AD-775 364

NONDESTRUCTIVE, THERMAL, AND MECHANICAL PROPERTIES EVALUATIONS OF COMPOSITE HEATSHIELD MATERIALS

James R. Brown, Jr., et al

Southern Research Institute

Prepared for:

Air Force Weapons Laboratory

January 1974

DISTRIBUTED BY:

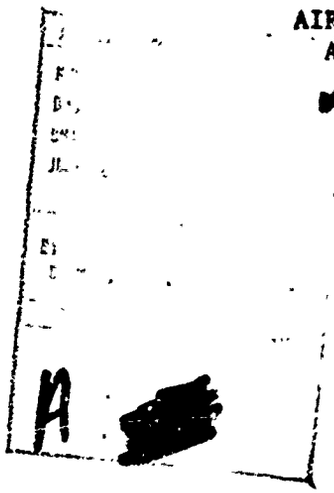
NTIS

National Technical Information Service
U. S. DEPARTMENT OF COMMERCE
5285 Port Royal Road, Springfield Va. 22151

Best
Available
Copy

AFWL-TR-73-189

AIR FORCE WEAPONS LABORATORY
Air Force Systems Command
Kirtland Air Force Base
New Mexico 87117



When US Government drawings, specifications, or other data are used for any purpose other than a definitely related Government procurement operation, the Government thereby incurs no responsibility nor any obligation whatsoever, and the fact that the Government may have formulated, furnished, or in any way supplied the said drawings, specifications, or other data, is not to be regarded by implication or otherwise, as in any manner licensing the holder or any other person or corporation, or conveying any rights or permission to manufacture, use, or sell any patented invention that may in any way be related thereto.

DO NOT RETURN THIS COPY. RETAIN OR DESTROY.

ib.

UNCLASSIFIED
Security Classification

DOCUMENT CONTROL DATA - R & D AD-775364
(Security classification of title, body of abstract and indexing annotation must be entered when the overall report is classified)

1. ORIGINATING ACTIVITY (Corporate author)
Southern Research Institute
2000 Ninth Avenue South
Birmingham, AL 35205

2a. REPORT SECURITY CLASSIFICATION
UNCLASSIFIED

2b. GROUP

3. REPORT TITLE
NONDESTRUCTIVE, THERMAL, AND MECHANICAL PROPERTIES EVALUATIONS OF COMPOSITE HEATSHIELD MATERIALS

4. DESCRIPTIVE NOTES (Type of report and inclusive dates)
October 1971 through December 1972

5. AUTHOR(S) (First name, middle initial, last name)
James R. Brown, Jr., H. G. Sanders, W. T. Engelke, and C. D. Pears

6. REPORT DATE
January 1974

7a. TOTAL NO. OF PAGES
614

7b. NO. OF REFS
4

8a. CONTRACT OR GRANT NO.
F29601-72-C-0042

b. PROJECT NO.
WDNA

c. Subtask AC 303

d.

9a. ORIGINATOR'S REPORT NUMBER(S)
AFWL-TR-73-189

9b. OTHER REPORT NO(S) (Any other numbers that may be assigned this report)

10. DISTRIBUTION STATEMENT
Approved for public release; distribution unlimited.

11. SUPPLEMENTARY NOTES

12. SPONSORING MILITARY ACTIVITY
AFWL (DYV)
Kirtland AFB, NM 87117

13. ABSTRACT
(Distribution Limitation Statement A)
This program involved material property characterization of both Advanced Heatshield Concept Assessment (AHCA) and Advanced Heatshield Program (AHP) materials. The first phase of this work involved nondestructive testing (NDT) characterization and evaluations of tensile, compressive, thermal expansion and thermal conductivity properties of arcs and plates of various AHP composite heatshield materials after simulated nuclear encounter by flyer plate impact. Physical and mechanical properties are presented as a function of the level of impact. A detailed discussion of the distribution of structure-change within the arcs is presented for all materials. The second phase of this work included quality control NDT of rings, arcs, and discs of various AHCA composite heatshield materials and a more extensive NDT characterization of selected rings and arcs from the quality control group. The results of the quality control inspections were also used to select certain rings for application to underground testing.

Details of illustrations in this document may be better studied on microfiche.

DD FORM 1 NOV 68 1473

UNCLASSIFIED
Security Classification

14 KEY WORDS	LINK A		LINK B		LINK C	
	ROLE	WT	ROLE	WT	ROLE	WT
Composite materials						
Nondestructive testing						
Mechanical properties evaluations						
Thermal properties evaluations						
Arcs						
Plates						
Rings						

AFWL-TR-73-189

NONDESTRUCTIVE, THERMAL, AND MECHANICAL PROPERTIES EVALUATIONS OF COMPOSITE HEATSHIELD MATERIALS

James R. Brown, Jr. et al.

Southern Research Institute

Final Report for Period October 1971 through December 1972

Approved for public release; distribution unlimited.

ic

FOREWORD

This report was prepared by the Southern Research Institute, Birmingham, Alabama, under Contract F29601-72-C-0042. The research was performed under Program Element 61102H, Project EDNA, Subtask AC 303.

Inclusive dates of research were October 1971 through December 1972. The report was submitted 1 November 1973 by the Air Force Weapons Laboratory Project Officer, Captain John A. Gordon (DYV).

In addition to the author listed on the cover, H. G. Sanders, W. T. Engelke, and C. D. Pears are also authors.

This technical report has been reviewed and is approved.

JOHN A. GORDON
Captain, USAF
Project Officer

DARRELL R. JAMES
Major, USAF
Chief, Radiation Response Branch

EDGAR A. O'HAIR, JR.
Colonel, USAF
Chief, Technology Division

ABSTRACT

(Distribution Limitation Statement A)

This program involved material property characterization of both Advanced Heatshield Concept Assessment (AHCA) and Advanced Heatshield Program (AHP) materials. The first phase of this work involved nondestructive testing (NDT) characterization and evaluations of tensile, compressive, thermal expansion and thermal conductivity properties of arcs and plates of various AHP composite heatshield materials after simulated nuclear encounter by flyer plate impact. Physical and mechanical properties are presented as a function of the level of impact. A detailed discussion of the distribution of structure-change within the arcs is presented for all materials.

The second phase of this work included quality control NDT of rings, arcs, and discs of various AHCA composite heatshield materials and a more extensive NDT characterization of selected rings and arcs from the quality control group. The results of the quality control inspections were also used to select certain rings for application to underground testing.

CONTENTS

Section		Page
I	INTRODUCTION	1
II	MATERIAL AND SPECIMEN PREPARATIONS	3
	Impacted Carbon-Carbon Composite Arcs	3
	Impacted Phenolic Composite Arcs	6
III	APPARATUSES AND PROCEDURES	10
	Nondestructive Testing and Monitor Evaluations	10
	Carbon-Carbon Composites	17
	Phenolic Composites	23
	Pre-Impact NDT Evaluations	24
	Nondestructive Ring Modulus Evaluations	25
IV	PROPERTIES OF IMPACTED ARCS AND SPECIMENS	27
	3D Carbon-Carbon Impacted Arcs	27
	Felt CC Impacted Plates	31
	R6300 Impacted Plates	34
	3D Quartz-Phenolic Impacted Arcs	35
	3D Carbon-Phenolic Portion of 3DC/QP Impacted Arcs #15A	36
	3D Quartz-Phenolic Portion of 3DC/QP Impacted Arcs #15B	38
V	DISTRIBUTION OF STRUCTURE-CHANGE IN ARCS	40
	3D Carbon-Carbon	40
	Felt CC	42
	AVCO R6300	44

CONTENTS (cont'd)

Section		Page
	AVCO 3D/QP	47
	Outer - 3DC/QP (Material #15A)	49
	Inner - 3DC/QP (Material #15B)	52
VI	RESULTS OF PRE-IMPACT NDT EVALUATIONS	53
	AVCO 3DC/QP	53
	AVCO 3DCP	53
	AVCO 3DCP (T400)	54
	AVCO R6300	55
	AVCO 3DCC	56
	Sandia Felt CC	58
	MOE Evaluations on Full Treatment NDT Rings	59
	APPENDIXES	
	A Ultimate Strength, Elastic Modulus, and Poisson's Ratio to 5500°F in Tension	313
	B Ultimate Strength, Elastic Modulus, and Poisson's Ratio to 5500°F in Compression	325
	C Thermal Expansion to 1800°F	335
	D Thermal Expansion to 5500°F	341
	E Thermal Conductivity to 1000°F	346
	F Thermal Conductivity to 5500°F by Radial Inflow Method	355
	G Tensile and Compressive Stress-Strain Curves for AVCO 3DCC - Material 8	367
	H Tensile and Compressive Stress-Strain Curves for Sandia Felt CC - Material 12	405

CONTENTS (cont'd)

I	Tensile and Compressive Stress-Strain Curves for AVCO R6300 - Material 10	433
J	Tensile and Compressive Stress-Strain Curves for AVCO 3DQP - Material 11	460
K	Tensile and Compressive Stress-Strain Curves for the Carbon-Phenolic Portion (15A) of AVCO 3DC/QP - Material 15	508
L	Tensile and Compressive Stress-Strain Curves for the Quartz-Phenolic Portion (15B) of AVCO 3DC/QP - Material 15	536
M	Anomalous Structure-Change Problem	566
DISTRIBUTION		585

ILLUSTRATIONS

Figure		Page
1	Construction of AVCO 3DCC	61
2	AVCO R6300 - Single Phase 2D, 20-Degree Angle Tape Wrap CP with AL (6061-T6) Backing Plate	62
3	AVCO Single Phase 3D Orthogonal Quartz-Phenolic - Material #11	63
4	AVCO Two Phase 3D Orthogonal Quartz-Phenolic - Material #15	64
5	Cutting Plan for Removing Circumferential Tensile Blanks from 3D Carbon-Carbon Impacted Arcs 8-AR-8, 8-AR-2, and 8-AR-5	65
6	Cutting Plan for Removing Circumferential Compressive Blanks from 3D Carbon-Carbon Impacted Arcs 8-AR-4, 8-AR-7, and 8-AR-1	66
7	Cutting Plan for Removing Axial Tensile Blanks from Felt Carbon-Carbon Impacted Plates 12-F-V, 12-F-16, and 12-F-13	67
8	Cutting Plan for Removing Axial Compressive Blanks from Felt Carbon-Carbon Impacted Plates 12-F-1, 12-F-15, 12-F-10, and 12-F-11	68
9	Cutting Plan for Removing Blanks from Phenolic Composite Impacted Arcs	69
10	Configuration of Specimen Strip for 3DCC Used in Radial Inflow Apparatus	70
11	Configuration of Specimen Strip for Felt CC Used in Radial Inflow Apparatus	71
12	Configuration of Axial Tensile Specimen Used for Evaluations of Specimens from 3D Carbon-Carbon Impacted Arcs	72
13	Modification to Tensile Specimen for Ultimate Strength Evaluations on Specimens from 3D Carbon-Carbon Impacted Arcs	73

ILLUSTRATIONS (cont'd)

Figure		Page
14	Configuration of Axial Tensile Specimen Used for Evaluations on Specimens from Felt Carbon-Carbon Impacted Plates	74
15	Configuration of Circumferential Compressive Specimen Used for Evaluations on Specimens from 3D Carbon-Carbon Impacted Arcs	75
16	Configuration of Axial Compressive Specimens Used for Evaluations on Specimens from Felt Carbon-Carbon Impacted Plates 12-F-15 and 12-F-10	76
17	Configuration of Axial Compressive Specimens Used for Evaluations on Specimens from Felt Carbon-Carbon Impacted Plates 12-F-11 and 12-F-1	77
18	Preparation of Thermal Expansion Specimens of 3DCC in Axial Direction from Used Compressive Specimens	78
19	Preparation of Thermal Expansion Specimen of 3DCC in Circumferential Direction from Used Compressive Specimen	79
20	Preparation of Thermal Expansion Specimen of Felt CC in the Circumferential Direction from Used Compressive Specimens	80
21	Preparation of Thermal Expansion Specimens of Felt CC in the Circumferential Direction from Used Compressive Specimen	81
22	Configuration of Thermal Conductivity Specimen Used in the Comparative Rod Apparatus for 3DCC	82
23	Configuration of Thermal Conductivity Specimen Used in the Comparative Rod Apparatus for Felt CC	83
24	Configuration of Axial Tensile Specimens Used for Evaluations on Specimens from R6300 Impacted Arcs	84
25	Configuration of Circumferential Tensile Specimens Used for Evaluations on Specimens from R6300 Impacted Arcs	85

ILLUSTRATIONS (cont'd)

Figure		Page
26	Configuration of Axial Compressive Specimens Used for Evaluations on Specimens from R6300 Impacted Arcs	86
27	Configuration of Circumferential Compressive Specimens Used for Evaluations on Specimens from R6300 Impacted Arcs	87
28	Configuration of Axial Tensile Specimens Used for Evaluations on Specimens from 3D Quartz-Phenolic Impacted Arcs	88
29	Configuration of Circumferential Tensile Specimens Used for Evaluations on Specimens from 3D Quartz-Phenolic Impacted Arcs	89
30	Configuration of Axial Compressive Specimens Used for Evaluations of Specimens from 3D Quartz-Phenolic Impacted Arcs	90
31	Configuration of Compressive Specimens Used for Evaluations on Specimens from 3D Quartz-Phenolic Impacted Arcs	91
32	Configuration of Axial Tensile Specimens for Evaluations on Specimens from 3D Carbon-Phenolic Portion of 3DC/QP Impacted Arcs	92
33	Configuration of Circumferential Tensile Specimens Used for Evaluations on Specimens from Carbon-Phenolic Portion of 3DC/QP Impacted Arcs	93
34	Configuration of Axial Compressive Specimen Used for Evaluation on Specimens from the 3D Carbon-Phenolic Portion of 3DC/QP Impacted Arcs	94
35	Configuration of Circumferential Compressive Specimen Used for Evaluations on Specimens from the 3D Carbon-Phenolic Portion of 3DC/QP Impacted Arcs	95
36	Configuration of Axial Tensile Specimens for Evaluations on Specimens from Quartz-Phenolic Portion of 3DC/QP Impacted Arcs	96

ILLUSTRATIONS (cont'd)

Figure		Page
37	Configuration of Circumferential Tensile Specimens Used for Evaluations on Specimens from Quartz-Phenolic Portion of 3DC/QP Impacted Arcs	97
38	Configuration of Axial Compressive Specimen Used for Evaluations on Specimens from the 3D Quartz-Phenolic Portion of 3DC/QP Impacted Arcs	98
39	Configuration of Circumferential Compressive Specimen Used for Evaluations on Specimens from the 3D Quartz-Phenolic Portion of 3DC/QP Impacted Arcs	99
40	Definition of Structure-Change Terms	100
41	SRI Indexing and Orientations for Arcs and Coupons	101
42	SRI Indexing and Orientation System for Rings	102
43	Ultrasonic Through-Transmission Setup Using the Pulsed Through-Transmission Technique	103
44	Setup for Determining Suspended Weight Saturated Specimen for Liquid Absorption Evaluation	104
45	Four-Point Bending Apparatus for Flexural Modulus of Elasticity (MOE) Evaluations	105
46	Specimen and Grip Configuration Used for Tensile Evaluations of Specimens from 3D Carbon-Carbon Impacted Arcs	106
47	Top View of Strip Specimen Assembly Employed in Radial Inflow Apparatus	107
48	Schematic of Chain Grip and Test Setup for Tensile Evaluations of Phenolic Composites	108
49	Assembly and Exploded View of Quartz-Phenolic Specimen and Specimen Tab Grips	109

ILLUSTRATIONS (cont'd)

Figure		Page
50	Specimen Configuration for Ultimate Tensile Strength Evaluation of Quartz-Phenolic Specimens	110
51	Schematic of Ring Flexure Setup Used for Modulus of Elasticity in Flexure (MOE) Evaluations	111
52	Schematic of Hydrostatic Ring Evaluation Setup Used for Compressive Modulus Evaluation	112
53	Group Photograph (1X) Showing Edges of Impacted 3D Carbon-Carbon Arcs	113
54a	Photographs Showing Visual Structure-Change in AVCO Arc 8-AR-8, 1.030 Kilotaps	114
54b	. . . . .	115
55a	Photographs Showing Visual Structure-Change in AVCO 3DCC Arc 8-AR-2, 2.200 Kilotaps	116
55b	. . . . .	117
56	Photographs Showing Visual Structure-Change in AVCO 3DCC Arc 8-AR-7	118
57a	Photographs Showing Visual Structure-Change in AVCO 3DCC Arc 8-AR-5, 3.360 Kilotaps	119
57b	. . . . .	120
58a	Photographs Showing Visual Structure-Change in AVCO 3DCC Arc 8-AR-1, 5.39 Kilotaps	121
58b	. . . . .	122
58c	. . . . .	123
59a	Photographs Showing Visual Structure-Change in AVCO 3DCC 8-AR-6, 7.56 Kilotaps	124
59b	. . . . .	125

ILLUSTRATIONS (cont'd)

Figure		Page
60	Photographs Showing Visual Structure-Change in AVCO 3DCC Arc 8-AR-3, 7.88 kilotaps	126
61	Group Radiograph in Axial Direction Showing Impacted Arc Rings from AVCO 3DCC	127
62a	Photomicrographs of Edges (Axial View) of Impulse Loaded Arcs from AVCO 3DCC	128
62b	. . . . .	129
62c	. . . . .	130
63	NDT Monitors and Flexural Modulus Versus Impact Level for AVCO 3DCC Material	131
64	Tensile, Compressive and Flexural Modulus of Elasticity for Specimens from 3D Carbon-Carbon Impacted Arcs	132
65	Tensile and Compressive Strength of Specimens from 3D Carbon-Carbon Impacted Arcs	133
66	Retained Modulus of Specimens from 3D Carbon-Carbon Impacted Arcs	134
67	Thermal Expansion of 3DCC in the Axial Direction After 3.045 KT Impact	135
68	Thermal Expansion of 3DCC in the Axial Direction After 5.39 KT Impact	136
69	Thermal Expansion of 3DCC in the Circumferential Direction After 2.2 KT Impact	137
70	Thermal Expansion of 3DCC in the Circumferential Direction After 3.36 KT Impact	138
71	Thermal Conductivity of 3DCC in the Radial Direction	139
72	Group Photograph of Most Severely Damaged Edges of Sandia Felt Carbon-Carbon Impacted Plates	140

ILLUSTRATIONS (cont'd)

Figure		Page
73a	Photographs Showing Visual Structure-Change in Sandia Felt CC Specimen 12-F-14	141
73b	. . . . .	142
73c	. . . . .	143
74	Photograph Showing Visual Structure-Change in Sandia Felt CC Specimen 12-F-10	144
75a	Photographs Showing Visual Structure-Change in Sandial Felt CC Specimen 12-F-11	145
75b	. . . . .	146
76	Group Radiograph in Axial Direction Showing Impacted Plates from Sandia Felt CC	147
77a	Photomicrographs of Sandia Felt CC	148
77b	. . . . .	149
77c	. . . . .	150
78	NDT Monitors and Flexural Modulus Versus Impact Level for Sandia Felt CC Material	151
79	Modulus of Elasticity for Specimens from Sandia Felt CC Impacted Plates	152
80	Axial Tensile Strength for Specimens from Sandia Felt CC Material Impacted Plates	153
81	Axial Compressive Strength for Specimens from Sandia Felt CC Impacted Plates	154
82	Retained Modulus for Specimens from Sandia Felt CC Material Impacted Plates	155
83	Thermal Expansion of Sandia Felt CC in the Axial Direction After 1.21 KT	156

ILLUSTRATIONS (cont'd)

Figure		Page
84	Thermal Expansion of Sandia Felt CC in the Axial Direction After 3.44 KT	157
85	Thermal Expansion of Sandia Felt CC in the Circumferential Direction After 1.21 KT	158
86	Thermal Expansion of Sandia Felt CC in the Circumferential Direction After 3.44 KT	159
87	Thermal Expansion of Sandia Felt CC in the Circumferential Direction After 6.14 KT	160
88	Thermal Conductivity of Sandia Felt CC in the Radial Direction	161
89	Group Photograph (1X) Showing Damaged Edges of Arc Rings from Material #10	162
90	Percentage Changes in Flexural MOE and NDT Monitors Versus Impulse in Taps for Aluminum-Backed Arc Specimens from Material #10 (AVCO TW 6300)	163
91	Results of Nondestructive Testing of Specimens from R6300 Impacted Arcs	164
92	Tensile and Compressive Strength of Specimens from R6300 Impacted Arcs	165
93	Tensile and Compressive Modulus of Specimens from R6300 Impacted Arcs	166
94	Group Photograph (1X) Showing Damaged Edges of Arc Rings from Material #11	167
95	Percentage Changes in Flexural MOE and NDT Monitors Versus Impulse in Taps for Arc Specimens from Material #11 (AVCO 3DQP)	168
96	Results of Nondestructive Testing on Specimens from 3D Quartz-Phenolic Impacted Arcs	169
97	Tensile and Compressive Strength of Specimens from 3D Quartz-Phenolic Impacted Arcs	170

ILLUSTRATIONS (cont'd)

Figure		Page
98	Tensile and Compressive Modulus of Specimens from 3D Quartz-Phenolic Impacted Arcs	171
99	Group Photograph (1X) Showing Damaged Edges of Arc Rings from Material #15	172
100	Percentage Changes in Flexural MOE and NDT Monitors Versus Impulse in Taps for Arc Specimens from Material #15 (AVCO 3DC/QP)	173
101	Results of Nondestructive Evaluations on Specimens from the 3D Carbon-Phenolic Portion, #15A, of 3DC/QP Impacted Arcs	174
102	Tensile and Compressive Strength of Specimens from the 3D Carbon-Phenolic Portion, #15A, of 3DC/QP Impacted Arcs	175
103	Tensile and Compressive Modulus of Specimens from the 3D Carbon-Phenolic Portion, #15A, of 3DC/QP Impacted Arcs	176
104	Results of Nondestructive Evaluations on Specimens from the 3D Quartz-Phenolic Portion #15B, of 3DC/QP Impacted Arcs	177
105	Tensile and Compressive Strength of the 3D Quartz-Phenolic Portion, #15B, of 3DC/QP Damaged Material	178
106	Tensile and Compressive Modulus of Specimens from the 3D Quartz-Phenolic Portion, #15B, of 3DC/QP Impacted Arcs	179
107	Sketch of Radiographic Results Showing Structure-Change Variations in AVCO 3DCC Arc 8-AR-7	180
108	Sketch of Radiographic Results Showing Structure-Change Variations in AVCO 3DCC Arc 8-AR-5	181
109	Sketch of Radiographic Results Showing Structure-Change Variations in AVCO 3DCC Arc 8-AR-1	182

ILLUSTRATIONS (cont'd)

Figure		Page
110	Sketch Showing Visual Inspection Results on Specimen Blanks from Felt CC Plate 12-F-10	183
111	Sketch Showing Visual Inspection Results on Specimen Blanks from Felt CC Plate 12-F-11	184
112	Radiograph in Circumferential Direction of Specimens from Felt CC Plate 12-F-11, 4.14 KT	185
113	Radiograph of Axial Compressive Specimens from R6300 Impacted Arcs	186
114	Radiograph of Circumferential Compressive Specimens from R6300 Impacted Arcs	187
115	Sketch of Structure-Change in Arc 10-AR-5	188
116	Radiograph of Axial Tensile Specimens from 3DQP Impacted Arcs	189
117	Radiograph of Circumferential Tensiel Specimens from 3DQP Impacted Arcs	190
118	Radiograph of Axial Compressive Specimens from 3DQP Impacted Arcs	191
119	Radiograph of Circumferential Compressive Specimens from 3DQP Impacted Arcs	192
120	Group Radiograph of Bulk Arcs of Impacted AVCO 3DC/QP Material	193
121	Radiograph of Axial Tensile Specimens from the Carbon-Phenolic Portion, #15A, of 3DC/QP Impacted Arcs	194
122	Radiograph of Circumferential Tensile Specimens from the Carbon-Phenolic Portion, #15A, of 3DC/QP Impacted Arcs	195
123	Radiograph of Axial Compressive Specimens from the Carbon-Phenolic Portion, #15A, of 3DC/QP Impacted Arcs	196

ILLUSTRATIONS (cont'd)

Figure		Page
124	Radiograph of Circumferential Compressive Specimens from the Carbon-Phenolic Portion, #15A, of 3DC/QP Impacted Arcs	197
125	Photographs Showing Typical AHCA AVCO 3DC/QP	198
126	Photograph Showing Typical AHP AVCO 3DC/QP	199
127	Typical AVCO 3DC/QP Structure Revealed by Radiography	200
128	Photographs Showing Typical AVCO 3DCP	201
129	Typical AVCO 3DCP Structure Revealed by Radiography	202
130	Photograph Showing Resin Rich Areas in AVCO 3DCP	203
131	Photograph Showing Resin Starved Areas Around Radials in Outer Surface of AVCO 3DCP	204
132	Photograph Showing Anomaly in AVCO 3DCP Arc 7 of Ring #6	205
133	Photographs Showing Locally Damaged Areas in AVCO 3DCP Rings #2 and #8	206
134	Photograph Showing High Porosity in AVCO 3DCP Ring #10	207
135a	Typical AVCO 3DCP (T 400) Structure Revealed by Radiography	208
135b	. . . . .	209
136	Radiograph Showing Typical Concentration Low-Absorptive Alignments in AVCO 3DCP (T 400)	210
137	Radiograph Showing Gross Circumferential Low-Absorptive Alignments in AVCO 3DCP (T 400) Ring #4	211

ILLUSTRATIONS (cont'd)

Figure		Page
138	Photograph Showing Typical AHCA AVCO R6300	212
139	Photograph Showing Occasional Visual Waviness in Tape Layup on Inner and Outer Surfaces of AVCO R6300	213
140	Typical AVCO R6300 Structure Revealed by Radiography	214
141	Photomicrographs in Axial Direction of AVCO R6300 Rings #2 and #4	215
142	Photographs Showing Typical Residual Porosity Between Tape Wraps in AVCO R6300	216
143	Photograph Showing Tape Wrap Discontinuity on Inner Surface of AVCO R6300 Ring #11, Arc 9	217
144	Photograph Showing Single 0.10 in. Void on Inner Surface of AVCO R6300 Ring #12, Arc 14	218
145	Photographs Showing Chips on Inner Edge of AVCO R6300, Ring #7	219
146	Radiographs Showing Material Anomalies in AVCO R6300 Ring #11, Arc 8 and Ring #11, Arc 9	220
147	Sketch Showing FT Inspection Results on AVCO R6300, Ring #2	221
148	Sketch Showing FT Inspection Results on AVCO R6300, Ring #4	222
149	Photographs Showing Typical AVCO 3DCC Material	223
150	Typical AVCO 3DCC Structure Revealed by Radiography	224
151	Photomicrographs in Axial Direction of AVCO Rings 1109-35-1 and 1109-35-5	225
152	Photograph Showing Typical Debonds in AVCO 3DCC Rings 110-35-1 through 1109-35-11	226

ILLUSTRATIONS (cont'd)

Figure		Page
153	Photographs Showing Visual Anomalies in AVCO 3DCC Discs #1 and #11	227
154	Photograph Showing Depressed Area in AVCO 3DCC, Ring #2B	228
155	Photograph Showing Machining Error in Bottom Edge of AVCO 3DCC Ring #4B	229
156	Photograph Showing Missing Axials and Circumferential in AVCO 3DCC, Ring #4B	230
157	Photograph Showing Large Visual Debond in AVCO 3DCC Ring #1A	231
158	Sketch Showing FT Inspection Results on AVCO 3DCC Ring 1109-35-1	232
159	Sketch Showing QC Inspection Results on AVCO 3DCC Ring 1109-35-2	233
160	Sketch Showing QC Inspection Results on AVCO 3DCC Ring 1109-35-3	234
161	Sketch Showing QC Inspection Results on AVCO 3DCC Ring 1109-35-4	235
162	Sketch Showing FT Inspection Results on AVCO 3DCC Ring 1109-35-5	236
163	Sketch Showing QC Inspection Results on AVCO 3DCC Ring 1109-35-6	237
164	Sketch Showing QC Inspection Results on AVCO 3DCC Ring 1109-35-7	238
165	Sketch Showing QC Inspection Results on AVCO 3DCC Ring 1109-35-8	239
166	Sketch Showing QC Inspection Results on AVCO 3DCC Ring 1109-35-9	240

ILLUSTRATIONS (cont'd)

Figure		Page
167	Sketch Showing QC Inspection Results on AVCO 3DCC Ring 1109-35-10	241
168	Sketch Showing QC Inspection Results on AVCO 3DCC Ring 1109-35-11	242
169	Sketch Showing QC Inspection Results on AVCO 3DCC Ring #1A	243
170	Sketch Showing QC Inspection Results on AVCO 3DCC Ring #2A	244
171	Sketch Showing QC Inspection Results on AVCO 3DCC Ring #1B	245
172	Sketch Showing QC Inspection Results on AVCO 3DCC Ring #2B	246
173	Sketch Showing QC Inspection Results on AVCO 3DCC Ring #3B	247
174	Sketch Showing QC Inspection Results on AVCO 3DCC Ring #4B	248
175	Photographs Showing Typical Sandia Felt CC	249
176	Typical Sandia Felt CC Structure Revealed by Radiography	250
177	Photomicrographs in Axial Direction of Sandia Felt CC Rings 2N-2 and 3N-2	251
178	Radiograph Showing Anomaly in Sandia Felt CC Ring #4P-2	252
179	Sketch Showing FT Inspection Results on Sandia Felt CC Ring #2N-2	253
180	Sketch Showing FT Inspection Results on Sandia Felt CC Ring #3N-2	254

ILLUSTRATIONS (cont'd)

Figure		Page
A-1	Picture of a Tensile Stress-Strain Facility	317
A-2	Schematic Arrangement of Gas-Bearing Universals, Specimen and Load Train	318
A-3	Tensile Specimen Configuration	319
A-4	Location of the Flag Attachments on the Tensile Specimens	320
A-5	Precision Collet Grip for Tensile Specimen 2:1 Scale	321
A-6	Small 5500°F Graphite Resistance Furnace	322
A-7	Arrangement of Optical Strain Analyzer	323
A-8	General Configuration of the Flag Attachment to Monitor Lateral Strain in Tension	324
B-1	Picture of the Compressive Facility with Gas Bearings and Optical Strain Analyzer	328
B-2	Schematic Arrangement of Gas-Bearing Universals, Specimen and Load Train	329
B-3	Compressive Specimen Configuration	330
B-4	Location of the Flag Attachments on the Compressive Specimen	331
B-5	Lateral Strain Flat Attachment for Compressive Specimen	332
B-6	Small 5500°F Graphite Resistance Furnace	333
B-7	Arrangement of Optical Strain Analyzer	334
C-1	Assembly of Quartz Tube Dilatometer for Thermal Expansion Measurements	336
C-2	Thermal Expansion of Fused Silica	337
C-3	Thermal Expansion of NBS Copper Standard SRM 736	338
C-4	Expansion of "A" Nickel	339
C-5	Thermal Expansion of ATJ Graphite (WG) Standard No. 5 In-House Optical Calibration	340

ILLUSTRATIONS (cont'd)

Figure		Page
D-1	Picture of the Graphite Dilatometer Tubes for Measuring Thermal Expansion to 5500°F	343
D-2	The Thermal Expansion of ATJ Graphite (WG) Standard No. 5 by In-House Optical Calibration	344
E-1	Schematic of Buildup Used for ASTM C177 Guarded Hot Plate Thermal Conductivity Apparatus	353
F-1	Picture of the Radial Thermal Conductivity Apparatus	359
F-2	Furnace with Thermal Conductivity Apparatus Installed	360
F-3	Cross-section Schematic of the Thermal Conductivity Apparatus	361
F-4	1.06-inch Diameter Thermal Conductivity Specimen for Radial Inflow Apparatus	362
F-5	Dimensions of 1.50-inch Diameter Specimen and Guards Used for Radial Inflow Thermal Conductivity Measurements	363
F-6	Thermal Conductivity of Tungsten Sheet Parallel to the Plane of the Sheet	364
F-7	Thermal Conductivity of ATJ Graphite, With Grain	365
F-8	Thermal Conductivity of AXM-5QI Graphite	366
M-1	AVCO Two Phase 3-D Orthogonal Quartz-Phenolic - Material #15	570
M-2	Photograph Showing Damage to AHCA Material #15 with Increased Impulse Levels	571
M-3	Photographs Showing Rear Delam in AHCA Material #15 Ring #4 Arc 3	572
M-4	Radiograph Showing AHP Mode for Material #15	
M-5	Photomicrographs Showing AHP and AHCA Material #15	574
M-6	Photomicrograph Showing Virgin AHCA Material #15 Between Radials	576

ILLUSTRATIONS (cont'd)

Figure		Page
M-7	Photomicrographs Showing Virgin AHP, and AHCA Cured Material #15	577
M-8	Photographs of Tab End #1 of Material #15	578
M-9	Photographs of Tab End #4A of Material #15	579
M-10	Photographs of Tab End of #5A of Material #15	580
M-11	Photomicrographs Showing Material #15 in Tab #1, #4A, and #5A	581

TABLES

Table		Page
1	Phase I Test Matrix for Carbon/Carbon Materials .	255
2	Phase I Test Matrix for Phenolic Composite Materials	256
3	Phase II Test Matrix for Underground Rings and Arcs	257
4	Results of NDT Monitor Evaluations of 3DCC, Material #8, Impacted Arcs	258
5	NDT Inspections for Structure-Change in AVCO 3DCC Impacted Arcs	259
6	Results of Tensile and Compressive Evaluations on 3D Carbon-Carbon Impacted Arcs	260
7	Thermal Expansion of 3DCC in the Axial Direction After 3.045 KT Measured in Graphite Dilatometer .	262
8	Thermal Expansion of 3DCC in the Circumferential Direction After 5.39 KT Measured in Graphite Dilatometer	263
9	Thermal Expansion of 3DCC in the Circumferential Direction After 2.2 KT Measured in Quartz Dilatometer	264
10	Thermal Expansion of 3DCC in the Circumferential Direction After 2.2 KT Measured in Quartz Dilatometer	265
11	Thermal Expansion of 3DCC in the Circumferential Direction After 3.36 KT Measured in Quartz Dilatometer	266
12	Thermal Expansion of 3DCC in the Circumferential Direction After 3.36 KT Measured in Graphite Dilatometer	267
13	Thermal Conductivity of 3DCC in the Radial Direction Exposed to 1.03 and 2.20 KT Using Comparative Rod Apparatus with Armco Iron References	268

TABLES (cont'd)

Table		Page
14	Thermal Conductivity of 3DCC in the Radial Direction Exposed to 1.03 KT Using Radial Inflow Apparatus (Strip Technique)	271
15	Results of NDT Monitor Evaluations of Felt CC, Material #12, Impacted Arcs	273
16	NDT Inspections for Structure-Change in Sandia Felt CC Impacted Arcs	274
17	Results of Tensile and Compressive Evaluations on Felt Carbon-Carbon Impacted Plates	275
18	Thermal Expansion of Felt CC in the Axial Direction After 1.21 KT Measured in Quartz Dilatometer . .	277
19	Thermal Expansion of Felt CC in the Axial Direction After 1.21 KT Measured in Graphite Dilatometer .	278
20	Thermal Expansion of Felt CC in the Axial Direction After 3.44 KT Measured in Quartz Dilatometer . .	279
21	Thermal Expansion of Felt CC in the Axial Direction After 3.44 KT Measured in Graphite Dilatometer .	280
22	Thermal Expansion of Felt CC in the Circumferential Direction After 1.21 KT Measured in Quartz Dilatometer	281
23	Thermal Expansion of Felt CC in the Circumferential Direction After 1.21 KT Measured in Graphite Dilatometer	282
24	Thermal Expansion of Felt CC in the Circumferential Direction After 3.44 KT Measured in Quartz Dilatometer	283
25	Thermal Expansion of Felt CC in the Circumferential Direction After 3.44 KT Measured in Graphite Dilatometer	284

TABLES (cont'd)

Table		Page
26	Thermal Expansion of Felt CC in the Circumferential Direction After 4.14 KT Measured in Quartz Dilatometer	285
27	Thermal Expansion of Felt CC in the Circumferential Direction After 4.14 KT Measured in Graphite Dilatometer	286
28	Thermal Conductivity of Felt CC in the Radial Direction Exposed to 1.21 and 3.44 KT Using Comparative Rod Apparatus with Armco Iron References	287
29	Thermal Conductivity of Felt CC in the Radial Direction Exposed to 0 KT Using Radial Inflow Apparatus (Strip Technique)	289
30	NDT/Monitor Inspection and MOE Results for Impacted Arc Rings from Material #10	291
31	Results of Tensile and Compressive Evaluations on R6300 Impacted Arcs	292
32	NDT/Monitor Inspection and MOE Results for Impacted Arc Rings from Material #11	294
33	Results of Tensile and Compressive Evaluations on 3D Quartz-Phenolic Impacted Arcs	295
34	NDT/Monitor Inspection and MOE Results for Impacted Arc Rings from Material #15	297
35	Results of Tensile and Compressive Evaluations on 3D Carbon-Phenolic Portion, #15A, of 3DC/QP Impacted Arcs	298
36	Results of Tensile and Compressive Evaluations on the Quartz-Phenolic Portion, #15B, of 3DC/QP Impacted Arcs	300
37	NDT Inspection Results for AVCO 3DC/QP	301

TABLES (cont'd)

Table		Page
38	NDT Inspection Results for AVCO 3DCP	302
39	NDT Inspection Results for AVCO 3DCP (T400)	303
40	NDT Inspection Results for AVCO R6300	305
41	NDT Inspection Results for AVCO 3DCC	308
42	NDT Inspection Results for Sandia Felt CC	310
43	Bulk MOE on AHCA Full Treatment Rings	311
D-1	Uncertainty in Thermal Expansion Measurements Made in Graphite Dilatometers	345
E-1	Calibrations of ASTM C177 Apparatuses and Procedures with Plexiglas and Pyrex 7740 Standards at About 150°F to 200°F	354
M-1	Comparison of AHCA #15 and #15 Outer ARCS	582
M-2	NDT Results on AHCA Material #15 and #15A Arcs in AHP and AHCA Geometry	583
M-3	NDT and Mechanical Results on AVCO Material 15 Tab Ends	584

SECTION I

INTRODUCTION

This program, entitled Advanced Heatshield Concept Assessment (AHCA), was involved with nondestructive, thermal and mechanical properties evaluations on various composite heatshield materials. The materials evaluated were 3D carbon-carbon (3DCC), Felt carbon-carbon (Felt CC), tape wrapped carbon-phenolic (R6300), 3D carbon-phenolic over 3D quartz-phenolic (3DC/QP), and 3D carbon-phenolic (3DCP).

This program was madeup of two separate but related phases. The first was an evaluation of carbon-carbon and phenolic composite arcs and plates which had been exposed to flyer plate impact loading. The evaluations on the carbon-carbon composites for this program included nondestructive testing of the arcs, bulk flexural modulus of the arcs, additional nondestructive testing, thermal expansion, thermal conductivity, tensile and compressive evaluations at room and elevated temperatures on specimens removed from the arcs. The Test Matrix, Table 1, outlines the numbers and types of specific evaluations. The purpose of the nondestructive testing (X-ray, visual and penetrant inspections) was to provide qualitative comparisons of the structure changes of the various specimens. The flexural modulus evaluations provided a measure of the change of a specific property. The remaining nondestructive evaluations (bulk density, ultrasonic velocity, ultrasonic transmission, open porosity and thickness measurements) were to provide monitors of structure/property changes. The thermal expansion, thermal conductivity, tensile and compressive properties were to provide first approximation properties necessary for analysis of structural/thermal response of heatshield structures and of flyer plate tests on rings.

The phenolic composite arcs of this program had been exposed to flyer plate impact loading and had previously had nondestructive and flexural modulus evaluations. The evaluations of this program on these arcs included nondestructive, tensile and compressive evaluations at room temperature on specimens removed from the arcs. The Test Matrix, Table 2, outlines the numbers and types of specific evaluations. The purposes for these evaluations were the same as for the carbon-carbon composites.

The second phase of this program consisted of non-destructive evaluations of arcs and rings which were to be exposed to flyer plate, or underground testing. This phase included carbon-carbon and phenolic composite materials. The Test Matrix, Table 3, outlines the numbers of evaluations as proposed and as completed. Quality control evaluation consisting of bulk density, visual inspection with photographic documentation and radiography was completed on 67 rings, 10 arcs and 11 discs. Using the quality control results as a guide and with agreement from the Air Force Project Officer 8 rings were selected for application in the underground test program and 5 arcs and 6 rings were selected for more extensive nondestructive evaluations for the AHCA Program. These evaluations included radial and axial ultrasonic velocity profiles, radial transmission profiles, open porosity, penetrant inspection, and 40X photomicrography. The 6 rings were then evaluated for elastic modulus by ring flexure and hydrostatic compression tests.

During the course of the program some redirection of effort was dictated by problems at other locations. Unexpected response of 3DC/QP materials to flyer plate testing brought on an extensive investigation of this material.

The results of the work on properties of impacted carbon-carbon arcs and plates and phenolic composite arcs are presented in Section IV. A discussion of distribution of structure-change in the impacted arcs is given in Section V. The results of pre-impact nondestructive evaluations of various arcs and rings are presented in Section VI. The work on the 3DC/QP response problem is discussed in Appendix M.

SECTION II

MATERIAL AND SPECIMEN PREPARATIONS

IMPACTED CARBON-CARBON COMPOSITE ARCS

Materials for this phase of the program included arcs of AVCO 3D Carbon-Carbon, Material #8, and plates of Sandia Felt Carbon-Carbon, Material #12. All but one of the 3DCC arcs had nominal dimensions of 0.450 in. thick by 1.50 in. width by 3.0 in. chordal length on an outside radius of 4.50 in. All but one of the Felt CC plates were nominally 2.0 in. square by 0.450 in. thick. The odd 3DCC Arc 8-AR-V, was nominally 0.450 in. thick by 1.50 in. width by 2.0 in. in chordal length. Felt CC Plate 12-F-1 was nominally 1.50 in. square by 0.45 in. thick. All of these arcs and plates except those labeled "V" (virgin) had previously been subjected to flyer plate impact loading.

The 3DCC was an orthogonal three-dimensional carbon-carbon composite. The composite was densified by phenolic impregnation, pyrolized and graphitized. The construction of this material is shown in Figure 1. A group photograph of the arcs evaluated is shown as Figure 53.

The Felt CC was a multidirectional carbon-carbon composite. A rayon felt carcass was assembled by needling, a process which pulled some of the fibers through the thickness direction of the various felt layers. The carcass was infiltrated with pyrolytic graphite, and finally graphitized. A group photograph of the plates is shown as Figure 72.

The arcs and plates supplied for this program were:

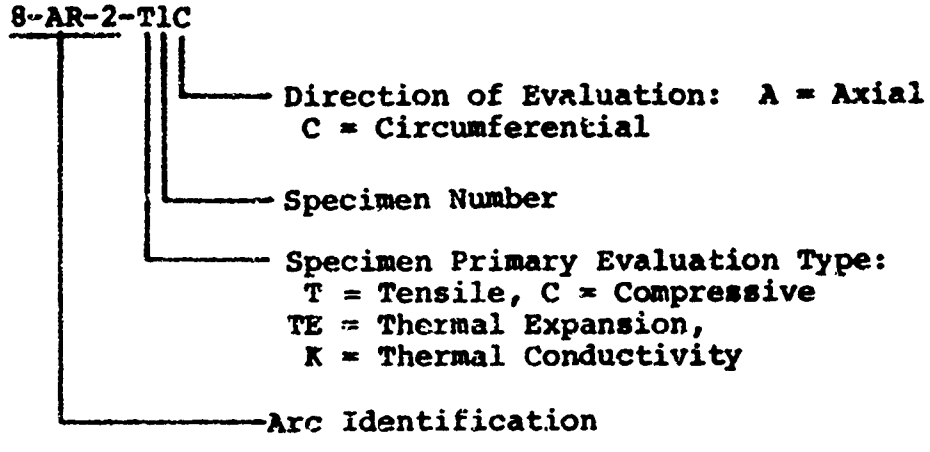
1. 3DCC (Material #8)	Impact Level (Kilotaps)
8-AR-V	0
8-AR-8	1.030
8-AR-4	1.640
8-AR-2	2.200
8-AR-7	3.045
8-AR-5	3.360
8-AR-1	5.390
8-AR-6	7.560
8-AR-3	7.880

2. Felt CC (Material #12)

	Impact Level (Kilotaps)
12-F-V	0
12-F-15	1.210
12-F-16	1.700
12-F-14	2.490
12-F- 1	2.430
12-F-13	3.070
12-F-10	3.440
12-F-11	4.140

Arcs 8-AR-6 and 8-AR-3 were too severly damaged during impact loading for evaluation in this program. Plate 12-F-14 was apparently an anomalous specimen which developed a midplane delamination and surface cracks at a relatively low impact level. An attempt was made to evaluate this specimen using NDT and bulk flexure. The results were considered questionable and no further evaluations were attempted.

After the NDT consisting of radiograph, visual inspection, 40X photomicrography, bulk density, ultrasonic velocity, ultrasonic transmission, open porosity, penetrant inspection, thickness measurement and bulk flexure evaluations, the 3DCC arcs and Felt CC plates were cut into blanks as shown in Figures 5 through 8. The 3DCC blanks were all oriented in the circumferential direction. The Felt CC blanks were supposed to be oriented in the circumferential direction also. A mixup in identification of the plate directions resulted in all Felt CC blanks being oriented in the axial direction. The specimens were identified as follows:



The size of the test matrix and the limited material available required that some specimens be used for several evaluations. The 3DCC arcs numbered 8-AR-8, 8-AR-2, and 8-AR-5, were designated for tensile evaluations. Felt CC specimens from plates 12-F-V, 12-F-16, and 12-F-13 were used for tensile evaluations. The remaining arcs were utilized for compressive evaluations. All blanks received NDT evaluations consisting of bulk density, radial and axial velocity, and radial ultrasonic transmission. Specimen blanks 8-AR-8-T1C through-T4C and 12-F-V-T1A through-T4A were used for thermal conductivity evaluations in the radial inflow apparatus prior to tensile evaluations. These specimen blanks were adapted for these evaluations by machining to the configurations shown in Figures 10 and 11. Specimen blanks 8-AR-5-T1C through-T4C, 8-AR-2-T1C through-T4C, 12-F-15-C1A through-C4A and 12-F-10-C1A through-C4A were used for thermal expansion evaluations prior to compressive evaluations. Two of these blanks from a given arc were stacked to give the 3.0 in. gage length for the expansion evaluations. This provided expansion specimens in the axial direction for Material #12 and in the circumferential direction for Material #8. After the thermal evaluations the tensile blanks were machined to the configurations shown in Figures 12 and 14 and the compressive blanks as shown in Figures 15, 16 and 17. The specimens were given NDT evaluations consisting of open porosity, visual inspection, and radiography. After the 3DCC tensile specimens were run for modulus they were remachined as shown in Figure 13 to improve the probability of tensile failures.

Used compressive specimen ends were employed for the expansion specimens in the circumferential direction for Felt CC and additional evaluations in both directions on the 3DCC material. The extraction of these specimens are illustrated in Figures 18 through 21.

As mentioned above, certain tensile specimen blanks were used for thermal evaluations prior to finish machining to tensile specimens. In addition, comparative rod thermal conductivity specimens were built up of pieces taken from scrap material from arcs 8-AR-8 and 8-AR-2 and plates 12-F-10 and 12-F-15. The configurations of these thermal conductivity specimens are shown in Figures 22 and 23.

IMPACTED PHENOLIC COMPOSITE ARCS

Materials for this phase of the program included arcs of R6300, 3D Quartz-Phenolic and 3D Carbon/Quartz-Phenolic. These arcs had previously been subjected to a flyer plate impact loading at Kaman Sciences and evaluated for structure change by nondestructive testing and flexural modulus determination at Southern Research Institute. These evaluations were reported in "Damage Study of Several Carbon-Phenolic Composite Materials" to Kaman Nuclear, Purchase Order 71P00657 dated July 6, 1971.

The arcs originally had nominal dimensions of 0.450 in. thick by 1.50 in. wide by 3.0 in. chordal length with an outside radius of 4.50 in. The width dimension in some cases was altered during the previous evaluations. The altered width aggravated the specimen geometry problems of the evaluations for this program.

The R6300 composite was a single phase 2D, 20 degree angle tape wrap phenolic-carbon with an aluminum (6061-T6) backing plate. A sketch of the construction of this material is shown in Figure 2. A group photograph of the arcs evaluated is shown in Figure 89.

The 3D Quartz-Phenolic (3DQP) was a single phase 3D orthogonal phenolic-quartz composite. A sketch of the construction of this material is shown in Figure 3. A group photograph of the arcs evaluated is shown in Figure 94.

The 3D Carbon/Quartz Phenolic (3DC/QP) was a two phase material made of 3D orthogonal phenolic-graphite over a 3D orthogonal phenolic-quartz. The radials were phenolic-carbon. A sketch showing the construction of this material is shown in Figure 4. A group photograph of the arcs evaluated is shown as Figure 99.

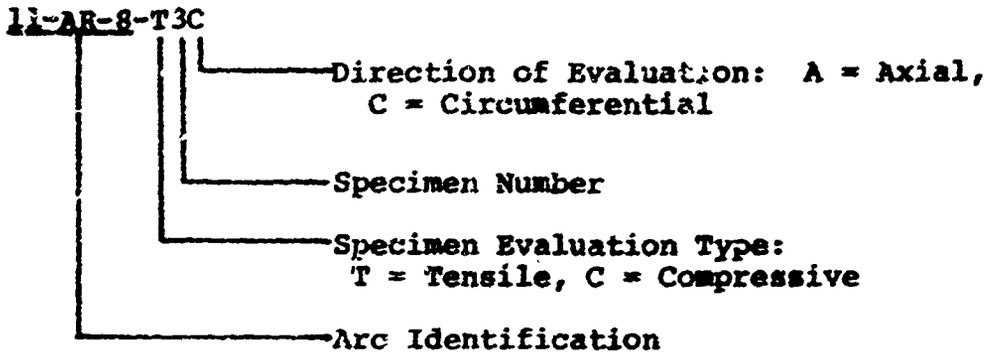
Included in the list of phenolic-composite arcs for this program were:

1. K6300 (Material #10)	Impact Level (Kilotaps)
10-AR-V	0
10-AR-4	0.490
10-AR-7	1.570
10-AR-6	1.660
10-AR-3	1.900
10-AR-1	1.990
10-AR-5	4.040
10-AR-2	

2. 3D Quartz-Phenolic, 3DQP (Material #11)	Impact Level (Kilotaps)
11-AR-V	0
11-AR-8	4.58
11-AR-5	7.54
11-AR-3	7.95
11-AR-7	8.61
11-AR-1	9.01
11-AR-2	9.01
11-AR-6	9.88

3. 3D Carbon/Quartz-Phenolic, 3DC/QP (Material #15)	Impact Level (Kilotaps)
15-AR-V	0
15-AR-3	4.09
15-AR-5	4.69
15-AR-6	5.18
15-AR-4	6.06
15-AR-7	6.52
15-AR-8	6.54

A common cutting plan was used for blanking all phenolic composite arcs, Figure 9. Two specimen blanks were oriented in the axial direction and two in the circumferential direction. Each 3DC/QP, Material #15, blank was further sliced into two smaller blanks which were predominantly 3DCP, designated #15A, and 3DQP, designated #15B. The specimen blanks were identified as follows:



Of the R6300 arcs from the earlier program, arc 10-AR-2 was considered too severely damaged and no attempt was made to machine specimens from it. The Virgin R6300 Arc, 10-AR-V, had no aluminum backing plate. The aluminum backing plate was removed from the remaining arcs by fly cutting in a milling machine. The specimens were blanked as previously described and blanks were designated for tensile evaluations from arcs 10-AR-4, 10-AR-6, and 10-AR-1. The remaining R6300 blanks were designated for compressive evaluations.

The 3DQP, Material #11, Arcs numbered 11-AR-8, 11-AR-3, 11-AR-7, and 11-AR-6 were designated for tensile evaluations. The remaining arcs were used for compressive evaluations. The arcs from the previous program were of varying widths and this distribution was chosen to utilize the longest axial direction specimen blanks for tensile evaluations.

The 3DC/QP, Material #15, Arcs numbered 15-AR-V, 15-AR-5, and 15-AR-4 were designated for tensile evaluations. The remaining arcs were used for compressive evaluations. In this distribution the two most severely damaged were chosen for compressive evaluations and the remaining distribution was selected generally to utilize the longest axial blanks for tensile evaluations and to distribute the tensile and compressive evaluations.

After NDT evaluations of the specimen blanks, they were machined to finished specimen configurations. Each specimen type, loading direction and material type was machined to its optimum configuration for the material available. Generally each specimen was the maximum possible thickness and length. The gage width of tensile specimens from the orthogonal composites, 3D Quartz-Phenolic, Material #15A and Material #15B was chosen to give two unit cells centered on the width. Compressive specimens from these materials used four unit cells centered on the gage widths. The gage width of the R5300 specimens was chosen to give a convenient and representative cross-section. Figures 24 through 39 show the configurations of the finished specimens.

SECTION III

APPARATUSES AND PROCEDURES

NONDESTRUCTIVE TESTING AND MONITOR EVALUATIONS

VISUAL AND LIGHT MICROSCOPY - For virgin material, visual inspections (1X to 10X) were made on exposed surfaces of bulk and specimen shapes to determine material macro-level typicality and surface anomalies. This was effective for detecting surface variations such as yarn bundle fraction variations, separations, macrovoids, discolorations, resin-rich and resin-starved areas, yarn bundle wrinkling and spacing variations, ply spacing variations, and void clusters. Results were documented photographically. Definitions of terms used to describe the structure-charges are shown in Figure 40. For micro-level characterization, photomicrographs at 40X were used to establish material typicality such as microcracking in yarn bundles, microcracking between matrix and yarn bundles, pore sizes, and pore size distributions. Such information was used to detect material variability (within single batch) and reproducibility (batch to batch variability).

For impacted materials, visual inspection (1X to 10X) were performed on the edges and surfaces of the specimens to assess macro-level structure change. Results were documented photographically. Photomicrographs (40X) were made on one edge (normal to axial direction) of specimens to assess micro-level structure change. Results from these inspections were compared to those from virgin material for assessment of structure-change. The photographs from both the visual inspection and the photomicrographs for the various levels of impact were compared with one another and with those from virgin material for assessment of structure-change. The Southern Research indexing and orientation systems used to locate a specific feature are shown in Figures 41 and 42.

GRAVIMETRIC BULK DENSITY - Bulk density measurements for specimens having a regular configuration were calculated from direct measurements of weights and lengths. An analytical balance having a sensitivity of ±0.0001 gram was used for weighing. Micrometers read to the nearest 0.0005 in. were used for measuring lengths, and a traveling microscope accurate to ±0.001 in. was used for measuring chord lengths.

RADIOGRAPHY - Radiography was performed using state-of-the-art X-ray techniques for low-absorptive materials. The radiographic unit used was a Radifluor 360 manufactured by Torr X-Ray Corporation, a division of Phillips Electronics. This unit is rated for operation from 0 to 120 kv at either 3 or 5 ma, making it ideal for phenolic and carbon-carbon type materials. The unit incorporates certain basic characteristics that are essential for examination of low-absorptive materials with high resolution and sensitivity. The focal spot size is 0.35 mm, and the X-ray tube window is 0.015 in. thick beryllium. A small focal spot size provides high sensitivity and distortion-free imaging of small discontinuities. Radiographic sensitivity using extra-fine grain file is within one percent (per MIL STD 453).

Operational and film development procedures were consistent with conventional good radiographic practices. For example, image sensitivity and contrast was enhanced by using minimum power settings for longer time periods. Sharp imaging was ensured by using extra-fine grain film (such as Eastman Type M) and by using a long FFD (up to 46 in.). Hand film processing in accordance to the film manufacturer's suggested procedure was used to assure maximum quality. Image quality was checked using penetrameters from similar material. Penetrameter hole sizes used are 1/2T, 1T and 2T (1T and 2T holes as defined by MIL-STD-453). Radiographs are inspected in a dark room using a high intensity (variable) spot illuminator.

ULTRASONICS - Basic apparatus used in the ultrasonic measurements of velocity, pulse-echo and through-transmission are a Sperry UM721 Reflectoscope and a Tektronix 564 Oscilloscope. Velocity is evaluated using the through-transmission, elapsed-time technique. The Sperry Um721 is used as the pulser, and the Tektronix 564 complete with a 3B3 time base (precision of 1 percent) and a 3A3 vertical amplifier is used as the signal measuring device. Inspection for flaws is done using the Sperry UM721 and the pulse-echo, reflection technique. Transmission measurements are made using the pulsed through-transmission technique with an in-line attenuator to simulate the varying degrees of structure-change. The Sperry UM721 is used as the signal pulser, the Tektronix 564 as the signal measuring device, and a Kay Model 20-0, 41dB in-line attenuator for assessing relative structure-changes in the various specimens.

In using the through-transmission, elapsed-time technique for measuring acoustic velocity, a short pulse of longitudinal-mode sound is transmitted through the specimen. An electrical pulse originates in a pulse generator and is applied to a ceramic piezoelectric crystal (SFZ). The pulse generated by this crystal is transmitted through a short delay line and inserted into the specimen. The time of insertion of the leading edge of this sound beam is the reference point on the time base of the oscilloscope which is used as a high-speed stopwatch. When the leading edge of this pulse of energy reaches the other end of the specimen, it is displayed on the oscilloscope. The difference between the entrance and exit times is used with the specimen length in calculating ultrasonic velocity. A short lucite delay line is used to allow time isolation of the sound wave from electrostatic coupling and to facilitate clear presentation of the leading edge of the entrant wave resulting in a more accurate "zero" for time.

Using 0.5/1.0 MHz transducers coupled with alcohol, the precision for this velocity measurement technique has been established for polygraphites such as ATJ-S as $\pm$0.002 in. per microsecond for a four in. long by 1/2 in. diameter specimen and as $\pm$0.010 in. per microsecond for a 1/4 in. long by 1/4 in. diameter specimen.

In using the pulse-echo, reflection technique to detect macroflaws, test blocks from ATJ-S polygraphite are used as calibration references for estimating the location, depth and size of discontinuities. These blocks are normally about 5/8 in. square by 2, 3, and 4 in. long. At one end, a single flat-bottom hole is drilled along the specimen axis to a depth of 1 in. The hole sizes range from 1/32 to 1/4 in. in 1/32 in. increments. The maximum penetrating signal frequency is used for maximum resolution, and instrument settings are duplicated as much as possible for evaluations of similar materials. Alcohol is used as the couplant. Two techniques, using a Tektronix Oscilloscope C-12 camera, are used in recording pulse-echo signals from specimens. The first technique involves taking photographs of the signal as transmitted from one or both ends of the specimen to determine "standing signals." The second technique involves recording a multiple trace (smear) of the signal. This is done by revolving the specimen on the face of the transducer on about a 1/8 in. radius with the camera shutter open. This technique tends to randomize the background noise and to define the more repetitive "standing signals."

In using the through-transmission technique for detecting structure variations, Figure 43, sound is transmitted through the specimen and displayed by the oscilloscope. The gain of the oscilloscope is held constant and a calibrated step attenuator located in the input circuit is used to maintain the displayed waveform at a constant amplitude. Values of transmission (called added dB) relative to a reference material may be read from the step attenuator. Measurements are made in an alcohol bath to minimize effects of contact coupling and near field effects. A suitable fixture is used to align the transducers and to hold the specimen squarely in the sound beam. When specimen geometry is such that part of the energy in the sound beam could by-pass the specimen, foam padding is used as a block to absorb this energy. The sensitivity of the calibrated attenuator is ± 1 dB with a minimum-maximum attenuation from 0 to 41 dB.

POROSITY BY LIQUID ABSORPTION - The evaluation of porosity and density of porous type materials such as polygraphites and carbon-carbon or carbon-phenolic composites are evaluated using a liquid absorption technique. Using this technique, mineral spirits (s.g. ~.76) is vacuum impregnated into samples of material. From measurements of dry weight, suspended weight and saturated weight, evaluations of absorption, density (bulk and apparent), and open porosity can be calculated directly. If the true density of the material sample is known, the total porosity and thus, the closed porosity of the material sample can be calculated.

The normal procedure used in making liquid absorption measurements involves first a thorough drying and then precise weighing of specimens to determine dry, suspended and saturated weights (recorded to nearest 0.0001 gram). First, the specimens are oven dried at temperature above 212°F for two hours to drive out absorbed moisture and then weighed to determine dry weight. Individual specimens are then placed in small beakers which are placed on their sides in a desiccator. After the desiccator is sealed off, a vacuum of 50 microns of Hg is pulled and held for two hours to remove entrapped air from the specimens. The dessicator is then purged with mineral spirits until the beakers containing the specimens are submerged. The desiccator is then vented, and the specimens are left in the desiccator for 20 minutes to allow vapor inside the specimens to condense.

The suspended weight is obtained by weighing the saturated specimen while suspended in the mineral spirits. The specimens are kept submerged by righting the beakers in the desiccator to maintain the mineral spirits level above the specimen. As shown in Figure 44, a basket is suspended from a balanced beam such that the level of mineral spirits in the individual beakers cover the specimen and basket at all times during the weighing operation. The tare weight of the basket, which is subtracted from the total suspended weight to determine the suspended weight of the specimen, is determined by weighing the suspended basket submerged in mineral spirits to the same depth that the specimen is weighed. Care is used to ensure that no air bubbles cling to the basket and that a clearance between the basket and sides of the beaker is maintained.

For determining saturated weight, the specimens are removed from the mineral spirits and wiped carefully to remove excessive surface mineral spirits. The specimens are then weighed immediately to determine the saturated weight.

From the three weights taken for each specimen (dry weight, suspended weight and saturated weight) percent water absorption, open porosity, bulk density and apparent density are determined. The total porosity can be determined also when the true density of the material is known. The equations used for these calculations are:

$$W_a = \left(\frac{W_{sa}-W_d}{W_d}\right) \frac{\rho_w}{\rho_m} \times 100 \text{ percent} \qquad (1)$$

$$P_o = \left(\frac{W_{sa}-W_d}{W_{sa}-W_{su}}\right) \times 100 \text{ percent} \qquad (2)$$

$$\rho_b = \left(\frac{W_d}{W_{sa}-W_{su}}\right) \times \rho_m \qquad (3)$$

$$\rho_a = \left(\frac{W_d}{W_d-W_{su}}\right) \times \rho_m \qquad (4)$$

$$P_t = \left[\frac{\frac{W_{sa}-W_{su}}{\rho_m} - \frac{W_d}{\rho_t}}{\frac{W_{sa}-W_{su}}{\rho_m}} \times 100 \text{ percent}\right] \qquad (5)$$

where

W_a = Water absorption

W_{sa} = Weight of sample when saturated with liquid m

W_d = Dry weight of sample

W_{su} = Weight of sample when suspended in liquid m

ρ_m = Density of liquid m (about 0.76 gm/cm^3 for mineral spirits - s. g. checked after each run)

ρ_w = Density of liquid water

ρ_t = True density of sample

ρ_b = Bulk density of sample

ρ_a = Apparent density of sample

P_o = Open porosity

P_t = Total porosity

Weights for this evaluation are determined using an analytical balance sensitive to 0.0001 gram. Instrument precision for measuring absorption is ±0.10, bulk density is ±0.002 gm/cm^3, open porosity is ±0.15 and total porosity is ±0.05.

FILTERED-PARTICLE PENETRANT INSPECTION - For inspecting porous materials whose particle size is 100 mesh or smaller, the filtered-particle inspection method is applicable. The filtered-particle system consists of a fluid (suspending medium) containing a dispersion of properly sized and shaped particles. Differential liquid absorption between an area containing a crack and one that does not is the phenomena which causes the particles to congregate about a surface discontinuity. For example, when the filtered-particle penetrant is applied, more liquid is absorbed at the site of a crack than anywhere else because of the extra absorption area within the defect. As the liquid enters the defect, the suspended particles are filtered out at the surface causing a higher concentration of particles along the defect.

The filtered-particle system used at Southern Research for phenolic and graphitic materials is Partek P-1A (in alcohol) manufactured by the Magnaflux Corporation. This system can be obtained with either an oil or alcohol base with a fluorescent particle which becomes clearly visible under black light.

The procedure for using the filtered-particle system consists first in applying the technique to a material which is applicable to the test. Partek P-1A when correctly used detects minute cracks which measure only about 0.002 to 0.003 in. wide on the surface. Application is by hand using an eye dropper, and inspection is done under black light. Results are recorded photographically using a Polaroid NP-3 camera with a Polaroid No. HNCP 37 x 0.030 in. filter and black light illumination.

ALCOHOL PENETRANT INSPECTION - Alcohol is used on porous materials such as graphites, phenolic and carbon-carbon composites as a nondestructive test for surface discontinuities such as gross porosity, wide density variations, large inclusions and cracks. When a material is wetted with alcohol, porous areas and cracks remain wet for a longer period of time than the surrounding material. The differential evaporation effect is discernible by visual observation. Although this technique is not quantitized (it probably could be), it is effective in revealing surface discontinuities

The alcohol inspection procedure involves the following:

1. Application of alcohol to surface of specimen usually for 5 to 10 seconds. This can be done by flooding, brushing, or immersing.

2. Inspection of specimen surface as alcohol evaporates. Porous areas will remain wetted while the surrounding smooth areas will dry. Cracks also will remain wetted depending primarily upon the depth and width of the crack.

3. Record is made of visual observations.

This technique is useful in revealing surface discontinuities. Other NDT methods of inspection such as ultrasonics and radiography can be used in conjunction with the penetrant test to determine the extent of the surface discontinuity internally.

CARBON-CARBON COMPOSITES

MODULUS OF ELASTICITY (MOE) IN FLEXURE - The evaluation of modulus of elasticity in flexure was performed in a four-point bending apparatus shown schematically in Figure 45. The apparatus consists of three sections: a support section, loading section, and deflection transducer support. The support section is a steel block with "V" guides for precise spacing and alignment of support pins, 0.500 in. in diameter, at a separation of 2.250 in. for the 3DCC arcs and 1.500 in. for the Felt CC plates. The loading section is a stiff steel loading ram with "V" grooves, 0.750 in. apart for the 3DCC arcs and 0.500 in. for the Felt CC plates, for precise spacing and alignment of loading pins, 0.375 in. in diameter. The loading ram is provided with guides which ride in "V" grooves in the support block to align the support block to the loading ram. Load is applied to the loading ram through a hardened steel ball in a recessed conical seat in the loading ram.

An attempt was made to determine flexural modulus using strain gages on the specimens. The attempt was successful for the Felt CC material but was not successful for the 3DCC material. The strain gages bonded readily to the 3DCC material but came off the arcs with a thin layer of the material when flexed. Using the strain gages the Felt CC plates were evaluated by loading incrementally and reading strain using a Baldwin strain indicator box. The flexural modulus was determined for the Felt CC plates by:

$$MOE = \frac{\sigma}{\varepsilon} = \frac{6M}{bh^2} \cdot \frac{1}{\varepsilon} = \frac{6Pa}{2bh^2} \frac{1}{\varepsilon} = \frac{3Pa}{bh^2} \cdot \frac{1}{\varepsilon}$$

where

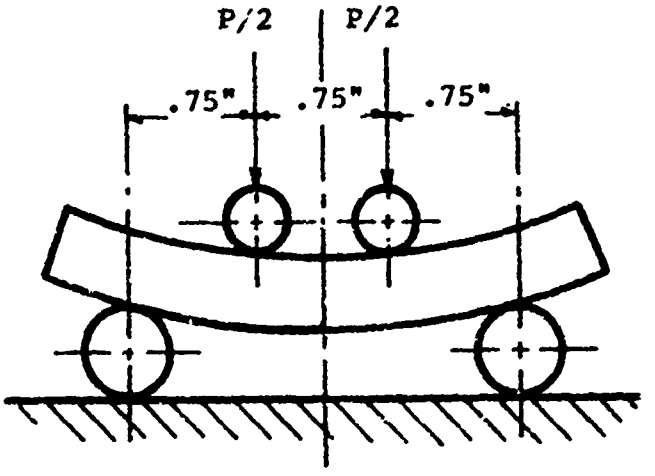
σ = Bending stress
ε = Strain gage reading
p = Applied load
a = 1/3 Beam span
b = Beam width
h = Beam depth

To conduct an MOE evaluation on the DCC arcs, a plate was inserted in the deflection transducer frame and centered. The specimen and transducer frame were placed on the support block and guides of the loading ram were inserted in the guide grooves of the support block. The specimen and frame were then carefully aligned such that the transducers' support frame arms were directly above the support rods. The assembled apparatus was placed between the crossheads of a 30,000 pound capacity Tinius-Olsen electromechanical testing machine. Load was applied to a maximum of 20 percent of the ultimate strength of the virgin material. Continuous load versus mid-point deflection plots were recorded on an X-Y recorder. A minimum of three loadings per side of the specimen constituted a run. The flexural modulus of elasticity (MOE) was calculated from the geometry and load-deflection curves by:

$$MOE = \frac{23a^3}{48I} \frac{P}{\delta}$$

where

a = 1/3 Beam span = 0.75 in.
I = Moment of Inertia = $\frac{bh^3}{12}$
b = Beam Width
h = Beam depth
$\frac{P}{\delta}$ = Slope of the load deflection curve



No allowance was made for curvature of the 3DCC specimens. Sample calculations showed this to be a negligible effect. The deflection measurement using the LVDT system includes a contribution due to compaction and one due to shear. Even though this shear deflection is of the same order of magnitude as the bending deflection it does not invalidate the data. The relative magnitudes of the flexural modulus values obtained in this manner provide a measure of property change. This test does prevent comparing data from the damaged and virgin 3DCC arcs since the latter arc had a different geometry and the shear deflection is strongly geometry dependent.

TENSILE EVALUATIONS - Tensile evaluations for the carbon-carbon composites, 3DCC and Felt CC, were run in the gas-bearing tensile facility. This facility utilizes precise alignments and gas-bearing universal joints to minimize the possibility (and magnitude) of external bending moments being applied to the specimen. The usual strain measuring system in this facility is our automatic optical strain analyzer. A complete description of the gas-bearing tensile testing facility is included as Appendix A.

Six specimens made from scrap material were evaluated to demonstrate the suitability of the Felt CC specimen design, Figure 17. These evaluations on the Felt CC specimens presented no problems. Evaluations as outlined in the Test Matrix, Table 4, were made on specimens from three of the impacted plates. Six specimens were evaluated at 3000°F and five at room temperature. Strain measurements were made using the optical strain analyzer. Specimens were loaded at a constant 10,000 psi per minute stress rate. Load was measured by a 2500 pound Strainsert load cell. Load versus strain was recorded on an X-Y recorder from which ultimate stress, elastic modulus and strain-to-failure were derived.

The 3DCC specimens presented several problems which were not completely overcome. First, the material available for each specimen was limited to 1.50 in. in length. The anticipated strength of the 3DCC material at 3000°F was 18,000 psi in tension and 1,200 psi in shear. The requirement that the specimen gage contain an integral number of unit cells centered on the gage set one gage dimension at either 0.10 or 0.20 in. (one or two unit cells). For a fixed grip length of 0.500 in. a gage cross section of 0.10 in. x 0.20 in. maximum was required to

limit the shear stress in the grip. During the specimen suitability demonstration higher failing loads were obtained with one unit cell in the width direction. The required elevated temperature tensile runs precluded using a combination mechanical-epoxy grip as used for the phenolic composites. The pull rod and specimen grip design which evolved are shown in Figure 46.

Another problem with the tensile evaluations on the 3DCC material was with the strain measurement. Strain measurements on initial runs on this material in the gas-bearing tensile facility were attempted using the optical strain analyzer. Seating of the specimen, bending of the specimen (due to the inevitable non-uniformity of the material) and lack of rigidity of the specimen, gave motions which the optical strain analyzer interpreted as strain. These erroneous strains made the analyzer output impossible to interpret. Clip-on strain gage extensometers do not suffer from these motions and were used to give interpretable stress-strain plots.

A specimen design suitability demonstration was attempted using seven specimens from scrap material from the AHP program. The grip lengths of these design suitability specimens were varied from 0.500 to 0.688 in. The ultimate failing stresses increased with increasing grip length. All failures were shear failures between the individual circumferential fibers and the matrix material. The only change in design which could increase the failing stress to a level where the mode was tension, rather than shear, would be to increase the grip length of the specimen. The material from the impacted arcs was not sufficient to increase the grip length.

The original specimen design, Figure 15, was retained but testing procedure was modified to assure the highest possible ultimate stresses. Stress-strain curves at room temperature were recorded to a level below the failing load of the specimen grip section. Elastic modulus was calculated from these curves. The specimens were then remachined as shown in Figure 16 to give the maximum possible specimen "grip" length. The specimens were rerun recording only a load-time plot for ultimate strength determination. These runs were at room temperature and 3000°F.

COMPRESSIVE EVALUATIONS - Compressive evaluations for the carbon-carbon composites, 3DCC and Felt CC, were run in our gas-bearing compressive facility. A complete description of this facility is included as Appendix B. The gas-bearings of this facility allow precise alignment of the load train. Prior to loading, the bearings are locked to provide riqid support to the specimen. This facility uses an automatic optical strain analyzer for strain measurements. Specimens were machined to the maximum possible dimensions allowed by the available material and the requirement that the 3DCC specimens contain an integral number of unit cells, centered on the gage section of the finished specimen, Figures 18, 19, and 20. Evaluations were run at room temperature and 4500°F.

THERMAL EXPANSION - The thermal expansion was determined with both the quartz and graphite dilatometers. The graphite dilatometers were employed over the total temperature range to 5000°F and the quartz dilatometers were employed up to 1700°F in order to confirm the data at the lower temperatures.

A complete description of the apparatuses and procedures with the estimated uncertainties in the measurements are included in Appendices C and D. Due to the small amount of material available for evaluation, the specimens employed were prepared by stacking smaller pieces to the required length as discussed previously.

The stacking of smaller pieces to provide a specimen of proper length has been found to provide data within the same uncertainty limits stated in the appendix, provided that no disruptions occur at the interfaces during exposure to temperature. For these carbon-carbon materials, no irregularities were observed at the interfaces after the run, therefore, the uncertainty remained unchanged.

THERMAL CONDUCTIVITY - The thermal conductivity of 3DCC and Felt CC were determined in the radial direction with both the comparative rod and radial inflow apparatuses. Complete descriptions of both apparatuses and the estimated uncertainty are included in Appendices E and F. Due to the limited amount of material available, modification in procedures and specimen configuration was necessary.

For the comparative rod apparatus the normal specimen of 1 in. diameter by 1 in. long could not be used. The specimens were prepared by glueing smaller pieces together and machining a configuration of maximum possible diameter by about 0.400 in. long.

The maximum diameters possible were 0.75 in. for the 3DCC and 0.65 in. for the Felt CC materials. The figures presented previously (Figure 25 and 26) illustrate the specimens prepared. All the other procedures were as discussed in the appendix.

A strip assembly was employed for the radial inflow apparatus. This assembly replaces the cylindrical specimen with four strips boxed around the central calorimeter as shown in Figure 47. The heat flowing radially inward toward the calorimeter transfers through the thickness of each strip. The temperature gradient across each strip is measured and the average value is used to calculate the thermal conductivity as shown in the following equation:

$$K = \frac{144}{4A} \frac{1}{\Delta T} \frac{Q}{\Delta T}$$

where
- K = Thermal conductivity
- 1 = Distance between the hot and cold temperature well in the specimen
- A = Cross-sectional area of gage section of one strip = 0.25 in.^{2}
- Q = Total measured heat flow - Btu/hr
- ΔT = Average temperature drop monitored in the strips

For a strip assembly it is desired to situate the strip such that the heat flows in the direction of low conductivity and perpendicular to the plane of high conductivity. This is desired since the specimen oriented in this fashion (in addition to the use of the pyrolytic strips shown in Figure 47) will tend to form flat and normal isotherms. This was accomplished with the gage of the specimen being oriented in the radial direction (probably lowest conductivity). The direction perpendicular to the gage was circumferential for the 3DCC and axial for the Felt CC.

Past experience in using the strip assembly with a high conductivity specimen indicated an error of no more than ± 10 percent provided the isotherms were not distorted significantly. Post-mortem analysis of the specimen and data for these runs indicated that the isotherms were reasonably normal to the heat flow and the uncertainty of ± 10 percent would apply here.

PHENOLIC COMPOSITES

TENSILE EVALUATIONS for the phenolic composites were run at room temperature in a Tinius-Olsen testing machine utilizing precision chain grips and precision specimen tabs. A sketch of the test set up is shown as Figure 48. Chain grips are used where failing loads of the specimens are likely to exceed the capacity of the gas-bearing facility.

The chain acts as a series of universal joints and is used to minimize the possibility of externally applied bending moments being introduced into the specimen. The chain is adapted to the grips by a centering bushing which locates the chain within 0.001 in. of the centerline of the grips. The chain and grips were pre-loaded above the chain rated load to assure good mating surfaces in the individual links and at the grip chain interface.

The specimens were machined to the maximum possible dimensions consistent with the material available and the requirement that the 3D orthogonal specimens be centered on the weave pattern and contain an integral number of unit cells. The elastic modulus desired was for the total thickness if possible. The resulting specimens were considerably smaller in length and width than good material testing would require. The tab grip utilizing both mechanical and epoxy bonding to grip the specimen was felt to the best approach. A sketch of an assembly of specimen and tab grips is shown as Figure 49.

The tab and specimen were machined to the same thickness. The specimen, tabs and covers were bonded together as one assembly using Shell Resinbond 907, (2,000 psi shear strength). The assembly was lightly clamped in an alignment jig under a small preload and cured at 150°F.

Strain measurements were made using clip-on strain gage extensometers. Load on the specimen was measured with the internal load cell in the testing machine. Load was applied at a constant rate of 10,000 psi per minute. Load and strain were recorded on an X-Y recorder.

Evaluations on the R6300, Material #10, and 3DCP, Material #15A, specimens were carried successfully to ultimate. The initial runs on the quartz-phenolic materials gave bending-shear failure within the tab grips. The majority of the 3DQP, Material #11, specimens were loaded to a level within the tab grip capability for evaluation of elastic modulus. The gage sections of these specimens were then machined as shown in Figure 50 to yield a higher gage stress for a given load. These specimens were then reloaded and gave specimen failure within the gage section and a much better estimate of the tensile strength of the material.

COMPRESSIVE EVALUATIONS for the phenolic composites, were run in the gas-bearing compressive facility. A complete description of this facility is included as Appendix B. The gas bearings of this facility allow precise alignment of the load train. Before loading the specimen, the bearings are locked and thus provide rigid support to the specimen. An automatic optical strain analyzer is used for strain measurement. Specimens were machined to the maximum possible dimensions allowed by the available material and the requirement that the specimens from the 3D orthogonal materials contain an integral number of unit cells centered on the gage section of the finished specimens. Two specimens from each arc were oriented in the axial direction and two in the circumferential direction. All specimens were loaded to failure at room temperature. Plots of load versus strain were recorded on an X-Y recorder.

PRE-IMPACT NDT EVALUATIONS

NDT characterization of arcs and rings for Phase II was conducted on as-received arcs and rings from AVCO 3DC/QP, AVCO 3DCP, AVCO 3DCC (T400), AVCO R6300, AVCO 3DCC and Sandia Felt CC. This work entailed characterization and quality control of 55 undegraded arcs, 67 rings, 11 discs, and 10 coupons. All specimens received quality control (QC) evaluation consisting of bulk density, visual inspection (1X) with photographic (1X to 10X) documentation, and radiography with one additional NDT monitor where questionable material uniformity or reproducibility appeared. Based on the QC results and agreement with the Air Force Project Officer, 5 arcs (AVCO 3DCP) and 6 rings (two each from AVCO R6300, AVCO 3DCC and Sandia Felt CC) were selected for more extensive NDT evaluation. This additional or full treatment (FT) NDT included inspections by ultrasonic velocity, radial ultrasonic transmission, liquid penetrants, 40X photomicrography, and bulk mechanical evaluations.

The test matrix for Phase II was presented in Table 3. The Southern Research indexing systems used for the various configurations are given in Figures 43 and 44.

NONDESTRUCTIVE RING MODULUS EVALUATIONS

The 6 rings which received the full treatment NDT evaluations received nondestructive modulus evaluations also. Two different methods were used: first, a ring flexure evaluation, and second, a hydrostatic compression evaluation. During these evaluations the rings were loaded to no greater than 20 percent of ultimate strength as defined by data from the AHP program.

A schematic drawing of the setup used for the ring flexure evaluations is shown as Figure 51. The ring was instrumented with four strain gages on the inside surface oriented in the circumferential direction. The ring to be evaluated was located between the crossheads of a Tinius-Olsen testing machine. Three dial indicators were located around the ring to measure radial deflection as shown in Figure 51. Strain was read using a Baldwin strain indicator. Load was read from an internal load cell in the testing machine. The ring was loaded incrementally and all dial indicator and strain gages read at each load increment. The ring was loaded to 20 percent or less of its ultimate strength. The sequence was repeated at least twice with the arbitrarily selected NDT zero orientation under the loading pad, rotated 45 degrees counterclockwise and at 90 degrees to the vertical. Modulus values were calculated using the classical ring equations.

The hydrostatic compression evaluation was run in a hydrostatic loading rig shown schematically in Figure 52. The loading medium was a thin wall rubber bladder which was connected to a hydraulic cylinder. The bladder was contained on the outside diameter by an outer closure ring and top and bottom closure plates. The bladder was contained on the inside diameter by the test ring and spacer rings. The spacer rings were sized to give an assembled height with the test ring in place which was 0.005 in. less than the outer closure ring. The bladder was oversized for the cavity in the rig and this combined with its thin wall ensured that the bladder supported a negligible portion of the hydraulic loading. The hydraulic system was filled and bled. The hydraulic cylinder was loaded in a tinius-Olsen testing machine. Load was measured by an internal load cell in the testing machine. This load was converted to hydraulic pressure and stresses were calculated using thick walled cylinder relationships.

$$\sigma = 2\rho \frac{R_2^2}{R_2^2 - R_1^2}$$

where

σ = Circumferential stress at I.D.
ρ = Hydraulic pressure
R_2 = Outside radius
R_1 = Inside Radius

Strain was read using a Baldwin strain indicator. From the stress and strain values, modulus was calculated using the Hook's Law relationship:

$$\sigma = E\varepsilon$$

SECTION IV

PROPERTIES OF IMPACTED ARCS AND SPECIMENS

3D CARBON-CARBON IMPACTED ARCS

NONDESTRUCTIVE TESTING - Results of the nondestructive monitors for the 3DCC impacted arcs are given in Table 4 and described graphically in Figure 63. The results of the subjective NDT evaluations are shown in Table 5 and are photographically documented in Figures 53 through 62. The ranges of monitor values measured on specimens from the arcs are also shown in Table 4 to give reinforcement to the magnitudes of the monitors on the arcs and an impression of the variability of the monitors with position on the arcs.

Visual (1X-10X) inspection of the impacted arcs indicated structure-change starting at the lowest impulse level of 1.03 kilotaps, Arc 8-AR-8. Structure-changes detected at this level were radial spall from one machined edge, bulk and aligned delaminations in edges, slight radial protrusion from front and rear faces, and occasional spall of radial ends from rear face, Figure 54. A rear delamination located about 0.1 in. from the rear face was detected at 2.20 kilotaps, Arc 8-AR-2, Figure 55. In addition, matrix spall from around radials on the front face was also detected at this level. Front yarn lift (circumferentials) at one edge was detected at 3.045 kilotaps, Arc 8-AR-7, Figure 56, and matrix spall from the edges was detected at 3.36 kilotaps, Arc 8-AR-5, Figure 57. Increased bulk and rear delaminations, rear radial recession, and a single front face crack were detected at 5.39 kilotaps, Arc 8-AR-1, Figure 58. A gross mid-thickness delamination with bulk delaminations, gross rear yarn lift and matrix spall, and a through-thickness crack were detected at 7.56 kilotaps, Arc 8-AR-6, Figure 59. At the highest impulse level of 7.88 kilotaps, Arc 8-AR-3, structure-change was similar to the 7.56 kilotap level except the specimen was totally separated near its middle, Figure 60.

Visual (10X) inspection did not reveal any new structure-change.

The group radiograph is shown in Figure 61. In comparing the before hit and after hit radiographs, no structure-change was detected for the 1.03, 1.64 and 2.20 kilotap levels; Arcs 8-AR-8, 8-AR-4 and 8-AR-2. Circumferential low-absorptive alignments measuring 0.6 and 0.7 in. long were detected at 0.1 in. from the rear face at 3.045 kilotaps, Arc 8-AR-7. Continuous, circumferential low-absorptive alignment at 0.1 and 0.35 in. from

the rear face and some volume oriented low-absorptive alignments were detected at 3.36 kilotaps, Arc 8-AR-5. Increased circumferential low-absorptive alignments at 0.1, 0.2, 0.3, and 0.4 in. from the rear face were detected at 5.39 kilotaps, Arc 8-AR-1. Gross circumferential alignments at 0.1 and 0.3 in. from the rear face and missing material from the rear face were detected at 7.56 and 7.88 kilotaps, Arcs 8-AR-6 and 8-AR-3. Aslo, a near through-thickenss radial low-absorptive alignment was revealed near the middle of Arc 8-AR-6 at the 7.56 kilotap level.

Photomicrographs (50X before reduction) are shown in Figure 62. Except for Arc 8-AR-2 at the 2.20 kilotap level, no gross macro structure-change was particularly obvious in single plane sections at up to the 5.39 kilotap level. At the 2.20 kilotap level, a circumferential separation was detected at 0.1 in. from the rear face even in single plane inspection. The separation occurred at a circumferential/axial bundle interface and was about macro-level structure-change consisted of fractured circumferentials and circumferential separations through axial bundles. Gross macro delaminations were incurred at the 7.56 and 7.88 kilotap levels.

The results of the monitors versus impact level for AVCO 3DCC arcs are plotted in Figure 63. The monitors bulk density and thickness measurements indicated slight material compaction at the lower impact levels and material expansion at the higher levels up through 3.045 kilotaps and expansion above this level. The magnitudes of the decreases in thickness, 0.001 in., at the lower impact levels would not usually be considered significant, but the significant and consistent increases in bulk density lend weight to the thickness changes. Open porosity measurements provided uniform values from the virgin arc through the 3.045 kilotap level. For these impulse levels, the virgin specimen had the highest open porosity of 11.8 percent with the 1.03 kilotap level specimen having the lowest at 10.5 percent. Open porosity increased to 12.2 and 13.0 percent at the 3.36 and 5.39 kilotap levels, respectively. Ultrasonic transmission measurements also indicated no significant structure-change up to 3.045 kilotaps. The transmission values ranged from 28.5 to 26 added dB over this range with the virgin arc having a transmission of 28 added dB. Transmission at 3.36 and 5.39 kilotaps decreased significantly to 17 and 19 added dB, respectively. Radial velocity was measured at both ends of the arc and at the center. The values in Table 4

are minimum and maximum values. The minimum values, which were considered more revealing of structure-change, indicated no change below 2.20 kilotaps, ranging from 0.1966 in./μsec at 2.20 kilotaps to 0.2025 in./μsec at 1.03 kilotaps (minimum values). Minimum values ranged from 0.1857 in./μsec at 3.045 kilotaps to 0.1585 in./μsec at 4.39 kilotaps. Maximum and minimum values of radial velocity for the various impulse levels are plotted in Figure 63.

Comparison of thickness and radial sonic transmission measurements before and after the MOE evaluations indicate that flexing the arcs had negligible effect.

MECHANICAL EVALUATIONS - The results of evaluations of flexural modulus are given in Table 4 and plotted in Figure 63. Tensile and compressive properties are given in Table 6 and are plotted in Figures 64, 65 and 66. Tensile and compressive stress strain curves are included in Appendix G. The flexural moduli in Table 4 and Figure 63 probably are not engineering values. The high modulus of the 3DCC material, the load levels imposed and the proportions of the arcs combined to give very small deflection signals from the flexural evaluations. Shear deflections aggravated by the delaminations inherent in this material and arc general compaction were included in the deflection signal measured and were probably large relative to the pure bending deflection which was desired. They do reflect structural change and their relative magnitudes should give a good approximation of the change in flexural modulus expected. The flexural modulus of the virgin specimen was not comparable to those of the impacted arcs since a different testing geometry was required. The flexural modulus of the impacted specimens showed a reasonably consistent decrease with increasing impact level. The most meaningful display of this consistency is shown in Figure 66, a plot of retained modulus versus impact level. The base for this plot of flexural modulus was obtained by extrapolation of the data for the impacted arcs back to a zero level of impact. The only significant deviation from a linear relation between the retained flexural modulus and impact level was at the 5.390 kilotap level. At this level data from the lower impact levels would have predicted a zero retained flexural modulus rather than the measured 18 percent.

Of the tensile and compressive data, Table 6 and Figures 64, 65 and 66, only the tensile modulus at room temperature and compressive strength at room temperature and 4500°F showed consistency. The tensile modulus decreased from about 12.8×10^6 psi for the virgin material (AHP data) to 7.09×10^6 psi for specimens from Arc 8-AR-5, 5.39 kilotaps. The minimum tensile strength was more consistent than the average strength and had values at room temperature of 11,500 psi for the virgin material

(AHP data), 11,040 psi at 1.030 kilotaps, 10,600 psi for 2.200 kilotaps and 9,280 psi for 3.360 kilotaps. At 3000°F the minimum tensile strength values were 16,240 psi for 1.030 kilotaps, 18,400 psi for 2.200 and 16,600 psi for 3.360 kilotaps. No data were available at 3000°F for the AHP material in the circumferential direction. As one would suspect the tensile strength was not very sensitive to impact level. The structure-changes observed in the visual inspection were predominantly in the matrix material between fibers and the tensile strength is related to the fibers.

The compressive strength showed variation with impact level. The strength at room temperature was 8,500 psi for the virgin material (AHP data), 5,760 psi at 1.640 kilotaps, 4,880 psi at psi at 3.045 kilotaps, and 4,030 psi at 5.390 kilotaps. At 3000°F the strength of the AHP material was 13,000 psi and at 4500°F for this program the strengths were 11,360 psi for virgin material, 10,970 psi at 1.640 kilotaps, 10,600 psi at 3.045 kilotaps and 7,430 psi at 5.390 kilotaps. Compressive modulus was not consistent. There were wide discrepancies between the two values at each temperature and impact level and extremely low values at 4500°F for the specimens from 8-AR-7, 3.045 kilotaps. These low values at 4500°F were not confirmed by low values at room temperature for this hit level.

THERMAL EXPANSION OF 3DCC - The thermal expansion values of 3D Carbon-Carbon in the axial and circumferential directions at various impact levels are shown in Figures 67 through 70 and Tables 7 through 12. In each figure the thermal expansion of a virgin specimen of 3D Carbon-Carbon evaluated under a previous program is plotted for a baseline reference.

Note that the expansion of the impacted material was always higher than that of the virgin material. The difference was most pronounced in the axial direction on the material impacted at a level of 5.39 kilotaps. The difference was only slight in the circumferential direction. The reason for the higher expansion of the impacted material may be due to separations between fabric and matrix. When the fabric and matrix separate, the expansion will no longer be controlled by the fabric. Lack of influence from the fabric would allow greater expansion.

In Figures 67 and 68 duplicate runs were made to 5000°F on the same specimen and in both cases the values measured during the second run after initial exposure to 5000°F were lower than those of the first. The slight inflection of the slope above 4000°F on all runs indicates some instability of this material at 5000°F.

THERMAL CONDUCTIVITY - The thermal conductivity of 3DCC in the radial direction at two impact levels, 1.03 and 2.20 kilotaps, is shown in Figure 71 and Tables 13 and 14. No trend in values was detected with impact level. A smooth curve was fitted to all the data and the values decreased from 275 Btu in./hr ft^2 °F at 100°F to a minimum of 132 Btu in./hr ft^2 °F at 3300°F, above which the values increased to 175 Btu in./hr ft^2 °F at 5000°F.

The thermal conductivity of the virgin material determined previously (AHP program) was lower than the impacted material. The reason for this anomoly probably is that the virgin material had a lower density and velocity than the impacted material. The respective densities were 1.63 gm/cm^3 and 1.68 gm/cm^3 and the velocities were 0.181 in./μsec compared to 0.20 in./μsec. Due to this density variation the effect of impact level could not be determined since the base line data does not appear to be representative of present specimens of 3DCC before impact.

The increase in conductivity above 3000°F is typical for some CC materials. As has been indicated with the results of the expansion evaluations the material is not stable at higher temperatures. Supporting this is the fact that the second run (after initial exposure to 5000°F) exhibited a slightly lower value in conductivity.

FELT CC IMPACTED PLATES

NONDESTRUCTIVE TESTING - Results of the non-destructive monitors of the Felt CC impacted plates are shown in Table 15 and described graphically in Figure 78. The ranges of values of the monitors on specimens removed from the plates are also shown in Table 15 to give reinforcement to the magnitudes of the monitors on the plates and an idea of the variability of the monitors with position on the plates.

Visual (1X-10X) inspection of the impacted plates indicated gross structure-change at 2.49 kilotaps, Plate 12-F-14, consisting of a gross delamination and a rear face crack, Figures 72 and 73. Structure-change at this impact level was much more severe than changes incurred at the higher impact levels. At 3.07 kilotaps, Plate 12-F-13, aligned hairline cracking in one edge located about 0.15 in. from the rear face was detected; however, cracking was not prominent enough at the surface for photographic documentation. At 3.44 kilotaps, Plate 12-F-10,

aligned cracking located about 0.2 in. from the rear face in two edges was apparent, Figure 74, and at 4.14 kilotaps, Plate 12-F-11, aligned cracking located about 0.2 in. from the rear face was apparent in all four edges, Figure 75. The only surface variations detected were at 2.49 kilotaps, Plate 12-F-14 which consisted of increased porosity and a rear face crack.

Visual inspection (10X) detected no structure-change to 2.43 kilotaps, and no additional structure-change to the changes detected at 1X at any of the higher impact levels.

The group radiograph is shown in Figure 76. Specimen 12-F-14 at 2.49 kilotaps showed a gross delamination for the full length of the plate. Otherwise, no structure-change was indicated at 1.21, 2.43 and 3.07 kilotaps. At 1.7 kilotaps, Plate 12-F-16, some low-absorptive alignments located about 0.1 in. from the rear face and running nearly the full length of the plate gave reason to suspect internal cracking. Since these plates were not radiographed before impact, no definite conclusion could be made from the radigraph. At 3.44 and 4.14 kilotaps, low-absorptive alignments located 0.25 in. from the rear face and at mid-thickness, respectively, were apparent. At 3.44 kilotaps, Plate 12-F-10, the alignments extended nearly the full length of the plate, and at 4.14 kilotaps, Plate 14-F-11, the alignments extended the full length of the plate and were more severe.

Photomicrographs (50X before reduction) are shown in Figure 77. No macro structure-change was indicated at any of the impact levels except in 12-F-14 at 2.49 kilotaps. As shown, missing material from a zone located between the gross delamination and the rear face was apparent. Macro cracking or delamination was also apparent at 3.44 and 4.14 kilotaps. Material adjacent to the macro cracking was virgin-appearing.

Liquid penetrants (Partek) detected some aligned cracking in two edges at 2.43 kilotaps, Plate 12-F-1. In addition, penetrants revealed aligned cracking in the third face of Plate 12-F-10 at 3.44 kilotaps (cracking in two faces by visual 1X) and rear face porosity in 12-F-14 at 2.49 kilotaps.

The results of the monitors versus impulse level for Felt CC plates are plotted in Figure 78. In general the NDT monitors did not indicate appreciable structure-change below the 4.140 kilotap level, excepting 12-F-14 at 2.49 kilotaps. The major exception to this was the bulk density of the plate 12-F-1 which

was far lower than the other plates. The low density apparently existed before flyer plate impact since the other NDT monitors did not detect any significant deviations in this plate. At 4.14 kilotaps, significant shifts in open porosity, velocity, and ultrasonic transmission were measured. Open porosity was 16.1 percent, velocity was 0.1034 in./μsec (lowest value), and transmission was 18 added dB. The average values at all of the other impulse levels (including virgin) were open porosity of 12.0 percent (range 10.3 - 13.1 percent), velocity of 0.1084 in./μsec (range 0.1057 - 0.1128 in./μsec), and transmission of 38 added dB (range 37 - 40 added dB). Monitor effectiveness was hampered by the lack of values before flyer plate impact.

Comparison of thickness, radial velocity and radial ultrasonic transmission measurements before and after MOE evaluations indicated that flexing had essentially no effect on the plates.

MECHANICAL EVALUATIONS - The results of flexural modulus evaluations on Felt CC are shown in Table 15 and Figures 78 and 82. Tensile and compressive properties are tabulated in Table 17 and are presented graphically in Figures 79 through 82. Tensile and compressive stress-strain curves are included as Appendix H. The flexural modulus value was 2.37×10^6 psi for the virgin specimen. Flexural modulus values indicated essentially no change below 3.070 kilotaps and decreases of about 10 percent at 3.070 kilotaps, 18 percent at 3.440 kilotaps, and 16 percent at 4.140 kilotaps. This indication of change above 3.070 kilotaps coincided with the appearance of macrocracking at 3.070 kilotaps and above.

Plate 12-F-14 had an anomalous response to flyer plate impact. It exhibited gross structure-change even though its impact level, 2.490 kilotaps was an intermediate value. Plate 12-F-1 was supplied to Kaman Sciences as a replacement for Plate 12-F-14. The geometry of Plate 12-F-1 differed from that of the other plates but this was not considered significant. After impact the bulk densities of this plate and the specimens from this plate were low compared to those of the other plates, even though none of the other NDT monitors detected significant deviations for this plate. The compressive strengths at both 70°F and 4500°F of the specimens from this plate were the highest of all of the plates. In view of the above data, plate 12-F-1 as well as 12-F-14 were concluded to have differed from the other plates prior to flyer plate impacting and cannot be compared to them for response after flyer plate impacting.

THERMAL EXPANSION - The thermal expansion of Felt CC in the axial and circumferential direction at various impact levels is shown in Figures 83 through 87 and Tables 18 through 27. In the axial direction the impact levels up to 3.44 kilotaps had no effect on the expansion as can be seen from the excellent agreement with the values measured on the virgin material evaluated previously (AHP program). In the circumferential direction the impacted specimens, from 1.2 to 4.2 kilotaps, had lower expansions than those of the virgin material. No trend could be detected with level of impact. The lower expansion of the impacted specimens is not fully understood; however, the possibility of the cracked areas acting as strain isolators may be the reason.

THERMAL CONDUCTIVITY - The thermal conductivity of Felt CC in the radial direction for both virgin and impacted specimens is shown in Figure 88 and Tables 28 and 29. The impacted material exhibited somewhat lower conductivity than that of the virgin and less than expected. No trend was observed for the two impact levels evaluated.

R6300 IMPACTED ARCS

NONDESTRUCTIVE TESTING - Results from prior evaluations on the R6300 arcs are included as Table 30 and Figure 90 for reference and a group photograph as Figure 89. During the earlier program no significant change in flexural modulus, MOE, had been measured even though significant structure-change had been detected visually. The most probable cause for the inability to measure a MOE change was the masking effect of the attached aluminum backing plate. Open porosity and radial ultrasonic transmission (attenuation in previous program) correlated somewhat with impact level.

Results from nondestructive testing of specimens from the R6300 arc are shown in Table 31 and Figure 91. From Figure 91 it was obvious that open porosity, ultrasonic transmission and ultrasonic velocity were sensitive monitors for the levels of impact. Bulk density differences shown in Figure 91 are not felt to be attributable to impact.

MECHANICAL EVALUATIONS - Results of tensile and compressive evaluations on the specimens from the R6300 arcs are shown in Table 31 and Figures 92 and 93. Compressive strengths in both axial and circumferential directions seem to be linearly related to impact level. The tensile and compressive moduli were not changed by impact levels. Only if the data from the AHP program

are used for virgin values does any change in tensile strength due to impact appear significant. The tensile strengths from the AHP program were respectively 5,800 psi and 9,000 psi in the axial and circumferential directions. The tensile strengths at 0.49 kilotaps were 3,480 psi and 6,800 psi and at 1.99 kilotaps 3,040 psi and 7,260 psi in the same order as above. Compressive strengths in the axial and circumferential directions changed almost linearly from 27,600 and 30,960 psi for the virgin specimens to 17,700 and 16,170 psi at 4.04 kilotaps. Radial sonic velocity and open porosity would seem to be useful as monitors of compressive strength after impact but monitors for other properties seemed to be lacking.

3D QUARTZ-PHENOLIC IMPACTED ARCS

NONDESTRUCTIVE TESTING - Results from the prior NDT evaluations on the 3D Quartz Phenolic arcs are presented as Table 32 and Figure 95 for reference. A group photograph of the arcs is included as Figure 94. During this earlier program significant changes in flexural modulus, MOE, were measured and a remarkably strong correlation with ultrasonic attenuation (transmission) was indicated. Ultrasonic velocity correlated very well up to the level where the signal became attenuated. Bulk density, open porosity and thickness changes also correlated with flexural modulus changes but their sensitivity was much less than the ultrasonic monitors.

Results from the NDT evaluations on the specimens from the 3D Quartz Phenolic arcs are shown in Table 33 and Figure 94. Unlike the NDT on the arcs, the monitors on the specimens were not sensitive to level of impact up to 7.95 kilotaps. In particular ultrasonic transmission indicated essentially no change at all. Above 7.95 kilotaps bulk density and open porosity changed linearly with change in impact level.

Visual inspection of the specimens revealed little that had not been noted earlier for the arcs. Generally for the lower levels of loading, occasional (volume) cracking was observed and for the higher levels aligned cracking and delamination primarily at midthickness were observed. The aligned cracking increased in severity with increasing impact level.

MECHANICAL EVALUATIONS - Results of tensile and compressive properties evaluations on specimens from the Quartz-Phenolic arcs are shown in Table 33 and Figures 97 and 98. Axial tensile strength decreased linearly from 42,400 psi for the virgin specimens (AHP data) to 32,590 psi at 7.95 kilotaps. At 9.88 kilotaps the axial tensile strength dropped sharply to 21,470 psi. Similar trends were observed for the circumferential tensile data with a linear decrease from 69,900 psi for the virgin specimens (AHP data) to 51,650 psi at 7.95 kilotaps. A sharp drop in strength to 21,500 psi at 9.88 kilotaps was also similar to that for the axial strength. Compressive strength decreased approximately linearly from 28,800 psi and 26,080 psi in the axial and circumferential directions for the virgin specimens to 11,180 psi and 11,520 psi at 9.01 kilotaps. Tensile moduli showed only slight change with impact level. The tensile moduli in the axial and circumferential directions decreased from 2.14×10^6 psi and 3.57×10^6 psi for the virgin specimens (AHP data) to 1.46×10^6 psi and 2.31×10^6 psi at 9.88 kilotaps. The compressive moduli in the axial and circumferential directions showed a small decrease from 2.65×10^6 psi and 2.78×10^6 psi for virgin specimens to 1.73×10^6 psi and 2.33×10^6 psi at 9.01 kilotaps. Again the AHP data were lower than the virgin data from this program. The NDT monitors seemed to correlate somewhat with strength in that they showed small decreases from the virgin specimens up to 7.95 kilotaps and a sharper decrease to 9.88 kilotaps.

3D CARBON-PHENOLIC PORTION OF 3DC/QP IMPACTED ARCS #15A

NONDESTRUCTIVE TESTING - Results from the prior NDT evaluations on the 3D Carbon/Quartz-Phenolic impacted arcs are presented as Table 34 and Figure 100 for reference. A group photograph of the arcs is shown as Figure 99. During these prior evaluations flexural modulus (MOE) decreased approximately linearly with increasing impact level. As for the 3D Quartz/Phenolic ultrasonic attenuation (transmission) was a very good correlator for MOE. Bulk density, open porosity and thickness changes showed some correlation to (but were not very sensitive) MOE changes.

Results from the NDT evaluations on the specimens from the 3D Carbon-Phenolic portion, #15A, of the 3DC/QP impacted arcs are shown in Table 35 and Figure 101. The NDT monitors for the specimens generally correlated with impact level but were less sensitive to changes in impact level than they were for the arcs. Ultrasonic transmission dropped significantly from the virgin specimens to the first impact level, 4.09 kilotaps, but showed little change above this level. Bulk density and open porosity changes showed correlation with impact level similar to those for the arcs.

Visual inspection of the specimens generally showed the same structure-changes as had been observed earlier for the arcs. These structure-changes were volume cracking at the lowest impact level, 4.09 kilotaps; increased volume cracking with occasional failed radials at 4.69 kilotaps; aligned cracking at the center of the Carbon-Phenolic portion of the arc at 5.18 kilotaps; and delaminations near the center of the Carbon-Phenolic portion of the arcs at the two highest impact levels, 6.06 and 6.51 kilotaps. The failure of ultrasonic transmission as a monitor of the impact level above 4.69 kilotaps is probably associated with the appearance of failed radials and delaminations.

MECHANICAL EVALUATIONS - Results of the evaluations of tensile and compressive properties of specimens from the Carbon-Phenolic portion of the 3DC/QP arcs are shown in Table 35 and Figures 102 and 103. Both tensile and compressive strengths decreased almost linearly from the virgin material to the highest impact levels tested. Axial tensile strength decreased from 16,980 psi for the virgin specimens to 1,240 psi at the 5.06 kilotaps. The circumferential tensile strength decreased from 22,520 psi for the virgin specimens to 200 psi at 6.06 kilotaps. These tensile strengths at 6.06 kilotaps can be considered essentially zero. Compressive strengths decreased from about 22,000 psi for both axial and circumferential virgin specimens (AHP data) to about 5,100 psi and 4,200 psi in the axial and circumferential directions respectively at 6.5 kilotaps.

Modulus values were difficult to obtain for these specimens. The extensive structure-changes prevented the material from behaving as a homogeneous material and this caused erratic strain behavior. Modulus values were obtained for axial tensile specimens, and circumferential compressive specimens. Axial tensile modulus decreased about linearly from 6.63×10^6 psi for the virgin specimens to 0.24×10^6 psi at 6.06 kilotaps. Circumferential tensile modulus was 6.10×10^5 psi for the virgin specimens and 1.25×10^6 psi at 4.69 kilotaps. Circumferential compressive modulus decreased eratically from 5.81×10^6 psi for the virgin specimens to 5.20×10^6 psi at 5.18 kilotaps and decreased sharply to 0.96×10^6 psi at 6.5 kilotaps.

The essentially linear decrease in tensile and compressive strengths and tensile moduli with impact level agreed with the approximately linear response of MOE for the complete arcs. The regular progression of structure-changes with impact level were thus reflected in flexural, tensile and compressive properties of the Carbon-Phenolic portion of the 3DC/QP material.

3D QUARTZ-PHENOLIC PORTION OF 3DC/QP IMPACTED ARCS #15B

NONDESTRUCTIVE TESTING - Results from the prior NDT evaluations on the 3D Carbon/Quartz-Phenolic are shown in Table 34 and Figure 100 and were discussed in the preceding section on the 3D Carbon-Phenolic portion of the 3DC/QP arc.

The results from the NDT evaluations on the specimens from the 3D Quartz-Phenolic portion, #15B, of the 3DC/QP impacted arcs are shown in Table 36 and Figure 104. The NDT monitors for these specimens seem to correlate generally with impact level but are less sensitive than these same monitors on the #15A specimens. Some structure-change is indicated by the monitors but significant changes were observed from visual inspection of the specimens only at the highest impact level, 6.5 kilotaps. Visual inspection of the arcs earlier had revealed some volume cracking at the lower impact levels and aligned cracking near the inner surface at the highest impact level, 6.5 kilotaps.

MECHANICAL EVALUATIONS - Results of the tensile and compressive properties evaluations on specimens from the Quartz-Phenolic portion of the 3DC/QP impacted arcs are shown in Table 36 and Figures 105 and 106. Tensile strengths in Table 36 and Figure 105 do not represent ultimate strengths. All specimens failed in the grip section. The failures were due to a combination of bending and shear. The strengths tabulated and plotted represent a lower bound above which the ultimate tensile strengths will lie. The axial tensile stress in the virgin specimens at failure was 35,500 psi which was about 25 percent less than the ultimate tensile strength from the AHP program of 57,550 psi. The circumferential tensile stress in the virgin specimen was 35,900 psi compared to 78,200 psi for the ultimate from the AHP program. Specimen 15B-AR-V-T4C was run once for modulus. The gage section was then reduced in an attempt to give a tensile failure in the gage section. This specimen was broken in loading into the load train.

The axial compressive strengths decreased almost linearly with impact level from 46,800 psi for the virgin specimens (AHP data) to 17,200 psi at 6.5 kilotaps The circumferential compressive strength decreased approximately linearly from 47,400 psi for the virgin material (AHP data) to 16,300 psi at 6.5 kilotaps.

The modulus values showed little change with increasing impact level. The axial tensile modulus decreased from 2.20×10^6 psi for the virgin specimens to 1.62×10^6 psi at 4.69 kilotaps and then increased again to 2.12×10^6 psi. Circumferential tensile modulus decreased slightly from 3.16×10^6 psi for the virgin specimens to 3.03×10^6 at 4.69 kilotaps and returned to 3.16×10^6 psi at 6.06 kilotaps. Axial compressive modulus decreased approximately linearly from 3.42×10^6 psi for virgin specimens (AHP data) to 2.37×10^6 psi at 6.5 kilotaps. Circumferential compressive modulus behaved irregularly, decreasing from 3.50×10^6 psi for virgin specimens to 2.84×10^6 psi at 4.09 kilotaps and then increasing to 3.26×10^6 psi at 6.5 kilotaps.

The only properties of these specimens which agreed well with the linear decrease of MOE with impact level on the complete arcs were the compressive strengths. Had the failure mode of the tensile specimens been tensile it is probable that tensile strengths would have also agreed with the linear MOE response. Tensile and compressive moduli did not agree with the MOE response.

SECTION V

DISTRIBUTION OF STRUCTURE-CHANGE IN ARCS

A study was made to determine distribution in the plane of the cylinder of structure-change within a given arc. Radial differences were obvious but not inspected quantitatively. The primary tools used were radiography of arcs and specimens from the arcs and visual inspection. Correlations were then made between these results, other NDT monitors and mechanical property results on specimens. Observe that a specimen represents a sample from an arc.

3D CARBON-CARBON

Radiographs of Arcs 8-AR-8, 8-AR-4 and 8-AR-2 indicated no structure-change. Radiographic and visual inspections of specimens from Arcs 8-AR-8 and 8-AR-4 indicated no structure-change. NDT monitor results and mechanical property results from these specimens were similar and this indicated uniform distribution of any structure-change. Radiographic inspection of Specimen 8-AR-2-T1C revealed a circumferential low-absorptive alignment over the full length of the specimen. Aligned cracking was detected visually about 0.10 in. from the rear face of the specimen. From the mechanical property results at 70°F, Specimen 8-AR-2-T1C had a tensile strength of 10,600 psi and elastic modulus of 5.97 x 10^6 psi which were significantly lower than values for 8-AR-2-T4C of 16,100 psi and 10.3 x 10^6 in. respectively. Thus, neither structure-change nor retained properties were uniform in Arc 8-AR-2. The mechanical property results at 3000°F and NDT monitor results of these specimens were similar indicating similar structures.

Structure-change was detected by radiography in bulk arcs at 3.045 kilotaps, Arc 8-AR-7. This change was indicated by low-absorptive alignments near both ends of the arc. A positive print of the radiograph was given in Figure 61, and a sketch showing this result is given in Figure 107. Radiographs of specimens from this arc revealed increased volume oriented low-absorptive alignments in the gage of Specimens 8-AR-7-C1C and 8-AR-7-C3C. Specimen 8-AR-7-C1C was considered more severe than 8-AR-7-C3C. Further, the radiographs of the specimens clearly showed the low-absorptive alignments detected in the ends of the bulk arc to lie only in Specimens 8-AR-7-C1C and 8-AR-7-C3C. Thus, the structure-change was not only located at the ends of the arc but was also local to one edge. From the mechanical property results at 70°F, Specimen 8-AR-7-C1C had a slightly lower strength and significantly lower modulus than Specimen 8-AR-7-C3C. These strength and modulus values were 4,600 psi and 4.82 x 10^6 psi for Specimen 8-AR-7-C1C and 5,100 psi and 7.26 x 10^6 for Specimen

8-AR-7-C3C. NDT monitor results for the specimens were similar except that radial velocity for Specimen 8-AR-7-C3C was higher, 0.2166 in./μsec for Specimen 8-AR-7-C3C and 0.1950 in./μsec for Specimen 8-AR-7-C1C. At 4500°F the mechanical property results were similar. Strengths and modulus values were 10,400 psi and 0.62×10^6 psi for Specimen 8-AR-7-C2C and 10,900 psi and 0.89×10^6 psi for Specimen 8-AR-7-C4C. It should be pointed out that these values for modulus (4500°F) did not align with the values measured at the other impact levels. For example, at 1.640 kilotaps the average modulus was 3.24×10^6 psi and at 5.39 kilotaps the average modulus was 1.94×10^6 psi. NDT monitor results for the 4500°F specimens indicated no significant variation of structure-change. This entire arc had significant structure-change but the change in NDT monitors and retained properties were not the same quantitatively.

Increased structure-change was detected by radiography at 3.360 kilotaps, (Arc 8-AR-5), Figure 108. Continuous low-absorptive alignments were detected at 0.10 and 0.35 in. from the rear face. Structure-change showed slight increase in intensity towards the ends of the arc. Radiographic results on the specimens indicated similar structures for all the specimens.

NDT monitor and mechanical results on specimens from ARC 8-AR-5 indicated some variation in values, but these were not significant enough to be conclusive of variations in structure-change. Tensile strengths at 70°F were 9,300 and 10,800 psi and at 3000°F were 18,600 and 16,600 psi. Modulus at 70°F for all four specimens ranged from 6.47×10^6 to 8.09×10^6 psi. Density ranged from 1.670 to 1.677 gm/cm^3; axial velocity from 0.4026 to 0.4682 in./μsec (mean and standard deviation for all specimens from the 3DCC Arcs were 0.4382 in./μsec and 0.0251 in./μsec); circumferential velocity ranged from 0.3669 to 0.4034 in./μsec (mean and standard deviation for all specimens were 0.3825 in./μsec and 0.0090 in./μsec). Open porosity ranged from 11.2 to 11.7 percent indicating a slight increase over specimens from the 2.20 and 1.64 kilotaps impulse levels. For this arc structure-change and retained properties varied but the degree of change was relatively uniform.

Increased structure-change (over 3.36 kilotaps) was detected by radiography at 5.37 kilotaps for Arc 8-AR-1, Figure 109. Increased, continuous circumferential low-absorptive alignments were indicated at 0.1, 0.2, 0.3, and 0.4 in. from the rear face. Again, a slight increase in intensity was indicated toward the ends of the arc. Radiographic results on specimens indicated several gross low-absorptive alignments (cracking). Distribution of cracking from specimen to specimen was fairly consistent with the widest

single indication being in Specimen 8-AR-1-C4C at 0.2 in. from the rear face. Mechanical results indicated similar strengths for the respective evaluations at 70°F and 3000°F with variations in modulus. At 70°F, Specimen 8-AR-1-C2C had a normal modulus of 9.0 x 10^6 psi, and Specimen 8-AR-1-C3C had a lower value of 4.86 x 10^6 psi. At 4500°F, Specimen 8-AR-1-C1C had a modulus of 2.24 x 10^6 psi, and Specimen 8-AR-1-C4C had a decreased value of 1.65 x 10^6 psi. NDT monitors indicated no variation in structure-change among the specimens. Density ranged from 1.651 to 1.662 gm/cm^3 (mean and standard deviation from all specimens from the 3DCC Arcs were 1.667 and 0.005 gm/cm^3); radial velocity ranged from 0.2014 to 0.2144 in./μsec (mean and standard deviation of all specimens were 0.2023 and 0.0100 in./μsec); circumferential velocity ranged from 0.3785 to 0.3914 in./μsec (mean and standard deviation of all specimens were 0.3825 and 0.0090 in./μsec). Open porosity ranging from 19.5 to 20.0 percent also, indicating a uniform structure for these specimens. For this arc, structure-change was extensive but rather uniform.

In summary, there was more gross structure-change observable visually at the circumferential ends of the arcs but damage was basically uniform in the axial direction, particularly at higher impact levels. One could assess the apparent structure-change by looking at the arcs axially and have a fairly good impression of structure-change internally . If one looked in the circumferential direction, the structure-change would erroneously appear more severe.

FELT CC

Radiographs and visual inspections on Plate 12-F-15 (1.21 kilotaps) indicated no structure-change (cracking). Mechanical and NDT monitor results indicated similar results for all specimens and therefore uniform structure.

For Plate 12-F-16 (1.70 kilotaps) visual and radiographic inspections on the plate and specimens from the plate indicated no structure-change. Radiography revealed low-absorptive alignments near the rear face in the plate which suggested cracking; however, visual inspection of the specimens later did not confirm this. The NDT monitor and mechanical results for the specimens were similar with one exception. Specimen 12-F-16-T2A (3000°F) had a high modulus value of 1.85 x 10^6 psi and a low strain-to-failure of 3.0 x 10^{-3} in./in. For comparison, Specimen 12-F-16-T3A (3000°F) had a lower modulus of 1.23 x 10^6 psi and a higher strain-to-failure of 6.6 x 10^{-3} in./in. The strengths were the same at 3,800 psi. Material variability as indicated by the low-absorptive areas may account for these differences.

For Plate 12-F-1 (2.430 kilotaps) visual and radiographic inspections on the plate revealed no structure-change; however, Partek penetrant inspection revealed hairline, aligned cracking in two opposite edges. This is important since it is near the design limit, even though this plate was "different." Post-mechanical, visual and penetrant inspections on the specimens revealed some mid-thickness hairline cracks aligned axially. In the outer Specimens, 12-F-1-C1A and -C3A, these cracks extended away from the fractured area and near the restrained base of the specimen but were not found in the center Specimen, - C2A. Recall that the center Specimen, 12-F-1-C2A, was not fractured due to excessive strain and overheating of the pushrods. NDT monitor and mechanical results on specimens indicated uniform structures through the bulk plate. Even though this may have been a "nonrepresentative" plate, circumferential cracks were found in both the plate and specimens suggesting uniformity across the arcs.

Visual inspection on the Plate 12-F-13 (3.07 kilotaps) detected hairline cracking at 0.15 in. from the rear face on one edge. No additional structure-change was revealed by radiography. On specimens from this plate visual inspections indicated no cracking, but radiography indicated several short, low-absorptive alignments-cracking suspected. NDT monitors and mechanical results were similar for the specimens indicating uniform structure. Thus structure-change in terms of circumferential cracks was rather uniform across the arcs.

On the Plate 12-F-10 (3.44 kilotaps) visual inspection revealed aligned and hairline cracking in two edges located about 0.2 in. from the rear face. Radiography revealed that this cracking extended nearly the full length of the plate. Liquid penetrants detected that the hairline cracking extended into the third edge. Visual inspection on specimens removed from this plate revealed that the cracking extended completely through all four specimens. A sketch showing these results is included as Figure 110. The NDT monitor and mechanical results were similar for all the specimens, also indicating uniform distribution of structure-change. Structure-change was rather uniform across this plate.

Characterization of distribution in Plate 12-F-11 (4.14 kilotaps) was similar to Plate 12-F-10 except that cracking was more severe. Gross through cracking in all four specimens was revealed by visual inspection, Figure 111. Radiography revealed gross cracking running the full length of Specimen 12-F-11-C1A and about 80 percent of the length of the other three specimens, Figure 112. Hairline cracking extended beyond the gross cracking

in these three specimens for the remaining 20 percent of the specimen length. Mechanical evaluations indicated similar results and uniform distribution of structure-change. NDT monitors also indicated similar results except for ultrasonic transmission in Specimen 12-F-11-C1A whose value was high at 24 added dB. Values for the other three specimens ranged from 16 to 18.5 added dB.

In summary, the structure-change was rather uniform across the plates being perhaps more severe on the circumferential ends and slightly less severe on the axial ends. Circumferential cracks were found near 2.5 kilotaps and definitely above 3 kilotaps. Criteria for this material may be small circumferential cracks if they are "extended" by "structural" loads during shock loading or if they can "turn" and "run" in temperature-stress loading.

AVCO R6300

No structure-change was indicated by any of the data for Arc 10-AR-4 (0.49 kilotaps). Visual inspection revealed occasional, short (~0.10 in.) hairline cracks in Arc 10-AR-7 (1.57 kilotaps). Radiography of the arc and of specimens from the arc did not reveal any structure-change. The NDT monitors did not show significant variation among the specimens. The mechanical properties, however, showed a difference in compressive strength between the two circumferential specimens. The strengths were 28,800 psi for Specimen 10-AR-7-C3C and 21,000 psi for Specimen 10-AR-7-C4C. Since there were no additional indications of more structure-change for Specimen 10-AR-7-C4C than for the other three specimens from this arc, it cannot be concluded that the difference in strength represents nonuniform structure-change. Visual inspection of specimens from this arc indicated hairline cracking in both axial specimens but none in the circumferential specimens. These visual results on the specimens indicate end to end distribution. Additional indications were not available.

None of the data for Arc 10-AR-6 (1.66 kilotaps) indicated any structure-change.

Visual inspection of Arc 10-AR-3 (1.90 kilotaps) revealed aligned, hairline cracking in the edges viewed axially but this did not extend to the circumferential ends of the arc. Radiographic inspection of this arc revealed occasional low-absorptive alignments which correlated with the visual hairline cracking.

Visual inspection of the specimens from this arc showed hairline cracking all around both axial specimens at about 0.10 in. from the inner surface and in the circumferential Specimen 10-AR-3-C4C. In Specimen 10-AR-3-C4C the hairline cracking tended to follow a tape wrap lamina. The only positive indication from radiography of the specimens was hairline cracking in Specimen 10-AR-3-C4C, Figure 114. Ultrasonic transmission for Specimen 10-AR-3-C4C was somewhat lower at 26 added dB than for the other three specimens (range 28 to 32 added dB). The other NDT monitors did not indicated variation among the specimens. The compressive strength of Specimen 10-AR-3-C4C was 20,210 psi which was significantly lower than the 27,520 psi strength of Specimen 10-AR-3-C3C. From the above it appears that the most significant structure-change in this arc occurred at the location of Specimen 10-AR-3-C4C which was at the bottom of the arc away from the indexed end.

Visual inspection of Arc 10-AR-1 (1.99 kilotaps) revealed aligned hairline circumferential cracking which covered a greater portion of the arc than on Arc 10-AR-3 but still did not extend to its ends. Even though visually the hairline cracking was more extensive than on Arc 10-AR-3 radiographic inspection did not show any structure-change. Visual inspections on the specimens from this arc revealed hairline cracks on both axial specimens on the ends located at the bottom of the arc and two short axial hairline cracks in the gage section of Specimen 10-AR-1-T1A. Specimen 10-AR-T4C had several hairline cracks which were located in the specimen near the bottom of the arc. The only structure-change revealed by radiography of the specimens was one hairline crack in Specimen 10-AR-1-T4C at about 0.05 in. from the inner surface. The only significant result from the NDT monitor and mechanical evaluations was a slightly low tensile strength for Specimen 10-AR-1-T4C. The strength of this specimen was 7,110 psi compared to 7,420 psi for Specimen 10-AR-1-T3C. In this arc, 10-AR-1, the structure-change appeared to be more severe at the bottom of the arc. Both structure-change and retained properties were reasonably uniform across the arcs except for the bottom edge.

Radiographic inspection of Arc 10-AR-5 (4.04 kilotaps) revealed cracking and hairline cracking to about 0.20 in. from the inner surface with a slight increase in number and severity at the ends of the arc. Visual inspection showed delaminations along and across the tape wrap laminae. As viewed from the ends of the arc the cracking at the top of the arc tended to remain generally parallel to the inner surface, Figure 115. At the bottom of the

arc the cracking tended to follow the tape wrap laminae and resulted in occasional material removal. The structure-changes seemed to be more severe at the corners. Radiographic inspection of Specimen 10-AR-5-C1A, Figure 113, showed severe cracking over the full length which was more severe at the top than in the center and most severe at the bottom of the arc. On Specimen 10-AR-5-C2A the pattern was the same as for Specimen 10-AR-5-C1A but the overall severity was less. Specimen 10-AR-5-C3C revealed multiple hairline cracking to a depth of about 0.20 in. from the inner surface, Figure 114. On Specimen 10-AR-5-C4C the cracking or delamination was severe. Visual inspection of the specimens coincided with the radiographic inspection results. Compressive strength measurements agreed well with the visual and radiographic results. The specimen with the more severe structure-change had the lower strength. Of the NDT monitors only ultrasonic transmission agreed with the visual and radiographic results. The severe structure-changes in this arc seemed to be confined to 0.20 in. from the inner surface. Structure-change was observed across the arc but cracks were more open at the corners.

The lowest impact level for which an indication of structure-change was found was 1.57 kilotaps (Arc 10-AR-7) where a significantly lower compressive strength was observed for the circumferential specimen nearest the bottom of the arc. Visual inspection of specimens from this arc indicated hairline cracking at the indexed end of the arc but not at the end where the low compressive strength was observed. At 1.66 kilotaps (Arc 10-AR-6) no structure-change was indicated. At 1.90 kilotaps (Arc 10-AR-3) visual inspection revealed cracking at the indexed end of the arc parallel to the inner surface and opposite the indexed end at the lower surface which followed the tape wrap laminae. Radiographic, strength and ultrasonic transmission data indicated that the most significant structure-change was at the end opposite the indexed end at the lower surface of the arc. At 1.99 kilotaps (Arc 10-AR-1) the overall structure-change seemed to be less severe than at 1.90 kilotaps (Arc 10-AR-3). Visual inspection revealed hairline cracking along the lower surface of the arc which tended to follow the tape wrap laminae. Radiographic and strength data indicated the most significant structure-change at the end of the arc opposite the indexed end at the lower surface. At 4.04 kilotaps (Arc 10-AR-5) visual inspection revealed severe cracking that was more severe at the corners of the arc than at the center of any of the edges. The cracks tended to remain parallel to the inner surface at the top of the arc but generally followed the tape wrap laminae near the lower surface. Radiographic inspection showed the structure-change to be more severe near the lower surface than at the top. Strength and ultrasonic transmission results confirmed the visual and radiographic findings.

In summary, structure-change was not uniform across the arc and seemed to be more severe near the edges. Radially, the damage was more severe at the inner portion. At about 1.5 kilotaps, structure-change (circumferential cracks) became apparent and influenced retained properties. Cracks between fabric layers occurred at about 1.5 kilotaps and across fabric layers at perhaps 4 kilotaps.

AVCO 3D/QP

Characterization of the bulk 3D/QP Arcs indicated structure-change starting with Arc 11-AR-8 (4.58 kilotaps). At this level, occasional bulk delaminations were detected by Partek penetrant only. On specimens from the arc some distribution in structure-change was indicated in that hairline and moderate discontinuous cracking was observed by visual inspection in all edges of Specimens -T1A, -T2A, and -T3C, but more severe cracking was apparent in Specimens -T4C. Radiography, Figures 116 and 117, revealed similar bulk delaminations in -T1A, and -T2A but revealed none in -T3C and -T4C, although visually apparent. NDT monitor and mechanical results indicated similar results for the specimens and uniform structure. Structure-change extended through the arc.

For Arc 11-AR-5 (7.54 kilotaps), visual inspection on the arc indicated apparent bulk delaminations and rear lift. Radiography indicated low-absorptive alignments at mid-thickness over the full length of the arc. On specimens from the arc some distribution in structure-change was indicated in that very slight cracking was observed in Specimens -C2A, -C3C, and C4C, but more severe cracking was apparent down both sides of -C1A. Distribution was further indicated by radiography, Figures 118 and 119, in that delaminations were revealed at mid-thickness for the full lengths of Specimens -C1A, and -C3C and nearly the full length of -C2A. A full-length delamination at mid-thickness was also indicated in Specimen -C4C but bulk delaminations were also dispersed on either side of the major delamination. Again, NDT monitor and mechanical results were similar among the specimens indicating uniform structure-change. Structure-change extended across the arc even though the delaminations opened more at some locations than at others.

For Arc 11-AR-3 (7.95 kilotaps), visual and radiographic inspections on the bulk arc clearly indicated full length mid-thickness delamination and rear lift. Visually, moderate and discontinuous cracking was detected at the middle of all edges of Specimen -T1A. More apparent cracking was observed in both sides of -T2A with no apparent cracking in the ends. Cracking was apparent at mid-thickness in Specimens -T3C and -T4C. Radiography, Figures 116 and 117, indicated mid-thickness delaminations running the full length of all four specimens with the

delaminations in -C4C appearing the least severe. Again, NDT monitor and mechanical results were similar among the specimens indicating uniform structure change. Generally, structure-change was uniform.

For Arc 11-AR-7 (8.61 kilotaps), visual and radiographic inspection on the bulk arc indicated increased full-length mid-thickness delamination with failed radials and rear lift. On specimens from the arc visual inspection indicated severe cracking at mid-thickness of all four specimens. Radiography, Figures 116 and 117, revealed severe full-length mid-thickness delaminations in all four specimens with the delamination in Specimen -T2A appearing less severe than -T1A. Mechanical results for the specimens were similar; however, some significant variations in the NDT monitors were measured indicating possible distribution in structure-change. The bulk density for -T4C was 1.542 gm/cm^3 compared to a range of 1.579 - 1.583 gm/cm^3 for the other three specimens; open porosity for -T3C was 9.7 percent compared to a range of 10.4 - 10.6 percent for the other three specimens; radial velocity for all four specimens had an overall range of 0.1793 - 0.1903 in./usec. Structure-change was generally uniform.

For Arcs 11-AR-1 and 11-AR-2 (9.01 kilotaps), visual and radiographic inspections revealed full-length mid-thickness delaminations and rear lift somewhat similar to 11-AR-7 above except the delamination in 11-AR-2 appeared less severe. On specimens from the arcs visual inspection revealed cracking in the middle of both edges over the full length of Specimens 11-AR-1-C1A, 11-AR-2-C1A, and 11-AR-2-C2A and nearly the full length of 11-AR-1-C2A. For Specimen 11-AR-2-C4C, cracking was apparent in the middle of all edges with one edge having more pronounced cracking. Except for apparent cracking in one end each of 11-AR-1-C4C and 11-AR-2-C3C, only slight cracking was evident in the remaining specimens. Radiography, Figures 118 and 119, indicated severe, full-length mid-thickness delaminations in all of the specimens. The NDT monitor and mechanical results gave some indication of distribution in structure-change; however, the low and high values of the respective measurements did not necessarily correlate with each other. Values for circumferential compressive strength for Specimens 11-AR-1-C3C and -C4C were 10,760 and 13,060 psi and for Specimens 11-AR-2-C3C and -C4C were 10,360 and 13,090 psi. Values for axial moduli for Specimens 11-AR-2-C1A and -C2A were 1.41×10^6 and 2.05×10^6 psi. Circumferential moduli values for 11-AR-2-C3C and -C4C were 1.86×10^6 and 2.84×10^6 psi. The bulk density for 11-AR-1-C4C was 1.534 gm/cm^3 compared to a range of 1.556 - 1.560 for the other three specimens from this arc. The bulk density for 11-AR-2-C3C was 1.581 compared to a range of 1.564 - 1.568 gm/cm^3 for the other three specimens from Arc 11-AR-2. Radial velocity for the four specimens removed from Arc 11-AR-1 ranged from 0.1707

(-C4C) to 0.1895 in./μsec (-C3C); for the four specimens removed from Arc 11-AR-2 the range was from 0.1778 (-C4C) to 0.1936 in./μsec (-C2A). Structure-change was uniform.

For Arc 11-AR-6 (9.88 kilotaps), visual and radiographic inspections revealed increased full-length mid-thickness delaminations with failed radials and increased rear lift. On specimens from the arc severe cracking was observed in the middle of all edges of Specimen -T1A and in three edges of Specimen -T2A. Very severe cracking was apparent at the middle of all edges in Specimens -T3C and -T4C. Radiography, Figures 116 and 117, indicated gross full length mid-thickness delaminations in all four specimens. NDT monitor and mechanical results indicated some distribution of structure-change. Again, the low and high values of the respective measurements did not necessarily correlate each other. Values for circumferential tensile strength for Specimens -T3C and -T4C were 24,330 and 18,670 psi. Values for axial moduli for Specimens -T1A and -T2A were 2.62×10^6 psi and 3.25×10^6 psi. Bulk density ranged from 1.517 to 1.543 gm/cm^3; open porosity ranged from 11.9 to 13.5 percent; radial velocity ranged from 0.1693 to 0.1881 in./μsec. Structure-change was uniform.

In summary the cracks seemed more open at the edges of the arcs but the cracks (and property degredation) persisted to the center. The difference was in the degree of opening of the cracks. Cracks seemed "randomly uniform" in that they would close and then open through an arc. Extensive delaminations were found at 4.50 kilotaps.

OUTER - 3DC/QP (MATERIAL #15A)

Characterization of outer material of the 3DC/QP bulk arcs indicated structure-change starting with Arc 15-AR-3 (4.09 kilotaps). At this level, bulk delaminations with a failed radial were apparent by visual inspection. On the axial specimens from the arc radiography, Figures 123 and 124, indicated bulk delaminations and short, volume oriented low-absorptive alignments indicating volume expansion. The circumferential specimens were not considered revealing. The mechanical results were reasonably consistent indicating uniform structure-change distribution. NDT monitor results from bulk density and open porosity measurements indicated some slight variation. The ranges for these data were 1.351 - 1.366 gm/cm^3 and 8.0 - 8.4 percent. Radial measurements of velocity and ultrasonic transmission were not revealing because of specimen thickness variations. Structure-change was uniform.

For Arc 15-AR-5 (4.69 kilotaps) outer, visual inspection of the bulk arc indicated increased cracking. Radiography, Figure 120, revealed a 0.4 in. long low-absorptive alignment in the central region. On axial specimens from the arc radiography indicated increased (over specimens from 15-AR-3) short, volume oriented low-absorptive alignments, Figure 121. In the circumferential specimens, however, full-length low-absorptive alignments were apparent, Figure 122. The mechanical results showed some wide variations. Specimens -T1A and -T2A had values of axial tensile strength of 8,650 and 4,900 psi and moduli of 3.3×10^6 and 0.84×10^6 psi. Specimens -T3C and-T4C had values of circumferential tensile strength of 1,340 and 2,290 psi. NDT monitor values of open porosity ranged from 7.5 to 8.3 percent. Structure-change was uniform.

For Arc 15-AR-6 (5.18 kilotaps) outer, visual and radiographic inspections of the bulk arc indicated mid-thickness delaminations particularly near the ends of the arc, Figure 120. On specimens from the arc, radiography indicated aligned cracking in all specimens. Cracking appeared more severe in Specimens -C2A and -C3C than in -C1A and -C4C. Similar to AVCO 3DQP (Material 11), some of the mechanical and NDT monitor results indicated structure-change distribution; however, the low and high values of the respective measurements did not necessarily correlate with each other. From the mechanical results, Specimens -C3C, and -C4C had values of circumferential strength of 6,410 and 4,580 psi. As mentioned above the radiographs of these specimens showed Specimen -C3C to have the more severe cracking. From NDT monitor results, bulk density ranged from 1.330 to 1.344 gm/cm^3, and open porosity ranged from 8.8 to 9.8 percent. Structure-change and retained properties were uniform except for -C4C where the cracks seemed milder but properties were lower.

For Arc 15-AR-4 (6.06) kilotaps) outer, visual and radiographic inspections of the bulk arc indicated mid-thickness delamination with failed radials, Figure 120. Radiography further indicated volume, low-absorptive alignments extending out from the mid-thickness delamination. On specimens from the arc radiography indicated multiple delaminations in all four specimens with the axial specimens indicating a slight increase in structure-change, Figures 122 and 123. The mechanical results indicated that the circumferential strength was essentially zero while the axial strength was about 1,250 psi. NDT monitors indicated some variations in density and open porosity. Bulk density ranged from 1.261 to 1.281 gm/cm^3, and open porosity ranged from 9.9 to 11.6 percent with the two axial specimens having the highest values. Overall, structure-change must be considered uniform.

For Arcs 15-AR-7 and 15-AR-8 (6.50 and 6.54 kilotaps) outer, visual and radiographic inspection indicated full-length mid-thickness delaminations with failed radials, Figure 120. Volume cracking and low-absorptive alignments also extended out from the major delaminations. On specimens from Arc 15-AR-7, radiography indicated severe volume low-absorptive alignments in Specimens -C1A and -C2A, Figure 123, and severe mid-thickness delaminations in Specimens -C3C and -C4C, Figure 124. From Arc 15-AR-8, very severe volume low-absorptive alignments in Specimens -C1A, and -C2A and less severe (than 15-AR-7-C3C and -C4C) mid-thickness delaminations with volume low-absorptive alignments located outside the major delaminations in Specimens -C3C and -C4C were revealed by radiography. Mechanical and NDT monitor results indicated structure variations. For Arc 15-AR-7, values of axial compressive strength for Specimens -C1A and -C2A were 4,820 and 6,000 psi. Values of circumferential compressive strength for Specimens -C3C and -C4C were 2,820 and 3,670 psi. From the NDT monitor results, bulk density ranged from 1.207 to 1.267 gm/cm^3, and open porosity ranged from 9.6 to 11.1 percent. For Arc 15-AR-8, the only variation in compressive strength was in the circumferential direction for Specimens -C3C and -C4C which had values of 5,940 and 4,340 psi. From the NDT monitor results, bulk density ranged from 1.239 to 1.288 gm/cm^3, and open porosity ranged from 8.6 to 9.6 percent. Previously for the other impact levels of this material, radial velocity was not discussed as a monitor for structure distribution primarily because of differences in thicknesses of specimens and because of uniformity in values. For Arc 15-AR-8, however, Specimen -C2A had a velocity of 0.1626 in./μsec compared to the range of 0.1803 to 0.1835 in./μsec for the other three specimens. Structure-change and retained properties were uniform except for 15-AR-7-C1A and 15-AR-8-C3C where structure-change seemed similar but properties differed.

In summary, structure-change did not appear uniform circumferentially and appeared to be more severe between the center and the ends of the bulk arc. Cracking without regard for appearance was rather uniformly distributed. Major structure-change to Material #15 occurred near the middle (radially) of the outer material. Structure-change was incurred at the first impulse level (4.09 kilotaps) which influenced retained properties. This change consisted of bulk delaminations in the outer material by visual and radiographic inspections. At higher impact levels mid-thickness delaminations with volume cracking were incurred.

INNER - 3DC/QP (MATERIAL #15B)

Characterization of the inner material from the 3DC/QP arcs indicated that structure-change was confined primarily near the inner (rear) surface starting with Arc 15-AR-5 (4.69 kilotaps). At this level, visual inspection of the bulk arc revealed cracking near the rear face to a depth of about four plies. Radiography, Figure 120, indicated an 0.15 in. long low-absorptive alignment at one end located about three plies behind the rear face. With increased impulse loadings on Arcs 15-AR-6 and -4 (5.18 and 6.06 kilotaps), increased cracking was apparent near the rear face. For Arcs 15-AR-7 and -8 (6.51 and 6.54 kilotaps), the cracking near the rear face was more aligned. On specimens from the arcs, radiography did not indicate structure-change below 6.51 kilotaps (Arcs 15-AR-7 and -8). At these levels, low-absorptive alignments were revealed near the rear face. The severity of these alignments were considered similar.

The nondestructive monitor and mechanical results did not in general show nonuniform distribution of structure-change. Several instances were found where a single value of one of the NDT monitors or mechanical properties differed from the other values for a given arc. In only two instances were there confirming data of nonuniform distribution. At 5.18 kilotaps (Arc 15-AR-6) the circumferential compressive Specimen 15B-AR-6-C4C had low strength, strain-to-failure and radial sonic velocity. These low values were: 14,900 psi (20,250 psi for Specimen 15B-AR-6-C3C), 0.0038 in./in. (0.0073 in./in. for Specimen 15B-AR-6-C3C, 0.1795 in./μsec (0.1820 to 0.1831 in./μsec for the other three specimens). At 6.54 kilotaps the axial compressive Specimens 15B-AR-8-C1A had low strength, bulk density and radial sonic velocity though the delamination seemed typical of the arcs. These low values were: 14,580 psi (21,400 psi for Specimen 15B-AR-8-C2A), 1.519 gm/cm^3 (1.541 to 1.576 for the other three specimens from this arc) and 0.1730 in./μsec (0.1836 in./μsec for Specimen 15-B-AR-8-C2A). In these two cited instances it may be concluded that nonuniformity of structure-change existed in these arcs; at least, there were differences in retained properties.

For the inner portion of the 3DC/QP arcs structure-change was apparent. At the 4.69 kilotap level, cracking near the rear face was revealed. With two exceptions the distribution of structure-change seemed to be uniform over the arcs. For the two exceptions to uniform distribution there was no location which seemed to be more susceptible to structure-change.

The conclusion drawn is that the exceptions were due to random material parameters.

SECTION VI

RESULTS OF PRE-IMPACT NDT EVALUATIONS

The test results for Phase II are given in Tables 37 through 42 and Figures 125 through 180. The presentation of the data according to material follows.

AVCO 3DC/QP

Nondestructive testing consisted of QC inspection of 11 arcs and 6 rings, and based on the QC inspection results, 1 ring was selected for underground FT inspection. The QC results are given in Table 37 and photographs of typical 3DC/QP structure in Figures 125 and 126. Typical structure as revealed by radiography in the radial and axial directions is shown in Figure 127.

No anomalies or problems were apparent. The porosity of the AHCA material was significantly lower than AHP material. Figures 125 and 126 show the comparison between the materials. At the time of this characterization, no problem with the AHCA material was suspected since it was to be an improvement over AHP material by impregnation.

AVCO 3DCP

Nondestructive testing consisted of QC inspection of 22 arcs and 10 rings from which 5 arcs were selected for AHCA FT inspection and 6 rings were selected for underground FT inspection. The results are given in Table 38 and Figures 128 through 134. Typical 3DCP material structure is described in Figures 128 and 129. Photographs depicting the material in the axial and circumferential directions are given in Figure 134. Typical structure as revealed by radiography in the radial and axial directions is shown in Figure 129. No photomicrographs were made on these specimens. However, photomicrographs were subsequently made on AHCA 3DC/QP during the characterization of the damage problem. Photomicrographs on both AHP and AHCA 3DC/QP are given in Appendix M under the discussion of this anomalous structure-change problem.

Similar to AVCO 3DC/QP, this material also had lower porosity than AHP material. In addition, visable resin rich areas along yarns and resin starved areas around radials were detected in the arcs and rings, Figures 130 and 131. The density of the arcs were the same as AHP material at 1.42 gm/cm^3. The density of the rings were slightly less at 1.41 gm/cm^3. Velocity results irom

the 5 FT arcs indicated values similar to AHP for axial velocity at 0.370 in./μsec, but no comparison for radial velocity was available. Radial ultrasonic transmission values ranged from 31 to 32 added dB.

Anomalies detected by visual inspection were of a mechanically induced nature. For Arc 7 of Ring 6, voids and raised axials were detected in the C edge, Figure 132; for Arcs 5 and 6 of Ring 6, chipped corners were apparent; for Ring 2, the outer edge was chipped or crushed at 25°, Figure 133; for Ring 8, an 0.16 inch long area in the top edge was indented, Figure 133; for Ring 10, local areas having high porosity were apparent, Figure 134. Radiography detected no anomalies in the arcs and rings. Typically, various concentrations of circumferential low-absorptive alignments were revealed by radiography in the axial direction for all the specimens. Ring 1 was probably the only exception as no significant variations were detectable. In addition for the rings, occasional through and part-through thickness low-absorptive alignments along the radials were observed. Such alignments were seen in Ring 3 at 45°, Ring 5 at 10-45° and 340°, Ring 9 at 135°, 190°, and 350°, Ring 10 at 240°, and Ring 12 at 245°.

Based on these inspections of the rings, the locations of most uniform material sites selected were as follows:

Ring No.	Most Uniform Material Centerline
1	Any
2	270°
3	225°
4	300°
5	255°
8	90°
9	Not Selected
10	45°
11	Not Selected
12	345°

AVCO 3DCP (T400)

Four rings and 4 arcs received QC nondestructive testing. The results are given in Table 39 and Figures 135 through 137. Typical structure revealed by radiography in the radial and axial directions is shown in Figure 135.

Generally, the material was uniform and sound. A background of residual pores or voids and striations were visually apparent in the surfaces and edges. No anomalies were detectable by the visual or radiographic inspection of the arcs. Visual inspection of Ring 3 revealed a circumferential delamination in the outer surface at 330°, voids on the inner surface at 220°, and voids on the bottom edge at 45°. Radiography revealed several concentrations of circumferential low-absorptive alignments in all 4 rings, Figure 136 depicts a typical alignment. The locations of these variations are detailed in Table 39. The only gross concentration of low-absorptive alignments indicated was in Ring 4 at 320-360°, Figure 137.

Based on the inspections of the rings, the locations of most uniform material sites were selected as follows:

Ring No.	Most Uniform Material Centerline
1	180°
2	150°
3	135°
4	240°

AVCO R6300

Nondestructive testing consisted of QC inspection of 18 arcs and 10 rings and FT inspections of 2 rings selected for AHCA and 1 ring selected for underground. These FT rings were selected from the QC rings. The results of the inspections are given in Table 40 and Figures 138 through 148.

The AHCA R6300 material was similar to the AHP material. Typical material structure is described in Figures 138 and 141. Photographs depicting the material are given in Figures 138 and 139. Typical structure as revealed by radiography in the radial and circumferential directions is shown in Figure 140. Photomicrographs at 50X (before reduction) showing microstructure are given in Figure 141. The density for AHP was about 1.33 gm/cm^3; whereas, for AHCA the density was slightly higher ranging from about 1.32 to 1.37 gm/cm^3. Ring 6 having a density of 1.301 gm/cm^3 was the only exception. Also, the AHCA material had higher surface porosity with a size to about 0.02 inch and more extensive aligned residual porosity between the tape wraps than did AHP material, Figures 138 and 142.

Some material anomalies were revealed by visual inspections. In Ring 11 Arc 9, a tape wrap discontinuity was apparent on the inner surface, Figure 143. (This anomally was also indicated by radial X-ray). In Ring 12 Arc 14, a single 0.10 inch long void was apparent on the inner surface, Figure 144. On Ring 7, the bottom inner edge was chipped from 130 to 180° and at 225°, Figure 145.

Some additional material anomalies were indicated by radiography in both the arcs and rings. About half of Ring 11 Arc 8 contained lower density material by radial X-ray, Figure 146. Low-absorptive alignments to about 3/4-inch in length were detected in Ring 11 Arc 9 by radial X-ray (tape wrap discontinuity by visual), Figure 146. Single 0.02 and 0.04 inch low-absorptive areas (voids) by axial X-ray were indicated in Rings 4, 6, and 9. A single 0.04 inch high-absorptive area (inclusion) was also indicated in Ring 6. Various volume oriented low-absorptive areas were indicated in the rings by axial X-ray. Although, these areas were not considered significant, they were avoided in selecting impact center lines.

From the QC inspections, Ring 9 was selected for underground test, and Rings 2 and 4 were selected for AHCA FT testing. The most uniform material sites for the QC rings were selected as follows:

Ring No.	Most Uniform Material Centerline
1	270°
3	55°
5	255°
6	255°
7	180°
8	135°
10	180°

Sketches showing QC and FT NDT inspection results and most uniform material sites on Rings 2 and 4 are given in Figures 147 and 148. Photomicrographs in the axial direction at 50X (before reduction) on FT Rings 2 and 4 were given in Figure 141.

AVCO 3DCC

Nondestructive testing consisted of QC inspection of 11 disc, 10 coupons, and 17 rings and FT nondestructive testing on 2 rings whose selection was based on the QC inspection. In addition, two underground rings were selected from these QC rings. Test results are given in Table 41 and in Figures 149 through 174.

Generally, this material was similar to AHP AVCO 3DCC material. Typical material structure is shown in Figures 149 through 151. Photographs depicting the material viewed in the radial and axial directions are given in Figure 149. Typical structure revealed by radiography in the radial and axial directions is shown in Figure 150. Photomicrographs at 50X (before reduction) showing microstructure are given in Figure 151. Debonds were generally similar to AHP except for the 1109-35 rings. Debonds in this material were more severe than AHP, Figure 152. Values of density and radial velocity for the AHP material were lower, 1.61 - 1.69 gm/cm^3 and 0.180 - 0.230 in./μsec for AHP compared to 1.63 -1.75 gm/cm^3 and 0.223 - 0.267 in./μsec for AHCA.

Single visual anomalies were detected in Discs 1 and 11. In Disc 1, visual inspection revealed that the inner edge had been bumped at 270° resulting in local material loss, Figure 153. In Disc 11, both visual and radiographic inspections revealed a through-thickness wrinkle, Figure 153. No visual anomalies were revealed in the coupons and the 1109-35 rings. Visual anomalies were detected in Rings 2B and 4B. In Ring 2B, a single 0.15 inch x 1 ply deep depressed area was located in the outer surface at 0° and about 0.20 inch from the bottom edge, Figure 154. In Ring 4B, two surface flaws were revealed. On the bottom edge at 180°, a machining error was made resulting in a surface mismatch at this location, Figure 155. On the outer surface at 300° next to the bottom edge, a local area measuring about 1.2 x 0.2 inch contained loose and missing pieces of axials and circumferentials, Figure 156.

The largest single visual debond detected in this group of specimens was found in Ring 1A. The debond had a length of about 3-1/2 inches and was located in the bottom edge from 150° to 210°, Figure 157. Radiography which did not reveal the debond indicated that the debond was only surface oriented.

Anomalies were revealed by radiography in Disc 11 and Coupon 5. In both cases, single through-thickness wrinkles were apparent. In addition to determining material anomalies, radiography was used for evaluating debonds. In the discs and coupons, the major debonds were continuous and were located about 0.10, 0.25, 0.35, and 0.40 inches from the inner edge (measurements on X-ray image). Axial radiographs on Rings 1 through 11 and 1A through 4B indicated a background of debonds with more severe ones also occuring. These were noted, and the locations of the most uniform material sites were selected away from the severest debond locations. Sketches showing these radiographic results are given in Figures 158 through 174. No material anomalies were detected in the rings. Except for the large visual debond located in the bottom edge, Ring 1A was considered uniform throughout.

Based on the QC inspections, Rings 2 and 3 were selected for underground test, and Rings 1 and 5 were selected for AHCA FT testing. The FT test results for these rings are depicted in Figures 158 through 160 and 162. The radiographic results for the QC rings are given in Figure 161 and Figures 163 through 174. The most uniform material sites selected were as follows:

Ring No.	Most Uniform Material Centerline
1109-35-1	230°
1109-35-2	315°
1109-35-3	320°
1109-35-4	315°
1109-35-5	30°
1109-35-6	270°
1109-35-7	315°
1109-35-8	220°
1109-35-9	155°
1109-35-10	315°
1109-35-11	270°
1A	Any
2A	165°
1B	135°
2B	225°
3B	180°
4B	105° and 270°

Photomicrographs in the axial direction on FT Rings 1109-35-1 and 1109-35-5 are given in Figure 151.

SANDIA FELT CC

Nondestructive testing consisted of QC inspection of 20 rings and FT inspection of 2 rings selected from the QC rings. Test results are given in Table 42 and Figures 175 through 180.

The Felt CC material supplied as rings for this program was similar to the AHP material which was supplied as cone plates. For AHP, the values of bulk density and radial velocity had ranges of 1.70 - 1.90 gm/cm^3 and 0.112 -1.24 in./μsec. This was comparable to ranges of 1.76 - 1.85 gm/cm^3 and 0.101 - 0.110 in./μsec for AHCA with the velocity values for AHCA material being based on measurements from the 2 FT rings only. Visually, the materials were similar except that AHCA indicated coarser needling and no discolorations in the edges. Residual porosity to about 0.012 inch resulting from needling was background. Typical AHCA material structure is described in Figures 175 through 177. Photographs depicting the material viewed in the radial and axial directions

are given in Figure 175. Typical structure revealed by radiography in the axial direction is shown in Figure 176. Photomicrographs at 50X (before reduction) showing microstructure are given in Figure 177.

No visual material anomalies were determined. However, during the polishing of FT Rings 2N-2 and 3N-2 for photomicrographs, both rings received slight surface scrapes in the polished edges. The locations of these scrapes were 245° - 260° for 2N-2 and 75° - 90° for 3N-2. Neither of the scrapes were considered severe enough to influence the performance of the material.

Radiography in the axial direction revealed significant, single circumferential low-absorptive alignments in Rings 4P-2 and 7P-2. In both cases, the signature was a single circumferential crack. The locations of these anomalies were 315° - 330° for 4P-2 and 335° - 345° for 7P-2. A printed radiograph showing the anomaly in 4P-2 is given in Figure 178. The anomaly in 7P-2 as radiographed could not be printed for reporting.

FT nondestructive characterization was conducted on Rings 2N-2 and 3N-2. The results of these inspections are depicted in Figures 179 and 180. For Ring 2N-2 liquid penetrants indicated void clusters to 0.2 inch in size in the outer surface at 55°, 295°, and 330°, Figure 179. Also, a mechanical surface indentation was indicated in the outer surface at the 0° orientation. No anomalies were detected by liquid penetrants in 3N-2. The velocity results were considered uniform for this material, Figures 179 and 180. Radial ultrasonic transmission indicated no variations greater than $\pm$ 1dB. Centerlines of most uniform material sites selected were 225° for 2N-2 and 270° for 3N-2. Photomicrographs in the axial direction are given in Figure 177.

MOE EVALUATIONS ON FULL TREATMENT NDT RINGS

The results of the MOE evaluations on the 6FT NDT rings (two each of 3DCC, Felt CC and R6300) are shown in Table 43. Modulus values were determined from three different measurements: (1) deflection measurements from ring flexure, (2) strain gage measurements from ring flexure and (3) strain gage measurements from hydrostatic compression. The first two values represent average flexure moduli and the third an average compressive modulus. The flexural moduli were generally less than the compressive modulus for the same ring.

The flexural moduli for the 3DCC rings 3109-35-1 and -5 were 9.4×10^6 psi and 10.0×10^6 psi based on strain gage measurements and 10.6×10^6 and 11.1×10^6 psi based on deflection measurements. The compressive moduli from the hydrostatic compression evaluations were 13.7×10^6 and 14.4×10^6 for rings -1 and -5. These compressive moduli seem somewhat high when compared to the range of circumferential modulus values of 7.66×10^6 to 10.4×10^6 which was measured on compressive specimens of the AHP project. The difference between the AHP and AHCA data may be due to the differences in specimen configuration.

The flexural moduli for the Sandia Felt CC rings 2N-2 and 3N-2 were 1.22×10^6 and 1.24×10^6 psi based on strain gage measurements and 1.34×10^6 and 1.38×10^6 psi based on deflection measurements. Hydrostatic compression gave values of the compressive moduli of 1.91×10^6 and 1.73×10^6 psi. Circumferential compressive moduli from the AHP program ranged from 1.30×10^6 to 1.91×10^6 psi.

The flexural moduli for the R6300 rings 2 and 4 were 1.47×10^6 and 1.50×10^6 psi based on strain gage measurements and 1.62×10^6 and 1.68×10^6 psi based on deflection measurements. Compressive moduli from the hydrostatic compression evaluations were 1.81×10^6 and 1.62×10^6 psi. The range of circumferential compressive moduli from the AHP program was 1.36×10^6 to 1.57×10^6 psi.

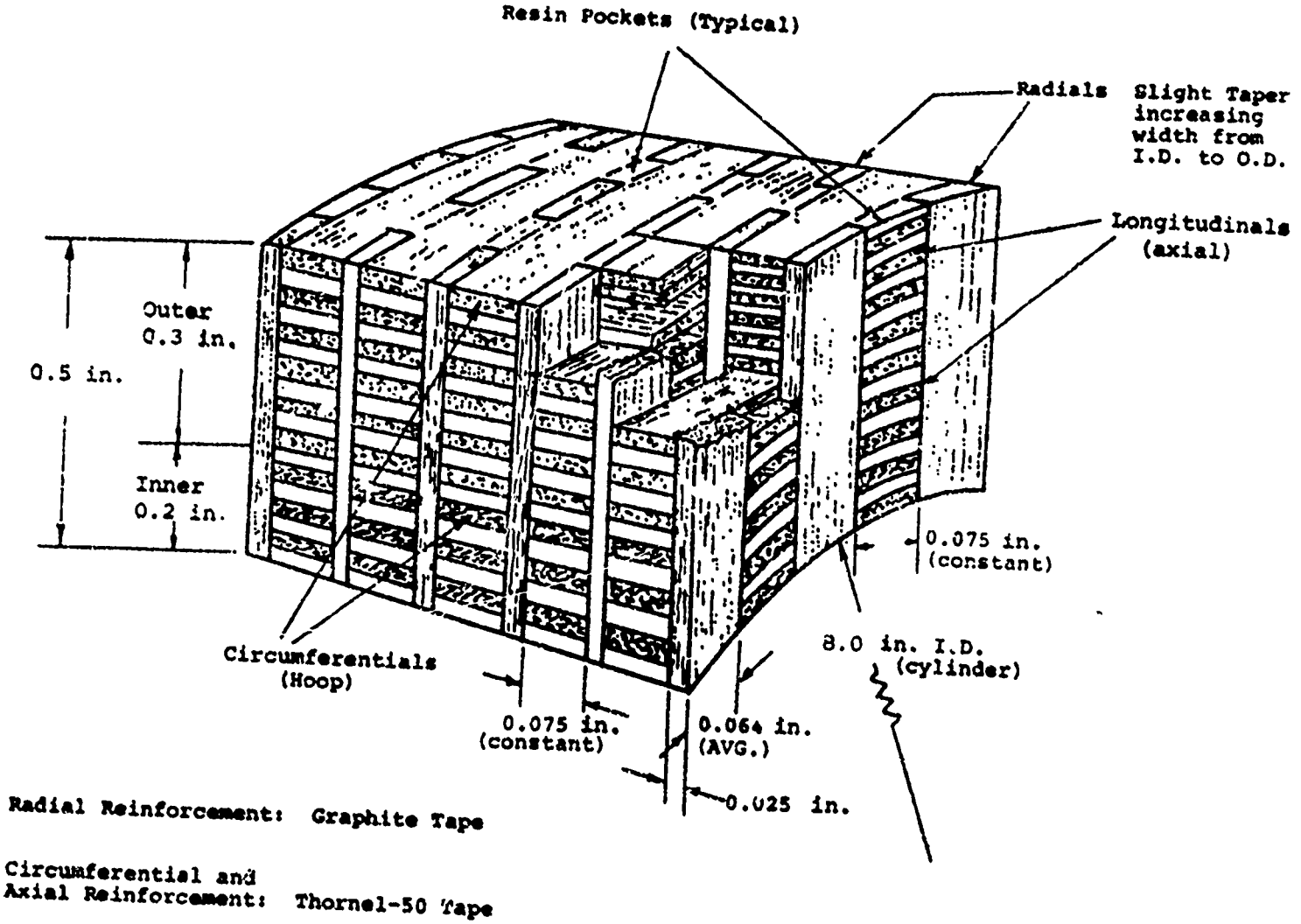
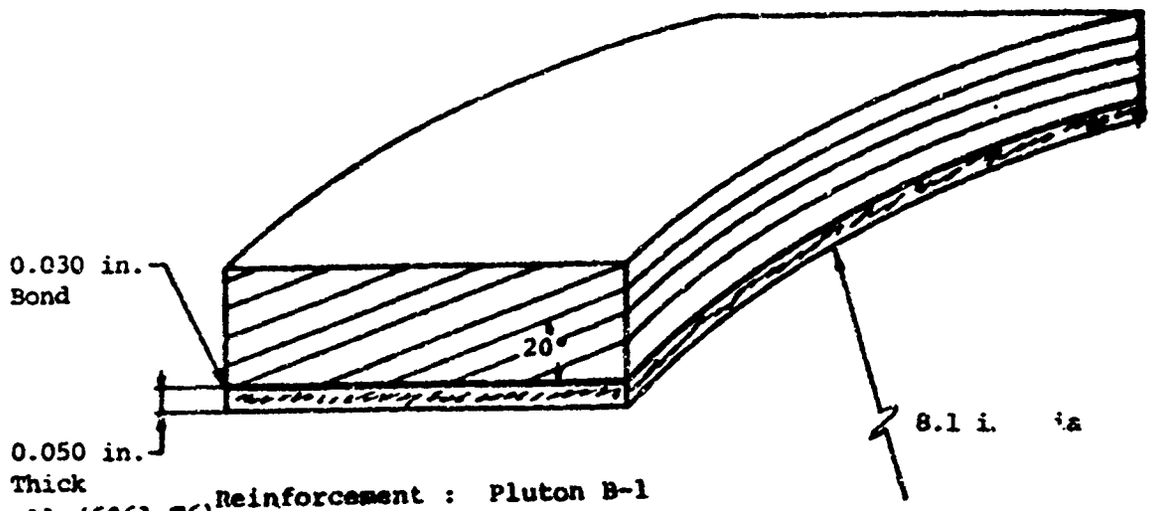


Figure 1. Construction of AVCO 3DCC



Aluminum understructure for
structural response
Sylgard 182 RTV Bond.

Figure 2. AVCO R6300 - Single Phase 2D, 20-Degree Angle Tape Wrap CP with Al (6061-T6) Backing Plate

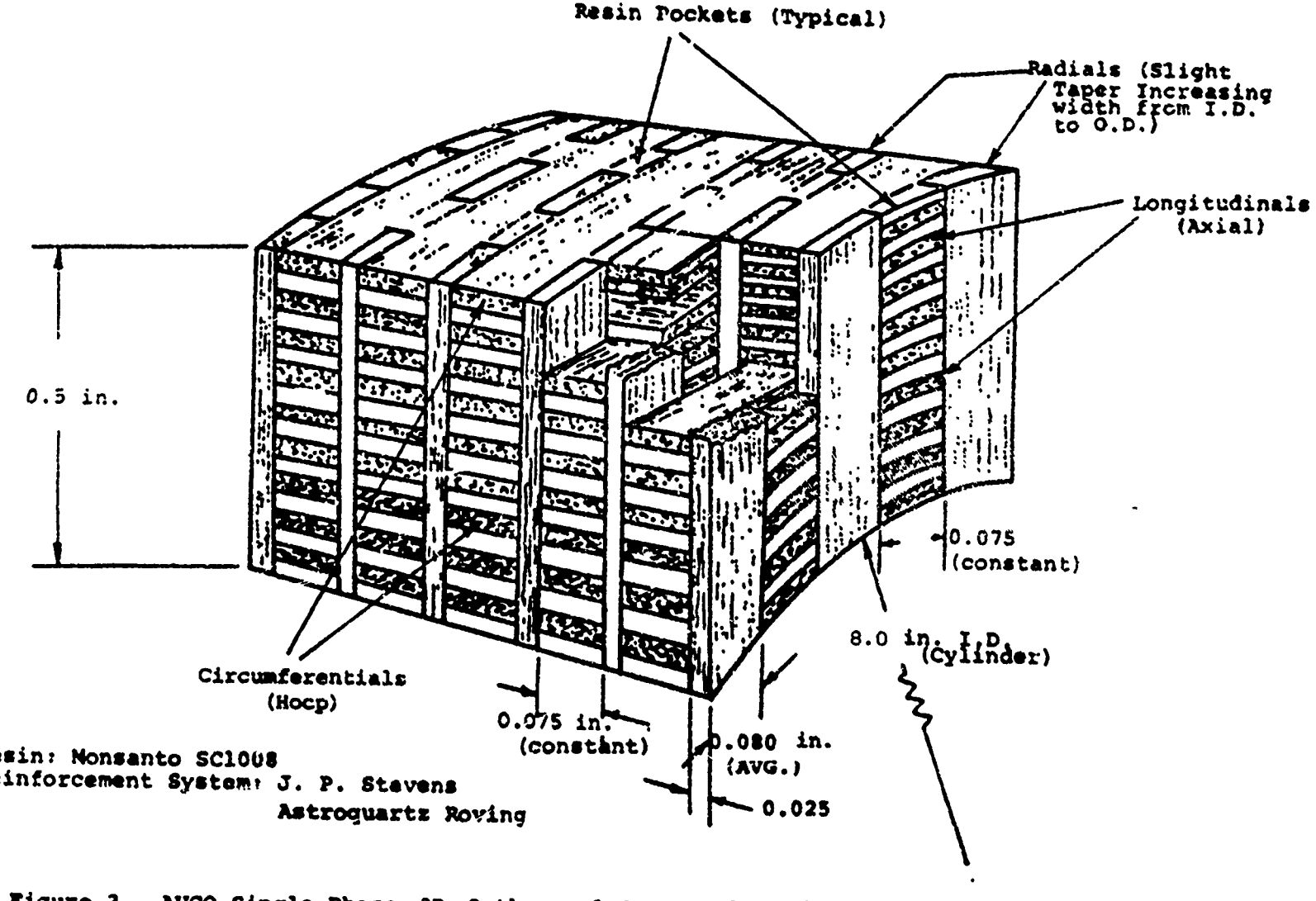


Figure 3. AVCO Single Phase 3D Orthogonal Quartz-Phenolic - Material #11

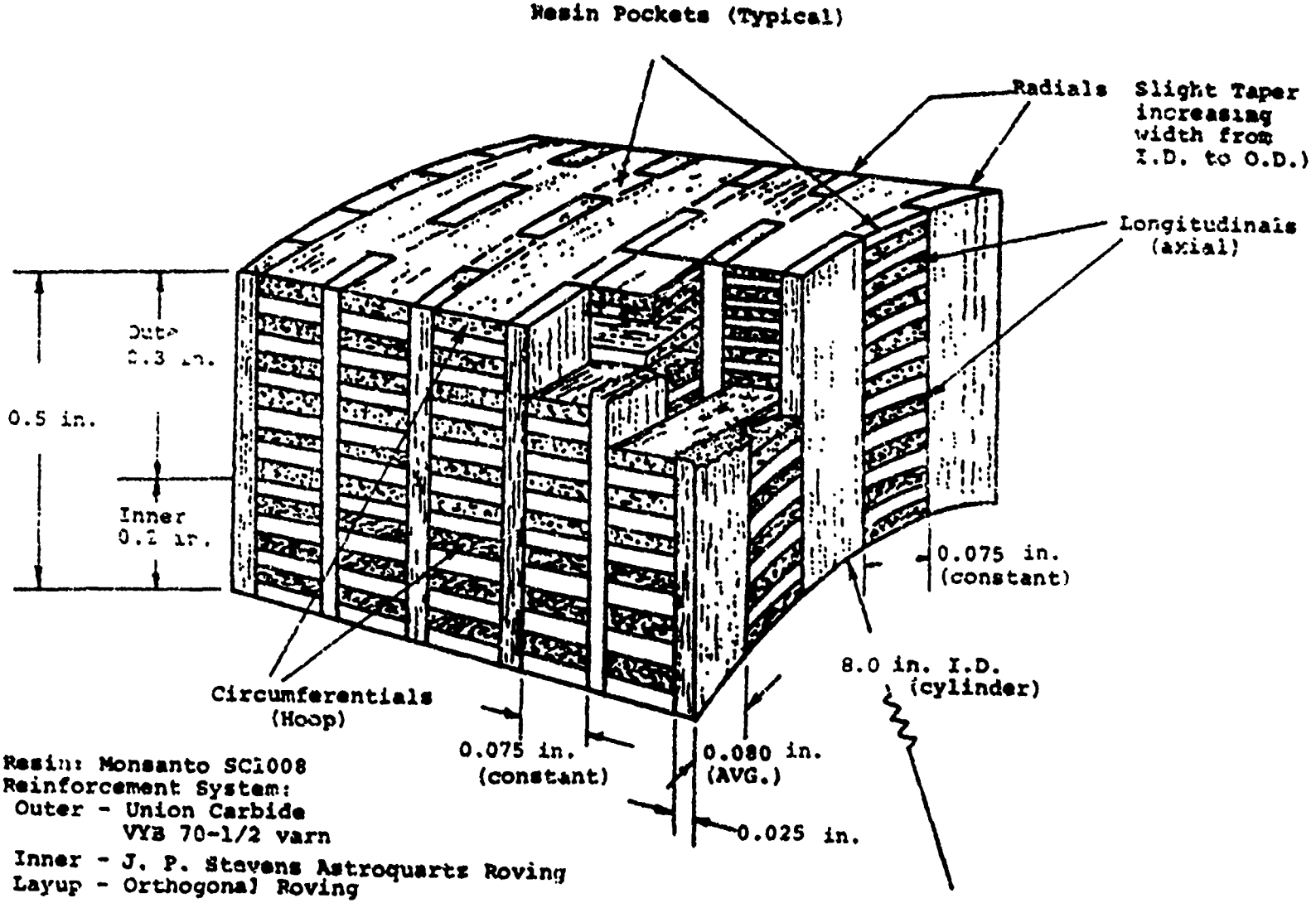


Figure 4. AVCO Two Phase 3D Orthogonal Quartz-Phenolic - Material #15

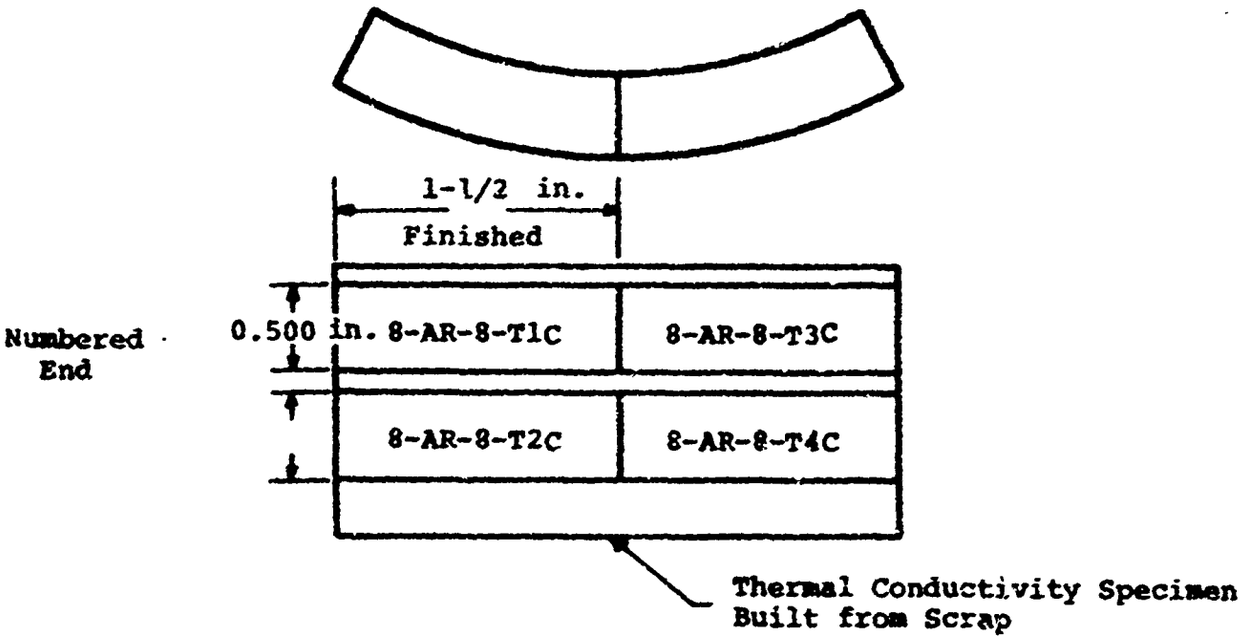


Figure 5 . Cutting Plan for Removing Circumferential Tensile Blanks from 3D Carbon-Carbon Impacted Area 8-AR-8, 8-AR-2 and 8-AR-5

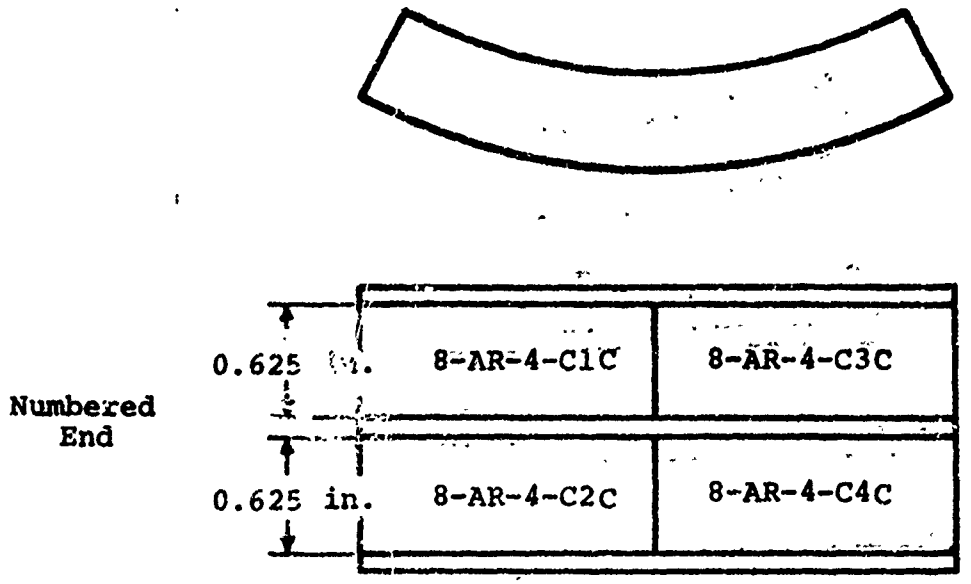


Figure 6. Cutting Plan for Removing Circumferential Compressive Blanks from 3D Carbon-Carbon Impacted Arcs 8-AR-4, 8-AR-7 and 8-AR-1

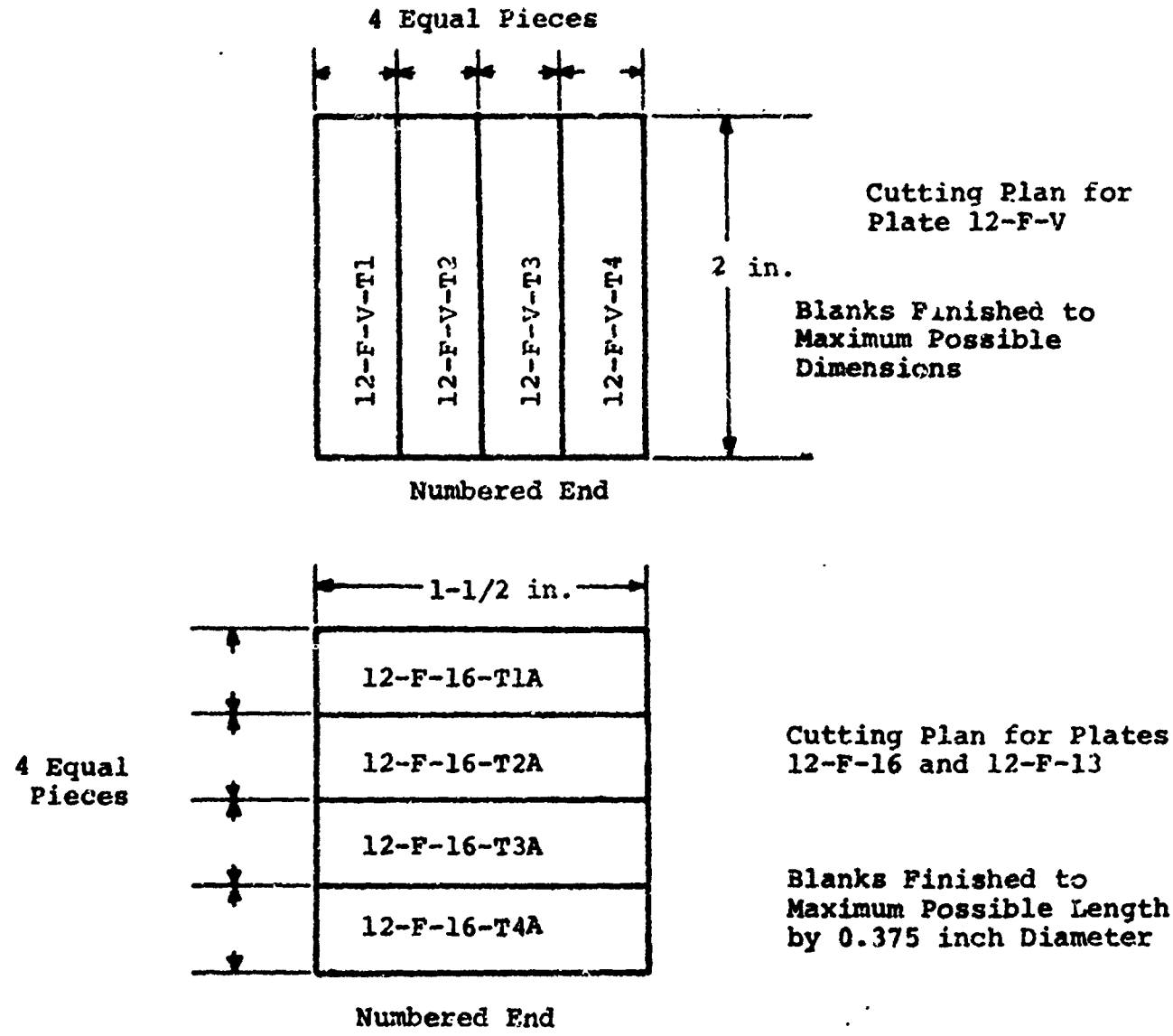


Figure 7. Cutting Plan for Removing Axial Tensile Blanks from Felt Carbon-Carbon Impacted Plates 12-F-V, 12-F-16 and 12-F-13

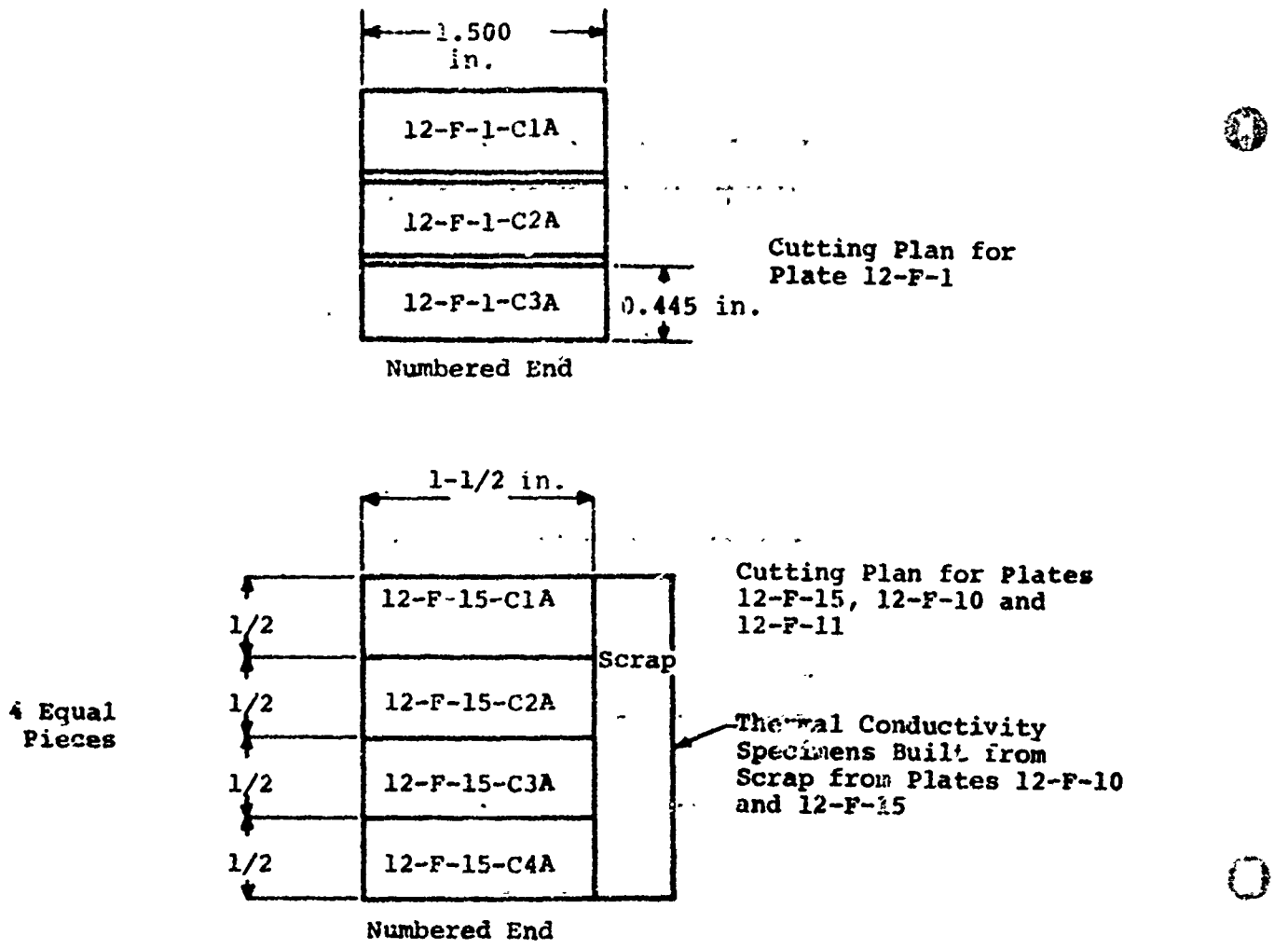


Figure 8. Cutting Plan for Removing Axial Compressive Blanks from Felt Carbon-Carbon Impacted plates 12-F-1, 12-F-15, 12-F-10, and 12-F-11

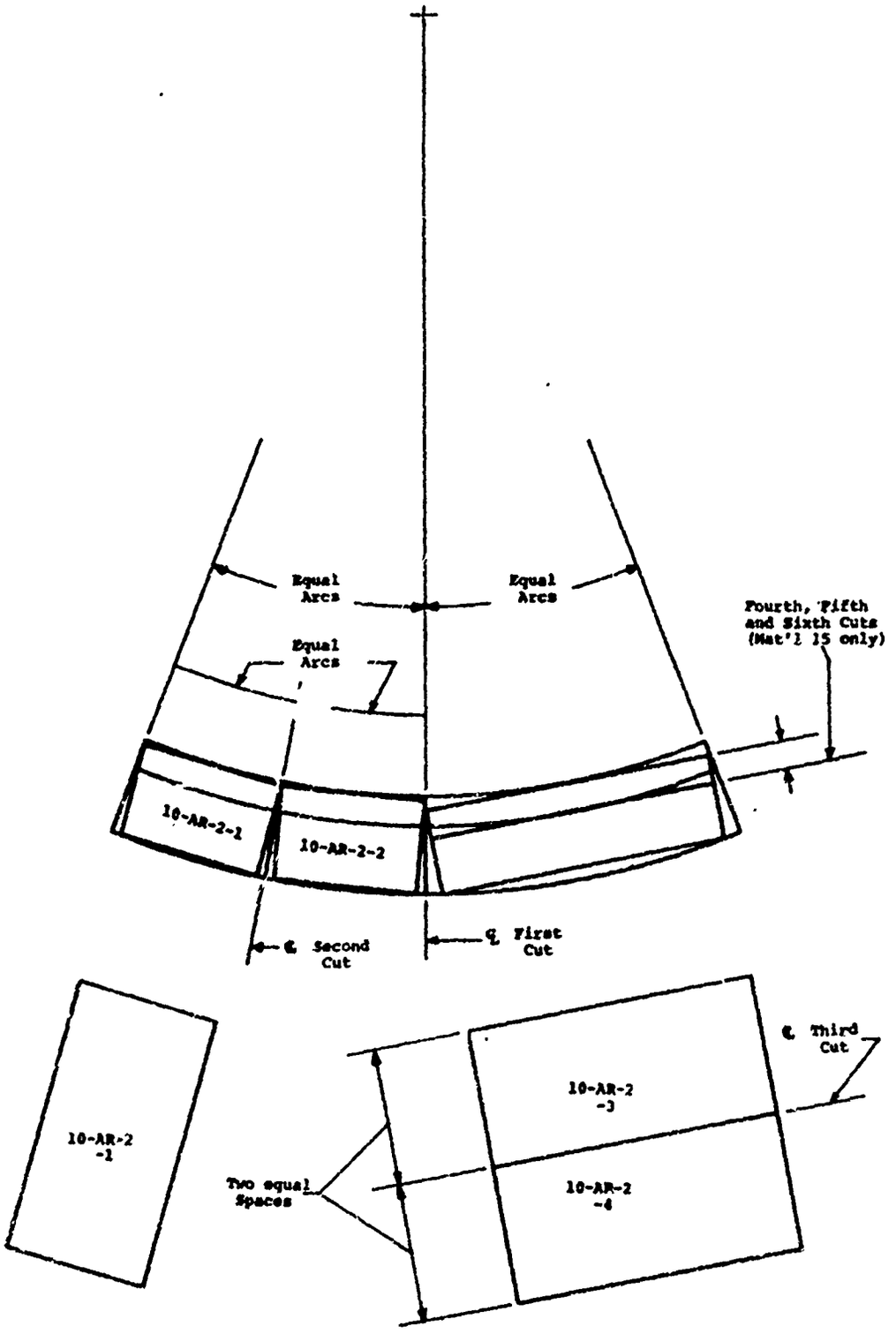


Figure 9. Cutting Plan for Removing Blanks from Phenolic Composite Impacted Arcs

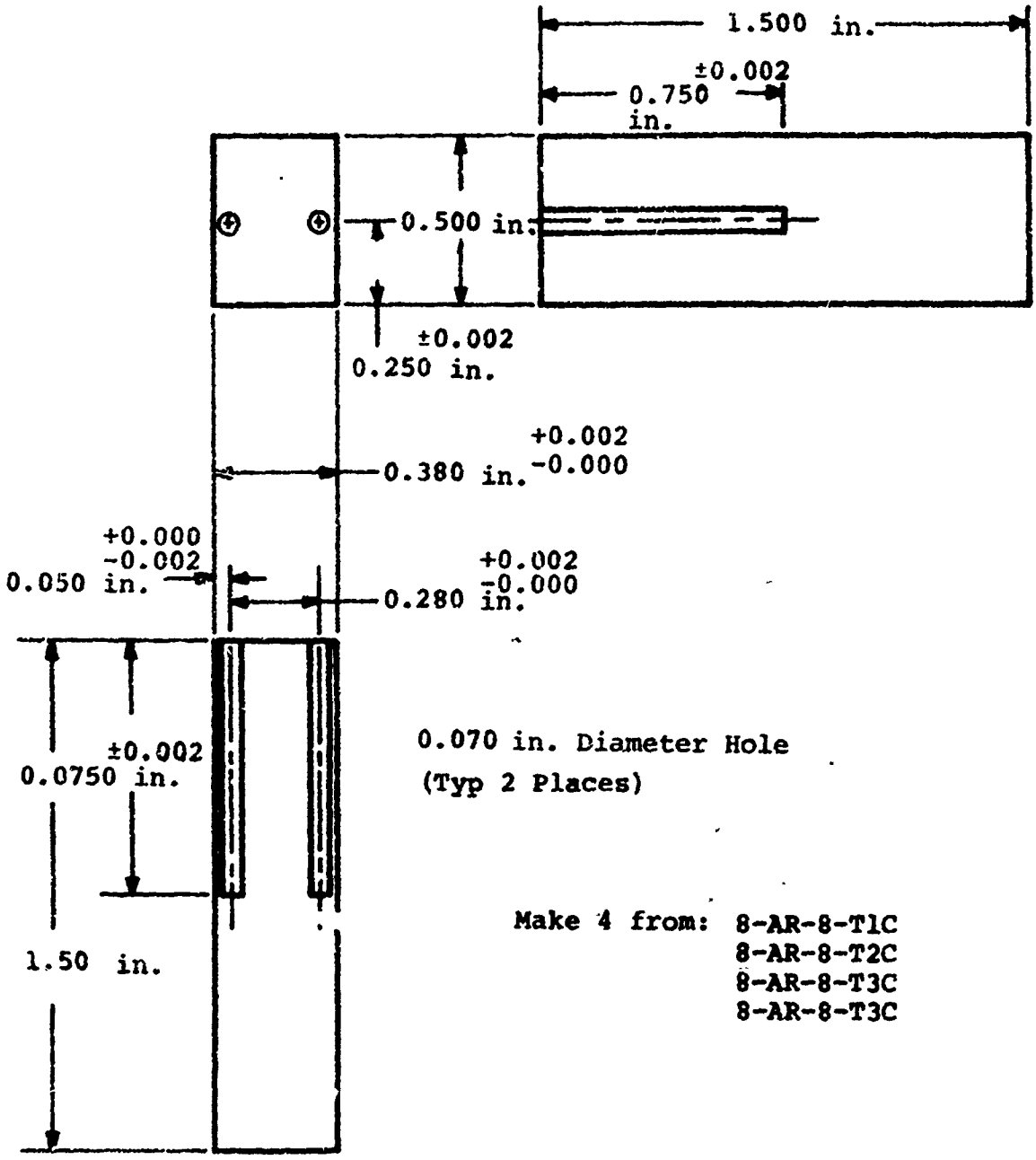


Figure 10. Configuration of Specimen Strip for 3DCC Used in Radial Inflow Apparatus

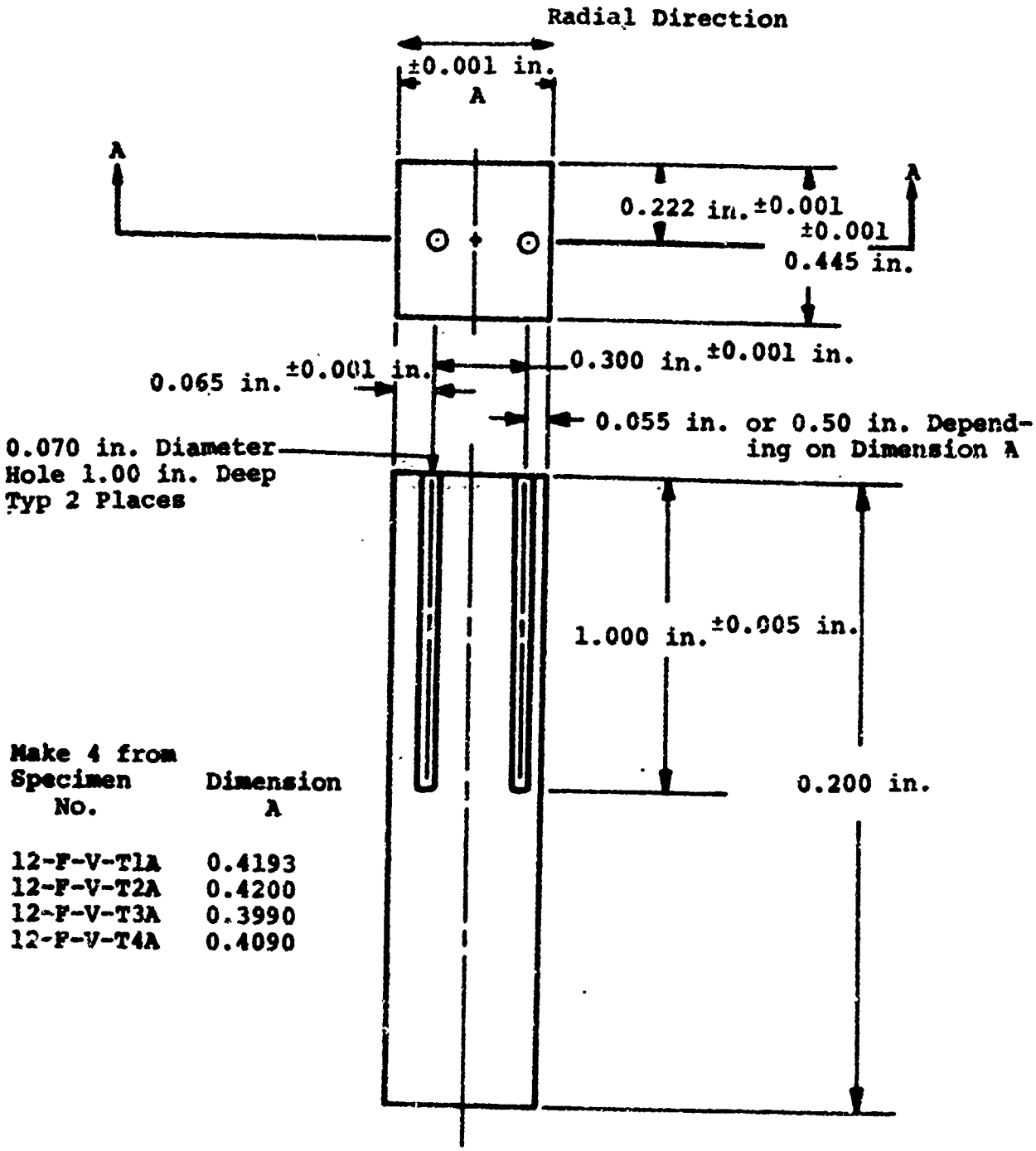


Figure 11. Configuration of Specimen Strip for Felt CC Used in Radial Inflow Apparatus

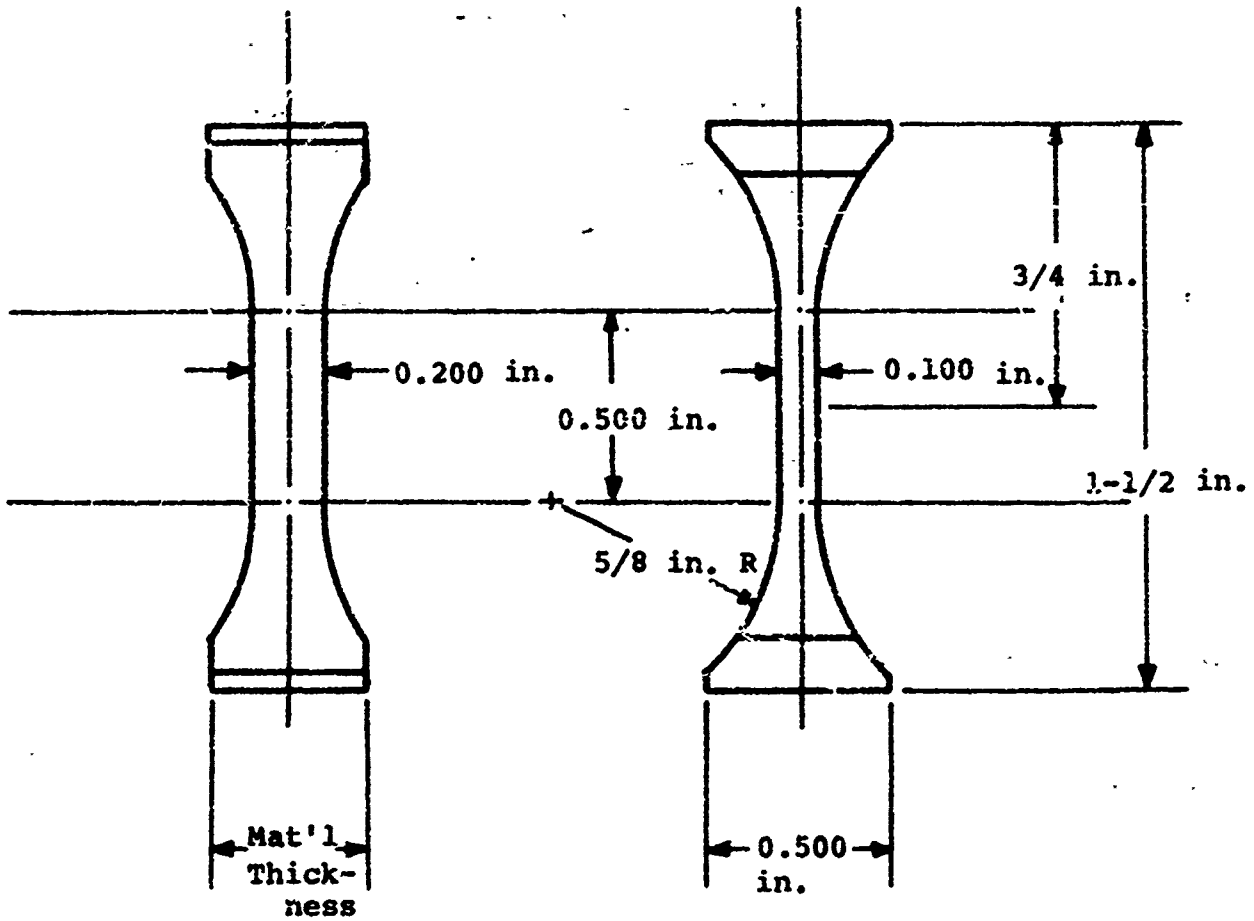


Figure 12. Configuration of Axial Tensile Specimen Used for Evaluations of Specimens from 3D Carbon-Carbon Impacted Arcs

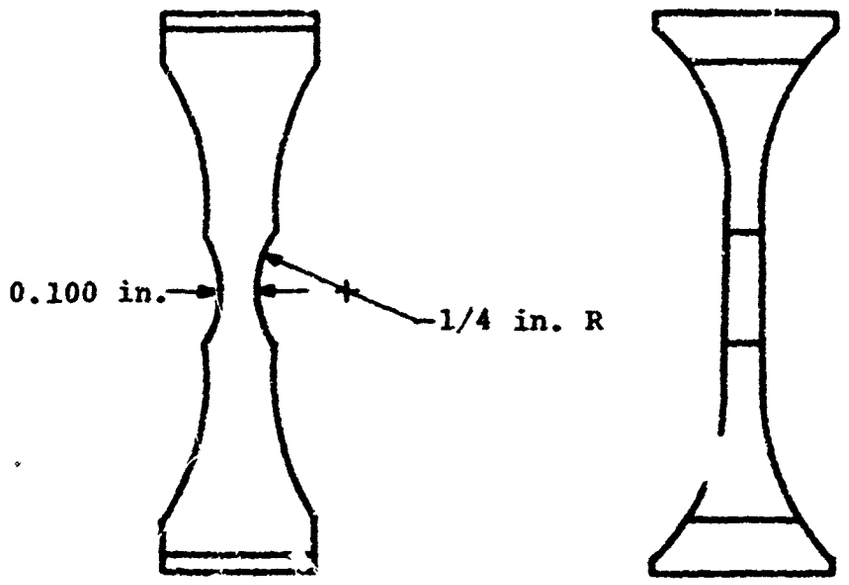
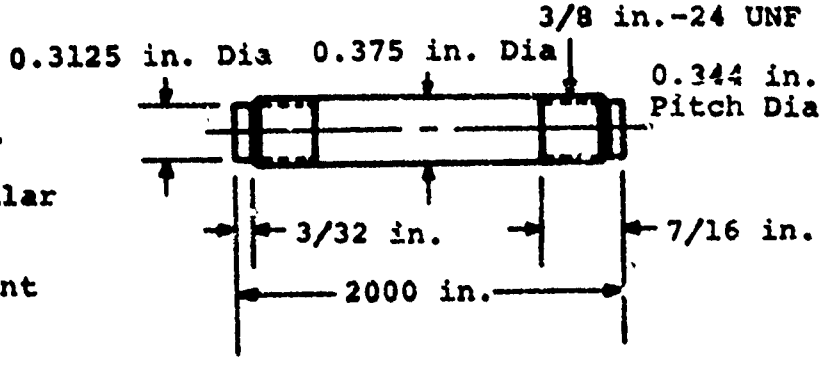


Figure 13. Modification to Tensile Specimen for Ultimate Strength Evaluations on Specimens from 3D Carbon-Carbon Impacted Arcs

Notes:

1. All Diameters True and Concentric to 0.0005 in.
2. Ends Flat and Perpendicular to 0.0005 in.
3. Do not Undercut at Tangent Points
4. Tolerances
   Lengths ± 0.005 in.
   Diameters ± 0.001 in.



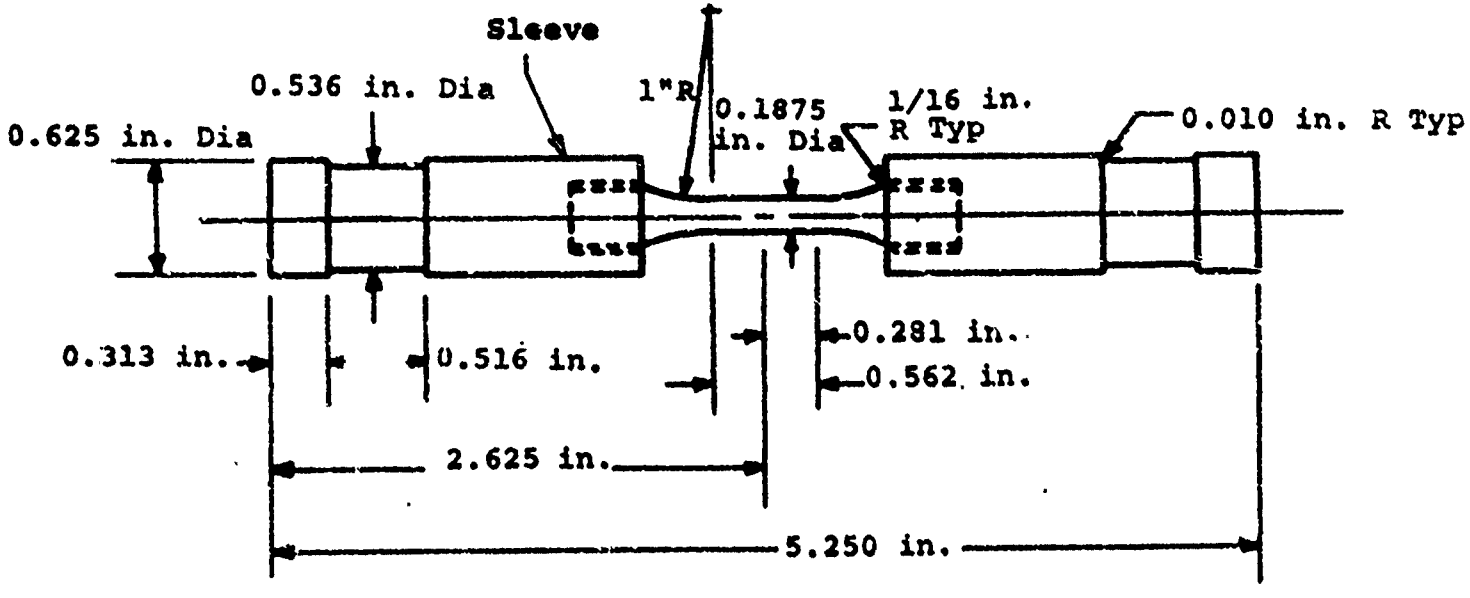


Figure 14. Configuration of Axial Tensile Specimen Used for Evaluations on Specimens from Felt Carbon-Carbon Impacted Plates

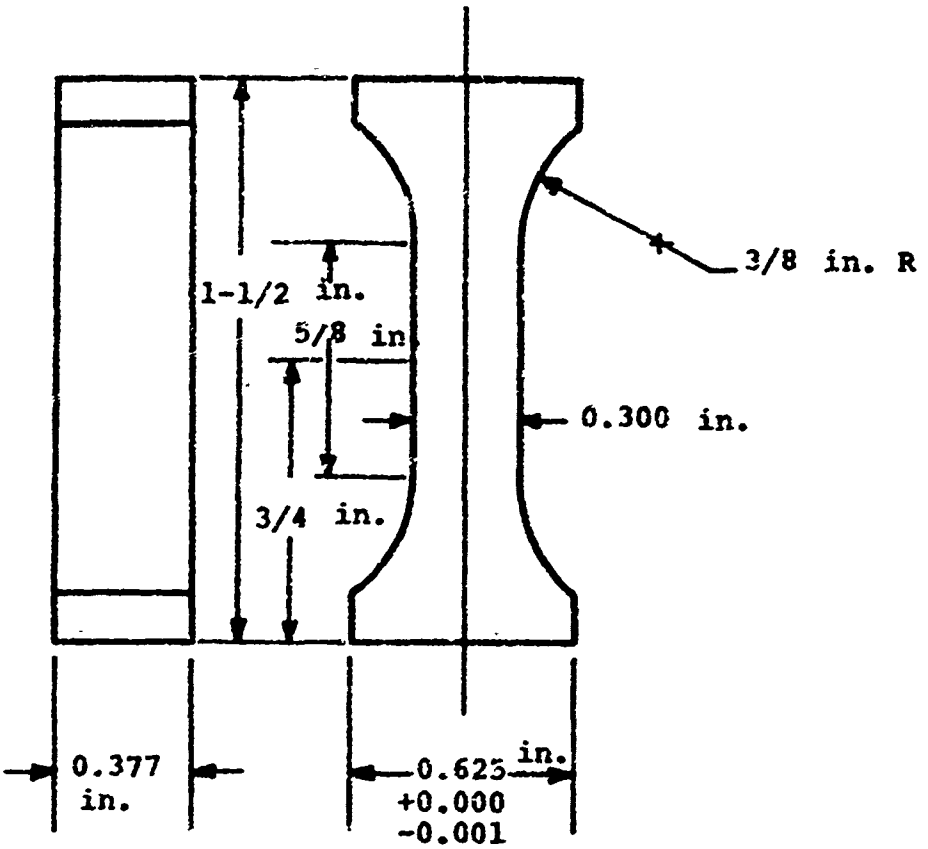


Figure 15. Configuration of Circumferential Compressive Specimen Used for Evaluations on Specimens from 3D Carbon-Carbon Impacted Arcs

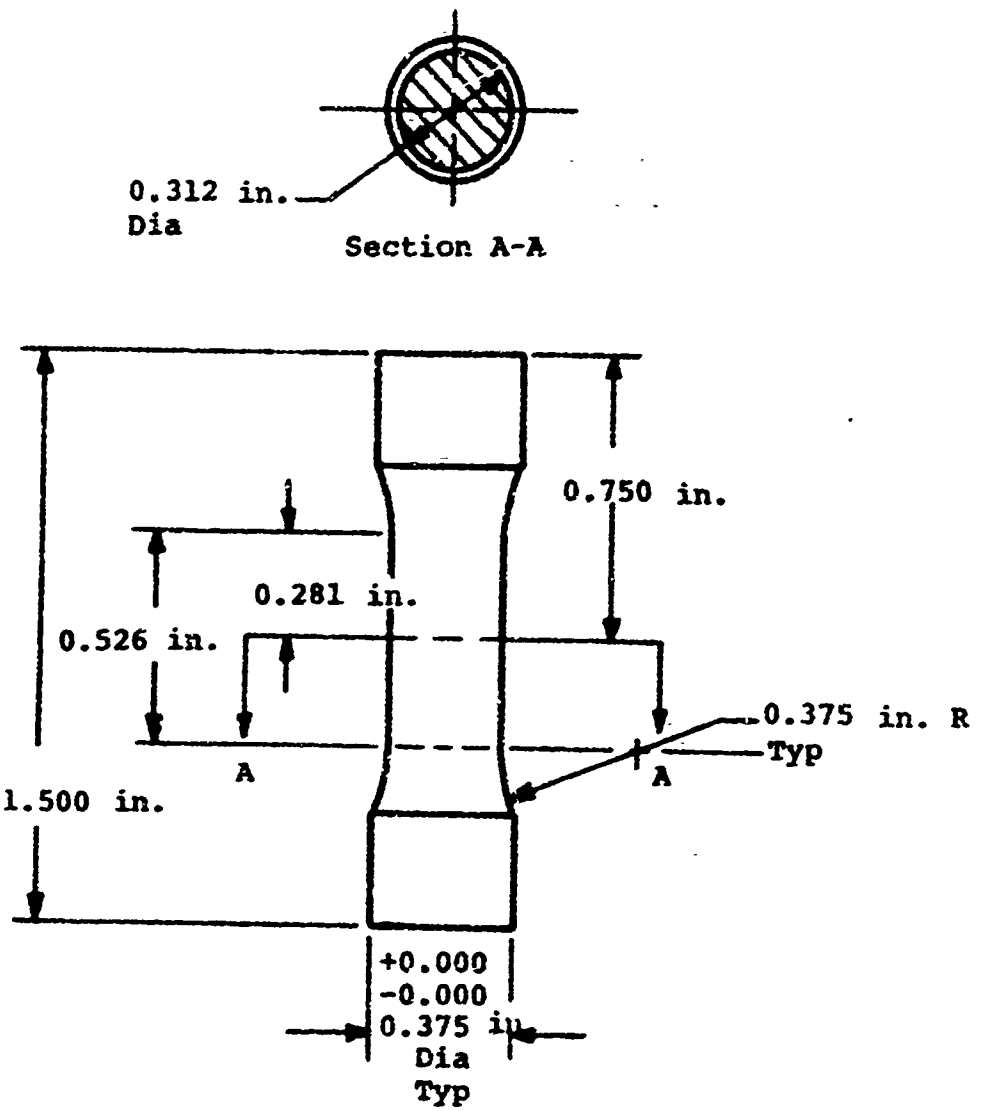


Figure 16. Configuration of Axial Compressive Specimens Used for Evaluations on Specimens from Felt Carbon-Carbon Impacted Plates 12-F-15 and 12-F-10

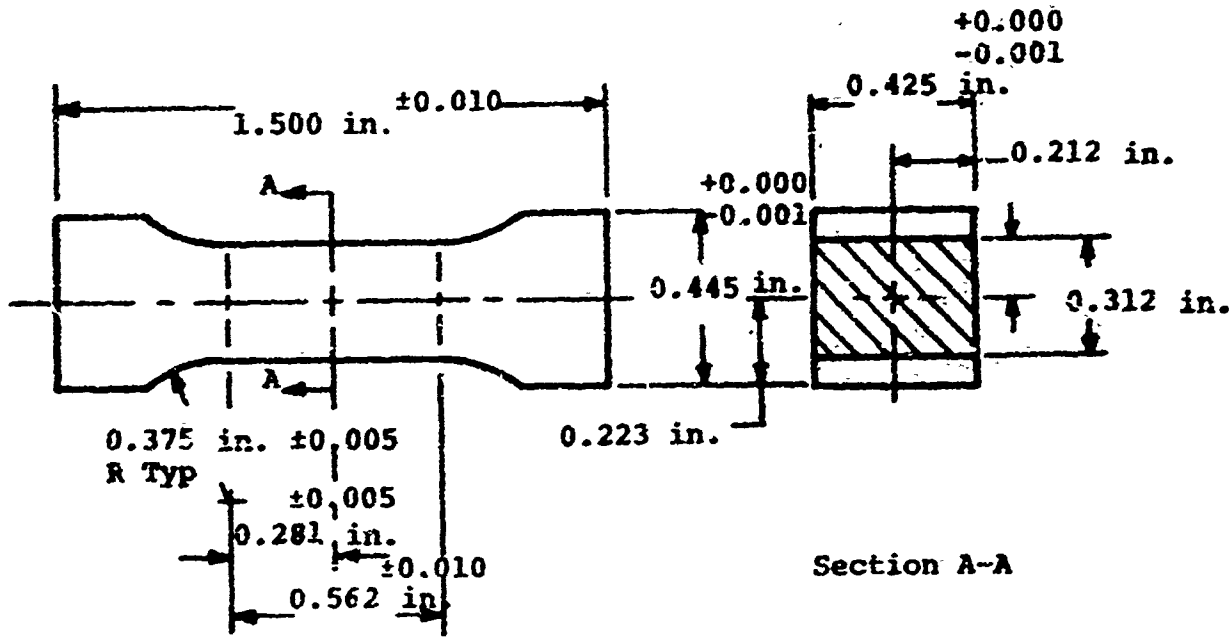
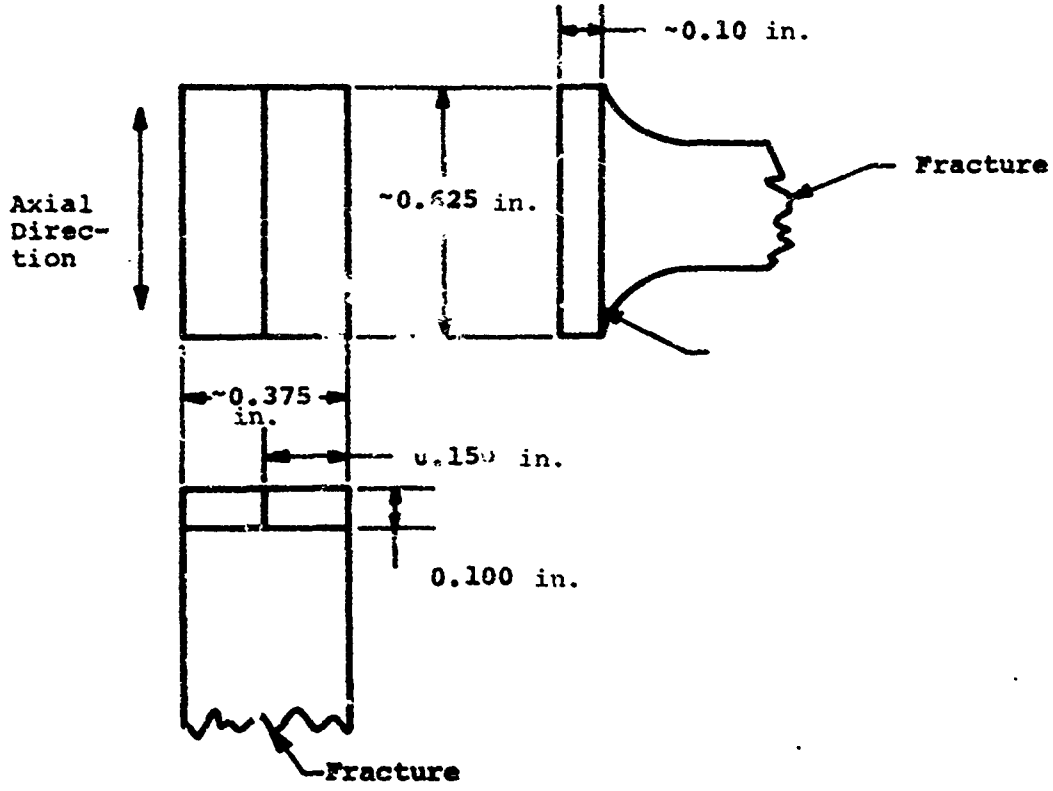
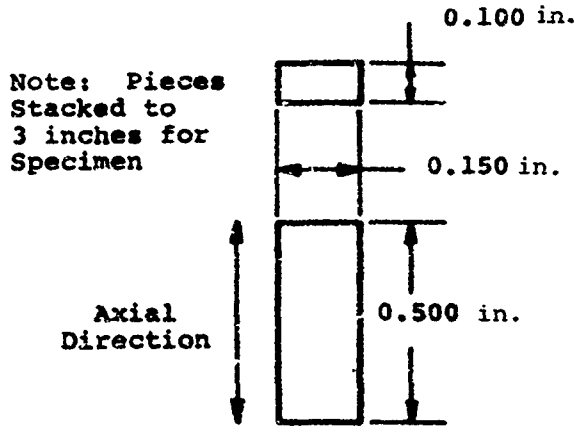


Figure 17. Configuration of Axial Compressive Specimens Used for Evaluations on Specimens from Felt Carbon-Carbon Impacted Plates 12-F-11 and 12-F-1



Cutting Plan for Ends of
8AR-7-C1 and 8AR-7-C3



Detail of Extracted Pieces

Figure 18. Preparation of Thermal Expansion Specimens of 3DCC in Axial Direction from Used Compressive Specimens

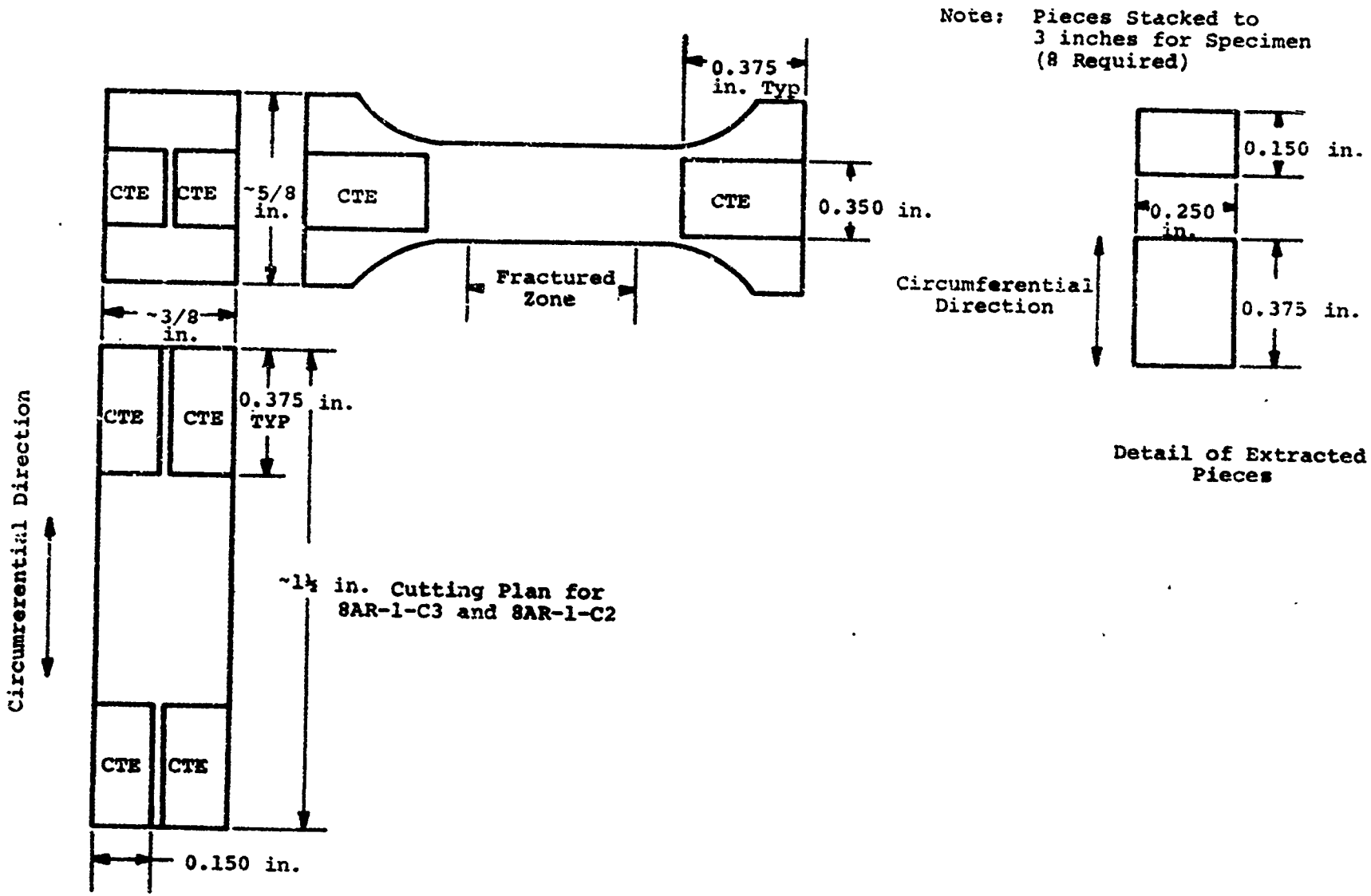


Figure 19. Preparation of Thermal Expansion Specimen of 3 DCC in Circumferential Direction from Used Compressive Specimen

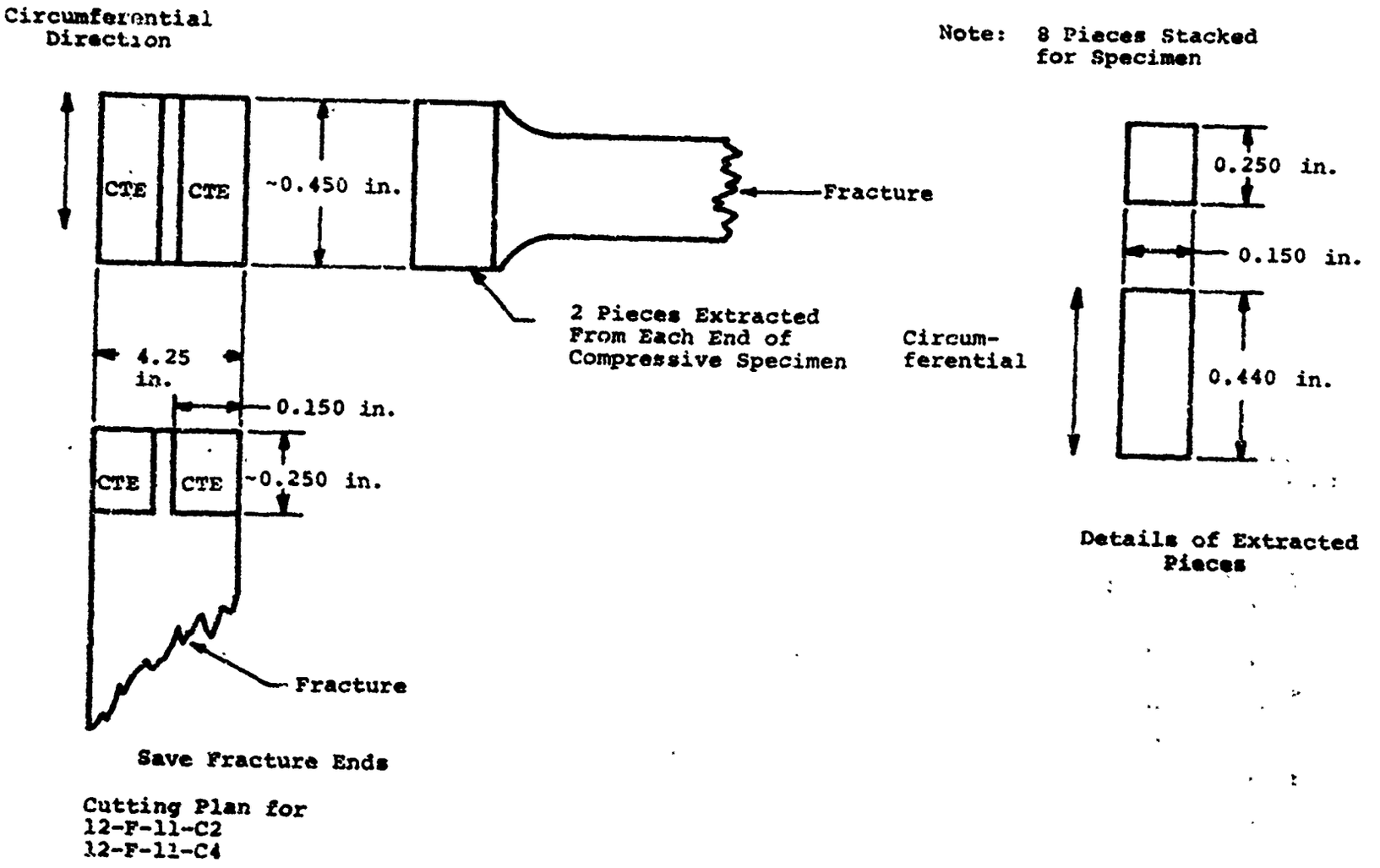
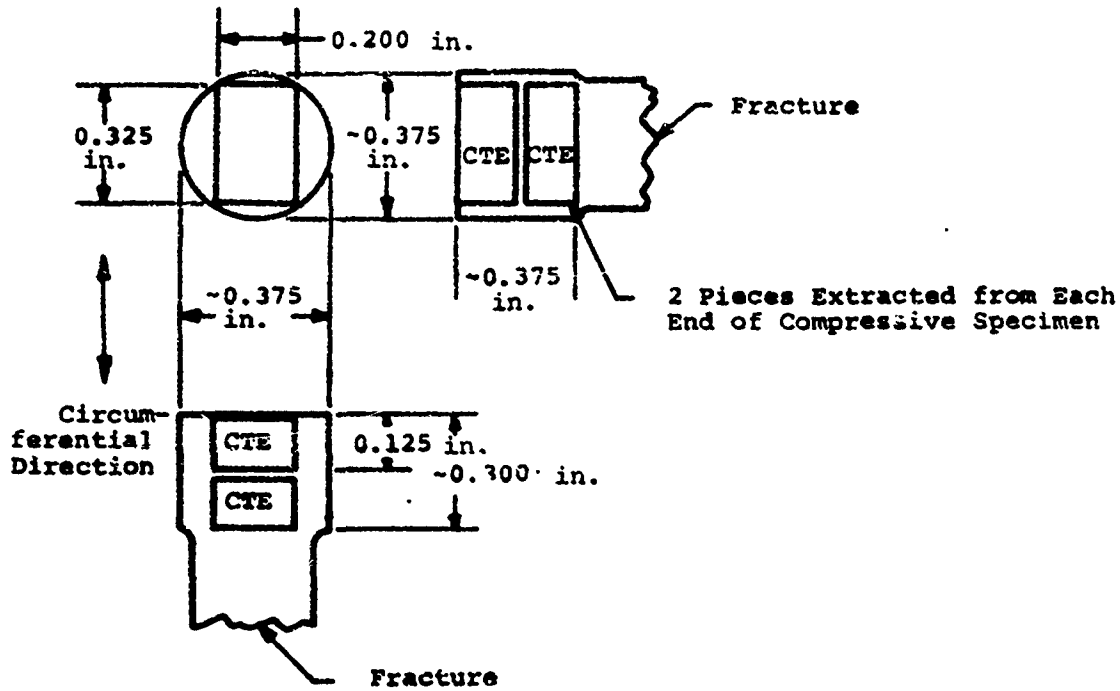
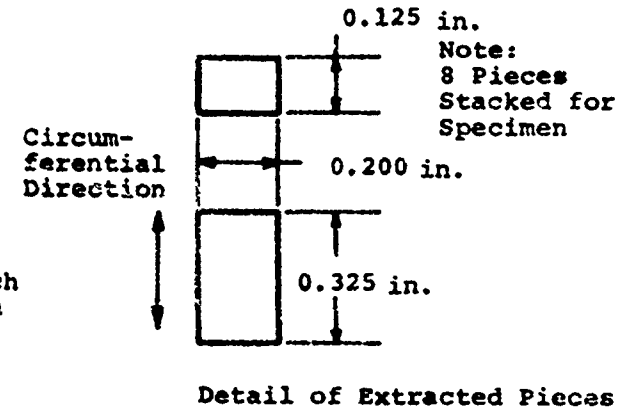


Figure 20. Preparation of Thermal Expansion Specimen of Felt CC in the Circumferential Direction from Used Compressive Specimens

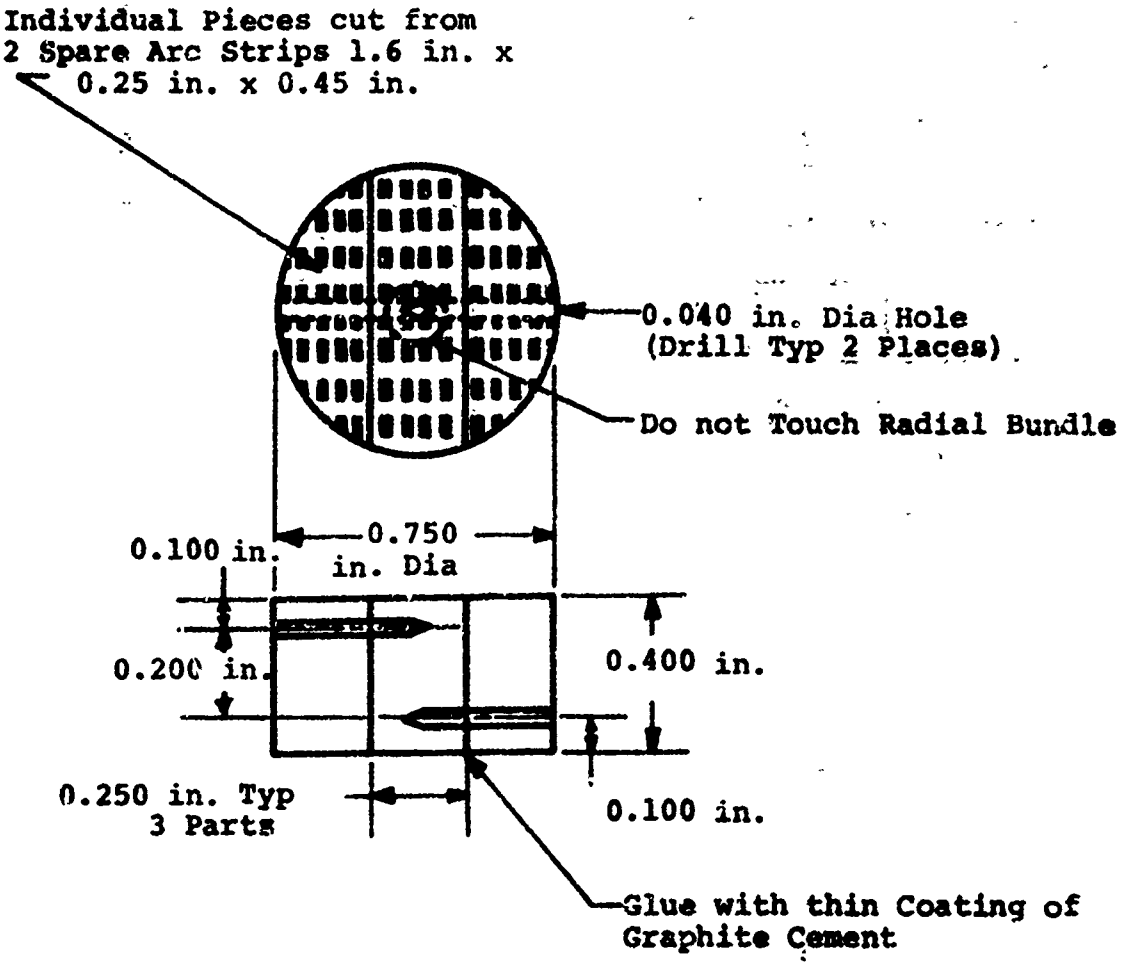


Cutting Plan for 12-F-10-C1, 12-F-10-C3 for First Specimen 12-F-15-C1 and 12-F-15-C4 for Second Specimen



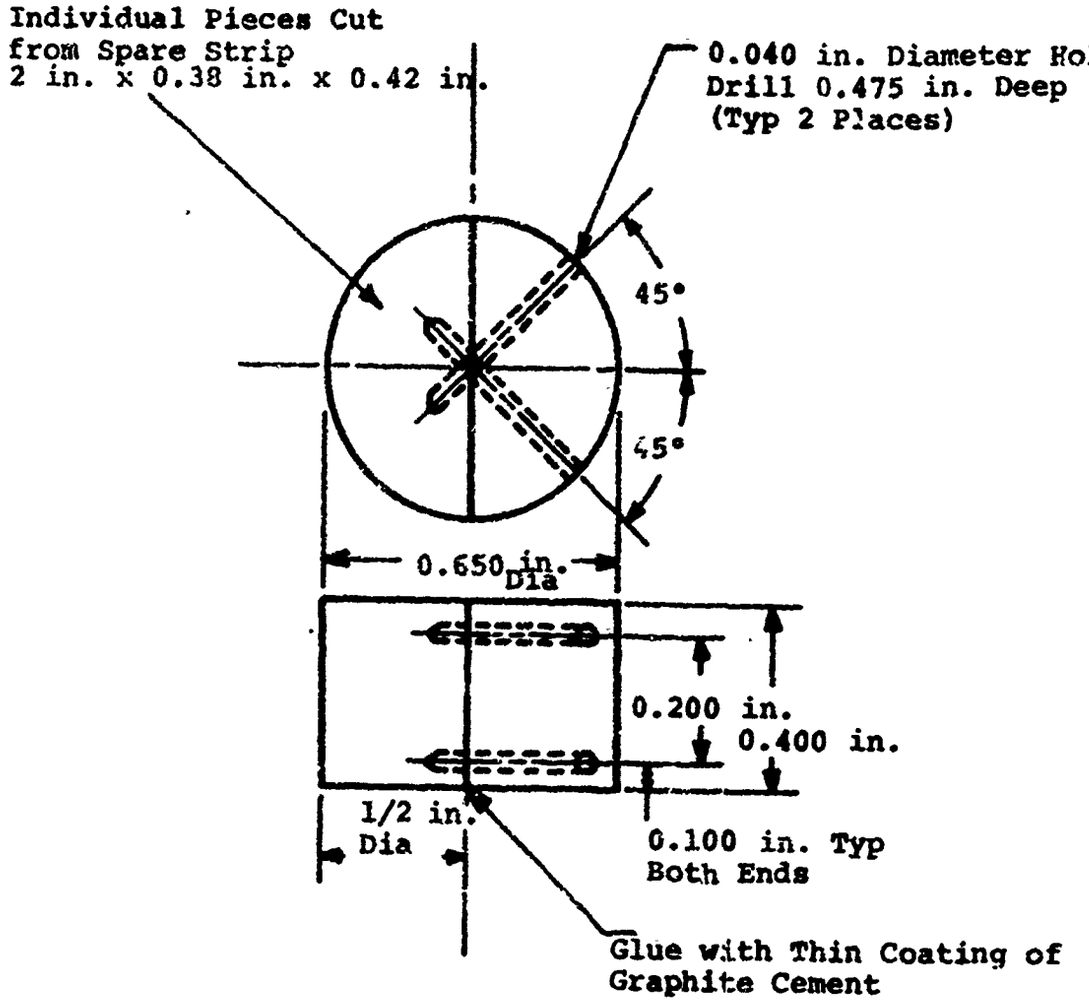
Detail of Extracted Pieces

Figure 21. Preparation of Thermal Expansion Specimens of Felt CC in the Circumferential Direction from Used Compressive Specimen



Specimens Made From 8-AR-2 and 8-AR-8

Figure 22. Configuration of Thermal Conductivity Specimen Used in the Comparative Rod Apparatus for 3DCC



Note: Specimens made from 12-F-10 and 12-F-15

Figure 23. Configuration of Thermal Conductivity Specimen Used in the Comparative Rod Apparatus for Felt CC

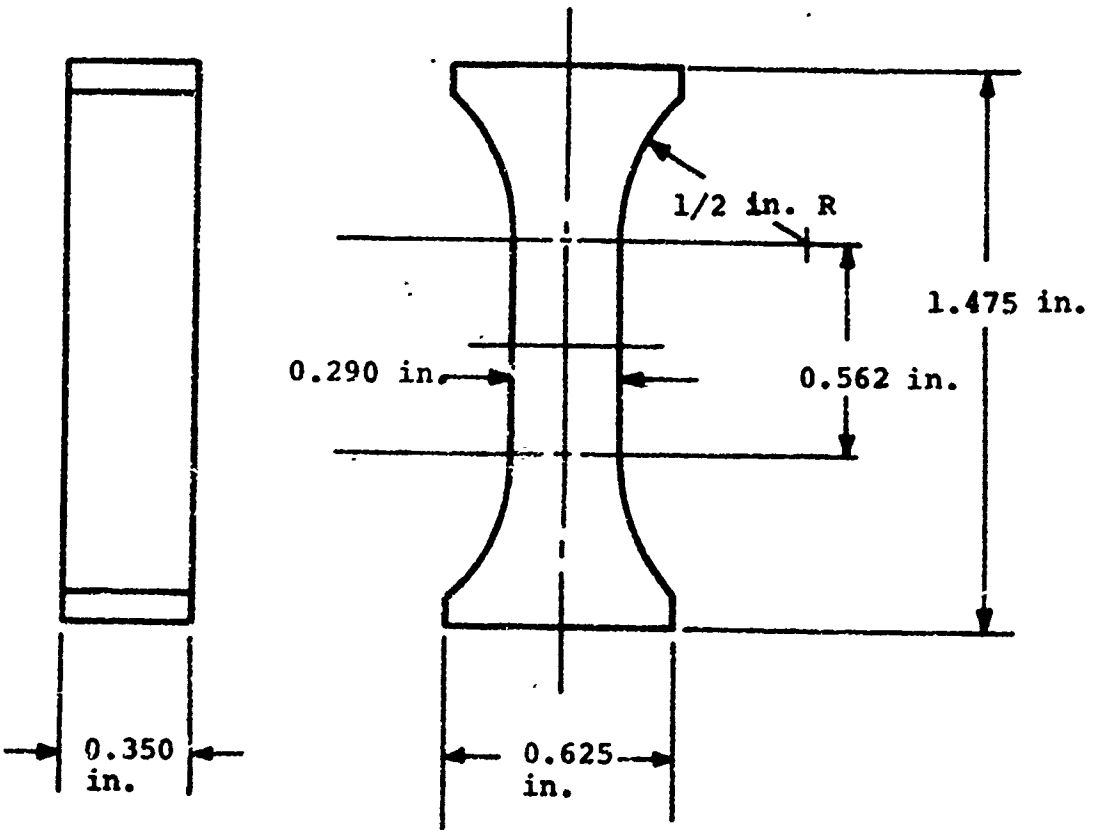


Figure 24. Configuration of Axial Tensile Specimens Used for Evaluations on Specimens From R6300 Impacted Arcs

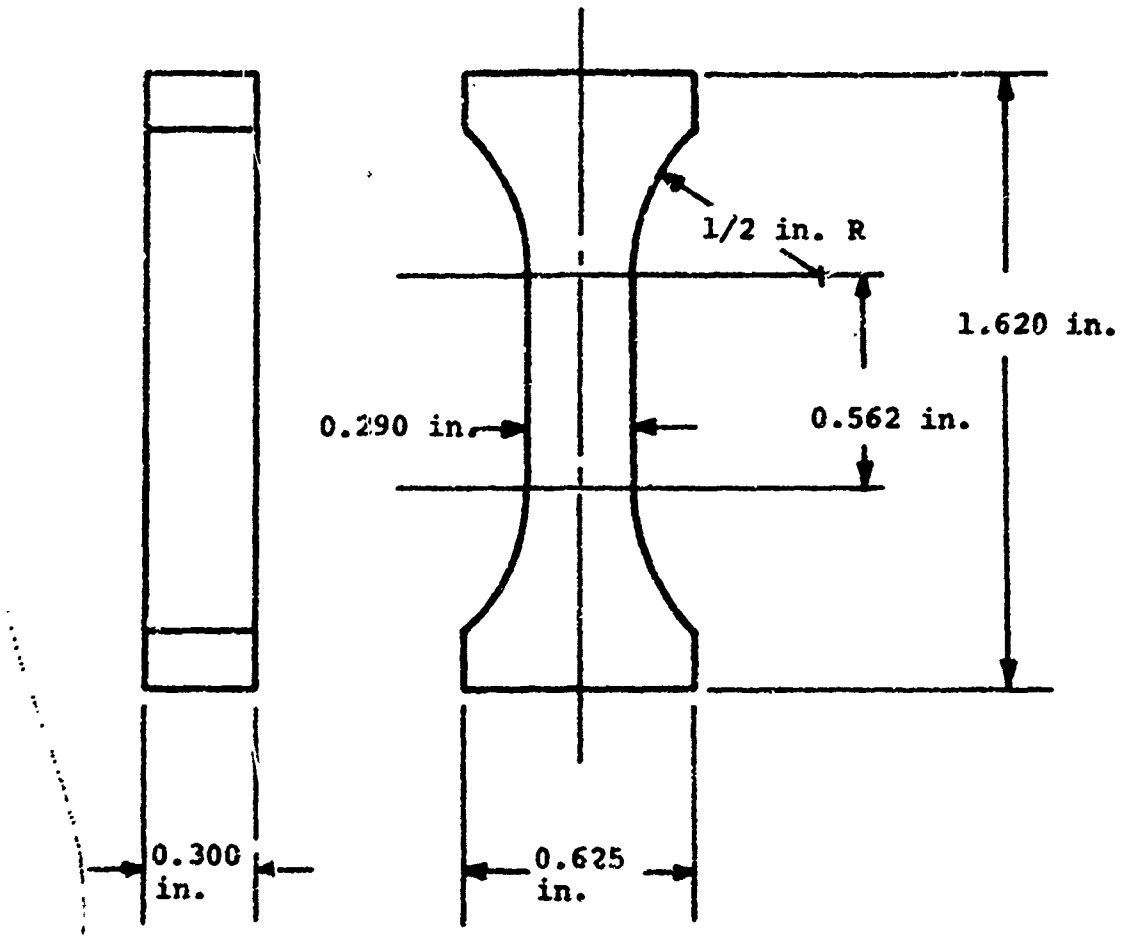


Figure 25. Configuration of Circumferential Tensile Specimens Used for Evaluations on Specimens From R6300 Impacted Arcs

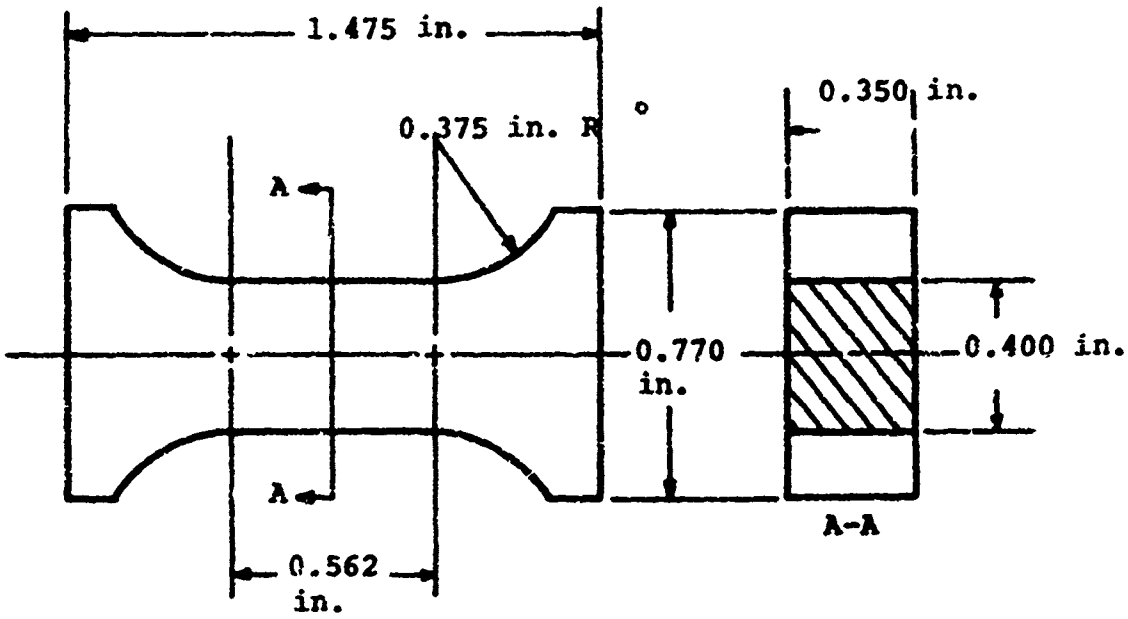


Figure 26. Configuration of Axial Compressive Specimens Used for Evaluations on Specimens from R6300 Impacted Arcs

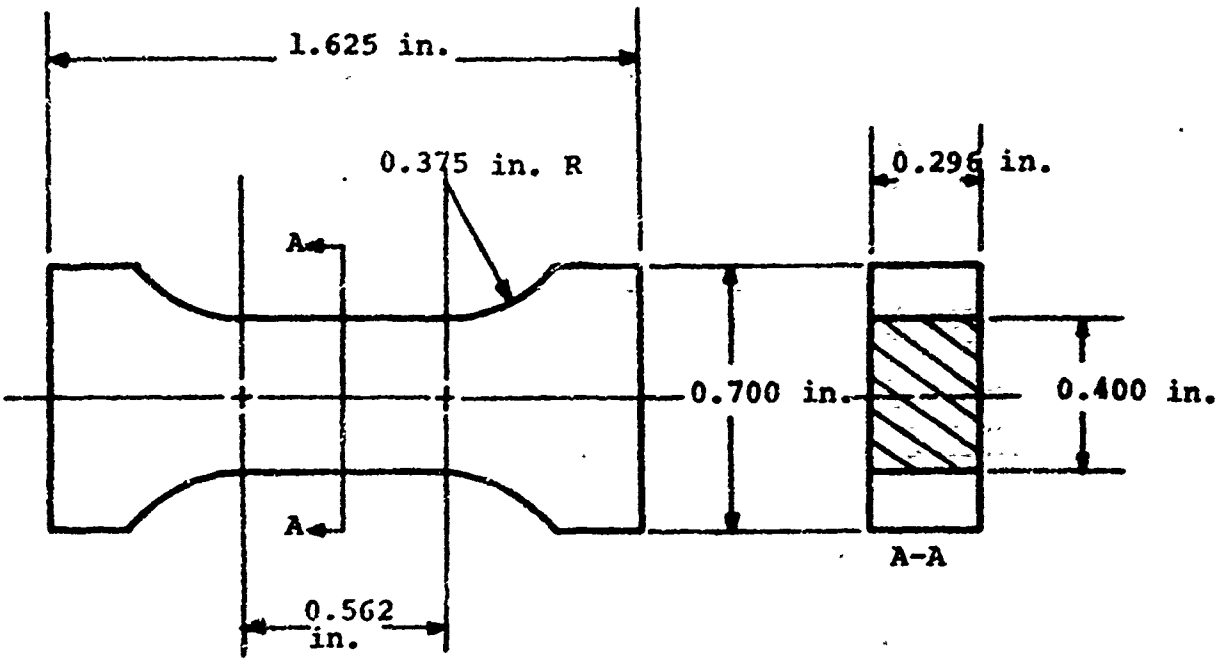


Figure 27. Configuration of Circumferential Compressive Specimens Used for Evaluations on Specimens From R6300 Impacted Arcs

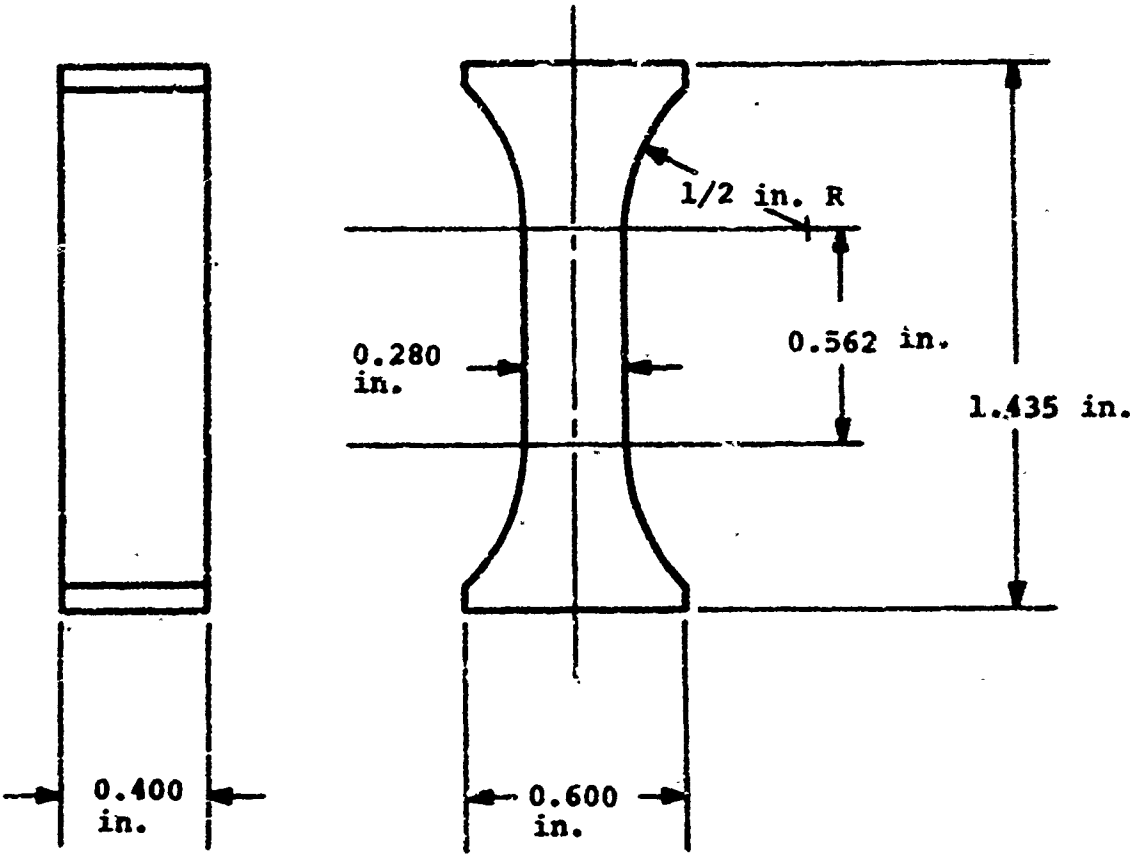


Figure 28. Configuration of Axial Tensile Specimens Used for Evaluations on Specimens from 3D Quartz-Phenolic Impacted Arcs

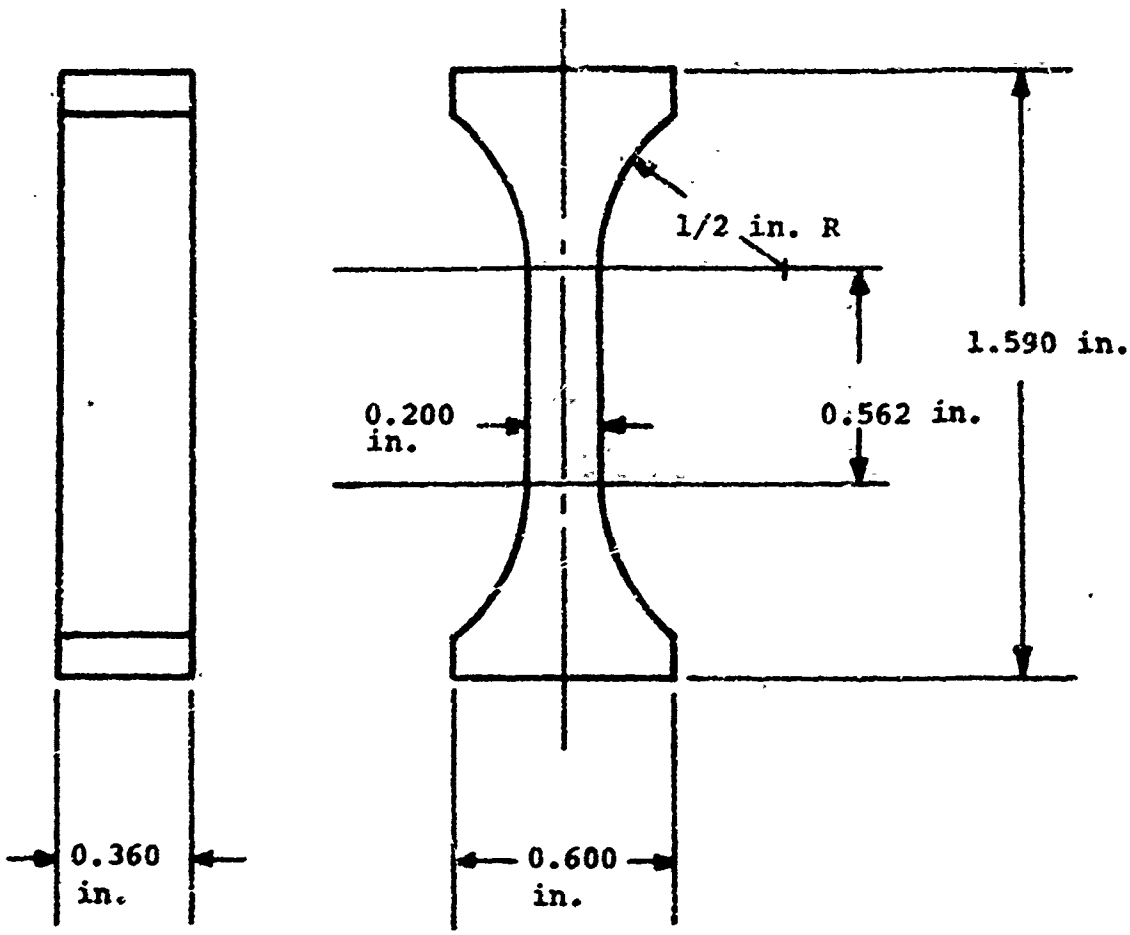
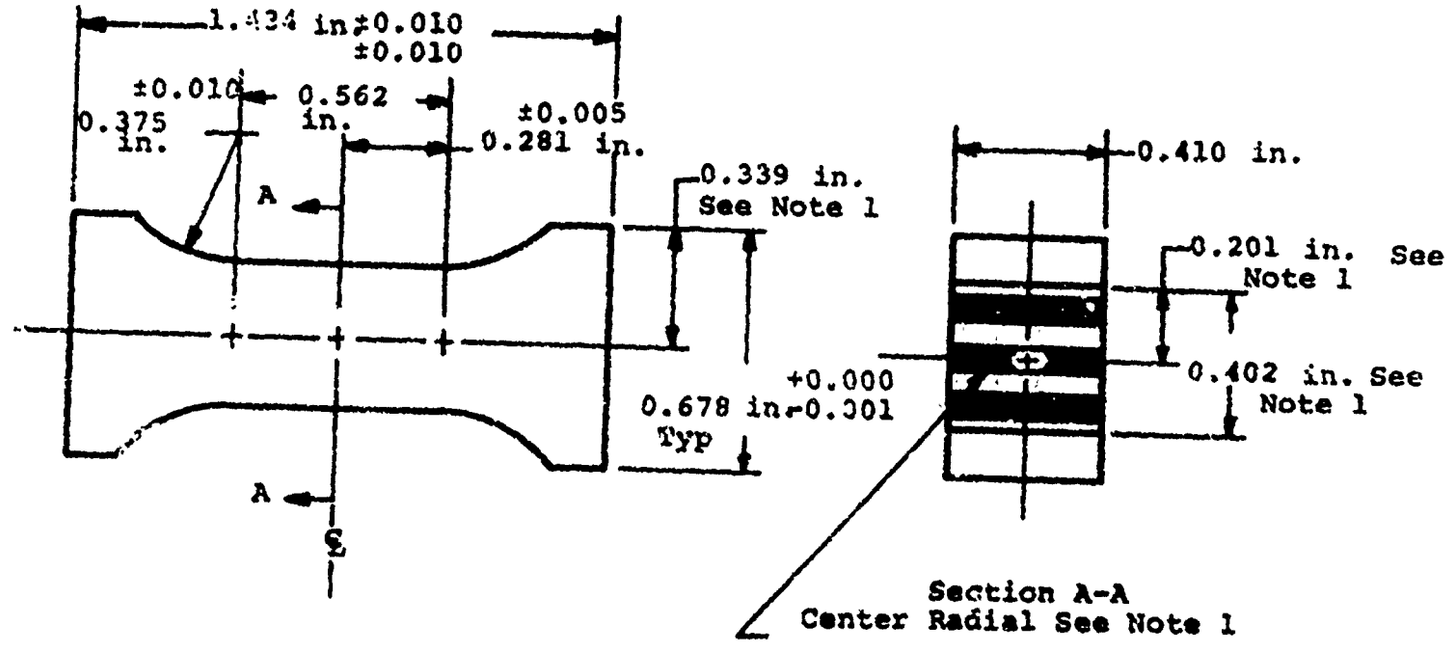
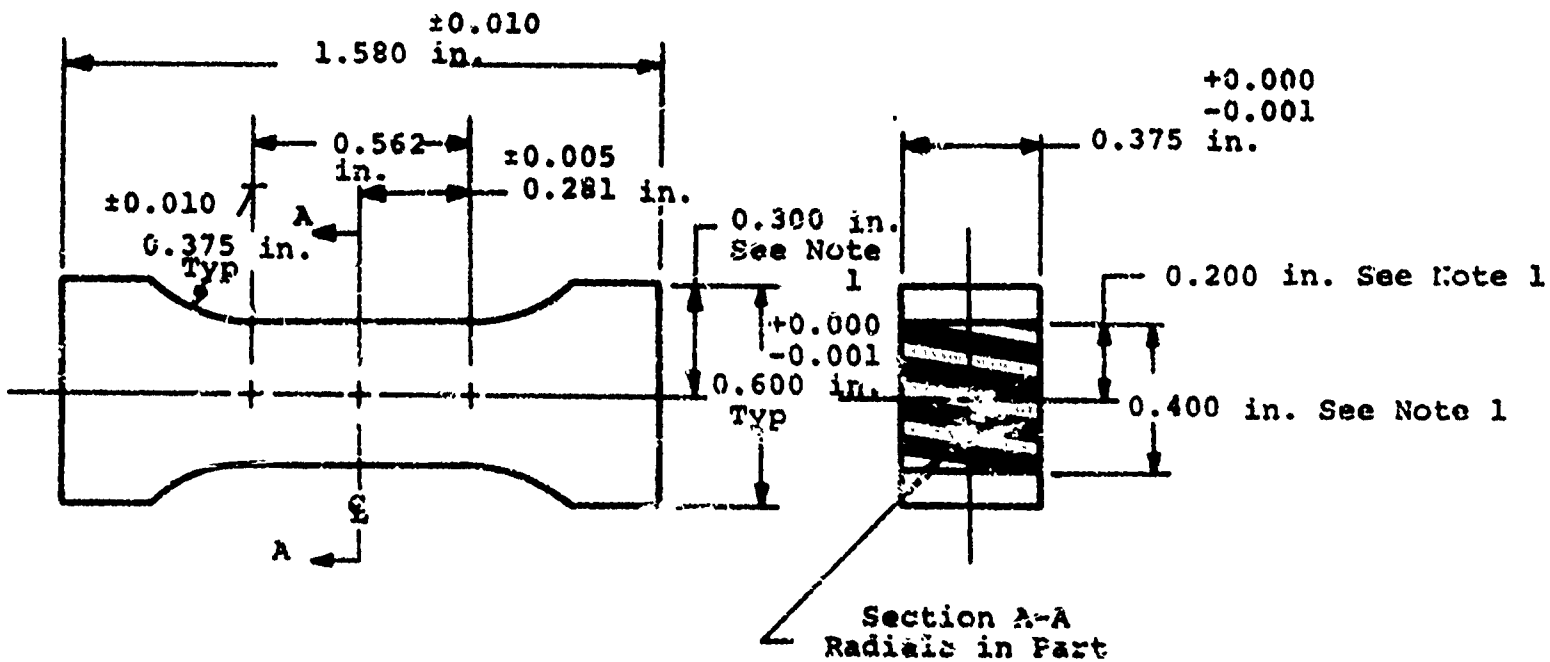


Figure 29. Configuration of Circumferential Tensile Specimens Used for Evaluations on Specimens from 3D Quartz-Phenolic Impacted Arcs



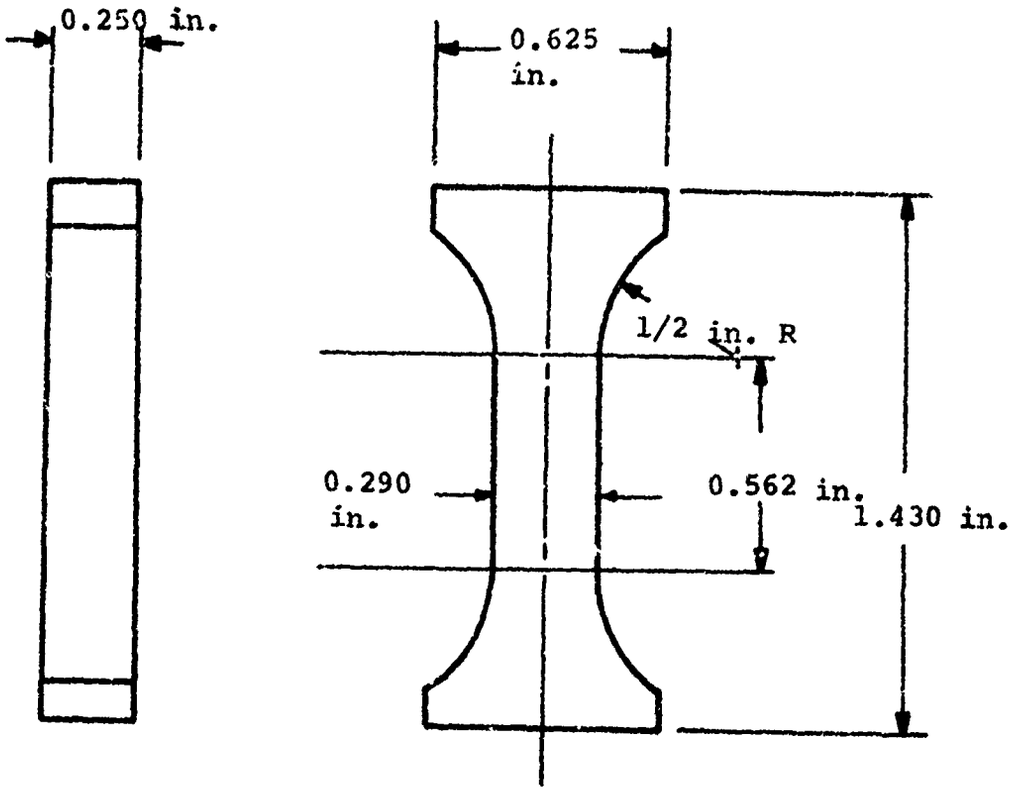
Notes:
1. Center Specimen on a Radial
2. Both Ends Flat and Perpendicular to 0.0005 in
3. Tolerances Unless Otherwise Noted ± 0.001 in

Figure 30. Configuration of Axial Compressive Specimens Used for Evaluations of Specimens from 3D Quartz-Phenolic Impacted Arcs



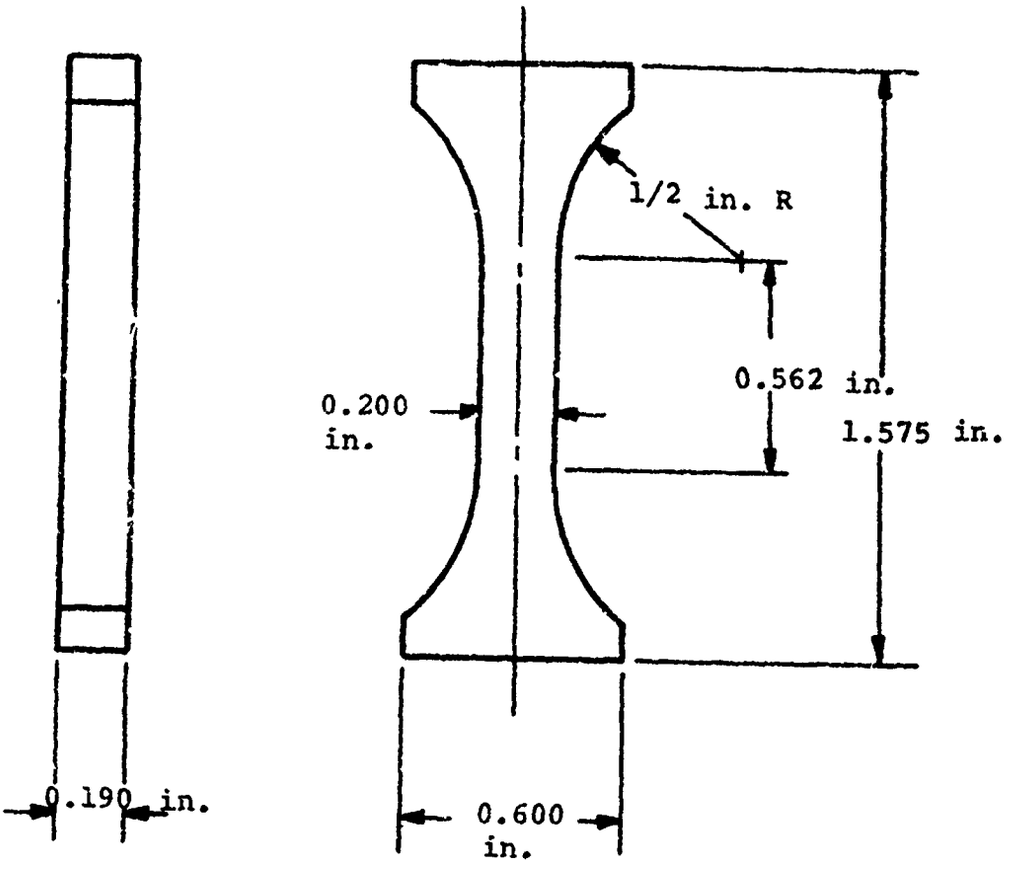
Notes: 1. Center Specimen Betwsen Radials
2. Both Ends Flat and Perpendicular to 0.0005
3. Tolerances Unless Otherwise Noted ± 0.001

Figure 31. Configuration of Compressive Specimens Used for Evaluations on Specimens from 3D Quartz-Phenolic Impacted Arcs



Center Specimen Between Radials

Figure 32. Configuration of Axial Tensile Specimens for Evaluations on Specimens from 3D Carbon-Phenolic Portion of 3DC/QP Impacted Arcs



Center Specimen Between Radials

Figure 33. Configuration of Circumferential Tensile Specimens Used for Evaluations on Specimens from Carbon-Phenolic Portion of 3DC/QP Impacted Arcs

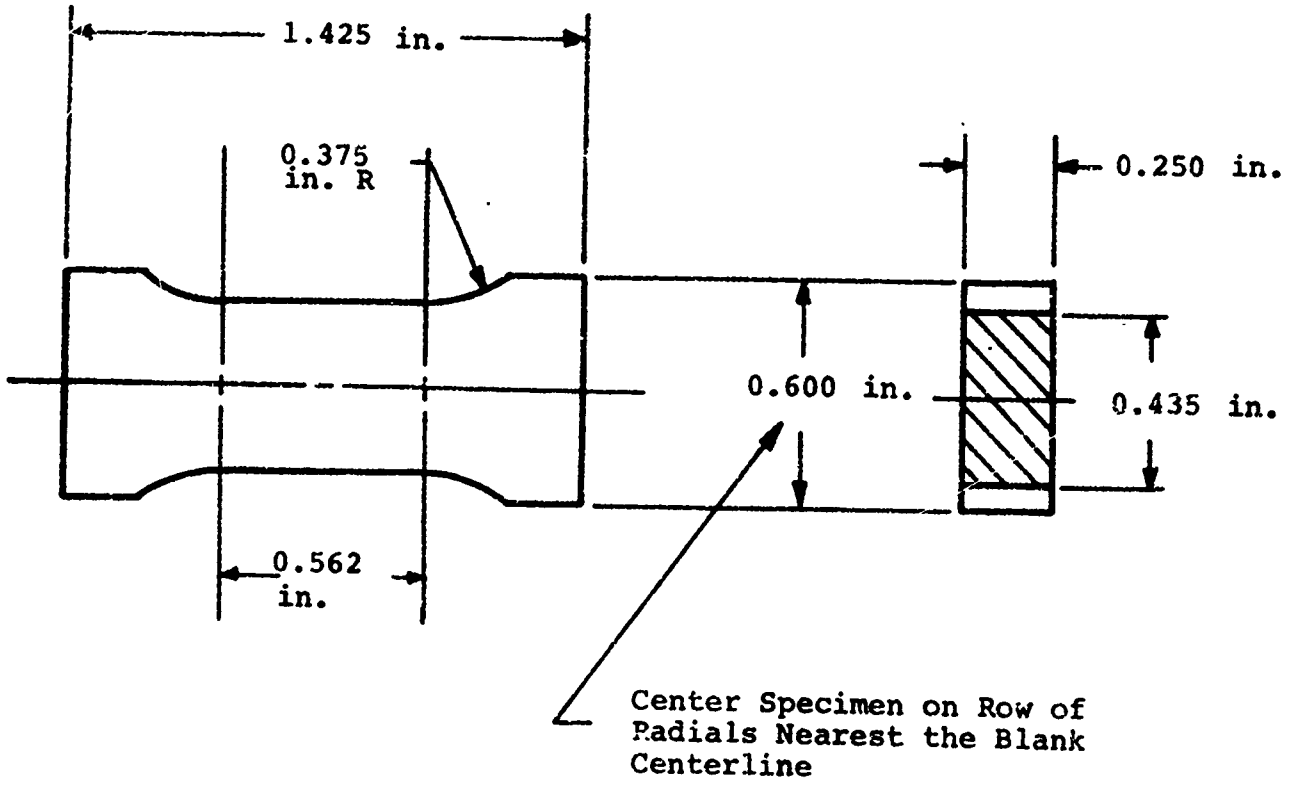


Figure 34. Configuration of Axial Compressive Specimen Used for Evaluation on Specimens from the 3D Carbon-Phenolic Portion of 3DC/QP Impacted Arcs

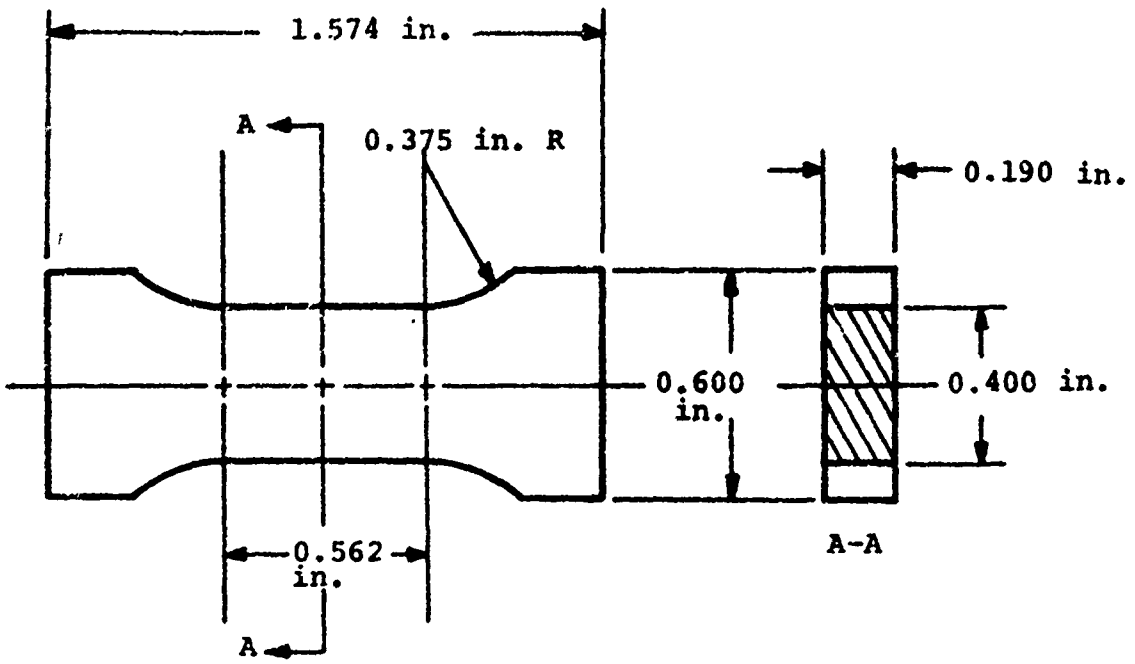
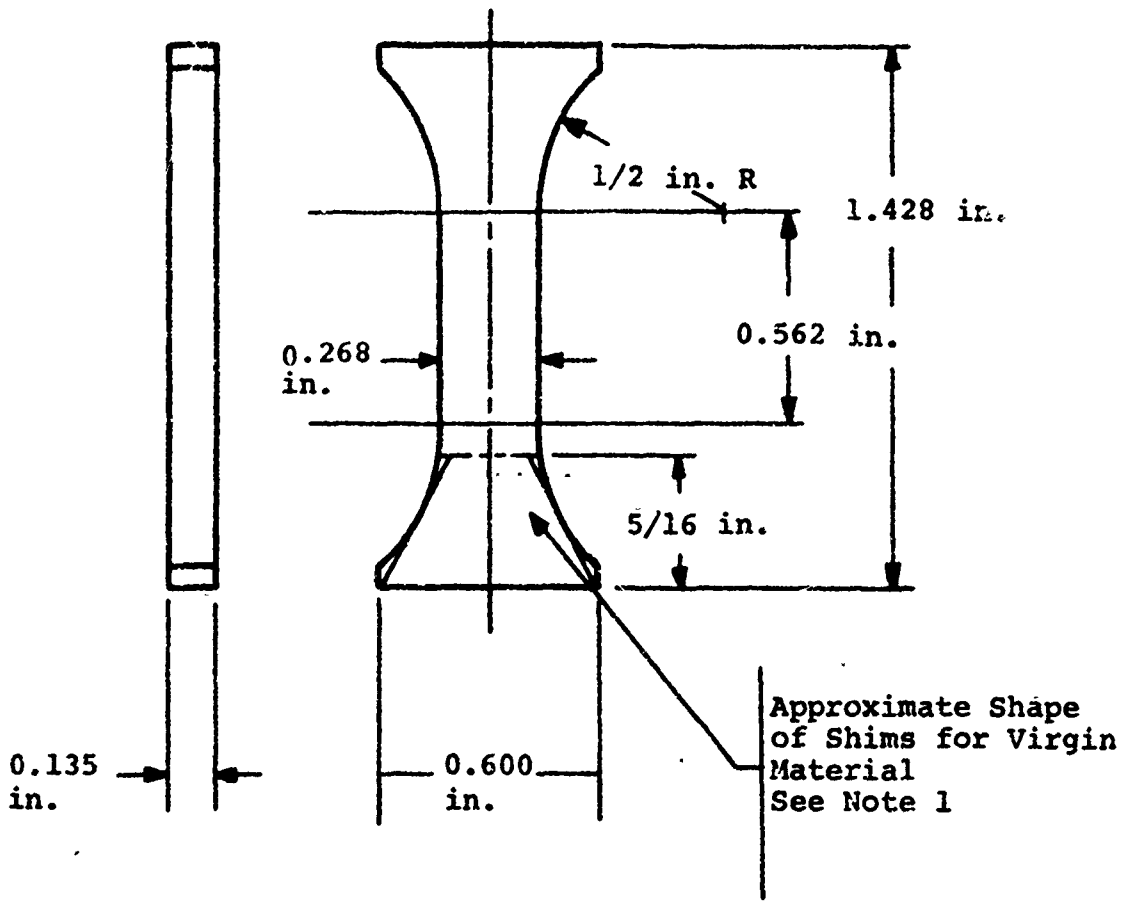
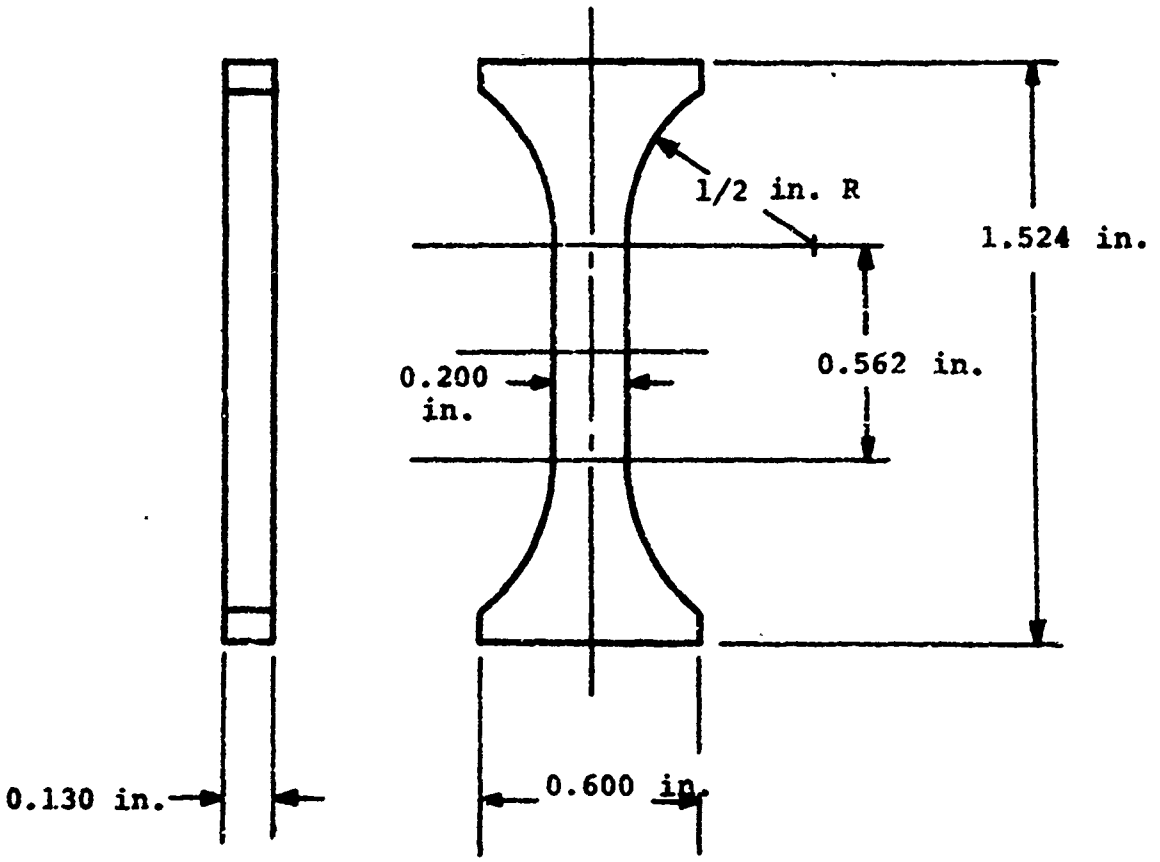


Figure 35. Configuration of Circumferential Compressive Specimen Used for Evaluations on Specimens from the 3D Carbon-Phenolic Portion of 3DC/QP Impacted Arcs



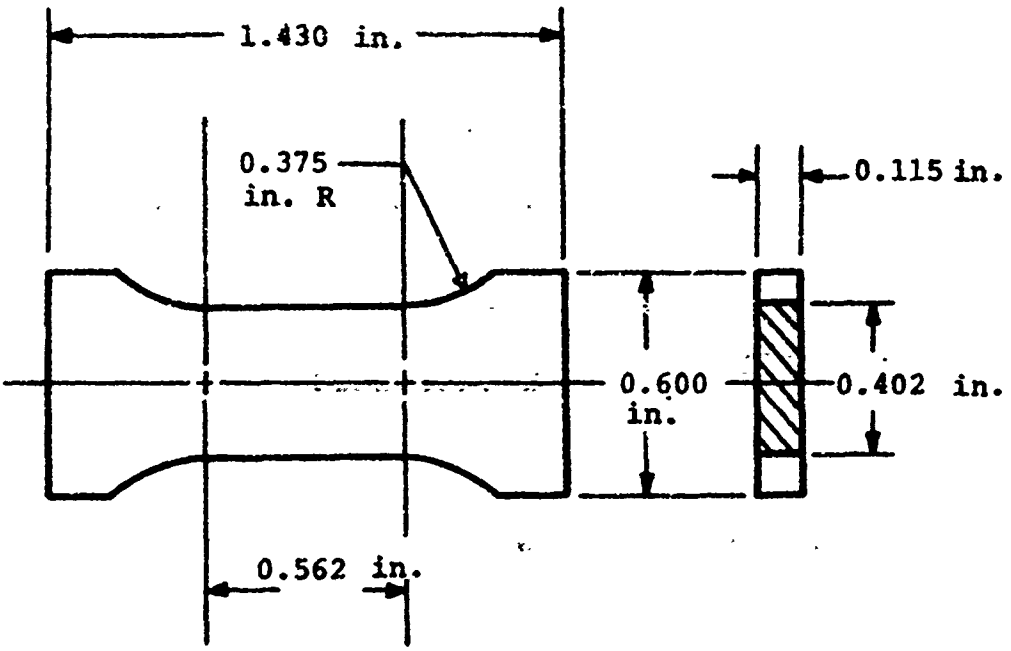
Notes: 1. Virgin Specimens 0.092 in.
2. Center Specimen Between Radials

Figure 36. Configuration of Axial Tensile Specimens for Evaluations on Specimens from Quartz-Phenolic Portion of 3DC/QP Impacted Arcs



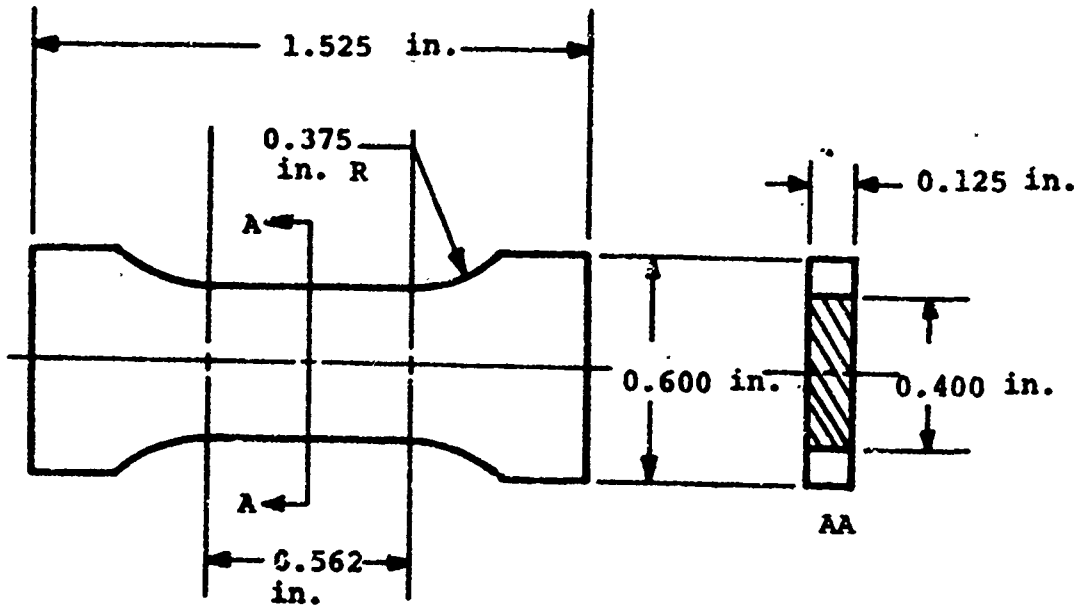
Center Specimen Between Radials

Figure 37. Configuration of Circumferential Tensile Specimens Used for Evaluations on Specimens from Quartz-Phenolic Portion of 3DC/QP Impacted Arcs



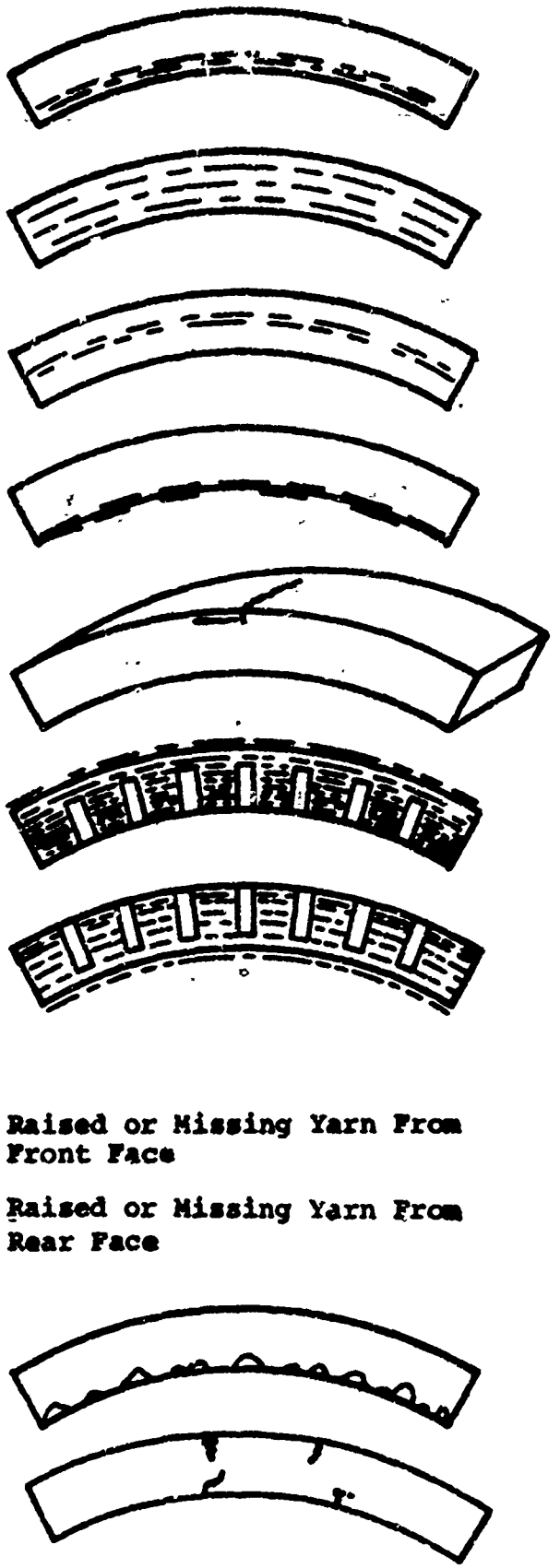
Center Specimen on Radials

Figure 38. Configuration of Axial Compressive Specimen Used for Evaluations on Specimens from the 3D Quartz-Phenolic Portion of 3DC/QP Impacted Arcs



Center Specimen Between Radials

Figure 39. Configuration of Circumferential Compressive Specimen Used for Evaluations on Specimens from the 3D Quartz-Phenolic Portion of 3DC/QP Impacted Arcs



Rear Delam (RD)

Bulk Delam (BD)

Mid Delam (MD)

Rear Lift (RL)

Front Face Crack (FFC)

Front Radial Recession (FRR)
(Bulk Expansion of Laterals
Toward Front Face)

Rear Radial Recession (RRR)
(Bulk Expansion of Laterals
Toward Rear Face)

Front Yarn Lift (FYL) — Raised or Missing Yarn From Front Face

Rear Yarn Lift (RYL) — Raised or Missing Yarn From Rear Face

Front Crush (FC)

Spall (S)

Buckle (B)

Figure 40. Definition of Structure-Change Terms

SECTION II

MATERIAL AND SPECIMEN PREPARATIONS

IMPACTED CARBON-CARBON COMPOSITE ARCS

Materials for this phase of the program included arcs of AVCO 3D Carbon-Carbon, Material #8, and plates of Sandia Felt Carbon-Carbon, Material #12. All but one of the 3DCC arcs had nominal dimensions of 0.450 in. thick by 1.50 in. width by 3.0 in. chordal length on an outside radius of 4.50 in. All but one of the Felt CC plates were nominally 2.0 in. square by 0.450 in. thick. The odd 3DCC Arc 8-AR-V, was nominally 0.450 in. thick by 1.50 in. width by 2.0 in. in chordal length. Felt CC Plate 12-F-1 was nominally 1.50 in. square by 0.45 in. thick. All of these arcs and plates except those labeled "V" (virgin) had previously been subjected to flyer plate impact loading.

The 3DCC was an orthogonal three-dimensional carbon-carbon composite. The composite was densified by phenolic impregnation, pyrolized and graphitized. The construction of this material is shown in Figure 1. A group photograph of the arcs evaluated is shown as Figure 53.

The Felt CC was a multidirectional carbon-carbon composite. A rayon felt carcass was assembled by needling, a process which pulled some of the fibers through the thickness direction of the various felt layers. The carcass was infiltrated with pyrolytic graphite, and finally graphitized. A group photograph of the plates is shown as Figure 72.

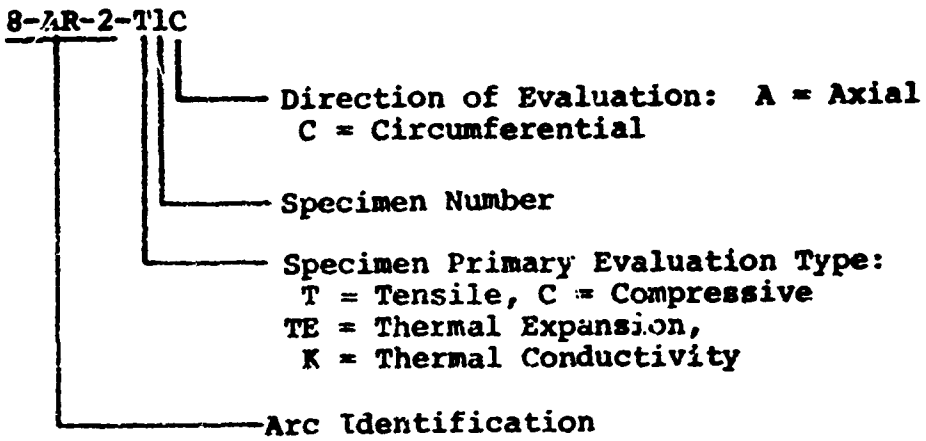
The arcs and plates supplied for this program were:

1. 3DCC (Material #8)	Impact Level (Kilotaps)
8-AR-V	0
8-AR-8	1.030
8-AR-4	1.640
8-AR-2	2.200
8-AR-7	3.045
8-AR-5	3.360
8-AR-1	5.390
8-AR-6	7.560
8-AR-3	7.880

2. Felt CC (Material #12)	Impact Level (Kilotaps)
12-F-V	0
12-F-15	1.210
12-F-16	1.700
12-F-14	2.490
12-F- 1	2.430
12-F-13	3.070
12-F-10	3.440
12-F-11	4.140

Arcs 8-AR-6 and 8-AR-3 were too severly damaged during impact loading for evaluation in this program. Plate 12-F-14 was apparently an anomalous specimen which developed a midplane delamination and surface cracks at a relatively low impact level. An attempt was made to evaluate this specimen using NDT and bulk flexure. The results were considered questionable and no further evaluations were attempted.

After the NDT consisting of radiograph, visual inspection, 40X photomicrography, bulk density, ultrasonic velocity, ultrasonic transmission, open porosity, penetrant inspection, thickness measurement and bulk flexure evaluations, the 3DCC arcs and Felt CC plates were cut into blanks as shown in Figures 5 through 8. The 3DCC blanks were all oriented in the circumferential direction. The Felt CC blanks were supposed to be oriented in the circumferential direction also. A mixup in identification of the plate directions resulted in all Felt CC blanks being oriented in the axial direction. The specimens were identified as follows:



The size of the test matrix and the limited material available required that some specimens be used for several evaluations. The 3DCC arcs numbered 8-AR-8, 8-AR-2, and 8-AR-5, were designated for tensile evaluations. Felt CC specimens from plates 12-F-V, 12-F-16, and 12-F-13 were used for tensile evaluations. The remaining arcs were utilized for compressive evaluations. All blanks received NDT evaluations consisting of bulk density, radial and axial velocity, and radial ultrasonic transmission. Specimen blanks 8-AR-8-T1C through-T4C and 12-F-V-T1A through-T4A were used for thermal conductivity evaluations in the radial inflow apparatus prior to tensile evaluations. These specimen blanks were adapted for these evaluations by machining to the configurations shown in Figures 10 and 11. Specimen blanks 8-AR-5-T1C through-T4C, 8-AR-2-T1C through-T4C, 12-F-15-C1A through-C4A and 12-F-10-C1A through-C4A were used for thermal expansion evaluations prior to compressive evaluations. Two of these blanks from a given arc were stacked to give the 3.0 in. gage length for the expansion evaluations. This provided expansion specimens in the axial direction for Material #12 and in the circumferential direction for Material #8. After the thermal evaluations the tensile blanks were machined to the configurations shown in Figures 12 and 14 and the compressive blanks as shown in Figures 15, 16 and 17. The specimens were given NDT evaluations consisting of open porosity, visual inspection, and radiography. After the 3DCC tensile specimens were run for modulus they were remachined as shown in Figure 13 to improve the probability of tensile failures.

Used compressive specimen ends were employed for the expansion specimens in the circumferential direction for Felt CC and additional evaluations in both directions on the 3DCC material. The extraction of these specimens are illustrated in Figures 18 through 21.

As mentioned above, certain tensile specimen blanks were used for thermal evaluations prior to finish machining to tensile specimens. In addition, comparative rod thermal conductivity specimens were built up of pieces taken from scrap material from arcs 8-AR-8 and 8-AR-2 and plates 12-F-10 and 12-F-15. The configurations of these thermal conductivity specimens are shown in Figures 22 and 23.

IMPACTED PHENOLIC COMPOSITE ARCS

Materials for this phase of the program included arcs of R6300, 3D Quartz-Phenolic and 3D Carbon/Quartz-Phenolic. These arcs had previously been subjected to a flyer plate impact loading at Kaman Sciences and evaluated for structure change by nondestructive testing and flexural modulus determination at Southern Research Institute. These evaluations were reported in "Damage Study of Several Carbon-Phenolic Composite Materials" to Kaman Nuclear, Purchase Order 71P00657 dated July 6, 1971.

The arcs originally had nominal dimensions of 0.450 in. thick by 1.50 in. wide by 3.0 in. chordal length with an outside radius of 4.50 in. The width dimension in some cases was altered during the previous evaluations. The altered width aggravated the specimen geometry problems of the evaluations for this program.

The R6300 composite was a single phase 2D, 20 degree angle tape wrap phenolic-carbon with an aluminum (6061-T6) backing plate. A sketch of the construction of this material is shown in Figure 2. A group photograph of the arcs evaluated is shown in Figure 89.

The 3D Quartz-Phenolic (3DQP) was a single phase 3D orthogonal phenolic-quartz composite. A sketch of the construction of this material is shown in Figure 3. A group photograph of the arcs evaluated is shown in Figure 94.

The 3D Carbon/Quartz Phenolic (3DC/QP) was a two phase material made of 3D orthogonal phenolic-graphite over a 3D orthogonal phenolic-quartz. The radials were phenolic-carbon. A sketch showing the construction of this material is shown in Figure 4. A group photograph of the arcs evaluated is shown as Figure 99.

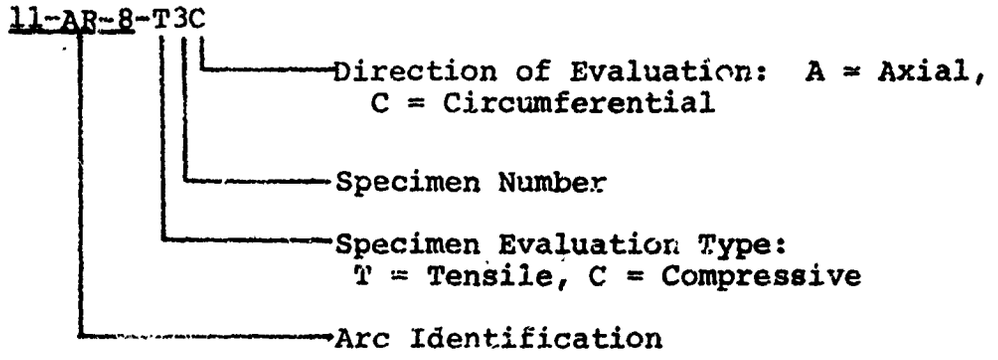
Included in the list of phenolic-composite arcs for this program were:

1. R6300 (Material #10)	Impact Level (Kilotaps)
10-AR-V	0
10-AR-4	0.490
10-AR-7	1.570
10-AR-6	1.660
10-AR-3	1.900
10-AR-1	1.990
10-AR-5	4.040
10-AR-2	

2. 3D Quartz-Phenolic, 3DQP (Material #11)	Impact Level (Kilotaps)
11-AR-V	0
11-AR-8	4.58
11-AR-5	7.54
11-AR-3	7.95
11-AR-7	8.61
11-AR-1	9.01
11-AR-2	9.01
11-AR-6	9.88

3. 3D Carbon/Quartz-Phenolic, 3DC/QP (Material #15)	Impact Level (Kilotaps)
15-AR-V	0
15-AR-3	4.09
15-AR-5	4.69
15-AR-6	5.18
15-AR-4	6.06
15-AR-7	6.51
15-AR-8	6.54

A common cutting plan was used for blanking all phenolic composite arcs, Figure 9. Two specimen blanks were oriented in the axial direction and two in the circumferential direction. Each 3DC/QP, Material #15, blank was further sliced into two smaller blanks which were predominantly 3DCP, designated #15A, and 3DQP, designated #15B. The specimen blanks were identified as follows:



Of the R6300 arcs from the earlier program, arc 10-AR-2 was considered too severely damaged and no attempt was made to machine specimens from it. The Virgin R6300 Arc, 10-AR-V, had no aluminum backing plate. The aluminum backing plate was removed from the remaining arcs by fly cutting in a milling machine. The specimens were blanked as previously described and blanks were designated for tensile evaluations from arcs 10-AR-4, 10-AR-6, and 10-AR-1. The remaining R6300 blanks were designated for compressive evaluations.

The 3DQP, Material #11, Arcs numbered 11-AR-8, 11-AR-3, 11-AR-7, and 11-AR-6 were designated for tensile evaluations. The remaining arcs were used for compressive evaluations. The arcs from the previous program were of varying widths and this distribution was chosen to utilize the longest axial direction specimen blanks for tensile evaluations.

The 3DC/QP, Material #15, Arcs numbered 15-AR-V, 15-AR-5, and 15-AR-4 were designated for tensile evaluations. The remaining arcs were used for compressive evaluations. In this distribution the two most severely damaged were chosen for compressive evaluations and the remaining distribution was selected generally to utilize the longest axial blanks for tensile evaluations and to distribute the tensile and compressive evaluations.

After NDT evaluations of the specimen blanks, they were machined to finished specimen configurations. Each specimen type, loading direction and material type was machined to its optimum configuration for the material available. Generally each specimen was the maximum possible thickness and length. The gage width of tensile specimens from the orthogonal composites, 3D Quartz-Phenolic, Material #15A and Material #15B was chosen to give two unit cells centered on the width. Compressive specimens from these materials used four unit cells centered on the gage widths. The gage width of the R6300 specimens was chosen to give a convenient and representative cross-section. Figures 24 through 39 show the configurations of the finished specimens.

SECTION III

APPARATUSES AND PROCEDURES

NONDESTRUCTIVE TESTING AND MONITOR EVALUATIONS

VISUAL AND LIGHT MICROSCOPY - For virgin material, visual inspections (1X to 10X) were made on exposed surfaces of bulk and specimen shapes to determine material macro-level typicality and surface anomalies. This was effective for detecting surface variations such as yarn bundle fraction variations, separations, macrovoids, discolorations, resin-rich and resin-starved areas, yarn bundle wrinkling and spacing variations, ply spacing variations, and void clusters. Results were documented photographically. Definitions of terms used to describe the structure-changes are shown in Figure 40. For micro-level characterization, photomicrographs at 40X were used to establish material typicality such as microcracking in yarn bundles, microcracking between matrix and yarn bundles, pore sizes, and pore size distributions. Such information was used to detect material variability (within single batch) and reproducibility (batch to batch variability).

For impacted materials, visual inspection (1X to 10X) were performed on the edges and surfaces of the specimens to assess macro-level structure change. Results were documented photographically. Photomicrographs (40X) were made on one edge (normal to axial direction) of specimens to assess micro-level structure change. Results from these inspections were compared to those from virgin material for assessment of structure-change. The photographs from both the visual inspection and the photomicrographs for the various levels of impact were compared with one another and with those from virgin material for assessment of structure-change. The Southern Research indexing and orientation systems used to locate a specific feature are shown in Figures 41 and 42.

GRAVIMETRIC BULK DENSITY - Bulk density measurements for specimens having a regular configuration were calculated from direct measurements of weights and lengths. An analytical balance having a sensitivity of ±0.0001 gram was used for weighing. Micrometers read to the nearest 0.0005 in. were used for measuring lengths, and a traveling microscope accurate to ±0.001 in. was used for measuring chord lengths.

RADIOGRAPHY - Radiography was performed using state-of-the-art X-ray techniques for low-absorptive materials. The radiographic unit used was a Radifluor 360 manufactured by Torr X-Ray Corporation, a division of Phillips Electronics. This unit is rated for operation from 0 to 120 kv at either 3 or 5 ma, making it ideal for phenolic and carbon-carbon type materials. The unit incorporates certain basic characteristics that are essential for examination of low-absorptive materials with high resolution and sensitivity. The focal spot size is 0.35 mm, and the X-ray tube window is 0.015 in. thick beryllium. A small focal spot size provides high sensitivity and distortion-free imaging of small discontinuities. Radiographic sensitivity using extra-fine grain file is within one percent (per MIL STD 453).

Operational and film development procedures were consistent with conventional good radiographic practices. For example, image sensitivity and contrast was enhanced by using minimum power settings for longer time periods. Sharp imaging was ensured by using extra-fine grain film (such as Eastman Type M) and by using a long FFD (up to 46 in.). Hand film processing in accordance to the film manufacturer's suggested procedure was used to assure maximum quality. Image quality was checked using penetrameters from similar material. Penetrameter hole sizes used are 1/2T, 1T and 2T (1T and 2T holes as defined by MIL-STD-453). Radiographs are inspected in a dark room using a high intensity (variable) spot illuminator.

ULTRASONICS - Basic apparatus used in the ultrasonic measurements of velocity, pulse-echo and through-transmission are a Sperry UM721 Reflectoscope and a Tektronix 564 Oscilloscope. Velocity is evaluated using the through-transmission, elapsed-time technique. The Sperry Um721 is used as the pulser, and the Tektronix 564 complete with a 3B3 time base (precision of 1 percent) and a 3A3 vertical amplifier is used as the signal measuring device. Inspection for flaws is done using the Sperry UM721 and the pulse-echo, reflection technique. Transmission measurements are made using the pulsed through-transmission technique with an in-line attenuator to simulate the varying degrees of structure-change. The Sperry UM721 is used as the signal pulser, the Tektronix 564 as the signal measuring device, and a Kay Model 20-0, 41dB in-line attenuator for assessing relative structure-changes in the various specimens.

In using the through-transmission, elapsed-time technique for measuring acoustic velocity, a short pulse of longitudinal-mode sound is transmitted through the specimen. An electrical pulse originates in a pulse generator and is applied to a ceramic piezoelectric crystal (SFZ). The pulse generated by this crystal is transmitted through a short delay line and inserted into the specimen. The time of insertion of the leading edge of this sound beam is the reference point on the time base of the oscilloscope which is used as a high-speed stopwatch. When the leading edge of this pulse of energy reaches the other end of the specimen, it is displayed on the oscilloscope. The difference between the entrance and exit times is used with the specimen length in calculating ultrasonic velocity. A short lucite delay line is used to allow time isolation of the sound wave from electrostatic coupling and to facilitate clear presentation of the leading edge of the entrant wave resulting in a more accurate "zero" for time.

Using 0.5/1.0 MHz transducers coupled with alcohol, the precision for this velocity measurement technique has been established for polygraphites such as ATJ-S as $\pm$0.002 in. per microsecond for a four in. long by 1/2 in. diameter specimen and as $\pm$0.010 in. per microsecond for a 1/4 in. long by 1/4 in. diameter specimen.

In using the pulse-echo, reflection technique to detect macroflaws, test blocks from ATJ-S polygraphite are used as calibration references for estimating the location, depth and size of discontinuities. These blocks are normally about 5/8 in. square by 2, 3, and 4 in. long. At one end, a single flat-bottom hole is drilled along the specimen axis to a depth of 1 in. The hole sizes range from 1/32 to 1/4 in. in 1/32 in. increments. The maximum penetrating signal frequency is used for maximum resolution, and instrument settings are duplicated as much as possible for evaluations of similar materials. Alcohol is used as the couplant. Two techniques, using a Tektronix Oscilloscope C-12 camera, are used in recording pulse-echo signals from specimens. The first technique involves taking photographs of the signal as transmitted from one or both ends of the specimen to determine "standing signals." The second technique involves recording a multiple trace (smear) of the signal. This is done by revolving the specimen on the face of the transducer on about a 1/8 in. radius with the camera shutter open. This technique tends to randomize the background noise and to define the more repetitive "standing signals."

In using the through-transmission technique for detecting structure variations, Figure 43, sound is transmitted through the specimen and displayed by the oscilloscope. The gain of the oscilloscope is held constant and a calibrated step attenuator located in the input circuit is used to maintain the displayed waveform at a constant amplitude. Values of transmission (called added dB) relative to a reference material may be read from the step attenuator. Measurements are made in an alcohol bath to minimize effects of contact coupling and near field effects. A suitable fixture is used to align the transducers and to hold the specimen squarely in the sound beam. When specimen geometry is such that part of the energy in the sound beam could by-pass the specimen, foam padding is used as a block to absorb this energy. The sensitivity of the calibrated attenuator is ± 1 dB with a minimum-maximum attenuation from 0 to 41 dB.

POROSITY BY LIQUID ABSORPTION - The evaluation of porosity and density of porous type materials such as polygraphites and carbon-carbon or carbon-phenolic composites are evaluated using a liquid absorption technique. Using this technique, mineral spirits (s.g. .76) is vacuum impregnated into samples of material. From measurements of dry weight, suspended weight and saturated weight, evaluations of absorption, density (bulk and apparent), and open porosity can be calculated directly. If the true density of the material sample is known, the total porosity and thus, the closed porosity of the material sample can be calculated.

The normal procedure used in making liquid absorption measurements involves first a thorough drying and then precise weighing of specimens to determine dry, suspended and saturated weights (recorded to nearest 0.0001 gram). First, the specimens are oven dried at temperature above 212°F for two hours to drive out absorbed moisture and then weighed to determine dry weight. Individual specimens are then placed in small beakers which are placed on their sides in a desiccator. After the desiccator is sealed off, a vacuum of 50 microns of Hg is pulled and held for two hours to remove entrapped air from the specimens. The dessicator is then purged with mineral spirits until the beakers containing the specimens are submerged. The desiccator is then vented, and the specimens are left in the desiccator for 20 minutes to allow vapor inside the specimens to condense.

The suspended weight is obtained by weighing the saturated specimen while suspended in the mineral spirits. The specimens are kept submerged by righting the beakers in the desiccator to maintain the mineral spirits level above the specimen. As shown in Figure 44, a basket is suspended from a balanced beam such that the level of mineral spirits in the individual beakers cover the specimen and basket at all times during the weighing operation. The tare weight of the basket, which is subtracted from the total suspended weight to determine the suspended weight of the specimen, is determined by weighing the suspended basket submerged in mineral spirits to the same depth that the specimen is weighed. Care is used to ensure that no air bubbles cling to the basket and that a clearance between the basket and sides of the beaker is maintained.

For determining saturated weight, the specimens are removed from the mineral spirits and wiped carefully to remove excessive surface mineral spirits. The specimens are then weighed immediately to determine the saturated weight.

From the three weights taken for each specimen (dry weight, suspended weight and saturated weight) percent water absorption, open porosity, bulk density and apparent density are determined. The total porosity can be determined also when the true density of the material is known. The equations used for these calculations are:

$$W_a = \left(\frac{W_{sa}-W_d}{W_d}\right) \frac{\rho_w}{\rho_m} \times 100 \text{ percent} \qquad (1)$$

$$P_o = \left(\frac{W_{sa}-W_d}{W_{sa}-W_{su}}\right) \times 100 \text{ percent} \qquad (2)$$

$$\rho_b = \left(\frac{W_d}{W_{sa}-W_{su}}\right) \times \rho_m \qquad (3)$$

$$\rho_a = \left(\frac{W_d}{W_d-W_{su}}\right) \times \rho_m \qquad (4)$$

$$P_t = \left[\frac{\frac{W_{sa}-W_{su}}{\rho_m} - \frac{W_d}{\rho_t}}{\frac{W_{sa}-W_{su}}{\rho_m}} \times 100 \text{ percent}\right] \qquad (5)$$

where

W_a = Water absorption

W_{sa} = Weight of sample when saturated with liquid m

W_d = Dry weight of sample

W_{su} = Weight of sample when suspended in liquid m

ρ_m = Density of liquid m (about 0.76 gm/cm^3 for mineral spirits - s. g. checked after each run)

ρ_w = Density of liquid water

ρ_t = True density of sample

ρ_b = Bulk density of sample

ρ_a = Apparent density of sample

P_o = Open porosity

P_t = Total porosity

Weights for this evaluation are determined using an analytical balance sensitive to 0.0001 gram. Instrument precision for measuring absorption is ±0.10, bulk density is ±0.002 gm/cm^3, open porosity is ±0.15 and total porosity is ±0.05.

FILTERED-PARTICLE PENETRANT INSPECTION - For inspecting porous materials whose particle size is 100 mesh or smaller, the filtered-particle inspection method is applicable. The filtered-particle system consists of a fluid (suspending medium) containing a dispersion of properly sized and shaped particles. Differential liquid absorption between an area containing a crack and one that does not is the phenomena which causes the particles to congregate about a surface discontinuity. For example, when the filtered-particle penetrant is applied, more liquid is absorbed at the site of a crack than anywhere else because of the extra absorption area within the defect. As the liquid enters the defect, the suspended particles are filtered out at the surface causing a higher concentration of particles along the defect.

The filtered-particle system used at Southern Research for phenolic and graphitic materials is Partek P-1A (in alcohol) manufactured by the Magnaflux Corporation. This system can be obtained with either an oil or alcohol base with a fluorescent particle which becomes clearly visible under black light.

The procedure for using the filtered-particle system consists first in applying the technique to a material which is applicable to the test. Partek P-1A when correctly used detects minute cracks which measure only about 0.002 to 0.003 in. wide on the surface. Application is by hand using an eye dropper, and inspection is done under black light. Results are recorded photographically using a Polaroid NP-3 camera with a Polaroid No. HNCP 37 x 0.030 in. filter and black light illumination.

ALCOHOL PENETRANT INSPECTION - Alcohol is used on porous materials such as graphites, phenolic and carbon-carbon composites as a nondestructive test for surface discontinuities such as gross porosity, wide density variations, large inclusions and cracks. When a material is wetted with alcohol, porous areas and cracks remain wet for a longer period of time than the surrounding material. The differential evaporation effect is discernible by visual observation. Although this technique is not quantitized (it probably could be), it is effective in revealing surface discontinuities.

The alcohol inspection procedure involves the following:

1. Application of alcohol to surface of specimen usually for 5 to 10 seconds. This can be done by flooding, brushing, or immersing.

2. Inspection of specimen surface as alcohol evaporates. Porous areas will remain wetted while the surrounding smooth areas will dry. Cracks also will remain wetted depending primarily upon the depth and width of the crack.

3. Record is made of visual observations.

This technique is useful in revealing surface discontinuities. Other NDT methods of inspection such as ultrasonics and radiography can be used in conjunction with the penetrant test to determine the extent of the surface discontinuity internally.

CARBON-CARBON COMPOSITES

MODULUS OF ELASTICITY (MOE) IN FLEXURE - The evaluation of modulus of elasticity in flexure was performed in a four-point bending apparatus shown schematically in Figure 45. The apparatus consists of three sections: a support section, loading section, and deflection transducer support. The support section is a steel block with "V" guides for precise spacing and alignment of support pins, 0.500 in. in diameter, at a separation of 2.250 in. for the 3DCC arcs and 1.500 in. for the Felt CC plates. The loading section is a stiff steel loading ram with "V" grooves, 0.750 in. apart for the 3DCC arcs and 0.500 in. for the Felt CC plates, for precise spacing and alignment of loading pins, 0.375 in. in diameter. The loading ram is provided with guides which ride in "V" grooves in the support block to align the support block to the loading ram. Load is applied to the loading ram through a hardened steel ball in a recessed conical seat in the loading ram.

An attempt was made to determine flexural modulus using strain gages on the specimens. The attempt was successful for the Felt CC material but was not successful for the 3DCC material. The strain gages bonded readily to the 3DCC material but came off the arcs with a thin layer of the material when flexed. Using the strain gages the Felt CC plates were evaluated by loading incrementally and reading strain using a Baldwin strain indicator box. The flexural modulus was determined for the Felt CC plates by:

$$MOE = \frac{\sigma}{\varepsilon} = \frac{6M}{bh^2} \cdot \frac{1}{\varepsilon} = \frac{6Pa}{2bh^2} \frac{1}{\varepsilon} = \frac{3Pa}{bh^2} \cdot \frac{1}{\varepsilon}$$

where

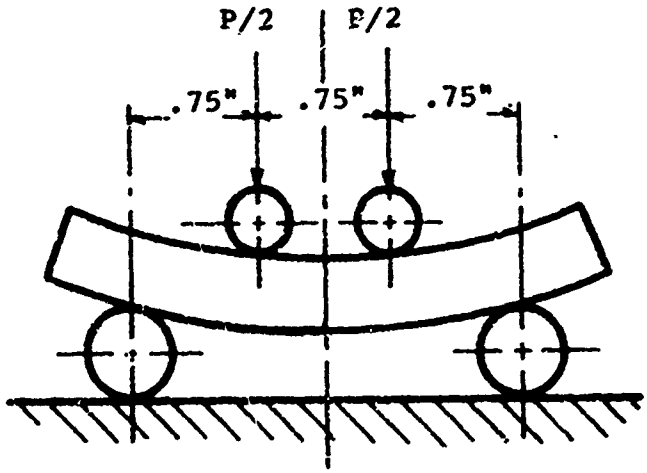
σ = Bending stress
ε = Strain gage reading
p = Applied load
a = 1/3 Beam span
b = Beam width
h = Beam depth

To conduct an MOE evaluation on the 3DCC arcs, a plate was inserted in the deflection transducer frame and centered. The specimen and transducer frame were placed on the support block and guides of the loading ram were inserted in the guide grooves of the support block. The specimen and frame were then carefully aligned such that the transducers' support frame arms were directly above the support rods. The assembled apparatus was placed between the crossheads of a 30,000 pound capacity Tinius-Olsen electromechanical testing machine. Load was applied to a maximum of 20 percent of the ultimate strength of the virgin material. Continuous load versus mid-point deflection plots were recorded on an X-Y recorder. A minimum of three loadings per side of the specimen constituted a run. The flexural modulus of elasticity (MOE) was calculated from the geometry and load-deflection curves by:

$$MOE = \frac{23a^3}{48I} \frac{P}{\delta}$$

where

a = 1/3 Beam span = 0.75 in.
I = Moment of Inertia = $\frac{bh^3}{12}$
b = Beam Width
h = Beam depth
$\frac{P}{\delta}$ = Slope of the load deflection curve



No allowance was made for curvature of the 3DCC specimens. Sample calculations showed this to be a negligible effect. The deflection measurement using the LVDT system includes a contribution due to compaction and one due to shear. Even though this shear deflection is of the same order of magnitude as the bending deflection it does not invalidate the data. The relative magnitudes of the flexural modulus values obtained in this manner provide a measure of property change. This test does prevent comparing data from the damaged and virgin 3DCC arcs since the latter arc had a different geometry and the shear deflection is strongly geometry dependent.

TENSILE EVALUATIONS - Tensile evaluations for the carbon-carbon composites, 3DCC and Felt CC, were run in the gas-bearing tensile facility. This facility utilizes precise alignments and gas-bearing universal joints to minimize the possibility (and magnitude) of external bending moments being applied to the specimen. The usual strain measuring system in this facility is our automatic optical strain analyzer. A complete description of the gas-bearing tensile testing facility is included as Appendix A.

Six specimens made from scrap material were evaluated to demonstrate the suitability of the Felt CC specimen design, Figure 17. These evaluations on the Felt CC specimens presented no problems. Evaluations as outlined in the Test Matrix, Table 4, were made on specimens from three of the impacted plates. Six specimens were evaluated at 3000°F and five at room temperature. Strain measurements were made using the optical strain analyzer. Specimens were loaded at a constant 10,000 psi per minute stress rate. Load was measured by a 2500 pound Strainsert load cell. Load versus strain was recorded on an X-Y recorder from which ultimate stress, elastic modulus and strain-to-failure were derived.

The 3DCC specimens presented several problems which were not completely overcome. First, the material available for each specimen was limited to 1.50 in. in length. The anticipated strength of the 3DCC material at 3000°F was 18,000 psi in tension and 1,200 psi in shear. The requirement that the specimen gage contain an integral number of unit cells centered on the gage set one gage dimension at either 0.10 or 0.20 in. (one or two unit cells). For a fixed grip length of 0.500 in. a gage cross section of 0.10 in. x 0.20 in. maximum was required to

limit the shear stress in the grip. During the specimen suitability demonstration higher failing loads were obtained with one unit cell in the width direction. The required elevated temperature tensile runs precluded using a combination mechanical-epoxy grip as used for the phenolic composites. The pull rod and specimen grip design which evolved are shown in Figure 46.

Another problem with the tensile evaluations on the 3DCC material was with the strain measurement. Strain measurements on initial runs on this material in the gas-bearing tensile facility were attempted using the optical strain analyzer. Seating of the specimen, bending of the specimen (due to the inevitable non-uniformity of the material) and lack of rigidity of the specimen, gave motions which the optical strain analyzer interpreted as strain. These erroneous strains made the analyzer output impossible to interpret. Clip-on strain gage extensometers do not suffer from these motions and were used to give interpretable stress-strain plots.

A specimen design suitability demonstration was attempted using seven specimens from scrap material from the AHP program. The grip lengths of these design suitability specimens were varied from 0.500 to 0.688 in. The ultimate failing stresses increased with increasing grip length. All failures were shear failures between the individual circumferential fibers and the matrix material. The only change in design which could increase the failing stress to a level where the mode was tension, rather than shear, would be to increase the grip length of the specimen. The material from the impacted arcs was not sufficient to increase the grip length.

The original specimen design, Figure 15, was retained but testing procedure was modified to assure the highest possible ultimate stresses. Stress-strain curves at room temperature were recorded to a level below the failing load of the specimen grip section. Elastic modulus was calculated from these curves. The specimens were then remachined as shown in Figure 16 to give the maximum possible specimen "grip" length. The specimens were rerun recording only a load-time plot for ultimate strength determination. These runs were at room temperature and 3000°F.

PHENOLIC COMPOSITES

TENSILE EVALUATIONS for the phenolic composites were run at room temperature in a Tinius-Olsen testing machine utilizing precision chain grips and precision specimen tabs. A sketch of the test set up is shown as Figure 48. Chain grips are used where failing loads of the specimens are likely to exceed the capacity of the gas-bearing facility.

The chain acts as a series of universal joints and is used to minimize the possibility of externally applied bending moments being introduced into the specimen. The chain is adapted to the grips by a centering bushing which locates the chain within 0.001 in. of the centerline of the grips. The chain and grips were pre-loaded above the chain rated load to assure good mating surfaces in the individual links and at the grip chain interface.

The specimens were machined to the maximum possible dimensions consistent with the material available and the requirement that the 3D orthogonal specimens be centered on the weave pattern and contain an integral number of unit cells. The elastic modulus desired was for the total thickness if possible. The resulting specimens were considerably smaller in length and width than good material testing would require. The tab-grip utilizing both mechanical and epoxy bonding to grip the specimen was felt to the best approach. A sketch of an assembly of specimen and tab grips is shown as Figure 49.

The tab and specimen were machined to the same thickness. The specimen, tabs and covers were bonded together as one assembly using Shell Resinbond 907, (2,000 psi shear strength). The assembly was lightly clamped in an alignment jig under a small preload and cured at 150°F.

Strain measurements were made using clip-on strain gage extensometers. Load on the specimen was measured with the internal load cell in the testing machine. Load was applied at a constant rate of 10,000 psi per minute. Load and strain were recorded on an X-Y recorder.

Evaluations on the R6300, Material #10, and 3DCP, Material #15A, specimens were carried successfully to ultimate. The initial runs on the quartz-phenolic materials gave bending-shear failure within the tab grips. The majority of the 3DQP, Material #11, specimens were loaded to a level within the tab grip capability for evaluation of elastic modulus. The gage sections of these specimens were then machined as shown in Figure 50 to yield a higher gage stress for a given load. These specimens were then reloaded and gave specimen failure within the gage section and a much better estimate of the tensile strength of the material.

COMPRESSIVE EVALUATIONS for the phenolic composites, were run in the gas-bearing compressive facility. A complete description of this facility is included as Appendix B. The gas bearings of this facility allow precise alignment of the load train. Before loading the specimen, the bearings are locked and thus provide rigid support to the specimen. An automatic optical strain analyzer is used for strain measurement. Specimens were machined to the maximum possible dimensions allowed by the available material and the requirement that the specimens from the 3D orthogonal materials contain an integral number of unit cells centered on the gage section of the finished specimens. Two specimens from each arc were oriented in the axial direction and two in the circumferential direction. All specimens were loaded to failure at room temperature. Plots of load versus strain were recorded on an X-Y recorder.

PRE-IMPACT NDT EVALUATIONS

NDT characterization of arcs and rings for Phase II was conducted on as-received arcs and rings from AVCO 3DC/QP, AVCO 3DCP, AVCO 3DCP (T400), AVCO R6300, AVCO 3DCC and Sandia Felt CC. This work entailed characterization and quality control of 55 undegraded arcs, 67 rings, 11 discs, and 10 coupons. All specimens received quality control (QC) evaluation consisting of bulk density, visual inspection (1X) with photographic (1X to 10X) documentation, and radiography with one additional NDT monitor where questionable material uniformity or reproducibility appeared. Based on the QC results and agreement with the Air Force Project Officer, 5 arcs (AVCO 3DCP) and 6 rings (two each from AVCO R6300, AVCO 3DCC and Sandia Felt CC) were selected for more extensive NDT evaluation. This additional or full treatment (FT) NDT included inspections by ultrasonic velocity, radial ultrasonic transmission, liquid penetrants, 40X photomicrography, and bulk mechanical evaluations.

The test matrix for Phase II was presented in Table 3. The Southern Research indexing systems used for the various configurations are given in Figures 43 and 44.

NONDESTRUCTIVE RING MODULUS EVALUATIONS

The 6 rings which received the full treatment NDT evaluations received nondestructive modulus evaluations also. Two different methods were used: first, a ring flexure evaluation, and second, a hydrostatic compression evaluation. During these evaluations the rings were loaded to no greater than 20 percent of ultimate strength as defined by data from the AHP program.

A schematic drawing of the setup used for the ring flexure evaluations is shown as Figure 51. The ring was instrumented with four strain gages on the inside surface oriented in the circumferential direction. The ring to be evaluated was located between the crossheads of a Tinius-Olsen testing machine. Three dial indicators were located around the ring to measure radial deflection as shown in Figure 51. Strain was read using a Baldwin strain indicator. Load was read from an internal load cell in the testing machine. The ring was loaded incrementally and all dial indicator and strain gages read at each load increment. The ring was loaded to 20 percent or less of its ultimate strength. The sequence was repeated at least twice with the arbitrarily selected NDT zero orientation under the loading pad, rotated 45° degrees counterclockwise and at 90 degrees to the vertical. Modulus values were calculated using the classical ring equations.

The hydrostatic compression evaluation was run in a hydrostatic loading rig shown schematically in Figure 52. The loading medium was a thin wall rubber bladder which was connected to a hydraulic cylinder. The bladder was contained on the outside diameter by an outer closure ring and top and bottom closure plates. The bladder was contained on the inside diameter by the test ring and spacer rings. The spacer rings were sized to give an assembled height with the test ring in place which was 0.005 in. less than the outer closure ring. The bladder was oversized for the cavity in the rig and this combined with its thin wall ensured that the bladder supported a negligible portion of the hydraulic loading. The hydraulic system was filled and bled. The hydraulic cylinder was loaded in a tinius-Olsen testing machine. Load was measured by an internal load cell in the testing machine. This load was converted to hydraulic pressure and stresses were calculated using thick walled cylinder relationships.

$$\sigma = 2\rho \frac{R_2^2}{R_2^2 - R_1^2}$$

where

σ = Circumferential stress at I.D.
ρ = Hydraulic pressure
R_2 = Outside radius
R_1 = Inside Radius

Strain was read using a Baldwin strain indicator. From the stress and strain values, modulus was calculated using the Hook's Law relationship:

$$\sigma = E\varepsilon$$

SECTION IV

PROPERTIES OF IMPACTED ARCS AND SPECIMENS

3D CARBON-CARBON IMPACTED ARCS

NONDESTRUCTIVE TESTING - Results of the nondestructive monitors for the 3DCC impacted arcs are given in Table 4 and described graphically in Figure 63. The results of the subjective NDT evaluations are shown in Table 5 and are photographically documented in Figures 53 through 62. The ranges of monitor values measured on specimens from the arcs are also shown in Table 4 to give reinforcement to the magnitudes of the monitors on the arcs and an impression of the variability of the monitors with position on the arcs.

Visual (1X-10X) inspection of the impacted arcs indicated structure-change starting at the lowest impulse level of 1.03 kilotaps, Arc 8-AR-8. Structure-changes detected at this level were radial spall from one machined edge, bulk and aligned delaminations in edges, slight radial protrusion from front and rear faces, and occasional spall of radial ends from rear face, Figure 54. A rear delamination located about 0.1 in. from the rear face was detected at 2.20 kilotaps, Arc 8-AR-2, Figure 55. In addition, matrix spall from around radials on the front face was also detected at this level. Front yarn lift (circumferentials) at one edge was detected at 3.045 kilotaps, Arc 8-AR-7, Figure 56, and matrix spall from the edges was detected at 3.36 kilotaps, Arc 8-AR-5, Figure 57. Increased bulk and rear delaminations, rear radial recession, and a single front face crack were detected at 5.39 kilotaps, Arc 8-AR-1, Figure 58. A gross mid-thickness delamination with bulk delaminations, gross rear yarn lift and matrix spall, and a through-thickness crack were detected at 7.56 kilotaps, Arc 8-AR-6, Figure 59. At the highest impulse level of 7.88 kilotaps, Arc 8-AR-3, structure-change was similar to the 7.56 kilotap level except the specimen was totally separated near its middle, Figure 60.

Visual (10X) inspection did not reveal any new structure-change.

The group radiograph is shown in Figure 61. In comparing the before hit and after hit radiographs, no structure-change was detected for the 1.03, 1.64 and 2.20 kilotap levels; Arcs 8-AR-8, 8-AR-4 and 8-AR-2. Circumferential low-absorptive alignments measuring 0.6 and 0.7 in. long were detected at 0.1 in. from the rear face at 3.045 kilotaps, Arc 8-AR-7. Continuous, circumferential low-absorptive alignment at 0.1 and 0.35 in. from

the rear face and some volume oriented low-absorptive alignments were detected at 3.36 kilotaps, Arc 8-AR-5. Increased circumferential low-absorptive alignments at 0.1, 0.2, 0.3, and 0.4 in. from the rear face were detected at 5.39 kilotaps, Arc 8-AR-1. Gross circumferential alignments at 0.1 and 0.3 in. from the rear face and missing material from the rear face were detected at 7.56 and 7.88 kilotaps, Arcs 8-AR-6 and 8-AR-3. Aslo, a near through-thickenss radial low-absorptive alignment was revealed near the middle of Arc 8-AR-6 at the 7.56 kilotap level.

Photomicrographs (50X before reduction) are shown in Figure 62. Except for Arc 8-AR-2 at the 2.20 kilotap level, no gross macro structure-change was particularly obvious in single plane sections at up to the 5.39 kilotap level. At the 2.20 kilotap level, a circumferential separation was detected at 0.1 in. from the rear face even in single plane inspection. The separation occurred at a circumferential/axial bundle interface and was about macro-level structure-change consisted of fractured circumferentials and circumferential separations through axial bundles. Gross macro delaminations were incurred at the 7.56 and 7.88 kilotap levels.

The results of the monitors versus impact level for AVCO 3DCC arcs are plotted in Figure 63. The monitors bulk density and thickness measurements indicated slight material compaction at the lower impact levels and material expansion at the higher levels up through 3.045 kilotaps and expansion above this level. The magnitudes of the decreases in thickness, 0.001 in., at the lower impact levels would not usually be considered significant, but the significant and consistent increases in bulk density lend weight to the thickness changes. Open porosity measurements provided uniform values from the virgin arc through the 3.045 kilotap level. For these impulse levels, the virgin specimen had the highest open porosity of 11.8 percent with the 1.03 kilotap level specimen having the lowest at 10.5 percent. Open porosity increased to 12.2 and 13.0 percent at the 3.36 and 5.39 kilotap levels, respectively. Ultrasonic transmission measurements also indicated no significant structure-change up to 3.045 kilotaps. The transmission values ranged from 28.5 to 26 added dB over this range with the virgin arc having a transmission of 28 added dB. Transmission at 3.36 and 5.39 kilotaps decreased significantly to 17 and 19 added dB, respectively. Radial velocity was measured at both ends of the arc and at the center. The values in Table 4

are minimum and maximum values. The minimum values, which were considered more revealing of structure-change, indicated no change below 2.20 kilotaps, ranging from 0.1966 in./μsec at 2.20 kilotaps to 0.2025 in./μsec at 1.03 kilotaps (minimum values). Minimum values ranged from 0.1857 in./μsec at 3.045 kilotaps to 0.1585 in./μsec at 4.39 kilotaps. Maximum and minimum values of radial velocity for the various impulse levels are plotted in Figure 63.

Comparison of thickness and radial sonic transmission measurements before and after the MOE evaluations indicate that flexing the arcs had negligible effect.

MECHANICAL EVALUATIONS - The results of evaluations of flexural modulus are given in Table 4 and plotted in Figure 63. Tensile and compressive properties are given in Table 6 and are plotted in Figures 64, 65 and 66. Tensile and compressive stress strain curves are included in Appendix G. The flexural moduli in Table 4 and Figure 63 probably are not engineering values. The high modulus of the 3DCC material, the load levels imposed and the proportions of the arcs combined to give very small deflection signals from the flexural evaluations. Shear deflections aggravated by the delaminations inherent in this material and arc general compaction were included in the deflection signal measured and were probably large relative to the pure bending deflection which was desired. They do reflect structural change and their relative magnitudes should give a good approximation of the change in flexural modulus expected. The flexural modulus of the virgin specimen was not comparable to those of the impacted arcs since a different testing geometry was required. The flexural modulus of the impacted specimens showed a reasonably consistent decrease with increasing impact level. The most meaningful display of this consistency is shown in Figure 66, a plot of retained modulus versus impact level. The base for this plot of flexural modulus was obtained by extrapolation of the data for the impacted arcs back to a zero level of impact. The only significant deviation from a linear relation between the retained flexural modulus and impact level was at the 5.390 kilotap level. At this level data from the lower impact levels would have predicted a zero retained flexural modulus rather than the measured 18 percent.

Of the tensile and compressive data, Table 6 and Figures 64, 65 and 66, only the tensile modulus at room temperature and compressive strength at room temperature and 4500°F showed consistency. The tensile modulus decreased from about 12.8×10^6 psi for the virgin material (AHP data) to 7.09×10^6 psi for specimens from Arc 8-AR-5, 5.39 kilotaps. The minimum tensile strength was more consistent than the average strength and had values at room temperature of 11,500 psi for the virgin material

(AHP data), 11,040 psi at 1.030 kilotaps, 10,600 psi for 2.200 kilotaps and 9,280 psi for 3.360 kilotaps. At 3000°F the minimum tensile strength values were 16,240 psi for 1.030 kilotaps, 18,400 psi for 2.200 and 16,600 psi for 3.360 kilotaps. No data were available at 3000°F for the AHP material in the circumferential direction. As one would suspect the tensile strength was not very sensitive to impact level. The structure-changes observed in the visual inspection were predominantly in the matrix material between fibers and the tensile strength is related to the fibers.

The compressive strength showed variation with impact level. The strength at room temperature was 8,590 psi for the virgin material (AHP data), 5,760 psi at 1.640 kilotaps, 4,880 psi at psi at 3.045 kilotaps, and 4,030 psi at 5.390 kilotaps. At 3000°F the strength of the AHP material was 13,000 psi and at 4500°F for this program the strengths were 11,360 psi for virgin material, 10,970 psi at 1.640 kilotaps, 10,600 psi at 3.045 kilotaps and 7,430 psi at 5.390 kilotaps. Compressive modulus was not consistent. There were wide discrepancies between the two values at each temperature and impact level and extremely low values at 4500°F for the specimens from 8-AR-7, 3.045 kilotaps. These low values at 4500°F were not confirmed by low values at room temperature for this hit level.

THERMAL EXPANSION OF 3DCC - The thermal expansion values of 3D Carbon-Carbon in the axial and circumferential directions at various impact levels are shown in Figures 67 through 70 and Tables 7 through 12. In each figure the thermal expansion of a virgin specimen of 3D Carbon-Carbon evaluated under a previous program is plotted for a baseline reference.

Note that the expansion of the impacted material was always higher than that of the virgin material. The difference was most pronounced in the axial direction on the material impacted at a level of 5.39 kilotaps. The difference was only slight in the circumferential direction. The reason for the higher expansion of the impacted material may be due to separations between fabric and matrix. When the fabric and matrix separate, the expansion will no longer be controlled by the fabric. Lack of influence from the fabric would allow greater expansion.

In Figures 67 and 68 duplicate runs were made to 5000°F on the same specimen and in both cases the values measured during the second run after initial exposure to 5000°F were lower than those of the first. The slight inflection of the slope above 4000°F on all runs indicates some instability of this material at 5000°F.

THERMAL CONDUCTIVITY - The thermal conductivity of 3DCC in the radial direction at two impact levels, 1.03 and 2.20 kilotaps, is shown in Figure 71 and Tables 13 and 14. No trend in values was detected with impact level. A smooth curve was fitted to all the data and the values decreased from 275 Btu in./hr ft^2 °F at 100°F to a minimum of 132 Btu in./hr ft^2 °F at 3300°F, above which the values increased to 175 Btu in./hr ft^2 °F at 5000°F.

The thermal conductivity of the virgin material determined previously (AHP program) was lower than the impacted material. The reason for this anomoly probably is that the virgin material had a lower density and velocity than the impacted material. The respective densities were 1.63 gm/cm^3 and 1.68 gm/cm^3 and the velocities were 0.181 in./μsec compared to 0.20 in./μsec. Due to this density variation the effect of impact level could not be determined since the base line data does not appear to be representative of present specimens of 3DCC before impact.

The increase in conductivity above 3000°F is typical for some CC materials. As has been indicated with the results of the expansion evaluations the material is not stable at higher temperatures. Supporting this is the fact that the second run (after initial exposure to 5000°F) exhibited a slightly lower value in conductivity.

FELT CC IMPACTED PLATES

NONDESTRUCTIVE TESTING - Results of the non-destructive monitors of the Felt CC impacted plates are shown in Table 15 and described graphically in Figure 78. The ranges of values of the monitors on specimens removed from the plates are also shown in Table 15 to give reinforcement to the magnitudes of the monitors on the plates and an idea of the variability of the monitors with position on the plates.

Visual (1X-10X) inspection of the impacted plates indicated gross structure-change at 2.49 kilotaps, Plate 12-F-14, consisting of a gross delamination and a rear face crack, Figures 72 and 73. Structure-change at this impact level was much more severe than changes incurred at the higher impact levels. At 3.07 kilotaps, Plate 12-F-13, aligned hairline cracking in one edge located about 0.15 in. from the rear face was detected; however, cracking was not prominent enough at the surface for photographic documentation. At 3.44 kilotaps, Plate 12-F-10,

aligned cracking locat l about 0.2 in. from the rear face in two edges was apparent, Figure 74, and at 4.14 kilotaps, Plate 12-F-11, aligned cracking located about 0.2 in. from the rear face was apparent in all four edges, Figure 75. The only surface variations detected were at 2.49 kilotaps, Plate 12-F-14 which consisted of increased porosity and a rear face crack.

Visual inspection (10X) detected no structure-change to 2.43 kilotaps, and no additional structure-change to the changes detected at 1X at any of the higher impact levels.

The group radiograph is shown in Figure 76. Specimen 12-F-14 at 2.49 kilotaps showed a gross delamination for the full length of the plate. Otherwise, no structure-change was indicated at 1.21, 2.43 and 3.07 kilotaps. At 1.7 kilotaps, Plate 12-F-16, some low-absorptive alignments located about 0.1 in. from the rear face and running nearly the full length of the plate gave reason to suspect internal cracking. Since these plates were not radiographed before impact, no definite conclusion could be made from the radigraph. At 3.44 and 4.14 kilotaps, low-absorptive alignments located 0.25 in. from the rear face and at mid-thickness, respectively, were apparent. At 3.44 kilotaps, Plate 12-F-10, the alignments extended nearly the full length of the plate, and at 4.14 kilotaps, Plate 14-F-11, the alignments extended the full length of the plate and were more severe.

Photomicrographs (50X before reduction) are shown in Figure 77. No macro structure-change was indicated at any of the impact levels except in 12-F-14 at 2.49 kilotaps. As shown, missing material from a zone located between the gross delamination and the rear face was apparent. Macro cracking or delamination was also apparent at 3.44 and 4.14 kilotaps. Material adjacent to the macro cracking was virgin-appearing.

Liquid penetrants (Partek) detected some aligned cracking in two edges at 2.43 kilotaps, Plate 12-F-1. In addition, penetrants revealed aligned cracking in the third face of Plate 12-F-10 at 3.44 kilotaps (cracking in two faces by visual 1X) and rear face porosity in 12-F-14 at 2.49 kilotaps.

The results of the monitors versus impulse level for Felt CC plates are plotted in Figure 78. In general the NDT monitors did not indicate appreciable structure-change below the 4.140 kilotap level, excepting 12-F-14 at 2.49 kilotaps. The major exception to this was the bulk density of the plate 12-F-1 which

was far lower than the other plates. The low density apparently existed before flyer plate impact since the other NDT monitors did not detect any significant deviations in this plate. At 4.14 kilotaps, significant shifts in open porosity, velocity, and ultrasonic transmission were measured. Open porosity was 16.1 percent, velocity was 0.1034 in./μsec (lowest value), and transmission was 18 added dB. The average values at all of the other impulse levels (including virgin) were open porosity of 12.0 percent (range 10.3 - 13.1 percent), velocity of 0.1084 in./μsec (range 0.1057 - 0.1128 in./μsec), and transmission of 38 added dB (range 37 - 40 added dB). Monitor effectiveness was hampered by the lack of values before flyer plate impact.

Comparison of thickness, radial velocity and radial ultrasonic transmission measurements before and after MOE evaluations indicated that flexing had essentially no effect on the plates.

MECHANICAL EVALUATIONS - The results of flexural modulus evaluations on Felt CC are shown in Table 15 and Figures 78 and 82. Tensile and compressive properties are tabulated in Table 17 and are presented graphically in Figures 79 through 82. Tensile and compressive stress-strain curves are included as Appendix H. The flexural modulus value was 2.37×10^6 psi for the virgin specimen. Flexural modulus values indicated essentially no change below 3.070 kilotaps and decreases of about 10 percent at 3.070 kilotaps, 18 percent at 3.440 kilotaps, and 16 percent at 4.140 kilotaps. This indication of change above 3.070 kilotaps coincided with the appearance of macrocracking at 3.070 kilotaps and above.

Plate 12-F-14 had an anomalous response to flyer plate impact. It exhibited gross structure-change even though its impact level, 2.490 kilotaps was an intermediate value. Plate 12-F-1 was supplied to Kaman Sciences as a replacement for Plate 12-F-14. The geometry of Plate 12-F-1 differed from that of the other plates but this was not considered significant. After impact the bulk densities of this plate and the specimens from this plate were low compared to those of the other plates, even though none of the other NDT monitors detected significant deviations for this plate. The compressive strengths at both 70°F and 4500°F of the specimens from this plate were the highest of all of the plates. In view of the above data Plate 12-F-1 as well as 12-F-14 were concluded to have differed from the other plates prior to flyer plate impacting and cannot be compared to them for response after flyer plate impacting.

THERMAL EXPANSION - The thermal expansion of Felt CC in the axial and circumferential direction at various impact levels is shown in Figures 83 through 87 and Tables 18 through 27. In the axial direction the impact levels up to 3.44 kilotaps had no effect on the expansion as can be seen from the excellent agreement with the values measured on the virgin material evaluated previously (AHP program). In the circumferential direction the impacted specimens, from 1.2 to 4.2 kilotaps, had lower expansions than those of the virgin material. No trend could be detected with level of impact. The lower expansion of the impacted specimens is not fully understood; however, the possibility of the cracked areas acting as strain isolators may be the reason.

THERMAL CONDUCTIVITY - The thermal conductivity of Felt CC in the radial direction for both virgin and impacted specimens is shown in Figure 88 and Tables 28 and 29. The impacted material exhibited somewhat lower conductivity than that of the virgin and less than expected. No trend was observed for the two impact levels evaluated.

R6300 IMPACTED ARCS

NONDESTRUCTIVE TESTING - Results from prior evaluations on the R6300 arcs are included as Table 30 and Figure 90 for reference and a group photograph as Figure 89. During the earlier program no significant change in flexural modulus, MOE, had been measured even though significant structure-change had been detected visually. The most probable cause for the inability to measure a MOE change was the masking effect of the attached aluminum backing plate. Open porosity and radial ultrasonic transmission (attenuation in previous program) correlated somewhat with impact level.

Results from nondestructive testing of specimens from the R6300 arc are shown in Table 31 and Figure 91. From Figure 91 it was obvious that open porosity, ultrasonic transmission and ultrasonic velocity were sensitive monitors for the levels of impact. Bulk density differences shown in Figure 91 are not felt to be attributable to impact.

MECHANICAL EVALUATIONS - Results of tensile and compressive evaluations on the specimens from the R6300 arcs are shown in Table 31 and Figures 92 and 93. Compressive strengths in both axial and circumferential directions seem to be linearly related to impact level. The tensile and compressive moduli were not changed by impact levels. Only if the data from the AHP program

are used for virgin values does any change in tensile strength due to impact appear significant. The tensile strengths from the AHP program were respectively 5,800 psi and 9,000 psi in the axial and circumferential directions. The tensile strengths at 0.49 kilotaps were 3,480 psi and 6,800 psi and at 1.99 kilotaps 3,040 psi and 7,260 psi in the same order as above. Compressive strengths in the axial and circumferential directions changed almost linearly from 27,600 and 30,960 psi for the virgin specimens to 17,700 and 16,170 psi at 4.04 kilotaps. Radial sonic velocity and open porosity would seem to be useful as monitors of compressive strength after impact but monitors for other properties seemed to be lacking.

3D QUARTZ-PHENOLIC IMPACTED ARCS

NONDESTRUCTIVE TESTING - Results from the prior NDT evaluations on the 3D Quartz Phenolic arcs are presented as Table 32 and Figure 95 for reference. A group photograph of the arcs is included as Figure 94. During this earlier program significant changes in flexural modulus, MOE, were measured and a remarkably strong correlation with ultrasonic attenuation (transmission) was indicated. Ultrasonic velocity correlated very well up to the level where the signal became attenuated. Bulk density, open porosity and thickness changes also correlated with flexural modulus changes but their sensitivity was much less than the ultrasonic monitors.

Results from the NDT evaluations on the specimens from the 3D Quartz Phenolic arcs are shown in Table 33 and Figure 94. Unlike the NDT on the arcs, the monitors on the specimens were not sensitive to level of impact up to 7.95 kilotaps. In particular ultrasonic transmission indicated essentially no change at all. Above 7.95 kilotaps bulk density and open porosity changed linearly with change in impact level.

Visual inspection of the specimens revealed little that had not been noted earlier for the arcs. Generally for the lower levels of loading, occasional (volume) cracking was observed and for the higher levels aligned cracking and delamination primarily at midthickness were observed. The aligned cracking increased in severity with increasing impact level.

MECHANICAL EVALUATIONS - Results of tensile and compressive properties evaluations on specimens from the Quartz-Phenolic arcs are shown in Table 33 and Figures 97 and 98. Axial tensile strength decreased linearly from 42,400 psi for the virgin specimens (AHP data) to 32,590 psi at 7.95 kilotaps. At 9.88 kilotaps the axial tensile strength dropped sharply to 21,470 psi. Similar trends were observed for the circumferential tensile data with a linear decrease from 69,900 psi for the virgin specimens (AHP data) to 51,650 psi at 7.95 kilotaps. A sharp drop in strength to 21,500 psi at 9.88 kilotaps was also similar to that for the axial strength. Compressive strength decreased approximately linearly from 28,800 psi and 26,080 psi in the axial and circumferential directions for the virgin specimens to 11,180 psi and 11,520 psi at 9.01 kilotaps. Tensile moduli showed only slight change with impact level. The tensile moduli in the axial and circumferential directions decreased from 2.14×10^6 psi and 3.57×10^6 psi for the virgin specimens (AHP data) to 1.46×10^6 psi and 2.31×10^6 psi at 9.88 kilotaps. The compressive moduli in the axial and circumferential directions showed a small decrease from 2.65×10^6 psi and 2.78×10^6 psi for virgin specimens to 1.73×10^6 psi and 2.33×10^6 psi at 9.01 kilotaps. Again the AHP data were lower than the virgin data from this program. The NDT monitors seemed to correlate somewhat with strength in that they showed small decreases from the virgin specimens up to 7.95 kilotaps and a sharper decrease to 9.88 kilotaps.

3D CARBON-PHENOLIC PORTION OF 3DC/QP IMPACTED ARCS #15A

NONDESTRUCTIVE TESTING - Results from the prior NDT evaluations on the 3D Carbon/Quartz-Phenolic impacted arcs are presented as Table 34 and Figure 100 for reference. A group photograph of the arcs is shown as Figure 99. During these prior evaluations flexural modulus (MOE) decreased approximately linearly with increasing impact level. As for the 3D Quartz/Phenolic ultrasonic attenuation (transmission) was a very good correlator for MOE. Bulk density, open porosity and thickness changes showed some correlation to (but were not very sensitive) MOE changes.

Results from the NDT evaluations on the specimens from the 3D Carbon-Phenolic portion, #15A, of the 3DC/QP impacted arcs are shown in Table 35 and Figure 101. The NDT monitors for the specimens generally correlated with impact level but were less sensitive to changes in impact level than they were for the arcs. Ultrasonic transmission dropped significantly from the virgin specimens to the first impact level, 4.09 kilotaps, but showed little change above this level. Bulk density and open porosity changes showed correlation with impact level similar to those for the arcs.

Visual inspection of the specimens generally showed the same structure-changes as had been observed earlier for the arcs. These structure-changes were volume cracking at the lowest impact level, 4.09 kilotaps; increased volume cracking with occasional failed radials at 4.69 kilotaps; aligned cracking at the center of the Carbon-Phenolic portion of the arc at 5.18 kilotaps; and delaminations near the center of the Carbon-Phenolic portion of the arcs at the two highest impact levels, 6.06 and 6.51 kilotaps. The failure of ultrasonic transmission as a monitor of the impact level above 4.69 kilotaps is probably associated with the appearance of failed radials and delaminations.

MECHANICAL EVALUATIONS - Results of the evaluations of tensile and compressive properties of specimens from the Carbon-Phenolic portion of the 3DC/QP arcs are shown in Table 35 and Figures 102 and 103. Both tensile and compressive strengths decreased almost linearly from the virgin material to the highest impact levels tested. Axial tensile strength decreased from 16,980 psi for the virgin specimens to 1,240 psi at the 6.06 kilotaps. The circumferential tensile strength decreased from 22,520 psi for the virgin specimens to 200 psi at 6.06 kilotaps. These tensile strengths at 6.06 kilotaps can be considered essentially zero. Compressive strengths decreased from about 22,000 psi for both axial and circumferential virgin specimens (AHP data) to about 5,100 psi and 4,200 psi in the axial and circumferential directions respectively at 6.5 kilotaps.

Modulus values were difficult to obtain for these specimens. The extensive structure-changes prevented the material from behaving as a homogeneous material and this caused erratic strain behavior. Modulus values were obtained for axial tensile specimens, and circumferential compressive specimens. Axial tensile modulus decreased about linearly from 6.63×10^6 psi for the virgin specimens to 0.24×10^6 psi at 6.06 kilotaps. Circumferential tensile modulus was 6.10×10^6 psi for the virgin specimens and 1.25×10^6 psi at 4.69 kilotaps. Circumferential compressive modulus decreased erratically from 6.81×10^6 psi for the virgin specimens to 5.20×10^6 psi at 5.18 kilotaps and decreased sharply to 0.96×10^6 psi at 6.5 kilotaps.

The essentially linear decrease in tensile and compressive strengths and tensile moduli with impact level agreed with the approximately linear response of MOE for the complete arcs. The regular progression of structure-changes with impact level were thus reflected in flexural, tensile and compressive properties of the Carbon-Phenolic portion of the 3DC/QP material.

3D QUARTZ-PHENOLIC PORTION OF 3DC/QP IMPACTED ARCS #15B

NONDESTRUCTIVE TESTING - Results from the prior NDT evaluations on the 3D Carbon/Quartz-Phenolic are shown in Table 34 and Figure 100 and were discussed in the preceding section on the 3D Carbon-Phenolic portion of the 3DC/QP arc.

The results from the NDT evaluations on the specimens from the 3D Quartz-Phenolic portion, #15B, of the 3DC/QP impacted arcs are shown in Table 36 and Figure 104. The NDT monitors for these specimens seem to correlate generally with impact level but are less sensitive than these same monitors on the #15A specimens. Some structure-change is indicated by the monitors but significant changes were observed from visual inspection of the specimens only at the highest impact level, 6.5 kilotaps. Visual inspection of the arcs earlier had revealed some volume cracking at the lower impact levels and aligned cracking near the inner surface at the highest impact level, 6.5 kilotaps.

MECHANICAL EVALUATIONS - Results of the tensile and compressive properties evaluations on specimens from the Quartz-Phenolic portion of the 3DC/QP impacted arcs are shown in Table 36 and Figures 105 and 106. Tensile strengths in Table 36 and Figure 105 do not represent ultimate strengths. All specimens failed in the grip section. The failures were due to a combination of bending and shear. The strengths tabulated and plotted represent a lower bound above which the ultimate tensile strengths will lie. The axial tensile stress in the virgin specimens at failure was 35,500 psi which was about 25 percent less than the ultimate tensile strength from the AHP program of 57,550 psi. The circumferential tensile stress in the virgin specimen was 35,900 psi compared to 78,200 psi for the ultimate from the AHP program. Specimen 15B-AR-V-T4C was run once for modulus. The gage section was then reduced in an attempt to give a tensile failure in the gage section. This specimen was broken in loading into the load train.

The axial compressive strengths decreased almost linearly with impact level from 46,800 psi for the virgin specimens (AHP data) to 17,200 psi at 6.5 kilotaps The circumferential compressive strength decreased approximately linearly from 47,400 psi for the virgin material (AHP data) to 16,300 psi at 6.5 kilotaps.

The modulus values showed little change with increasing impact level. The axial tensile modulus decreased from 2.20×10^6 psi for the virgin specimens to 1.62×10^6 psi at 4.69 kilotaps and then increased again to 2.12×10^6 psi. Circumferential tensile modulus decreased slightly from 3.16×10^6 psi for the virgin specimens to 3.03×10^6 at 4.69 kilotaps and returned to 3.16×10^6 psi at 6.06 kilotaps. Axial compressive modulus decreased approximately linearly from 3.42×10^6 psi for virgin specimens (AHP data) to 2.37×10^6 psi at 6.5 kilotaps. Circumferential compressive modulus behaved irregularly, decreasing from 3.50×10^6 psi for virgin specimens to 2.84×10^6 psi at 4.09 kilotaps and then increasing to 3.26×10^6 psi at 6.5 kilotaps.

The only properties of these specimens which agreed well with the linear decrease of MOE with impact level on the complete arcs were the compressive strengths. Had the failure mode of the tensile specimens been tensile it is probable that tensile strengths would have also agreed with the linear MOE response. Tensile and compressive moduli did not agree with the MOE response.

SECTION V

DISTRIBUTION OF STRUCTURE-CHANGE IN ARCS

A study was made to determine distribution in the plane of the cylinder of structure-change within a given arc. Radial differences were obvious but not inspected quantitatively. The primary tools used were radiography of arcs and specimens from the arcs and visual inspection. Correlations were then made between these results, other NDT monitors and mechanical property results on specimens. Observe that a specimen represents a sample from an arc.

3D CARBON-CARBON

Radiographs of Arcs 8-AR-8, 8-AR-4 and 8-AR-2 indicated no structure-change. Radiographic and visual inspections of specimens from Arcs 8-AR-8 and 8-AR-4 indicated no structure-change. NDT monitor results and mechanical property results from these specimens were similar and this indicated uniform distribution of any structure-change. Radiographic inspection of Specimen 8-AR-2-T1C revealed a circumferential low-absorptive alignment over the full length of the specimen. Aligned cracking was detected visually about 0.10 in. from the rear face of the specimen. From the mechanical property results at 70°F, Specimen 8-AR-2-T1C had a tensile strength of 10,600 psi and elastic modulus of 5.97 x 10^6 psi which were significantly lower than values for 8-AR-2-T4C of 16,100 psi and 10.3 x 10^6 in. respectively. Thus, neither structure-change nor retained properties were uniform in Arc 8-AR-2. The mechanical property results at 3000°F and NDT monitor results of these specimens were similar indicating similar structures.

Structure-change was detected by radiography in bulk arcs at 3.045 kilotaps, Arc 8-AR-7. This change was indicated by low-absorptive alignments near both ends of the arc. A positive print of the radiograph was given in Figure 61, and a sketch showing this result is given in Figure 107. Radiographs of specimens from this arc revealed increased volume oriented low-absorptive alignments in the gage of Specimens 8-AR-7-C1C and 8-AR-7-C3C. Specimen 8-AR-7-C1C was considered more severe than 8-AR-7-C3C. Further, the radiographs of the specimens clearly showed the low-absorptive alignments detected in the ends of the bulk arc to lie only in Specimens 8-AR-7-C1C and 8-AR-7-C3C. Thus, the structure-change was not only located at the ends of the arc but was also local to one edge. From the mechanical property results at 70°F, Specimen 8-AR-7-C1C had a slightly lower strength and significantly lower modulus than Specimen 8-AR-7-C3C. These strength and modulus values were 4,600 psi and 4.82 x 10^6 psi for Specimen 8-AR-7-C1C and 5,100 psi and 7.26 x 10^6 for Specimen

8-AR-7-C3C. NDT monitor results for the specimens were similar except that radial velocity for Specimen 8-AR-7-C3C was higher, 0.2166 in./μsec for Specimen 8-AR-7-C3C and 0.1950 in./μsec for Specimen 8-AR-7-C1C. At 4500°F the mechanical property results were similar. Strengths and modulus values were 10,400 psi and 0.62×10^6 psi for Specimen 8-AR-7-C2C and 10,900 psi and 0.89×10^6 psi for Specimen 8-AR-7-C4C. It should be pointed out tha these values for modulus (4500°F) did not align with the values measured at the other impact levels. For example, at 1.640 kilo taps the average modulus was 3.24×10^6 psi and at 5.39 kilotaps the average modulus was 1.94×10^6 psi. NDT monitor results for the 4500°F specimens indicated no significant variation of struc ture-change. This entire arc had significant structure-change but the change in NDT monitors and retained properties were not the same quantitatively.

Increased structure-change was detected by radiography at 3.360 kilotaps, (Arc 8-AR-5), Figure 108. Continuous low-absorpt alignments were detected at 0 10 and 0.35 in. from the rear face. Structure-change showed slight increase in intensity towards the ends of the arc. Radiographic results on the specimens indi cated similar structures for all the specimens.

NDT monitor and mechanical results on specimens from ARC 8-AR-5 indicated some variation in values, but these were not significant enough to be conclusive of variations in structure-chan Tensile strengths at 70°F were 9,300 and 10,800 psi and at 3000° were 18,600 and 16,600 psi. Modulus at 70°F for all four specimens ranged from 6.47×10^6 to 8.09×10^6 psi. Density ranged from 1.670 to 1.677 gm/cm^3; axial velocity from 0.4026 to 0.4682 in./μsec (mean and standard deviation for all specimens from the 3DCC Arcs were 0.4382 in./μsec and 0.0251 in./μsec); circumferential velocity ranged from 0.3669 to 0.4034 in./μsec (mean and standard deviation for all specimens were 0.3825 in./μsec and 0.0090 in./μsec). Open porosity ranged from 11.2 to 11.7 percent indicating a slight increase over specimens from the 2.2 and 1.64 kilotaps impulse levels. For this arc structure-change and retained properties varied but the degree of change was relatively uniform.

Increased structure-change (over 3.36 kilotaps) was detecte by radiography at 5.37 kilotaps for Arc 8-AR-1, Figure 109. Increased, continuous circumferential low-absorptive alignments we indicated at 0.1, 0.2, 0.3, and 0.4 in. from the rear face. Aga a slight increase in intensity was indicated toward the ends of the arc. Radiographic results on specimens indicated several gr low-absorptive alignments (cracking). Distribution of cracking from specimen to specimen was fairly consistent with the widest

single indication being in Specimen 8-AR-1-C4C at 0.2 in. from the rear face. Mechanical results indicated similar strengths for the respective evaluations at 70°F and 3000°F with variations in modulus. At 70°F, Specimen 8-AR-1-C2C had a normal modulus of 9.0 x 10^6 psi, and Specimen 8-AR-1-C3C had a lower value of 4.86 x 10^6 psi. At 4500°F, Specimen 8-AR-1-C1C had a modulus of 2.24 x 10^6 psi, and Specimen 8-AR-1-C4C had a decreased value of 1.65 x 10^6 psi. NDT monitors indicated no variation in structure-change among the specimens. Density ranged from 1.651 to 1.662 gm/cm^3 (mean and standard deviation from all specimens from the 3DCC Arcs were 1.667 and 0.005 gm/cm^3); radial velocity ranged from 0.2014 to 0.2144 in./μsec (mean and standard deviation of all specimens were 0.2023 and 0.0100 in./μsec); circumferential velocity ranged from 0.3785 to 0.3914 in./μsec (mean and standard deviation of all specimens were 0.3825 and 0.0090 in./μsec). Open porosity ranging from 19.5 to 20.0 percent also, indicating a uniform structure for these specimens. For this arc, structure-change was extensive but rather uniform.

In summary, there was more gross structure-change observable visually at the circumferential ends of the arcs but damage was basically uniform in the axial direction, particularly at higher impact levels. One could assess the apparent structure-change by looking at the arcs axially and have a fairly good impression of structure-change internally . If one looked in the circumferential direction, the structure-change would erroneously appear more severe.

FELT CC

Radiographs and visual inspections on Plate 12-F-15 (1.21 kilotaps) indicated no structure-change (cracking). Mechanical and NDT monitor results indicated similar results for all specimens and therefore uniform structure.

For Plate 12-F-16 (1.70 kilotaps) visual and radiographic inspections on the plate and specimens from the plate indicated no structure-change. Radiography revealed low-absorptive alignments near the rear face in the plate which suggested cracking; however, visual inspection of the specimens later did not confirm this. The NDT monitor and mechanical results for the specimens were similar with one exception. Specimen 12-F-16-T2A (3000°F) had a high modulus value of 1.85 x 10^6 psi and a low strain-to-failure of 3.0 x 10^{-3} in./in. For comparison, Specimen 12-F-16-T3A (3000°F) had a lower modulus of 1.23 x 10^6 psi and a higher strain-to-failure of 6.6 x 10^{-3} in./in. The strengths were the same at 3,800 psi. Material variability as indicated by the low-absorptive areas may account for these differences.

For Plate 12-F-1 (2.430 kilotaps) visual and radiographic inspections on the plate revealed no structure-change; however, Partek penetrant inspection revealed hairline, aligned cracking in two opposite edges. This is important since it is near the design limit, even though this plate was "different." Post-mechanical, visual and penetrant inspections on the specimens revealed some mid-thickness hairline cracks aligned axially. In the outer Specimens, 12-F-1-C1A and -C3A, these cracks extended away from the fractured area and near the restrained base of the specimen but were not found in the center Specimen, - C2A. Recall that the center Specimen, 12-F-1-C2A, was not fractured due to excessive strain and overheating of the pushrods. NDT monitor and mechanical results on specimens indicated uniform structures through the bulk plate. Even though this may have been a "nonrepresentative" plate, circumferential cracks were found in both the plate and specimens suggesting uniformity across the arcs.

Visual inspection on the Plate 12-F-13 (3.07 kilotaps) detected hairline cracking at 0.15 in. from the rear face on one edge. No additional structure-change was revealed by radiography. On specimens from this plate visual inspections indicated no cracking, but radiography indicated several short, low-absorptive alignments-cracking suspected. NDT monitors and mechanical results were similar for the specimens indicating uniform structure. Thus structure-change in terms of circumferential cracks was rather uniform across the arcs.

On the Plate 12-F-10 (3.44 kilotaps) visual inspection revealed aligned and hairline cracking in two edges located about 0.2 in. from the rear face. Radiography revealed that this cracking extended nearly the full length of the plate. Liquid penetrants detected that the hairline cracking extended into the third edge. Visual inspection on specimens removed from this plate revealed that the cracking extended completely through all four specimens. A sketch showing these results is included as Figure 110. The NDT monitor and mechanical results were similar for all the specimens, also indicating uniform distribution of structure-change. Structure-change was rather uniform across this plate.

Characterization of distribution in Plate 12-F-11 (4.14 kilotaps) was similar to Plate 12-F-10 except that cracking was more severe. Gross through cracking in all four specimens was revealed by visual inspection, Figure 111. Radiography revealed gross cracking running the full length of Specimen 12-F-11-C1A and about 80 percent of the length of the other three specimens, Figure 112. Hairline cracking extended beyond the gross cracking

in these three specimens for the remaining 20 percent of the specimen length. Mechanical evaluations indicated similar results and uniform distribution of structure-change. NDT monitors also indicated similar results except for ultrasonic transmission in Specimen 12-F-11-C1A whose value was high at 24 added dB. Values for the other three specimens ranged from 16 to 18.5 added dB.

In summary, the structure-change was rather uniform across the plates being perhaps more severe on the circumferential ends and slightly less severe on the axial ends. Circumferential cracks were found near 2.5 kilotaps and definitely above 3 kilotaps. Criteria for this material may be small circumferential cracks if they are "extended" by "structural" loads during shock loading or if they can "turn" and "run" in temperature-stress loading.

AVCO R6300

No structure-change was indicated by any of the data for Arc 10-AR-4 (0.49 kilotaps). Visual inspection revealed occasional, short (~0.10 in.) hairline cracks in Arc 10-AR-7 (1.57 kilotaps). Radiography of the arc and of specimens from the arc did not reveal any structure-change. The NDT monitors did not show significant variation among the specimens. The mechanical properties, however, showed a difference in compressive strength between the two circumferential specimens. The strengths were 28,800 psi for Specimen 10-AR-7-C3C and 21,000 psi for Specimen 10-AR-7-C4C. Since there were no additional indications of more structure-change for Specimen 10-AR-7-C4C than for the other three specimens from this arc, it cannot be concluded that the difference in strength represents nonuniform structure-change. Visual inspection of specimens from this arc indicated hairline cracking in both axial specimens but none in the circumferential specimens. These visual results on the specimens indicate end to end distribution. Additional indications were not available.

None of the data for Arc 10-AR-6 (1.66 kilotaps) indicated any structure-change.

Visual inspection of Arc 10-AR-3 (1.90 kilotaps) revealed aligned, hairline cracking in the edges viewed axially but this did not extend to the circumferential ends of the arc. Radiographic inspection of this arc revealed occasional low-absorptive alignments which correlated with the visual hairline cracking.

Visual inspection of the specimens from this arc showed hairline cracking all around both axial specimens at about 0.10 in. from the inner surface and in the circumferential Specimen 10-AR-3-C4C. In Specimen 10-AR-3-C4C the hairline cracking tended to follow a tape wrap lamina. The only positive indication from radiography of the specimens was hairline cracking in Specimen 10-AR-3-C4C, Figure 114. Ultrasonic transmission for Specimen 10-AR-3-C4C was somewhat lower at 26 added dB than for the other three specimens (range 28 to 32 added dB). The other NDT monitors did not indicated variation among the specimens. The compressive strength of Specimen 10-AR-3-C4C was 20,210 psi which was significantly lower than the 27,520 psi strength of Specimen 10-AR-3-C3C. From the above it appears that the most significant structure-change in this arc occurred at the location of Specimen 10-AR-3-C4C which was at the bottom of the arc away from the indexed end.

Visual inspection of Arc 10-AR-1 (1.99 kilotaps) revealed aligned hairline circumferential cracking which covered a greater portion of the arc than on Arc 10-AR-3 but still did not extend to its ends. Even though visually the hairline cracking was more extensive than on Arc 10-AR-3 radiographic inspection did not show any structure-change. Visual inspections on the specimens from this arc revealed hairline cracks on both axial specimens on the ends located at the bottom of the arc and two short axial hairline cracks in the gage section of Specimen 10-AR-1-T1A. Specimen 10-AR-T4C had several hairline cracks which were located in the specimen near the bottom of the arc. The only structure-change revealed by radiography of the specimens was one hairline crack in Specimen 10-AR-1-T4C at about 0.05 in. from the inner surface. The only significant result from the NDT monitor and mechanical evaluations was a slightly low tensile strength for Specimen 10-AR-1-T4C. The strength of this specimen was 7,110 psi compared to 7,420 psi for Specimen 10-AR-1-T3C. In this arc, 10-AR-1, the structure-change appeared to be more severe at the bottom of the arc. Both structure-change and retained properties were reasonably uniform across the arcs except for the bottom edge.

Radiographic inspection of Arc 10-AR-5 (4.04 kilotaps) revealed cracking and hairline cracking to about 0.20 in. from the inner surface with a slight increase in number and severity at the ends of the arc. Visual inspection showed delaminations along and across the tape wrap laminae. As viewed from the ends of the arc the cracking at the top of the arc tended to remain generally parallel to the inner surface, Figure 115. At the bottom of the

arc the cracking tended to follow the tape wrap laminae and resulted in occasional material removal. The structure-changes seemed to be more severe at the corners. Radiographic inspection of Specimen 10-AR-5-C1A, Figure 113, showed severe cracking over the full length which was more severe at the top than in the center and most severe at the bottom of the arc. On Specimen 10-AR-5-C2A the pattern was the same as for Specimen 10-AR-5-C1A but the overall severity was less. Specimen 10-AR-5-C3C revealed multiple hairline cracking to a depth of about 0.20 in. from the inner surface, Figure 114. On Specimen 10-AR-5-C4C the cracking or delamination was severe. Visual inspection of the specimens coincided with the radiographic inspection results. Compressive strength measurements agreed well with the visual and radiographic results. The specimen with the more severe structure-change had the lower strength. Of the NDT monitors only ultrasonic transmission agreed with the visual and radiographic results. The severe structure-changes in this arc seemed to be confined to 0.20 in. from the inner surface. Structure-change was observed across the arc but cracks were more open at the corners.

The lowest impact level for which an indication of structure-change was found was 1.57 kilotaps (Arc 10-AR-7) where a significantly lower compressive strength was observed for the circumferential specimen nearest the bottom of the arc. Visual inspection of specimens from this arc indicated hairline cracking at the indexed end of the arc but not at the end where the low compressive strength was observed. At 1.66 kilotaps (Arc 10-AR-6) no structure-change was indicated. At 1.90 kilotaps (Arc 10-AR-3) visual inspection revealed cracking at the indexed end of the arc parallel to the inner surface and opposite the indexed end at the lower surface which followed the tape wrap laminae. Radiographic, strength and ultrasonic transmission data indicated that the most significant structure-change was at the end opposite the indexed end at the lower surface of the arc. At 1.99 kilotaps (Arc 10-AR-1) the overall structure-change seemed to be less severe than at 1.90 kilotaps (Arc 10-AR-3). Visual inspection revealed hairline cracking along the lower surface of the arc which tended to follow the tape wrap laminae. Radiographic and strength data indicated the most significant structure-change at the end of the arc opposite the indexed end at the lower surface. At 4.04 kilotaps (Arc 10-AR-5) visual inspection revealed severe cracking that was more severe at the corners of the arc than at the center of any of the edges. The cracks tended to remain parallel to the inner surface at the top of the arc but generally followed the tape wrap laminae near the lower surface. Radiographic inspection showed the structure-change to be more severe near the lower surface than at the top. Strength and ultrasonic transmission results confirmed the visual and radiographic findings.

In summary, structure-change was not uniform across the arc and seemed to be more severe near the edges. Radially, the damage was more severe at the inner portion. At about 1.5 kilotaps, structure-change (circumferential cracks) became apparent and influenced retained properties. Cracks between fabric layers occurred at about 1.5 kilotaps and across fabric layers at perhaps 4 kilotaps.

AVCO 3D/QP

Characterization of the bulk 3D/QP Arcs indicated structure-change starting with Arc 11-AR-8 (4.58 kilotaps). At this level, occasional bulk delaminations were detected by Partek penetrant only. On specimens from the arc some distribution in structure-change was indicated in that hairline and moderate discontinuous cracking was observed by visual inspection in all edges of Specimens -T1A, -T2A, and -T3C, but more severe cracking was apparent in Specimens -T4C. Radiography, Figures 116 and 117, revealed similar bulk delaminations in -T1A, and -T2A but revealed none in -T3C and -T4C, although visually apparent. NDT monitor and mechanical results indicated similar results for the specimens and uniform structure. Structure-change extended through the arc.

For Arc 11-AR-5 (7.54 kilotaps), visual inspection on the arc indicated apparent bulk delaminations and rear lift. Radiography indicated low-absorptive alignments at mid-thickness over the full length of the arc. On specimens from the arc some distribution in structure-change was indicated in that very slight cracking was observed in Specimens -C2A, -C3C, and C4C, but more severe cracking was apparent down both sides of -C1A. Distribution was further indicated by radiography, Figures 118 and 119, in that delaminations were revealed at mid-thickness for the full lengths of Specimens -C1A, and -C3C and nearly the full length of -C2A. A full-length delamination at mid-thickness was also indicated in Specimen -C4C but bulk delaminations were also dispersed on either side of the major delamination. Again, NDT monitor and mechanical results were similar among the specimens indicating uniform structure-change. Structure-change extended across the arc even though the delaminations opened more at some locations than at others.

For Arc 11-AR-3 (7.95 kilotaps), visual and radiographic inspections on the bulk arc clearly indicated full length mid-thickness delamination and rear lift. Visually, moderate and discontinuous cracking was detected at the middle of all edges of Specimen -T1A. More apparent cracking was observed in both sides of -T2A with no apparent cracking in the ends. Cracking was apparent at mid-thickness in Specimens -T3C and -T4C. Radiography, Figures 116 and 117, indicated mid-thickness delaminations running the full length of all four specimens with the

delaminations in -C4C appearing the least severe. Again, NDT monitor and mechanical results were similar among the specimens indicating uniform structure change. Generally, structure-change was uniform.

For Arc 11-AR-7 (8.61 kilotaps), visual and radiographic inspection on the bulk arc indicated increased full-length mid-thickness delamination with failed radials and rear lift. On specimens from the arc visual inspection indicated severe cracking at mid-thickness of all four specimens. Radiography, Figures 116 and 117, revealed severe full-length mid-thickness delaminations in all four specimens with the delamination in Specimen -T2A appearing less severe than -T1A. Mechanical results for the specimens were similar; however, some significant variations in the NDT monitors were measured indicating possible distribution in structure-change. The bulk density for -T4C was 1.542 gm/cm^3 compared to a range of 1.579 - 1.583 gm/cm^3 for the other three specimens; open porosity for -T3C was 9.7 percent compared to a range of 10.4 - 10.6 percent for the other three specimens; radial velocity for all four specimens had an overall range of 0.1793 - 0.1903 in./usec. Structure-change was generally uniform.

For Arcs 11-AR-1 and 11-AR-2 (9.01 kilotaps), visual and radiographic inspections revealed full-length mid-thickness delaminations and rear lift somewhat similar to 11-AR-7 above except the delamination in 11-AR-2 appeared less severe. On specimens from the arcs visual inspection revealed cracking in the middle of both edges over the full length of Specimens 11-AR-1-C1A, 11-AR-2-C1A, and 11-AR-2-C2A and nearly the full length of 11-AR-1-C2A. For Specimen 11-AR-2-C4C, cracking was apparent in the middle of all edges with one edge having more pronounced cracking. Except for apparent cracking in one end each of 11-AR-1-C4C and 11-AR-2-C3C, only slight cracking was evident in the remaining specimens. Radiography, Figures 118 and 119, indicated severe, full-length mid-thickness delaminations in all of the specimens. The NDT monitor and mechanical results gave some indication of distribution in structure-change; however, the low and high values of the respective measurements did not necessarily correlate with each other. Values for circumferential compressive strength for Specimens 11-AR-1-C3C and -C4C were 10,760 and 13,060 psi and for Specimens 11-AR-2-C3C and -C4C were 10,360 and 13,090 psi. Values for axial moduli for Specimens 11-AR-2-C1A and -C2A were 1.41×10^6 and 2.05×10^6 psi. Circumferential moduli values for 11-AR-2-C3C and -C4C were 1.86×10^6 and 2.84×10^6 psi. The bulk density for 11-AR-1-C4C was 1.534 gm/cm^3 compared to a range of 1.556 - 1.560 for the other three specimens from this arc. The bulk density for 11-AR-2-C3C was 1.581 compared to a range of 1.564 - 1.568 gm/cm^3 for the other three specimens from Arc 11-AR-2. Radial velocity for the four specimens removed from Arc 11-AR-1 ranged from 0.1707

(-C4C) to 0.1895 in./μsec (-C3C); for the four specimens removed from Arc 11-AR-2 the range was from 0.1778 (-C4C) to 0.1936 in./μsec (-C2A). Structure-change was uniform.

For Arc 11-AR-6 (9.88 kilotaps), visual and radiographic inspections revealed increased full-length mid-thickness delaminations with failed radials and increased rear lift. On specimens from the arc severe cracking was observed in the middle of all edges of Specimen -T1A and in three edges of Specimen -T2A. Very severe cracking was apparent at the middle of all edges in Specimens -T3C and -T4C. Radiography, Figures 116 and 117, indicated gross full length mid-thickness delaminations in all four specimens. NDT monitor and mechanical results indicated some distribution of structure-change. Again, the low and high values of the respective measurements did not necessarily correlate each other. Values for circumferential tensile strength for Specimens -T3C and -T4C were 24,330 and 18,670 psi. Values for axial moduli for Specimens -T1A and -T2A were 2.62×10^6 psi and 3.25×10^6 psi. Bulk density ranged from 1.517 to 1.543 gm/cm^3; open porosity ranged from 11.9 to 13.5 percent; radial velocity ranged from 0.1693 to 0.1881 in./μsec. Structure-change was uniform.

In summary the cracks seemed more open at the edges of the arcs but the cracks (and property degredation) persisted to the center. The difference was in the degree of opening of the cracks. Cracks seemed "randomly uniform" in that they would close and then open through an arc. Extensive delaminations were found at 4.50 kilotaps.

OUTER - 3DC/QP (MATERIAL #15A)

Characterization of outer material of the 3DC/QP bulk arcs indicated structure-change starting with Arc 15-AR-3 (4.09 kilotaps). At this level, bulk delaminations with a failed radial were apparent by visual inspection. On the axial specimens from the arc radiography, Figures 123 and 124, indicated bulk delaminations and short, volume oriented low-absorptive alignments indicating volume expansion. The circumferential specimens were not considered revealing. The mechanical results were reasonably consistent indicating uniform structure-change distribution. NDT monitor results from bulk density and open porosity measurements indicated some slight variation. The ranges for these data were 1.351 - 1.366 gm/cm^3 and 8.0 - 8.4 percent. Radial measurements of velocity and ultrasonic transmission were not revealing because of specimen thickness variations. Structure-change was uniform.

For Arc 15-AR-5 (4.69 kilotaps) outer, visual inspection of the bulk arc indicated increased cracking. Radiography, Figure 120, revealed a 0.4 in. long low-absorptive alignment in the central region. On axial specimens from the arc radiography indicated increased (over specimens from 15-AR-3) short, volume oriented low-absorptive alignments, Figure 121. In the circumferential specimens, however, full-length low-absorptive alignments were apparent, Figure 122. The mechanical results showed some wide variations. Specimens -T1A and -T2A had values of axial tensile strength of 8,650 and 4,900 psi and moduli of 3.3×10^6 and 0.84×10^6 psi. Specimens -T3C and-T4C had values of circumferential tensile strength of 1,340 and 2,290 psi. NDT monitor values of open porosity ranged from 7.5 to 8.3 percent. Structure-change was uniform.

For Arc 15-AR-6 (5.18 kilotaps) outer, visual and radiographic inspections of the bulk arc indicated mid-thickness delaminations particularly near the ends of the arc, Figure 120. On specimens from the arc, radiography indicated aligned cracking in all specimens. Cracking appeared more severe in Specimens -C2A and -C3C than in -C1A and -C4C. Similar to AVCO 3DQP (Material 11), some of the mechanical and NDT monitor results indicated structure-change distribution; however, the low and high values of the respective measurements did not necessarily correlate with each other. From the mechanical results, Specimens -C3C, and -C4C had values of circumferential strength of 6,410 and 4,580 psi. As mentioned above the radiographs of these specimens showed Specimen -C3C to have the more severe cracking. From NDT monitor results, bulk density ranged from 1.330 to 1.344 gm/cm^3, and open porosity ranged from 8.8 to 9.8 percent. Structure-change and retained properties were uniform except for -C4C where the cracks seemed milder but properties were lower.

For Arc 15-AR-4 (6.06) kilotaps) outer, visual and radiographic inspections of the bulk arc indicated mid-thickness delamination with failed radials, Figure 120. Radiography further indicated volume, low-absorptive alignments extending out from the mid-thickness delamination. On specimens from the arc radiography indicated multiple delaminations in all four specimens with the axial specimens indicating a slight increase in structure-change, Figures 122 and 123. The mechanical results indicated that the circumferential strength was essentially zero while the axial strength was about 1,250 psi. NDT monitors indicated some variations in density and open porosity. Bulk density ranged from 1.261 to 1.281 gm/cm^3, and open porosity ranged from 9.9 to 11.6 percent with the two axial specimens having the highest values. Overall, structure-change must be considered uniform.

For Arcs 15-AR-7 and 15-AR-8 (6,50 and 6.54 kilotaps) outer, visual and radiographic inspection indicated full-length mid-thickness delaminations with failed radials, Figure 120. Volume cracking and low-absorptive alignments also extended out from the major delaminations. On specimens from Arc 15-AR-7, radiography indicated severe volume low-absorptive alignments in Specimens -C1A and -C2A, Figure 123, and severe mid-thickness delaminations in Specimens -C3C and -C4C, Figure 124. From Arc 15-AR-8, very severe volume low-absorptive alignments in Specimens -C1A, and -C2A and less severe (than 15-AR-7-C3C and -C4C) mid-thickness delaminations with volume low-absorptive alignments located outside the major delaminations in Specimens -C3C and -C4C were revealed by radiography. Mechanical and NDT monitor results indicated structure variations. For Arc 15-AR-7, values of axial compressive strength for Specimens -C1A and -C2A were 4,820 and 6,000 psi. Values of circumferential compressive strength for Specimens -C3C and -C4C were 2,820 and 3,670 psi. From the NDT monitor results, bulk density ranged from 1.207 to 1.267 gm/cm^3, and open porosity ranged from 9.6 to 11.1 percent. For Arc 15-AR-8, the only variation in compressive strength was in the circumferential direction for Specimens -C3C and -C4C which had values of 5,940 and 4,340 psi. From the NDT monitor results, bulk density ranged from 1.239 to 1.288 gm/cm^3, and open porosity ranged from 8.6 to 9.6 percent. Previously for the other impact levels of this material, radial velocity was not discussed as a monitor for structure distribution primarily because of differences in thicknesses of specimens and because of uniformity in values. For Arc 15-AR-8, however, Specimen -C2A had a velocity of 0.1626 in./μsec compared to the range of 0.1803 to 0.1835 in./μsec for the other three specimens. Structure-change and retained properties were uniform except for 15-AR-7-C1A and 15-AR-8-C3C where structure-change seemed similar but properties differed.

In summary, structure-change did not appear uniform circumferentially and appeared to be more severe between the center and the ends of the bulk arc. Cracking without regard for appearance was rather uniformly distributed. Major structure-change to Material #15 occurred near the middle (radially) of the outer material. Structure-change was incurred at the first impulse level (4.09 kilotaps) which influenced retained properties. This change consisted of bulk delaminations in the outer material by visual and radiographic inspections. At higher impact levels mid-thickness delaminations with volume cracking were incurred.

INNER - 3DC/QP (MATERIAL #15B)

Characterization of the inner material from the 3DC/QP arcs indicated that structure-change was confined primarily near the inner (rear) surface starting with Arc 15-AR-5 (4.69 kilotaps). At this level, visual inspection of the bulk arc revealed cracking near the rear face to a depth of about four plies. Radiography, Figure 120, indicated an 0.15 in. long low-absorptive alignment at one end located about three plies behind the rear face. With increased impulse loadings on Arcs 15-AR-6 and -4 (5.18 and 6.06 kilotaps), increased cracking was apparent near the rear face. For Arcs 15-AR-7 and -8 (6.51 and 6.54 kilotaps), the cracking near the rear face was more aligned. On specimens from the arcs, radiography did not indicate structure-change below 6.51 kilotaps (Arcs 15-AR-7 and -8). At these levels, low-absorptive alignments were revealed near the rear face. The severity of these alignments were considered similar.

The nondestructive monitor and mechanical results did not in general show nonuniform distribution of structure-change. Several instances were found where a single value of one of the NDT monitors or mechanical properties differed from the other values for a given arc. In only two instances were there confirming data of nonuniform distribution. At 5.18 kilotaps (Arc 15-AR-6) the circumferential compressive Specimen 15B-AR-6-C4C had low strength, strain-to-failure and radial sonic velocity. These low values were: 14,900 psi (20,250 psi for Specimen 15B-AR-6-C3C), 0.0038 in./in. (0.0073 in./in. for Specimen 15B-AR-6-C3C, 0.1795 in./μsec (0.1820 to 0.1831 in./μsec for the other three specimens). At 6.54 kilotaps the axial compressive Specimens 15B-AR-8-C1A had low strength, bulk density and radial sonic velocity though the delamination seemed typical of the arcs. These low values were: 14,580 psi (21,400 psi for Specimen 15B-AR-8-C2A), 1.519 gm/cm^3 (1.541 to 1.576 for the other three specimens from this arc) and 0.1730 in./μsec (0.1836 in./μsec for Specimen 15-B-AR-8-C2A). In these two cited instances it may be concluded that nonuniformity of structure-change existed in these arcs; at least, there were differences in retained properties.

For the inner portion of the 3DC/QP arcs structure-change was apparent. At the 4.69 kilotap level, cracking near the rear face was revealed. With two exceptions the distribution of structure-change seemed to be uniform over the arcs. For the two exceptions to uniform distribution there was no location which seemed to be more susceptible to structure-change.

The conclusion drawn is that the exceptions were due to random material parameters.

SECTION VI

RESULTS OF PRE-IMPACT NDT EVALUATIONS

The test results for Phase II are given in Tables 37 through 42 and Figures 125 through 180. The presentation of the data according to material follows.

AVCO 3DC/QP

Nondestructive testing consisted of QC inspection of 11 arcs and 6 rings, and based on the QC inspection results, 1 ring was selected for underground FT inspection. The QC results are given in Table 37 and photographs of typical 3DC/QP structure in Figures 125 and 126. Typical structure as revealed by radiography in the radial and axial directions is shown in Figure 127.

No anomalies or problems were apparent. The porosity of the AHCA material was significantly lower than AHP material. Figures 125 and 126 show the comparison between the materials. At the time of this characterization, no problem with the AHCA material was suspected since it was to be an improvement over AHP material by impregnation.

AVCO 3DCP

Nondestructive testing consisted of QC inspection of 22 arcs and 10 rings from which 5 arcs were selected for AHCA FT inspection and 6 rings were selected for underground FT inspection. The results are given in Table 38 and Figures 128 through 134. Typical 3DCP material structure is described in Figures 128 and 129. Photographs depicting the material in the axial and circumferential directions are given in Figure 134. Typical structure as revealed by radiography in the radial and axial directions is shown in Figure 129. No photomicrographs were made on these specimens. However, photomicrographs were subsequently made on AHCA 3DC/QP during the characterization of the damage problem. Photomicrographs on both AHP and AHCA 3DC/QP are given in Appendix M under the discussion of this anomalous structure-change problem.

Similar to AVCO 3DC/QP, this material also had lower porosity than AHP material. In addition, visable resin rich areas along yarns and resin starved areas around radials were detected in the arcs and rings, Figures 130 and 131. The density of the arcs were the same as AHP material at 1.42 gm/cm^3. The density of the rings were slightly less at 1.41 gm/cm^3. Velocity results from

the 5 FT arcs indicated values similar to AHP for axial velocity at 0.370 in./μsec, but no comparison for radial velocity was available. Radial ultrasonic transmission values ranged from 31 to 32 added dB.

Anomalies detected by visual inspection were of a mechanically induced nature. For Arc 7 of Ring 6, voids and raised axials were detected in the C edge, Figure 132; for Arcs 5 and 6 of Ring 6, chipped corners were apparent; for Ring 2, the outer edge was chipped or crushed at 25°, Figure 133; for Ring 8, an 0.16 inch long area in the top edge was indented, Figure 133; for Ring 10, local areas having high porosity were apparent, Figure 134. Radiography detected no anomalies in the arcs and rings. Typically, various concentrations of circumferential low-absorptive alignments were revealed by radiography in the axial direction for all the specimens. Ring 1 was probably the only exception as no significant variations were detectable. In addition for the rings, occasional through and part-through thickness low-absorptive alignments along the radials were observed. Such alignments were seen in Ring 3 at 45°, Ring 5 at 10-45° and 340°, Ring 9 at 135°, 190°, and 350°, Ring 10 at 240°, and Ring 12 at 245°.

Based on these inspections of the rings, the locations of most uniform material sites selected were as follows:

Ring No.	Most Uniform Material Centerline
1	Any
2	270°
3	225°
4	300°
5	255°
8	90°
9	Not Selected
10	45°
11	Not Selected
12	345°

AVCO 3DCP (T400)

Four rings and 4 arcs received QC nondestructive testing. The results are given in Table 39 and Figures 135 through 137. Typical structure revealed by radiography in the radial and axial directions is shown in Figure 135.

Generally, the material was uniform and sound. A background of residual pores or voids and striations were visually apparent in the surfaces and edges. No anomalies were detectable by the visual or radiographic inspection of the arcs. Visual inspection of Ring 3 revealed a circumferential delamination in the outer surface at 330°, voids on the inner surface at 220°, and voids on the bottom edge at 45°. Radiography revealed several concentrations of circumferential low-absorptive alignments in all 4 rings, Figure 136 depicts a typical alignment. The locations of these variations are detailed in Table 39. The only gross concentration of low-absorptive alignments indicated was in Ring 4 at 320-360°, Figure 137.

Based on the inspections of the rings, the locations of most uniform material sites were selected as follows:

Ring No.	Most Uniform Material Centerline
1	180°
2	150°
3	135°
4	240°

AVCO R6300

Nondestructive testing consisted of QC inspection of 18 arcs and 10 rings and FT inspections of 2 rings selected for AHCA and 1 ring selected for underground. These FT rings were selected from the QC rings. The results of the inspections are given in Table 40 and Figures 138 through 148.

The AHCA R6300 material was similar to the AHP material. Typical material structure is described in Figures 138 and 141. Photographs depicting the material are given in Figures 138 and 139. Typical structure as revealed by radiography in the radial and circumferential directions is shown in Figure 140. Photomicrographs at 50X (before reduction) showing microstructure are given in Figure 141. The density for AHP was about 1.33 gm/cm^3; whereas, for AHCA the density was slightly higher ranging from about 1.32 to 1.37 gm/cm^3. Ring 6 having a density of 1.301 gm/cm^3 was the only exception. Also, the AHCA material had higher surface porosity with a size to about 0.02 inch and more extensive aligned residual porosity between the tape wraps than did AHP material, Figures 138 and 142.

Some material anomalies were revealed by visual inspections. In Ring 11 Arc 9, a tape wrap discontinuity was apparent on the inner surface, Figure 143. (This anomally was also indicated by radial X-ray). In Ring 12 Arc 14, a single 0.10 inch long void was apparent on the inner surface, Figure 144. On Ring 7, the bottom inner edge was chipped from 130 to 180° and at 215°, Figure 145.

Some additional material anomalies were indicated by radiography in both the arcs and rings. About half of Ring 11 Arc 8 contained lower density material by radial X-ray, Figure 146. Low-absorptive alignments to about 3/4-inch in length were detected in Ring 11 Arc 9 by radial X-ray (tape wrap discontinuity by visual), Figure 146. Single 0.02 and 0.04 inch low-absorptive areas (voids) by axial X-ray were indicated in Rings 4, 6, and 9. A single 0.04 inch high-absorptive area (inclusion) was also indicated in Ring 6. Various volume oriented low-absorptive areas were indicated in the rings by axial X-ray. Although, these areas were not considered significant, they were avoided in selecting impact center lines.

From the QC inspections, Ring 9 was selected for underground test, and Rings 2 and 4 were selected for AHCA FT testing. The most uniform material sites for the QC rings were selected as follows:

Ring No.	Most Uniform Material Centerline
1	270°
3	55°
5	255°
6	255°
7	180°
8	135°
10	180°

Sketches showing QC and FT NDT inspection results and most uniform material sites on Rings 2 and 4 are given in Figures 147 and 148. Photomicrographs in the axial direction at 50X (before reduction) on FT Rings 2 and 4 were given in Figure 141.

AVCO 3DCC

Nondestructive testing consisted of QC inspection of 11 disc, 10 coupons, and 17 rings and FT nondestructive testing on 2 rings whose selection was based on the QC inspection. In addition, two underground rings were selected from these QC rings. Test results are given in Table 41 and in Figures 149 through 174.

Generally, this material was similar to AHP AVCO 3DCC material. Typical material structure is shown in Figures 149 through 151. Photographs depicting the material viewed in the radial and axial directions are given in Figure 149. Typical structure revealed by radiography in the radial and axial directions is shown in Figure 150. Photomicrographs at 50X (before reduction) showing microstructure are given in Figure 151. Debonds were generally similar to AHP except for the 1109-35 rings. Debonds in this material were more severe than AHP, Figure 152. Values of density and radial velocity for the AHP material were lower, 1.61 - 1.69 gm/cm^3 and 0.180 - 0.230 in./μsec for AHP compared to 1.63 -1.75 gm/cm^3 and 0.223 - 0.267 in./μsec for AHCA.

Single visual anomalies were detected in Discs 1 and 11. In Disc 1, visual inspection revealed that the inner edge had been bumped at 270° resulting in local material loss, Figure 153. In Disc 11, both visual and radiographic inspections revealed a through-thickness wrinkle, Figure 153. No visual anomalies were revealed in the coupons and the 1109-35 rings. Visual anomalies were detected in Rings 2B and 4B. In Ring 2B, a single 0.15 inch x 1 ply deep depressed area was located in the outer surface at 0° and about 0.20 inch from the bottom edge, Figure 154. In Ring 4B, two surface flaws were revealed. On the bottom edge at 180°, a machining error was made resulting in a surface mismatch at this location, Figure 155. On the outer surface at 300° next to the bottom edge, a local area measuring about 1.2 x 0.2 inch contained loose and missing pieces of axials and circumferentials, Figure 156.

The largest single visual debond detected in this group of specimens was found in Ring 1A. The debond had a length of about 3-1/2 inches and was located in the bottom edge from 150° to 210°, Figure 157. Radiography which did not reveal the debond indicated that the debond was only surface oriented.

Anomalies were revealed by radiography in Disc 11 and Coupon 5. In both cases, single through-thickness wrinkles were apparent. In addition to determining material anomalies, radiography was used for evaluating debonds. In the discs and coupons, the major debonds were continuous and were located about 0.10, 0.25, 0.35, and 0.40 inches from the inner edge (measurements on X-ray image). Axial radiographs on Rings 1 through 11 and 1A through 4B indicated a background of debonds with more severe ones also occuring. These were noted, and the locations of the most uniform material sites were selected away from the severest debond locations. Sketches showing these radiographic results are given in Figures 158 through 174. No material anomalies were detected in the rings. Except for the large visual debond located in the bottom edge, Ring 1A was considered uniform throughout.

Based on the QC inspections, Rings 2 and 3 were selected for underground test, and Rings 1 and 5 were selected for AHCA FT testing. The FT test results for these rings are depicted in Figures 158 through 160 and 162. The radiographic results for the QC rings are given in Figure 161 and Figures 163 through 174. The most uniform material sites selected were as follows:

Ring No.	Most Uniform Material Centerline
1109-35-1	230°
1109-35-2	315°
1109-35-3	320°
1109-35-4	315°
1109-35-5	30°
1109-35-6	270°
1109-35-7	315°
1109-35-8	220°
1109-35-9	155°
1109-35-10	315°
1109-35-11	270°
1A	Any
2A	165°
1B	135°
2B	225°
3B	180°
4B	105° and 270°

Photomicrographs in the axial direction on FT Rings 1109-35-1 and 1109-35-5 are given in Figure 151.

SANDIA FELT CC

Nondestructive testing consisted of QC inspection of 20 rings and FT inspection of 2 rings selected from the QC rings. Test results are given in Table 42 and Figures 175 through 180.

The Felt CC material supplied as rings for this program was similar to the AHP material which was supplied as cone plates. For AHP, the values of bulk density and radial velocity had ranges of 1.70 - 1.90 gm/cm^3 and 0.112 -1.24 in./μsec. This was comparable to ranges of 1.76 - 1.85 gm/cm^3 and 0.101 - 0.110 in./μsec for AHCA with the velocity values for AHCA material being based on measurements from the 2 FT rings only. Visually, the materials were similar except that AHCA indicated coarser needling and no discolorations in the edges. Residual porosity to about 0.012 inch resulting from needling was background. Typical AHCA material structure is described in Figures 175 through 177. Photographs depicting the material viewed in the radial and axial directions

are given in Figure 175. Typical structure revealed by radiography in the axial direction is shown in Figure 176. Photomicrographs at 50X (before reduction) showing microstructure are given in Figure 177.

No visual material anomalies were determined. However, during the polishing of FT Rings 2N-2 and 3N-2 for photomicrographs, both rings received slight surface scrapes in the polished edges. The locations of these scrapes were 245° - 260° for 2N-2 and 75° - 90° for 3N-2. Neither of the scrapes were considered severe enough to influence the performance of the material.

Radiography in the axial direction revealed significant, single circumferential low-absorptive alignments in Rings 4P-2 and 7P-2. In both cases, the signature was a single circumferential crack. The locations of these anomalies were 315° - 330° for 4P-2 and 335° - 345° for 7P-2. A printed radiograph showing the anomaly in 4P-2 is given in Figure 178. The anomaly in 7P-2 as radiographed could not be printed for reporting.

FT nondestructive characterization was conducted on Rings 2N-2 and 3N-2. The results of these inspections are depicted in Figures 179 and 180. For Ring 2N-2 liquid penetrants indicated void clusters to 0.2 inch in size in the outer surface at 55°, 295°, and 330°, Figure 179. Also, a mechanical surface indentation was indicated in the outer surface at the 0° orientation. No anomalies were detected by liquid penetrants in 3N-2. The velocity results were considered uniform for this material, Figures 179 and 180. Radial ultrasonic transmission indicated no variations greater than $\pm$ 1dB. Centerlines of most uniform material sites selected were 225° for 2N-2 and 270° for 3N-2. Photomicrographs in the axial direction are given in Figure 177.

MOE EVALUATIONS ON FULL TREATMENT NDT RINGS

The results of the MOE evaluations on the 6FT NDT rings (two each of 3DCC, Felt CC and R6300) are shown in Table 43. Modulus values were determined from three different measurements: (1) deflection measurements from ring flexure, (2) strain gage measurements from ring flexure and (3) strain gage measurements from hydrostatic compression. The first two values represent average flexure moduli and the third an average compressive modulus. The flexural moduli were generally less than the compressive modulus for the same ring.

The flexural moduli for the 3DCC rings 1109-35-1 and -5 were 9.4×10^6 psi and 10.0×10^6 psi based on strain gage measurements and 10.6×10^6 and 11.1×10^6 psi based on deflection measurements. The compressive moduli from the hydrostatic compression evaluations were 13.7×10^6 and 14.4×10^6 for rings -1 and -5. These compressive moduli seem somewhat high when compared to the range of circumferential modulus values of 7.66×10^6 to 10.4×10^6 which was measured on compressive specimens of the AHP project. The difference between the AHP and AHCA data may be due to the differences in specimen configuration.

The flexural moduli for the Sandia Felt CC rings 2N-2 and 3N-2 were 1.22×10^6 and 1.24×10^6 psi based on strain gage measurements and 1.34×10^6 and 1.38×10^6 psi based on deflection measurements. Hydrostatic compression gave values of the compressive moduli of 1.91×10^6 and 1.73×10^6 psi. Circumferential compressive moduli from the AHP program ranged from 1.30×10^6 to 1.91×10^6 psi.

The flexural moduli for the R6300 rings 2 and 4 were 1.47×10^6 and 1.50×10^6 psi based on strain gage measurements and 1.62×10^6 and 1.68×10^6 psi based on deflection measurements. Compressive moduli from the hydrostatic compression evaluations were 1.81×10^6 and 1.62×10^6 psi. The range of circumferential compressive moduli from the AHP program was 1.36×10^6 to 1.57×10^6 psi.

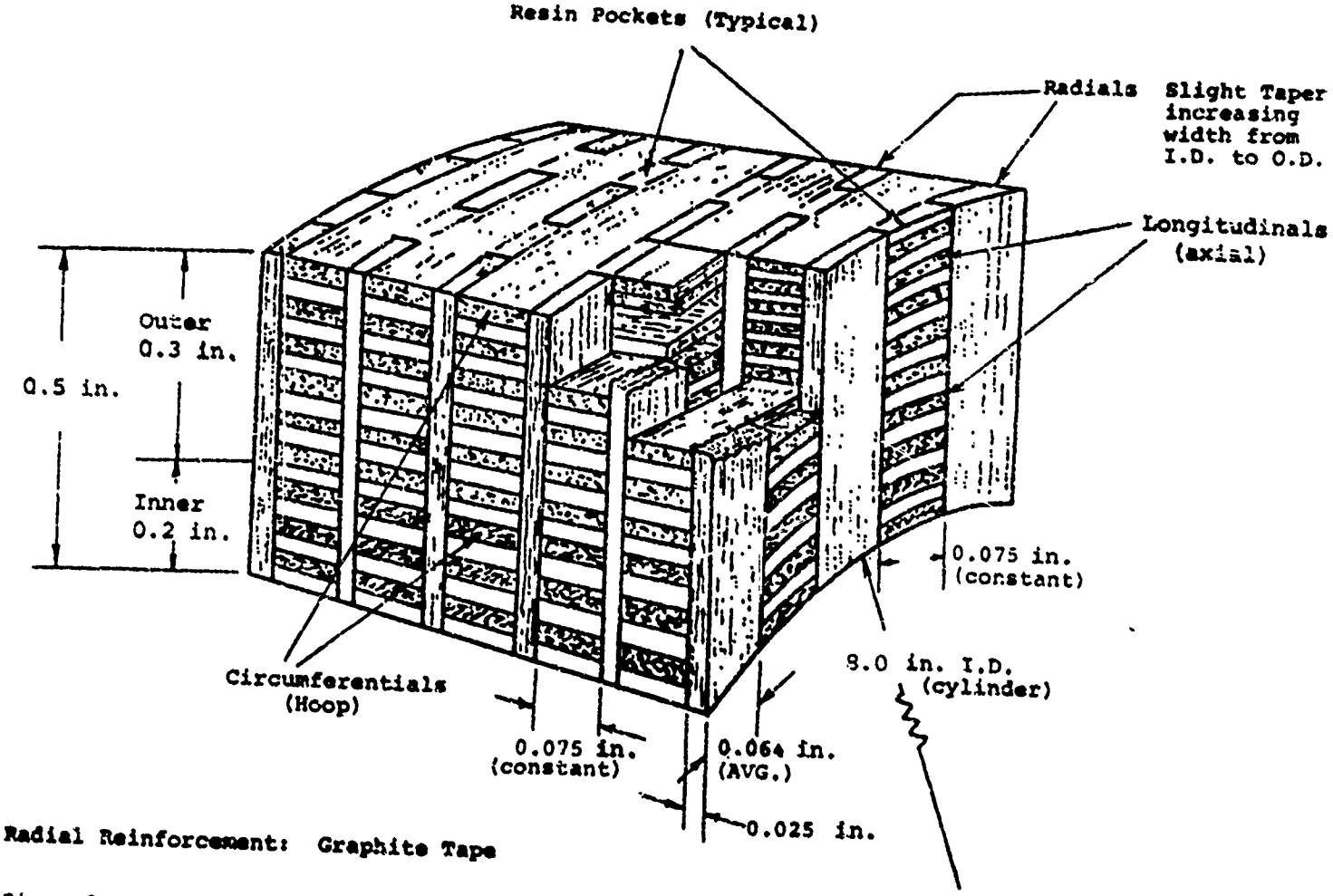


Figure 1. Construction of AVCO 3DCC

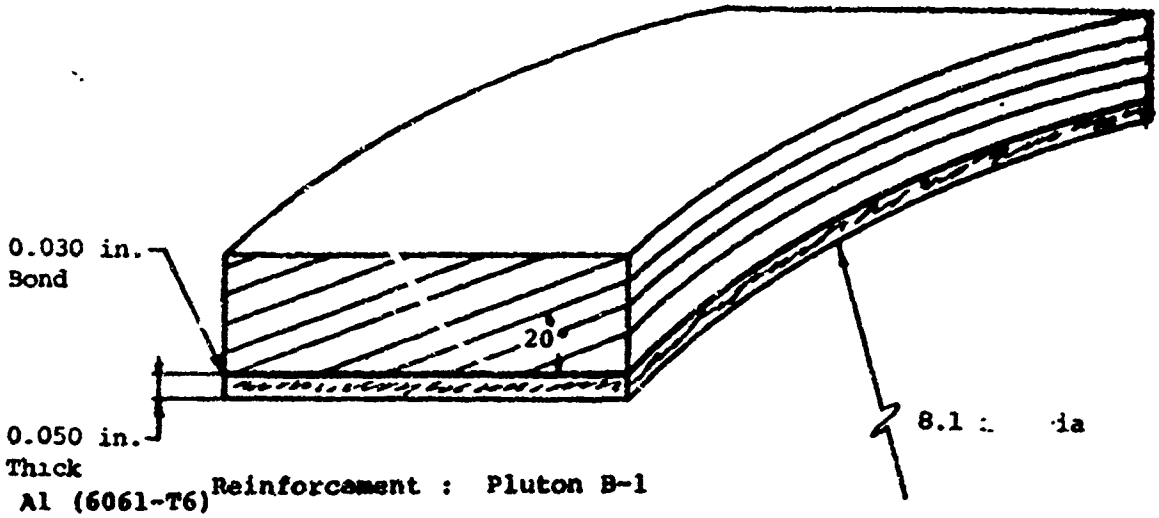


Figure 2. AVCO R6300 - Single Phase 2D, 20-Degree Angle Tape Wrap CP with Al (6061-T6) Backing Plate

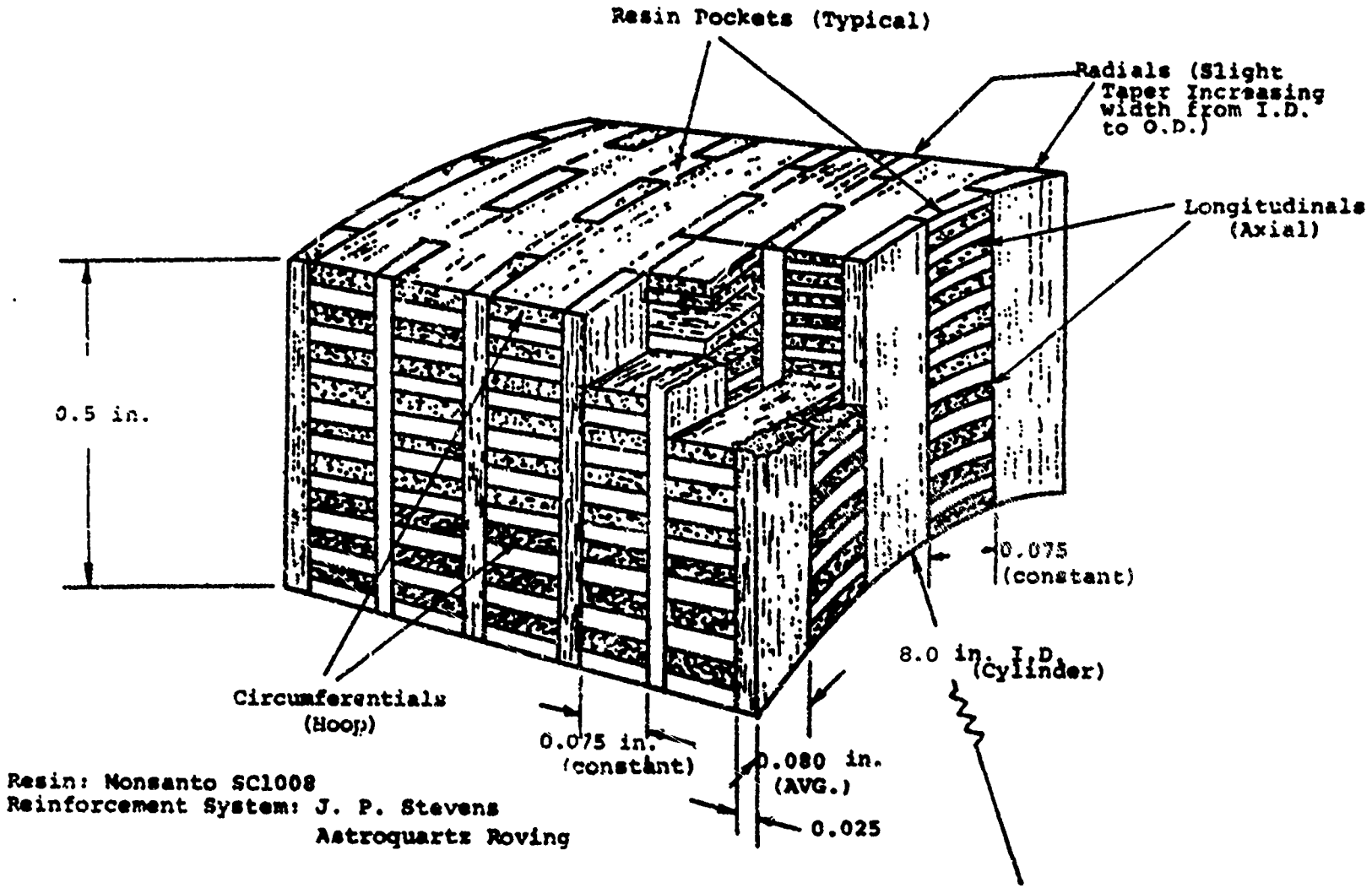


Figure 3. AVCO Single Phase 3D Orthogonal Quartz-Phenolic - Material #11

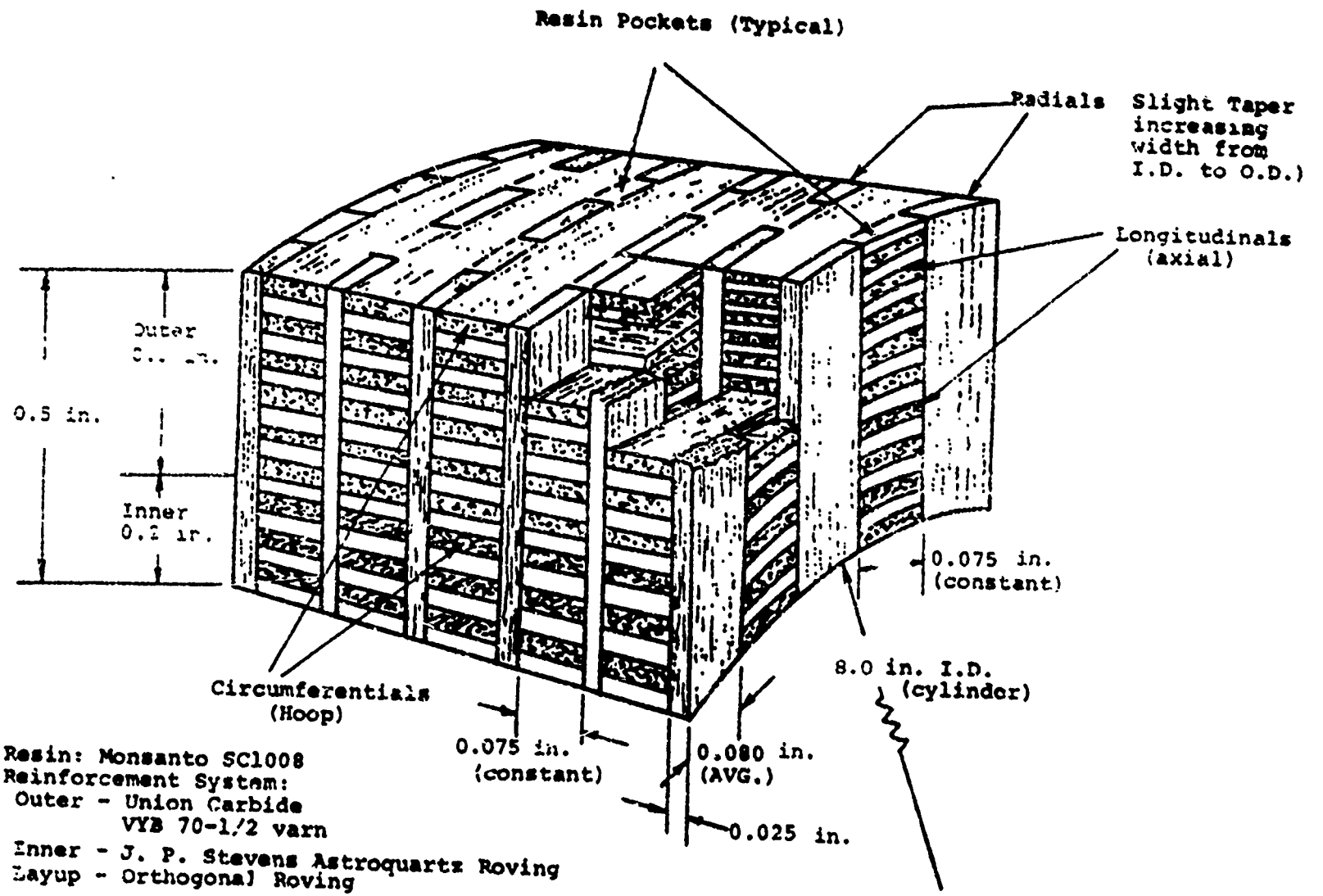


Figure 4. AVCO Two Phase 3D Orthogonal Quartz-Phenolic - Material #15

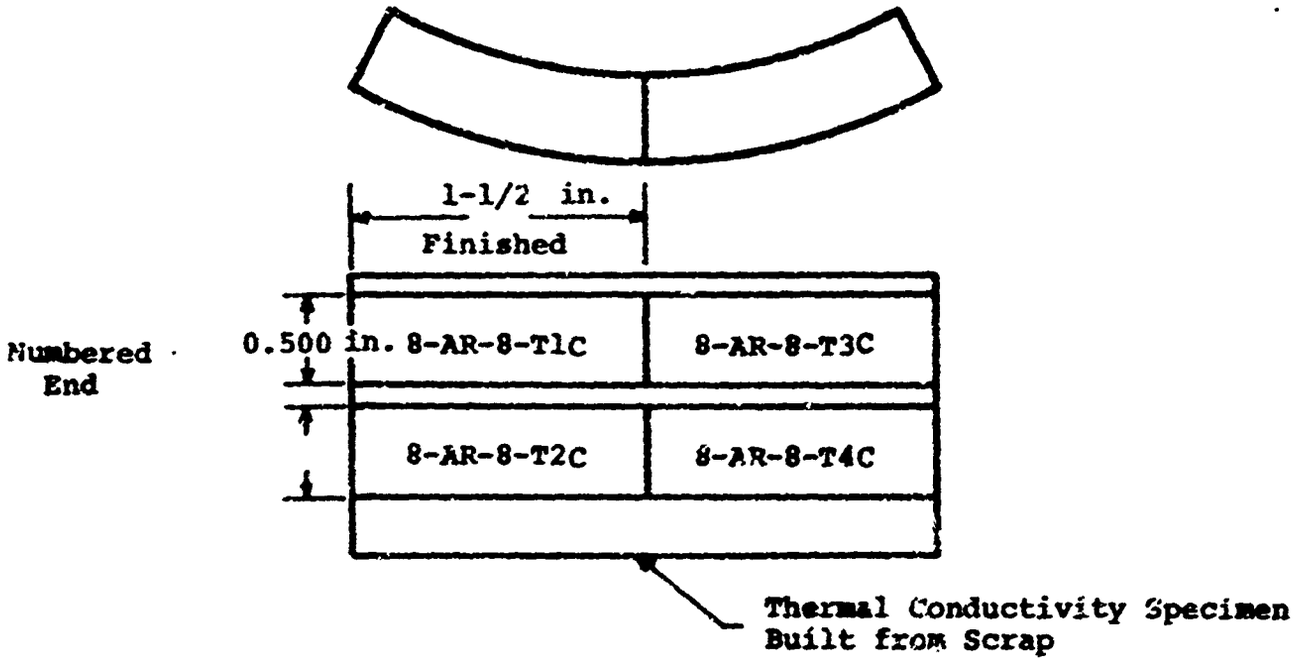


Figure 5 . Cutting Plan for Removing Circumferential Tensile Blanks from 3D Carbon-Carbon Impacted Arcs 8-AR-8, 8-AR-2 nd 8-AR-5

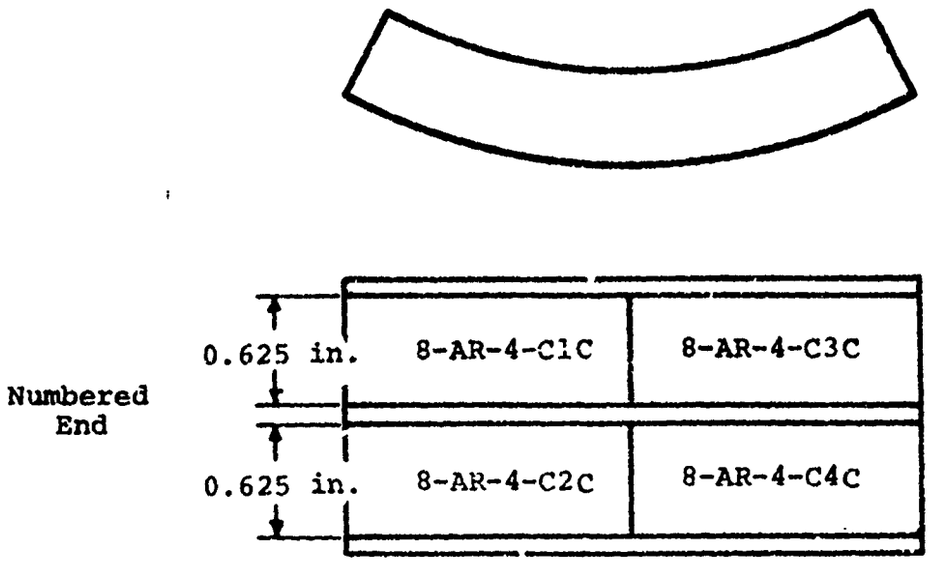


Figure 6. Cutting Plan for Removing Circumferential Compressive Blanks from 3D Carbon-Carbon Impacted Arcs 8-AR-4, 8-AR-7 and 8-AR-1

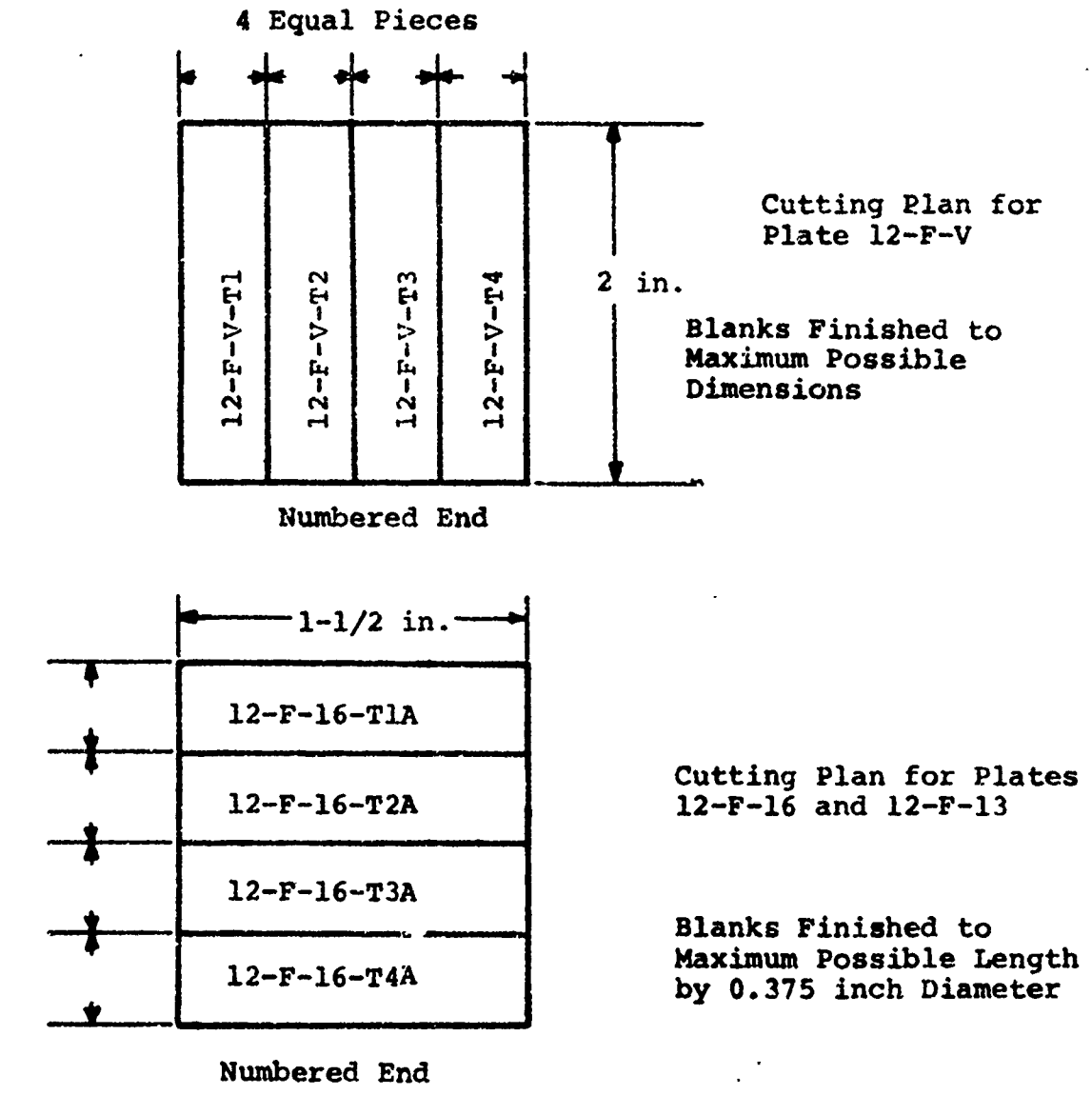


Figure 7. Cutting Plan for Removing Axial Tensile Blanks from Felt Carbon-Carbon Impacted Plates 12-F-V, 12-F-16 and 12-F-13

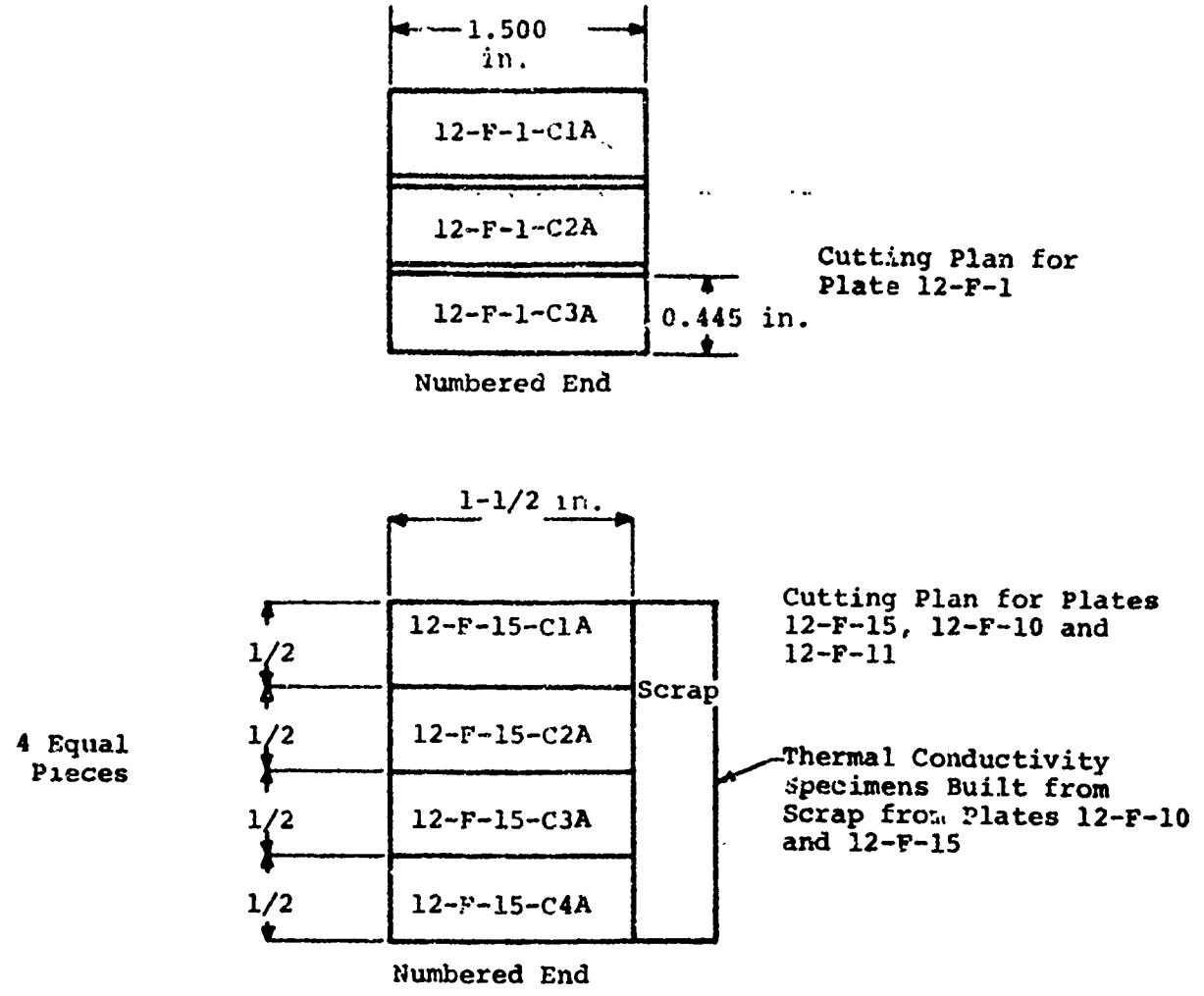


Figure 8. Cutting Plan for Removing Axial Compressive Blanks from Felt Carbon-Carbon Impacted plates 12-F-1, 12-F-15, 12-F-10, and 12-F-11

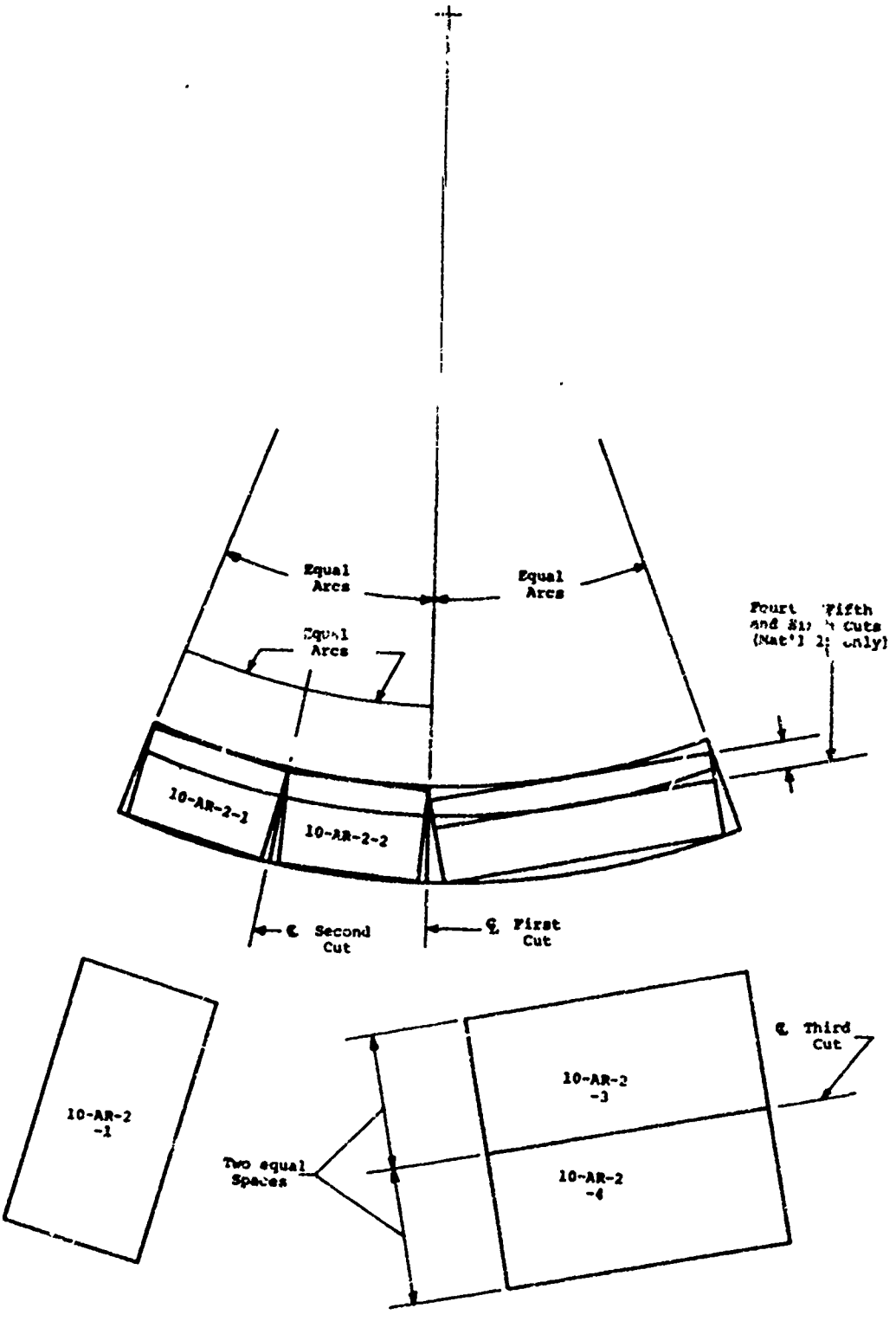


Figure 9. Cutting Plan for Removing Blanks from Phenolic Composite Impacted Arcs

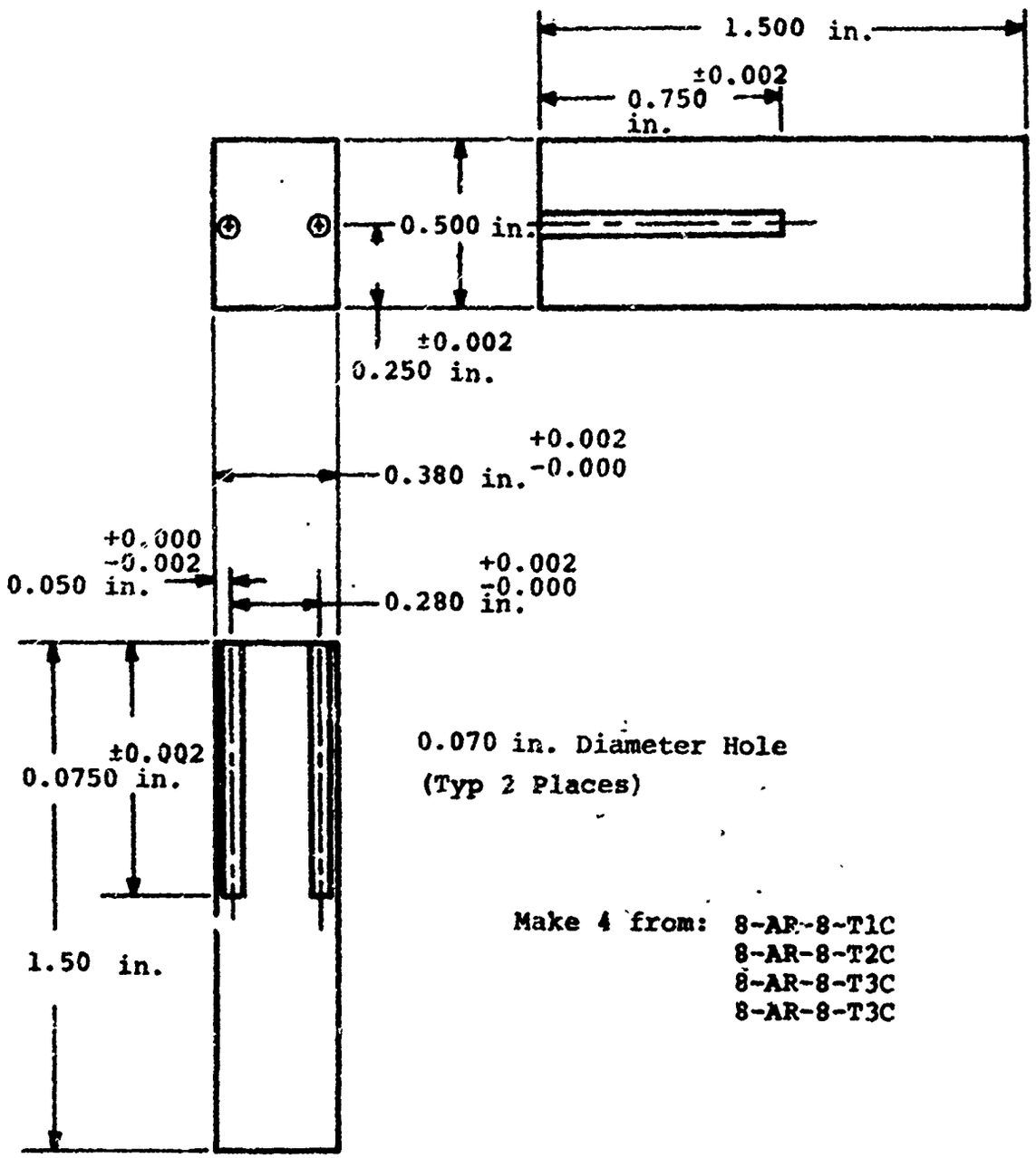


Figure 10. Configuration of Specimen Strip for 3DCC Used in Radial Inflow Apparatus

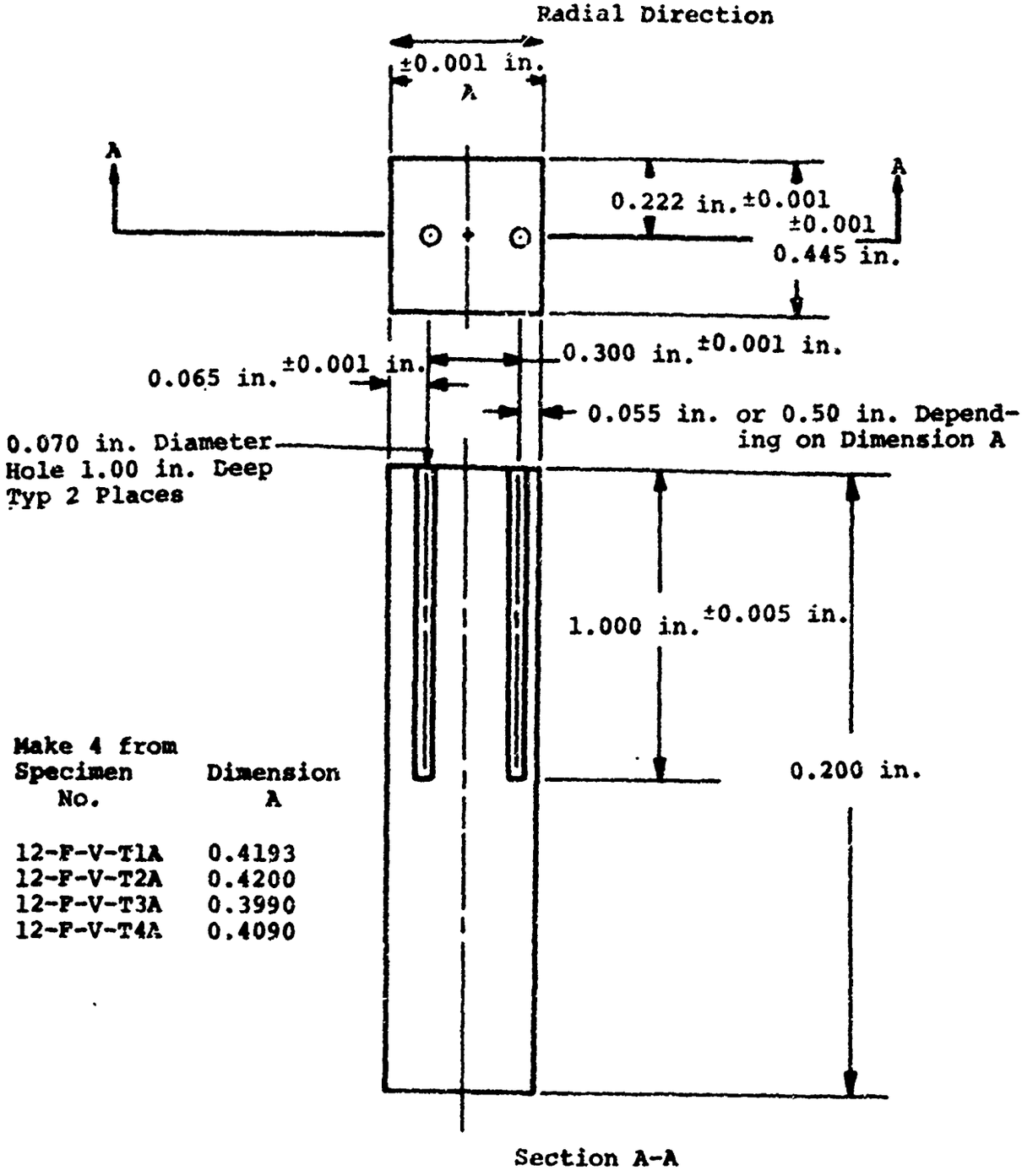


Figure 11. Configuration of Specimen Strip for Felt CC Used in Radial Inflow Apparatus

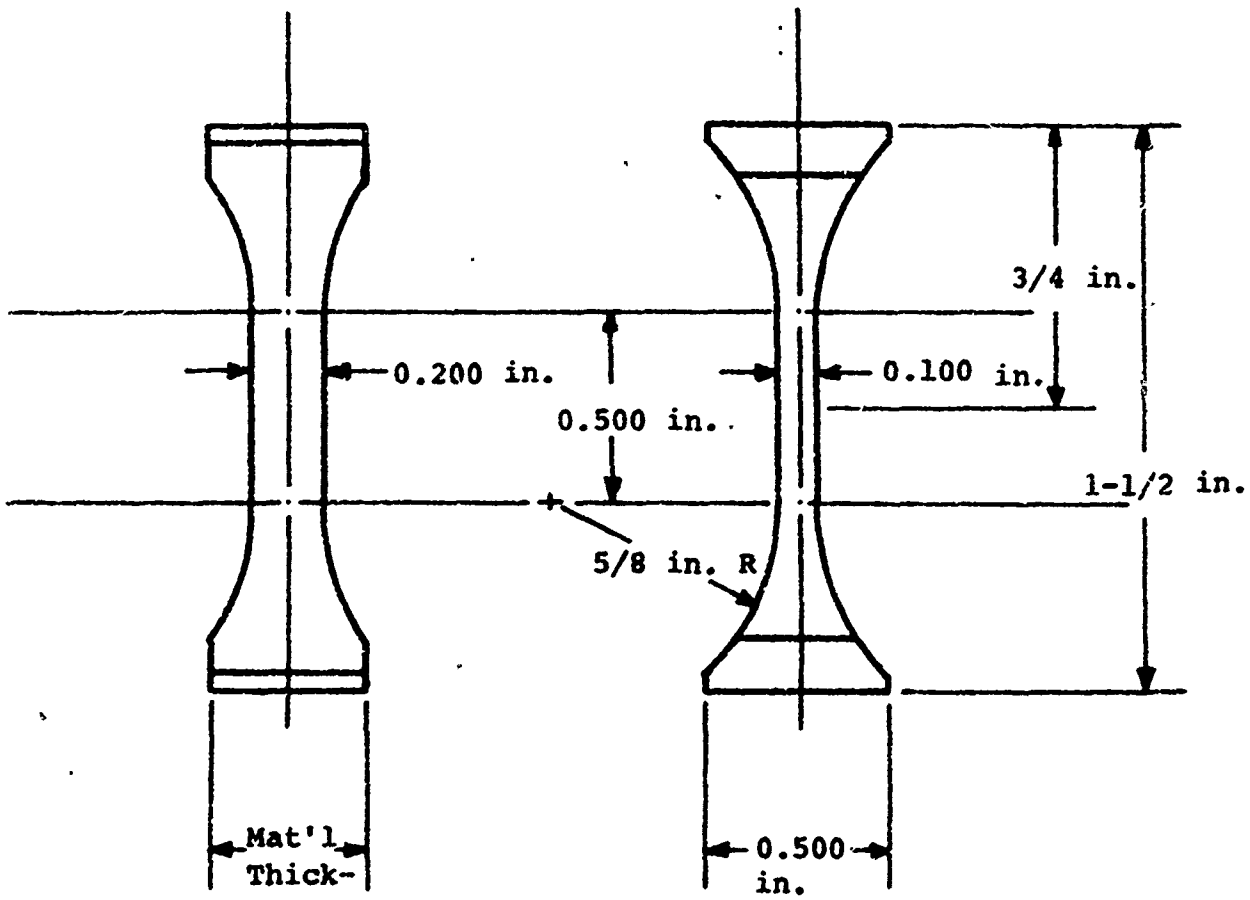


Figure 12. Configuration of Axial Tensile Specimen Used for Evaluations of Specimens from 3D Carbon-Carbon Impacted Arcs

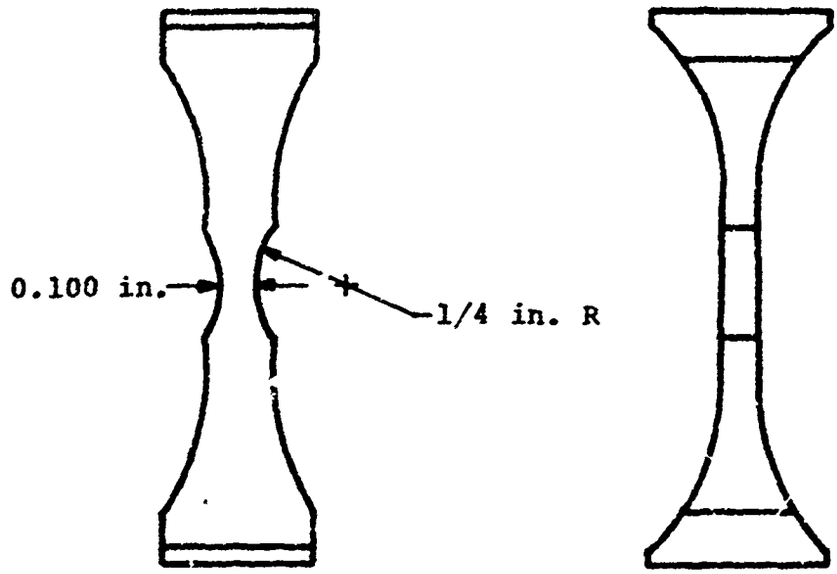
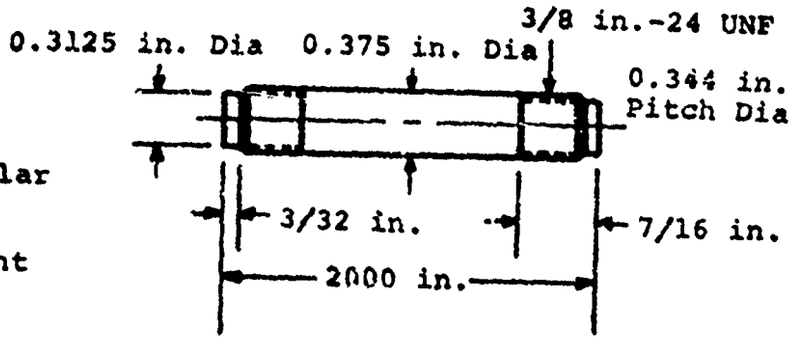


Figure 13. Modification to Tensile Specimen for Ultimate Strength Evaluations on Specimens from 3D Carbon-Carbon Impacted Arcs

Notes:

1. All Diameters True and Concentric to 0.0005 in.
2. Ends Flat and Perpendicular to 0.0005 in.
3. Do not Undercut at Tangent Points
4. Tolerances
   Lengths ± 0.005 in.
   Diameters ± 0.001 in.



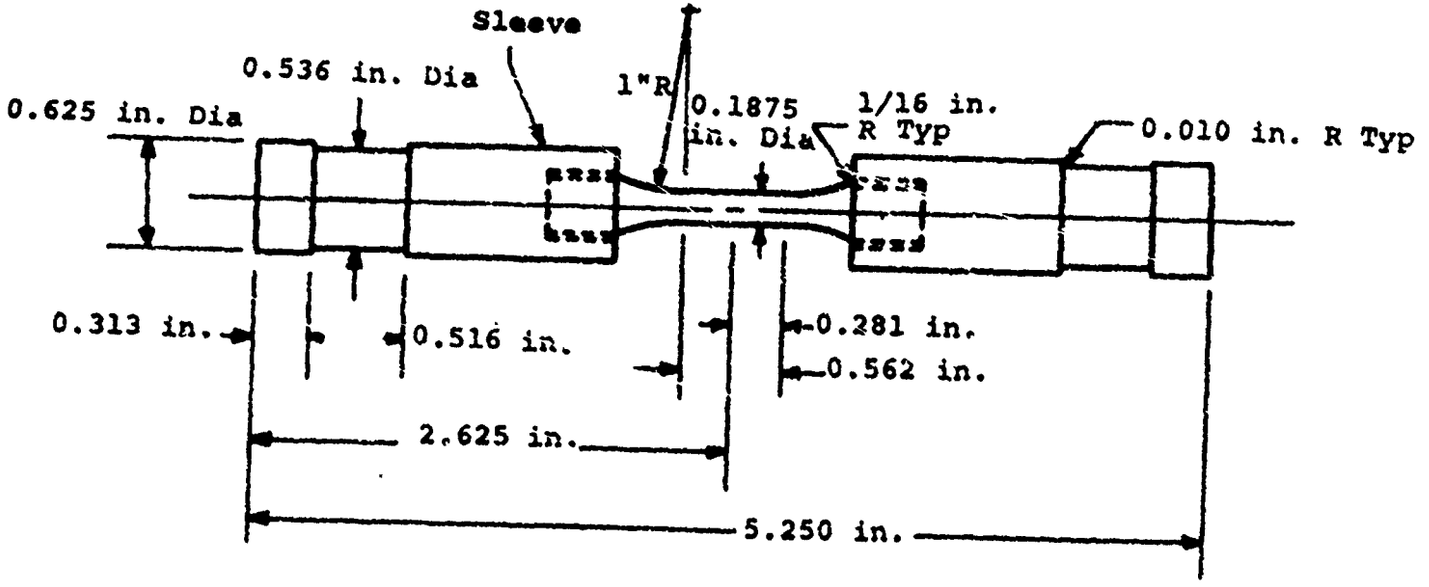


Figure 14. Configuration of Axial Tensile Specimen Used for Evaluation Specimens from Felt Carbon-Carbon Impacted Plates

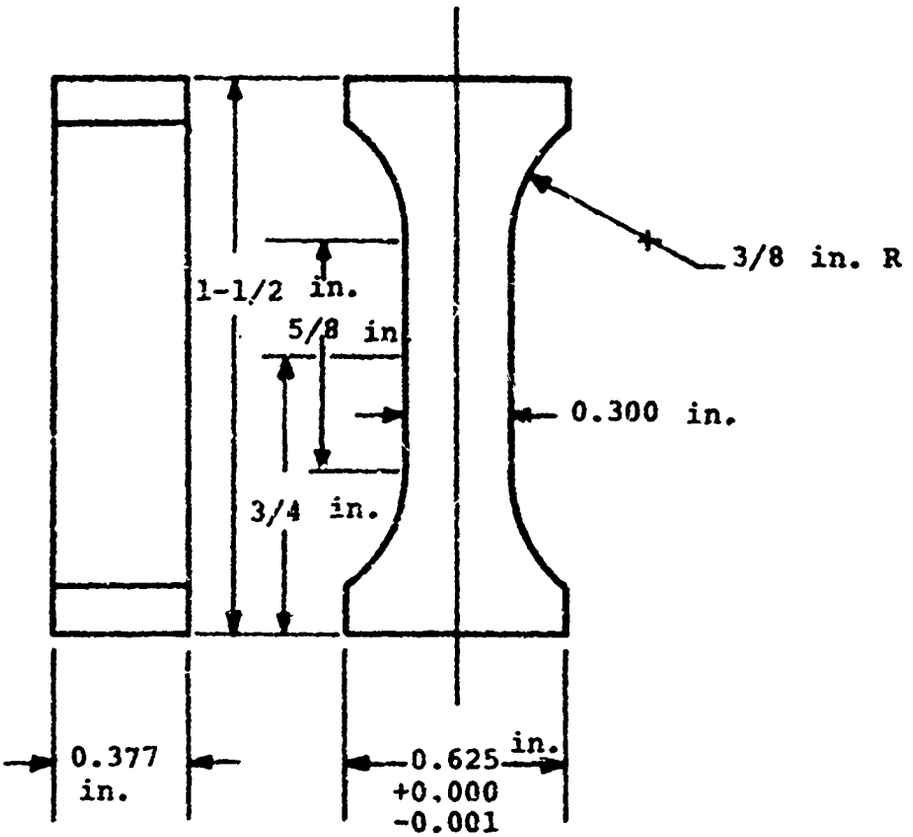


Figure 15. Configuration of Circumferential Compressive Specimen Used for Evaluations on Specimens from 3D Carbon-Carbon Impacted Arcs

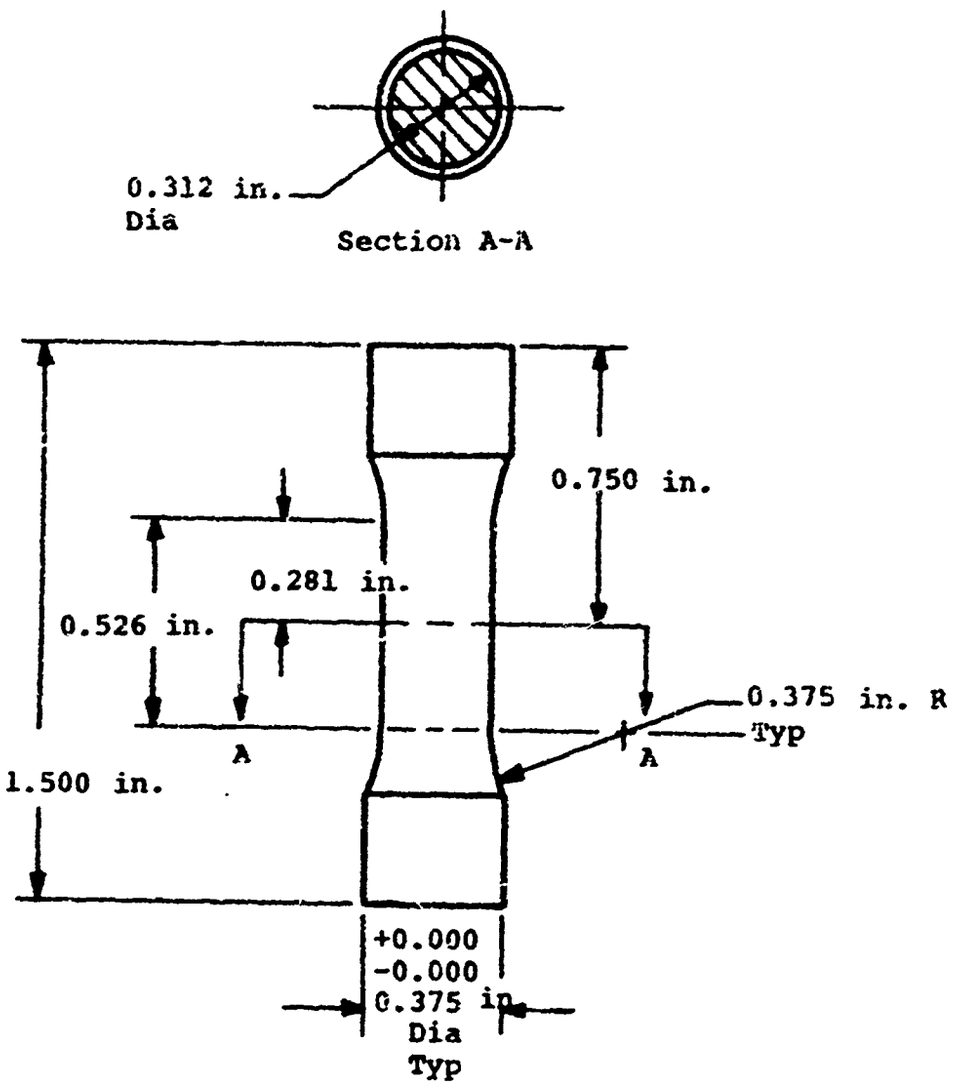


Figure 16. Configuration of Axial Compressive Specimens Used for Evaluations on Specimens from Felt Carbon-Carbon Impacted Plates 12-F-15 and 12-F-10

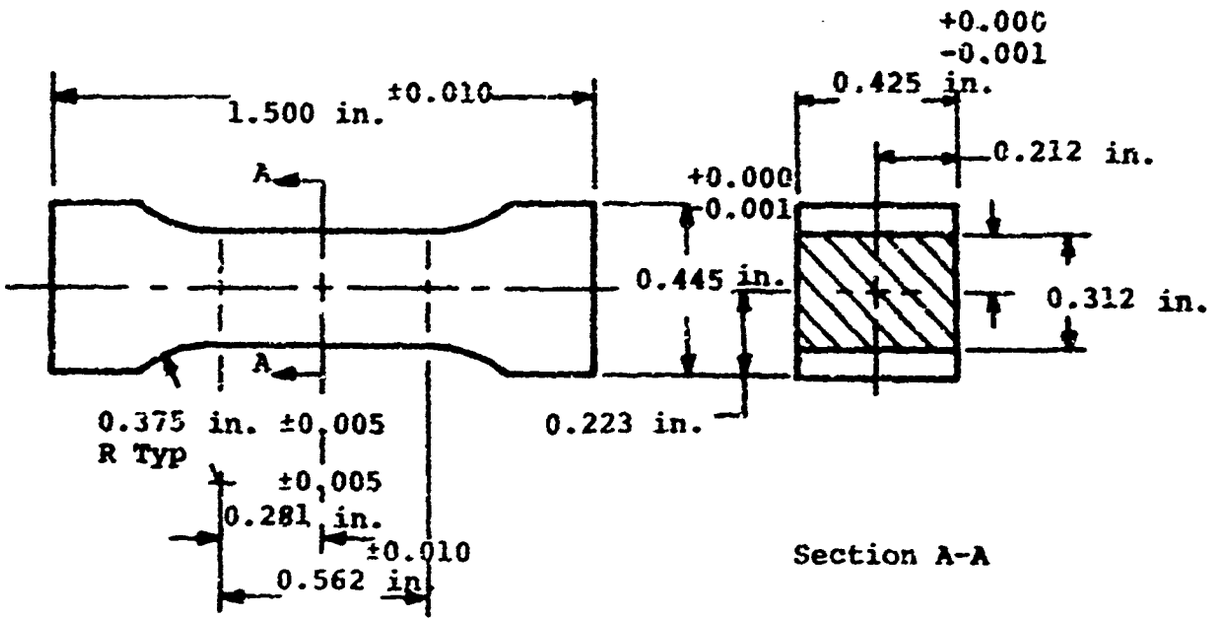
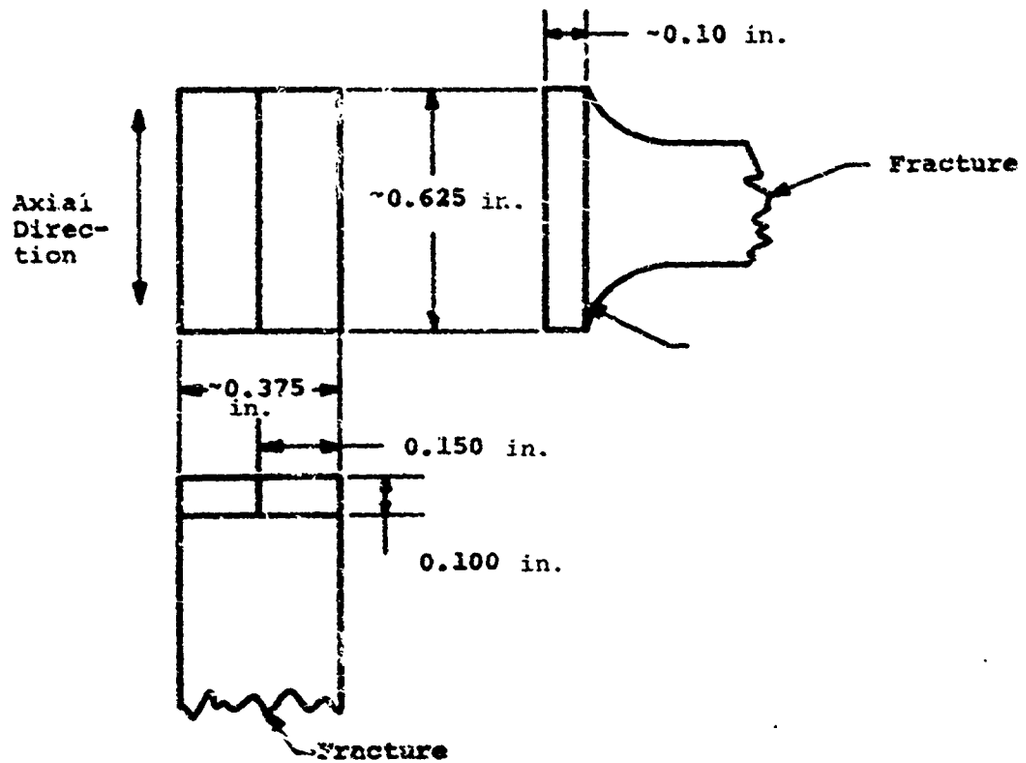
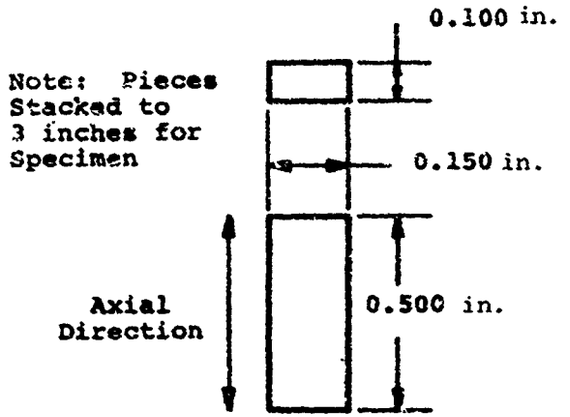


Figure 17. Configuration of Axial Compressive Specimens Used for Evaluations on Specimens from Felt Carbon-Carbon Impacted Plates 12-P-11 and 12-P-1



Cutting Plan for Ends of 8AR-7-C1 and 8AR-7-C3



Detail of Extracted Pieces

Figure 18. Preparation of Thermal Expansion Specimens of 3DCC in Axial Direction From Used Compressive Specimens

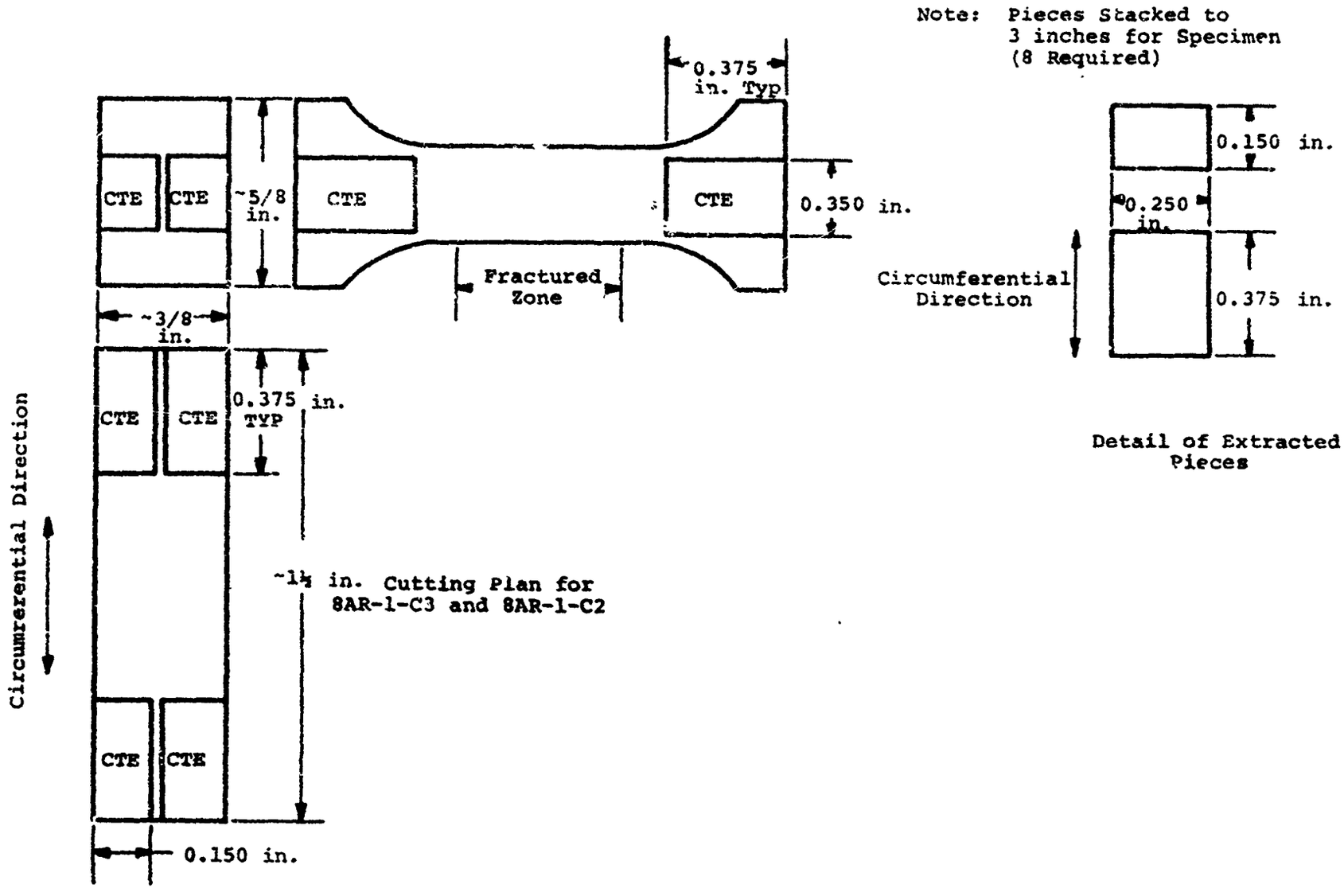


Figure 19. Preparation of Thermal Expansion Specimen of 3 DCC in Circumferential Direction from Used Compressive Specimen

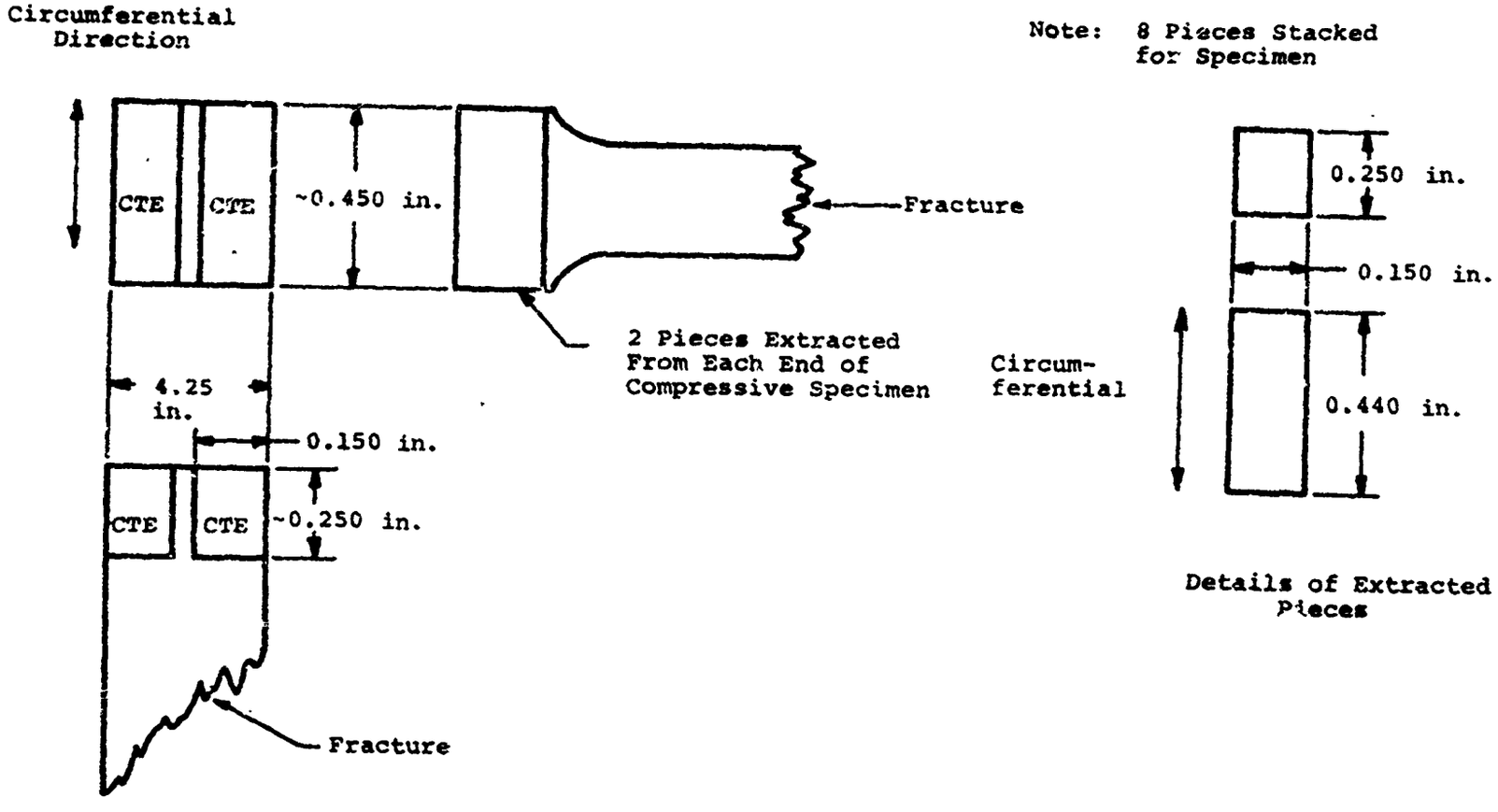
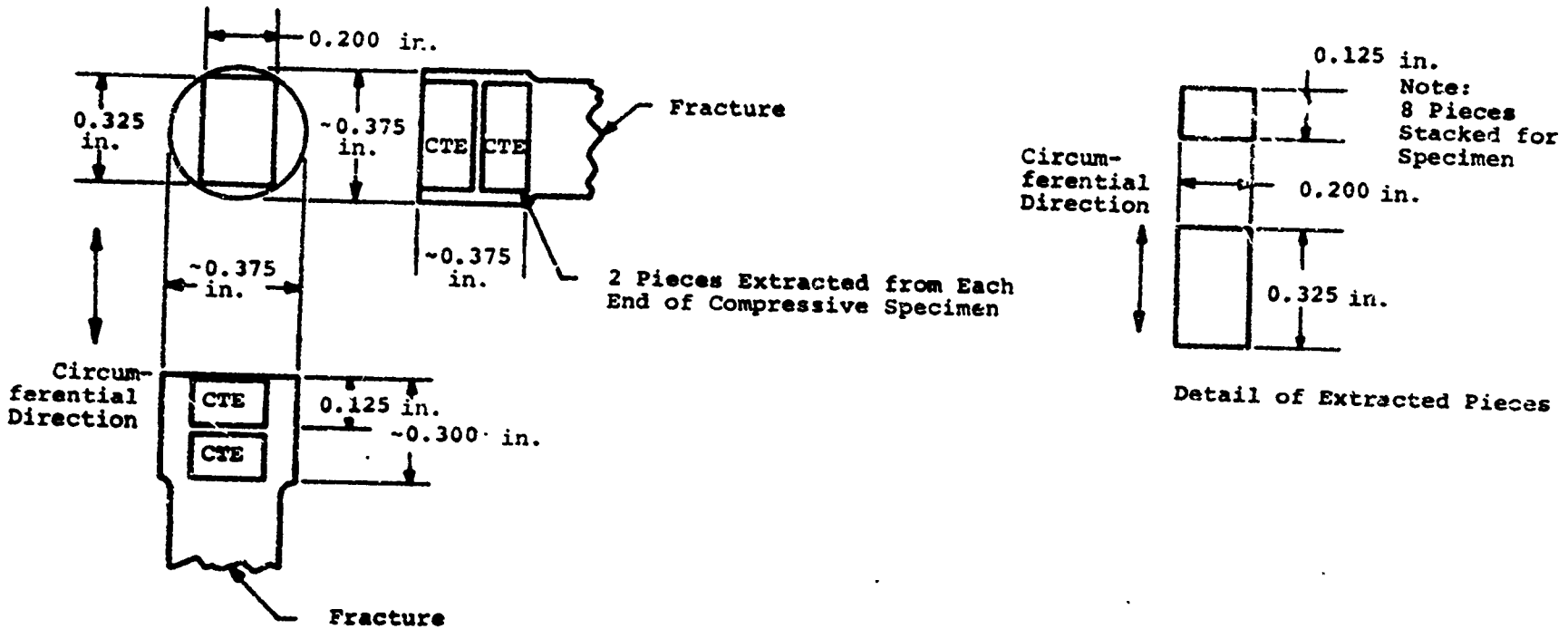
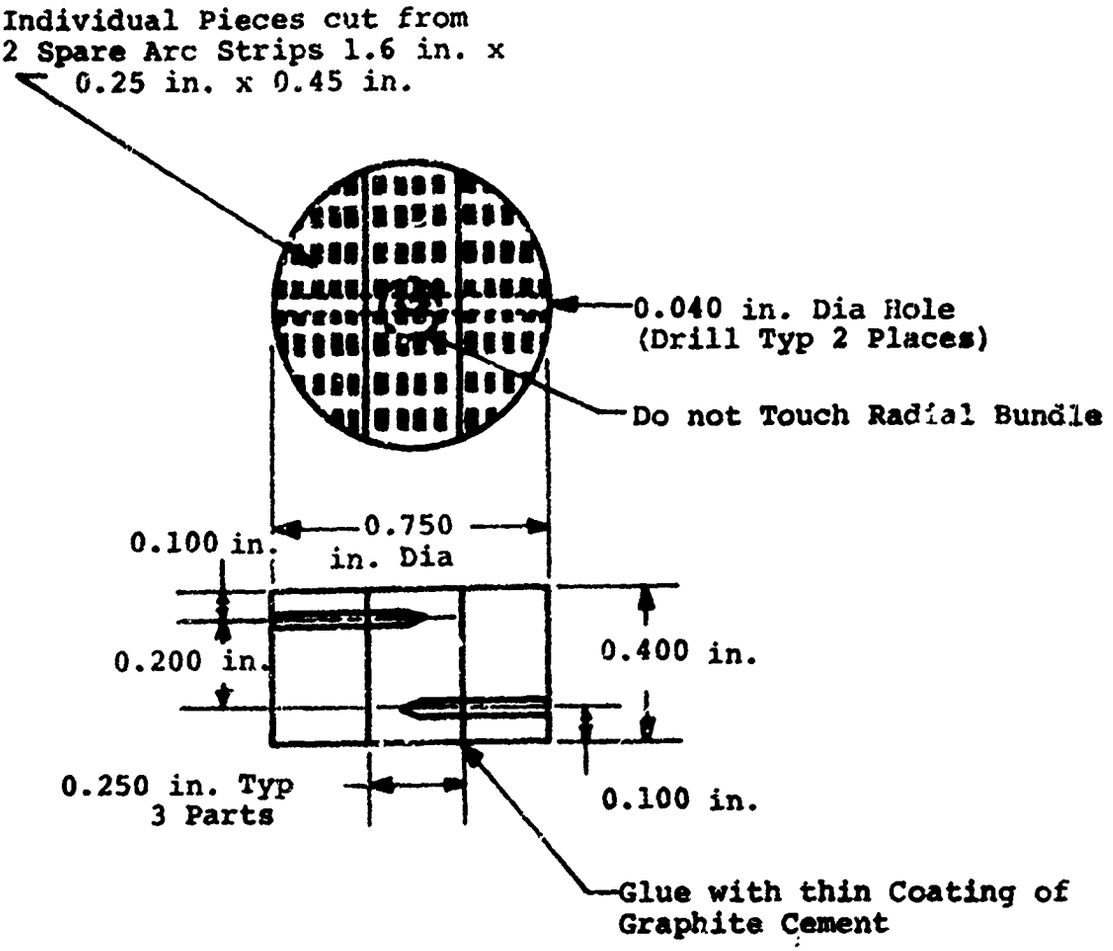


Figure 20. Preparation of Thermal Expansion Specimen of Felt CC in the Circumferential Direction from Used Compressive Specimens



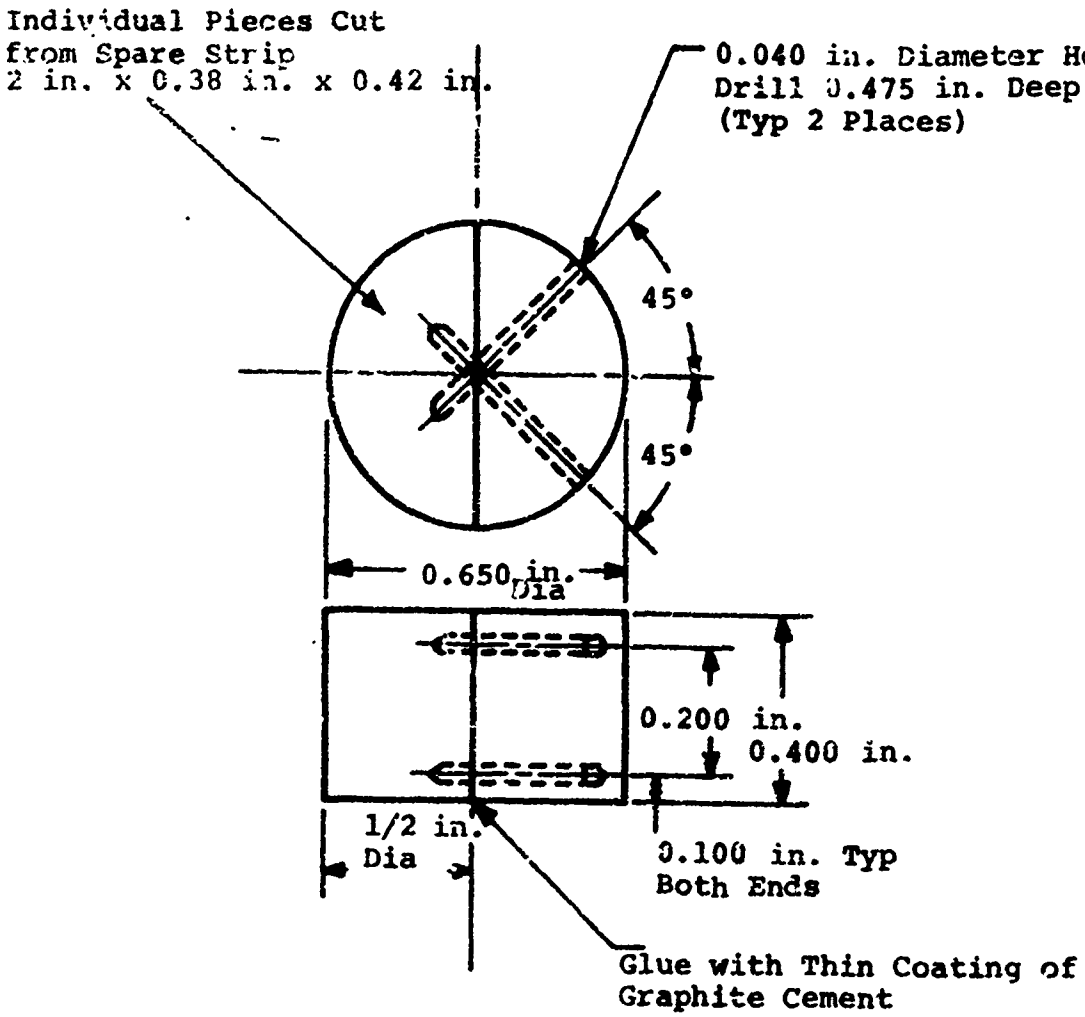
Cutting Plan for 12-F-10-C1, 12-F-10-C3 for First Specimen 12-F-15-C1 and 12-F-15-C4 for Second Specimen

Figure 21. Preparation of Thermal Expansion Specimens of Felt CC in the Circumferential Direction from Used Compressive Specimen



Specimens Made From 8-AR-2 and 8-AR-8

Figure 22. Configuration of Thermal Conductivity Specimen Used in the Comparative Rod Apparatus for 3DCC



Note: Specimens made from 12-F-10 and 12-F-15

Figure 23. Configuration of Thermal Conductivity Specimen Used in the Comparative Rod Apparatus for Felt CC

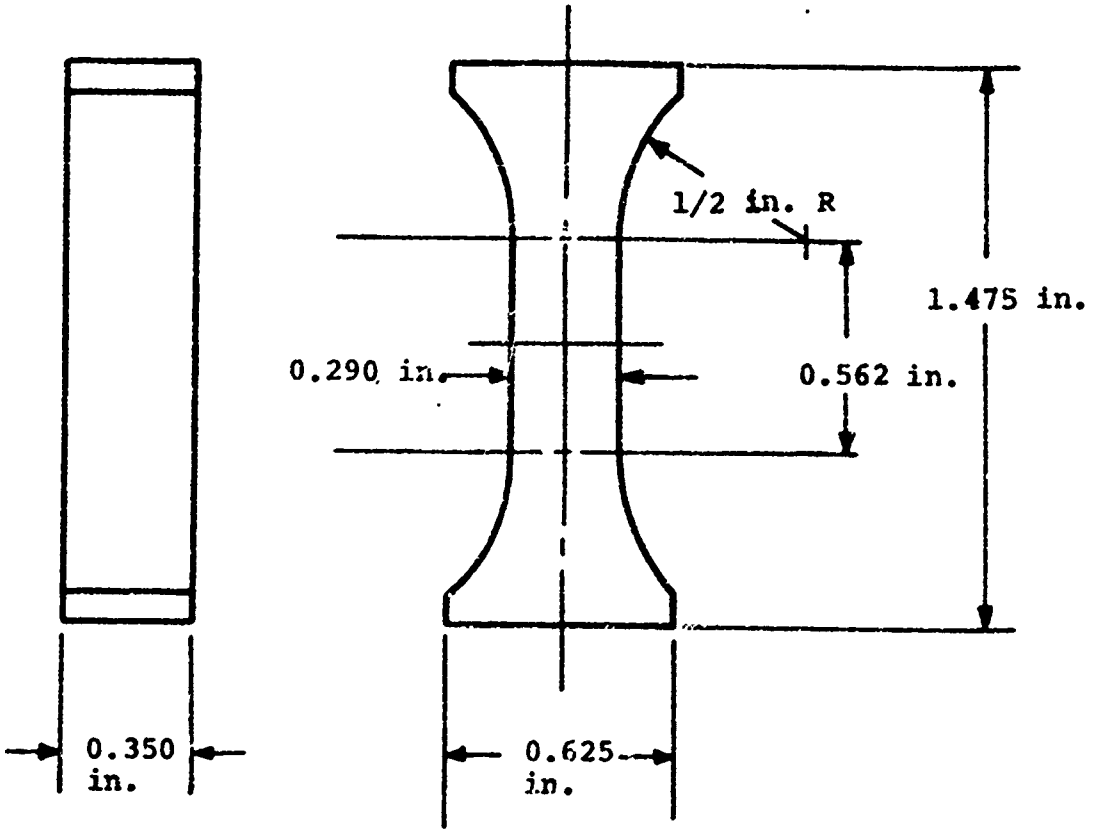


Figure 24. Configuration of Axial Tensile Specimens Used for Evaluations on Specimens From R6300 Impacted Arcs

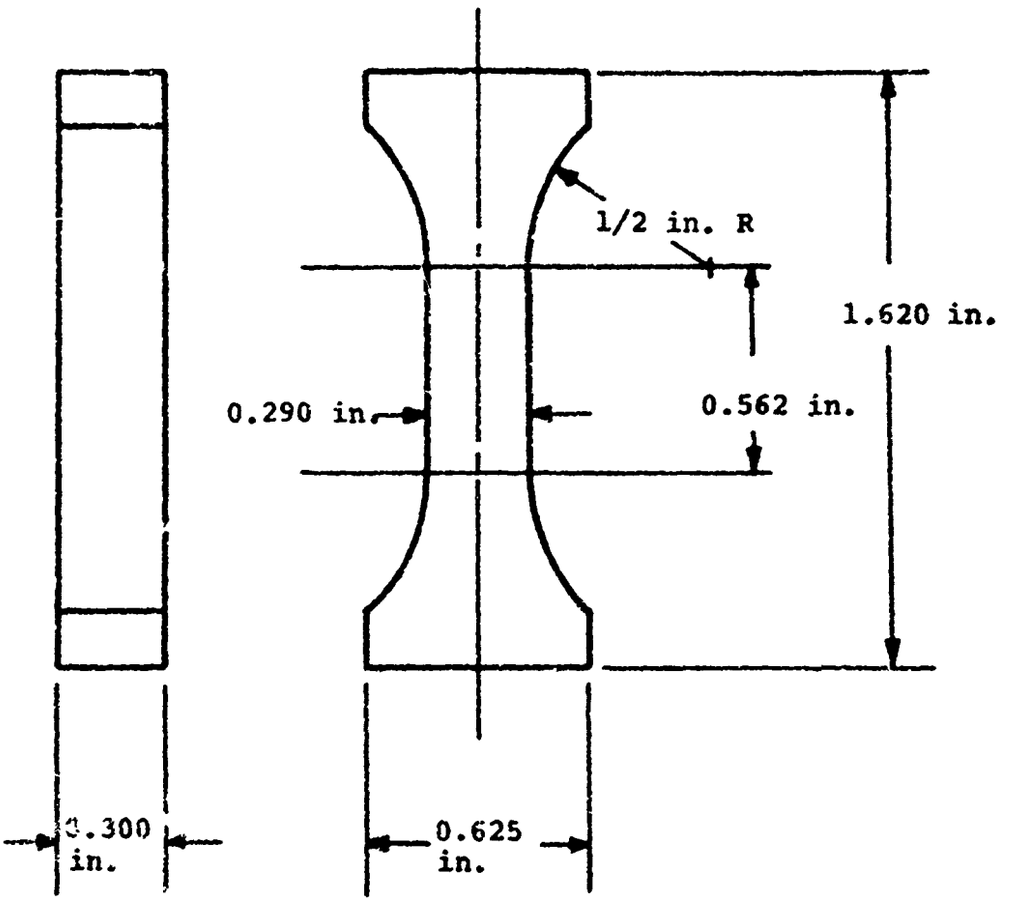


Figure 25. Configuration of Circumferential Tensile Specimens Used for Evaluations on Specimens From R6300 Impacted Arcs

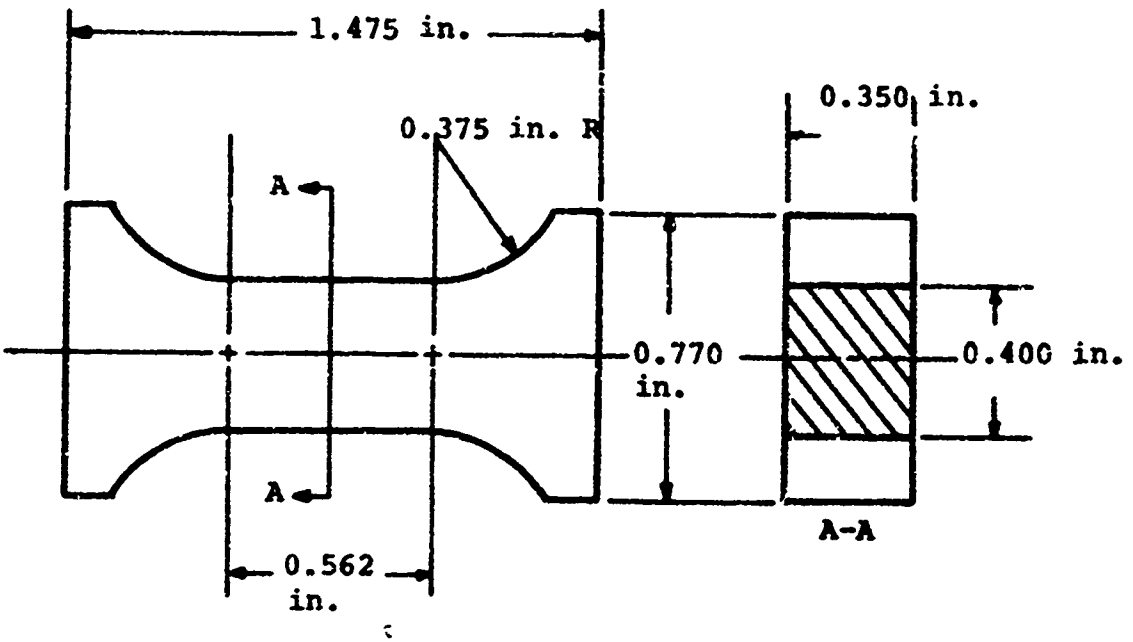


Figure 26. Configuration of Axial Compressive Specimens Used for Evaluations on Specimens from R6300 Impacted Arcs

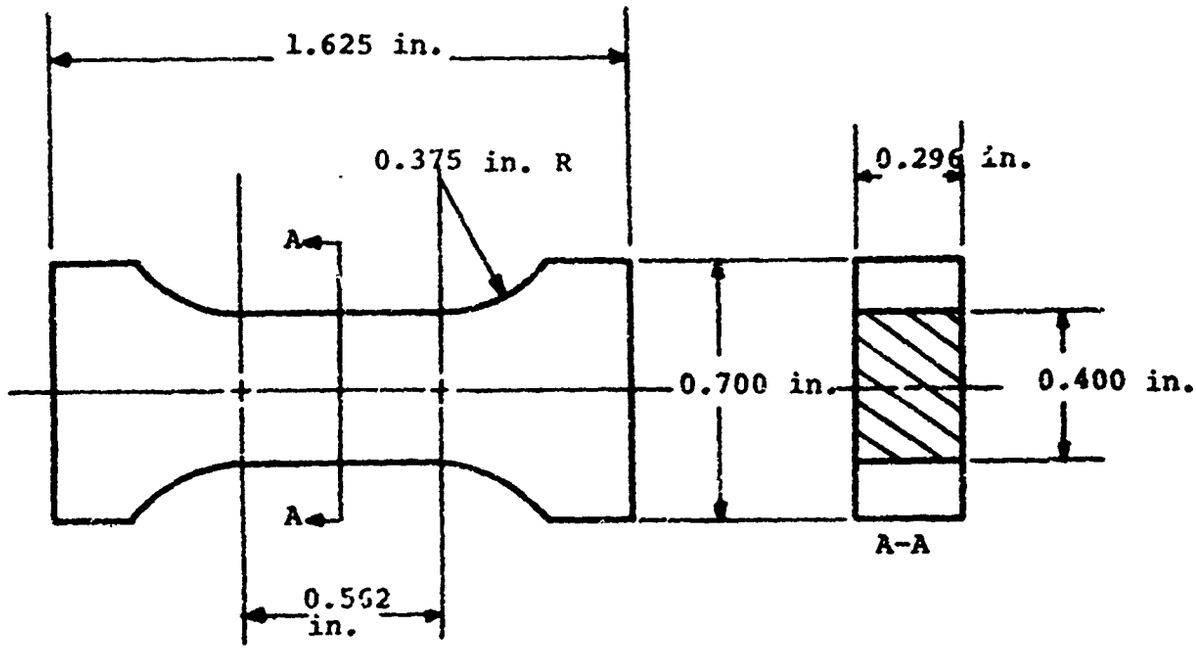


Figure 27. Configuration of Circumferential Compressive Specimens Used for Evaluations on Specimens From R6300 Impacted Arcs

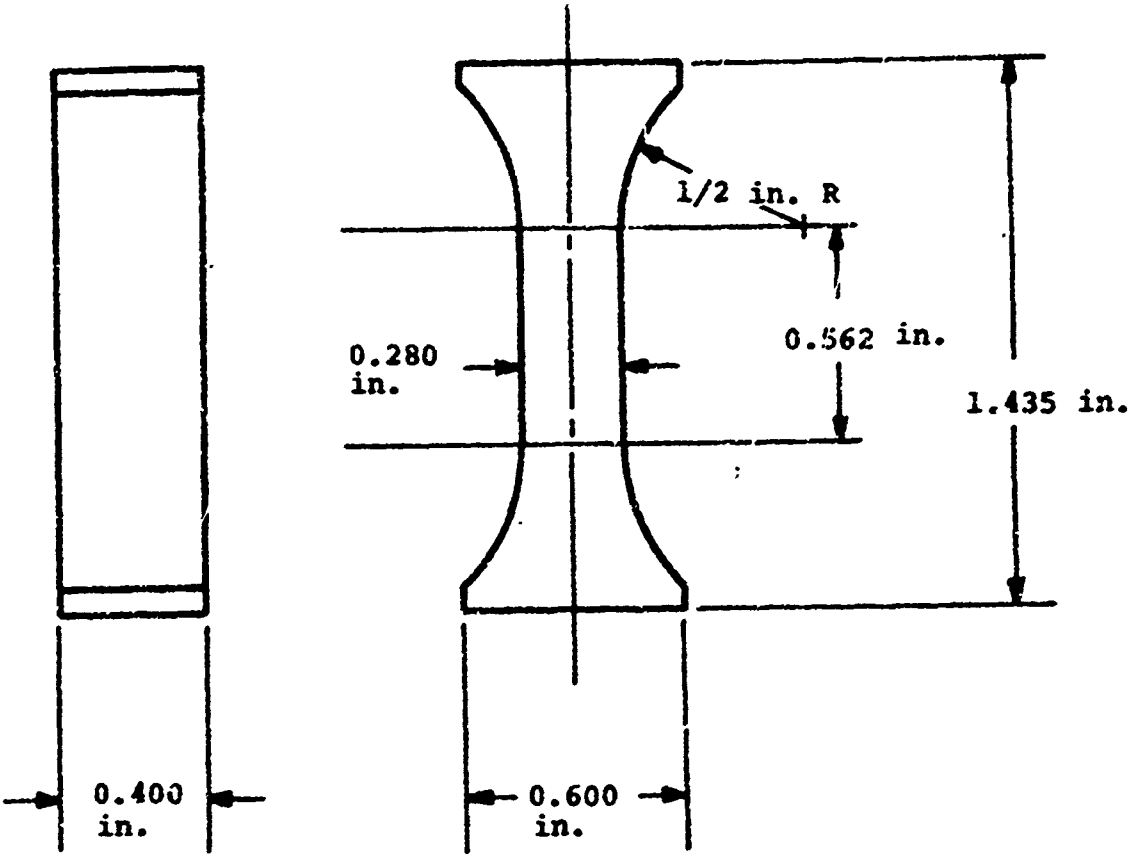


Figure 28. Configuration of Axial Tensile Specimens Used for Evaluations on Specimens from 3D Quartz-Phenolic Impacted Arcs

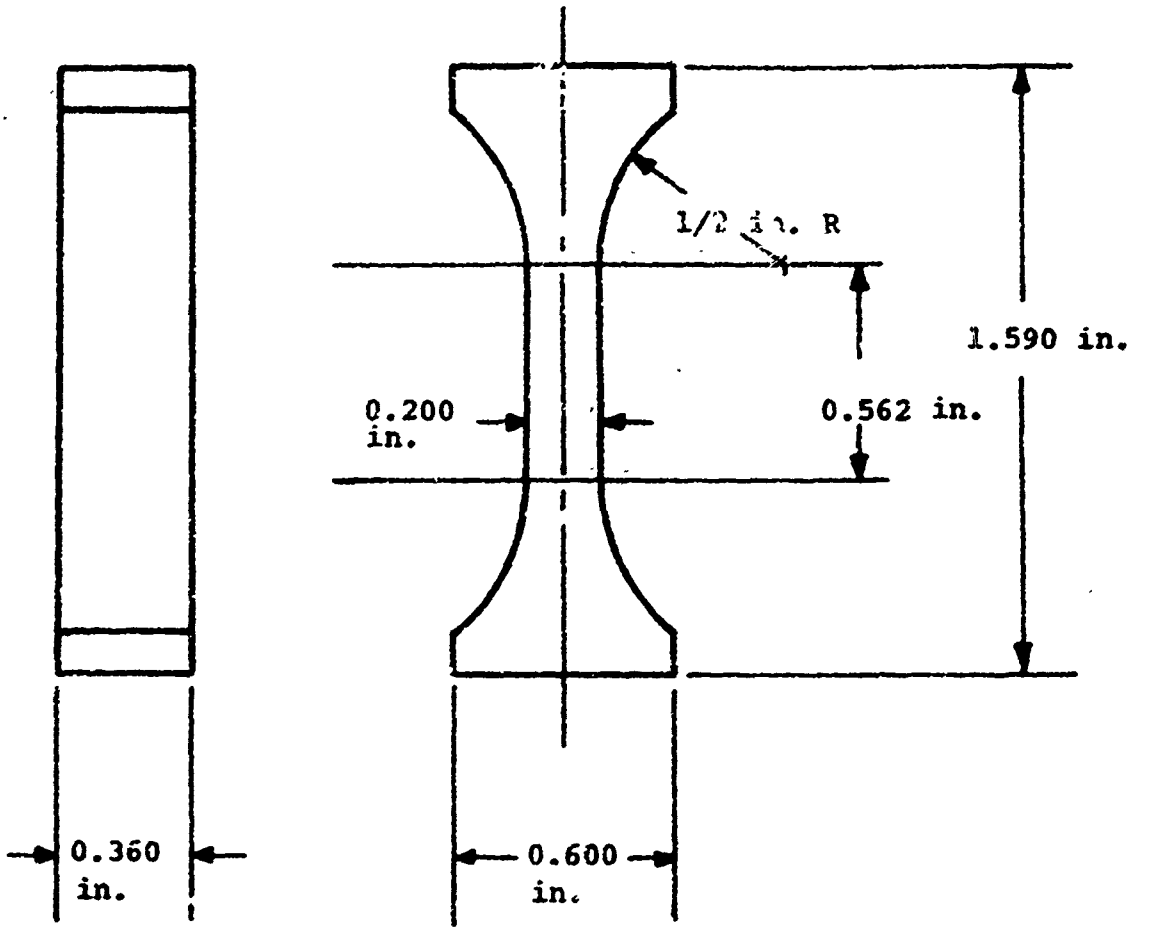
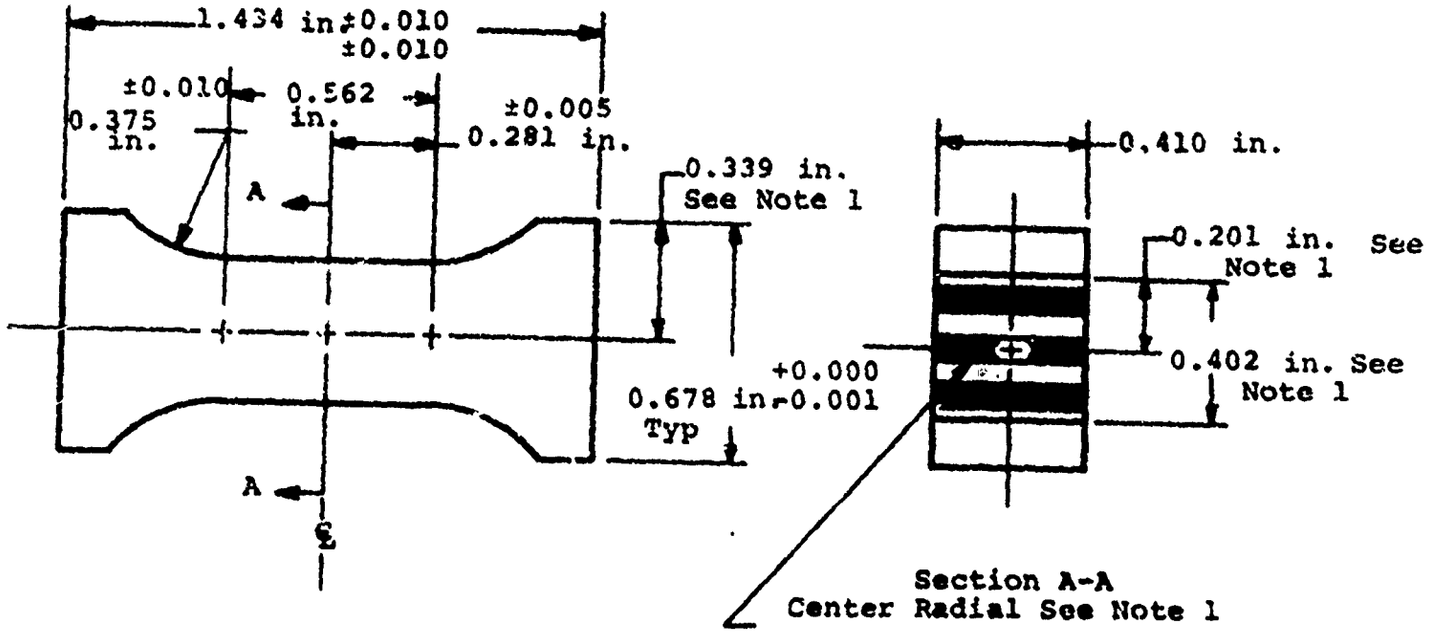
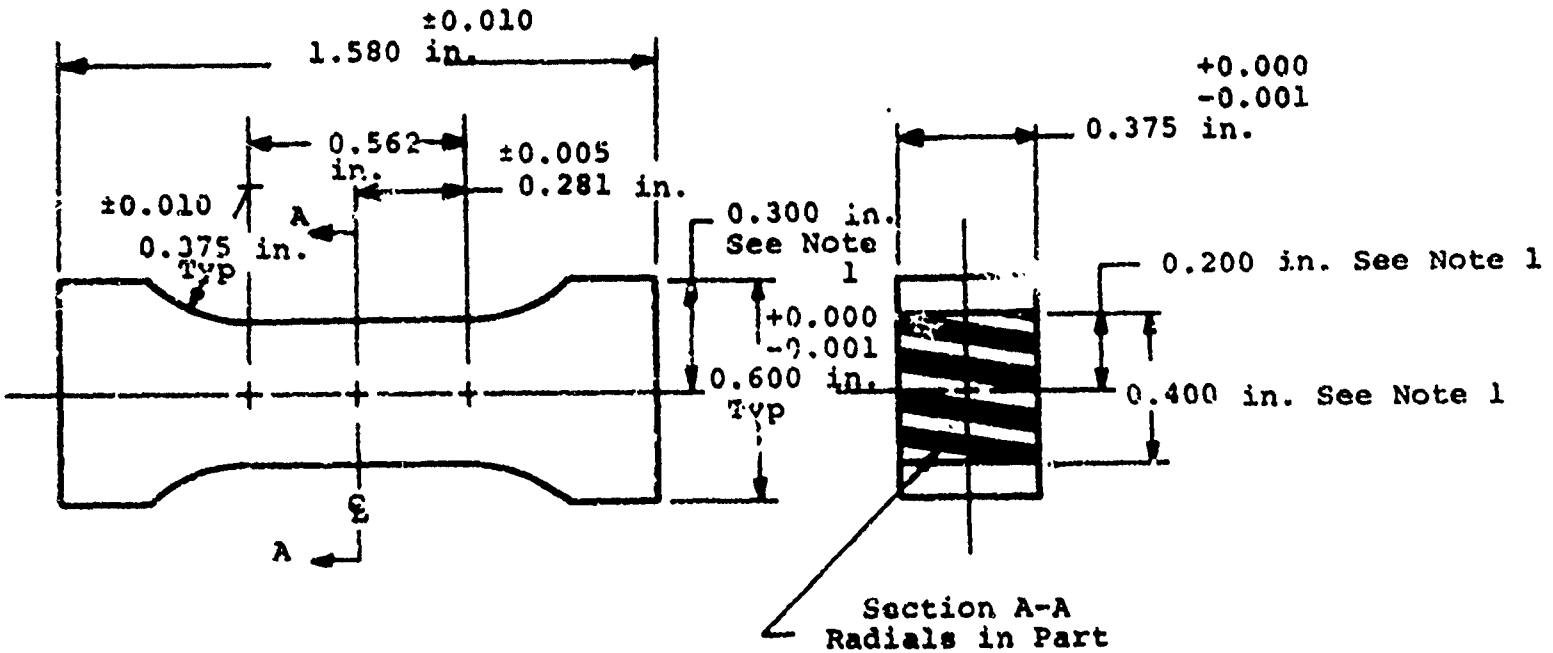


Figure 29. Configuration of Circumferential Tensile Specimens Used for Evaluations on Specimens from 3D Quartz-Phenolic Impacted Arcs



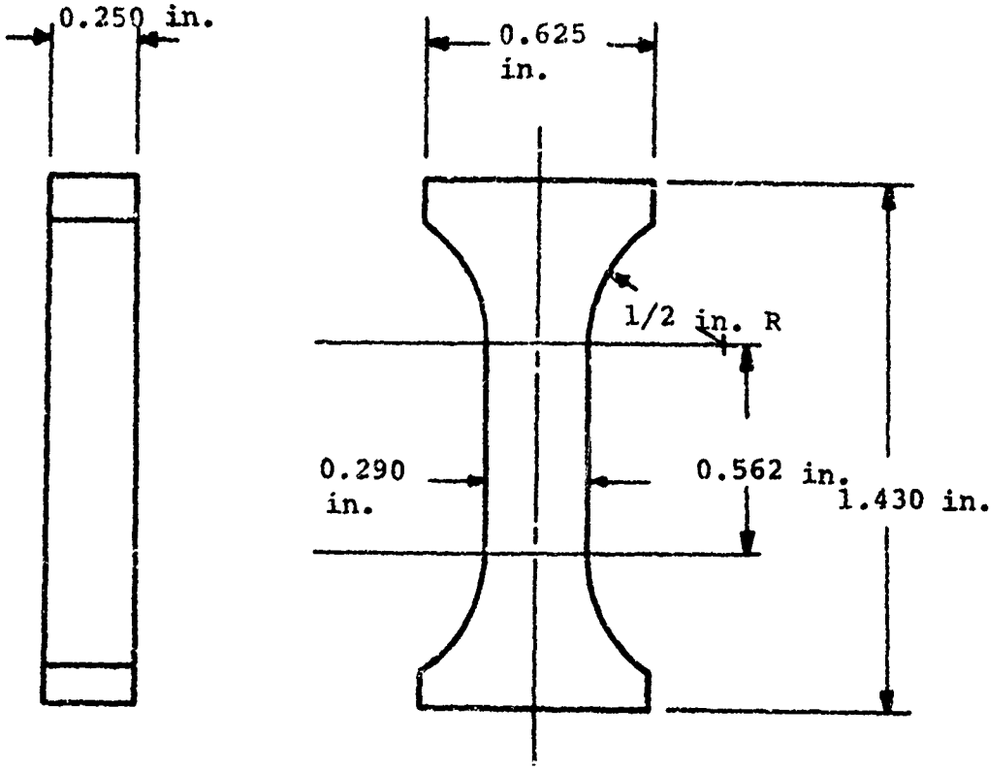
Notes:
1. Center Specimen on a Radial
2. Both Ends Flat and Perpendicular to 0.0005 in
3. Tolerances Unless Otherwise Noted ± 0.001 in

Figure 30. Configuration of Axial Compressive Specimens Used for Evaluations of Specimens from 3D Quartz-Phenolic Impacted Arcs



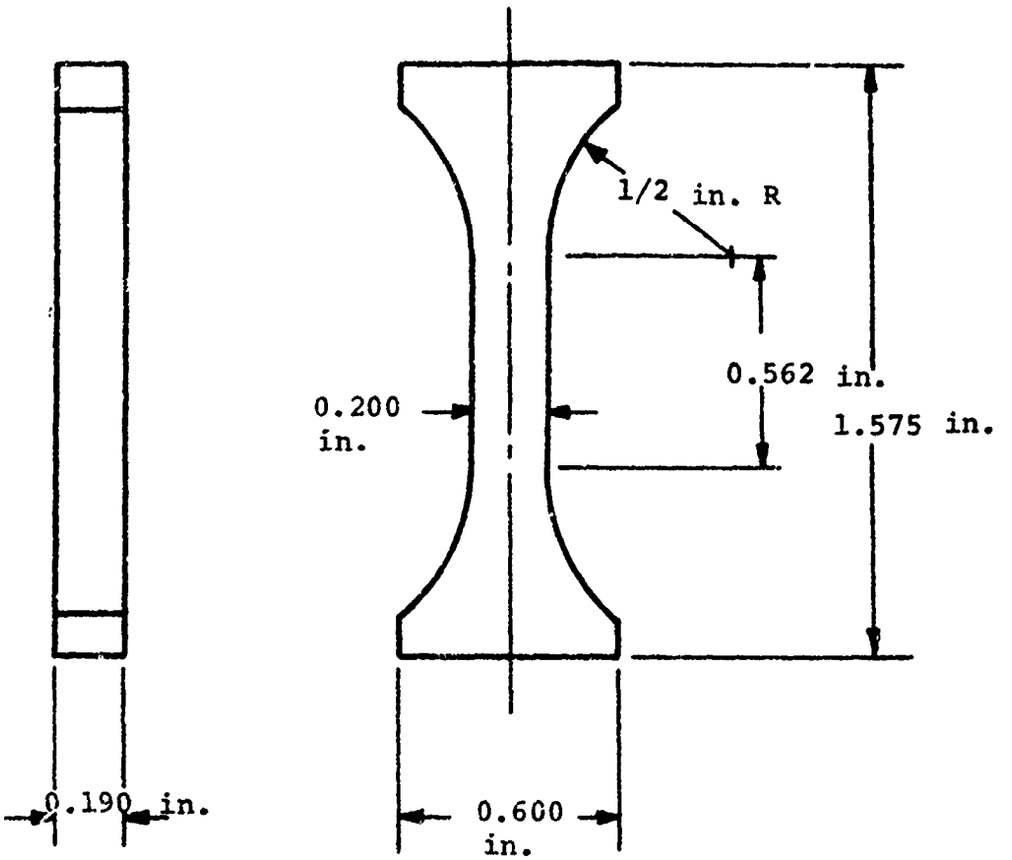
Notes:
1. Center Specimen Between Radials
2. Both Ends Flat and Perpendicular to 0.0005
3. Tolerances Unless Otherwise Noted ± 0.001

Figure 31. Configuration of Compressive Specimens Used for Evaluations on Specimens from 3D Quartz-Phenolic Impacted Arcs



Center Specimen Between Radials

Figure 32. Configuration of Axial Tensile Specimens for Evaluations on Specimens from 3D Carbon-Phenolic Portion of 3DC/QP Impacted Arcs



Center Specimen Between Radials

Figure 33. Configuration of Circumferential Tensile Specimens Used for Evaluations on Specimens from Carbon-Phenolic Portion of 3DC/QP Impacted Arcs

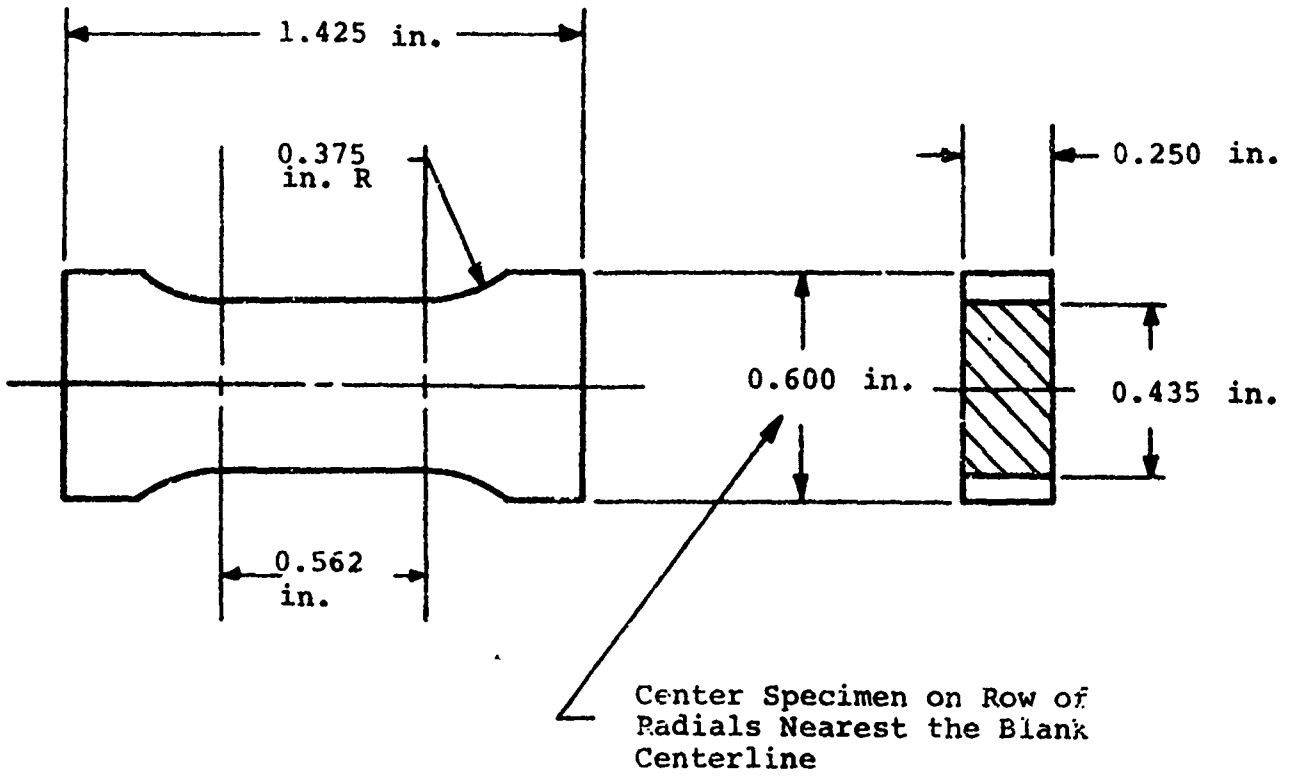


Figure 34. Configuration of Axial Compressive Specimen Used for Evaluation on Specimens from the 3D Carbon-Phenolic Portion of 3DC/QP Impacted Arcs

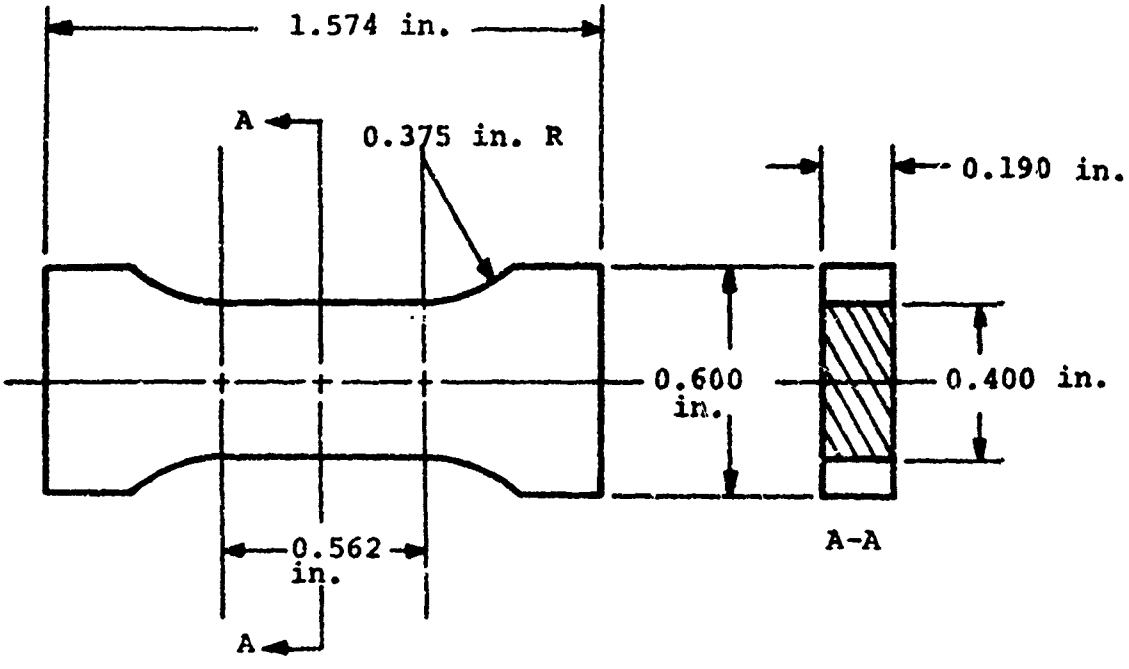
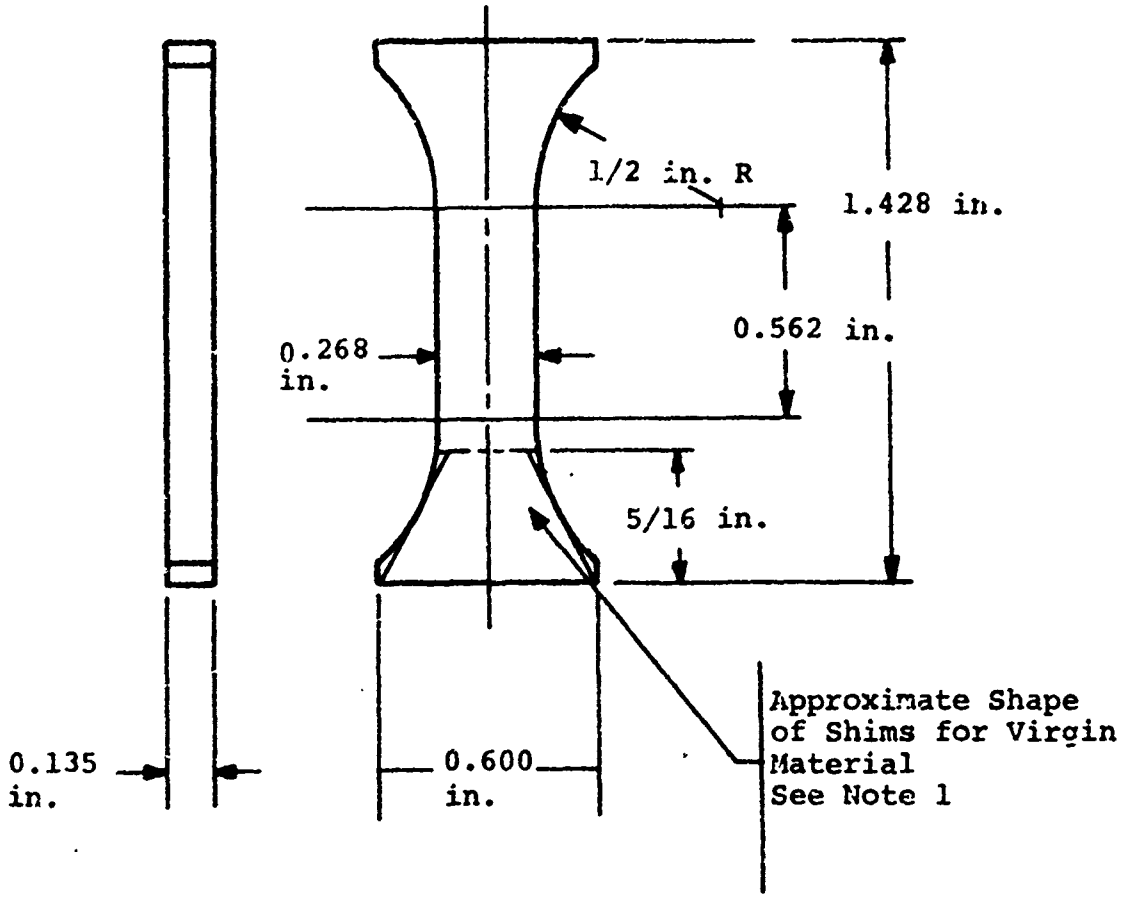
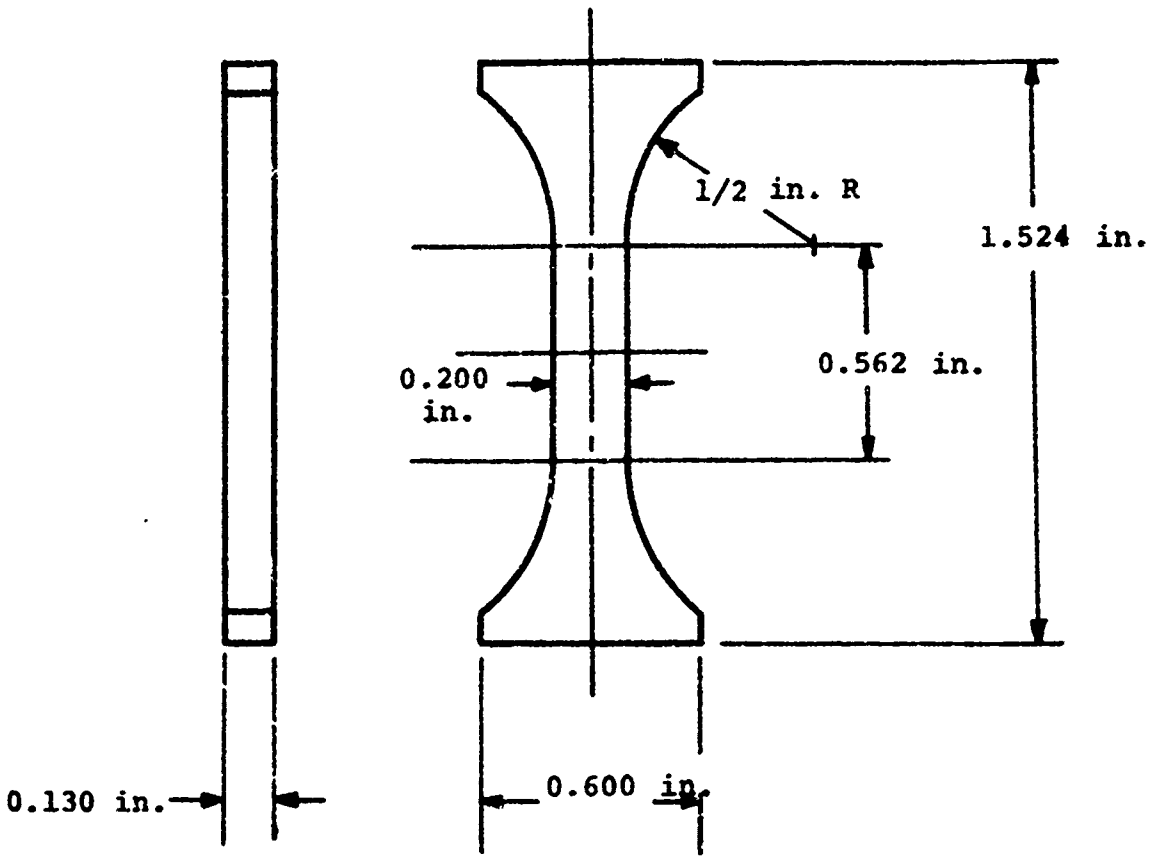


Figure 35. Configuration of Circumferential Compressive Specimen Used for Evaluations on Specimens from the 3D Carbon-Phenolic Portion of 3DC/QP Impacted Arcs



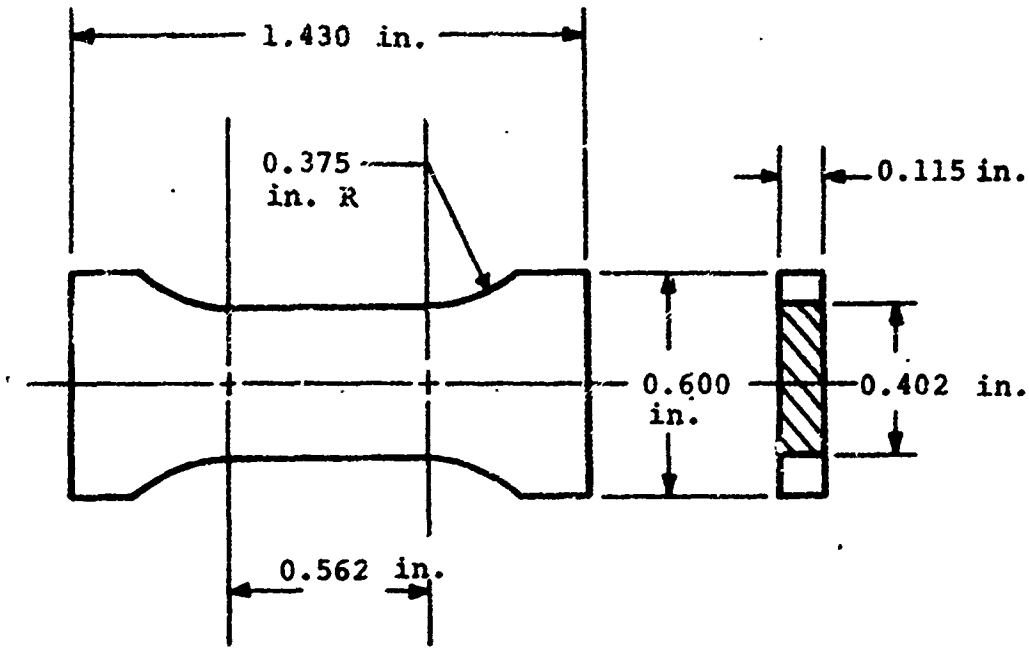
Notes: 1. Virgin Specimens 0.092 in.
2. Center Specimen Between Radials

Figure 36. Configuration of Axial Tensile Specimens for Evaluations on Specimens from Quartz-Phenolic Portion of 3DC/QP Impacted Arcs



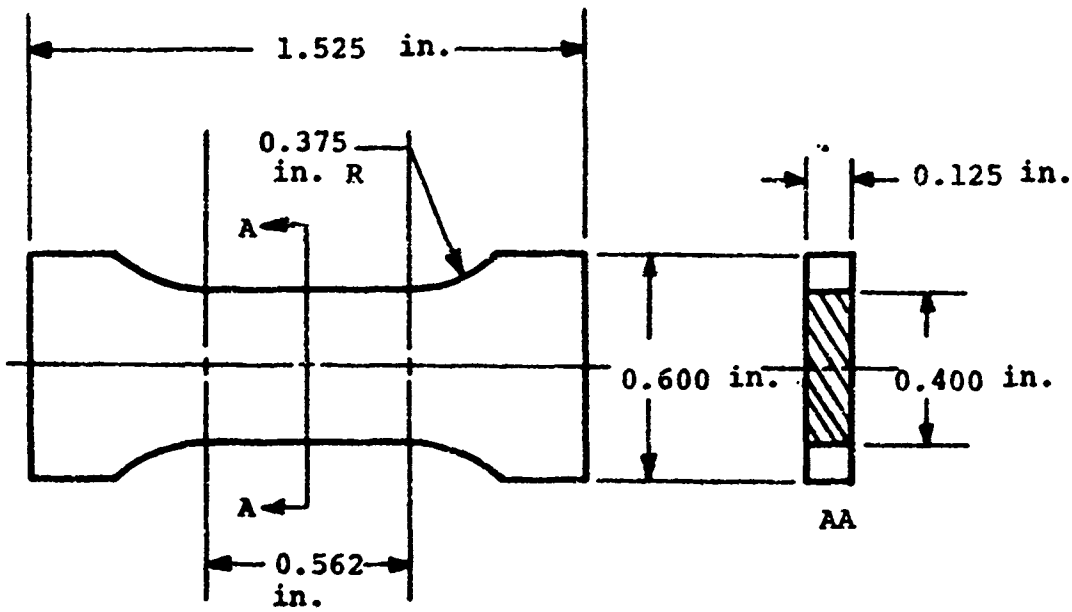
Center Specimen Between Radials

Figure 37. Configuration of Circumferential Tensile Specimens Used for Evaluations on Specimens from Quartz-Phenolic Portion of 3DC/QP Impacted Arcs



Center Specimen on Radials

Figure 38. Configuration of Axial Compressive Specimen Used for Evaluations on Specimens from the 3D Quartz-Phenolic Portion of 3DC/QP Impacted Arcs



Center Specimen Between Radials

Figure 39. Configuration of Circumferential Compressive Specimen Used for Evaluations on Specimens from the 3D Quartz-Phenolic Portion of 3DC/QP Impacted Arcs

Rear Delam (RD)

Bulk Delam (BD)

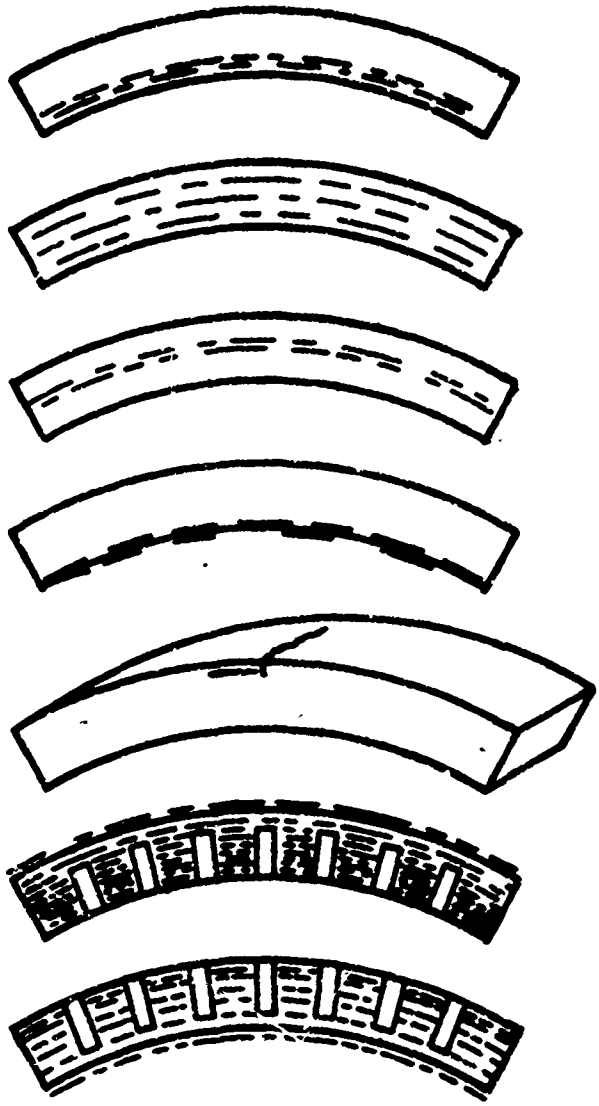
Mid Delam (MD)

Rear Lift (RL)

Front Face Crack (FFC)

Front Radial Recession (FRR)
(Bulk Expansion of Laterals
Toward Front Face)

Rear Radial Recession (RRR)
(Bulk Expansion of Laterals
Toward Rear Face)



Front Yarn Lift (FYL) — Raised or Missing Yarn From Front Face

Rear Yarn Lift (RYL) — Raised or Missing Yarn From Rear Face

Front Crush (FC)

Spall (S)

Buckle (B)

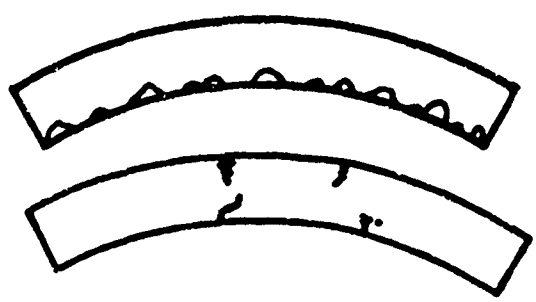


Figure 40. Definition of Structure-Change Terms

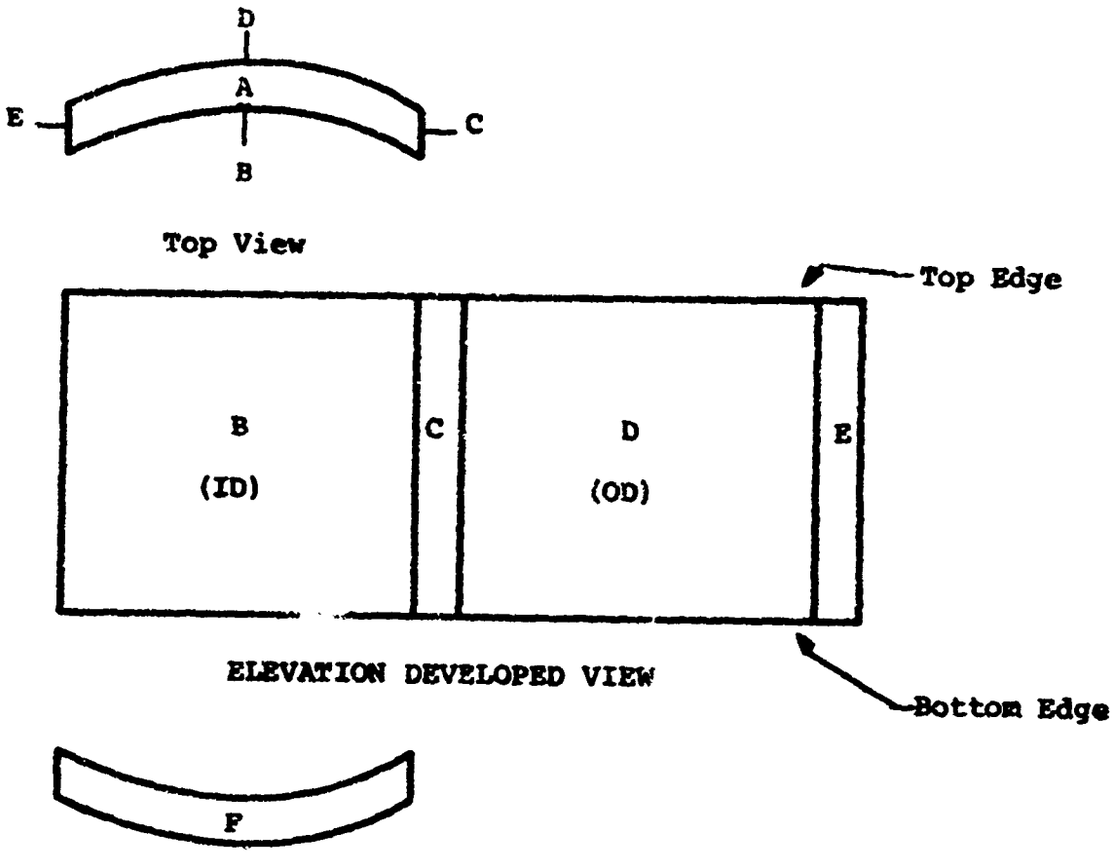
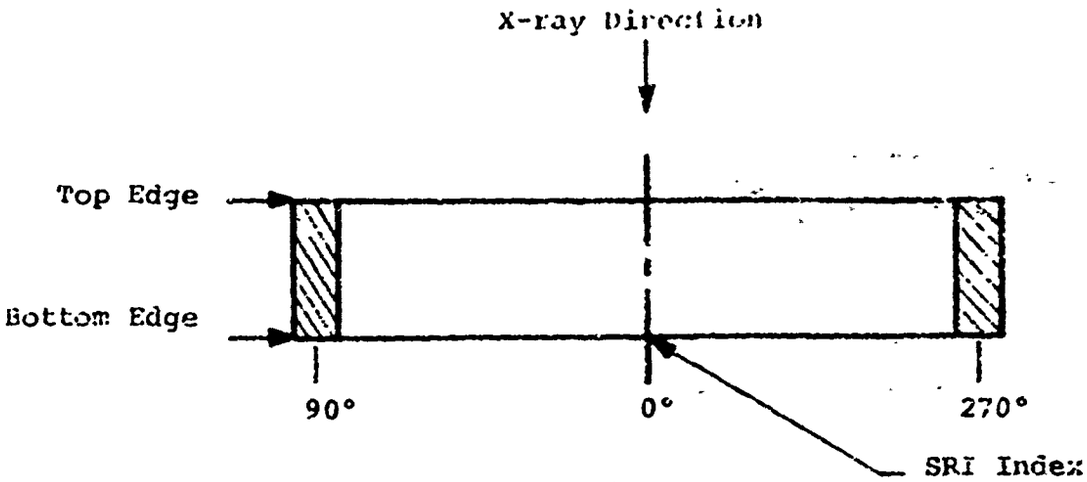
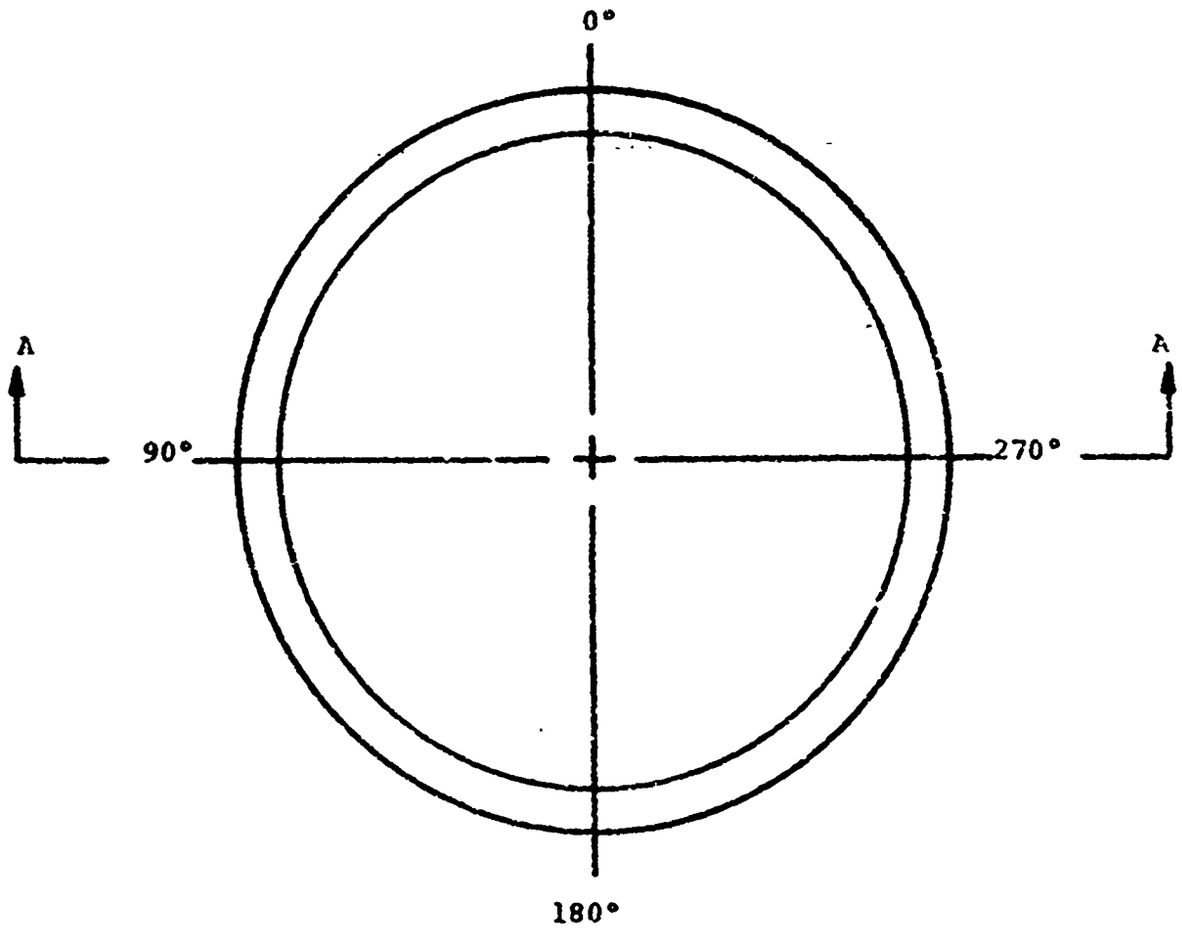


Figure 41. SRI Indexing and Orientations for Arcs and Coupons



Section A-A



Top View

Figure 42. SRI Indexing and Orientation System for Rings

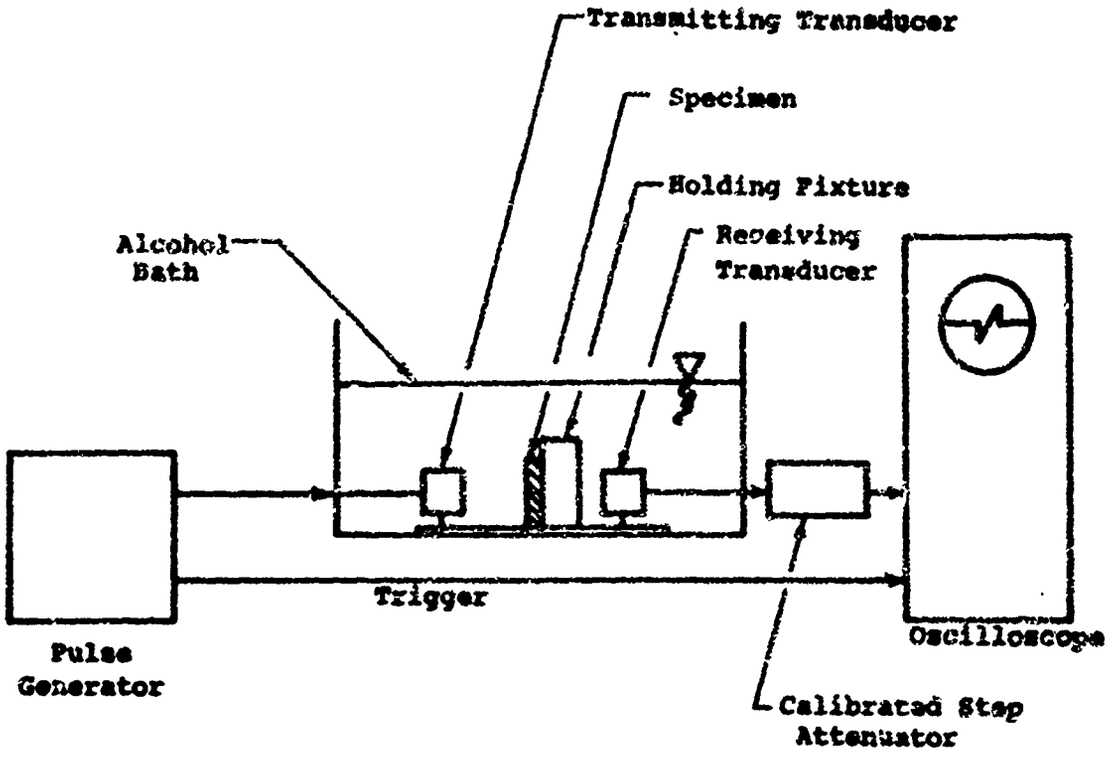


Figure 43. Ultrasonic Attenuation Setup Using the Pulsed Through-Transmission Technique

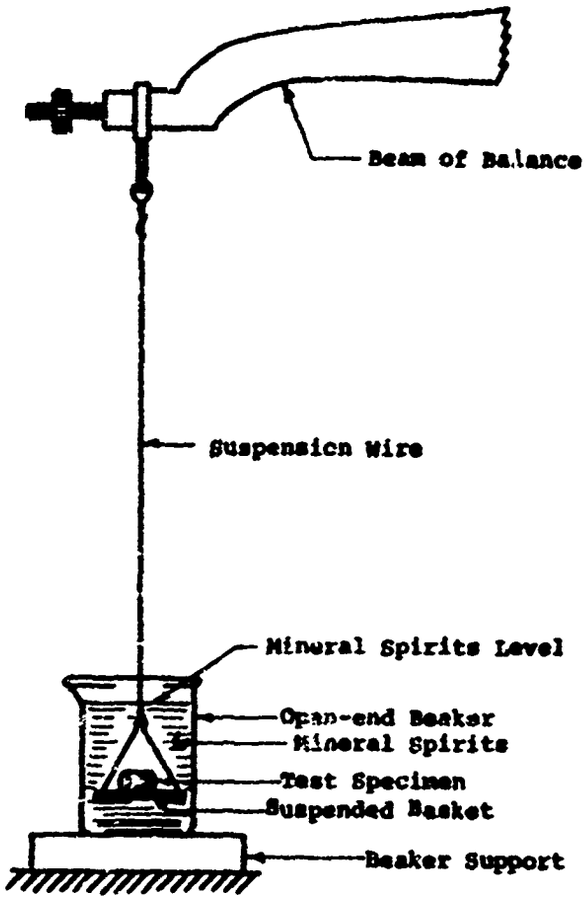


Figure 44. Setup for Determining Suspended Weight of Saturated Specimen for Liquid Absorption Evaluation

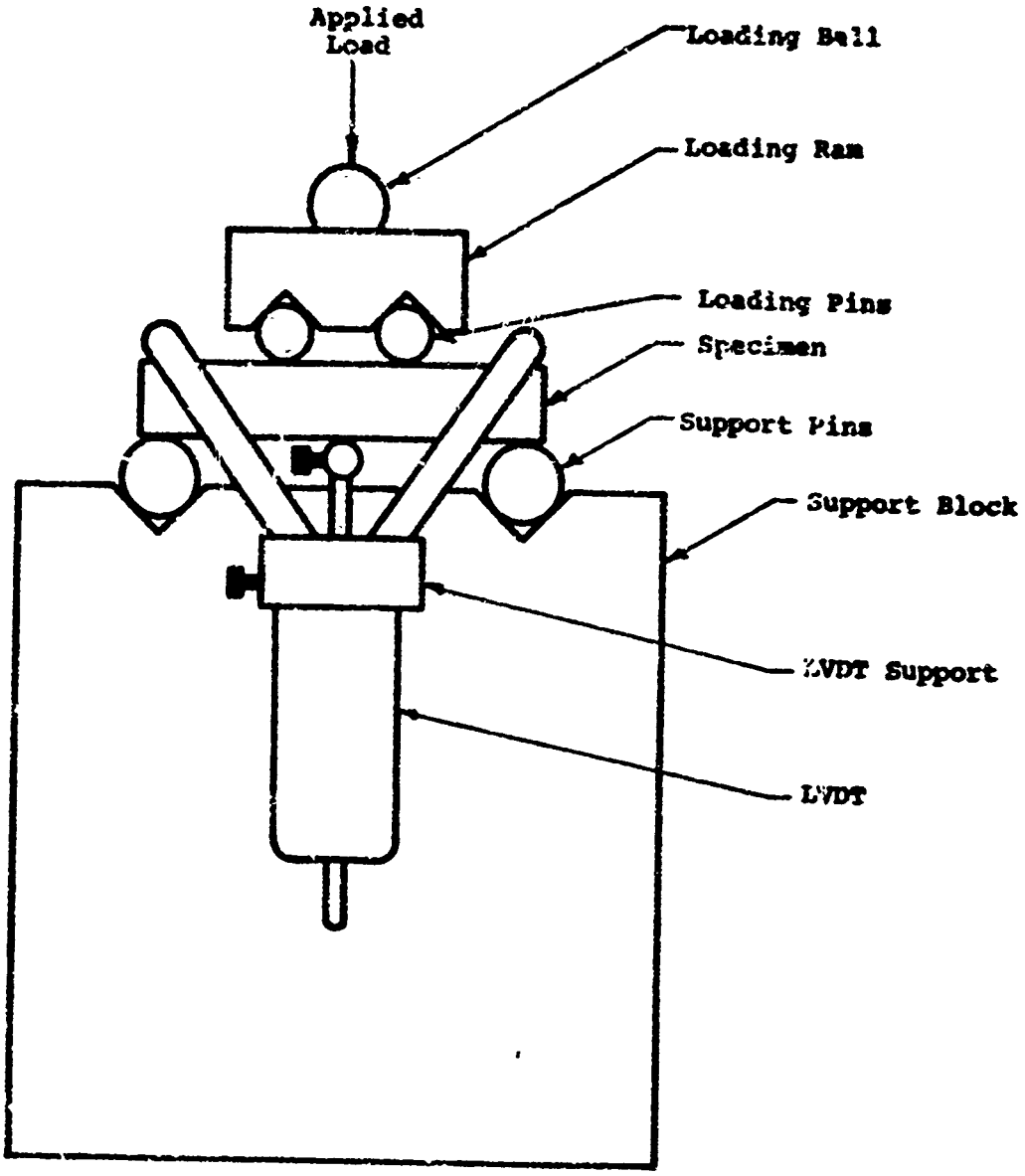


Figure 45. Four-Point Bending Apparatus for Flexural Modulus of Elasticity (MOE) Evaluations

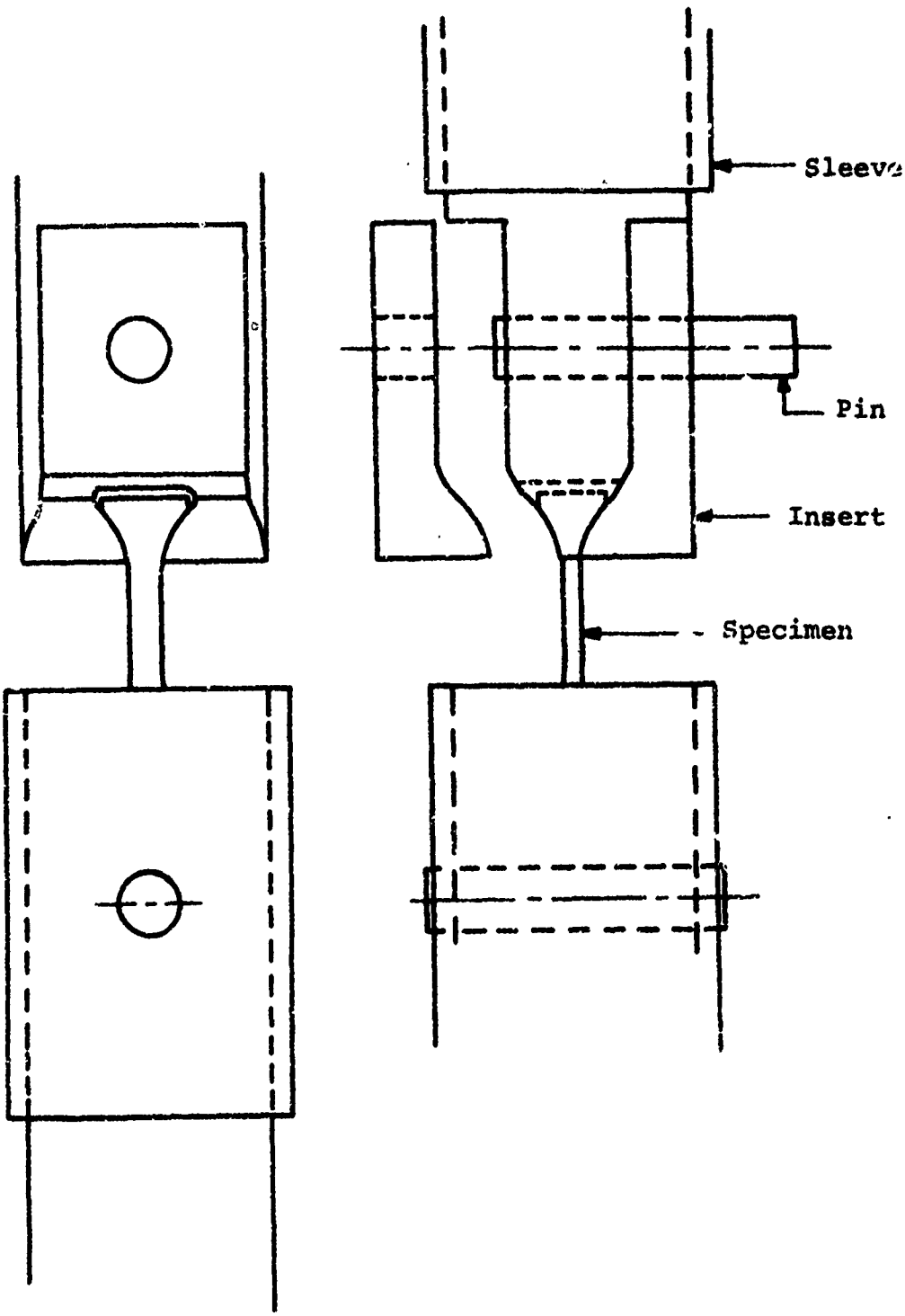


Figure 46. Specimen and Grip Configuration Used for Tensile Evaluations of Specimens From 3D Carbon-Carbon Impacted Arcs

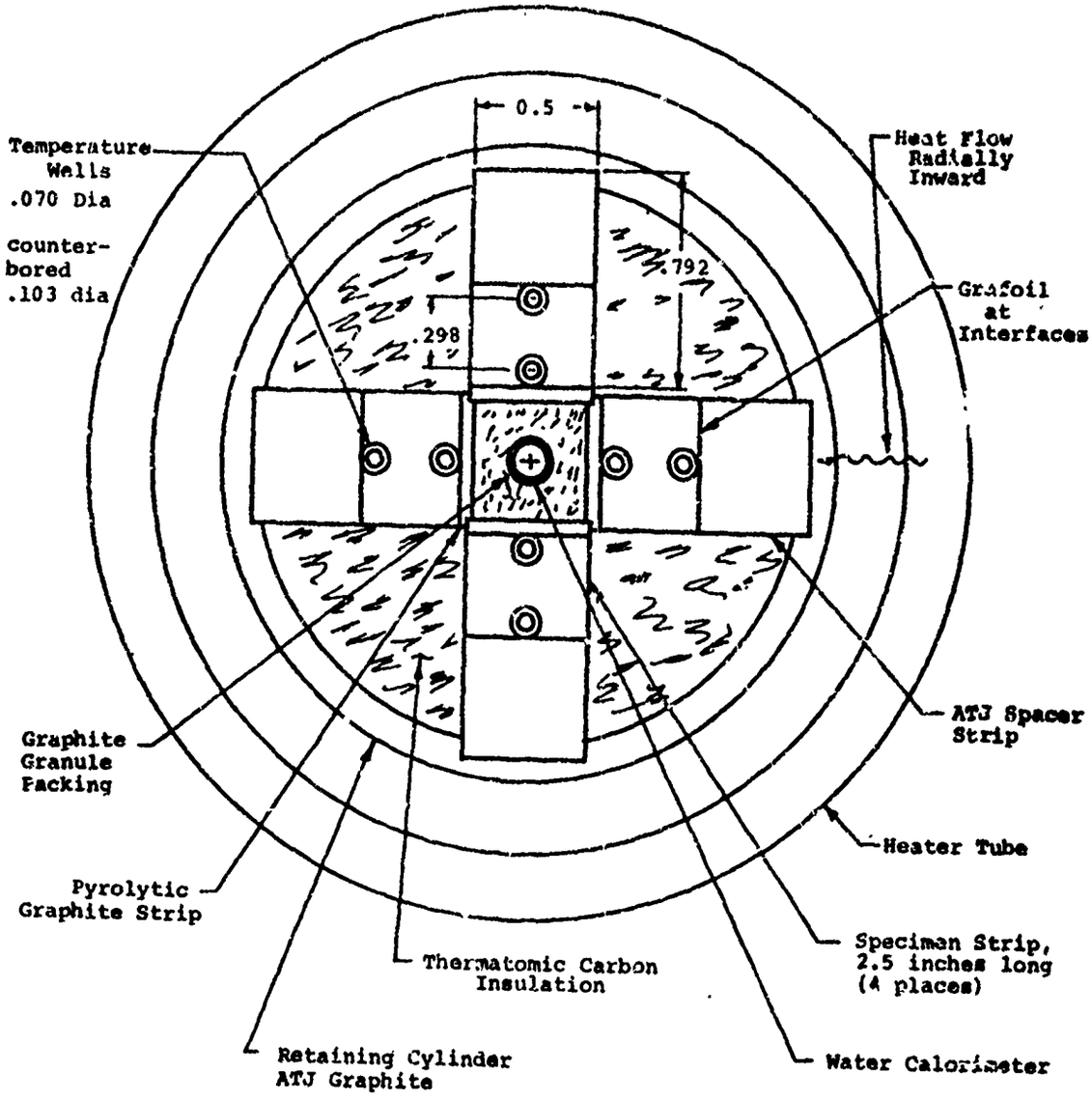


Figure 47. Top View of Strip Specimen Assembly Employed in Radial Inflow Apparatus

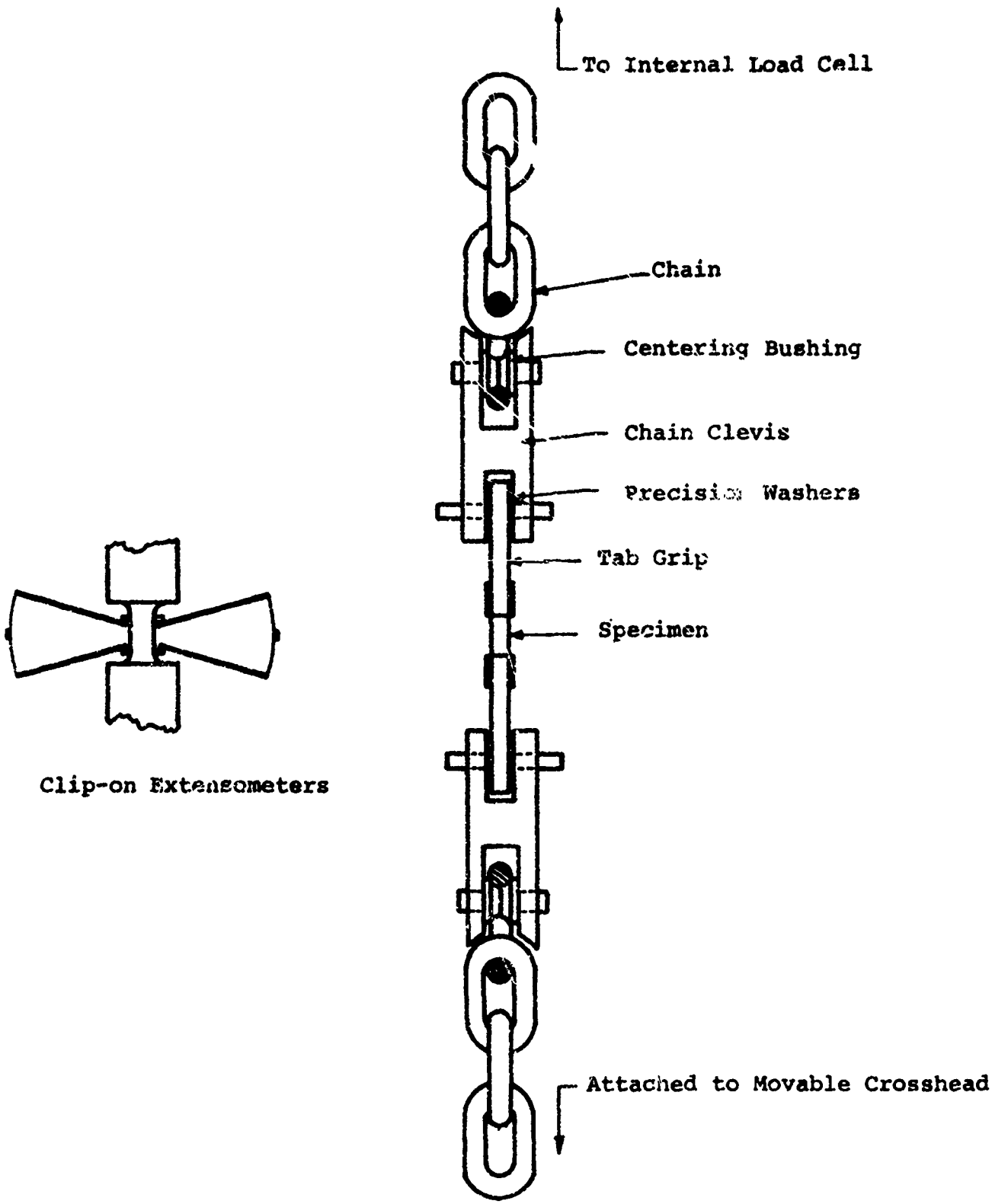


Figure 48. Schematic of Chain grip and Test Setup for Tensile Evaluations of Phenolic Composites

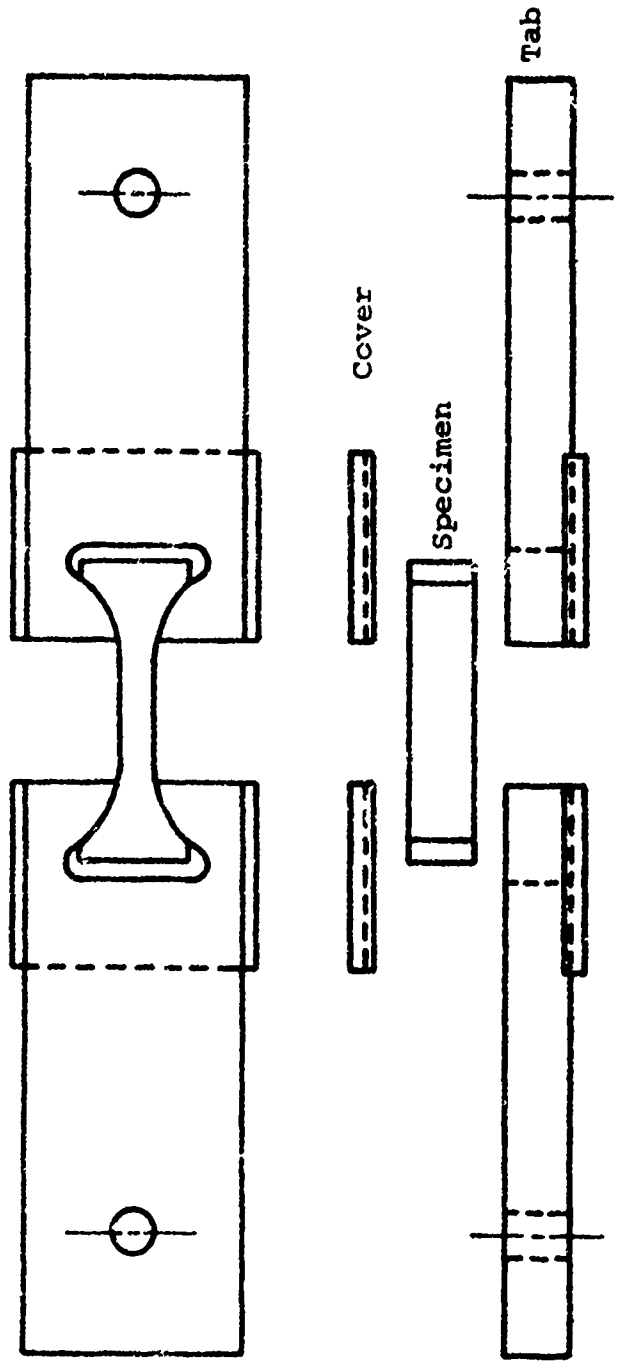


Figure 49. Assembly and Exploded View of Quartz-Phenolic Specimen and Specimen Tab Grips

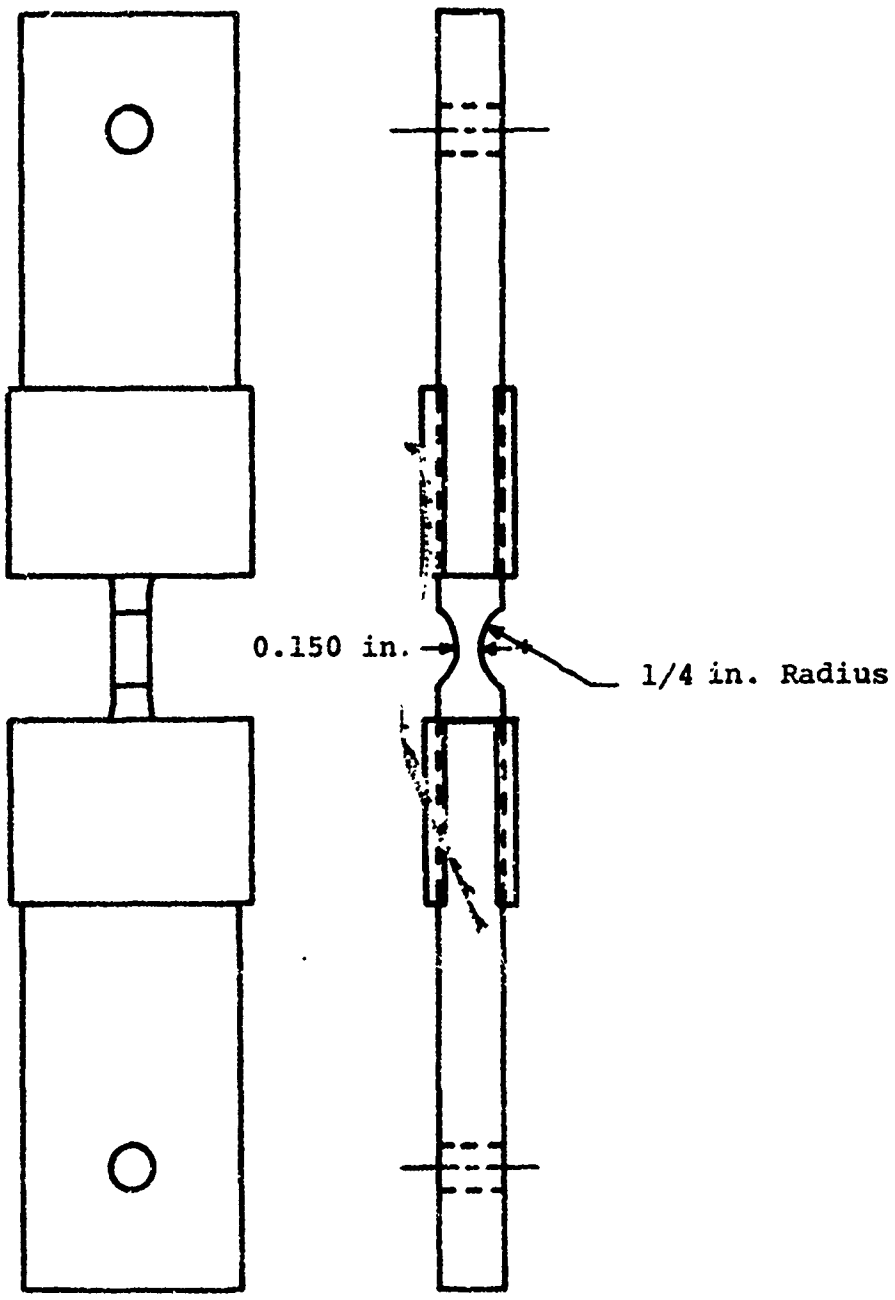


Figure 50. Specimen Configuration for Ultimate Tensile Strength Evaluation of Quartz-Phenolic Specimens

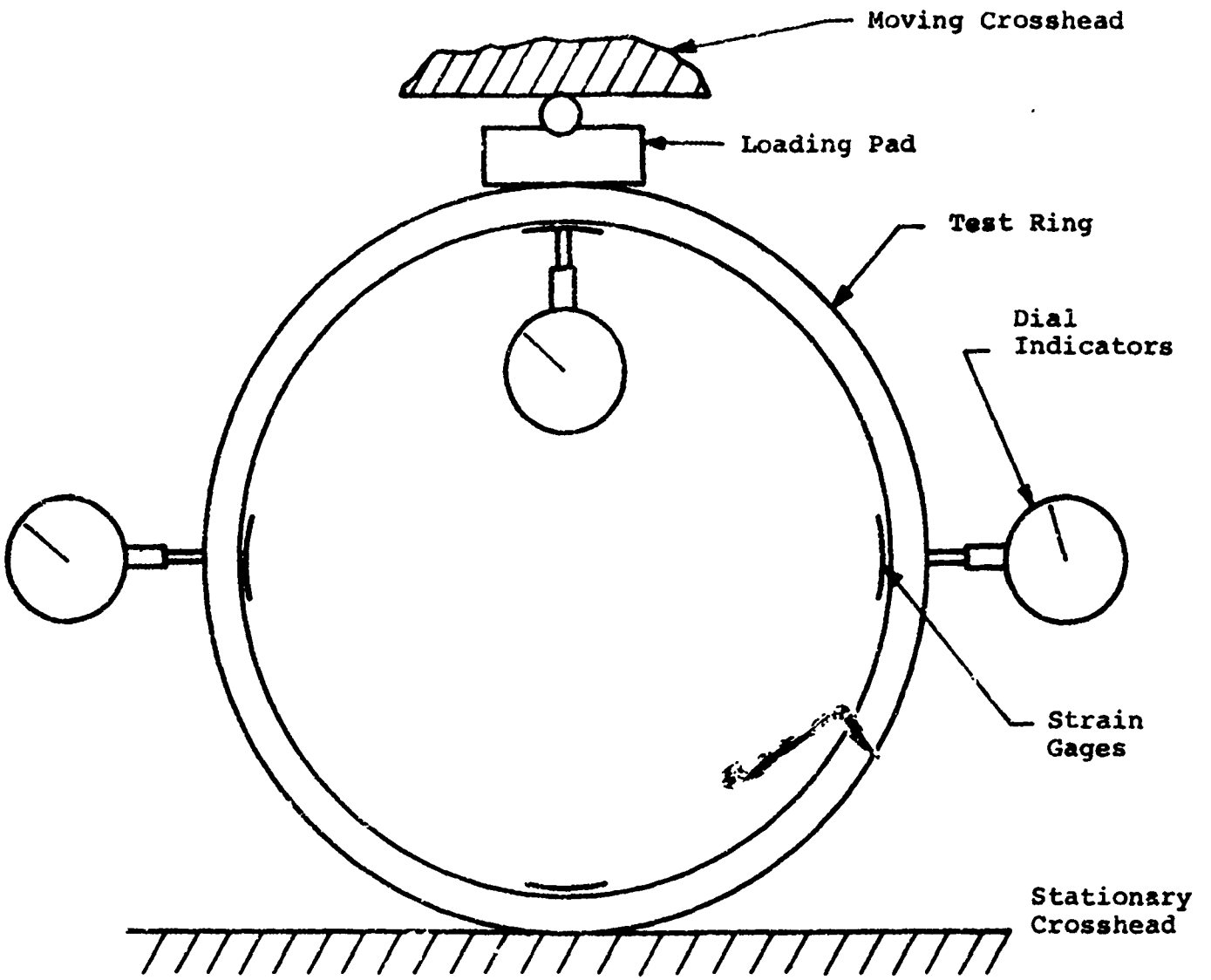


Figure 51. Schematic of Ring Flexure Setup Used For Modulus of Elasticity in Flexure (MOE) Evaluations

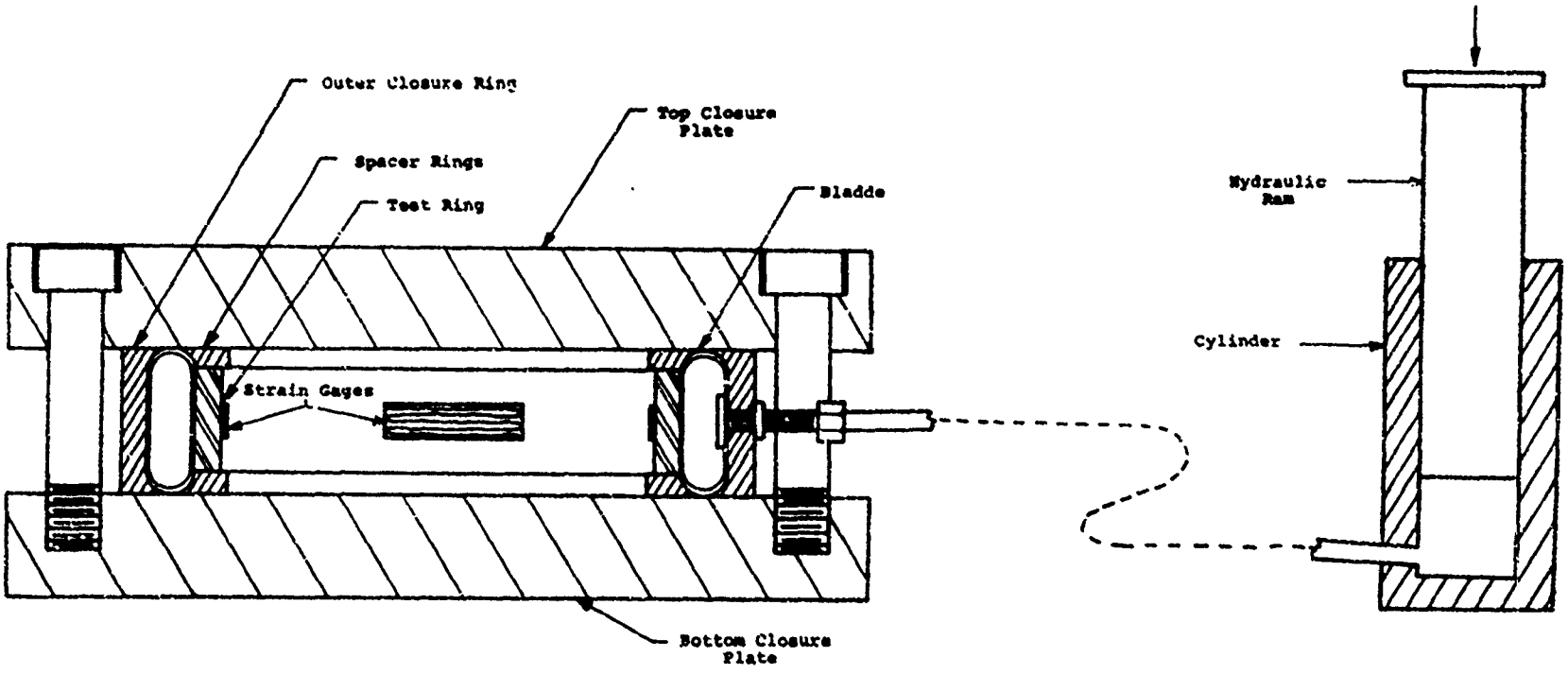
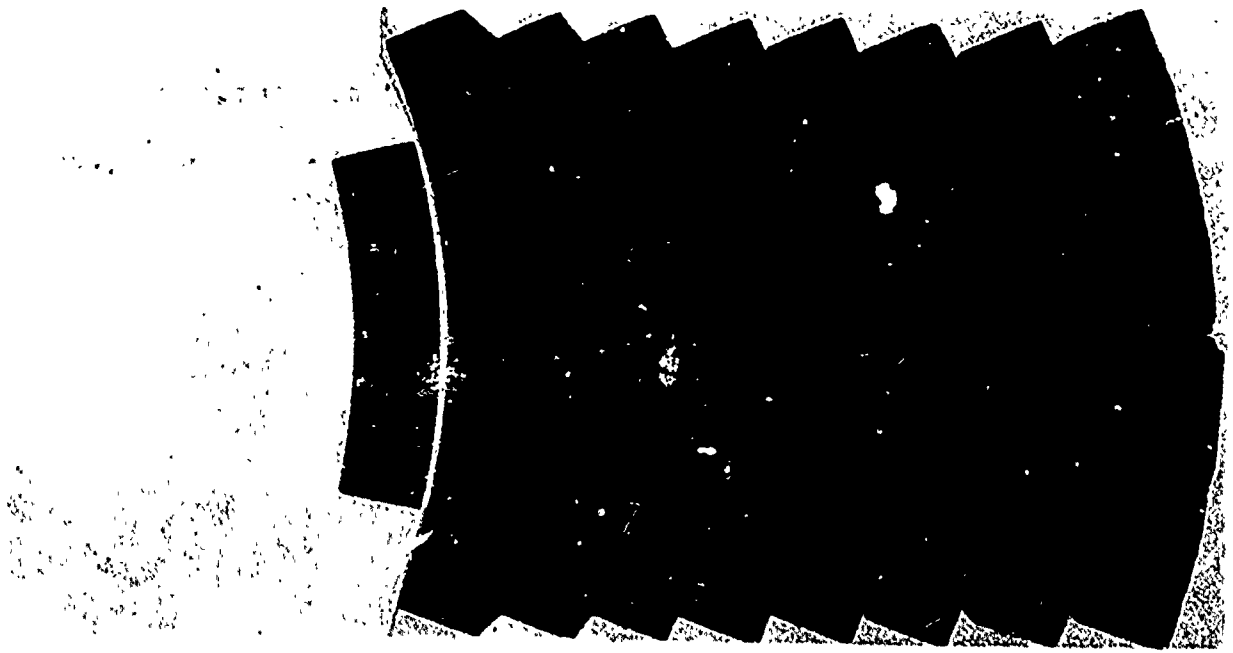
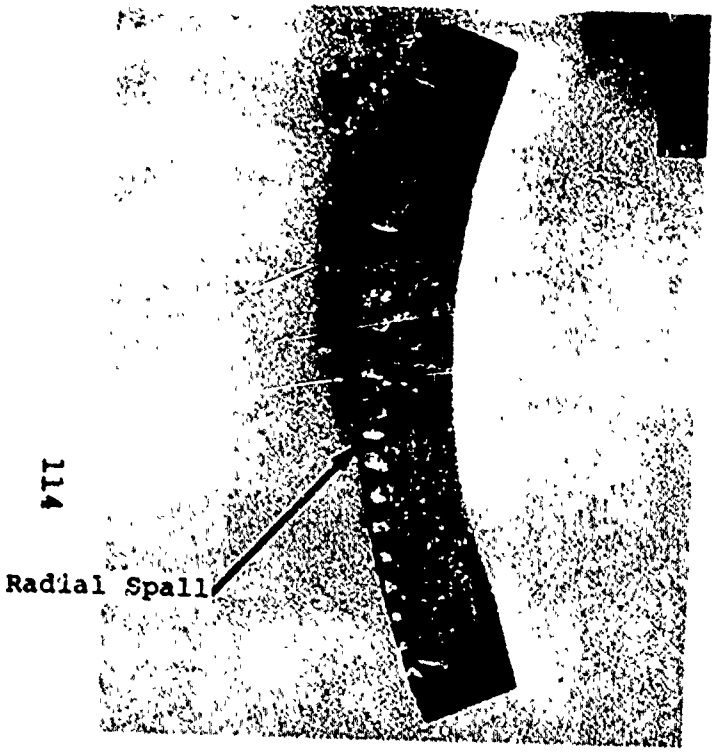


Figure 52. Schematic of Hydrostatic Ring Evaluation Setup Used for Compressive Modulus Evaluation

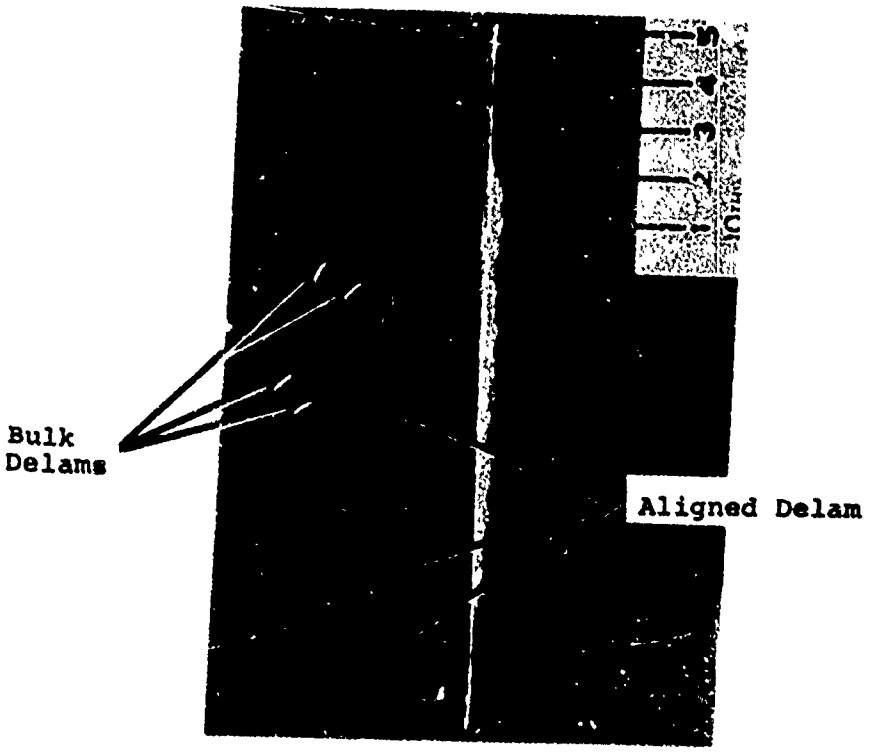


ARC No. V	8	4	2	7	5	1	6	3
Impact Level (Kilotaps)	1.030	1.640	2.200	3.045	3.360	5.390	7.560	7.880

Figure 53. Group Photograph (1X) Showing Edges of Impacted 3D Carbon-Carbon Arcs

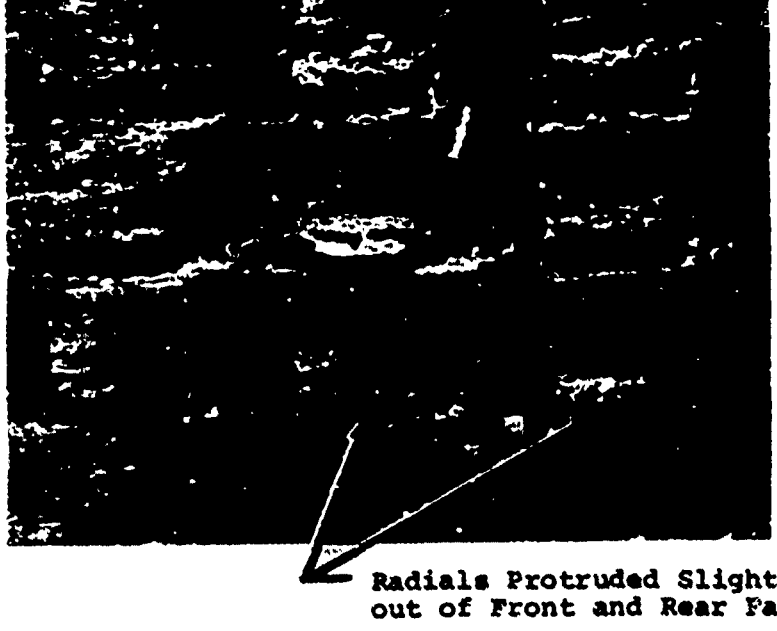


(Scale Shown)



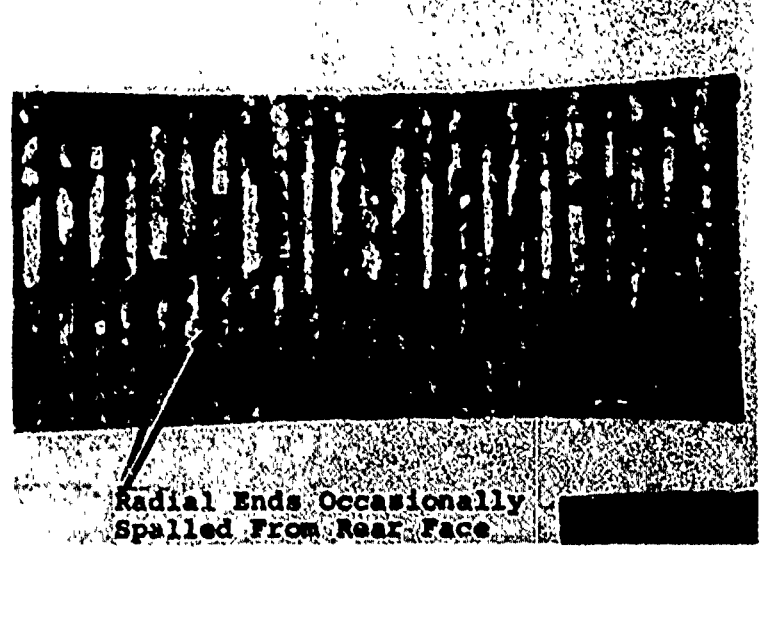
(Scale Shown)

Figure 54a. Photographs Showing Visual Structure-Change in AVCO 3DCC Arc 8-AR-8, 1.030 Kilotaps



Radials Protruded Slightly
out of Front and Rear Faces

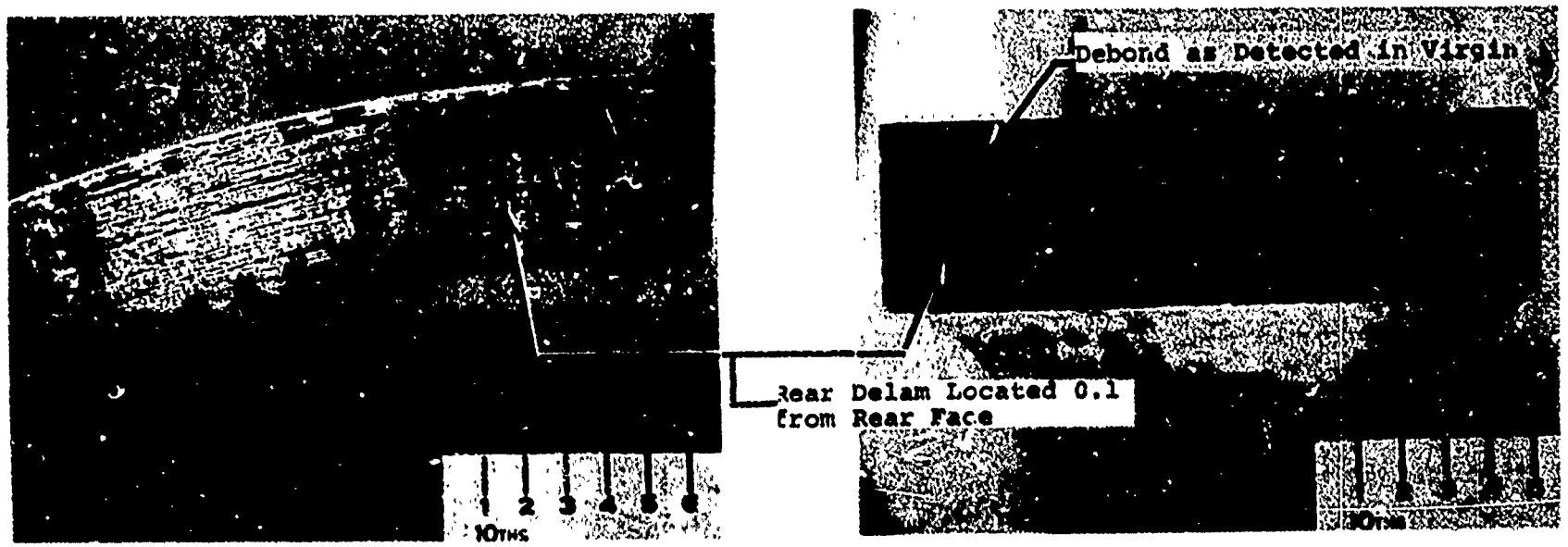
(10X)



Radial Ends Occasionally
Spalled From Rear Face

(Scale Shown)

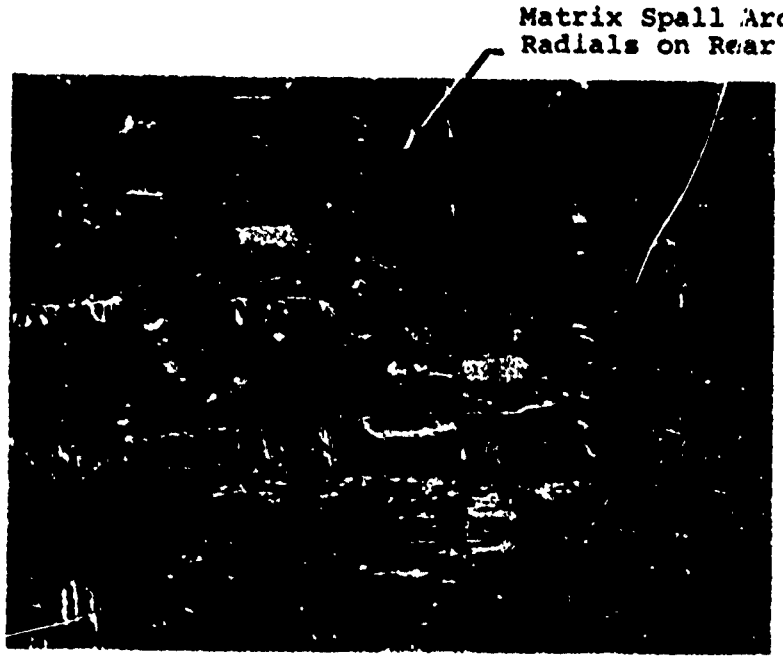
Figure 54b.



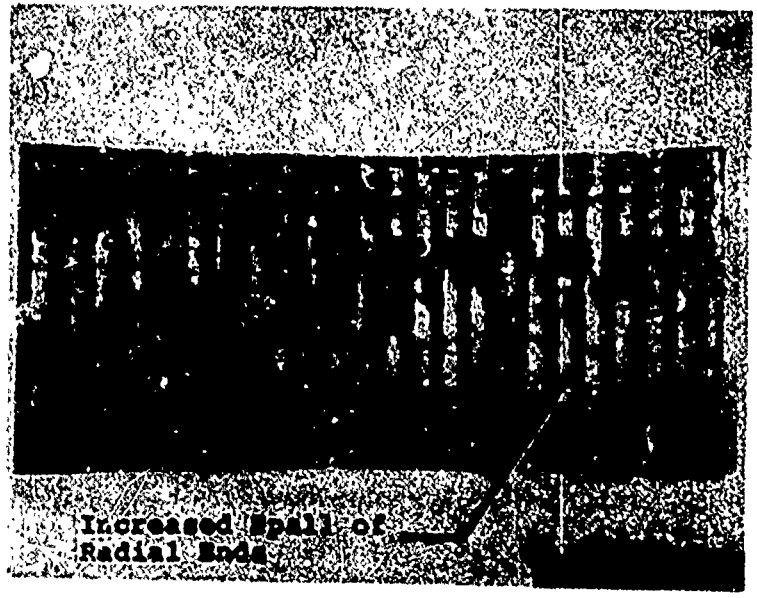
Axial View
(Scale Shown)

Circumferential View
(Scale Shown)

Figure 55a. Photographs Showing Visual Structure-Change in AVCO 3DCC Arc 8-AR-2, 2.200 Kilotaps

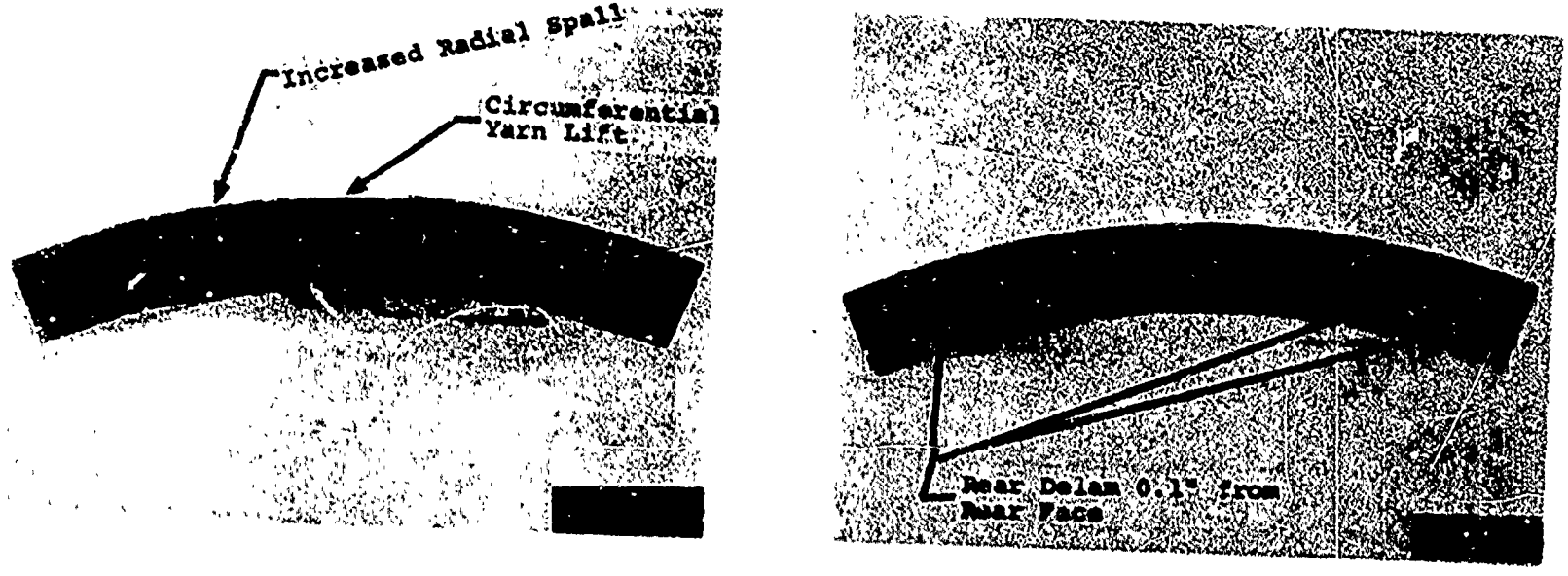


(No Scale)



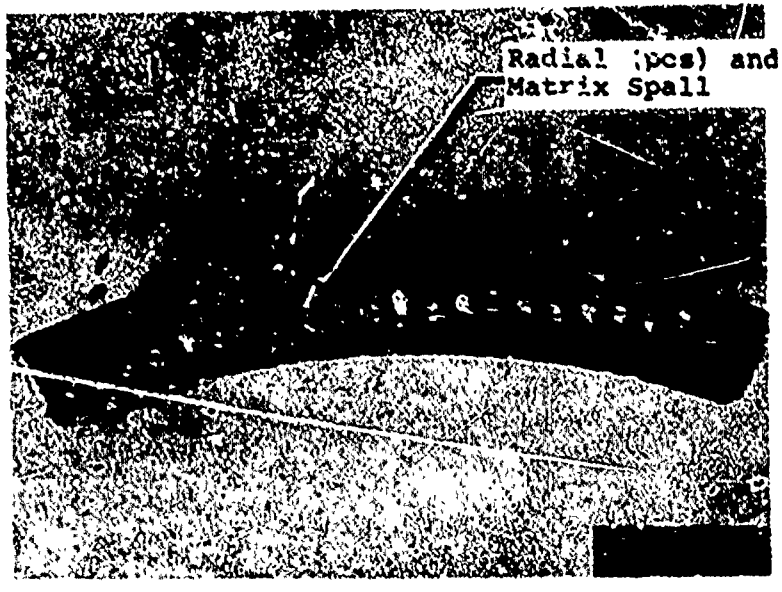
(Scale Shown)

Figure 55b.



(Scale Shown)

Figure 56. Photographs Showing Visual Structure-Change AVCO 3DCC Arc 8-AR-7

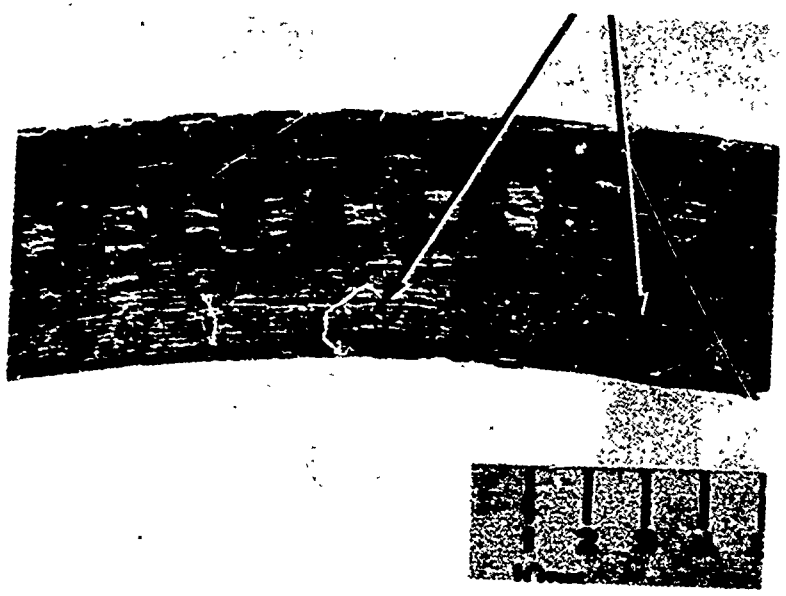


Axial View
(Scale Shown)

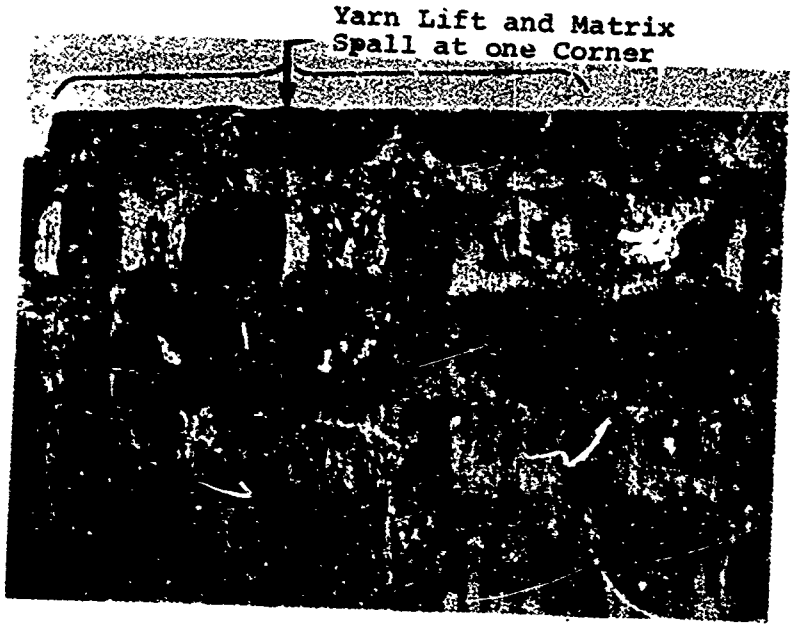


Circumferential View
(Scale Shown)

Figure 57a. Photographs Showing Visual Structure-Change in AVCO 3DCC
Arc 8-AR-5, 3.360 Kilotaps

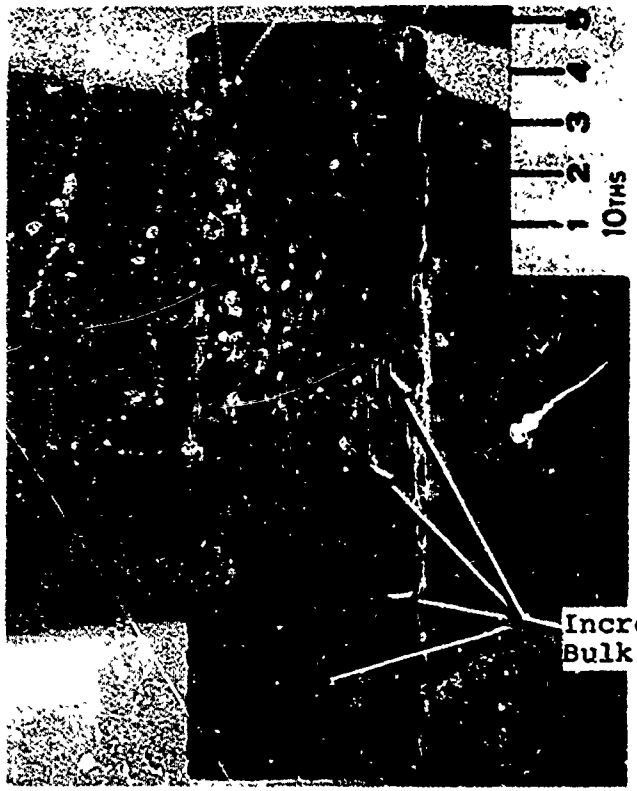


Axial View
(Scale Shown)

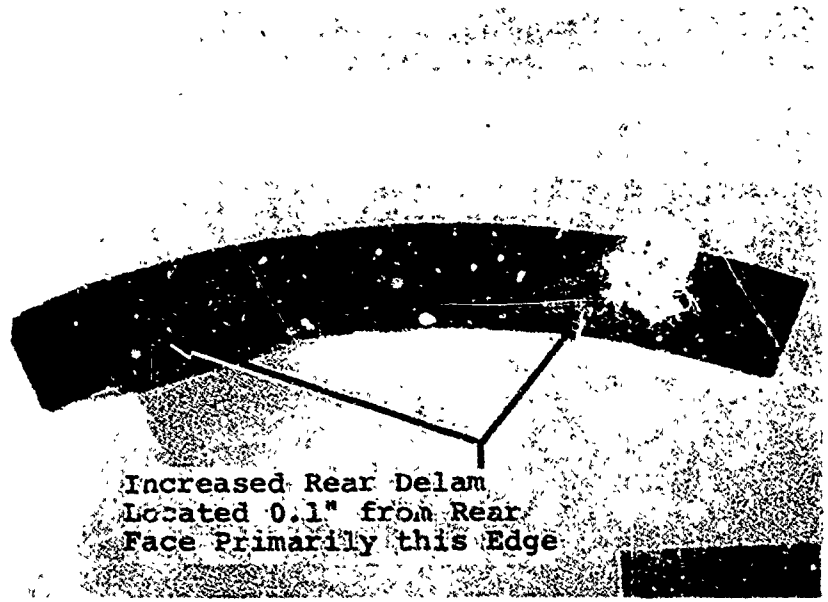


Radial View
(10X)

Figure 57b.

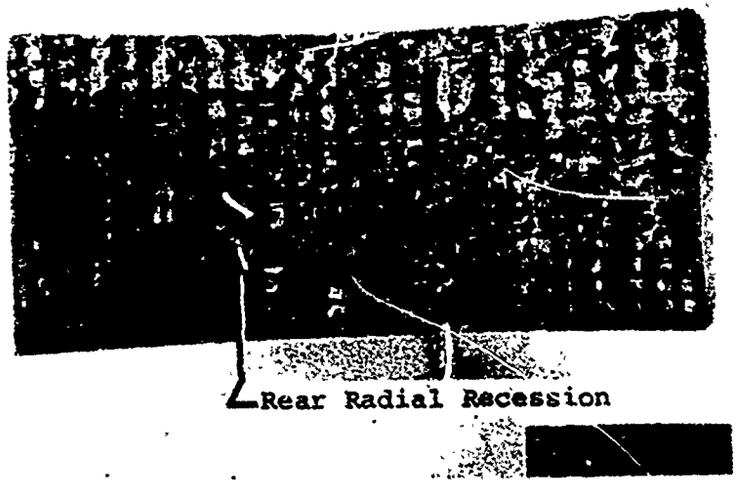


Circumferential View
(Scale Shown)

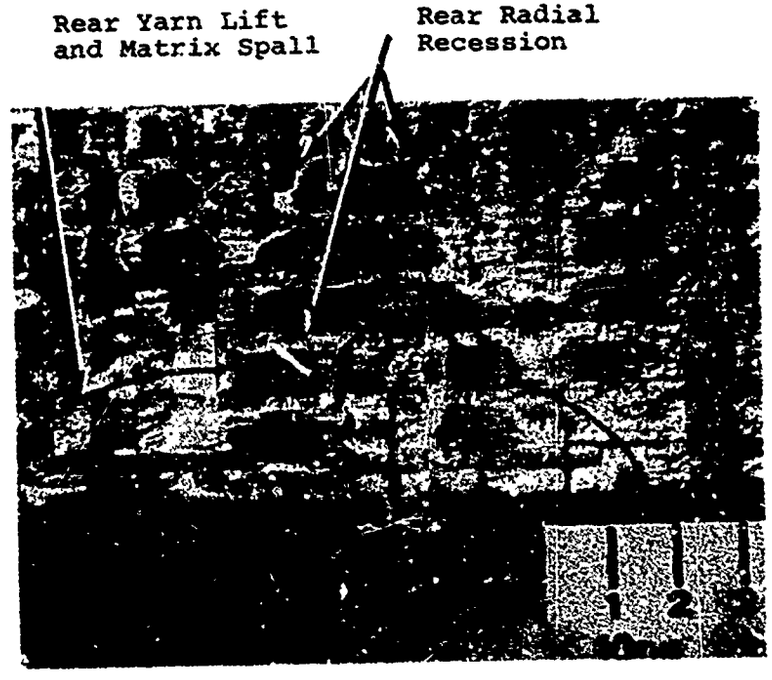


Axial View
(Scale Shown)

Figure 58a. Photographs Showing Visual Structure-Change in AVCO 3DCC Arc 8-AR-1, 5.39 Kilotaps

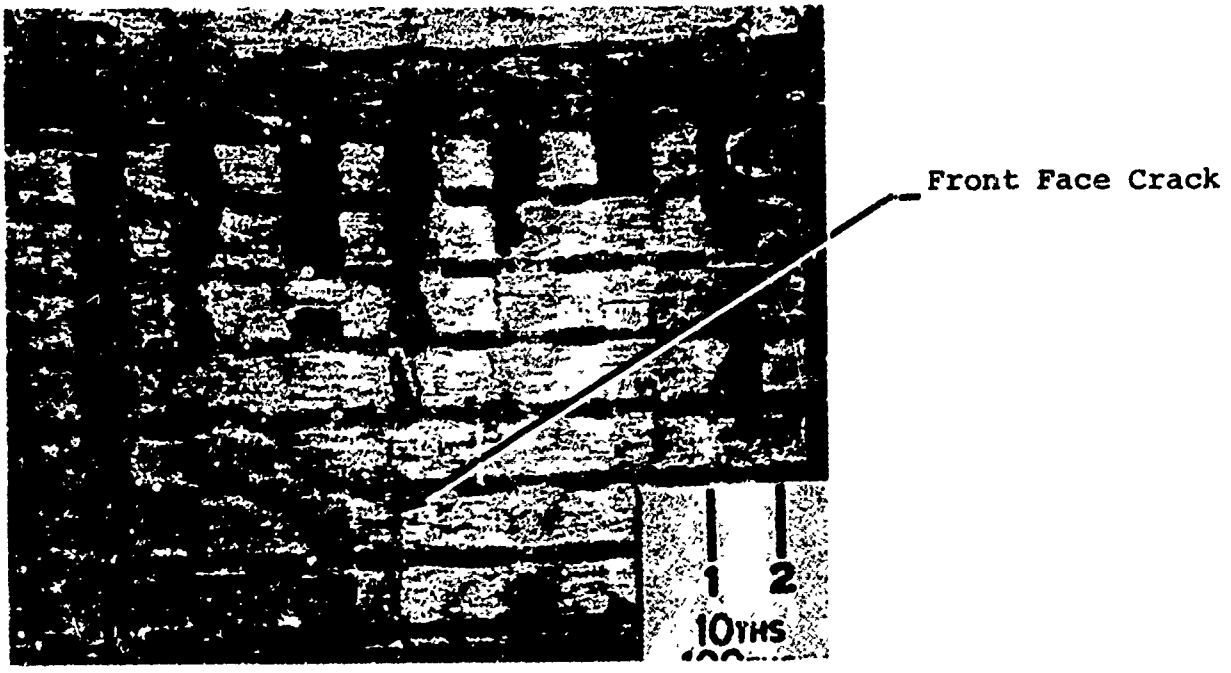


Radial View
(Scale Shown)



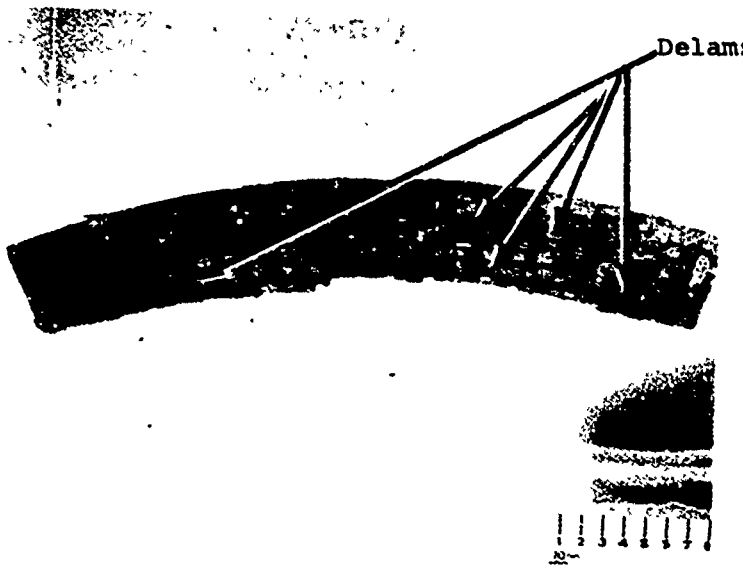
Radial View
(Scale Shown)

Figure 58b.

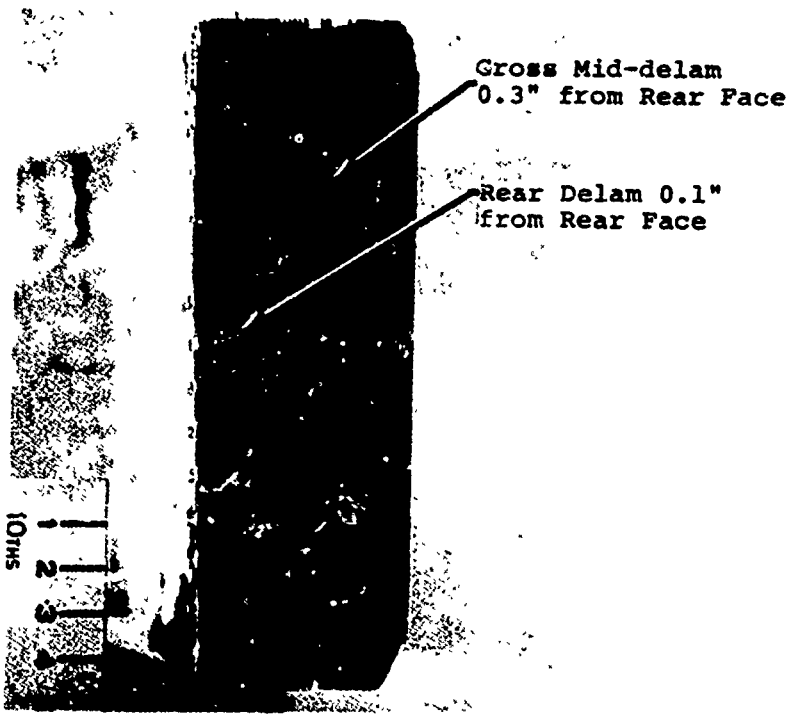


Radial View
(Scale Shown)

Figure 58c.

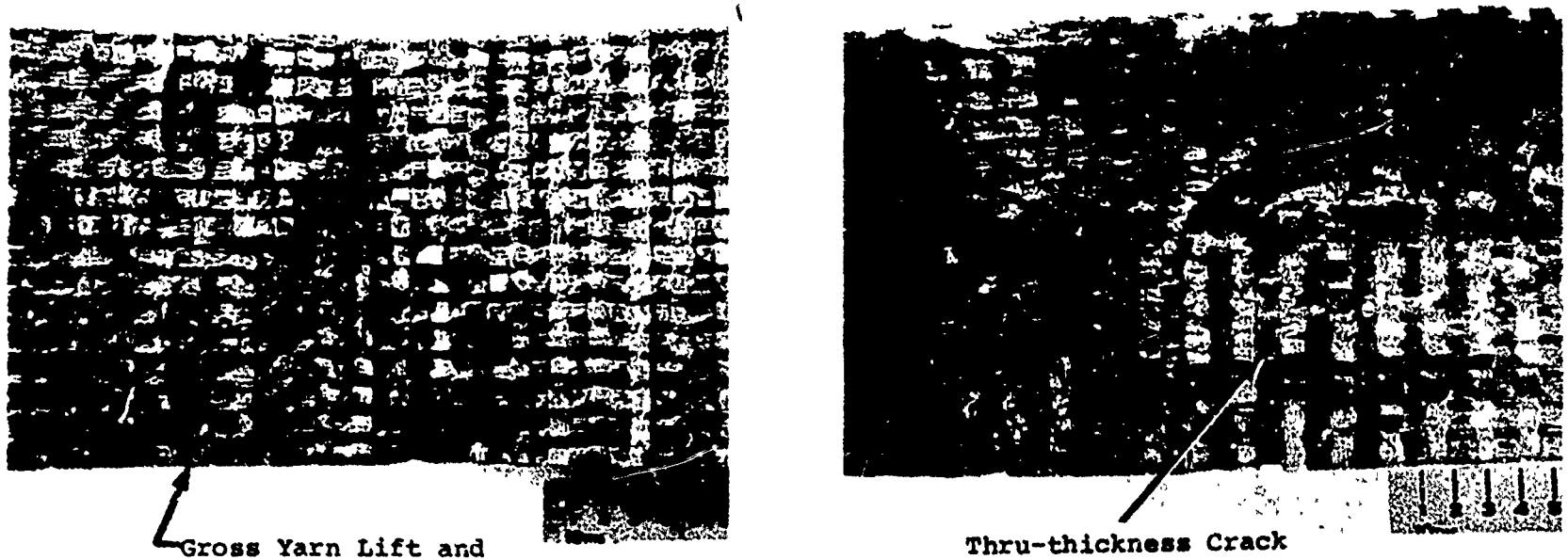


Axial View
(Scale Shown)



Circumferential View
(Scale Shown)

Figure 59a. Photographs Showing Visual Structure-Change in AVCO 3DCC Arc 8-AR-6, 7.560 Kilotaps

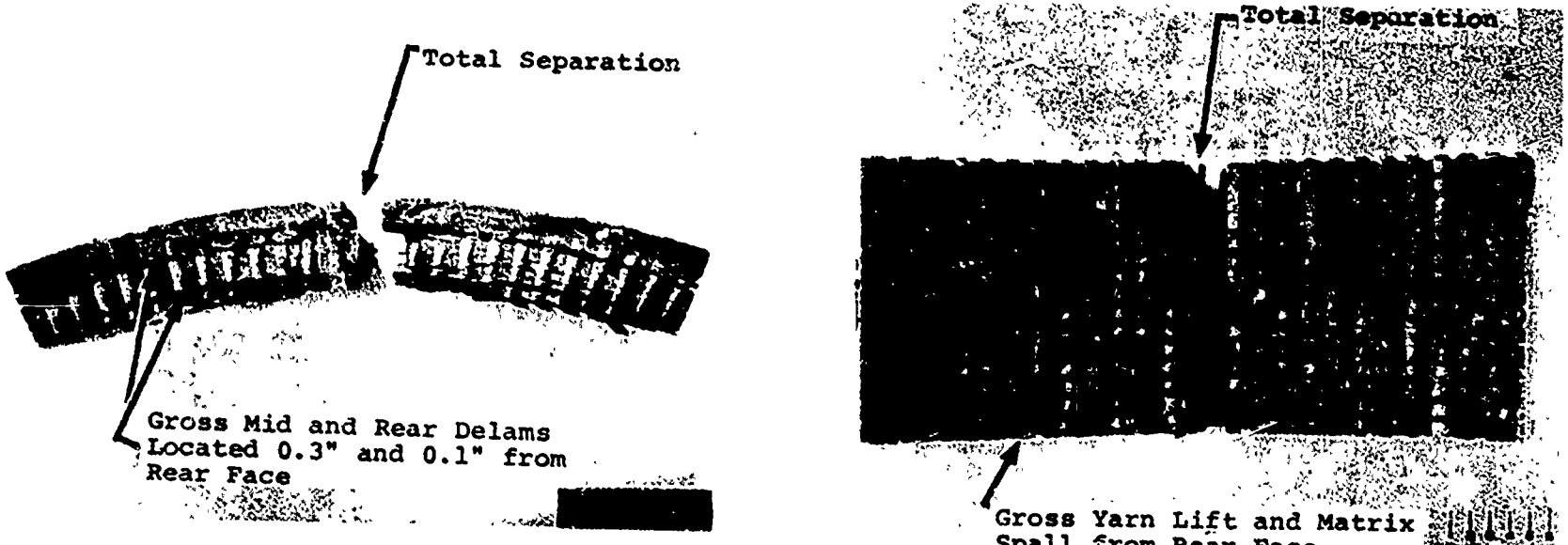


Radial View
Inside Surface

(Scale Shown)

Radial View
Outside Surface

Figure 59b.



Axial View
(Scale Shown)

Radial View
(Scale Shown)

Figure 60. Photographs Showing Visual Structure-Change in AVCO 3DCC Arc 8-AR-3, 7.88 Kilotaps

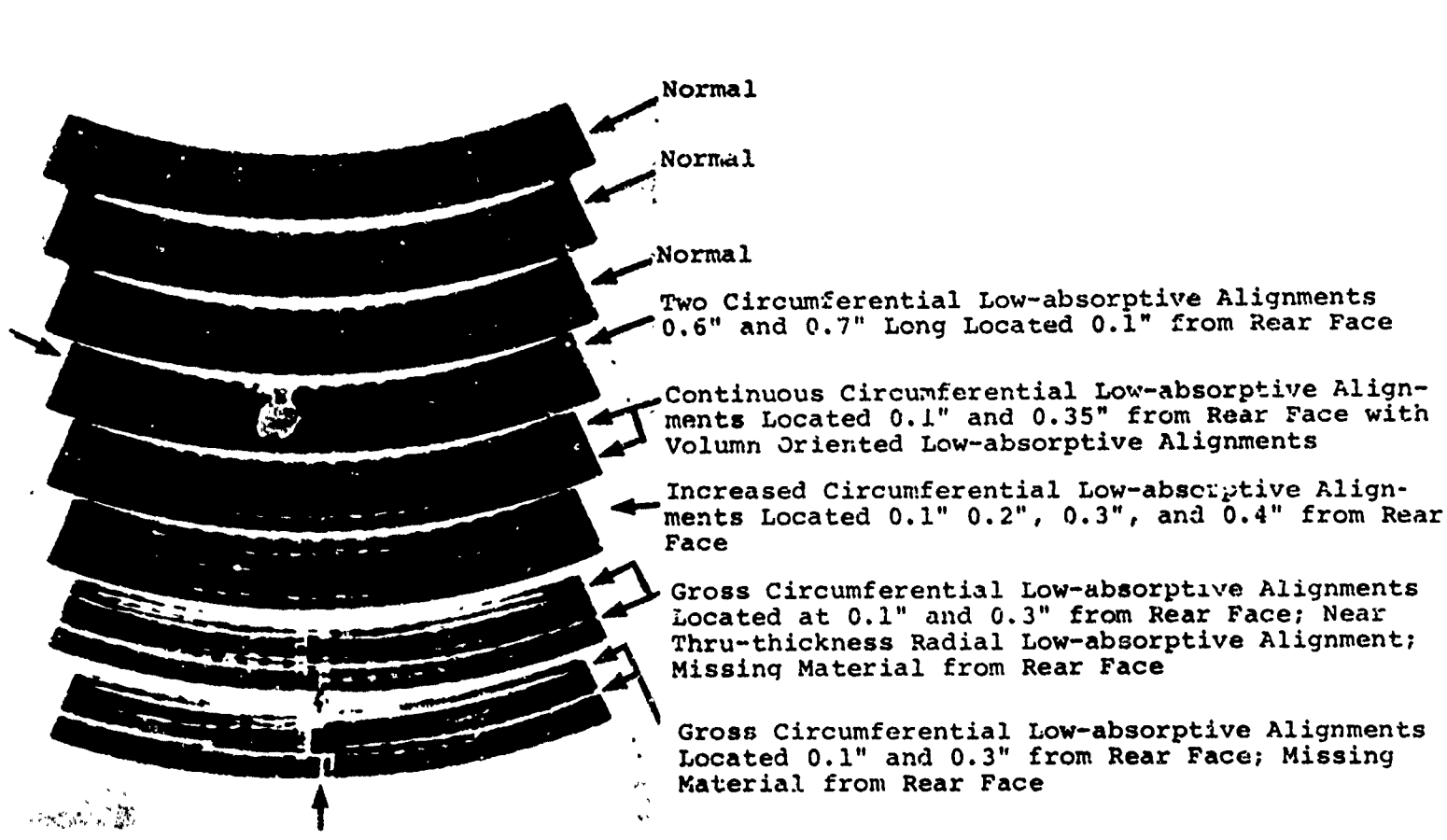


Figure 61. Group Radiograph in Axial Direction Showing Impacted Arc Rings from AVCO 3DCC

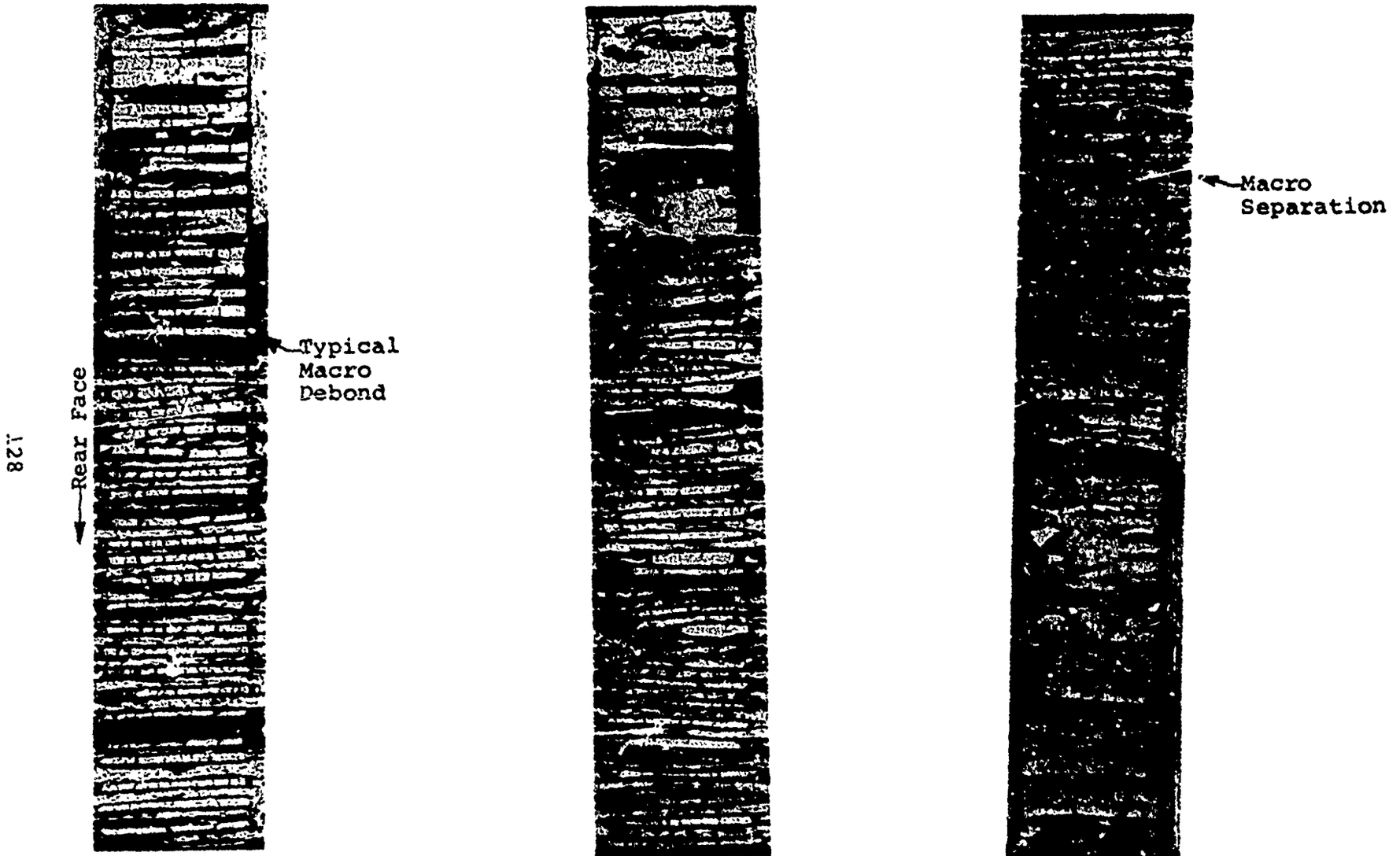
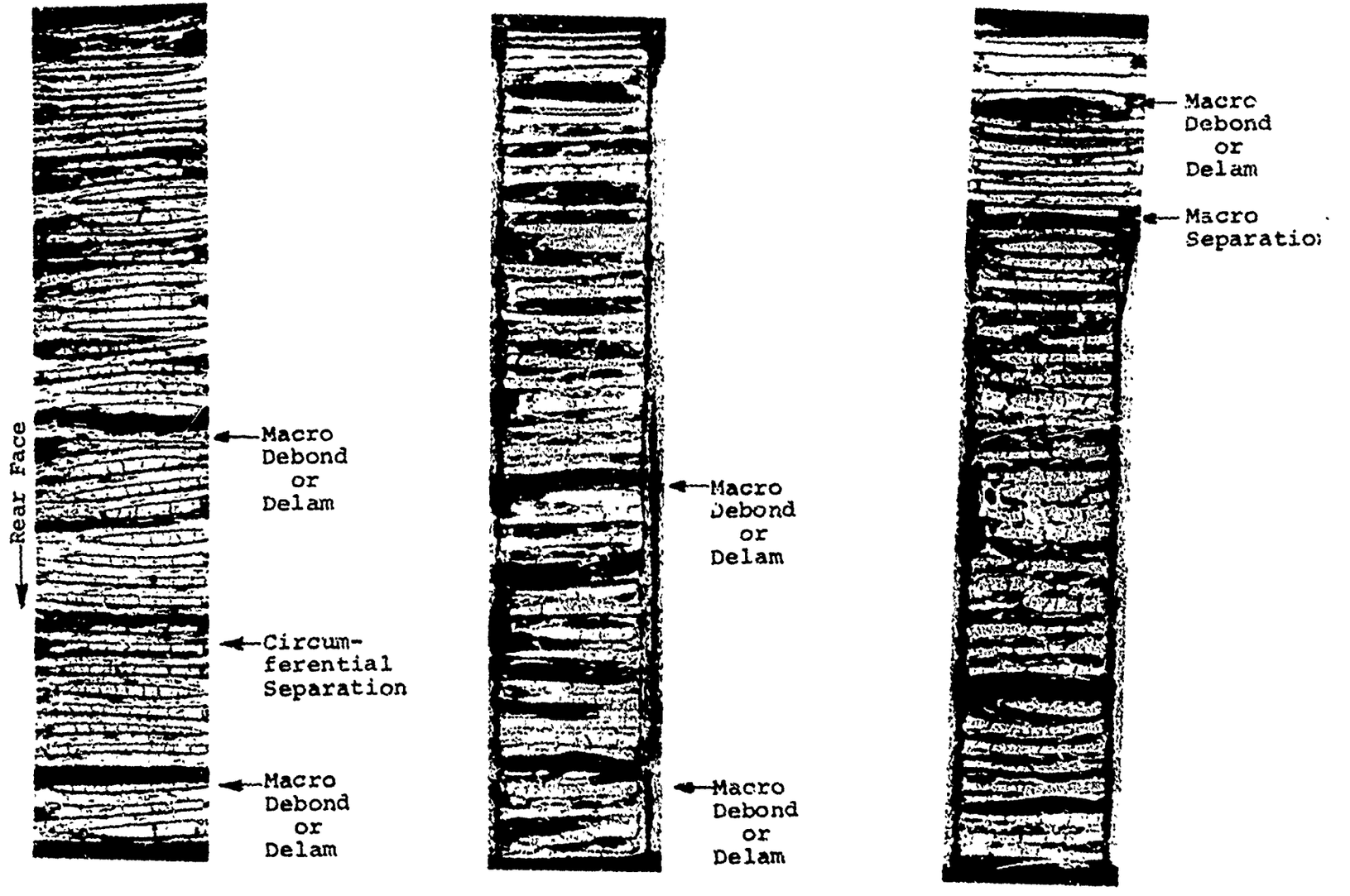


Figure 62a. Photomicrographs of Edges (Axial View) of Impulse Loaded Arcs from AVCO 3DCC



8-AR-2, 2.20 KT

8-AR-7 (Normal Micro) 3.04 KT

8-AR-5 (Normal Micro) 3.36 KT

Figure 62b.

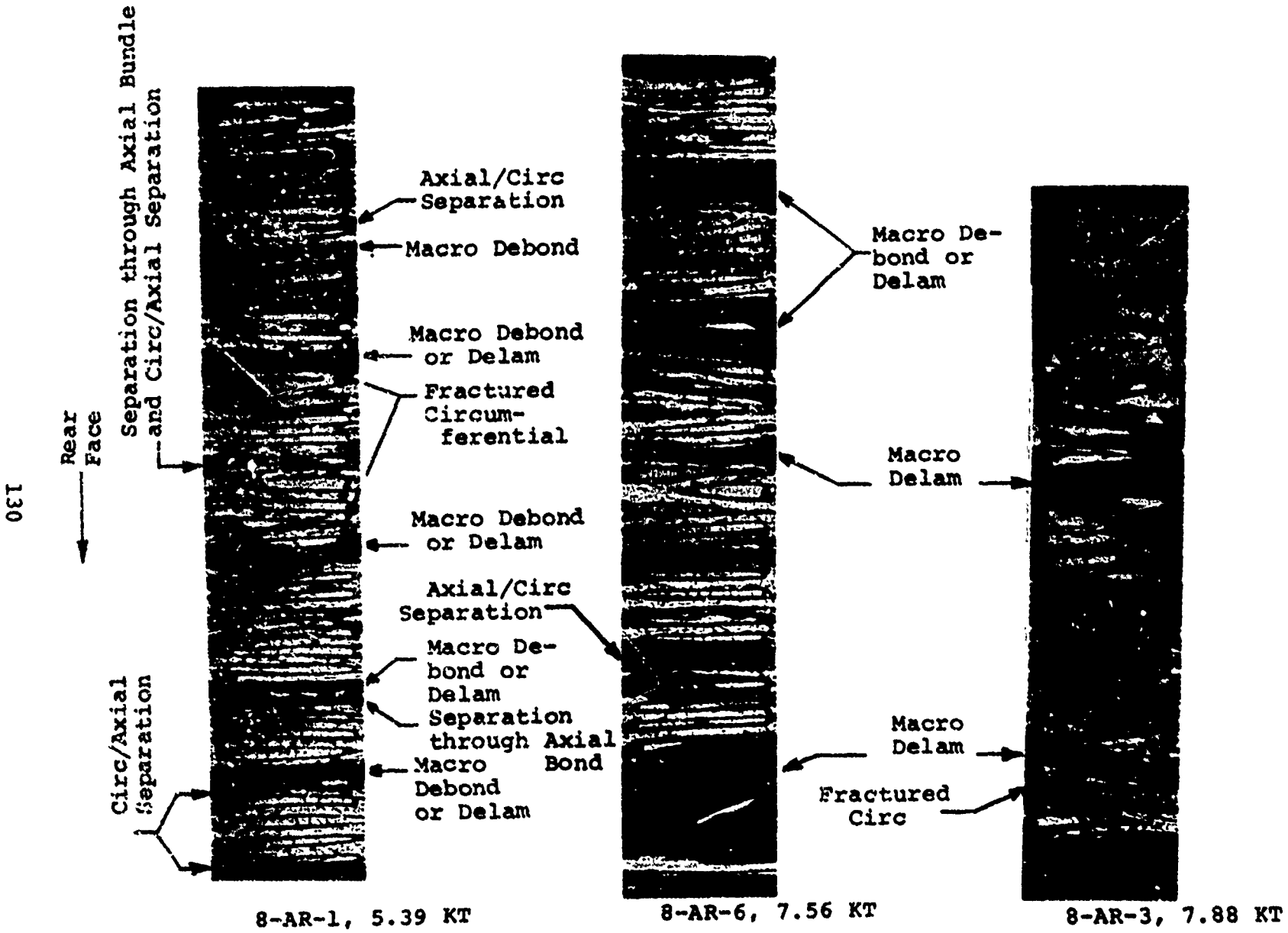

130
Rear Face
Separation through Axial Bundle and Circ/Axial Separation
Axial/Circ Separation
Macro Debond
Macro Debond or Delam
Fractured Circum-ferential
Macro Debond or Delam
Axial/Circ Separation
Macro De-bond or Delam
Separation through Axial Bond
Macro Debond or Delam
Circ/Axial Separation
Macro De-bond or Delam
Macro Delam
Macro Delam
Fractured Circ
8-AR-1, 5.39 KT
8-AR-6, 7.56 KT
8-AR-3, 7.88 KT

Figure 62c

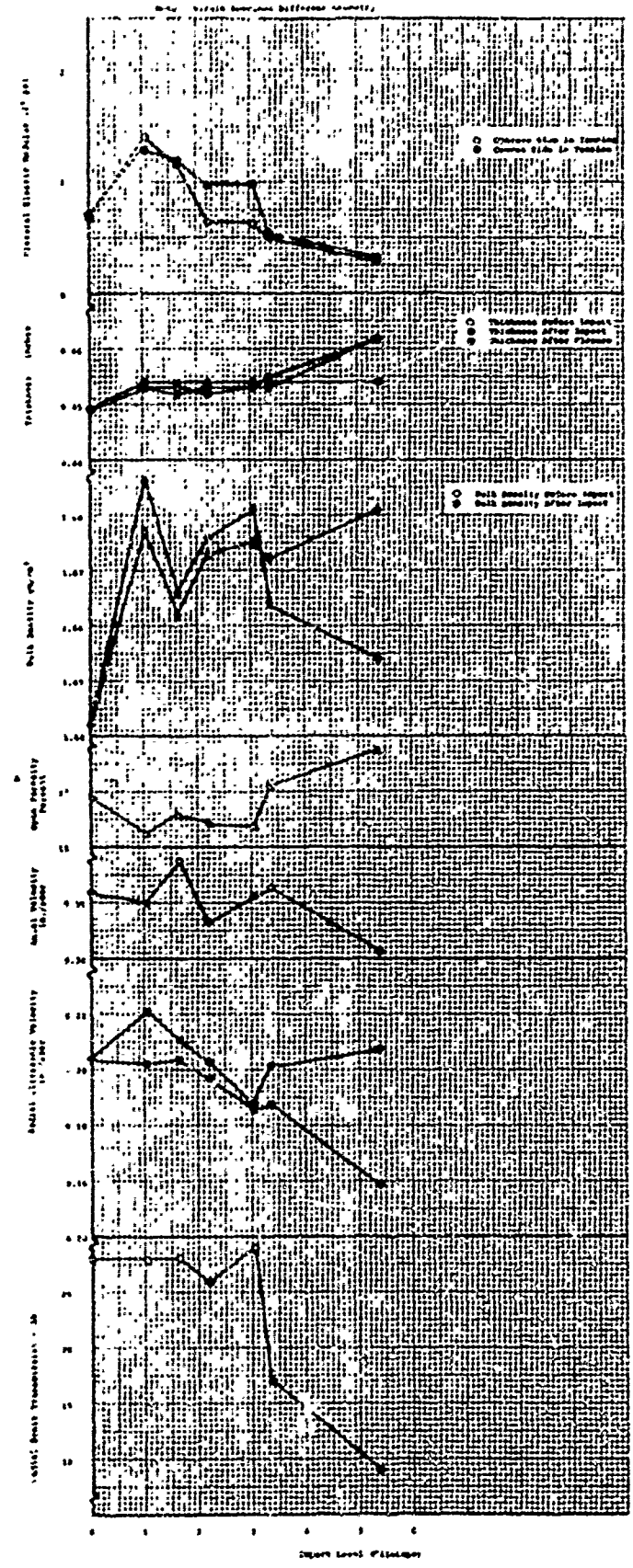


Figure 63. NDT Monitors and Flexural Modulus versus Impact Level for AVCC 3DCC Material

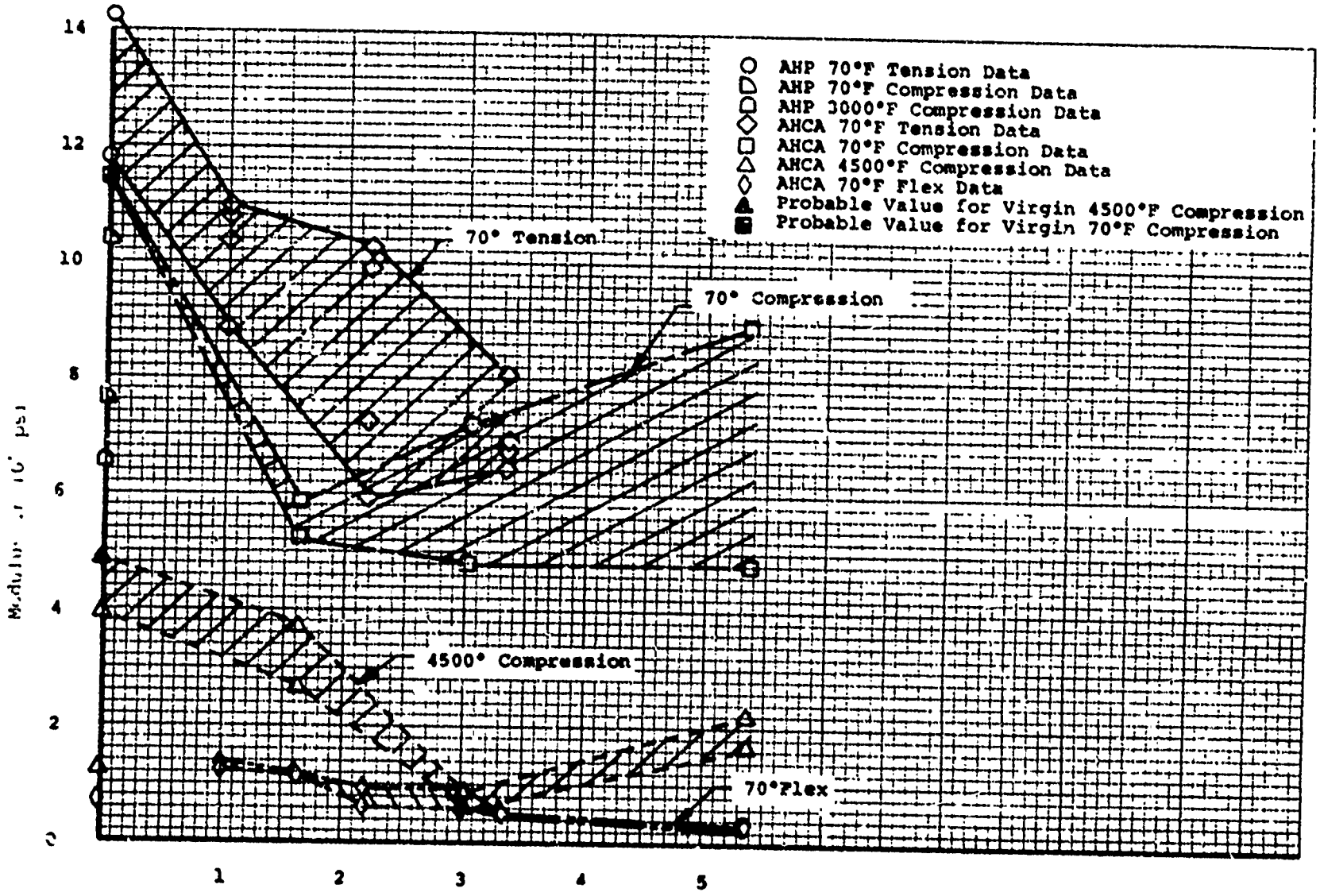


Figure 64. Tensile, Compressive and Flexural Modulus of Elasticity for Specimens from 3D Carbon-Carbon Impacted Arcs

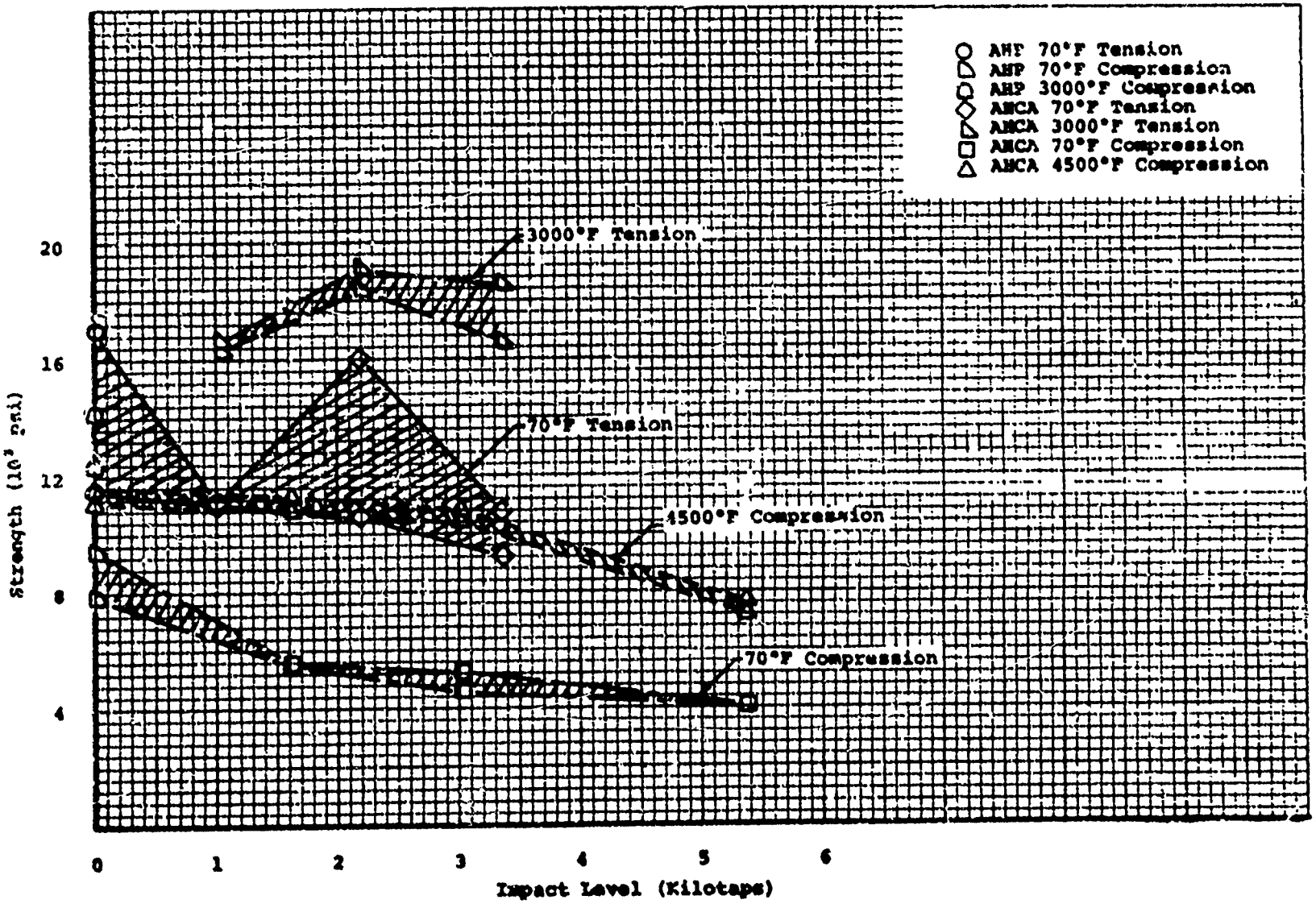


Figure 65. Tensile and Compressive Strength of Specimens from 3D Carbon-Carbon Impacted Arcs

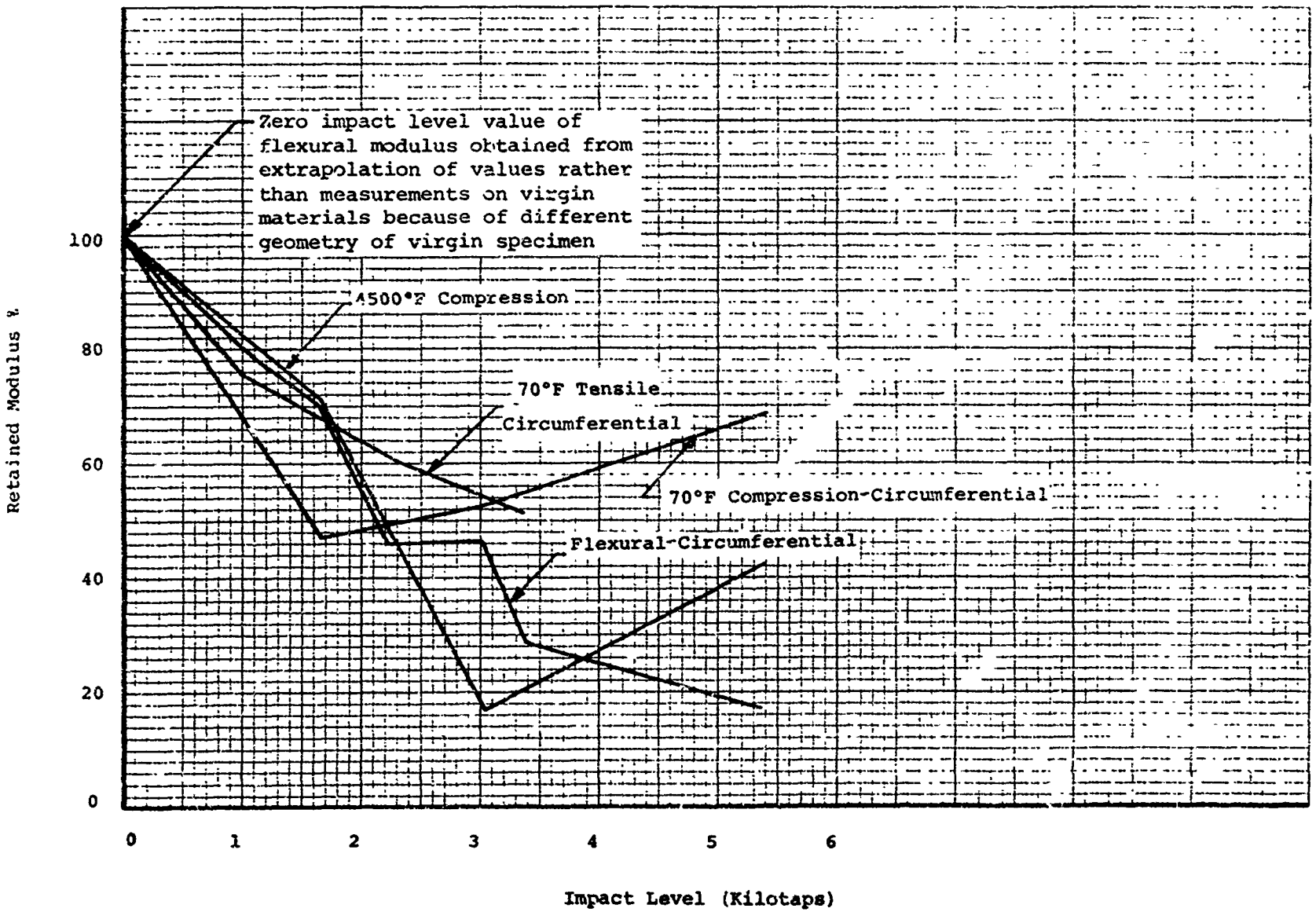


Figure 66. Retained Modulus of Specimens From 3D Carbon-Carbon Impacted Arcs

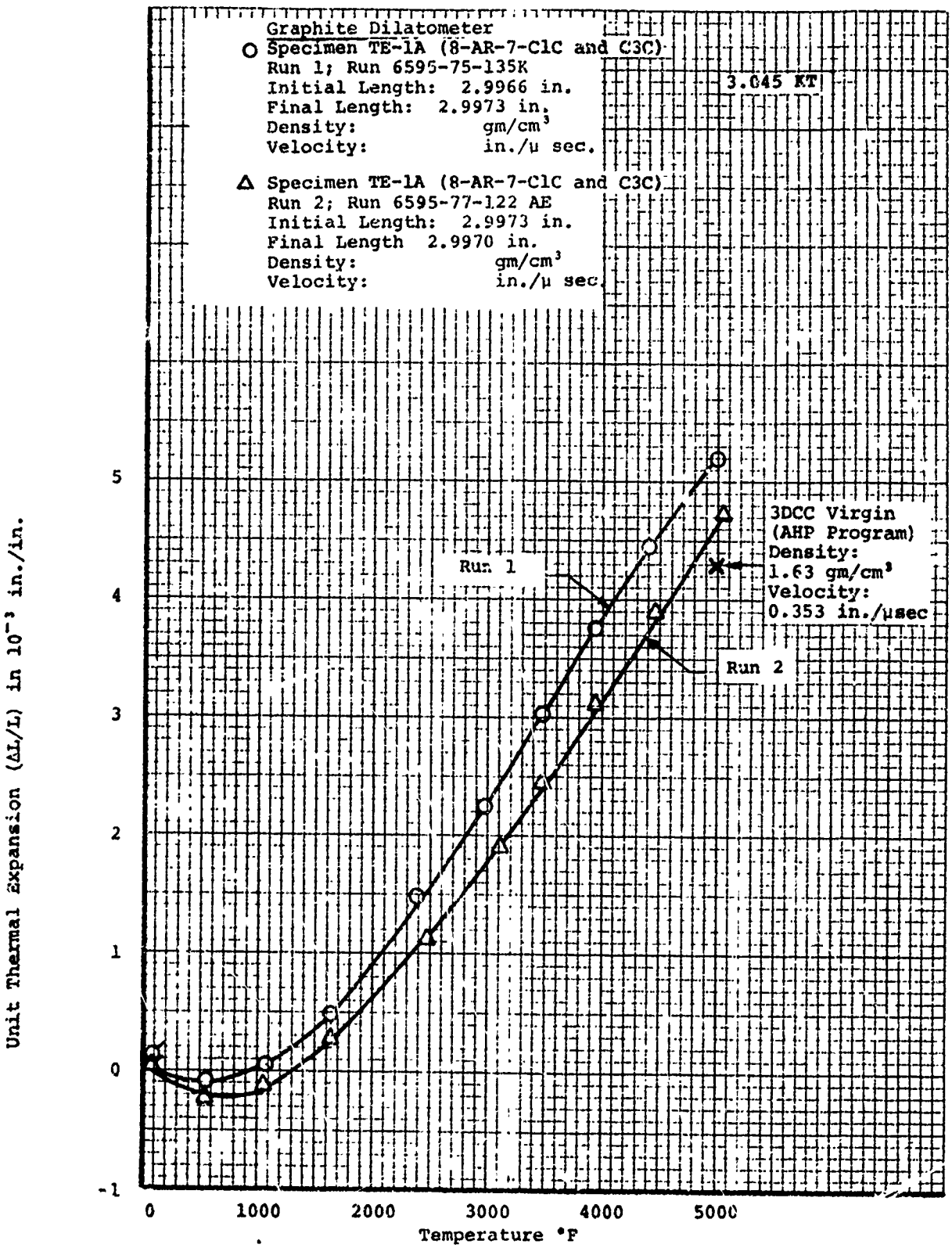


Figure 67. Thermal Expansion of 3DCC in the Axial Direction After 3.045 KT

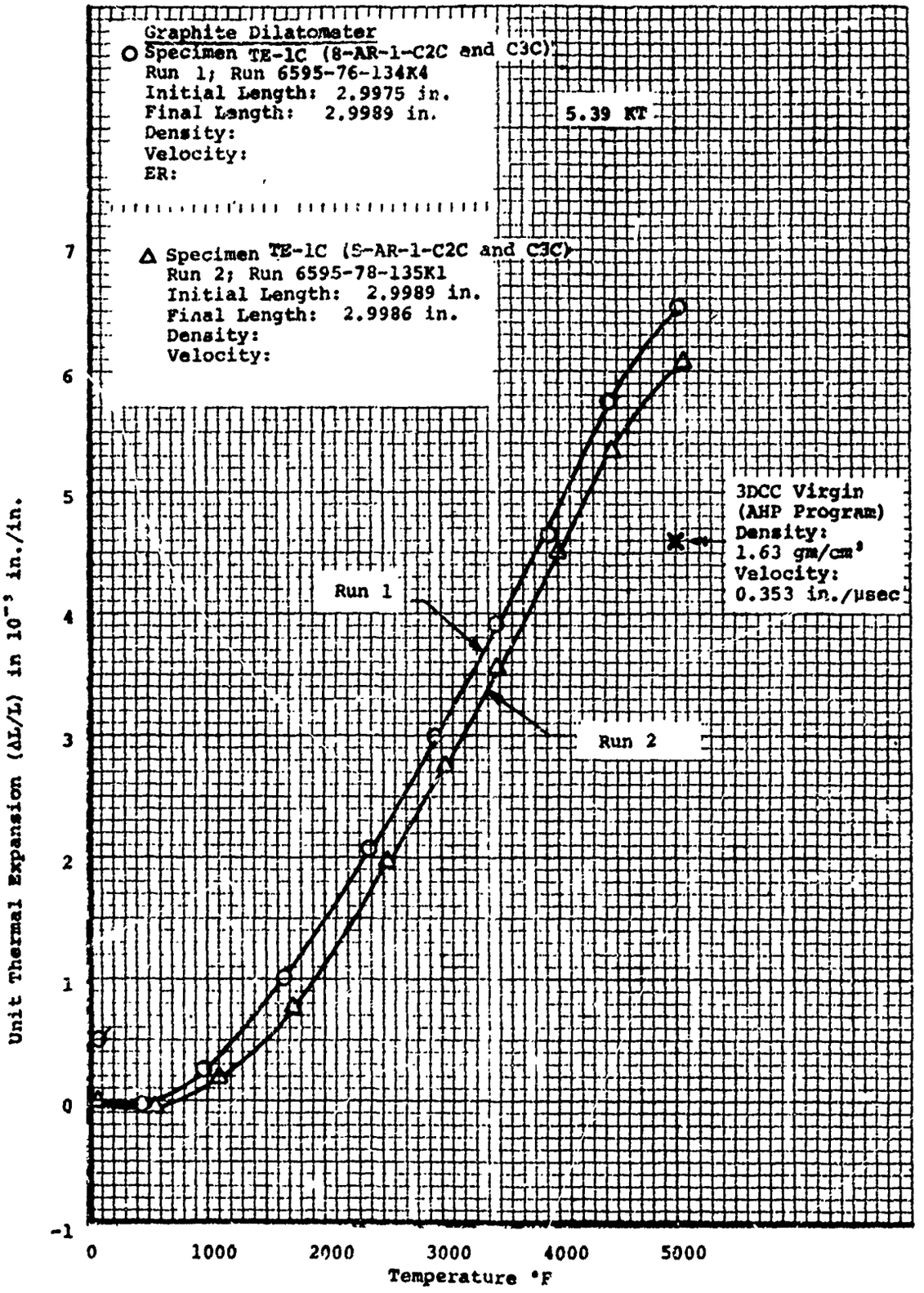


Figure 68. Thermal Expansion of 3DCC in the Axial Direction After 5.39 KT Impact

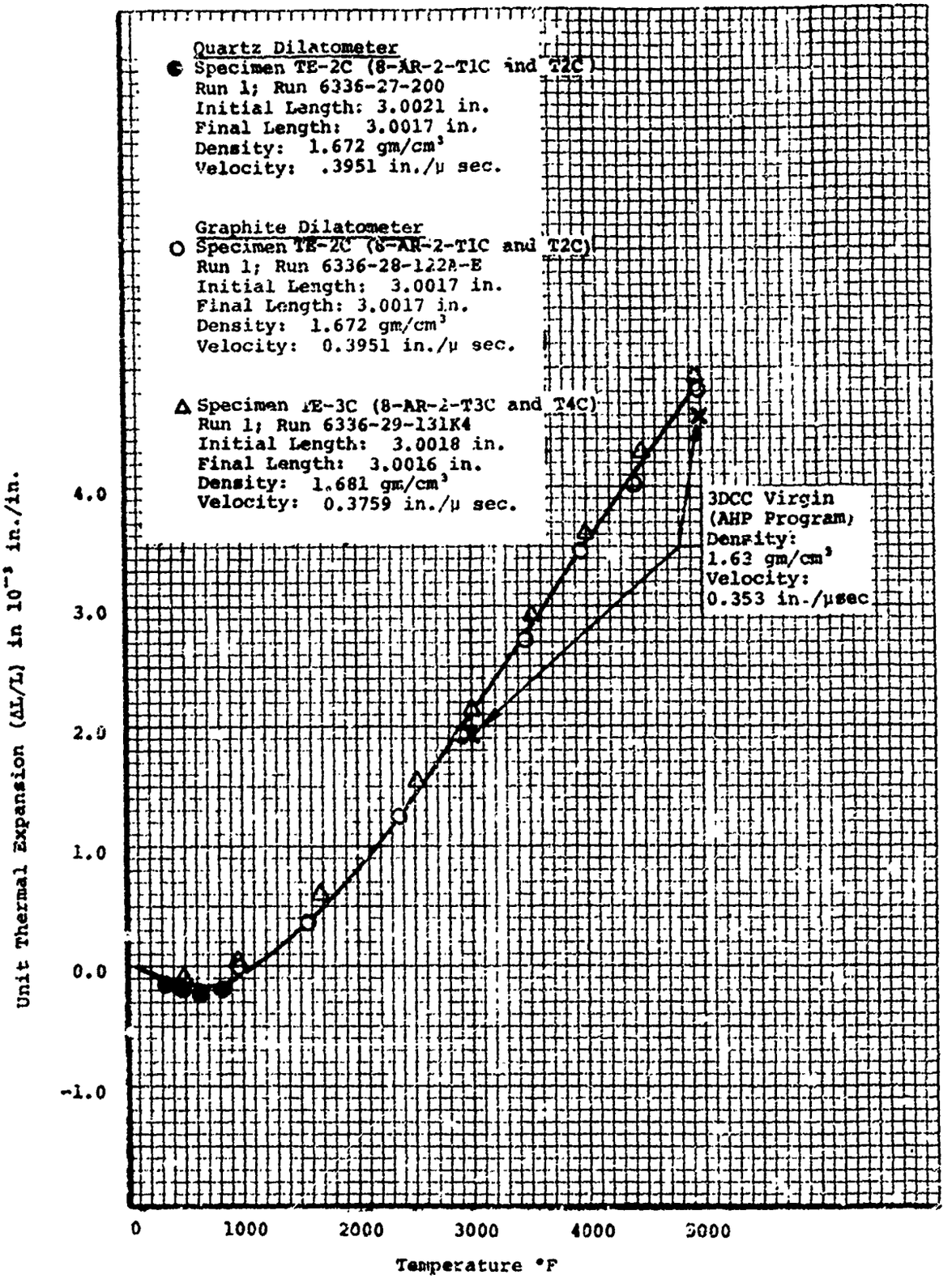


Figure 69. Thermal Expansion of 3DCC in the Circumferential Direction After 2.2 KT Impact

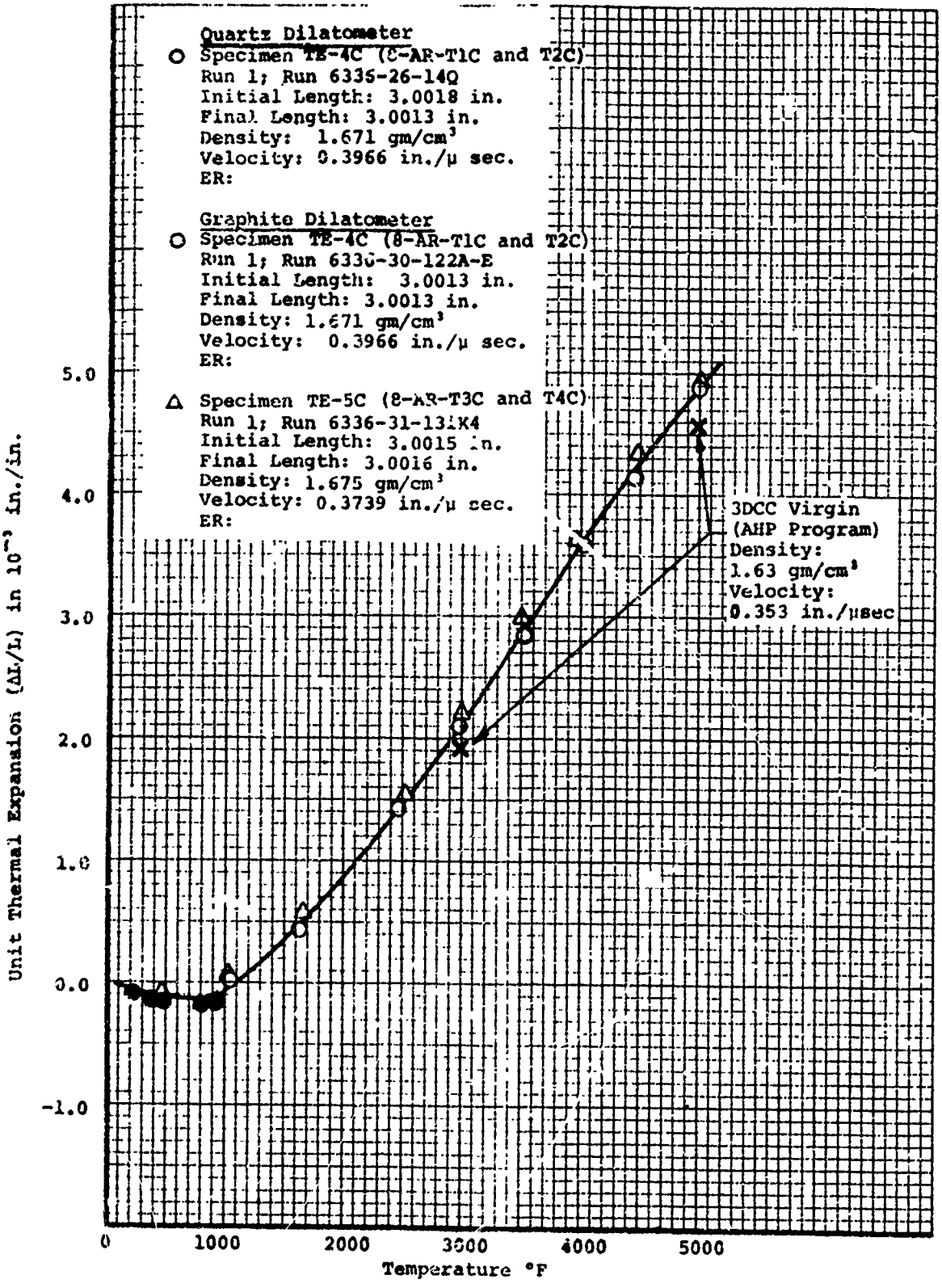


Figure 70. Thermal Expansion of 3DCC in the Circumferential Direction After 3.36 KT Impact

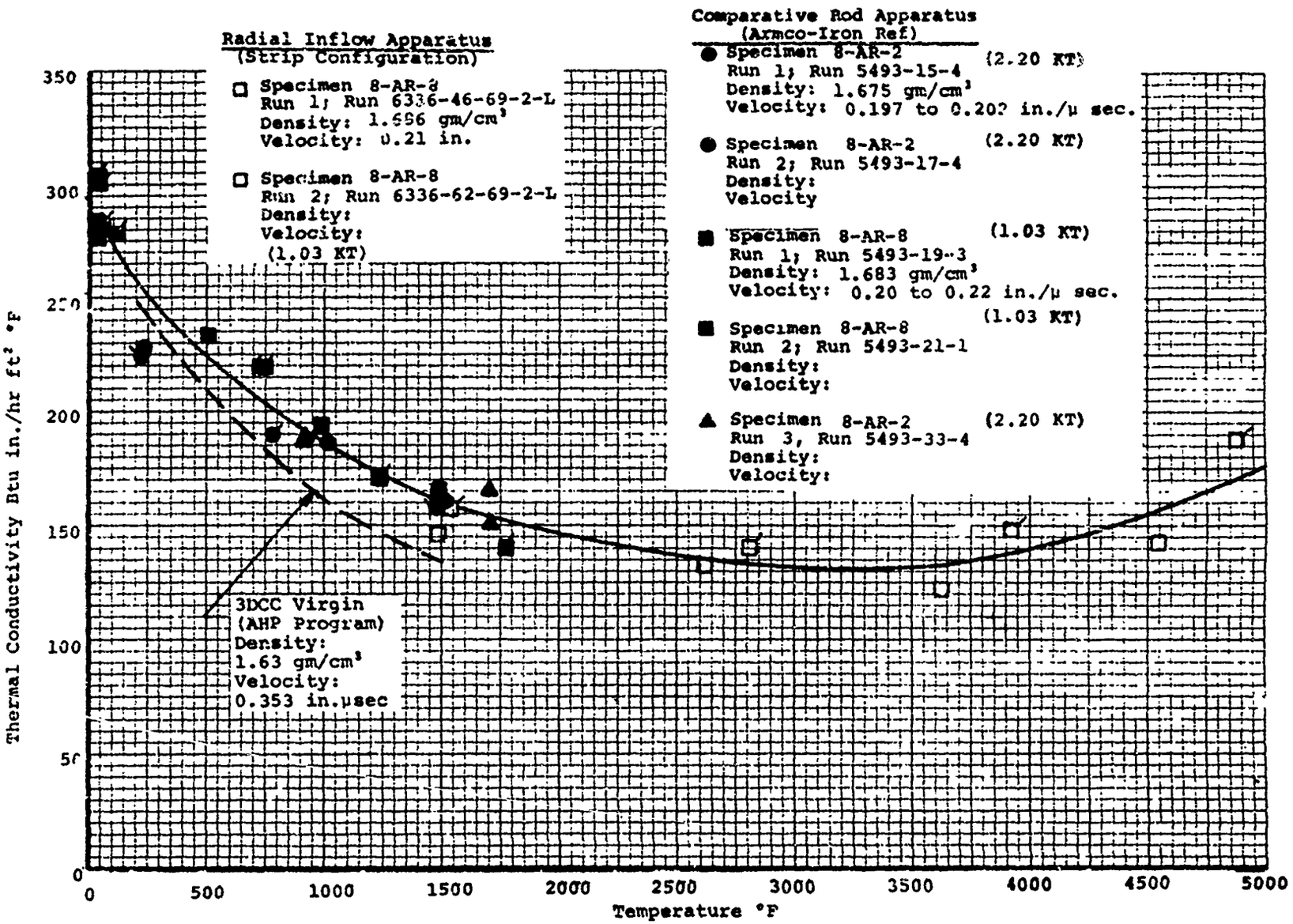


Figure 71. Thermal Conductivity of 3DCC in the Radial Direction

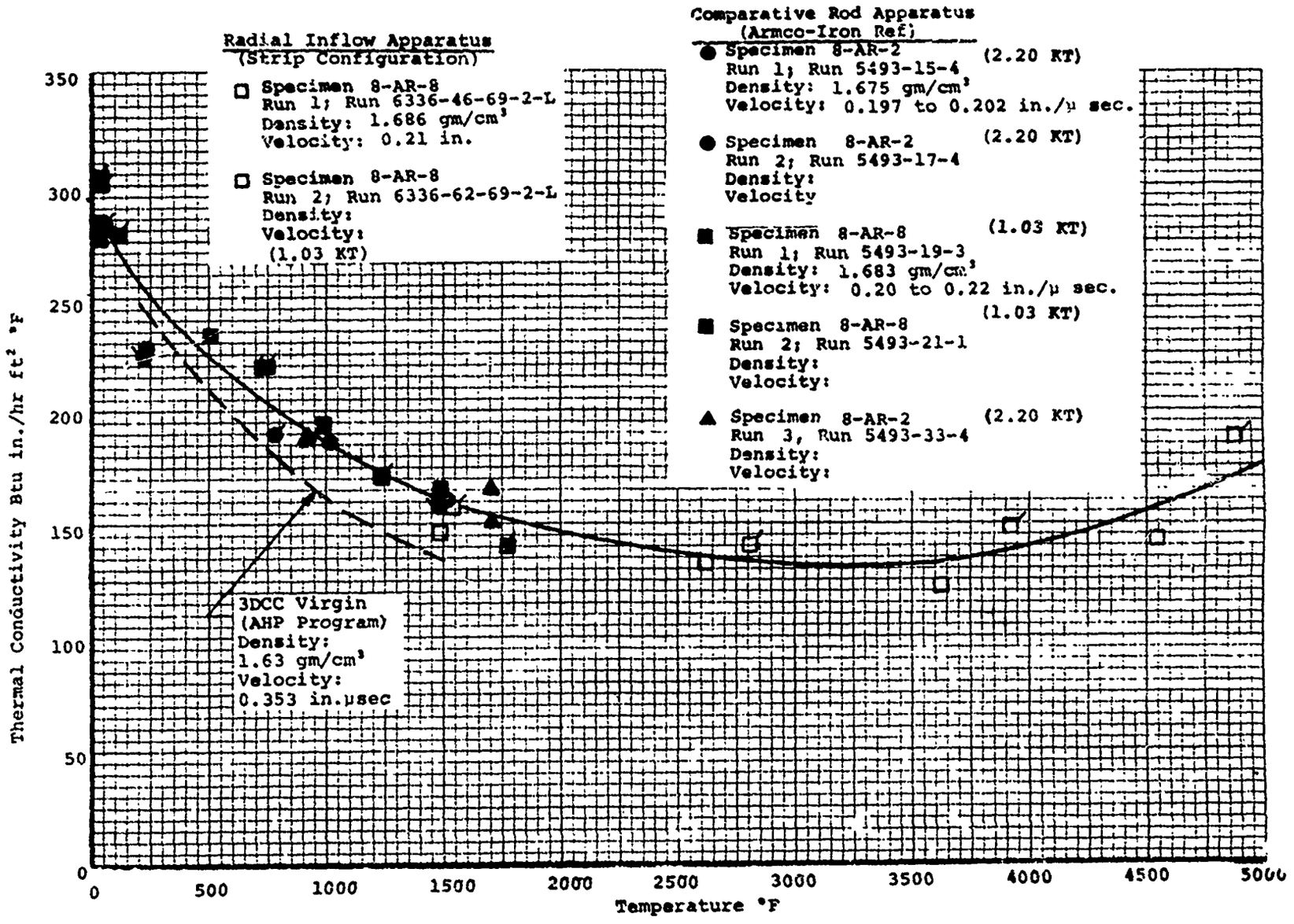
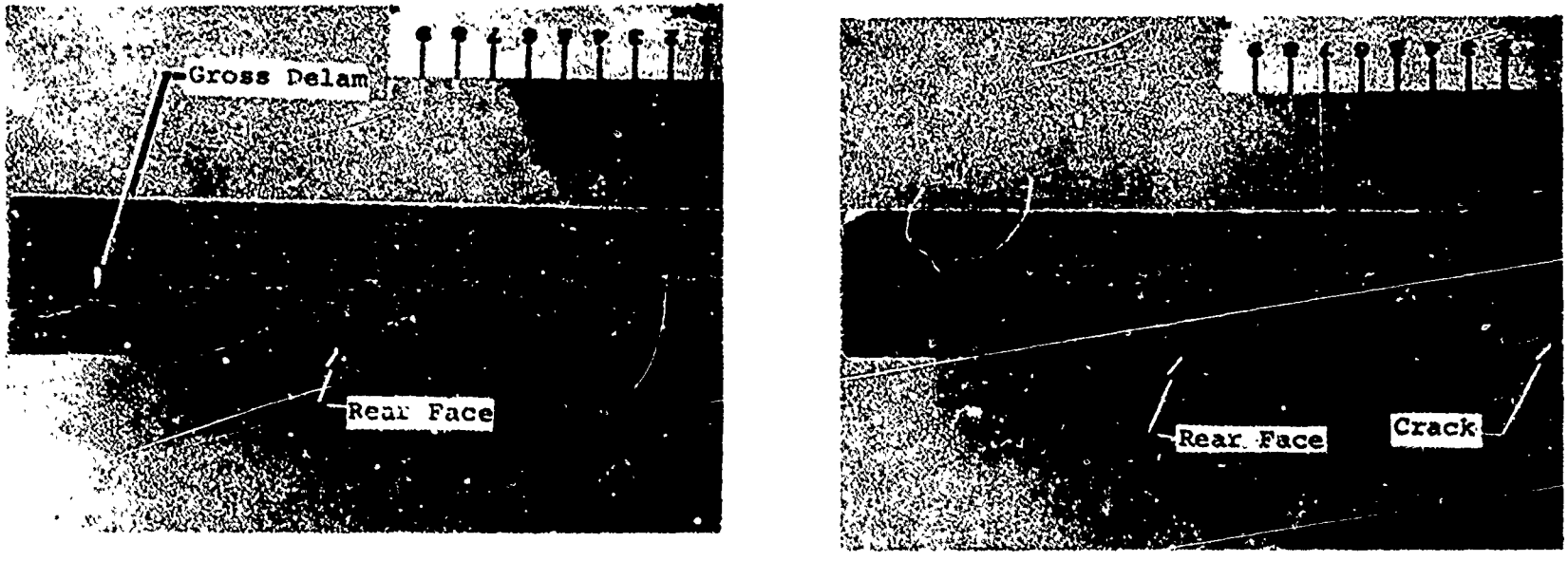


Figure 71. Thermal Conductivity of 3DCC in the Radial Direction



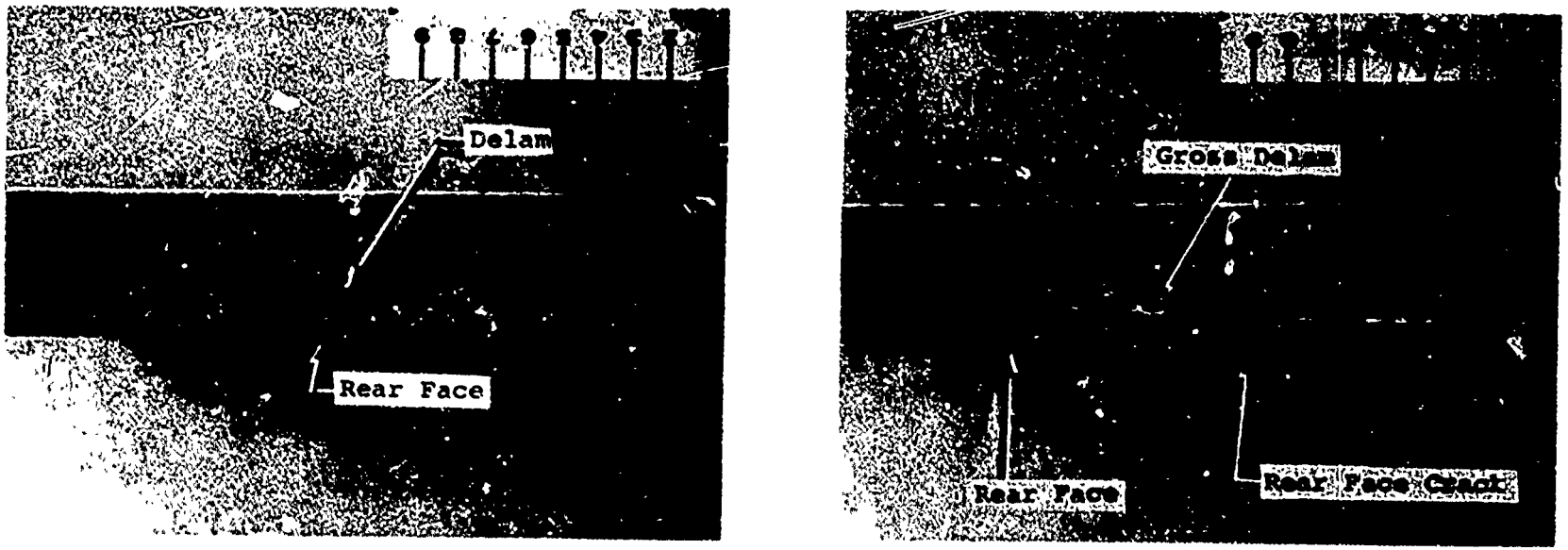
Plate No.	15	16	1	14	13	10	11
Impact Level (Kilotaps)	1.210		2.430		3.070		4.140
		1.700		2.490		3.440	

Figure 72. Group Photograph of Most Severely Damaged Edges of Sandia Felt Carbon-Carbon Impacted Plates



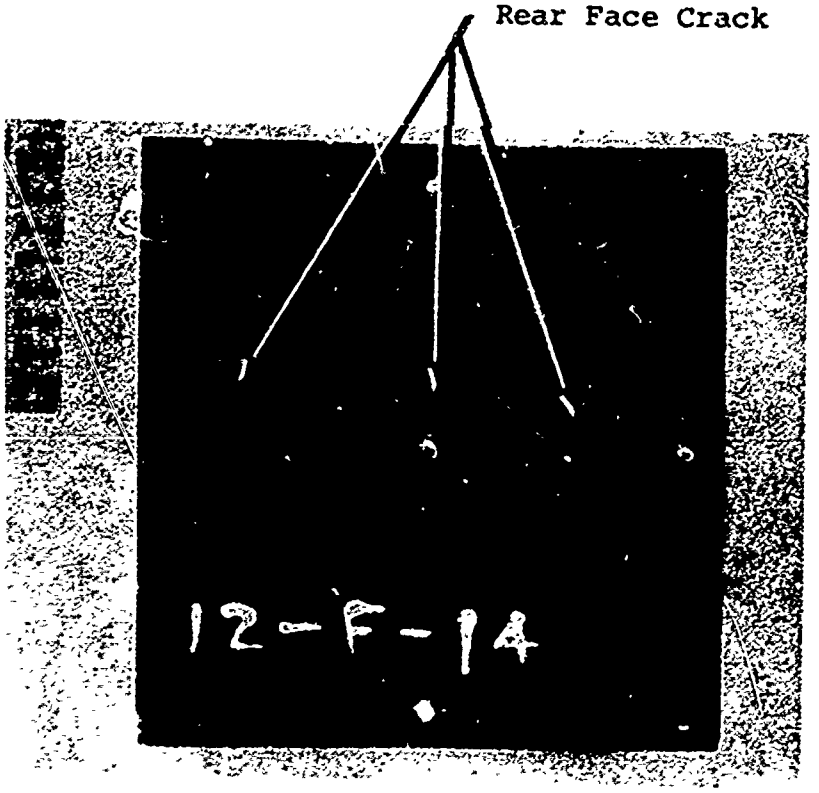
(Scale Shown)

Figure 73a. Photographs Showing Visual Structure in Sandia Felt CC Specimen 12-F-14, 2.49 KT



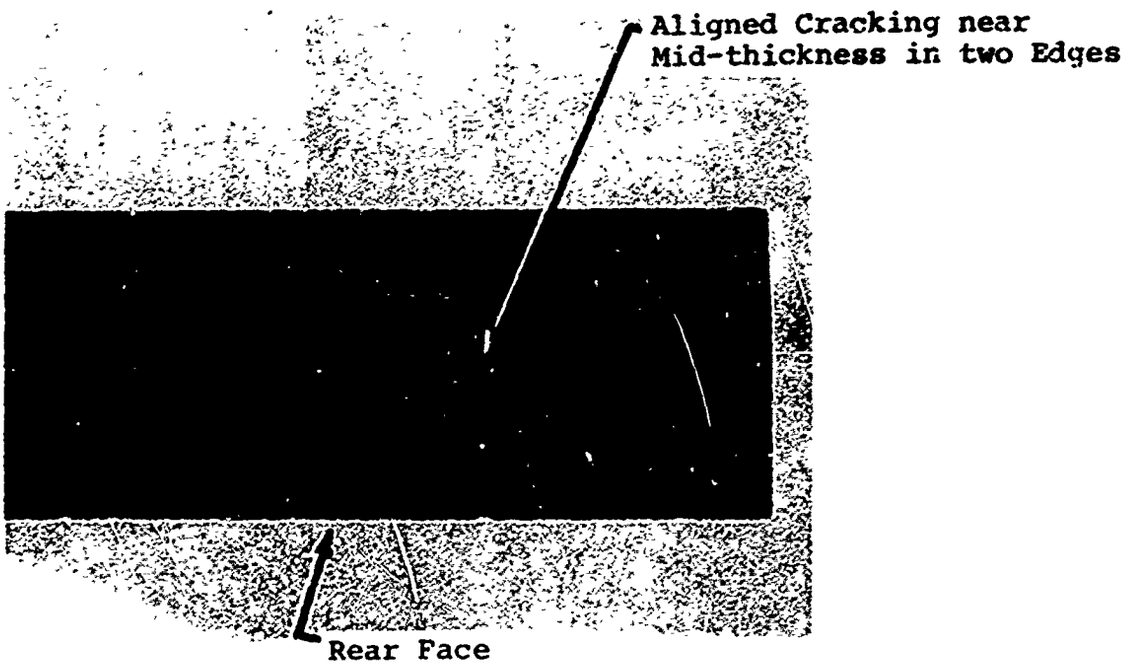
(Scale Shown)

Figure 73b.



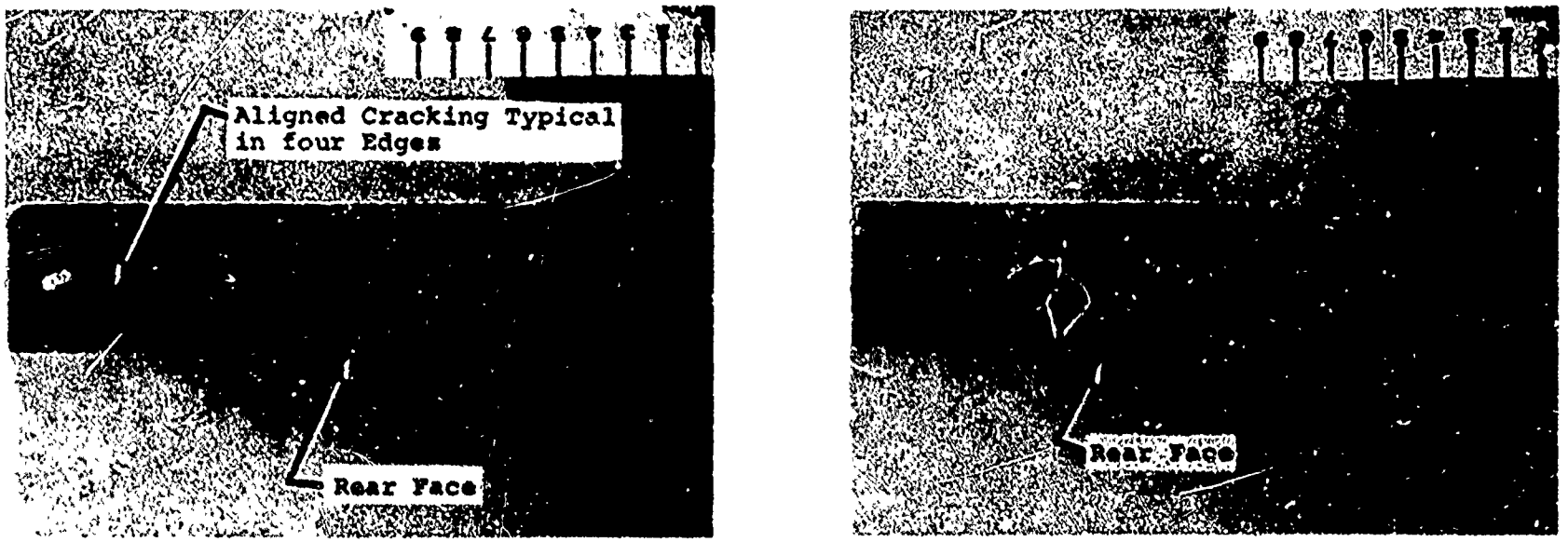
Scale Shown

Figure 73c.



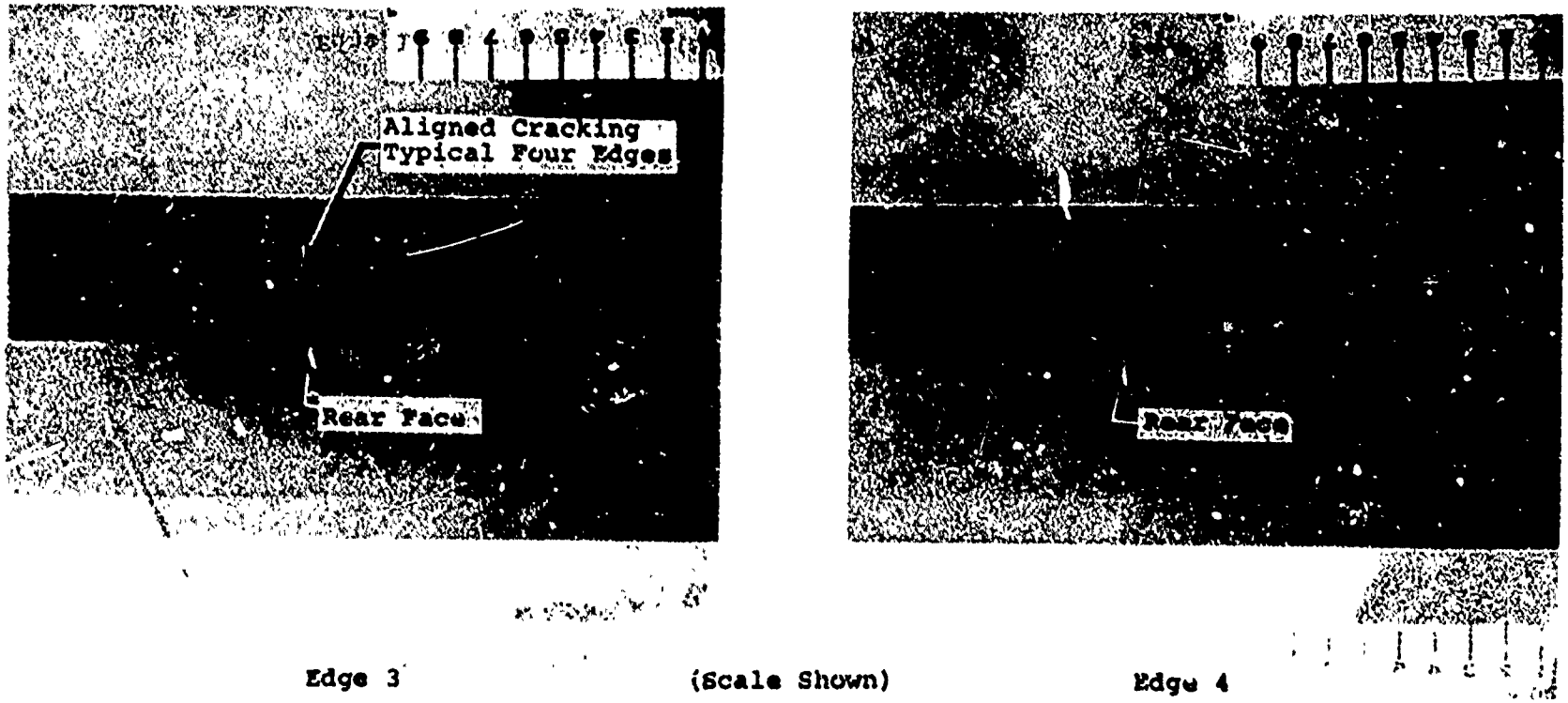
(3.8X)

Figure 74. Photograph Showing Visual Structure-Change in Sandia Felt CC Specimen 12-F-10, 3.44 KT



Edge 1 (Scale Shown) Edge 2

Figure 75a. Photographs Showing Visual Structure Change in Sandia Felt CC Specimen 12-F-11, 4.14 KT



Edge 3 (Scale Shown) Edge 4

Figure 75b.

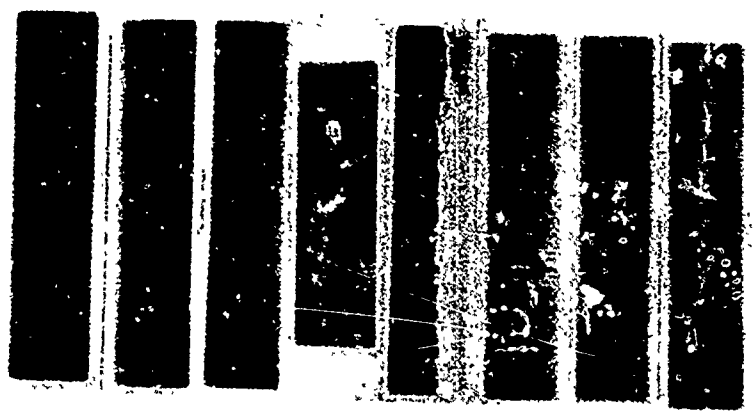


Plate No.	V	15	16	1	14	13	10	11
Impact Level Kilotaps	0		1.700		2.490		3.440	
	1.210		2.430		3.070		4.140	

Positive Prints from Individual Radiographs

Figure 76. Group Radiograph in Axial Direction Showing Impacted Plates from Sandia Felt CC

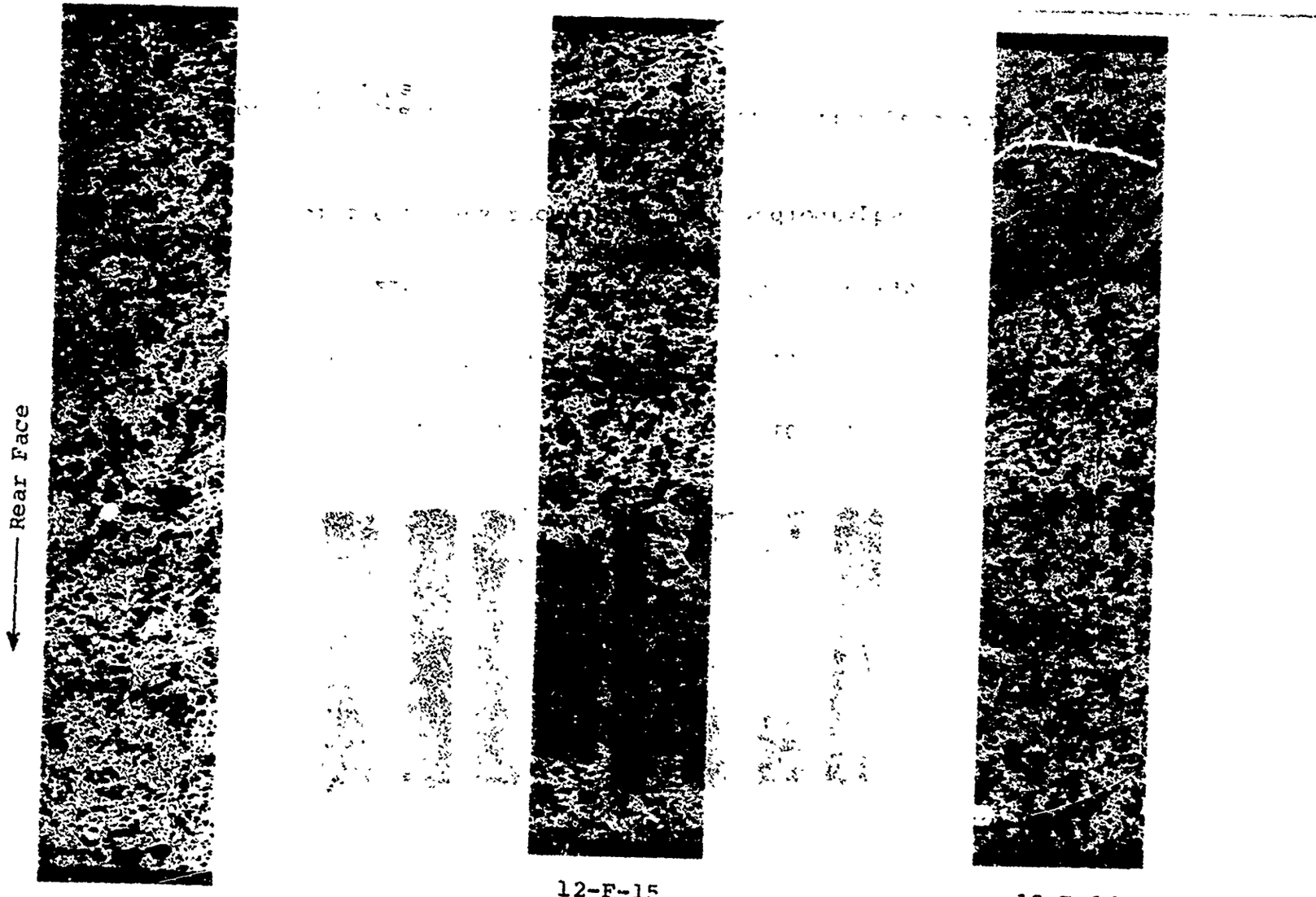


Figure 77a. Photomicrographs of Edges (Axial View) of Impulse Loaded Plates from Sandia Felt CC

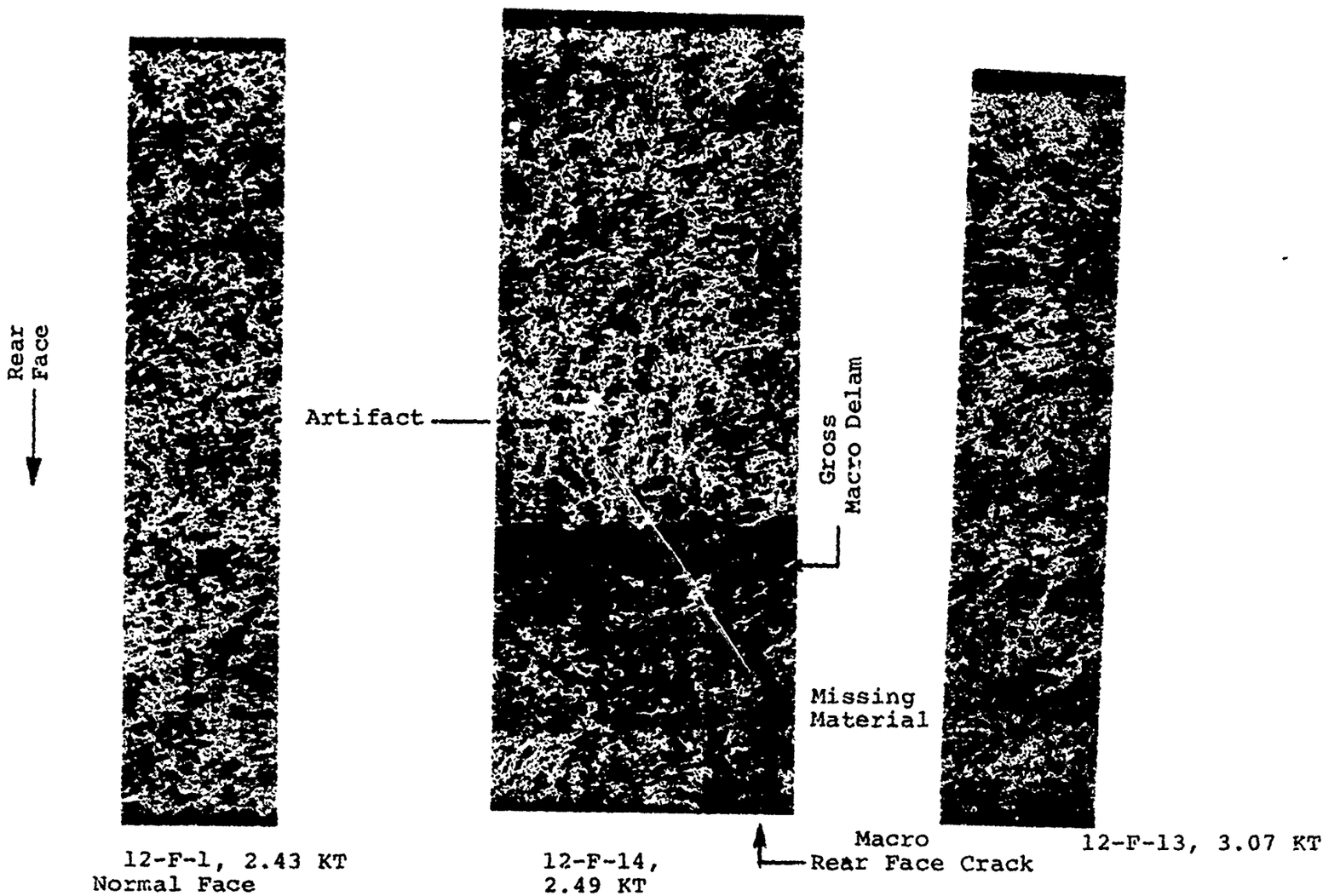
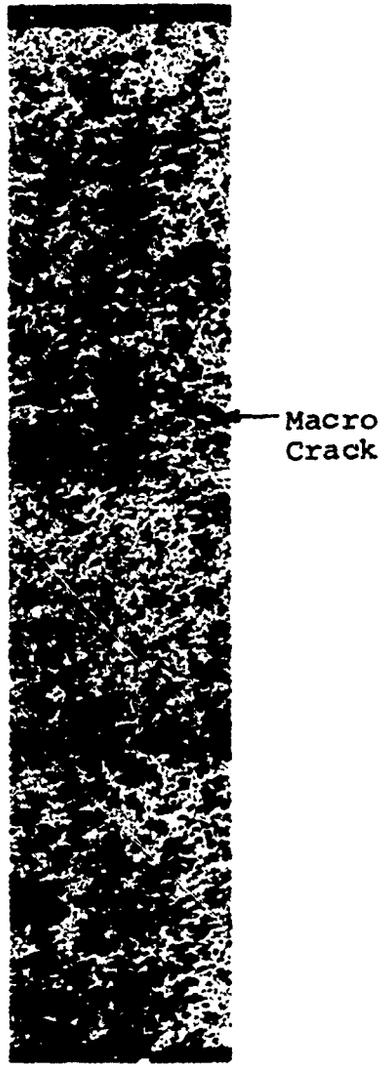
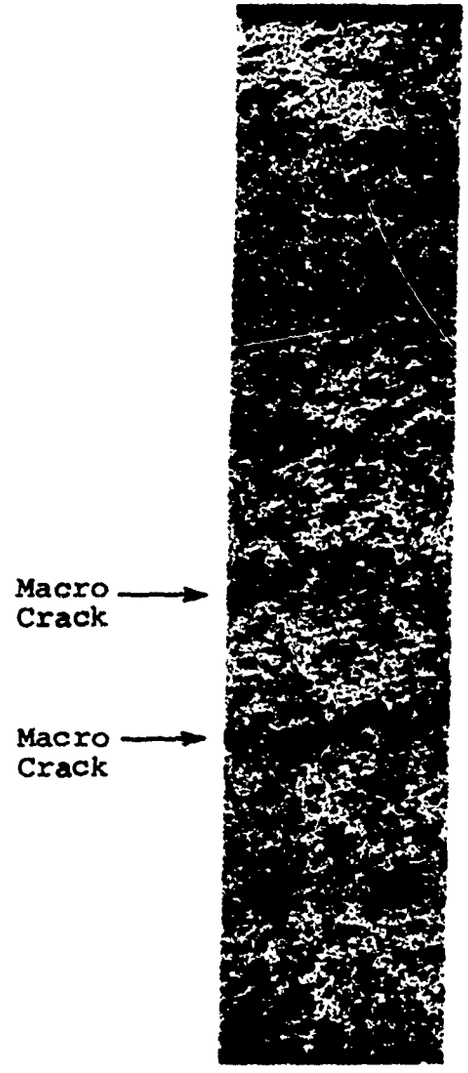

Rear Face
Artifact
Gross Macro Delam
Missing Material
Macro Rear Face Crack
12-F-1, 2.43 KT Normal Face
12-F-14, 2.49 KT
12-F-13, 3.07 KT

Figure 77b.



12-F-10
(Normal Micro) 3.44 KT



12-F-11
(Normal Micro) 4.14 KT

Figure 77c.

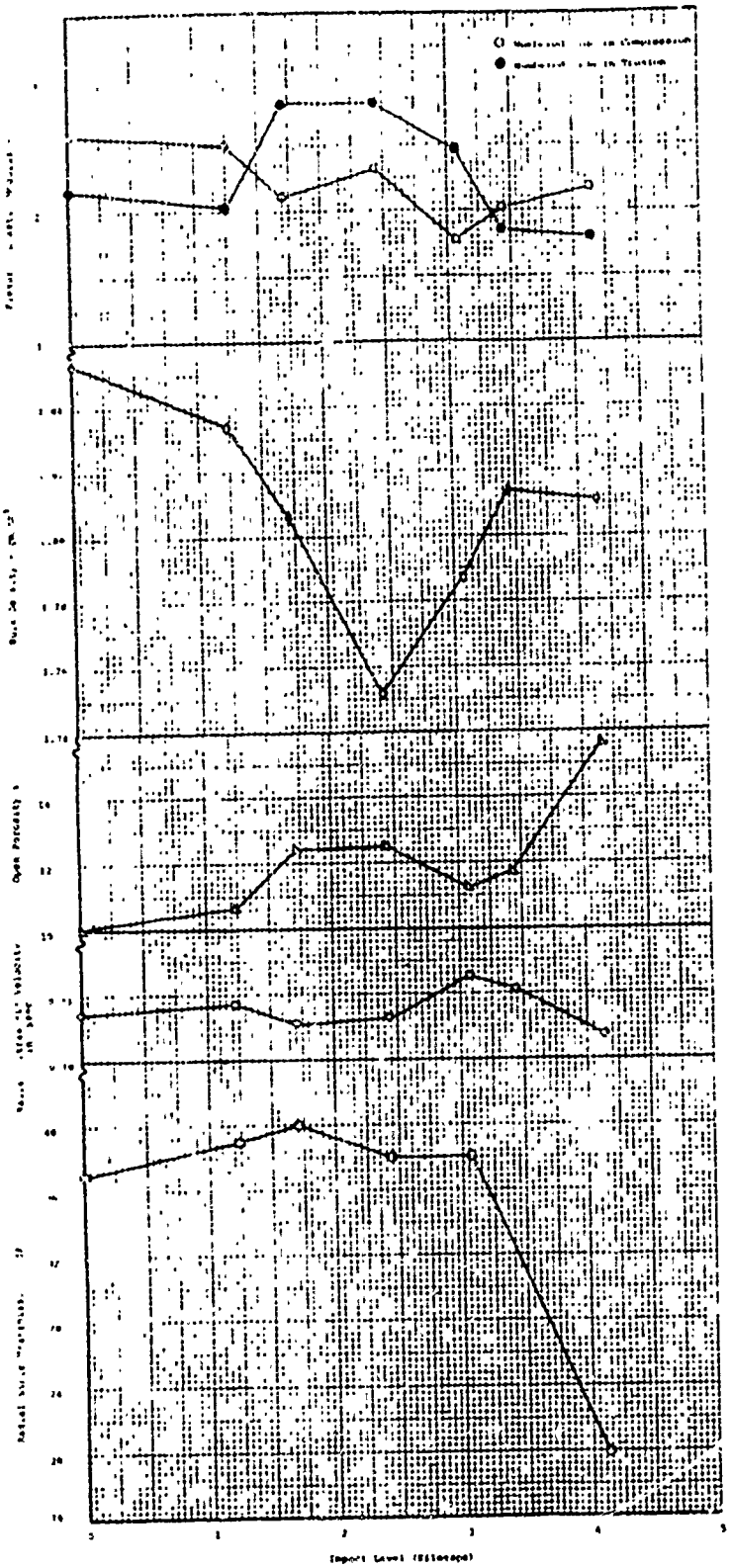


Figure 78. NDT Monitors and Flexural Modulus versus Impact Level for Sandia Felt CC Material

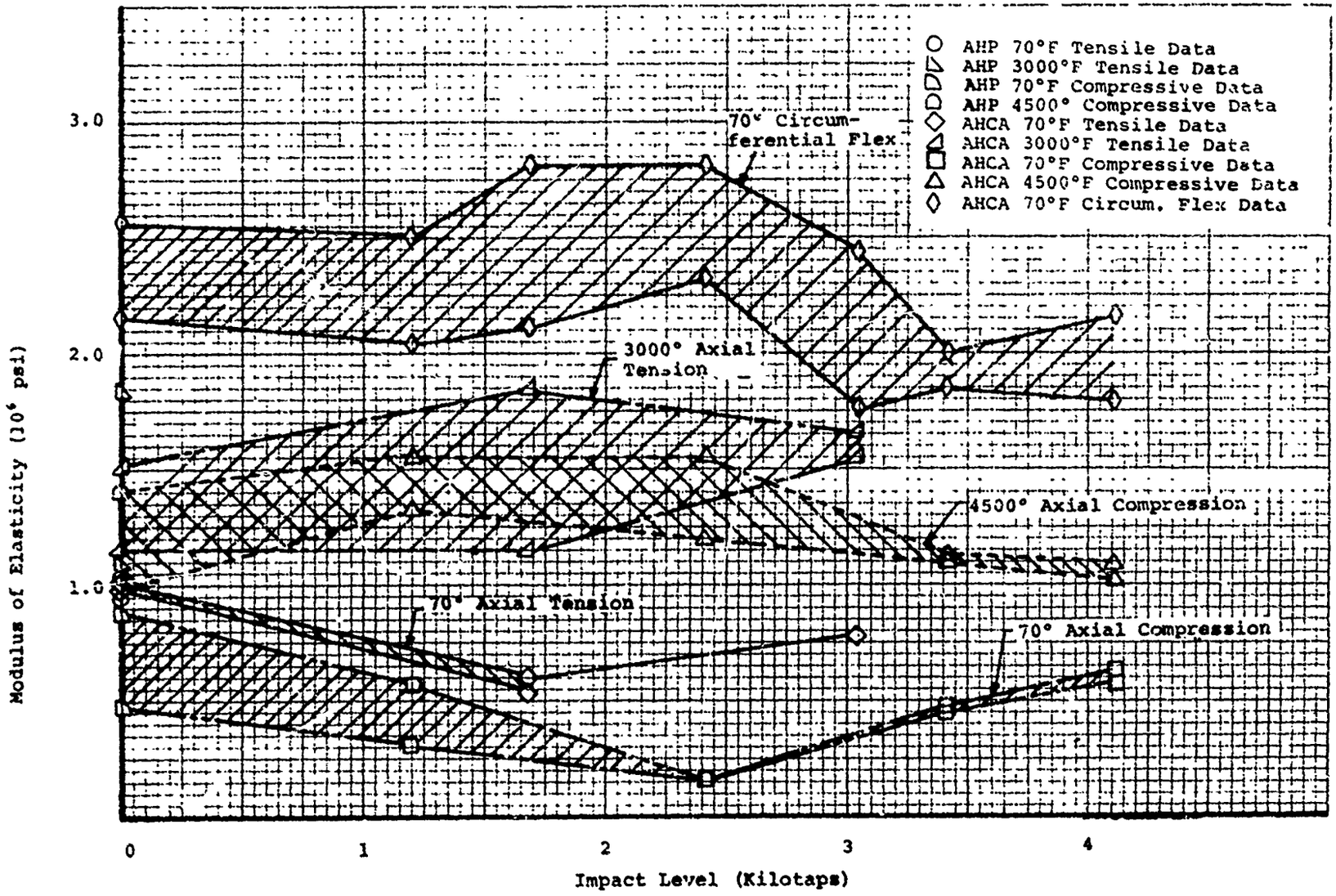


Figure 79. Modulus of Elasticity for Specimens from Sandia Felt CC Impacted Plates

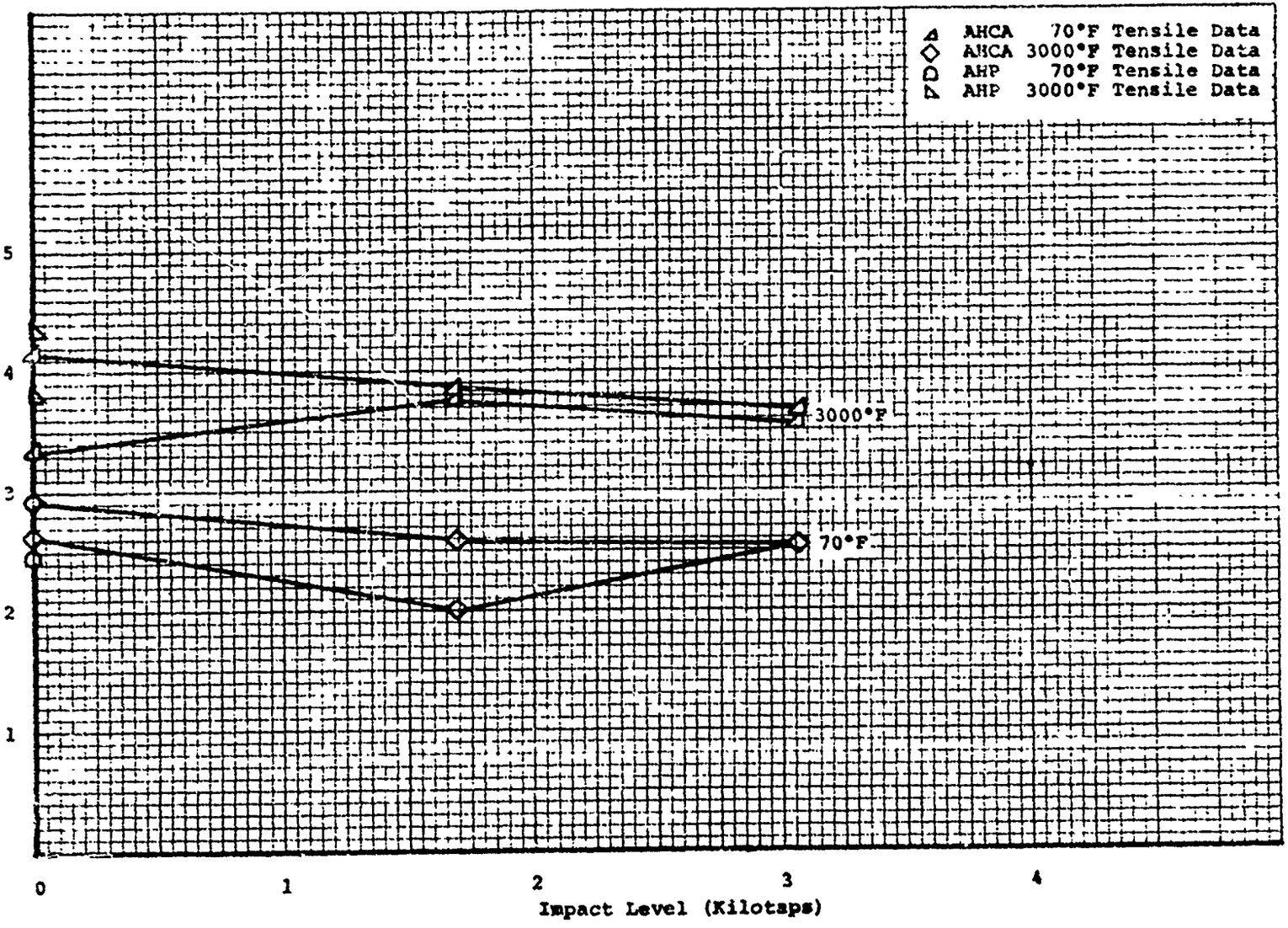


Figure 80. Axial Tensile Strength for Specimens from Sandia Felt CC Material Impacted Plates

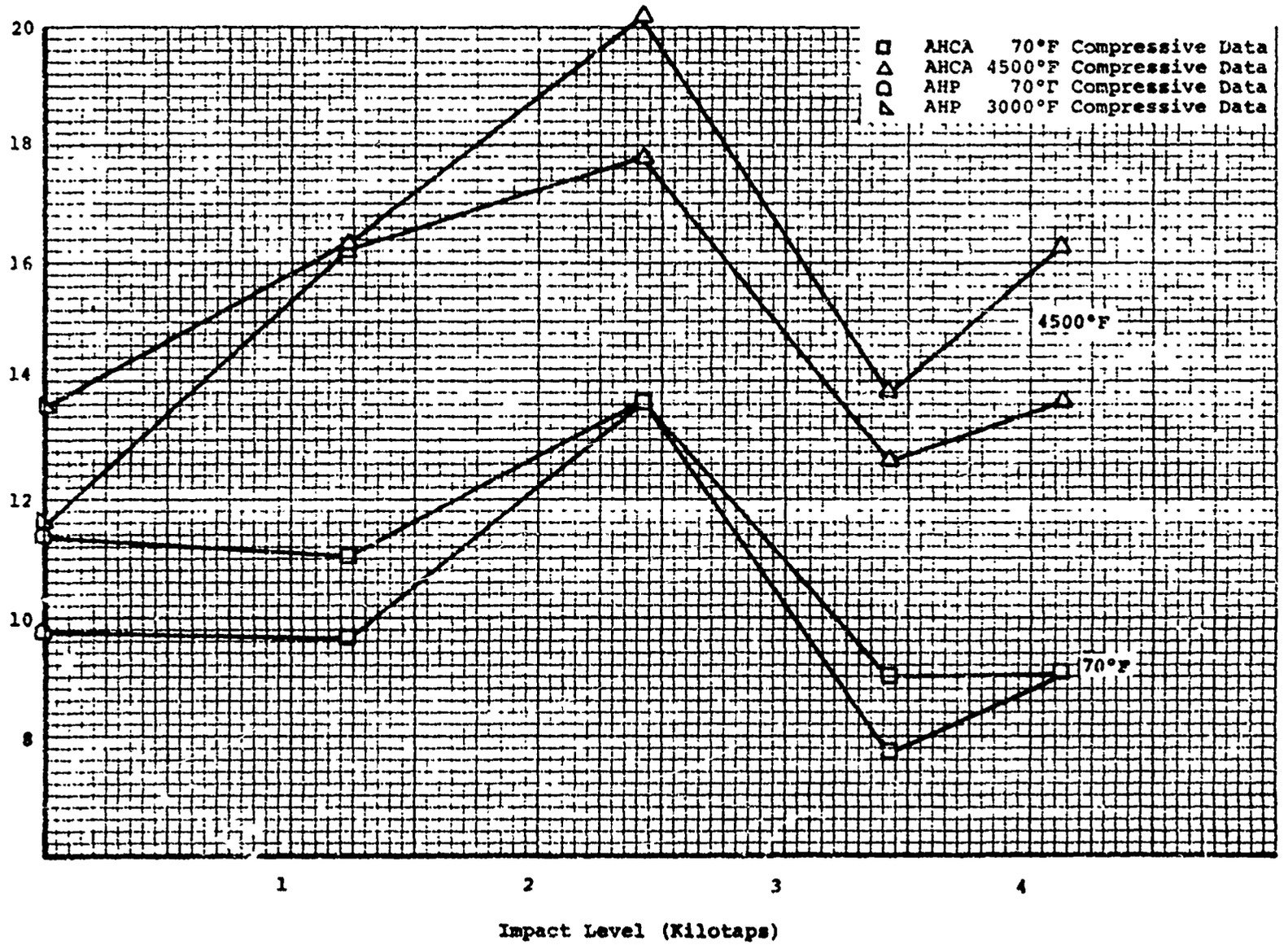


Figure 81. Axial Compressive Strength for Specimens from Sandia Felt CC Impacted Plates

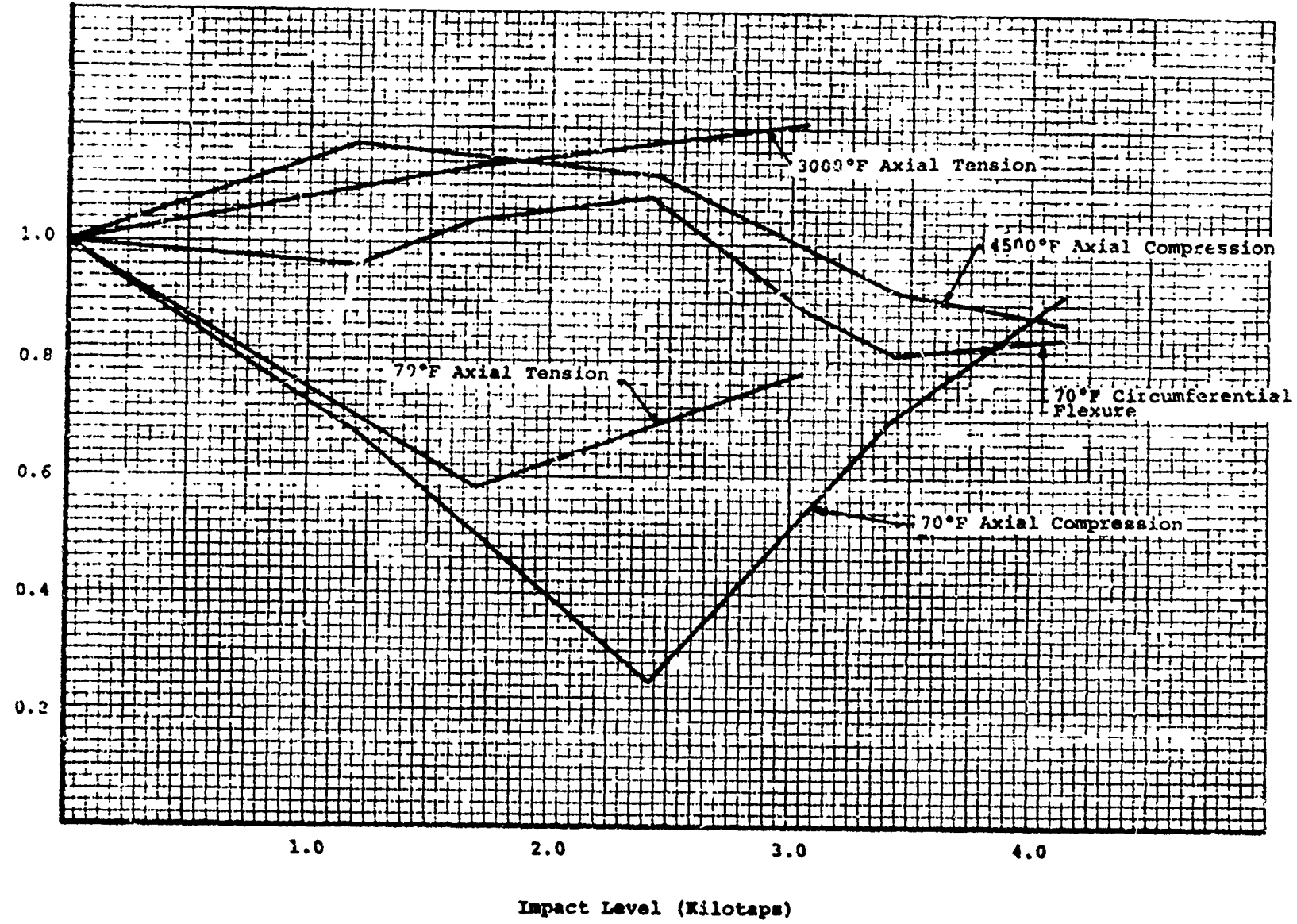


Figure 82. Retained Modulus for Specimens from Sandia Felt CC Material Impacted Plates

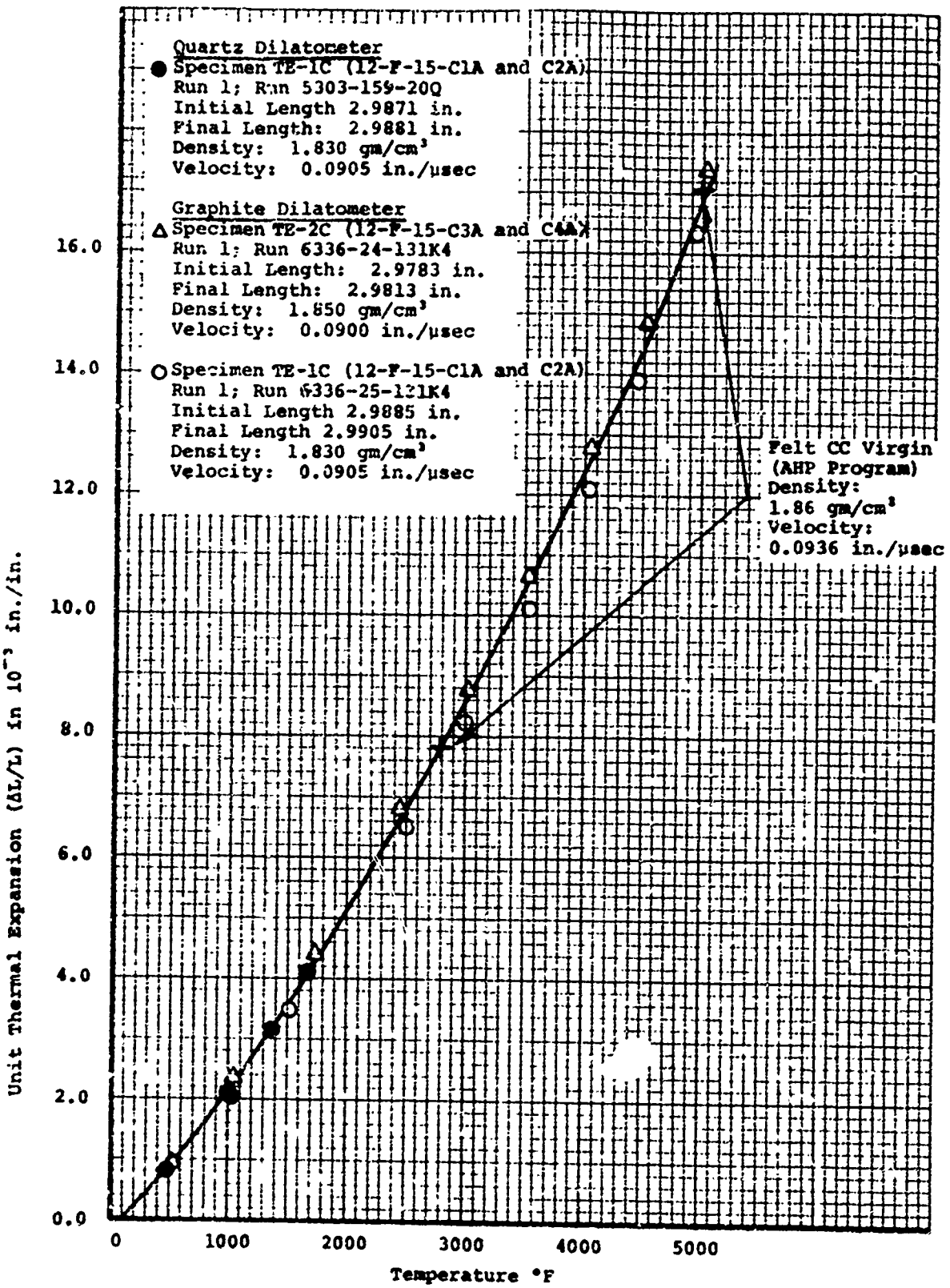


Figure 83. Thermal Expansion of Felt CC in the Axial Direction After 1.21 KT

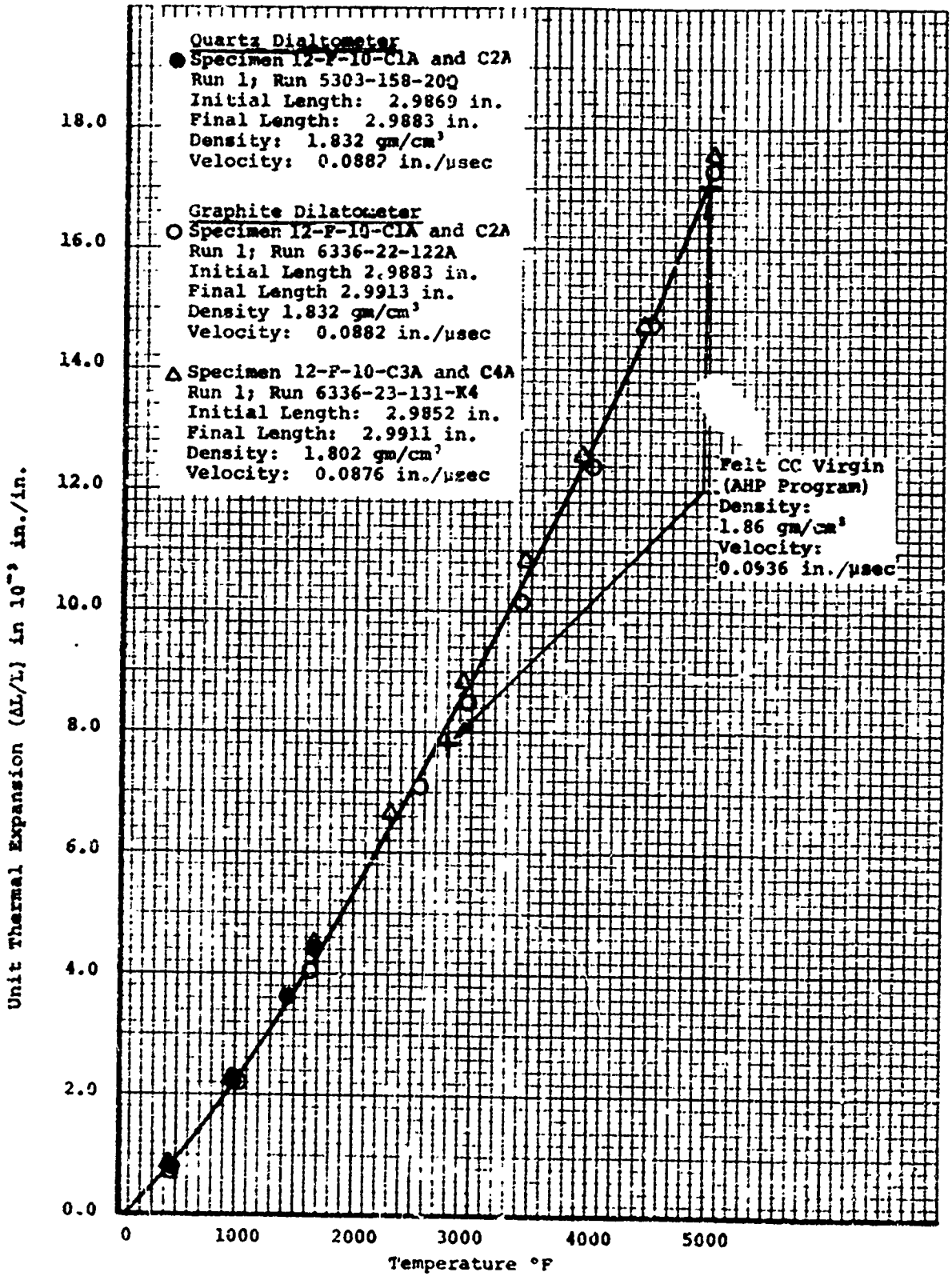


Figure 84. Thermal Expansion of Felt CC in the Axial Direction After 3.44 KT

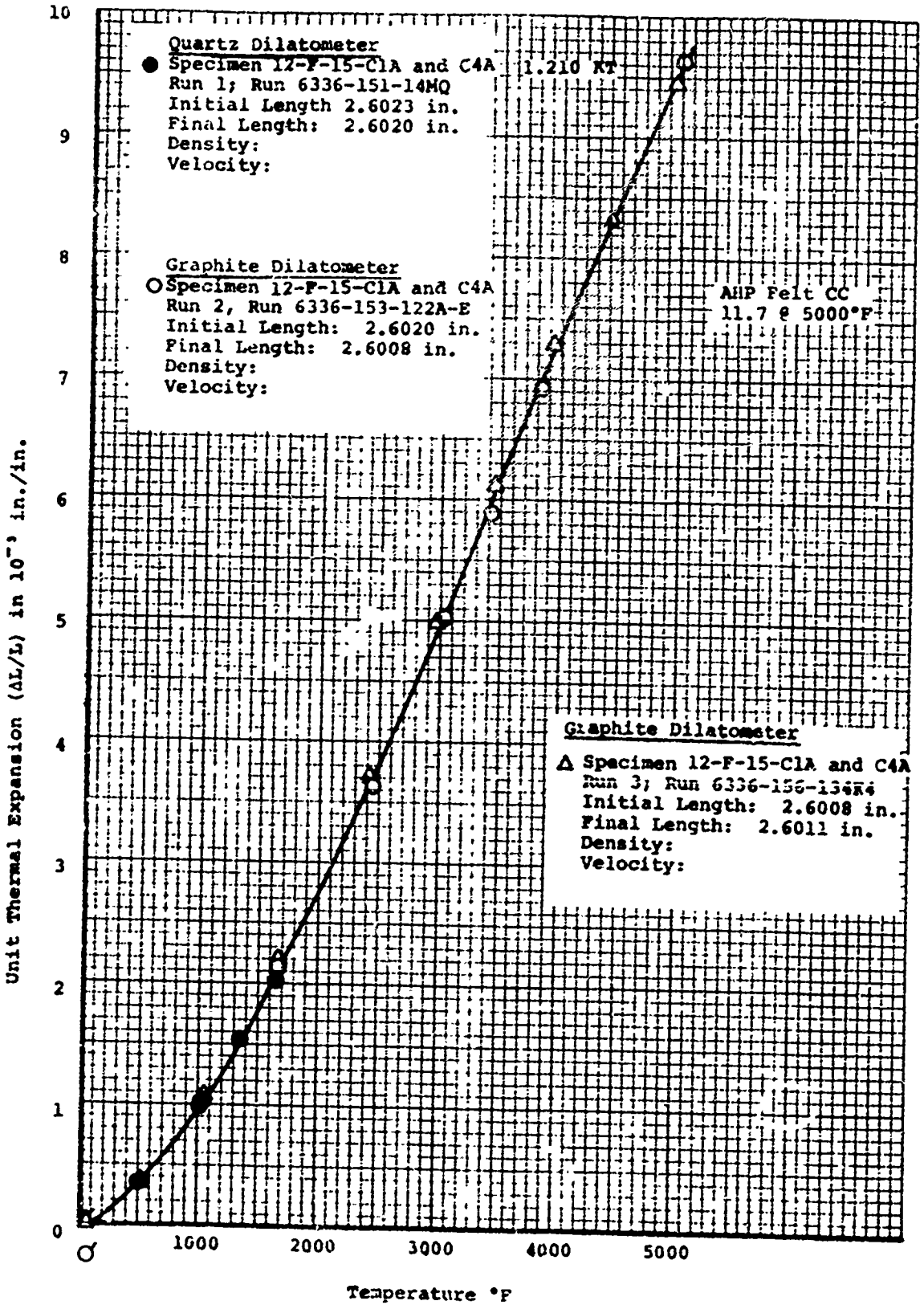


Figure 85. Thermal Expansion of Felt CC in the Circumferential Direction After 1.21 KT

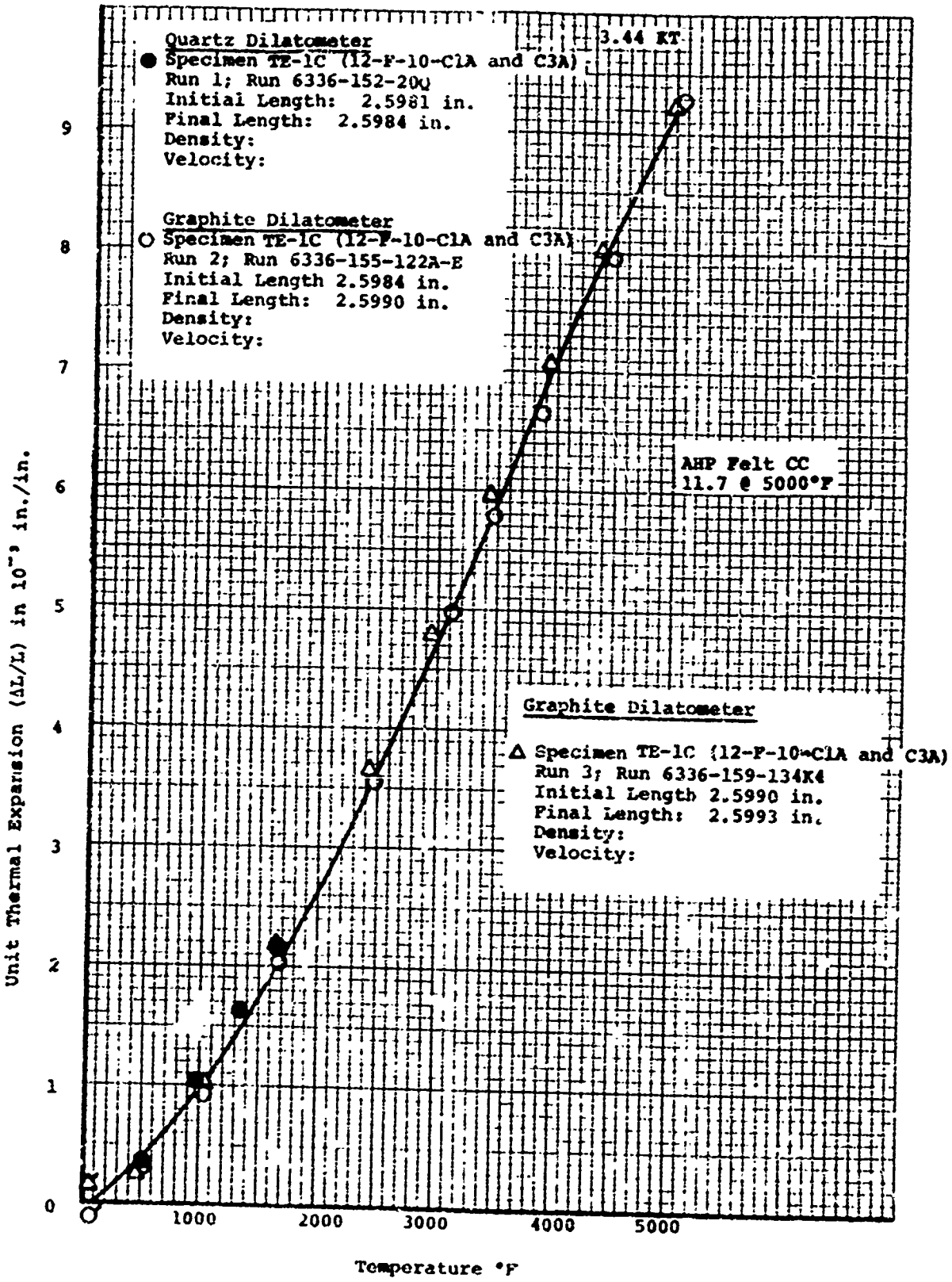


Figure 86. Thermal Expansion of Felt CC in the Circumferential Direction After 3.44 KT

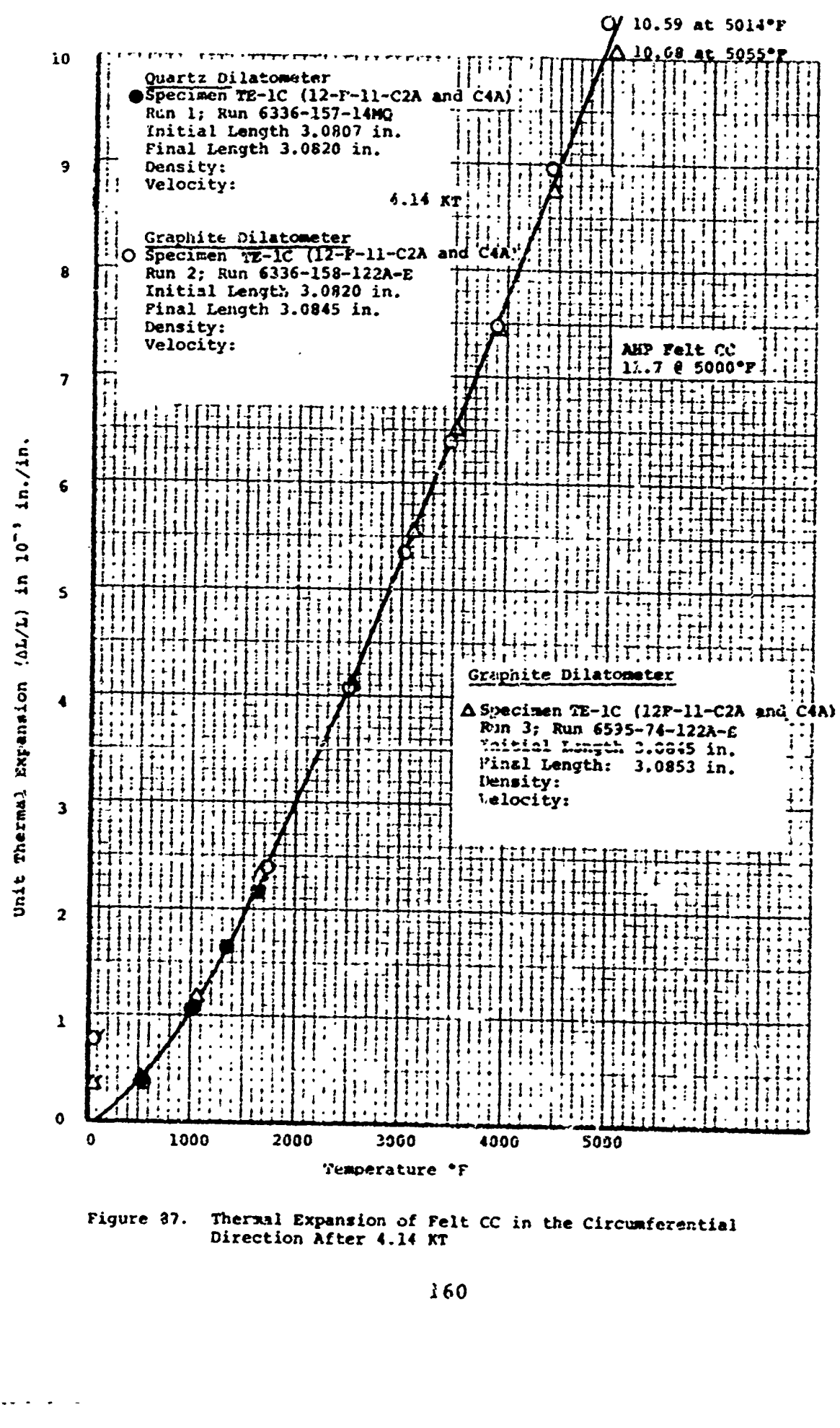


Figure 87. Thermal Expansion of Felt CC in the Circumferential Direction After 4.14 KT

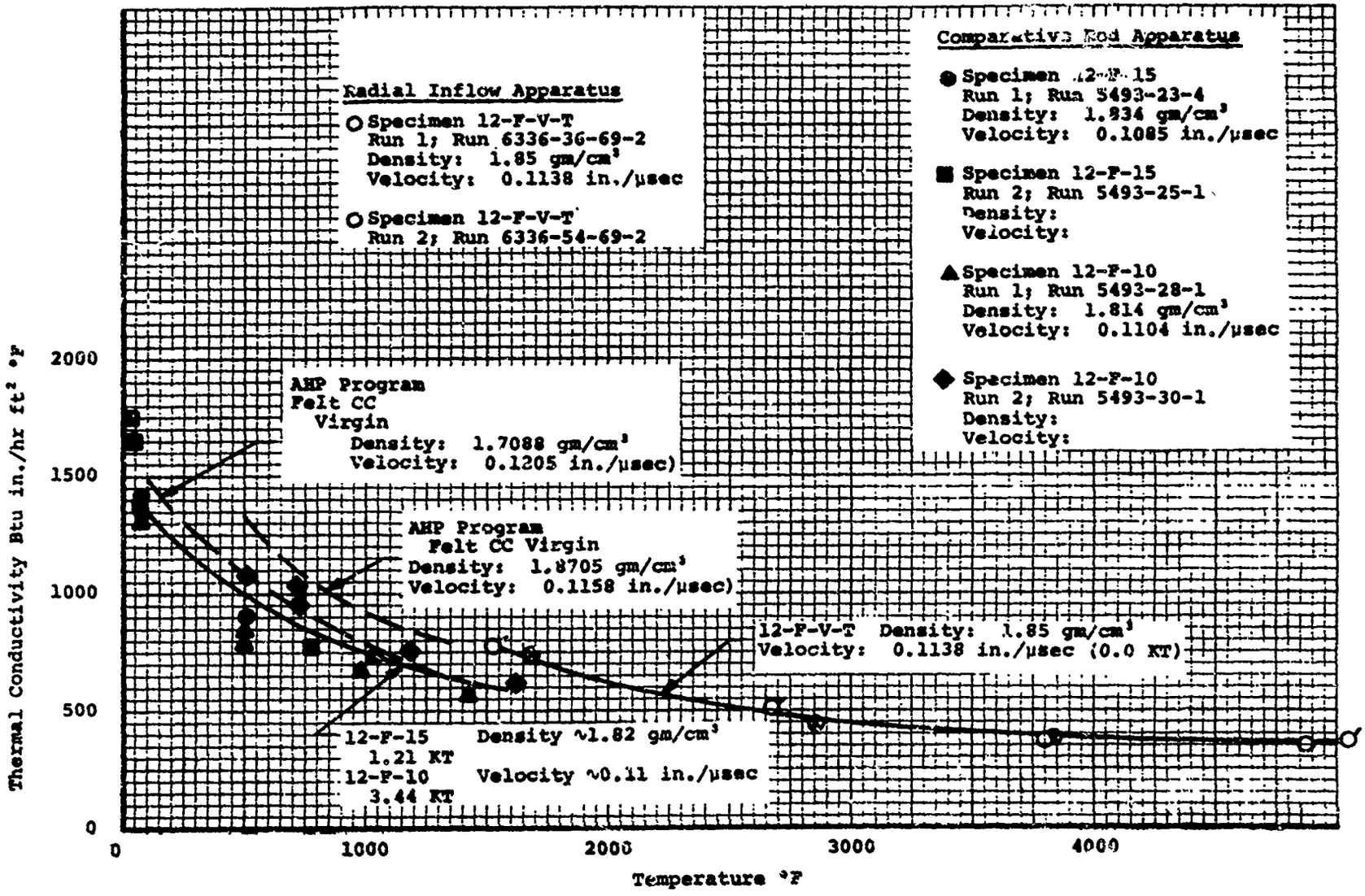
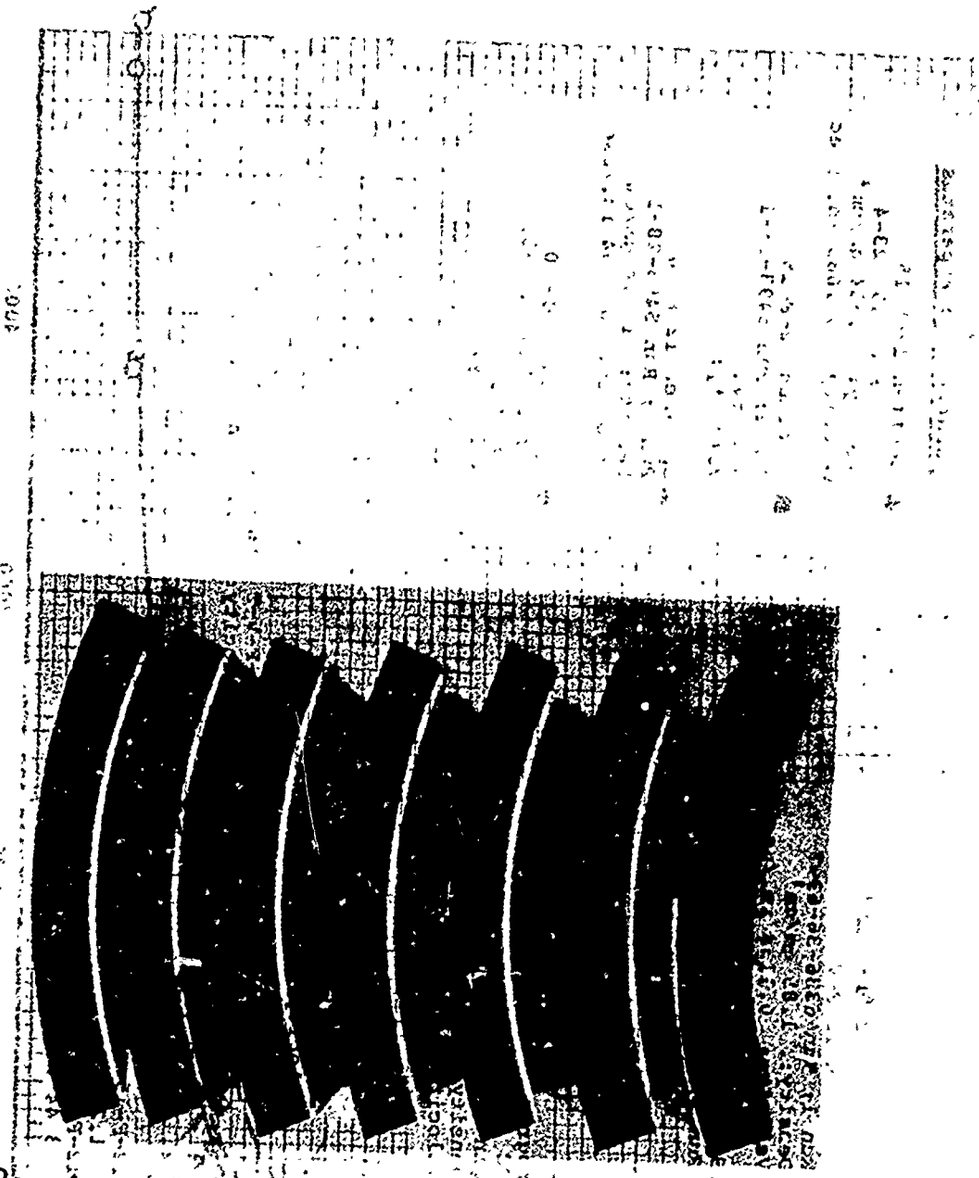


Figure 88. Thermal Conductivity of Felt CC in the Radial Direction



Specimen No.	4	7	6	3	1	5	2
Impulse Level KT	0.49	1.59	1.66	1.90	1.99	4.04	4.48

Figure 89. Group Photograph (1X) Showing Impacted Edges of Arc Rings from Material 10

The percentage change in MOE, bulk density, sonic velocity, sonic attenuation* and thickness are defined as:

$$\text{Percentage change} = \frac{\text{Virgin value} - \text{Specimen value}}{\text{Virgin value}} \times 100\%$$

For Open Porosity: Specimen value (%) - Virgin value (%)

*By definition:

$$\text{Percentage sonic attenuation} = \frac{\text{attenuation of specimen (db)} - \text{attenuation of virgin (db)}}{\text{attenuation of virgin (db)}} \times 100\%$$

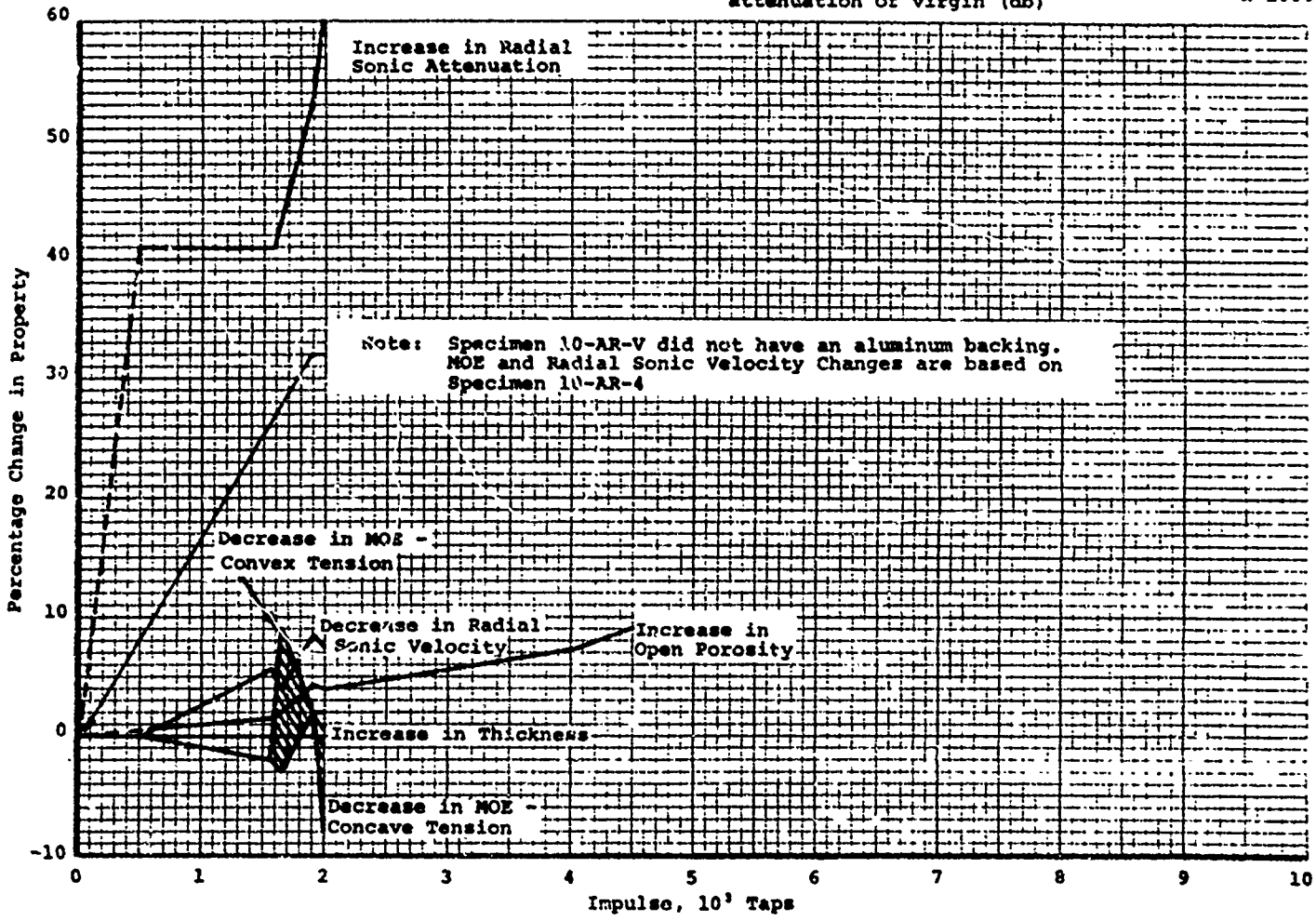


Figure 90. Percentage Changes in Flexural MOE and NDT Monitors versus Impulse in Taps for Aluminum-Backed Arc Specimens from Material 10 (AVCO TW R6300)

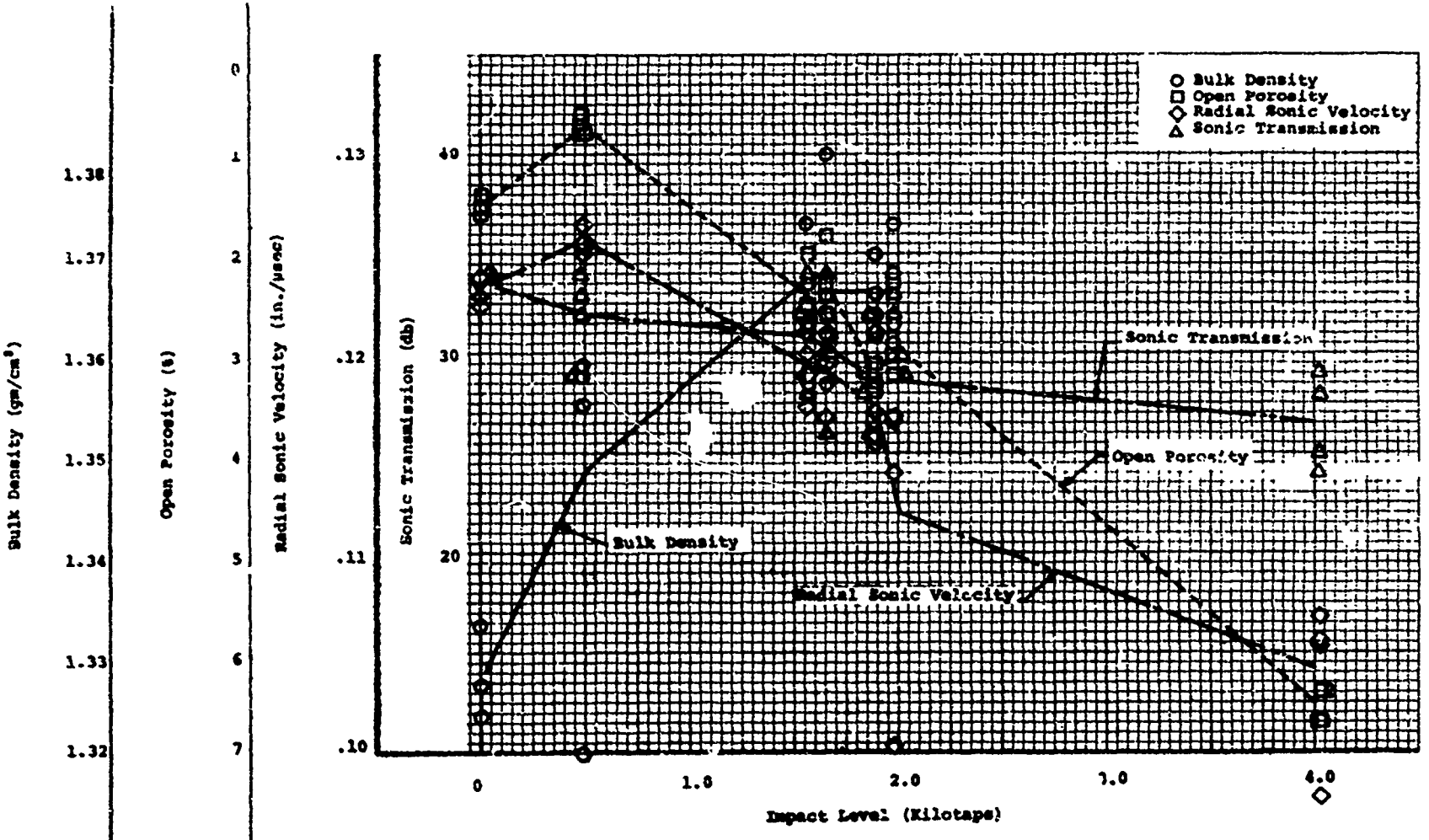


Figure 91. Results of Non Destructive Testing of Specimens from R6300 Impacted Arcs

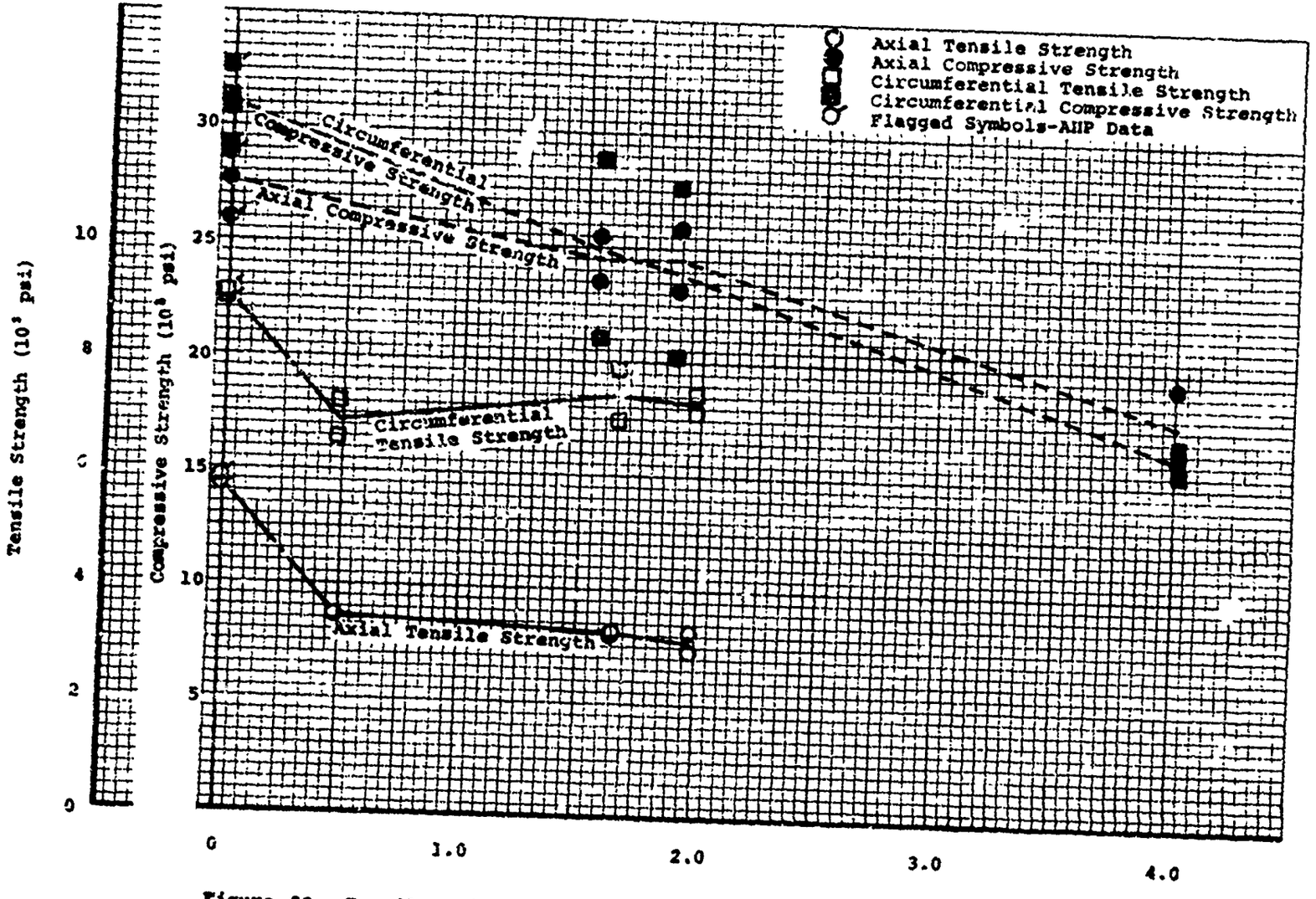


Figure 92. Tensile and Compressive Strength of Specimens from R6300 Impacted Arcs

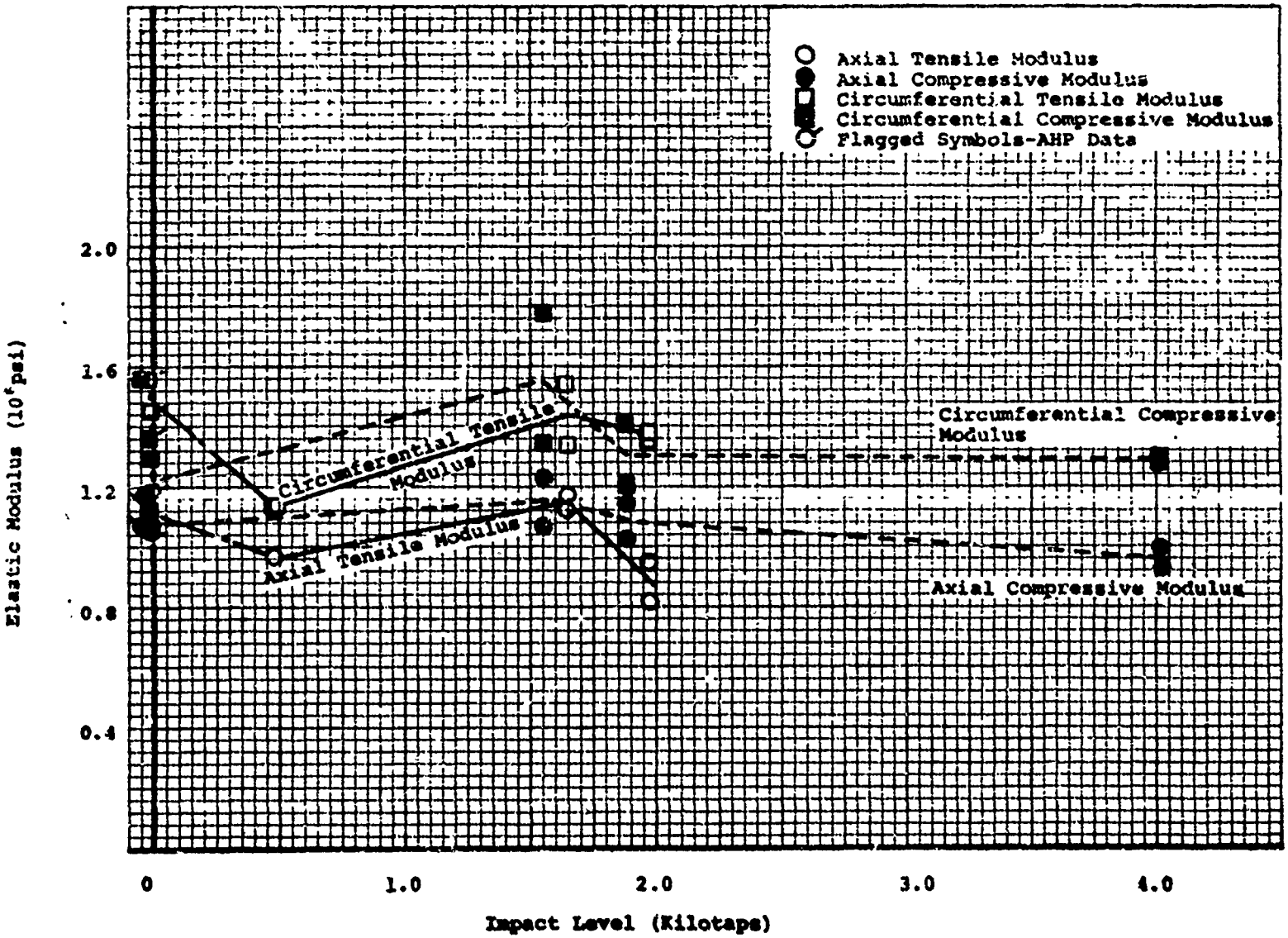
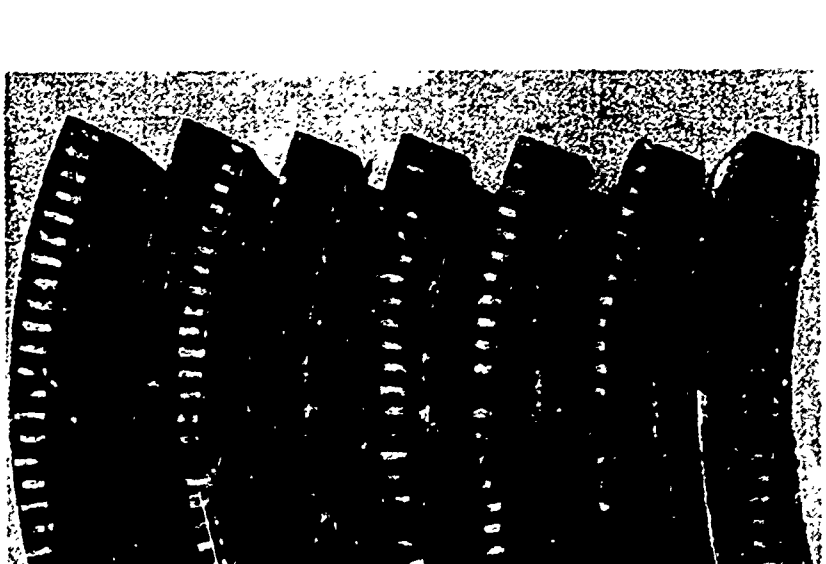


Figure 93. Tensile and Compressive Modulus of Specimens from R6300 Impacted Arcs



Specimen No.	8	5	3	7	1	2	6
Impulse Level KT	4.58	7.54	7.95	8.61	9.01	9.01	9.88

Figure 94. Group Photograph (1X) Showing Impacted Edges of Arc Rings from Material 11

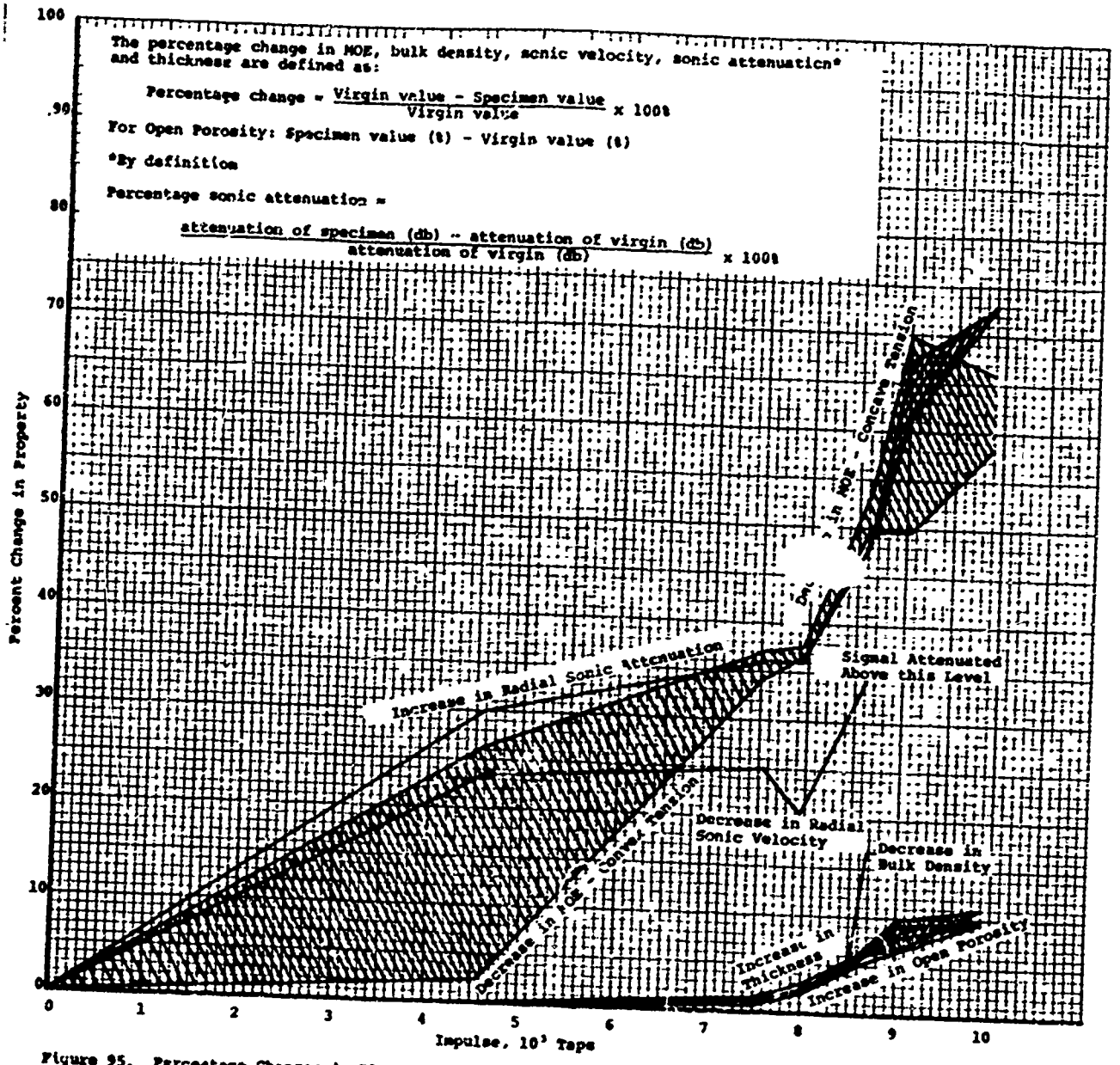


Figure 95. Percentage Changes in Flexural MOE and NDT Monitors versus Impulse in Taps for Arc Specimens from Material 11 (AVCO 3D Q?)

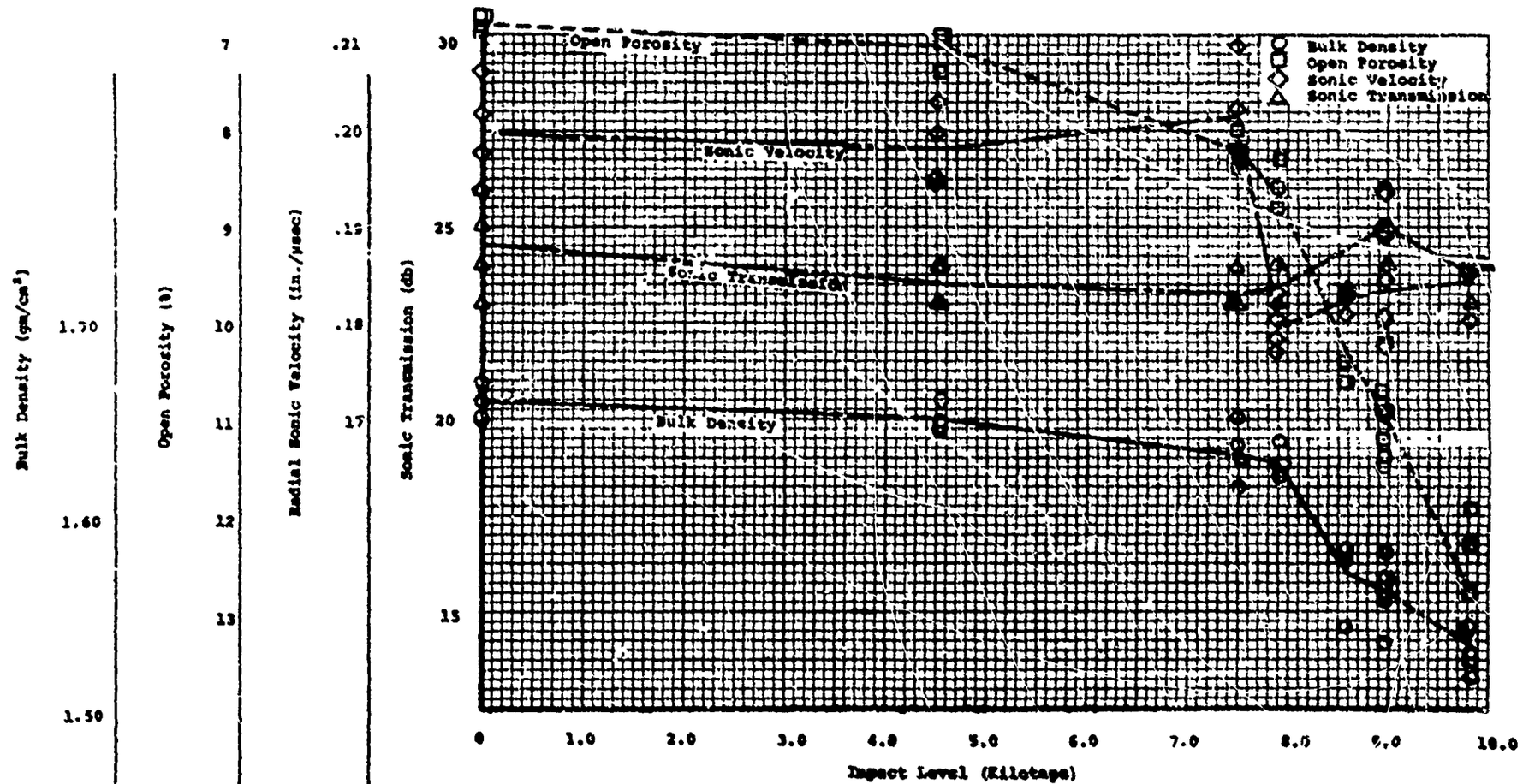


Figure 96. Results of Nondestructive Testing on Specimens from S.. ..uarts-Phenolic Impacted Area

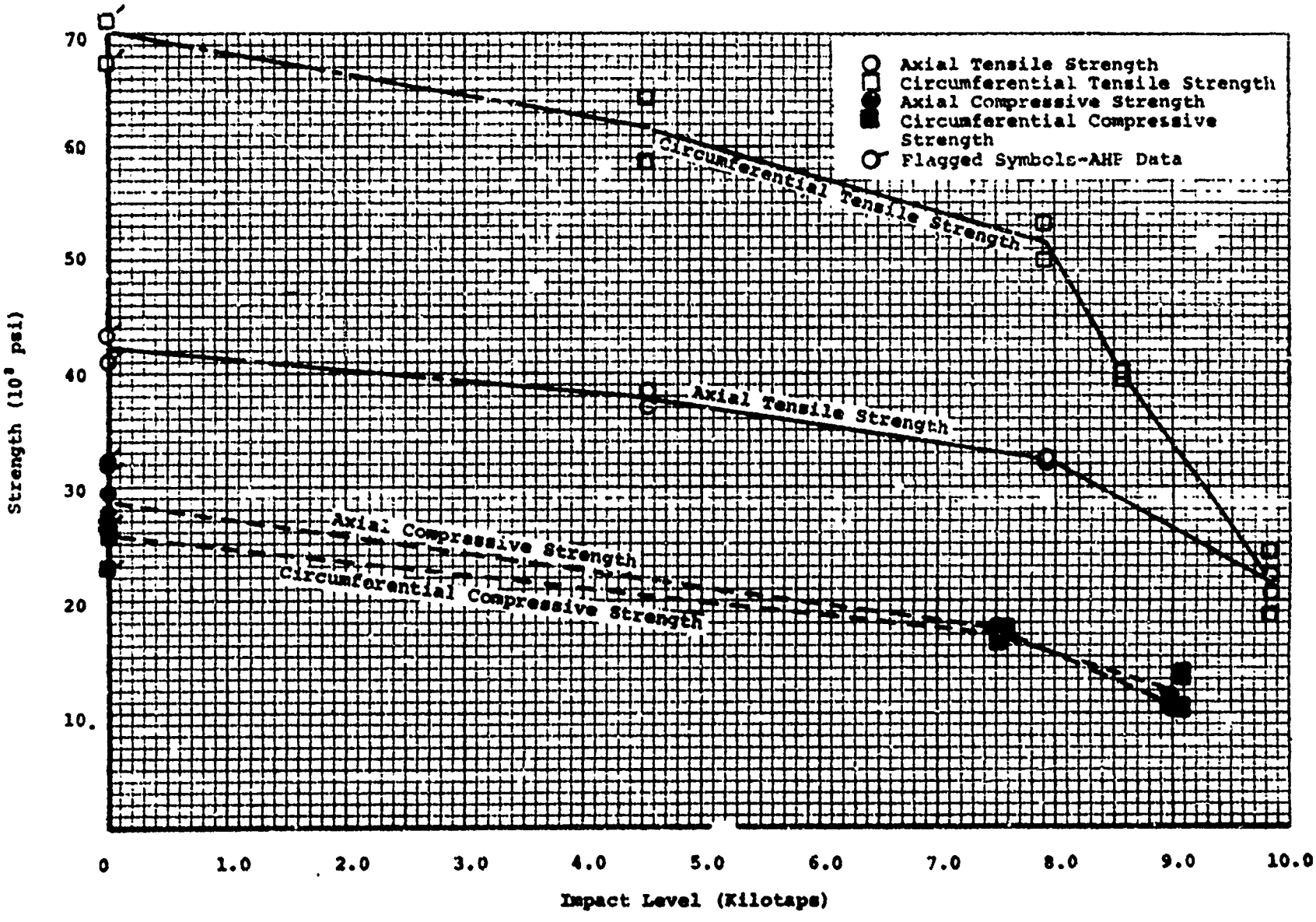


Figure 97. Tensile and Compressive Strength of Specimens from 3D Quartz-Phenolic Impacted Arcs

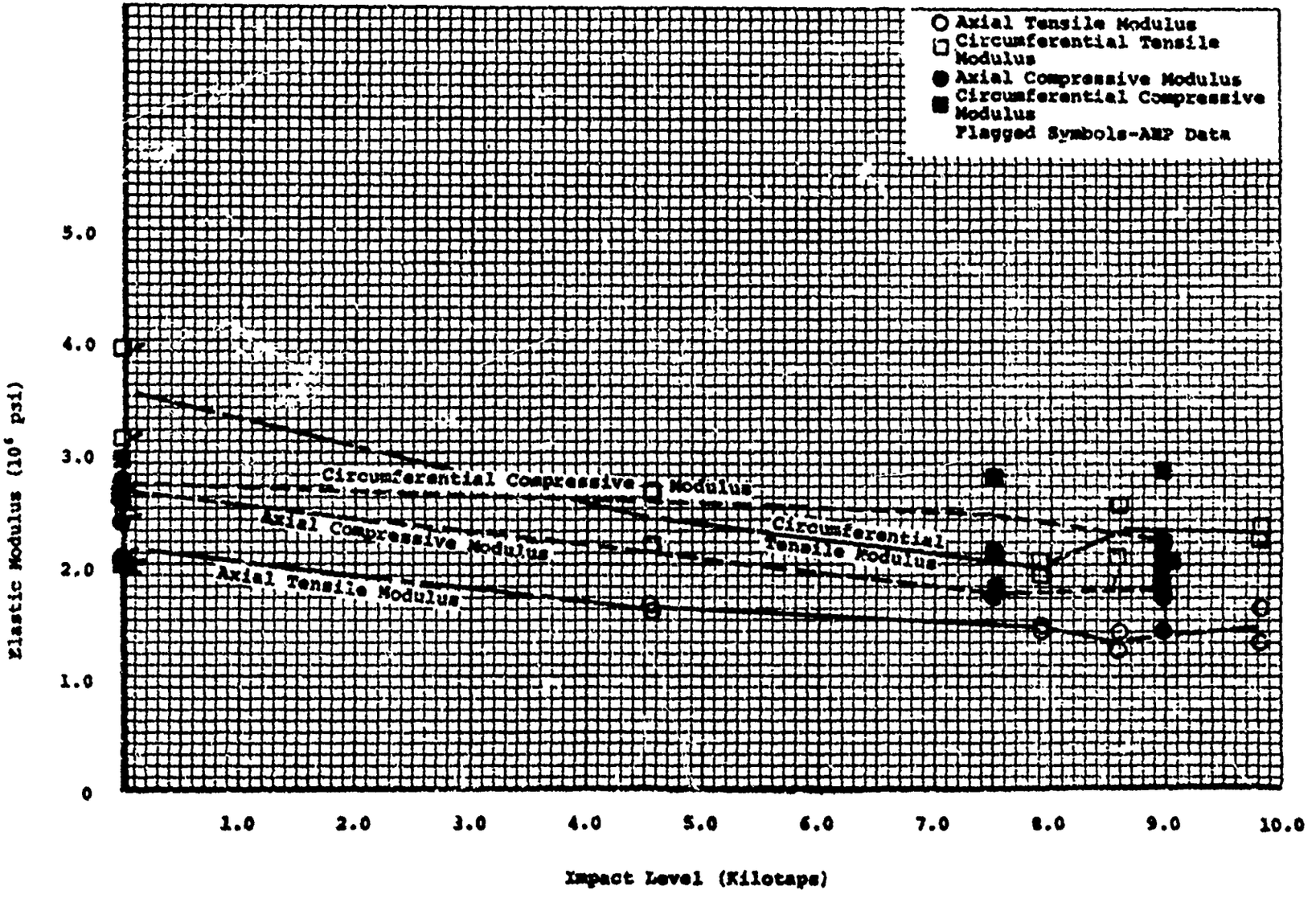
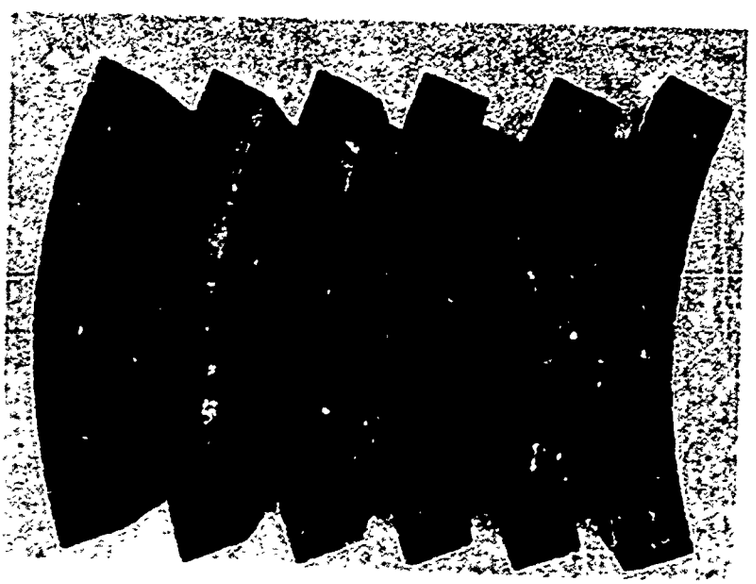


Figure 98. Tensile and Compressive Modulus of Specimens from 3D Quartz-Phenolic Impacted Area



Specimen No.	3	5	6	4	7	8
Impulse Level KT	4.09	4.69	5.18	6.06	6.51	6.54

Figure 99. Group Photographs (1X) Showing Impacted Edges of Arc Rings from Material 15

The percentage change in MOE, bulk density, sonic velocity, sonic attenuation* and thickness are defined as:

$$\text{Percentage change} = \frac{\text{Virgin value} - \text{Specimen value}}{\text{Virgin value}} \times 100\%$$

For Open Porosity: Specimen value (%) - Virgin value (%)

*By Definition:

$$\text{Percentage sonic attenuation} = \frac{\text{attenuation of specimen (db)} - \text{attenuation of virgin (db)}}{\text{attenuation of virgin (db)}} \times 100\%$$

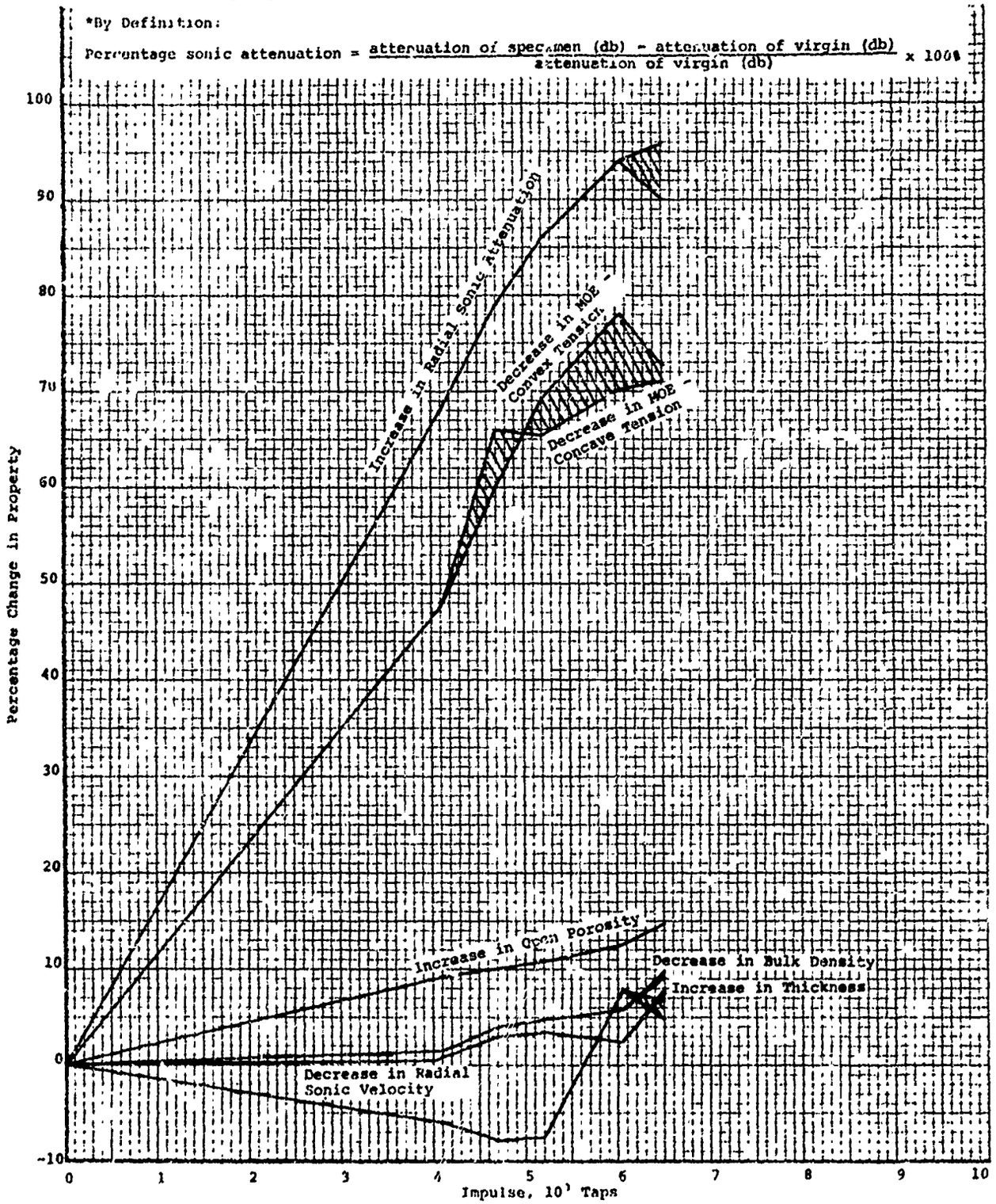


Figure 100. Percentage Changes in Flexural MOE and NDT Monitors versus Impulse in Taps for Arc Specimens from Material 15 (AVCO 3D COP)

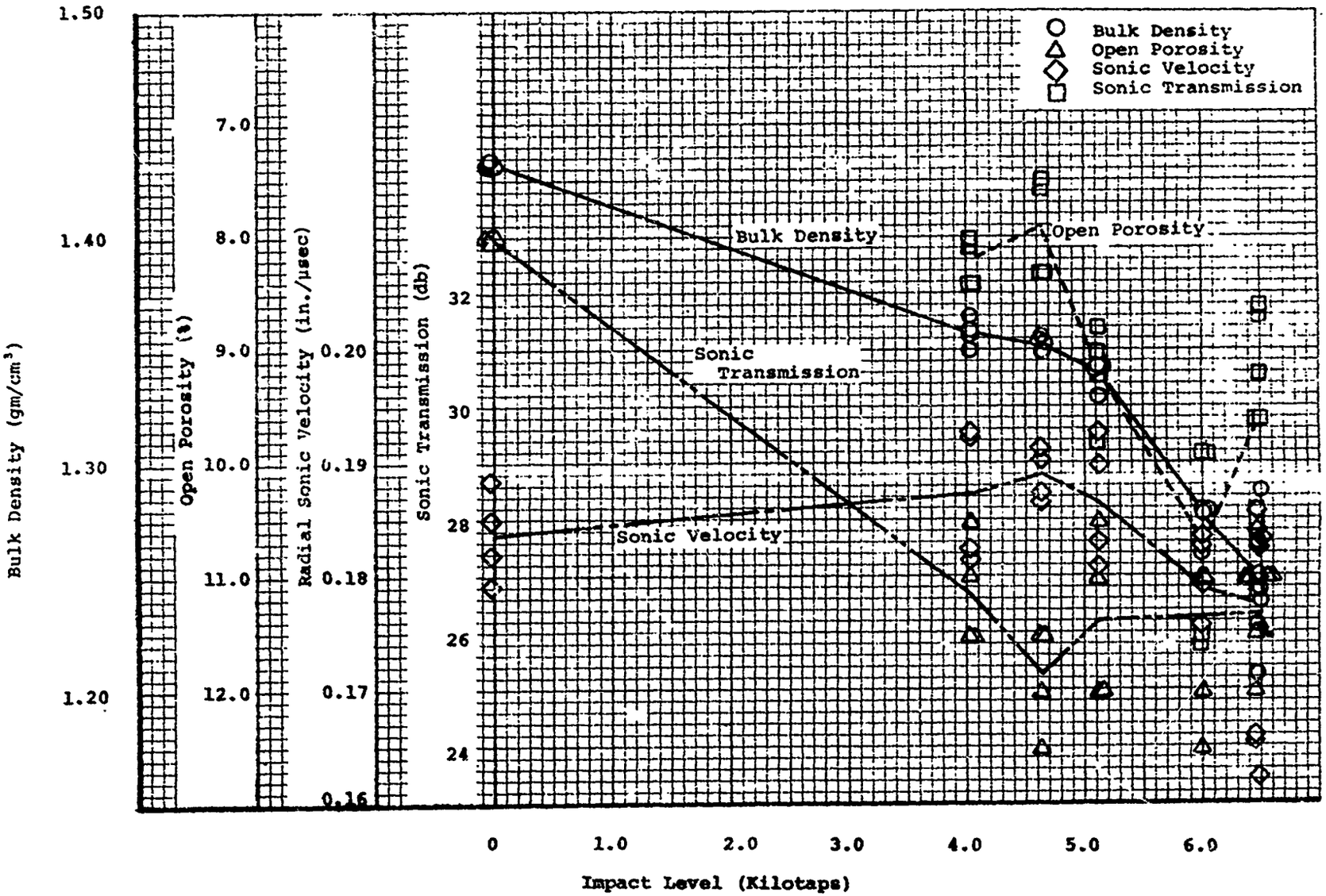


Figure 101. Results of Nondestructive Evaluations on Specimens from the 3D Carbon-Phenolic Portion, #15A, of 3DC/QP Impacted arcs

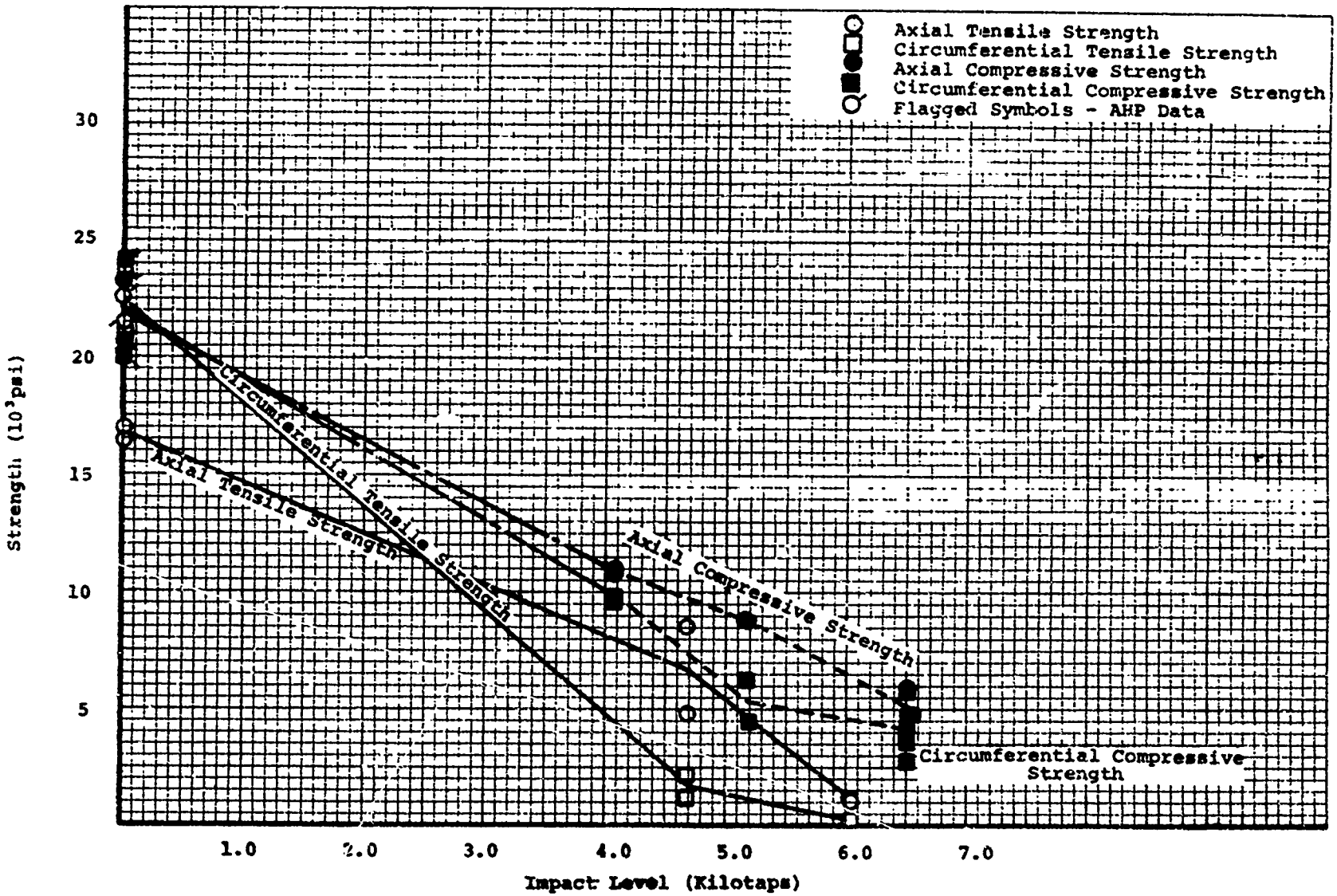


Figure 102. Tensile and Compressive Strength of Specimens from the 3D Carbon-Phenolic Portion, #15A, of 3DC/QP Impacted Arcs

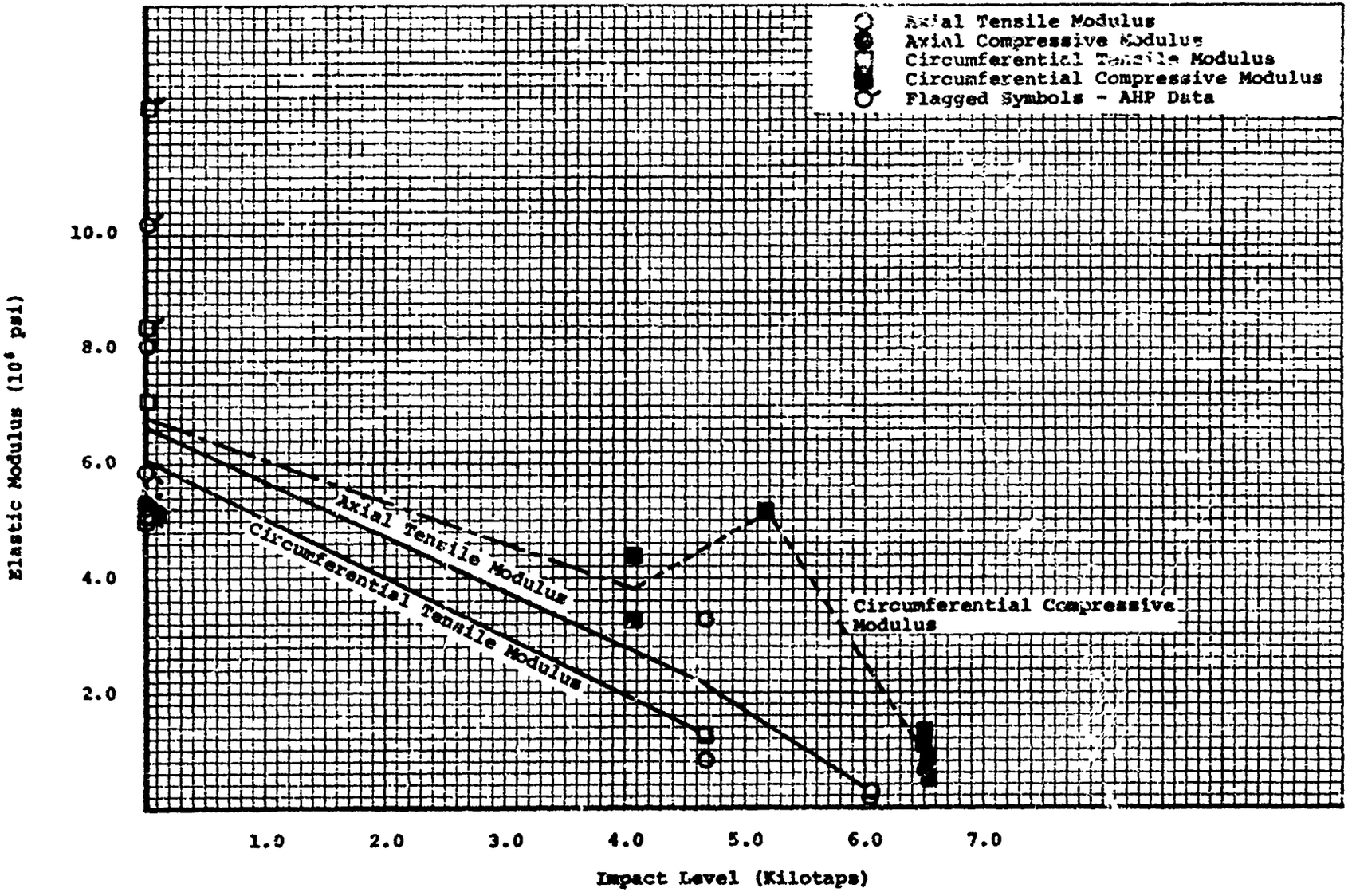


Figure 103. Tensile and Compressive Modulus of Specimens from the 3D Carbon-Phenolic Portion, #15A, of 3DC/QP Impacted Arcs

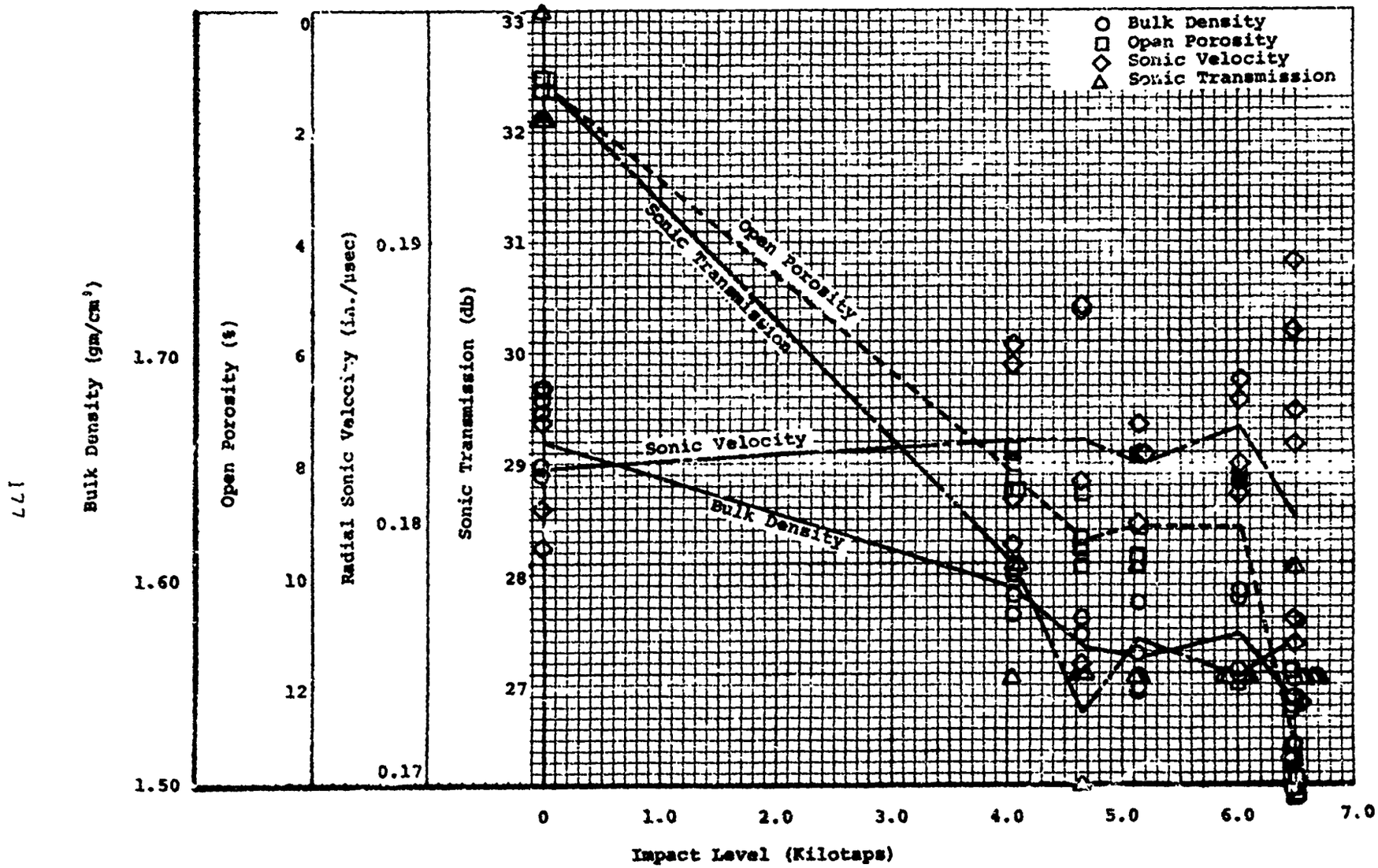


Figure 104. Results of Non Destructive Evaluations on Specimens from the 3D Quartz-Phenolic Portion #153, of 3DC/QP Impacted Arcs

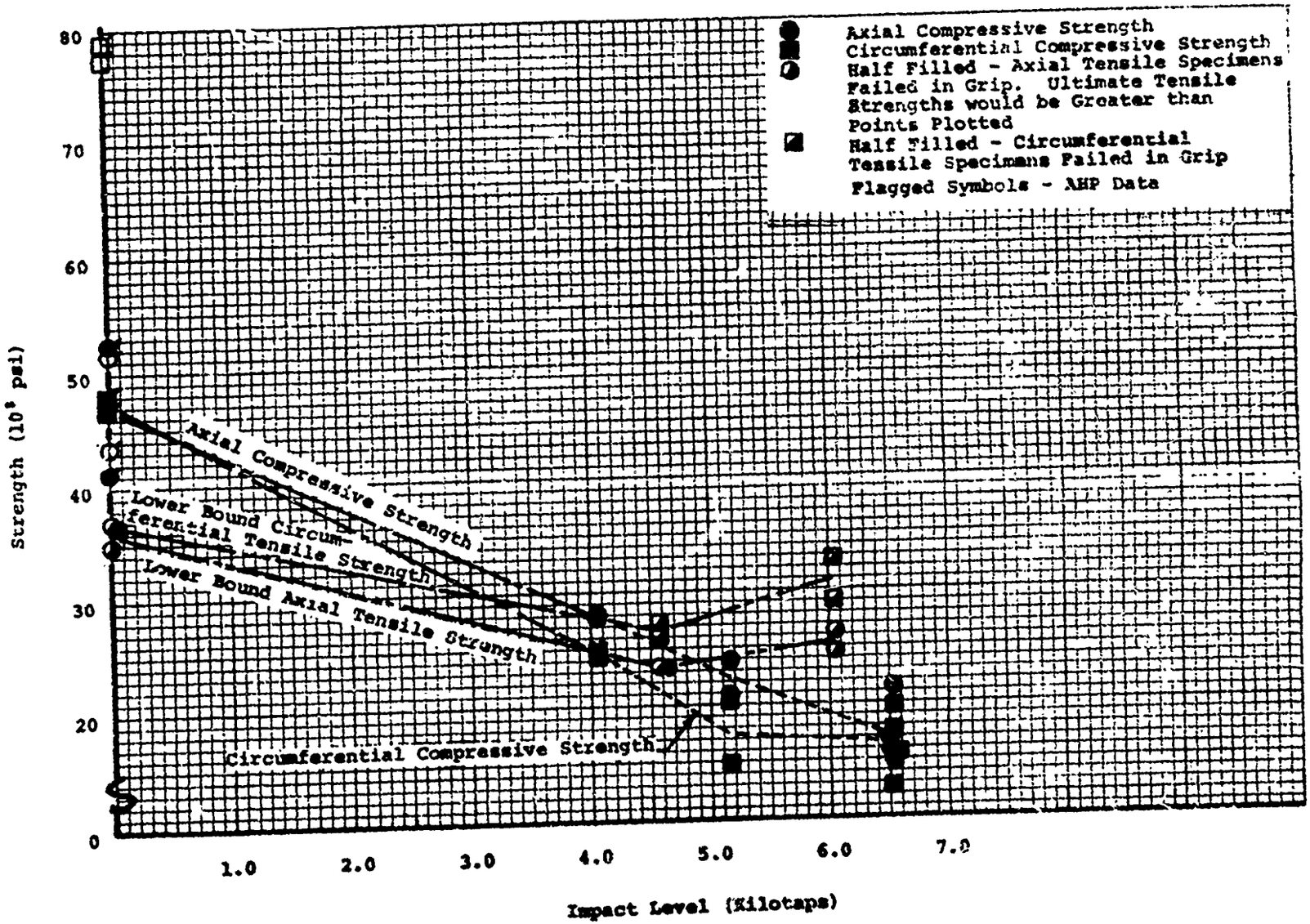


Figure 105. Tensile and Compressive Strength of the 3D Quartz-Phenolic Portion, #15B, of 3DC/QP Damaged Material

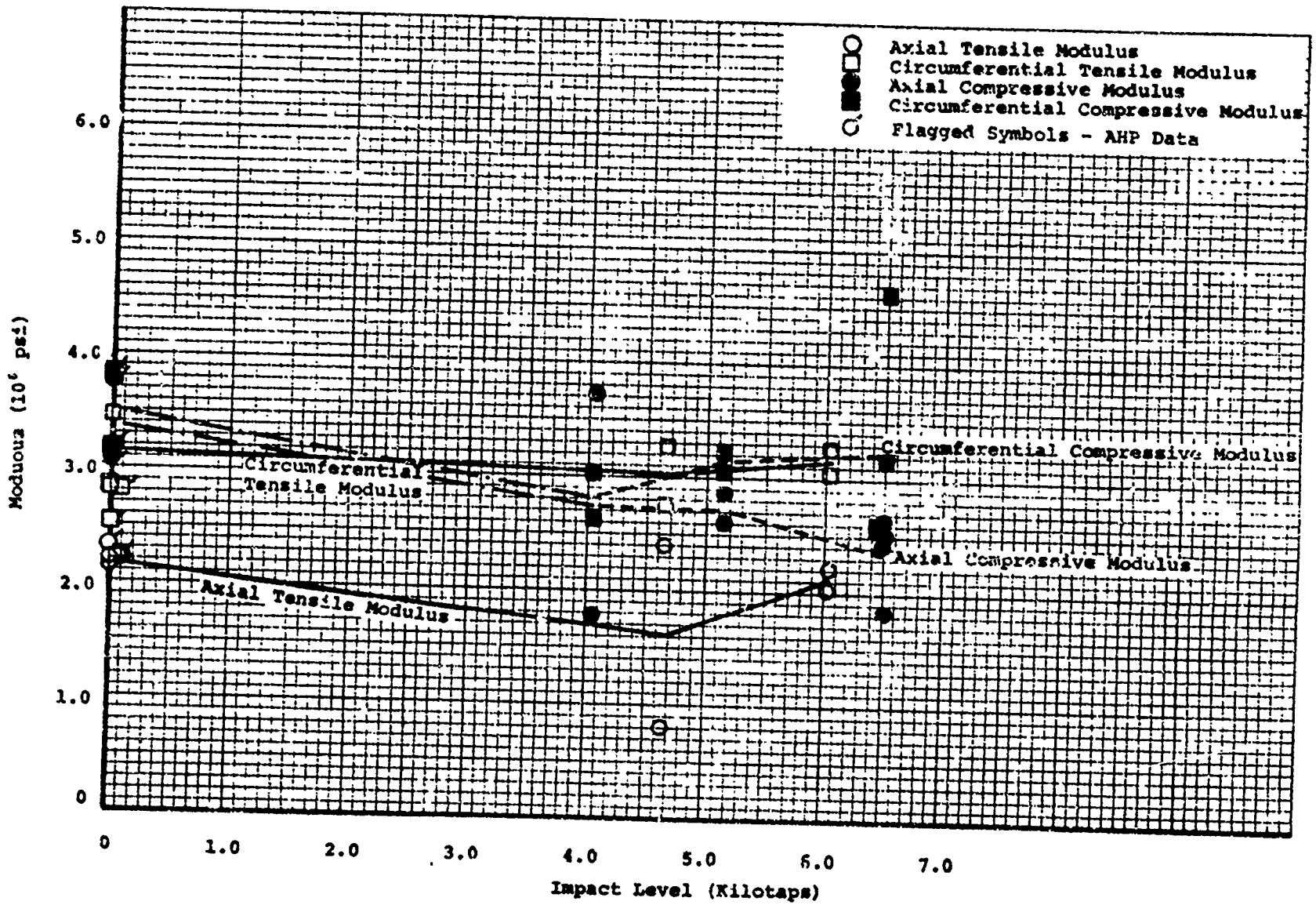


Figure 106. Tensile and Compressive Modulus of Specimens from the 3D Quartz-Phenolic Portion, #15B, of 3DC/QP Impacted Arcs



——Low-Absorptive Alignments
Indicating Structure Change.

Figure 107. Sketch of Radiographic Results Showing Structure Change Variations in AVCO 3DCC Arc 8-AR-7, 3.045 KT



——Low-Absorptive Alignments Indicating Structure Change

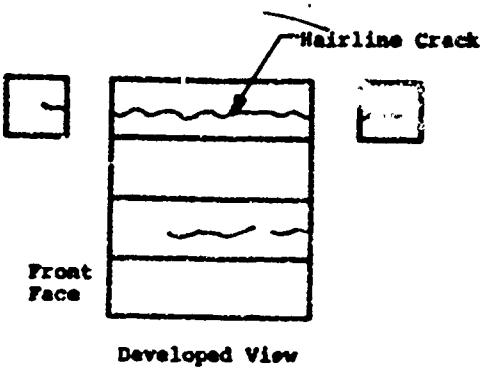
Figure 106. Sketch of Radiographic Results Showing Structure Change Variations in AVCO 3DCC Arc 8-AR-5



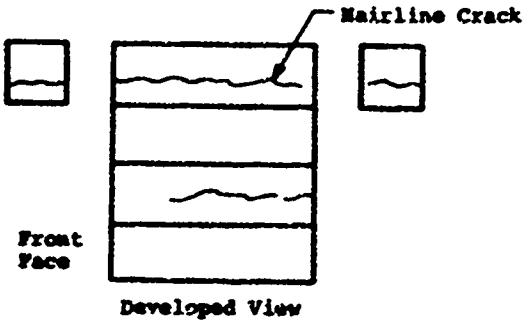
——Low-Absorptive Alignments
Indicating Structure Change

Figure 109. Sketch of Radiographic Results Showing Structure Change Variations in AVCO 3DCC Arc 8-AR-1, 5.39 ET

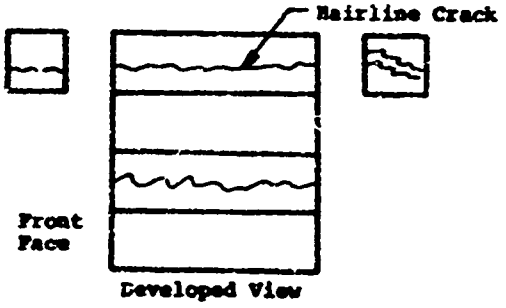
12-F-10-C1A



12-F-10-C2A



12-F-10-C3A



12-F-10-C4A

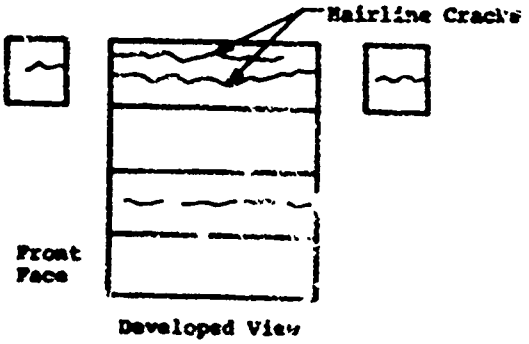
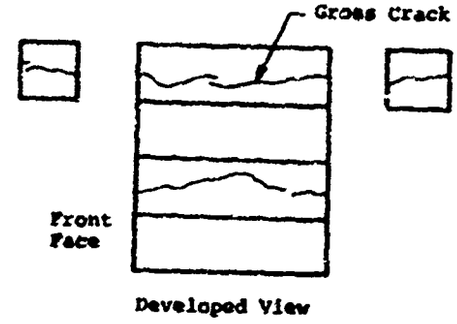
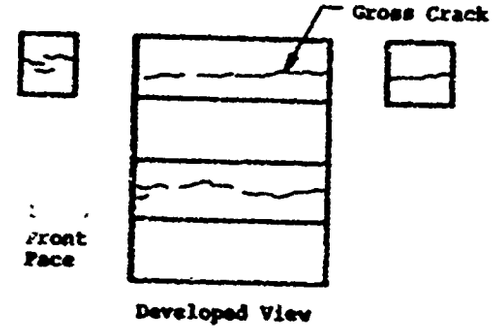


Figure 110. Sketch Showing Visual Inspection Results on Specimen Blanks from Felt CC Plate 12-F-10

12-F-11-C1A



12-F-11-C2A



12-F-11-C3A Similar to 12-F-11-C2A above

12-F-11-C4A

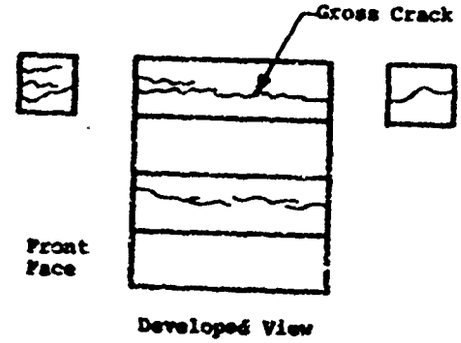
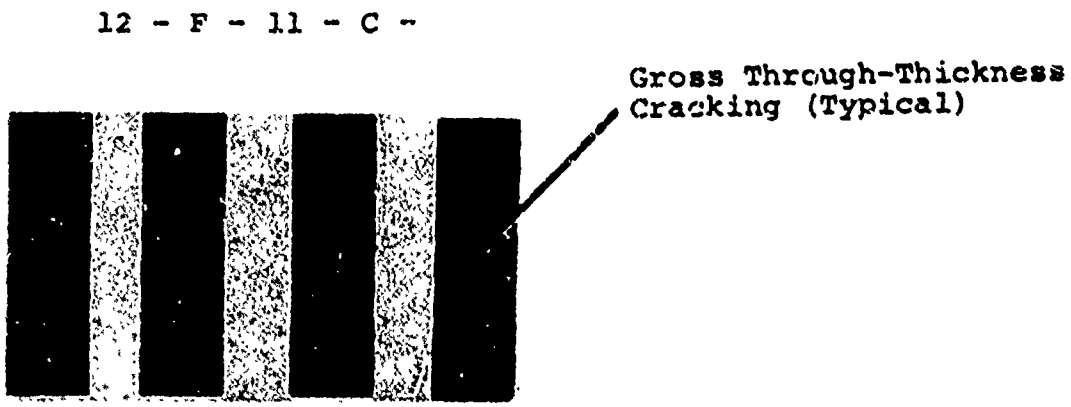


Figure 111. Sketch Showing Visual Inspection Results on Specimen Blanks from Pelt CC Plate 12-F-11, 4.14 KT



(Positive Print)

Figure 112. Radiograph in Circumferential Direction of Specimens from Felt CC Plate 12-F-11, 4.14 KT

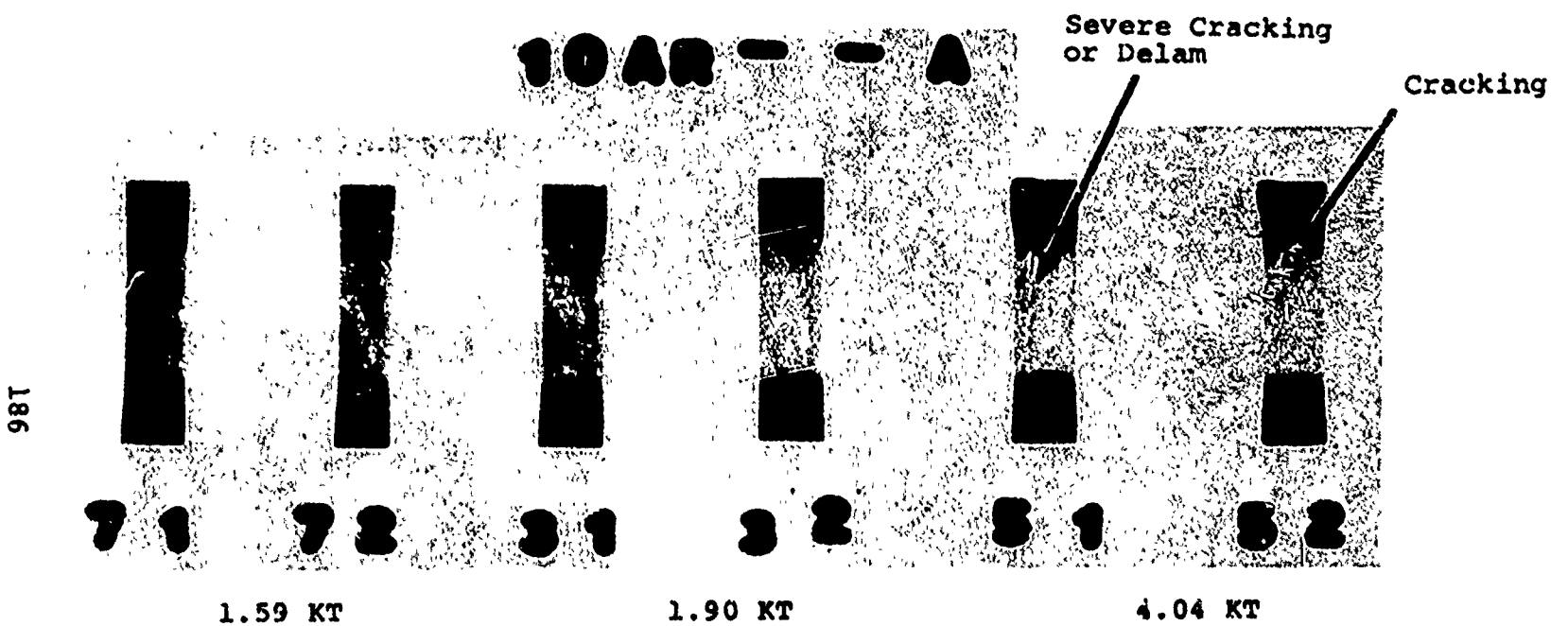


Figure 113. Radiograph of Axial Compressive Specimens from R6300 Impacted Arcs

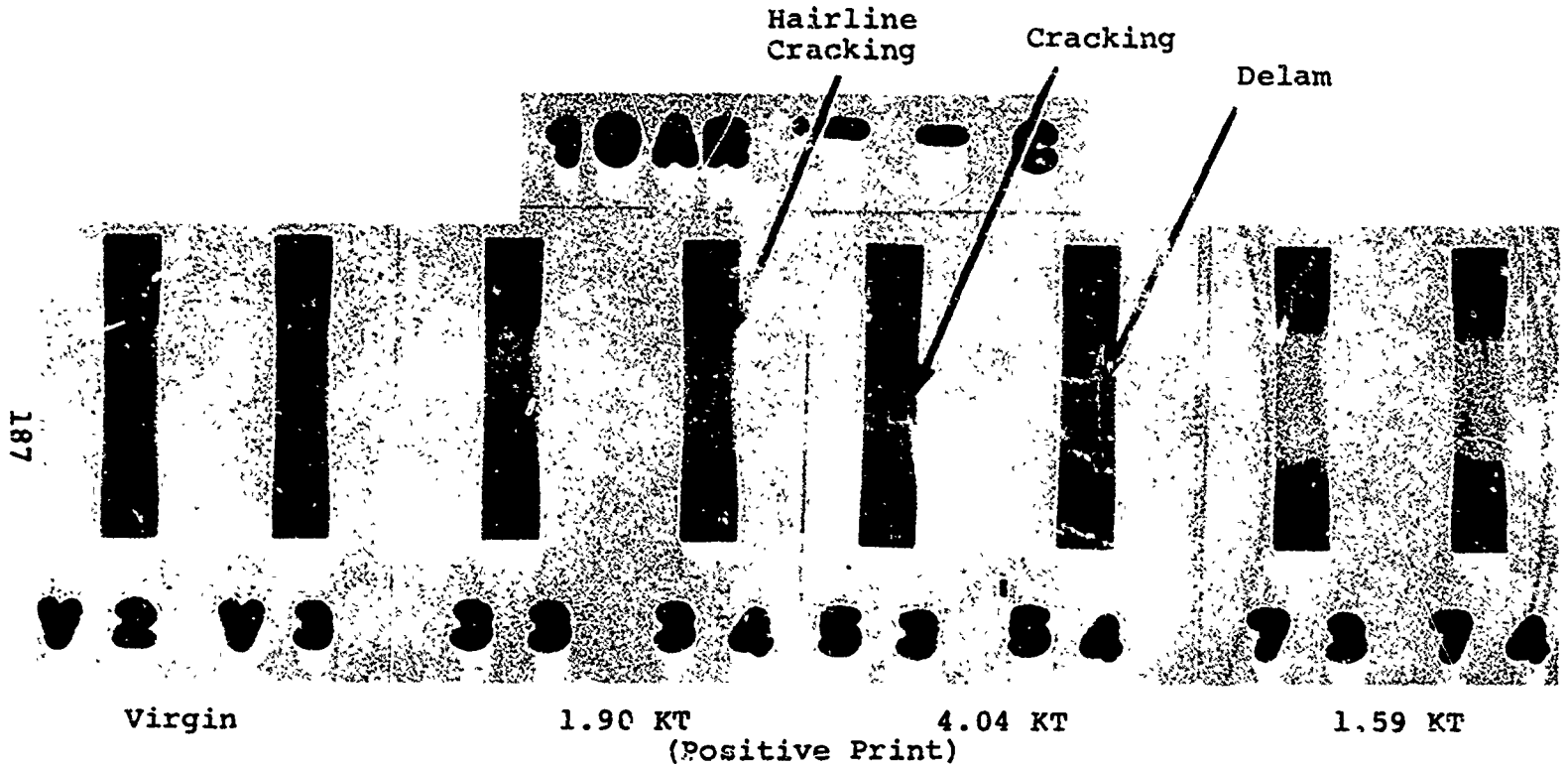


Figure 114. Radiograph of Circumferential Compressive Specimens from R6300 Impacted Arcs

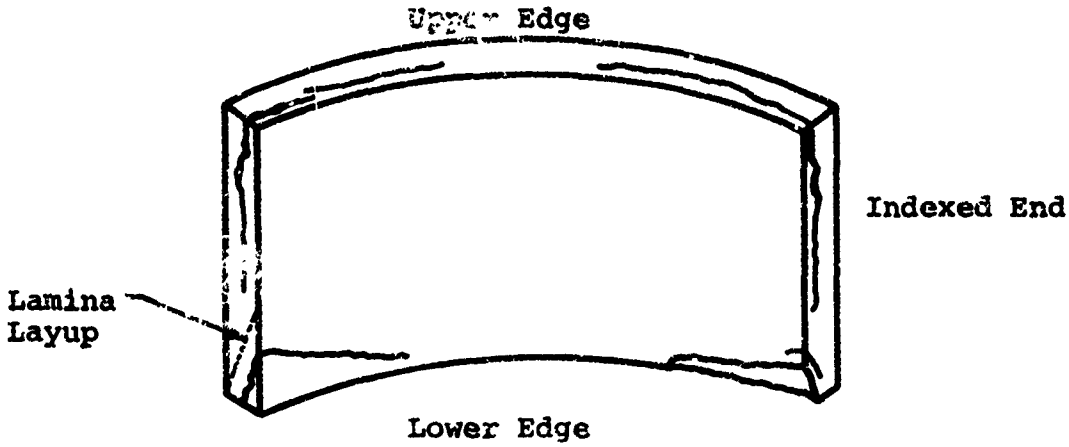
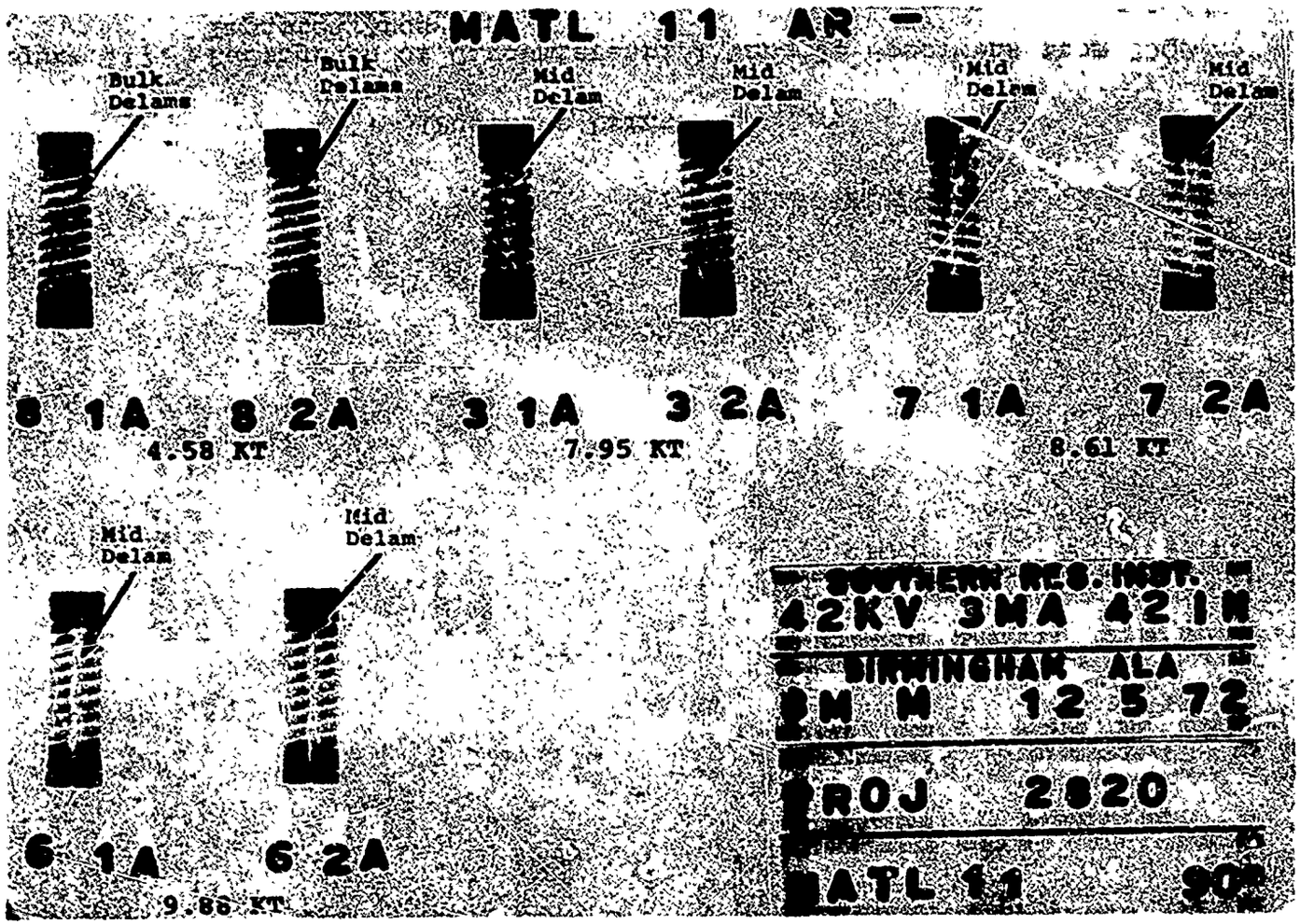
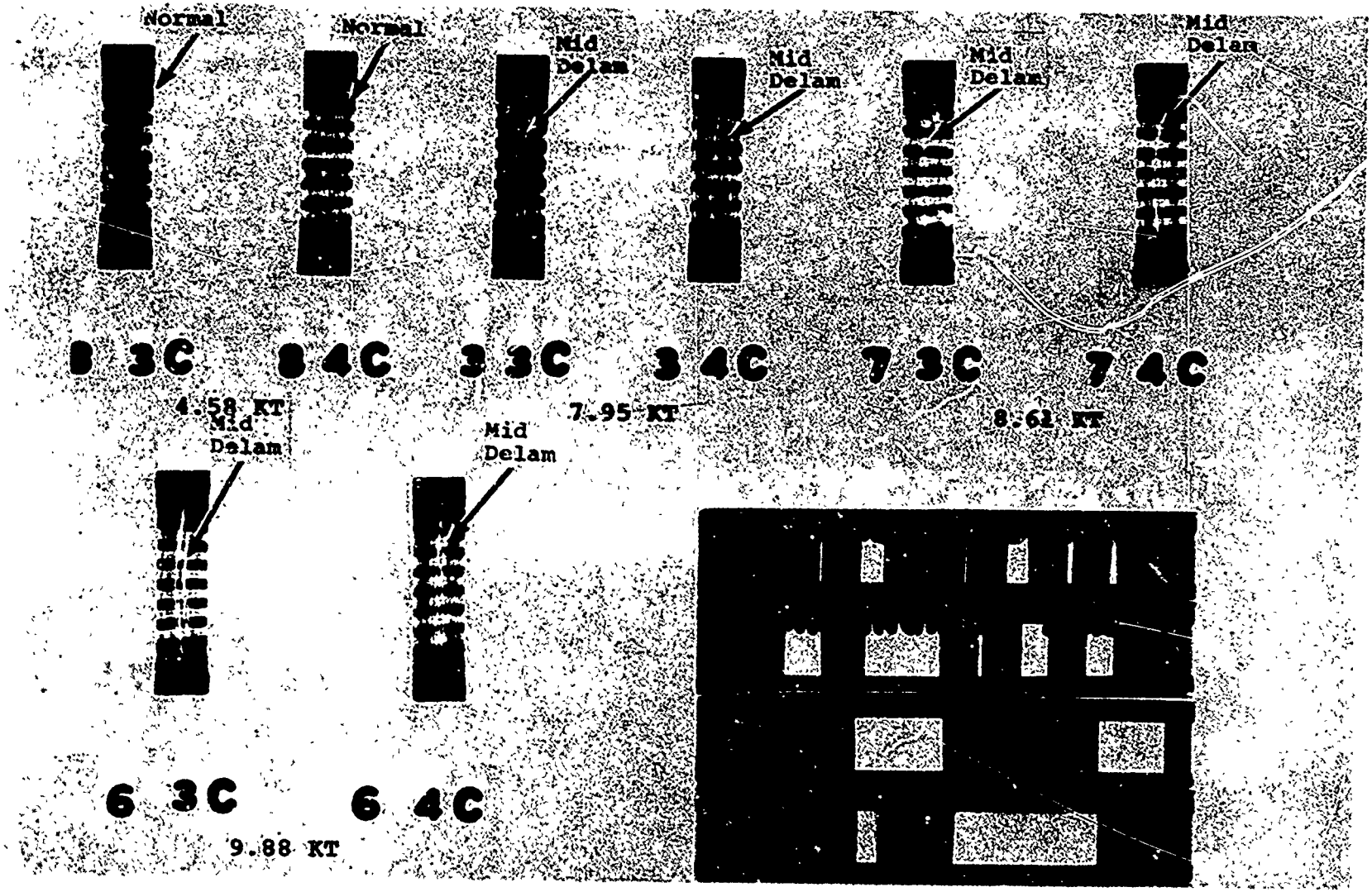


Figure 115. Sketch of Structure Change in Arc 10-AR-5



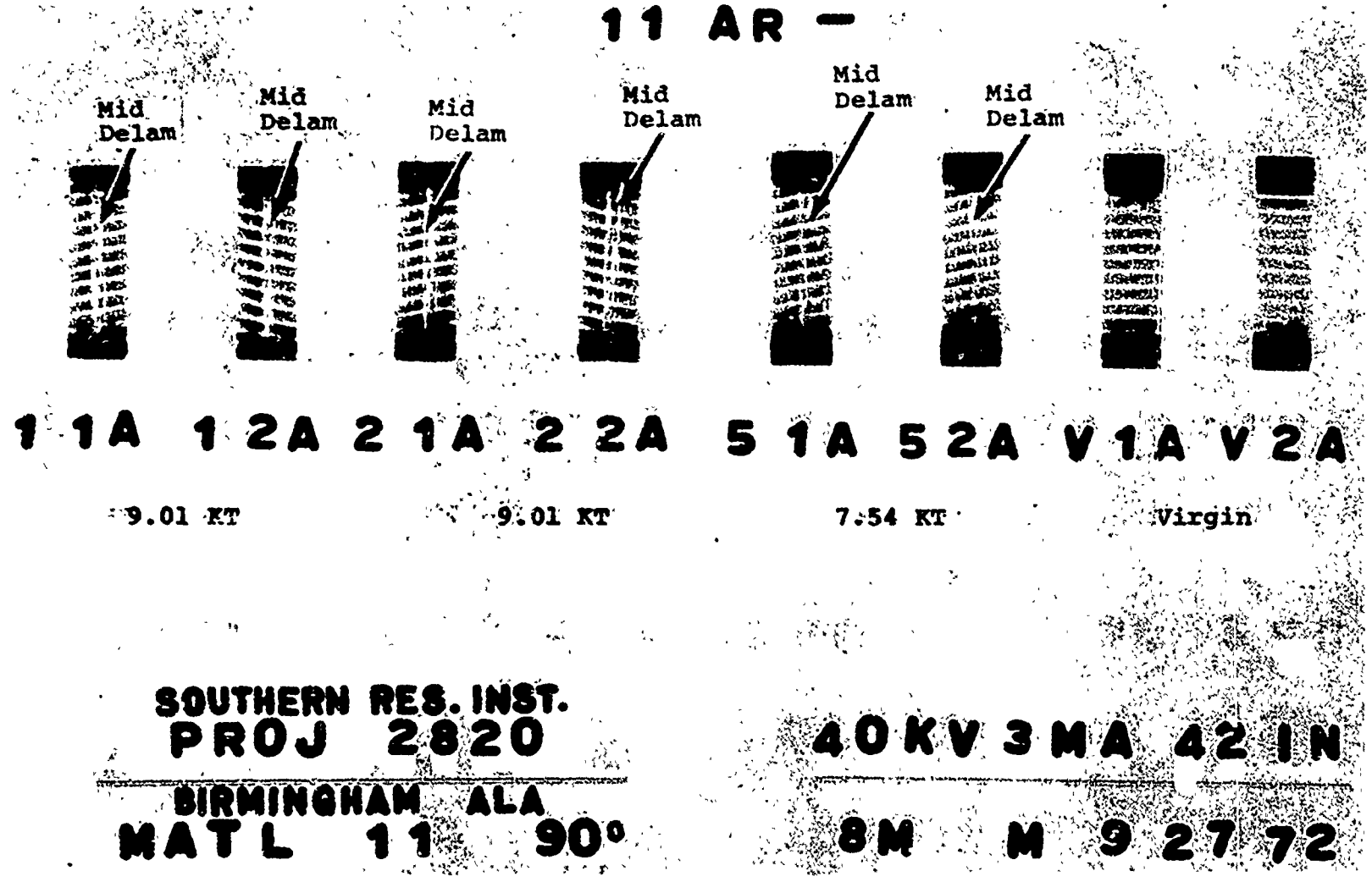
(Positive Print)

Figure 116. Radiograph of Axial Tensile Specimens from 3DQP Impacted Arcs



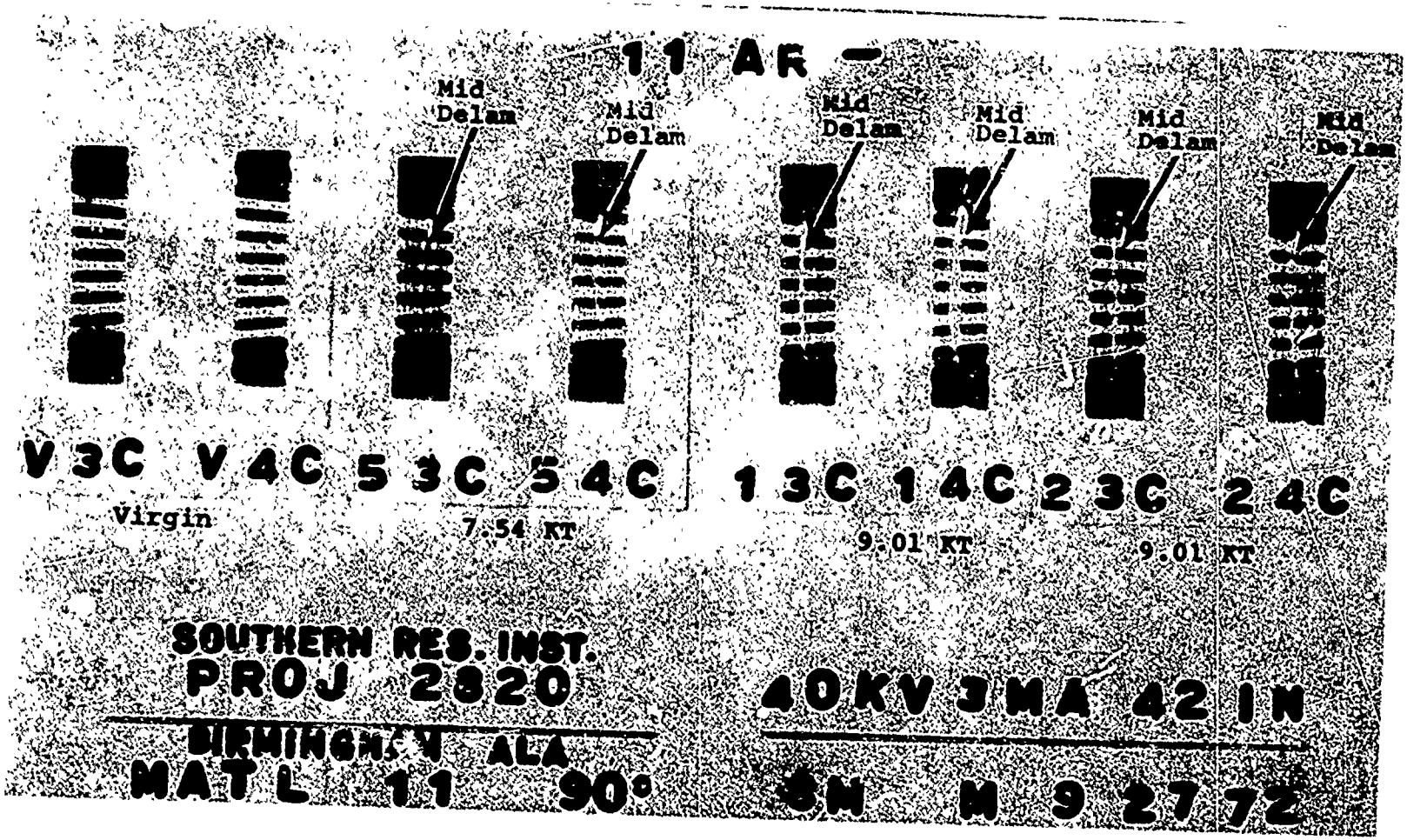
(Positive Print)

Figure 117. Radiograph of Circumferential Tensile Specimens from 3DQP Impacted Arcs



(Positive Print)

Figure 118. Radiograph of Axial Compressive Specimens from 3DQP Impacted Arcs



(Positive Print)

Figure 119. Radiograph of Circumferential Compressive Specimens from 3DQP Impacted Arcs

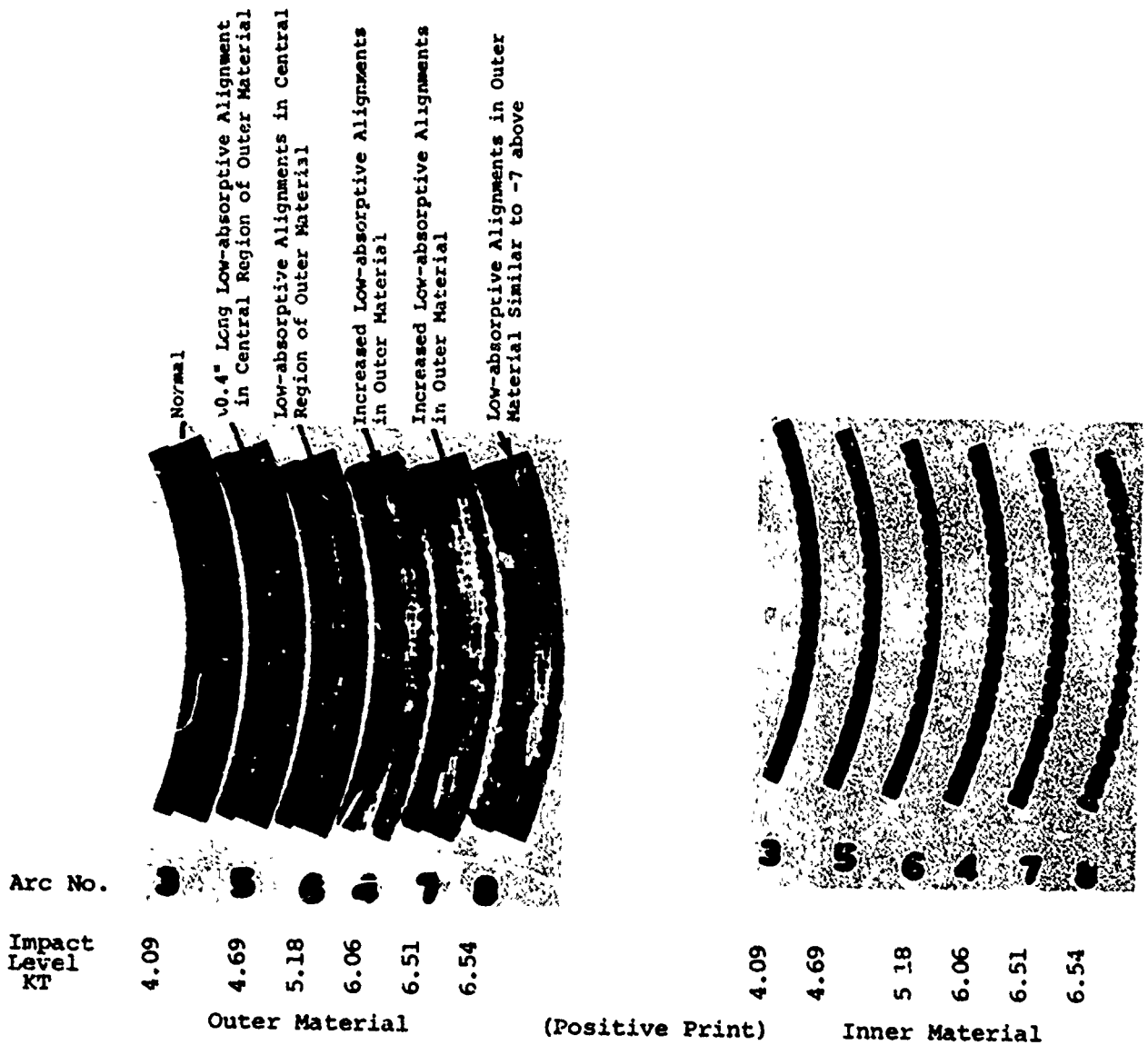


Figure 120. Group Radiograph of Bulk Arcs of Impacted AVCO 3DC/QP Material

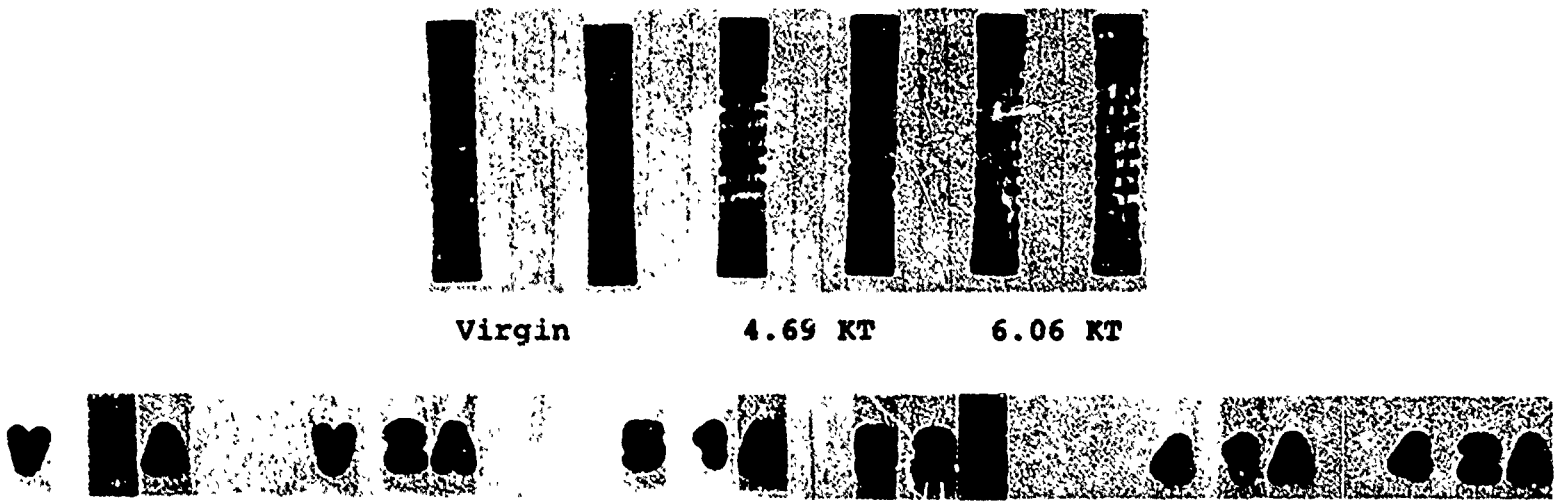
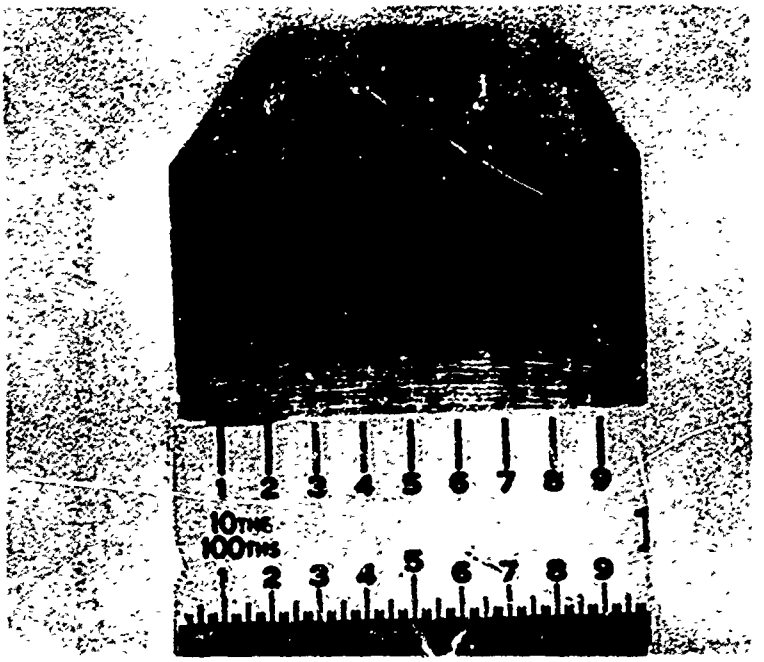


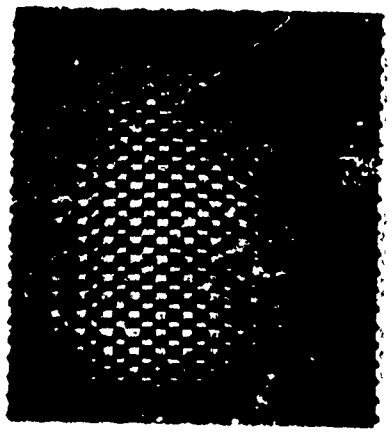
Figure 121. Radiograph of Axial Tensile Specimens from the Carbon-Phenolic Portion, #15A, of 3DC/QP Impacted Arcs



(2X)

Axial View

Figure 126. Photograph Showing Typical AHP AVCO 3DC/QP



Radial Direction



Axial Direction

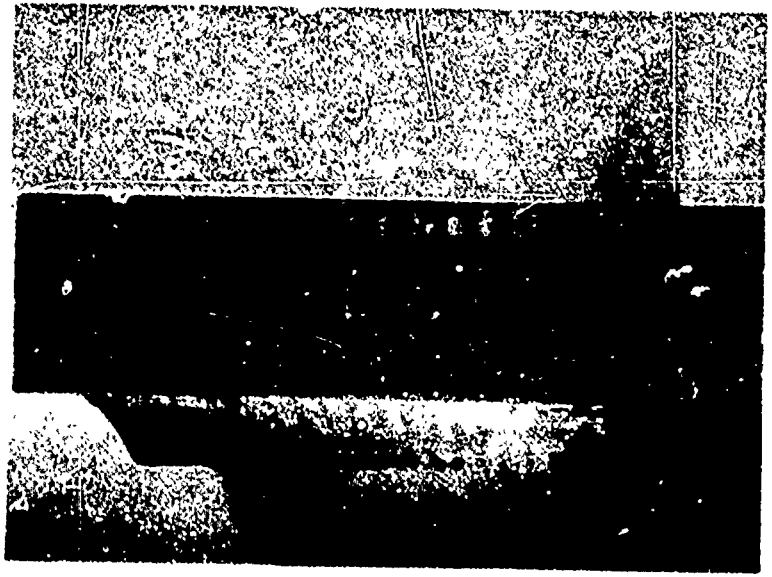
(Positive Prints)

Figure 127. Typical AVCO 3DC/QP Structure Revealed by Radiography



(2X)

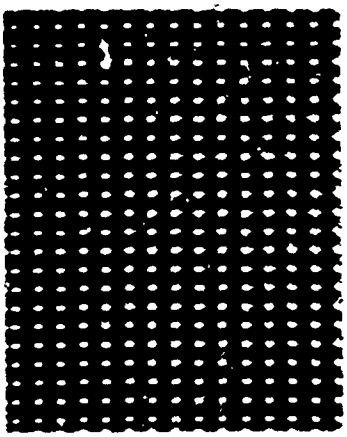
Axial View



(2X)

Circumferential View

Figure 128. Photographs Showing Typical AVCO 3DCP



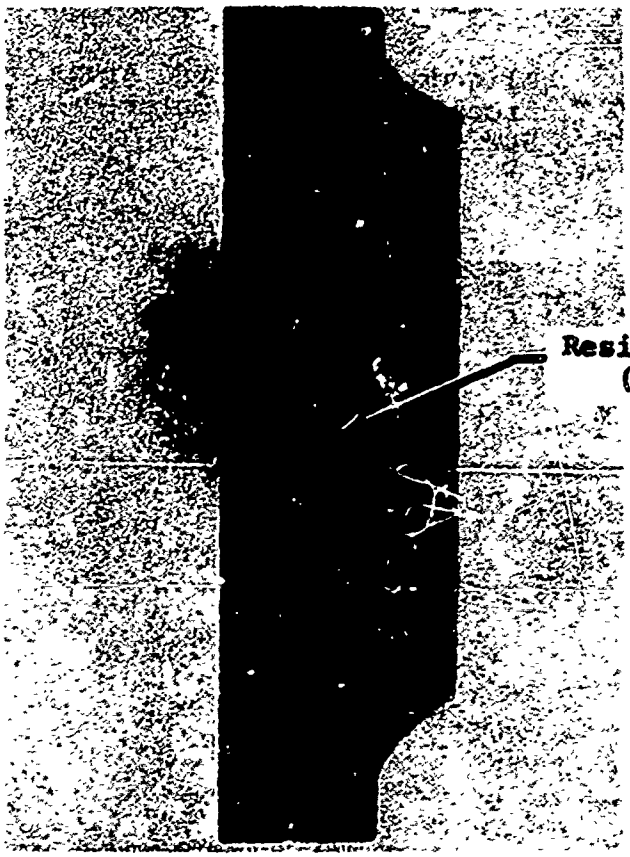
Radial Direction



Axial Direction

Positive Print

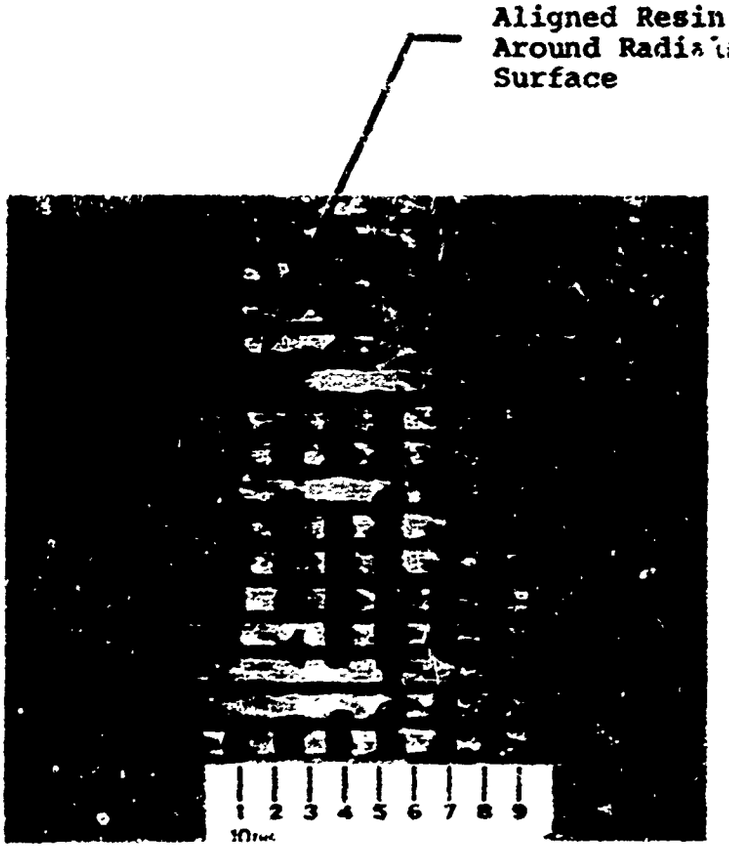
Figure 129. Typical AVCO 3DCP Structure Revealed by Radiography



(2X)

Circumferential View

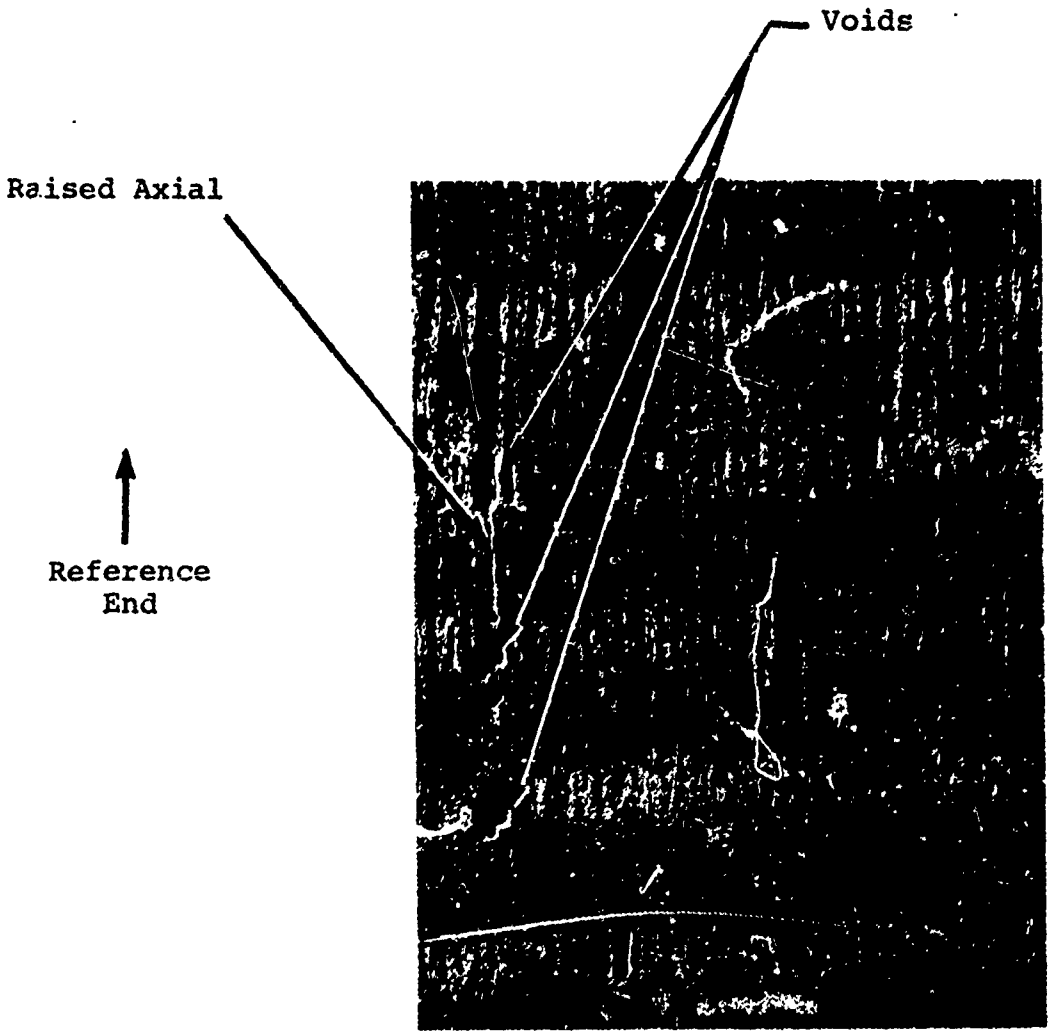
Figure 130. Photograph Showing Resin Rich Areas in AVCO 3DCP



(2X)

Radial View of Outer Surface

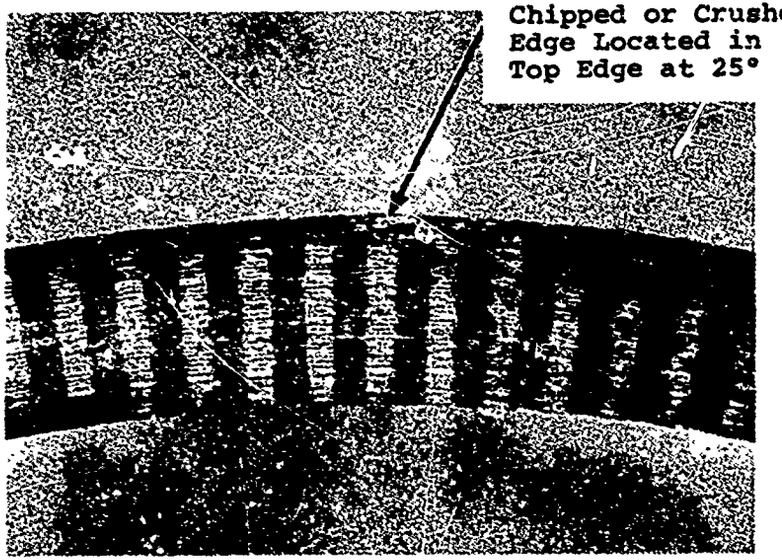
Figure 131. Photograph Showing Resin Starved Areas Around Radials in Outer Surface of AVCO 3DCP



(10X)

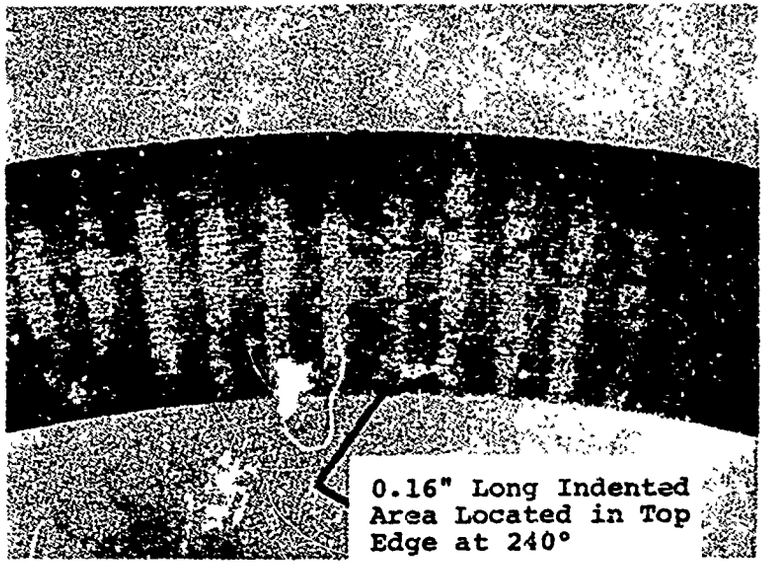
Circumferential View
of C Edge

Figure 132. Photograph Showing Anomaly in AVCO 3DCP Arc 7 of Ring #6



(2.6X)

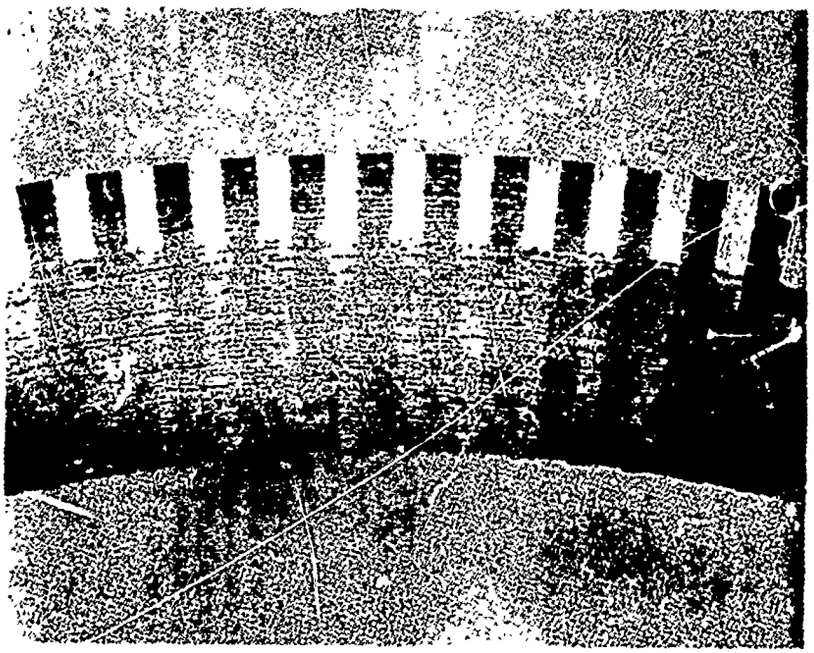
Ring #2



(2.9X)

Ring #8

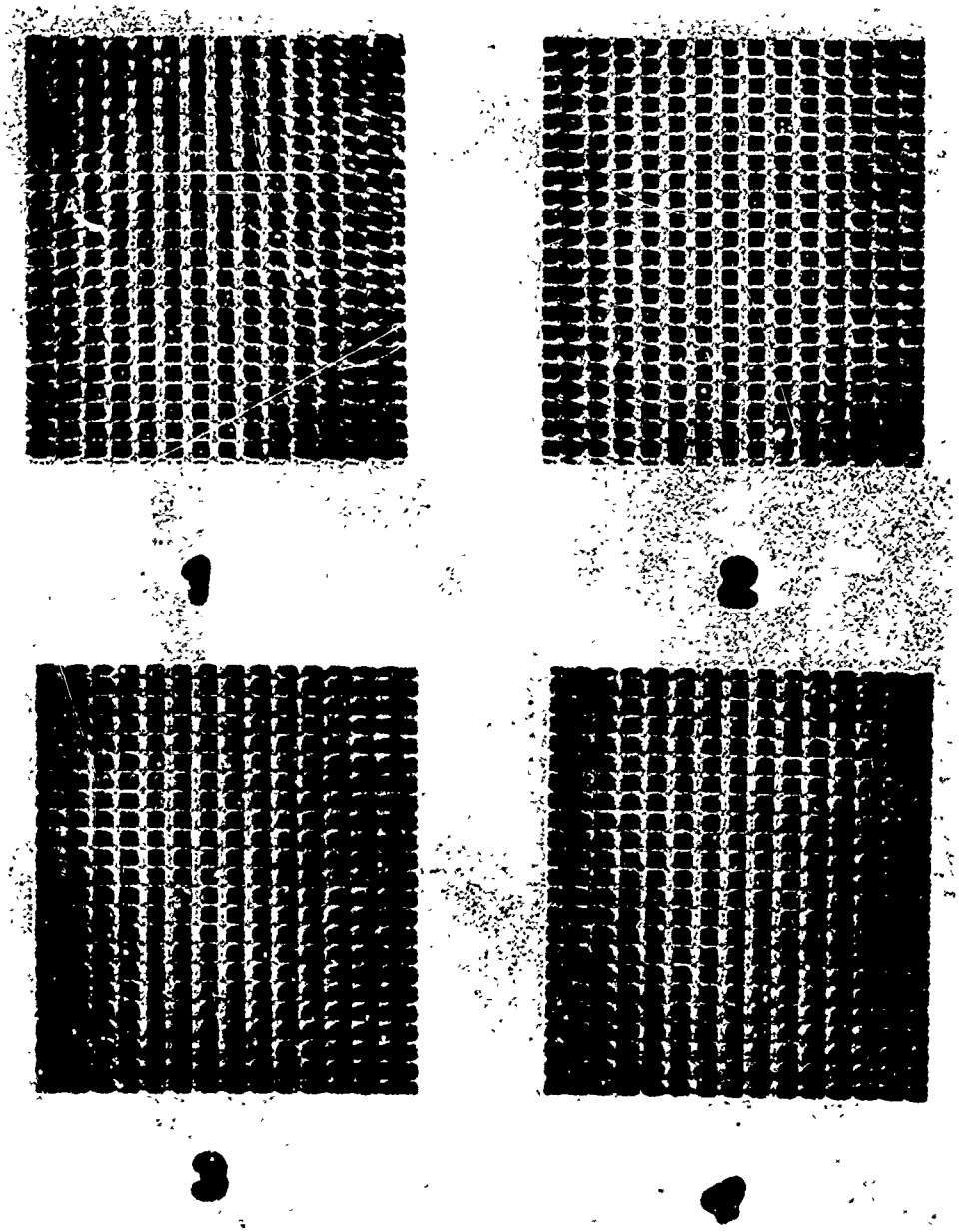
Figure 133. Photographs Showing Locally Damaged Areas in AVCO 3DCP Rings #2 and #8



(2.6X)

Axial View

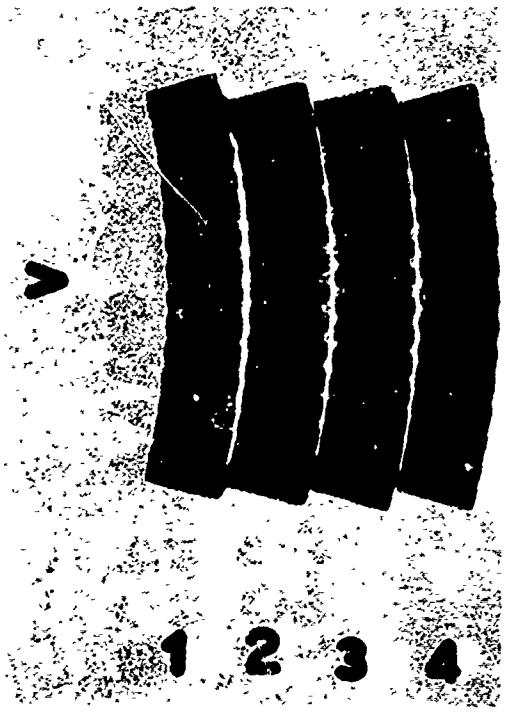
Figure 134. Photograph Showing High Porosity in AVCO 3DCP Ring #10



Radial Direction

Positive Print

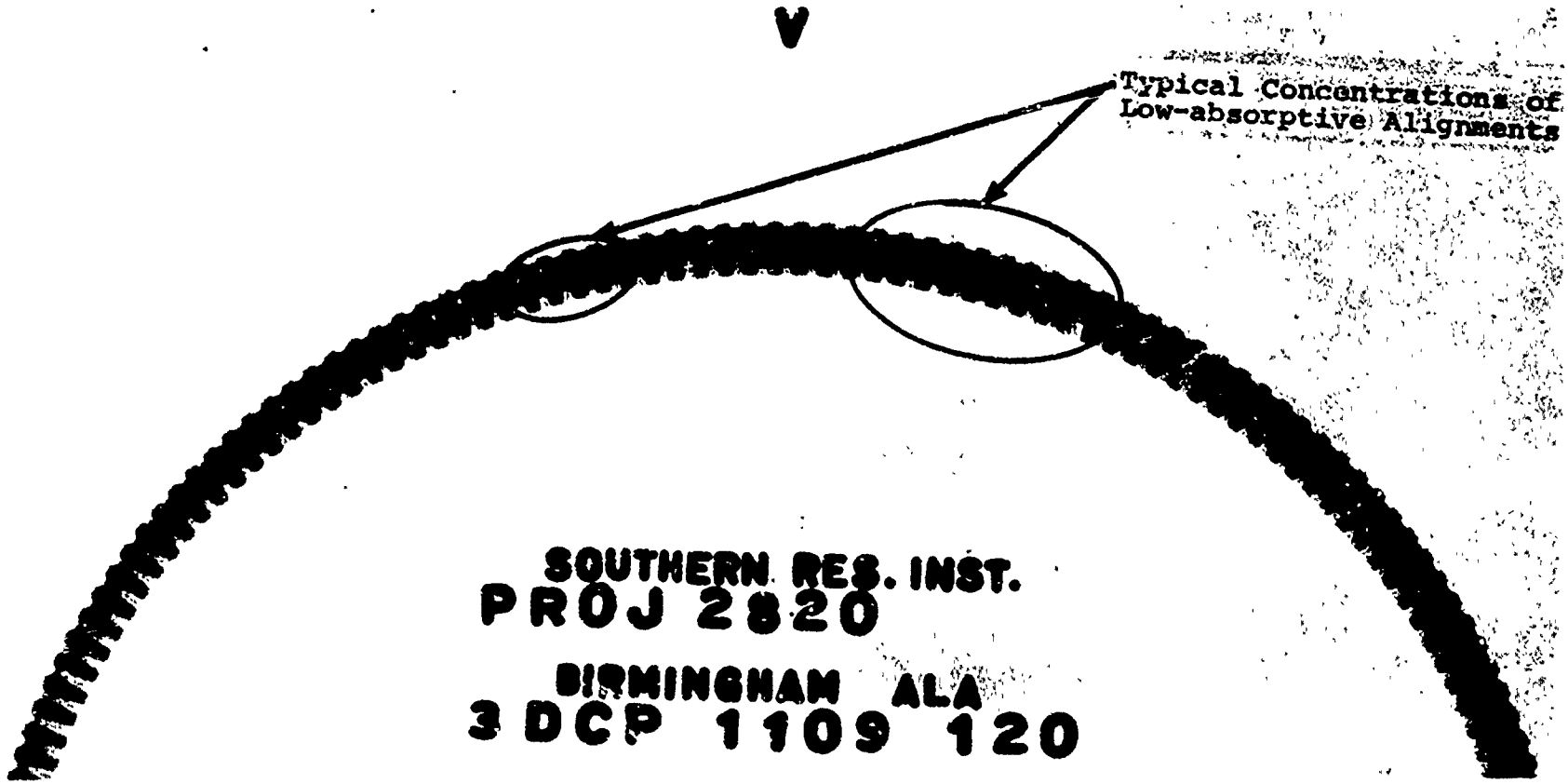
Figure 135a. Typical AVCO 3DCP (T400) Structure Revealed by Radiography



Axial Direction

Positive Print

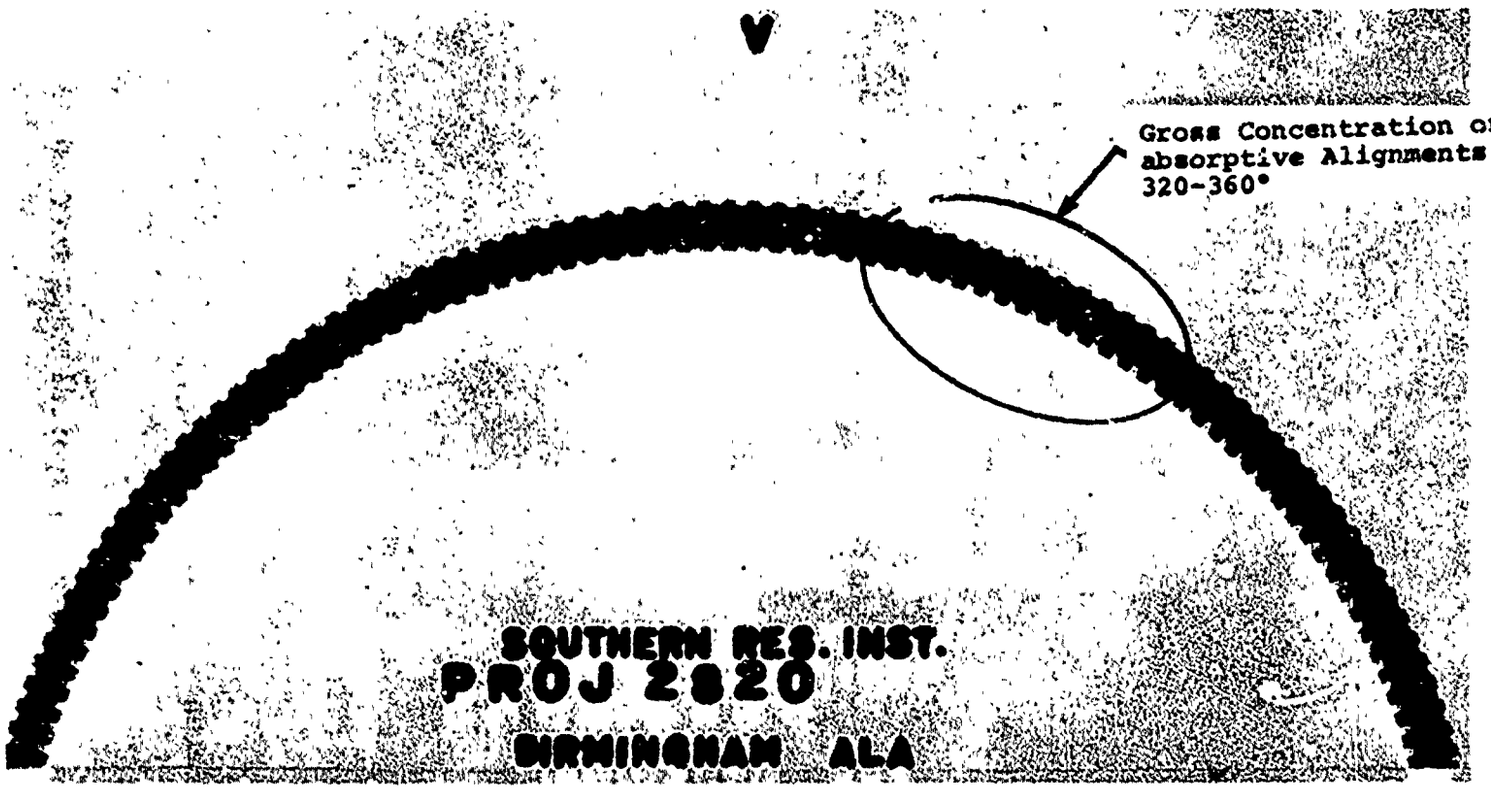
Figure 135b.



Positive Print

Axial Direction

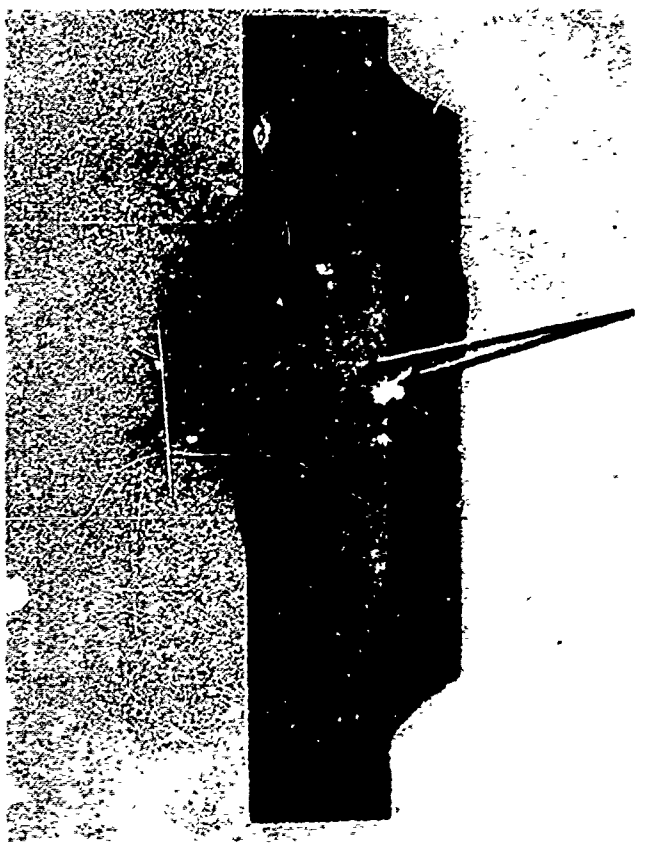
Figure 136. Radiograph Showing Typical Concentration Low-Absorptive Alignments in AVCO 3DCP (T400)



Positive Print

Axial Direction

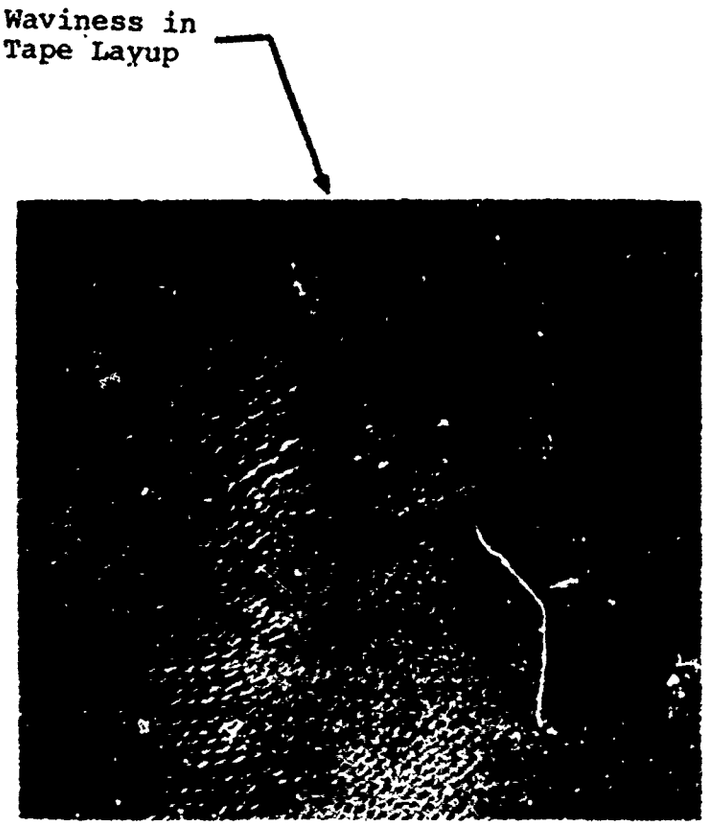
Figure 137. Radiography Showing Gross Circumferential Low-Absorptive Alignments in AVCO 3DCP (T400) Ring #4



(1.85X)

Circumferential View

Figure 138. Photograph Showing Typical AHCA AVCO R6300



(1.82X)

Radial View of Outer Surface

Figure 139. Photograph Showing Occasional Visual Waviness in Tape Layup on Inner and Outer Surfaces of AVCO R6300



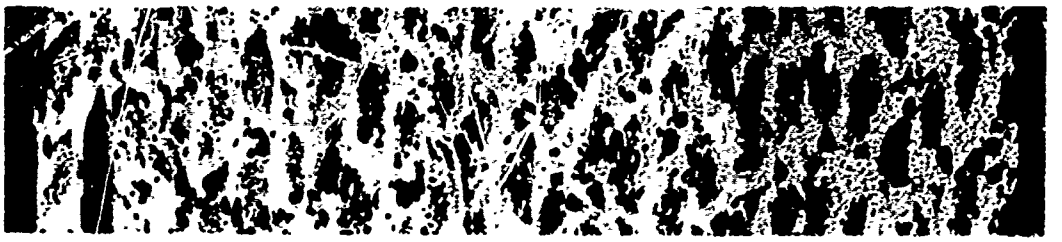
Radial Direction

Circumferential Direction

Positive Prints

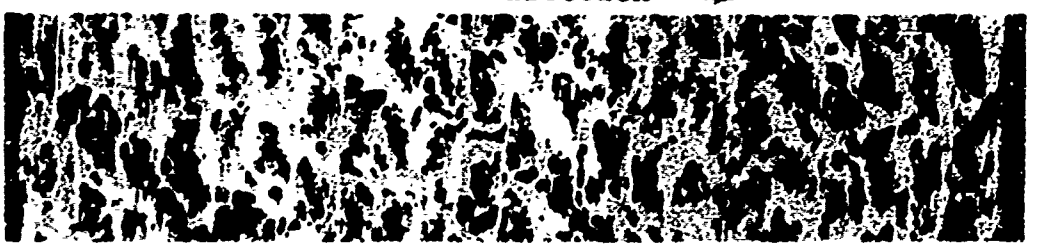
Figure 140. Typical AVCO R6300 Structure Revealed by Radiography

Radial Direction ⟶



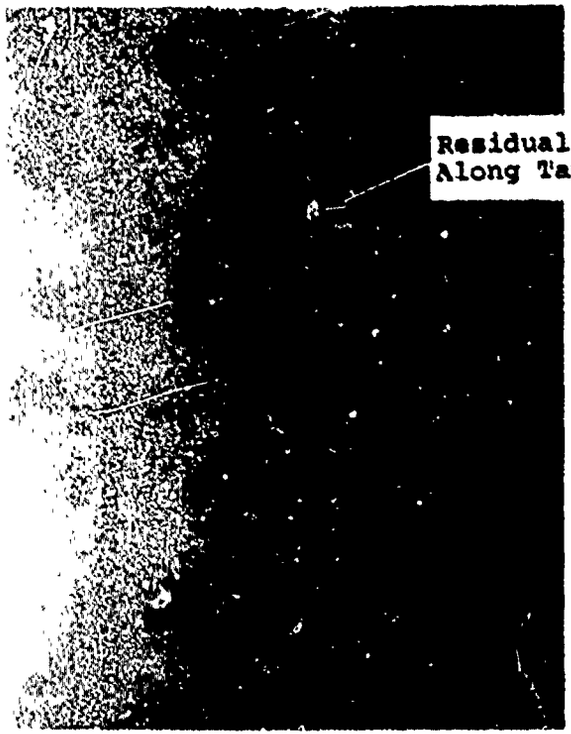
R6300 Ring #4
(50X Before Reduction)

Radial Direction ⟶



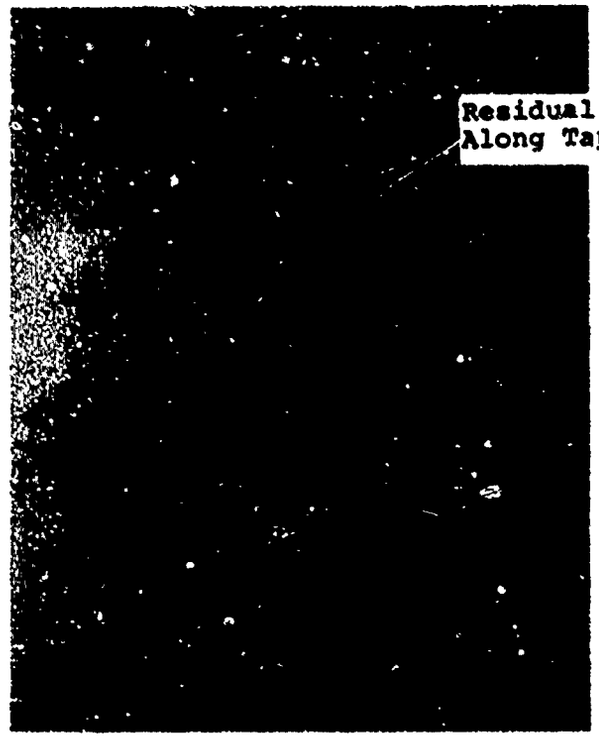
R6300 Ring #2
(50X Before Reduction)

Figure 141. Photomicrographs in Axial Direction of AVCO R6300 Rings #2 and #4



(1.93X)

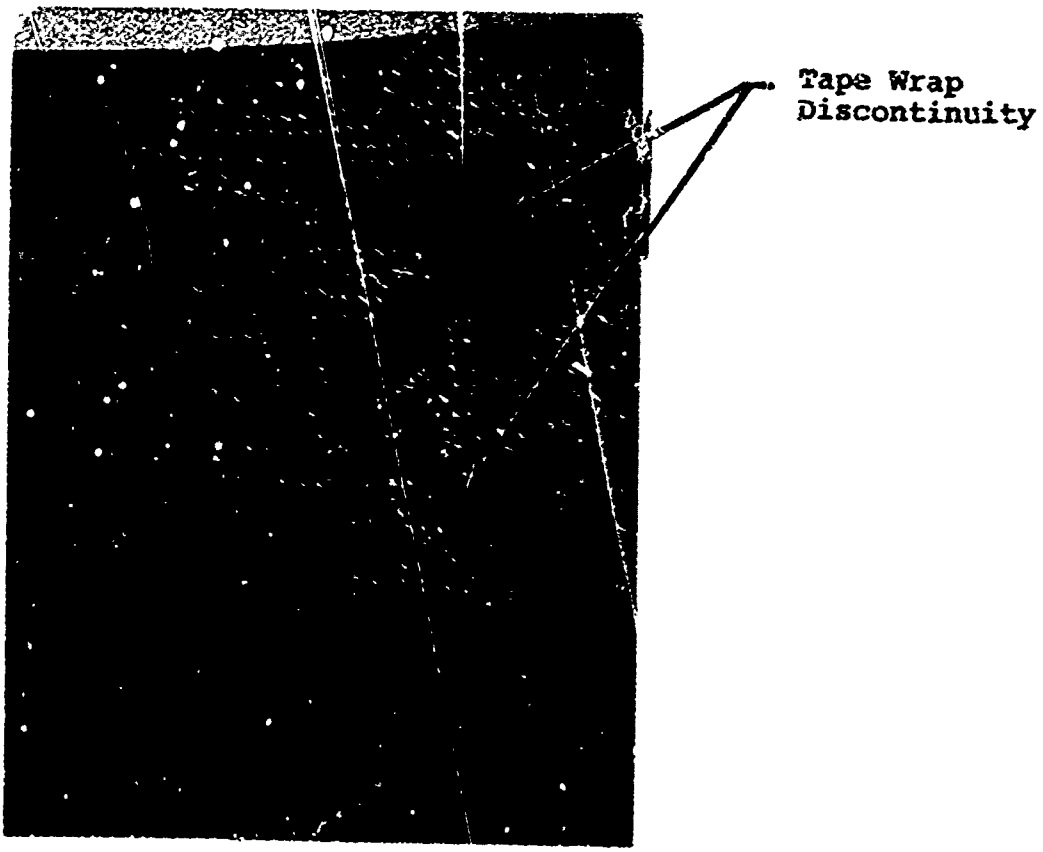
Circumferential View
Ring 11 Arc 3



(1.93X)

Circumferential View
Ring 12 Arc 15

Figure 142. Photographs Showing Typical Residual Porosity Between Tape Wraps in AVCO R6300



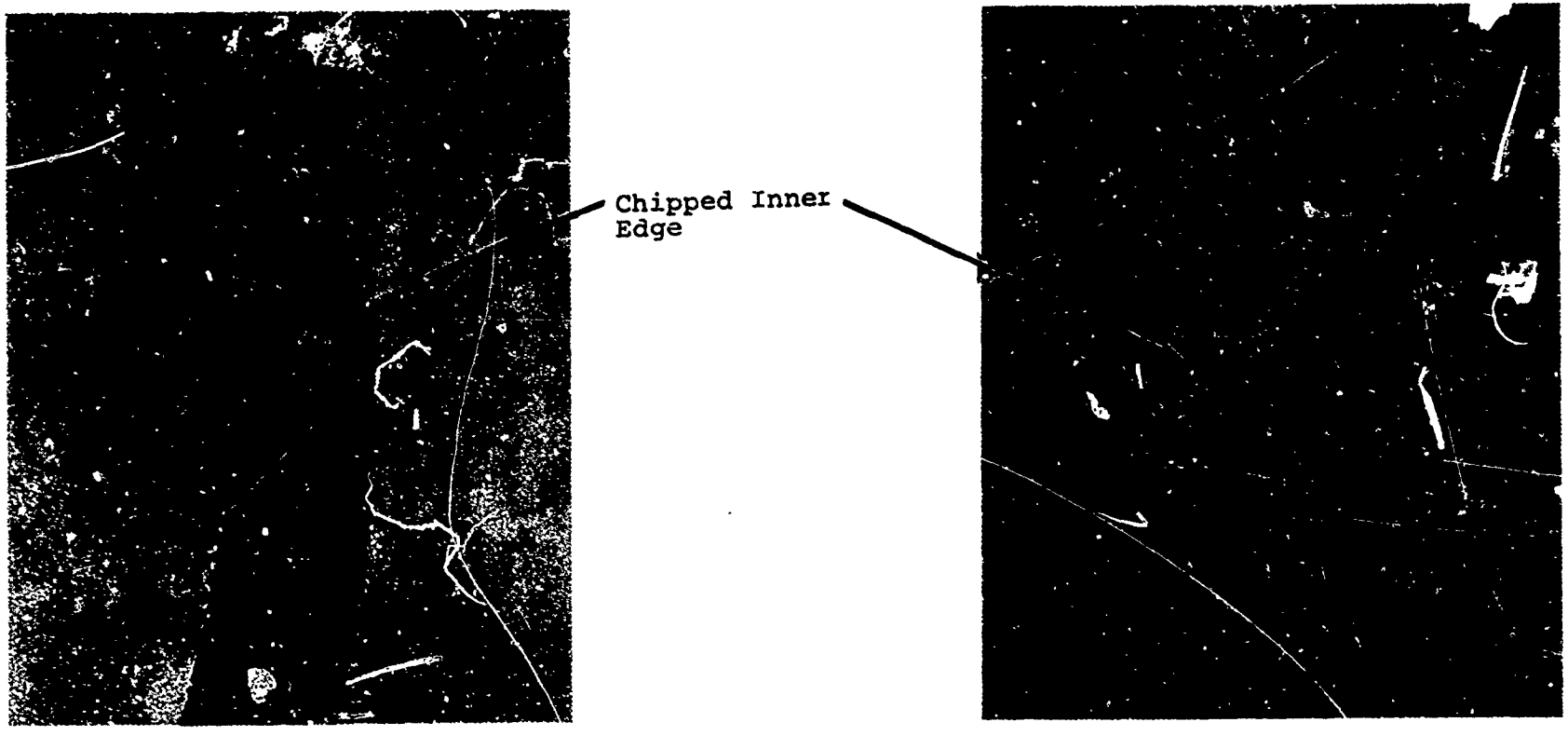
(2X)

Figure 143. Photograph Showing Tape Wrap Discontinuity on Inner Surface of AVCO R6300 Ring #11 of Arc 9



(2X)

Figure 144. Photograph Showing Single 0.10 inch Void on Inner Surface of AVCO R6300 Ring #12 Arc 14



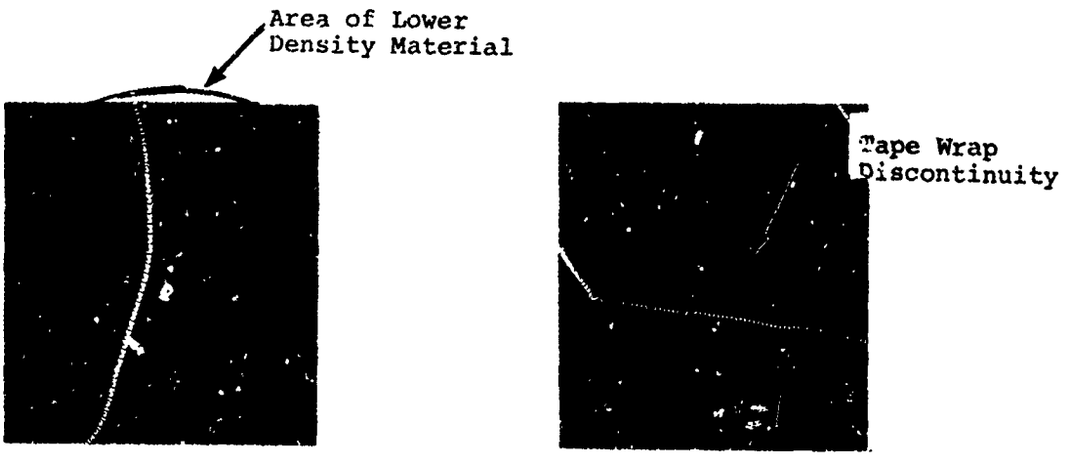
(2.2X)

(2.7X)

Bottom, Inner Edge Chipped from 130-180°

Bottom, Inner Edge Chipped at 215°

Figure 145. Photographs Showing Chips on Inner Edge of AVCO R6300 Ring #7



Radial Direction

Ring 11 Arc 8

Radial Direction

Ring 11 Arc 9

Positive Prints

Figure 146. Radiographs Showing Material Anomalies in AVCO R6300 Ring #11 Arc 8 and Ring #11 Arc 9

General Notes:

1. ⬡ Radial velocity in in./μsec and ultrasonic transmission in added db (Higher values denote lower material attenuation)
2. ↓ Axial velocity in in./μsec
3. Radiography was not revealing of any material anomalies
4. Visual and penetrant inspection was not revealing of any material anomalies
b. Bulk density = 1.324 gm/cm³

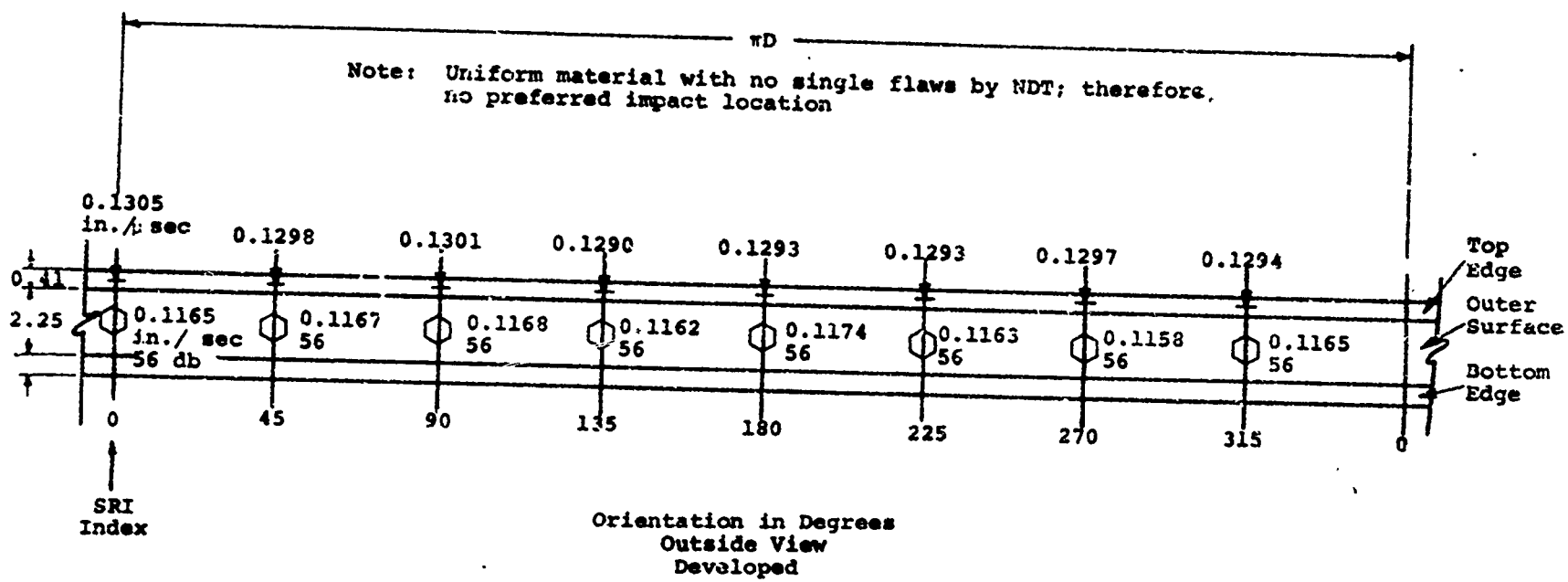


Figure 147. Sketch Showing FT Inspection Results on AVCO R6300 Ring 2

General Notes:

1. ⬡ Radial velocity in in./μsec and ultrasonic transmission in added db (higher values denote lower material attenuation)
2. + Axial velocity in in./μsec
3. Visual and penetrant inspection was not revealing of any material anomalies
4. Bulk density = 1.330 gm/cm³

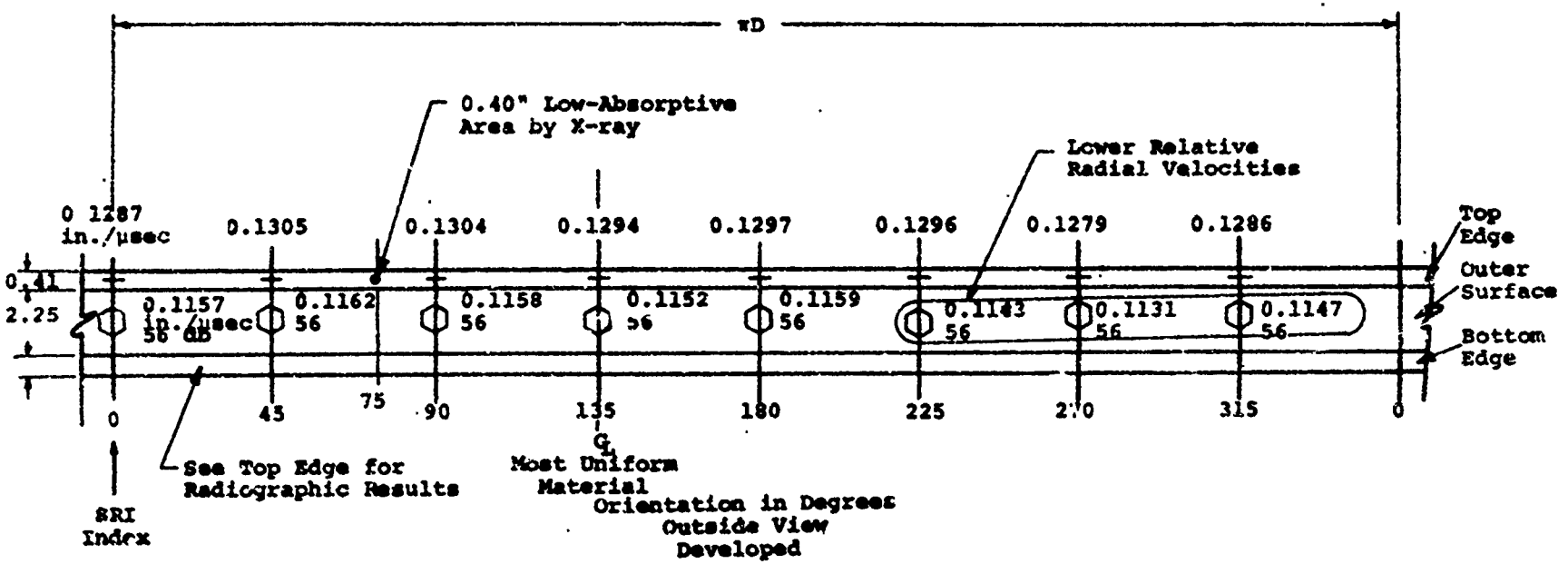
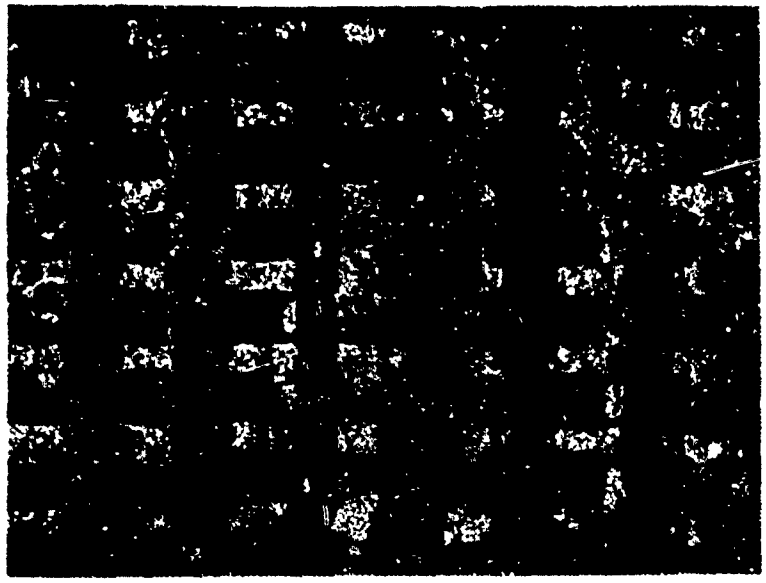
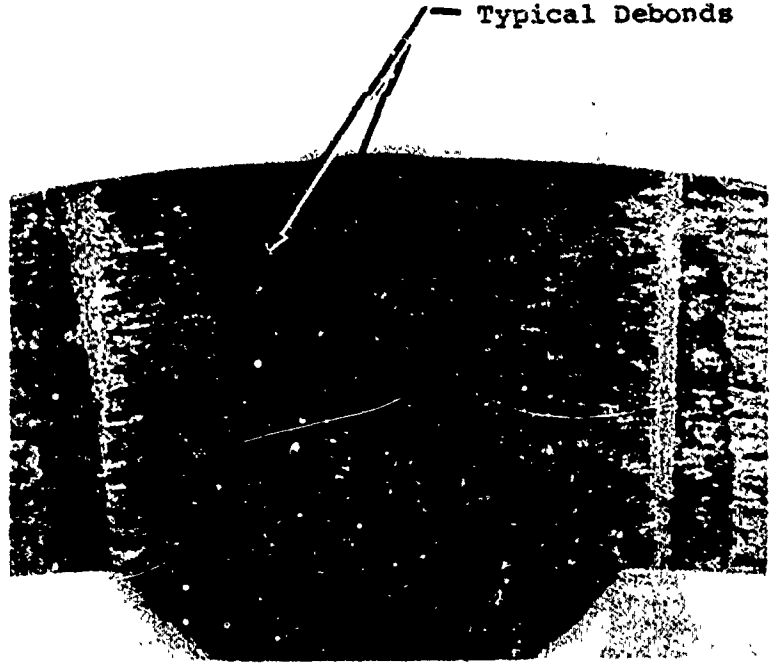


Figure 148. Sketch Showing FT Inspection Results on AVCO R6300 Ring 4

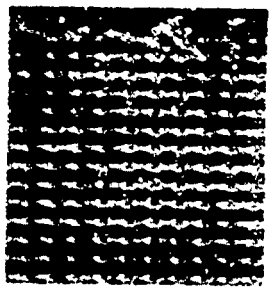


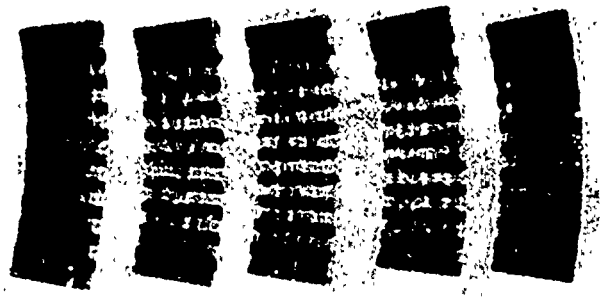
Radial View
5X



Axial View
5X

Figure 149. Photographs Showing Typical AVCO 3DCC Material





Radial Direction

Axial Direction

Positive Prints

Figure 150. Typical AVCO 3DCC Structure Revealed by Radiography

Radial Direction ⟶



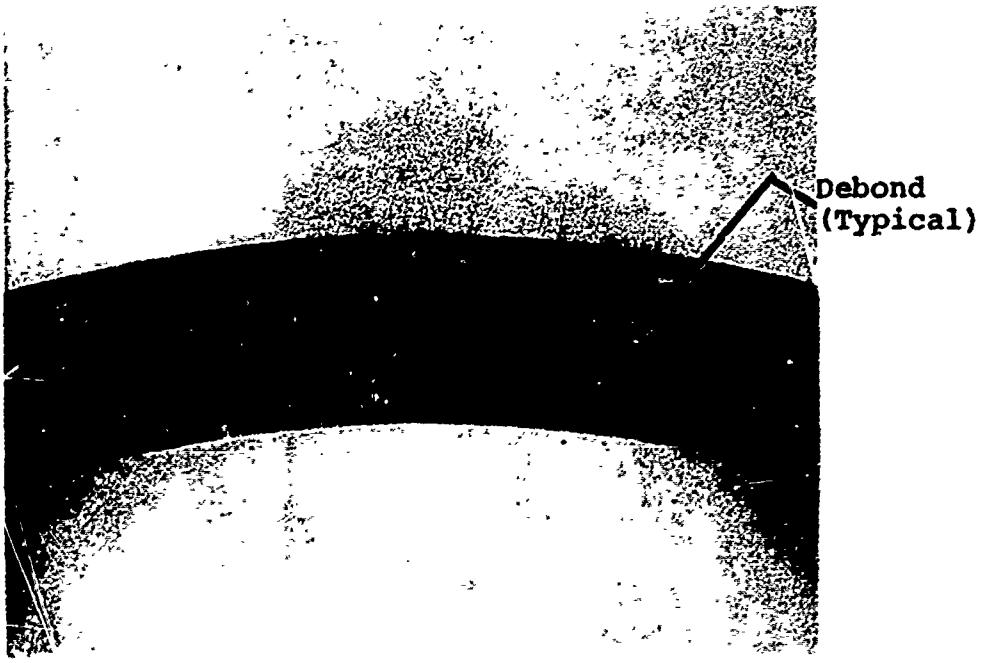
Ring 1109-35-1
(50X Before Reduction)

Radial Direction ⟶



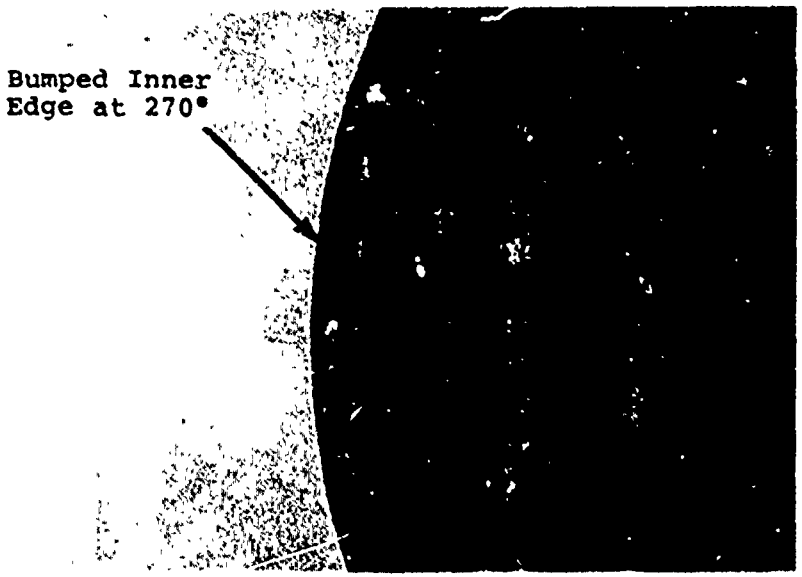
Ring 1109-35-5
(50X Before Reduction)

Figure 151. Photomicrographs in Axial Direction of AVCO Rings 1109-35-5 and 1109-35-5

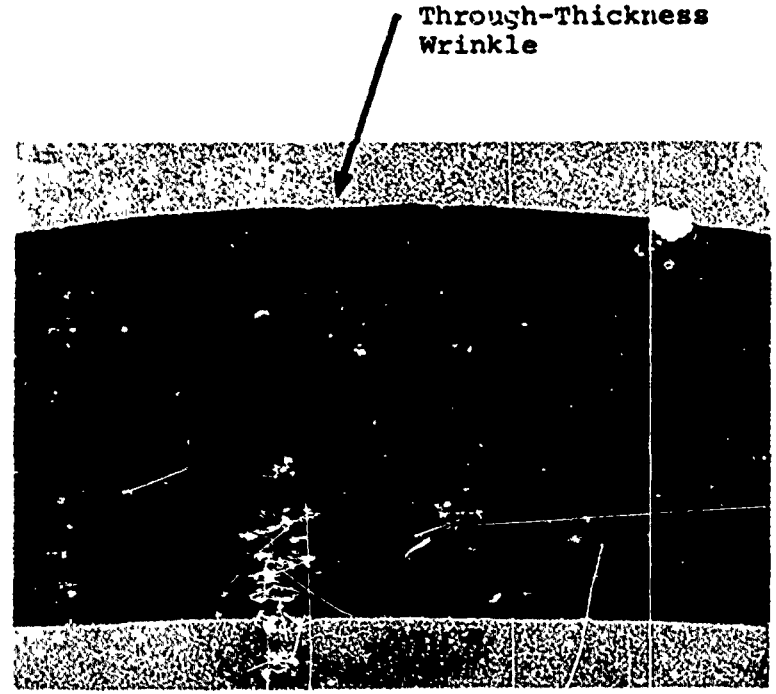


Axial View
(2X)

Figure 152. Photograph Showing Typical Debonds in AVCO 3DCC Rings #1109-35-1 through #1109-35-11

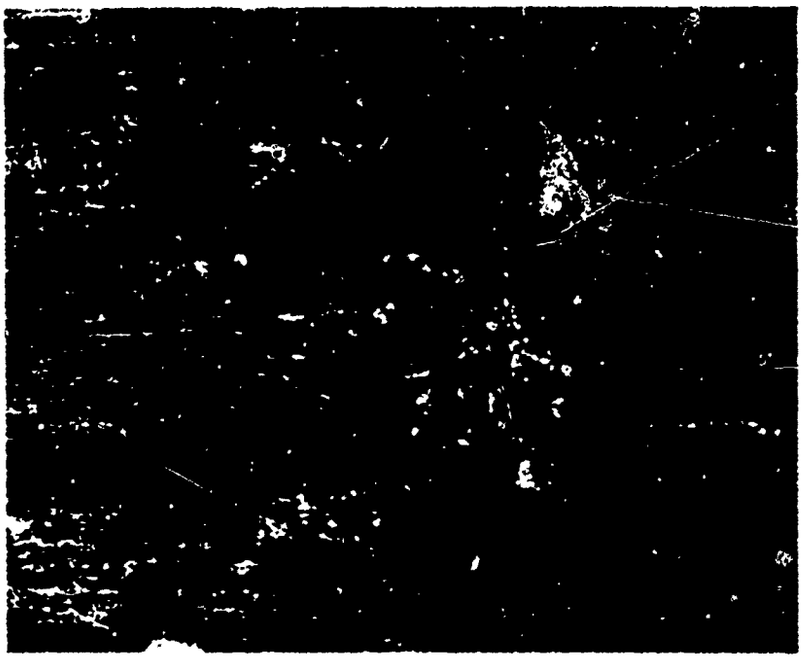


Radial View
Disc #1
5X



Axial View
Disc #11
5X

Figure 153. Photographs Showing Visual Anomalies in AVCO 3DCC Discs #1 and #11

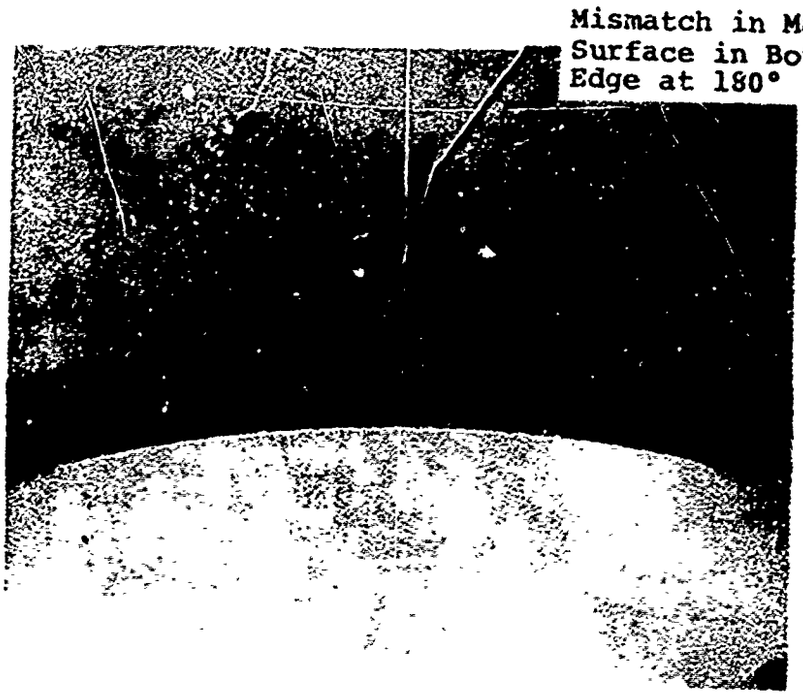


0.15 inch X
0.15 inch X
1 Ply Deep
Depressed Area
in Outer Surface
Located at
0° and 0.20 inch
from Bottom Edge

(10X)

Radial View

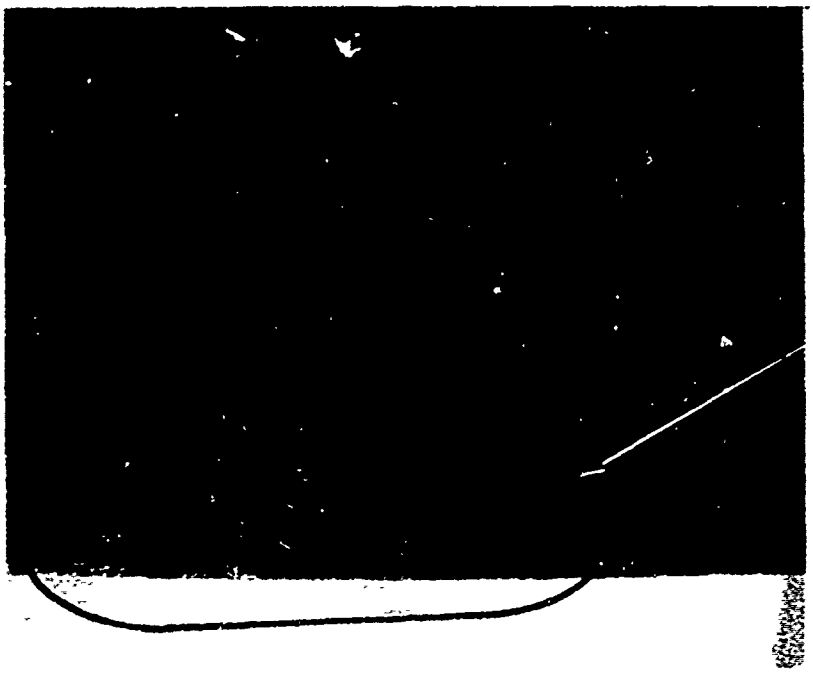
Figure 154. Photograph Showing Depressed Area in AVCO 3DCC Ring #2B



(2X)

Axial View

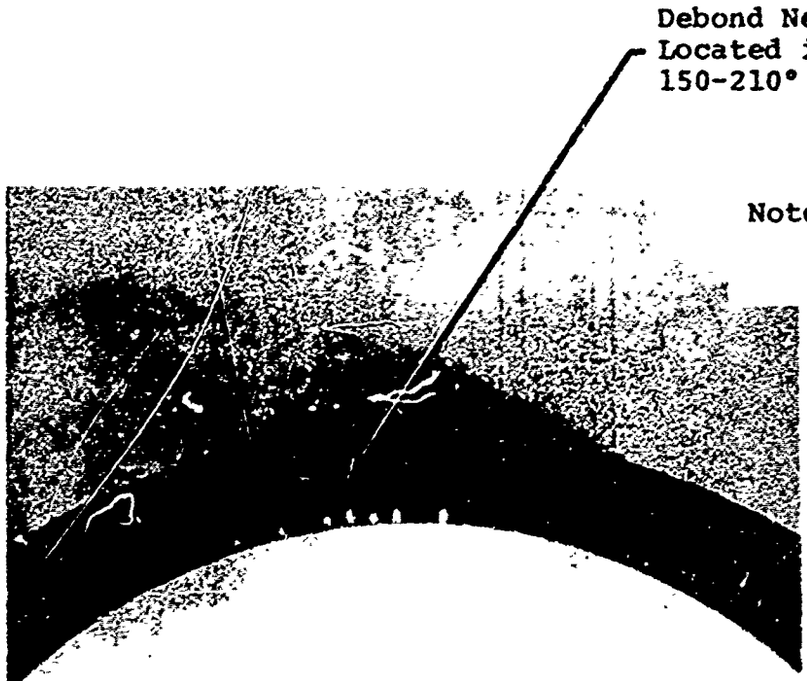
Figure 155. Photograph Showing Machining Error in Bottom Edge of AVCO 3DCC Ring #4B



Local Area
(1.2 inch x 0.2 inch
of Loose and Missing
Pieces of Axials and
Circumferentials
Located on Outer
Surface at 300°
and Bottom Edge

Radial View
2X

Figure 156. Photograph Showing Missing Axials and Circumferentials in AVCO 3DCC Ring #4B



(1X)

Axial View

Figure 157. Photograph Showing Large Visual Debond in AVCO 3DCC in Ring #1A

General Notes:

1. ⬡ Radial Velocity in in./μsec and ultrasonic transmission in added db (Higher values denote lower material attenuation)
2. ↕ Axial velocity in in./μsec
3. Bulk Density = 1.626 gm/cm³
4. Visual and Penetrant inspection not revealing of material anomalies

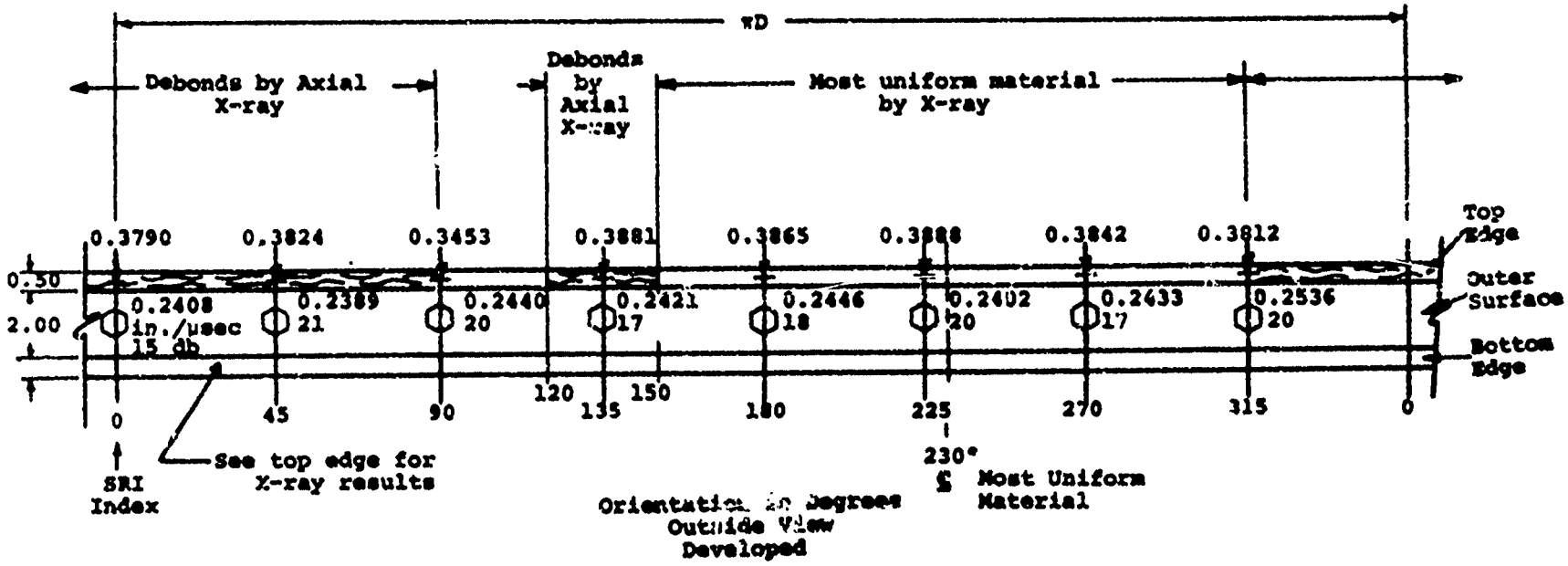


Figure 158. Sketch Showing PT Inspection Results on AVCO 3DCC Ring 1109-35-1

Notes:

1. QC nondestructive test results only. Ring was selected for underground test
2. Bulk Density: 1.638 gm/cm³

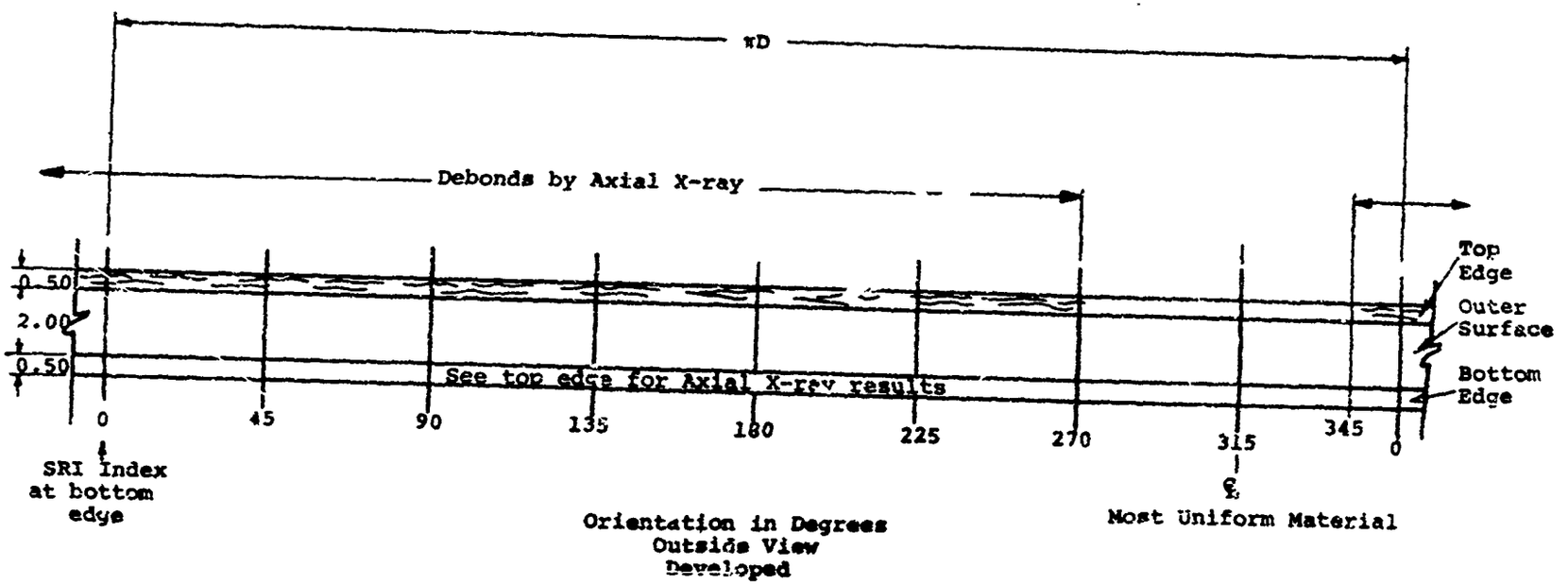


Figure 159. Sketch Showing QC Inspection Results on AVCO 3DCC Ring 1109-[illegible]-2

Notes:

1. QC nondestructive test results only. Ring was selected for underground test.
2. Bulk density: 1.645 gm/cm³

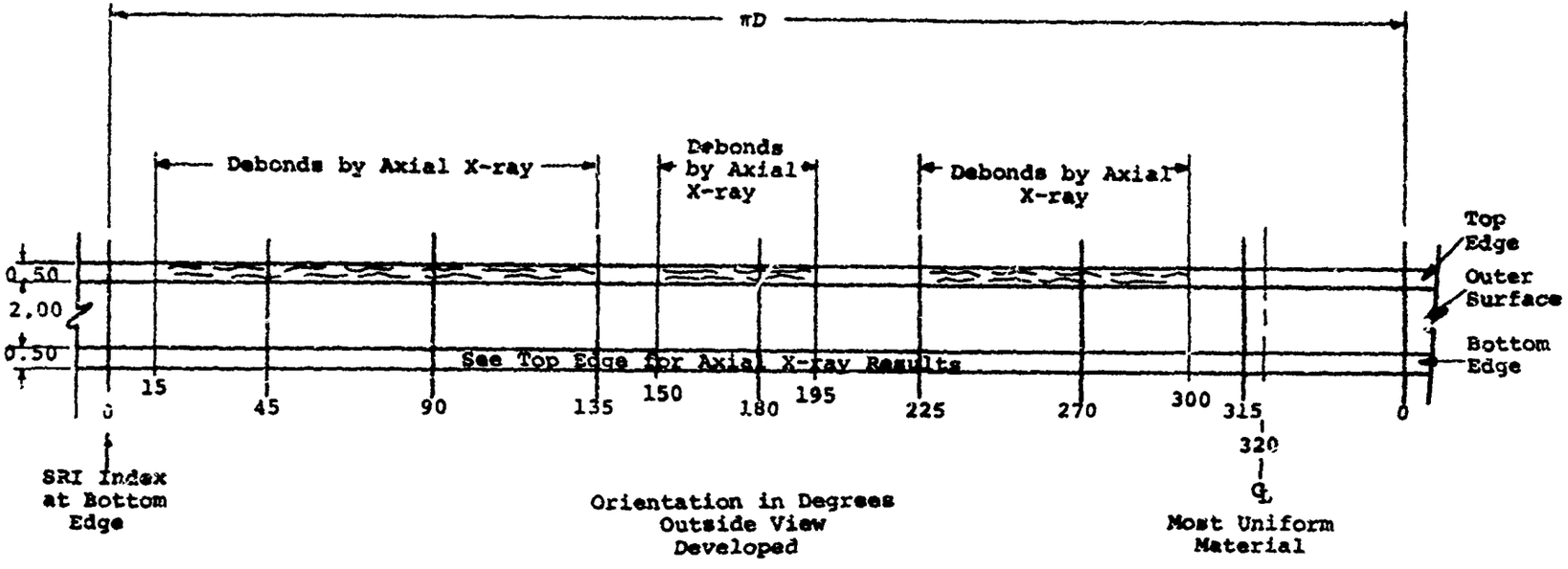


Figure 160. Sketch Showing QC Inspection Results on AVCO 3DCC Ring 1109-35-3

Notes:

1. Q.C. nondestructive testing only
2. Bulk density: 1.646 gm/cm^3

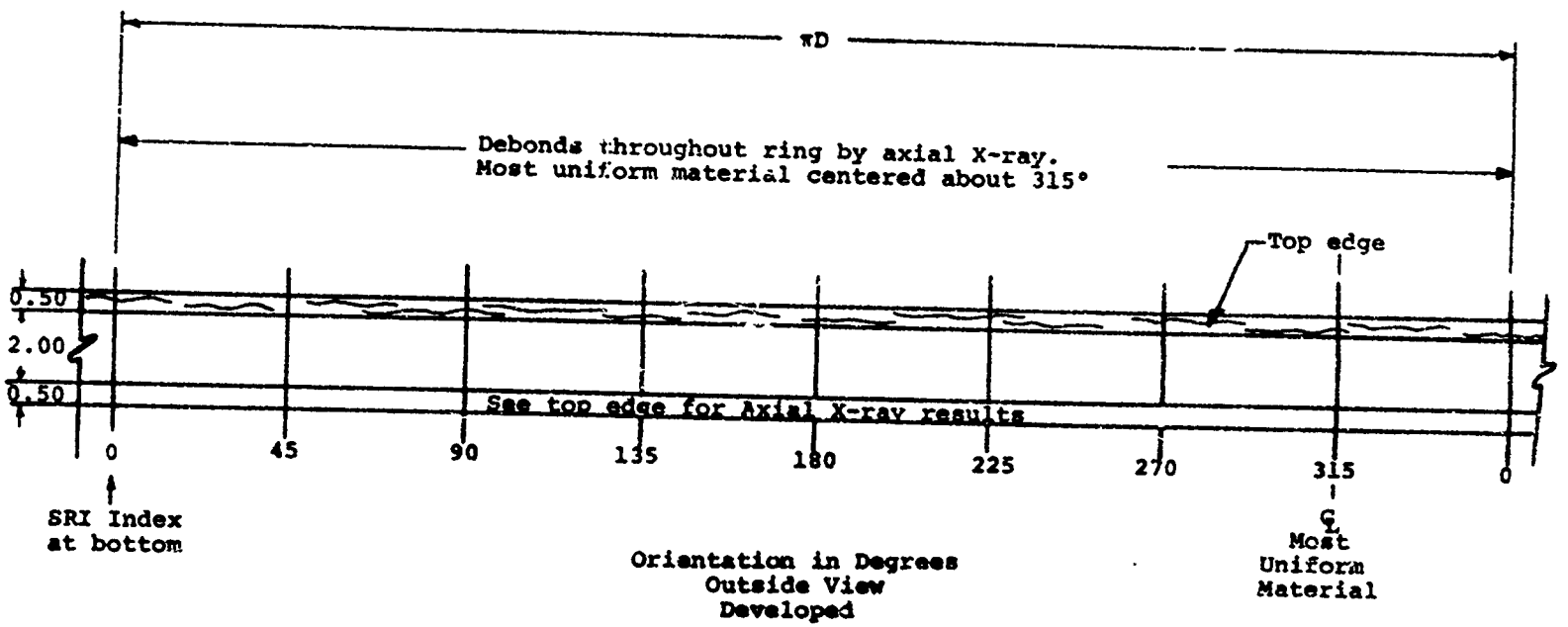


Figure 161. Sketch Showing QC Inspection Results on AVCO 3DCC Ring 1109-35-4

Notes:

1. ⬡ Radial velocity in in./μsec and ultrasonic transmission in added db (Higher values indicate lower material attenuation)
2. ↓ Axial velocity in in./μsec
3. Bulk Density = 1.646 gm/cm³

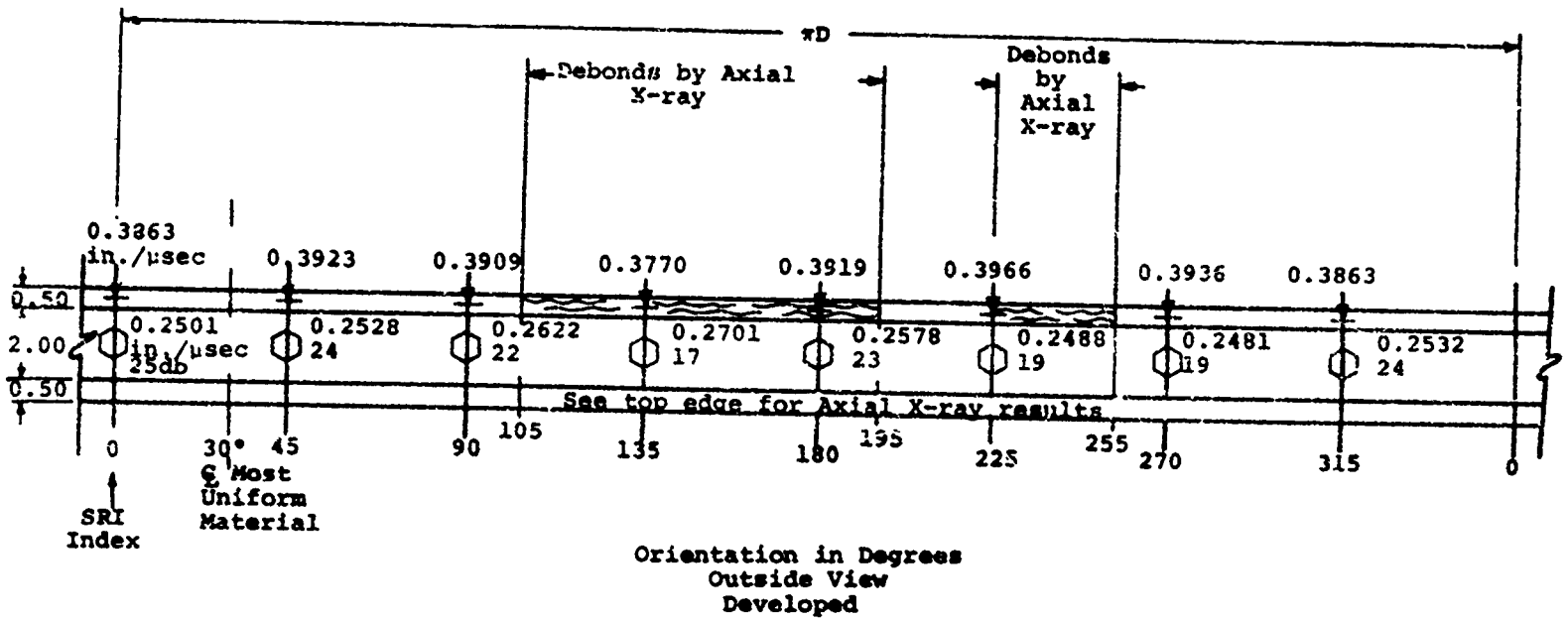


Figure 162. Sketch Showing FT Inspection Results on AVCO 3DCC Ring 1109-35-5

Notes:

1. Q.C. nondestructive testing only
2. Bulk density: 1.664 gm/cm^3

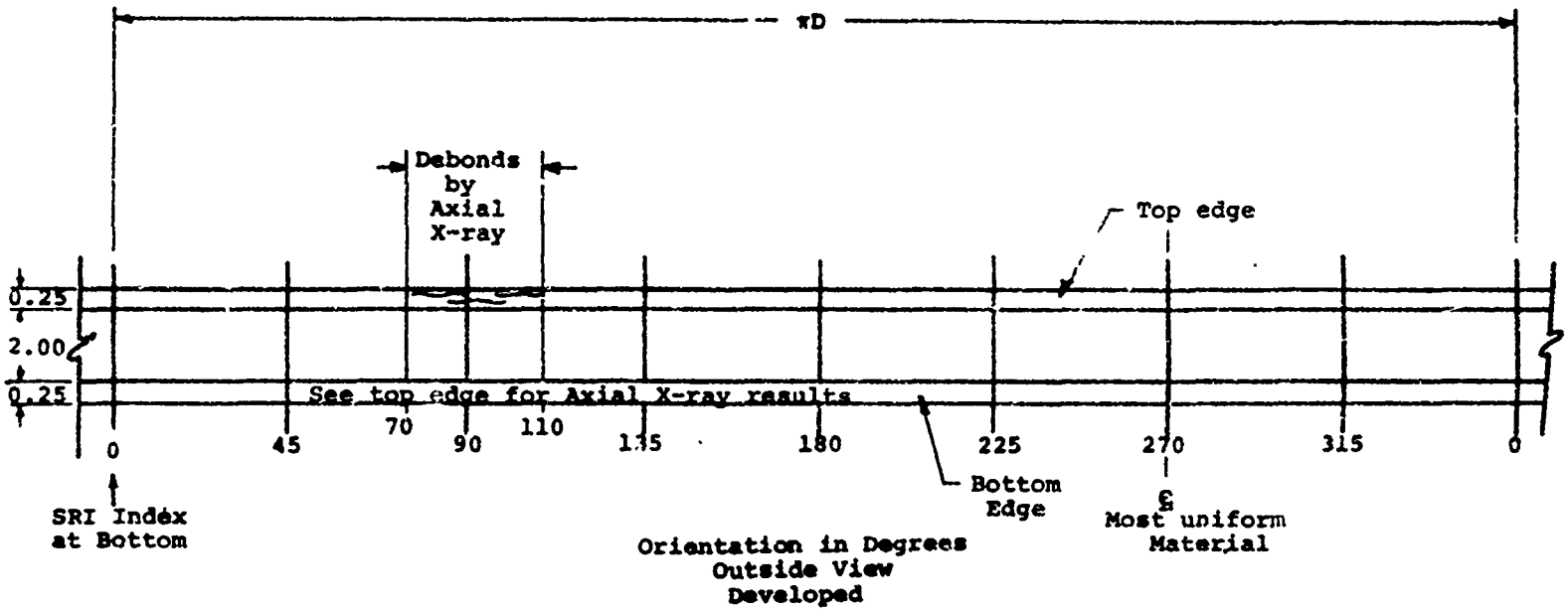


Figure 163. Sketch Showing QC Inspection Results on AVCO 3DCC Ring 1109-35-6

Notes:

1. Q.C. nondestructive testing only
2. Bulk density: 1.654 gm/cm^3

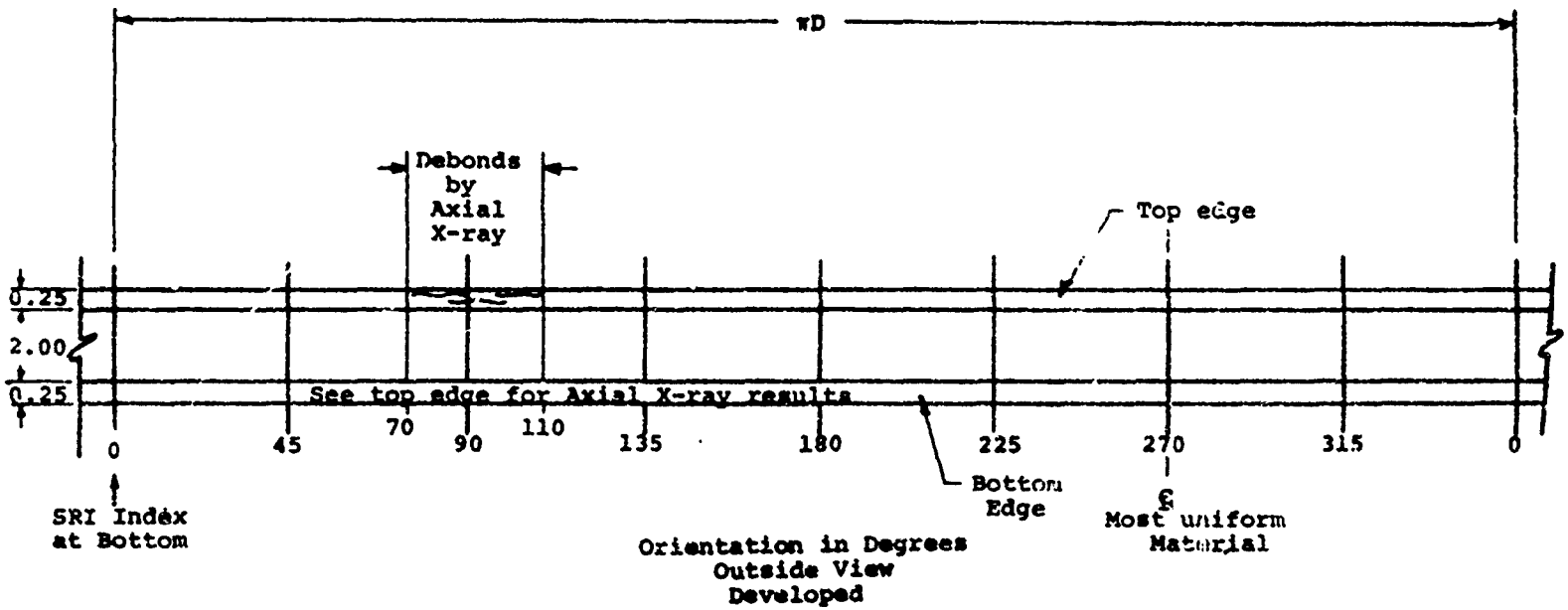


Figure 163. Sketch Showing QC Inspection Results on AVCO 3DCC Ring 1109-35-6

Notes:

1. Q.C. nondestructive testing only
2. Bulk density: 1.675 gm/cm^3

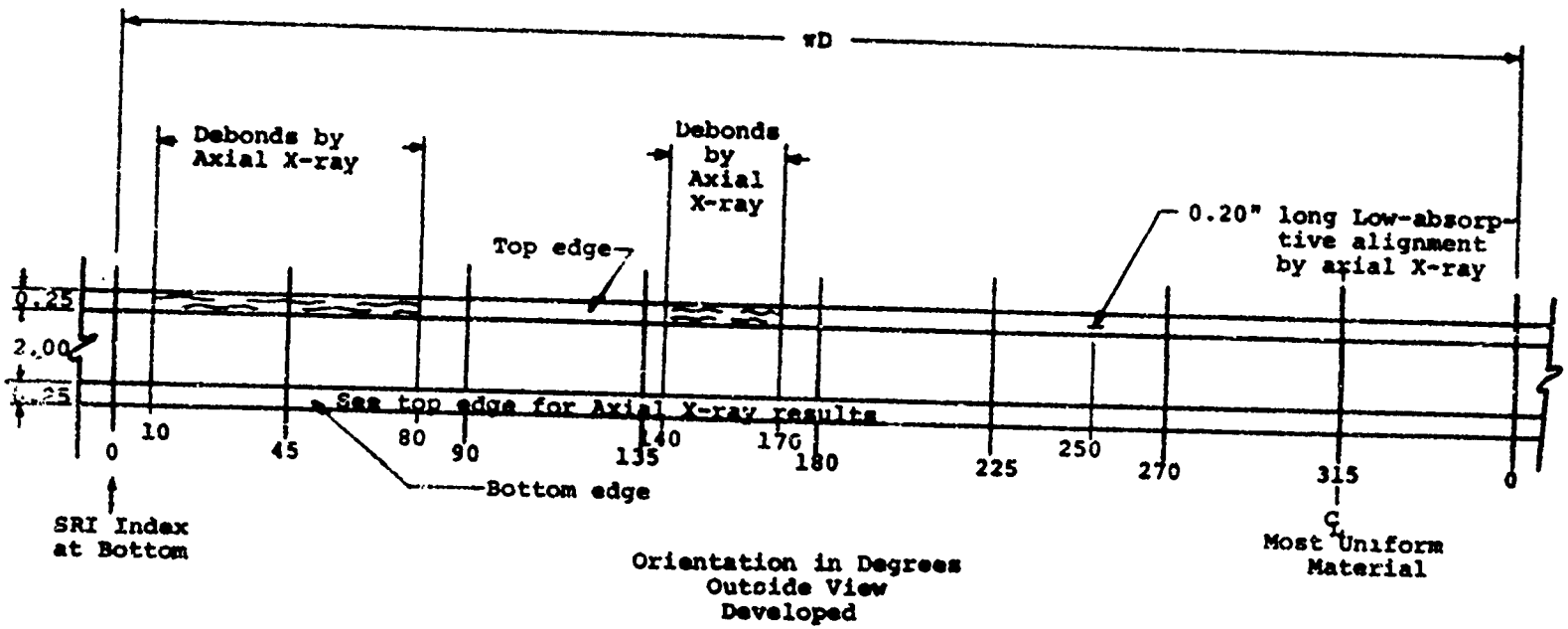


Figure 164. Sketch Showing QC Inspection Results on AVCO 3DCC Ring 1109-35-7

Notes:

1. Q.C. nondestructive testing only
2. Bulk density: 1.685 gm/cm^3

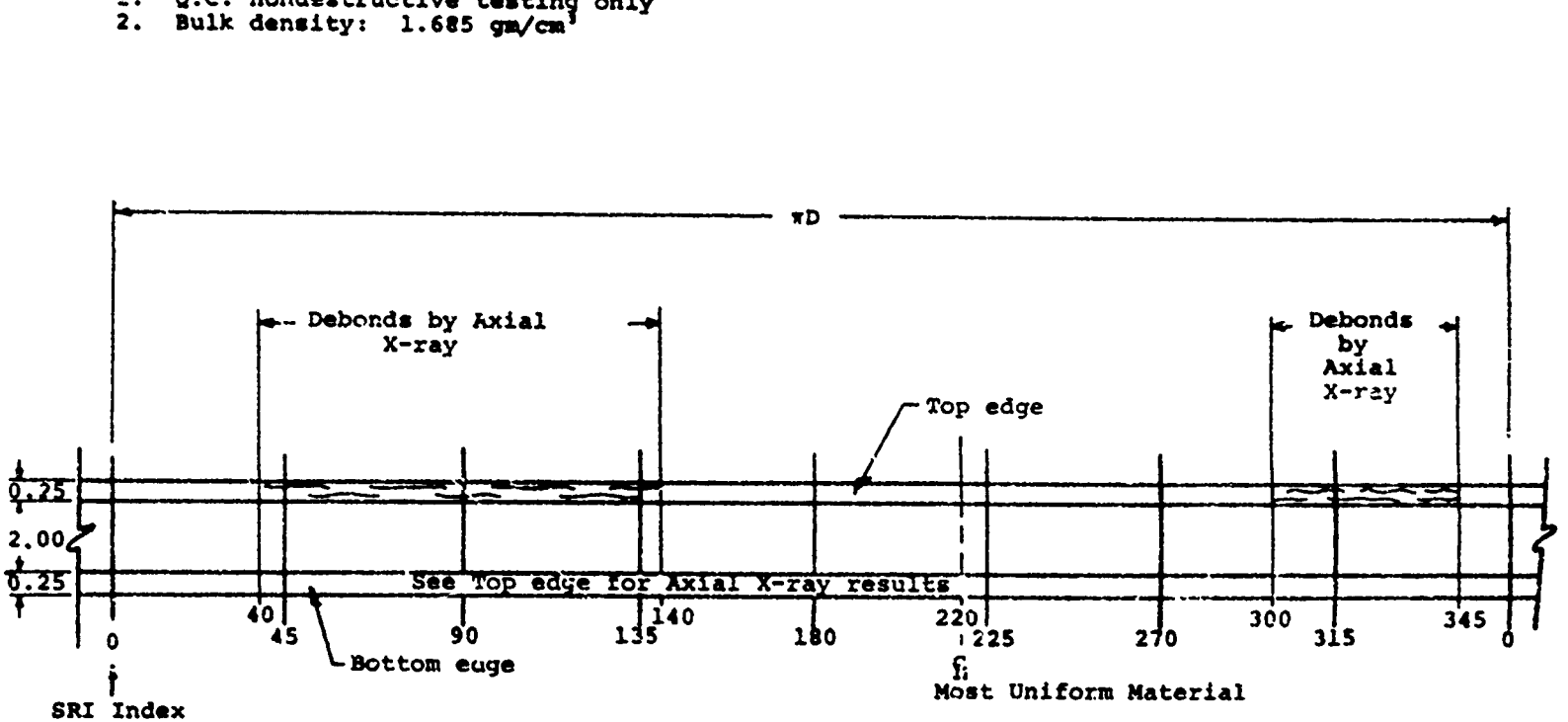


Figure 165. Sketch Showing QC Inspection Results on AVCO 3DCC Ring 1109-35-8

Notes:

1. Q.C. nondestructive testing only
2. Bulk density: 1.673 gm/cm^3

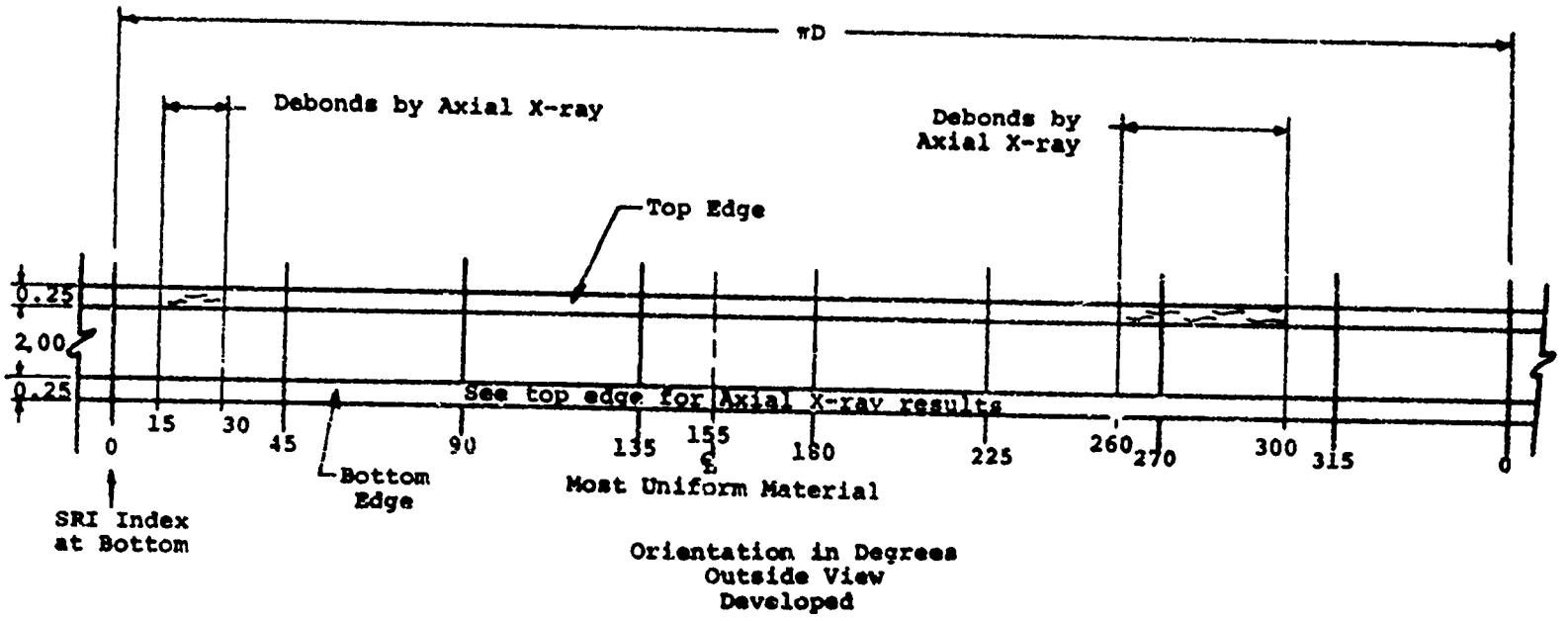


Figure 166. Sketch Showing QC Inspection Results on AVCO 3DCC Ring 1109-35-9

Notes:

1. Q.C. nondestructive testing only
2. Bulk density: 1.698 gm/cm^3

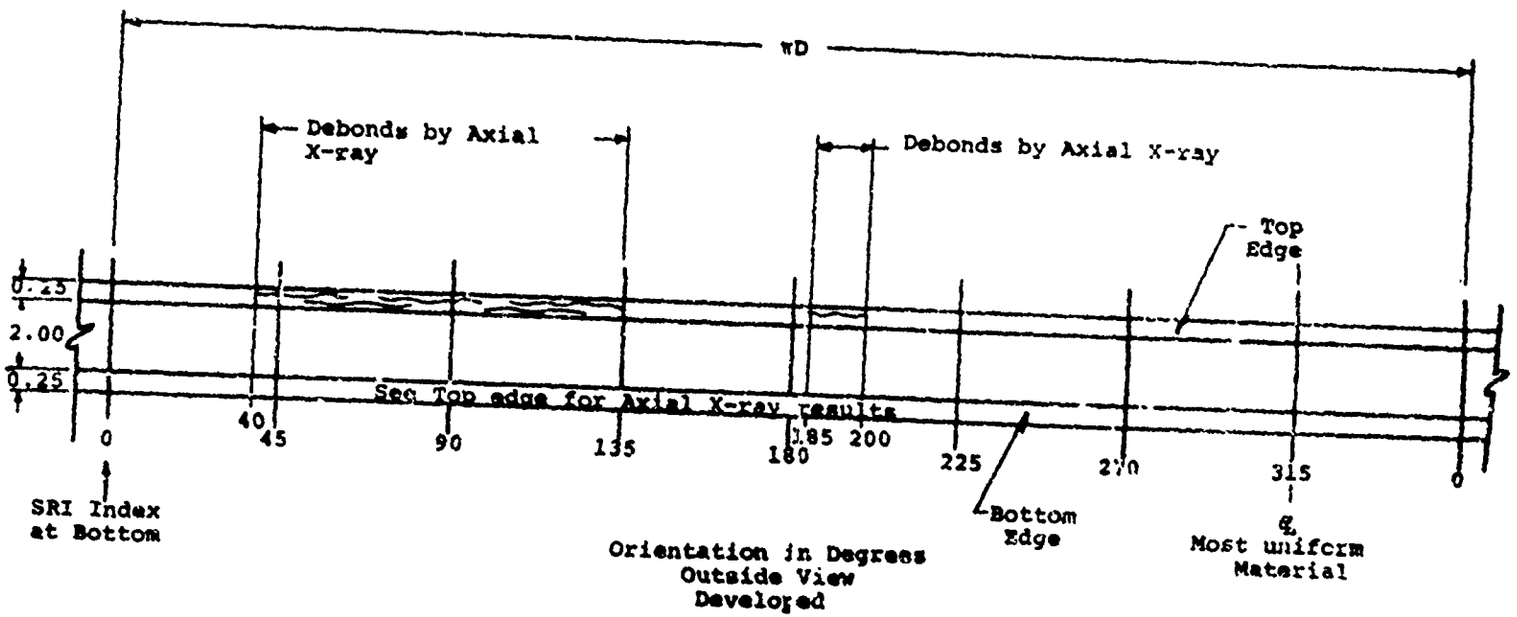


Figure 167. Sketch Showing QC Inspection Results AVCO 3DCC Ring 1109-35-10

Notes:

1. Q.C. nondestructive testing only
2. Bulk density: 1.691 gm/cm^3

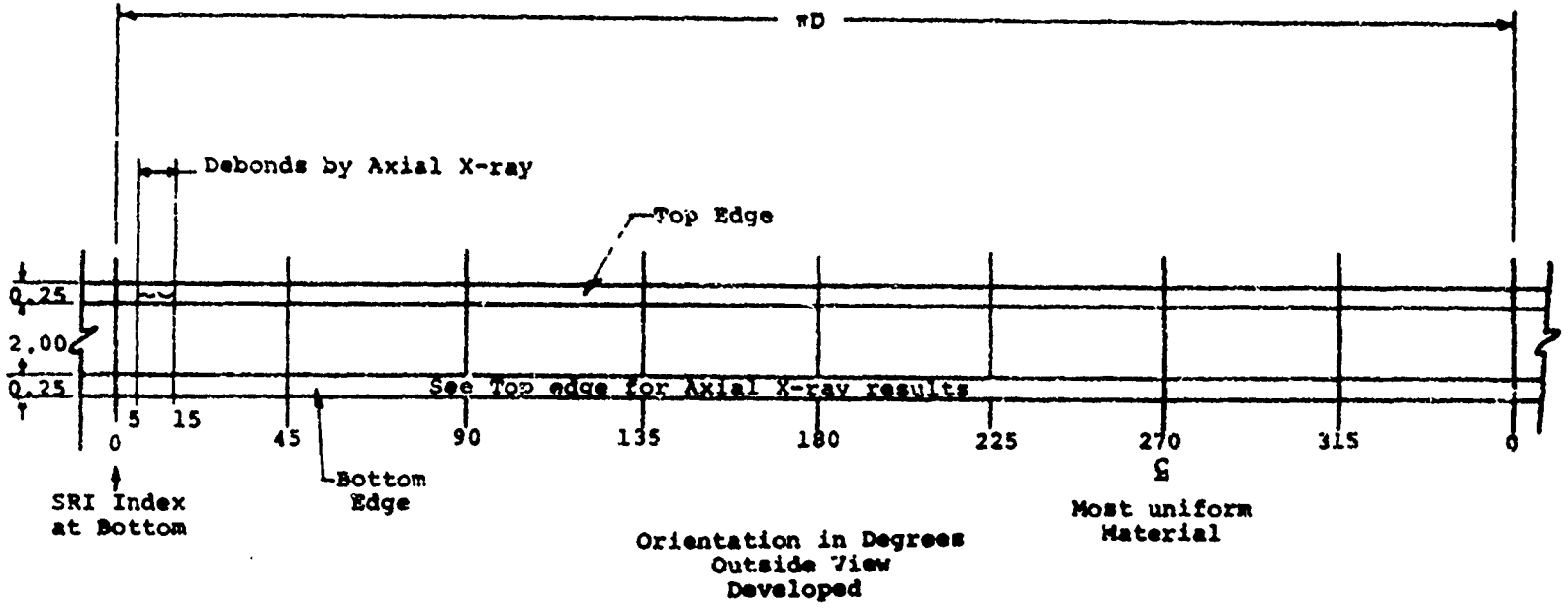


Figure 168. Sketch Showing QC Inspection Results on AVCO 3DCC Ring 1109-35-11

Notes:

1. QC nondestructive testing only
2. Radiography indicated the ring to be uniform throughout
3. Ring considered uniform throughout. Note visual debond in bottom edge.
4. Bulk density: 1.677 gm/cm³

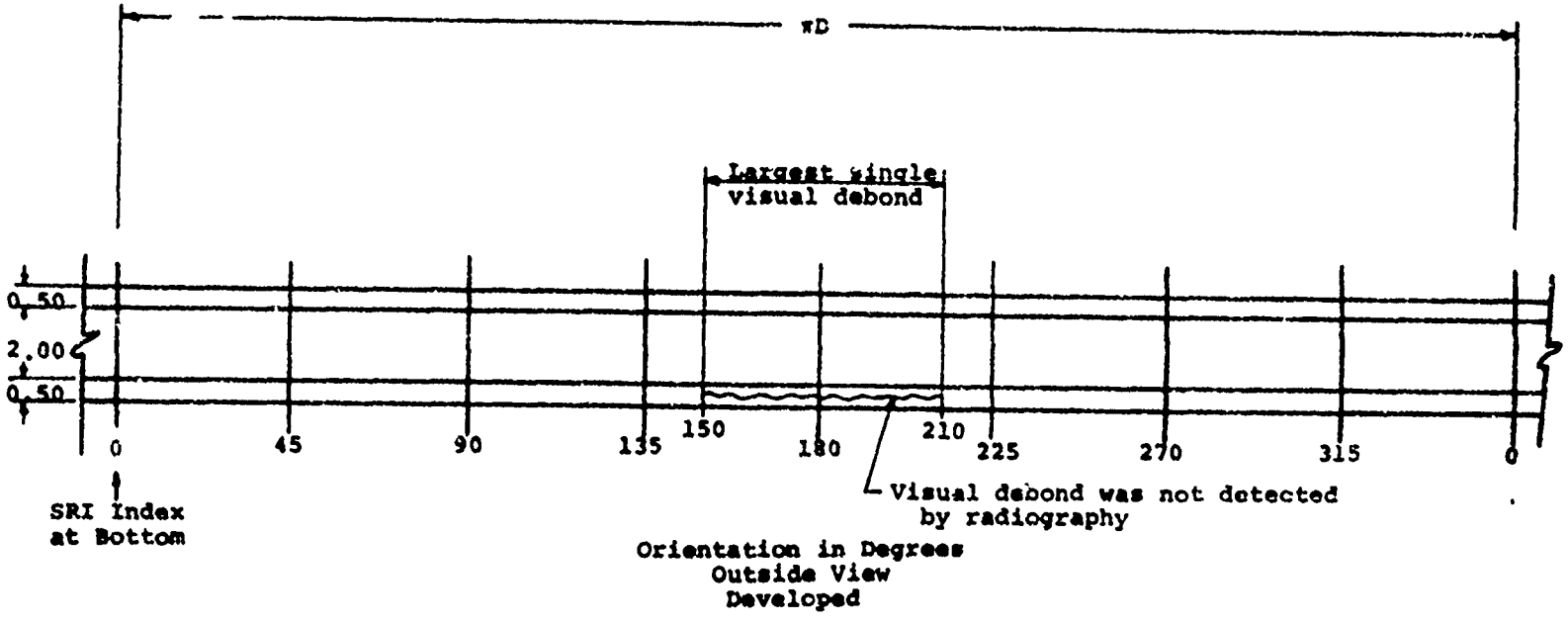


Figure 169. Sketch Showing QC Inspection Results on AVCO 3DCC Ring 1A

Notes:

1. Q.C. nondestructive testing only
2. Bulk density: 1.680 gm/cm³

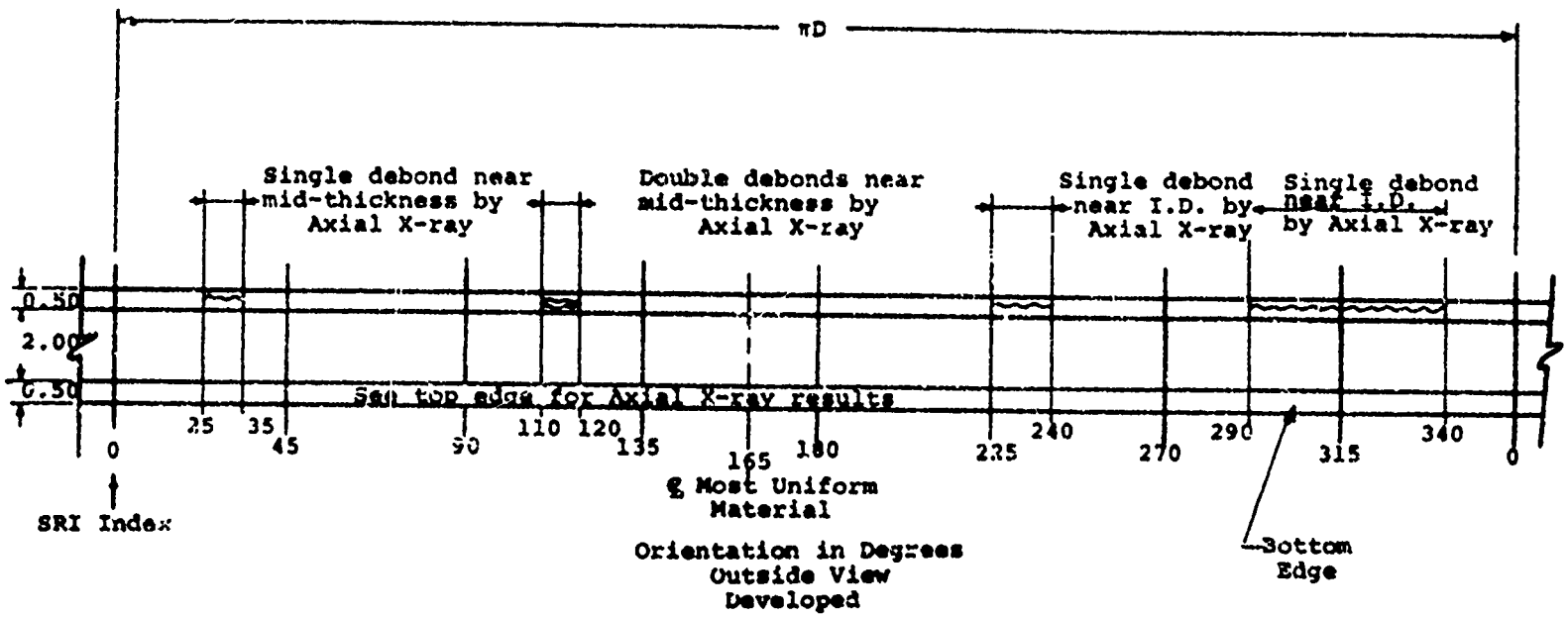


Figure 170. Sketch Showing QC Inspection Results on AVCO 3DCC Ring 2A

Notes:

1. Q.C. nondestructive testing only
2. Bulk density: 1.680 gm/cm³

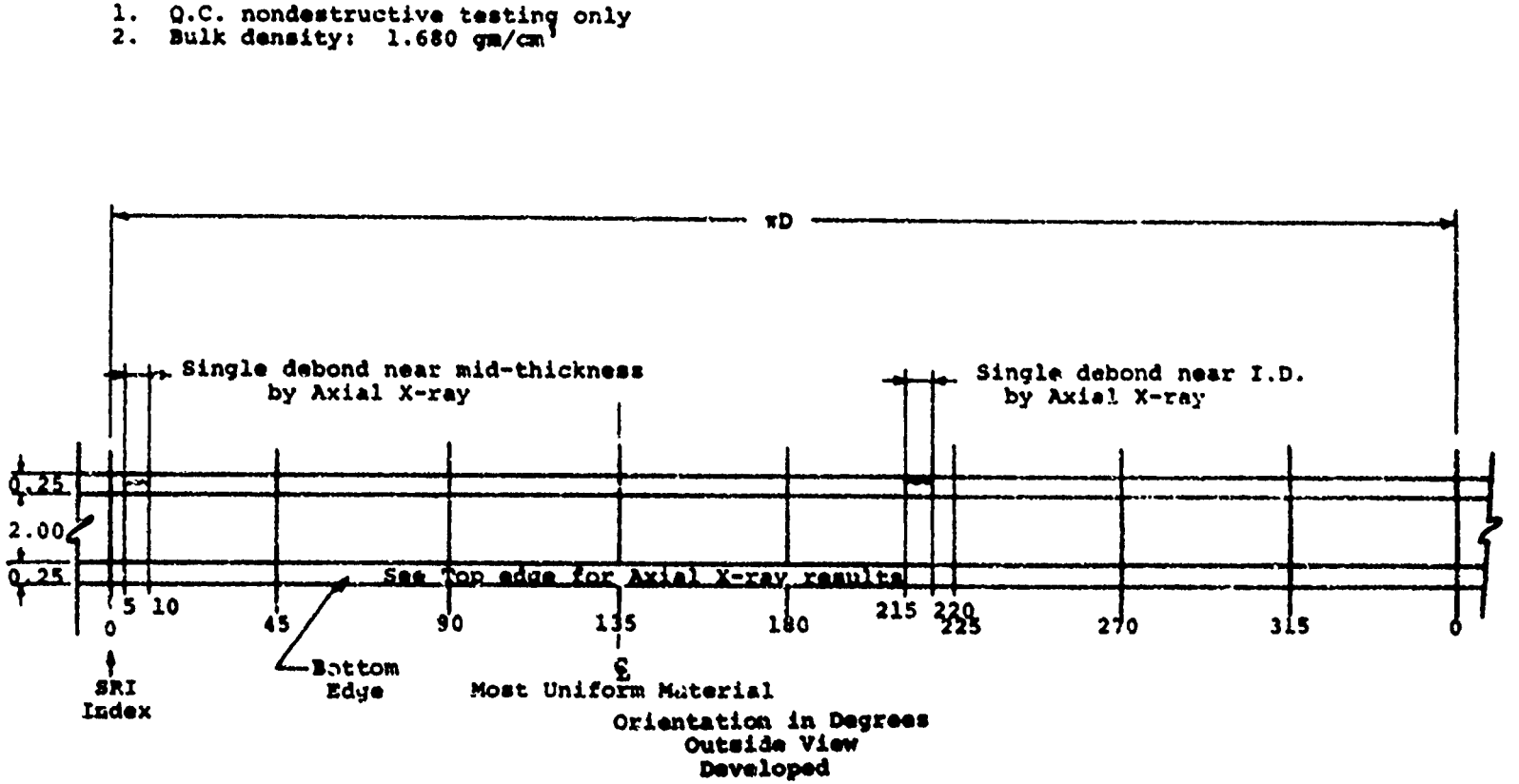


Figure 171. Sketch Showing QC Inspection Results on AVCO 3DCC Ring 1B

Notes:

1. Q.C. nondestructive testing only
2. Bulk density: 1.672 gm/cm^3

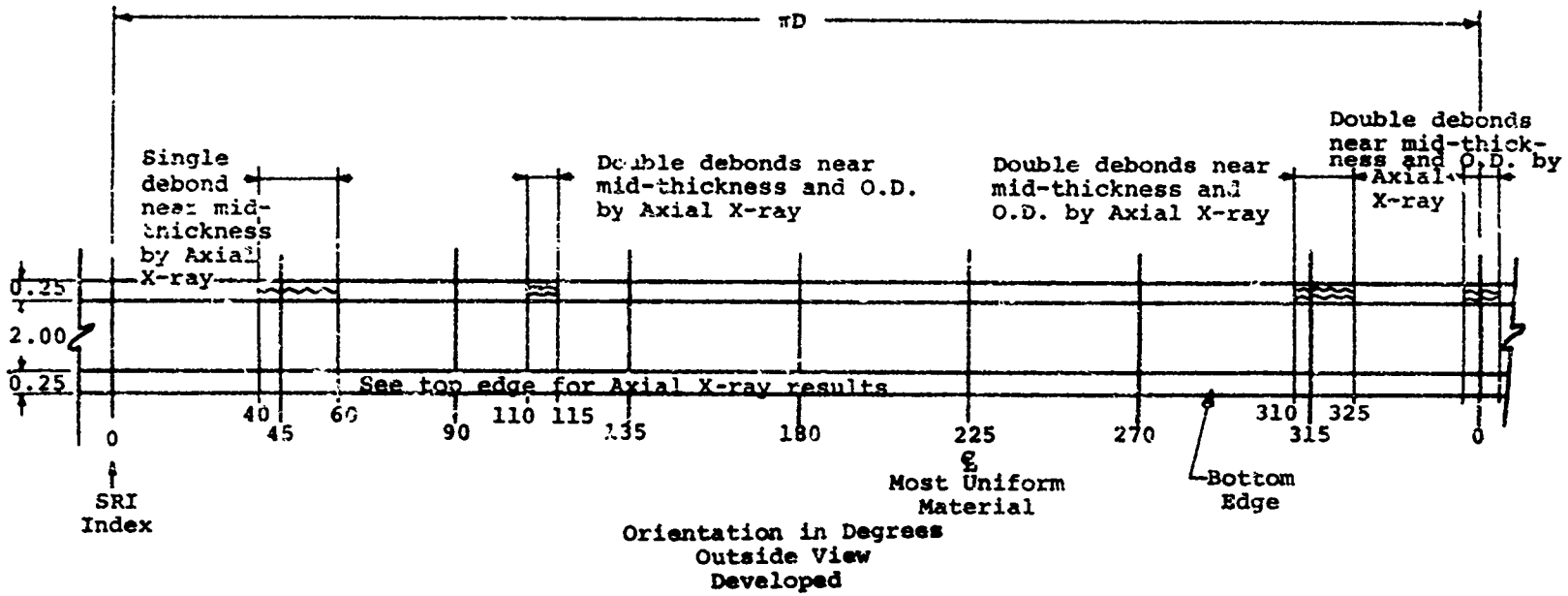


Figure 172. Sketch Showing QC Inspection Results on AVCO 3DCC Ring 2B

Notes:

1. Q.C. nondestructive testing only
2. Bulk density: 1.673 gm/cm³

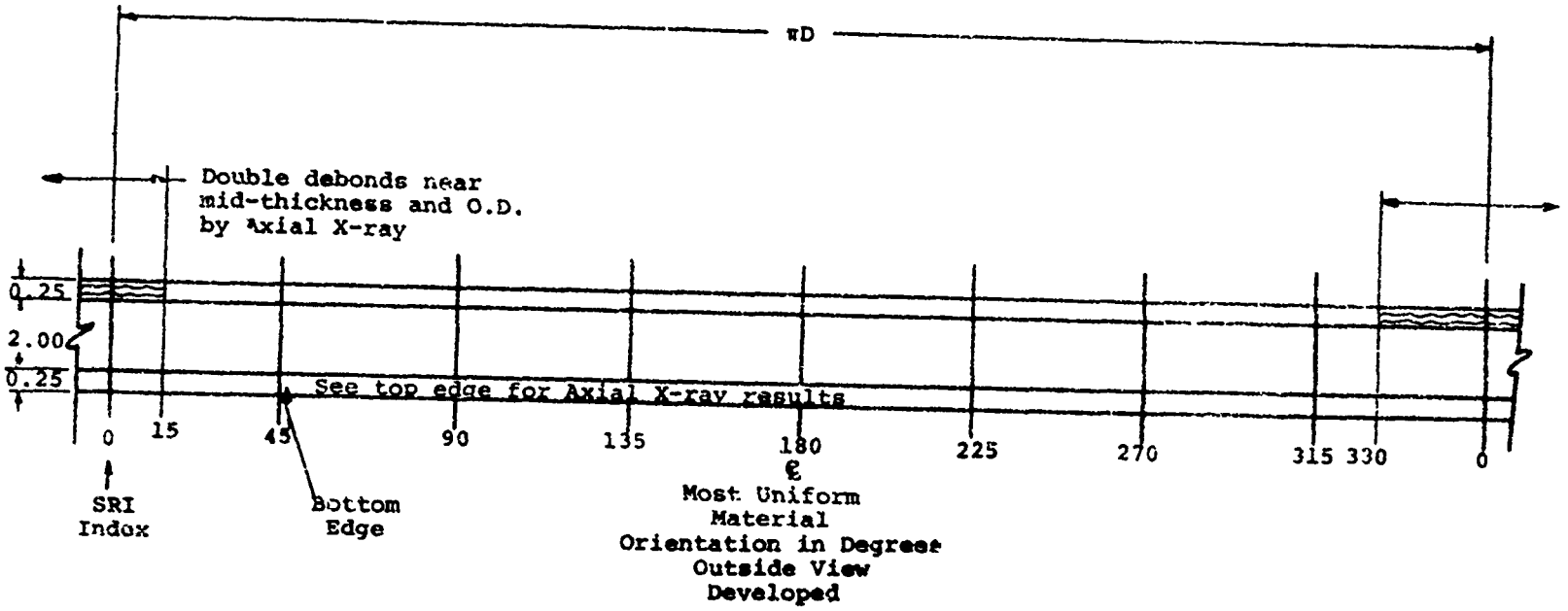


Figure 173. Sketch Showing QC Inspection Results on AVCO 3DCC Ring 3B

Notes:

1. Q.C. nondestructive testing only
2. Bulk density: 1.675 gm/cm³

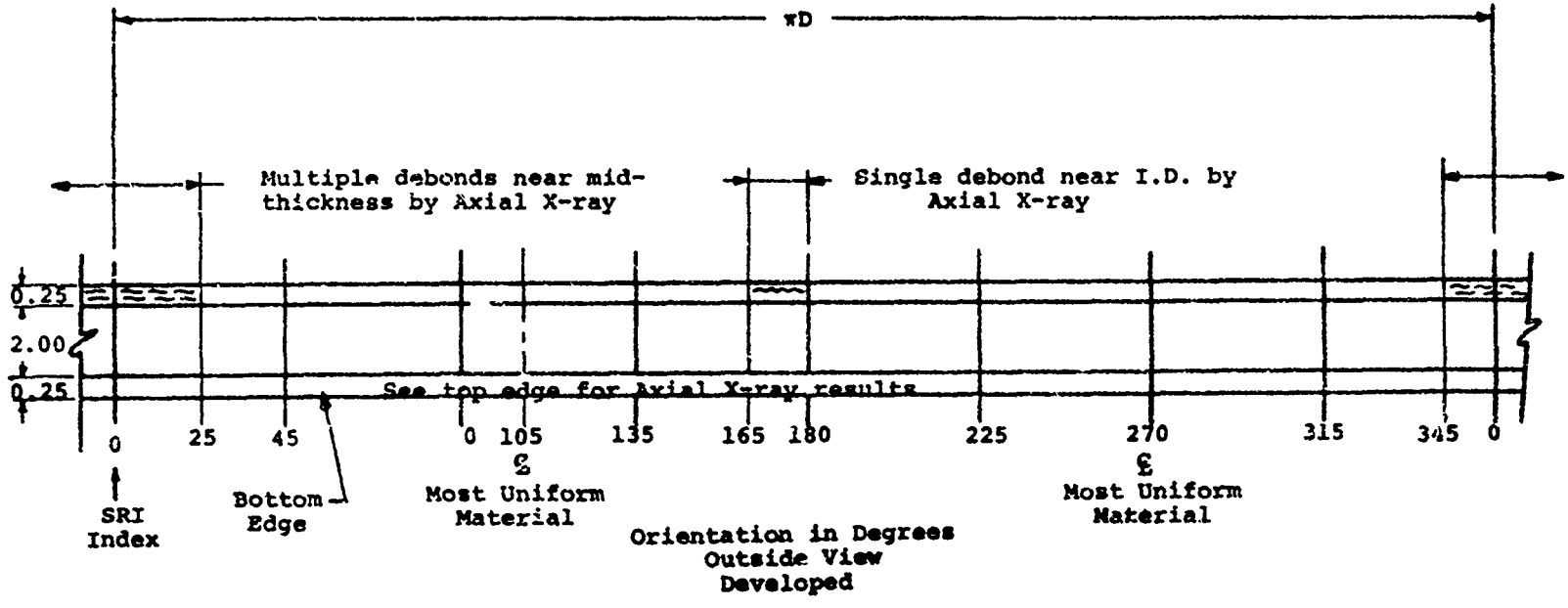
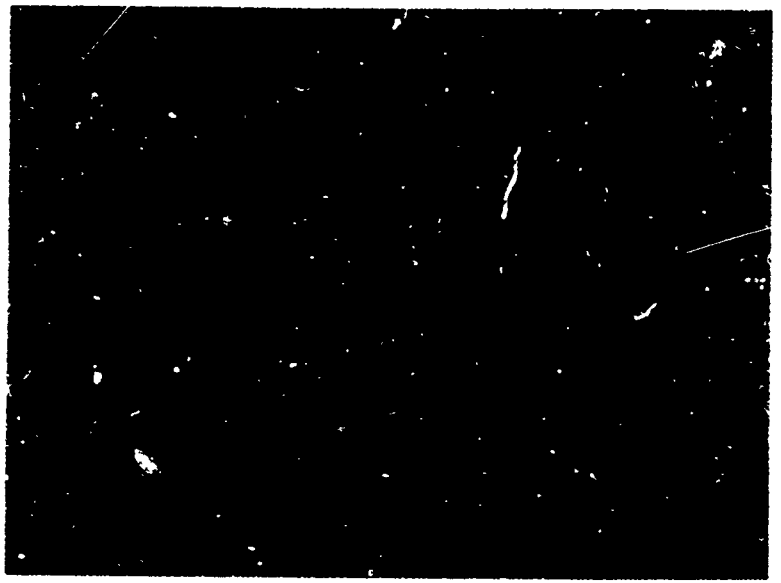
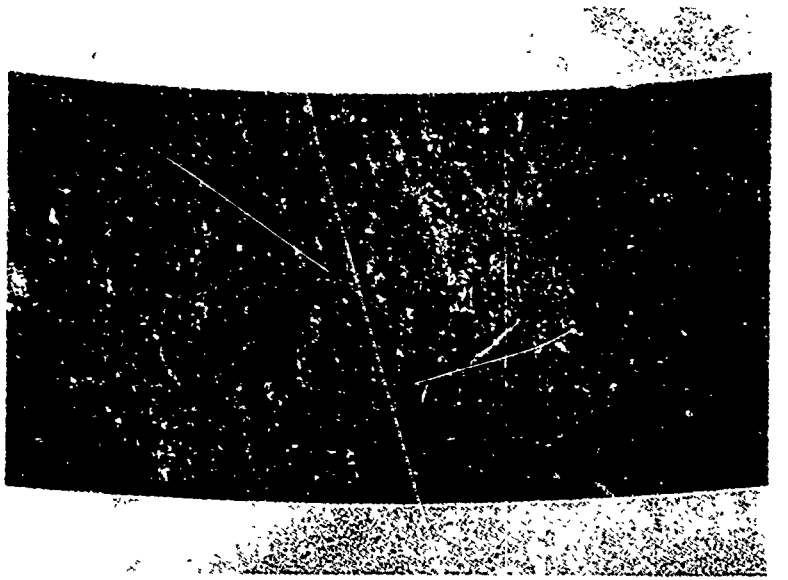


Figure 174. Sketch Showing QC Inspection Results on AVCO 3DCC Ring 4B



(5X)

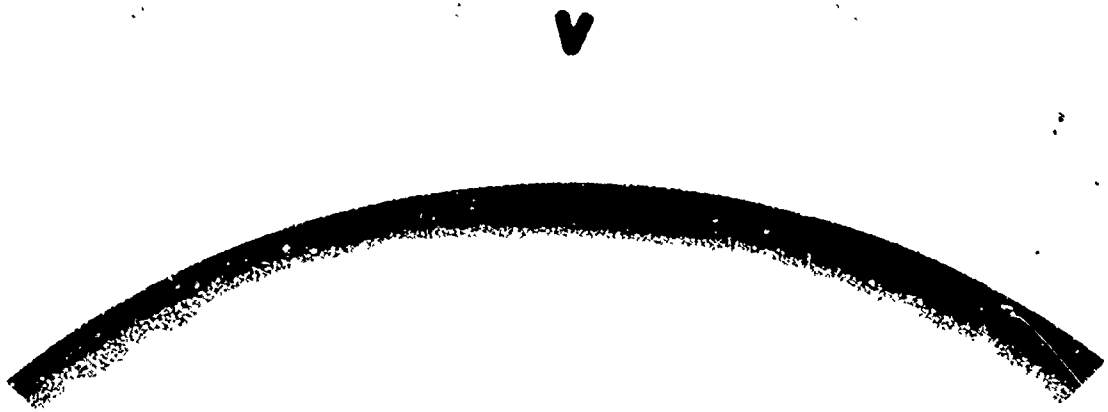
Radial View



(5X)

Axial View

Figure 175. Photographs Showing Typical Sandia Felt CC



Axial View

Positive Print

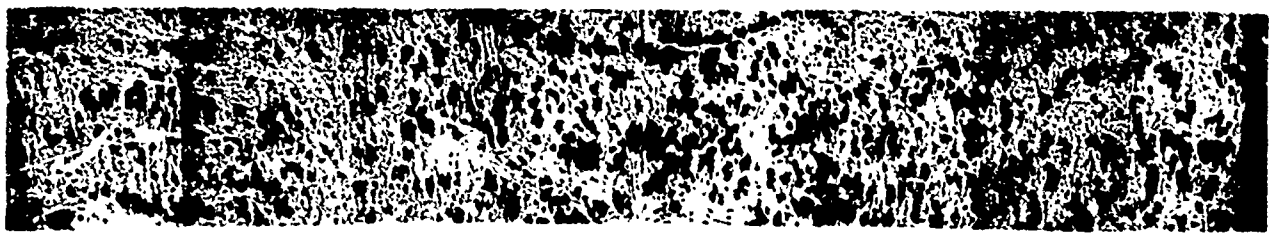
Figure 176. Typical Sandia Felt CC Structure Revealed by Radiography

Radial Direction



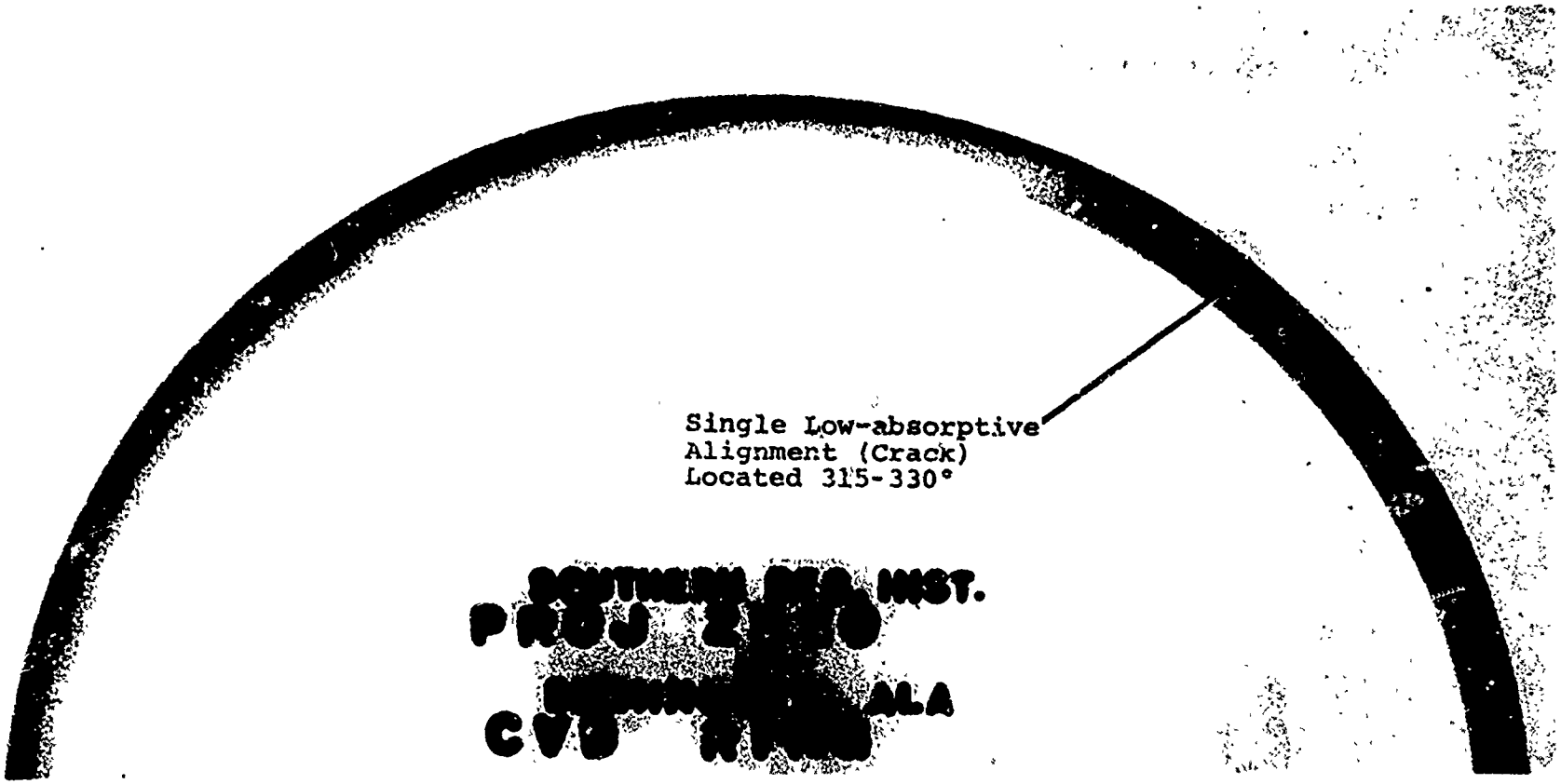
Ring 2N-2
(50X Before Reduction)

Radial Direction



Ring 3N-2
(50X Before Reduction)

Figure 177. Photomicrographs in Axial Direction of Sandia Felt CC Rings 2N-2 and 3N-2



Axial View

Positive Print

Figure 178. Radiograph Showing Anomaly in Sandia Felt CC Ring #4P-2

General Notes:

1. ⬡ Radial Velocity in in./μsec and ultrasonic transmission in added db (higher values denote lower material attenuation)
2. ↕ Axial velocity in in./μsec
3. Radiography was not revealing of any material anomalies
4. Bulk density - 1.805 gm/cm³
5. Liquid penetrant indications are shown in sketch

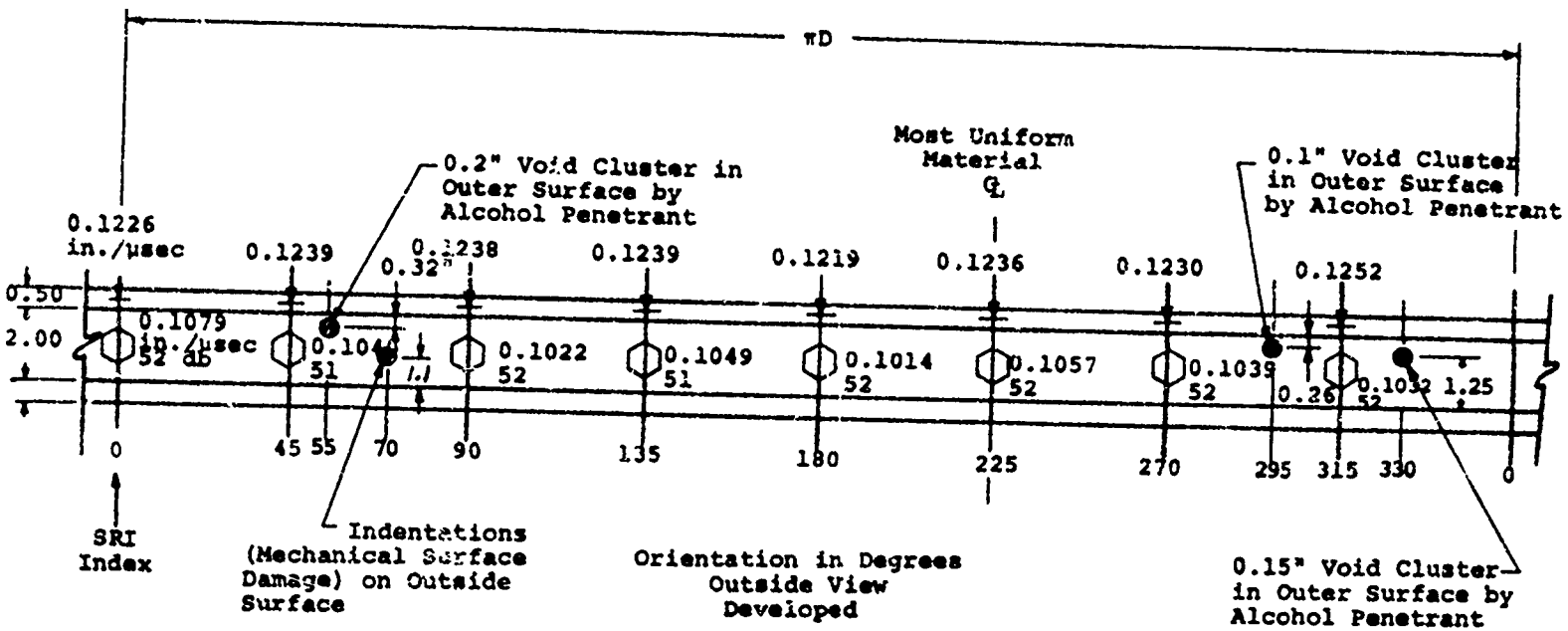


Figure 179. Sketch Showing FT Inspection Results on Sandia Felt CC Ring 2N-2

Notes:

1. ⬡ Radial Velocity in in./μsec and ultrasonic transmission in added db (Higher values denote lower material attenuation)
2. ↓ Axial Velocity in in./μsec
3. Radiography was not revealing of any material anomalies
4. Bulk density = 1.802 gm/cm³
5. Liquid penetrants not revealing of any material anomalies

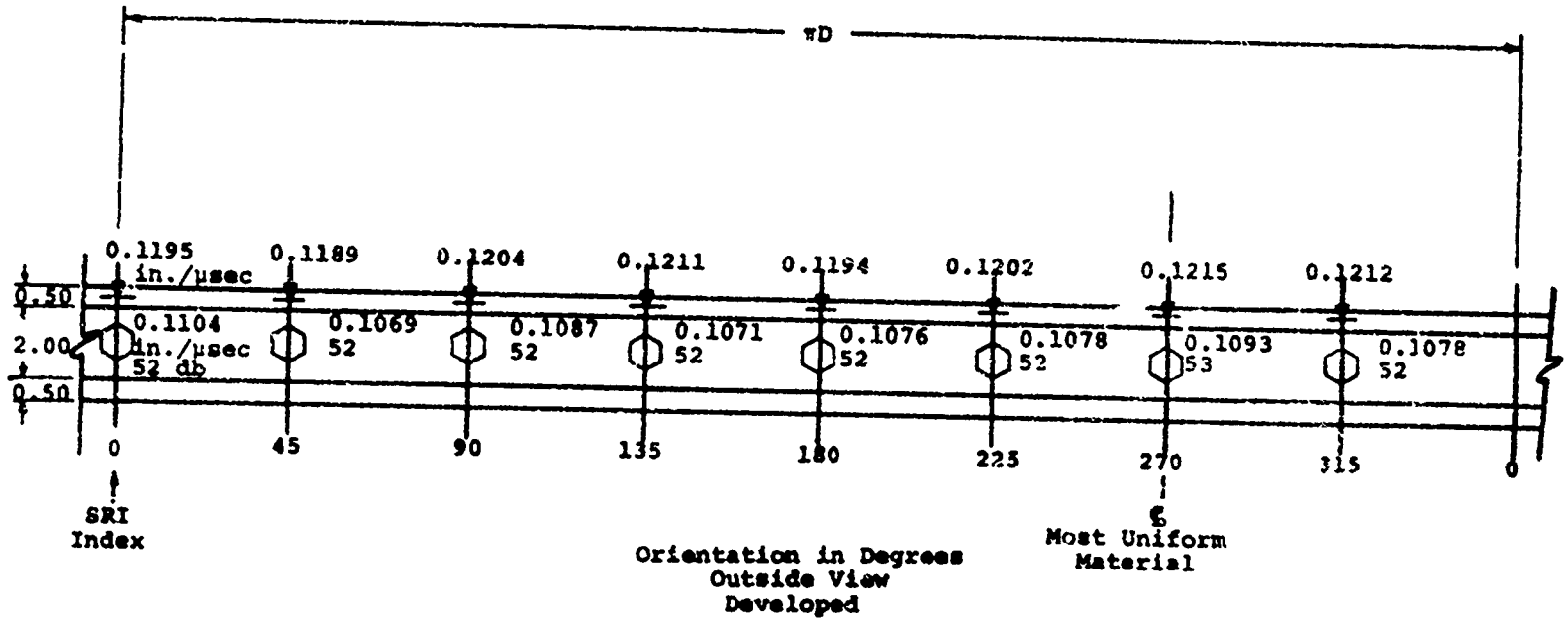


Figure 190. Sketch Showing FT Inspection Results on Sandia Felt CC Ring 3N-2

Table 1

Phase I Test Matrix for Carbon/Carbon Materials

Test	Number of[a] Specimens	Direction	Temp. °F	Damage Levels	Repetition	Total Tests
Full NDT on Arcs	7, (6)	------	----	7, (6)	----	13
Bulk Modulus of Elasticity	7 arcs (6) arcs	------	70	7, (6)	2, (2)	26
NDT on blanks[b]	38, (46)	------	----	------	------	84
NDT on coupons[c]	38, (46)	------	----	------	------	84
Stress-strain to failure (tension)	6, (8) 6, (8)	Cir. Cir.	70 3000	3, (3) 3, (3)	2 ea 2 ea	12 12
Stress-strain to failure (comp.)	6, (8) 6, (8)	Cir. Cir.	70 4500	3, (3) 3, (3)	2 ea[d] 2 ea	11 12
Thermal Expansion Coefficient	6, (6) 2, (2)	Cir. Axial	70-5000 70-5000	3, (3) 1, (1)	2 ea 2 ea	12 4
Thermal Conductivity	4, (4) 2, (2)	Radial Radial	70-2000 2000-5000	2, (2) 1, (1)	2 ea 2 ea	8 4
Gage Suitability	(8)	------	70	4 sm. spec. 4 lge. spec.		(8)

Notes:

[a] 3DCC - Material # 8 -- X
Felt CC - Material #12 -- (X)

[b] NDT on blanks consists of bulk grav density, radial and axial ultrasonic velocity, and radial ultrasonic transmission tests

[c] NDT on coupons consists of open porosity, visual inspection, and radiography tests

[d] Virgin 70°F compression singleton data only for Material #12

TABLE 2

PHASE I TEST MATRIX PHENOLIC COMPOSITE MATERIALS

Test	Loading Direction	Number of Specimens[a]	Total No. of Tests
NDT on blanks[b]	-----	28, (28), [28A], [23B]	112
NDT on coupons[c]	-----	28, (28), [28A], [28B]	112
Stress-strain to failure (tension)	Axial Cir.	7, (7), [7A], [7B] 7, (7), [7A], [7B]	28 28
Stress-strain to failure (compression)	Axial Cir.	7, (7), [7A], [7B] 7, (7), [7A], [7B]	28 28

Notes:

[a]

Material	No. of Spec.
R6300 - Material #10	X
3DQP - Material #11	(X)
3DCP - Material #15A	[XA]
3DC/QP - Material #15B	[XB]

[b] NDT on blanks consists of bulk grav density, radial and axial ultrasonic velocity, and radial ultrasonic attenuation tests

[c] NDT on coupons consists of open porosity, visual inspection and radiography tests

TABLE 3

PHASE II TEST MATRIX FOR UNDEGRADED RINGS AND ARCS

		Material	Number of Rings or Arcs	Full NDT[b]	Q. C. NDT[a]	Mechanical Bulk Test
Proposed	Rings	3DCC - # 8	15	2	13	4[c]
		Felt CC - #12	18	2	16	4[c]
		R6300 - #10	9	2	7	4[c]
		3DC/QP - #15	11	4	7	8[c]
		3DCP - #15A	12	4	8	8[c]
	Arcs	R6300 - #10	15	-	15	-
		3DC/QP - #15	21	6	15	6
		3DCP - #15A	37	12	25	12
		Total Tests ---	Rings-65 Arcs -73	Rings-14 Arcs -18	Rings-51 Arcs -55	Rings-14 Arcs -18
Actual	Rings	3DCC - # 8	17	2	15	2[c]
		Felt CC - #12	20	2	18	2[c]
		R6300 - #10	10	2	8	2[c]
		3DC/QP - #15	6	-	6	-
		3DCP - #15A	10	-	10	-
		3DCP(T400)	4	-	4	-
	Arcs	3DCC - # 8	21	-	21	-
		R6300 - #10	18	-	18	-
		3DC/QP - #15	11	-	11	-
		3DCP - #15A	22	5	17	-
		3DCP(T400)	4	-	4	-
	Arcs	3DC/QP - #15 Problem	8	8	-	2
		Total Tests ---		Rings- 6 Arcs -13	Rings-61 Arcs -71	Rings-6 Arcs -?

Notes:

[a]Quality control nondestructive tests consisted of visual (1X) and photos (1X to 10X), bulk density measurements and radiography

[b]Full NDT consists of all of the quality control evaluations plus ultrasonic velocity, ultrasonic transmission, open porosity, penetrant inspection, and 40X photomicrography

[c]Ring flexure and hydrostatic compression tests for each ring

TABLE 4

RESULTS OF NDE MONITOR EVALUATIONS OF 3DCC, MATERIAL #8, IMPACTED ARCS

Specimen	Impact Level (K Tape)	Thickness (Inches)			ARC Bulk Density (gm/cm³)		Specimen Bulk Density Range (gm/cm³)	ARC Porosity		ARC Velocity			Specimen Velocity		Barre	ARC Sonic Transmission		Specimen Sonic Transmission Radial Added (db)	ARC NOE (10⁶ psi)
		Before Impact	After Impact	After NOE	Before Impact	After Impact		Open After Impact (%)		Axial - Before Impact (in./usec)	Radial - After Impact (in./usec)	Radial - After NOE (in./usec)	Axial (in./usec)	Circum (in./usec)	Radial (in./use.	Radial - After Impact Added (db)	Radial - After NOE Added (db)		
9-AR-V	0	0.449	0.449	0.449	1.643	1.642	1.639 1.650	11.0	11.9	0.3352	0.2039	-	0.3668 0.3791		0.1878 0.1866	28	24	26	0.69[1] 0.72
9-AR-6	1.030	0.454	0.453	0.453	1.677	1.686	1.679 1.684	10.5	10.3 10.7	0.3502	0.2035 0.2200	-	0.4363 0.4592	0.3693 0.3923	-	28	25.5	15 17	1.40 1.28
9-AR-4	1.643	0.454	0.453	0.453	1.662	1.666	1.656 1.666	11.2	-	0.3578	0.2034 0.2189	-	-	0.3725 0.3916	0.2025 0.2092	28	25	-	1.46 1.20
9-AR-2	2.203	0.454	0.453	0.453	1.673	1.676	1.671 1.686	10.9	10.3 10.8	0.3669	0.1946 0.2026	-	0.4032 0.4732	0.3738 0.3557	-	24	23.5	16 19	0.64 0.97
9-AR-1	3.045	0.454	0.453	0.453	1.675	1.681	1.666 1.676	10.9	-	0.3514	0.1857 0.1873	-	-	0.3713 0.3887	0.1874 0.2166	23.5	24.5	-	0.63 0.95
9-AR-5	3.362	0.454	0.455	0.453	1.672	1.664	1.670 1.677	11.2	11.3 11.7	0.3530	0.1875 0.2012	-	0.4026 0.4682	0.3669 0.4034	-	17	14.5	13 9	0.52 0.56
9-AA-1	5.390	0.454	0.462	0.462	1.681	1.654	1.649 1.662	13.5	-	0.3614	0.1585 0.2077	-	-	0.3785 0.3914	0.2014 0.2146	9	13	-	0.29 0.32

1. NOE values for 3DCC arcs are not engineering values. These NOE values include effects of shear deflections and are therefore dependent on specimen and test geometry. Geometry for virgin 3DCC specimen different.

2. Radial velocity before impulse loading was not measurable because of signal attenuation. Signal treatment was later improved.

TABLE 1

[illegible] INSPECTIVE PRE-STRUCTURE-CRACK
IN AMCO 1020 IMPACTED ARCS

Specimen	% Impact Level	In Group Polaroid	Visual (1X) Edge Appearance	Visual (1X) Surface Appearance	Visual (1X) Edge & Inner Surface Appearance	Liquid Penetrant	Loose Wedge Axial	SEM Fractomicrographs	Radial Polar Echo
0-AP-8	0%	Fig 53	1. Spalled radials to one edge Fig 54a 2. Bulk & aligned (axial) delams on one edge. Fig 54a	1. Radials protruded slightly out of front and rear faces (primarily exterr. Fig 54b 2. Radial ends occasionally visible at rear face. Fig 54c	Rev. cooling of any radial-circ. interfaces		Normal	Micro Normal Fig 60a	Material Before Explosion
0-AP-9	1 Lvl	Fig 53	1. Spalled radials to one edge similar to 0-AP-8 above. 2. Bulk & aligned (axial) delams one edge similar to 0-AP-8 above	2. Increased radial protrusion from front and rear faces. 3. Radial ends at rear face occasionally spalled similar to 0-AP-8 above.		Bulk & aligned (axial) delams to one edge more severe than 0-AP-8 (Partial)	Normal	Micro normal; Micro Separation located 0.36 inch from rear face for side	
0-AP-2	2 Lvl	Fig 53	1. Spalled radials to one edge similar to 0-AP-8 above 2. Rear delam is sted 0.1 inch from rear face. Delam measured 1.3 inch in one edge and about 1 inch in adjacent edge Fig 53a . Also, bulk delams between rear delam and rear face. 3. Decreased bulk delams (axial) in other edge than 0-AP-8.	1. Slight radial protrusion in front face with matrix/ spall around radials Fig 53b 2. Increased radial protrusion in rear face. 3. Increased spall of radial ends at rear face Fig 53b			Normal	Circ Separation at 0.1 inch from rear face. Fig 63b	
0-AP-3	3 Lvl	Fig 53	1. Increased spalled radials one edge. Fig 54 2 Bulk delams one edge similar to 0-AP 5 below. 3 Rear delam (also) primarily one edge 0.1 inch from rear face Fig 54 4. Some lift (also) at edge of front face Fig 54	1. Slight increase in radial protrusion at front & rear faces. 2. Increased spall of radial ends at front & rear faces.			Two circ low-absorptive alignments 18.6 inch & 0.7 inch long located 0.3 inch from rear face. Fig 61	Micro Normal Fig 63b	
0-AP-5	4 Lvl	Fig 53	1 Increased spalled radials (one) to two edges. Fig 57a. 2. Bulk (primarily delams to one edge Fig 57a 3 matrix spall primarily from two edges 4 Rear delam (also) primarily one edge 0.1 inch from rear face. Fig 57b 5. Some lift & matrix spall at one corner. Fig 57b	1 Radial protrusion & spall of radial ends at front & rear faces similar to 0-AP-7 above. One radial protruded 0.2 inch out from front face.			Continuous circ. low-absorptive alignments 0.1 inch & 0.75 in from rear face. Also, several sml. orientat circ. low-absorptive alignments. Fig 61	Micro Normal Fig 63b	
0-AP-1	5.3%	Fig 53	1. Increased bulk (axial) delams one edge. Fig 58a 2. Increased rear delam (circ) primarily one edge 1.1 inch from rear face. Fig 58a	1. Increased radial protrusion from front face 2. Increased spall of radial ends from rear face. 3 Rear radial rupturation. Fig 58b . 4. Rear more lift & matrix spall over edges on rear face Fig 58b . 5. Front face crack extending 0.4 inch across gage bounded from one edge - located about center of arc. Fig 58c			Increase circ low-absorptive alignments 0 inch, 0.2 inch 0.3 inch & 0.6 inch from rear face. Fig 61	1. Fractured circ along radials. Fig 63c 2. Separations through radials at 0.1 inch & 0.28 inch from rear face. Fig 63c 3. Circ/axial separations at various locations Fig 63c	
0-AP-4	7.4%	Fig 53	1 Some axial-delam 0.1 inch from rear face. Fig 59a 2 Some bulk delams Fig 59a. 3 Rear delam 0.1 inch from rear face. Fig 5a	1. Some more lift & matrix spall from rear face. Fig 59a 2 The circumferen crack near center of arc. Fig 59b			1. Some circ low-absorptive alignments 1 & inch and 3.3 inch from rear face Fig 61 2. Rear through thickness radial low-absorptive alignment near center of arc. Fig 61 3. Plastic material from rear face Fig 61	1. Fractured circ Fig 63d 2. Some, micro delams	
0-AP-	7.6%	Fig 53	1 Some broken (totally or partial) at corner; other wise, similar to 0 AP 4 at 7% with grease and rear delams to stand at 0.2 inch and 0.1 inch from rear face. Fig 59	1 Some more lift & matrix spall from rear face Fig 59			1 Some circ low-absorptive alignments at 0.1 inch & 0.3 inch from rear face. Fig 61 2 Plastic material from rear face. Fig 61	Similar to 0 AP-4 Above	

TABLE 6

RESULTS OF TENSILE AND COMPRESSIVE EVALUATIONS ON 3D CARBON-CARBON IMPACTED ARCS

Specimen Number	Impact Level (K Taps)	Temp F°	Bulk Density gm/cm³	Tensile Ultimate Strength psi	Tensile Initial Elastic Modulus 10^6 psi	Axial Sonic Velocity in./μsec	Circum Sonic Velocity in./μsec	Open Porosity %
8-AR-8-T01C	1.030	70	1.684	11,120	11.0	0.4496	0.3913	10.2
T04C		70	1.683	11,040	8.87	0.4536	0.3829	10.7
8-AR-2-T01C	2.200	70	1.672	10,600	5.97	0.4032	0.3957	10.8
T04C		70	1.677	16,100	10.3	0.4112	0.3781	10.6
8-AR-5-T01C	3.360	70	1.672	9,280	6.47	0.4296	0.3898	11.3
T04C		70	1.673	10,800	8.09	0.4545	0.3809	11.7
8-AR-8-T02C	1.030	3000	1.679	16,240	10.8[1]	0.4363	0.3821	10.6
T03C		3000	1.682	16,600	10.4	0.4592	0.3793	10.6
8-AR-2-T02C	2.200	3000	1.671	18,400	7.28	0.4732	0.3945	10.8
T03C		3000	1.686	19,120	9.95	0.4169	0.3738	10.3
8-AR-5-T02C	3.360	3000	1.670	18,570	6.98	0.4026	0.4034	11.3
T03C		3000	1.677	16,600	6.82	0.4682	0.3669	11.2

TABLE 6 CONTINUED

Specimen Number	Impact Level (K Taps)	Temp F°	Bulk Density gm/cm³	Compressive Ultimate Strength psi	Compressive Initial Elastic Modulus 10^6 psi	Radial Sonic Velocity in./μsec	Circum Sonic Velocity in./μsec	Sonic Trans-mission (Added db)
8-AR-4-C01C	1.640	70	1.663	5,540	5.85	0.2078	0.3807	21.0
C04C		70	1.664	5,990	5.05	0.2053	0.3725	21.0
8-AR-7-C01C	3.045	70	1.666	4,550	4.82	0.1956	0.3841	20.5
C03C		70	1.675	5,220	7.26	0.2165	0.3713	20.5
8-AR-1-C02C	5.390	70	1.662	4,030	9.0	0.2103	0.3846	19.5
C03C		70	1.649	4,030	4.86	0.2111	0.3904	20.0
8-AR-[illegible]C020		4500	1.629	11,100	1.22	0.1886	0.3660	26.0
C01C	0	4500	1.630	11,620	2.98	0.1878	0.3791	26.0
8-AR-4-C02C		4500	1.666	11,270	3.79	0.2092	0.3824	20.5
C03C	1.640	4500	1.656	10,680	2.68	0.2025	0.3844	21.0
8-AR-7-C02C		4500	1.676	10,400	0.62	0.1951	0.3724	22.0
C04C	3.045	4500	1.674	10,860	0.89	0.1874	0.3887	20.5
8-AR-1-C01C		4500	1.660	7,210	2.24	0.2144	0.3785	19.5
C04C	5.390	4500	1.651	7,650	1.65	0.2014	0.3914	20.0

[1]All tensile modulus evaluations at room temperature

TABLE 7

THERMAL EXPANSION OF 3DCC IN THE AXIAL DIRECTION AFTER 3.045 KT
MEASURED IN GRAPHITE DILATOMETER

Specimen and Run No.	Temp. °F	Time	Observed Total Elongation (10^{-3} in.)	Observed Unit Elongation (10^{-3} in./in.)	Unit Correction for Dilatometer Motion (10^{-3} in./in.)	Corrected Specimen Unit Elongation (10^{-3} in./in.)
Specimen: TE-1-A	59	8:05	0.0	0.0	0.0	0.0
8AR-7-C1 & C3	555	8:45	-2.32	-0.77	0.69	-0.08
Run: 1	1080	9:25	-4.87	-1.63	1.70	0.07
Run: 6595-75-135K1	1633	10:05	-7.32	-2.44	2.92	0.48
Initial length:	2493	10:50	-10.57	-3.53	5.01	1.48
2.9966 in.	2982	11:30	-12.26	-4.09	6.34	2.25
Final length:	3493	12:10	-14.02	-4.68	7.72	3.04
2.9973 in.	3943	12:50	-15.67	-5.23	9.00	3.77
Initial weight:	4415	1:30	-17.78	-5.93	10.39	4.46
1.2554 gm	5004	2:05	-20.87	-6.96	12.16	5.20
Final weight:	60	7:55	0.42	0.14	0.0	0.14
1.2529 gm						
Density: gm/cm³						
Specimen: 8AR-7-C1&C3	59	7:45	0.0	0.0	0.0	0.0
Run: 2	535	8:25	-1.79	-0.60	0.38	-0.22
Run: 6595-77-122A-E	1043	9:05	-3.50	-1.17	1.04	-0.13
Initial length:	1634	9:45	-5.27	-1.76	2.03	0.27
2.9973	2468	10:25	-7.31	-2.44	3.57	1.13
Final length:	3104	11:05	-8.90	-2.97	4.89	1.92
2.9970	3488	11:45	-9.80	-3.27	5.71	2.44
Initial weight:	3949	12:25	-10.86	-3.62	6.73	3.11
1.2529 gm	4476	1:05	-12.11	-4.04	7.94	3.90
Final weight:	5055	1:40	-13.74	-4.58	9.30	4.72
1.2473 gm	60	6:20	0.17	0.06	0.0	0.06
Density: gm/cm³						

TABLE 8

THERMAL EXPANSION OF 3DCC IN THE CIRCUMFERENTIAL DIRECTION AFTER 5.39 KT
MEASURED IN GRAPHITE DILATOMETER

Specimen and Run No.	Temp. °F	Time	Observed Total Elongation (10^{-3} in.)	Observed Unit Elongation (10^{-3}in./in.)	Unit Correction for Dilatometer Motion (10^{-3} in./in.)	Corrected Specimen Unit Elongation (10^{-3} in./in.)
Specimen: TE-1C	59	8:05	0.0	0.0	0.0	0.0
8AR-1-C2&C3	449	8:45	-1.50	-0.50	0.48	-0.02
Run: 1	993	9:25	-3.63	-1.21	1.48	0.27
Run: 6595-76-134K4	1650	10:05	-5.87	-1.96	2.97	1.01
Initial length:	2392	10:50	-7.75	-2.59	4.67	2.08
2.9975 in.	2932	11:30	-9.07	-3.03	6.03	3.00
Final length:	3463	12:10	-10.69	-3.57	7.48	3.91
2.9989 in.	3918	12:50	-12.16	-4.06	8.71	4.65
Initial weight:	4440	1:30	-13.29	-4.43	10.20	5.77
3.0774 gm	5014	2:05	-16.06	-5.36	11.88	6.52
Final weight:	60	7:55	1.49	0.50	0.0	0.50
3.0736 gm						
Density: gm/cm^3						
Specimen: TE-2C	59	7:45	0.0	0.0	0.0	0.0
8AR-1-C2&C3	535	8:25	-2.08	-0.69	0.64	-0.05
Run: 2	1099	9:05	-4.56	-1.52	1.72	0.20
Run: 6595-78-135K1	1713	9:45	-6.95	-2.32	3.09	0.77
Initial length:	2528	10:25	-9.44	-3.15	5.12	1.97
2.9989 in.	3028	11:05	-11.15	-3.72	6.48	2.76
Final length:	3483	11:45	-12.42	-4.14	7.71	3.57
2.9986 in.	3999	12:25	-13.97	-4.66	9.17	4.51
Initial weight:	4466	1:05	-15.55	-5.18	10.52	5.34
3.0736 gm	5065	1:40	-18.67	-6.23	12.33	6.10
Final weight:	60	6:20	0.03	0.01	0.0	0.01
3.0718 gm						
Density: gm/cm^3						

TABLE 9

THERMAL EXPANSION OF 3DCC IN THE CIRCUMFERENTIAL DIRECTION AFTER 2.2 KT
MEASURED IN QUARTZ DILATOMETER

Specimen	Time	Specimen Temperature - °F				Observed Total Elongation 10^{-3} in.	Observed Unit Elongation 10^{-3} in./in.	Unit Elongation Correction for Dilatometer Motion 10^{-3} in./in.	Corrected Specimen Unit Elongation 10^{-3} in./in.
		Top	Middle	Bottom	Average				
Spec: 8-AR-3-T1 & T2 Run: 1 Run: 6336-27-20Q Density: 1.672 gm/cm³ Velocity: 0.3951 in./usec		Initial Length: 3.0021 in. Final Length: 3.0017 in.					Initial Weight: 16.5075 gm Final Weight: 16.4975 gm		
	11:00	74	-	74	74	0.0	0.0	0.0	0.0
	11:25	214	-		214	-0.40	-0.13	0.02	-0.11
	11:33	297	-		297	-0.58	-0.19	0.05	-0.14
	11:37	328	-		328	-0.65	-0.22	0.06	-0.16
	11:45	396	-		396	-0.78	-0.26	0.07	-0.19
	11:55	451	-		451	-0.85	-0.28	0.09	-0.19
	12:10	484	-	484	484	-0.91	-0.30	0.10	-0.20
	12:30	612	-		612	-1.11	-0.37	0.14	-0.23
	12:47	823	-		823	-1.23	-0.41	0.21	-0.20

TABLE 10

THERMAL EXPANSION OF 3DCC IN THE CIRCUMFERENTIAL DIRECTION AFTER 2.2 KT
MEASURED IN QUARTZ DILATOMETER

Specimen and Run No.	Temp. °F	Time	Observed Total Elongation (10^{-3} in.)	Observed Unit Elongation (10^{-3} in./in.)	Unit Correction for Dilatometer Motion (10^{-3} in./in.)	Corrected Specimen Unit Elongation (10^{-3} in./in.)
Specimen: 8-AR-2 T1&T2	76	7:40	0.0	0.0	0.0	0.0
	460	8:15	-1.27	-0.42	0.23	-0.14
Run: 1	964	8:50	-2.80	-0.93	0.92	-0.01
Run: 6336-28-122A-E	1577	9:30	-4.48	-1.49	1.87	0.38
Initial length: 3.0017 in.	2372	10:10	-6.41	-2.14	3.37	1.23
	2917	10:45	-7.74	-2.58	4.51	1.93
Final length: 3.0017 in.	3483	11:20	-8.98	-2.99	5.71	2.72
	3959	11:55	-10.01	-3.33	6.80	3.47
Initial weight: 16.4975 gm	4425	12:30	-11.49	-3.83	7.86	4.03
	4963	1:05	-13.16	-4.38	9.21	4.83
Final weight: 16.4791 gm	75	7:15	0.32	0.11	0.0	0.11
Density: 1.672 gm/cm^3						
Velocity: 0.3951 in./μsec						
Specimen: 8-AR-2 T3&T4	76	7:45	0.0	0.0	0.0	0.0
	493	8:20	-1.79	-0.60	0.51	-0.09
Run: 1	974	8:55	-3.74	-1.25	1.29	0.04
Run: 6336-29-131K4	1689	9:35	-6.33	-2.11	2.71	0.60
Initial length: 3.0018 in.	2513	10:15	-9.40	-3.13	4.69	1.56
	3002	10:50	-11.16	-3.72	5.90	2.18
Final length: 3.0016 in.	3513	11:25	-12.93	-4.31	7.23	2.92
	4004	12:00	-14.83	-4.94	8.57	3.63
Initial weight: 16.6305 gm	4496	12:35	-16.80	-5.60	9.90	4.30
	4983	1:10	-19.10	-6.36	11.31	4.95
Final weight: 16.6037 gm	75	7:15	0.28	0.09	0.0	0.09
Density: 1.681 gm/cm^3						
Velocity: 0.3759 in./μsec						

TABLE 11

THERMAL EXPANSION OF 3DCC IN THE CIRCUMFERENTIAL DIRECTION AFTER 3.36 KT
MEASURED IN QUARTZ DILATOMETER

Specimen	Time	Specimen Temperatura - °F				Observed Total Elongation 10^{-3} in.	Observed Unit Elongation 10^{-3} in./in.	Unit Elongation Correction for Dilatometer Motion 10^{-3} in./in.	Corrected Specimen Unit Elongation 10^{-3} in./in.
		Top	Middle	Bottom	Average				
Spec: 8-AR-5-T1 & T2 Run: 1 Run: 6336-26-14MQ Density: 1.671 gm/cm³ Velocity: 0.3966 in./μsec		Initial Length: 3.0018 in. Final Length: 3.0013 in.				Initial Weight: 16.5147 gm Final Weight: 16.6012 gm			
	11:00	74	-	74	74	0.0	0.0	0.0	0.0
	11:25	213	-		213	-0.34	-0.11	0.04	-0.07
	11:33	293	-		293	-0.50	-0.17	0.07	-0.10
	11:37	327	-		327	-0.58	-0.19	0.08	-0.11
	11:45	384	-		384	-0.69	-0.23	0.09	-0.12
	11:55	443	-		443	-0.78	-0.26	0.11	-0.15
	12:10	493	-	493	493	-0.85	-0.28	0.12	-0.16
	12:30	632	-		632	-1.02	-0.34	0.16	-0.18
	12:47	806	-		806	-1.10	-0.37	0.20	0.17

TABLE 12

THERMAL EXPANSION OF 3DCC IN THE CIRCUMFERENTIAL DIRECTION AFTER 3.36 KT MEASURED IN GRAPHITE DILATOMETER

Specimen and Run No.	Temp. °F	Time	Observed Total Elongation (10^{-3} in.)	Observed Unit Elongation (10^{-3} in./in.)	Unit Correction for Dilatometer Motion (10^{-3} in./in.)	Corrected Specimen Unit Elongation (10^{-3} in./in.)
Specimen: 8-AR-5 T1 & T2	78	7:55	0.0	0.0	0.0	0.0
	488	8:35	-1.28	-0.43	0.29	-0.14
Run: 1	1063	9:15	-3.00	-1.00	1.03	0.03
Run: 6336-30-122A-E	1621	9:55	-4.50	-1.50	1.96	0.46
Initial length: 3.0013 in.	2473	10:35	-6.44	-2.15	3.58	1.43
	2992	11:15	-7.64	-2.55	4.66	2.11
Final length: 3.0013 in.	3523	11:55	-8.80	-2.93	5.80	2.87
	4040	12:35	-10.06	-3.35	6.97	3.62
Initial weight: 16.6012 gm	4466	1:15	-11.30	-3.77	7.95	4.18
	5004	1:50	-13.11	-4.37	9.28	4.91
Final weight: 16.5780 gm	75	7:15	0.64	0.21	0.0	0.21
Density: 1.671 gm/cm³						
Velocity: 0.3966 in./μsec						
Specimen: 8-AR-5 T3 & T4	78	8:00	0.0	0.0	0.0	0.0
	493	8:40	-1.84	-0.61	0.51	-0.10
Run: 1	1017	9:20	-3.94	-1.31	1.39	0.08
Run: 6336-31-131K4	1684	10:00	-6.33	-2.11	2.70	0.59
Initial length: 3.0015 in.	2523	10:40	-9.31	-3.10	4.66	1.56
	3002	11:20	-11.01	-3.67	5.89	2.22
Final length: 3.0016 in.	3503	12:00	-12.63	-4.21	7.22	3.01
	3979	12:40	-14.48	-4.82	8.48	3.66
Initial weight: 16.5877 gm	4496	1:20	-16.61	-5.53	9.90	4.37
	5014	2:00	-19.36	-6.45	11.42	4.97
Final weight: 16.5524 gm	75	7:15	0.51	0.17	0.0	0.17
Density: 1.675 gm/cm³						
Velocity: 0.3739 in./μsec						

TABLE 13

THERMAL CONDUCTIVITY OF 3DCC IN THE RADIAL DIRECTION
EXPOSED TO 1.03 AND 2.20 KT USING COMPARATIVE ROD APPARATUS WITH ARMCO IRON REFERENCES

Specimen and Time	Mean Temperature of Specimen °F	Thermal Conductivity of Specimen k_s Btu in./hr ft² °F	ΔT through Specimen °F	Mean Temperature of Lower Reference °F	Thermal Conductivity of Lower Reference k_1 Btu in./hr ft² °F	ΔT through Lower Reference ΔT_1 °F	Mean Temperature of Upper Reference °F	Thermal Conductivity of Upper Reference k_2 Btu in./hr ft² °F	ΔT through Upper Reference ΔT_2 °F
Spec: 8-AR-2 Run: 5493-15-4 Density: (2.20 KT)	L_s = 0.1984 in. L_1 and L_2 = 0.750 in. Specimen Diameter = 0.750 in.			Initial Thickness: 0.3984 in. Final Thickness: 0.3983 in.					
7-19-72 9:25a.m.	44	282	12.5	1.5	528	24.3	85.0	502	27.6
10:10a.m.	58	277	13.3	15.2	525	25.6	101.1	497	29.0
7-20-72 7:30a.m.	492	229	13.1	449.	404	26.7	533.	385	31.1
8:00a.m.	493	229	13.2	449.	404	26.7	533.	385	31.3
10:30a.m.	1,023	187	27.0	936.	300	61.5	1,111.	368	73.3
10:55a.m.	1,022	187	26.77	936.	300	61.1	1,110.	268	72.5
1:15p.m.	1,497	162	42.23	1,355.	228	110.9	1,645.	195	136.3
2:00p.m.	1,531	161	43.05	1,385.	221	115.53	1,679.	197	135.9
Spec: 8-AR-2 Run: 5493-17-4 Density: (2.20 KT)	L_s = 0.198 in. L_1 and L_2 = 0.750 in. Specimen Diameter = 0.750 in.			Initial Thickness: 0.3983 in. Final Thickness: 0.3983 in.					
7-21-72 2:15p.m.	62	259	14.6	19	522	27.3	108	495	29.2
2:30p.m.	66	259	14.6	23	521	27.0	112	494	29.3
7-24-72 9:25a.m.	479	225	13.3	438	403	27.3	520	388	29.9
3:10p.m.	790	191	28.7	708	347	59.3	886	308	68.1
3:45p.m.	790	192	28.7	708	347	59.2	886	308	68.3
7-25-72 10:45a.m.	1,489	159	43.8	1,350	228	112.7	1,646	195	137.1
11:05a.m.	1,498	162	42.2	1,360	226	112.2	1,654	195	134.1
1:05p.m.	1,758	126	41.2	1,648	195	95.8	1,885	200	102.5
1:25p.m.	1,758	125	41.3	1,648	195	96.1	1,885	200	102.0

TABLE 13 CONTINUED

Specimen and Time	Mean Temperature of Specimen °F	Thermal Conductivity of Specimen k_s Btu in./hr ft² °F	ΔT through Specimen °F	Mean Temperature of Lower Reference °F	Thermal Conductivity of Lower Reference k_1 Btu in./hr ft² °F	ΔT through Lower Reference ΔT_1 °F	Mean Temperature of Upper Reference °F	Thermal Conductivity of Upper Reference k_2 Btu in./hr ft² °F	ΔT through Upper Reference ΔT_2 °F
Spec: 8-AR-2 Run: 5493-33-4 Density: (2.20 MT)	L_s = 0.1984 in. L_1 and L_2 = 0.750 in. Specimen Diameter = 0.7506 in.			Initial Thickness: 0.3970 in. Final Thickness: 0.3970 in.			Initial Weight: 4.9198 gm Final Weight: 4.9188 gm		
8-9-72 12:40p.m.	919	188	28.9	836	320	64.4	1,017	283	73.0
1:00p.m.	929	186	29.2	847	319	64.3	1,027	282	73.3
3:45p.m.	1,723	157	28.8	1,756	195	87.8	1,844	200	85.5
4:05p.m.	1,705	167	27.0	1,618	195	88.1	1,827	200	84.9
Spec: 8-AR-8 Run: 5493-19-3 Density: (1.03 MT)	L_s = 0.1970 in. L_1 and L_2 = 0.750 in. Specimen Diameter = 0.7506in.			Initial Thickness: 0.3970 in. Final Thickness: 0.3969 in.			Initial Weight: 4.8405 gm Final Weight: 4.8137 gm		
7-26-72 3:05p.m.	74	261	12.8	37	518	24.6	113	493	25.6
3:20p.m.	77	250	13.1	38	518	24.1	115	493	25.7
7:15p.m.	502	234	15.7	451	402	33.1	553	380	38.3
7:30p.m.	503	234	15.4	450	402	33.0	552	380	37.1
7-27-72 10:45a.m.	980	195	27.3	894	368	64.7	1,074	273	75.6
11:05a.m.	979	195	27.3	894	308	64.4	1,073	273	75.4
2:40p.m.	1,463	164	44.0	1,318	232	117.9	1,623	155	141.1
3:00p.m.	1,469	166	43.5	1,316	233	118.0	1,628	195	140.5

TABLE 13 CONTINUED

Specimen and Time	Mean Temperature of Specimen °F	Thermal Conductivity of Specimen k_s Btu in./hr ft² °F	ΔT through Specimen °F	Mean Temperature of Lower Reference °F	Thermal Conductivity of Lower Reference k_1 Btu in./hr ft² °F	ΔT through Lower Reference ΔT_1 °F	Mean Temperature of Upper Reference °F	Thermal Conductivity of Upper Reference k_2 Btu in./hr ft² °F	ΔT through Upper Reference ΔT_2 °F
Spec: S-AR-8 Run: 5493-21-1 Density:	l_s = 0.1970 in. l_1 and l_2 = 0.750 in. Specimen Diameter = 0.7506 in.			Initial Thickness: 0.3970 in. Final Thickness: 0.3970 in.			Initial Weight: 4.9395 gm Final Weight: 4.9381 gm		Weight with surrounding wire	
(1.03 KT)										
7-31-72 10:55a.m.	82	302	10.6	46	512	23.4	115	492	25.2
11:15a.m.	84	305	10.4	46	511	23.3	117	491	25.1
4:00p.m.	745	220	27.8	657	359	63.6	838	319	74.6
4:15p.m.	752	220	27.5	664	358	63.3	843	318	73.8
8-01-72 12:30p.m.	1,234	171	39.6	1,112	268	96.3	1,368	225	114.8
12:55p.m.	1,235	172	39.8	1,114	268	96.7	1,368	225	115.7
3:00p.m.	1,775	134	45.6	1,632	195	123.8	1,910	201	112.4

Notes: 1. All measurements made with helium purge. Apparatus was not evacuated prior to determination
2. Thermal conductivity (k_s) of specimen calculated from following equation

$$k_s = \left[\frac{k_1 \Delta T_1}{l_1} + \frac{k_2 \Delta T_2}{l_2}\right] \frac{l_s}{2\Delta T_s}$$

where

k = thermal conductivity
ΔT = temperature drop over gage length
l = gage length

and subscripts 1, 2, and s refer to lower reference, upper reference, and specimen, respectively.

TABLE 14

THERMAL CONDUCTIVITY OF 3DCC IN THE RADIAL DIRECTION EXPOSED TO 1.03 KT
USING RADIAL INFLOW APPARATUS (STRIP TECHNIQUE)

Specimen and Run Number	Time	Strip Location	Average ΔT Each Strip	Heat Flow to Calorimeter Btu/hr	Specimen Average Mean Temperature	Average Thermal Conductivity Btu in./hr ft² °F
Spec: S-AR-T-1,2,3,4 Run: 6336-46-69-2-L		Front	79	281		
		Left	91	288		
		Back	77	294		
		Right	83	308		
				312		
	9:25			297	1,495	146
		Front	132	496		
		Left	161	469		
		Back	146	487		
		Right	151	509		
				491		
				494		
	10:45			491	2,618	134
		Front	196	648		
		Left	237	662		
		Back	222	667		
		Right	216	661		
				658		
				654		
	11:55			659	3,631	122
		Front	237	905		
		Left	283	888		
		Back	250	910		
		Right	250	910		
				901		
				906		
	1:00			904	4,541	143

TABLE 14 CONTINUED

Specimen and Run Number	Time	Strip Location	Average ΔT Each Strip	Heat Flow to Calorimeter Btu/hr	Specimen Average Mean Temperature	Average Thermal Conductivity Btu in./ht ft²°F
Spec: 8-AR-8T Run: 6336-62-69-2		Front	95	363		
		Left	91	360		
		Back	98	362		
		Right	80	360		
				349		
				362		
	8:55			359	1,546	159
		Front	195	674		
		Left	198	678		
		Back	194	671		
		Right	181	679		
				673		
				652		
	10:15			672	2,805	147
		Front	265	921		
		Left	262	939		
		Back	256	931		
		Right	235	951		
				943		
				955		
	11:20			941	3,935	149
		Front	280	1,190		
		Left	263	1,214		
		Back	267	1,216		
		Right	225	1,226		
				1,198		
				1,181		
	12:15			1,204	4,886	187

Mean temperature calculated as the average of temperature readings.

$$k = \frac{t\,Q}{A_{\Delta}T}$$

where

k = thermal conductivity
t = distance between outside and inside hole = 0.3 in.
Q = heat to calorimeter gage
A = area of specimen = 1.0 in.²
$_{\Delta}T$ = temperature drop from outside to inside hole

TABLE 15

RESULTS OF NDT MONITOR EVALUATIONS OF FELT CC, MATERIAL #12, IMPACTED ARCs

Specimen	Impact Level (K Taps)	Thickness (Inches)			ARC Bulk Density (gm/cm³)		Specimen Bulk Density Range (gm/cm³)	ARC Open Porosity	Specimen Porosity	ARC Velocity			Specimen Velocity		Range	ARC Sonic Transmission		Specimen Sonic Transmission Radial Added (db)	ARC MOE
		Before Impact	After Impact	After MOE	Before Impact	After Impact		After Impact (%)		Axial - Before Impact (in./μsec)	Radial - After Impact (in./μsec)	Radial - After MOE (in./μsec)	Axial (in./μsec)	Circum (in./μsec)	Radial (in./μsec)	Radial - After Impact Added (db)	Radial - After MOE Added (db)		(10⁶ psi)
12-F-V	0	-	0.455	0.455	-	1.852	1.850 1.855	10.3	-	-	0.1069	0.1057	0.0950 0.0972	-	0.1131 0.1146	38	38	28 30	2.57 2.16
12-F-15	1.210	-	0.428	0.428	-	1.836	1.825 1.857	11.2	-	-	0.1085	0.1065	0.0892 0.0918	-	0.1069 0.1116	39	39	31 33	2.51 2.04
12-F-16	1.700	-	0.425	0.425	-	1.806	1.793 1.810	13.9	-	-	0.1057	0.1020	0.0883 0.0950	-	0.1053 0.1095	49	39	-	2.12 2.62
12-F-1	2.430	-	0.454	0.454	-	1.752	1.750 1.758	13.1	12.9 13.6	-	0.1061	0.1053	0.0916 0.0929	-	0.1128 0.1147	38	35	32	2.33 2.82
12-F-13	3.070	-	0.429	0.429	-	1.787	1.750 1.811	11.8	-	-	0.1128	0.1050	0.0846 0.0864	-	0.1021 0.1105	50	36	-	1.77 2.45
12-F-10	3.040	-	0.430	0.430	-	1.814	1.802 1.839	12.3	-	-	0.1103	0.1071	0.0876 0.0893	-	0.1051 0.1093	37	37	25 29	2.01 1.85
12-F-11	4.140	-	0.433	0.433	-	1.811	1.818 1.839	16.1	-	-	0.1036	0.0969	0.0868 0.0987	-	0.1003 0.1069	18	21	15 25	2.17 1.80

TABLE 16

NDT INSPECTIONS FOR STRUCTURE-CHANGE
IN SAMOIA FELT CC IMPACTED ARCS

Specimen	(K Taps) Impulse Level	1X Group Polaroid	Visual (1X) Edge Appearance	Visual (1X) Surface Appearance	Visual (10X) Edge & Inner Surface Appearance	Group X-ray Axial	50X Photomicrographs	Liquid Penetrant	Radia Pulse-Echo
12-F-15	1.210	Fig 72	Normal	Normal	Normal	Normal Fig 76	Micro Normal Fig 77	Normal	Material defies evaluation
12-F-16	1.290	Fig 72	Normal	Normal	Normal	Suspect low-absorbtive alignment about 0.1 inch from rear face - runs nearly full length. Fig 76	Micro Normal Fig 77	Normal	
12-F-1	2.430	Fig 72	Normal	Normal (Size: 1.52 x 1.56 inch)	Normal	Normal Fig 76	Micro Normal Fig 77	Hairline aligned cracking in two edges by Fartek	
12-F-14	2.490	Fig 72	Gross delam located 0.1-0.2 inch from rear face. Fig 73	1. Single 1.4 inch long rear face crack. Fig 73 2. Rear face was more porous	No additional structure-change.	Gross delam 0.15 inch from rear face. Fig 76	1. Gross Macro delam and front face crack. 2. Missing material between delam and rear face. Fig 77	Rear face more porous	
12-F-13	3.070	Fig 72	Aligned hairline cracking in one edge located 0.15 inch from rear face.	Normal	No additional structure-change.	Normal Fig 76	Micro Normal Fig 77	Normal	
12-F-10	3.440	Fig 72	Aligned cracking in two edges located 0.2 inch from rear face. Fig 74	Normal	No additional structure-change	Low-absorptive alignment about 0.25 inch from rear face extending nearly full length. Fig 76	Micro Normal Fig 77	Aligned cracking in three edges located 0.2-0.3 inch from rear face	
12-F-11	4.140	Fig 72	Aligned cracking in four edges located 0.2 inch from rear face. Fig 75	Normal	No additional structure-change	Increased low-absorptive alignment at mid-thickness extending full length. Fig 76	Micro Normal Fig 77	No additional structure-change	

TABLE 17

RESULTS OF TENSILE AND COMPRESSIVE EVALUATIONS ON FELT CARBON-CARBON IMPACTED PLATES-

Specimen Number	Impact Level (K Taps)	Temp F°	Bulk Density gm/cm³	Tensile Ultimate Strength psi	Tensile Initial Elastic Modulus 10^6 psi	Total Unit Axial Strain in./in.	Axial Sonic Velocity in./μsec	Radial Sonic Velocity in./μsec	Sonic Transmission (db)
12-F-V T03A	0	70	1.853	2,630	1.01	0.0070	0.0950	0.1131	
T04A		70	1.853	2,930	0.98	0.0060	0.0962	0.1146	
12-F-16 T01A	1.700	70	1.801	2,590	0.62	0.0052	0.0886	0.1080	---
T04A		70	1.810	2,000	0.55	0.0062	0.0900	0.1095	---
12-F-13 T03A	3.070	70	1.798	2,520	0.79	0.0052	0.0850	0.1092	---
T01A		70	1.750	---	---	---	0.0864	0.1044	---
12-F-V T01A	0	3000	1.855	3,420	1.52	0.0023	0.0972	0.1142	
T02A		3000	1.850	4,080	1.16	0.0042	0.0950	0.1138	
12-F-16 T02A	1.700	3000	1.795	3,820	1.85	0.0030	0.0900	0.1060	---
T03A		3000	1.793	3,750	1.23	0.0066	0.0883	0.1053	---
12-F-13 T02A	3.070	3000	1.783	3,630	1.67	0.0034	0.0846	0.1021	---
T04A		3000	1.811	3,560	1.55	0.0033	0.0855	0.1105	---

TABLE 17 CONTINUED

Specimen Number	Impact Level (K Taps)	Temp F°	Bulk Density gm/cm³	Compressive Ultimate Strength psi	Compressive Initial Elastic Modulus 10^6 psi	Axial Sonic Velocity in./usec	Radial Sonic Velocity in./usec	Radial Sonic Transmission (db)
12-F-15 C01A	1.210	70	1.825	9,720	0.32	0.0918	0.1069	31.5
C04A		70	1.857	11,060	0.58	0.0906	0.1116	32.0
12-F-1 C03A	2.430	70	1.750	13,660	0.17	0.0922	0.1136	38.0
12-F-10 C01A	3.440	70	1.839	9,000	0.46	0.0883	0.1072	29.0
C03A		70	1.802	7,940	0.48	0.0877	0.1091	28.5
12-F-11 C02A	4.140	70	1.818	9,040	0.65	0.0868	0.1003	16.0
C04A		70	1.830	9,040	0.58	0.0887	0.1053	18.5
12-F-15 C02A	1.210	4500	1.834	16,280	1.33	0.0892	0.1086	32.0
C03A		4500	1.843	16,380	1.56	0.0895	0.1098	32.0
12-F-1 C01A	2.430	4500	1.758	20,200	1.21	0.0929	0.1128	38.0
C02A		4500	1.752	17,800	1.55	0.0916	0.1136	38.0
12-F-10 C02A	3.440	4500	1.828	13,800	1.10	0.0881	0.1093	29.0
C04A		4500	1.802	12,620	1.14	0.0876	0.1051	25.5
12-F-11 C01A	4.140	4500	1.826	13,680	1.10	0.0877	0.1052	24.0
C03A		4500	1.925	16,280	1.02	0.0869	0.1069	18.5

1. Broken in Handling

TABLE 18

THERMAL EXPANSION OF FELT CC IN THE AXIAL DIRECTION AFTER 1.21 KT
MEASURED IN QUARTZ DILATOMETER

Specimen	Time	Specimen Temperature - °F				Observed Total Elongation 10^{-3} in.	Observed Unit Elongation 10^{-3} in./in.	Unit Elongation Correction for Dilatometer Motion 10^{-3} in./in.	Corrected Specimen Unit Elongation 10^{-3} in./in.
		Top	Middle	Bottom	Average				
Spec: 12-F-15-C1 & C2 Run: 1 Run: 5303-159-20Q Density: 1.830 gm/cm³ Velocity: 0.0905 in./usec	Initial Length: 2.9871 in. Final Length: 2.9881 in.					Initial Weight: 9.9538 gm Final Weight: 9.9489 gm			
	8:05	74	-	74	74	0.0	0.0	0.0	0.0
	9:05	492	-	492	492	2.13	0.71	0.10	0.81
	10:00	1001	-	1001	1001	5.52	1.85	0.28	2.13
	10:55	1381	-	1381	1381	8.33	2.79	0.40	3.19
	11:40	1690	-	1690	1690	10.87	3.64	0.50	4.14
	8:00	75	-	75	75	0.34	0.11	0.0	0.11

TABLE 19

THERMAL EXPANSION OF FELT CC IN THE AXIAL DIRECTION AFTER 1.21 KT
MEASURED IN GRAPHITE DILATOMETER

Specimen and Run No.	Temp. °F	Time	Observed Total Elongation (10^{-3} in.)	Observed Unit Elongation (10^{-3} in./in.)	Unit Correction for Dilatometer Motion (10^{-3} in./in.)	Corrected Specimen Unit Elongation (10^{-3} in./in.)
TE-1C						
Specimen: 12-F-15 C1 & C2	77	8:10	0.0	0.0	0.0	0.0
	494	8:55	0.89	0.30	0.51	0.81
Run: 1	1029	9:35	1.98	0.66	1.40	2.06
Run: 6336-25-131-K4	1565	10:15	3.22	1.08	2.45	3.53
Initial length: 2.9885 in.	2513	10:55	5.57	1.86	4.67	6.53
	3018	11:35	6.92	2.32	5.94	8.26
Final length: 2.9905 in.	3554	12:15	8.43	2.82	7.34	10.16
	4060	12:55	10.22	3.42	8.70	12.12
Initial weight: 9.9500 gm	4486	1:35	12.19	4.08	9.88	13.96
	4973	2:10	15.25	5.10	11.29	16.39
Final weight: 9.9471 gm	75	7:00	2.57	0.86	0.0	0.86
Density: 1.830 gm/cm³						
Velocity: 0.0905 in./μsec						
TE-2C						
Specimen: 12-F-15 C3 & C4	77	7:40	0.0	0.0	0.0	0.0
	529	8:20	1.15	0.39	0.57	0.96
Run: 1	1056	9:00	2.68	0.90	1.47	2.37
Run: 6336-24-131-K4	1757	9:50	4.61	1.55	2.90	4.45
Initial length: 2.9783 in.	2478	10:30	6.80	2.28	4.58	6.86
	3028	11:10	8.47	2.84	5.97	8.81
Final length: 2.9813 in.	3548	11:50	10.10	3.39	7.30	10.69
	4080	12:35	12.07	4.05	8.78	12.83
Initial weight: 10.0194 gm	4547	1:15	14.52	4.88	10.03	14.91
	5034	1:50	17.77	5.97	11.47	17.44
Final weight: 10.0140 gm	75	7:20	3.09	1.04	0.0	1.04
Density: 1.850 gm/cm³						
Velocity: 0.0900 in./μsec						

TABLE 20

THERMAL EXPANSION OF FELT CC IN THE AXIAL DIRECTION AFTER 3.44 KT
MEASURED IN QUARTZ DILATOMETER

Specimen	Time	Specimen Temperature - °F				Observed Total Elongation 10^{-3} in.	Observed Unit Elongation 10^{-3} in./'	Unit Elongation Correction for Dilatometer Motion 10^{-3} in./in.	Corrected Specimen Unit Elongation 10^{-3} in./in.
		Top	Middle	Bottom	Average				
Spec: 12-F-10-C1 & C2 Run: 1 Run. 5303-153-20Q Density: Velocity:		Initial Length: 2.9869 in. Final Length: 2.9883 in.				Initial Weight: 9.9280 gm Final Weight: 9.9236 gm			
	9:00	75	-	75	75	0.0	0.0	0.0	0.0
	10:10	453	-	453	453	2.17	0.73	0.09	0.82
	11:20	971	-	971	971	5.86	1.96	0.26	2.22
	12:30	1432	-	1432	1432	9.70	3.25	0.42	3.67
	1:10	1674	-	1674	1674	11.83	3.96	0.50	4.46
	6:45	75	-	75	75	1.31	0.44	0.0	0.44

TABLE 20

THERMAL EXPANSION OF FELT CC IN THE AXIAL DIRECTION AFTER 3.44 KT
MEASURED IN QUARTZ DILATOMETER

Specimen	Time	Specimen Temperature - °F				Observed Total Elongation 10^{-3} in.	Observed Unit Elongation 10^{-3} in./in.	Unit Elongation Correction for Dilatometer Motion 10^{-3} in./in.	Corrected Specimen Unit Elongation 10^{-3} in./in.
		Top	Middle	Bottom	Average				
Spec: 12-F-10-C1 & C2 Run: 1 Run: 5303-158-200 Density: Velocity:		Initial Length: 2.9869 in. Final Length: 2.9883 in.				Initial Weight: 9.9280 gm Final Weight: 9.9236 gm			
	9:00	75	-	75	75	0.0	0.0	0.0	0.0
	10:10	453	-	453	453	2.17	0.73	0.09	0.82
	11:20	971	-	971	971	5.86	1.96	0.26	2.22
	12:30	1432	-	1432	1432	9.70	3.25	0.42	3.67
	1:10	1674	-	1674	1674	11.83	3.96	0.50	4.46
	6:45	75	-	75	75	1.31	0.44	0.0	0.44

TABLE 21

THERMAL EXPANSION OF FELT CC IN THE AXIAL DIRECTION AFTER 3.44 KT
MEASURED IN GRAPHITE DILATOMETER

Specimen and Run No.	Temp. °F	Time	Observed Total Elongation (10^{-3} in.)	Observed Unit Elongation (10^{-3} in./in.)	Unit Correction for Dilatometer Motion (10^{-3} in./in.)	Corrected Specimen Unit Elongation (10^{-3} in./in.)
Specimen: 12-F-10 C1 & C2	75	8:05	0.0	0.0	0.0	0.0
Run: 1	472	8:45	1.47	0.49	0.28	0.77
Run: 6336-22-122A-E	1044	9:25	3.89	1.30	0.91	2.21
Initial length: 2.9883 in.	1656	10:05	6.44	2.16	1.89	4.05
Final length: 2.9913 in.	2578	10:45	10.35	3.46	3.64	7.10
Initial weight: 9.9236 gm	2982	11:25	12.02	4.02	4.49	8.51
Final weight: 9.9217 gm	3432	12:05	13.92	4.66	5.49	10.15
Density: gm/cm³	4009	12:45	16.81	5.63	6.80	12.43
	4537	1:25	20.02	6.70	8.07	14.77
	5034	2:00	23.94	8.01	9.33	17.34
	75	6:50	3.63	1.21	0.0	1.21
Specimen: 12-F-10 C3 & C4	75	8:45	0.0	0.0	0.0	0.0
Run: 1	455	9:20	1.15	0.39	0.48	0.87
Run: 6336-23-131-K4	969	9:55	2.97	0.99	1.29	2.28
Initial length: 2.9852 in.	1679	10:35	5.45	1.83	2.70	4.53
Final length: 2.9911 in.	2311	11:15	7.43	2.49	4.18	6.67
Initial weight: 9.7172 gm	2937	11:50	9.37	3.14	5.71	8.85
Final weight: 9.7135 gm	3483	12:25	11.04	3.70	7.16	10.86
Density: gm/cm³	3948	1:05	12.62	4.23	8.39	12.62
	4466	1:45	14.91	4.96	9.81	14.77
	5044	2:20	18.25	6.11	11.48	17.59
	75	6:50	5.84	1.96	0.0	1.96

TABLE 22

THERMAL EXPANSION OF FELT CC IN THE CIRCUMFERENTIAL DIRECTION AFTER 1.21 MT
MEASURED IN QUARTZ DILATOMETER

Specimen	Time	Specimen Temperature - °F				Observed Total Elongation 10^{-3} in.	Observed Unit Elongation 10^{-3} in./in.	Unit Elongation Correction for Dilatometer Motion 10^{-3} in./in.	Corrected Specimen Unit Elongation 10^{-3} in./in.
		Top	Middle	Bottom	Average				
Spec: 12-F-15-C1 & C4			Initial Length: 2.6023 in.				Initial Weight: 2.0735 gm		
Run: 1			Final Length: 2.6020 in.				Final Weight: 2.0710 gm		
Run: 633[illegible]-151-14MO									
Density:									
Velocity:									
	11:05	76	-	76	76	0.0	0.0	0.0	0.0
	12:00	495	-	495	495	0.56	0.22	0.13	0.35
	1:10	999	-	1002	1001	2.03	0.78	0.22	1.00
	2:05	1336	-	1343	1340	3.33	1.28	0.26	1.54
	3:00	1649	-	1665	1657	4.52	1.74	0.30	2.04
	7:00	70	-	70	70	0.0	0.0	0.0	0.0

TABLE 23

THERMAL EXPANSION OF FELT CC IN THE CIRCUMFERENTIAL DIRECTION AFTER 1.21 KT MEASURED IN GRAPHITE DILATOMETER

Specimen and Run No.	Temp. °F	Time	Observed Total Elongation (10^{-3} in.)	Observed Unit Elongation (10^{-3} in./in.)	Unit Correction for Dilatometer Motion (10^{-3} in./in.)	Corrected Specimen Unit Elongation (10^{-3} in./in.)
Spec: 12-F-15-C1 & C4	64	8:45	0.0	0.0	0.0	0.0
Run: 1	492	9:30	-0.10	-0.04	0.39	0.35
Run: 6336-153-122A-E	1047	10:10	-0.07	-0.03	1.06	1.03
Initial Length: 2.6020 in.	1684	10:50	0.09	0.03	2.12	2.15
	2432	11:30	0.40	0.15	3.50	3.65
Final Length: 2.6008 in.	3048	12:10	0.70	0.27	4.77	5.04
	3422	12:50	0.85	0.33	5.58	5.91
Initial Weight: 2.0710 gm	3852	1:30	1.04	0.40	6.54	6.94
	4466	2:10	0.90	0.35	7.90	8.25
Final Weight: 2.0706 gm	5034	2:45	1.02	0.39	9.25	9.64
	60	7:00	-0.72	-0.28	0.0	-0.28
Spec: 12-F-15-C1 & C4	59	8:25	0.0	0.0	0.0	0.0
Run: 2	508	9:15	-0.55	-0.21	0.57	0.36
Run: 6336-156-134-K4	1046	9:55	-1.32	-0.51	1.60	1.09
Initial Length: 2.6008 in.	1665	10:35	-2.01	-0.77	2.99	2.22
	2422	11:15	-2.62	-1.01	4.74	3.73
Final Length: 2.6011 in.	2987	11:55	-3.03	-1.17	6.17	5.00
	3473	12:30	-3.43	-1.32	7.47	6.15
Final Weight: 2.0705 gm	3959	1:10	-4.01	-1.54	8.84	7.30
	4445	1:50	-4.82	-1.85	10.21	8.36
Initial Weight: 2.0706 gm	4984	2:25	-6.06	-2.33	11.80	9.47
	60	6:40	0.02	0.01	0.0	0.01

TABLE 24

THERMAL EXPANSION OF FELT CC IN THE CIRCUMFERENTIAL DIRECTION AFTER 3.44 MT
MEASURED IN QUARTZ DILATOMETER

Specimen	Time	Specimen Temperature - °F				Observed Total Elongation 10^{-3} in.	Observed Unit Elongation 10^{-3} in./in.	Unit Elongation Correction for Dilatometer Motion 10^{-3} in./in.	Corrected Specimen Unit Elongation 10^{-3} in./in.
		Top	Middle	Bottom	Average				
Spec: 12-F-10-C1 & C3 Run: 1 Run: 6336-152-20Q Density: Velocity:	Initial Length: 2.5981 in. Final Length: 2.5984 in.						Initial Weight: 1.9644 gm Final Weight: 1.9628 gm		
	11:05	76	-	76	76	0.0	0.0	0.0	0.0
	12:00	508	-	508	508	0.64	0.25	0.11	0.36
	1:10	980	-	980	980	1.92	0.74	0.27	1.01
	2:05	1345	-	1348	1347	3.22	1.24	0.39	1.63
	3:00	1650	-	1658	1654	4.38	1.69	0.49	2.18
	7:00	70	-	70	70	0.28	0.11	0.0	0.11

TABLE 25

THERMAL EXPANSION OF FELT CC IN THE CIRCUMFERENTIAL DIRECTION AFTER 3.44 KT MEASURED IN GRAPHITE DILATOMETER

Specimen and Run No.	Temp. °F	Time	Observed Total Elongation (10^{-3} in.)	Observed Unit Elongation (10^{-3} in./in.)	Unit Correction for Dilatometer Motion (10^{-3} in./in.)	Corrected Specimen Unit Elongation (10^{-3} in./in.)
Specimen: 12-F-10 C1 & C3	59	8:25	0.0	0.0	0.0	0.0
Run: 1	535	9:15	-0.21	-0.08	0.39	0.31
Run: 6336-155-122A-E	1038	9:55	-0.30	-0.12	1.04	0.92
Initial length: 2.5984 in.	1685	10:35	-0.22	-0.08	2.12	2.04
	2478	11:15	-0.05	-0.02	3.59	3.57
Final length: 2.5990 in.	3114	11:55	0.19	0.07	4.91	4.98
	3483	12:30	0.27	0.10	5.71	5.81
Initial weight: 1.9628 gm	3873	1:10	0.28	0.11	6.56	6.67
	4476	1:50	0.11	0.04	7.93	7.97
Final weight: 1.9624 gm	5065	2:25	-0.09	-0.03	9.32	9.29
	60	6:40	-0.31	-0.12	0.0	-0.12
Density: gm/cm³						
Specimen: 12-F-10 C1 & C3	59	7:55	0.0	0.0	0.0	0.0
Run: 2	464	8:35	-0.64	-0.25	0.51	0.26
Run: 6336-159-134K4	1030	9:20	-1.45	-0.56	1.56	1.00
Initial length: 2.5990 in.	1655	10:05	-2.13	-0.82	2.99	2.17
	2422	10:50	-2.75	-1.06	4.74	3.68
Final length: 2.5993 in.	2937	11:30	-3.22	-1.24	6.04	4.80
	3442	12:10	-3.69	-1.42	7.39	5.97
Initial weight: 1.9624 gm	2908	12:50	-4.30	-1.65	8.84	7.19
	4379	1:25	-5.03	-1.94	10.03	8.09
Final weight: 1.9626 gm	4984	1:55	-6.64	-2.55	11.80	9.25
	60	6:20	0.48	0.18	0.0	0.18
Density: gm/cm³						

TABLE 26

THERMAL EXPANSION OF FELT CC IN THE CIRCUMFERENTIAL DIRECTION AFTER 4.14 KI
MEASURED IN QUARTZ DILATOMETER

Specimen	Time	Specimen Temperature - °F				Observed Total Elongation 10^{-3} in.	Observed Unit Elongation 10^{-3} in./in.	Unit Elongation Correction for Dilatometer Motion 10^{-3} in./in.	Corrected Specimen Unit Elongation 10^{-3} in./in.
		Top	Middle	Bottom	Average				
Spec: 12-F-11-C2 & C4 Run: 1 Run: 6336-157-14MQ Density: Velocity:		Initial Length: 3.0807 in. Final Length: 3.0820 in.					Initial Weight: 3.4608 gm Final Weight: 3.4563 gm		
	11:10	76	-	76	76	0.0	0.0	0.0	0.0
	12:10	510	-	510	510	0.86	0.28	0.13	0.41
	1:05	997	-	1001	999	2.63	0.85	0.22	1.07
	2:00	1340	-	1350	1345	4.28	1.39	0.26	1.65
	2:50	1639	-	1659	1649	5.76	1.87	0.30	2.17
	6:15	70	-	70	70	0.34	0.11	0.0	0.11

TABLE 27

THERMAL EXPANSION OF FELT CC IN THE CIRCUMFERENTIAL DIRECTION AFTER 4.14 °T MEASURED IN GRAPHITE DILATOMETER

Specimen and Run No.	Temp. °F	Time	Observed Total Elongation (10^{-3} in.)	Observed Unit Elongation (10^{-3} in./in.)	Unit Correction for Dilatometer Motion (10^{-3} in./in.)	Corrected Specimen Unit Elongation (10^{-3} in./in.)
Spec: 12-F-11-C2 & C4	59	7:55	0.0	0.0	0.0	0.0
Run: 1	509	8:35	0.05	0.02	0.36	0.38
Run: 6336-158-122A-E	1011	9:20	0.21	0.07	1.00	1.07
Initial Length: 3.0820 in.	1718	10:05	0.70	0.23	2.16	2.39
	2503	10:50	1.35	0.44	3.64	4.08
Final Length: 3.0845 in.	3043	11:30	1.84	0.60	4.76	5.36
	3478	12:10	2.13	0.69	5.70	6.39
Initial Weight: 3.4563 gm	3908	12:50	2.53	0.82	6.66	7.48
	4456	1:25	3.28	1.06	7.89	8.95
Final Weight: 3.4560 gm	5014	1:55	4.31	1.40	9.19	10.59
	60	6:20	2.36	0.77	0.0	0.77
Spec: 12-F-11-C2 & C4	59	8:00	0.0	0.0	0.0	0.0
Run: 2	509	8:40	0.07	0.02	0.36	0.38
Run: 6595-74-122A-E	1067	9:20	0.28	0.09	1.09	1.18
Initial Length: 3.0845 in.	1679	10:00	0.69	0.22	2.11	2.33
	2518	10:45	1.37	0.44	3.67	4.11
Final Length: 3.0853 in.	3134	11:25	1.89	0.61	4.96	5.57
	3539	12:05	2.11	0.68	5.83	6.51
Initial Weight: 3.4560 gm	3928	12:45	2.36	0.77	6.70	7.47
	4496	1:25	2.38	0.77	7.97	8.74
Final Weight: 3.4558 gm	5055	1:00	2.42	0.78	9.30	10.08
	60	7:50	1.02	0.33	0.0	0.33

TABLE 28

THERMAL CONDUCTIVITY OF FELT CC IN THE RADIAL DIRECTION
EXPOSED TO 1.21 and 3.44 KT USING COMPARATIVE ROD APPARATUS WITH ARMCO IRON REFERENCES

Specimen and Time	Mean Temperature of Specimen °F	Thermal Conductivity of Specimen k_s Btu in./hr ft² °F	ΔT through Specimen °F	Mean Temperature of Lower Reference °F	Thermal Conductivity of Lower Reference k_1 Btu in./hr ft² °F	ΔT through Lower Reference ΔT_1 °F	Mean Temperature of Upper Reference °F	Thermal Conductivity of Upper Reference k_2 Btu in./hr ft² °F	ΔT through Upper Reference ΔT_2 °F
Spec: 12-F-10 Run: 5492-28-1 Density: (3.44 KT)	ℓ_s = 0.1993 in. ℓ_1 and ℓ_2 = 0.750 in. Specimen Diameter = 0.6495 in.			Initial Thickness: 0.3993 in. Final Thickness: 0.3993 in.			Initial Weight: 3.9238 gm Final Weight: 3.9179 gm		
8-1-72 5:45p.m.	82	1,334	2.9	53	501	28.1	111	495	31.0
6:05p.m.	82	1,301	3.0	53	501	28.1	111	495	30.9
8-2-72 8:15a.m.	493	855	4.8	457	401	36.0	533	385	41.8
8:35a.m.	493	829	4.9	457	401	36.2	532	385	41.8
12:20p.m.	996	679	9.2	922	300	76.8	1,074	273	87.3
12:40p.m.	997	668	9.4	123	300	78.0	1,076	273	87.4
2:40p.m.	1,419	573	14.3	1,301	235	132.8	1,551	198	152.9
2:55p.m.	1,425	565	14.4	1,306	235	133.4	1,556	198	150.8
Spec: 12-F-10 Run: 5493-30-2 Density: (3.44 KT)	ℓ_s = 0.1993 in. ℓ_1 and ℓ_2 = 0.750 in. Specimen Diameter = 0.6495 in.			Initial Thickness: 0.3993 in. Final Thickness: 0.3993 in.			Initial Weight: 3.9179 gm Final Weight: 3.9165 gm		
8-8-72 11:00a.m.	82	1,342	2.4	56	510	23.5	107	495	25.6
11:15a.m.	83	1,486	2.3	57	510	24.9	109	495	25..
5:20p.m.	722	951	5.3	670	355	54.2	777	33[illegible]	57.2
5:35p.m.	718	1,048	4.8	668	356	53.5	772	332	55.5
8-9-72 1:05p.m.	1,179	757	10.6	1,076	272	109.9	1,296	236	129.9
1:30p.m.	1,189	769	10.5	1,087	271	110.1	1,307	235	130.4
3:45p.m.	1,602	625	14.6	1,458	210	156.8	1,761	198	179.3

TABLE 28 CONTINUED

Specimen and Time	Mean Temperature of Specimen °F	Thermal Conductivity of Specimen k_s Btu in./hr ft² °F	ΔT through Specimen °F	Mean Temperature of Lower Reference °F	Thermal Conductivity of Lower Reference k_1 Btu in./hr ft² °F	ΔT through Lower Reference ΔT_1 °F	Mean Temperature of Upper Reference °F	Thermal Conductivity of Upper Reference k_2 Btu in./hr ft² °F	ΔT through Upper Reference ΔT_2 °F
Spec: 12-F-15 Run: 5493-23-4 Density: (1.21 RT)	l_s = 0.1990 in. l_1 and l_2 = 0.750 in. Specimen Diameter = 0.6508 in.			Initial Thickness: 0.3990 in. Final Thickness: 0.3990 in.			Initial Weight: 3.9058 gm Final Weight: 3.8917 gm		
7-27-72 3:05p.m.	72	1,400	3.50	34	528	38.3	114	493	36.9
3:25p.m.	74	1,391	3.60	35	518	37.8	116	493	36.8
6:15p.m.	505	906	4.77	464	400	41.3	549	382	42.0
6:40p.m.	508	907	4.72	458	398	41.2	552	380	41.9
7-28-72 12:20p.m.	1,046	711	10.50	956	295	96.7	1,147	260	106.8
12:40p.m.	1,047	734	10.15	956	295	97.1	1,148	260	107.0
Spec: 12-F-15 Run: 5493-25-1 Density: (1.21 RT)	l_s = 0.1990 in. l_1 and l_2 = 0.750 in. Specimen Diameter = 0.6508 in.			Initial Thickness: 0.3990 in. Final Thickness: 0.3990 in.			Initial Weight: 3.8917 gm Final Weight: 3.8859 gm		
8-4-72 7:30p.m.	43	1,654	3.3	3	529	39.20	84	500	39.6
8:00p.m.	44	1,763	3.1	4	528	39.1	85	500	39.8
8-7-72 5:20p.m.	787	880	8.7	704	348	82.7	875	311	93.4
5:40p.m.	785	792	9.4	704	348	80.8	870	312	83.1
8-8-73 3:10p.m.	1,205	698	14.2	1,076	273	134.5	1,352	228	166.1
3:30p.m.	1,211	694	14.1	1,084	272	134.0	1,358	226	165.1

Notes: 1. All measurements made with helium purge. Apparatus was not evacuated prior to determination
2. Thermal conductivity (k_s) of specimen calculated from following equation

$$k_s = \left[\frac{k_1 \Delta T_1}{l_1} + \frac{k_2 \Delta T_2}{l_2}\right] \frac{l_s}{2\Delta T_s}$$

where

k = thermal conductivity
ΔT = temperature drop over gage length
l = gage length

and subscripts 1, 2, and s refer to lower reference, upper reference, and specimen, respectively.

TABLE 29

THERMAL CONDUCTIVITY OF FELT CC IN THE RADIAL DIPECTION EXPOSED TO 0 KT
USING RADIAL INFLOW APPARATUS (STRIP TECHNIQUE)

Specimen and Run Number	Time	Strip Location	Average ΔT Each Strip	Heat Flow to Calorimeter Btu/hr	Specimen Average Mean Temperature	Average Thermal Conductivity Btu in./hr ft²°F
Spec: 12-F-V-T 1,2,3,4, Run: 6336-36-69-2-L		Front	15	273		
		Left	20	278		
		Back	15	278		
		Right	18	273		
				276		
				275		
	8:35		17	276	1,526	788
		Front	38	506		
		Left	57	506		
		Back	49	523		
		Right	55	516		
				533		
				541		
	9:40			521	2,675	506
		Front	85	706		
		Left	116	727		
		Back	92	736		
		Right	94	793		
				736		
				780		
	10:50			737	3,802	369
		Front	110	968		
		Left	154	974		
		Back	120	991		
		Right	142	981		
				954		
	11:45			575	5,084	361

TABLE 29 CONTINUED

Specimen and Run Number	Time	Strip Location	Average ΔT Each Strip	Heat Flow to Calorimeter Btu/hr	Specimen Average Mean Temperature	Average Thermal Conductivity Btu in./hr ft² °F
Spec: 12-F-V-T-1,2,3,4 Run: 6336-54-69-2-L		Front	17	248		
		Left	18	259		
		Back	19	273		
		Right	16	293		
				300		
				297		
	9:00			278	1,687	750
		Front	46	412		
		Left	45	431		
		Back	54	449		
		Right	47	447		
				459		
				470		
	10:20			445	2,847	450
		Front	74	586		
		Left	77	587		
		Back	80	608		
		Right	75	604		
				609		
				611		
	11:40			600	3,822	378
		Front	100	782		
		Left	101	791		
		Back	130	775		
		Right	108	785		
				791		
				801		
	12:35			787	4,868	350

Mean temperature calculated as the average of temperature readings.

$$k = \frac{t\,Q}{A_{\Delta}T}$$

where

k = thermal conductivity
t = distance between outside and inside hole = 0.3 in.
Q = heat to calorimeter gage
A = area of specimen = 0.89 in.²
$_{\Delta}T$ = temperature drop from outside to inside hole

TABLE 30

NDT/MONITOR INSPECTION AND MOE RESULTS FOR IMPACTED ARC RINGS FROM MATERIAL 6

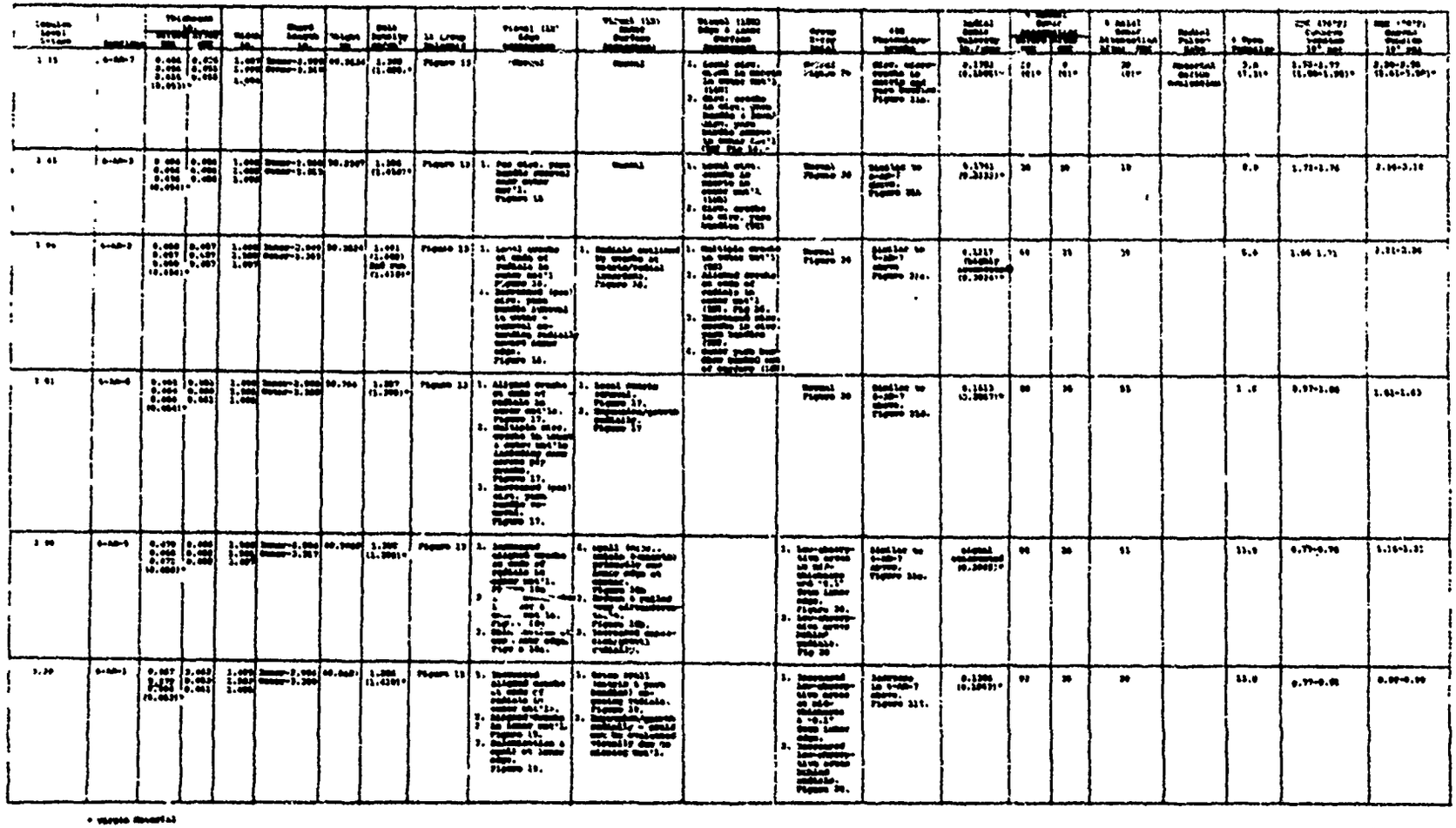


TABLE 31

RESULTS OF TENSILE AND COMPRESSIVE EVALUATIONS ON R6300 IMPACTED ARCS

Specimen Number	Impact Level (K Taps)	Tensile Strength psi		Tensile Modulus 10^6 psi		Tensile Strain in./in.		Bulk Density gm/cm³	Open Porosity %	Axial Sonic Velocity in./usec	Radial Sonic Velocity in./usec	Radial Sonic Transmission (db)
		Axial	Circum.	Axial	Circum	Axial	Circum					
10-AR-4-T1A	0.49	--[1]		--[1]		--[1]		..358	0.8	0.1244	0.1256	29.0
T2A		3,480		0.97		0.0040		1.359	0.7	0.1239	0.1256	32.0
T3C			7,200		1.14		0.0075	1.320	0.6	0.1316	0.1286	32.0
T4C			6,560		1.14		0.0079	1.355	0.8	0.1243	0.1215	34.0
10-AR-6-T1A	1.66	3,270		1.12		0.0092		1.362	1.3	0.1231	0.1197	36.0
T2A		3,240		1.17		0 0090		1.366	2.6	0.1221	0.1197	30.0
T3C			7,850		1.34		0.0079	1.357	2.4	0.1234	0.1213	34.0
T4C			6,960		1.54		0.0056	1.380	1.8	0.1362	0.1201	31.0
10-AR-1-T1A	1.99	3,150		0.95		0.0039		1.363	3.2	0.1222	0.1205	30.0
T2A		2,930		0.82		0.0041		1.368	3.2	0.1215	0.1169	29.0
T3C			7,420		1.37		0.0073	1.373	2.3	0.1360	0.1168	33.0
T4C			7,110		1.39		0.0070	1.361	3.0	0.1352	0.1141	32.0

TABLE 31 CONTINUED

Specimen Number	Impact Level (K Taps)	Compressive Strength psi		Compressive Modulus 10^6 psi		Compressive Strain in./in.		Bulk Density gm/cm³	Open Porosity %	Axial Sonic Velocity in./μsec	Radial Sonic Velocity in./μsec	Radial Sonic Transmission (db)
		Axial	Circum	Axial	Circum	Axial	Circum					
10-AR-V-C1A	0	27,600		1.08		0.0346		1.327	1.5	0.1241	0.1239	34.0
C2C			30,700		1.30		0.0316	1.324	1.6	0.1296	0.1224	34.0
C3C			31,220		1.13		0.0408	1.333	1.4	0.1303	0.1238	33.0
10-AR-7-C1A	1.57	23,500		1.23		0.0203		1.363	2.5	0.1249	0.1211	28.0
C2A		25,400		1.09		0.0349		1.367	2.6	0.1223	0.1174	25.0
C3C			28,800		1.35		0.0184	1.357	2.6	0.1226	0.1190	24.0
C4C			21,000		1.78		0.0185	1.383	2.0	0.1360	0.1300	32.0
10-AR-3-C1A	1.90	23,100		1.15		0.0273		1.364	3.3	0.1216	0.1155	28.0
C2A		25,850		1.03		0.0298		1.362	3.4	0.1214	0.1159	29.0
C3C			27,520		1.21		0.0289	1.366	3.2	0.1323	0.1171	32.0
C4C			20,210		1.41		0.0150	1.370	3.1	0.1325	0.1212	26.0
10-AR-5-C1A	4.04	16,100		1.00		0.0413		--[2]	6.7	0.1167	0.1057	28.0
C2A		19,300		0.94		0.0275		--[2]	6.7	0.1189	0.1063	29.0
C3C			16,820		1.28		0.0138	--[2]	6.4	0.1300	0.0988	25.0
C4C			15,520		1.30		0.0078	--[2]	6.4	0.1315	0.1053	24.0

[1] Broken in handling
[2] Specimens heavily chipped. Bulk density not available

TABLE 32

NDT/MONITOR INSPECTION AND MOE RESULTS FOR IMPACTED ARC RINGS FROM MATERIAL #11

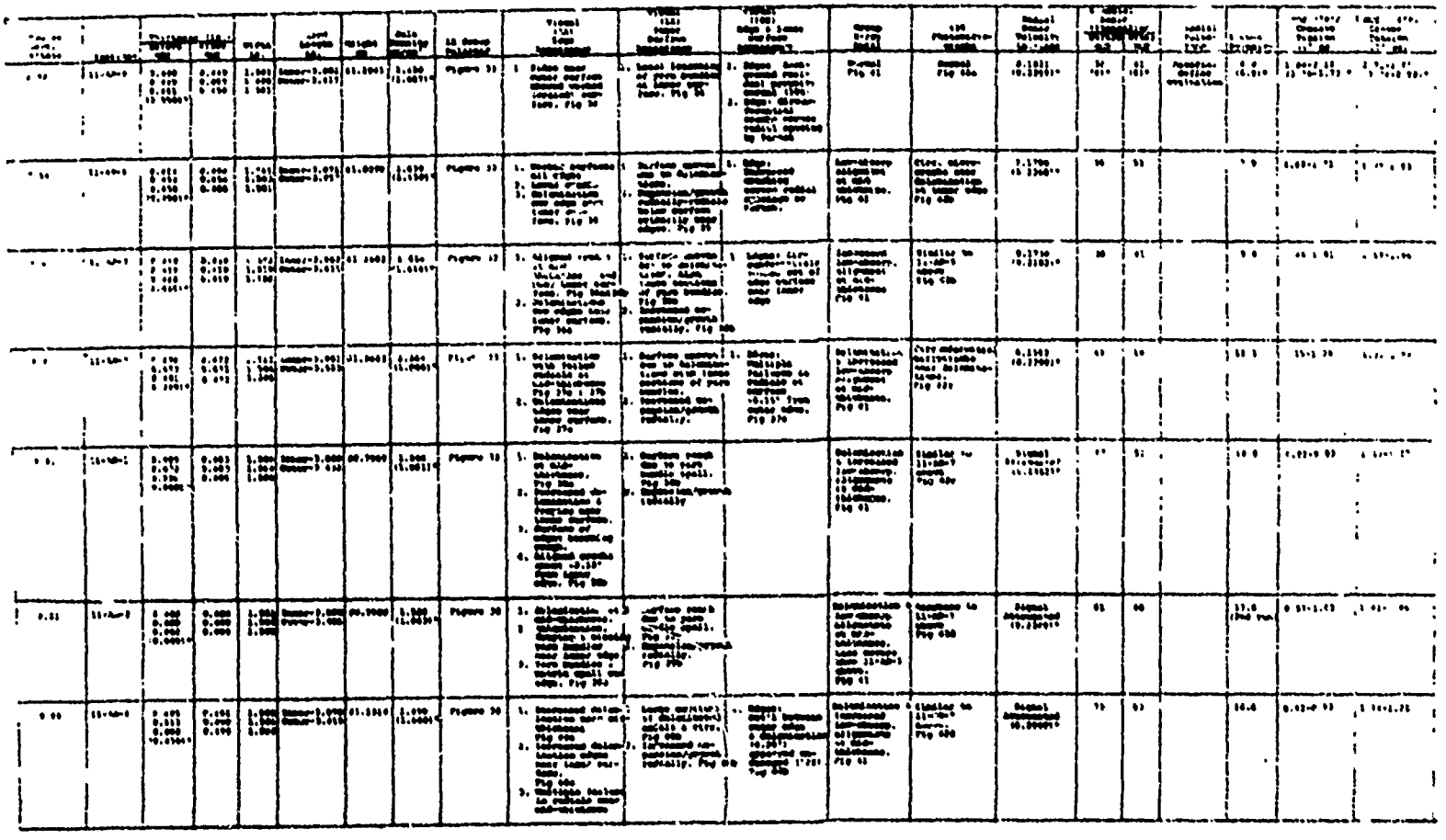


TABLE 33

RESULTS OF TENSILE AND COMPRESSIVE EVALUATIONS ON 3D QUARTZ-PHENOLIC IMPACTED ARCS

Specimen Number	Impact Level (K Taps)	Tensile Strength psi		Tensile Modulus 10^6psi		Tensile Strain in./in.		Bulk Density gm/cm³	Open Porosity %	Axial Sonic Velocity in./μsec	Radial Sonic Velocity in./μsec	Radial Sonic Transmission (db)
		Axial	Circum	Axial	Circum	Axial	Circum					
11-AR-8-T1A	4.58	37,320		1.64				1.649	7.0	0.1769	0.1943	24.0
T2A		38,570		1.58				1.646	7.0	0.1773	0.2030	24.0
T3C			58,830		2.18			1.660	7.4	0.1813	0.1987	23.0
T4C			64,300		2.67			1.644	7.1	0.1810	0.1950	23.0
11-AR-5-T1A	7.95	32,770		1.46				1.627	8.8	0.1771	0.1930	24.0
T2A		32,410		1.42				1.627	8.3	0.1783	0.1932	25.0
T3C			53,300		2.05			1.639	8.6	0.1831	0.2030	24.0
T4C			50,000		1.92			1.620	8.3	0.1805	0.1922	24.0
11-AR-7-T1A	8.61	--[1]		1.41				1.580	10.6	0.1838	0.1903	23.0
T2A		--[1]		1.22				1.583	10.6	0.1810	0.1854	24.0
T3C			40,330		2.08			1.579	9.7	0.1828	0.1793	23.0
T4C			39,670		2.53			1.542	10.4	0.1834	0.1799	24.0
11-AR-6-T1A	9.88	22,140		1.31				1.540	11.9	0.1804	0.1693	24.0
T2A		20,800		1.62				1.543	12.3	0.1855	0.1722	24.0
T3C			24,330		2.27			1.528	13.5	0.1862	0.1881	23.0
T4C			28,670		2.35			1.517	12.8	0.1860	0.1753	24.0

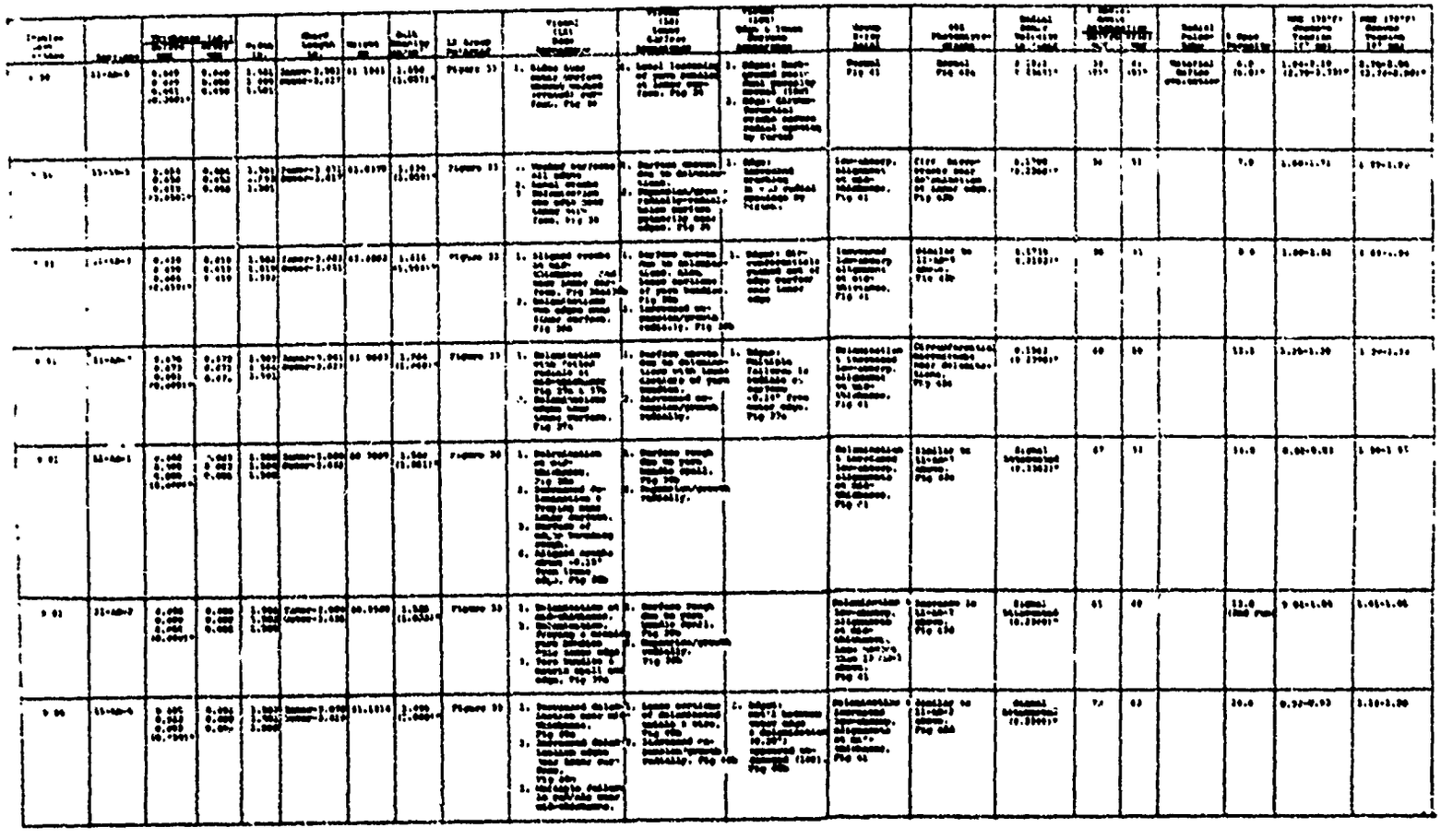
TABLE 33 CONTINUED

Specimen Number	Impact Level (K Taps)	Compressive Strength psi		Compressive Modulus 10^6 psi		Compressive Strain in./in.		Bulk Density gm/cm³	Open Porosity %	Axial Sonic Velocity in./μsec	Radial Sonic Velocity in./μsec	Radial Sonic Transmission (db)
		Axial	Circum	Axial	Circum	Axial	Circum					
11-AR-V-C1A	0	28,000		2.77		0.0148		1.651	6.8	0.1770	0.2016	23.0
C2A		29,750		2.54		0.0104		1.659	7.0	0.1759	0.1935	25.0
C3C			25,950		2.93		0.0121	1.668	6.8	0.1803	0.2060	24.0
C4C			26,200		2.84		0.0165	1.650	6.9	0.1812	0.1976	26.0
11-AR-5-C1A	7.54	17,100		1.81		0.0250		1.629	8.2	0.1792	0.2025	24.0
C2A		17,580		1.71		0.0296		1.637	8.0	0.1770	0.1980	23.0
C3C			16,250		2.12		0.0107	1.651	8.2	0.1832	0.2089	23.0
C4C			17,930		2.80		0.0060	1.615	8.4	0.1819	0.1971	23.0
11-AR-1-C1A	9.01	10,960		2.02		0.0110		1.560	10.9	0.1845	0.1809	26.0
C2A		10,300		1.73		0.0108		1.556	11.2	0.1848	0.1807	25.0
C3C			10,760		2.04		0.0107	1.557	11.5	0.1830	0.1895	25.0
C4C			13,060		2.22		0.0060	1.534	11.4	0.1828	0.1707	25.0
11-AR-2-C1A	9.01	11,680		1.41		>0.0300		1.568	10.8	0.1823	0.1847	26.0
C2A		10,430		2.05		0.0093		1.568	10.9	0.1808	0.1936	26.0
C3C			10,260		1.86		0.0095	1.581	10.7	0.1828	0.1892	24.0
C4C			13,900		2.83		0.0047	1.564	10.2	0.1802	0.1778	24.0

[1]Specimens failed in grip section at a low stress level

TABLE 34

NDT/MONITOR INSPECTION AND MOE RESULTS FOR IMPACTED ARC RINGS FROM MATERIAL 11



* Single value.

TABLE 35

RESULTS OF TENSILE AND COMPRESSIVE EVALUATIONS ON THE 3D CARBON-PHENOLIC PORTION, #15A, OF 3DC/QP IMPACTED ARCS

Specimen Number	Impact Level (K Taps)	Tensile Strength psi		Tensile Modulus 10^6 psi		Tensile Strain in./in.		Bulk Density gm/cm^3	Open Porosity %	Axial Sonic Velocity in./usec	Radial Sonic Velocity in./usec	Radial Sonic Transmission (db)
		Axial	Circum	Axial	Circum	Axial	Circum					
15A-AR-V-T1A	0	17,150		8.06		0.0028		1.435	--[3]	0.3015	0.1888	33.0
T2A		16,700		5.21		0.0033		1.432	--[3]	0.3649	0.1851	33.0
T3C			23,850		5.06		0.0071	1.432	--[3]	0.3694	0.1794	33.0
T4C			21,200		7.15		0.0082	1.432	--[3]	0.3709	0.1821	33.0
15A-AR-5-T1A	4.69	8,650		3.30		0.0049		1.357	8.3	0.3540	0.1915	25.0
T2A		4,900		3.84		0.0093		1.348	8.3	0.3579	0.1904	24.0
T3C			1,340		1.25		0.0067	1.354	7.5	0.3456	0.1875	26.0
T4C			2,290		--		0.0090	1.354	7.6	0.3488	0.1871	26.0
15A-AR-4-T1A	6.06	1,100		0.17		0.0097		1.261	11.6	0.3248	0.1758	24.0
T2A		1,380		0.31		0.0100		1.281	11.5	0.3122	0.1792	25.0
T3C			300[1]		--[1]		--[1]	1.279	9.9	0.3119	0.1837	27.0
T4C			--[2]		--[2]		--[2]	1.281	9.9	0.3033	0.1827	27.0

TABLE 35 CONTINUED

Specimen Number	Impact Level (K Taps)	Compressive Strength psi		Compressive Modulus 10^6 psi		Compressive Strain in./in.		Bulk Density gm/cm^3	Open Porosity %	Axial Sonic Velocity in./μsec	Radial Sonic Velocity in./μsec	Radial Sonic Transmission (db)
		Axial	Circum	Axial	Circum	Axial	Circum					
15A-AR-3-C1A	4.09	10,900		--[1]		>0.0180		1.357	8.1	0.3595	0.1817	26.0
C2A		11,000		--[1]		>0.0180		1.351	8.4	0.3603	0.1826	26.0
C3C			10,000		3.22		>0.0024	1.359	8.0	0.3557	0.1926	28.0
C4C			9,820		4.40		>0.0020	1.366	8.4	0.3688	0.1928	27.0
15A-AR-6-C1A	5.18	8,960		--[1]		0.0350		1.344	9.8	0.3219	0.1930	25.0
C2A		8,980		--[1]		>0.0280		1.343	8.8	0.3487	0.1810	25.0
C3C			6,410		5.20		>0.0030	1.330	9.2	0.3391	0.1832	27.0
C4C			4,580		--		--	1.344	9.0	0.3234	0.1900	28.0
15A-AR-7-C1A	6.51	4,820		--[1]		>0.0084		1.267	11.1	0.3313	0.1655	26.0
C2A		6,000		--[1]		>0.0214		1.265	10.4	0.3343	0.1664	25.0
C3C			2,820		1.39		0.0055	1.207	9.6	0.3205	0.1860	27.0
C4C			3,670		1.09		>0.0026	1.229	10.5	0.3201	0.1841	27.0
15A-AR-8-C1A	6.54	4,640		--[4]		>0.0280		1.288	9.6	0.3554	0.1828	26.0
C2A		4,860		--[4]		>0.0080		1.239	9.2	0.3606	0.1626	26.0
C3C			5,940		0.87		>0.0100	1.244	8.6	0.3113	0.1835	27.0
C4C			4,340		0.49		>0.0100	1.249	8.7	0.2943	0.1803	27.0

[1]Stress-strain curve not readable. Ultimate load only available
[2]Specimen broke under weight of load train. Strength < 100 psi
[3]Bleeding specimens. Open porosity not obtained
[4]The initial strain readings were much too low to give a reasonable modulus value

TABLE 36

RESULTS OF TENSILE AND COMPRESSIVE EVALUATIONS ON THE 3D QUARTZ-PHENOLIC PORTION, #15B, OF 3DC/QP IMPACTED ARCS

Specimen Number	Impact Level (K Tape)	Tensile Strength ^{1}psi		Tensile Modulus 10^{6}psi		Tensile Strain in./in.		Bulk Density gm/cm^{3}	Open Porosity %	Axial Sonic Velocity in./μsec	Radial Sonic Velocity in./μsec	Radial Sonic Transmission (db)
		Axial	Circum	Axial	Circum	Axial	Circum					
15B-AR-V-T1A	0	35,000		2.18				1.669	1.4	0.1782	0.1844	32.0
T2A		36,000		2.22				1.674	1.4	0.1763	0.1809	32.0
T3C			35,900		2.84			1.645	1.2	0.2089	0.1831	33.0
T4C			-		3.48			1.641	1.2	0.2035	0.1785	32.0
15B-AR-5-T1A	4.69	23,400		2.42				1.568	10.0	0.1779	0.1745	27.0
T2A		23,400		0.83				1.577	9.7	0.1789	0.1872	27.0
T3C			27,200		2.78			1.556	8.7	0.2058	0.1810	27.0
T4C			26,000		3.28			1.554	9.5	0.1959	0.1874	26.0
15B-AR-4-T1A	6.06	26,200		2.03				1.588	8.4	0.1807	0.1847	27.0
T2A		24,600		2.22				1.585	8.5	0.1794	0.1817	27.0
T3C			29,000		3.04			1.553	12.1	0.1864	0.1806	27.0
T4C			32,800		3.28			1.552	8.2	0.1879	0.1840	27.0

TABLE 36 CONTINUED

Specimen Number	Impact Level (K Taps)	Compressive Strength psi		Compressive Modulus 10^6 psi		Compressive Strain in./in.		Bulk Density gm/cm^3	Open Porosity %	Axial Sonic Velocity in./μsec	Radial Sonic Velocity in./μsec	Radial Sonic Transmission (db)
		Axial	Circum	Axial	Circum	Axial	Circum					
15B-AR-3-C1A	4.09	27,800		1.80		0.0152		1.599	8.4	0.1804	0.1804	29.0
C2A		28,000		3.73		0.0059		1.596	8.6	0.1790	0.1788	28.0
C3C			24,900		3.04		0.0109	1.587	8.6	0.2042	0.1860	27.0
C4C			24,550		2.63		0.0133	1.578	7.9	0.2070	0.1853	28.0
15B-AR-6-C1A	5.18	21,000		2.88		0.0083		1.560	10.0	0.1759	0.1831	27.0
C2A		23,900		2.61		0.0124		1.584	9.8	0.1742	0.1820	27.0
C3C			20,250		3.08		0.0073	1.545	9.3	0.1982	0.1820	27.0
C4C			14,900		3.23		0.0038	1.543	8.0	0.2026	0.1795	28.0
15B-AR-7-C1A	6.51	15,800		2.67		0.0108		1.536	12.4	0.1805	0.1761	27.0
C2A		16,900		2.43		0.0137		1.541	11.9	0.1789	0.1710	27.0
C3C			15,670		2.58		0.0092	1.534	14.0	0.1881	0.1890	28.0
C4C			12,640		2.64		0.0053	1.510	14.2	0.1897	0.1865	27.0
15B-AR-8-C1A	6.54	14,560		1.86		0.0090		1.519	13.8	0.1919	0.1730	27.0
C2A		21,400		2.52		0.0077		1.576	14.1	0.1814	0.1836	27.0
C3C			19,600		4.63		0.0054	1.548	12.5	0.1916	0.1824	27.0
C4C			17,300		3.19		0.0064	1.541	13.5	0.1957	0.1752	28.0

[1]Failures were all in the grip area of the specimen. Strength and strain values therefore not representative of ultimate tensile strength and tensile strain to failure but relative magnitudes should represent structure change and a lower bound of strength

TABLE 37

NDT INSPECTION RESULTS FOR AVCO 3DCQP

Specimen Configuration	Specimen	Number	Type NDT QC	Type NDT FT	Bulk Density gm/cm³	Velocity in./μsec Radial	Velocity in./μsec Axial	Ultrasonic Transmission (Added db) Radial	Ultrasonic Transmission (Added db) Axial	Remarks
ARC	Ring 4	AR 1	X		1.480					Visual Results 1. Material similar to AHP material except surface porosity was lower and circumferentials were straighter. Figure 125. 2. No material anomalies. Radiographic Results 1. No material anomalies.
		2	X		1.481					
		3	X		1.477					
		4	X		1.479					
		5	X		1.480					
		6	X		1.481					
		7	X		1.478					
		8	X		1.480					
		9	X		1.474					
		10	X		1.476					
		11	X		1.478					
		$\bar{X}$			1.479					
		Sd			0.002					
Ring		1	X		1.473					
		2	X		1.473					
		3	X		1.476					
		5	X		1.472					
		6	X		1.470					
		7	X		1.472					
		$\bar{X}$			1.473					
		Sd			0.002					

TABLE 38

NDT INSPECTION RESULTS FOR AVCO 3DCP

Specimen Configuration	Specimen Number	Type NDT QC	Type NDT FT	Bulk Density gm/cm³	Velocity in./μsec Radial	Velocity in./μsec Axial	Ultrasonic Transmission (Added db) Radial	Ultrasonic Transmission (Added db) Axial	Remarks
ARC	Ring 6 Arc 1	X		1.415					Visual Results
	" 6 " 2		X	1.417	0.1811	0.3714	31		1. Material similar to AHP material except surface porosity was lower and circumferentials were straighter. Figure 128 and 129.
	" 6 " 3	X		1.417					
	" 6 " 4		X	1.415	0.1864	0.3734	31.5		
	" 6 " 5		X	1.419	0.1833	0.3757	32.5		
	" 6 " 6	X		1.417					
	" 6 " 7	X		1.416					2. Occasional resin rich areas between axials and circumferentials Figure 130.
	" 6 " 8		X	1.418	0.1851	0.3685	32		
	" 6 " 9	X		1.420					
	" 6 " 10		X	1.416	0.1827	0.3683	32		
	" 6 " 11	X		1.418					3. Resin starved areas aligned circumferentially around radials in outer surface. Figure 131.
	$\bar{X}$			1.417	0.1837	0.3715	31.8		
	Sd			0.002	0.0021	0.0032	0.6		
									4. Voids and raised axial in right edge of Arc 7 of Ring 6. Located in C edge, 0.35" from bottom edge, 0.38" from inner surface. Figure 132.
ARC	Ring 7 Arc 1	X		1.417					
	" 7 " 2	X		1.417					
	" 7 " 3	X		1.413					
	" 7 " 4	X		1.415					
	" 7 " 5	X		1.418					5. Arcs 5 and 6 from Ring 6 had chipped corners probably incurred in handling.
	" 7 " 6	X		1.418					
	" 7 " 7	X		1.417					
	" 7 " 8	X		1.415					
	" 7 " 9	X		1.415					6. Ring #2 had 0.4" long chipped or crushed top outer edge at 25°. Figure 133.
	" 7 " 10	X		1.419					
	" 7 " 11	X		1.420					
	$\bar{X}$			1.417					
	Sd			0.002					

TABLE 38 CONTINUED

Specimen Configuration	Specimen Number	Type NDT QC	Type NDT FT	Bulk Density gm/cm³	Velocity in./μsec Radial	Velocity in./μsec Axial	Ultrasonic Transmission (Added db) Radial	Ultrasonic Transmission (Added db) Axial	Remarks
Ring	1	X		1.406					7. Ring #8 had 0.16" long indented area located in top edge, 0.08" from inner surface at 240°. Fig 133.
	2	X		1.415					
	3	X		1.414					
	4	X		1.409					
	5	X		1.411					
	8	X		1.412					8. Ring #10 had local areas of high porosity (and lowest density). Fig 134.
	9	X		1.413					
	10	X		1.403					
	11	X		1.404					Liquid Penetrants Results
	12	X		1.405					
	$\bar{X}$			1.409					Partek P-18 on edges and alcohol on flats were not revealing of any new material flaws.
	Sd			0.004					
									Radiographic Results
									1. No material anomalies in arcs from Rings 6 & 7. Occasional circumferential low-absorptive alignments & residual porosity apparent.
									2. Ring #1 was not revealing of any variations.
									3. Various volume oriented circumferential low-absorptive alignments were revealed in Rings #2,3,4,5,10,11, and 12.
									4. Occasional through and part-through thickness low-absorptive alignments along radials in Rings #3 (45°), #5 (10-45° and 340°), #9 (135°, 190°, and 350°), #10 (240°), and #12 (245°).

TABLE 39

NDT INSPECTION RESULTS FOR AVCO 3DCP (T400)

Specimen Configuration	Specimen Number	Type NDT QC	Type NDT FT	Bulk Density gm/cm³	Velocity in./μsec Radial	Velocity in./μsec Axial	Ultrasonic Transmission (Added db) Radial	Ultrasonic Transmission (Added db) Axial	Remarks
ARC	1	X		1.445					**Visual Results**
	2	X		1.451					1. Material contained some residual pores or voids in faces and edges and striations.
	3	X		1.457					
	4	X		1.457					2. No visual anomalies were detectable in the arcs.
	$\bar{X}$			1.452					
	Sd			-					3. Rings in general were symmetrical.
Ring	1	X		1.462					
	2	X		1.458					4. Ring 3 contained a circumferential delam in outer surface at 330°, voids on inner surface at 220°, and voids on bottom edge at 45°.
	3	X		1.455					
	4	X							**Radiographic Results**
	$\bar{X}$			1.459					
	Sd			-					1. No anomalies were detectable in the arcs.
									2. Ring 1 had increased circumferential low-absorptive alignments at 15°, 40°, 275-285°, and 315-350°, Figure 136 for typical.
									3. Ring 2 had increased circumferential low-absorptive alignments at 0-90°, 210°, 255-280°, and 315°, Figure 136 for typical.
									4. Ring 3 had increased circumferential low-absorptive alignments at 0-60°, 210-220°, 285-300°, and 315-340°, Figure 136 for typical.
									5. Ring 4 had increased circumferential low-absorptive alignments at 25-45°, 125°, and 140-170°. A gross consentration of low-absorptive alignments were indicated at 320-360°, Figure 137

TABLE 40

NDT INSPECTION RESULTS FOR AVCO R6300

Specimen Configuration	Specimen	Number	Type NDT QC	Type NDT FT	Bulk Density gm/cm³	Velocity in./μsec Radial	Velocity in./μsec Axial	Ultrasonic Transmission (Added db) Radial	Ultrasonic Transmission (Added db) Axial	Remarks
ARC	Ring 12	ARC 1	X		1.368	0.1261	0.13.6			Visual Results
		2	X		1.357	0.1252	0.1308			
		3	X		1.361	0.1253	0.1310			1. Similar to AHP material with following exceptions: a. Density of AHCA was slightly higher, density of AHP about 1.33 gm/cm³ and density of AHCA ranged from 1.32 to 1.37 gm/cm³ b. Residual Porosity (to 0.02 inch in size) was higher for AHCA, Figure 138.
		13	X		1.344					
		14	X		1.369					
		15	X		1.367					
		$\bar{X}$			1.361	0.1255	0.1311			
		Sd			0.010	-	-			
ARC	Ring 11	ARC 1	X		1.344					2. Typical of AHP R6300, inner and outer surfaces had occasional waviness because of variations in tape layup, Figure 139.
		2	X		1.346					
		3	X		1.369					
		4	X		1.345					
		5	X		1.367					
		6	X		1.345					
		7	X		1.347					
		8	X		1.355					
		9	X		1.371					3. Viewed circumferentially aligned residual porosity between tape wraps, Figure 142. Was not typical for AHP R6300.
		10	X		1.373					
		11	X		1.366					
		12	X		1.332					
		$\bar{X}$			1.355					4. Tape wrap discontinuities on inner surface of Ring 11, Arc 9, Figure 143.
		Sd			0.014					

TABLE 40 CONTINUED

Specimen Configuration	Specimen Number	Type NDT QC	Type NDT FT	Bulk Density gm/cm³	Velocity in./μsec Radial	Velocity in./μsec Axial	Ultrasonic Transmission (Added db) Radial	Ultrasonic Transmission (Added db) Axial	Remarks
Ring	1	X		1.322					**Visual Results Cont'd**
	2		X	1.324	$\bar{X}$ 0.1165	$\bar{X}$ 0.1296	$\bar{X}$ 56		5. Single 0.10 inch long void on inner surface of Ring 12 Arc 14, Figure 144.
	3	X		1.337	Sd0.0005	Sd0.0005	Sd 0		
	4		X	1.330	$\bar{X}$ 0.1151	$\bar{X}$ 0.1294	$\bar{X}$ 56		6. Bottom, inner edge of Ring 7 was chipped from 130 to 180° and at 215°, Figure 145.
	5	X		1.322	Sd0.0010	Sd0.0009	Sd 0		
	6	X		1.301					**Radiographic Results**
	7	X		1.333					1. No flaws by radiography in circumferential direction. Low-absorptive alignments were occasionally revealed between tape wraps, Figure 140
	8	X		1.337					2. About half of Ring 11 Arc 8 contained lower density material by radial X-ray, Figure 146.
	9	X		1.330					3. Low-absorptive alignments to about 3/4-inch in Ring 11 Arc 9 by radial X-ray, Figure 146.
	10	X		1.356					4. Single 0.04 inch low-absorptive area (void) located at 75° in Ring 4 by axial X-ray.
	X			1.330					5. Single 0.04 inch low-absorptive area (void) located at 95° and 0.04 inch high-absorptive area (inclusion) located at 140° in Ring 6 by axial X-ray.
	Sd			0.014					6. Single 0.02 inch low-absorptive area (void) located at 290° in Ring 9 by axial X-ray.
									Note: Various volume oriented low-absorptive areas were revealed in the rings by axial X-ray. Although, these areas were not considered to be of any real consequence, hit orientations were specified away from such areas.
									Liquid Penetrant Results FT Rings 2 and 4 were inspected, but no additional material anomalies were revealed.

TABLE 41

NDT INSPECTION RESULTS FOR AVCO 3DCC

Specimen Configuration	Specimen Number	Type NDT QC	Type NDT PT	Bulk Density gm/cm³	Velocity in./μsec Radial	Velocity in./μsec Axial	Ultrasonic Transmission (Added db) Radial	Ultrasonic Transmission (Added db) Axial	Remarks
DISC (AHP-0006/ W250)	1			1.707	0.2491				Visual Results
	2			1.711	0.2673				1. Generally material similar to AHP material with debonds uniformly distributed, Figure 149 through 151 for typical.
	3			1.708	0.2234				
	4			1.711	0.2504				
	5			1.710	0.2480				
	6			1.712	0.2464				
	7			1.729	0.2563				
	8			1.714	0.2593				2. The debonds in the 1109-35 rings appeared more severe than AHP, Figure 152.
	9			1.717	0.2508				
	10			1.714	0.2476				
	11			1.719	0.2518				
	X			1.714	0.2495				3. Visual anomalies in Discs: a. #1: Inner edge bumped at 270°, Figure 153; b. #11: Single through-thickness wrinkle, Figure 153;
	Sd			0.006	0.0110				
Coupon (AHP-0007 3DCC 1109-34)	1	X		1.700					4. No visual anomalies in coupons.
	2	X		1.706					
	3	X		1.709					5. No visual anomalies in 1109-35 rings.
	4	X		1.709					
	5	X		1.725					
	6	X		1.720					6. Visual anomalies in Rings 2B and 4B a. #2B: Single 0.15 inch x 0.15 inch x 1 ply deep depressed area located in outer surface at 0° and 0.20 inch from bottom edge, Figure 154.
	7	X		1.715					
	8	X		1.709					
	9	X		1.709					
	10	X		1.705					
	X			1.711					
	Sd			0.007					

TABLE 41 CONTINUED

Specimen Configuration	Specimen Number	Type NDT QC	Type NDT PT	Thickness inch	Bulk Density gm/cm³	Velocity in./μsec Radial	Velocity in./μsec Axial	Ultrasonic Transmission (Added db) Radial	Ultrasonic Transmission (Added db) Axial	Remarks
Ring	1109-35-1		X	1/2	1.626	X̄ 0.2434 Sd0.0045	X̄ 0.3794 Sd0.0142	X̄ 18.5 Sd 2.1		Visual Results Cont'd
	2	X		1/2	1.638					b. #43: Machining error resulted in surface mismatch in bottom edge at 180°, Figure 155; local area 0.2 inch x 1.2 inch of loose and missing material in outer surface at 300° and bottom edge, Figure 156.
	3	X		1/2	1.645					
	4	X		1/2	1.646					
	5		X	1/2	1.646	X̄ 0.2554 Sd0.0076	X̄ 0.3894 Sd0.0061	X̄ 21.9 Sd 3.0		
	6	X		1/4	1.664					
	7	X		1/4	1.675					7. Ring 11 had largest single visual debond, Figure 137. Debond measured 3-1/2 inches and was located in bottom edge at 150°-210°. Debond was not detectable by radiography.
	8	X		1/4	1.685					
	9	X		1/4	1.673					
	10	X		1/4	1.698					
	11	X		1/4	1.691					
	X̄				1.662					
	Sd				0.024					
										Radiographic Results
Ring	1A	X		1/2	1.677					1. Major debonds in discs and coupons were continuous and regularly spaced at about 0.10, 0.25, 0.35, and 0.40 inch from I.D.
	2A	X		1/2	1.680					
	1B	X		1/4	1.680					
	2B	X		1/4	1.672					2. Through-thickness wrinkle in Disc #11 by axial X-ray, also apparent visually, Figure 153.
	3B	X		1/4	1.673					
	4B	X		1/4	1.675					3. Through-thickness wrinkle in Coupon #5 by axial X-ray.
	X̄				1.676					
	Sd				0.003					4. Axial radiographs on Rings 1 through 11 and 1A through 4B revealed a background debonds. The more severe ones were noted, and the locations of the most uniform material were selected away from these sites. Sketches showing these results are given in Figure 158 through 174. Ring 1A was considered uniform throughout
										Liquid Penetrants Results
										FT Rings 1 and 5 were inspected, but no additional material anomalies were revealed.

TABLE 42

NDT INSPECTION RESULTS FOR SANDIA FELT CC

Specimen Configuration	Specimen Number	Type NDT QC	Type NDT PT	Thickness inch	Bulk Density gm/cm³	Velocity in./μsec Radial	Velocity in./μsec Axial	Ultrasonic Transmission (Added db) Radial	Ultrasonic Transmission (Added db) Axial	Remarks
Ring	2N-1	X		0.45	1.778					Visual Results
	2N-2		X	0.50	1.805	$\bar{X}$ 0.1042 Sd 0.0020	$\bar{X}$ 0.1235 Sd0.0010	$\bar{X}$ 51.8 Sd 0.5		1. Material similar to AMP except needling was coarser incurring background residual porosity of about 0.012 inch, Figure 175.
	2N-3	X		0.25	1.793					
	2P-1	X		0.25	1.777					
	3N-2		X	0.50	1.802	$\bar{X}$ 0.1087 Sd 0.0012	$\bar{X}$ 0.1203 Sd0.0009	$\bar{X}$ 52.1 Sd 0.4		
	4N-1	X		0.45	1.782					2. No visual material anomalies.
	4N-2	X		0.50	1.804					
	4P-2	X		0.50	1.796					3. During polishing, PT Ring 2N-2 incurred a 1.1 inch long scrap in polished edge (top) located 245°-260°.
	7N-1	X		0.45	1.763					
	7N-2	X		0.25	1.823					
	7P-1	X		0.25	1.831					4. During polishing, PT Ring 3N-2 incurred a 0.7 inch long scrap in polished (top) edge located 75°-90°.
	7P-2	X		0.25	1.837					
	8N-1	X		0.25	1.789					
	8N-2	X		0.50	1.798					Radiographic Results
	8P-1	X		0.50	1.831					
	8P-2	X		0.50	1.827					1. Circumferential low-absorptive alignment (crack) in Ring 7P-2 located 335°-345° (1 inch length).
	10N-1	X		0.25	1.792					
	10N-2	X		0.25	1.806					2. Circumferential low-absorptive alignment (crack) in Ring 4P-2 located at 315°-330°, Figure 178.
	10P-1	X		0.25	1.845					
	10P-2	X		0.25	1.846					Liquid Penetrants on PT Rings 2N-2 and 3N-2
	-									
	$\bar{X}$				1.806					1. Rings 2N-2: a. Void clusters to 0.2 inch revealed by alcohol on outer surface at 55°, 295°, and 330° Figure 180. b. Mechanical surface indentations in outer surface at 0°.
	Sd				0.024					
										2. No additional material anomalies were revealed in Ring 3N-2.

TABLE 43

BULK MOE ON AHCA FULL TREATMENT RINGS

Material	Ring No.	Ring Flexure		Hydrostatic Compression
		From Deflections Measurements	From Strain Gage Measurements	From Strain Gage Measurements
3DCC	1109-35-1	7.9*	9.4	13.7
	-5	8.2	10.0	14.4
Felt CC	2N2	1.34	1.22	1.91
	3N2	1.38	1.24	1.73
R6300	-2	1.62	1.47	1.81
	-4	1.68	1.50	1.62

*Note: Units of MOE are 10^6 psi

APPENDIX A

ULTIMATE STRENGTH, ELASTIC MODULUS AND POISSON'S RATIO TO 5500°F IN TENSION

A typical tensile facility shown in Figures A-1 and A-2 consists of the gas-bearings, the load frame, the mechanical drive system, the 5500°F furnace, the optical strain analyzers and associated instrumentation for measurement of load and strain. The load capacity is 15,000 pounds.

The load frame and mechanical drive system are similar to those of many good facilities. The upper crosshead is positioned by a small electric motor connected to a precision screw jack. This crosshead is stationary during loading and is moved only when assembling the load train. The lower crosshead is used to apply the load to the specimen through a precision screw jack chain driven by a variable speed motor and gear reducer.

Nonuniaxial loading, and therefore bending stresses, may be introduced in tensile specimens not only from (1) misalignment of the load train at the attachment to the crossheads, but also from (2) eccentricity within the load train, (3) unbalance of the load train and (4) external forces applied to the load train by such items as electrical leads and clip-on extensometers. Although the bending moments from some of these sources may seem relatively slight, the resulting stress distortions are quite significant in the evaluation of the extremely sensitive brittle materials. Now consider each individually.

To confirm that the gas-bearings had eliminated nonuniaxial loading at the point of attachment of the load train to the crossheads, the frictional moment was determined at a load of 5000 pounds by measuring the torque required to produce initial motion within the system with the bearings in operation. This torque was found to be a maximum of 6.6×10^{-3} inch-pounds. The equation

$$M_O = \frac{2\mu P}{3} \left[\frac{R_2^3 - R_1^3}{R_2^2 - R_1^2}\right] \qquad (1)$$

was then applied to the system to calculate the kinetic friction where M_O was the resisting moment due to kinetic friction and μ represented the coefficient of kinetic friction. The calculated value of μ was then equal to a maximum of only 4.5×10^{-7}.

The classic equation

$$S = \frac{Mc}{I} \qquad (2)$$

was then employed to obtain the stress that could be induced in the specimen due to this bending moment. This value was 0.16 psi, or less than 0.002 percent of the tensile stress produced within a typical graphite specimen. These low values clearly indicate the elimination of problems of bending stress in the specimen imposed by misalignment at the crosshead attachments, either initially or during loading.

Emphases in the design of the load train were placed on (1) large length-to-diameter ratios at each connection, (2) close sliding fits (less than 0.005 inch) of all mating connections, (3) the elimination of threaded connections, (4) the use of pin connections wherever possible and (5) increasing the size of components to permit precise machining of all mating surfaces. All members were machined true and concentric to within 0.0005 inch, and the entire load train was checked regularly to ensure overall alignment following assembly of the individual members. This process ensures concentricity and no kinks in the system.

The problems of unbalance within the load train and of external forces applied to the load train have been explored and corrected. The entire load train is statically balanced to less than 0.01 inch-pound for normal operation.

One configuration of the tensile specimen is shown in Figure A-3. This specimen provides a relatively large L/D ratio in the gripping area to ensure good alignment. All surfaces in the gripping area are cylindrical in order to make precision machining easier and repeatable from specimen to specimen. This specimen also has double breakdown radii from the gripping area to the gage section. This double breakdown allows a uniform transition of the stress pattern and reduces the frequency of radius (out of gage) fractures. This specimen provides a uniform gage section which gives a definable volume of material under stress and permits accurate measurements of strain. The flags for the measurement of axial strain are positioned one inch apart so that unit strain is recorded directly. The flag attachment for measurement of lateral strain is positioned between the flags for axial strain (see Figure A-4).

A schematic of the precision tensile grip is shown in Figure A-5. The design is much like the jaws of a lathe head or the chuck of a drill motor made with precision. Observe from the figure the long surface contact of the mating parts and the close fits to establish precise alignment with the specimen. As the load is applied, the wedges maintain alignment to fracture.

Figure A-6 is a sketch of the 5500°F furnace used for tension showing the basic components. The furnace consists of a resistively heated graphite element insulated from a water-cooled shell by thermatomic carbon. The furnace and specimen are purged with helium to provide an inert atmosphere. Ports with visual openings are provided on opposite sides of the furnace as a means of allowing the strain analyzers to view the gage flags on the specimen. Specimen temperatures are determined by optical pyrometer readings taken through another small sight port containing a sapphire window. A calibration curve was established for the loss through the sapphire window, and since the furnace cavity acts essentially as a blackbody, true temperature readings are obtained. Power is supplied to the heating element by means of a 25 KVA variable transformer.

Strain measurement consists of measuring optically the elongation between two flags, or targets, which are mounted on the specimen and separated initially by a predetermined gage length. The travel of the targets is measured by sensing the displacemnt of the image of the edge of the targets and then electromechanically following the image displacement. The relative travel of the two targets provides the strain. Readout is continuous and automatic on a millivolt recorder. A schematic of the analyzer is shown in Figure A-7.

A brief summary of the mechanical motions of the components involved in monitoring the strain is helpful in understanding the detailed performance. A tracking telescope follows the upper target and carries a second telescope mounted on its carriage. The second telescope is capable of independent motion to follow the lower target. The relative displacement between the upper and lower telescope, as strain occurs, defines the strain. The system usually is operated so that the tracking telescope follows the upper target and the strain is monitored by the relative displacement of the aperture rather than the telescope following the lower target. With this procedure the maximum range is the maximum displacement available for the lower aperture, of about 1/8 inch, and the sensitivity is limited by the optics and the noise level of the detector. Using both telescopes, the range is about 3/4 inch.

To provide optical references on the specimens, targets are affixed to the test specimen as mentioned. When the specimen is heated to temperature, the targets are self-luminous and are observed optically. The optics view past the luminous targets into a cooled cavity in the opposite furnace wall. The self-luminous targets are then visible against a dark background. To obtain data below 2000°F, a light beam is directed from behind the flags providing a shadow image for the detection system.

The image of the flowing target is focused through a rotating shutter (chopper) and onto a rectangular aperture. Small slits in the aperture pass a portion of the upper and lower edges of the light beam. A photocell receives the light thus transmitted, and an electronic circuit detects whether the energy passed by the two slits is equal. A servo drives the apertures to let a balanced quantity of light pass through the two slits and thus maintains an optical null.

To obtain lateral strain, a strain analyzer is supported horizontally on the tensile frame to view the diametrical or lateral strain of the specimen. A flag attachment, with the general configuration as shown in Figure A-8, was developed to follow and transmit lateral motions of up to a few mils. The three-piece assembly consists of a ring and two rams bearing on the specimen.

Calibrations of the analyzers are performed in various ways including absolute correlations to precision micrometers, strain gage extensometers, and direct plots of stress-strain for reference materials such as steel, plexiglas, magnesium and aluminum. Precision is within ±0.000020 inch.

Instrumentation includes primarily a stress-strain measurement system composed of a 1000-pound SR-4 Baldwin load cell, constant d.c. voltage power supply, two optical strain analyzers, and two X-Y recorders. Specimen temperature is monitored with an optical pyrometer. Stress (load) is measured by a commercial load cell. The cell receives a constant d.c. voltage input from the power supply and transmits a millivolt signal (directly proportional to load) to an X-Y recorder. Simultaneously, the optical strain analyzers measure both the axial and lateral strain and transmit a millivolt signal (proportional to strain) to the X-Y recorders. Thus, continuous plots of stress-axial strain and axial strain-lateral strain are recorded simultaneously.

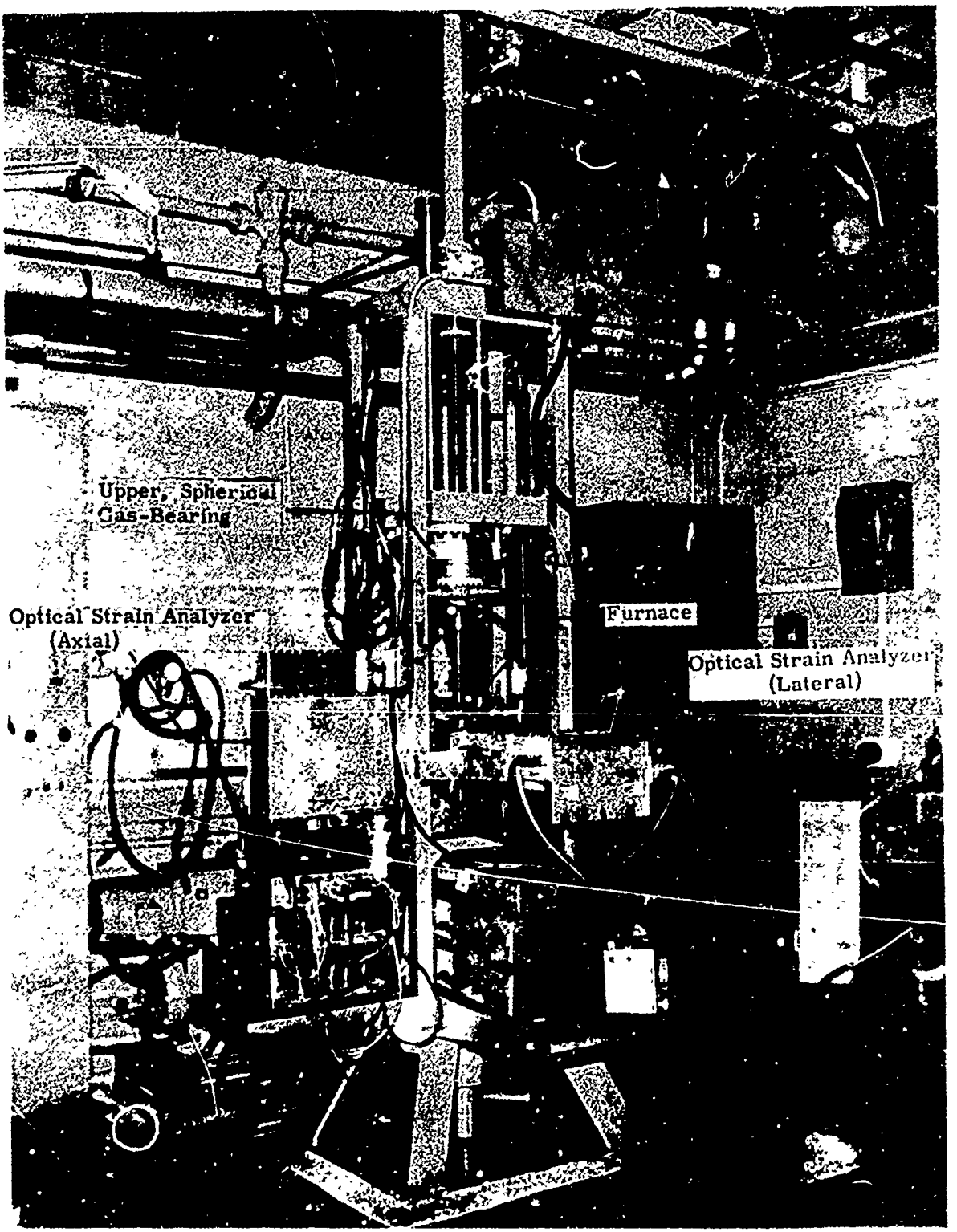


Figure A-1. Picture of a Tensile Stress-Strain Facility

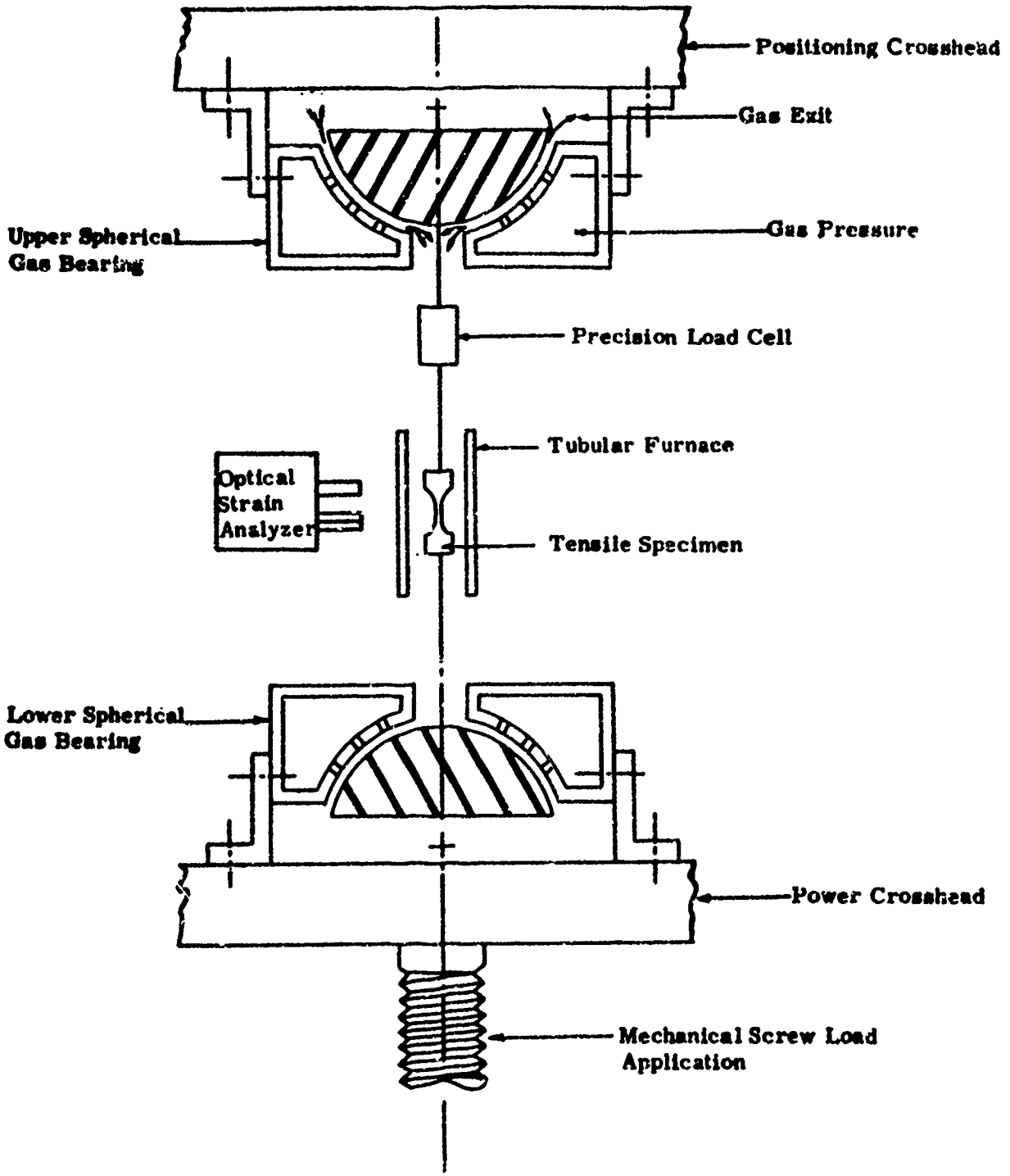


Figure A-2. Schematic Arrangement of Gas-Bearing Universals, Specimen and Load Train

Notes:

1. All Diameters True and Concentric to Within 0.0005"
2. Do Not Undercut Radii At Tangent Points
3. Both Ends Flat and Perpendicular to and to Within 0.0005"
4. All Dimensions are in Inches
5. Tolerances are $\pm$ 0.001 on Diameters
   $\pm$ 0.005 on Lengths
   $\pm \frac{1}{64}$ on Fractions

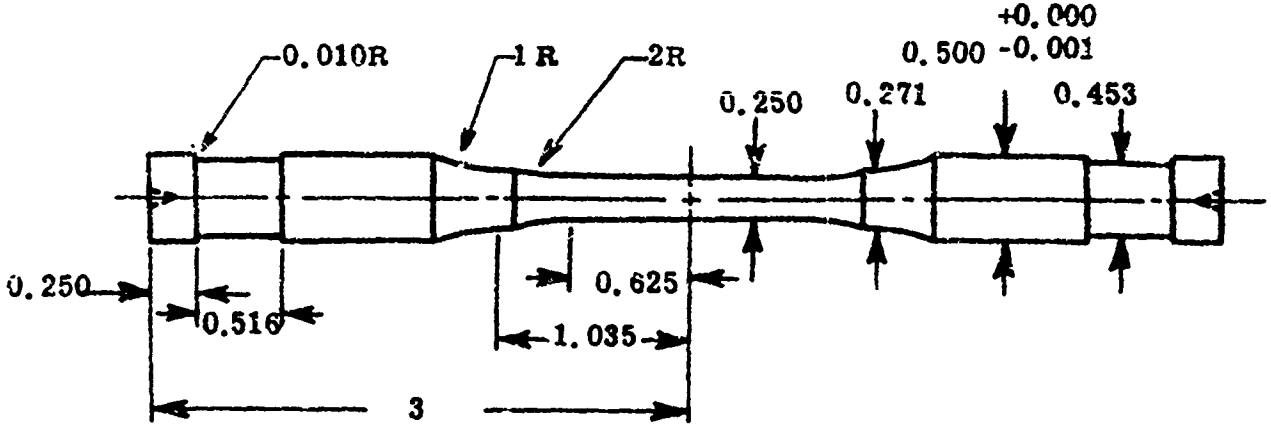


Figure A-3. Tensile Specimen Configuration

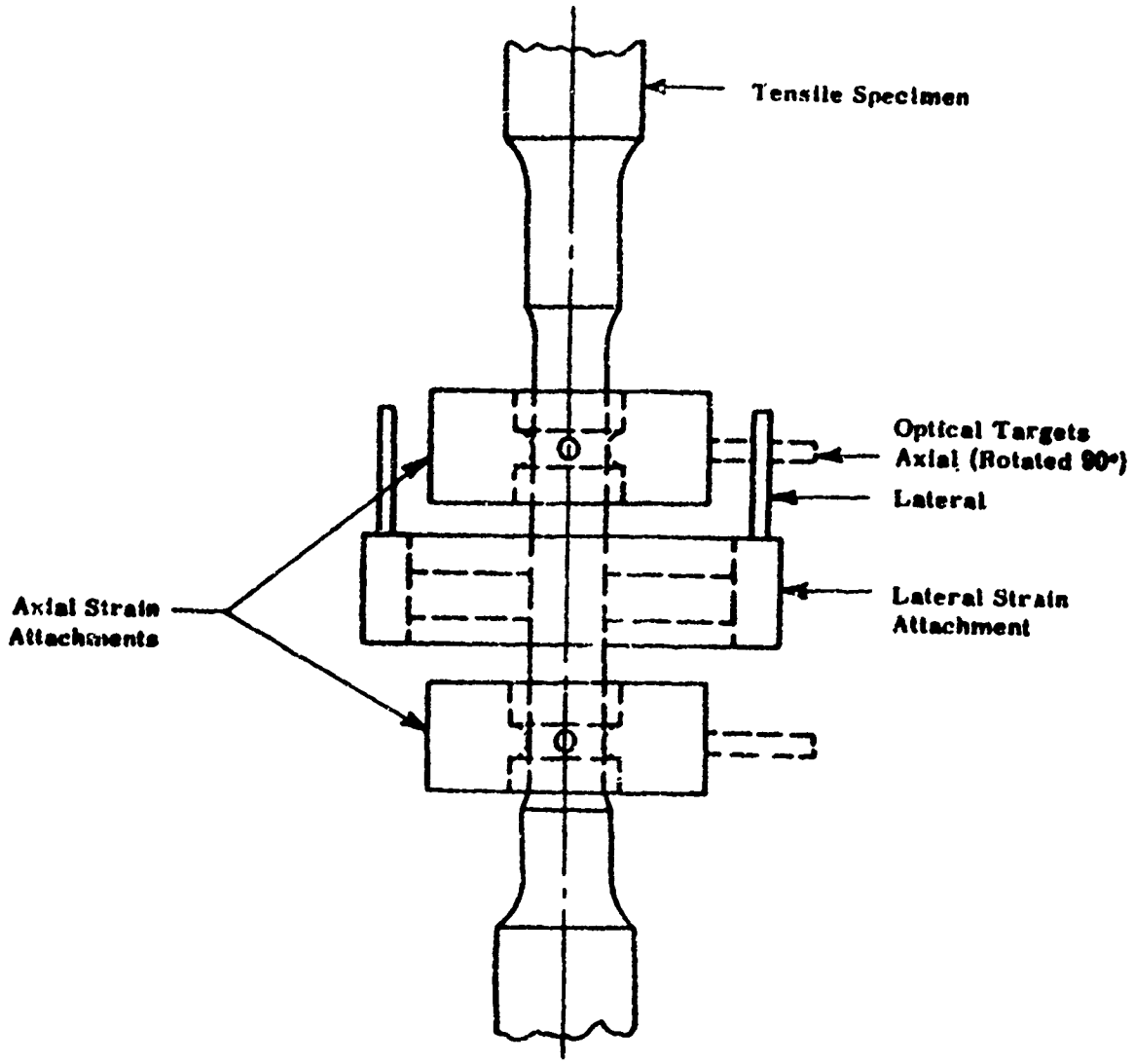


Figure A-4. Location of the Flag Attachments on the Tensile Specimens

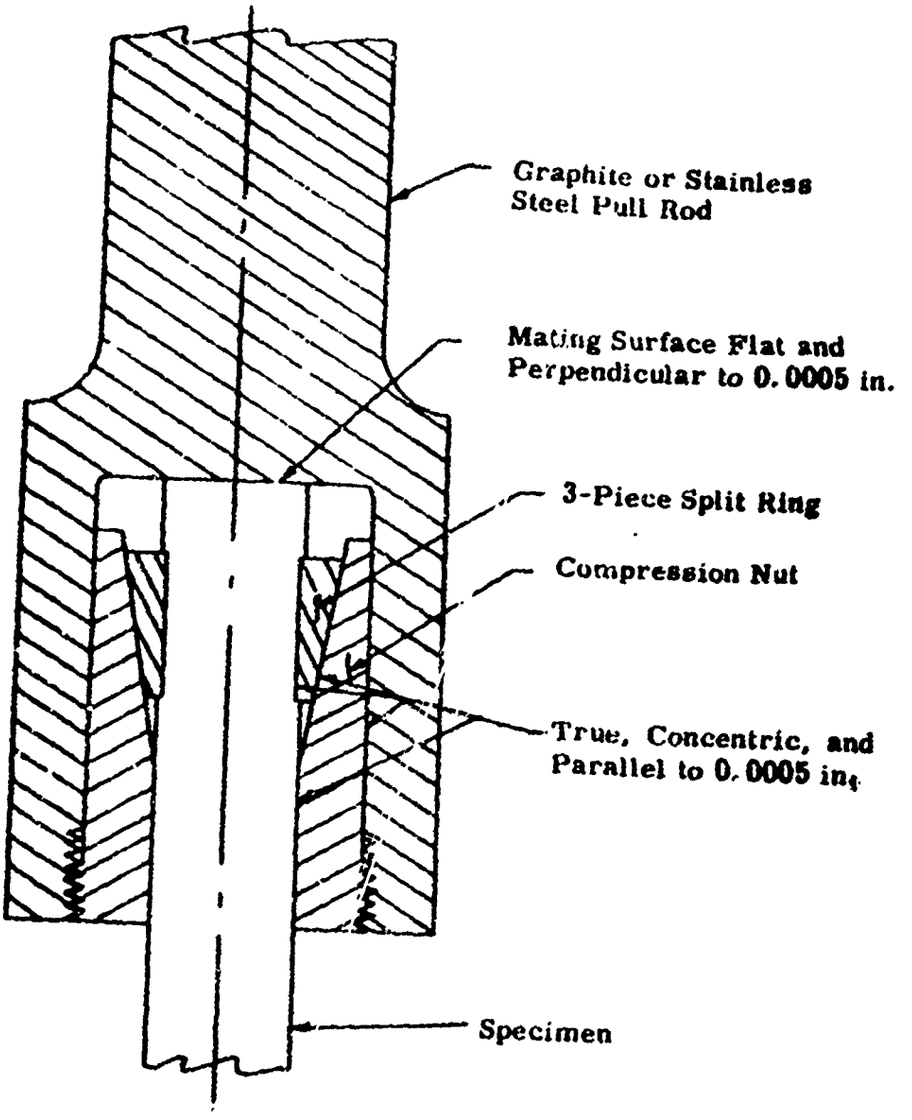


Figure A-5. Precision Collet Grip for Tensile Specimen 2:1 Scale

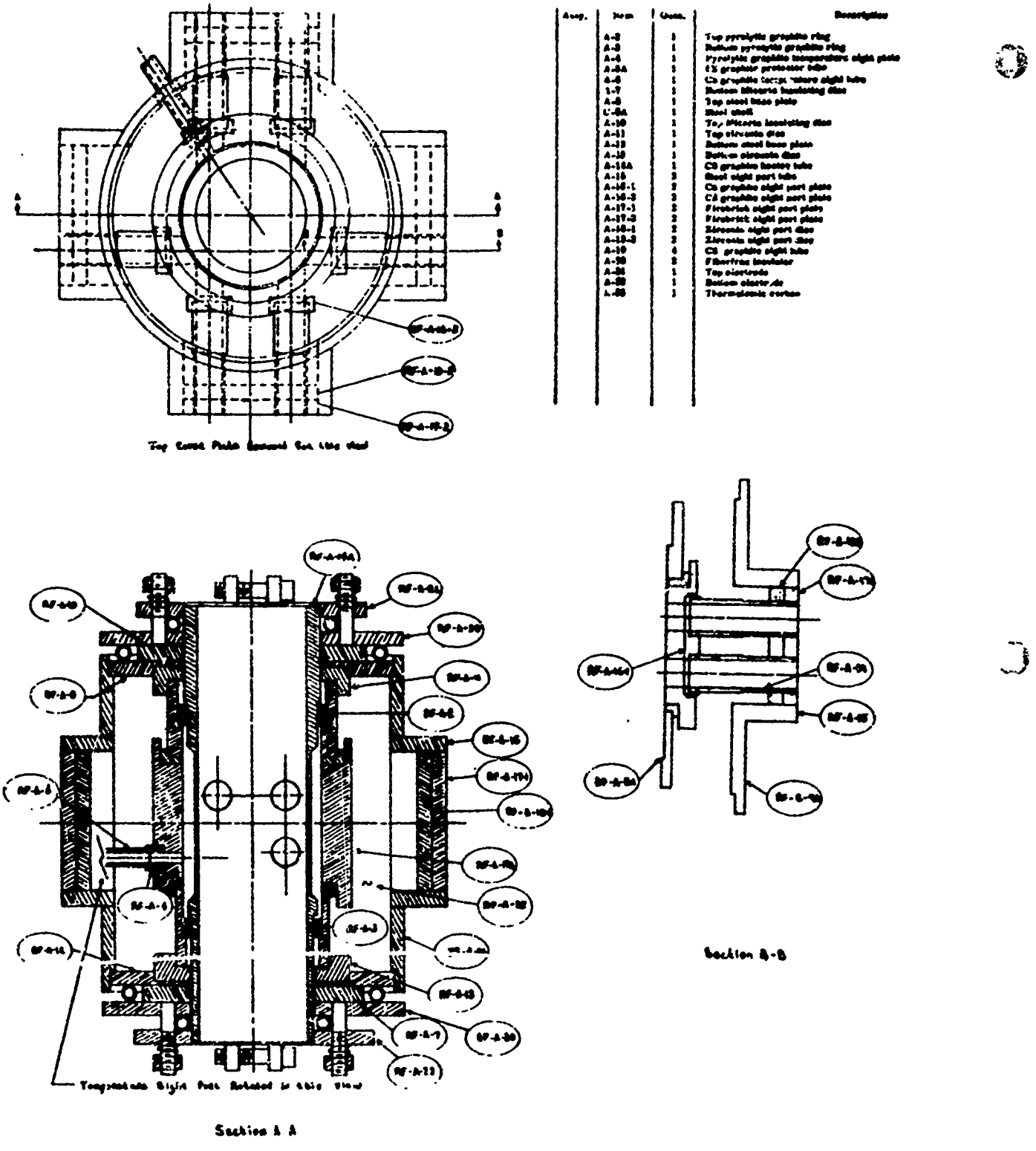


Figure A-6. Small 5500°F Graphite Resistance Furnace

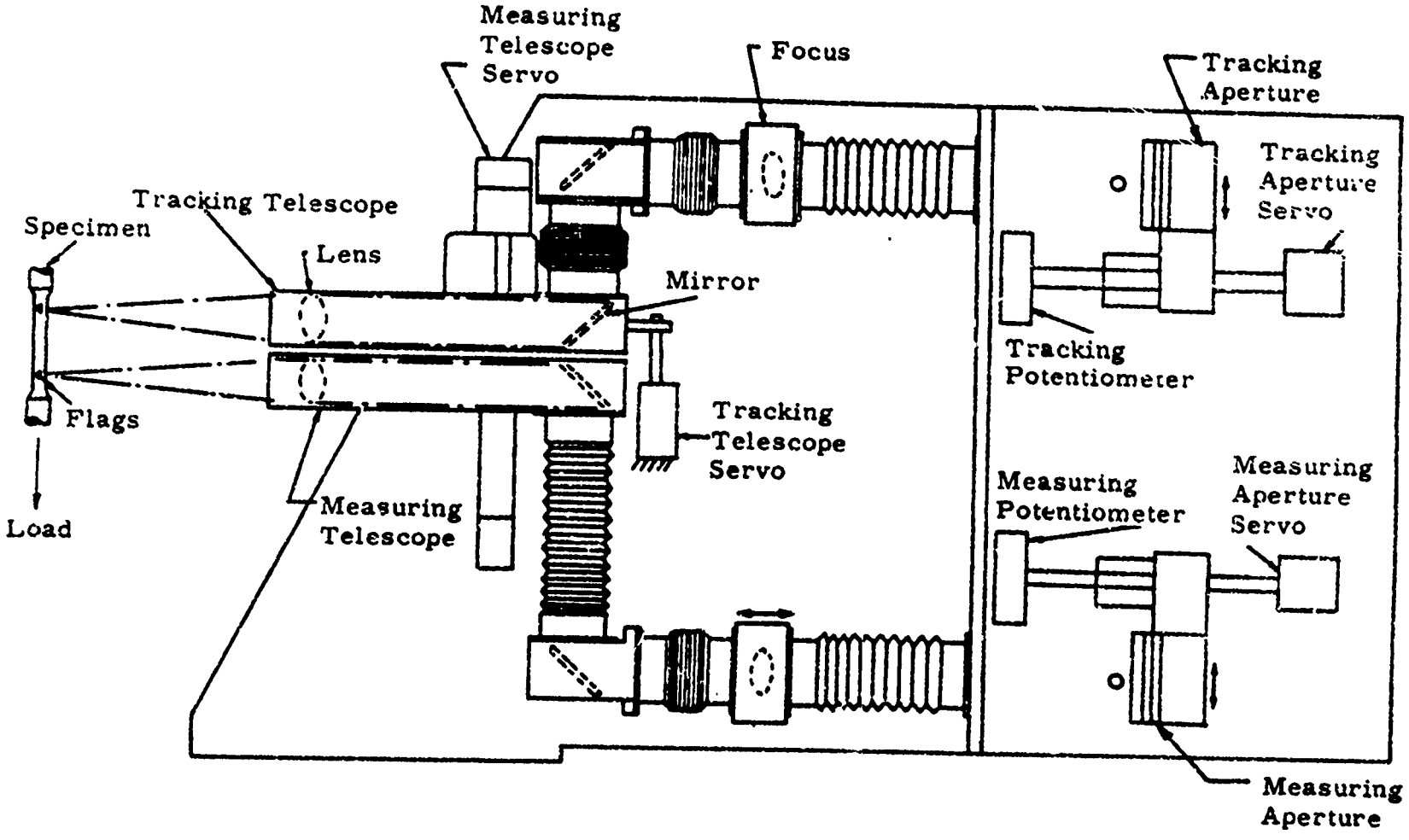


Figure A-7. Arrangement of Optical Strain Analyzer

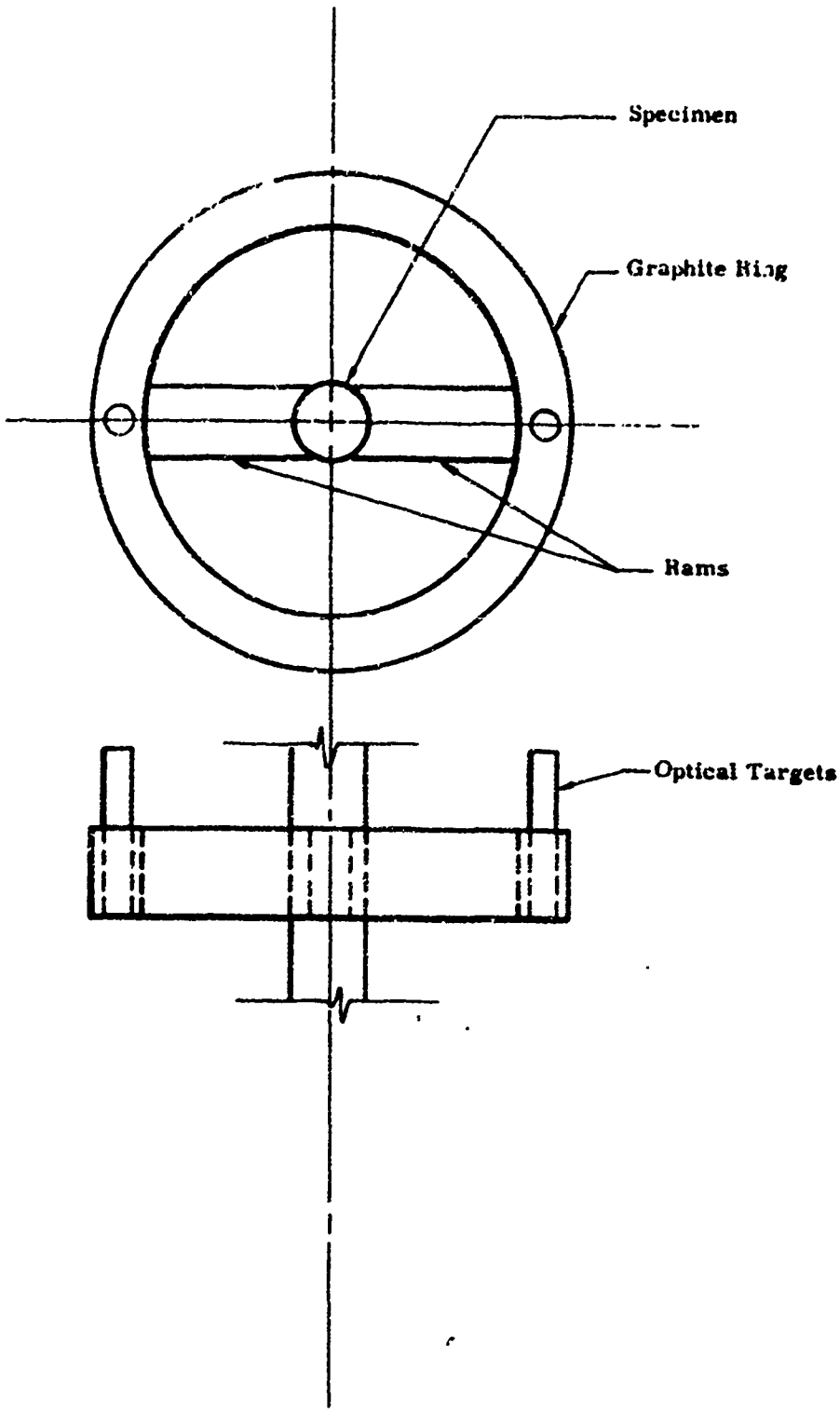


Figure A-8. General Configuration of the Flag Attachment to Monitor Lateral Strain in Tension

APPENDIX B

ULTIMATE STRENGTH, ELASTIC MODULUS, AND POISSON'S RATIO TO 5500°F IN COMPRESSION

The compressive apparatus shown in Figures B-1 and B-2 consists primarily of a load frame, gas bearings, load train, 50-ton screw jack, variable speed mechanical drive system, strain analyzers, 5500°F furnace, and associated instrumentation for the measurement of load and train.

The load frame is similar to most standard frames. It was designed to carry a maximum load of 100,000 pounds and to support the furnace, optical strain analyzers and other related equipment.

Gas bearings are installed at each end of the load train to permit precise alignment of the loading train to the specimen. The upper bearing is spherical on a radius of 6.5 inches. This radius is the distance from the top of the specimen to the spherical bearing surface. The load train, not the specimen, shifts to maintain radial alignment. The lower bearing is flat and is about 6 inches in diameter. The lower bearing permits transverse alignment of the load train. The gas bearings are floated for only a small initial amount of load so that precise alignment of the load train can be attained.

The load train near the furnace consists of the specimen loaded on each side by graphite and water-cooled steel push rods. The graphite push rods are counter-bored to permit insertion of a pyrolytic graphite disc which serves as a heat dam and to align the specimen to the center-line of the load train. Extreme care is exercised in the preparation of all parts of the load train to ensure concentricity of the mating parts to less than 0.0005 inch.

The 50-ton jack is a power screw type. The mechanical drive system consists of a gear reducer driven by a Louis Allis Synchro-Spede Unit (300-3000 rpm). The gear reducer is connected to the Synchro-Spede Unit through a chain coupling and to the 50-ton jack by a single roller chain and sprocket system. Different load rates are obtained by adjustment of the variable speed setting on the Synchro-Spede and by changeout of sprockets on the gear reducer and screw jack.

Figure B-4 shows details of the "dumbbell" specimen which maintains a 0.500 inch diameter over the 1.2 inch long gage section. The specimen provides sufficient room for the flag attachments that follow the axial and lateral strains and also minimizes the influence of end restraint.

The flag attachments for the measurement of axial strain are positioned one inch apart so that unit strain is recorded directly. The flag attachment for the measurement of lateral strain is positioned between the flags for axial strain; see Figure B-4. The lateral flag attachment used in compression is shown in Figure B-5. The 4-piece assembly consists of a ring, two rams bearing on the specimen, and a screw to adjust the contact pressure. The ring was designed to track lateral motions as great as 0.030 inch without breaking.

Figure B-6 is a sketch of the 5500°F furnace used for compression showing the basic components. The furnace consists of a resistivity heated graphite element insulated from a water-cooled shell by thermatomic carbon. The furnace and specimen are purged with helium to provide an inert atmosphere. Ports with visual openings are provided on opposite sides of the furnace as a means of allowing the strain analyzers to view the gage flags on the specimen. Specimen temperatures are determined by optical pyrometer readings taken through another small sight port containing a sapphire window. A calibration curve was established for the loss through the sapphire window, and since the furnace cavity acts essentially as a blackbody, true temperature readings are obtained. Power is supplied to the heating element by means of a 25 KVA variable transformer.

Strain measurement consists of measuring optically the elongation between two flags, or targets, which are mounted on the specimen and separated initially by a predetermined gage length. The travel of the targets is measured by sensing the displacement of the image of the edge of the targets and then electromechanically following the image displacement. The relative travel of the two targets provides the strain. Readout is continuous and automatic on a millivolt recorder. A schematic of the analyzer is shown in Figure B-7.

A brief summary of the mechanical motions of the components involved in monitoring the strain is helpful in understanding the detailed performance. A tracking telescope follows the upper target and carries a second telescope mounted on its carriage. The second telescope is capable of independent motion to follow the lower target. The relative displacement between the upper and lower telescope, as strain occurs, defines the strain. The system usually is operated so that the tracking telescope follows the

upper target and the strain is monitored by the relative displacement of the aperture rather than the telescope following the lower target. With this procedure the maximum range is the maximum displacement available for the lower aperture, or about 1/8 inch, and the sensitivity is limited by the optics and the noise level of the detector. Using both telescopes, the range is about 3/4 inch.

To provide optical references on the specimens, targets are affixed to the test specimen as mentioned. When the specimen is heated to temperature, the targets are self-luminous and are observed optically. The optics view past the luminous targets into a cooled cavity in the opposite furnace wall. The self-luminous targets are then visible against a dark background. To obtain data at below 2000°F, a light beam is directed from behind the flags providing a shadow image for the detection system.

The image of the glowing target is focused through a rotating shutter (chopper) and onto a rectangular aperture. Small slits in the aperture pass a portion of the upper and lower edges of the light beam. A photocell receives the light thus transmitted, and an electronic circuit detects whether the energy passed by the two slits is equal. A servo drives the apertures to let a balanced quantity of light pass through the two slits and thus maintains an optical null.

To obtain lateral strain, a strain analyzer is supported horizontally on the load frame to view the diametrical or lateral strain of the specimen.

Calibrations of the analyzers are performed in various ways including absolute correlations to precision micrometers, strain gage extensometers, and direct plots of stress-strain for reference materials such as steel, plexiglas, magnesium, and aluminum. Precision is ±0.000020 inch.

Instrumentation includes primarily a stress-strain measurement system composed of a 20,000-pound SR-4 Baldwin load cell, constant d.c. voltage power supply, two optical strain analyzers, and two X-Y recorders. Specimen temperature is monitored with an optical pyrometer. Stress (load) is measured by a commercial load cell. The cell receives a constant d.c. voltage input from the power supply and transmits a millivolt signal (directly proportional to load) to an X-Y recorder. Simultaneously, the optical strain analyzers measure both the axial and lateral strain and transmit a millivolt signal (proportional to strain) to the X-Y recorders. Thus, continuous plots of stress-axial strain and axial strain-lateral strain are recorded simultaneously.

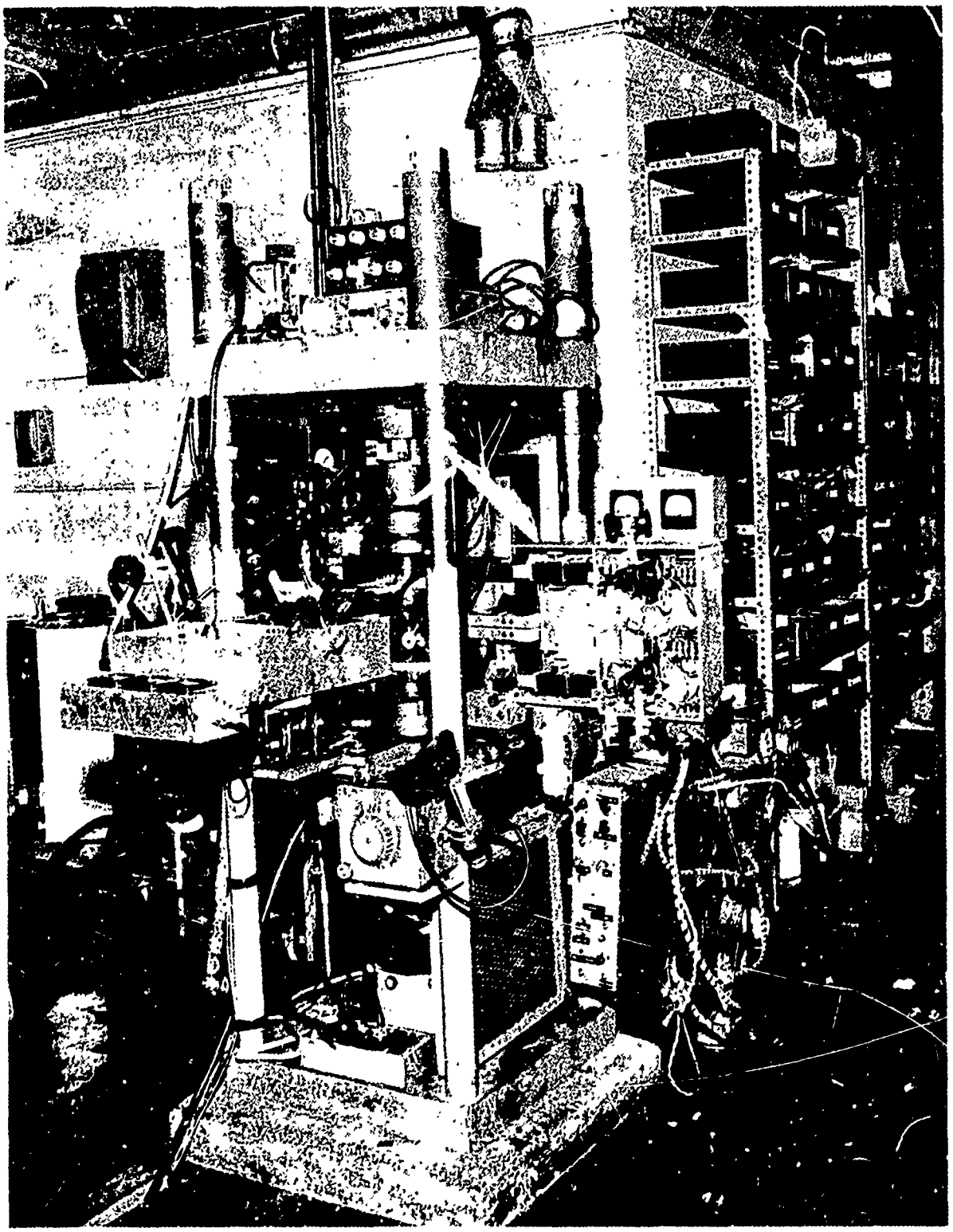


Figure B-1. Picture of the Compressive Facility with Gas Bearings and Optical Strain Analyzer

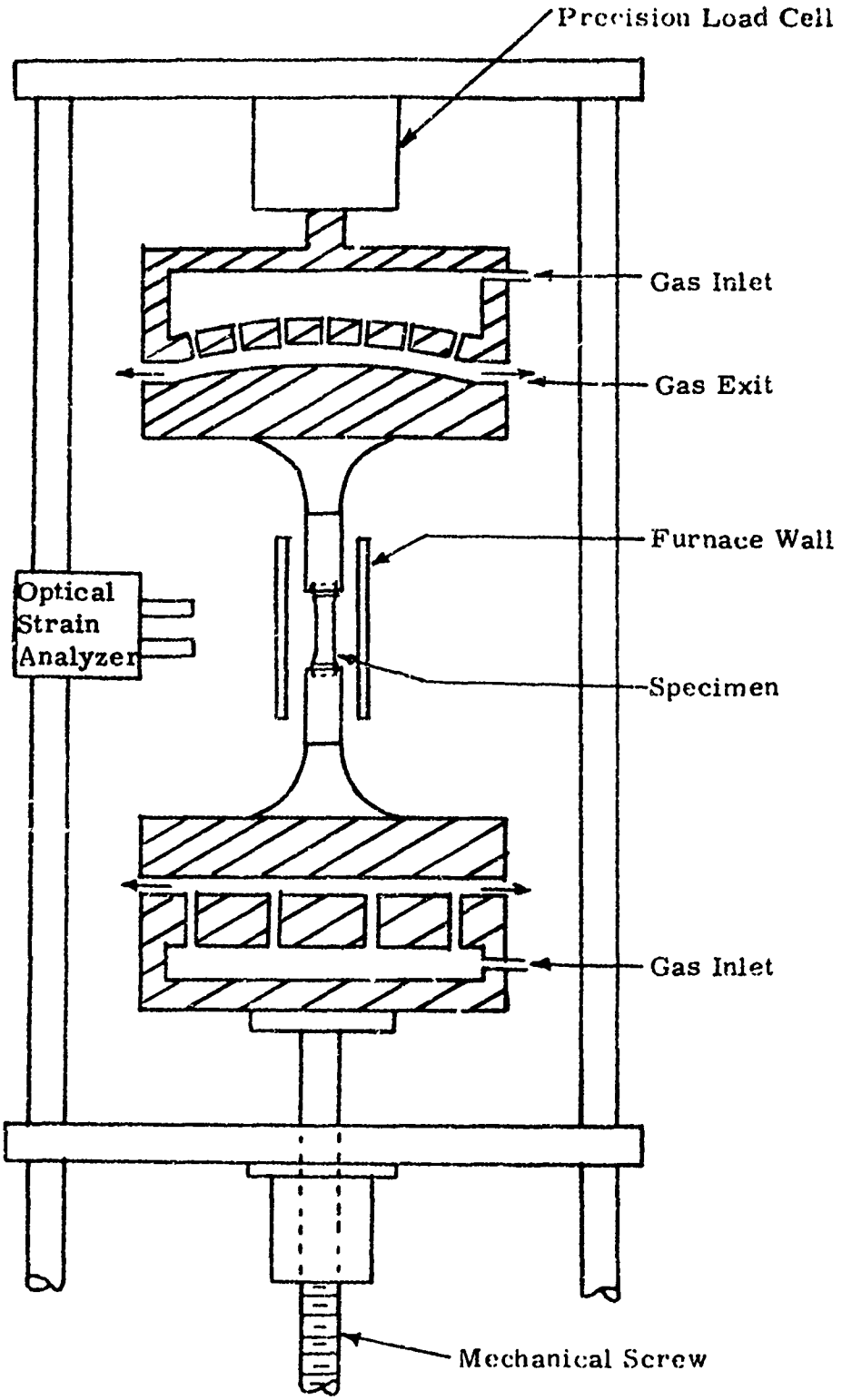


Figure B-2. Schematic Arrangement of Gas-Bearing Universals, Specimen and Load Train

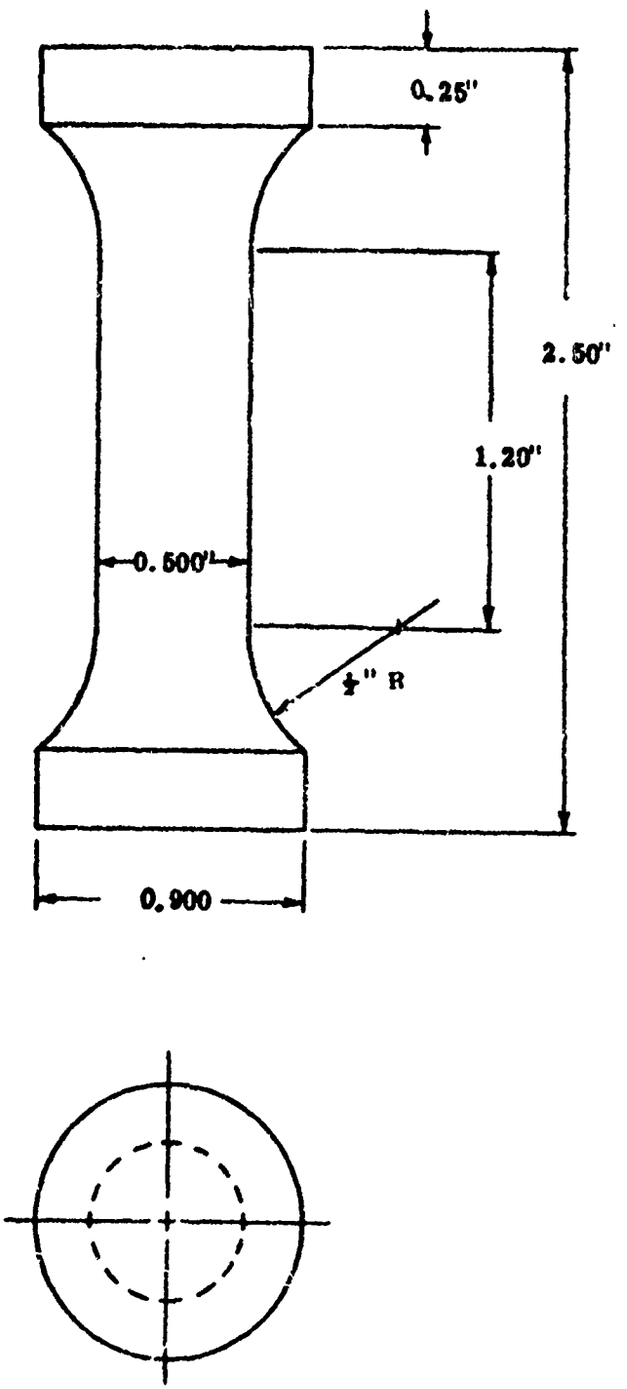


Figure B-3. Compressive Specimen Configuration

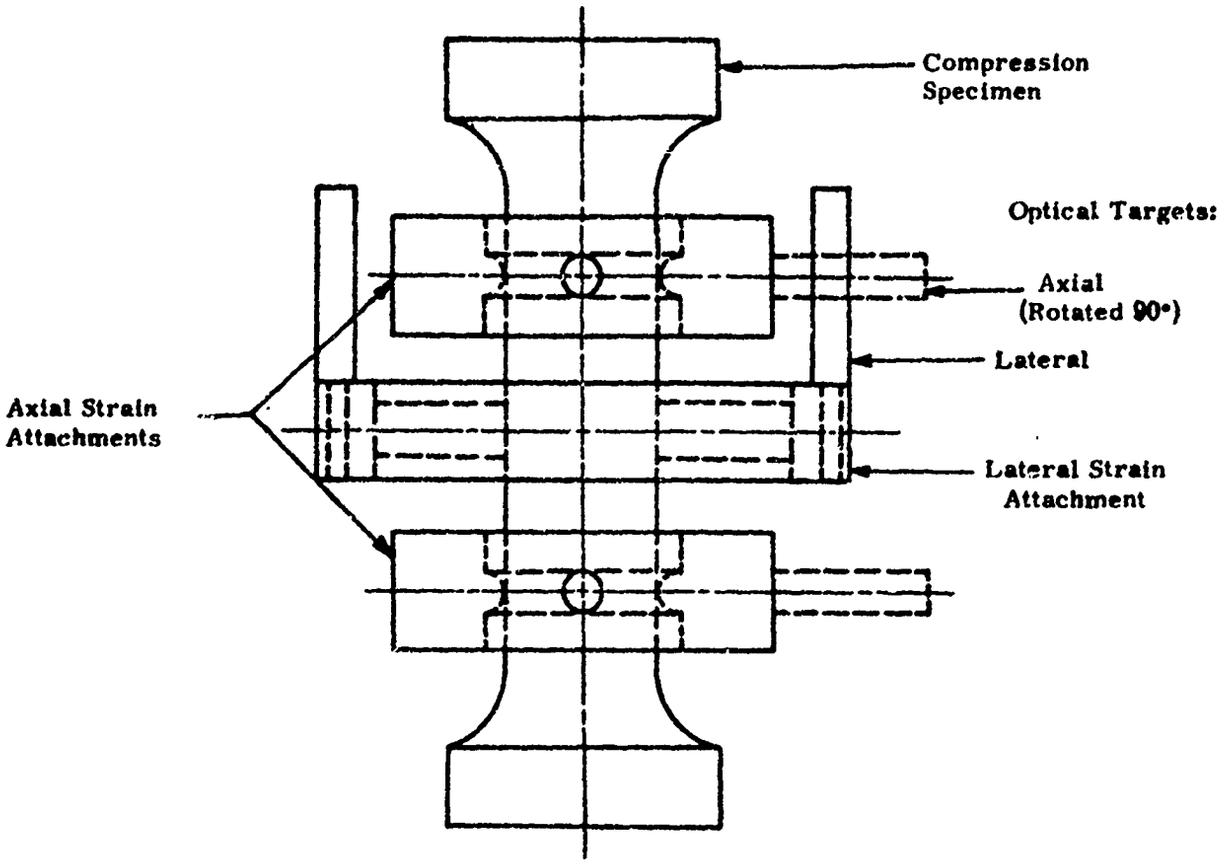


Figure B-4. Location of the Flag Attachments on the Compressive Specimen

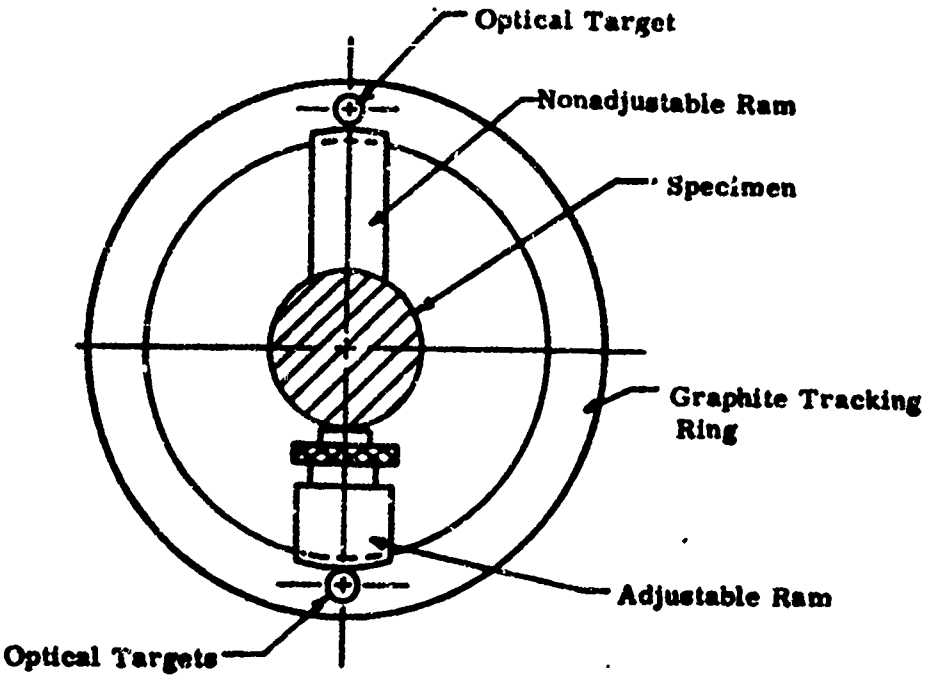


Figure B-5. Lateral Strain Flat Attachment for Compressive Specimen

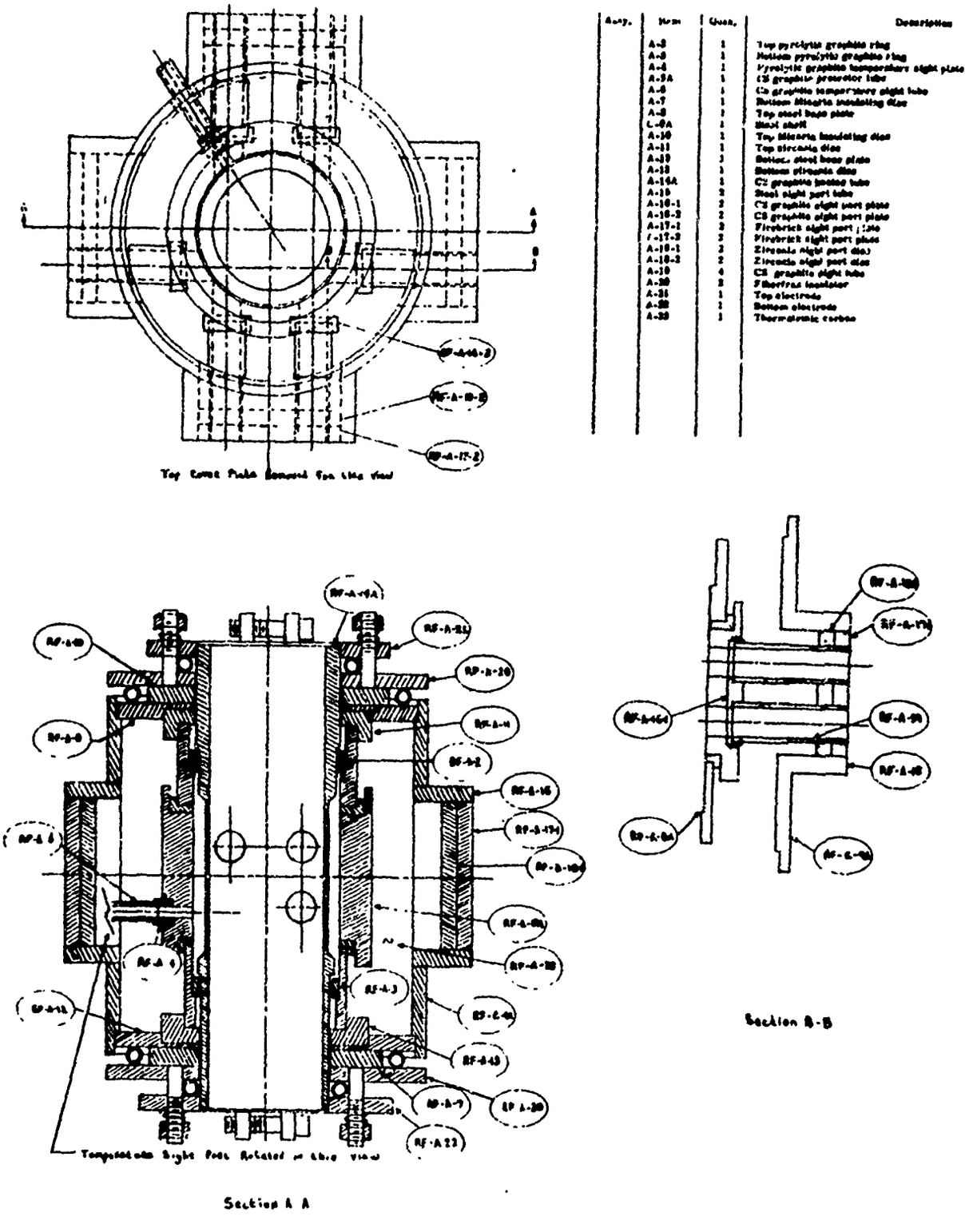


Figure B-6. Small 5500°F Graphite Resistance Furnace

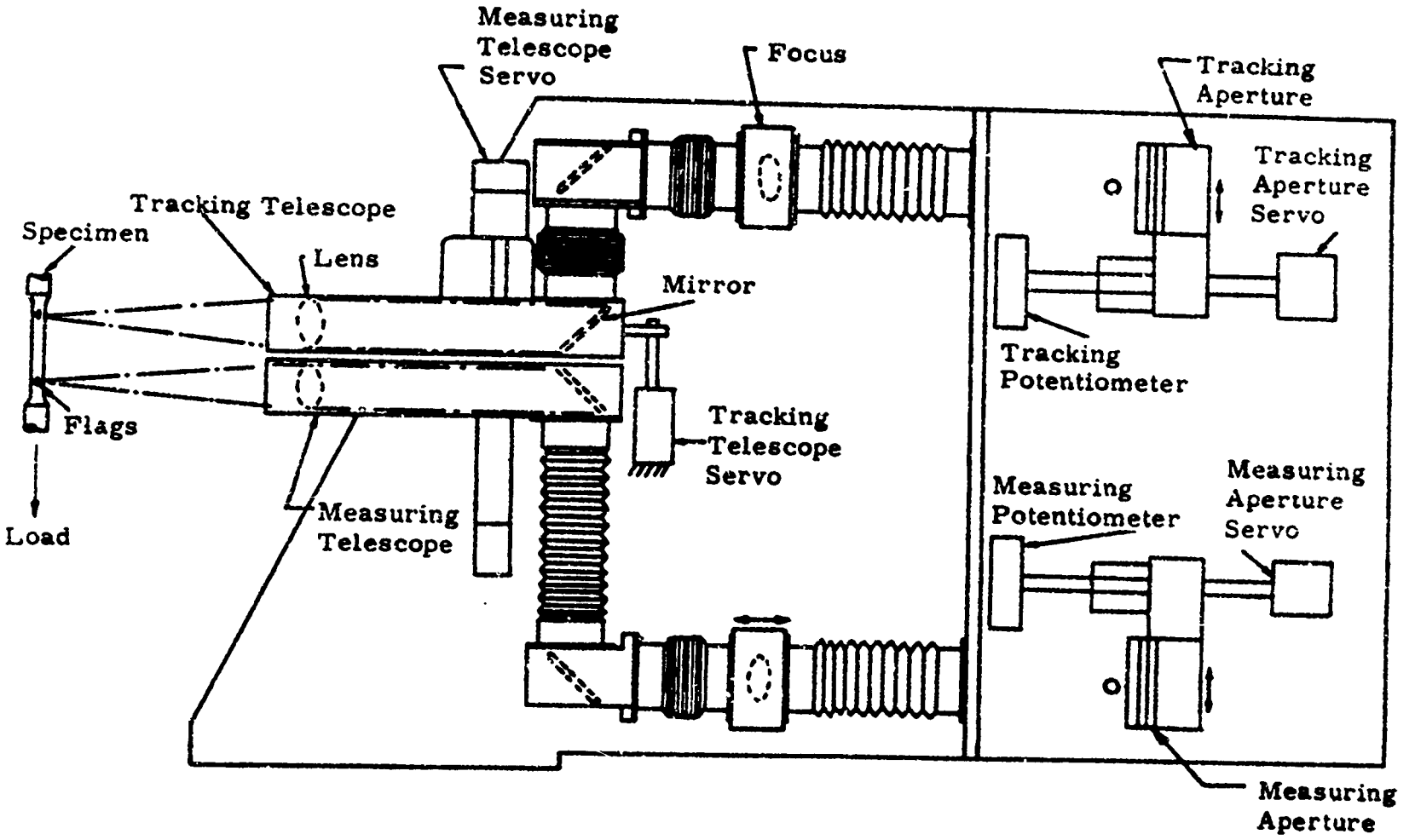


Figure B-7. Arrangement of Optical Strain Analyzer

APPENDIX C

THERMAL EXPANSION TO 1800°F

Thermal expansion measurements are made utilizing quartz tube dilatometers of the Bureau of Standards design. The dial gages (B. C. Ames Co., Model 212, Shockless) are graduated in 0.0001-inch divisions with a total range of 0.500 inch. The manufacturer's stated mechanical accuracy for any given reading is ±0.0001 inch at any point in the range. This accuracy has been checked with a precision micrometer.

The extensions from the dial, which are made of stainless steel, are finned to facilitate cooling. The temperatures of the fins are continually monitored and air cooled when necessary to eliminate differential expansion between the dial gage mount and the extension (see Figure C-1).

For temperatures above room temperature, each dilatometer is heated by an individual heater. The temperature of the heater is maintained by a manual setting of a variable voltage transformer.

Cold specimen temperatures are obtained by use of a Dewar flask filled with dry ice and trichloroethylene. The flask surrounds the dilatometer tubes and the cold liquid level rises to a height above the specimens.

Liquid nitrogen is used in the Dewar flask for temperatures down to -300°F. A cooling coil has also been designed to provide better control of temperatures in the cryogenic range.

Thermocouples are placed at each end and the center of the specimens to monitor the temperature throughout. The specimens are nominally 1/2-inch diameter by 3 inches in length with the ends rounded on a 3-inch radius. Other diameters and cross-sectional configurations are employed where necessary due to configuration of supplied material.

To calibrate the dilatometers we employ a fused silica specimen, the expansion of which is known and is shown in Figure C-2.

The accuracy of the apparatus to 1800°F has been checked by running the NBS copper standard and other in-house standards of graphite and nickel. Figures C-3, C-4, and C-5 include the expansion values measured in the quartz dilatometers on these standards. Note the excellent agreement between the measured values and the data reported by NBS on the copper. For the graphite and nickel standards, good agreement was observed between the values measured in the quartz dilatometer and that reported in the literature and the values measured at SRI by optically tracking.

The above data and our experience have demonstrated the excellent precision and accuracy of this equipment. We have observed no systematic uncertainty with the equipment and, based on 5 runs with the graphite standard, the random uncertainty is $\pm 0.05 \times 10^{-3}$ in./in. at 1500°F with a 95 percent confidence interval.

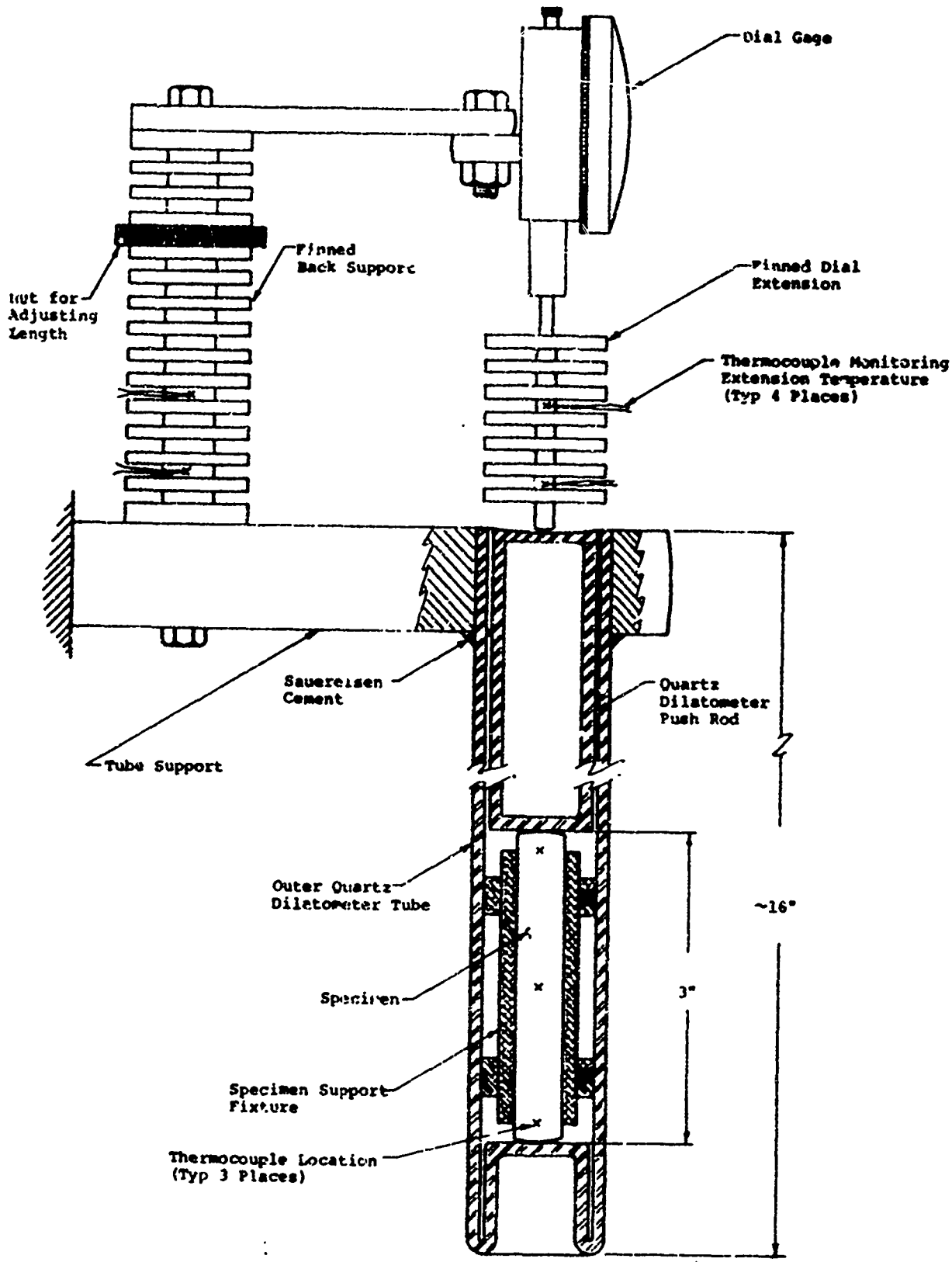


Figure C-1. Assembly of Quartz Tube Dilatometer for Thermal Expansion Measurements

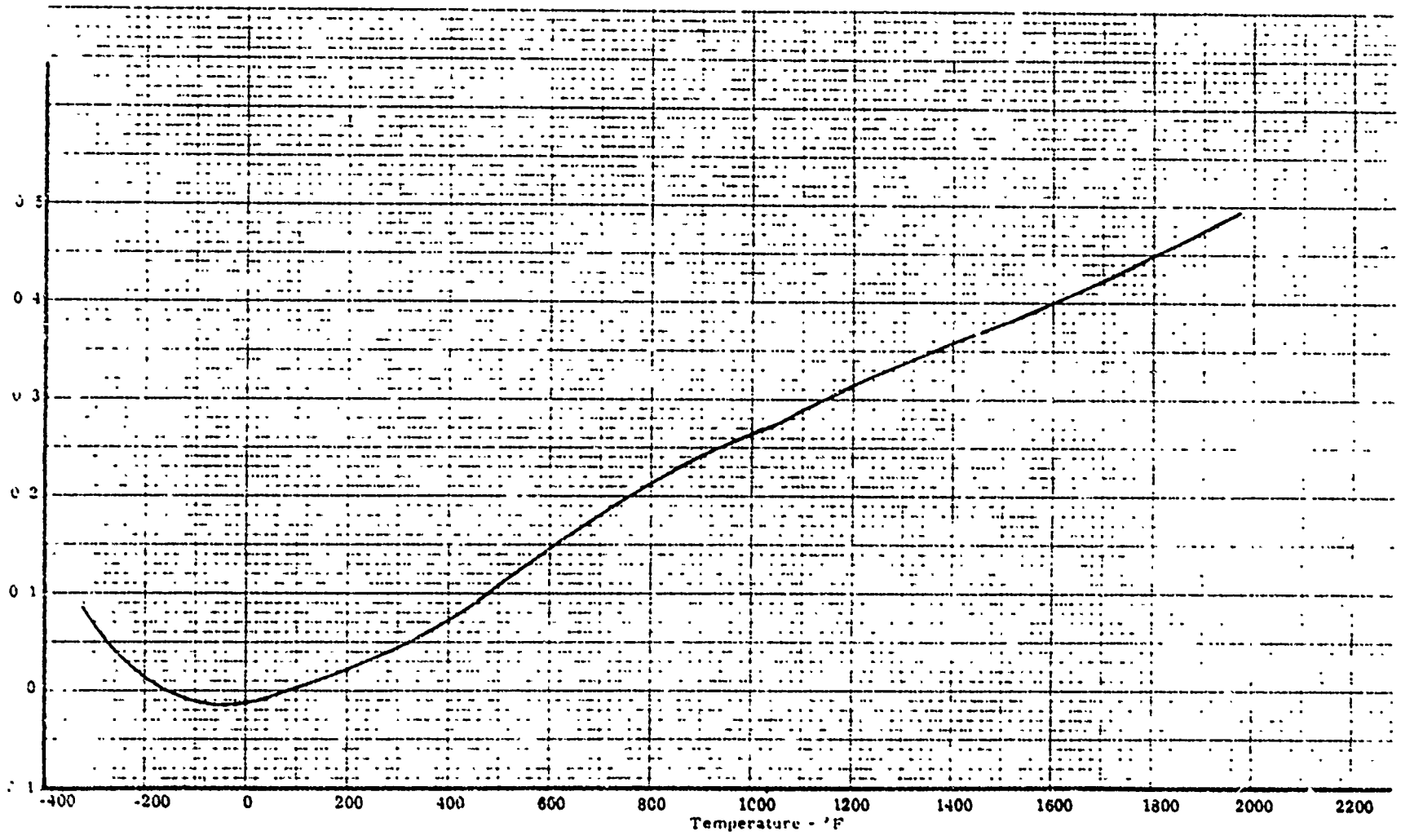


Figure C-2. Thermal Expansion of Fused Silica (Taken from Souder and Hidnert, "Measurements on Thermal Expansion of Fused Silica" Scientific Papers of the Bureau of Standards, No. 524)

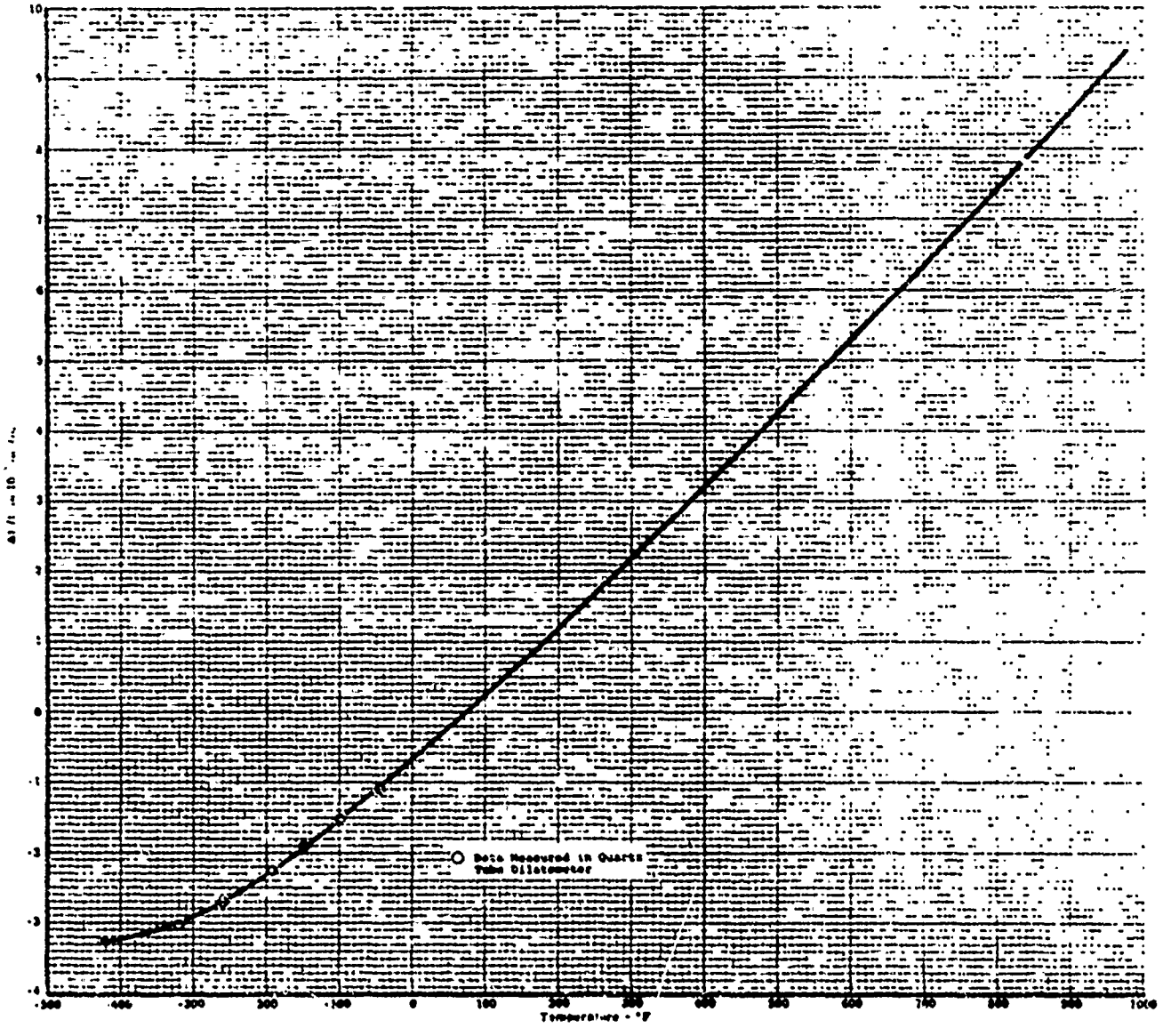


Figure C-3. Thermal Expansion of NBS Copper Standard SRM 736

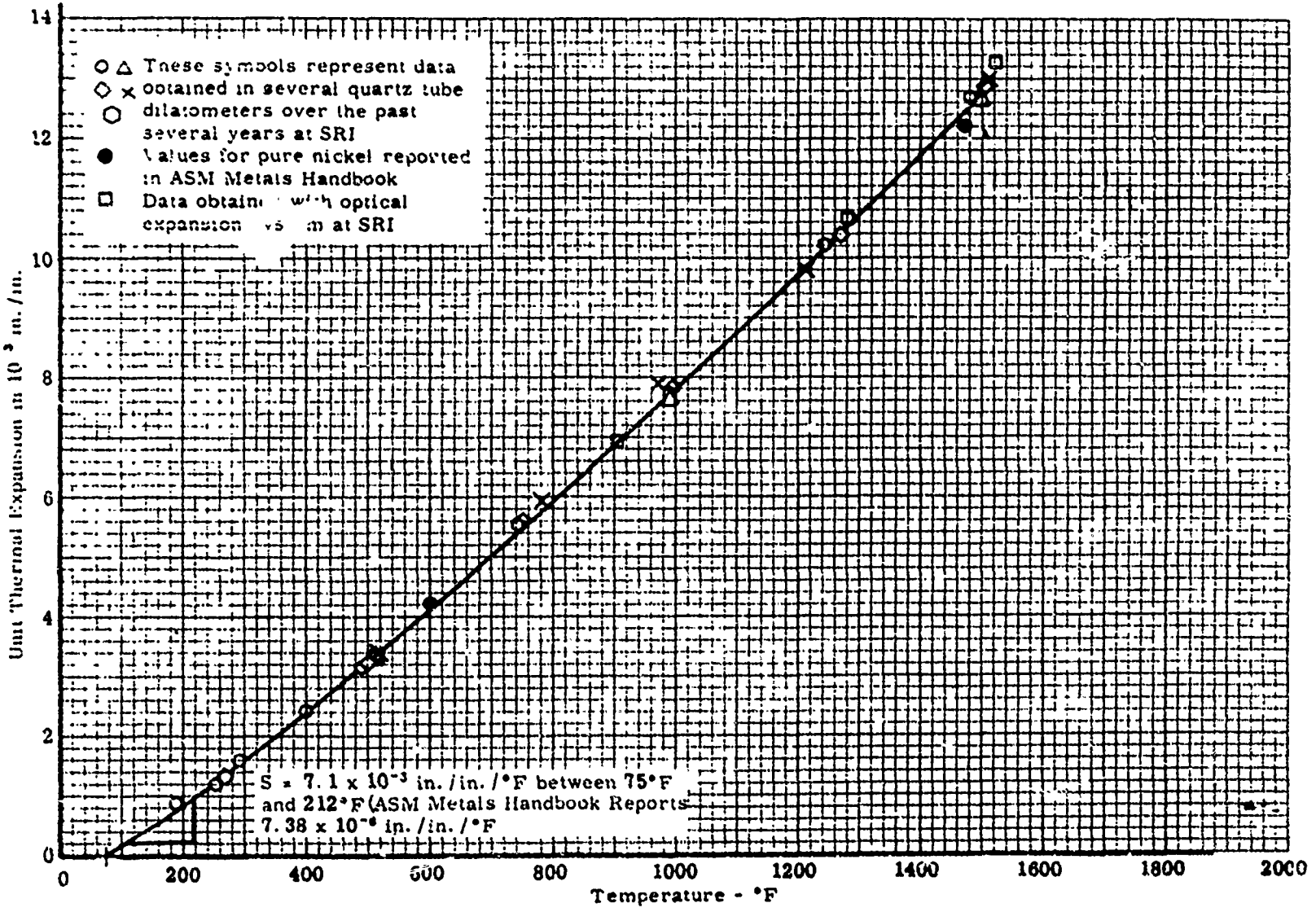


Figure C-4. Expansion of "A" Nickel (Calibration Standard Specimen)

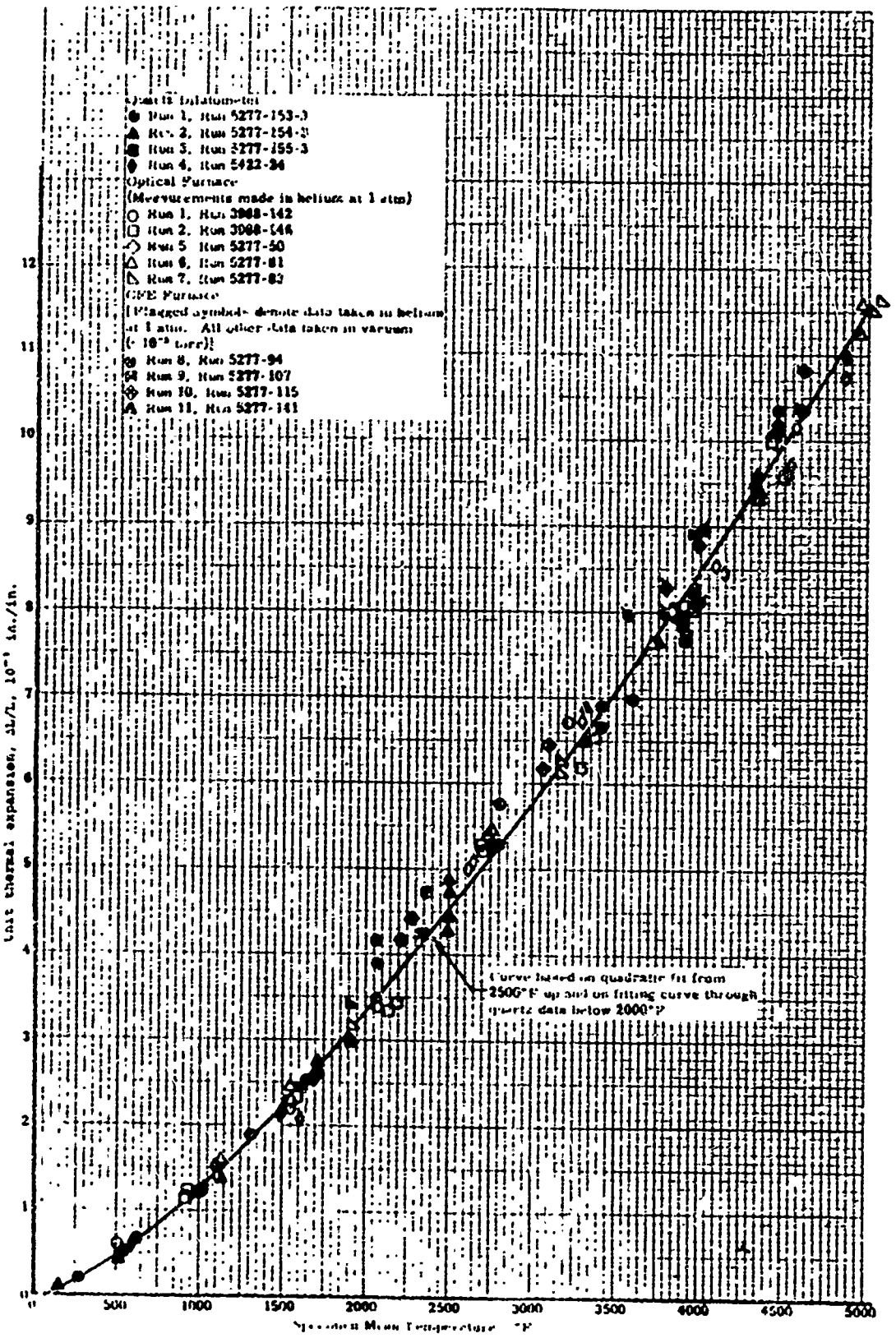


Figure C-5. Thermal Expansion of ATJ Graphite (WG) Standard No. 5 In-House Optical Calibration

APPENDIX D

THERMAL EXPANSION TO 5500°F

Thermal expansion is measured in a graphite tube dilatometer developed by Southern Research Institute for performance to 5500°F, see Figure D-1. The specimen required is about 1/2 inch diameter and 3 inches long, although the exact size can vary somewhat if it appears desirable from the standpoint of specimen availability. Specimens 3/4 inch in diameter and only 1/4 inch thick can be evaluated, but with a reduced precision. Discs can be stacked to provide more length in many cases. Of course, specimens can always be pinned together from smaller pieces to provide both length and columnar strength.

In the dilatometer, the specimen rests on the bottom of the cylinder with a graphite extension rod resting on the specimen to extend to the top of the cylinder. When required, tungsten pads are inserted at the ends of the specimens to eliminate graphite diffusion from the dilatometer parts into the specimen. This entire assembly is inserted into one of the 5000°F furnaces described in another brochure.

The motion of the specimen is measured by a dial gage attached to the upper end of the cylinder with the stylus bearing on the extension rod. The system accurately indicates total motions of 0.0001 inch or less than 0.00004 per inch of specimen.

Either a helium or an argon environment can be employed. Nitrogen has been used on occasion. The equipment will permit operation at hard vacuums, but this procedure is rarely used.

A CS graphite, which has a fairly low expansion relative to other grades of graphite, is used as the material for the dilatometer. Prior to calibrations, the dilatometers are heat soaked to a temperature several hundred degrees above the maximum temperature to which they would be exposed during normal service. Dimensional stability is confirmed by measuring the lengths of the dilatometer tube and rod after each run. Past experience has shown that following the initial heat soak the expansion is reproducible in subsequent repeated cycles to lower temperatures. Reproducibility is also confirmed by repeated runs on standards.

To calibrate the dilatometers we have developed in-house primary and secondary standards of ATJ graphite. ATJ graphite was selected as a standard because of our vast experience with it, its stability after repeated exposure to high temperatures, and its relatively low expansion.

The true expansion of the primary standard was determined by a direct optical technique using a traveling Gaertner telescope. The total error in the telescope readings, based on calibration data, was estimated to be 0.2×10^{-3} in./in. For the direct optical measurements, the 3.5 inch long specimen was heated in a graphite furnace, and the expansion was determined by sighting on "knife" edges machined on the ends of the specimen. Typically a total of 11 runs have been made in two different furnaces both in vacuum and helium environments. The two environments are used to check effects of refraction as reported in the literature. The same standard was then machined to the configuration of a regular dilatometer specimen and several runs were made in our precision quartz dilatometers. The optical expansion data were fitted to a quadratic equation over the temperature range from 2500°F to 5000°F using the method of least squares and statistically analyzed to determine the uncertainty (primarily the scatter). Below 2500°F, the quartz dilatometer data were fitted by hand since the uncertainty of this apparatus has been well established, and the imprecision is small ($<0.1 \times 10^{-3}$ in./in.). A typical plot of all data points with the curve fit is shown in Figure D-2.

A check of the expansion of the standard was obtained by making runs on round robin specimens of various graphites and synthetic sapphire which had been previously evaluated by others, including the National Bureau of Standards. Our data on these specimens agreed within a 2.5 percent random difference with the data reported by the other laboratories.

After establishing the expansion of the ATJ standard, several graphite dilatometers were then calibrated by making runs on this standard. These dilatometers were used to establish the expansion of secondary standards (also ATJ graphite) which are used to calibrate new dilatometers and to make periodic checks on dilatometers currently in service. This use of secondary standards thus minimizes the wear and tear on the primary standard and prolongs its life.

Table 1 lists the uncertainties in the dilatometer measurements in 10^{-3} in./in. Observe that most of the uncertainty is in the expansion of the standard and includes both random and systematic uncertainties. Other sources of uncertainty, resulting from such factors as dial gage and temperature measurement, are small amounting to less than 0.2×10^{-3} in./in. at any temperature. The precision in the dilatometer measurements is quite good and amounts to about 0.1×10^{-3} in./in. From Table 1, it can be seen that the maximum total uncertainty, which occurs at a temperature of 4500°F, is $\pm 0.45 \times 10^{-3}$ in./in. For a low expansion graphite, such as ATJ, this amounts to an uncertainty of ±4.5 percent at 4500°F (see Figure D-2). For graphites having higher expansions, the percentage uncertainty would be lower.

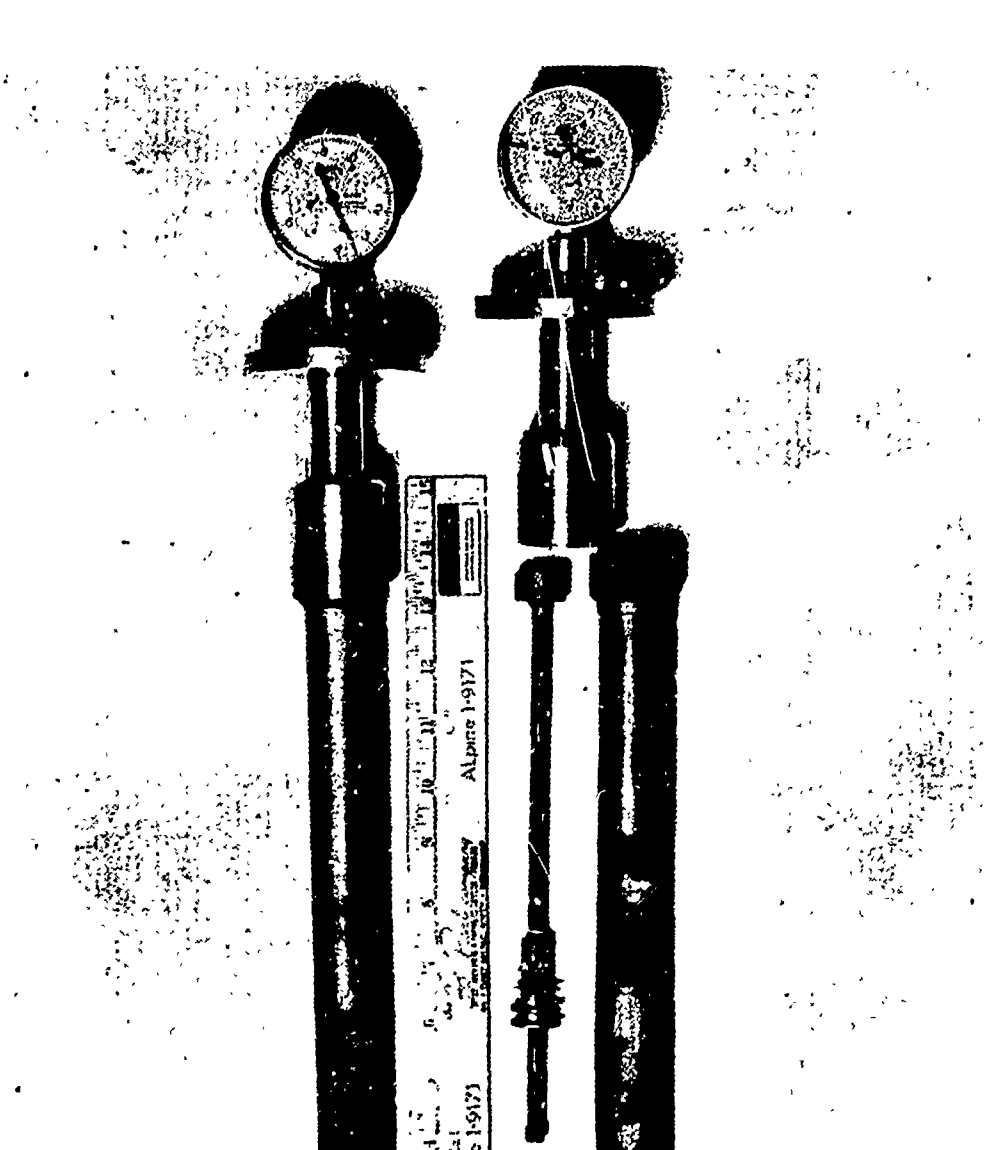


Figure D-1. Picture of the Graphite Dilatometer Tubes for Measuring Thermal Expansion to 5500°F

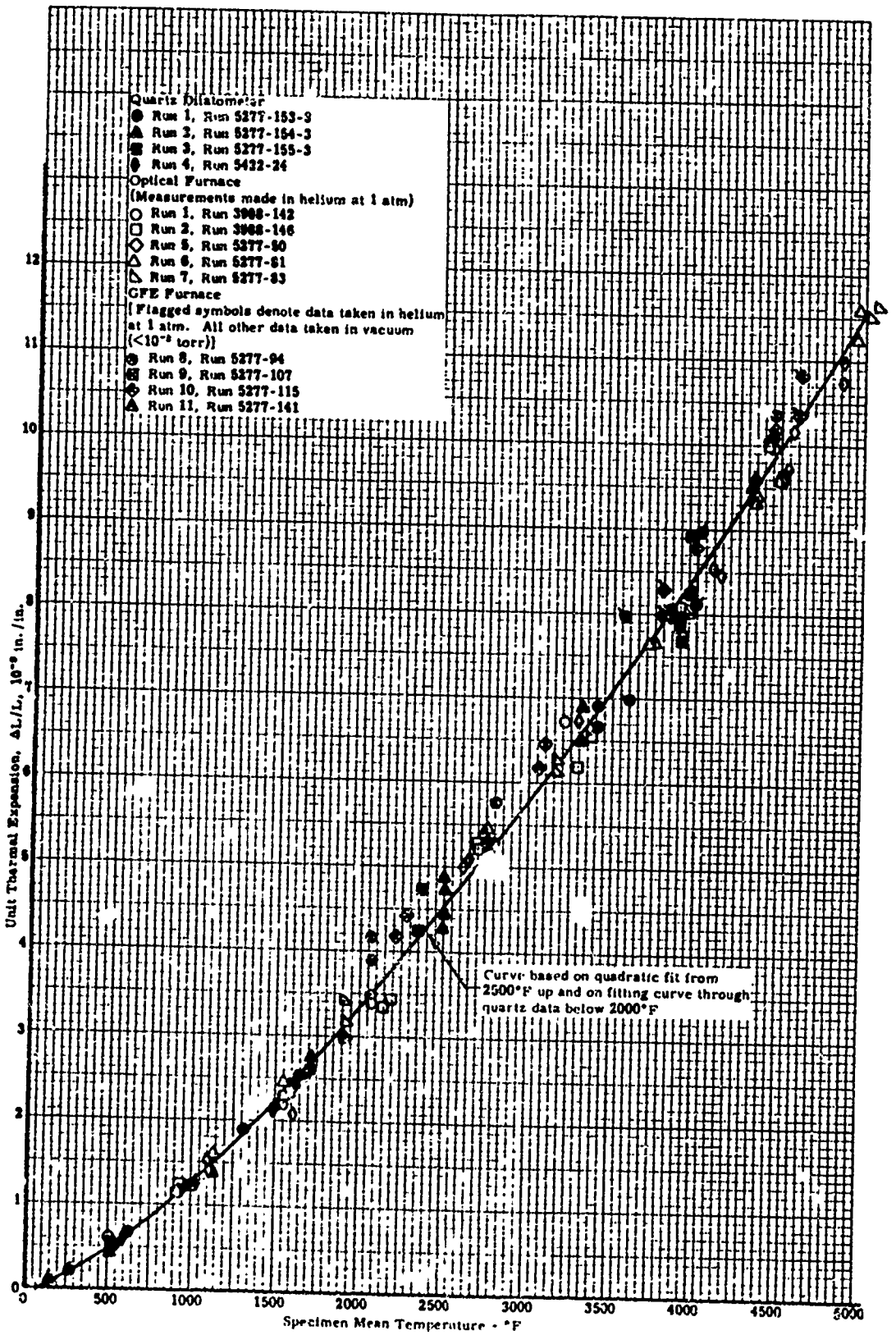


Figure D-2. The Thermal Expansion of AXF Graphite (wg) Standard No. 5 by In-House Optical Calibration

Table D-1

Uncertainty in Thermal Expansion Measurements
Made in Graphite Dilatometers

Temp °F	Uncertainty in Expansion of Standard in 10^{-3} in./in. Random Uncertainty (See Note 1)	Uncertainty in Expansion of Standard in 10^{-3} in./in. Systematic Uncertainty (See Note 2)	Random Uncertainty in Dilatometer Measurements in 10^{-3} in./in.	Total Uncertainty in Dilatometer Measurements from all Sources in 10^{-3} in./in. +	Total Uncertainty in Dilatometer Measurements from all Sources in 10^{-3} in./in. -
500	±0.04	0	±0.03	0.05	0.05
1000	±0.04	0	±0.03	0.05	0.05
1500	±0.05	0	±0.04	0.07	0.07
2000	±0.17	+0.03	±0.05	0.21	0.18
2500	±0.11	+0.20	±0.07	0.33	0.13
3000	±0.12	+0.21	±0.08	0.35	0.14
3500	±0.19	-0.02	±0.10	0.21	0.23
4000	±0.14	-0.09	±0.12	0.18	0.27
4500	±0.14	±0.25	±0.14	0.45	0.45
5000	±0.19	-0.12	±0.16	0.25	0.37

Notes:

1. 95% confidence limits.

2. Represents deviation between average measured value and least squares curve through all data.

APPENDIX E

THERMAL CONDUCTIVITY TO 1000°F

Apparatus and Procedure

Thermal conductivity runs can be made with any of the three guarded hot plate apparatuses which are slightly modified from the standard ASTM C177-45 design. All three are identical in operating procedure and design except in size and are classified as either the 14-inch, 7-inch, or 3-inch apparatus depending on the diameter of the specimen used. Actually the diameters for the 7-inch and 3-inch apparatuses are 7-3/8 inches and 3-1/4 inches, respectively. Specimen thicknesses are from from 1/8 inch to 3 inches and duplicate specimens are required per run. Figure E-1 is a schematic of a typical assembly used for all three apparatuses.

The apparatus consists of a central heater plate surrounded by a guard heater, each separately controlled. The guard ring is maintained at the same temperature as the central heater so that all of the heat flow is normal to the specimen surfaces. The temperature differences between the guard and central sections are measured by means of differential-thermocouple junctions connected in series. The 14-inch and 7-inch apparatuses contain eight differential junctions, whereas the 3-inch apparatus contains four. The heater plate is sandwiched between layers of filler material, the hot-face thermocouples, the specimen, cold-face thermocouples, filler material, a copper plate, and finally a cold source to dissipate the heat. The cold source consists of a copper coil enclosed in an aluminum box on the 14-inch apparatus, a copper coil soldered to a copper plate on the 7-inch apparatus, and a spiral baffled copper container on the 3-inch apparatus. In addition to the thermocouples in contact with the specimen, thermocouples are located in the central heater and the outer copper cold plates.

To provide intimate contact at all interfaces, the entire sandwich assembly is pressed firmly together by spring loading with the total load application desired, which is usually 600 pounds.

Normally for the determinations between -50°F to 150°F, a filler material of gum rubber is used. From 150°F to 1000°F Fiberfrax paper is used as a filler. The overlapping data at 150°F provides a check on any possible uncertainty due to poor intimate contact resulting from either specimen or filler surface irregularities. If the data agree within approximately 5 percent, the run is continued; however, if the agreement is not within 5 percent, the thermocouples are replaced, the specimen is removed, surfaces are resanded, and the run is repeated.

The thermocouples used on the hot and cold side of the specimen are made from 0.005-inch diameter chromel-alumel wire electrically insulated with 0.003-inch Teflon tape. The junction is made by soldering the wires to a small square of 0.002-inch thick brass shim stock called a "getter". The Teflon insulated leads are sandwiched between the specimen and filler material to ensure isothermal conditions along the length of the wire. This arrangement ensures that there is no air film between the specimen and the thermocouples and that good intimate contact exists at all interfaces.

Single thermocouples in the center of the heater plate and cold plate monitor the temperatures of the heater and cold plates in order to obtain the overall temperature drop through the assembly.

The assembly is arranged to operate with the specimen placed in the apparatus horizontally as shown in Figure E-1. The specimen required are flat panels sized to fit the apparatus. The assembly is insulated around the edges by either Fiberfrax or glass wool batt.

A constant voltage transformer is used in conjunction with variable voltage transformers to ensure a constant power supply at each setting. The central heater and guard heater are controlled individually by the variable voltage transformers. The voltage and current to the central heater are monitored by means of a voltmeter and an ammeter which are switched out of the circuit except when actually being read. The voltage to the guard heater is monitored constantly by a voltmeter.

All of the thermocouple readings are taken on a Leeds and Northrup K-3 potentiometer in conjunction with a galvanometer of 0.43 microvolts per mm deflection sensitivity.

To obtain mean sample temperatures above room temperature, water is circulated through the cooling section. For mean sample temperatures below room temperature, cold trichloroethylene is pumped through the cooling section. This coolant is chilled by circulating it through copper coils in a trichloroethylene dry-ice bath. Equilibrium conditions are certified before readings are taken.

Coefficients of thermal conductivity are calculated from the expression:

$$k_s = \frac{Ql_s}{A\Delta t}$$

Q = total heat flow - Btu/hr

l_s = average thickness of specimens - inches

A = area of central heater section - square feet

Δt = sum of temperature drop across each sample - °F

Theoretically, Q, the heat input, should split, with exactly half of the input flowing through each sample. The temperature drops indicate that this condition rarely exists. Instead, there is a slight unbalance in the heat flow. The above formula then permits a calculation of the arithmetic average for the two panels. In this calculation the temperatures are measured directly at the faces of the specimen by the "getters," resulting in a "direct" method.

As a check, the thermal conductivity is calculated for the specimen with a "series-resistance" or "composite" expression. This method utilizes the same run data, except that the temperature difference between the heater plate and the cold plate is utilized and, since the resistance of the filler is measured separately in the same apparatus, the following series-resistance equation can be used to determine the thermal conductivity of the specimen:

$$k_s = \frac{l_s}{(l_T/k_T) - (l_F/k_F)} \qquad (2)$$

l_s = thickness of the specimen - inches

k_s = thermal conductivity of the specimen - Btu in./hr ft^2°F

(l_T/k_T) = thermal resistance of the total composite of filler and specimen, calculated from the temperature difference between the hot and cold plate

(l_F/k_F) = thermal resistance of the filler alone, determined under the same conditions that exist for (l_T/k_T)

The (l_F/k_F) term for the gum rubber filler is determined both with and without copper plates inserted between the rubber pads to simulate interface resistance that is present during the evaluation of the specimen.

Improvement and Calibrations on the ASTM C177-5 Technique

The ASTM C177-45 guarded hot plate apparatus is only recommended for determining values below 5 Btu in./hr $ft^2°F$. Due to the higher conductivities of many of the new reinforced plastics such as the phenolic graphites and carbons, considerable work was necessary before the above procedures were incorporated, which provides accurate data between 5 and 10 Btu in./hr $ft^2°F$. The following is a resume of the work and analysis performed which extended the range to 10 Btu in./hr $ft^2°F$.

It was decided at the beginning of the investigation that data from -50°F to 150°F would be determined using a filler of gum rubber and determining the conductivity of the specimen by both "direct" measurement of the temperature drop across the specimen and a "series-resistance" or "composite" method, as explained. From 150°F to the maximum temperature, the data would be obtained by using an asbestos filler and determining the conductivity by a "direct" calculation from the measured face temperatures of the specimen. Both methods were used at the 150°F to determine if any uncertainty existed due to poor intimate contact resulting from either specimen or filler surface irregularities.

Considerable deviation of approximately 20 percent to 30 percent occurred between the values obtained for the "composite" method and the "direct" method for the higher conductivity materials. The evaluations with Plexiglas and Pyrex at that time indicated the following (see Table 1):

1. The "composite" method, when calibrated with pyrex and Plexiglas, exhibited somewhat high values of 8 Btu in./hr $ft^2°F$ at 150°F and 11.23 Btu in./hr $ft^2°F$ at 150°F, respectively. The major difficulty was the great scatter between different data.

2. The "direct" method, when calibrated with pyrex, was in error by exhibiting values averaging about 20 percent low. However, the Plexiglas calibration indicated excellent agreement.

The above results indicated that the conductivity data for values above 5 Btu in./hr $ft^2°F$ should be determined using the composite method, with the direct method employed for the lower values. However, the composite method is much too critical under certain conditions, and data scatter was as high as 30 percent. By considering equation 2 in close detail, it was found that normal experimental error in determining (l_F/k_F) can result in a magnified error of k_s if (l_F/k_F) is critically close to (l_T/k_T). With certain conditions,

an error of 3 percent in (l_F/k_F) can result in a 10 percent to 50 percent error in k_s. Therefore, it was mandatory that the direct method be improved for use over the entire range of values, and that the composite be used onlv as a check.

It was determined that a majority of the errors obtained with the direct method was due to the lack of intimate contact at the interfaces of the specimens when the load and fillers were improperly selected. This error was magnified (even percentagewise) when the conductivities were about 5 Btu in./hr ft^2°F. In order to obtain intimate contact at the interfaces, proper selection of compaction load and filler material for each test material is required. An extensive evaluation was performed on the effect of measured conductivity of increased compaction loading using either no filler material or fillers of gum rubber, Fiberfrax, or asbestos. The specimens used in this evaluation were Plexiglas, Pyrex, and other plastic materials, which represented a range of conditions including different surface finish, flatness, flexibility, and conductivity. Table E-1 presents the calibration data obtained for Pyrex and Plexiglas in the 3-inch and 7-inch diameters and 14-inch square ASTM C177-45 guarded hot plate apparatuses.

Under the normal compaction load of approximately 600 pounds, the 3-inch diameter apparatus provided reliable data for Plexiglas using either filler or no filler, and for Pyrex using the filler only. Under the normal load, the 14-inch apparatus provided accurate data for Plexiglas; however, the values were occasionally low on the Pyrex using the direct method of calculation. The 7-inch diameter apparatus provided data about 8 percent low for Pyrex under normal load with a gum rubber filler. For Plexiglas, the 7-inch diameter apparatus provided accurate data under normal compaction loads with no filler and gum rubber of Fiberfrax filler; however, the data were 7 percent low using an asbestos filler. Subsequent work indicated that the 7-inch apparatus was somewhat erratic, so the heater was rebuilt and the agreement with standard improved even more to within about 5 percent, although the trend remained similar. Such extensive data were not reobtained.

Under varying load, the 7-inch diameter apparatus with gum rubber filler provided values for Pyrex that increased 7.5 percent as the load was increased from 100 pounds to 600 pounds and only increased 3 percent more from 600 pounds to 4000 pounds. The excessively high compaction pressures provided values on Plexiglas with a gum rubber filler that were not orderly and were noticeably higher than reported in the literature for this material regardless of the technique.

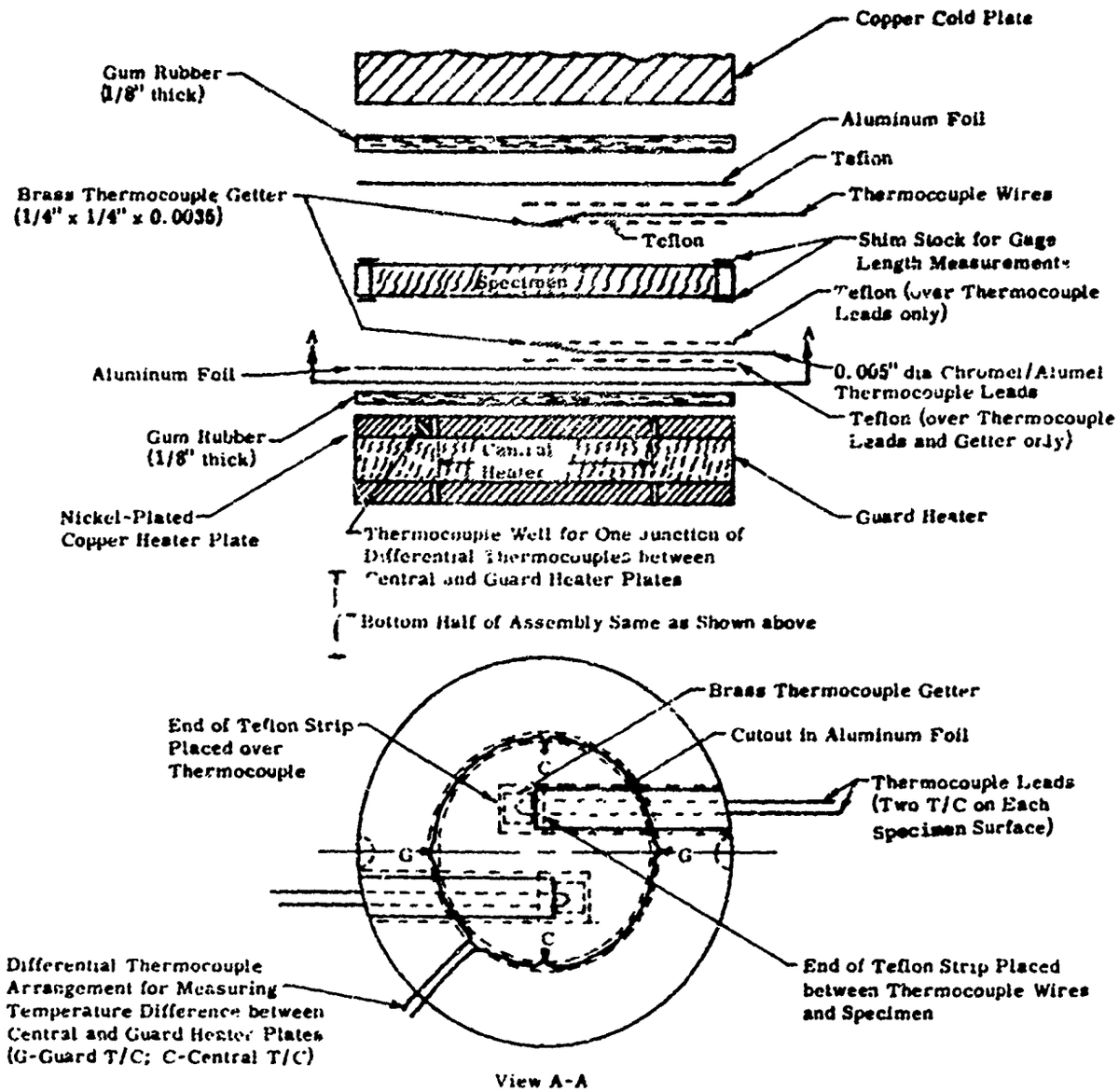
The data obtained with increasing load on the other plastic materials (not standards) demonstrated in most cases that an increase in compaction load from the normal 600 pounds did not increase the values insignificantly but did introduce unorderly changes. It was apparent, therefore, that excessively high loadings were neither required nor desirable. As a matter of fact, the bonds between the resin and reinforcement on some materials could be influenced, thermally, by such high pressures. Further, stress fields are created and data obtained here have indicated an influence of stress on the conductivity of the structures involved for a material such as Plexiglas. The mechanism is probably one of the induced alignment of the chains.

The major requirements was to provide intimate thermal contact on all faces, which could be done by the proper selection of compaction load and filler, depending on the properties of the particular specimen. The actual load on the sandwich was more important than the pressure since it is the load and not the pressure that best correlates with flattening a curved plate or specimen. For example, it requires more load to flatten a 7-inch plate than it does a 14-inch plate. So, if the same pressure were maintained on the two apparatuses, the lower compaction force on the smaller one would not flatten the bow. The pressure would be important in providing deformations, locally, of the filler and/or specimen where a low or high spot may exist; however, the data on Plexiglas and Pyrex with rubber and Fiberfrax, particularly, clearly demonstrated that small compaction loads were sufficient to provide enough pressure to deform the filler into local areas. The compaction load needed was not as excessive as had been suggested in some literature in which the pressure was considered of major importance. An indication of the importance of the load-filler combination rather than pressure was apparent from the data, which provided higher conductivities on the 7-inch rig with the rubber filler and 600 pound load than on the same rig with no filler at 3000 pound load. Higher conductivities were obtained with the lower pressure by substituting the proper combination of load-filler.

From the above, it has been decided that the higher thermal conductivity materials can be evaluated accurately by the direct measurement method using a filler if the flat surfaces are held flat, and the compaction loads are held at a nominal level sufficient to provide intimate contact at the interfaces. The amount of loading depends on the flatness, the flexibility of the specimen, and the type of filler used. For very rigid materials like Pyrex, it is doubtful if enough pressure could be applied when run without filler without breaking the specimen. No one technique is adequate for the determination of the conductivity of all specimens over the full temperature range. Careful judgement is required by the investigator in each case to select the compaction load, the filler (or no filler), the heat flow level, and to evaluate the condition of the apparatus.

The above analysis led to the modifications and improvements which have been made on the ASTM apparatuses beyond those normally employed to assure better accuracy of the data. The screw loading device on the 14-inch apparatus has been modified to incorporate spring loading at the center and edge clamps to ensure more uniform loading, and thus provide flatter surfaces and more intimate contact. The edges are monitored with 1-mil pullout tabs to ensure that no gaps existed in the plates. The thermocouple wires are more carefully placed along the isothermal surface of the specimen. The Fiberfrax paper has been adopted as a high temperature filler, since it conformed to any irregularities on the surface exceptionally well allowing the placement of the small thermocouple wires, electrically insulated with 0.003-inch Teflon tape, without disrupting the intimate contact required. It has also been noted that decreasing the heat level, and thus the temperature difference, across the specimen provides less deviation at the 150°F overlap temperature. The minimum heat flow level depends on the conductivity of the material and cannot be defined at a given temperature drop. The random deviation between values on the same specimen as evaluated with rubber filler from -50°F to 150°F, and with Fiberfrax filler from 150°F to 1000°F, has been reduced to a maximum of about 5 percent. Past experience has shown that the Fiberfrax filler provides slightly higher data on 30 percent of the runs and slightly lower data on the remaining runs at the change-over temperature (from one filler to the other) at about 150°F.

Table E-1 presents the many calibrations performed on the apparatuses for both before and after the above improvements were incorporated.



Notes:

1. Buildup shown is used up to 150°F.
2. Above 150°F, gum rubber on hot surface of specimen is replaced by two Fiberfrax discs each 1/8 inch thick and a Fiberfrax disc of the same thickness is placed between the gum rubber and the specimen on the cold surface.
3. At elevated temperatures, an asbestos disc can be placed between the gum rubber and Fiberfrax at the cold surfaces to control temperature drop across the specimen.

Figure E-1. Schematic of Buildup Used for ASTM C177 Guarded Hot Plate Thermal Conductivity Apparatus

TABLE I

CALIBRATIONS OF ALTH C177 APPARATUSES AND PROCEDURES WITH PLEXIGLAS AND PYREX 7740 STANDARDS AT ABOUT 150°F TO 200°F (DIRECT METHOD UNLESS OTHERWISE NOTED)

Apparatus	Plexiglas Thermal Conductivity Btu in./hr ft² °F	Pyrex Thermal Conductivity Btu in./hr ft² °F
14 in. rig with asbestos or rubber filler, composite method and 600 pounds	1.33 to 1.39	7.1 to 8.9
14 in. rig with asbestos filler and 600 pounds	1.17 to 1.20	5.96
14 in. rig and rubber filler and 600 pounds	1.19 to 1.22 to 1.30	7.35 to 7.39
14 in. rig with Fiberfrax filler and 600 pounds after improvements made	1.34	7.64 to 7.83
7 in. diameter rig with rubber filler and compaction of:		
100 pounds	1.25	-7.36
600 pounds	1.26 to 1.09 with Q	0%, 7.74
1000 pounds	1.25	0%
3000 pounds	-	+2.0%
4000 pounds	1.14 to 1.33 with Q	+2.1%
7 in. diameter rig with asbestos filler and compaction of:		
100 pounds	-	
600 pounds	1.11 to 1.17	5.0
1000 pounds	1.11	
3000 pounds	-	
4000 pounds	1.16	
7 in. diameter rig with no filler with compaction loads of:		
100 pounds	1.12	
600 pounds	1.21	4.0
1000 pounds	1.23	
3000 pounds	1.27	
4000 pounds	1.29	
7 in. diameter rig with Fiberfrax and 600 pounds after improvements made	1.14	7.13 to 8.1
3 in. diameter rig with rubber filler and 600 pounds	1.17	7.34 to 7.6
3 in. diameter rig with Fiberfrax filler and 600 pounds	1.15, 1.18, 1.19, 1.41 to 1.19	7.4 to 7.6
3 in. diameter rig with asbestos filler and 600 pounds	1.16, 1.16, 1.16	7.28
3 in. diameter rig without filler and 600 pounds	1.18 to 1.19	6.79 to 6.79

1. Literature and previous work reports the thermal conductivity of Plexiglas to be 1.19.

2. Literature reports the thermal conductivity of 7740 Pyrex to be from 7.1 to 8.1 at about 200°F by Knapp, American Ceramic Society, 1942, and the NBS, respectively. The NBS data are by the series resistance or composite technique. Prior values by the NBS using direct method were about 7.4 to 7.6.

3. Thicknesses of specimens vary with investigator.

APPENDIX F

THERMAL CONDUCTIVITY TO 5500°F BY RADIAL INFLOW METHOD

The thermal conductivity is determined with a radial heat inflow apparatus that utilizes a central specimen 1 inch long. This apparatus is normally employed for measurements over the temperature range from 1500°F to 5500°F. Comparative rod apparatus is used at temperatures below 1500°F where radiant heating is less effective. The radial inflow apparatus gives a direct measurement of the thermal conductivity rather than a measurement relative to some standard reference material. A picture of the apparatus ready to be installed in the furnace is shown in Figure F-1. The furnace and associated equipment for the therman conductivity work is shown in Figure F-2. In addition to the specimen, the apparatus consists primarily of (1) a water calorimeter that passes axially through the center of the specimen, (2) guards made from the same specimen material at both ends of the specimens to reduce axial heat losses, (3) sight tubes that allow the temperature at selected points in the specimen to be determined either by thermocouples or optical pyrometer and (4) an external radiant heat source (see Figure F-3). The water calorimeter provides a heat sink at the center of the specimen to create a substantial heat flow through the specimen and allows the absolute value of the heat flow to be determined. Thermocouples mounted 1/2 inch apart in the calorimeter water stream measure the temperature rise of the water as it passes through the gage portion of the specimen. By metering the water flow through the calorimeter, it is possible to calculate the total radial heat flow through the 1/2-inch gage section of the specimen from the standard relationship $Q = MC\Delta T$. M is the weight of water flowing per hour, C is the specific heat of water and ΔT is the temperature rise of the water as it passes through the gage section.

The standard specimen configuration is shown in Figure F-4. The specimen is 1.062 inches O.D. x 0.250 inch I.D. x 1 inch long. Holes 0.073 inch in diameter are drilled on radii of 0.233 and 0.437 inch to permit measurement of the radial temperature gradient. In specimens which are anisotropic in the diametral plane (for example, certain graphites), a second pair of holes is drilled 90° to the first pair. The diameters joining each pair of holes is located to coincide with the principal planes of anisotropy in the material.

A 1/2 inch long upper guard and a 1/2 inch long lower guard of specimen material are placed above and below the 1 inch long specimen to maintain a constant radial temperature gradient throughout the entire specimen length and thereby prevent axial heat flow in the specimen. The outer ends of the specimen guards are insulated with graphite tubes filled with thermatomic carbon. These tubes also hold the specimen in alignment. The combined effect of specimen guards and thermatomic carbon insulation permits a minimum axial temperature gradient within the specimen. This gradient is not detectable by optical pyrometer readings. Visual inspection of the specimens after runs have verified that no large axial temperature gradient exists in the specimen. The guards, made of specimen material, display axial distortion of the isothermal lines for approximately 1/4 inch from the outer ends before reaching an apparent constant axial temperature.

When sufficient material is available, the alternate specimen configuration shown in Figure F-5 is employed. This specimen, being 1.5 inches in diameter, provides a larger gage length (0.357 inch) between temperature wells and allows the installation of three holes on each radius without excessively distorting the radial temperature profiles. Thus this specimen configuration permits a more precise measurement of the average temperature at each radial location. As with the smaller specimen, the location of the temperature wells must be altered for transversely anisotropic specimens.

The annulus between the specimen inside diameter and the 7/32 inch outside diameter of the calorimeter tube is packed with either copper granules, graphite or zirconia powder. This packing provides a positive method for centering the calorimeter within the specimen and promotes good heat transfer between specimen and calorimeter.

Temperatures up to 2000°F are measured with chromel alumel thermocouples inserted into the specimen through the sight tubes. At high temperatures, the temperatures are measured through the vertical sight tubes using a right-angle mirror device and optical pyrometer.

In Figures F-1 and F-3 showing a typical conductivity calorimeter apparatus ready for insertion into a furnace for a run, a water-cooled copper section can be seen at the top of the unit. This section provides permanent sight

tubes to within about 2-1/2 inches of the guard specimen, in addition to the permanent mount for the right-angle mirror device used with the optical pyrometer. Within the short zone between the water-cooled section and the top guard, thin-walled graphite sight tubes are fitted. The remainder of the annulus is filled with thermatomic carbon insulation.

During thermal conductivity runs, the following data are recorded: (1) power input, (2) specimen face termperature, (3) specimen temperatures in the gage section at the two radii, (4) temperature of the calorimeter water at two points 1/2 inch apart axially within the specimen center and (5) water flow rate through the calorimeter. At least five readings are made at each general temperature range to determine the normal data scatter and to minimize the error that might be encountered in a single reading.

All thermocouple readings are measured on a Leeds and Northrup K-3 null balance potentiometer used in conjunction with a galvanometer of 0.43 microvolt per mm deflection sensitivity. All optically measured temperatures are read with a Leeds and Northrup Type 8622 optical pyrometer. The flow rate of the calorimeter water is measured with a Fischer and Porter Stabl-Vis Flowrater.

The thermal conductivity values are computed from the relation

$$K = \frac{Q \ln \frac{r_2}{r_1}}{2\pi L \, (T_{r_2} - T_{r_1})}$$

where

Q = the heat flow to and measured by the calorimeter

r_2 = the radius to the outer temperature well

r_1 = the radius to the inner temperature well

T_{r_2} = temperature at r

T_{r_1} = temperature at r

L = the gage length over which the calorimeter ΔT is measured, for our present calorimeter is 1/2 inch

Based on an extensive error analysis and calibrations on homogeneous isotropic materials of known thermal conductivities, such as Armco iron and tungsten, the precision (coefficient of variation) in the measurements has been established at ±7 percent over the temperature range. For multiple runs on samples having similar properties, the uncertainty in a smooth curve through the data can be established to within ±7 percent. A detailed error analysis has been presented in a paper by Mann and Pears.[1]

Data obtained here on several high-temperature materials are presented in Figures F-6, F-7, and F-8. Figure F-6 is a plot of data obtained here on tungsten. The specimen for these determinations were fabricated from stacks of 0.060-inch washers cut from hot rolled sheet stock. Also plotted are values reported by other investigators including "recommended values" given by Powell, Ho and Liley[2] based on a compilation of 103 sets of data. Agreement of the recommended values is excellent throughout the temperature range.

Figure F-7 shows data obtained here on ATJ graphite, with grain. This material is premium grade, medium grain graphite having a density range of 1.73 to 1.78 gm/cm^3. The crosses (+) shown in the figure are "recommended values" given by Ho, Powell and Liley.[3] Again agreement is excellent.

Figure F-8 shows data obtained on AXM-5Q1. These data were obtained under a program sponsored by the Air Force Materials Laboratory to develop high temperature thermal conductivity standards. Measurements were made on this material by four laboratories in addition to Southern Research Institute. The bands shown in Figure 31 represent the range of data reported by the other participating organizations. A complete presentation and discussion of the data are given in AFML-TR-69-2.[4]

---

[1]Mann, W. H. Jr., and C. D. Pears, A Radial Heat Flow Method for Measurement of Thermal Conductivity to 5200°F, presented at the Conference on Thermal Conductivity Methods, Battelle Memorial Institute, October 26-28, 1961.

[2]Powell, R. W., C. Y. Ho and P. E. Liley, Thermal Conductivity of Selected Materials, NSRDS-NBS 8, National Standard Reference Data Series - National Bureau of Standards - 8, 1966, pp. 11, 54-59.

[3]Ho, C. Y., R. W. Powell and P. E. Liley, Thermal Conductivity of Selected Materials, Part 2, NSRDS-NBS 16 National Standard Reference Data Series - National Bureau of Standards - 16, pp. 89-128.

[4]Little, Arthur D., Inc., AFML-TR-69-2, Development of High Temperature Thermal Conductivity Standards, Under Contract AF33(615)-2874, 1969, pp. 115-127.

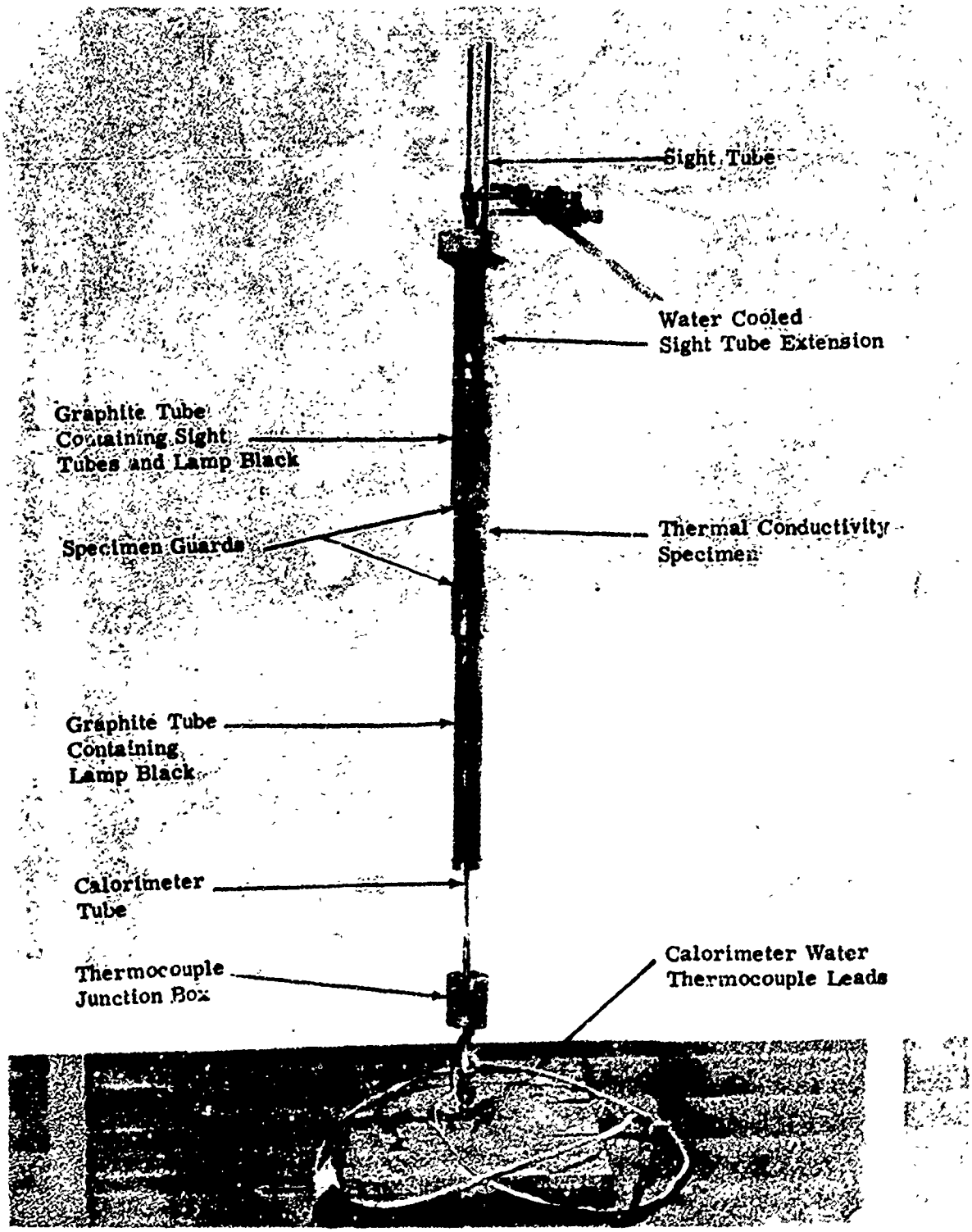


Figure F-1. Picture of the Radial thermal Conductivity Apparatus

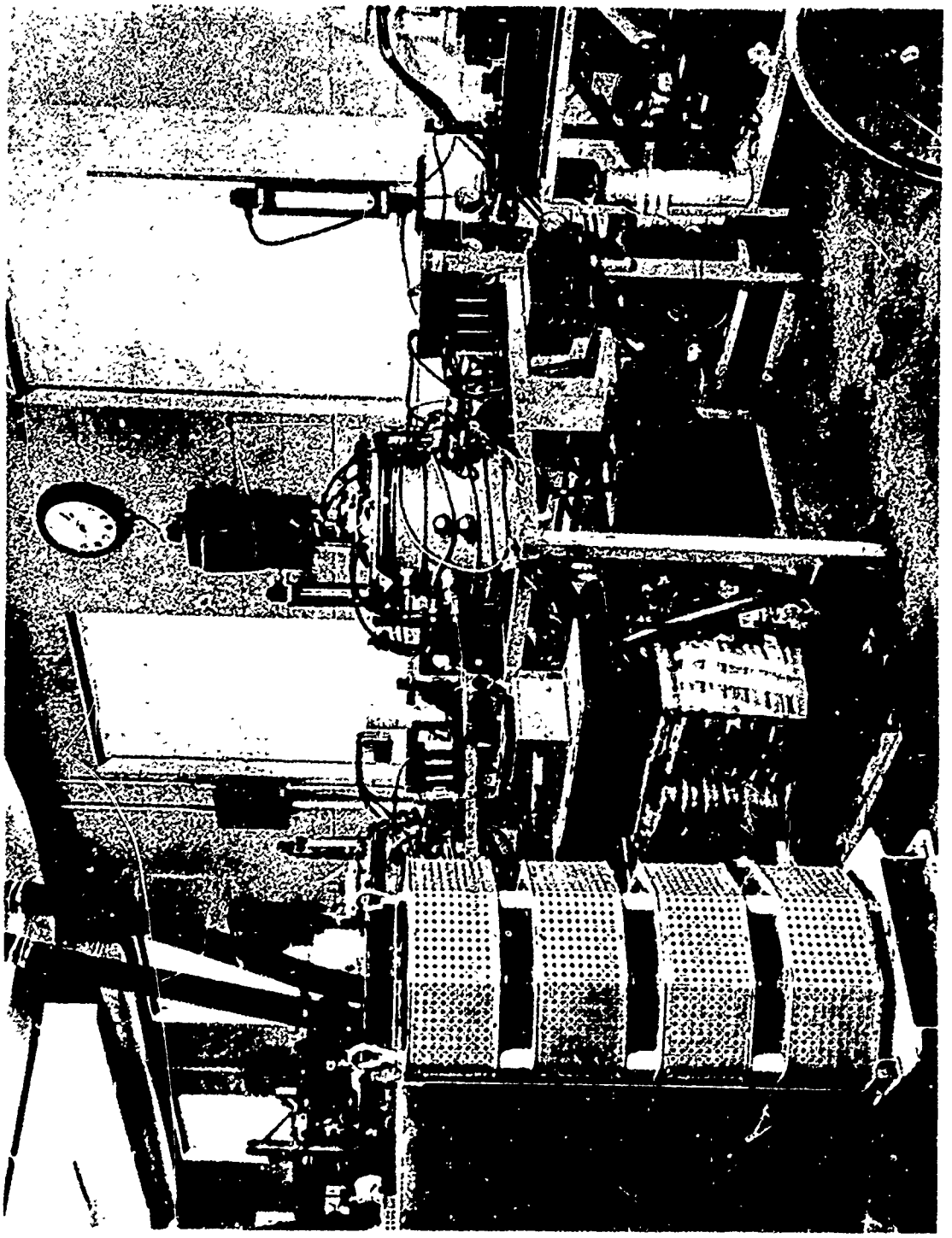


Figure F-2. Furnace with Thermal Conductivity Apparatus Installed

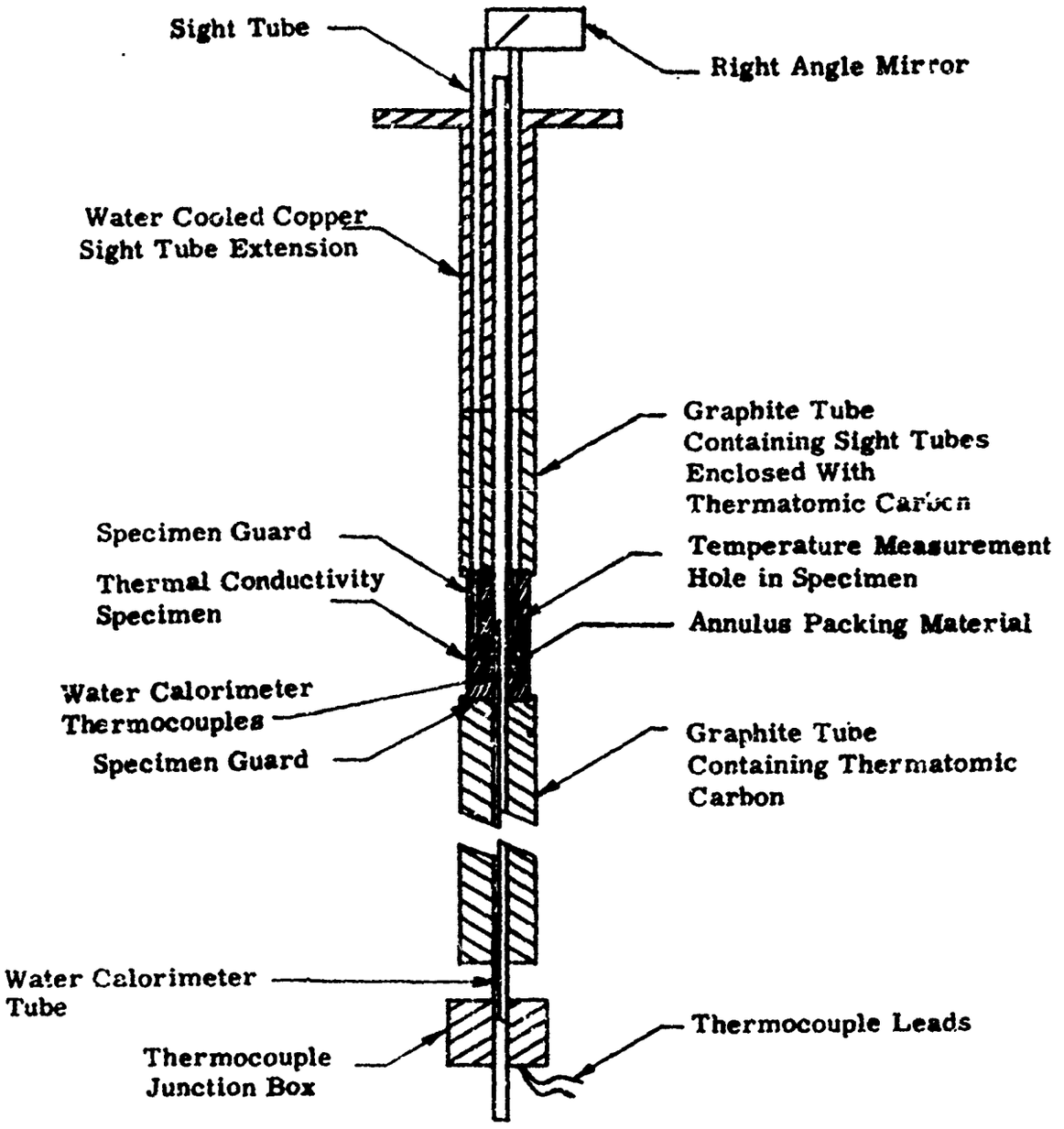


Figure F-3. Cross-section Schematic of the Thermal Conductivity Apparatus

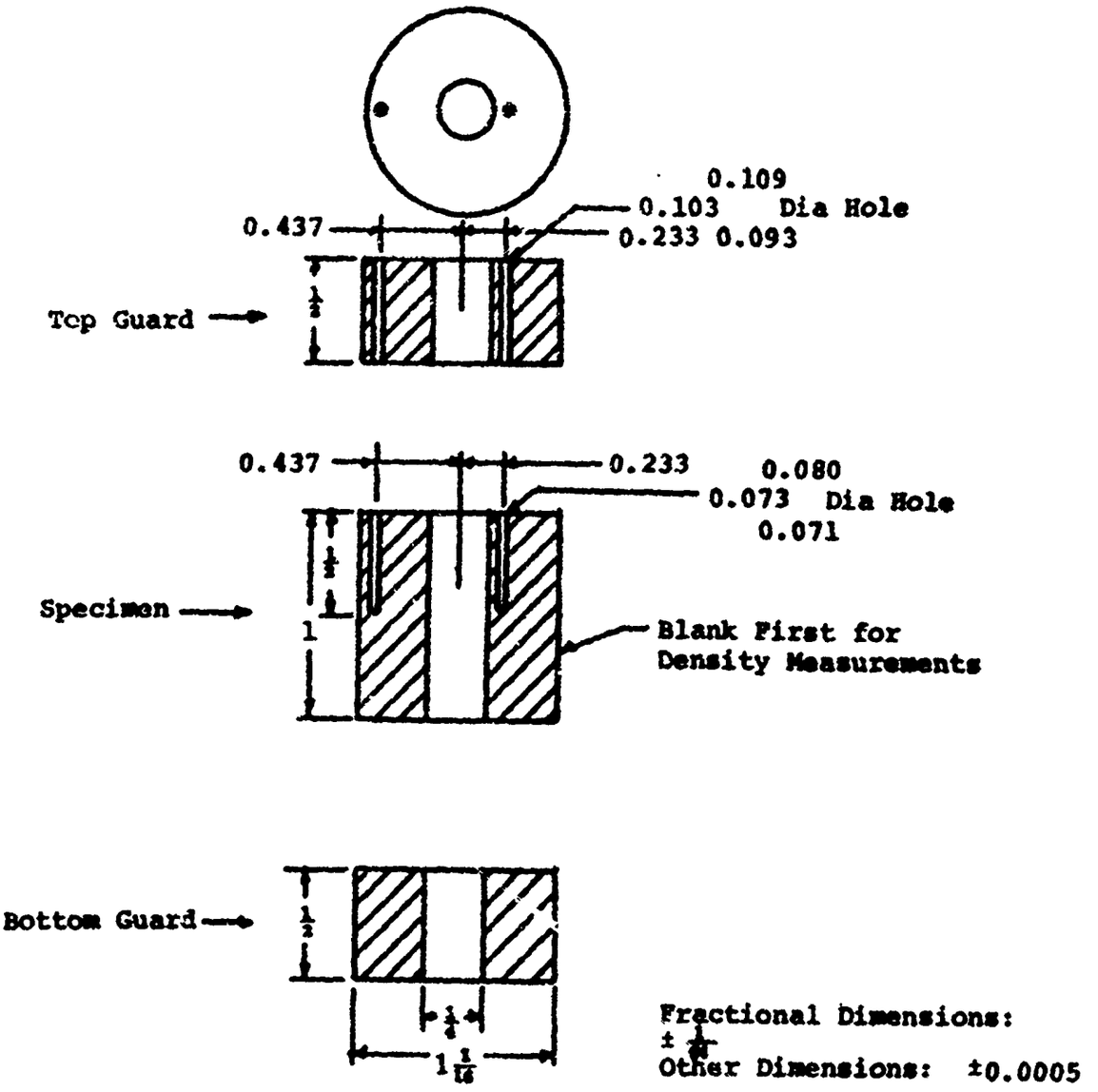


Figure F-4. 1.06-inch Diameter Thermal Conductivity Specimen for Radial inflow Apparatus

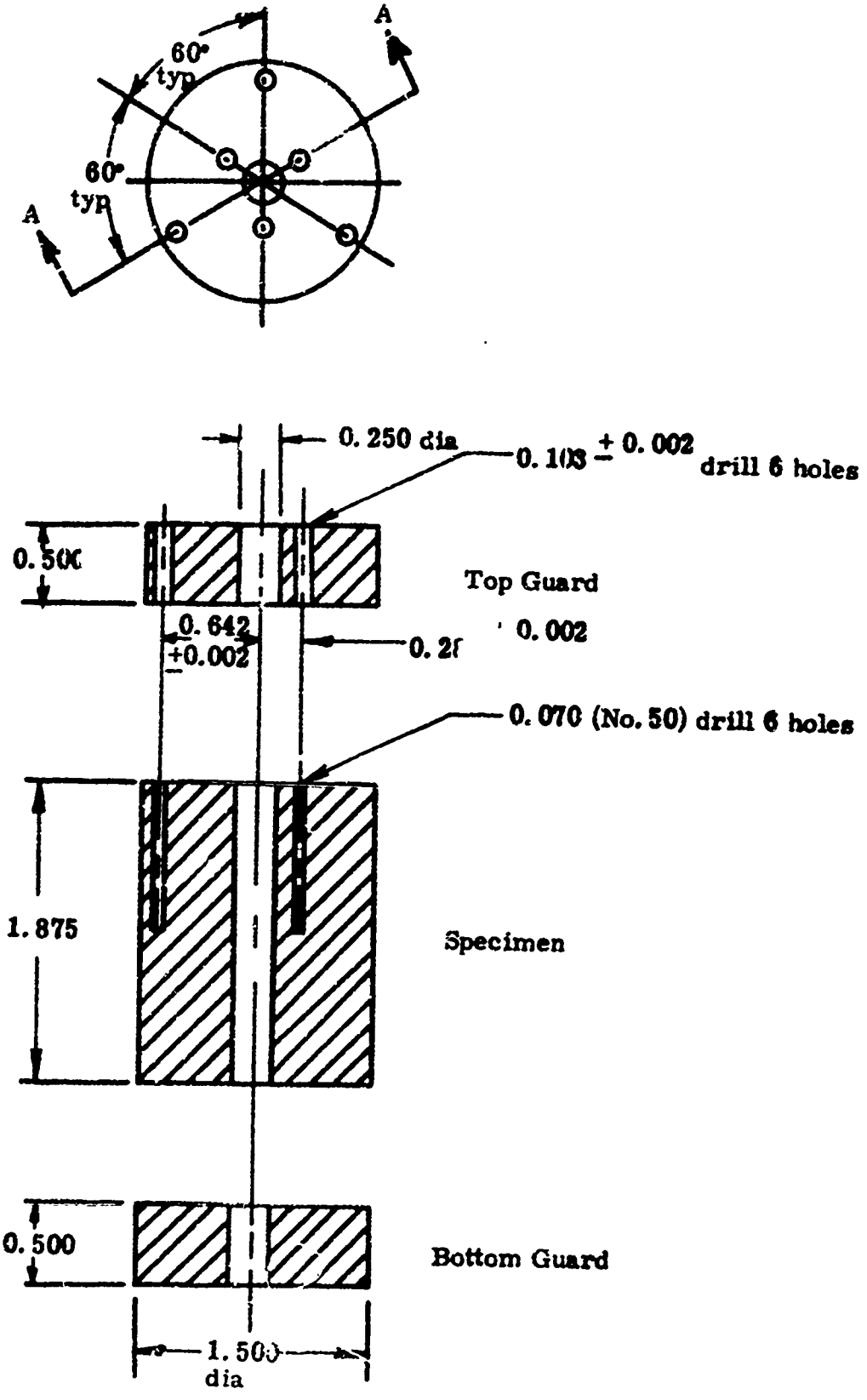


Figure F-5. Dimensions of 1.50 Inch Diameter Specimen and Guards Used for Radial Inflow Thermal Conductivity Measurements

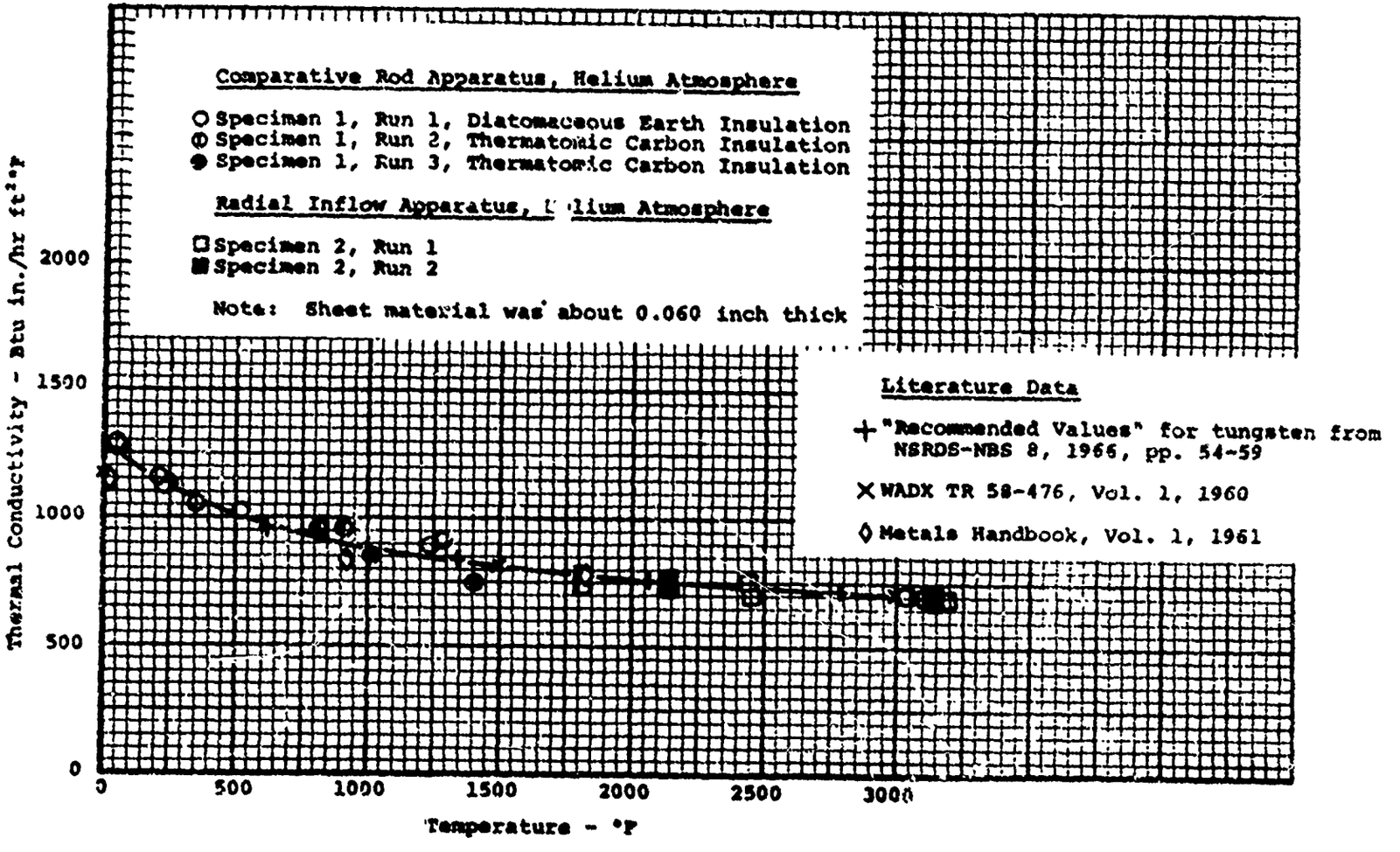


Figure F-6. Thermal Conductivity of Tungsten Sheet Parallel to the Plane of the Sheet

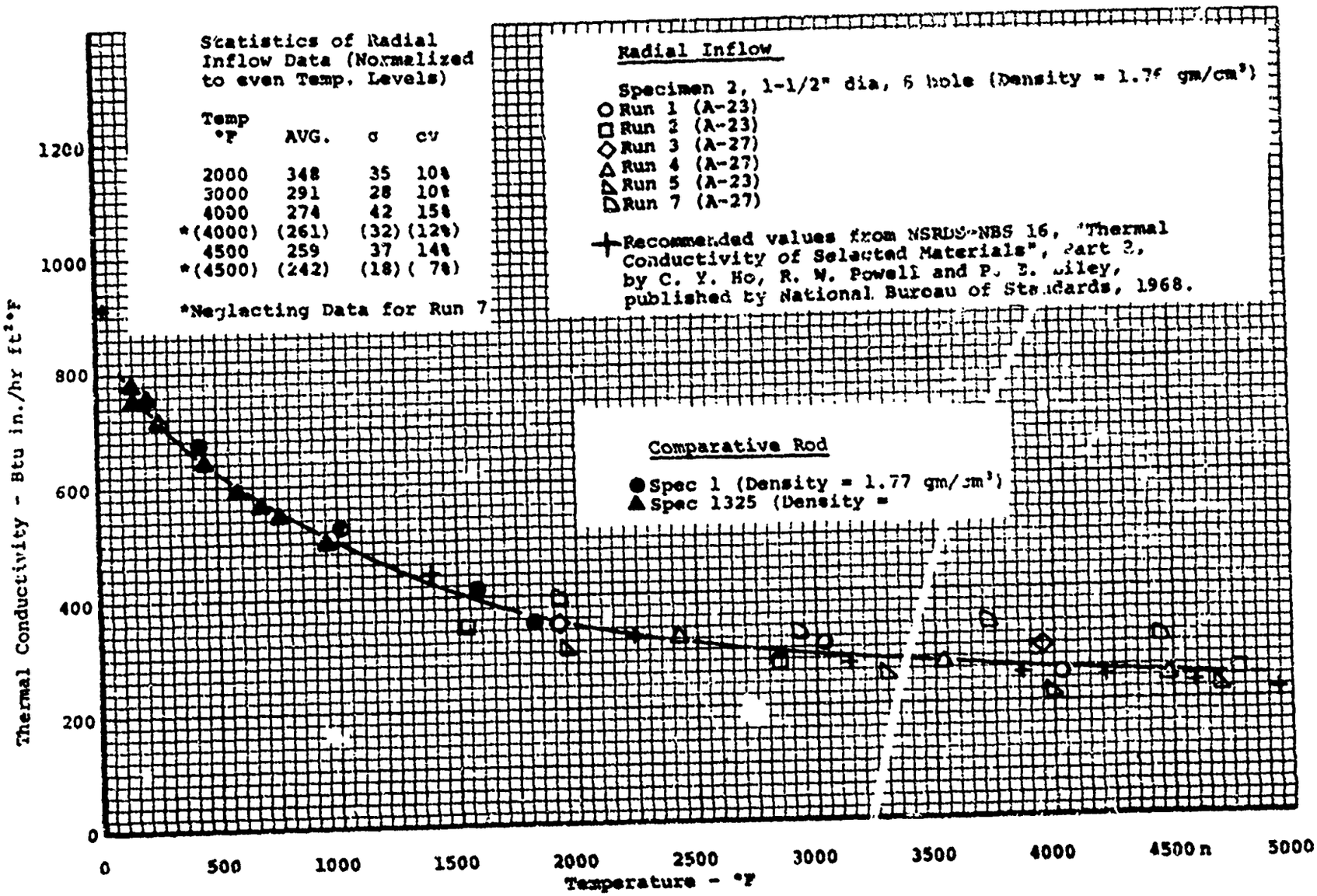


Figure F-7. Thermal Conductivity of ATJ Graphite, With Grain

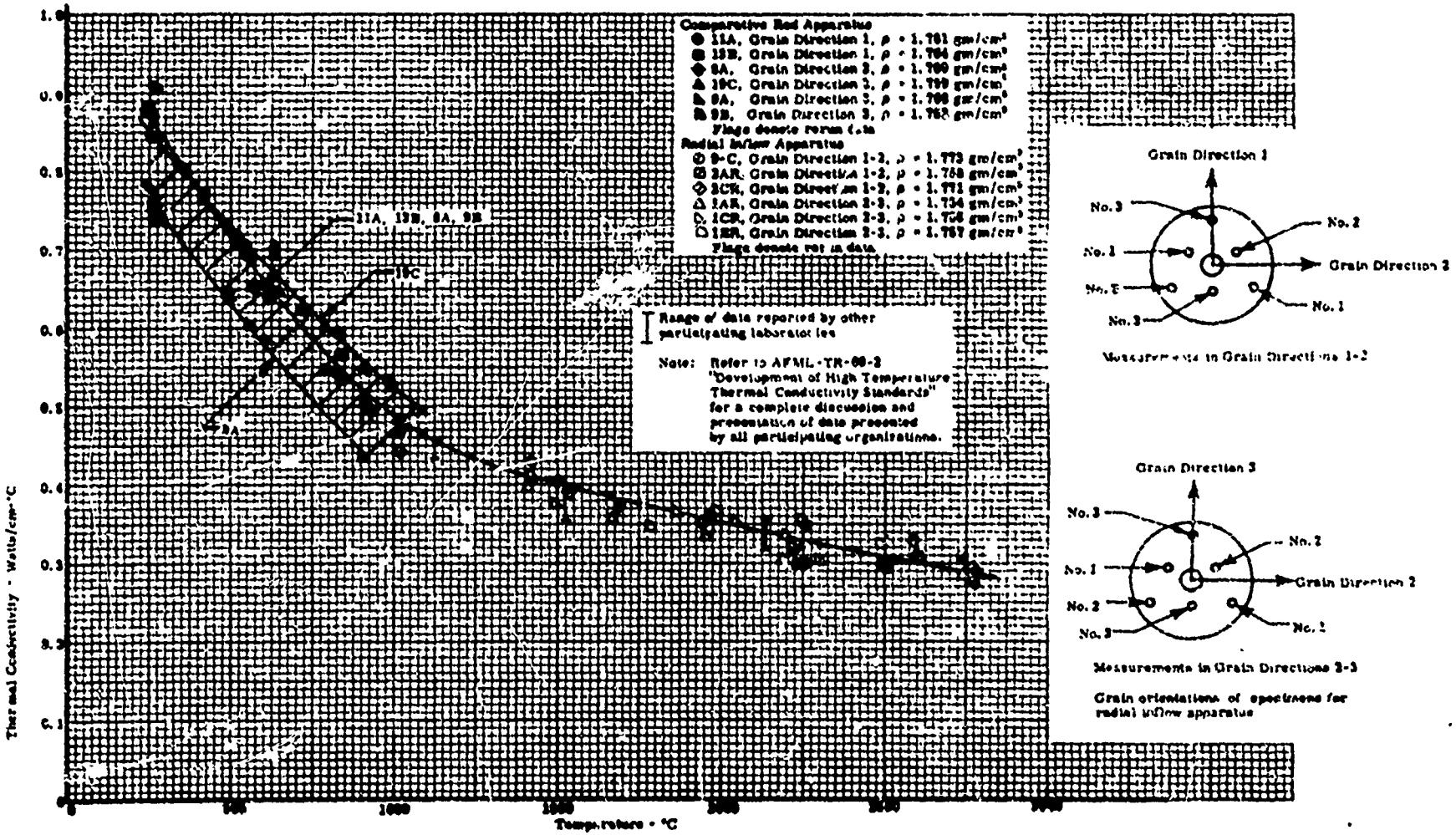
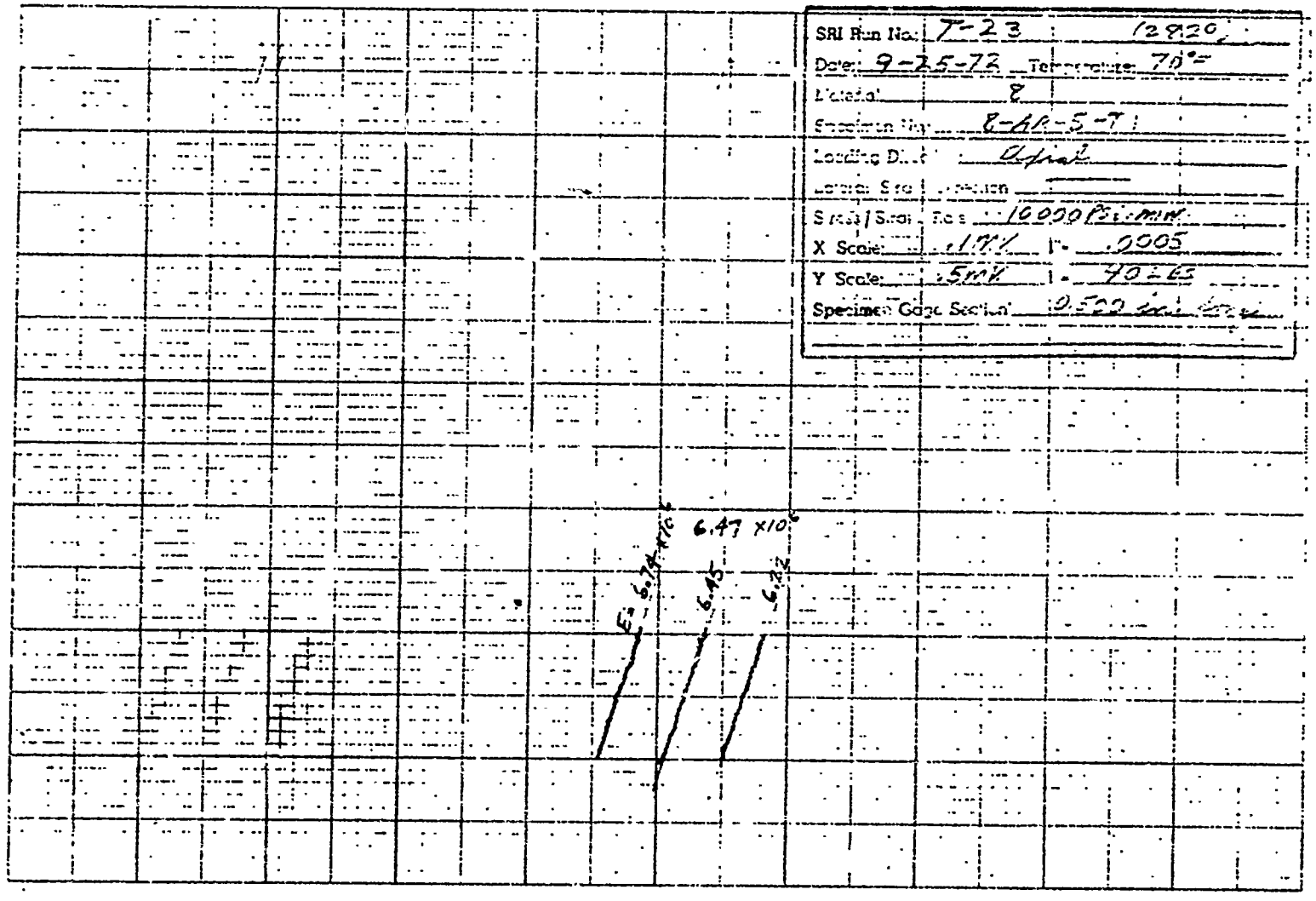
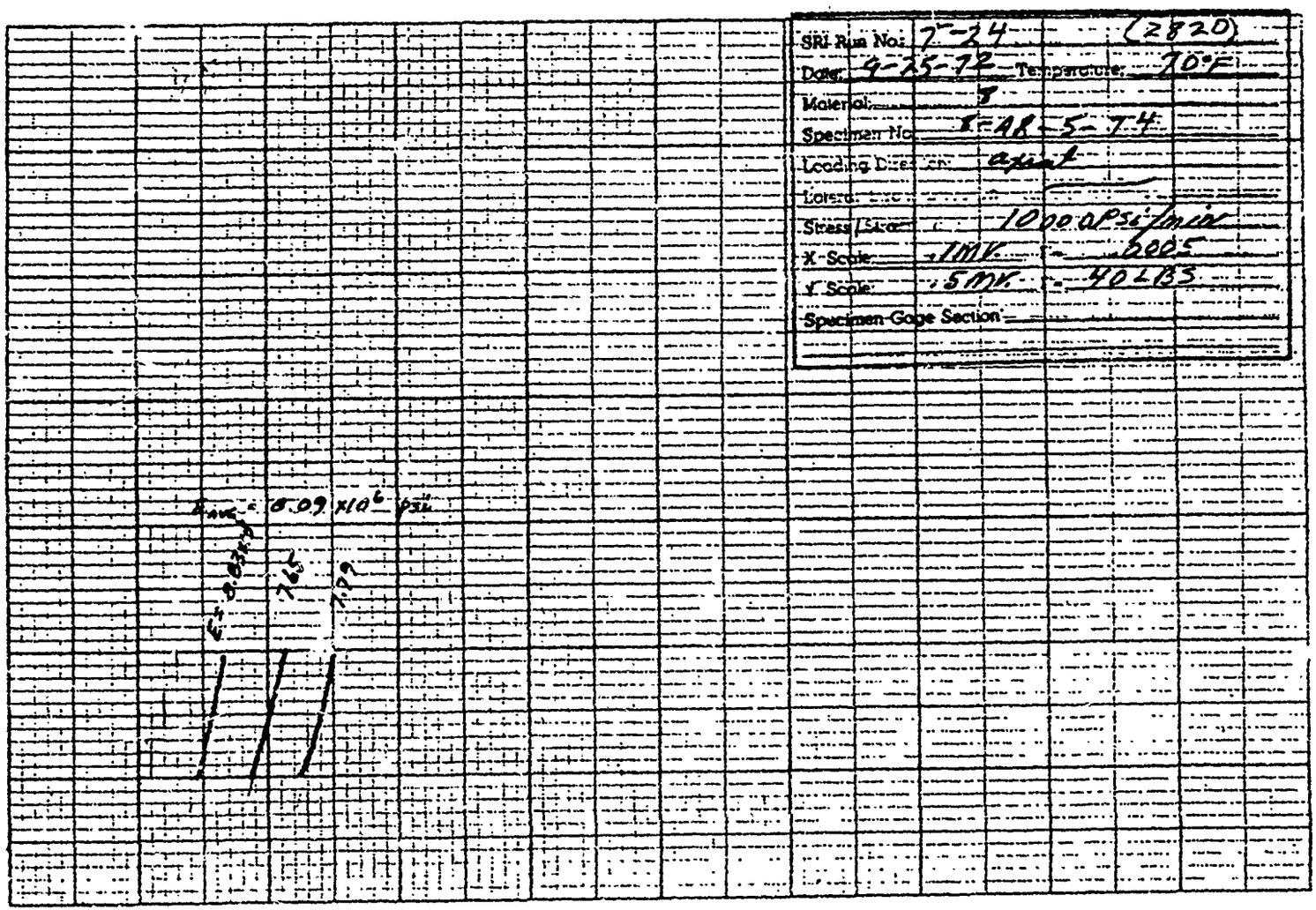


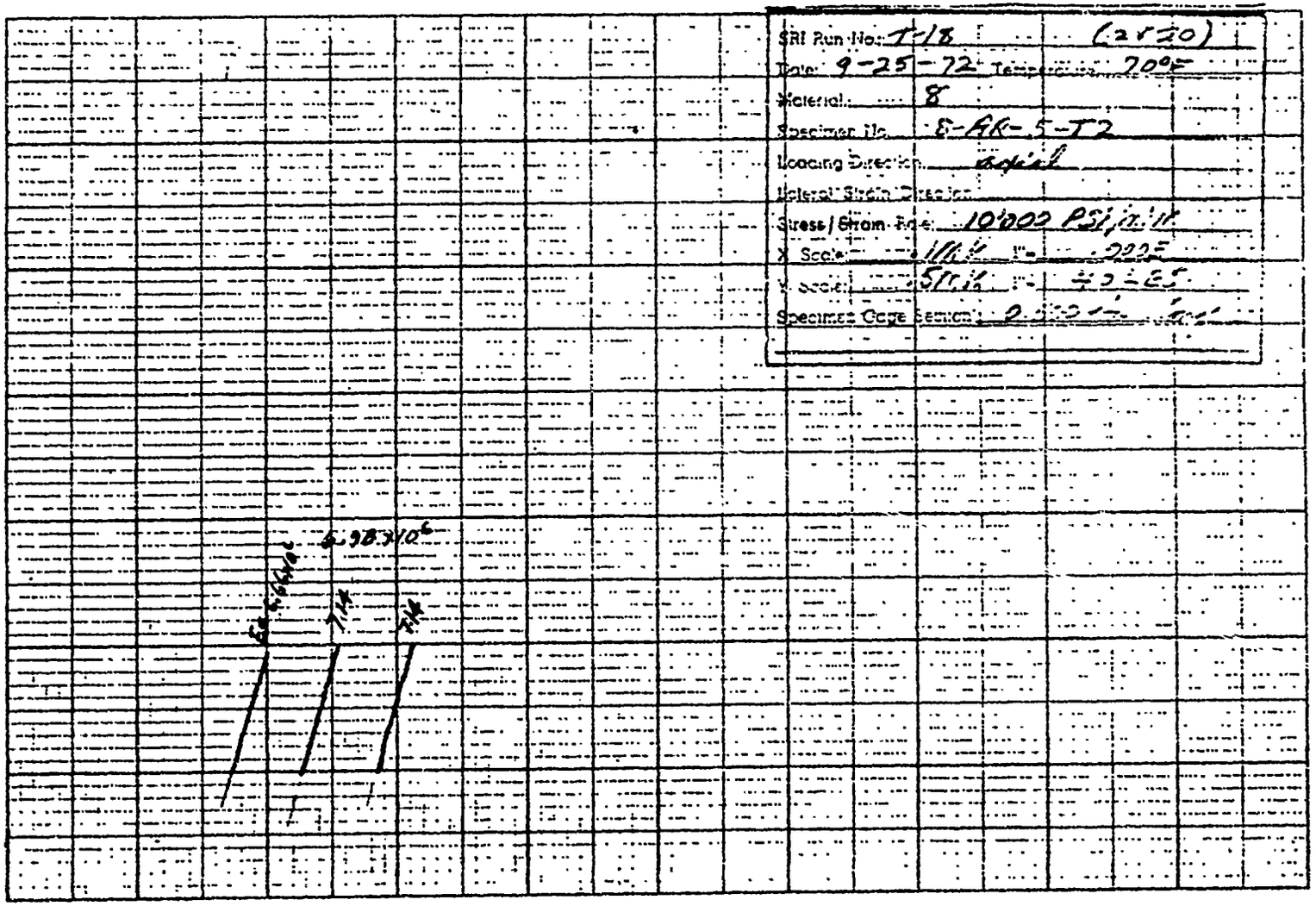
Figure F-8. Thermal Conductivity of AXM-5QI Graphite

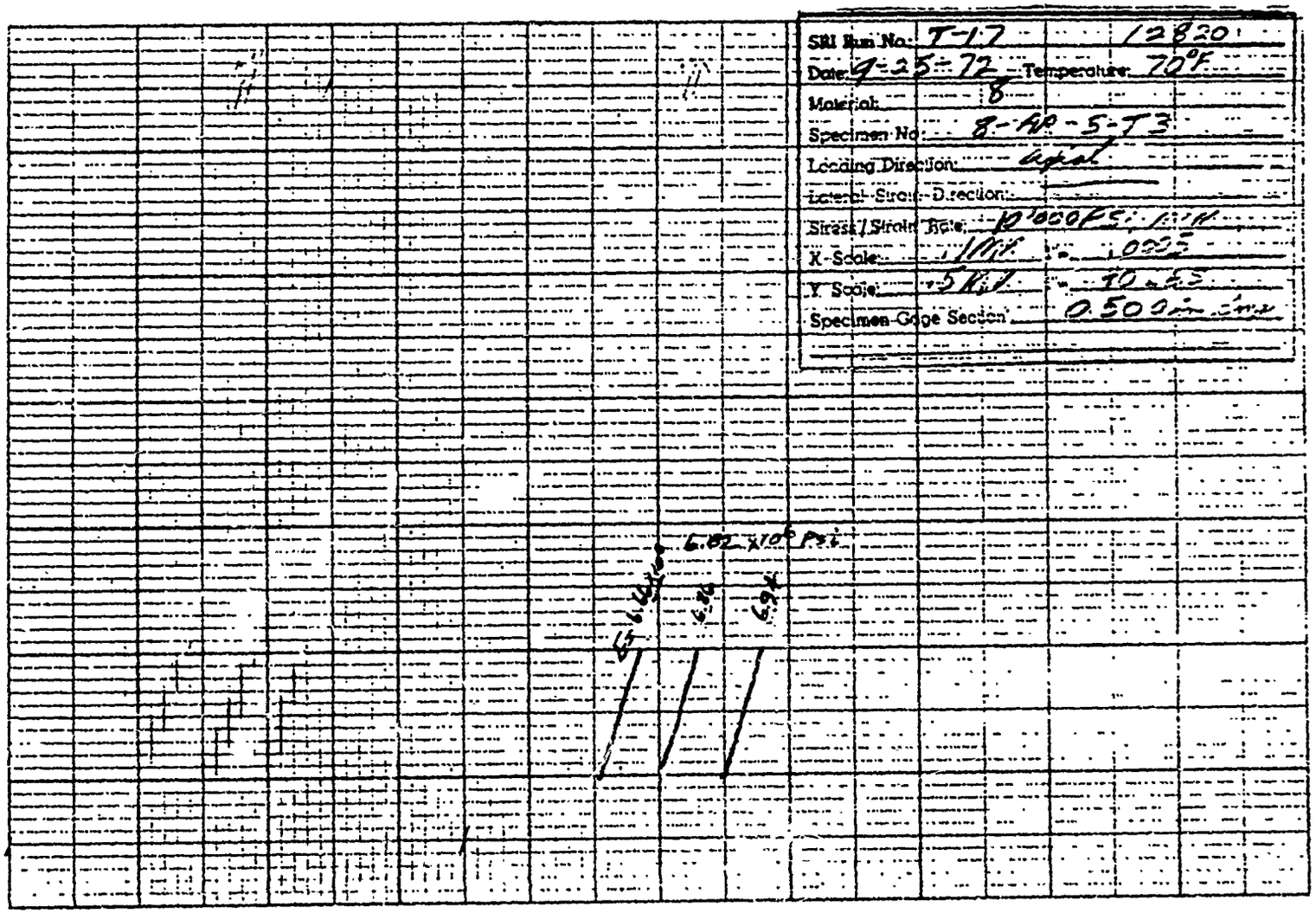
APPENDIX C

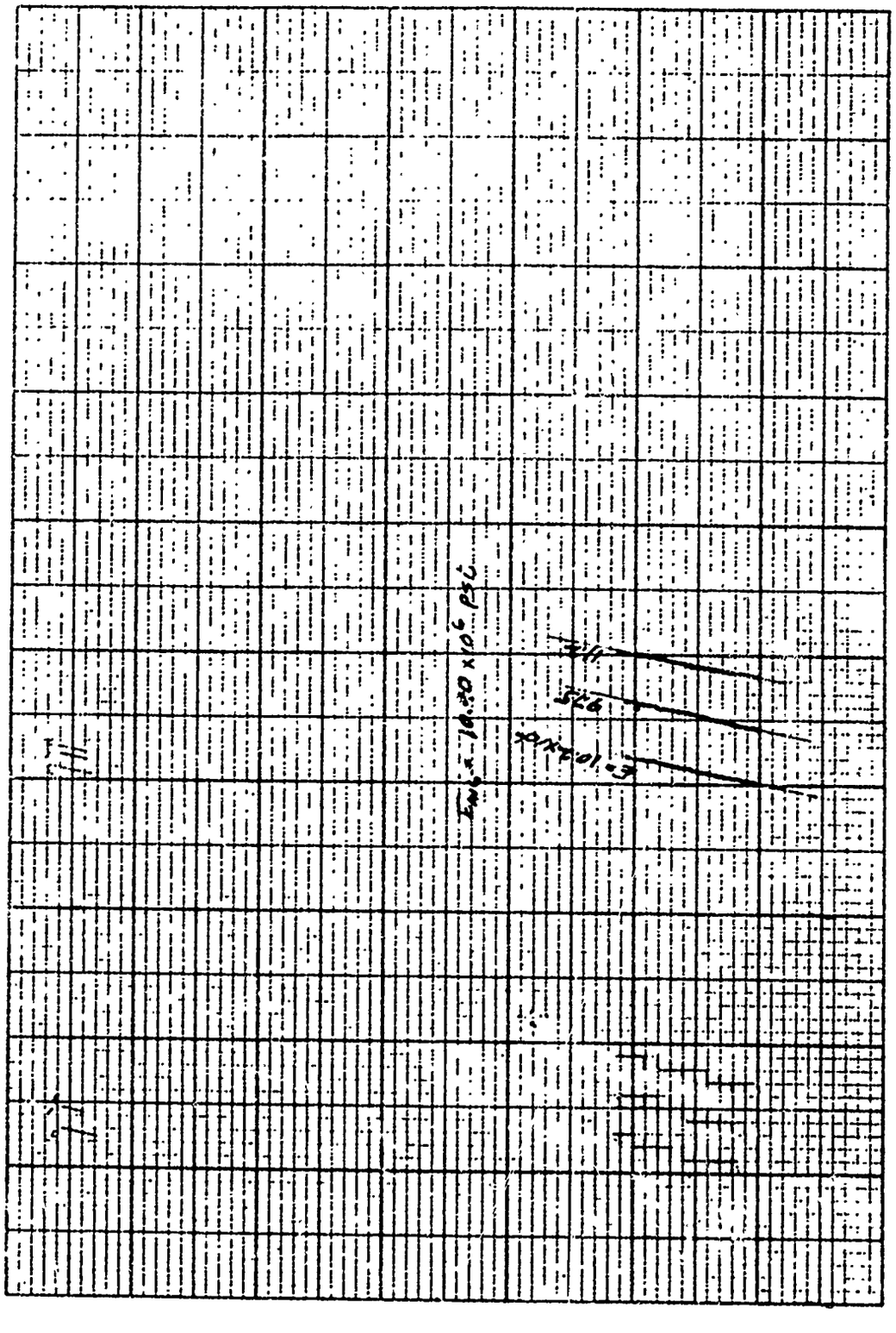
TENSILE AND COMPRESSIVE STRESS-STRAIN CURVES FOR AVCO 3DCC MATERIAL 8

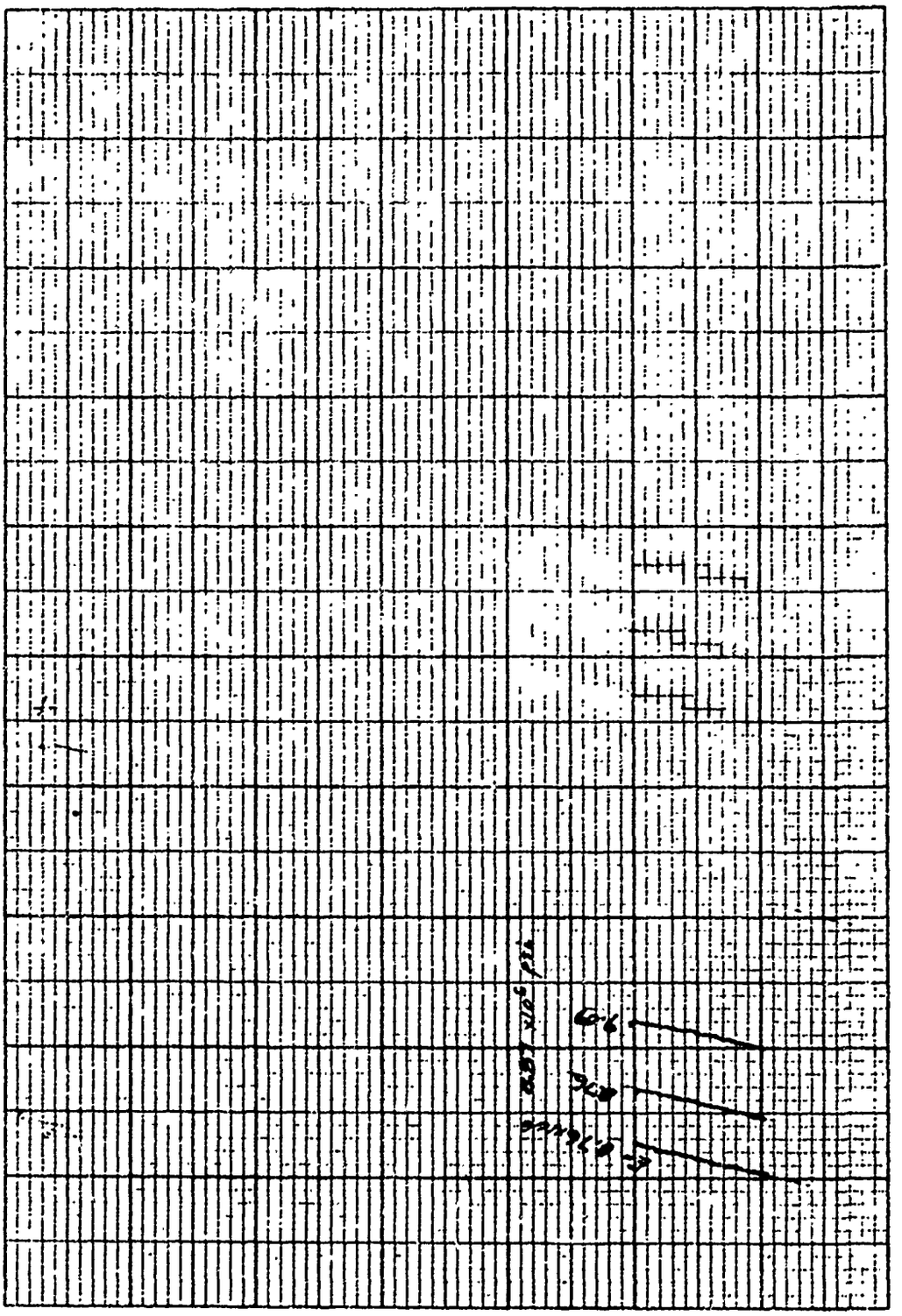

SRI Run No: T-23 12820
Date: 9-25-72 Temperature: 78°F
Specimen No: 8-AR-5-T
Loading Direction: Axial
Strain Rate: 10000 μin/min
X Scale: .1"/" 1" = .0005
Y Scale: .5"/" 1" = 70.63
Specimen Gage Section: 0.500 sq. in.
6.47 x10^6
6.45
6.22

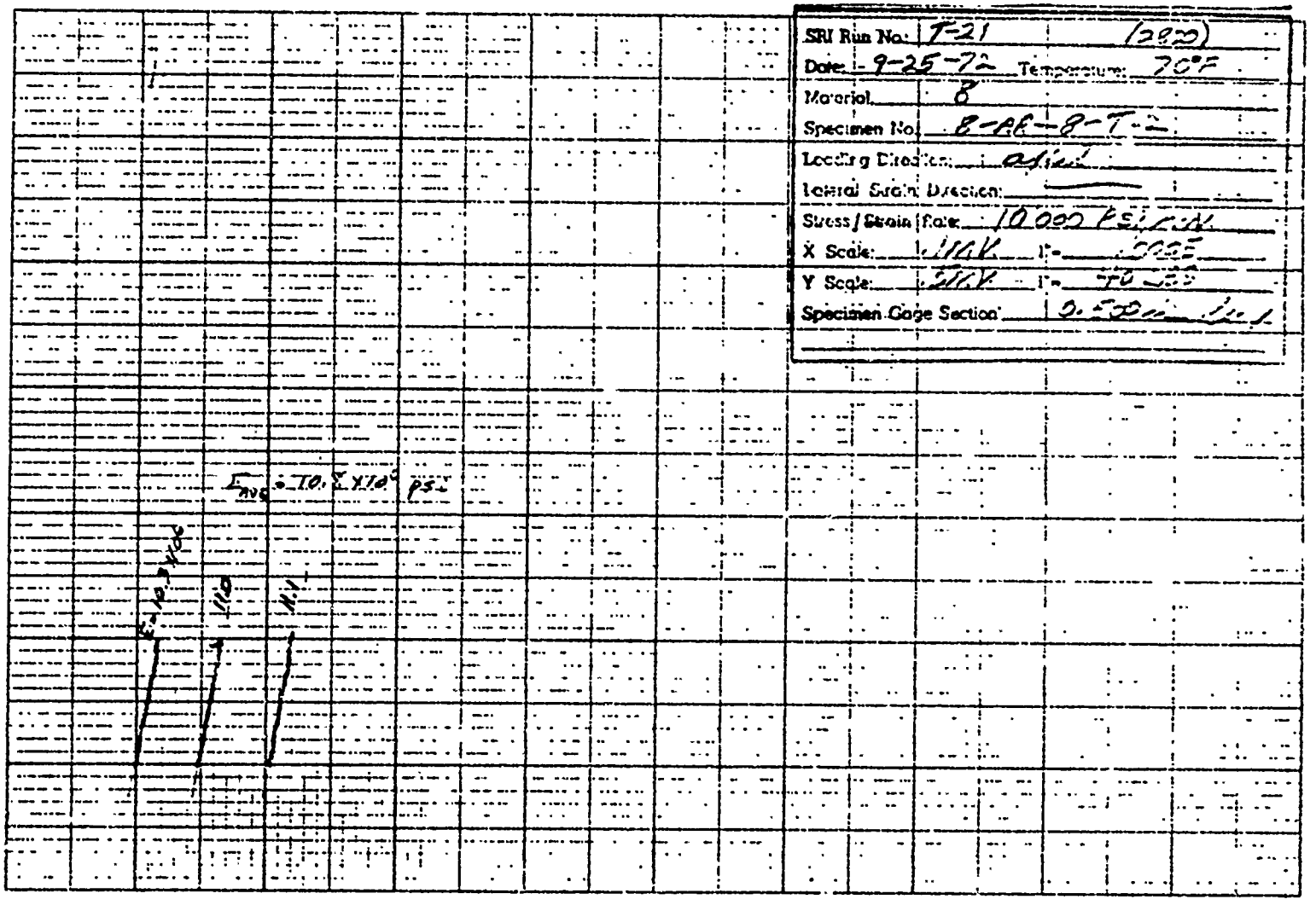

SRI Run No: 7-24 (2820)
Date: 9-25-72 Temperature: 70°F
Material: 8
Specimen No: 8-AR-5-74
Loading Direction: axial
Loading Rate: 1000 psi/min
X-Scale: .1 IN. = .005
Y-Scale: .5 IN. = 40 LBS
Specimen Gage Section:
E = 8.03 x 10^6 psi
765
779

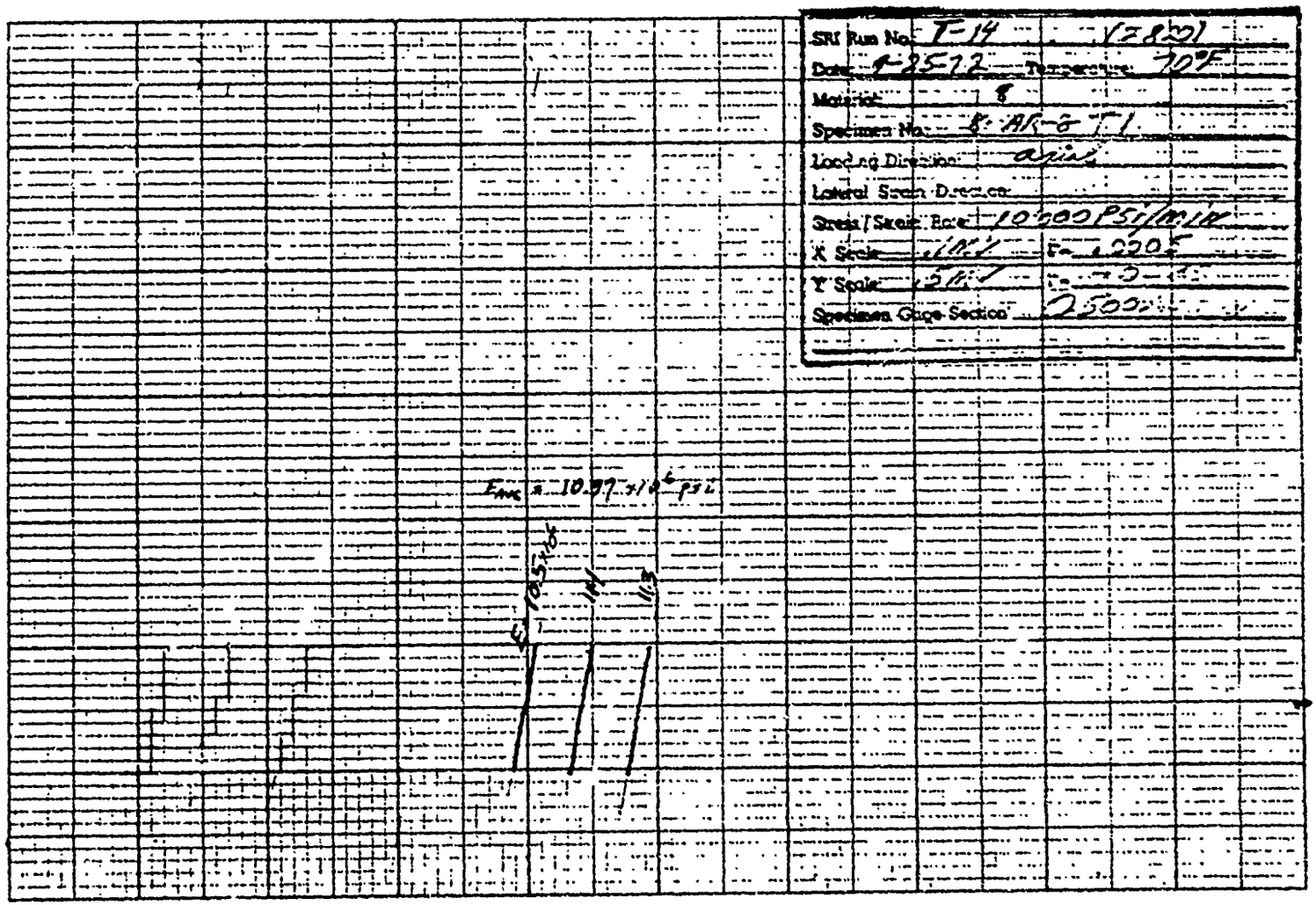

SRI Run No: T-18 (2-20)
Date: 9-25-72 Temperature: 70°F
Material: 8
Specimen No: E-AK-5-T2
Loading Direction: axial
Lateral Strain Direction:
Stress/Strain Rate: 10,000 PSI/in/in
X Scale: 111/2" = .025
Y Scale: 5"/1" = 43.65
Specimen Gage Section: 2.0" x .501"
E = 5.98x10^6
7114
7114

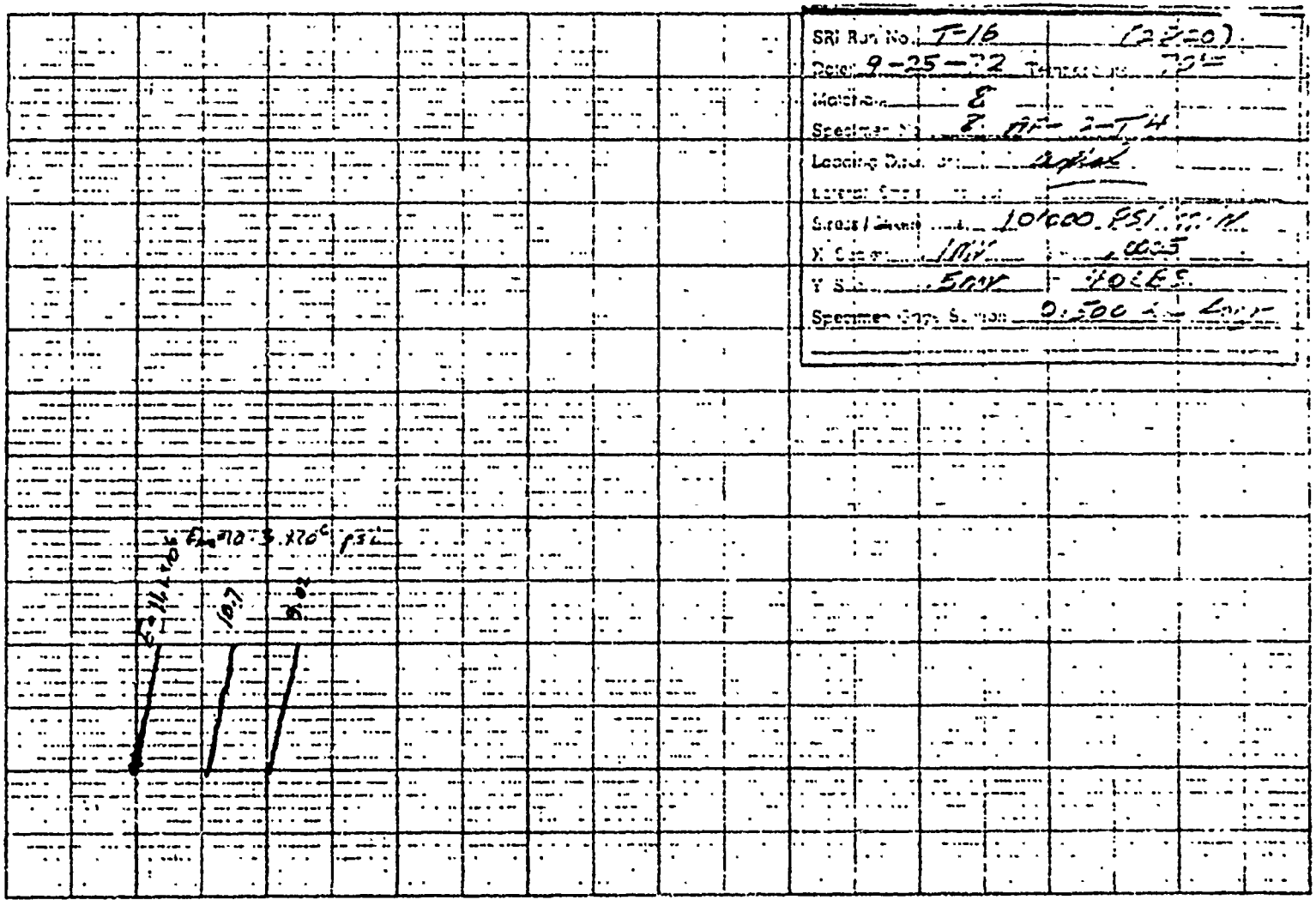

SRI Run No: T-17 12820
Date: 9-25-72 Temperature: 70°F
Material: 8
Specimen No: 8-AP-5-T3
Loading Direction: Axial
Lateral Strain Direction:
Stress/Strain Rate: 10,000 PSI/MIN
X-Scale: .1 IN. = .005
Y Scale: 5 KSI = 10 KSI
Specimen Gage Section: 0.500 in. dia
6.82 x10⁶ PSI
6.84
6.94

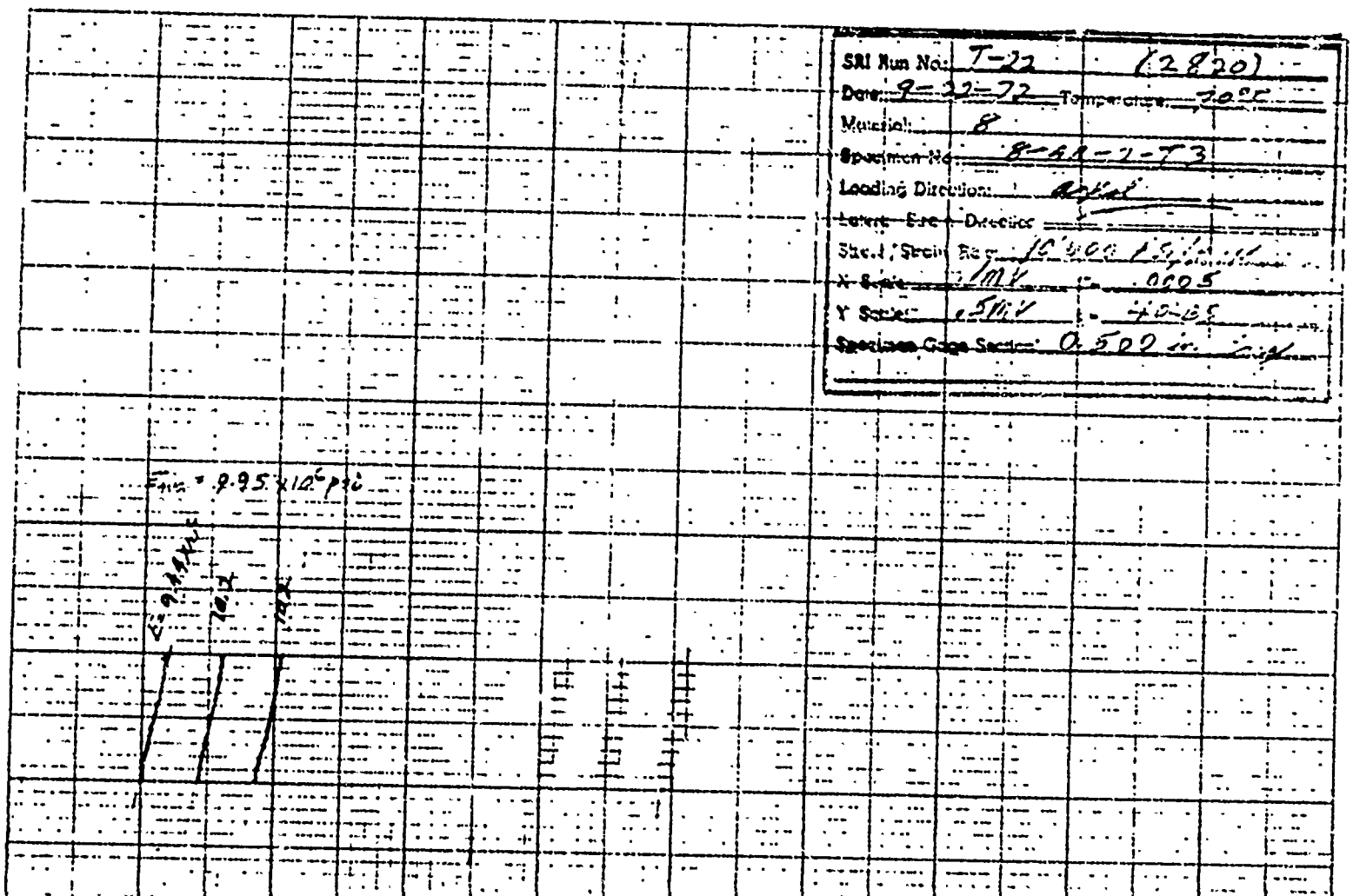

E = 10.30 x 10^6 psi
1/4
5/16
3/8



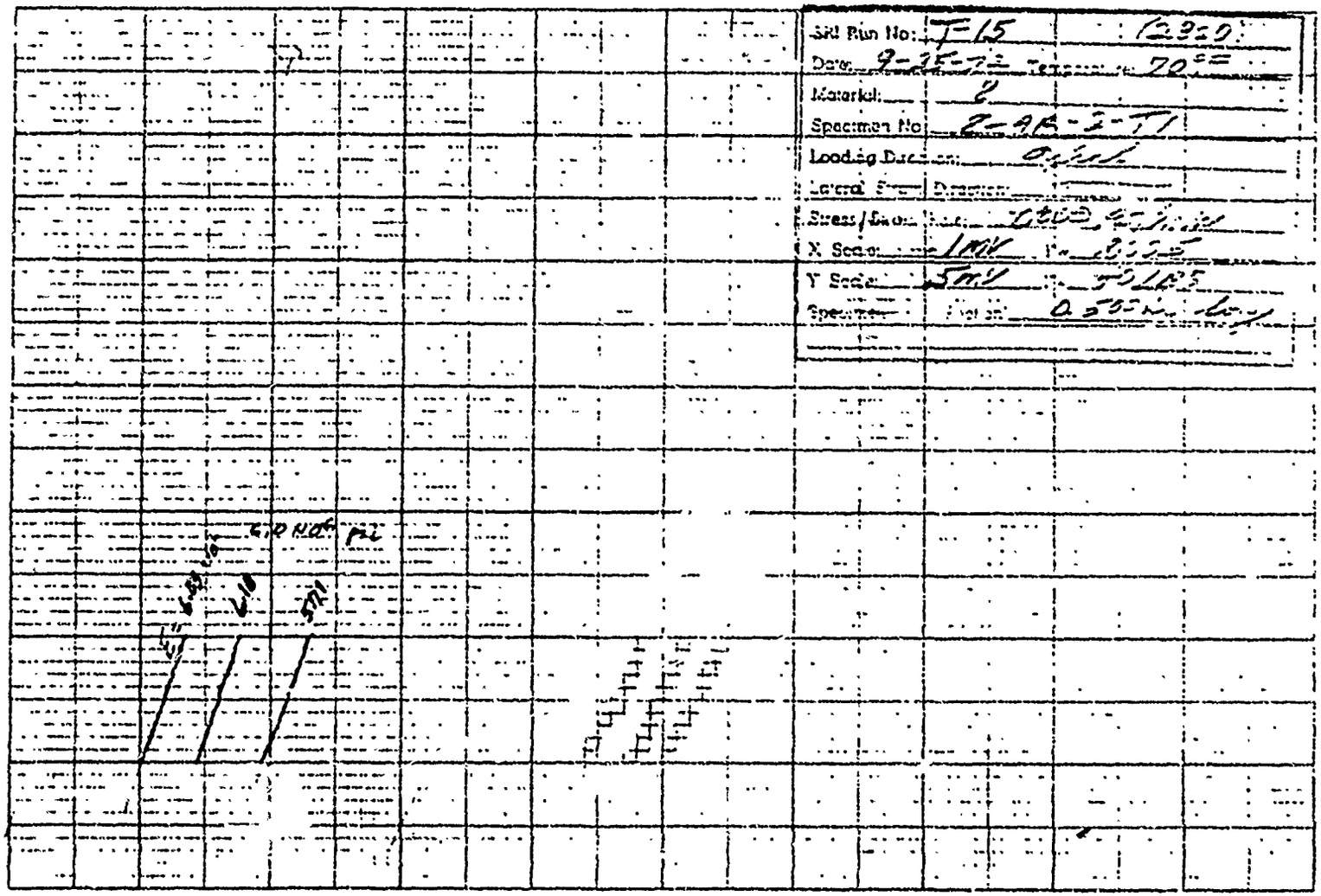

SRI Run No: T-21 (2820)
Date: 9-25-72 Temperature: 70°F
Material: 8
Specimen No: 8-AE-8-T-2
Loading Direction: axial
Lateral Strain Direction:
Stress / Strain Rate: 10,000 PSI/MIN
X Scale: 1 MIN 1" = 2000
Y Scale: 200K 1" = 20,000
Specimen Gage Section: 0.500 in. dia.
E_AVG = 10.8 X 10^6 PSI
E = 10.8 X 10^6
110
111

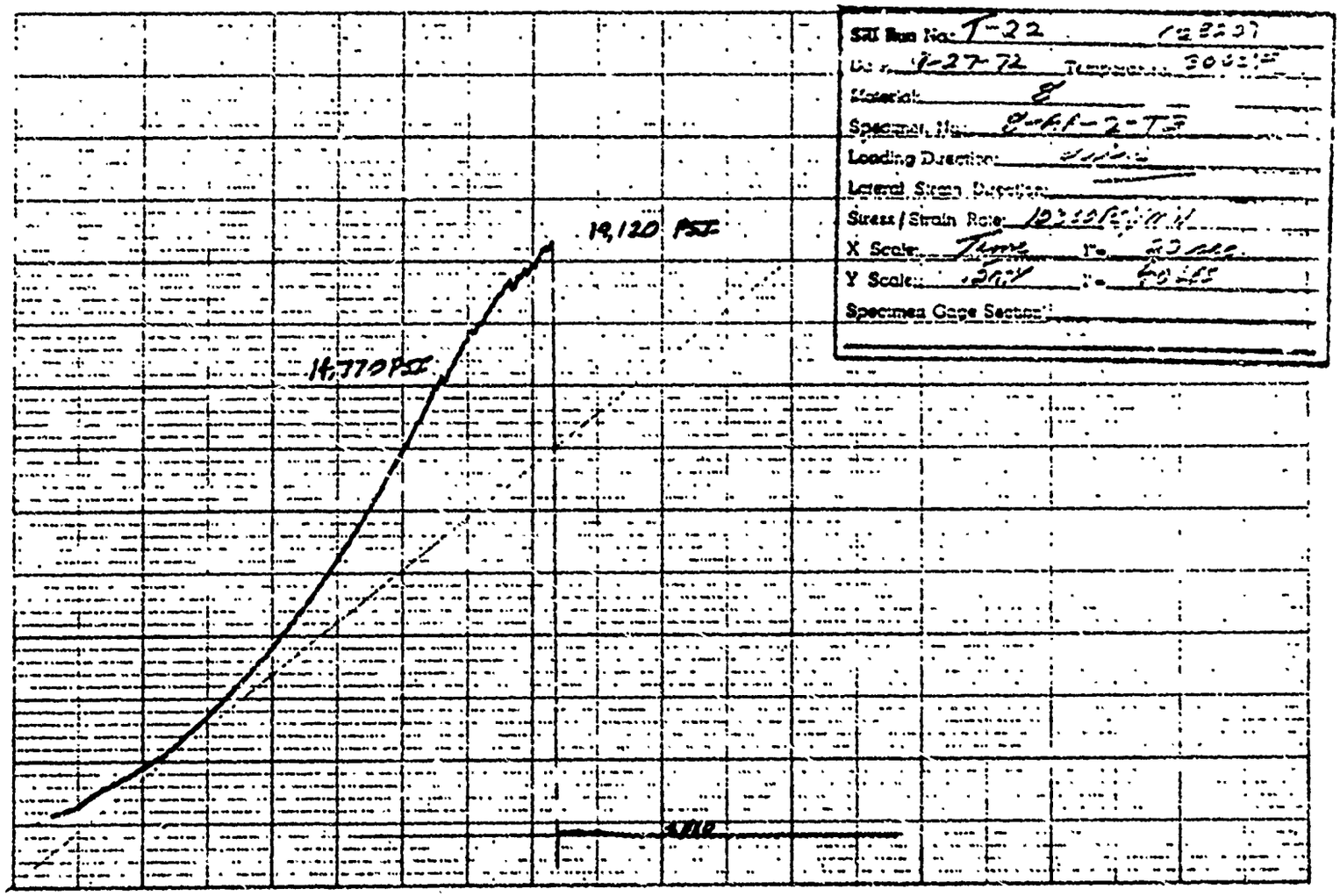

SRI Run No. T-14
Date 8-25-72
Temperature 70°F
Material B
Specimen No. B-AR-8 T-1
Loading Direction axial
Lateral Strain Direction
Stress / Strain Base 10,000 PSI/INCH
X Scale .1 IN/
Y Scale .5 IN/
Specimen Gage Section 2.500
E_INIT = 10.97 x 10^6 PSI
E_TAN x 10^6
INIT
E_SEC

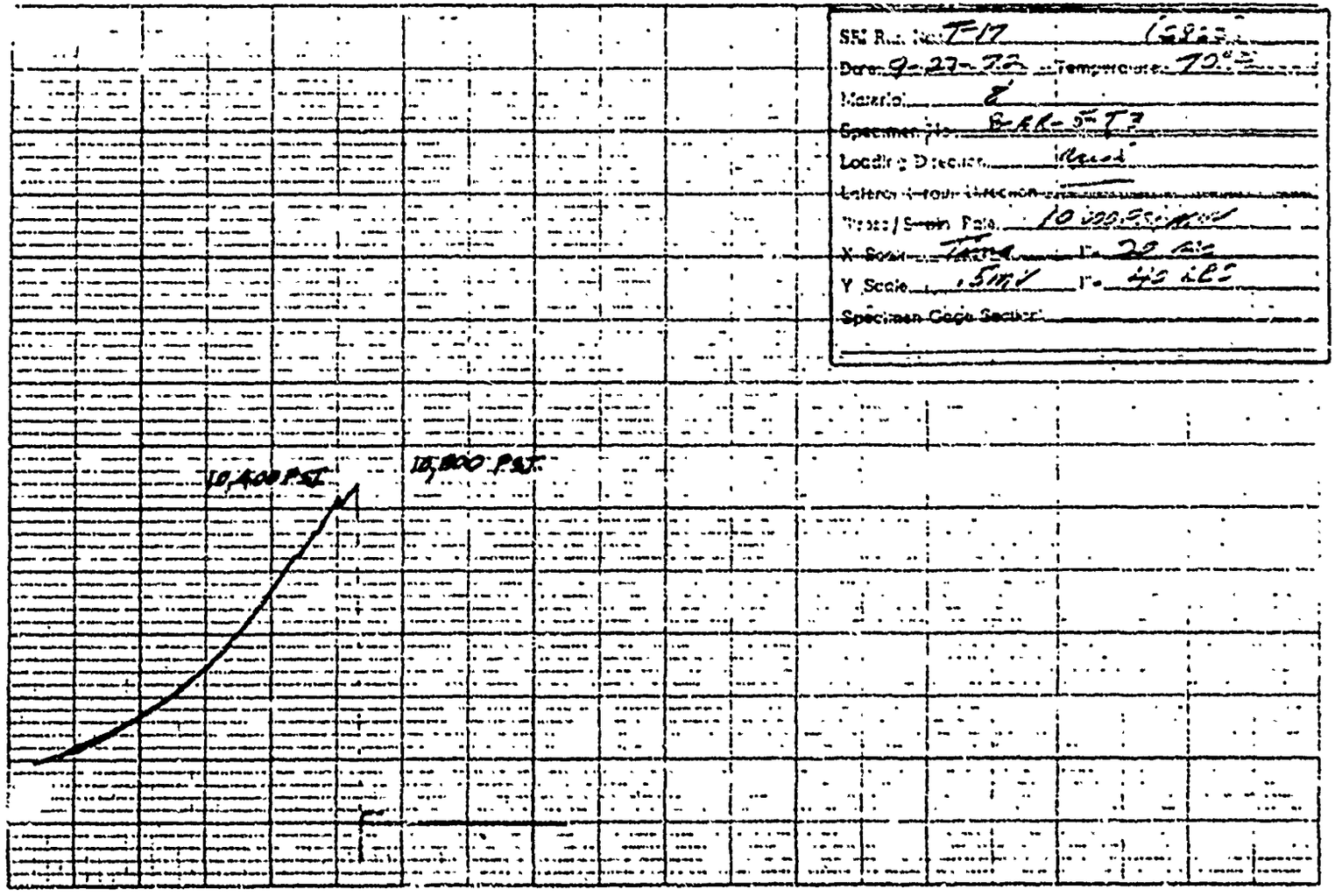

SRI Run No. T-16 (22-0)
Date 9-25-72
Material E
Specimen No. E 0F- 2-T4
Loading Rate Axial
Stress Level 10000 PSI
Y Scale 50K 20KIPS
Specimen Gage Section 0.500 x 2.000
E=10.3 X10^6 PSI
Load
Strain

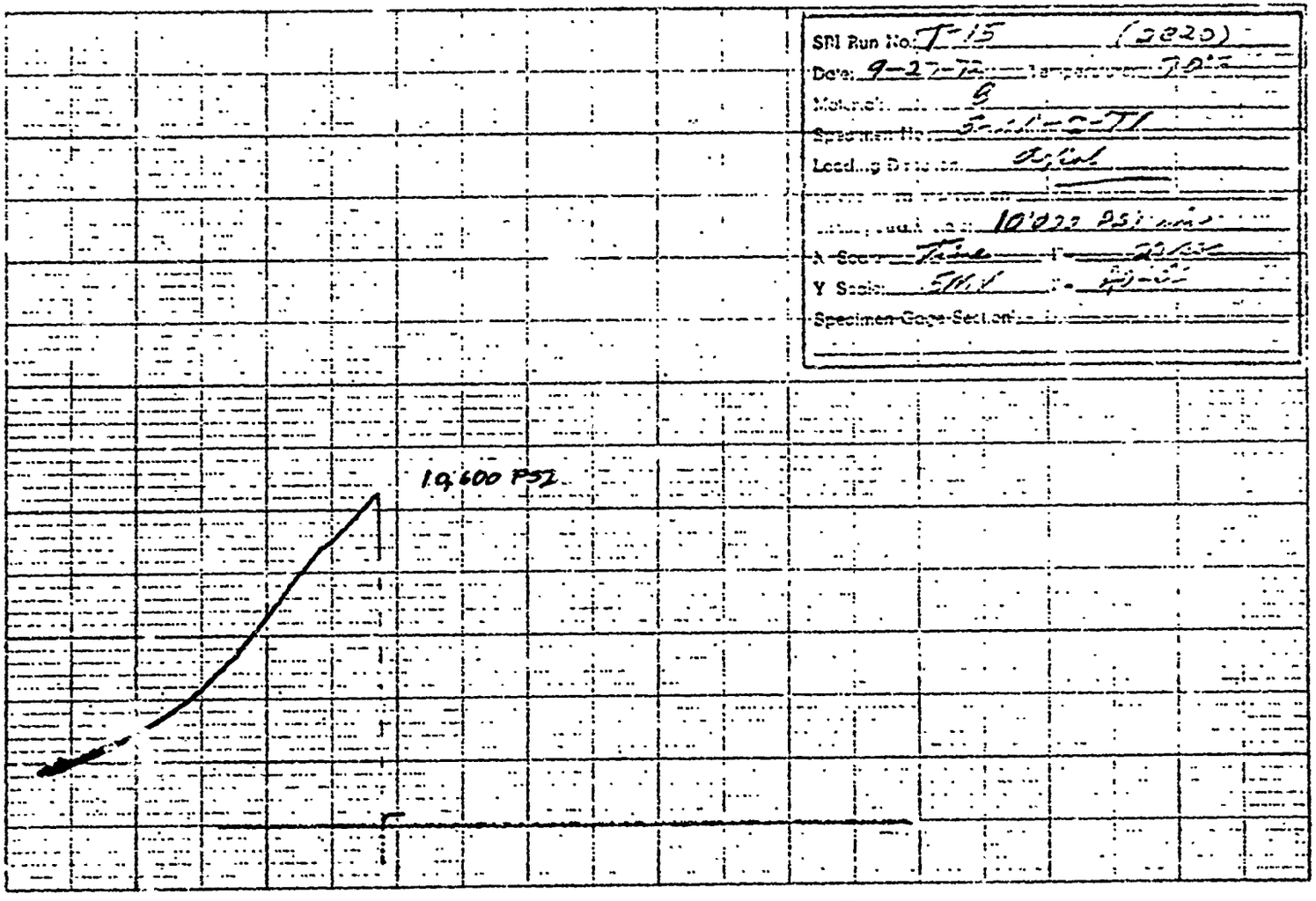

SRI Run No: T-22 (2820)
Date: 9-22-72 Temperature: -10°C
Material: 8
Specimen No: 8-AA-1-T3
Loading Direction: Axial
Load Exc - Direction
Strain Rate: 10,000 psi/min
X Scale: .1 in = .0005
Y Scale: .5 in = .0005
Specimen Gage Section: 0.500 in. long
$E_{min} = 9.95 \times 10^6$ psi
$E = 9.94 \times 10^6$ psi
10^7
$1.4 \times$

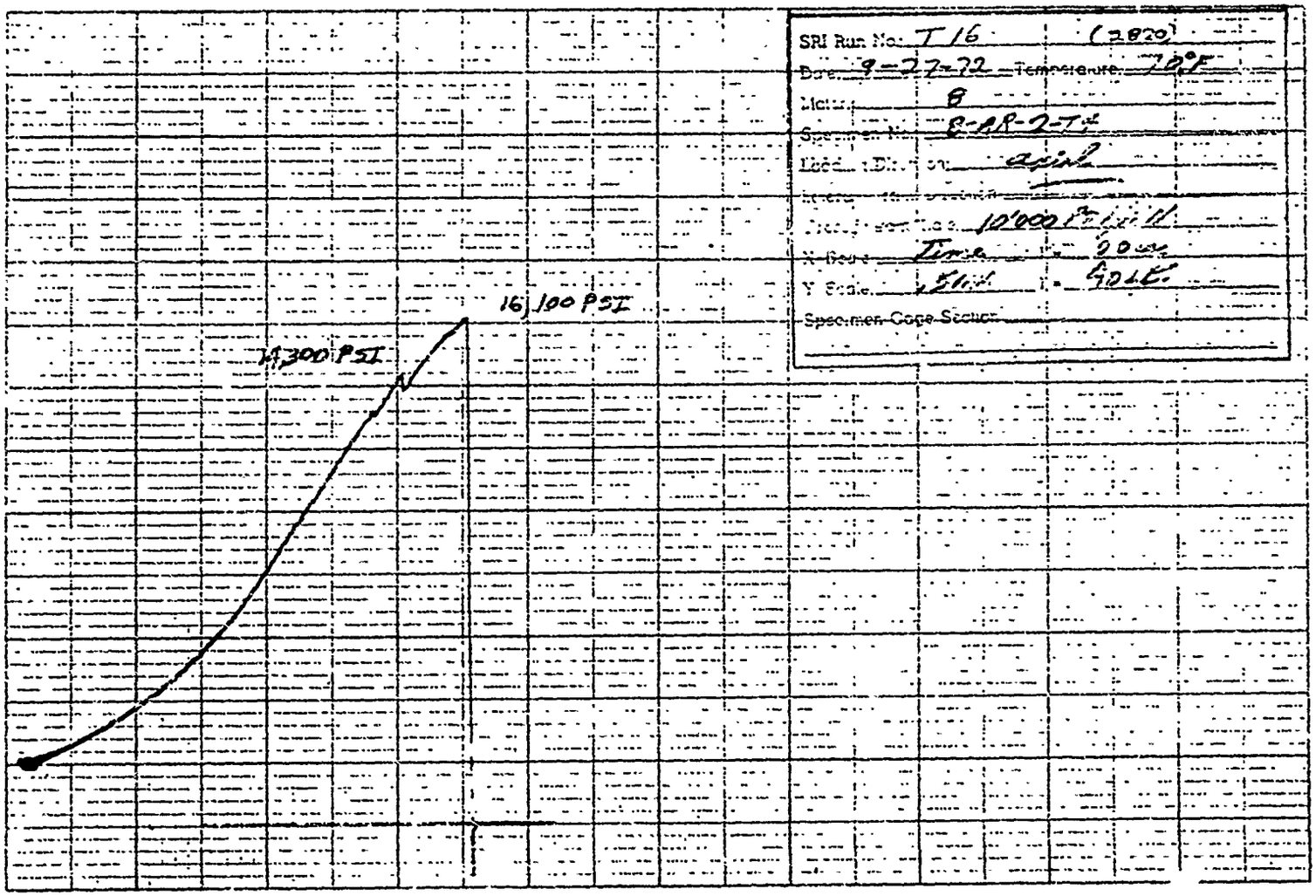
Reproduced from best available copy.

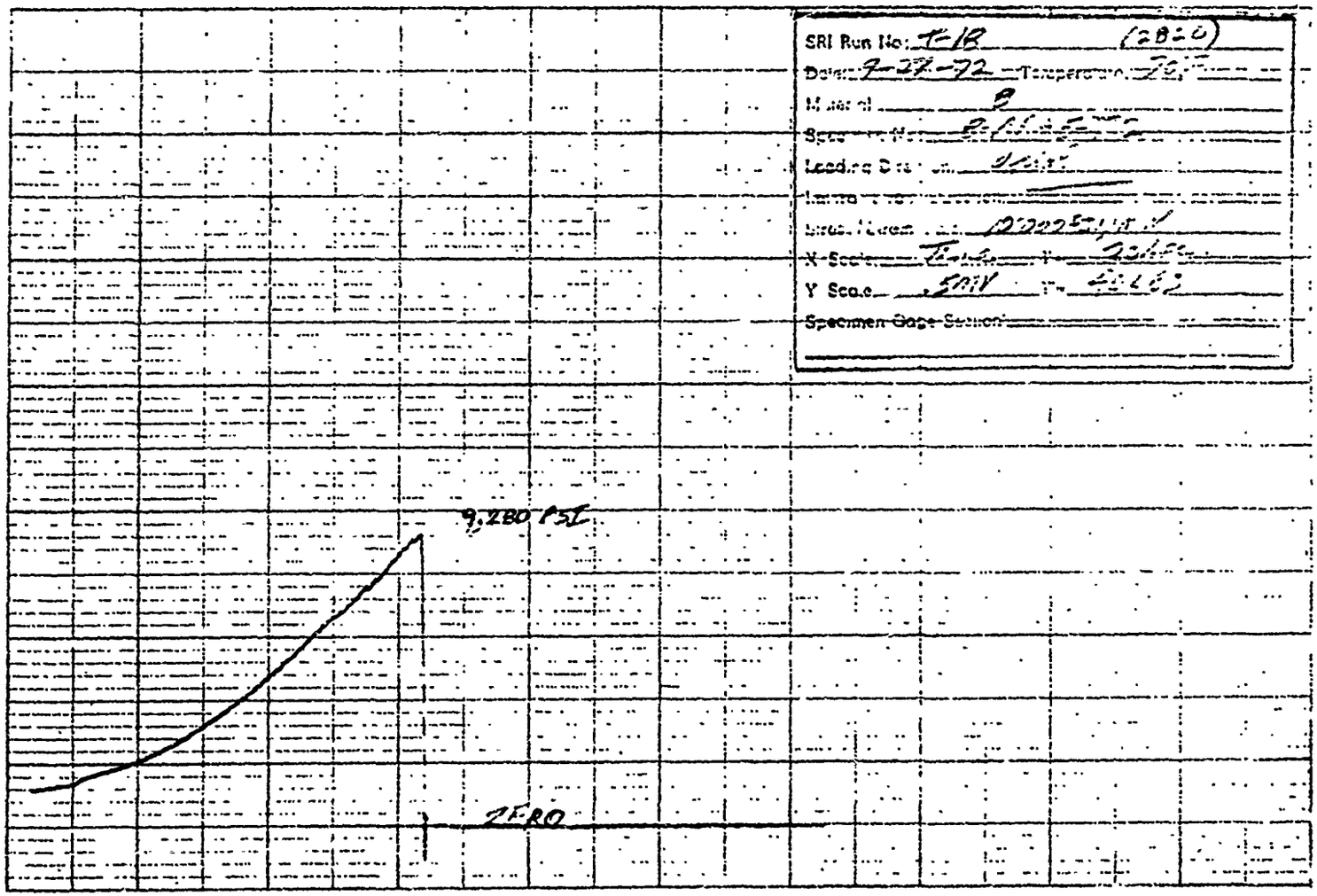

SR1 Run No: T-15
Date: 9-25-72
Material:
Specimen No:
Loading Direction:
Lateral
Stress/Strain
X Scale: 1MK
Y Scale: 5MK
Specimen
END NOT PLL
5MK

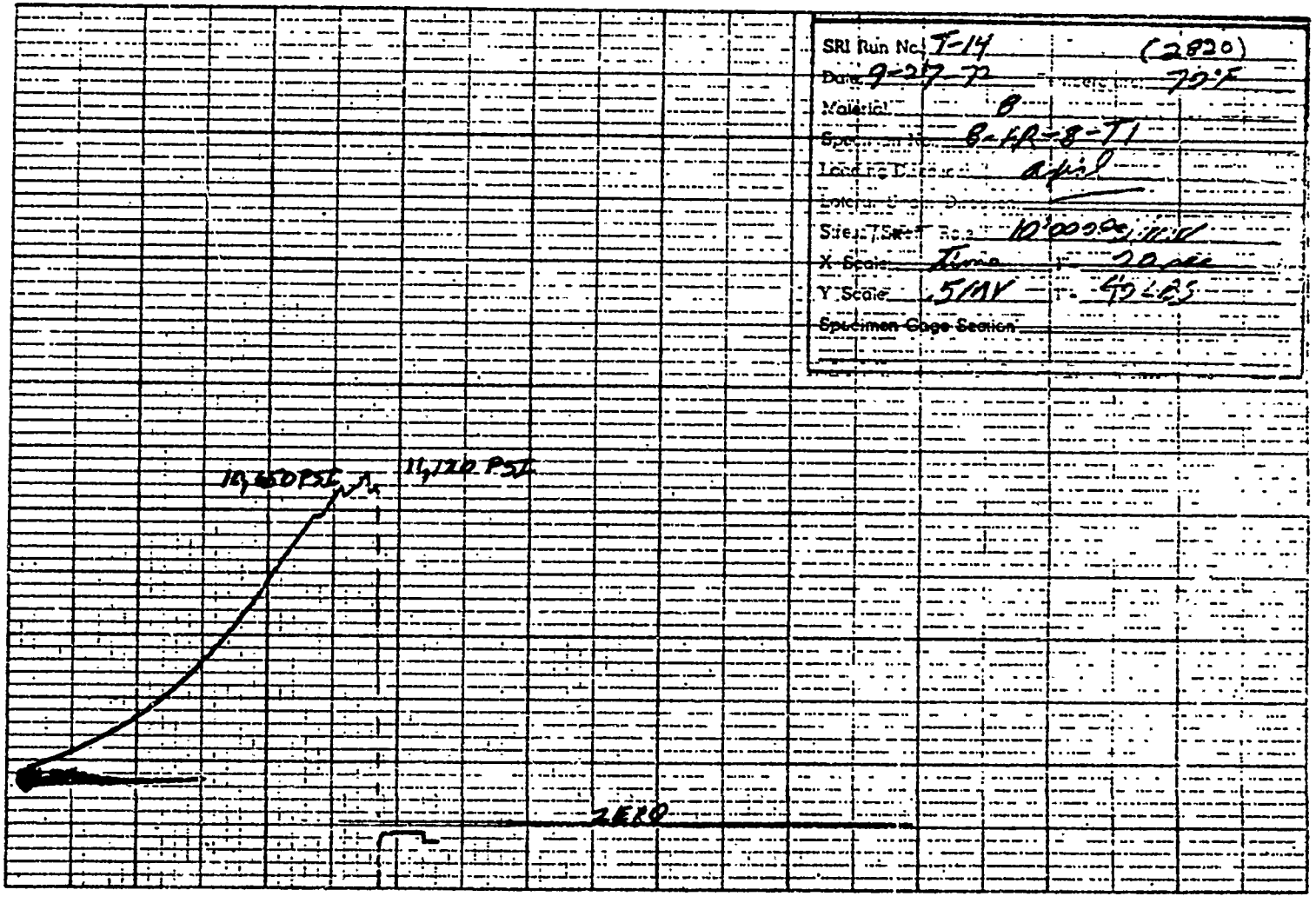

SRI Run No. T-22
Date 1-27-72 Temperature 3000°F
Material C
Specimen No. C-Ref-2-T3
Loading Direction Axial
Lateral Stress Direction
Stress / Strain Rate 12,000 psi/min
X Scale Time 1" = 20 sec
Y Scale Load 1" = 5000 lbs
Specimen Gage Section
19,120 PSI
14,770 PSI

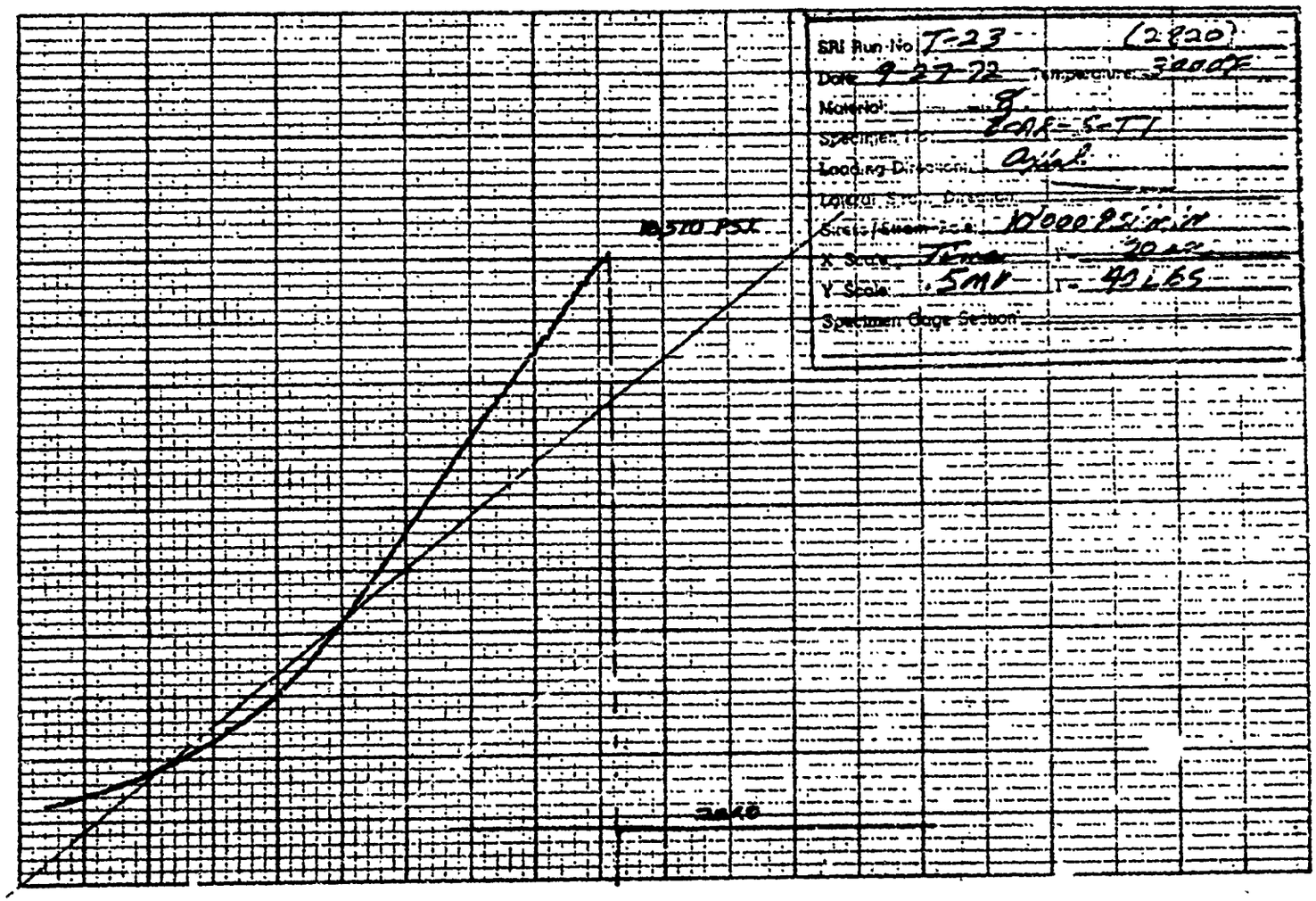

SR No. T-17
Date 9-27-72
Temperature 70°F
Material E
Specimen No. E-RR-5-T7
Loading Direction Radial
Load / Strain Rate 10,000 psi/min
X Scale .5 in = 20 ksi
Y Scale .5 in = 40 ksi
Specimen Gage Section
10,400 PSI
10,800 PSI

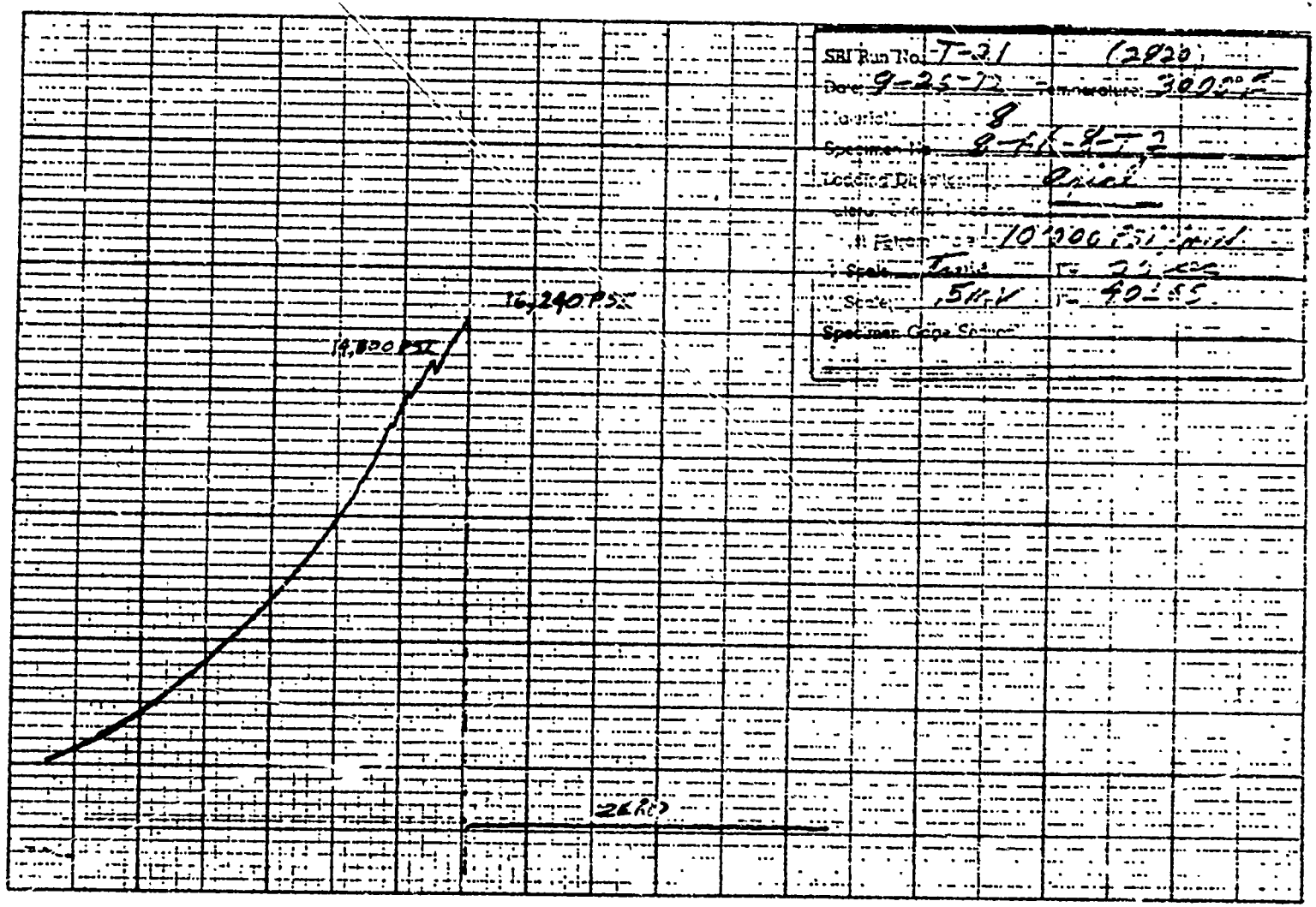

SRI Run No: T-15 (3020)
Date: 9-27-72
Material: G
Specimen No: G-III-C-T1
Loading Direction: Axial
10,000 PSI/inch
X Scale: Fine
Y Scale: 500
Specimen Gage Section:
19,600 PSI

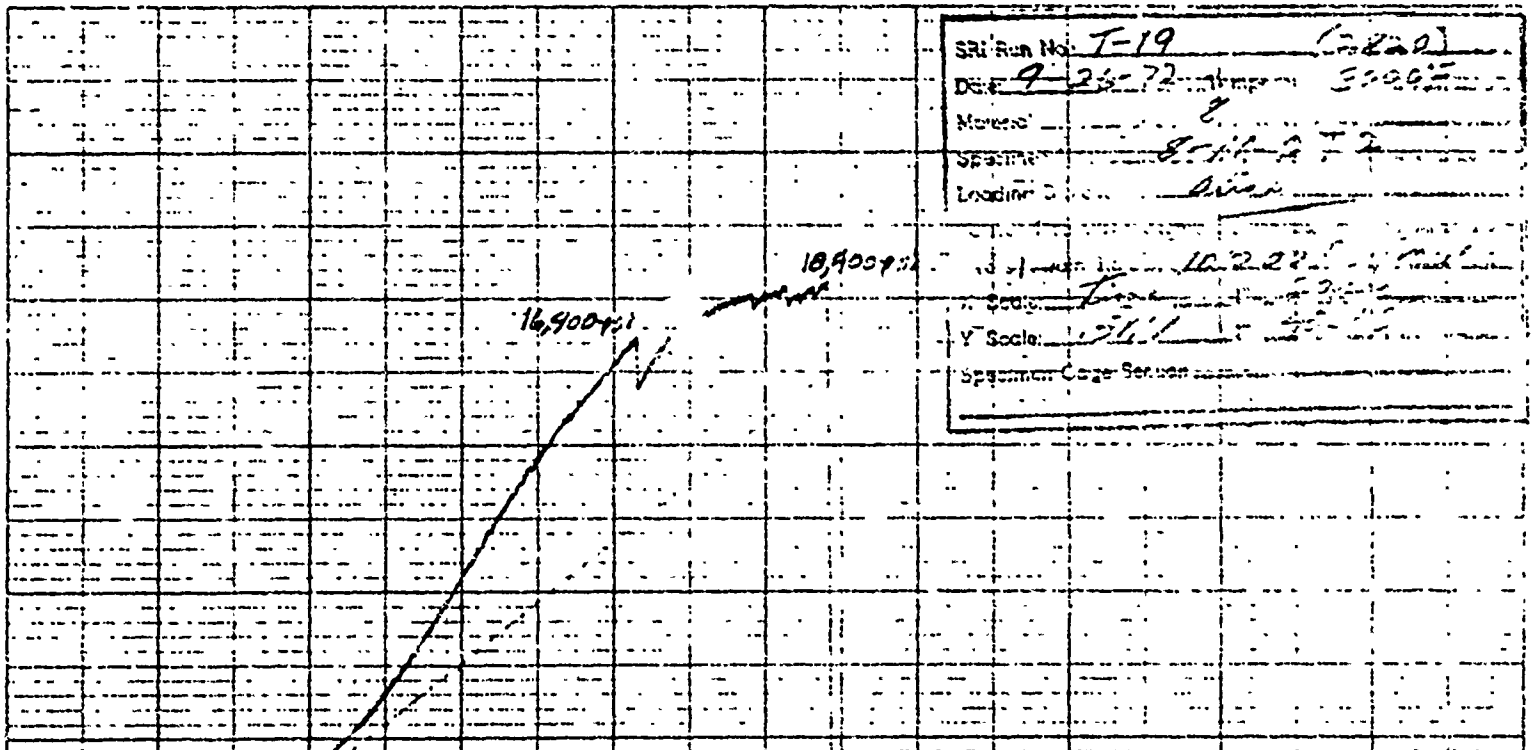

SRI Run No: T16 (2820)
Date: 9-27-72 Temperature: 70°F
Material: B
Specimen No: B-AR-2-T2
Load Direction: axial
Load: 10000 lbs full
X Scale: Time 20 sec
Y Scale: Full 40 KSI
Specimen Cage Section
16,100 PSI
14,300 PSI

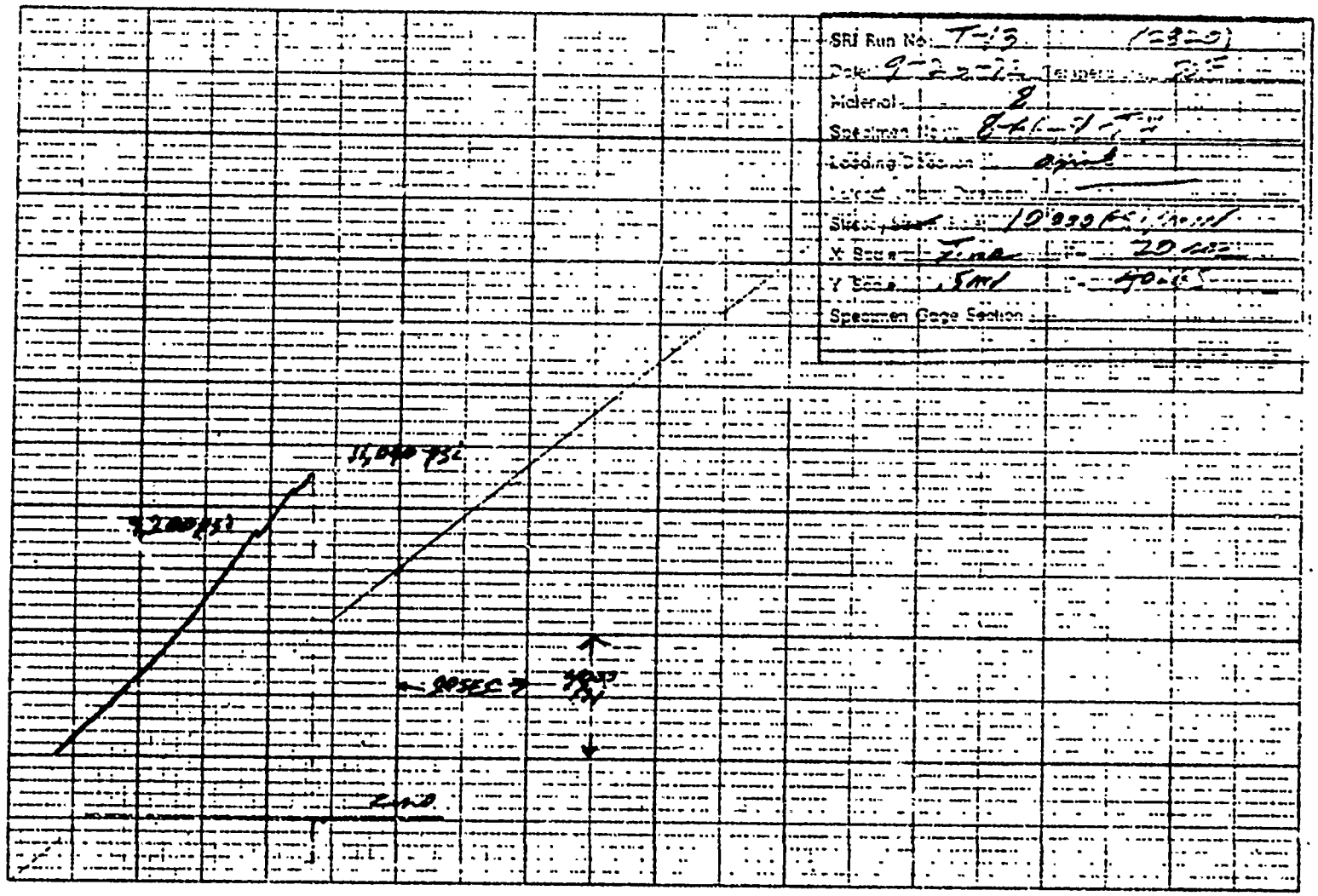

SRI Run No: T-18 (28-0)
Date: 9-27-72 Temperature: 70°
Material: 9
Specimen No: P-18-5-5
Loading Rate: 0.05"
Instron Head: 0.2" F.S. 1"
X-Scale: 1" = 2000#
Y Scale: .5"/V = 2000#
Specimen Gage Section:
9,280 PSI
ZERO

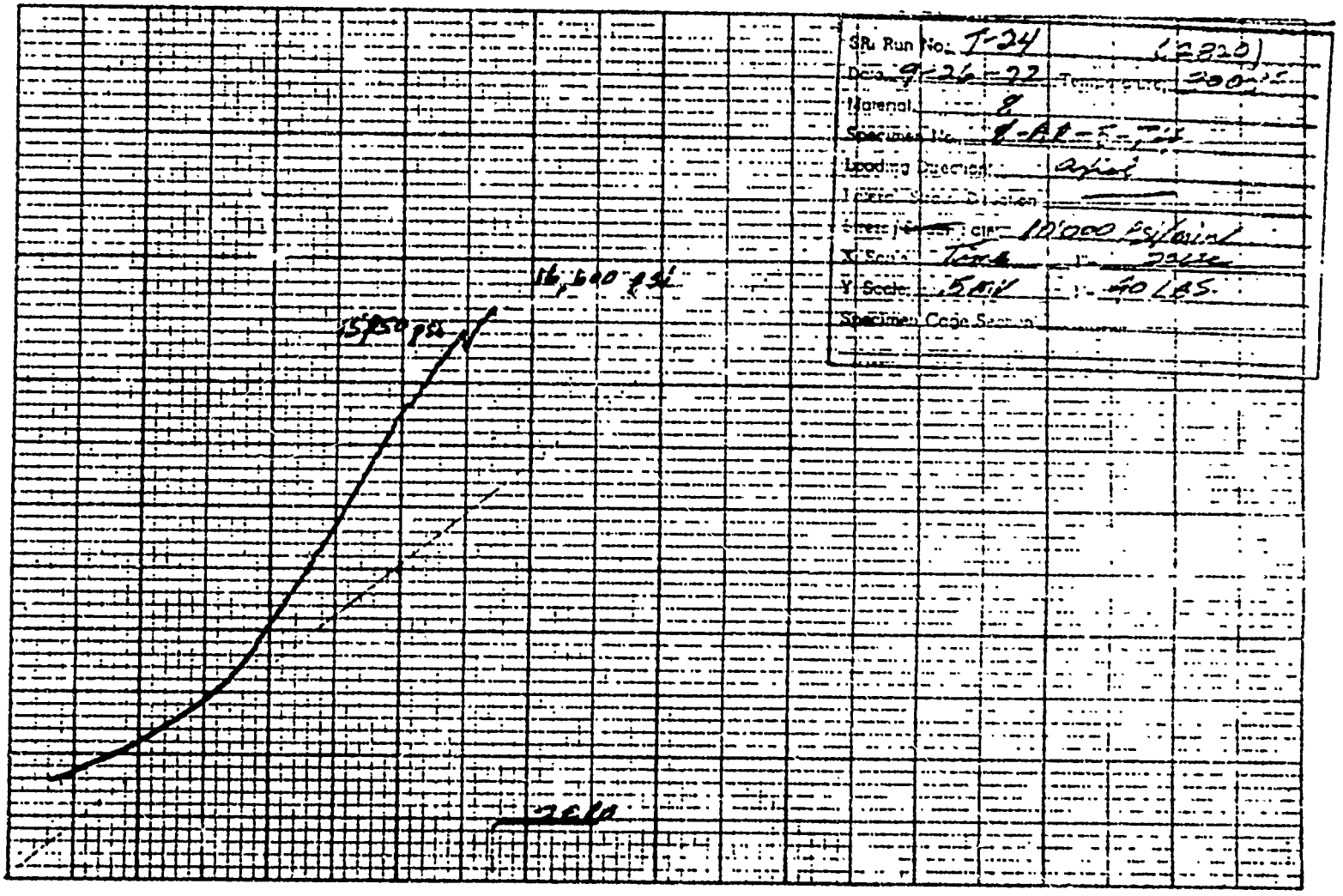

SRI Run No. T-14 (2820)
Date 9-27-72 70°F
Material B
Specimen No. B-4R-8-T1
Loading Direction axial
Strain Rate 10"/0.09 sec/in/in
X Scale Time 20 sec
Y Scale 5 KIP 40 LBS
Specimen Gage Section
14,660 PSI
14,720 PSI
ZERO

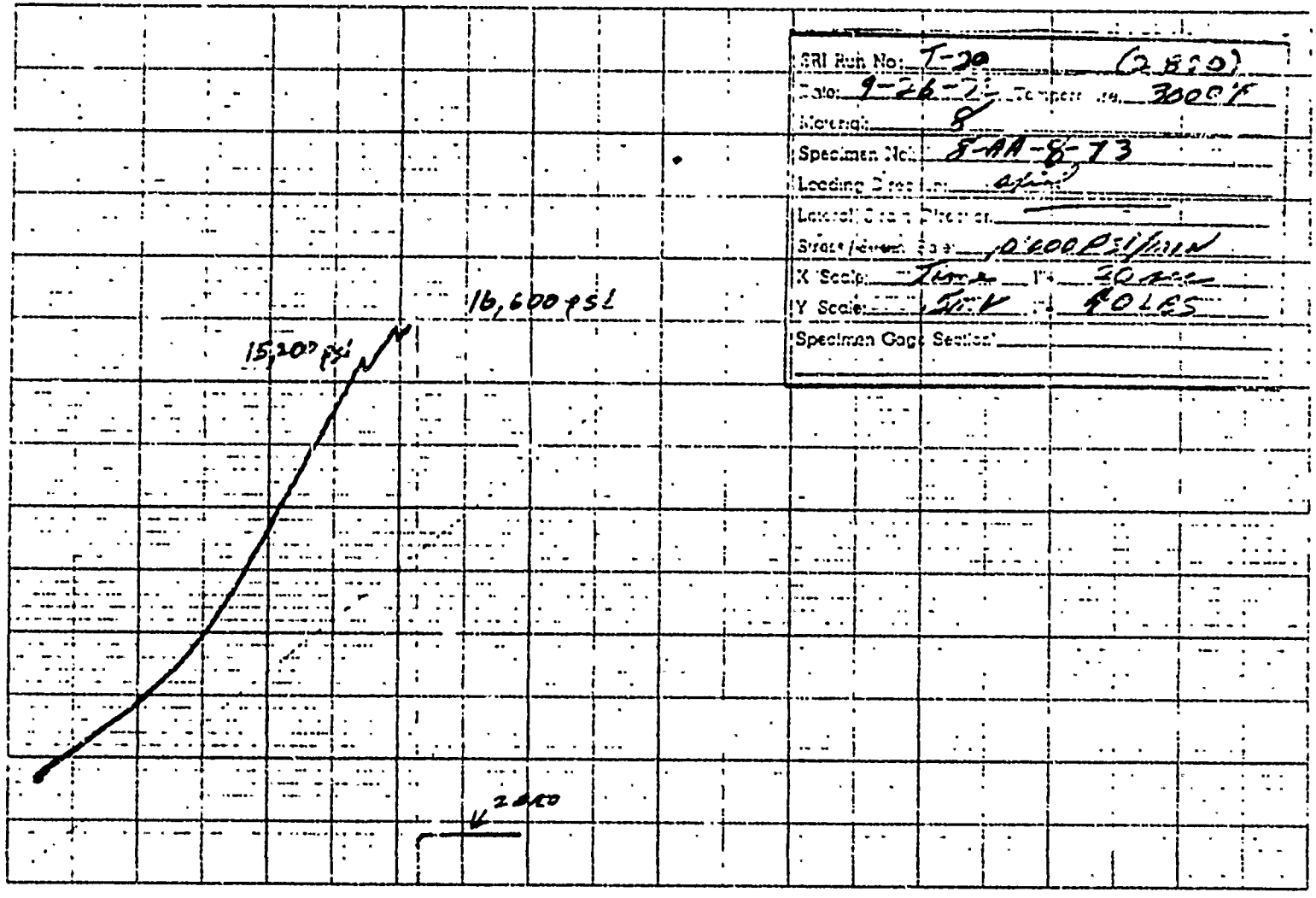

SRI Run No. T-23 (2820)
Date 9-27-72 Temperature 3000F
Material G
Specimen No. ZOAS-SCT
Loading Direction Axial
Load or Stress Direction
Stress/Strain Scale 10000 psi/in
X Scale Time 20 sec/in
Y Scale 5M# 1" = 93165
Specimen Gage Section
10,510 PSI
Time

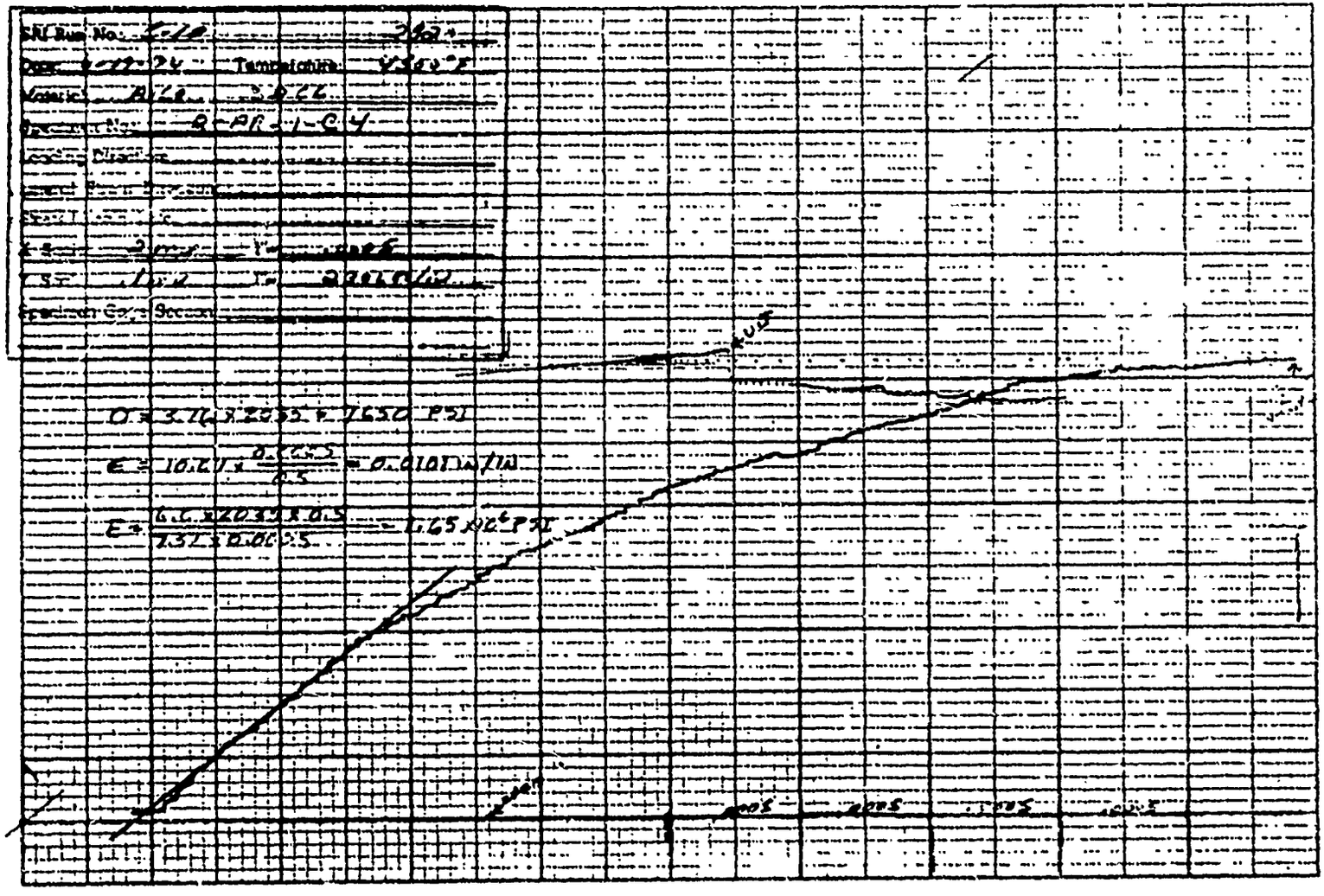

SBI Run No: T-31
Date: 9-25-72
Specimen No: 8
Specimen Type: 9-5½-8-T-2
Loading Direction: Axial
Test Temperature: 300°F
Strain Rate: 10,000 PSI/min
Scale: Force 1" = 2½ Kips
Scale: 5K-V 1" = 40 Kips
Specimen Gage Stress
16,240 PSI
19,820 PSI
ZERO

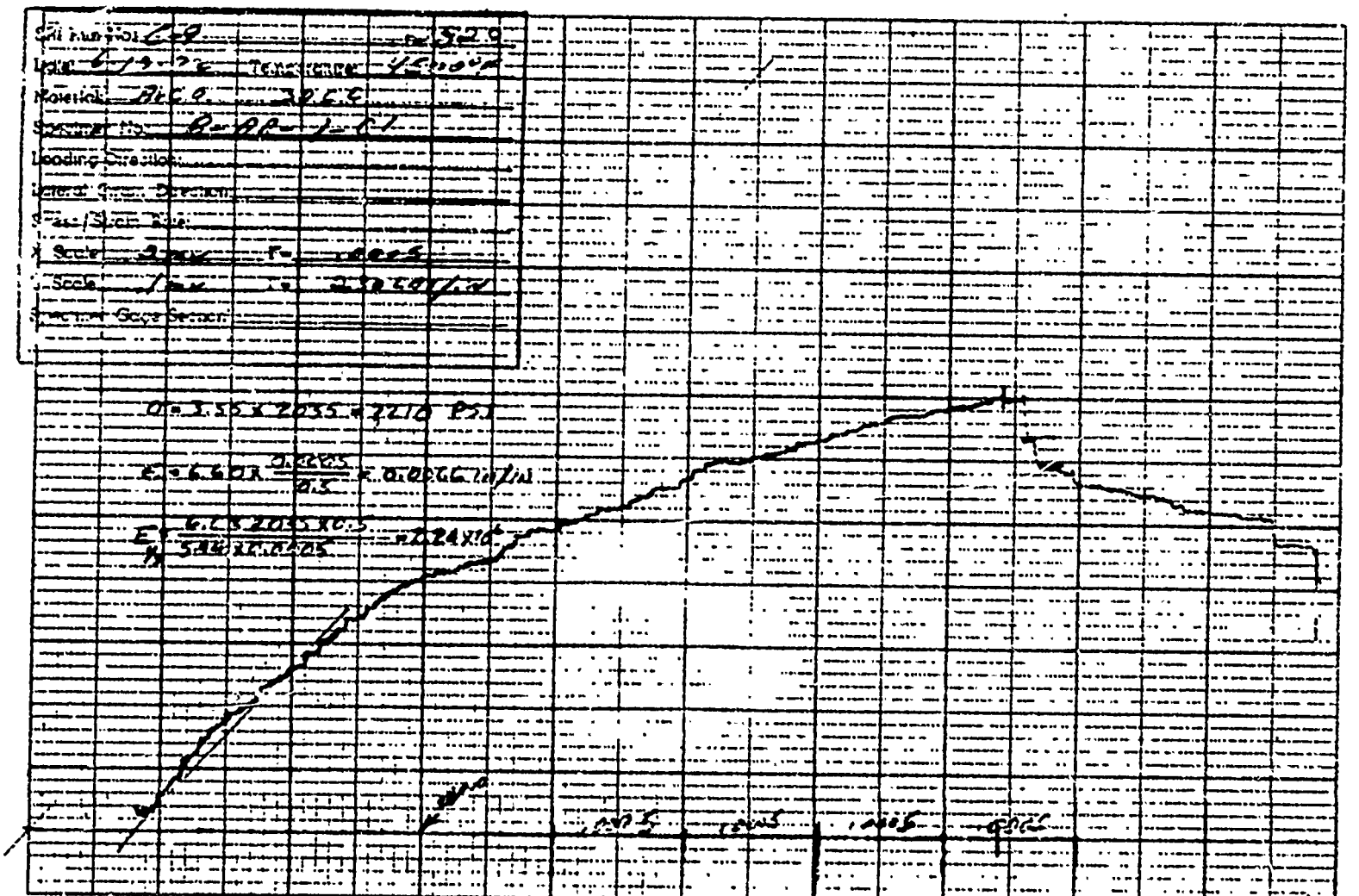

SRI Run No: T-19
Date: 9-25-72
Material:
Specimen:
Loading:
Scale:
Y Scale:
Specimen Gage Section
16,900 psi
18,900 psi
ZERO

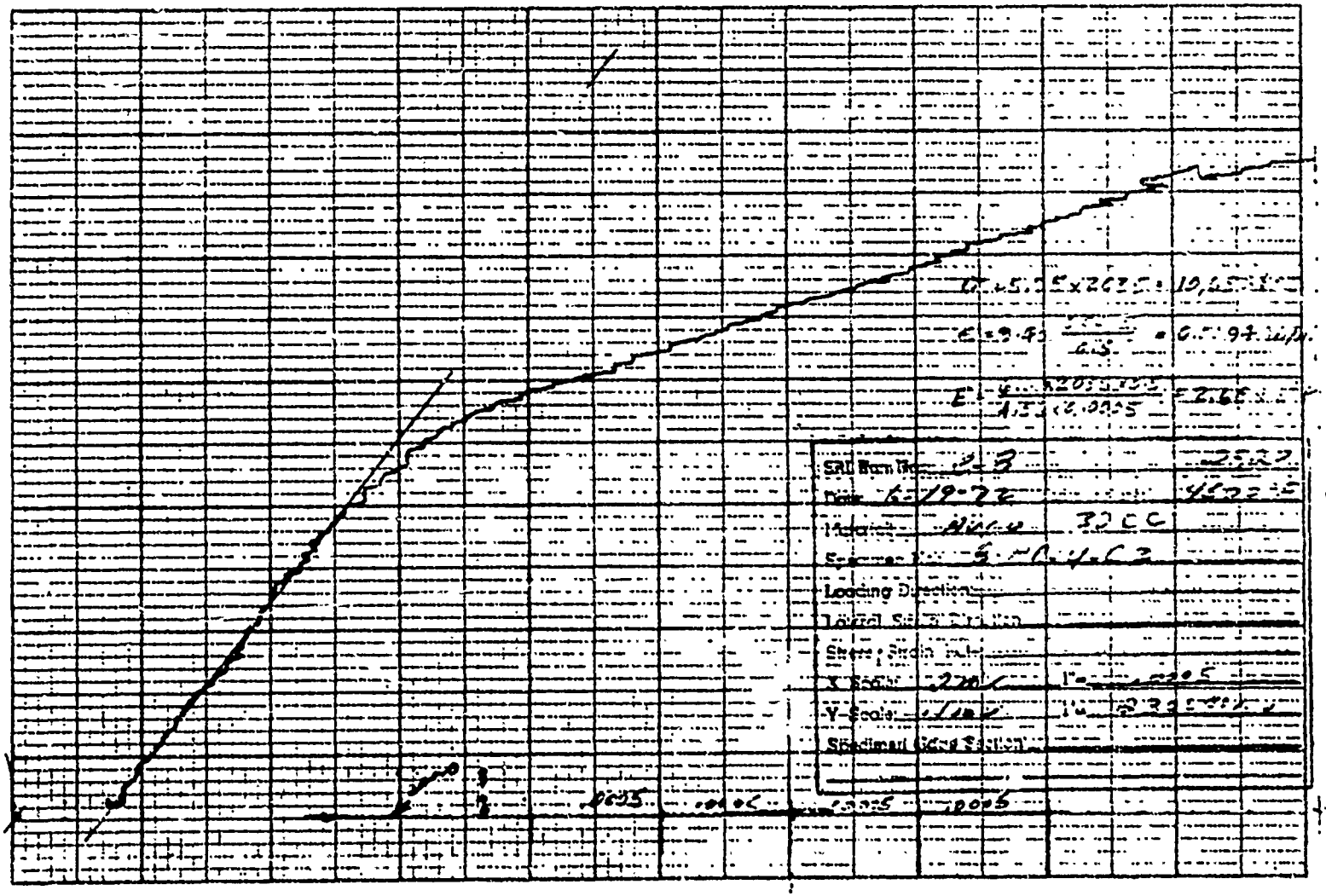

SRI Run No. T-13
Material
Specimen No.
Loading Direction
Strain Rate
X Scale
Y Scale
Specimen Gage Section
11,000 PSI
20 MSEC

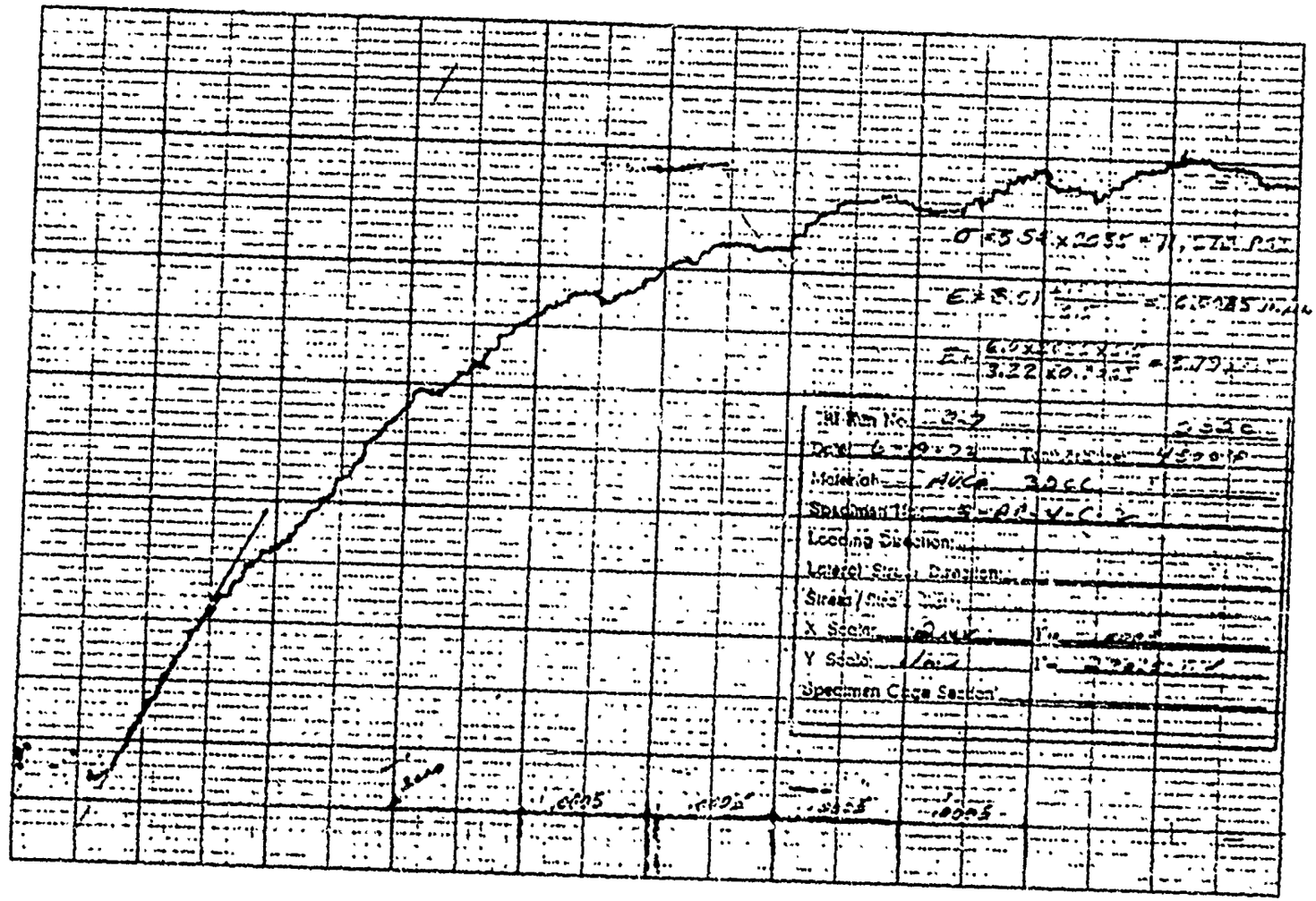

SR Run No. T-24
Date 9-26-22
Material 8
Specimen No. 8-At-5-T-L
Loading Direction Axial
Stress [illegible] cir. 10'000 psi/inch
X Scale Time 1" = 2 min
Y Scale 5 KK 1" = 40 LBS.
Specimen Cage Section
16,640 #
15850 psi
390


SRI Run No: T-20 (2 of 2)
Date: 9-26-72 Temperature 300°F
Material: 8
Specimen No: 8-AA-8-T3
Loading Direction: axial
Lateral Strain Direction:
Stress Level Rate: 40,000 PSI/min
X Scale: Time 1" = 20 sec
Y Scale: Stress 1" = 40 KSI
Specimen Gage Section:
16,600 psi
15,200 psi
2000


SRL Run No. [illegible]
Temperature [illegible]°F
Material [illegible]
Specimen No. [illegible]
Loading Direction
Specimen Geometry
Strain Gage Factor
Poisson's Ratio
Specimen Geometry
σ = 3.76 x 2033.5 = 7650 PSI
ε = 10.21 x 0.5 = 0.0010 in/in
E = 6.6 x 2033.5 x 0.5 / 7.32 x 0.0025 = 7.65 x 10^6 PSI


Gage Number: C-9
Date: 6-9-72
Temperature: 75°F
Material: Alc 9 20 C E
Specimen No.: B-BB-1-51
Loading Direction:
Lateral Gage Direction:
Gage/Strain Box:
X Scale: 2 psi/in
Y Scale: 1 in = 2000 psi
Specimen Gage Section:
σ = 3.56 x 2035 = 7210 PSI
E = 6.603 x 0.0005/0.5 x 0.000066 in/in
E = 6.6 x 2035 x 0.5 / 5846 x 0.0005 = 0.0024 x 10^6


Date 6-19-72
Material
Specimen
Loading Direction
Strain Rate
X-Scale
Y-Scale
Stress-Strain Curve Section


Material
Specimen Type
Loading Direction
Specimen Cross Section

SPI Run No: 5-12 S-20

Date: 6-19-72 Temperature: 4500 °F

Material: A-C 3256

Specimen No: S-MR-0-C

Loading Direction:

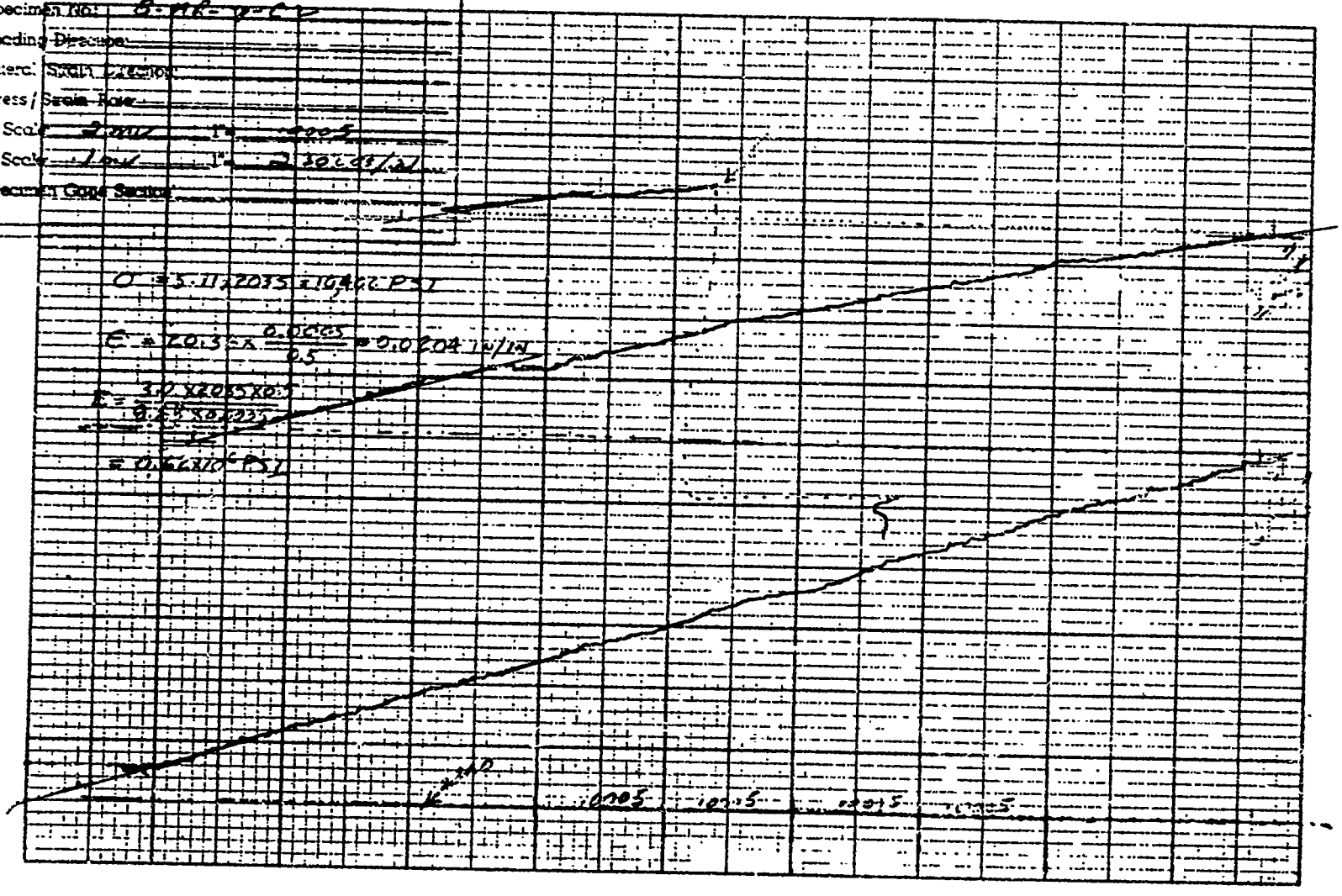
Lateral Strain Control:

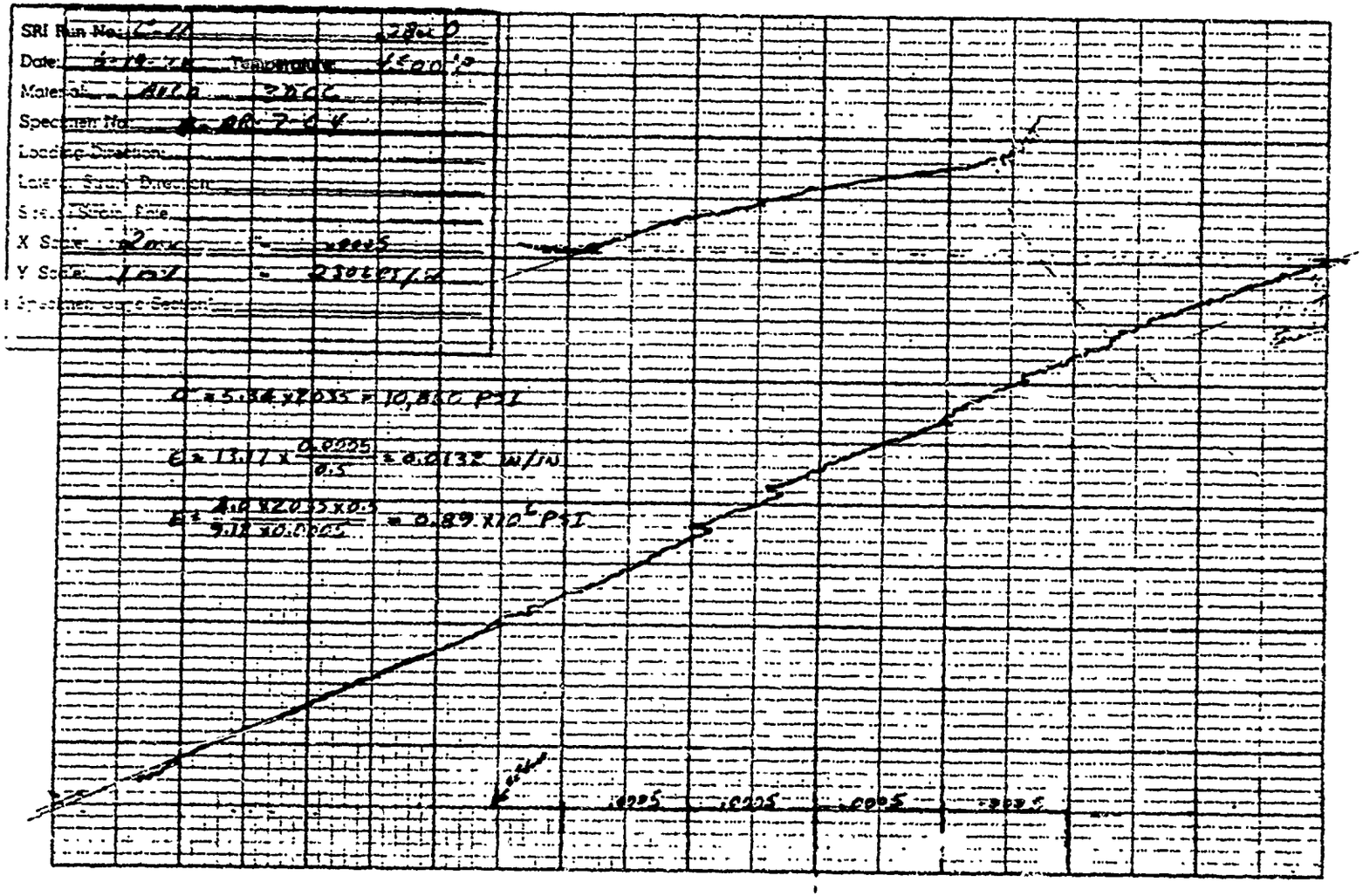
Stress/Strain Rate:

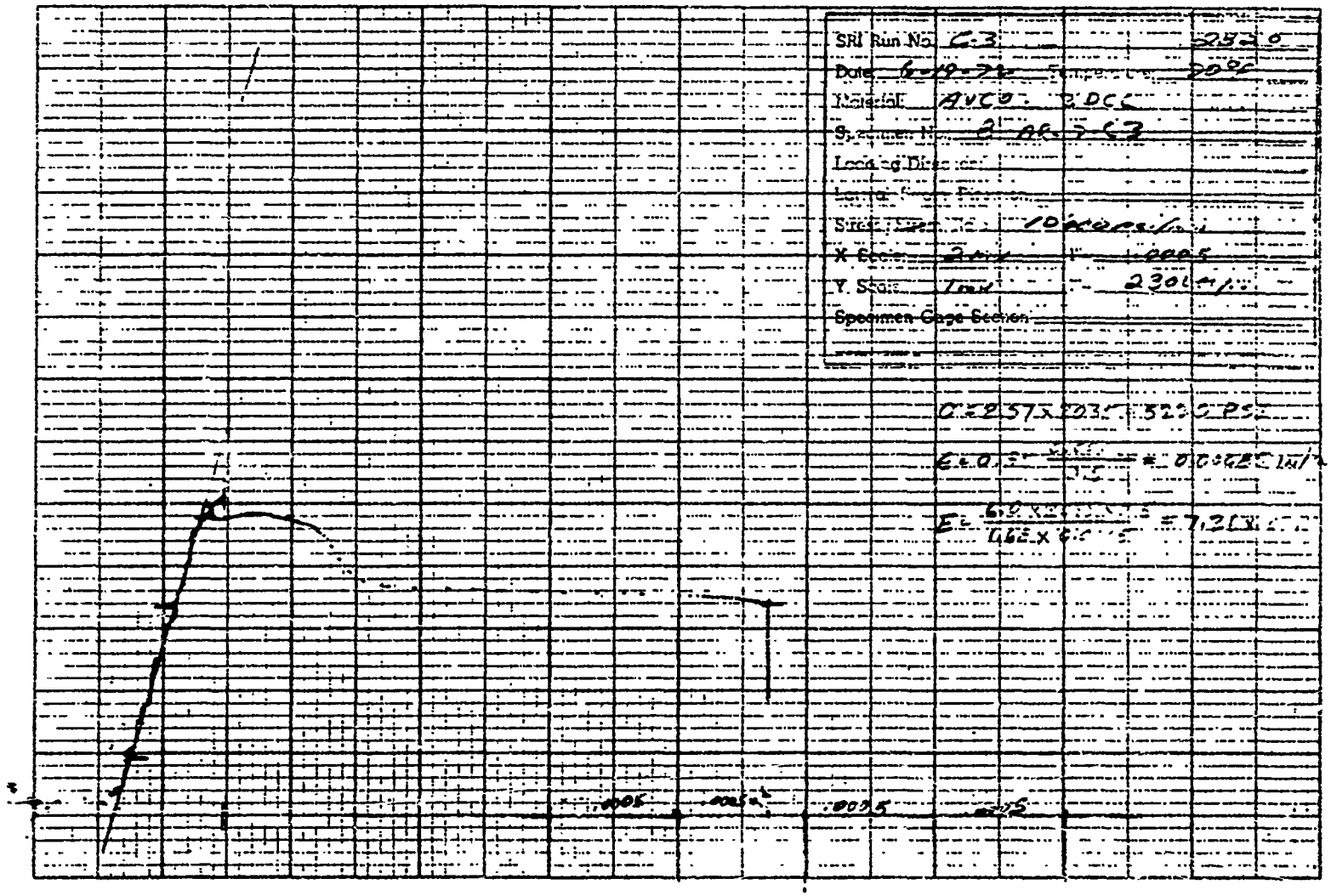
X Scale: 2 ksi/in 1" = .0005

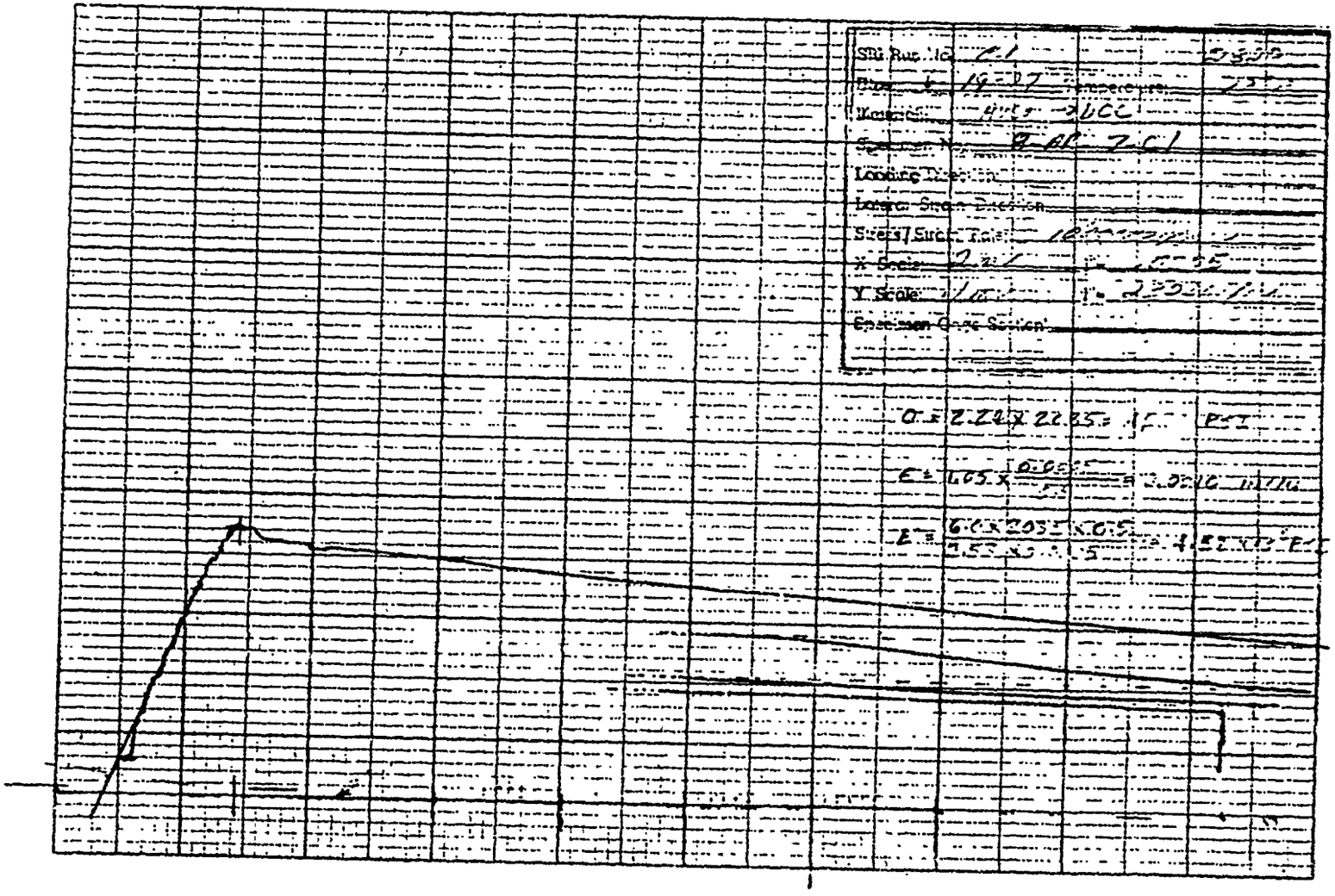
Y Scale: 1 ksi/in 1" = 20.03 ksi

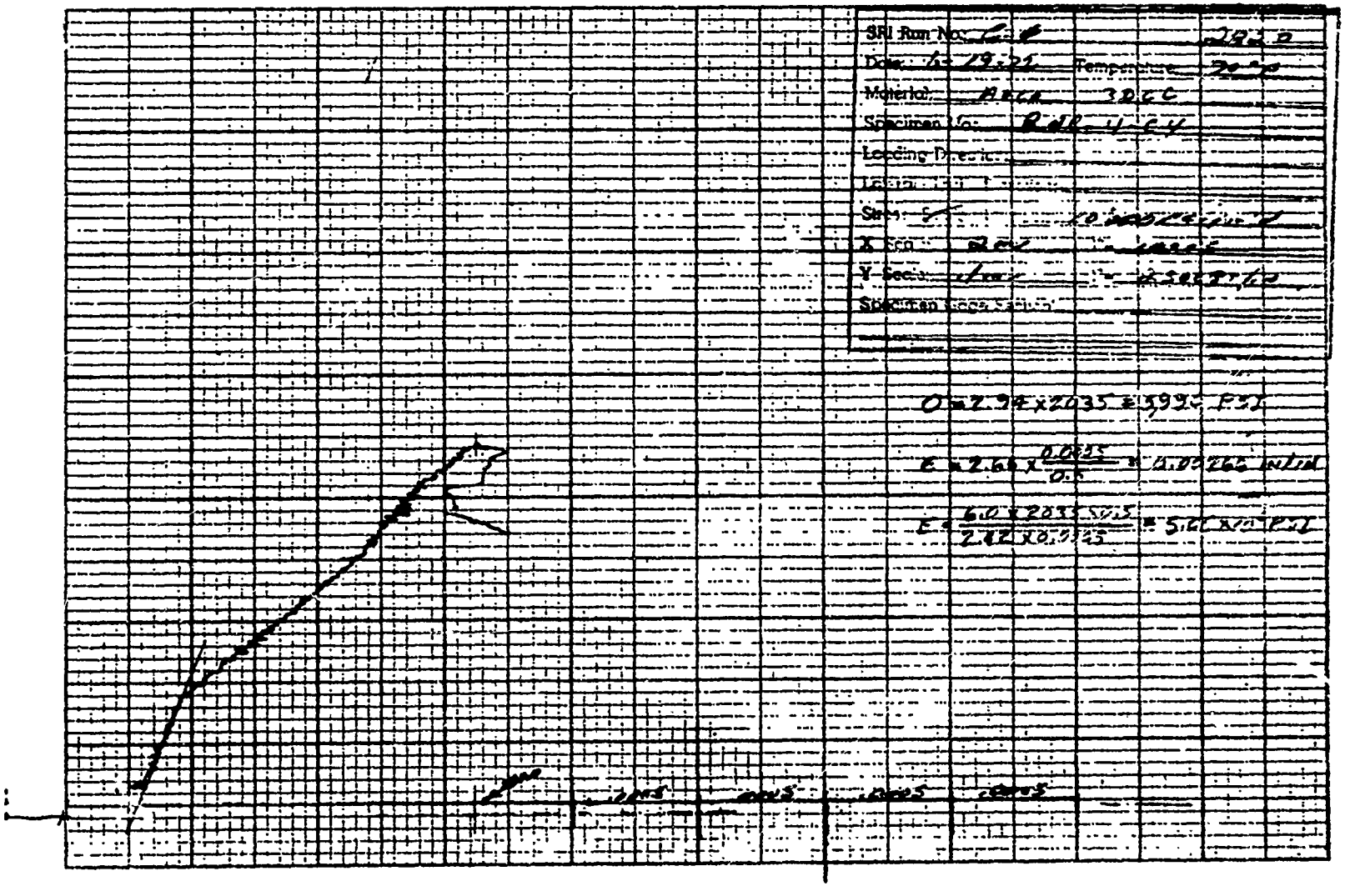
Specimen Gage Section:

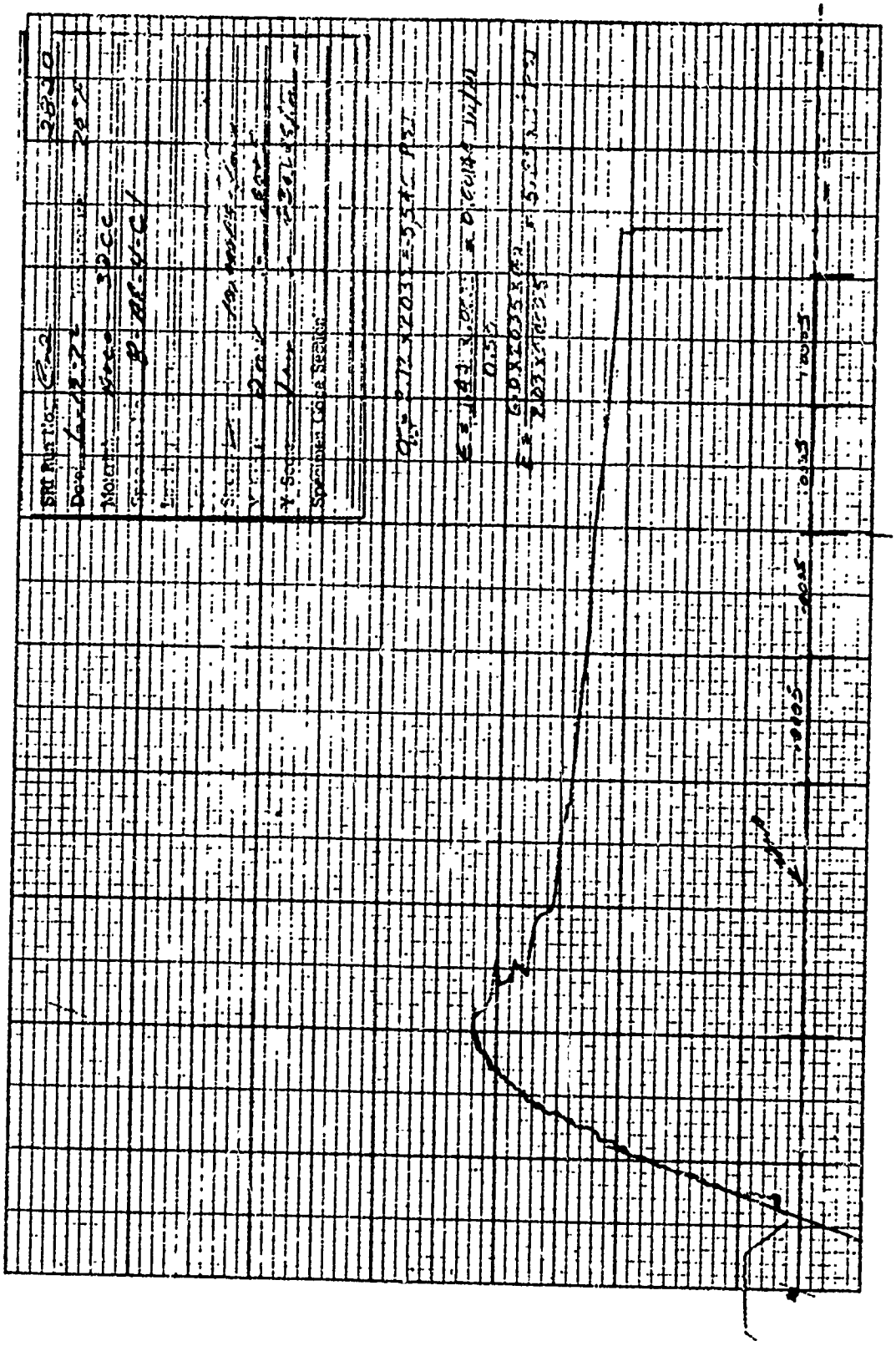


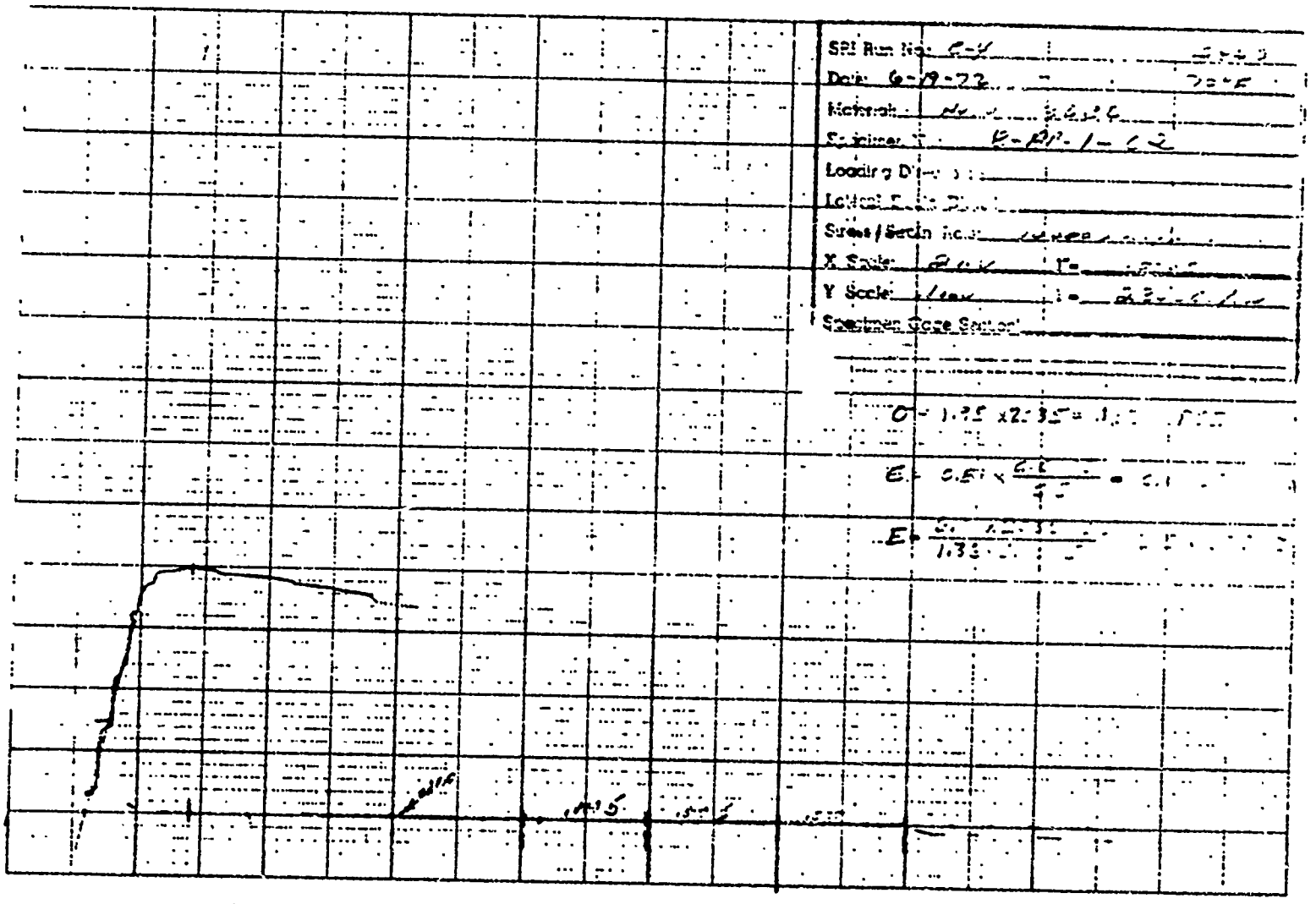

SRI Run No:
Date:
Temperature
Material
Specimen No:
Loading Direction:
Lateral Gage Direction:
Strain Rate:
X Scale:
Y Scale:
Specimen Cross-Section:
σ = 5.34 x 2033 = 10,860 PSI
ε = 13.17 x 0.0005/0.5 = 0.0132 in/in
E = 9.18 x 2033 x 0.5 / 9.18 x 0.0005 = 0.89 x 10^6 PSI
.0025
.0125
.005

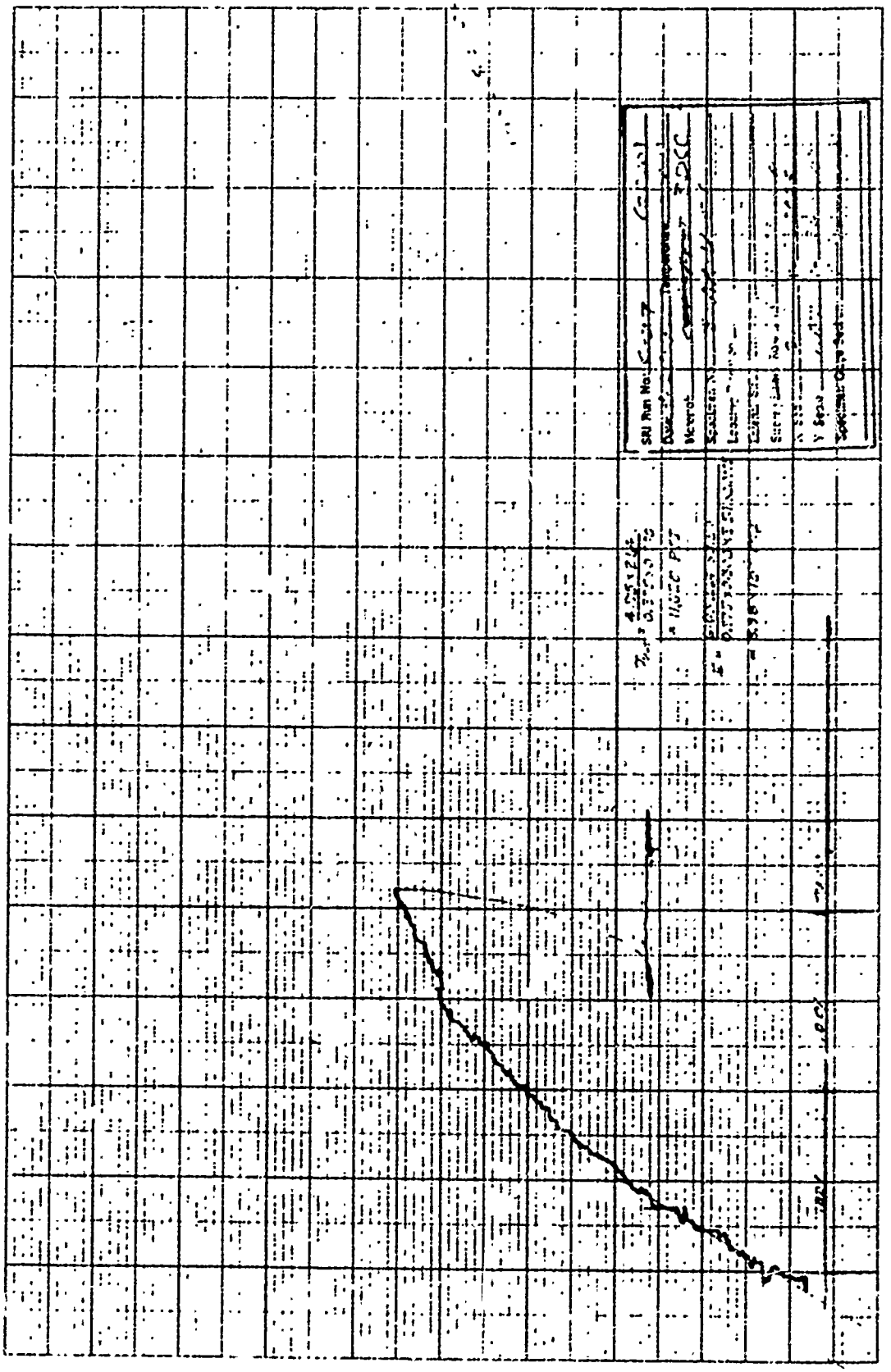

SRI Run No. C-3
Date 6-19-72
Material AVCO 2DC
Specimen No. 2 DC-3-C3
Location Direction
Location from Face
Strain Gage
X Gage
Y Gage
Specimen Gage Section
10 Kpsi/in.
.0005
2300 μ in.
.005
.0025

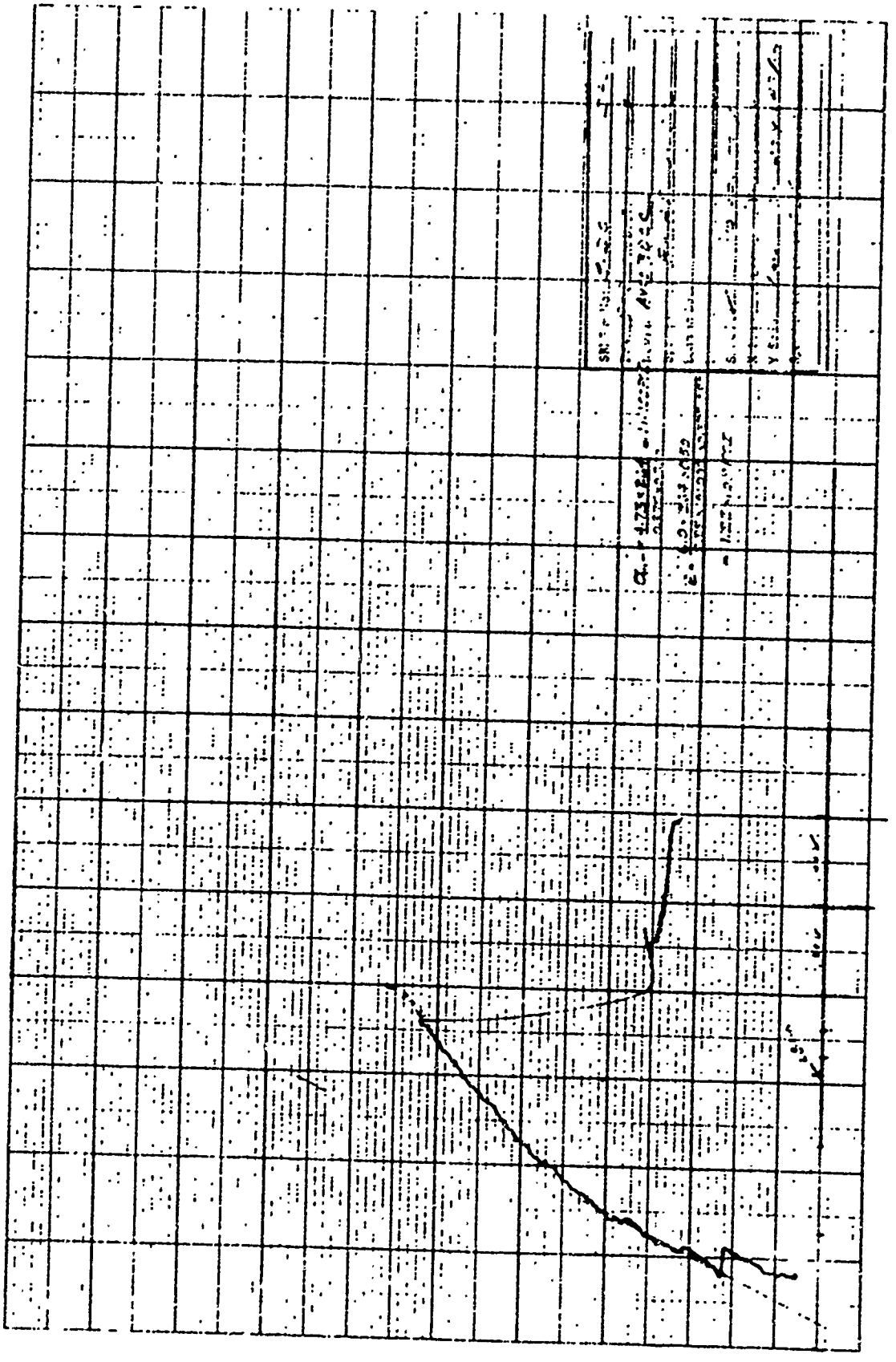

Strain Rate
Temperature
Material
Specimen No.
Loading Direction
Longit. Strain Direction
Stress/Strain Ratio
X Scale
Y Scale
Specimen Gage Section


SRI Run No:
Date:
Temperature
Material:
Specimen No:
Loading Direction
Size:
X Scale
Y Scale
Specimen Description
400



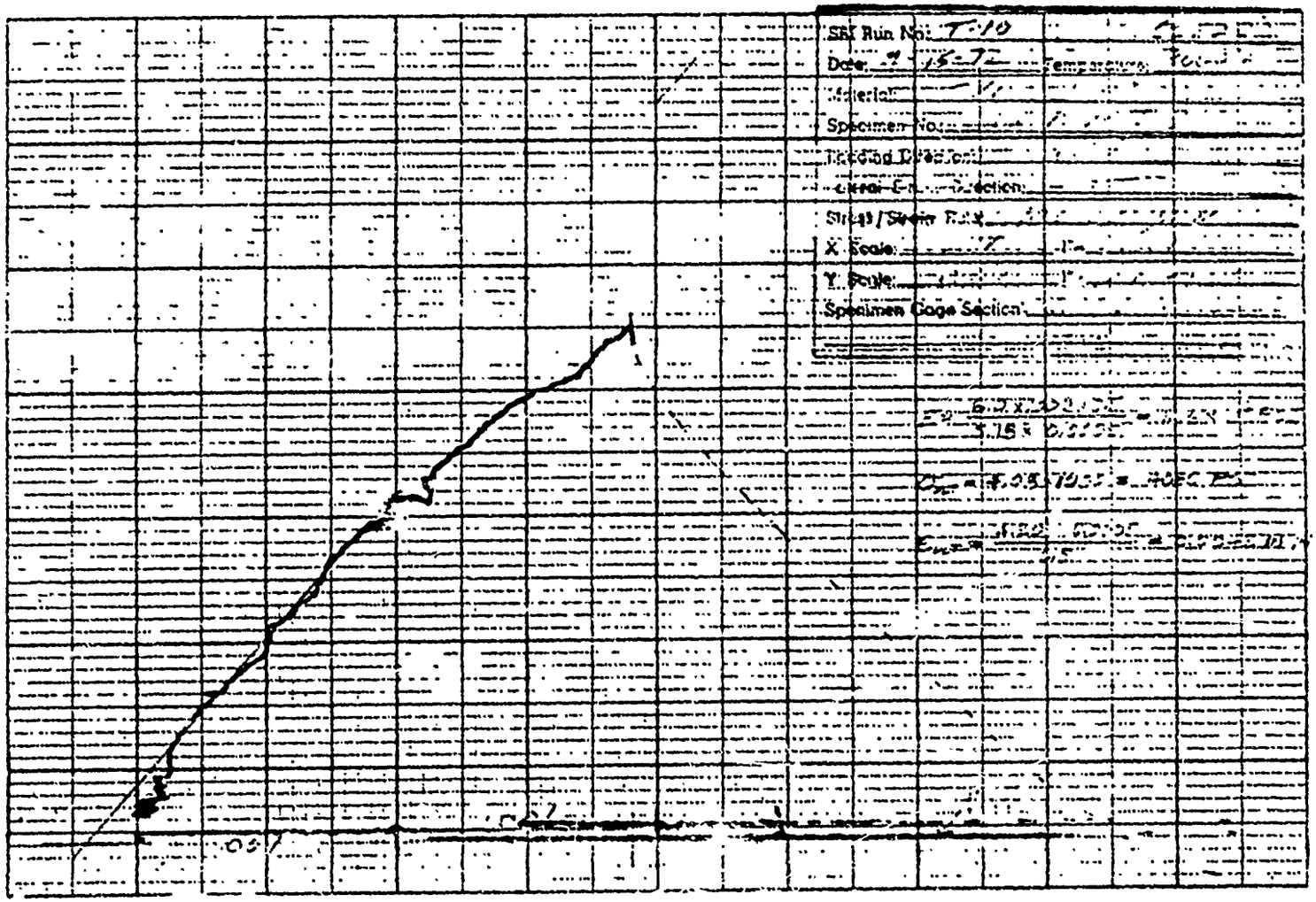

Date: 6-19-22
Material:
Loading Direction:
Stress/Section Inc.:
X Scale:
Y Scale:
Specimen Gage Section:
E = 0.5 x
E =

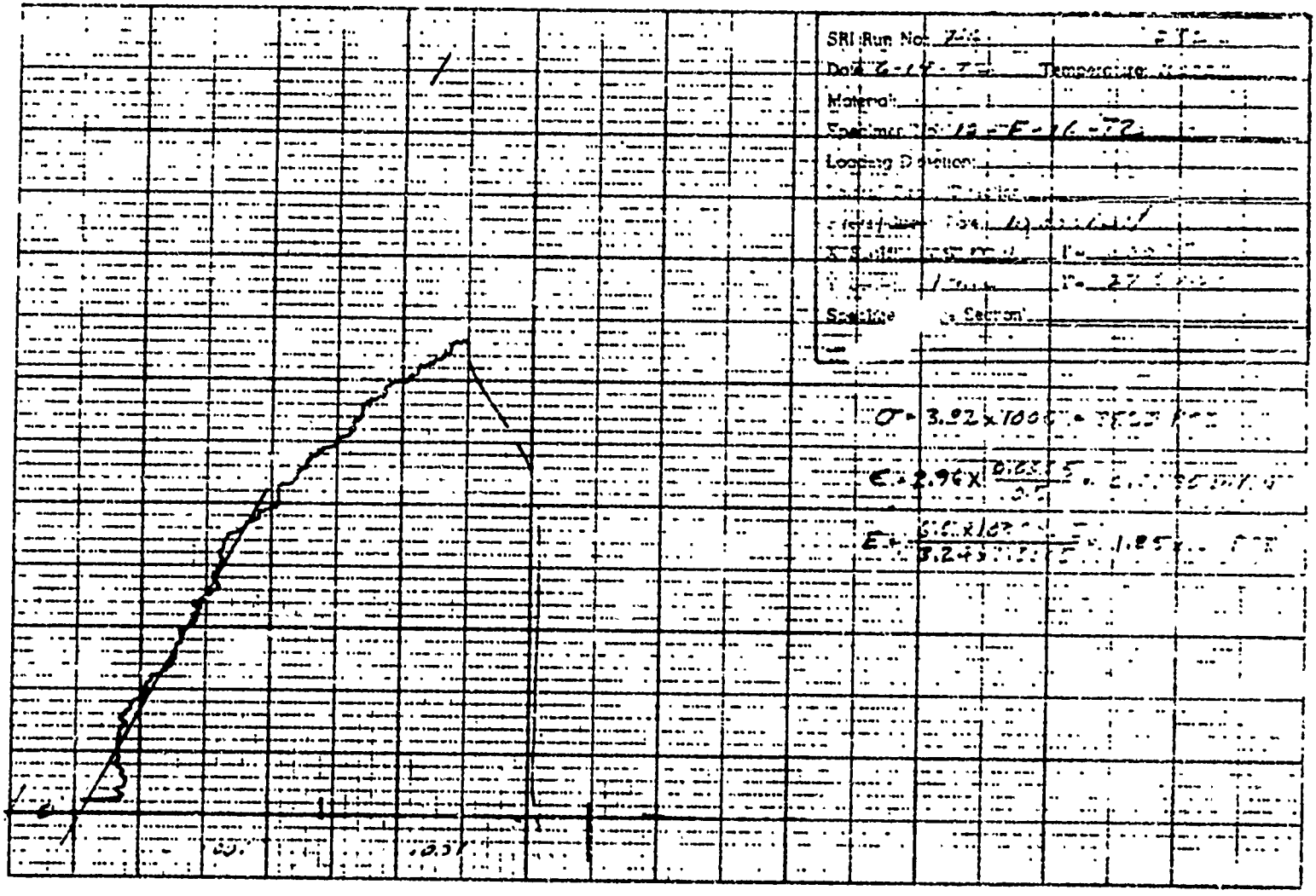


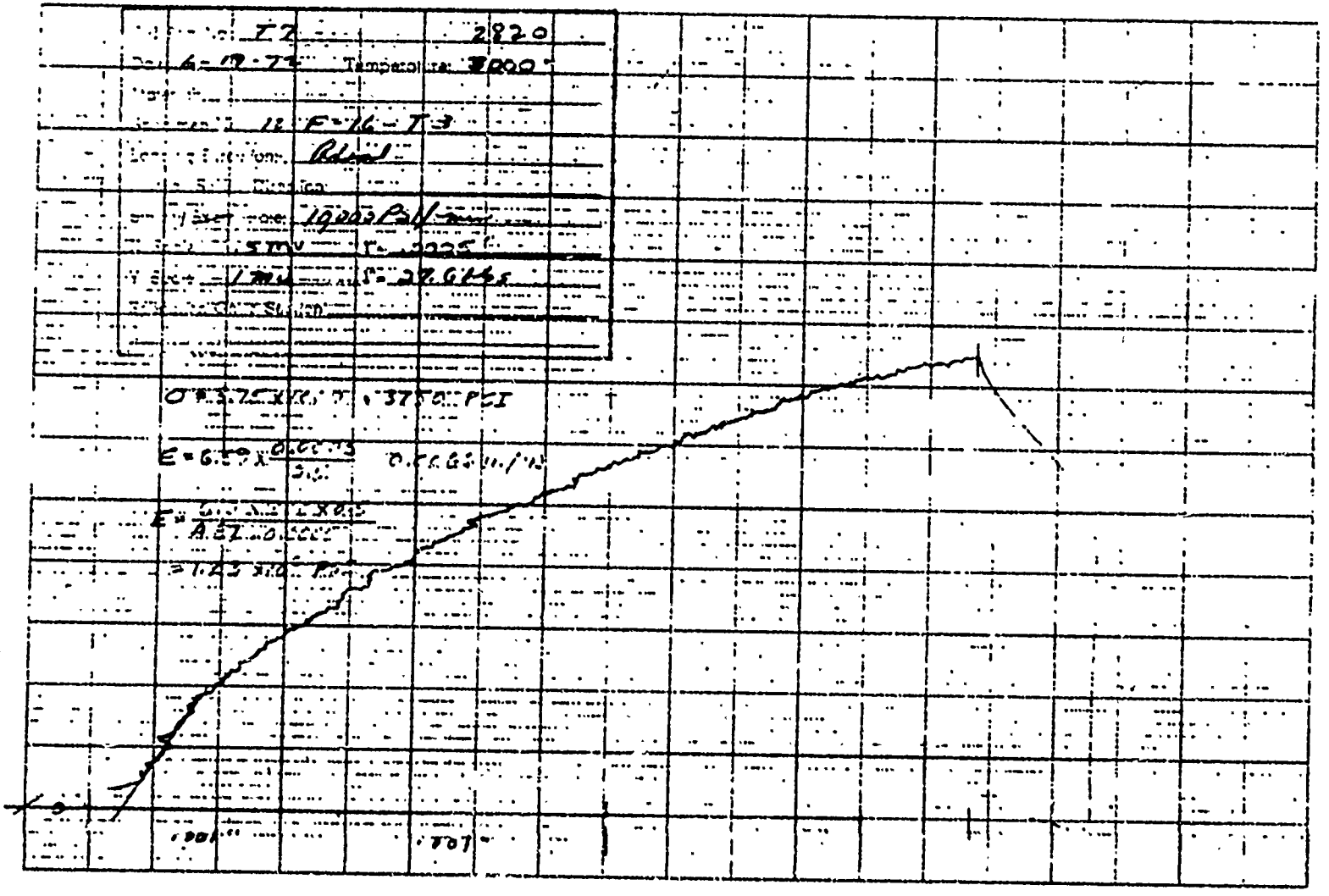


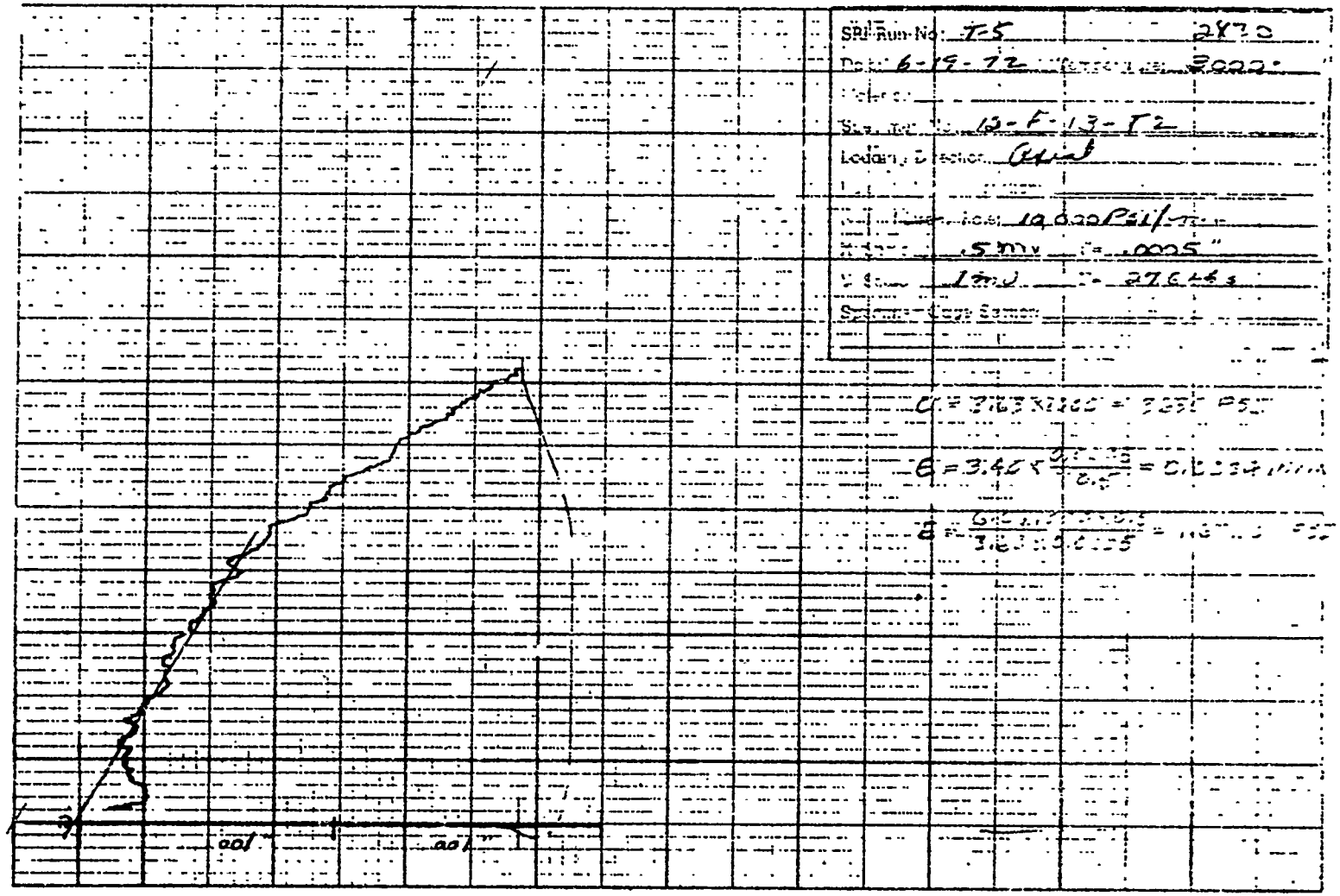
APPENDIX H

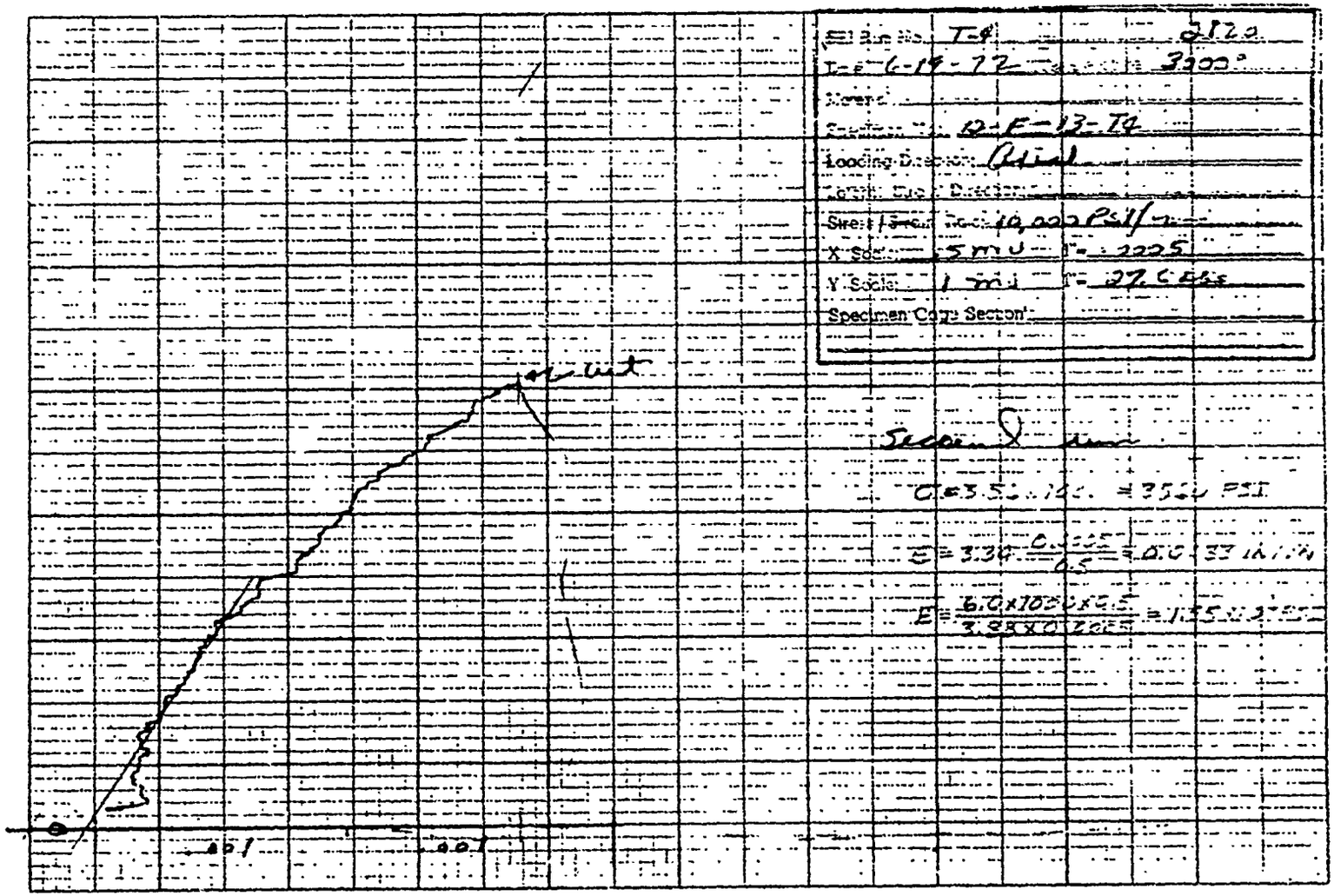
TENSILE AND COMPRESSIVE STRESS-STRAIN CURVES FOR SANDIA FELT CC - MATERIAL 12

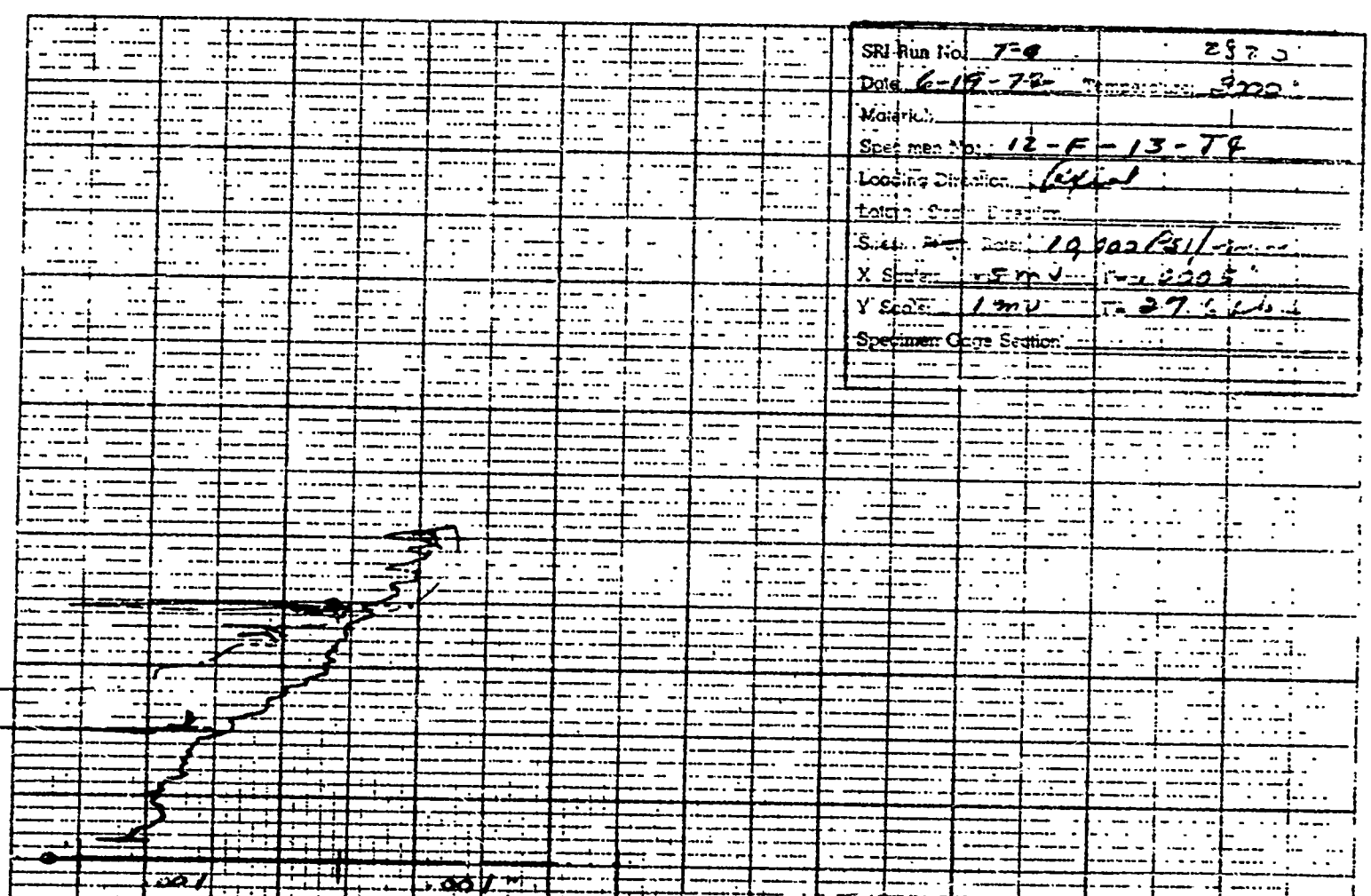

SRI Run No: T-10
Date: 4-15-72
Material:
Specimen No:
Loading Direction:
Load-Extension:
Stress/Strain Rate:
X Scale:
Y Scale:
Specimen Gage Section:


SRI Run No:
Date:
Temperature:
Material:
Specimen No:
Loading Direction:
Specimen
Section
σ = 3.92 x 100
ε = 2.96 x
E = 6.6 x 10
3.243

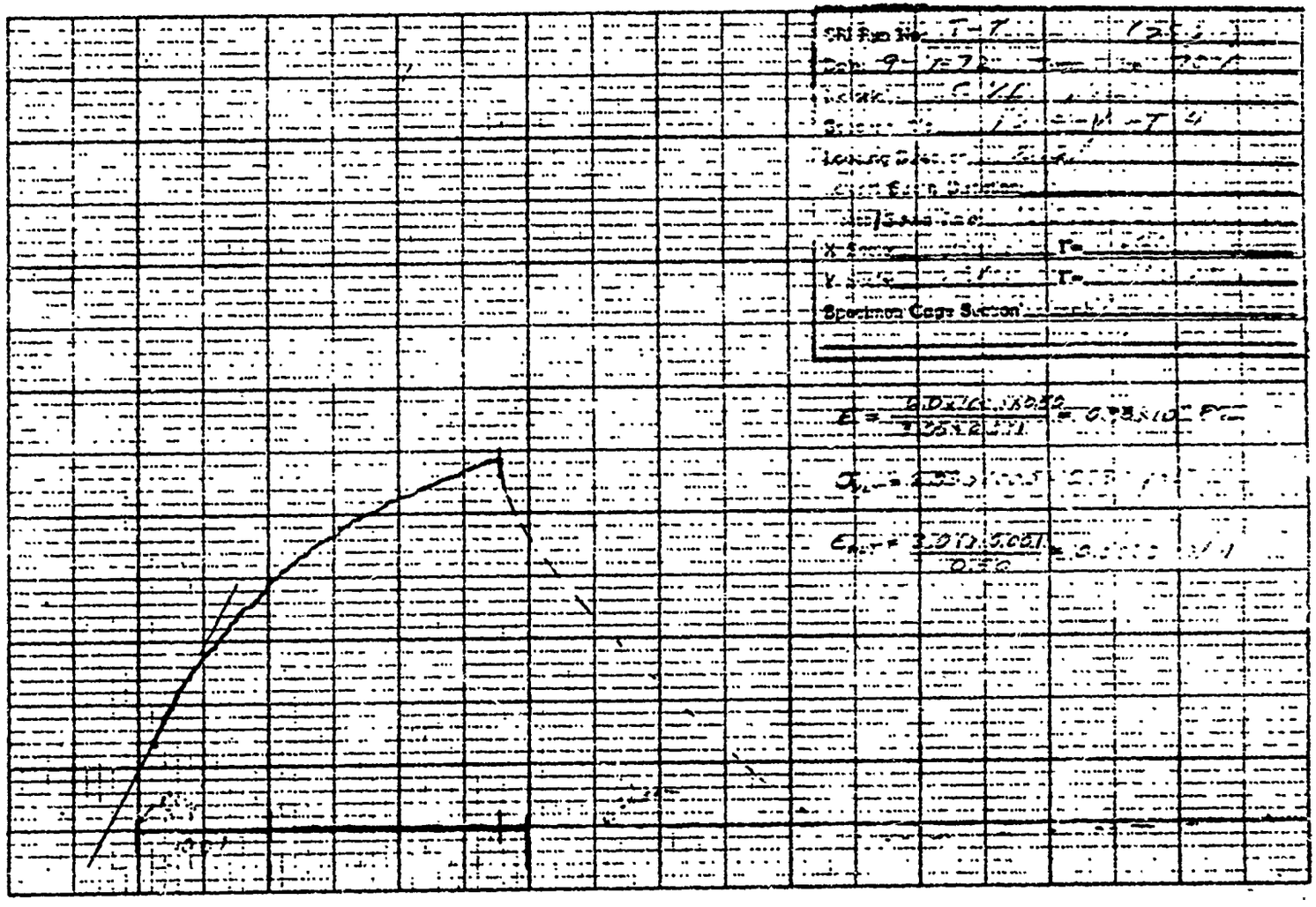

T2 2820
Temperature 2800°
Alloy
Tensile Strength 19000 Psi
Yield Strength
.901"
.907"

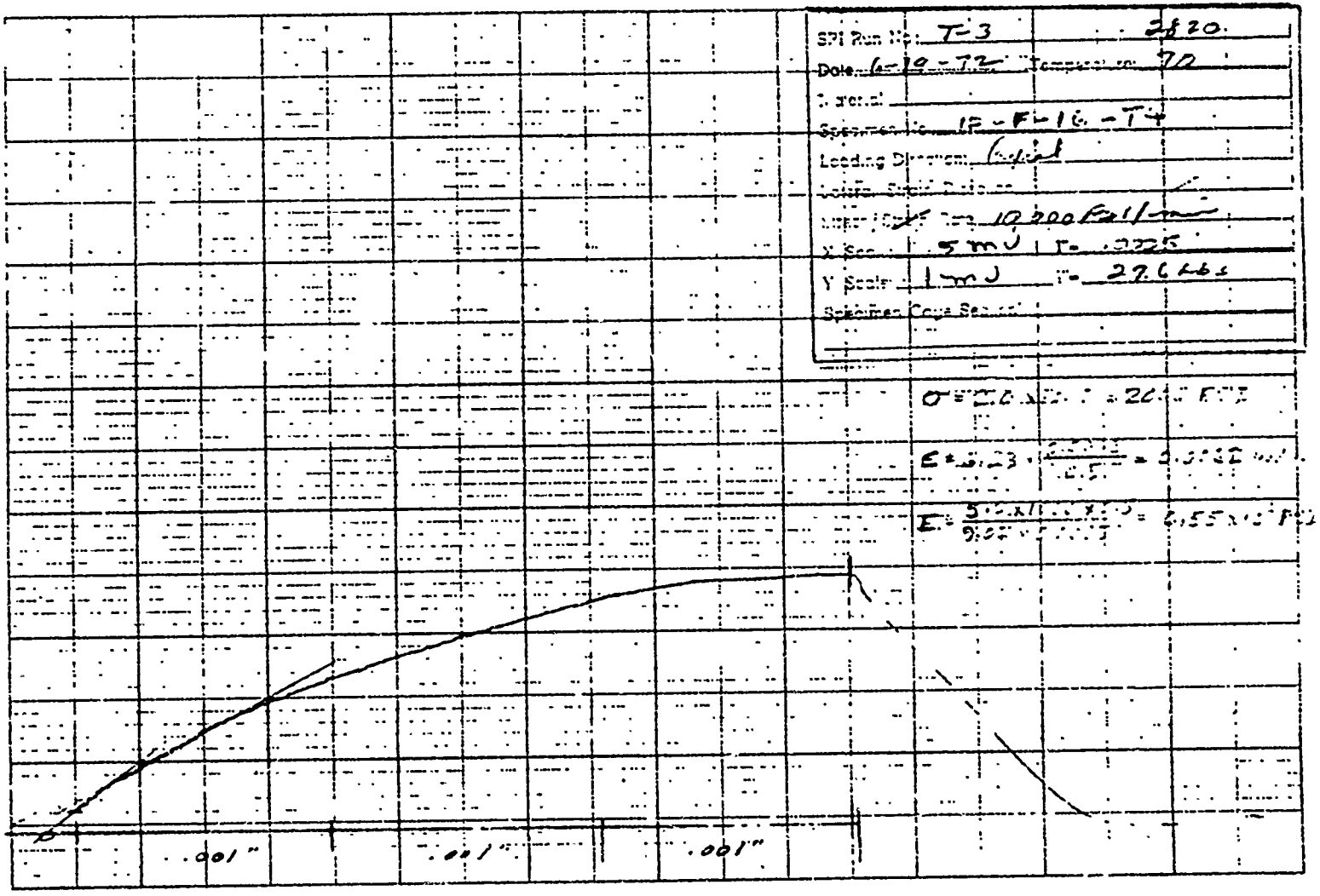

SRI Run No: T-5
2870
Date: 6-19-72
Load: 19,020 Psi/Tr
.5mv
.0025"
1mv
Sample Dia: 2.000"
Loading Direction: Axial
Test Type: 12-6-13-72
001
001

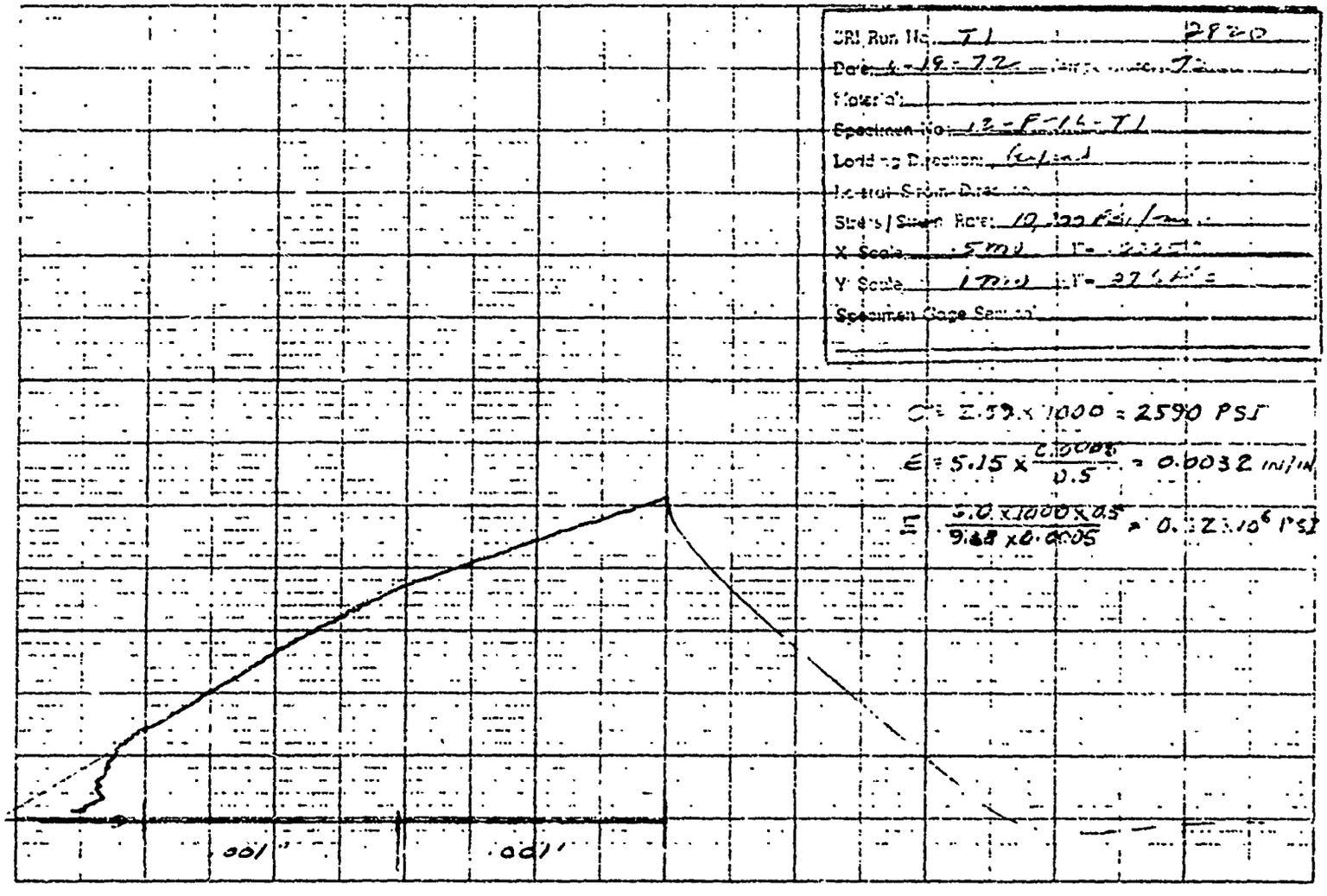

Spec No. T-9
T-E 6-19-72
Material
Condition W-E-13-T9
Loading Direction Radial
Strain Rate Direction
Stress / Strain Rate 10,000 PSI/min
X Scale .5 min = 1" = .1225
Y Scale 1 min = 1" = 27,648
Specimen Cross Section
Second Cycle
E = 3.34 × 10⁶ PSI

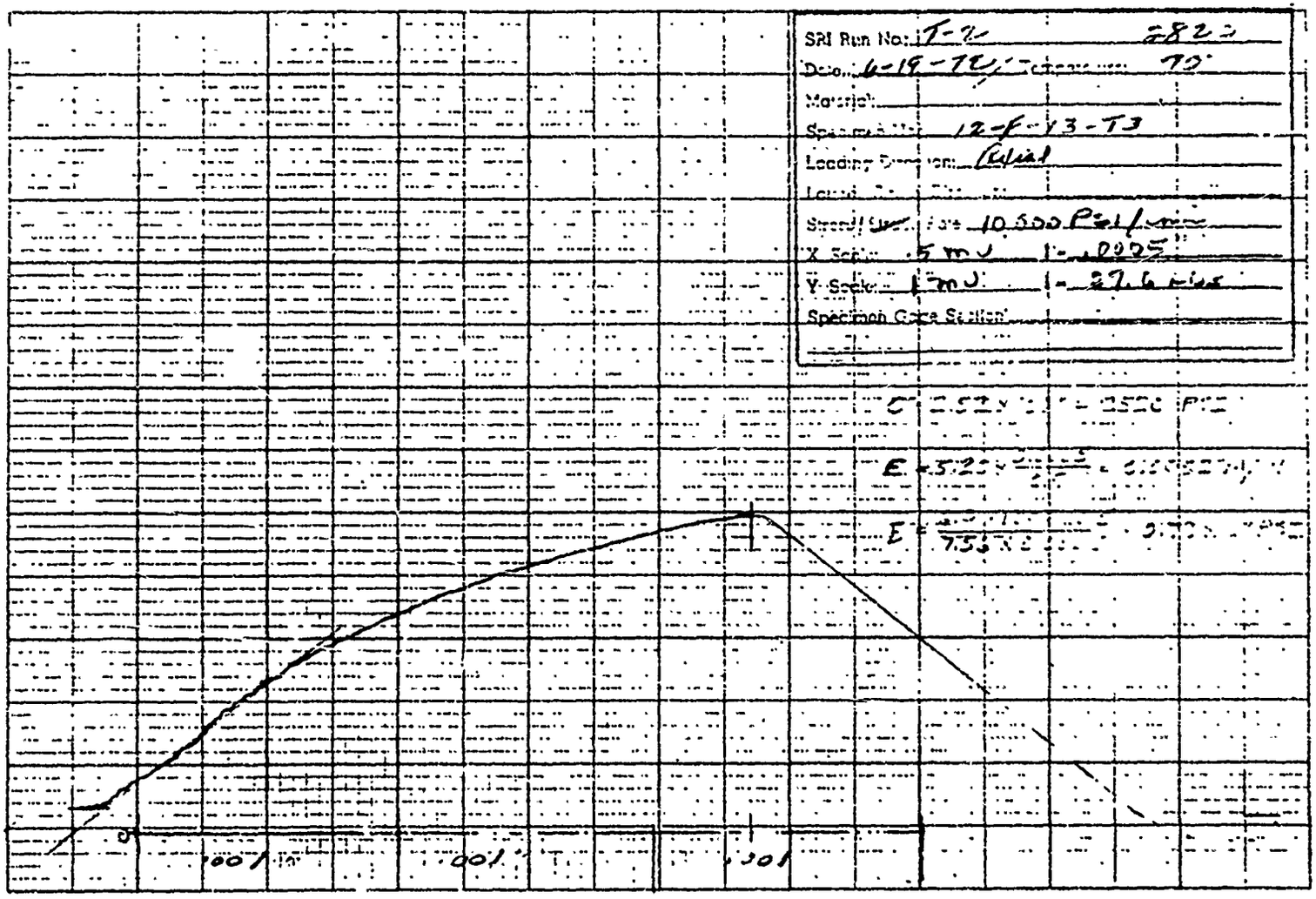

SRI Run No: T-9
Date: 6-19-78
Material:
Specimen No: 12-F-13-T4
Loading Direction: Lateral
Testing Temperature:
Strain Rate: 10 in/in/sec
X Scale: 5 mV
Y Scale: 1 mV
Specimen Gage Section:
.001
.001

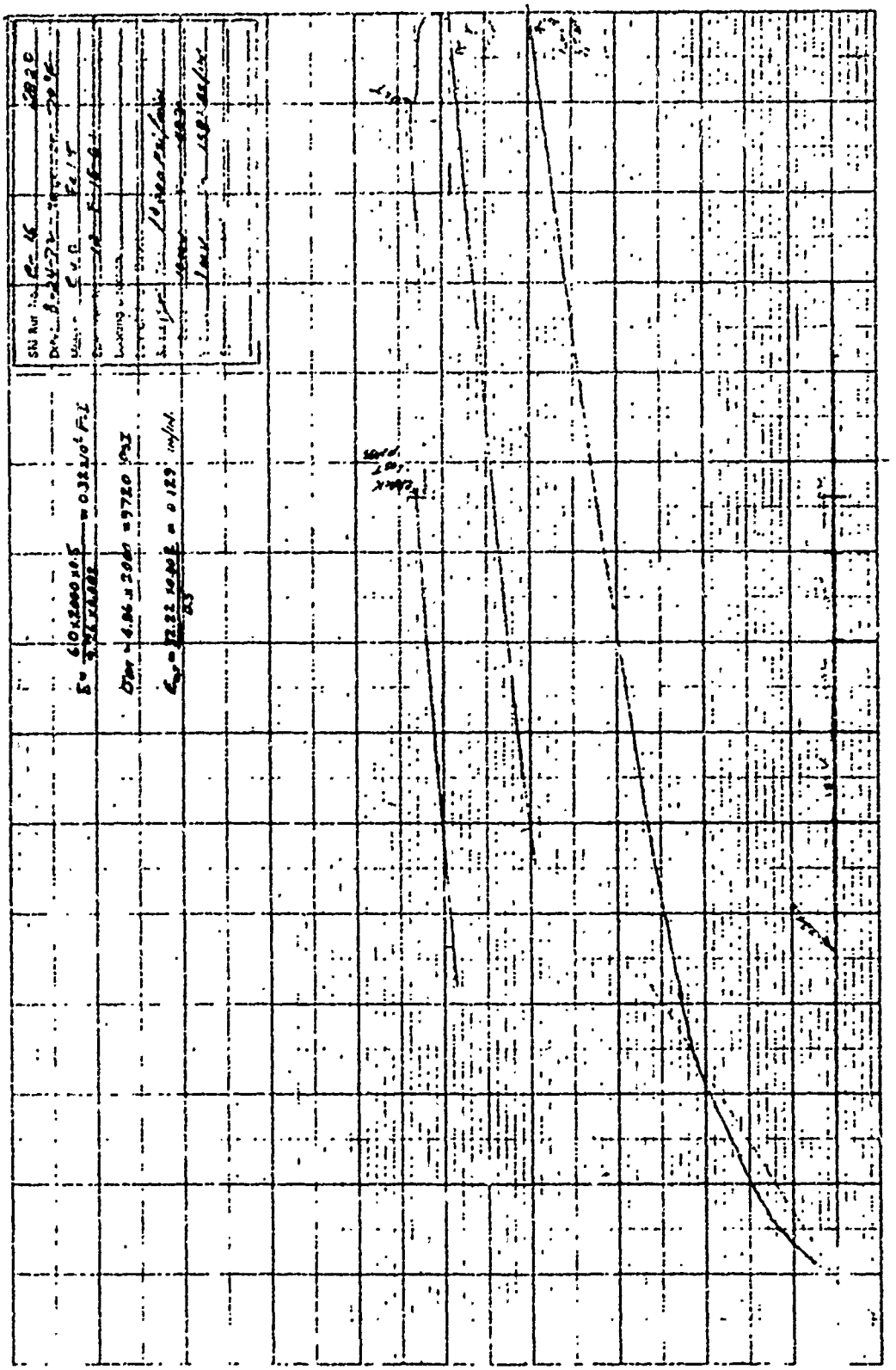
412

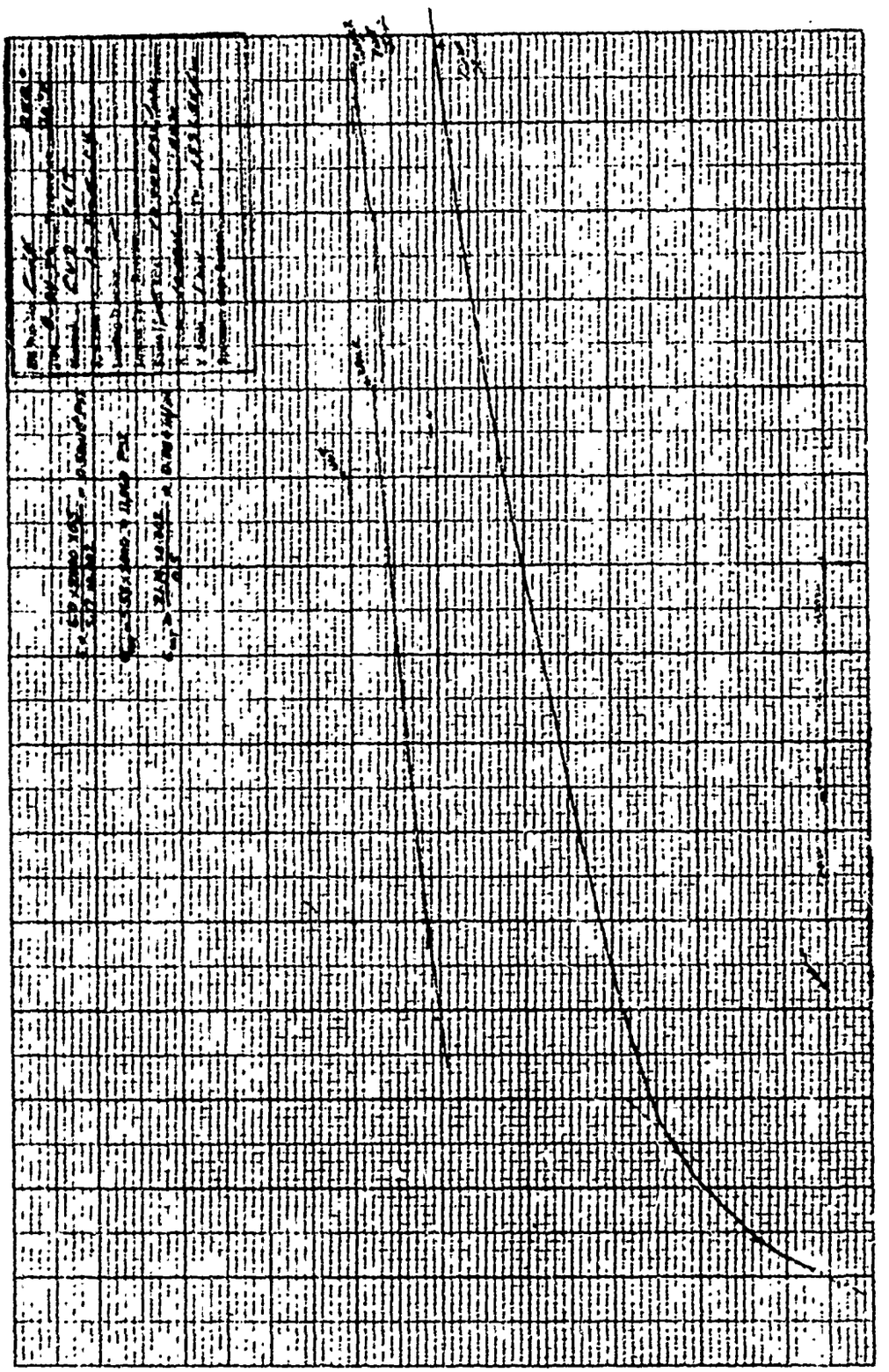

Specimen Cage Section

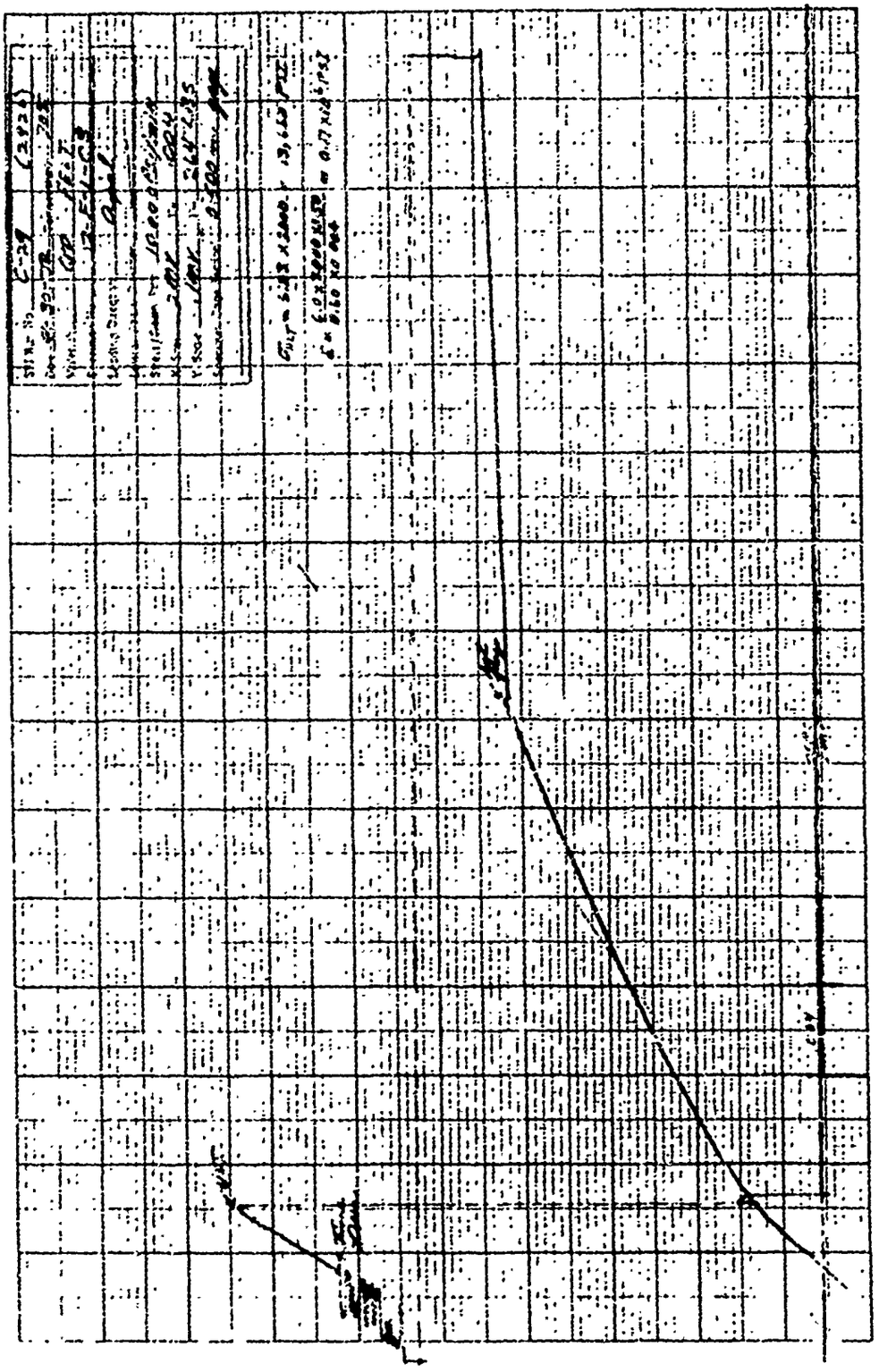

SPI Run No: T-3
Date: 6-19-72
Specimen No: 1F-F-16-T4
Loading Direction: Radial
Upper Cut-off Freq: 10,000 Full-min
X Scale: 5 mJ
Y Scale: 1 mJ
.001"
.001"
.001"

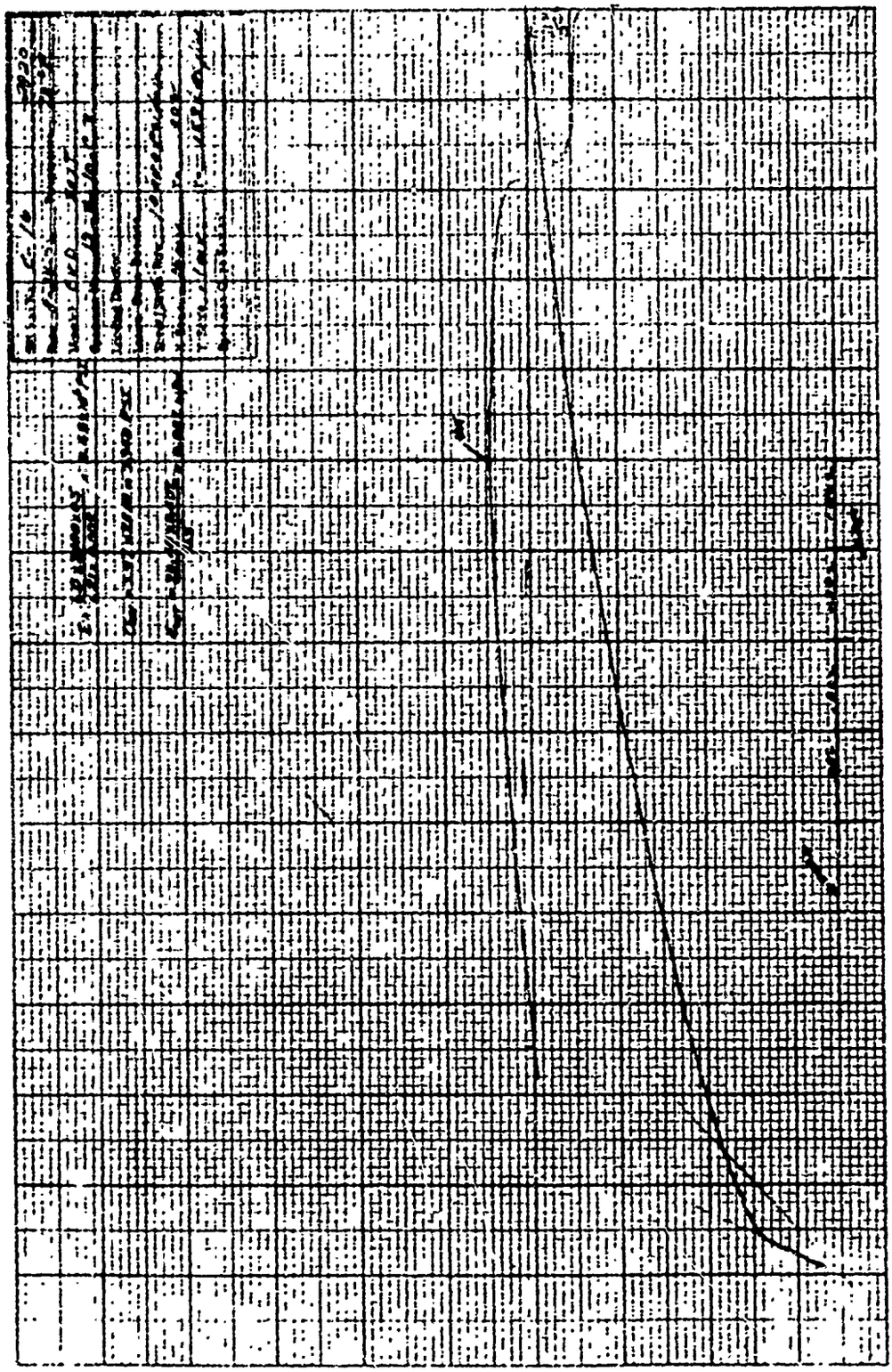

SRI Run No. T1
Date: 6-19-72
Material:
Specimen No: 12-F-16-T1
Loading Direction: Radial
Strain/Strain Rate:
X Scale: .5 mV
Y Scale: 1 mV
Specimen Gage Section
σ = 2.59 x 1000 = 2590 PSI
ε = 5.15 x .00005/0.5 = 0.0032 in/in
E = 5.0 x 1000 x 0.5 / 9.88 x 0.0005 = 0.51 x 10^6 PSI
.001"
.001"

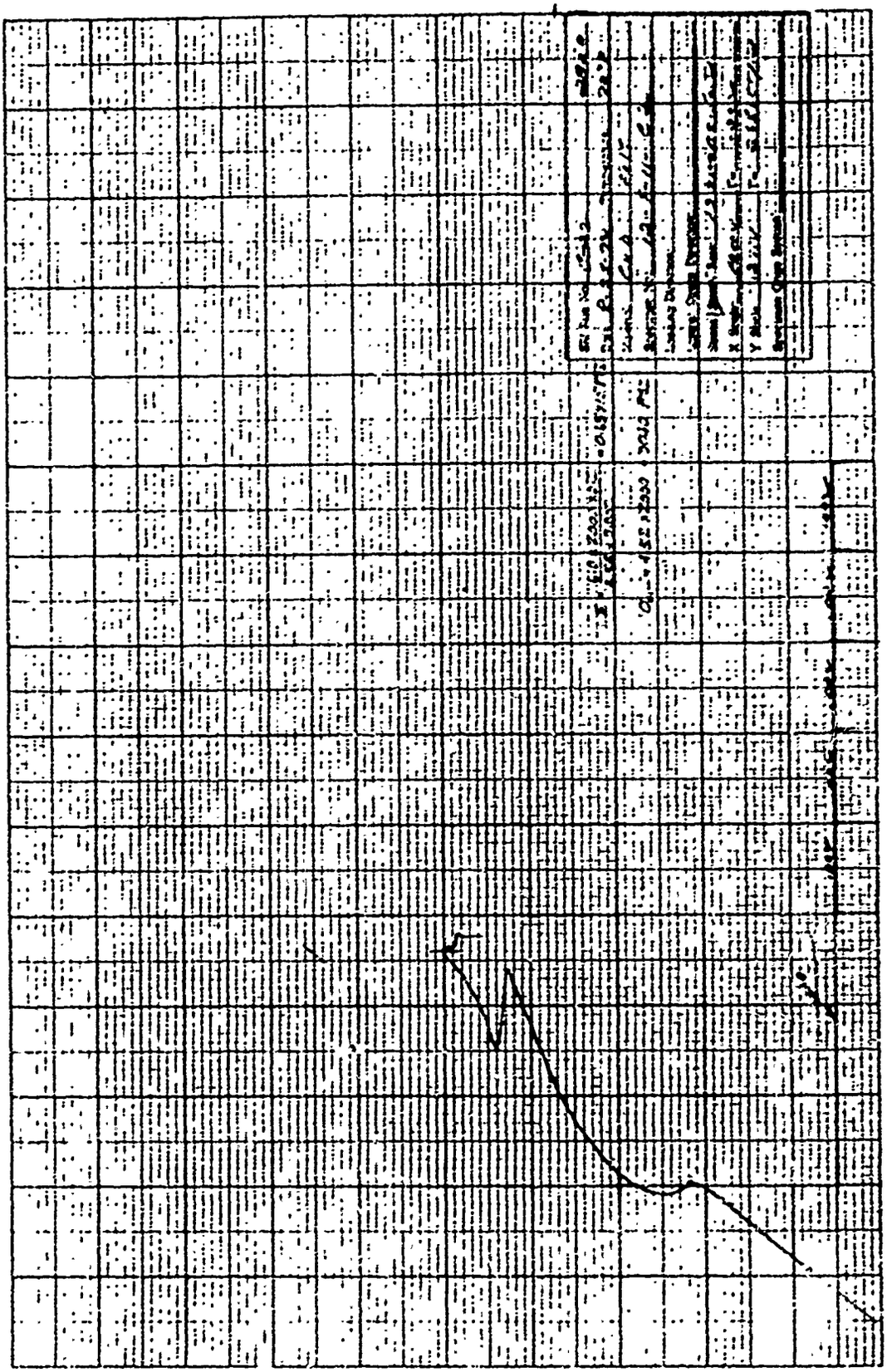

SRI Run No: T-7- 2822
Date: 6-19-72 Temp: 75°
Material:
Specimen No: 12-F-Y3-T3
Loading Direction: Radial
Location:
Speed/Cycles: Rate 10,500 Psi/min
X Scale: .5 mV 1" = .025"
Y Scale: 1 mV 1" = 27.6 ksi
Specimen Gage Section:
E = 7.55 x
0
.001"
.001"
.001"

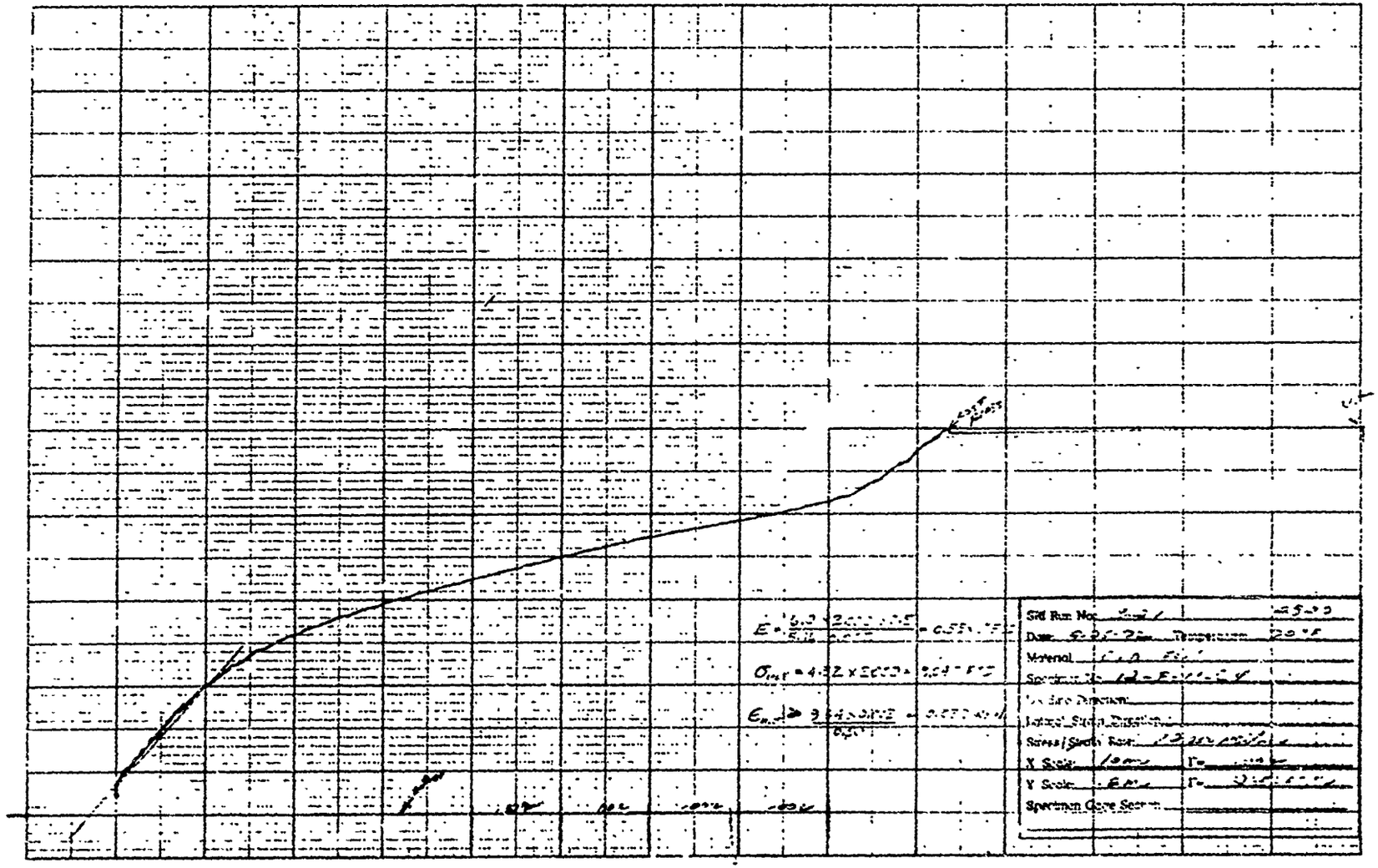


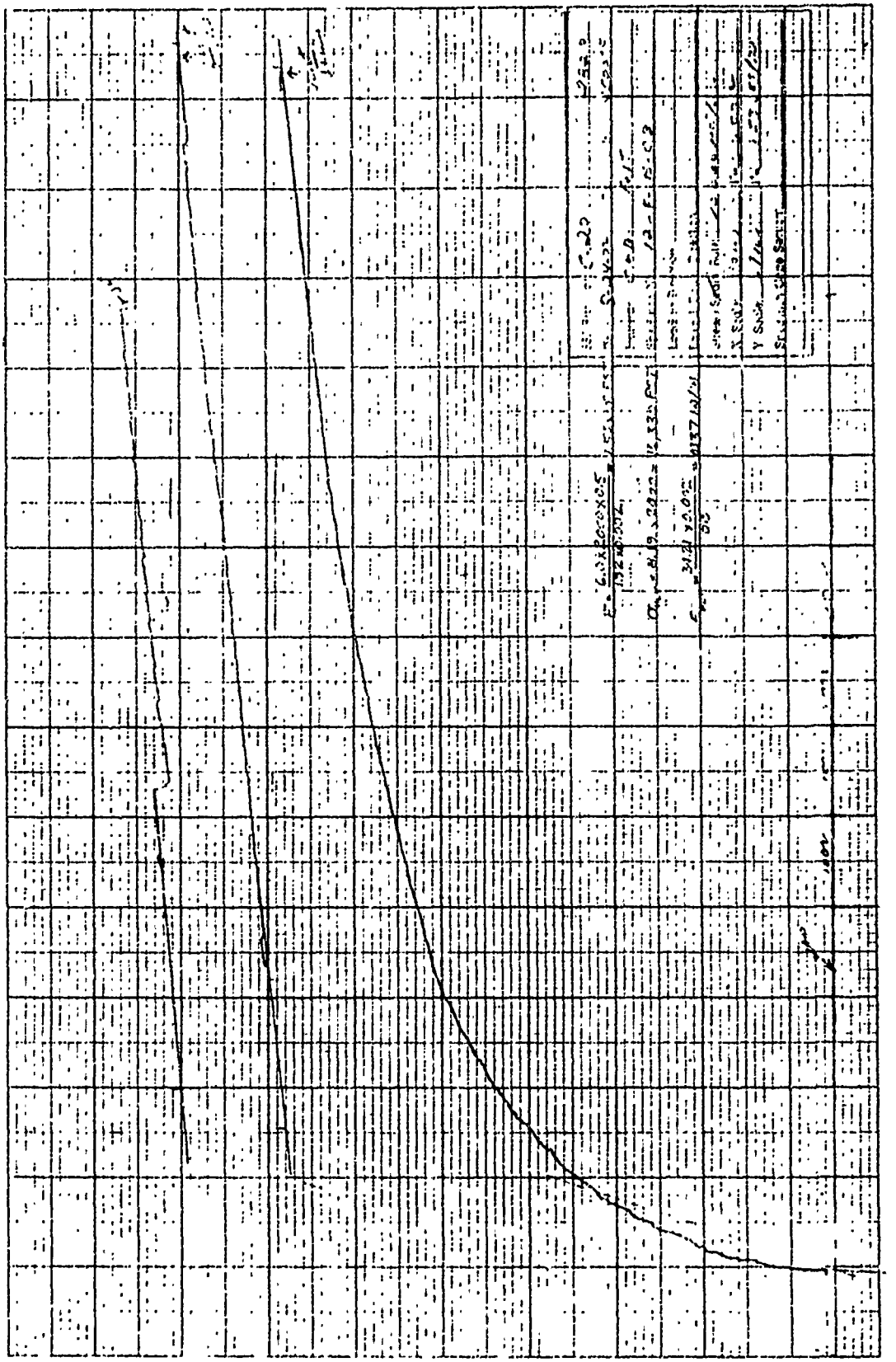


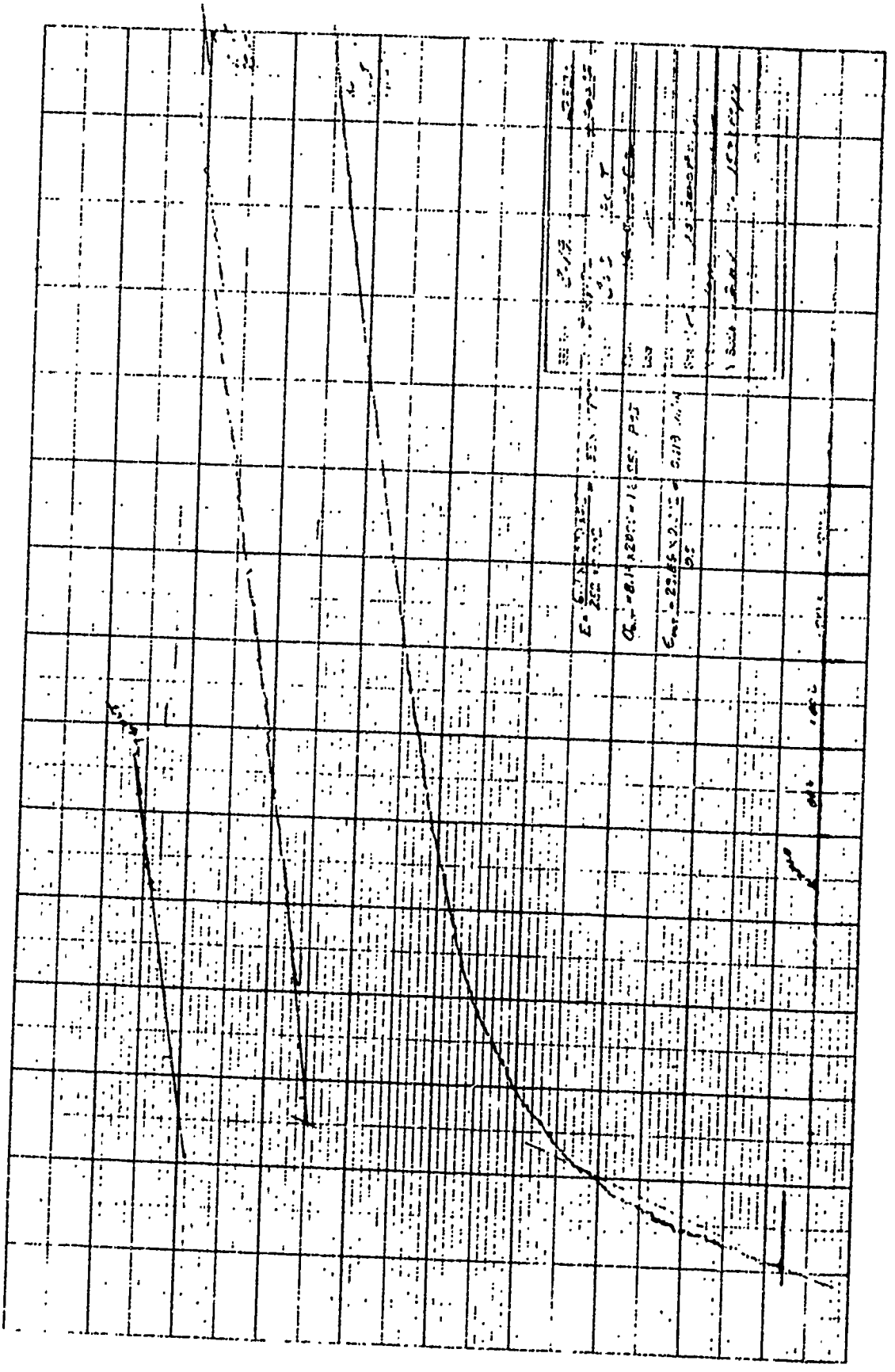


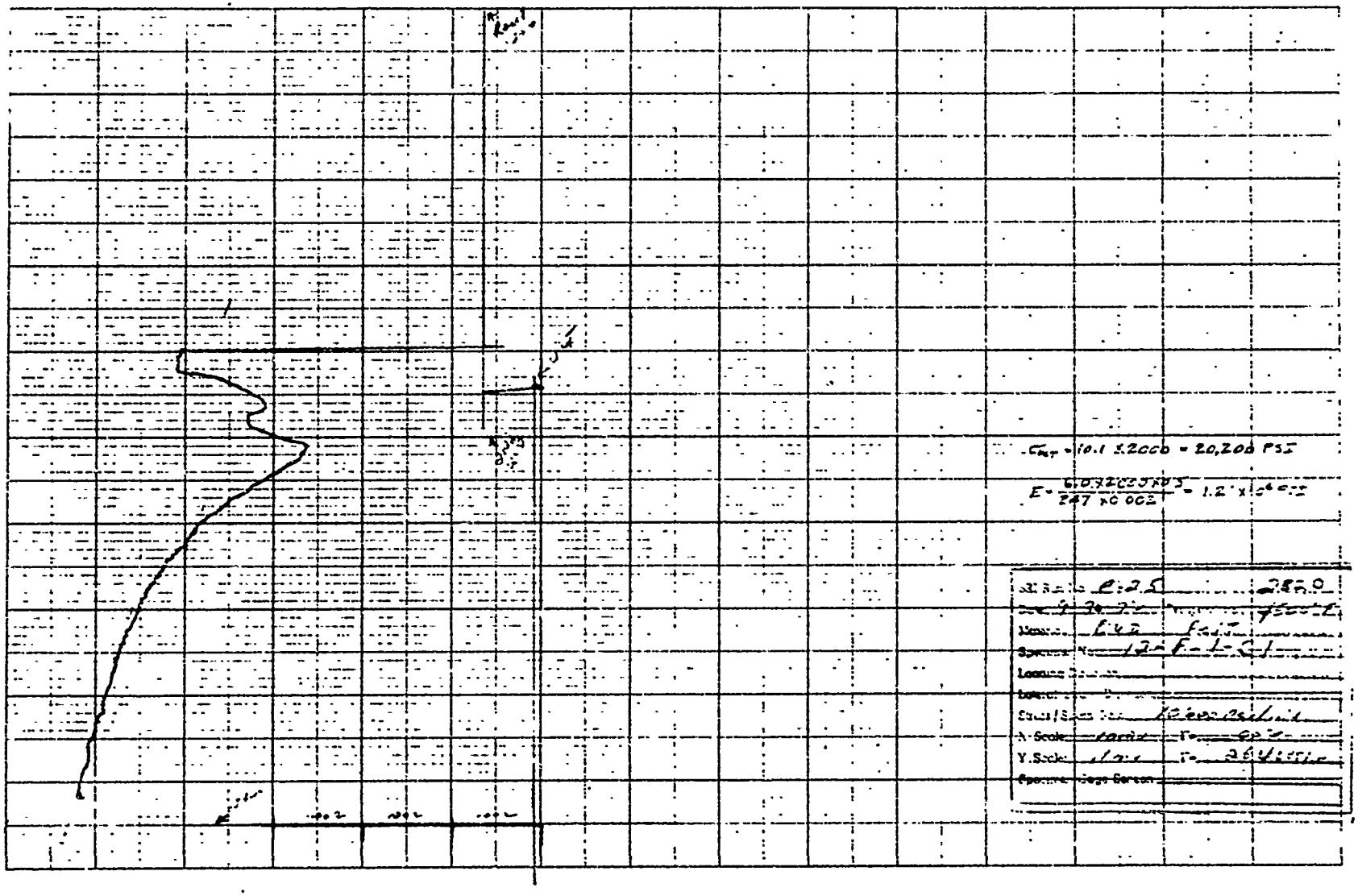


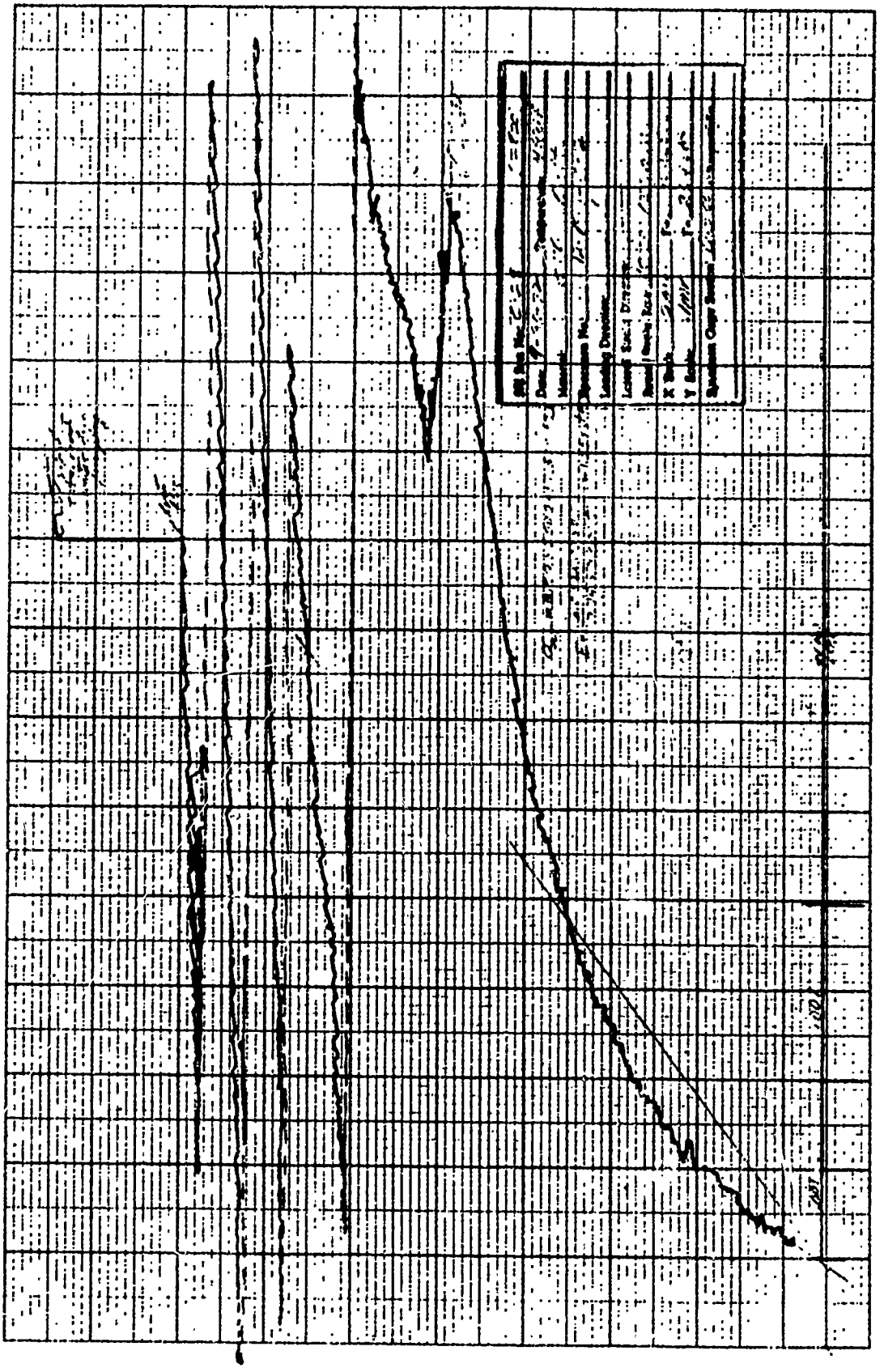


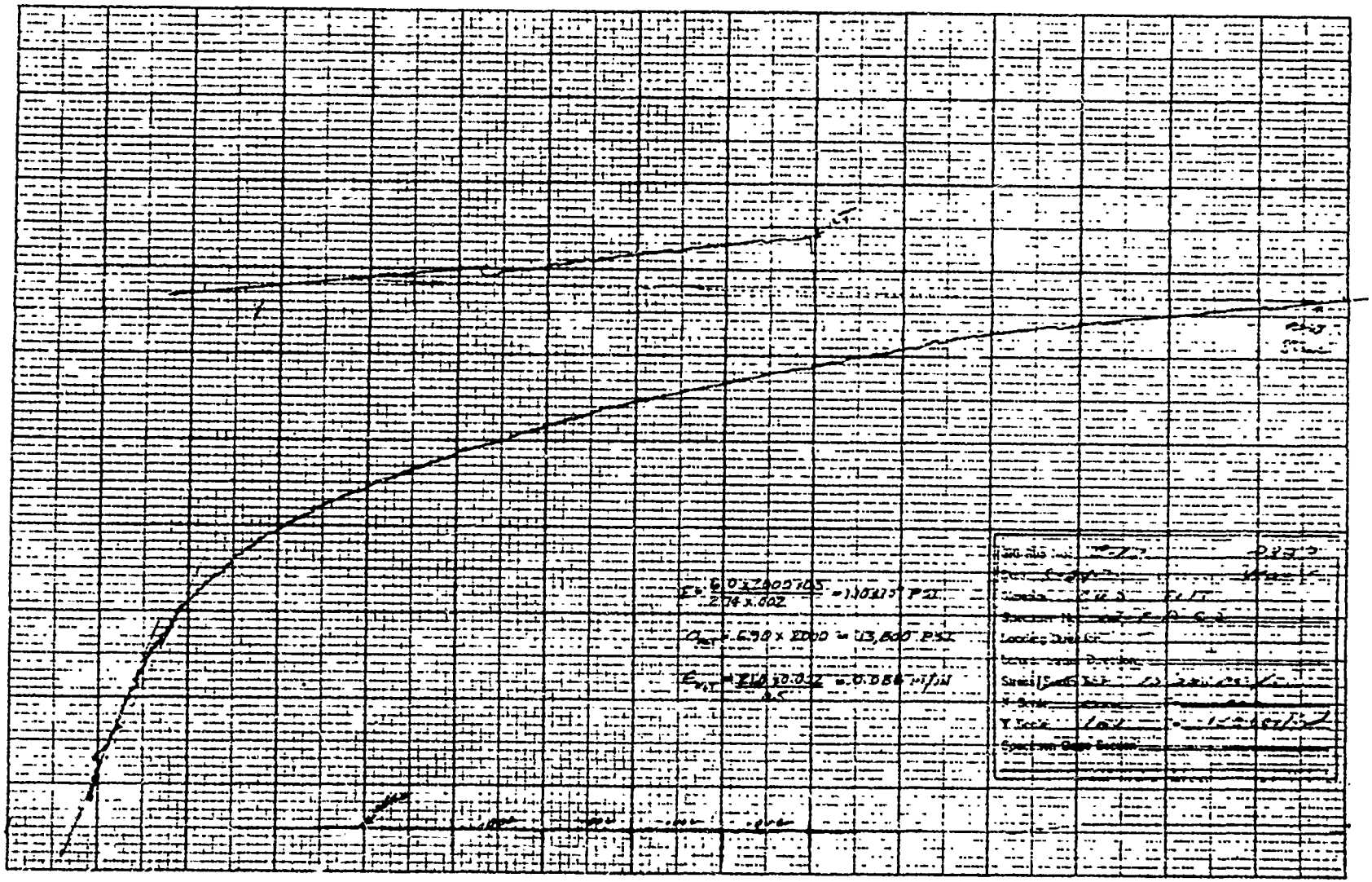

Std Run No:
Date:
Temperature:
Material:
Specimen No:
Test Axis Direction:
Initial Strain Direction:
Stress / Strain Rate:
X Scale:
Y Scale:
Specimen Gage Section:

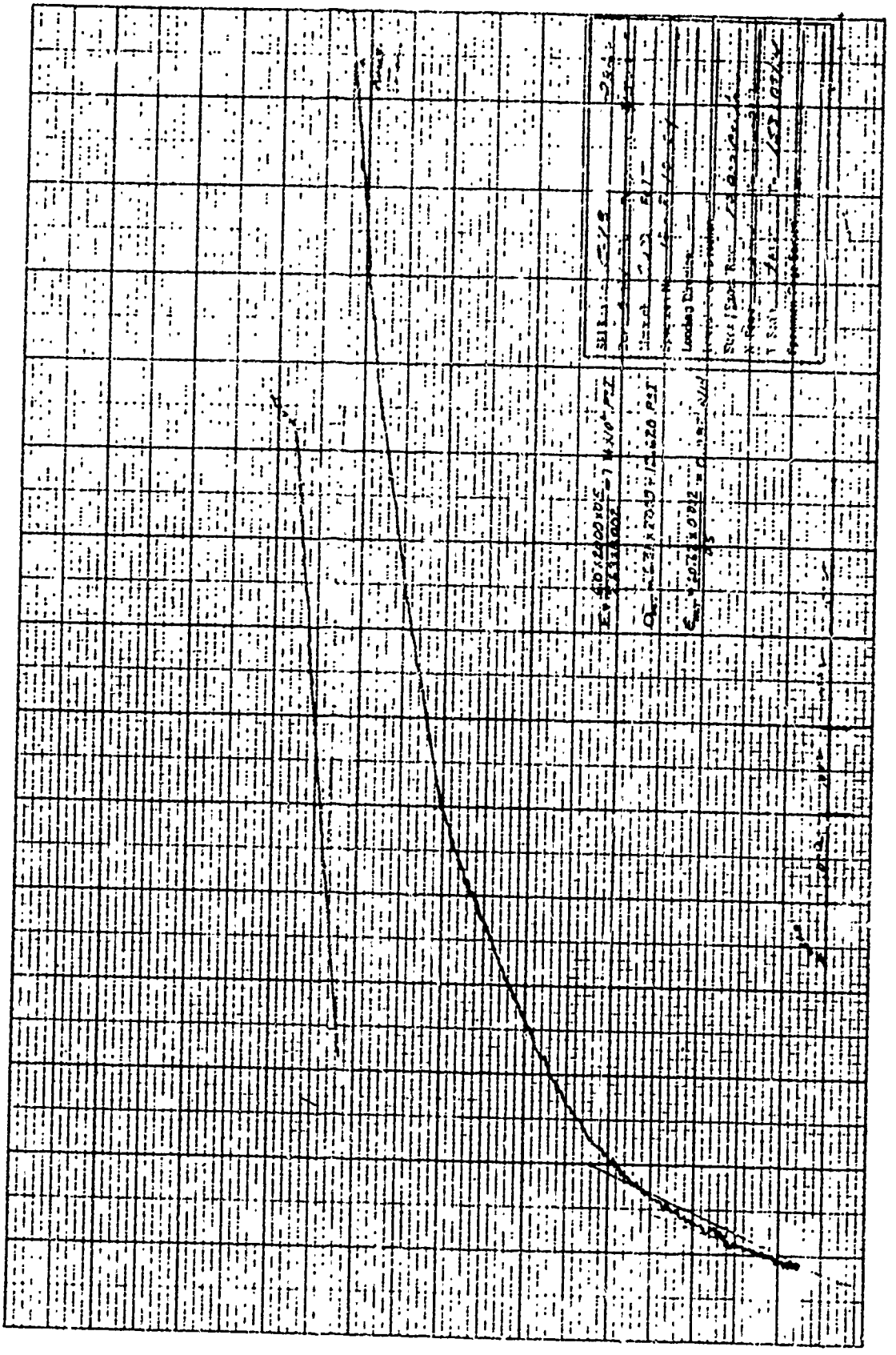


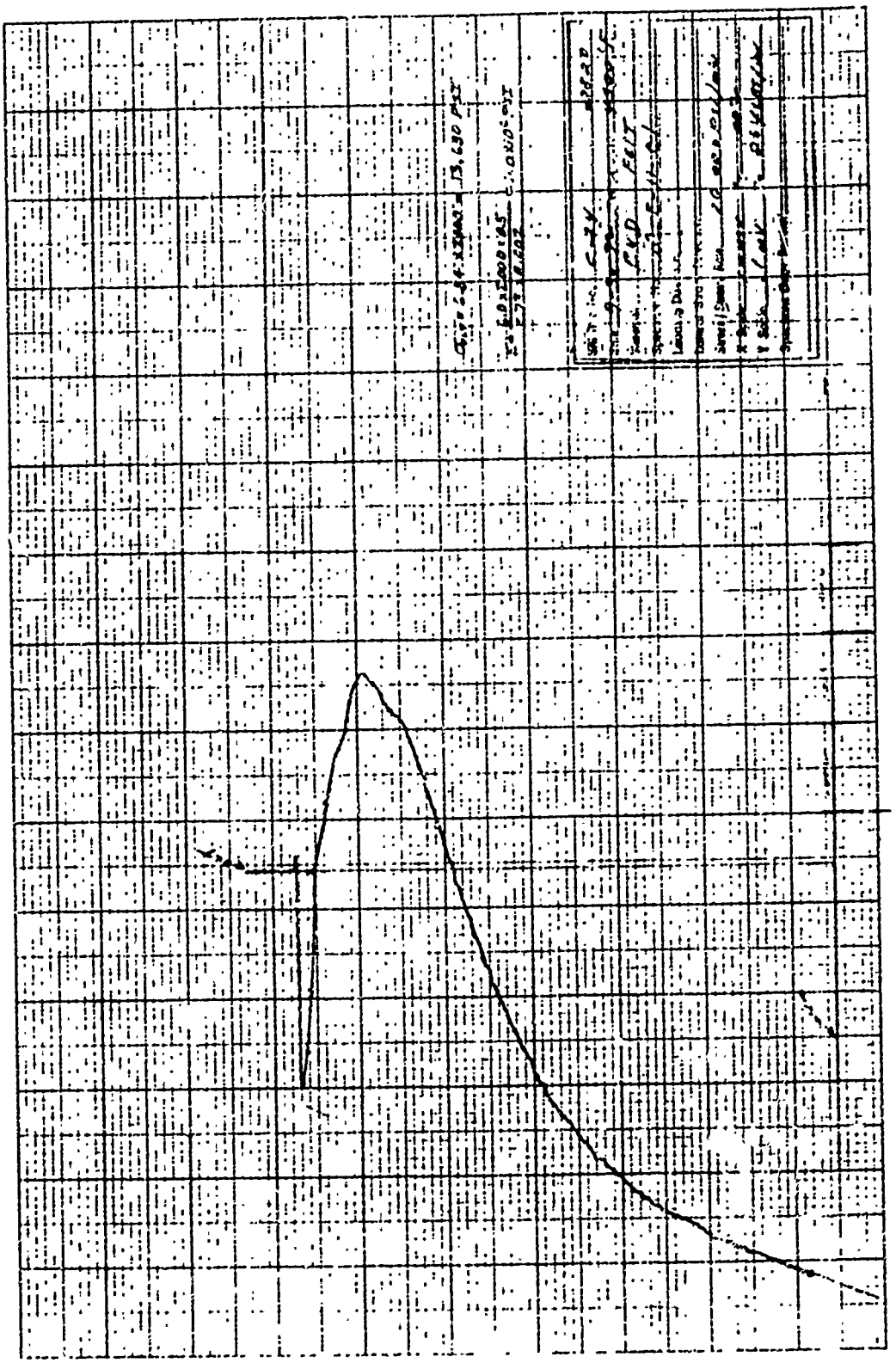


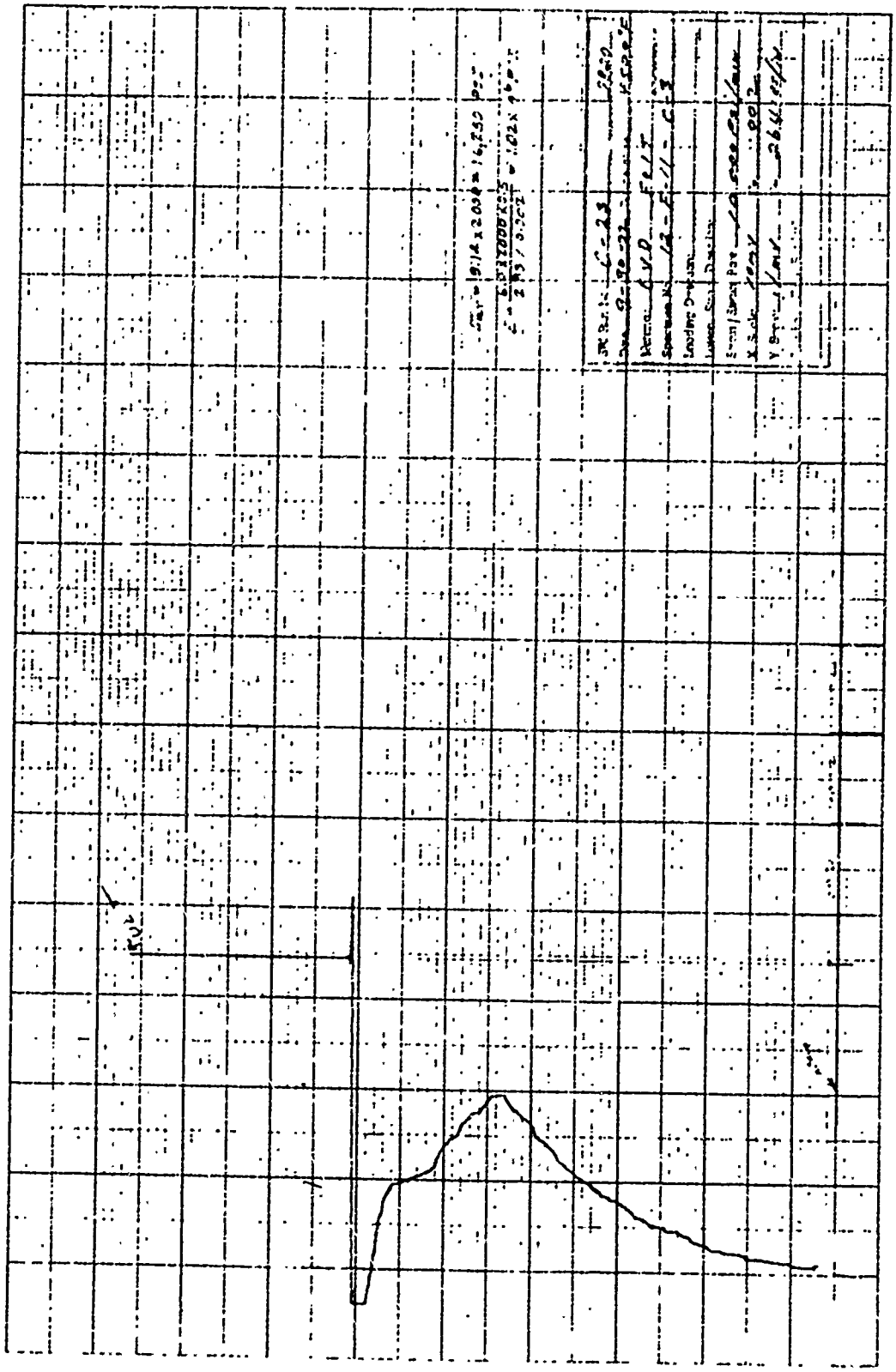

$\sigma_{max} = 10.1 \times 2000 = 20,200$ PSI
$E = \frac{6.0 \times 2000 \times 0.5}{247 \times 0.002} = 1.2 \times 10^6$ PSI




$E = \frac{6.0 \times 2000 \times 10^5}{2.04 \times .002} = 14.71 \times 10^6$ PSI
$\sigma_{PL} = .6.90 \times 2000 = 13,800$ PSI
$\epsilon_{PL} = \frac{2000}{E} = \frac{.0136}{\Delta \epsilon}$ in/in

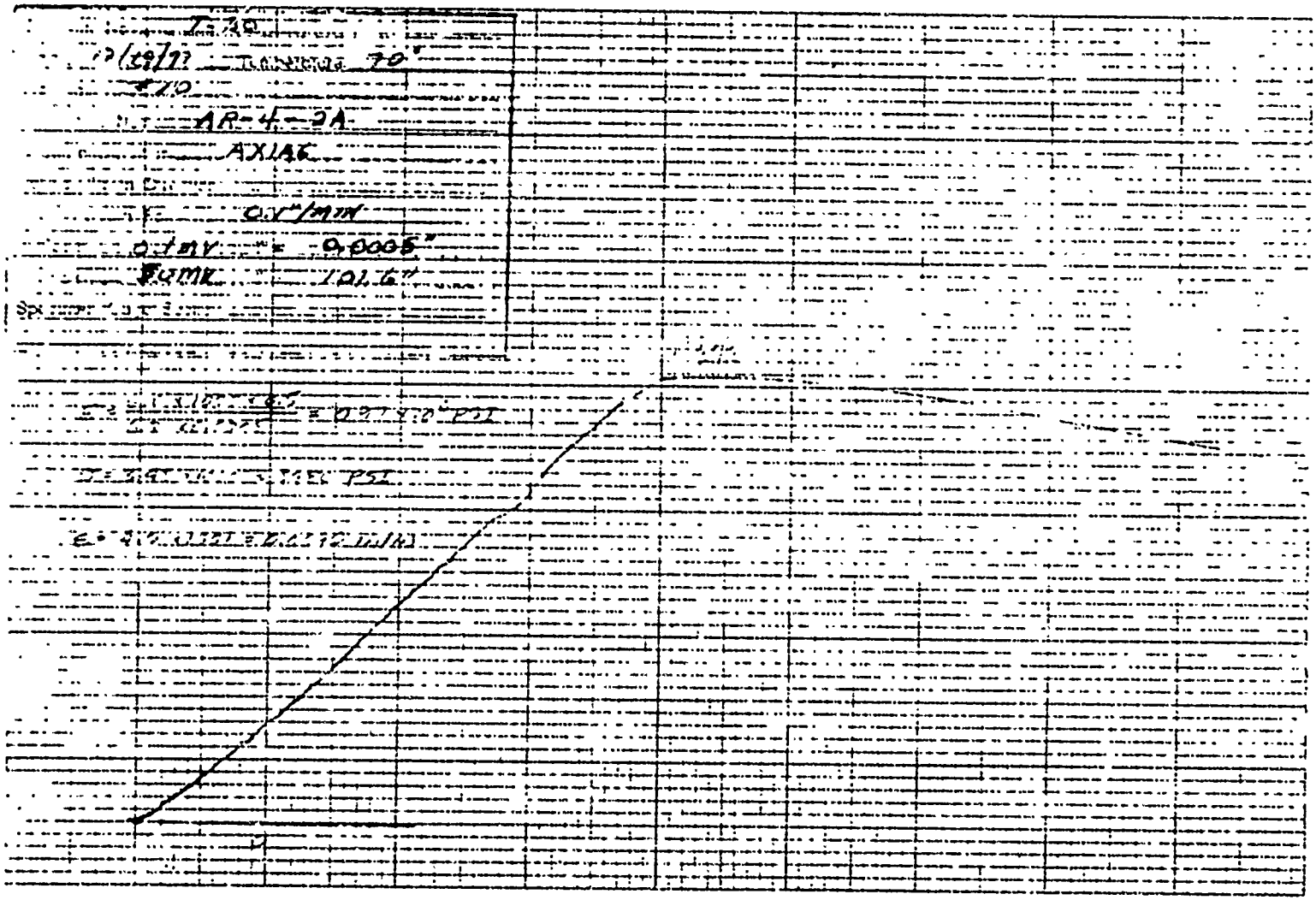


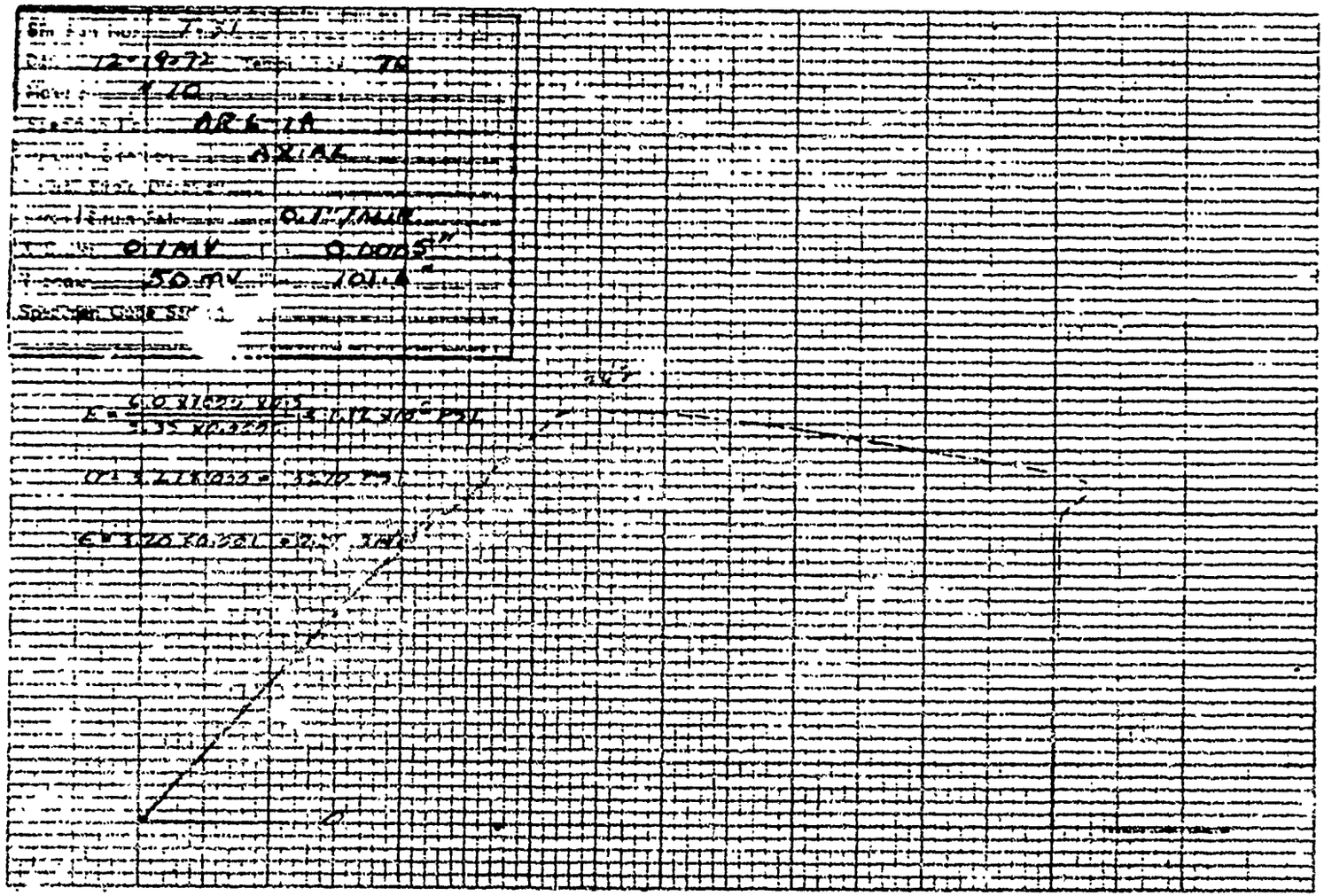


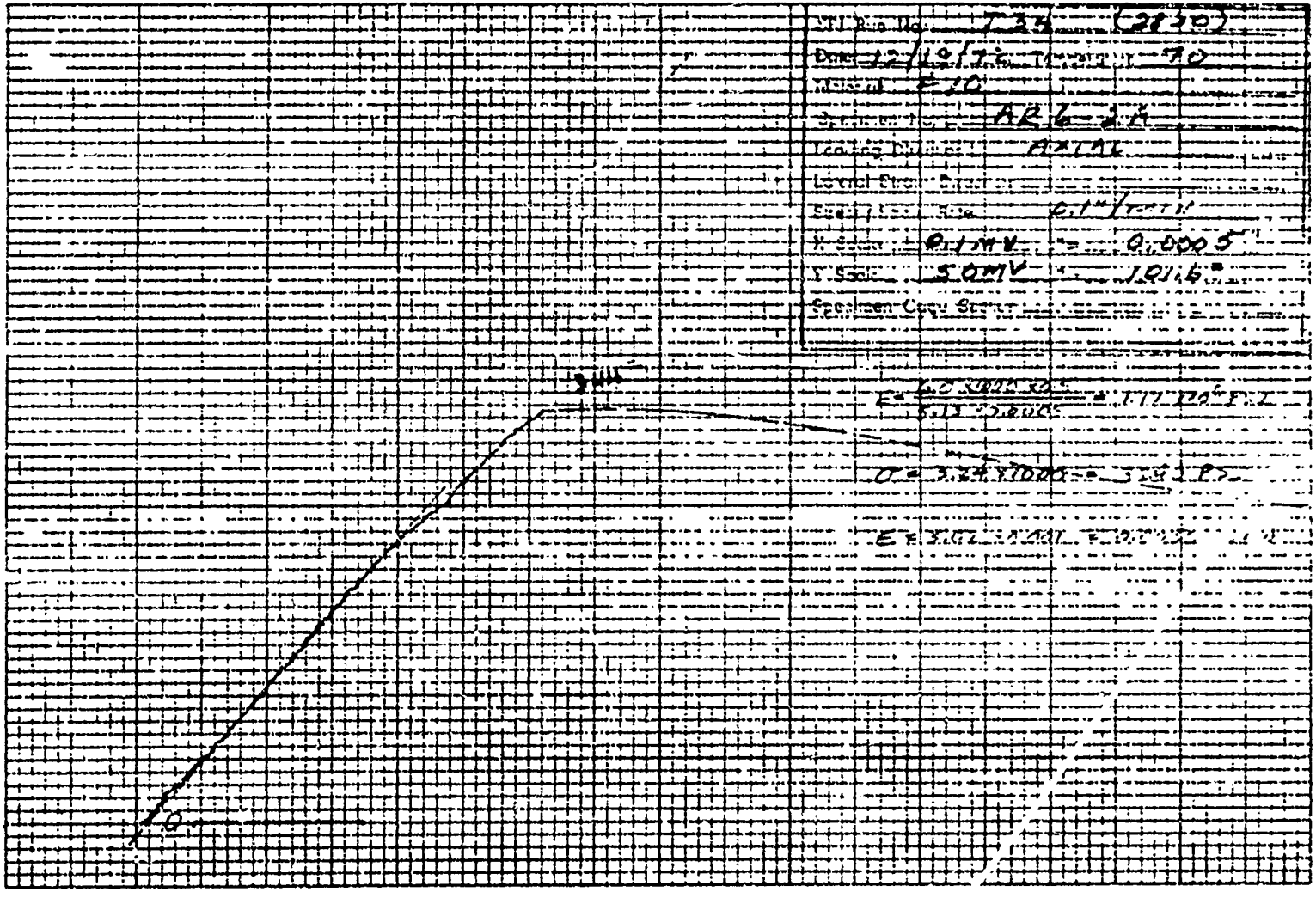


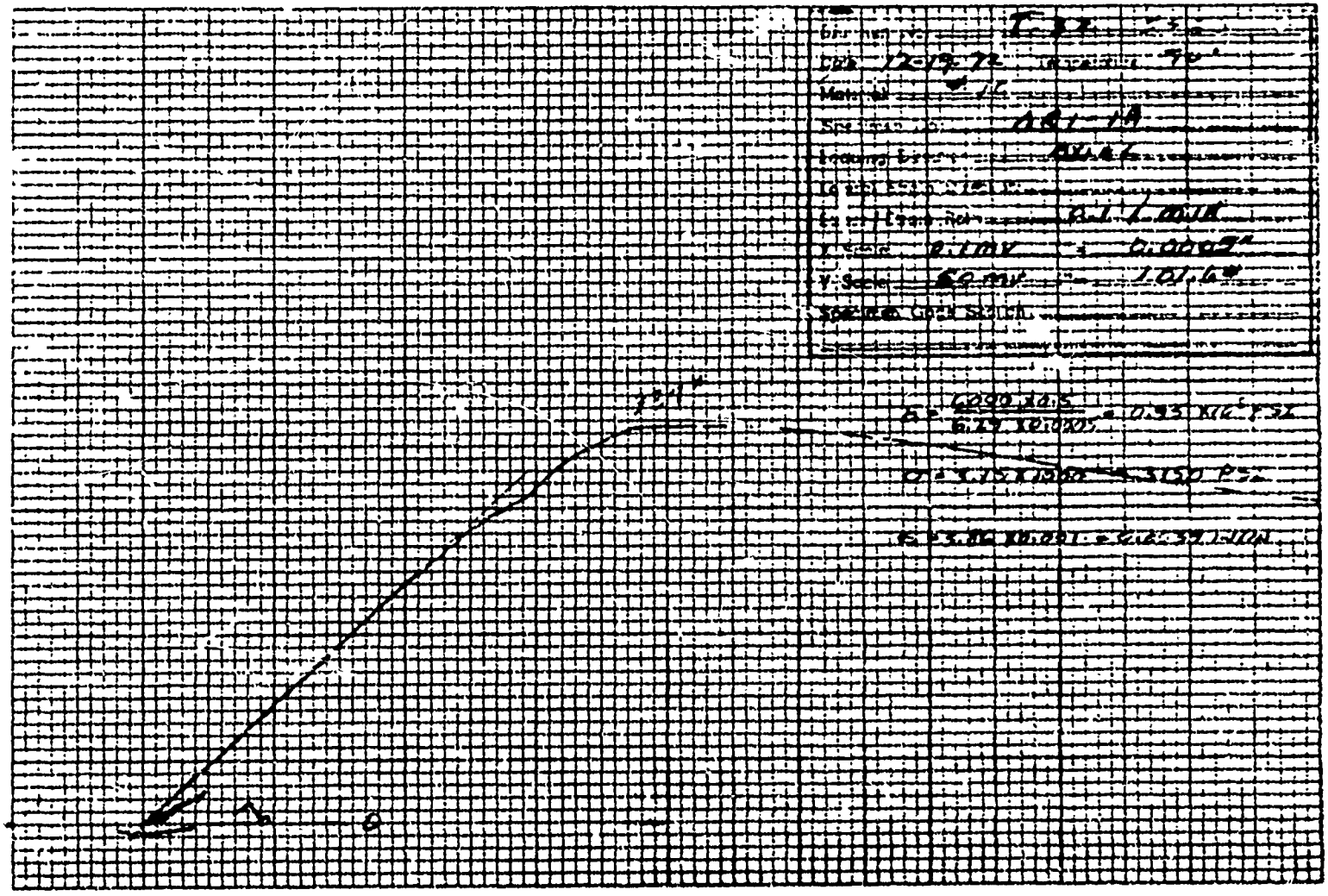
APPENDIX I

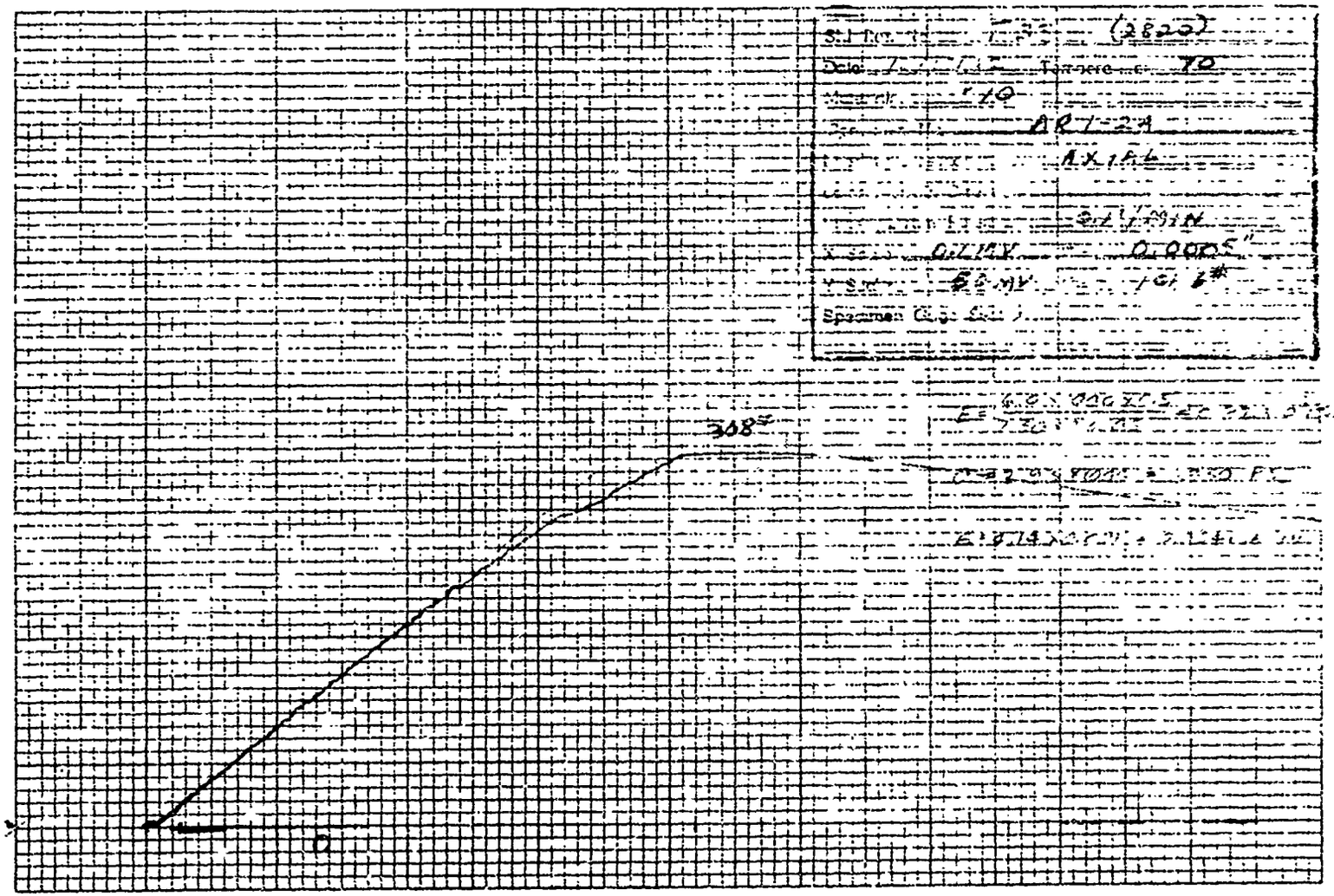
TENSILE AND COMPRESSIVE STRESS-STRAIN CURVES FOR AVCO R6300 - MATERIAL 10

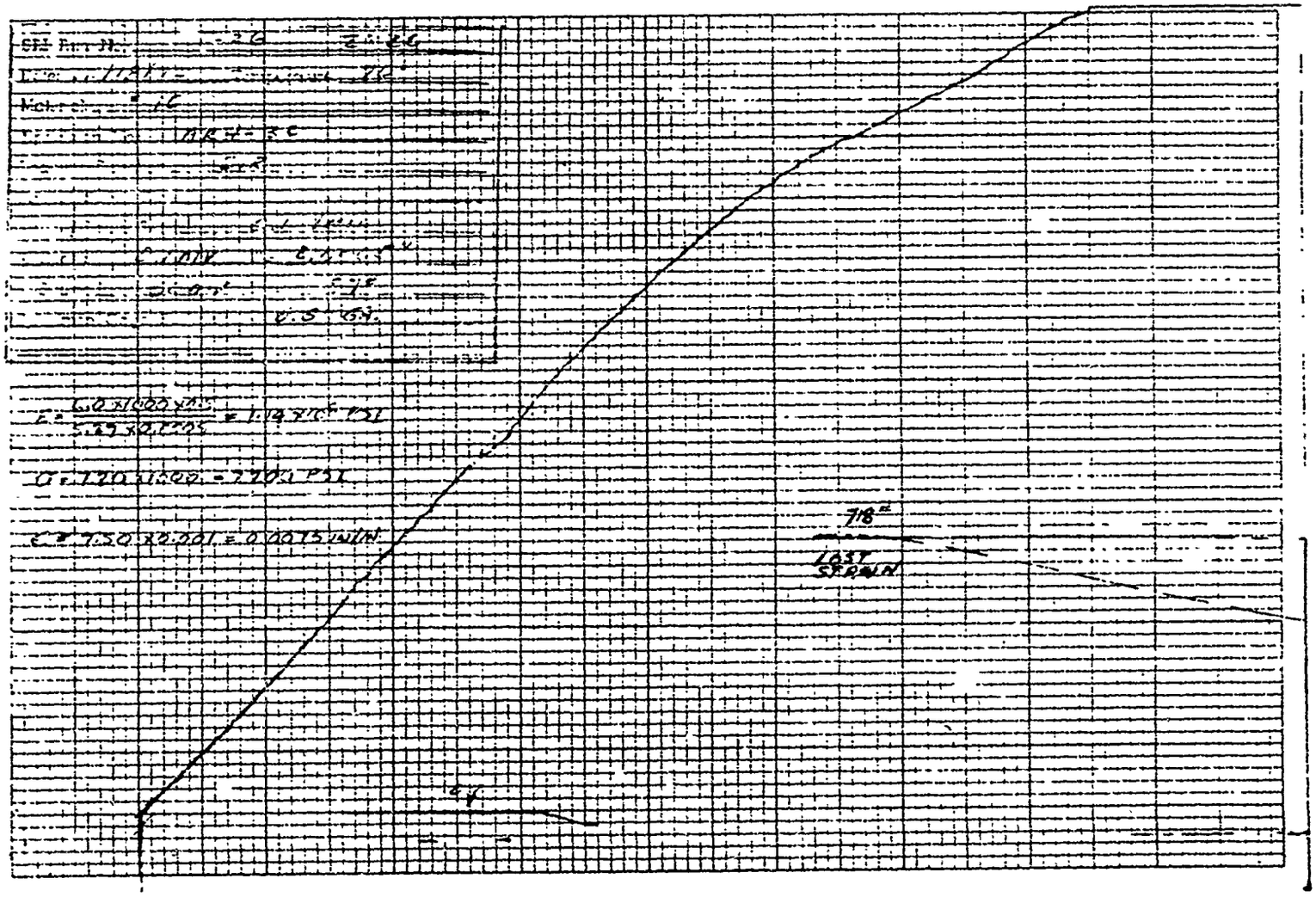

T-70
12/28/77
TEMPERATURE 70°
F-10
AR-4-2A
AXIAL
CYC/MIN
DISP = .0005"
FCMK 101.6"

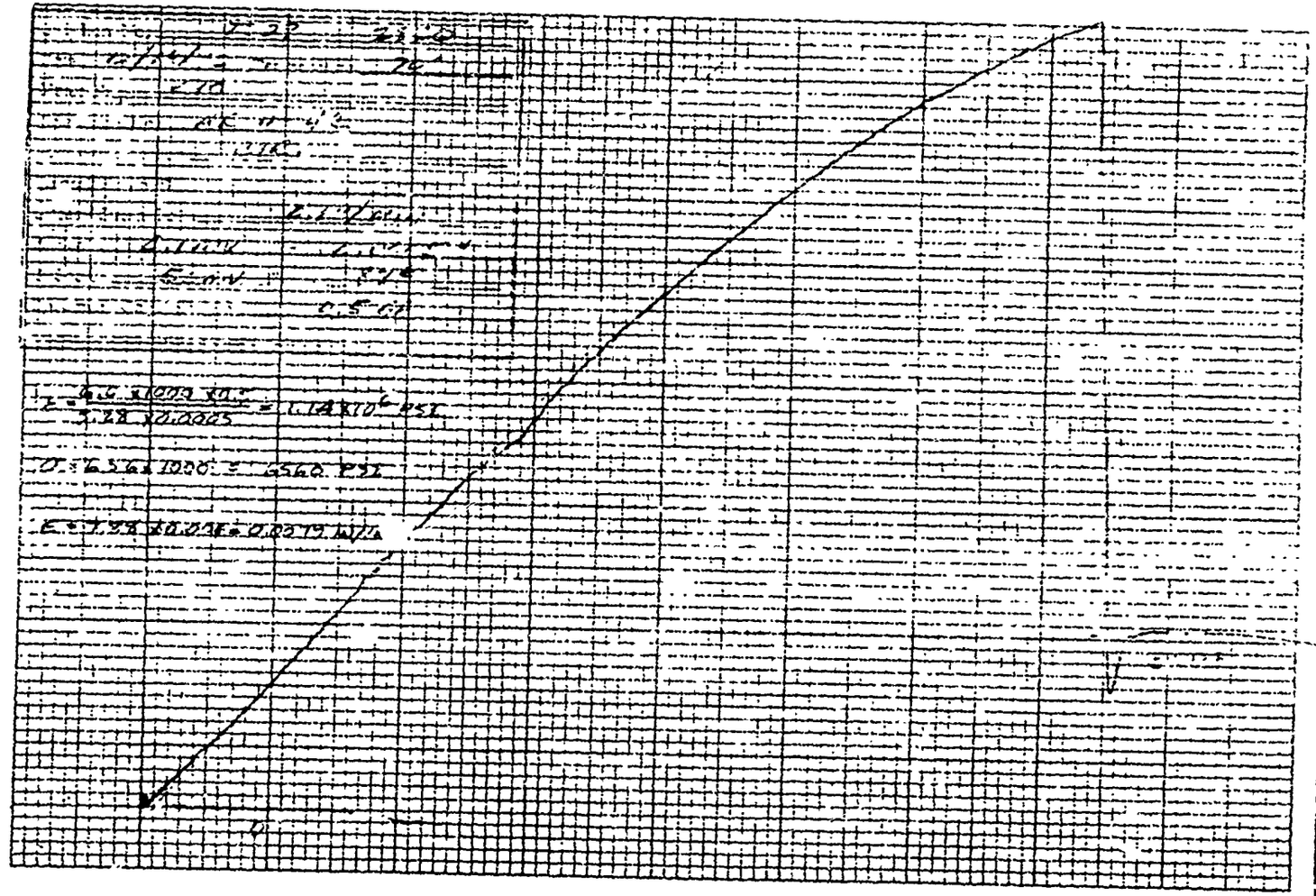

12-19-72
AR 6-1A
AXIAL
0.1 TMIN
0.0005"
50 mV
Specimen Gage SN

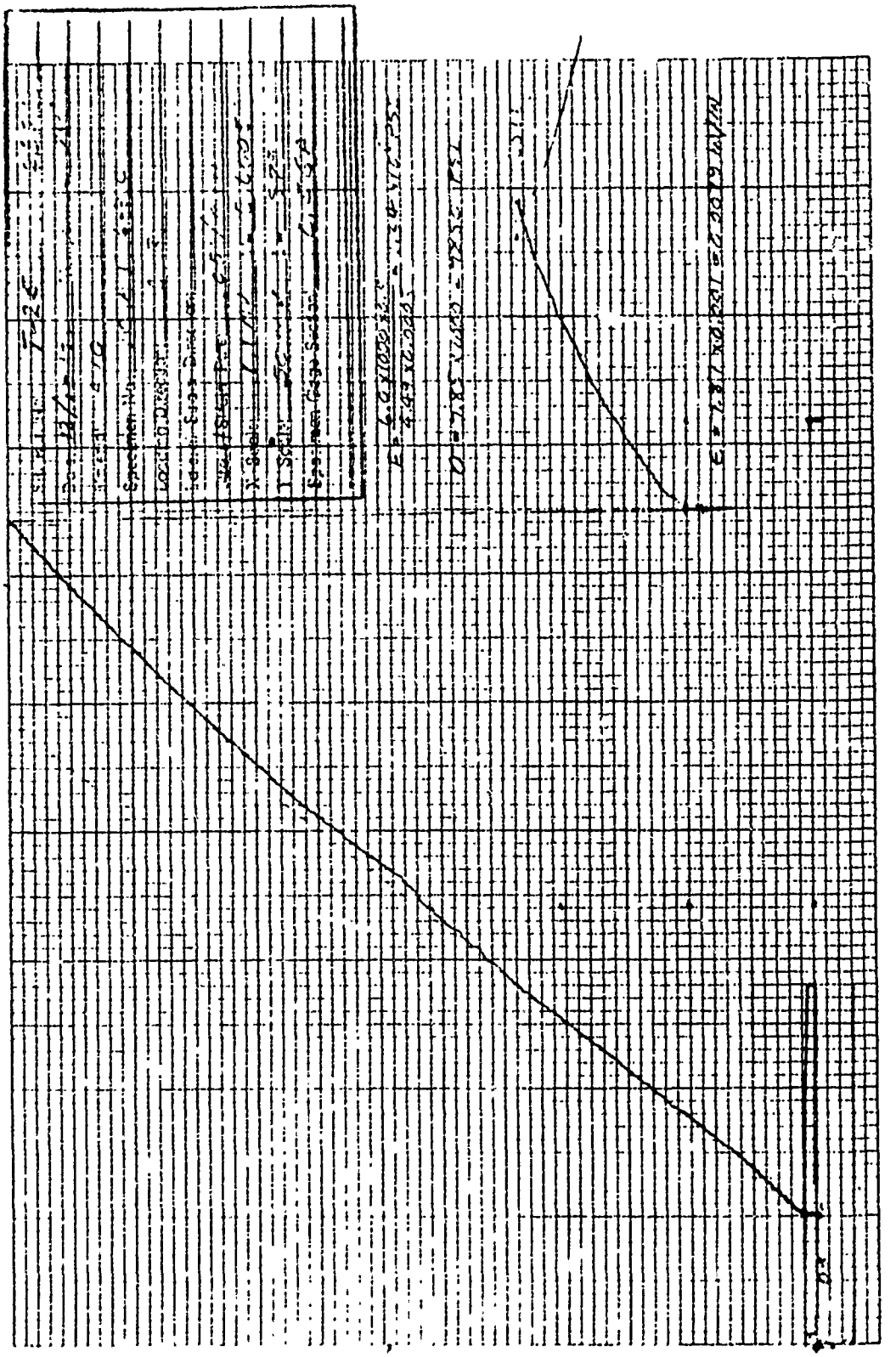

Date 12/10/77
Material
Specimen
Loading Direction
Lateral Strain
Scale
Y Scale
Specimen Cross Sec
AR 6-2 A
AXIAL
0.1"/INCH
0.1mV = 0.0005"
50mV = 101.6"
E=
σ = 3.24 x 10000 =
E =
Y
0

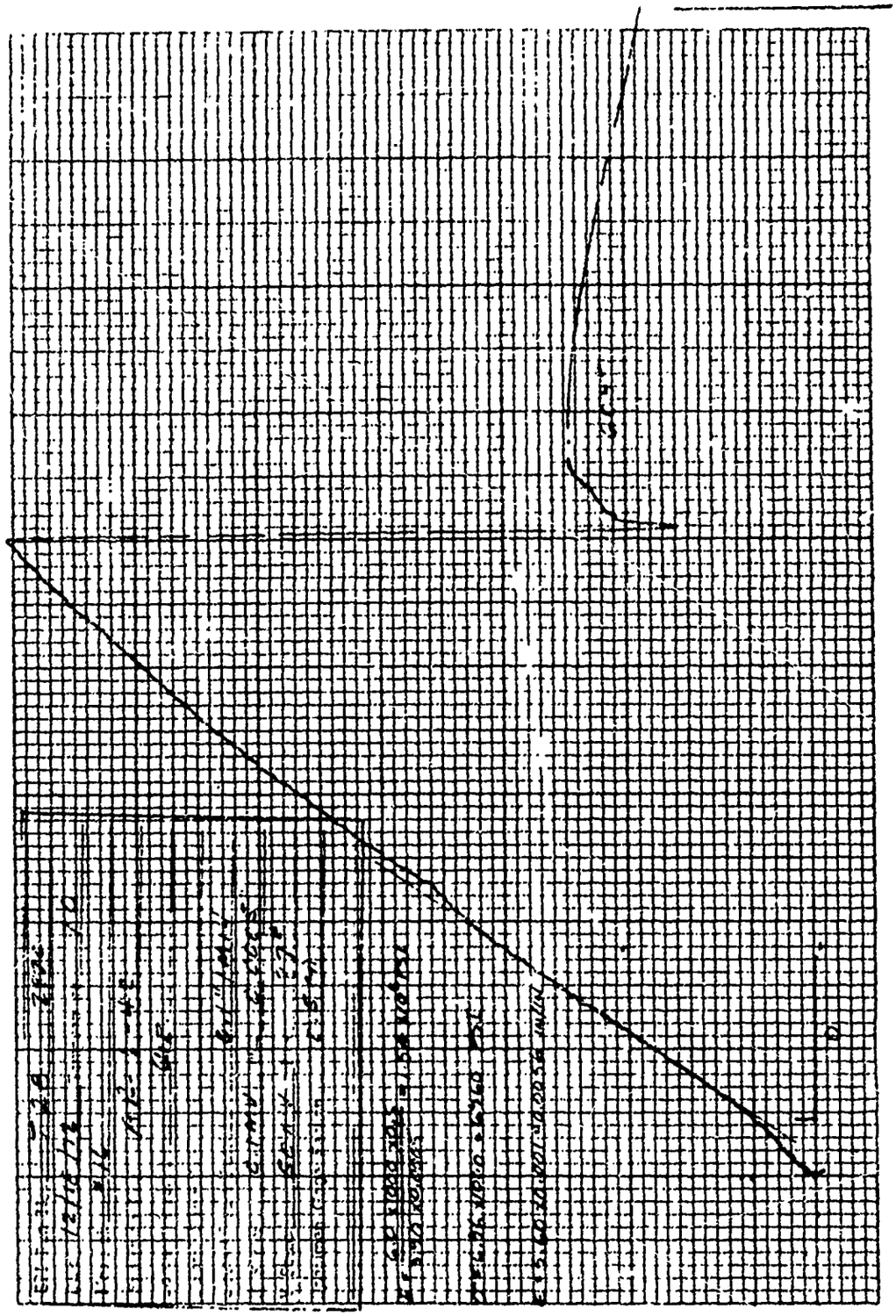

Test
Date 12-19-72
Material
Strain Gage
Loading Device
Gage Factor
Gage Resistance
Bridge Voltage
Y-Scale
Specimen Cross Section
Y
b
a

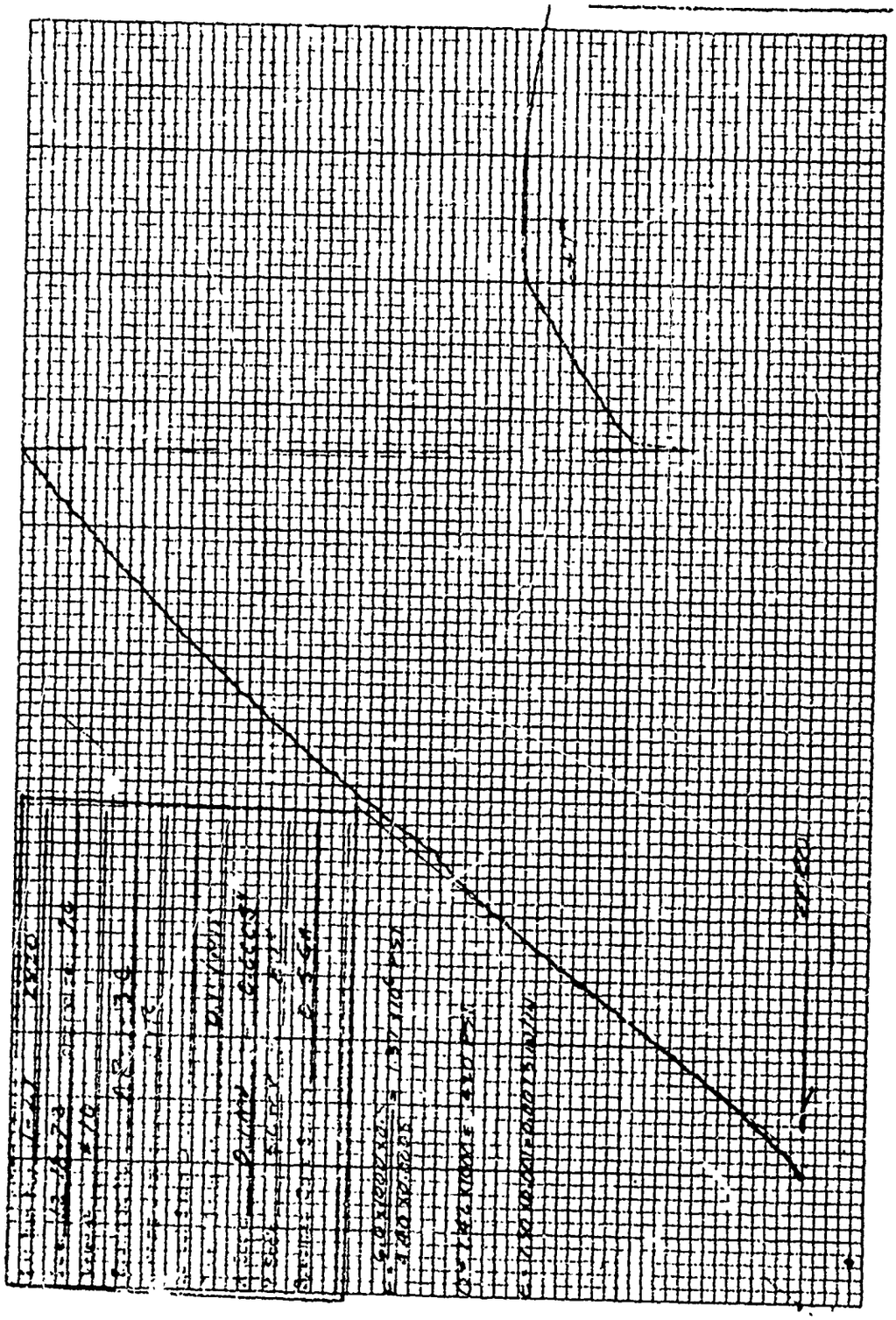

(2820)
Tempre
70
AR-214
1X1A4
0.0005"
308°
D

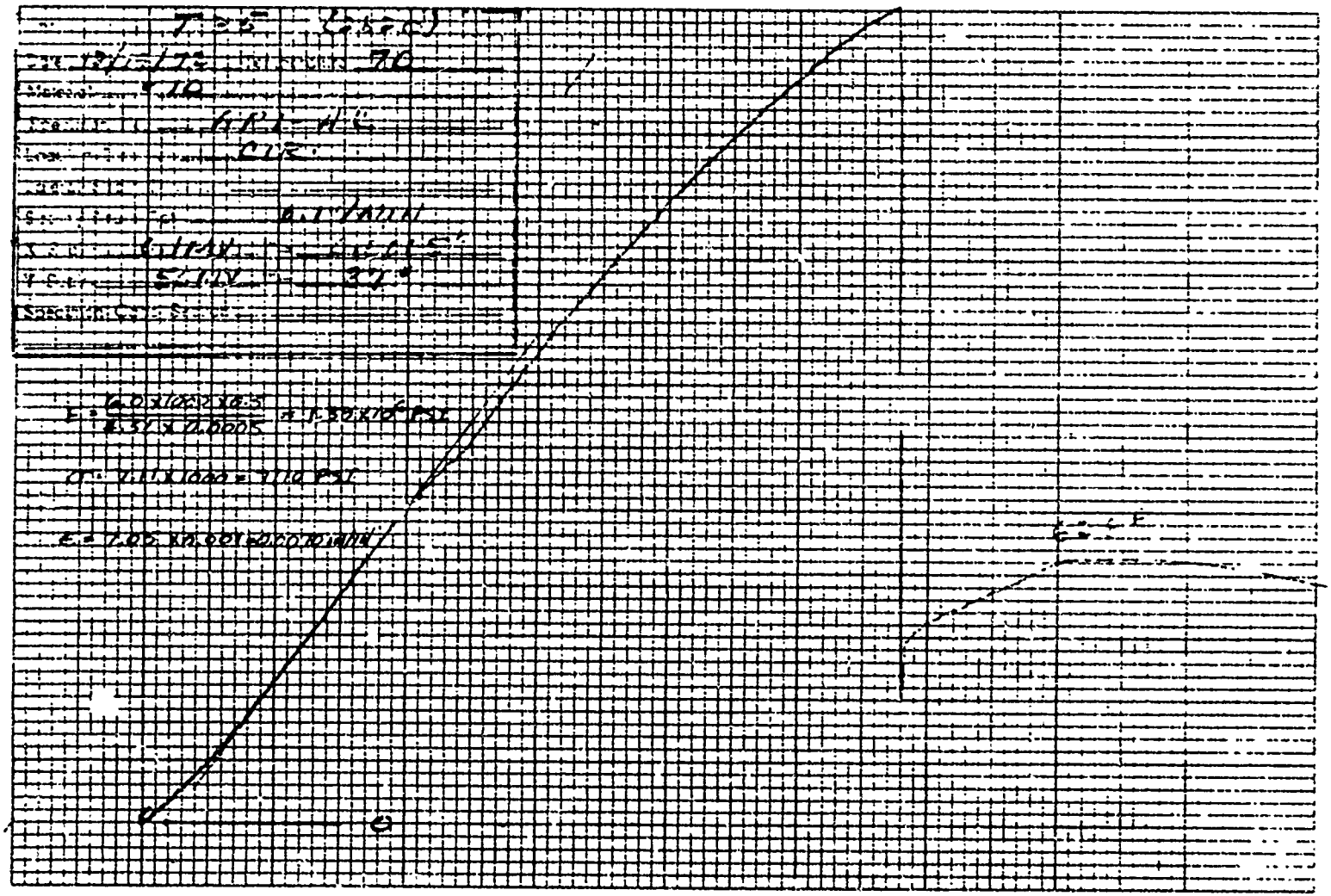

7/8"
LOST
STRAIN
4f

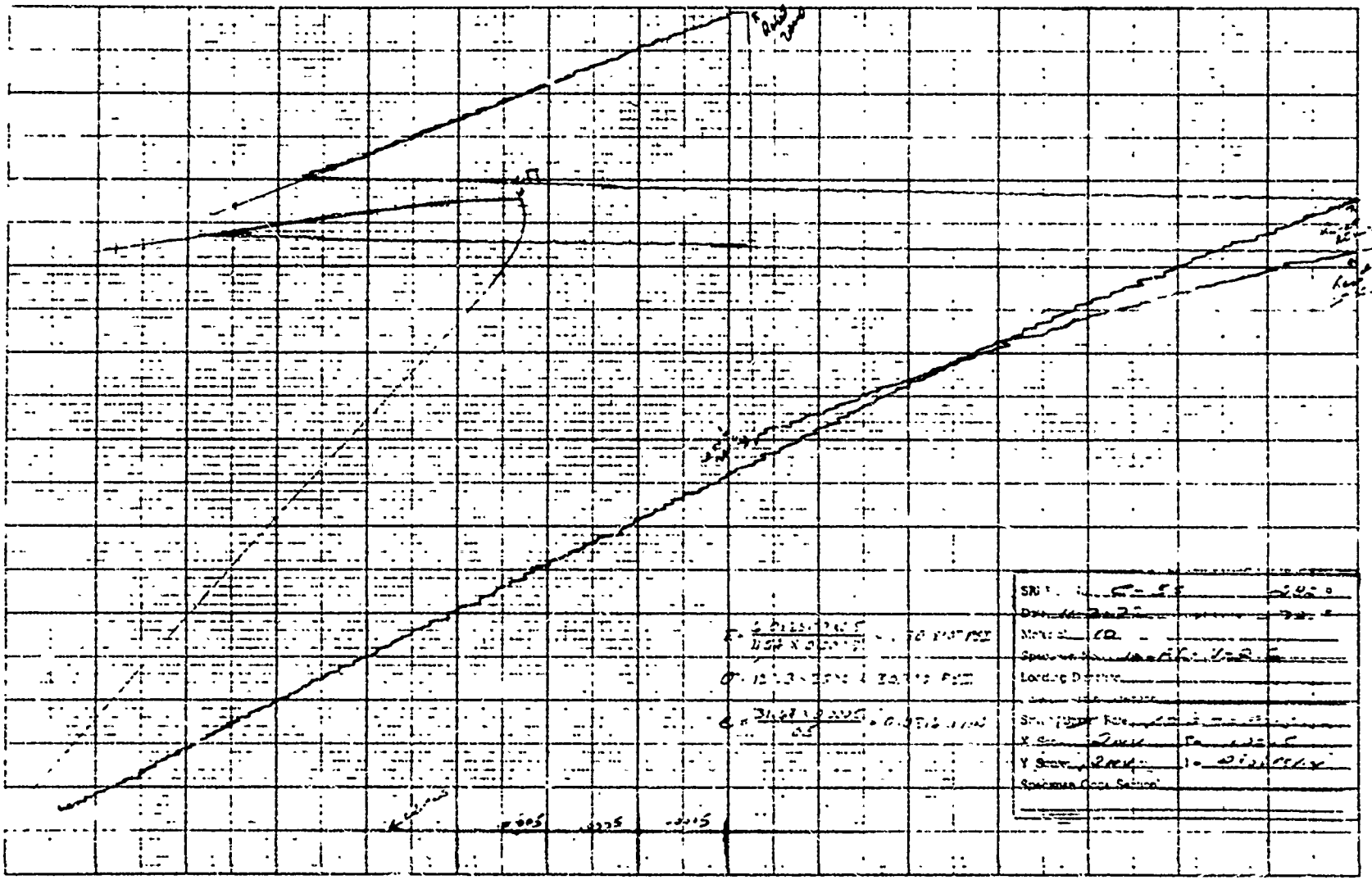


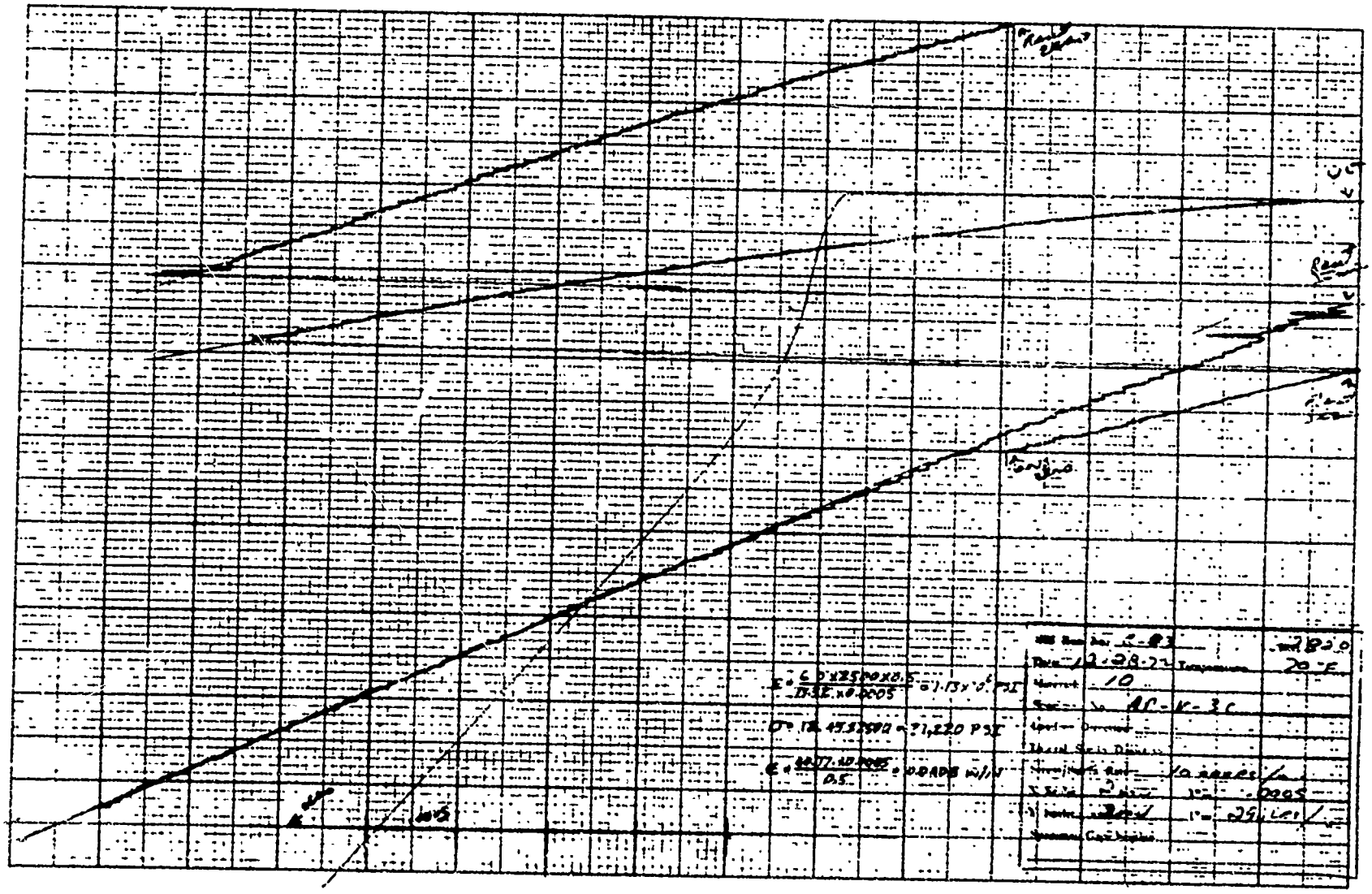


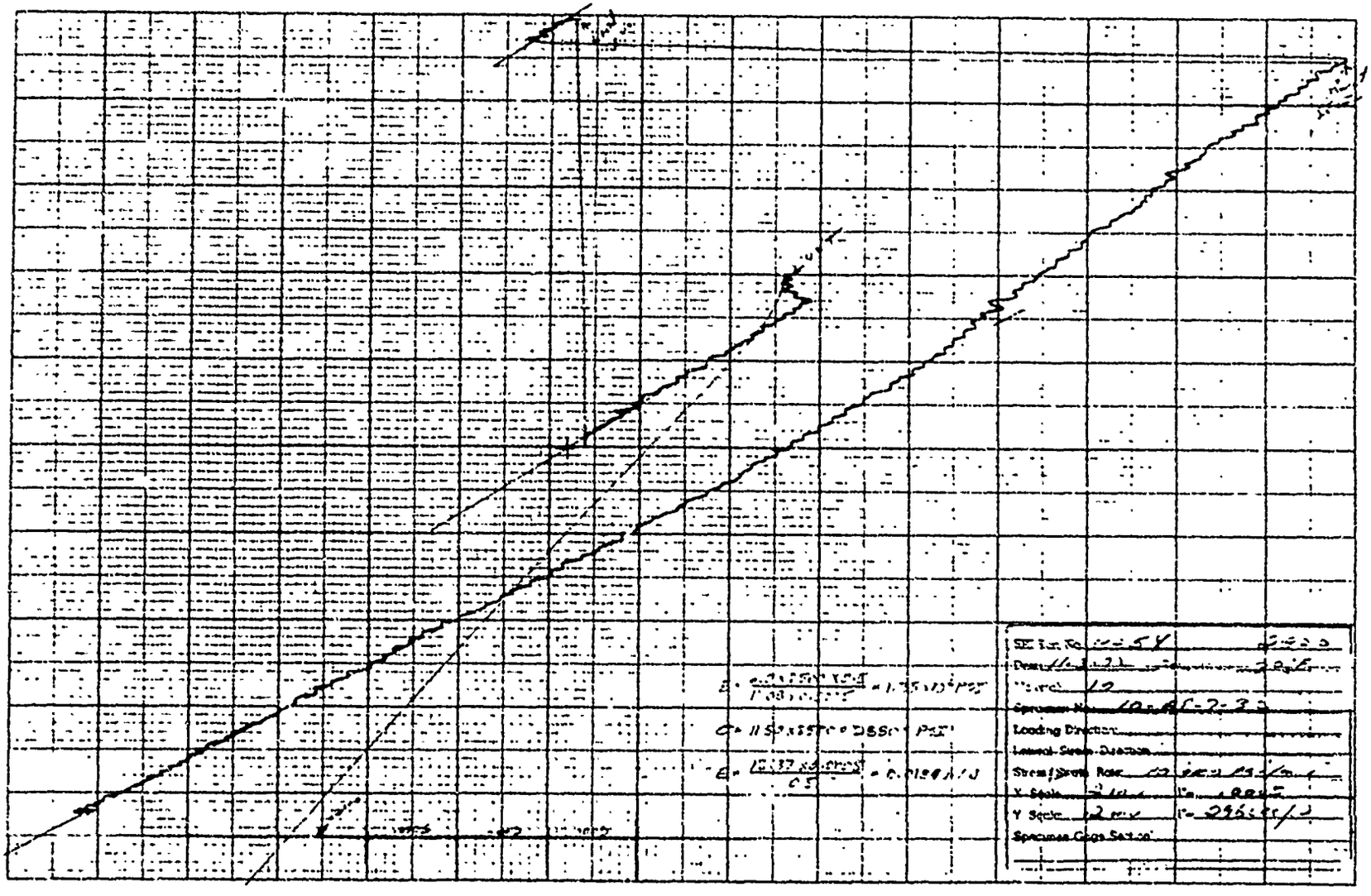


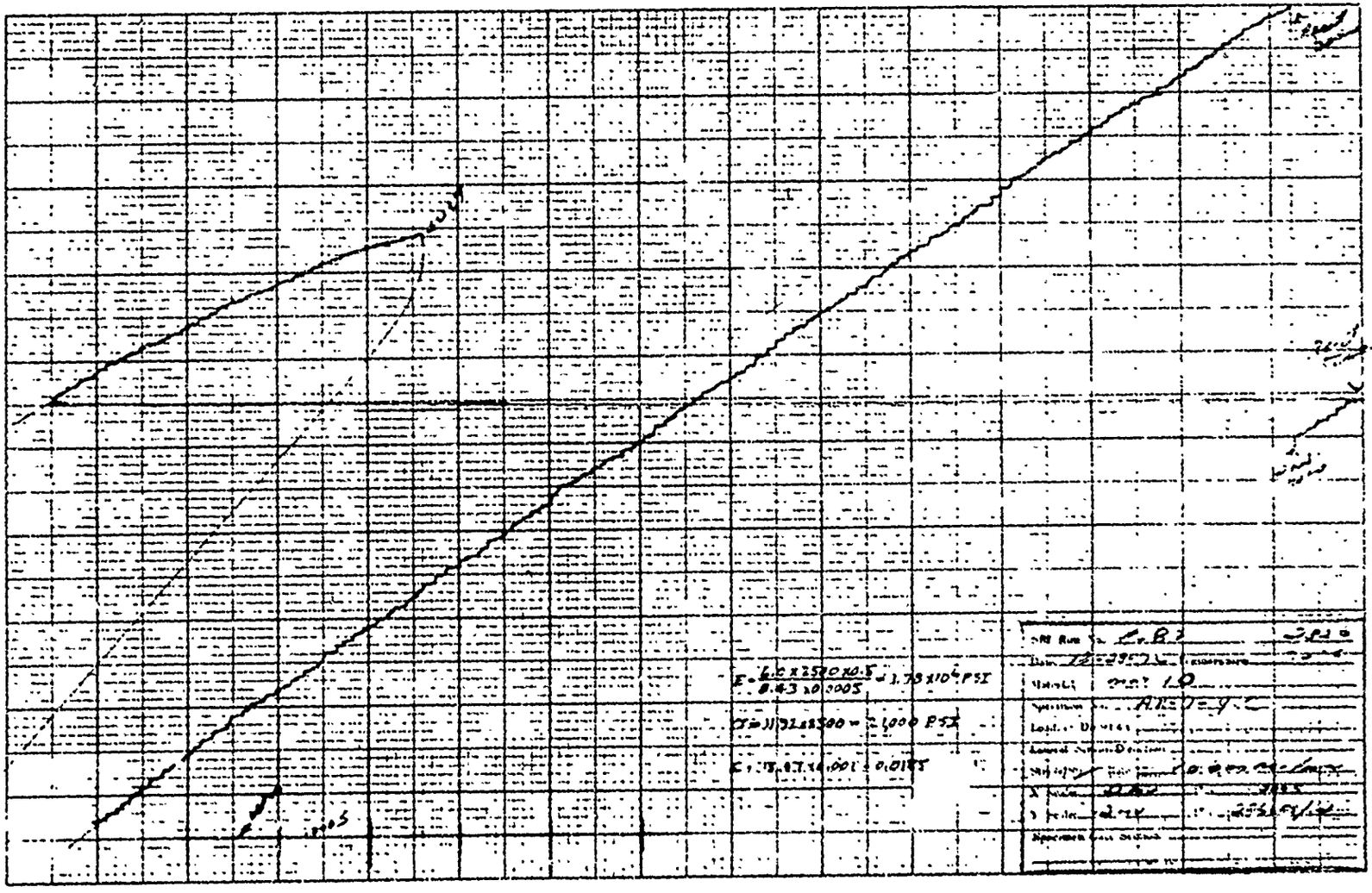


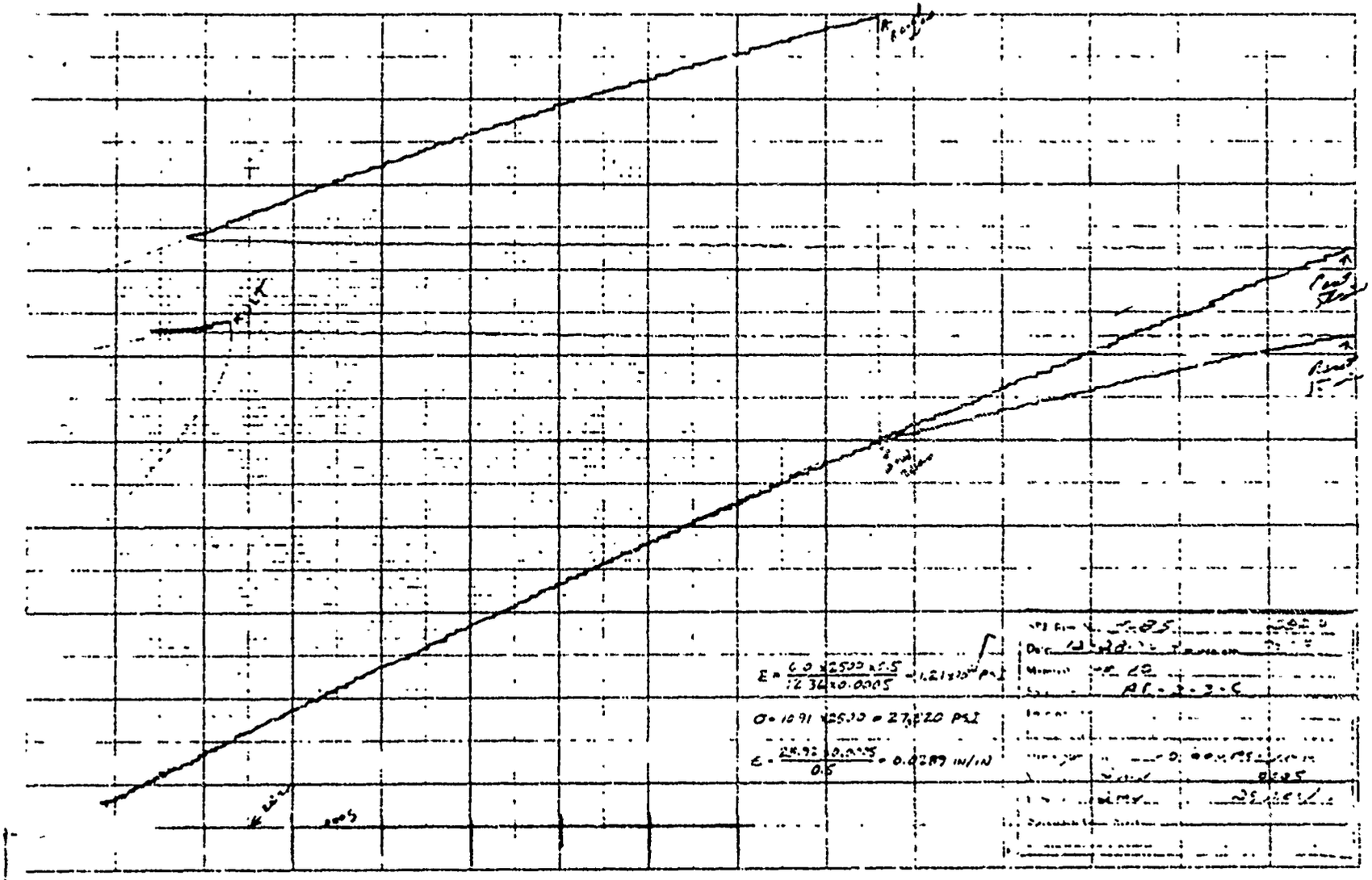


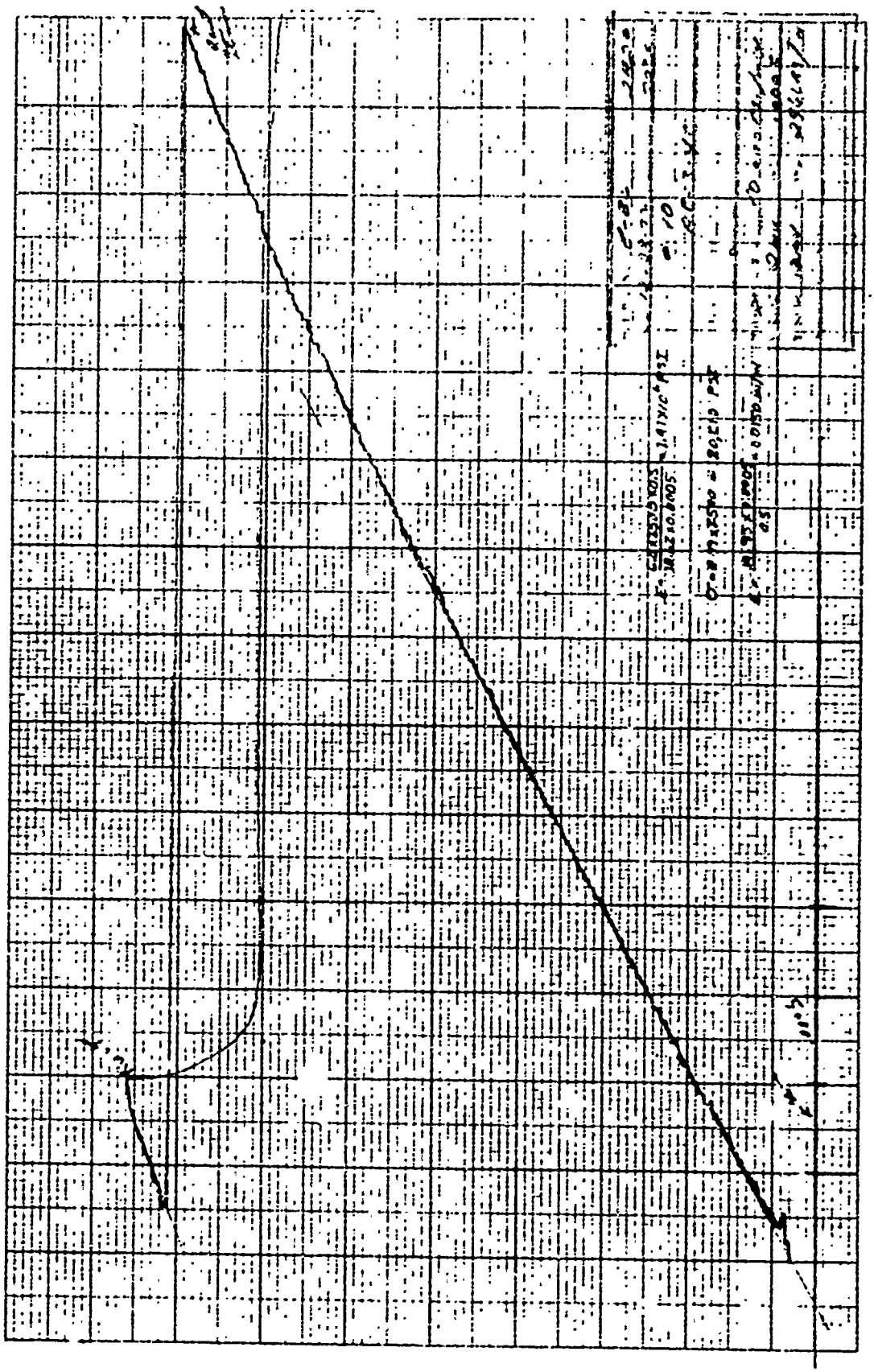


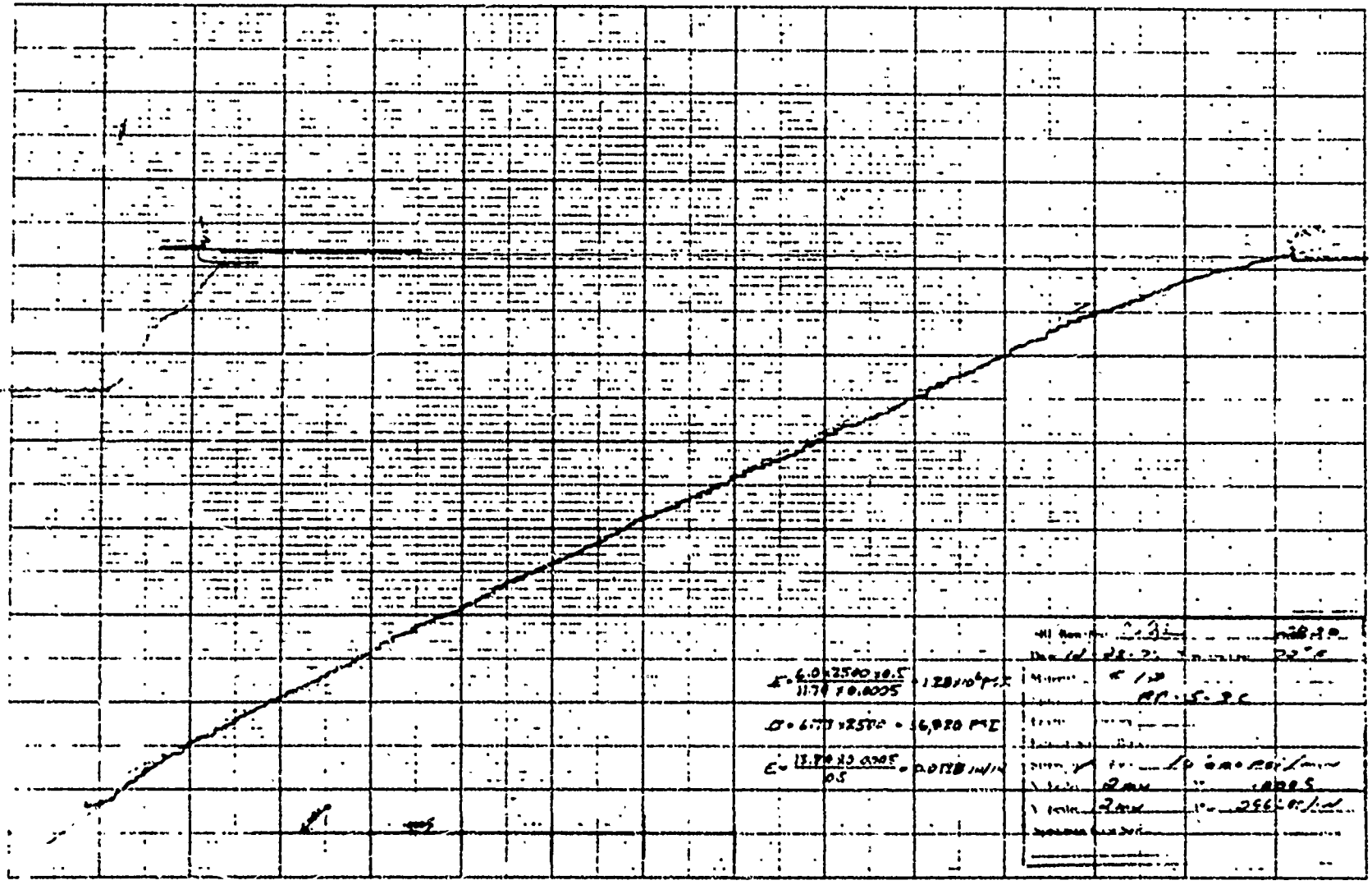

$\varepsilon = \frac{6.0 \times 25{,}000 \times 0.5}{D.S.E. \times 0.0005} = 61.13 \times 10^6$ PSI
$D = 12.45 \times 5900 = 71{,}220$ PSI
$\varepsilon = \frac{44{,}177.40 \times 0.0005}{0.5} = 0.0884$ IN/IN
20-F
AC-K-3C
10

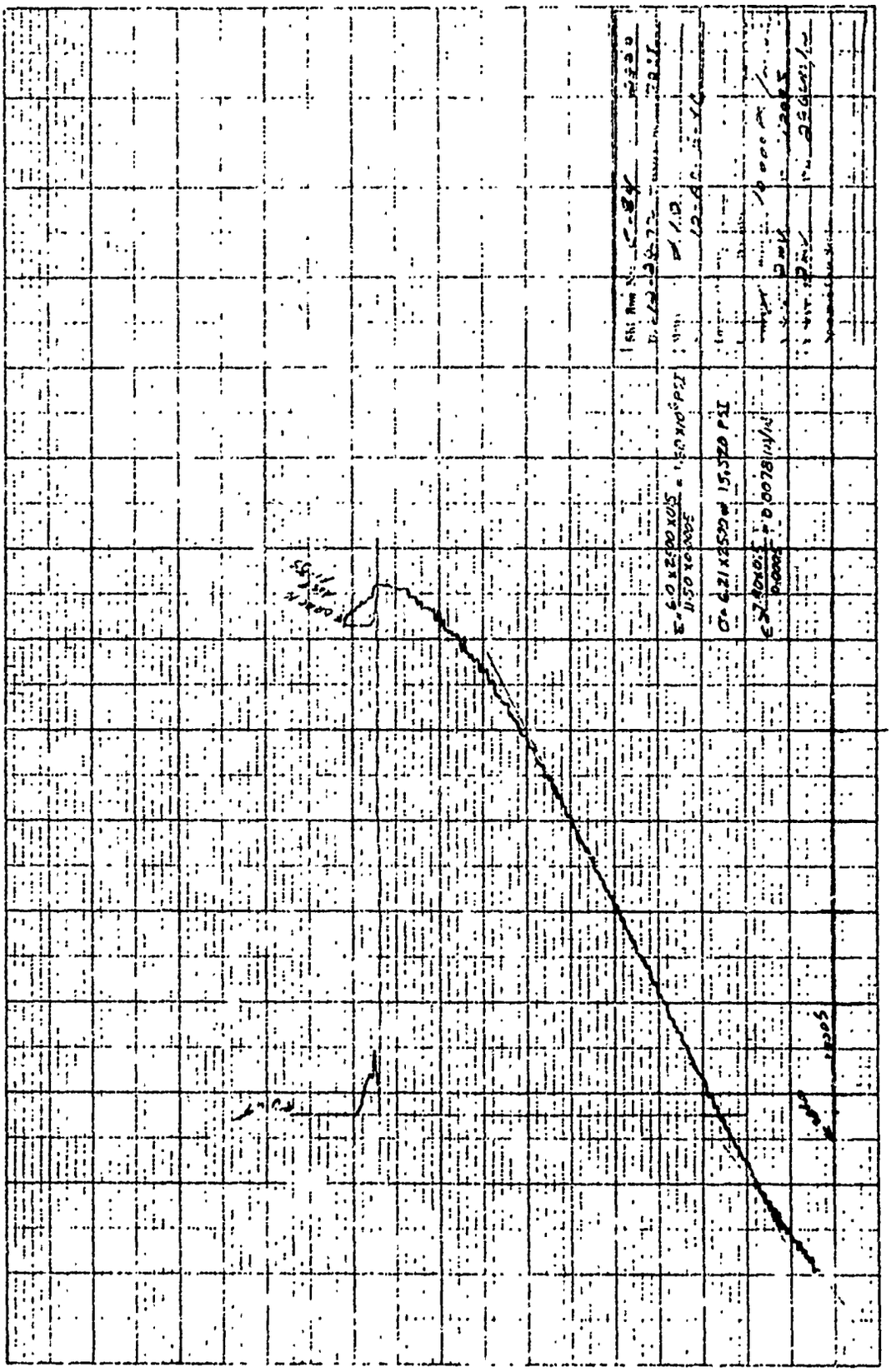

Loading Direction
Lateral Strain Direction
Y Scale
Specimen Gage Setup

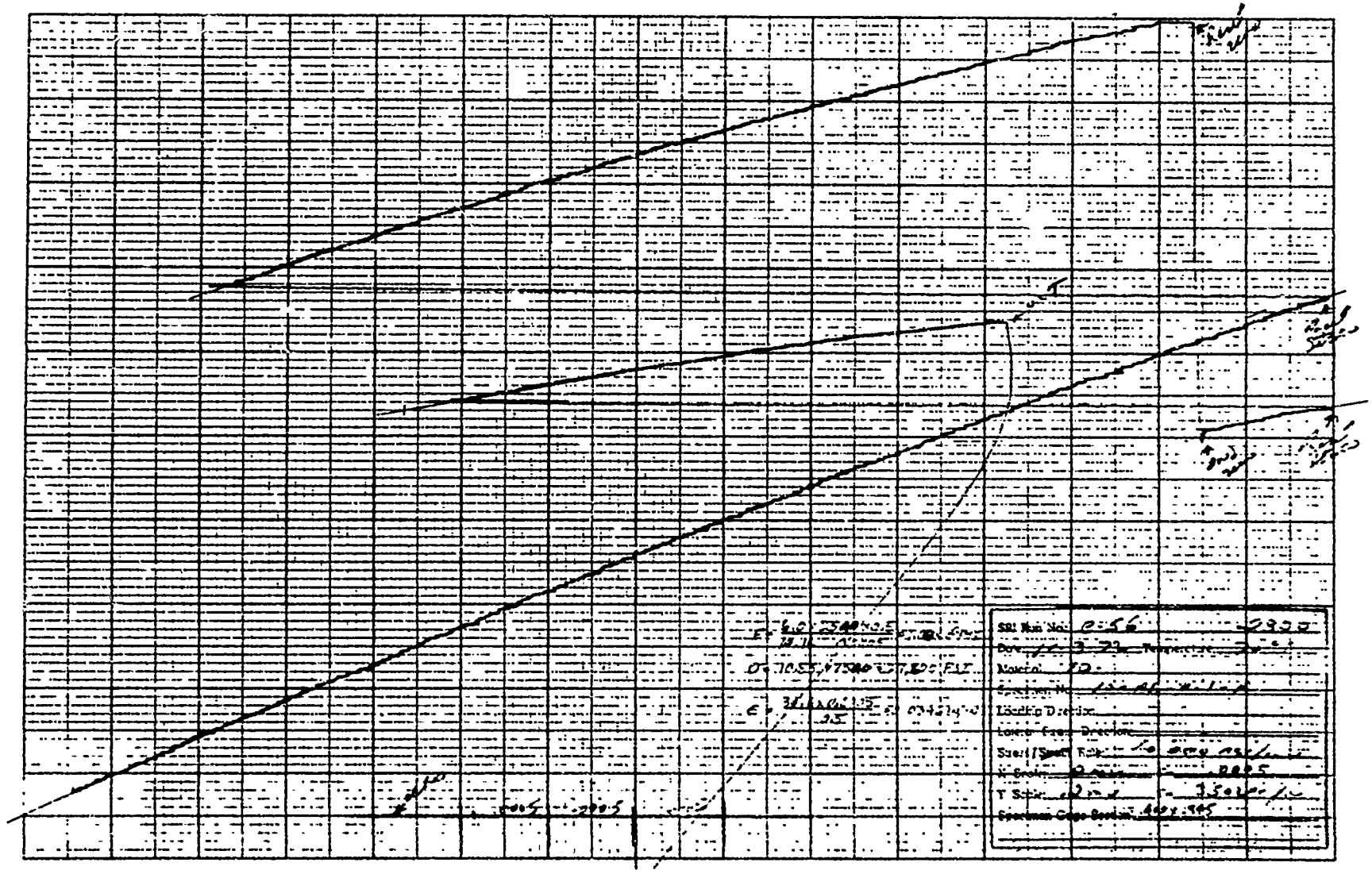

$E = \frac{6.0 \times 2570 \times 0.5}{8.43 \times 0.0005} = 3.79 \times 10^6$ PSI
$\sigma = 11,732 \times 500 = 4000$ PSI
$\varepsilon = 15,874 \times .001 = 0.01585$

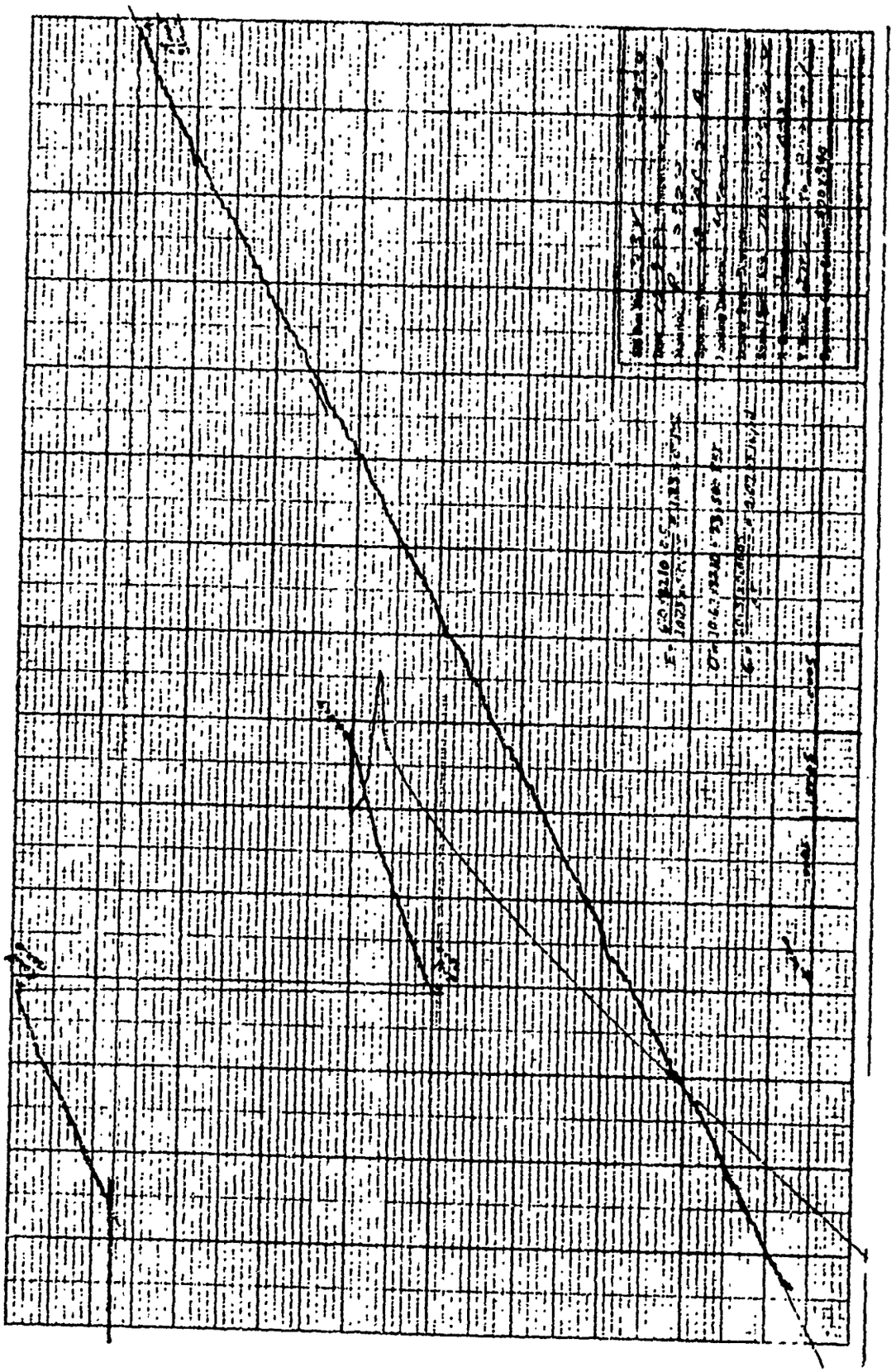

$E = \frac{6.0 \times 2500 \times 1.5}{12.34 \times 0.0005} = 1.21 \times 10^{6}$ PSI
$\sigma = 10.91 \times 2530 = 27,620$ PSI
$\epsilon = \frac{28.92 \times 0.005}{0.5} = 0.0289$ IN/IN

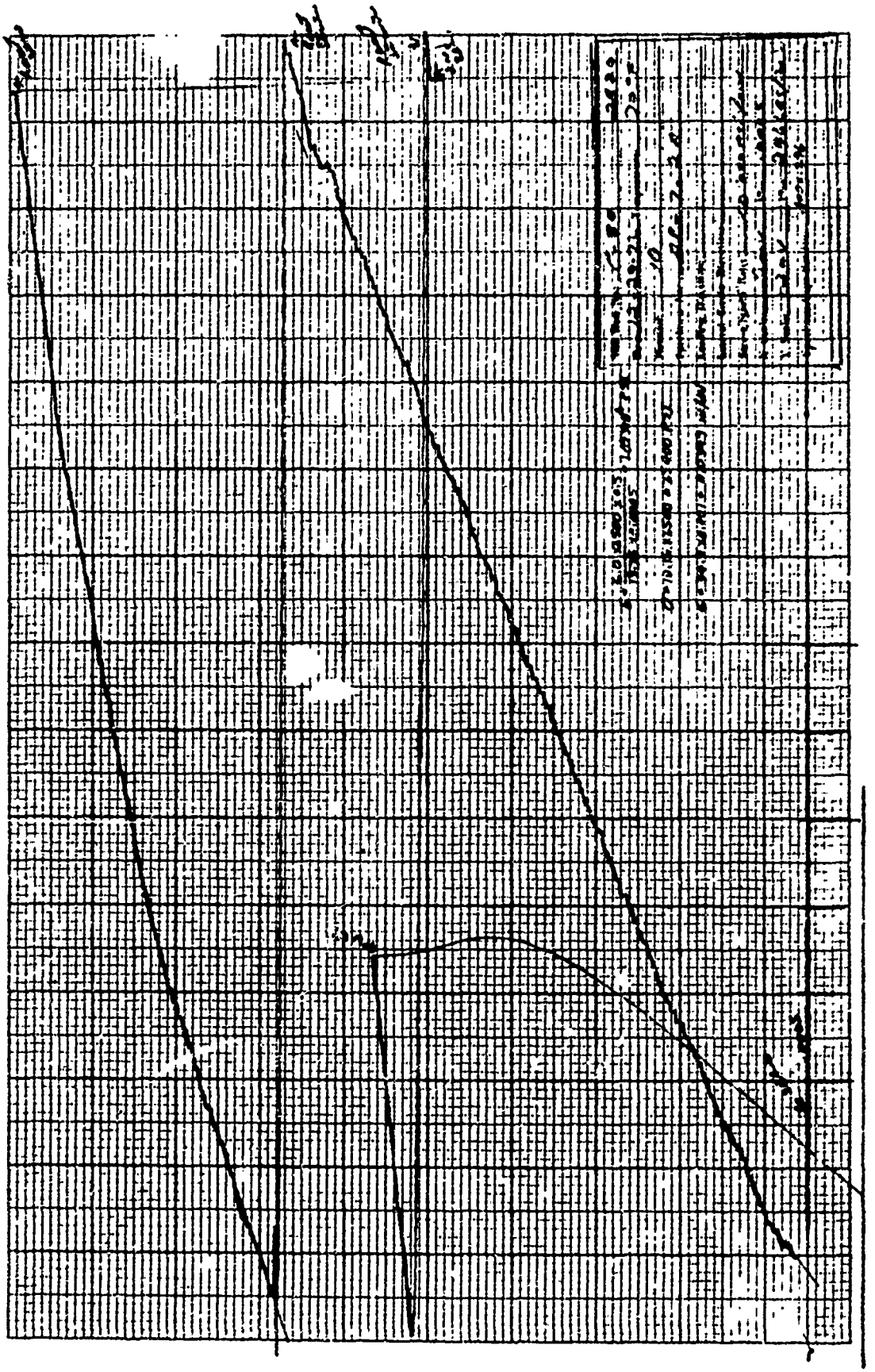


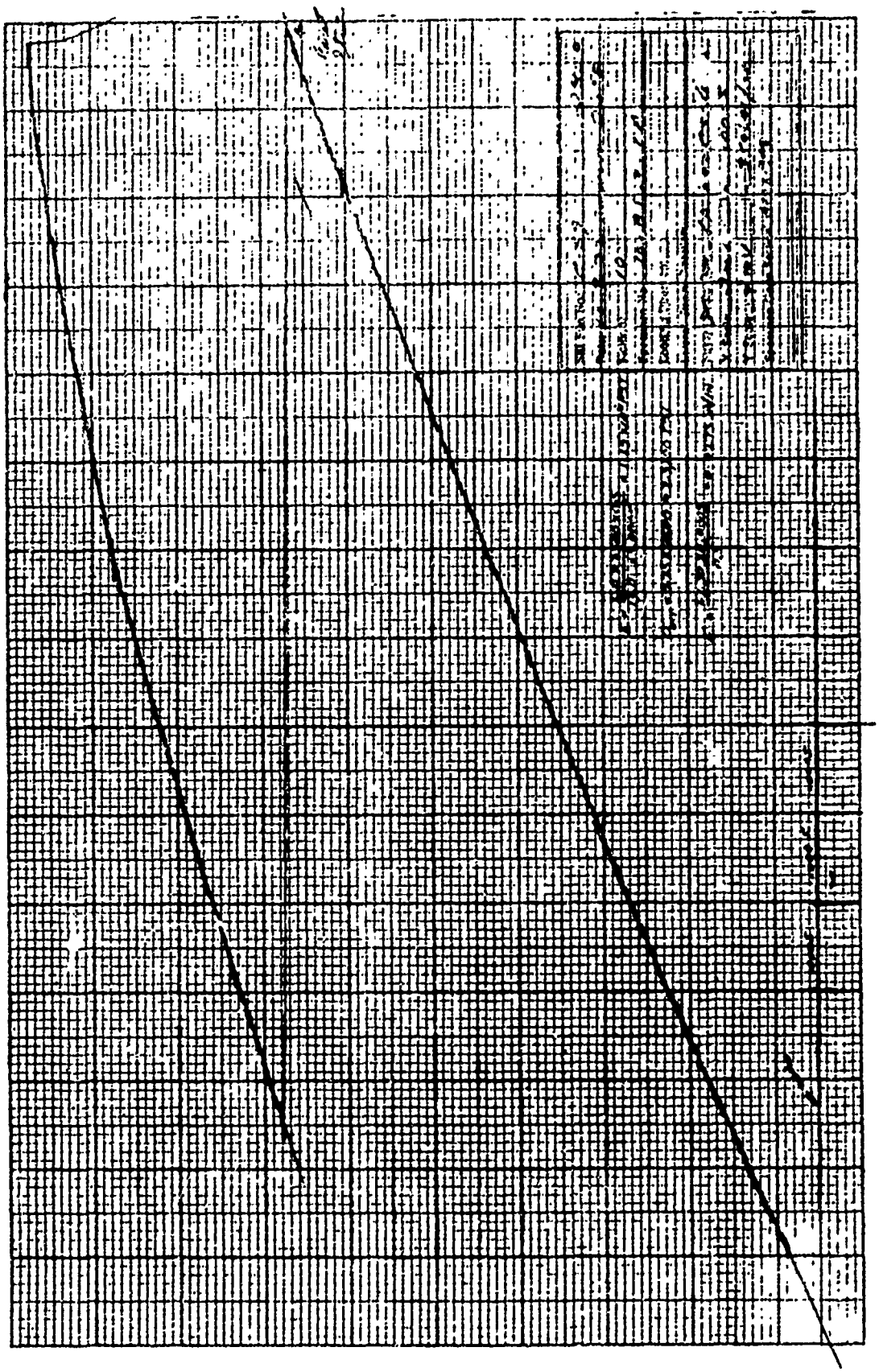


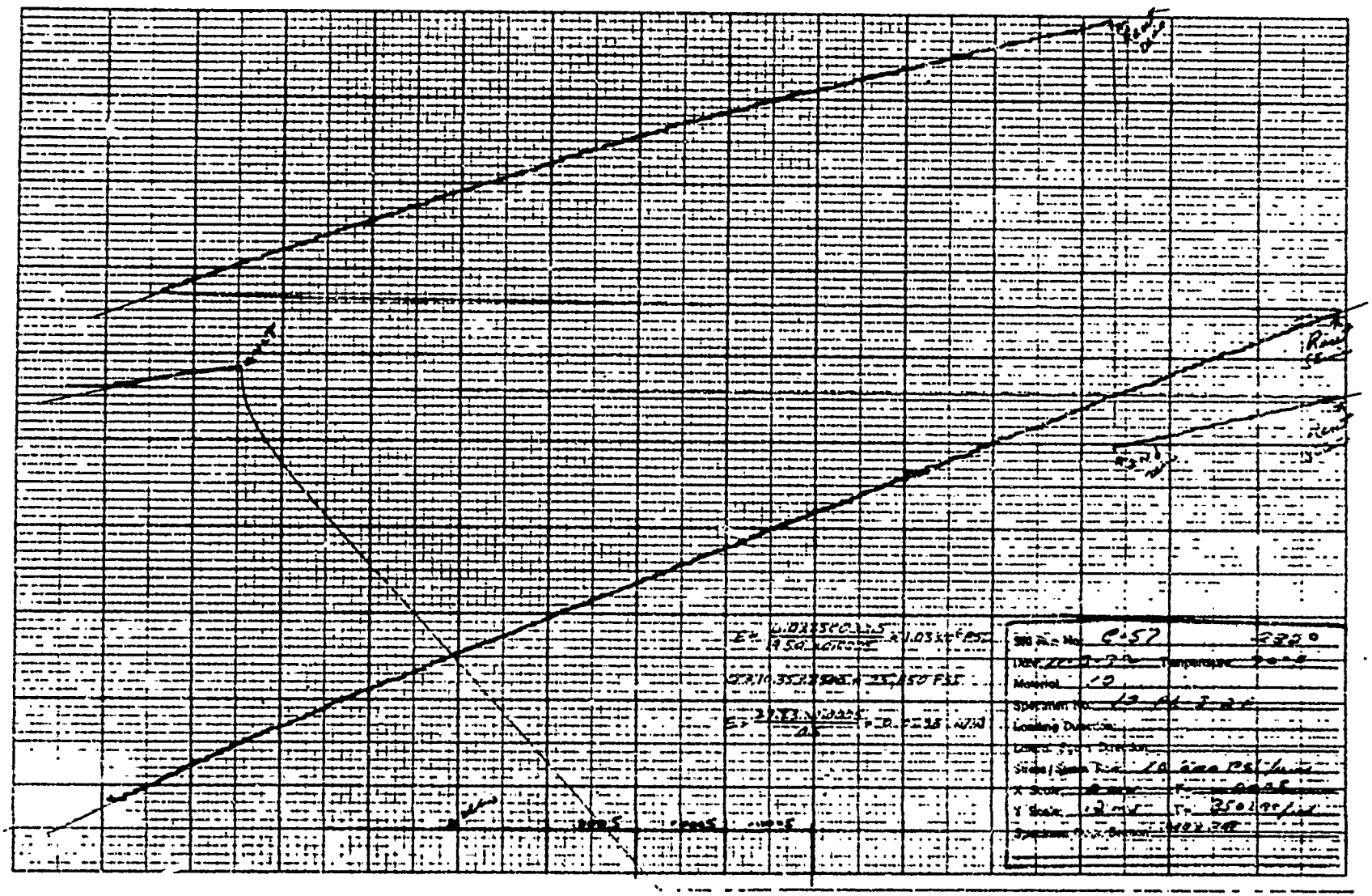


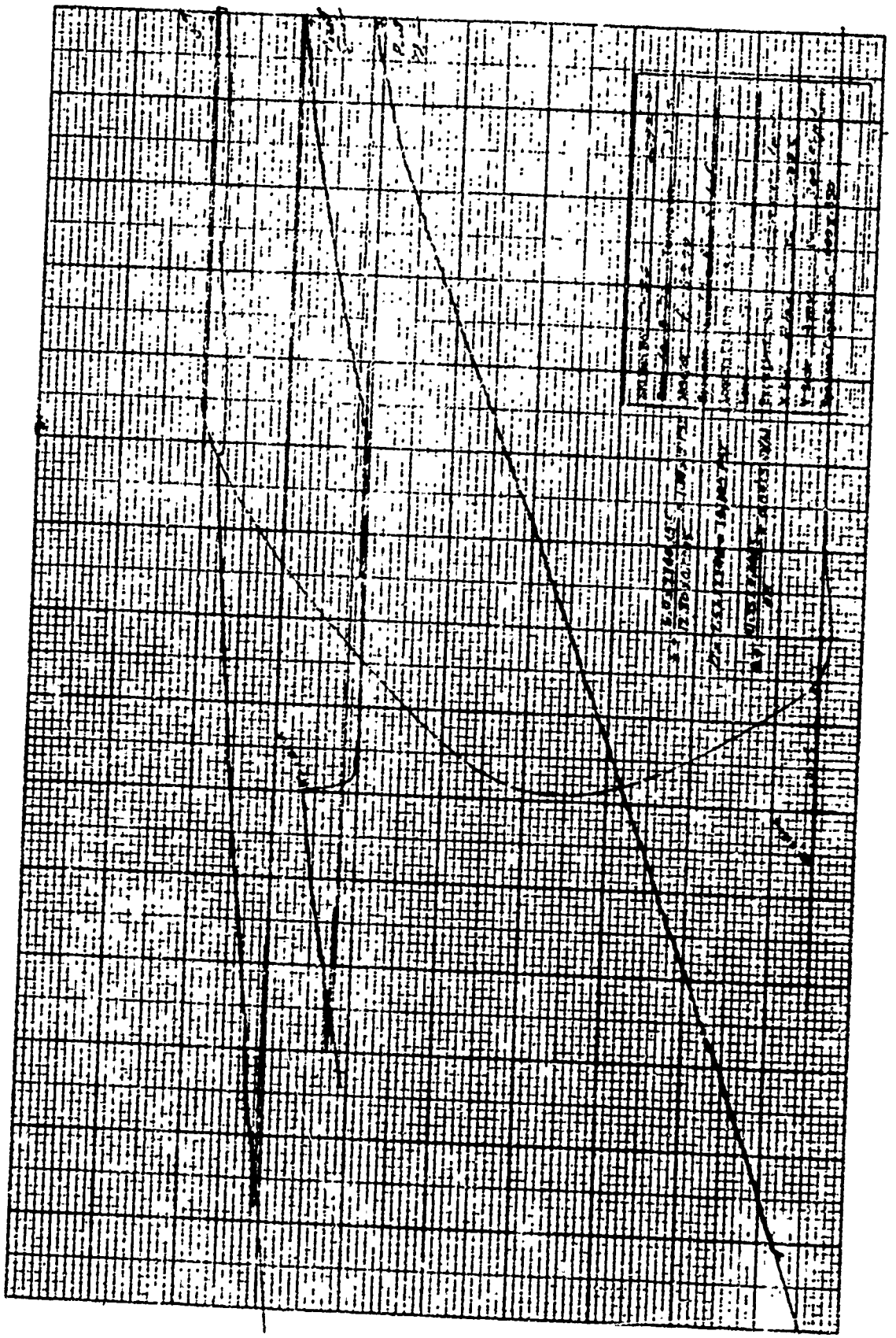


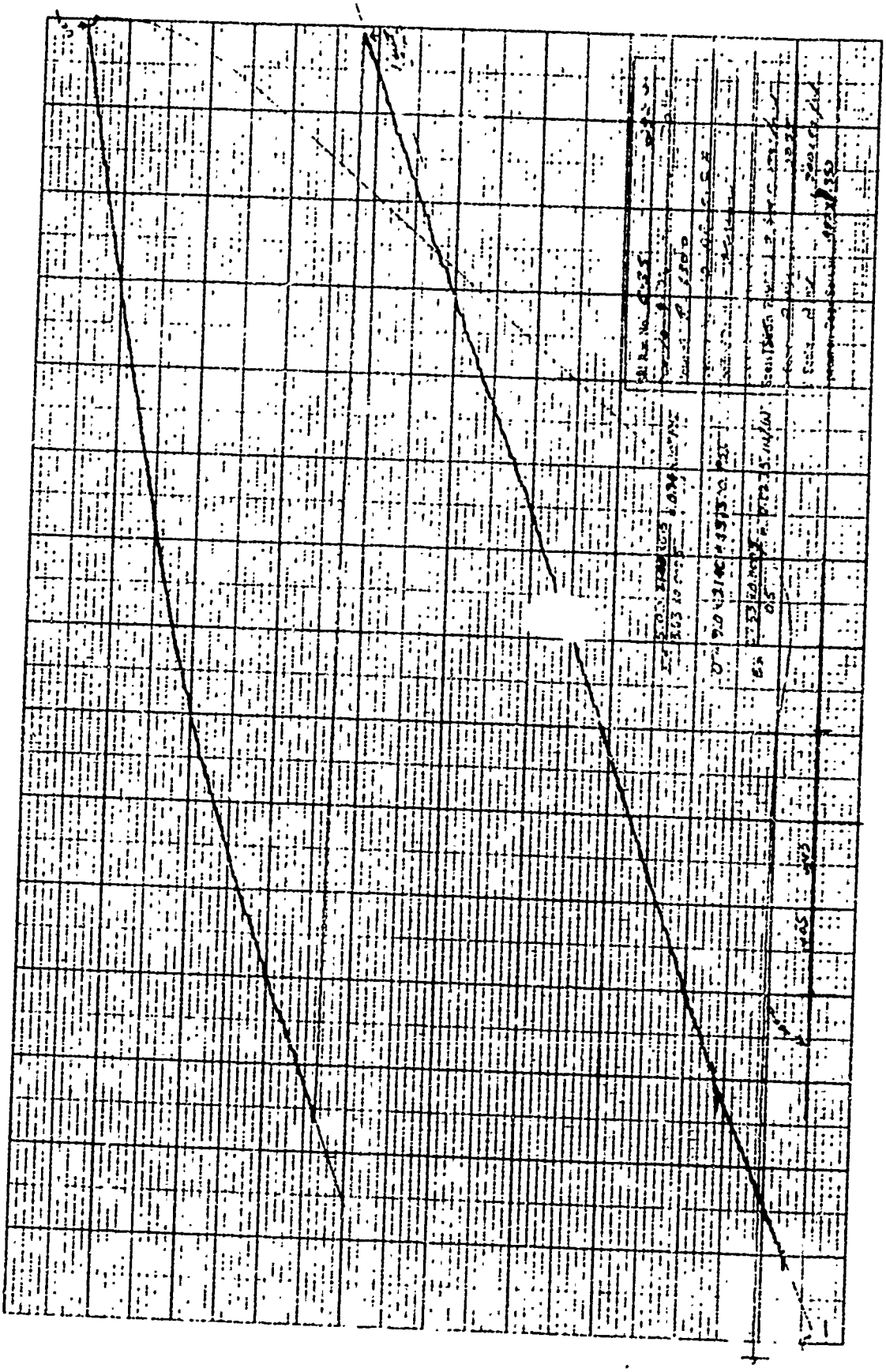







Material LO
Temperature
Loading Direction
Direction
Strain Rate
X Scale
Y Scale





APPENDIX J

TENSILE AND COMPRESSIVE STRESS-STRAIN CURVES FOR AVCO 3DQP - MATERIAL 11

Test Run No. T67 (2420)

Date: 2/10/72 Temperature: 70

Material: 11

Specimen No: 4E-8-1C

Location: AX18L

Integral Digital Display:

Strain Gage Scale: 0.2" = 1 cm

X Scale: 0.2 MV = 0.801"

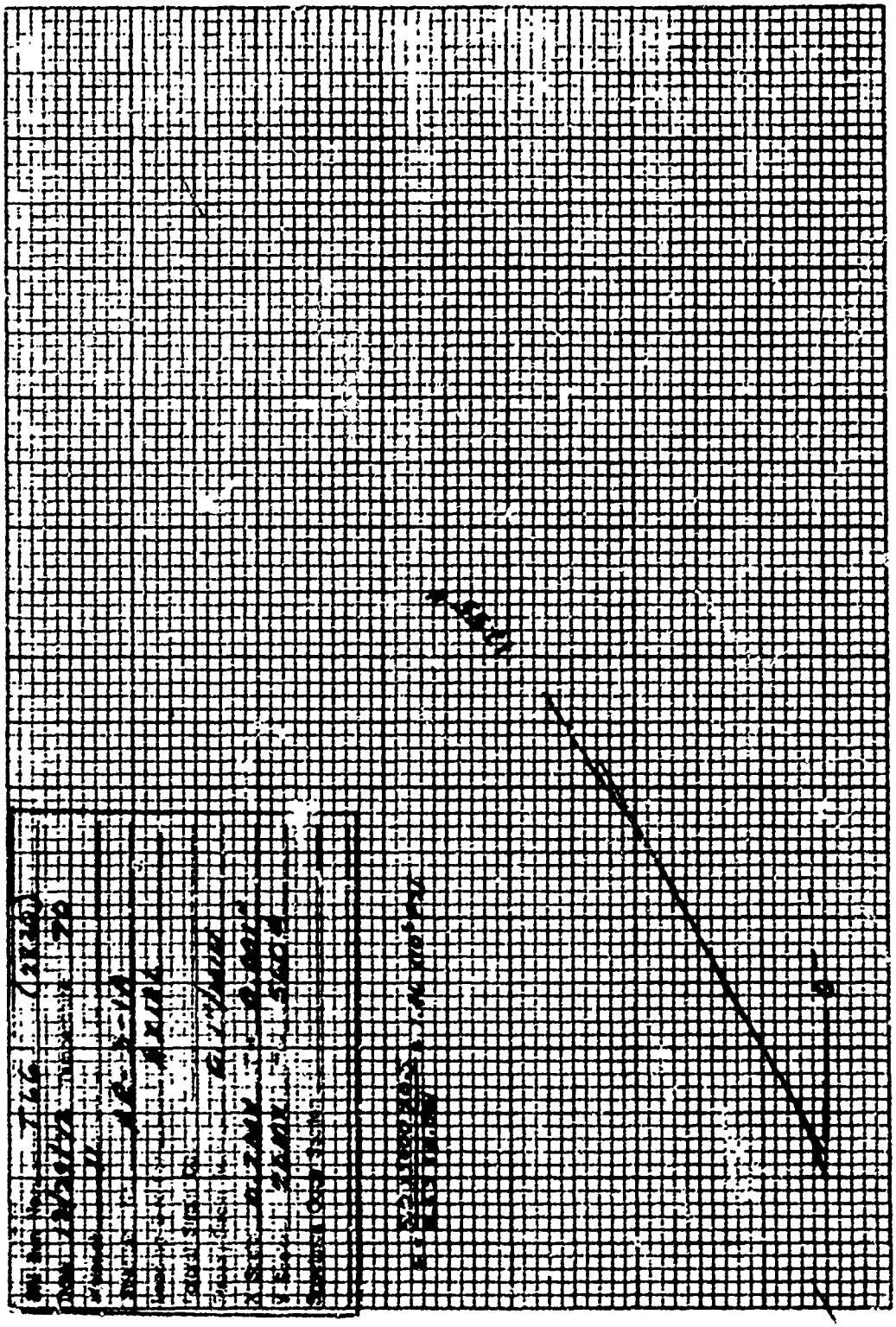
Y Scale: 20 MV = 360°

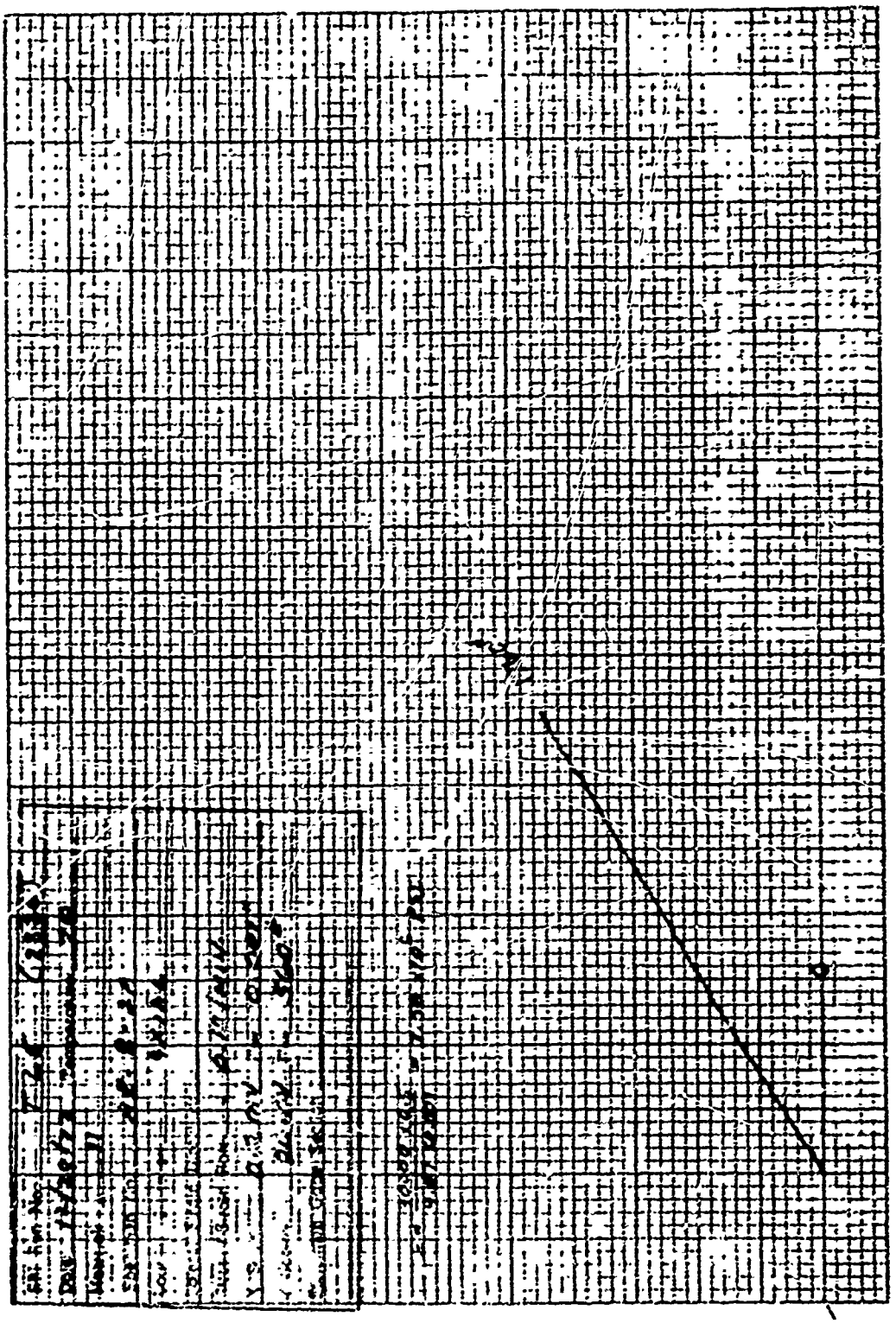
Specimen Cross Section: .666 x 0.370

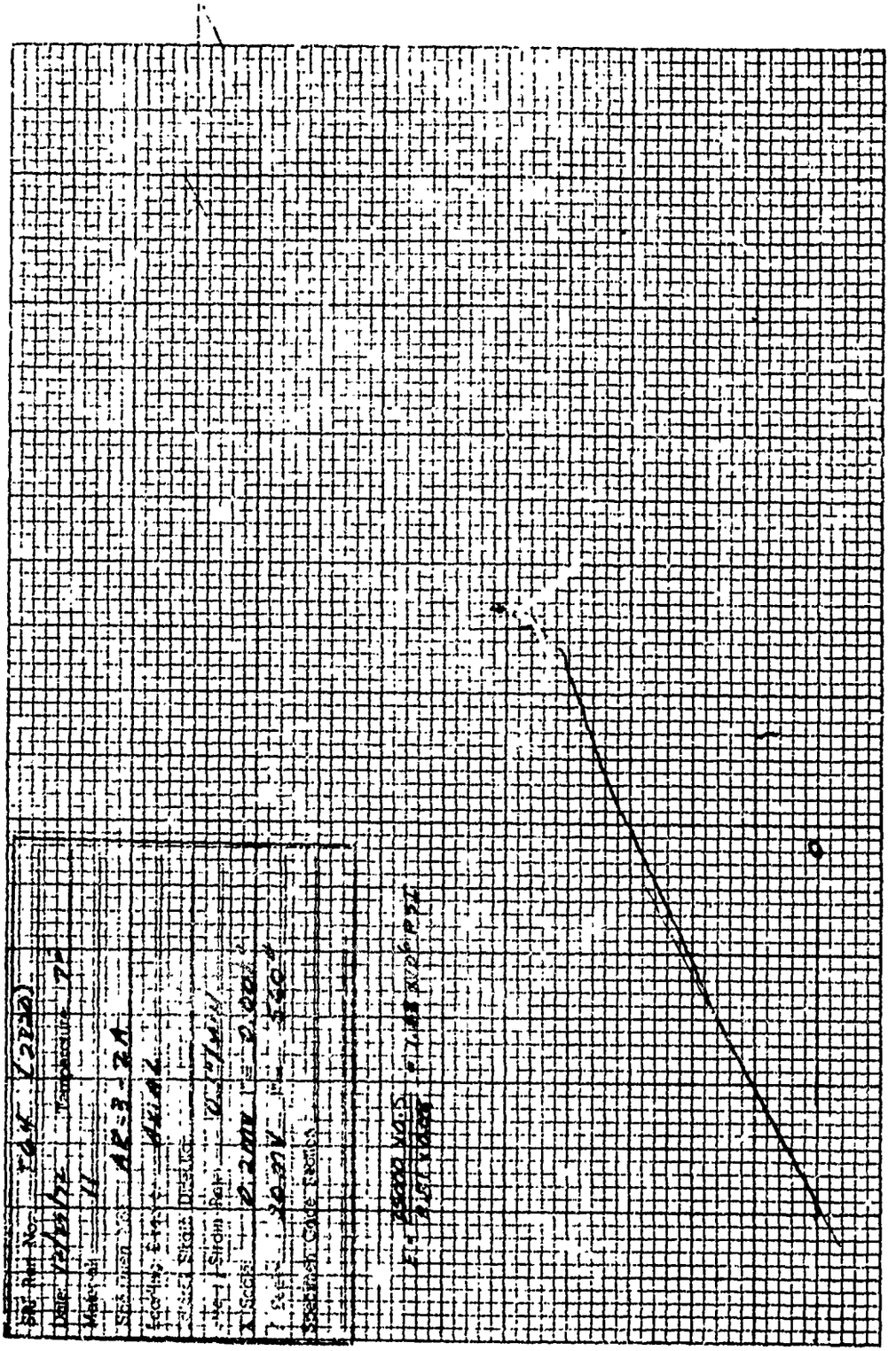
$K = \frac{60 \times 5000 \times 0.5}{\pi \times 0.801} = 1.19 \times 10^5$ PSI

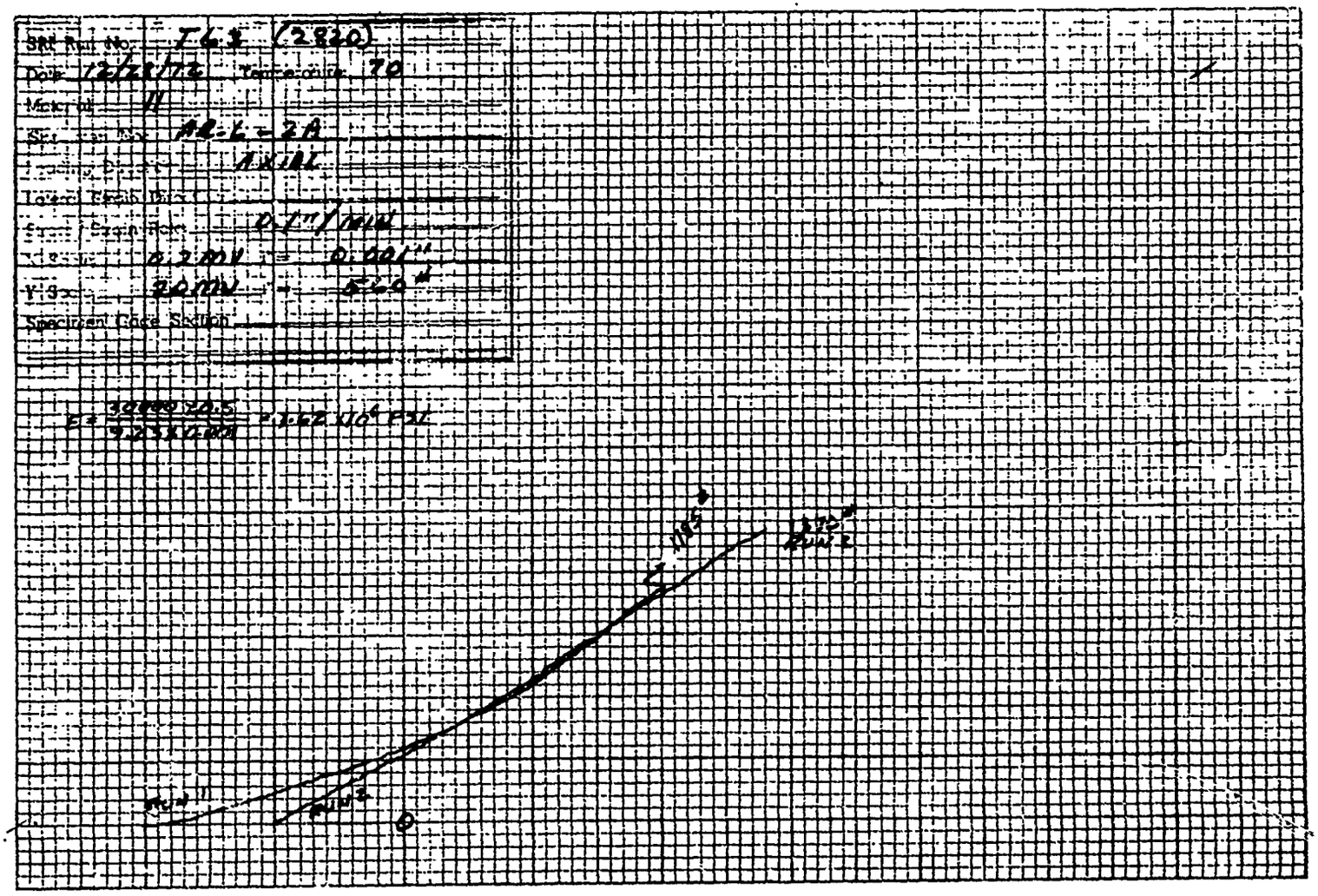
360°

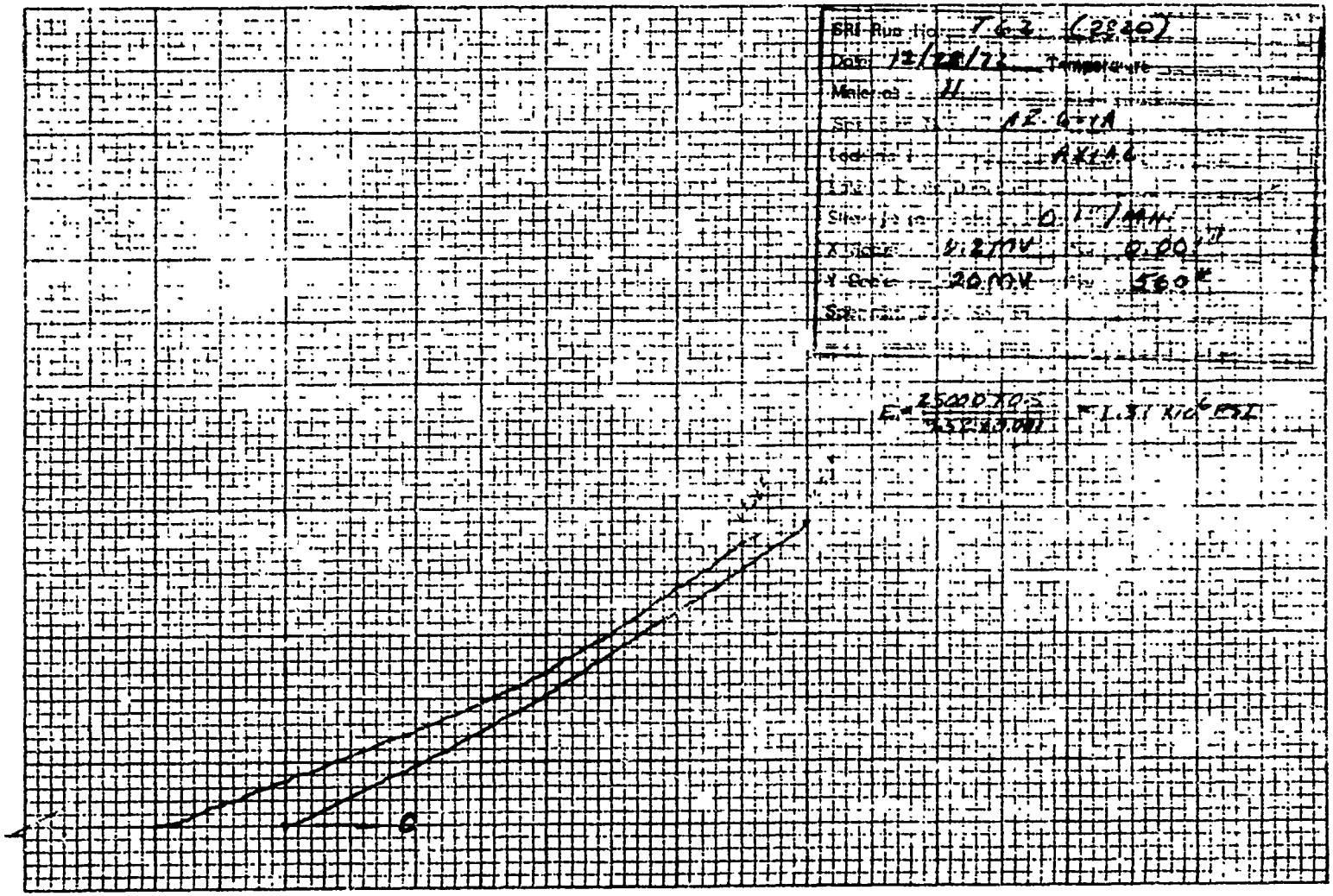
0

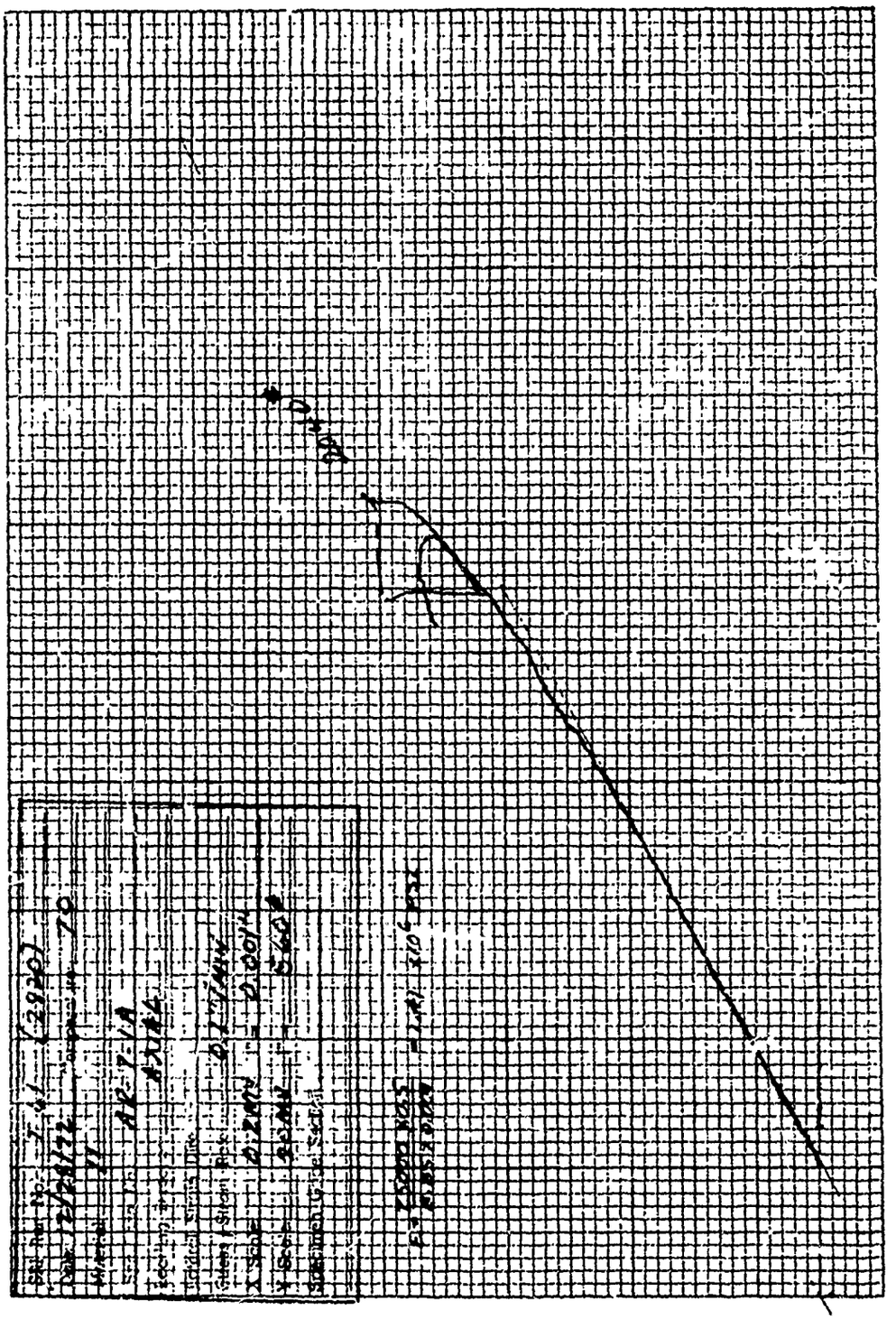


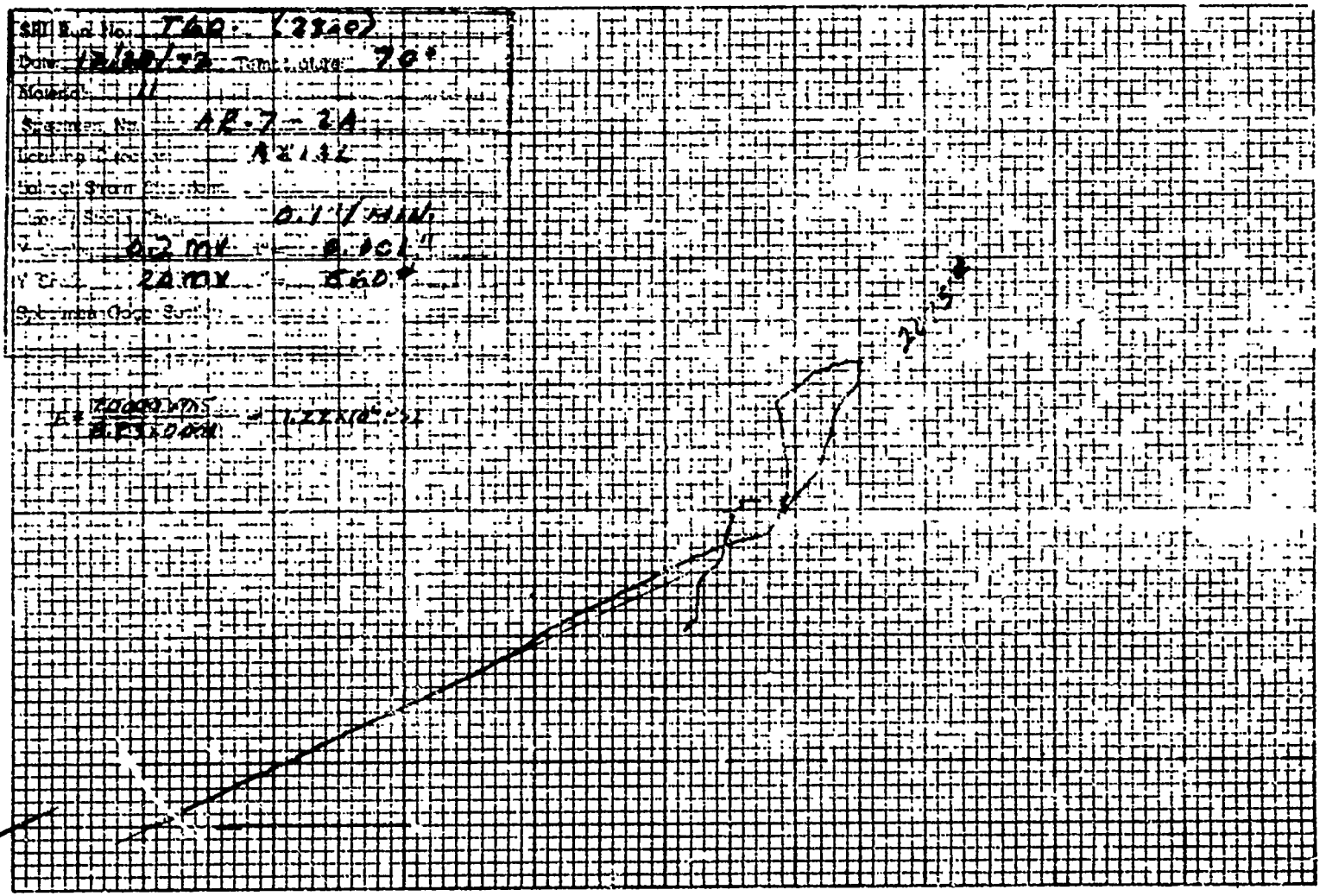


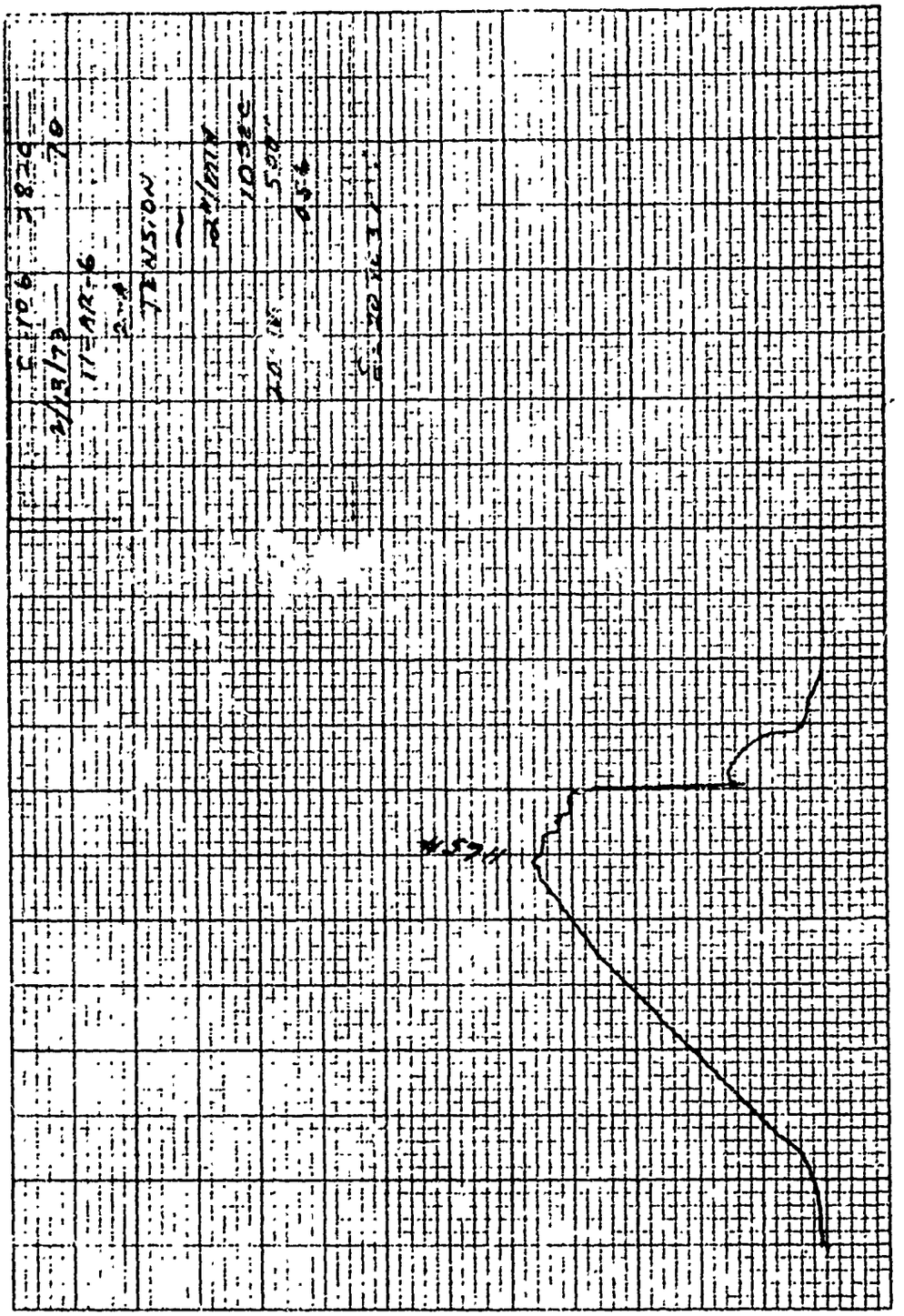

Temperature 72
AR=3-24
2.2MW
30.3KV
340°
Specimen Code Item

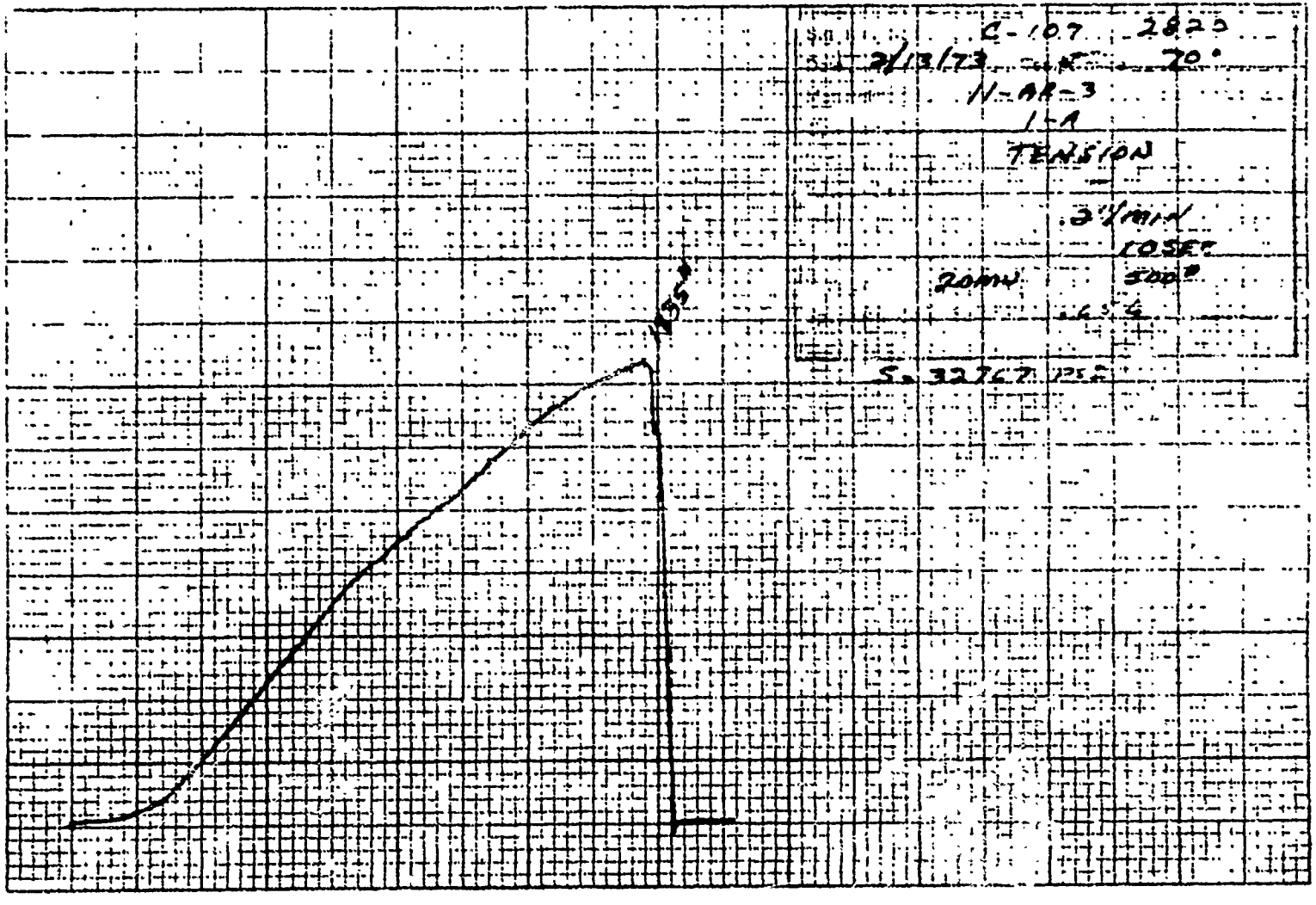

Std Run No. T4S (2820)
Date 12/28/72 Temperature 70
Material 11
Specimen No. AE-L-2A
Loading Direction AXIAL
Lower Limit Dial 0.1" / INCH
Upper Limit Dial 0.2 INCH = 0.001"
Y Sc. 20 MV = 5 ksi
Specimen Face Section
E = 30000 x 0.5 / 9.253 x 0.001 = 1.62 x 10^6 PSI
11.5°
12.75°

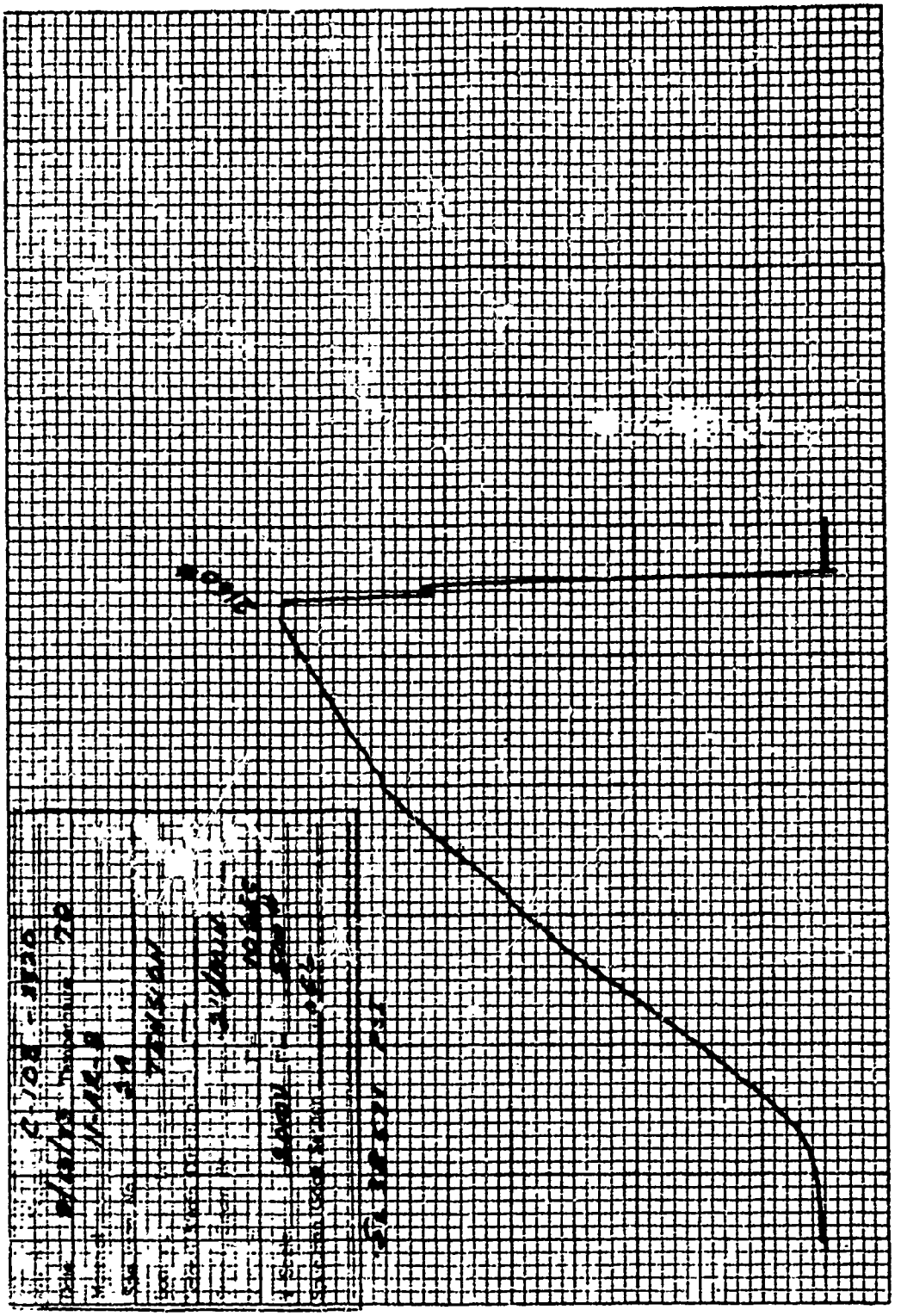

SRI Run no: T-6-2 (2540)
Date: 12/28/72 Temperature
Material: U
Spl: 12.6 x 1A
Load: 4 x 4.6
Slit: 0.1 mm
X Scale: 2.2 MV 0.00 in
Y Scale: 20 MV 550 K
Spl:
E = 25000 x 0.5 / 3.52 x 3.082 = 1.51 x 10^6 PSI
6

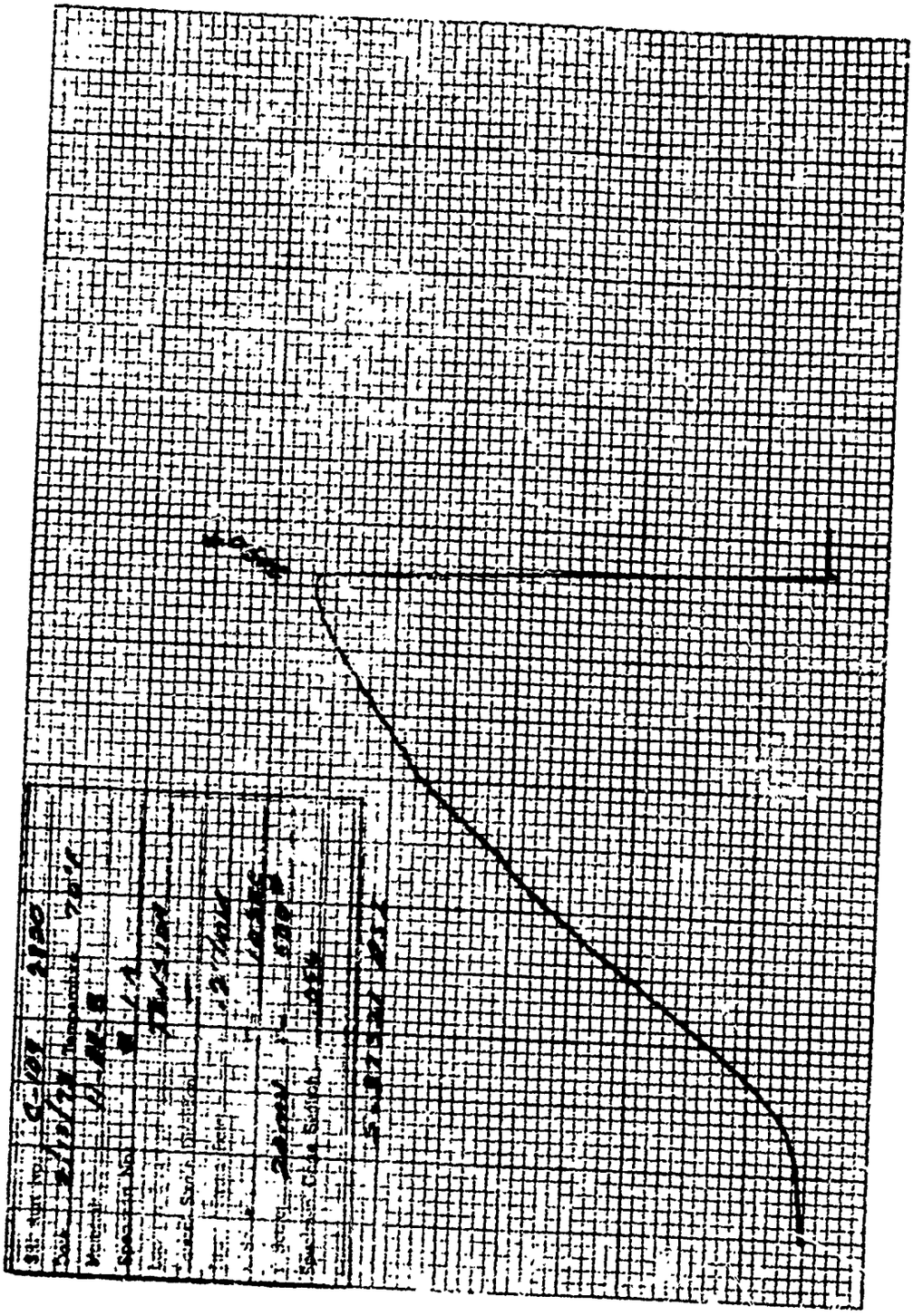


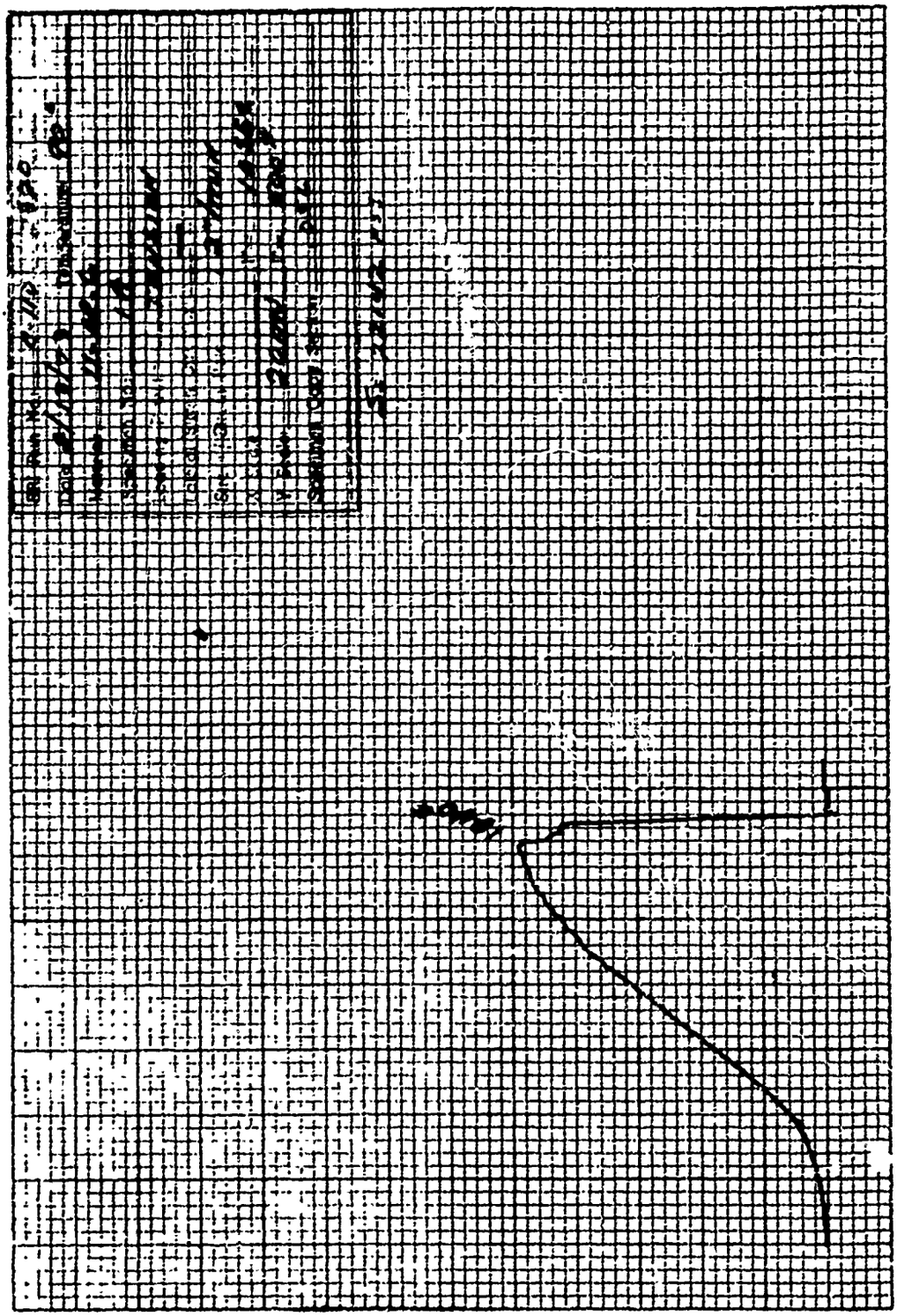

Test No. T60 (2340)
Date 12/20/72 Time: start 70°
Material: Al
Specimen No. AR.7-24
Lot No. Al 1.2
Initial Strain Rate 0.1 /min
Y Axis .02 inx = 8 ksi
X Axis .2 inx = 560#
Specimen Gage Sur.
A= 20000 mm
8.75x10000
= 1.22x10^-4

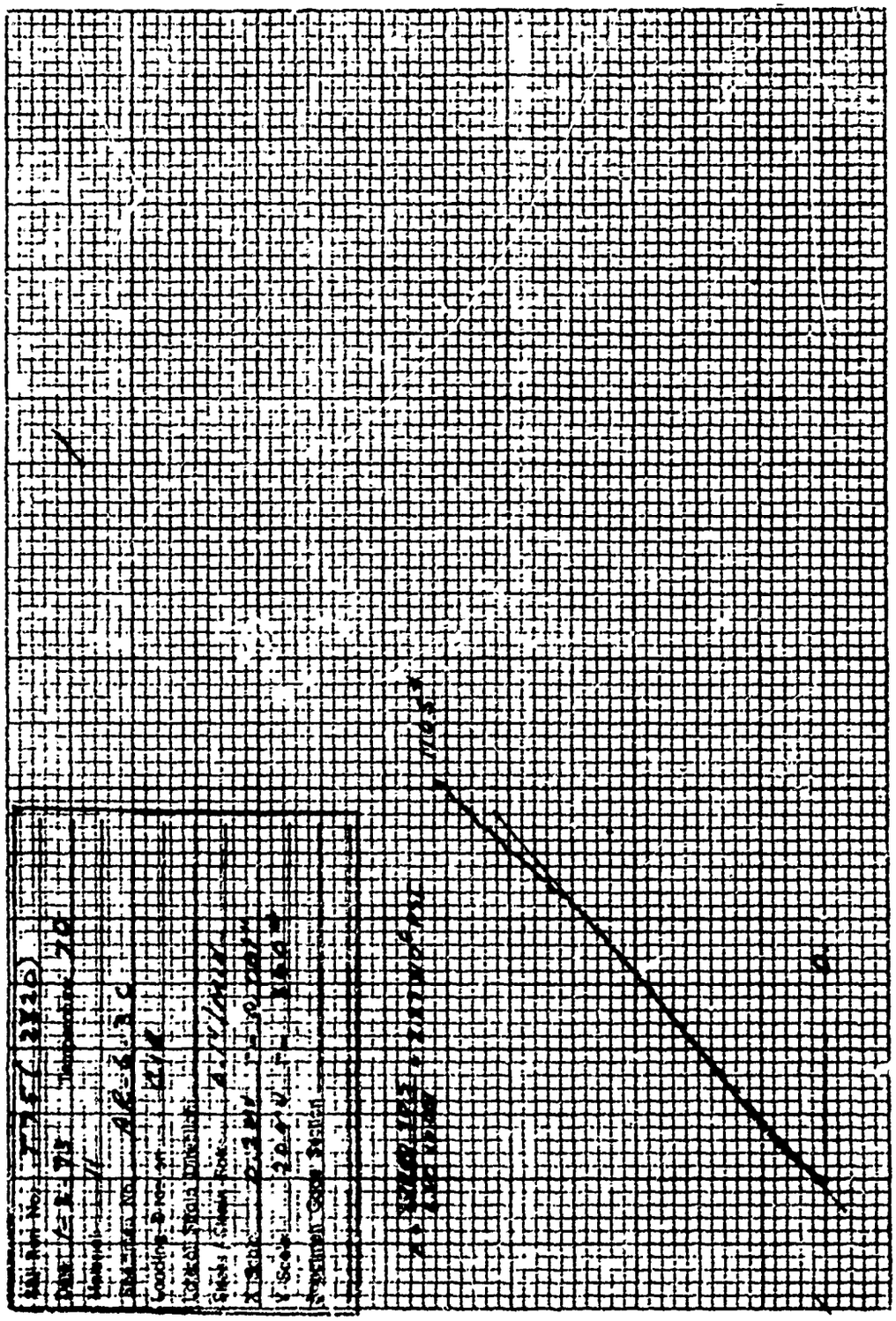



C-107 2825
2/13/73 F 70°
N-AR-3
1-A
TENSION
3½ min
COSET
500#
ROHN
S. 32767



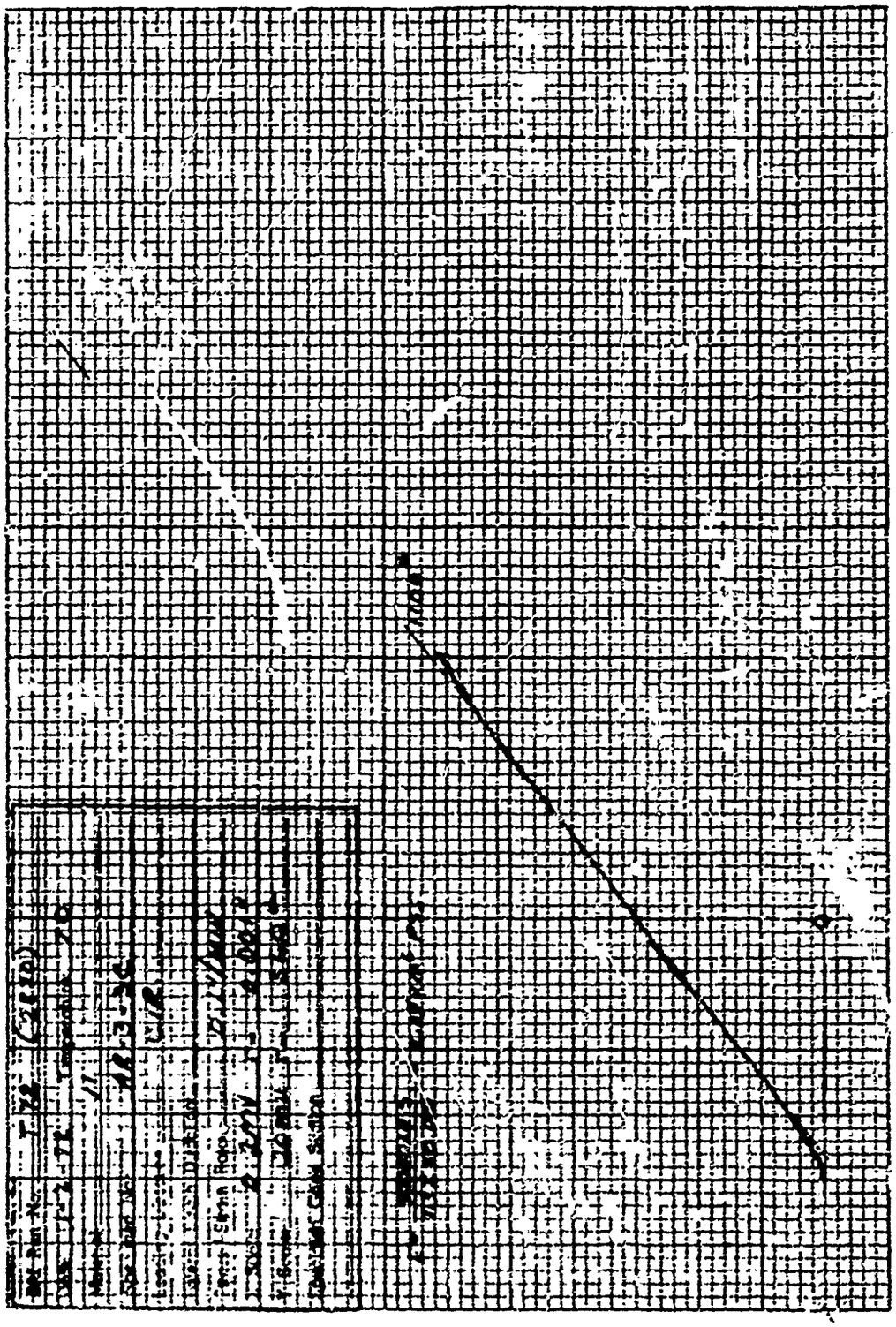


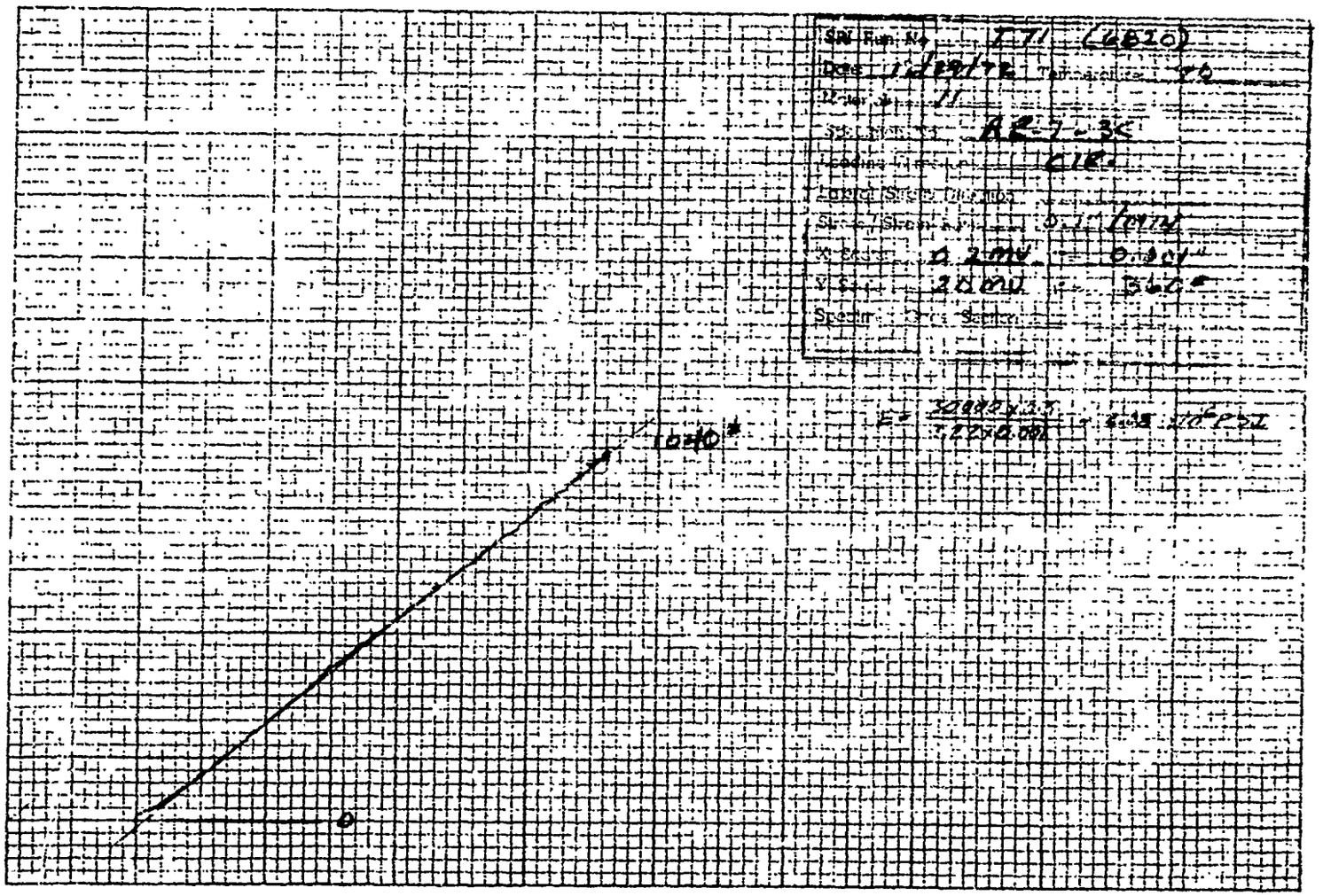


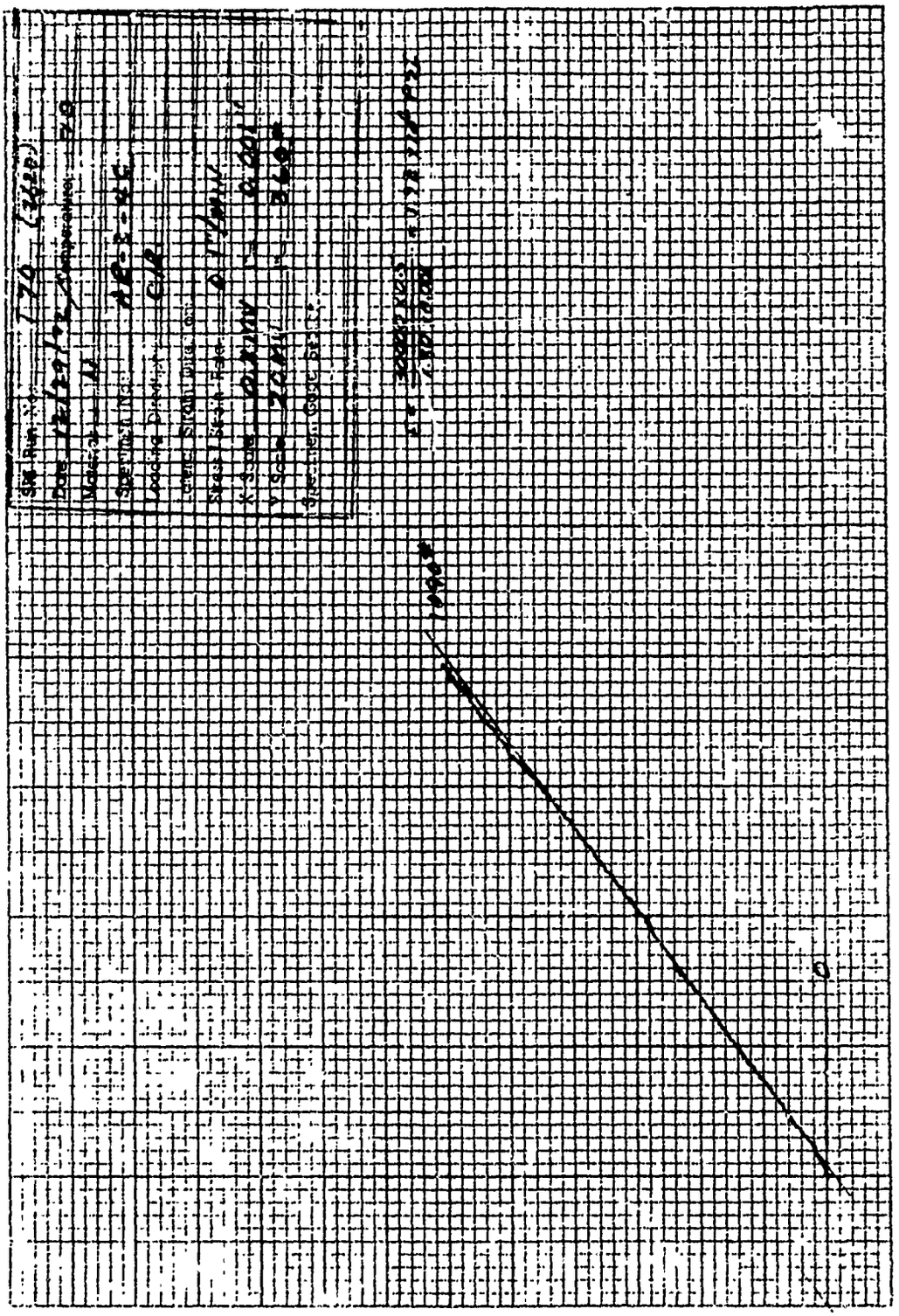


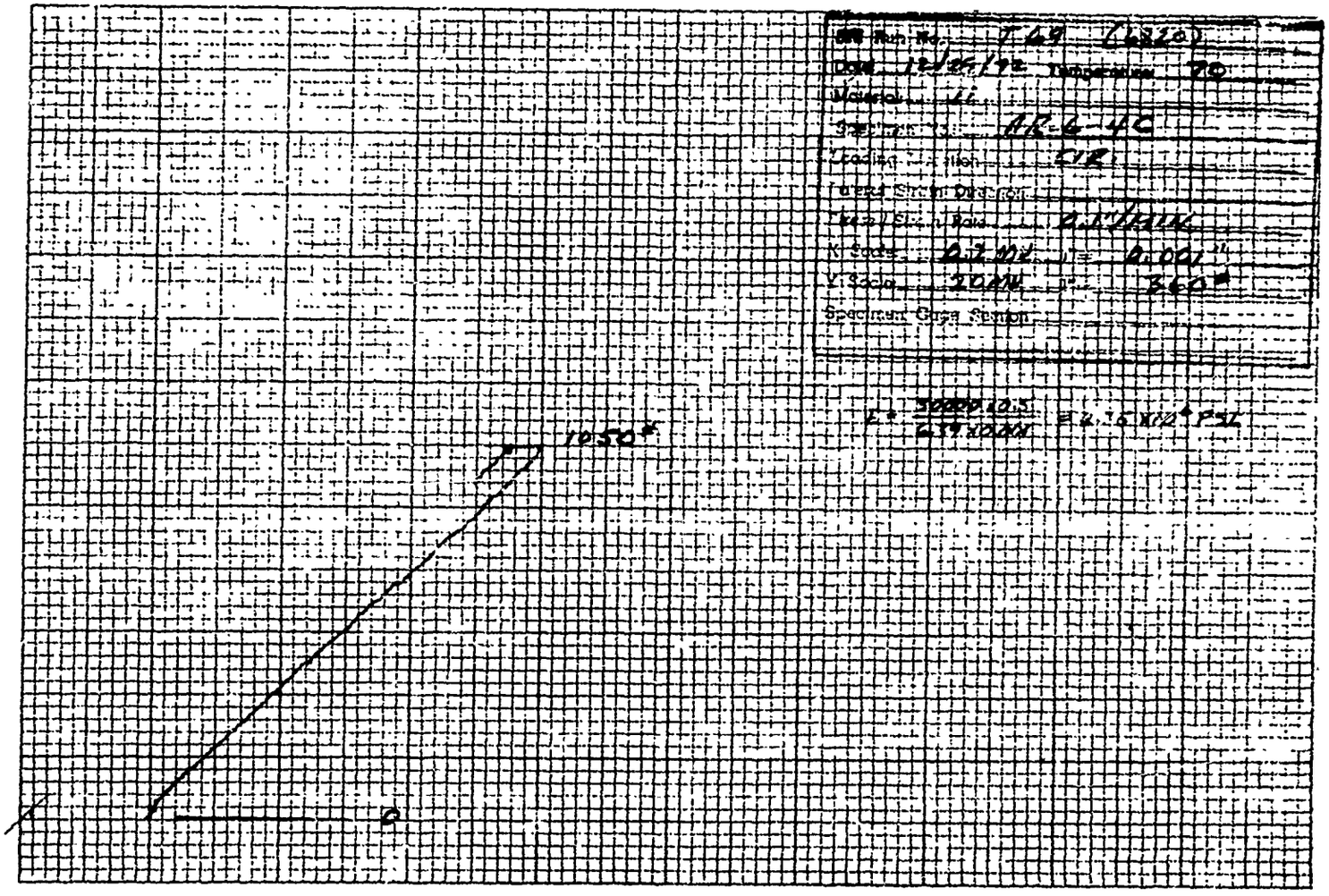


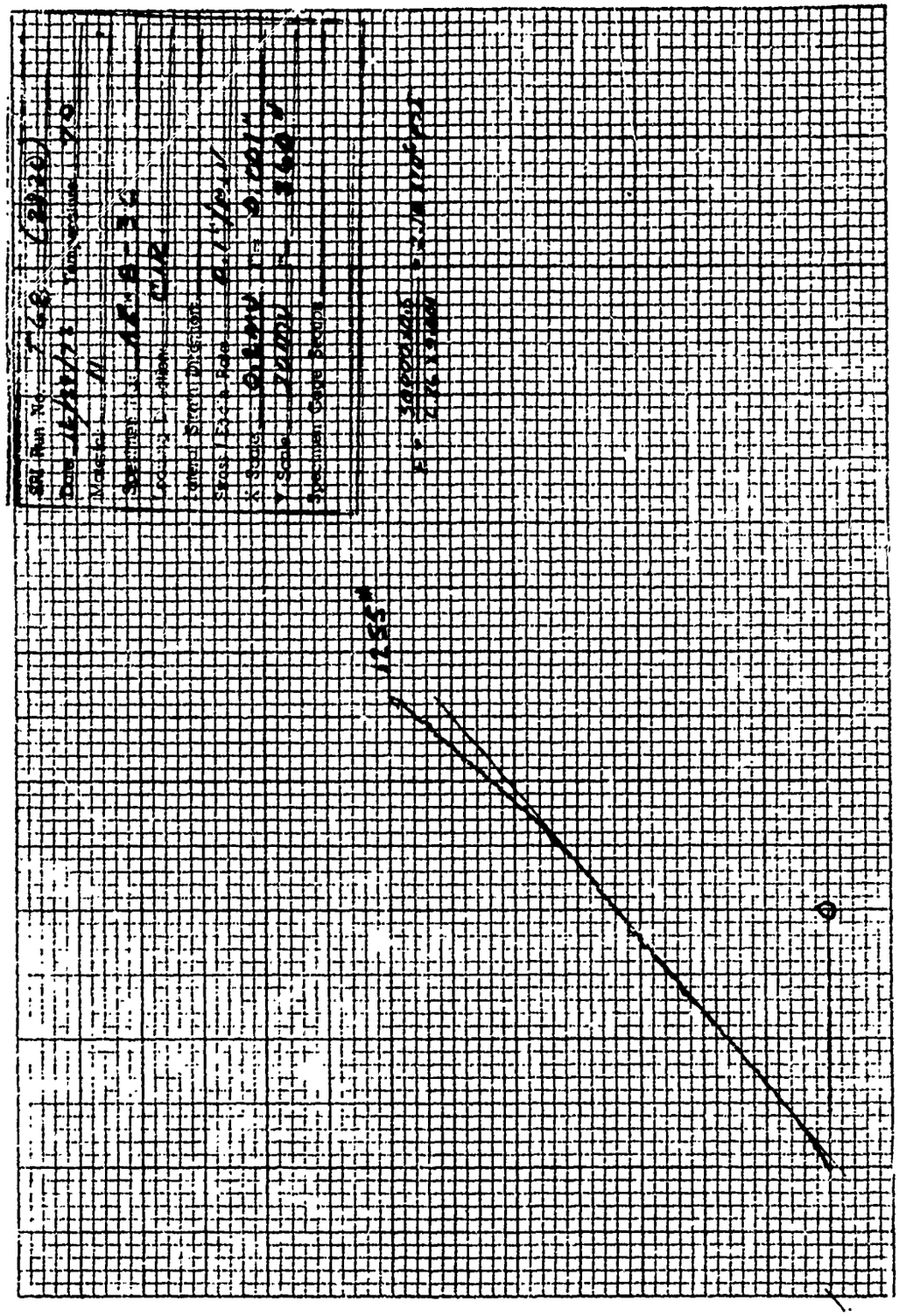

SBF Run No: 773 (2820)
Date: 1-24-73
Temperature: 70
Material: Aluminum
Specimen: 2-2-45
Beam Properties: 2MeV
Current:
Beam Energy: 2.1" Lucite
X Scan: 2MV 0.2cm
Y Scan: 2MV 360°
Specimen Goal: Scratch
11:45 Y
0

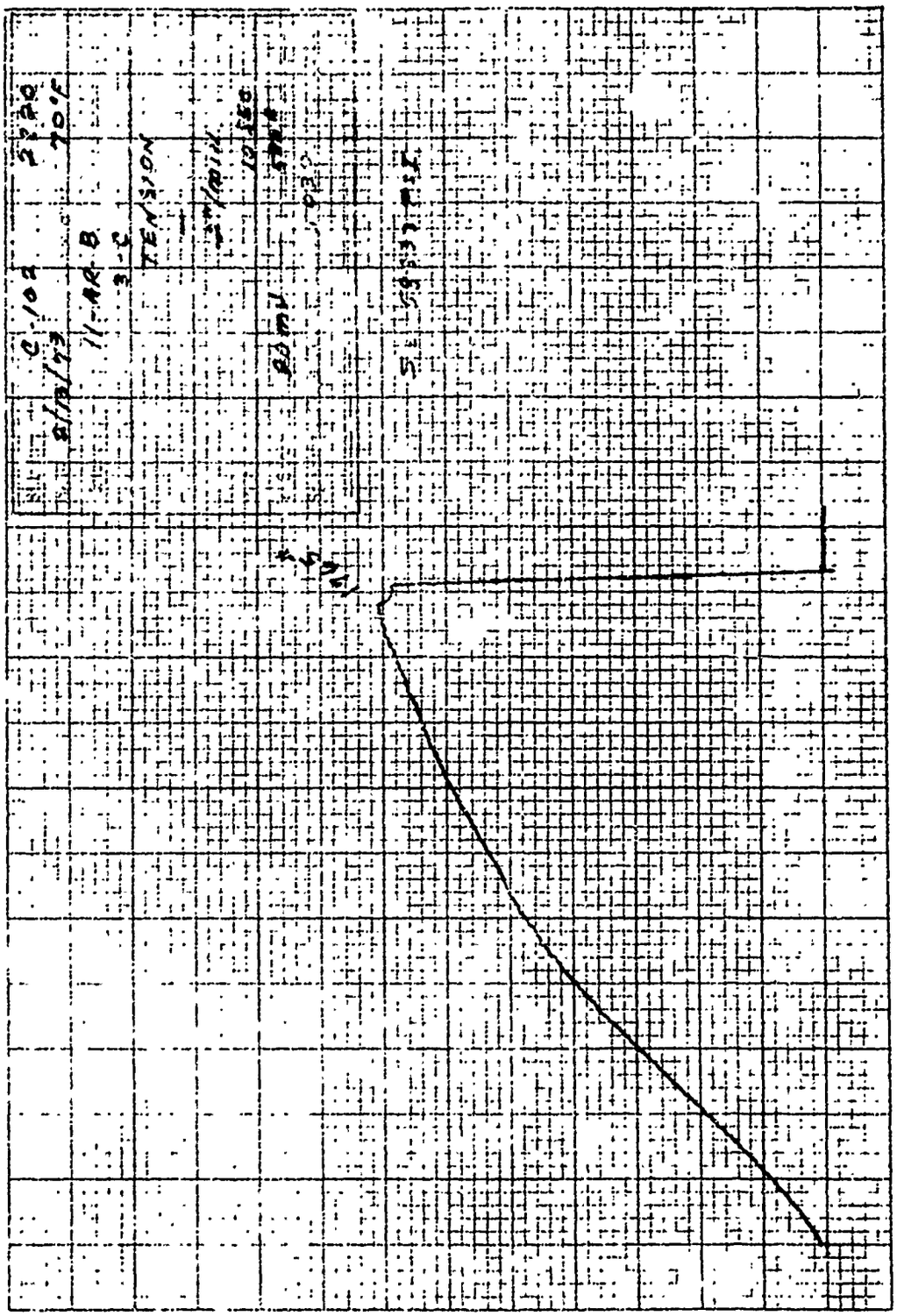


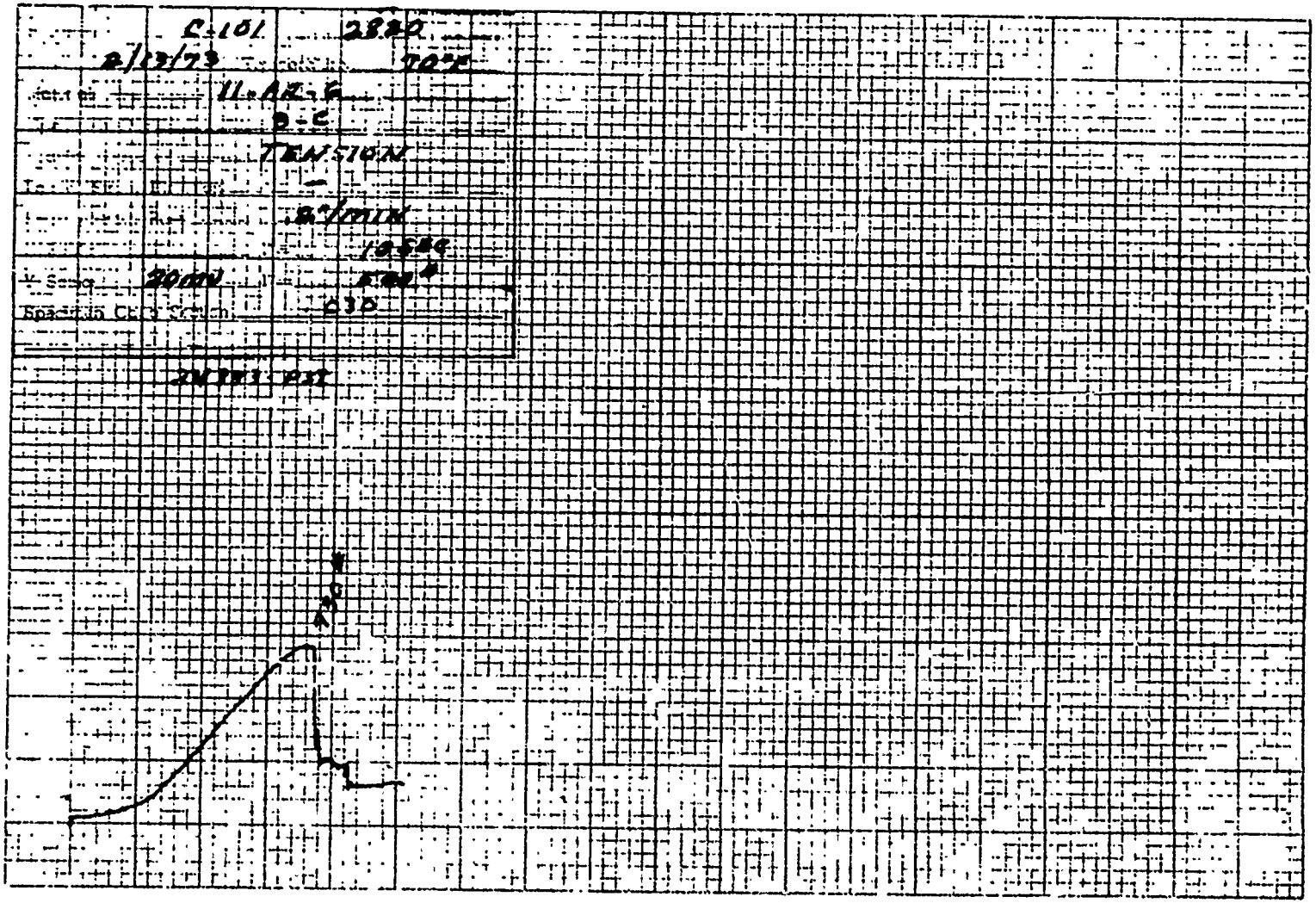

10:40

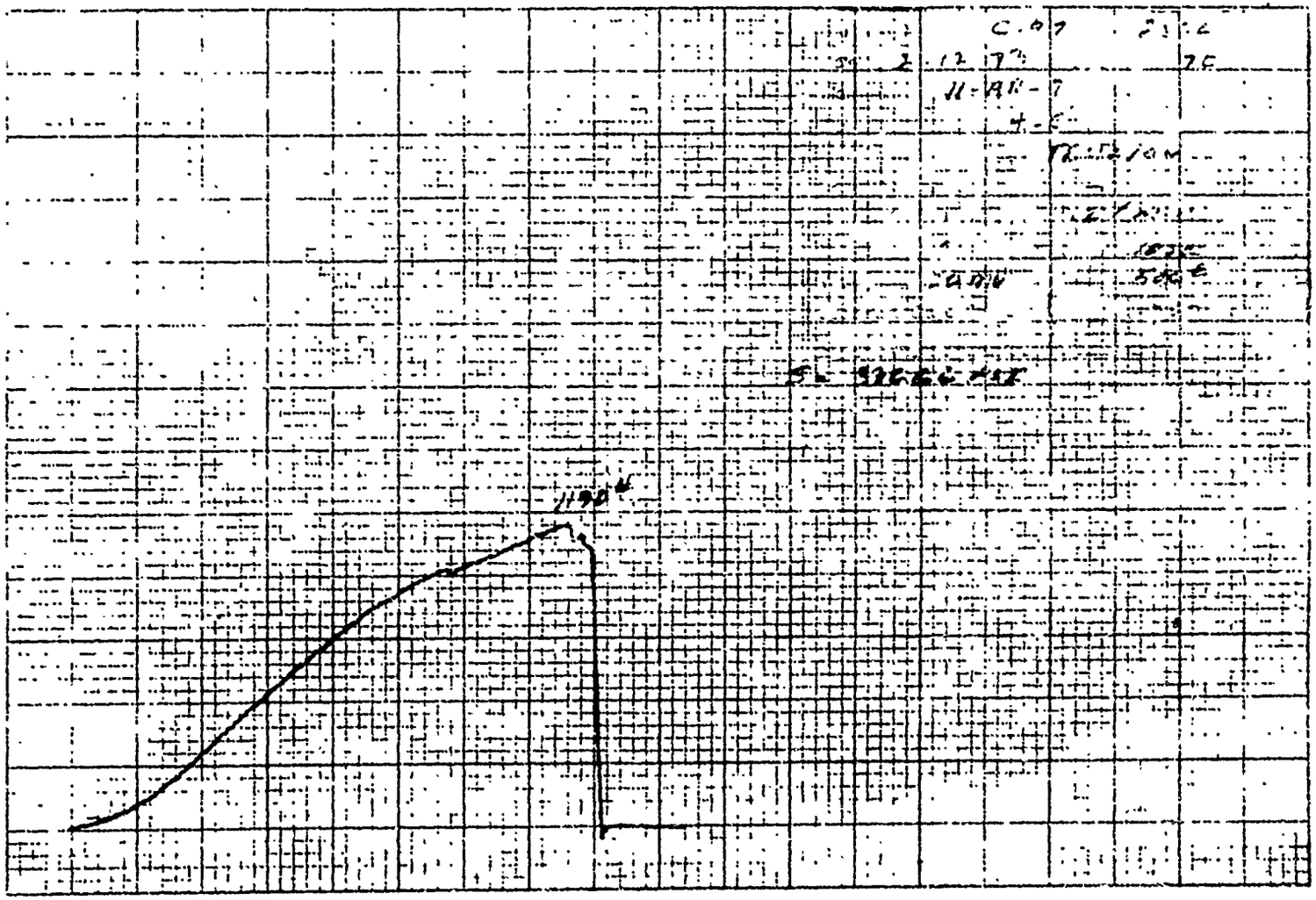


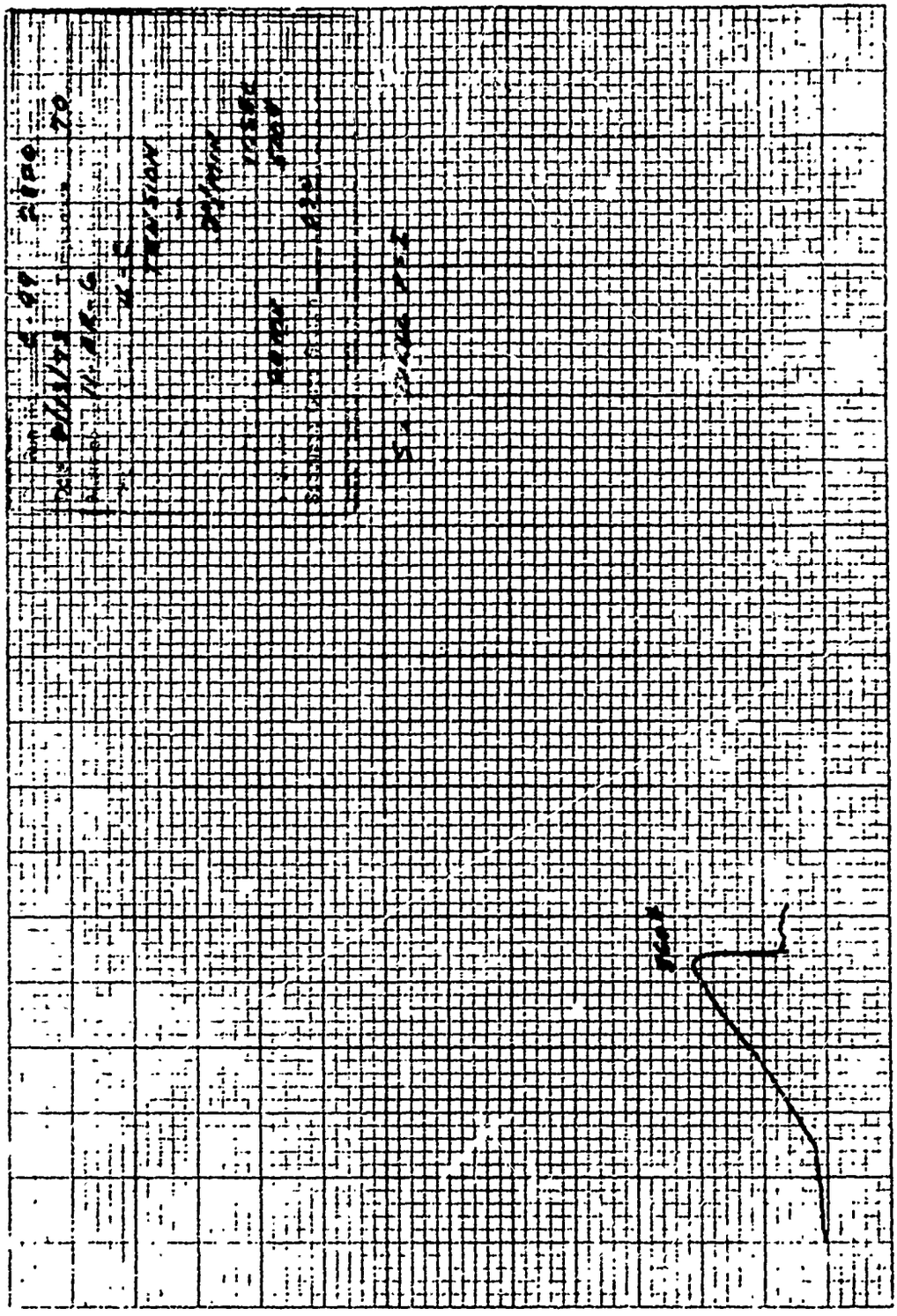

Test Run No. T-69 (Cast 20)
Date 12/26/92 Temperature 70
Material 4L
Specimen AR-4-4C
Loading Direction CIR.
Area/Strain Rosette 0.1"/in/in
K Scale 0.2 Ml/in = 0.001 in/in
V Scale 20 kN/in = 360 lb
Specimen Gage Section
E = 30000 ksi / 6.39 x 10^6 psi = 4.7 x 10^3 psi
1050 lb
0

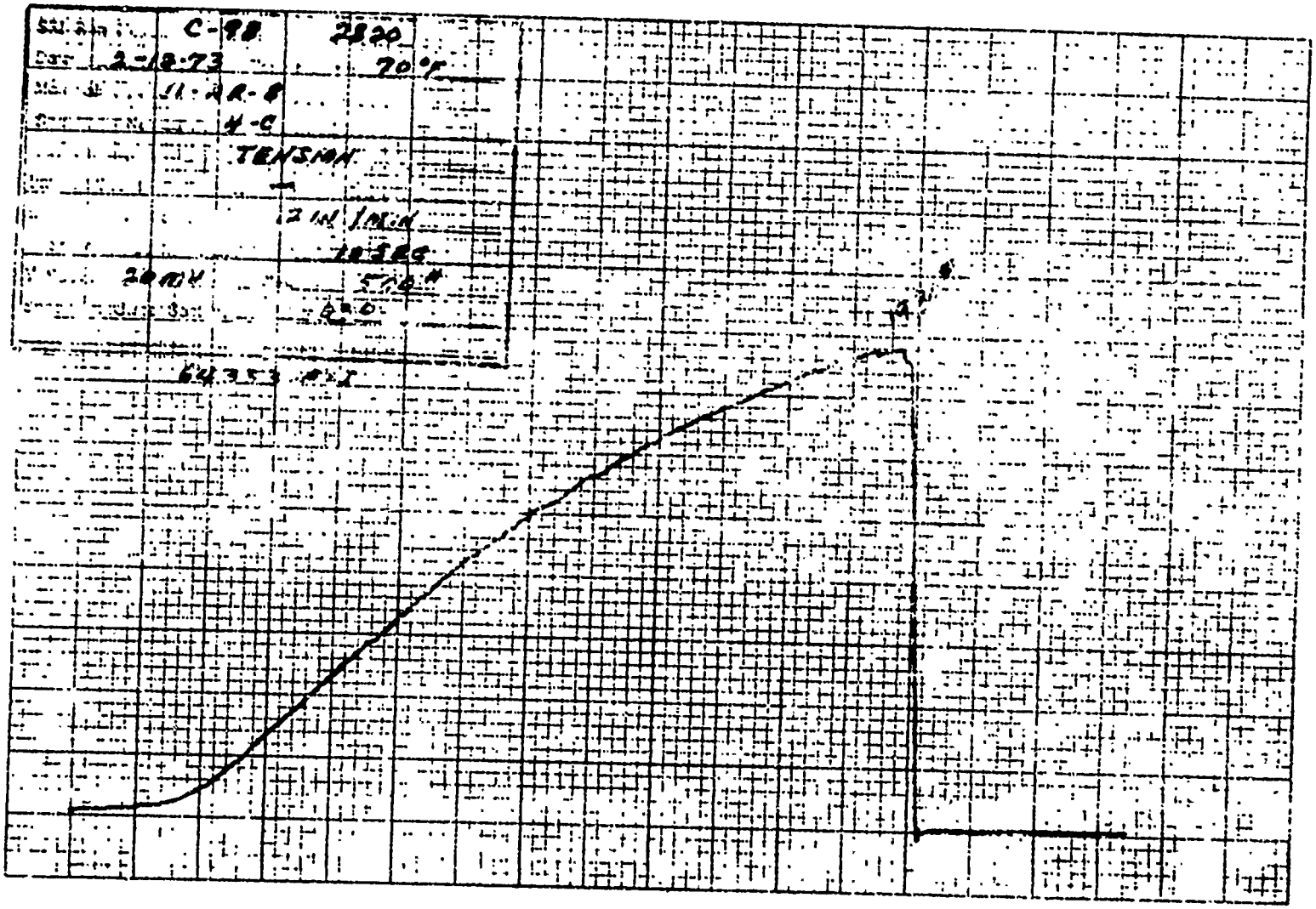


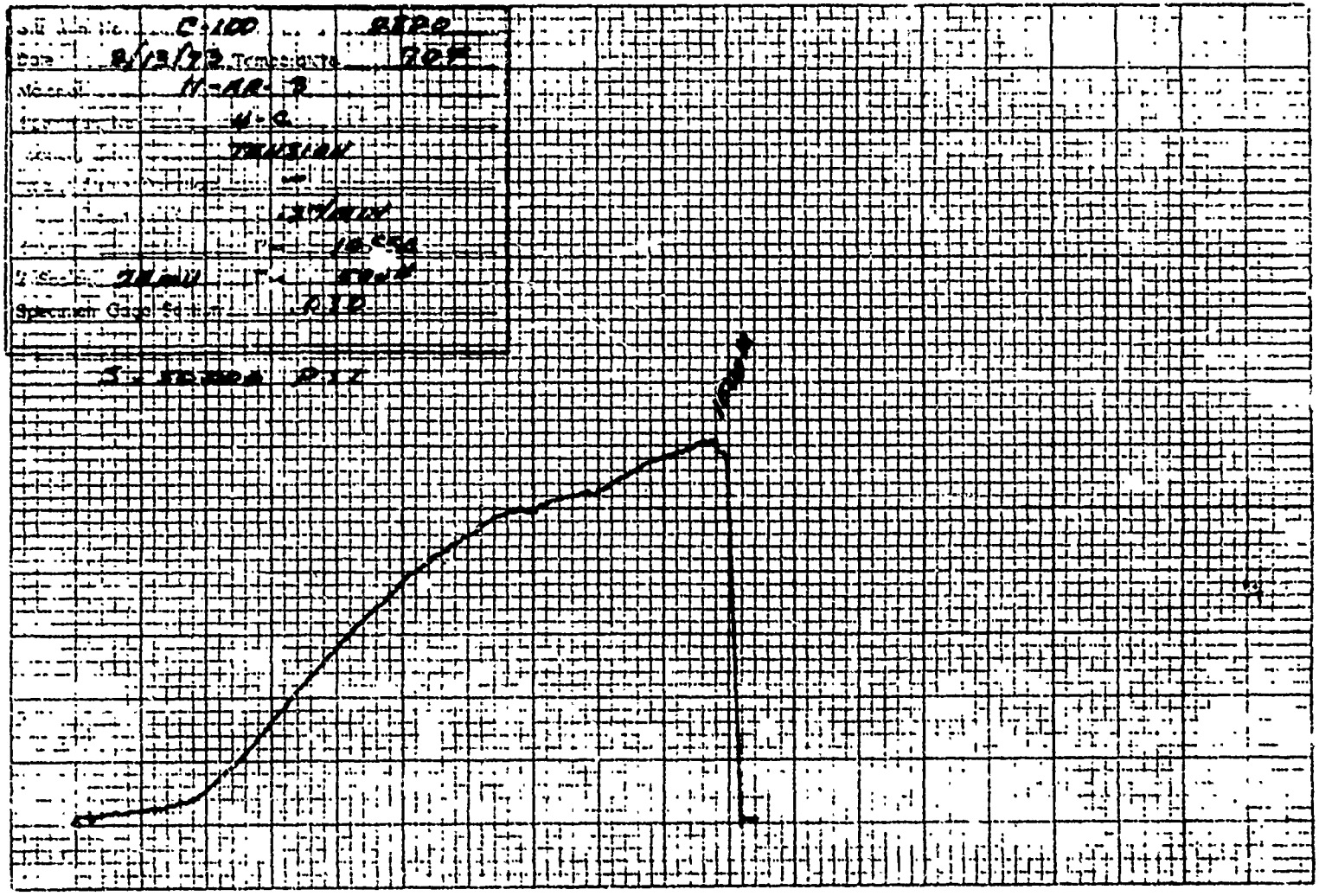

G-10 2 5.2Q
8/13/73 70°F
11-NA-B
3-C
TENSION
50 mil

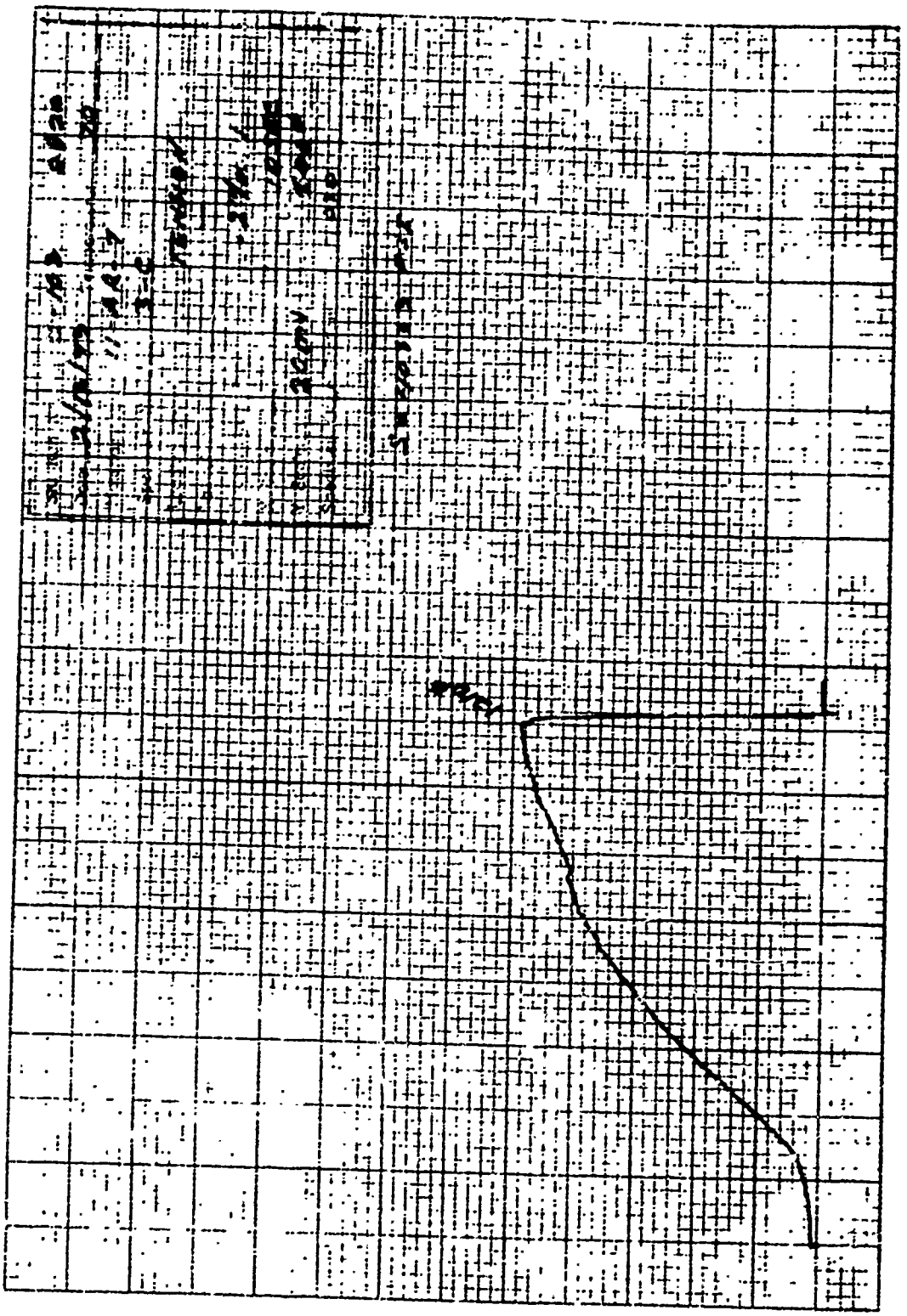

C-101
2820
2/13/73
70°F
11 AZ-5
D-C
TEN-10M
8"/MIN
20MV
D3D

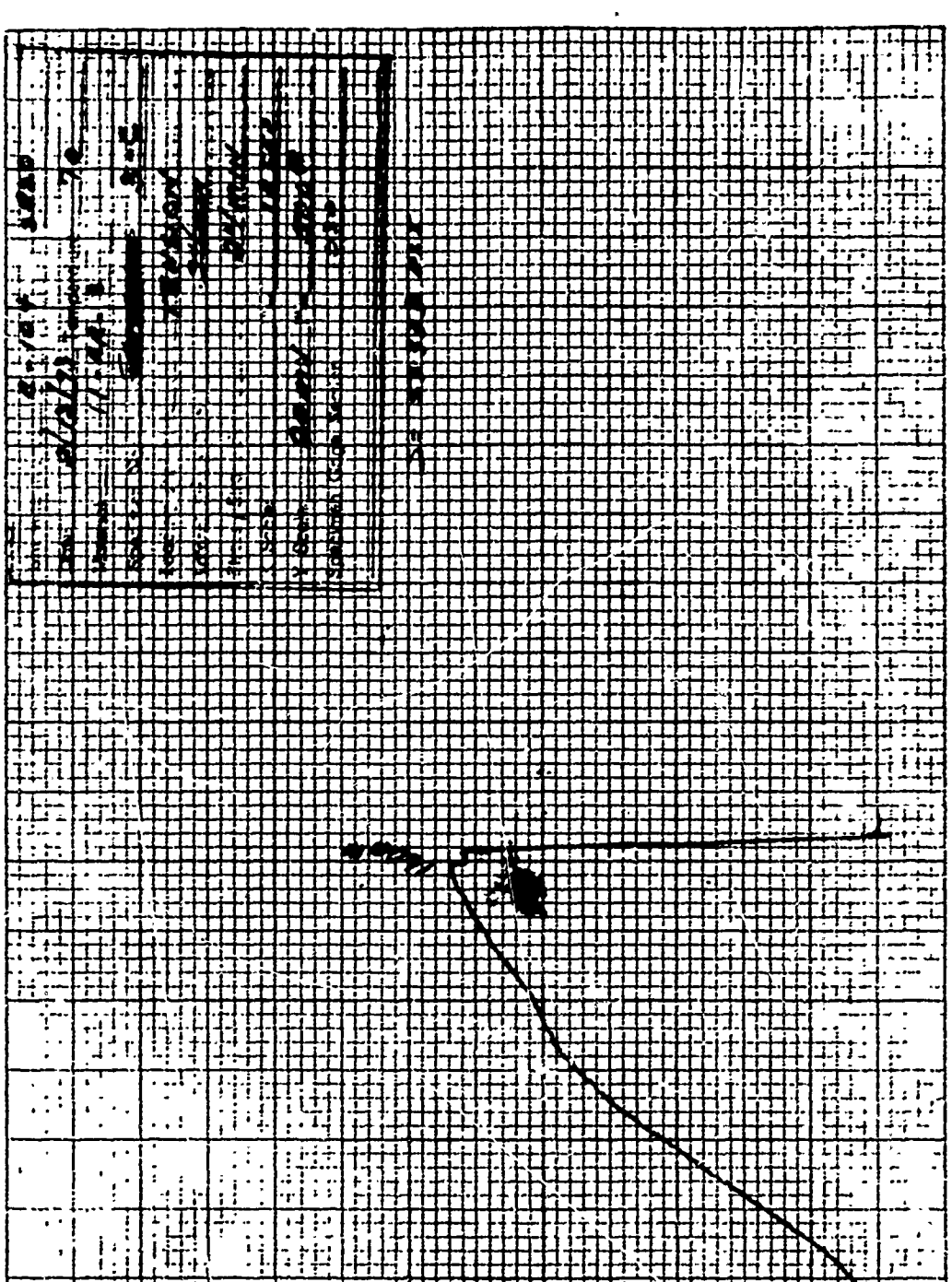

1190

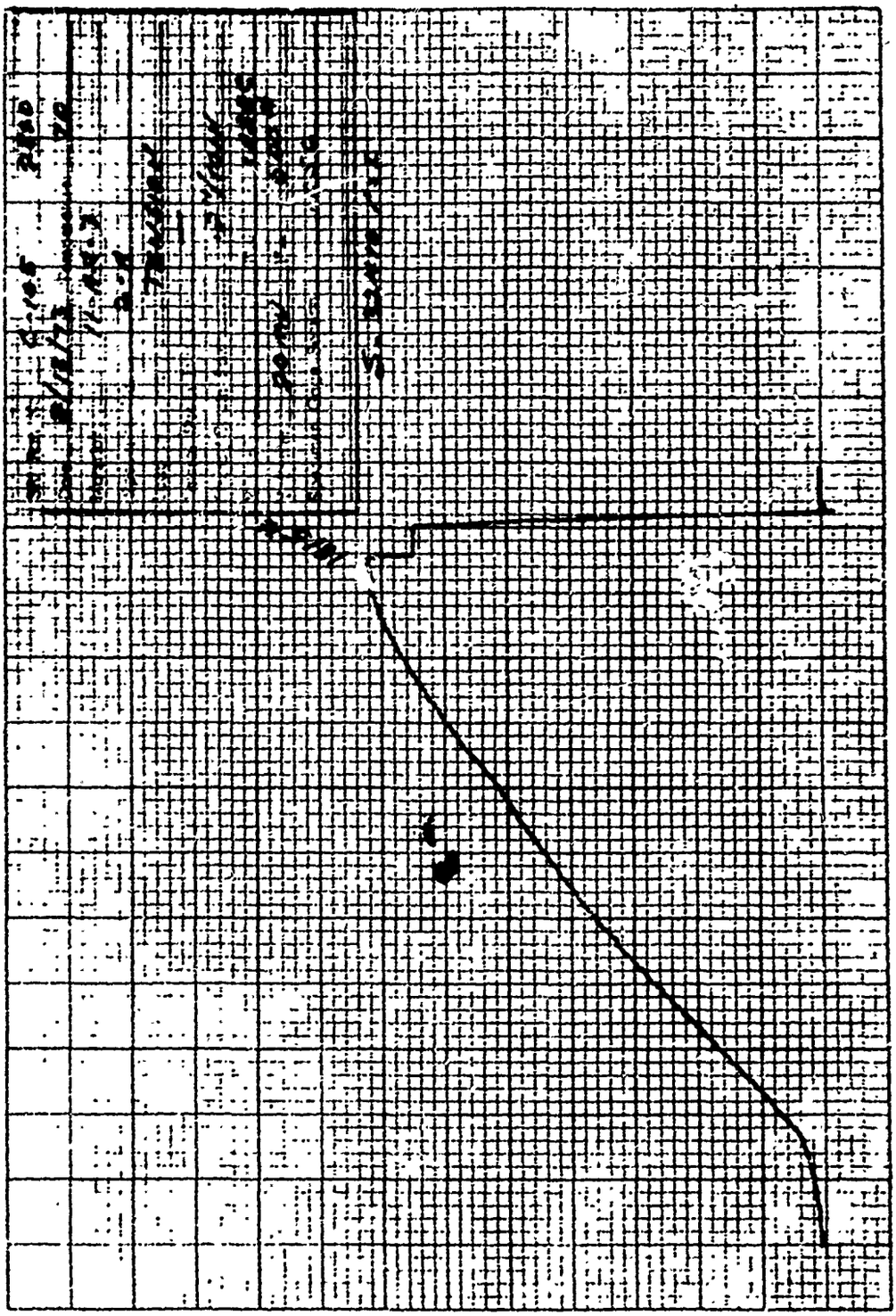


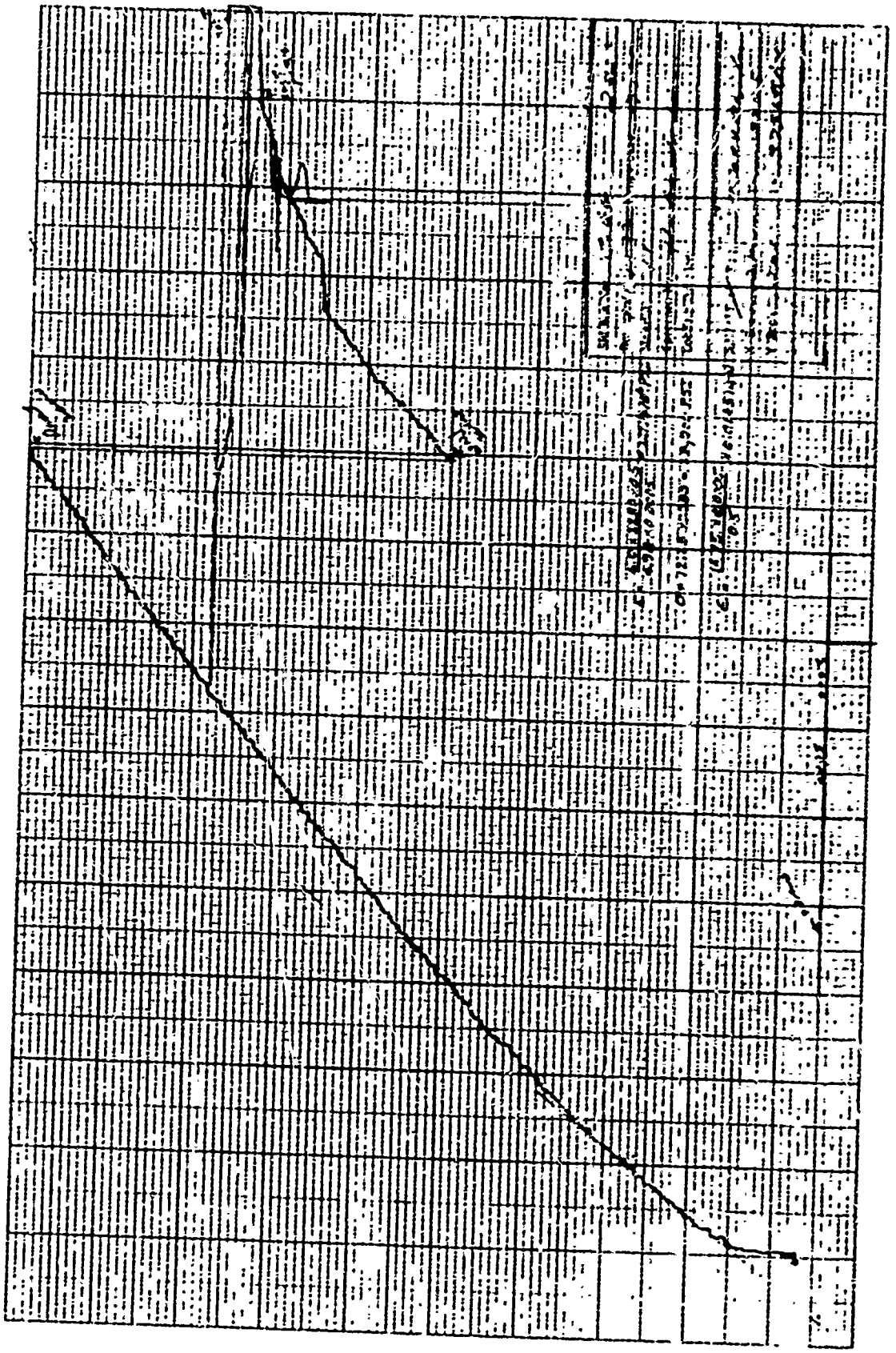

C-98
2820
2-18-73
70°F
11-AA-8
4-C
TENSION
12 IN/MIN
20 KIP
5.0 K
64.353 K-I

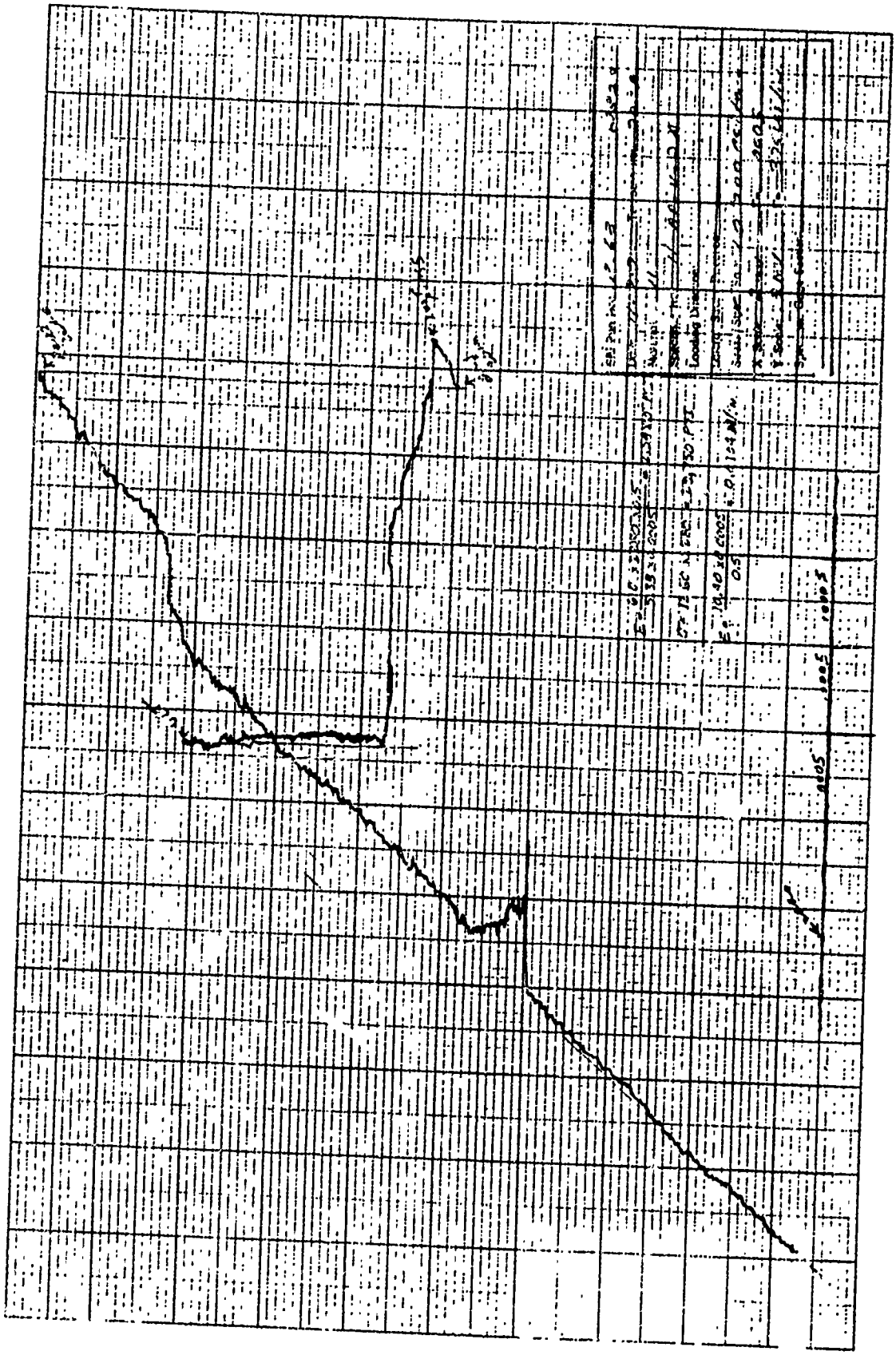

C-100
8/13/72
Temperature
Material
Type
Specimen Gage Section

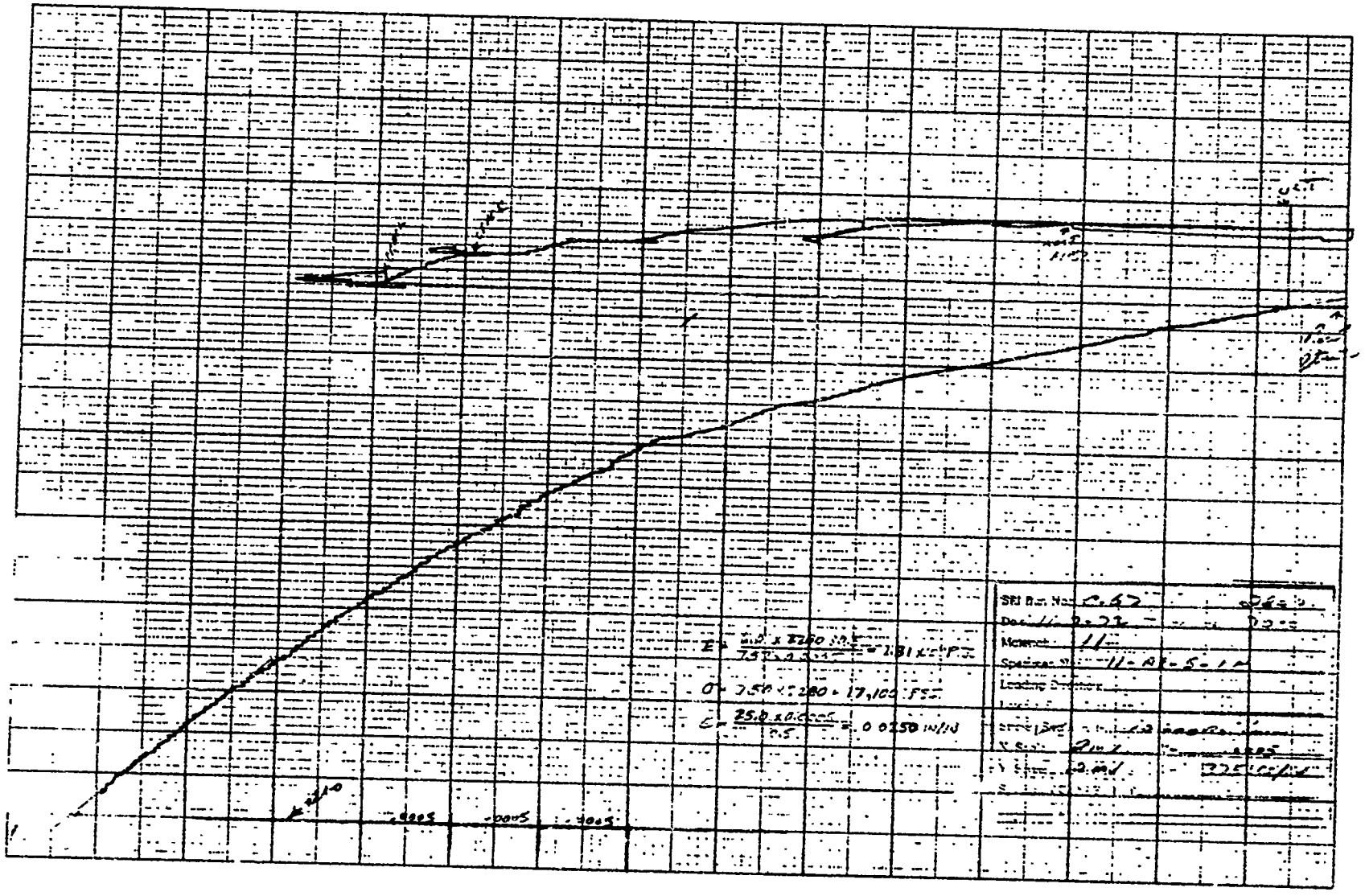


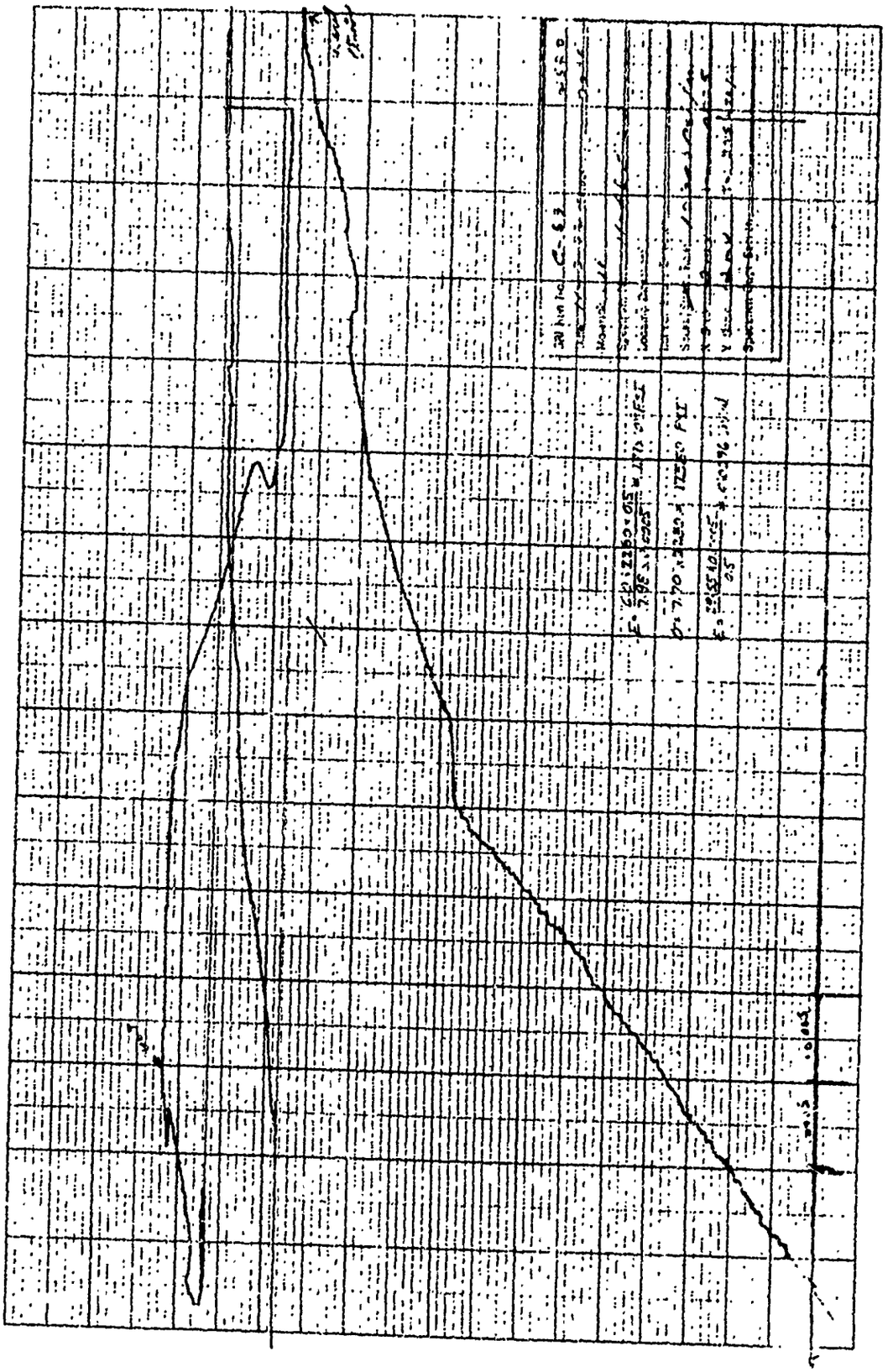


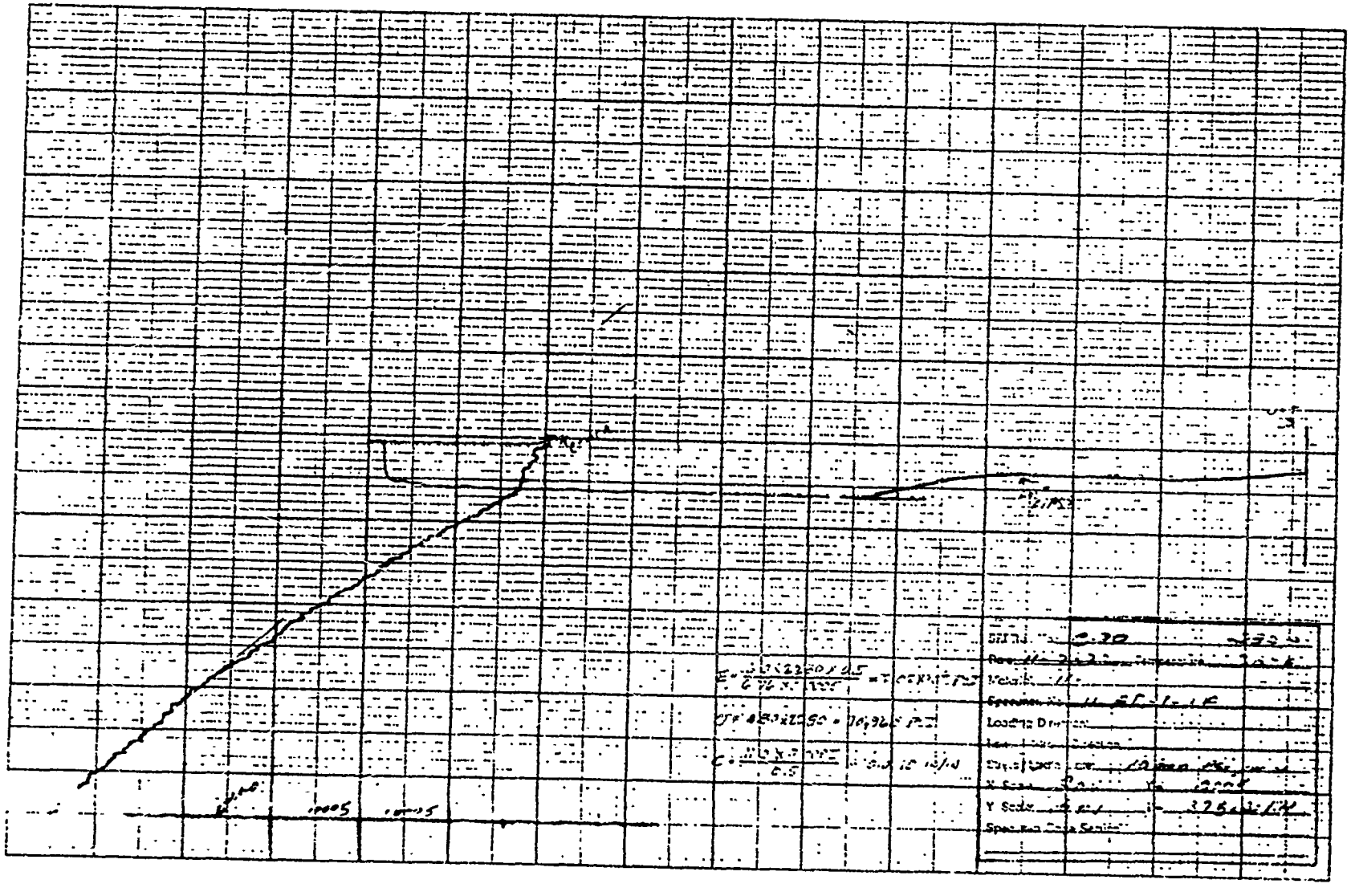


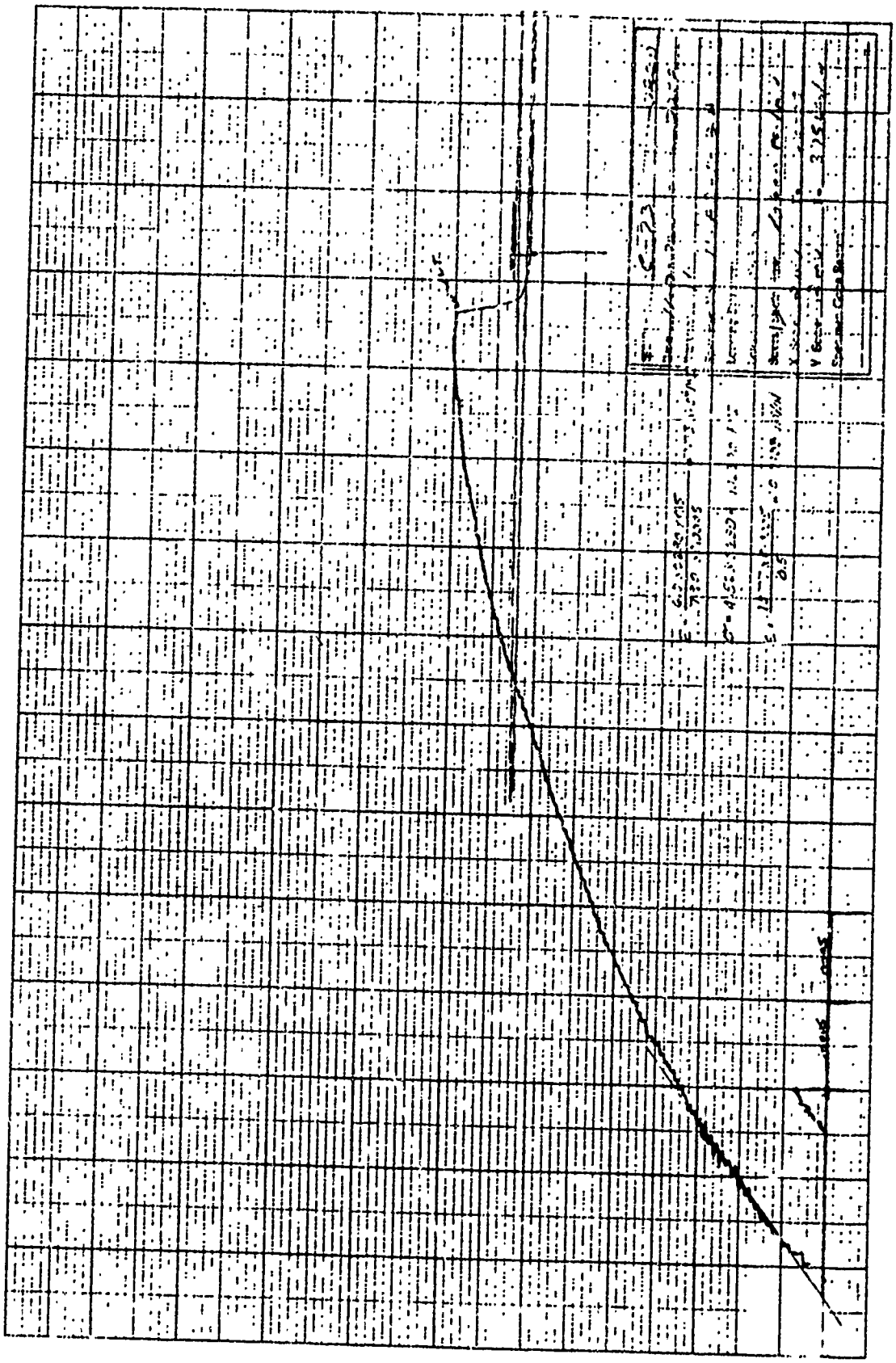


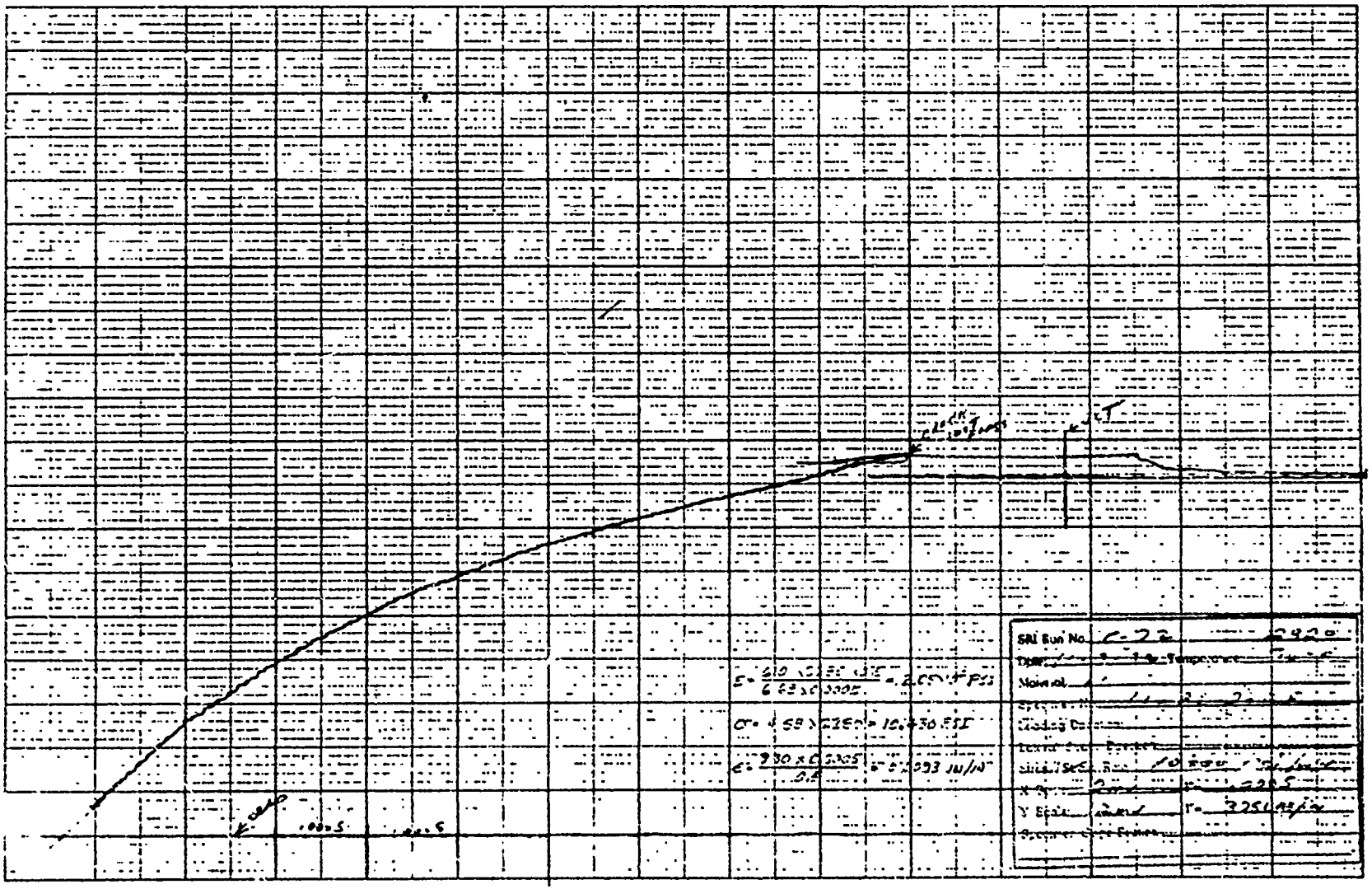


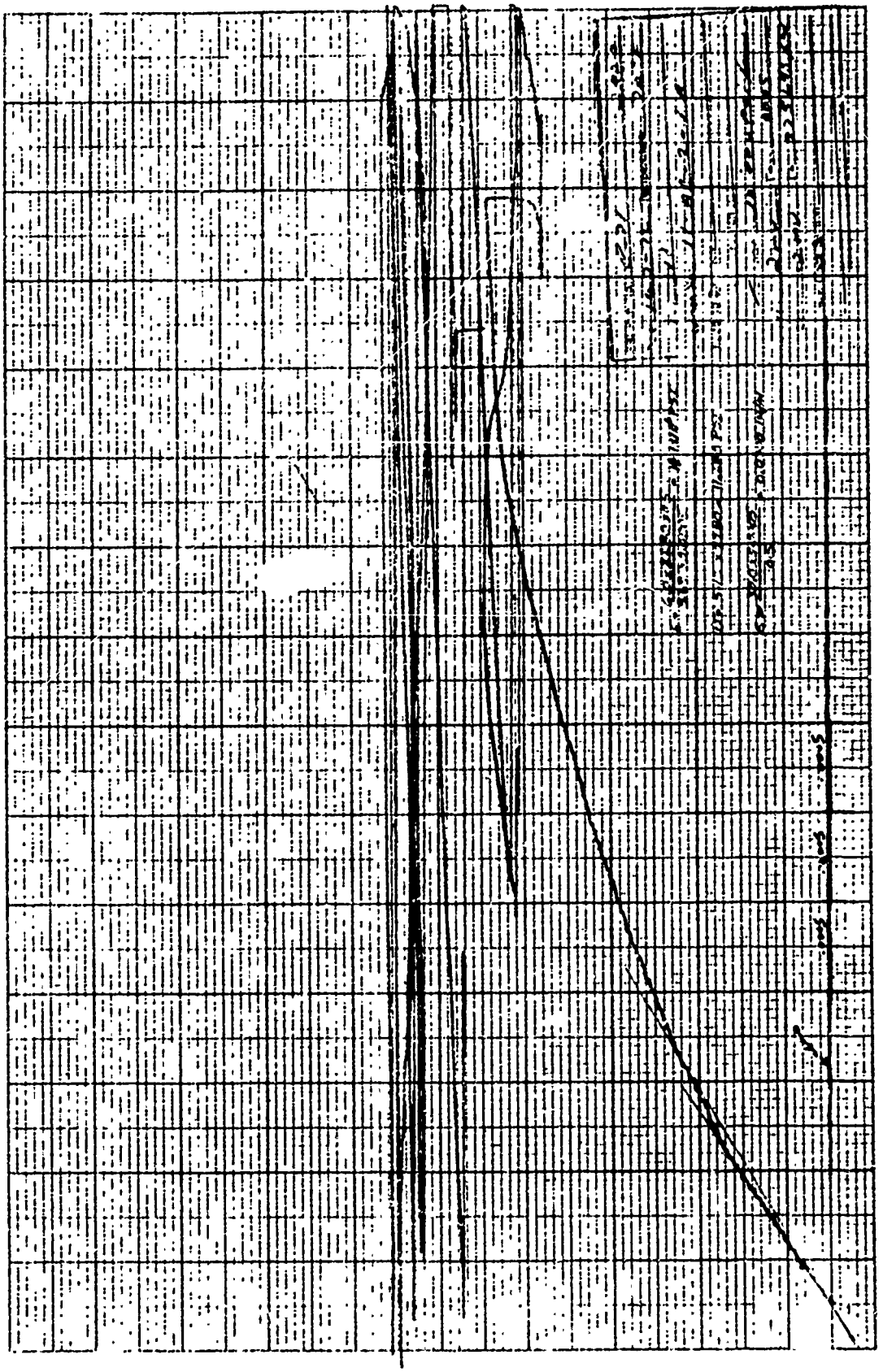

.0005
.0005
.0005

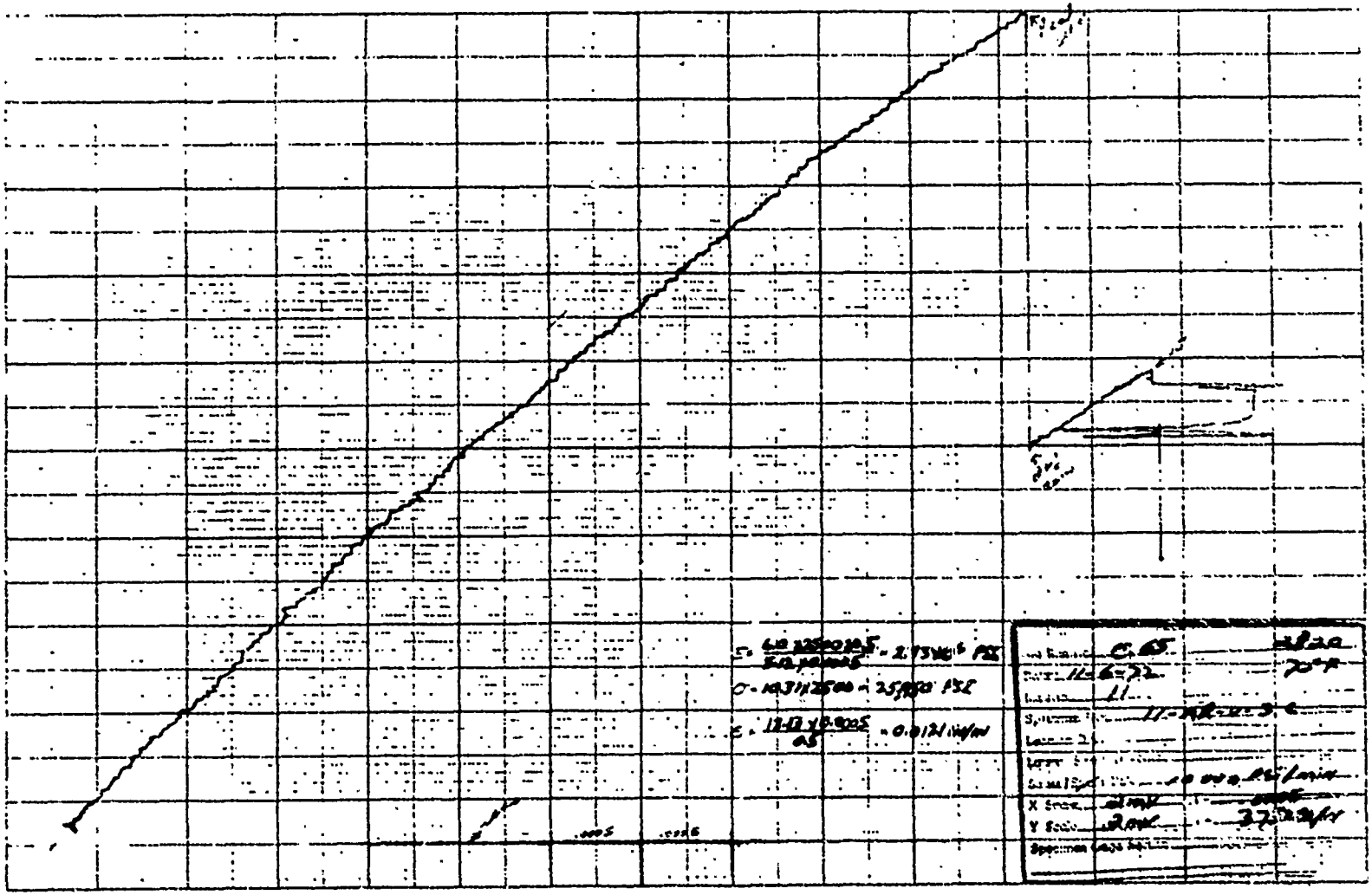


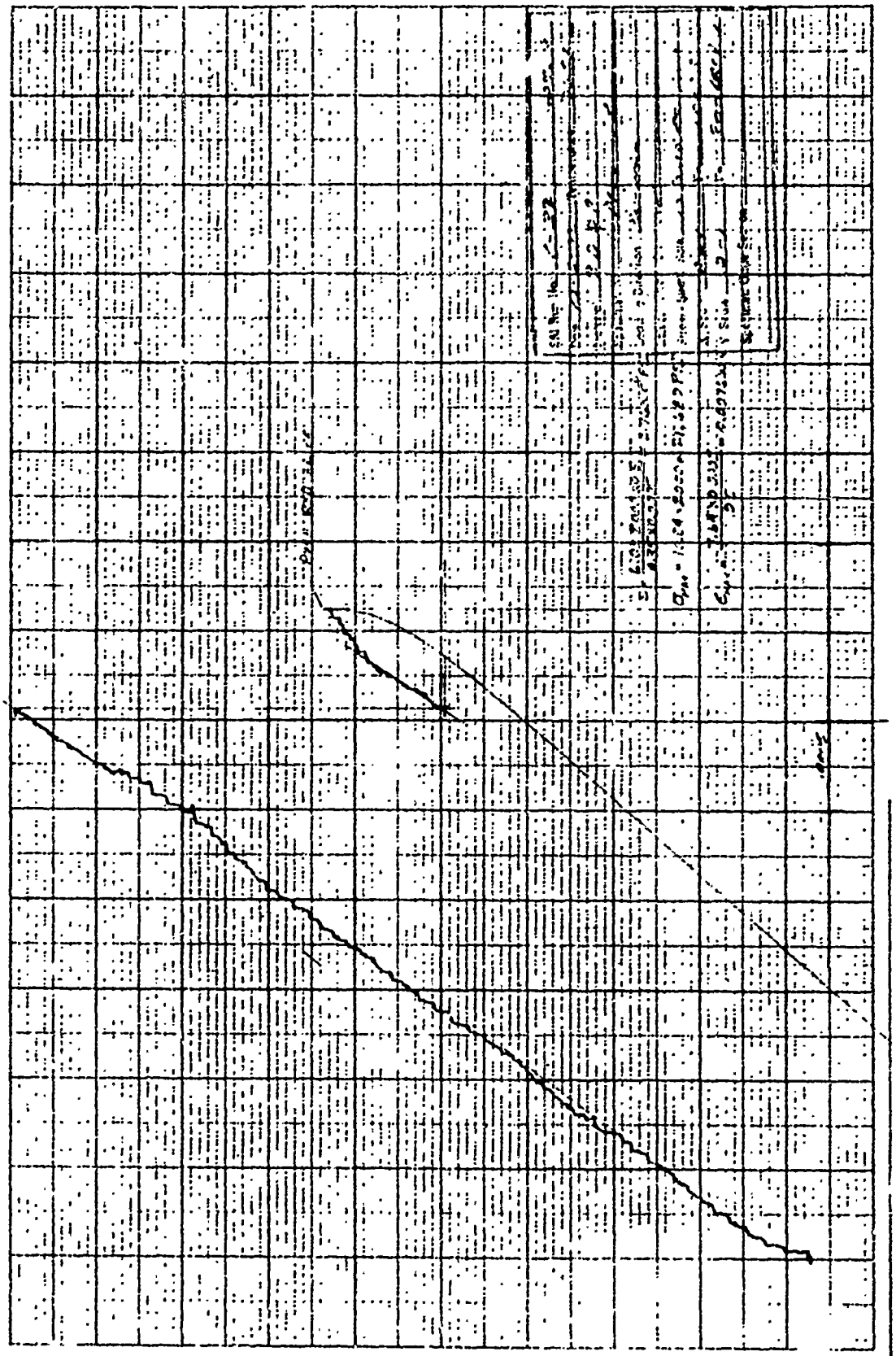


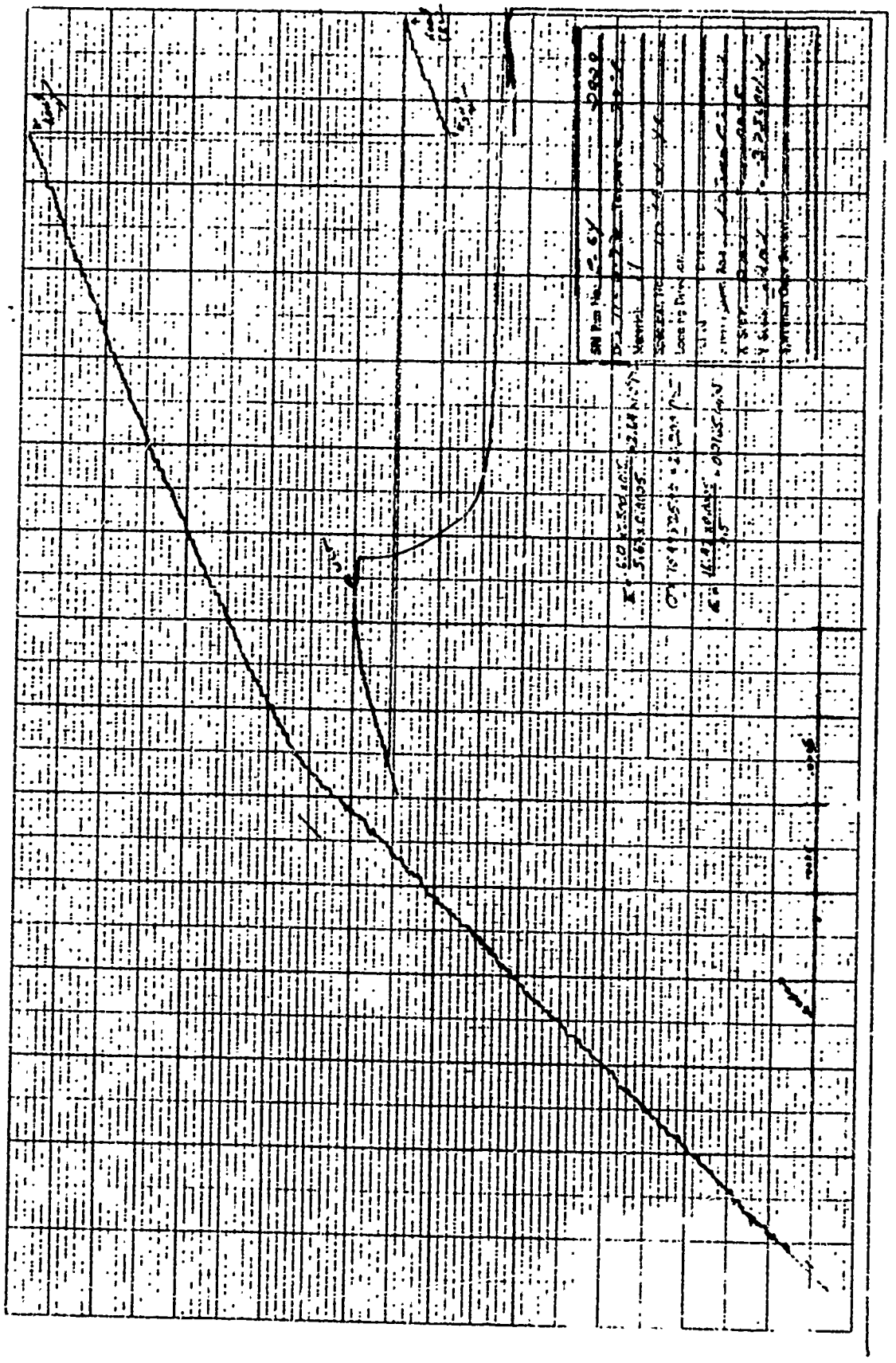


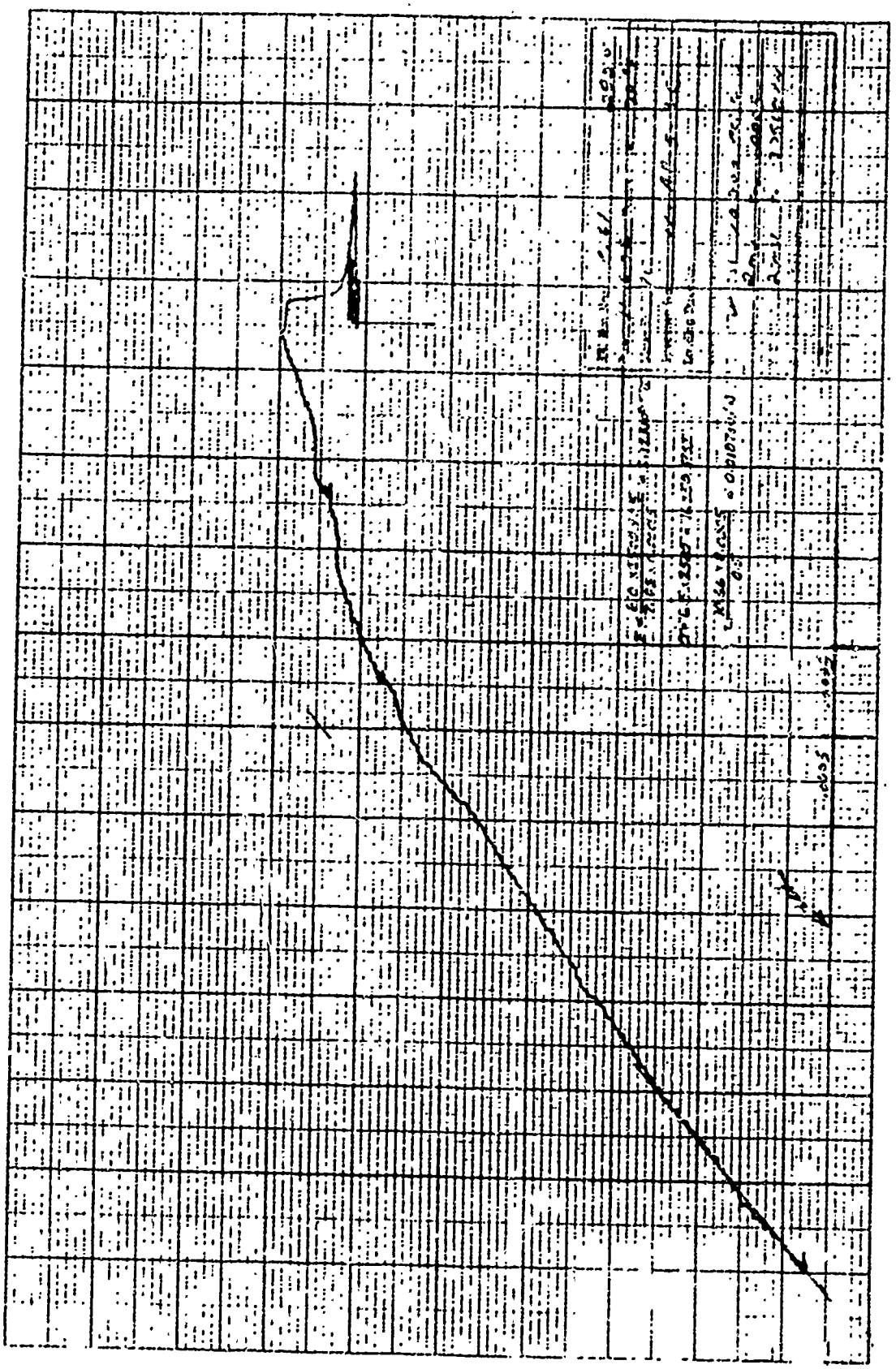

SRI Run No.
Date:
Temperature
Material
Operator
Testing Date
Tested by
Specimen Size
Area
Gage Length
Y Span
Comments: Type Failure

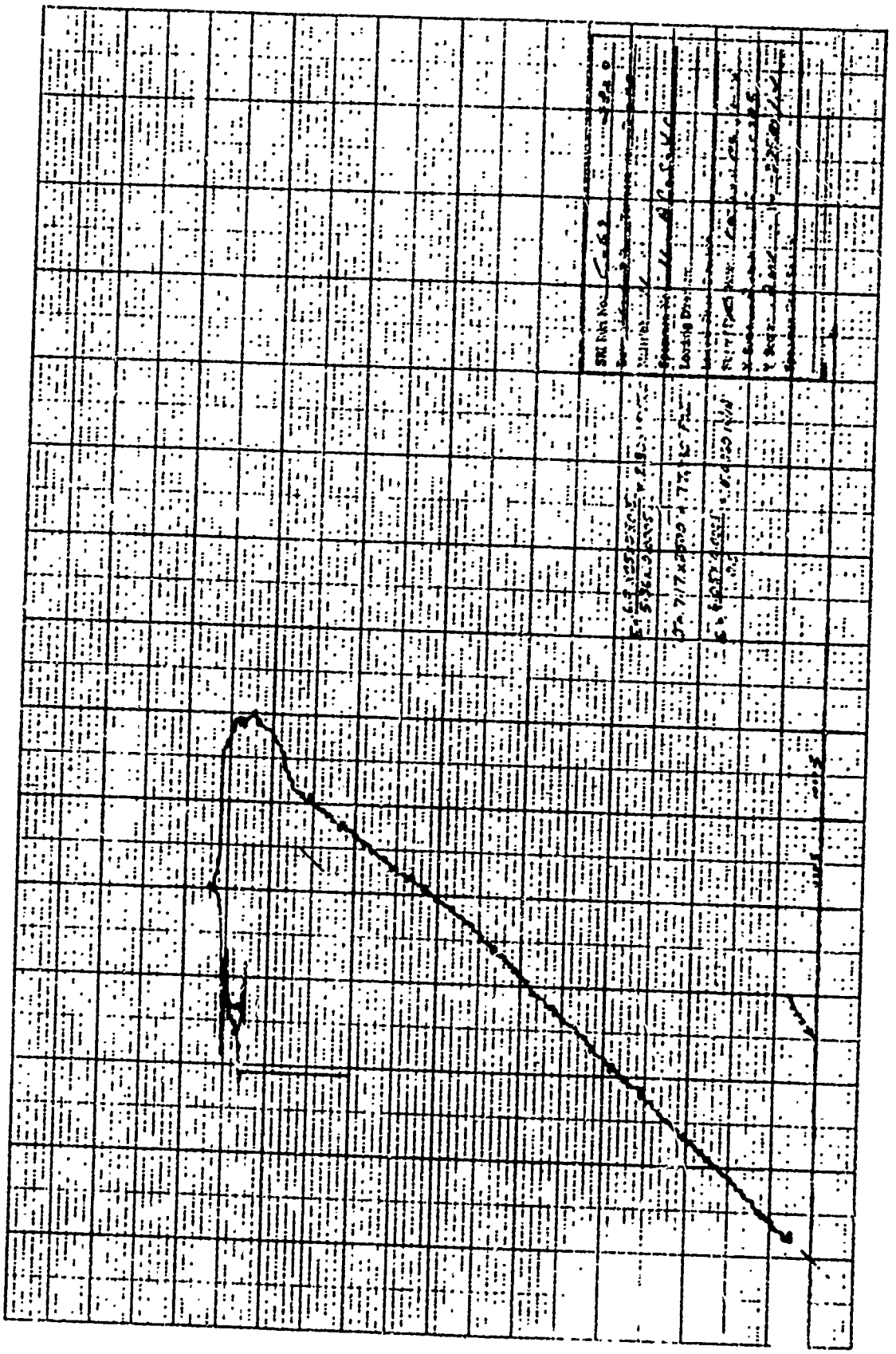


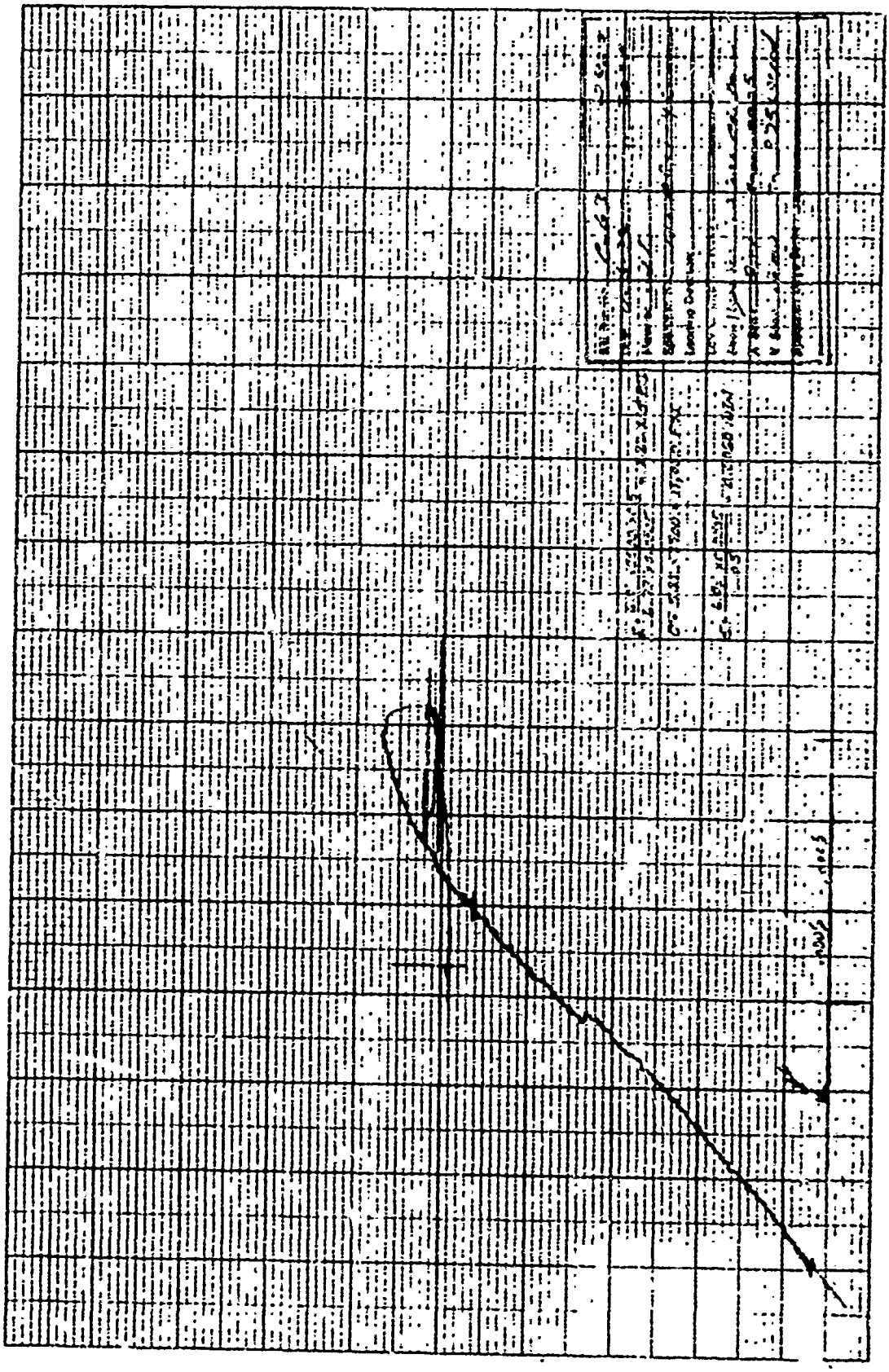

E = 4π 1250 10.5 / 5π 0.0005 = 2.73 x 10^6 PSI
σ = 14311.2500 = 25,000 PSI
E = 12.0 x 0.0005 / 0.5 = 0.0121 in/in

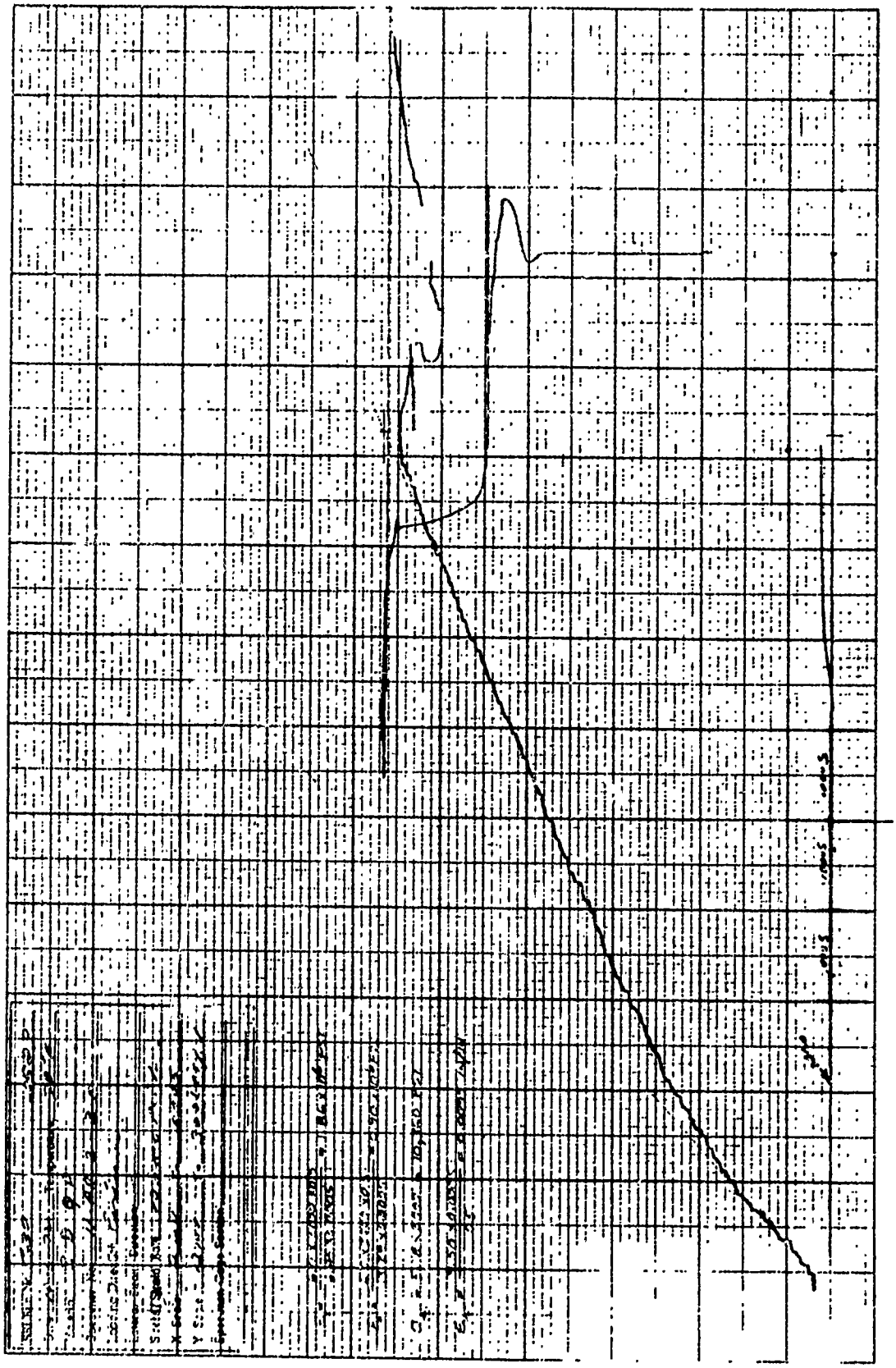


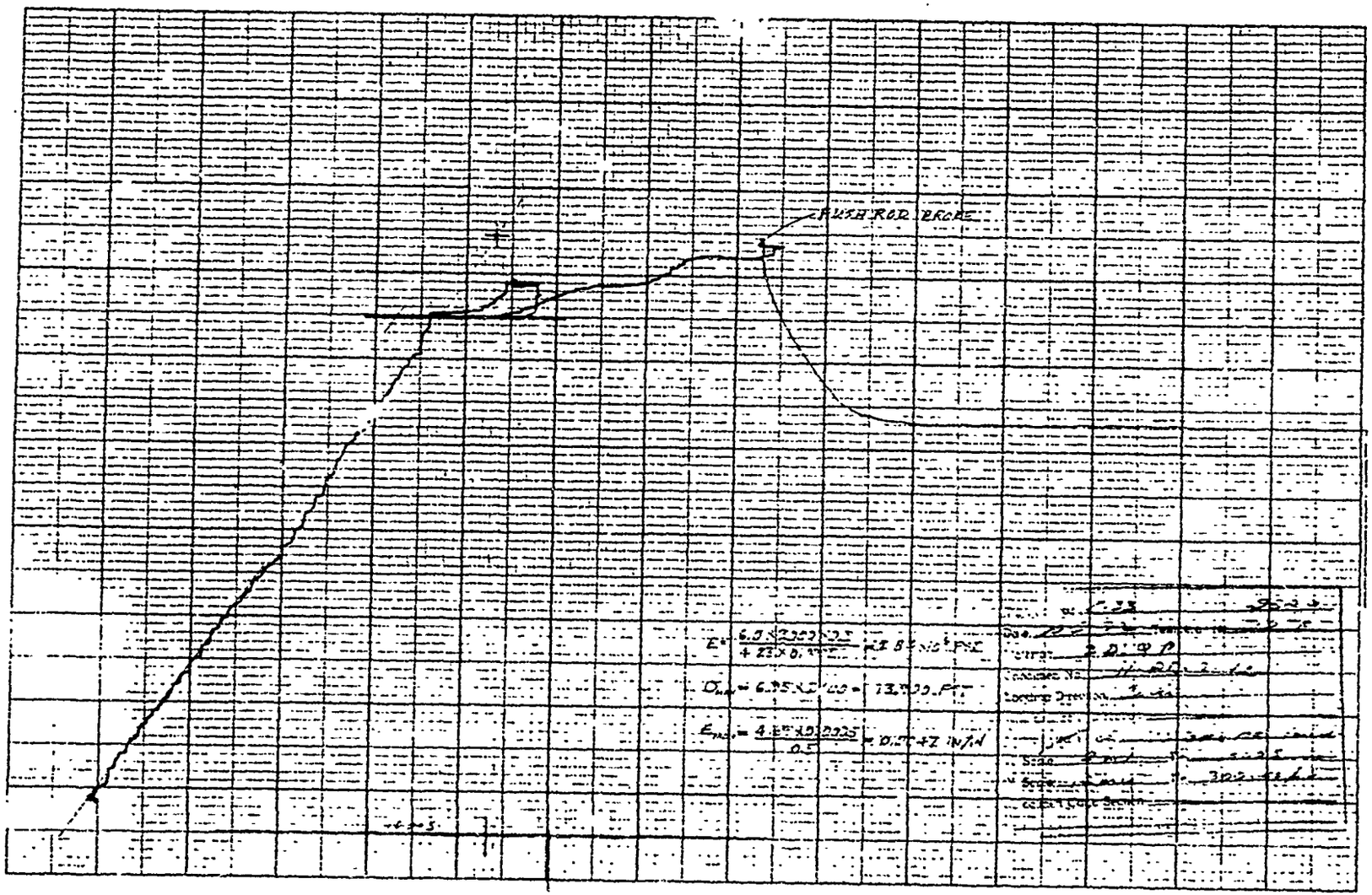






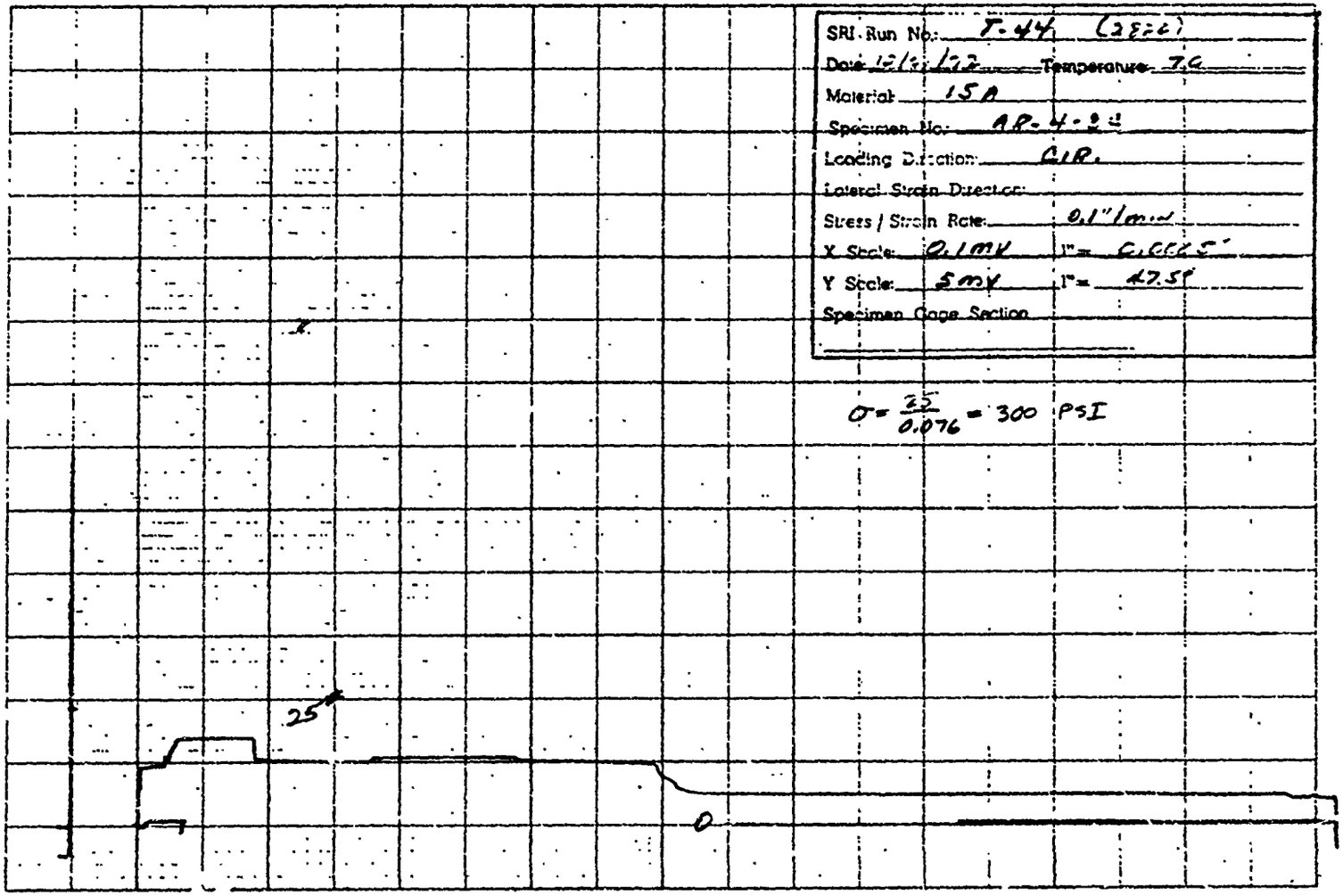


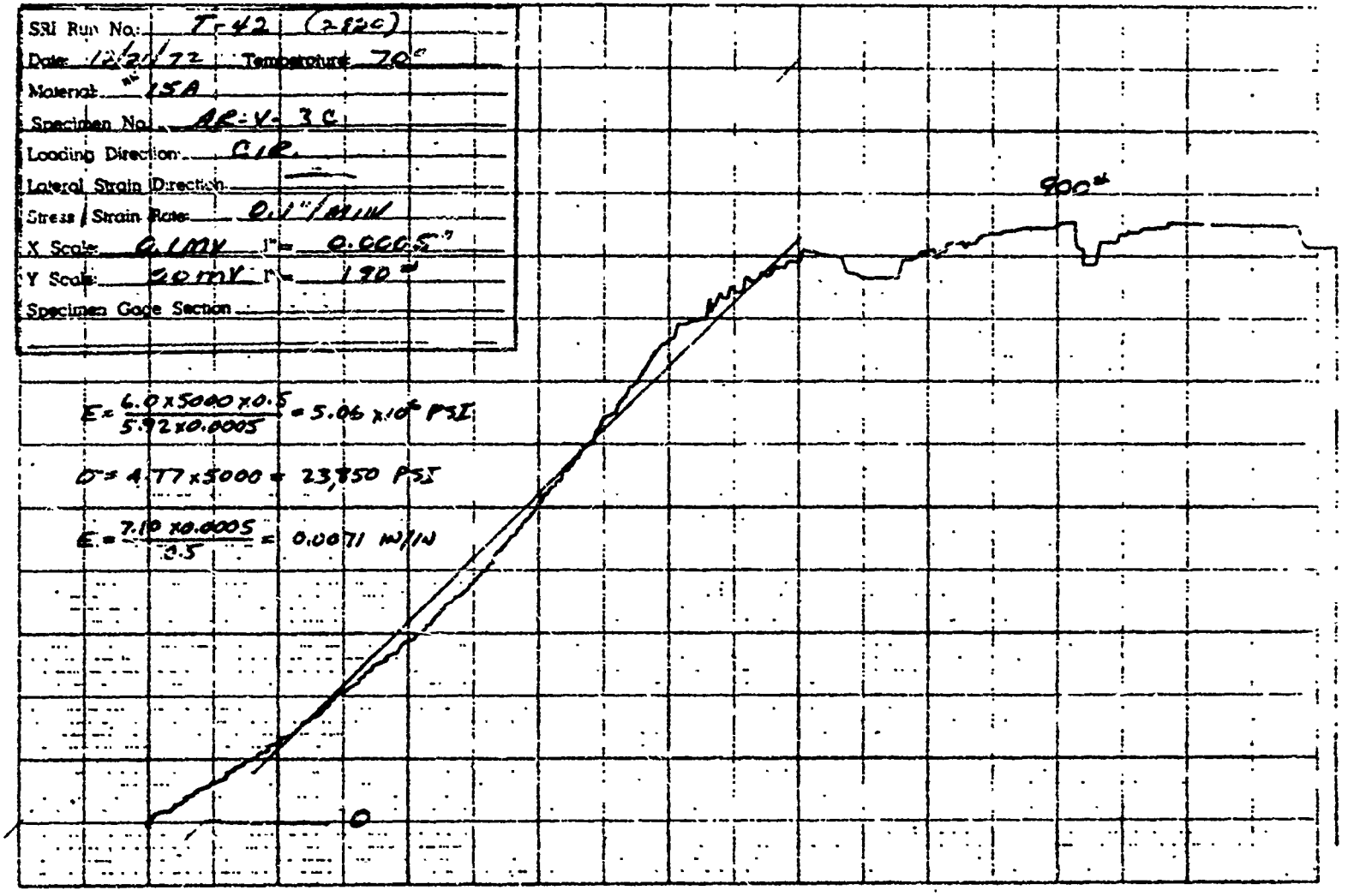


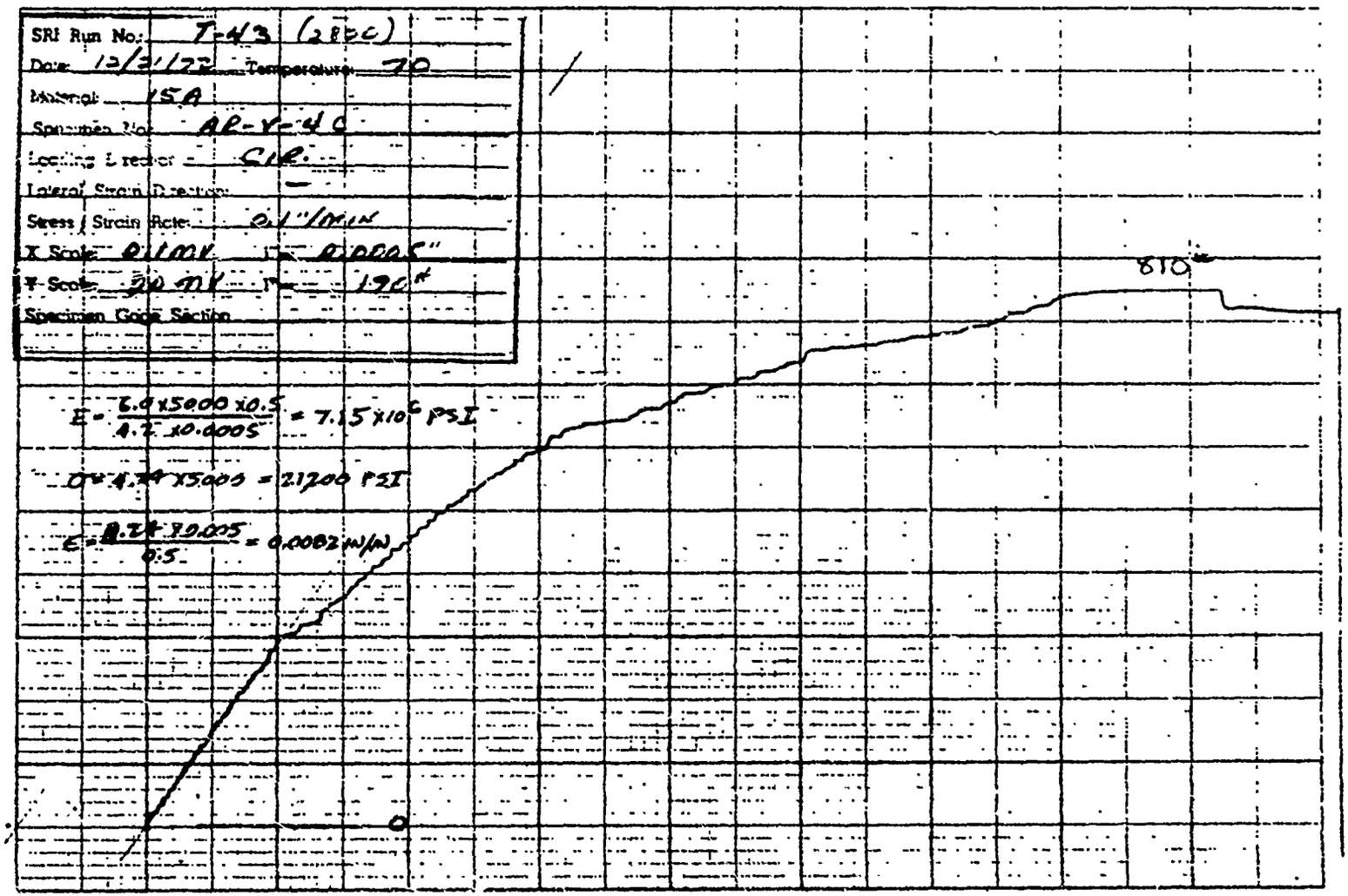

PUSH ROD BRACE

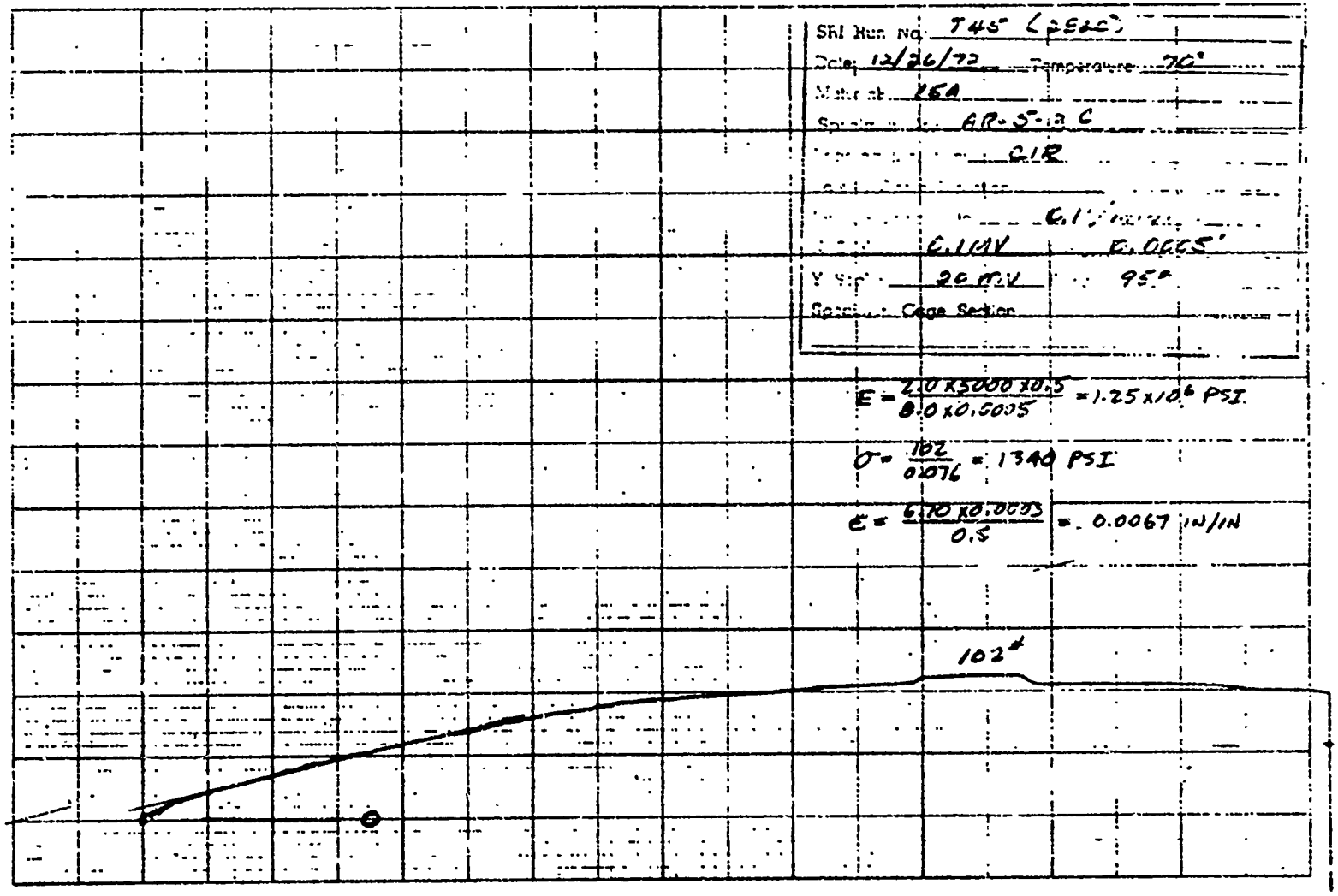
APPENDIX K

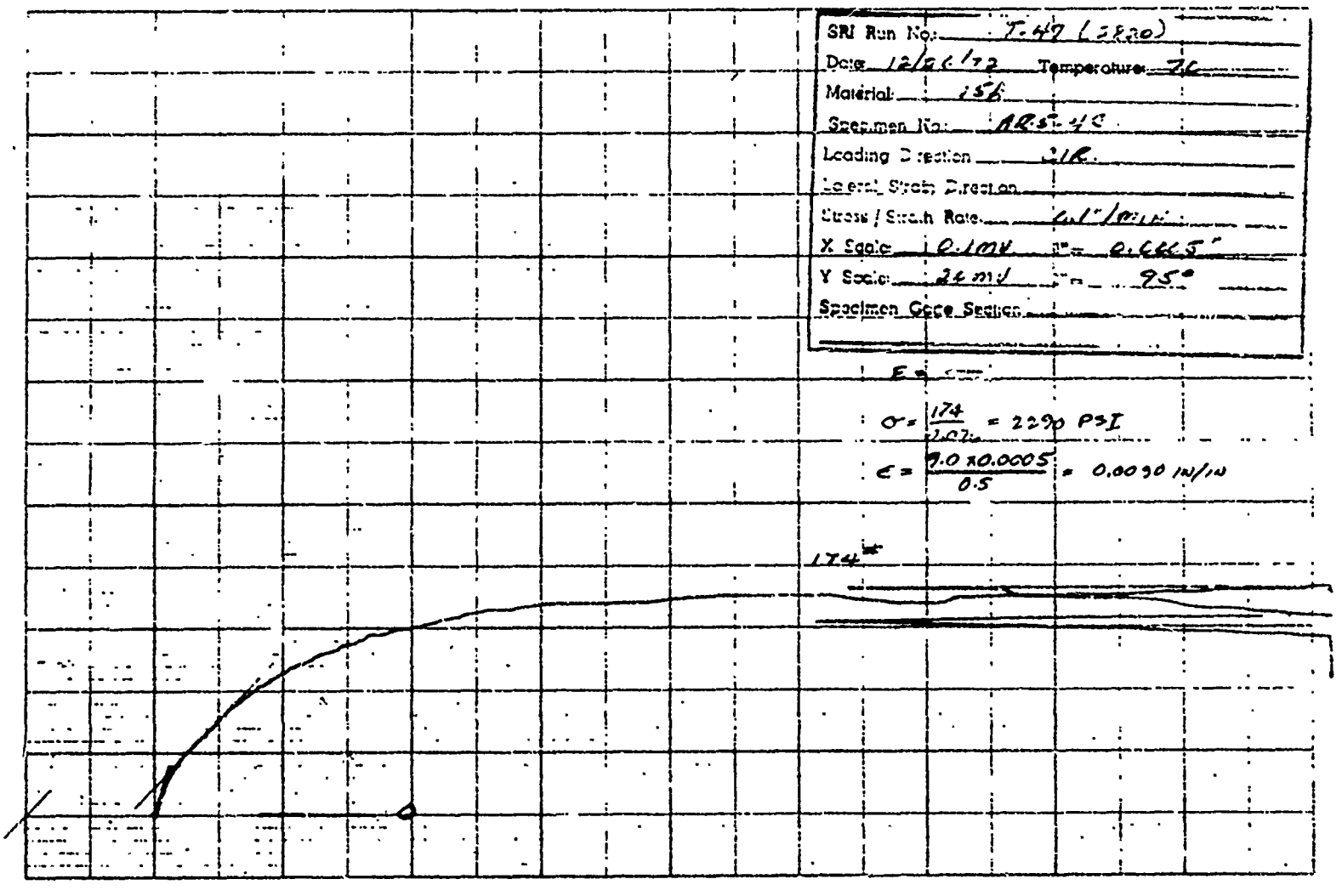
TENSILE AND COMPRESSIVE STRESS-STRAIN CURVES FOR THE CARBON-PHENOLIC PORTION (#15A) OF AVCO 3DC/QP - MATERIAL 15

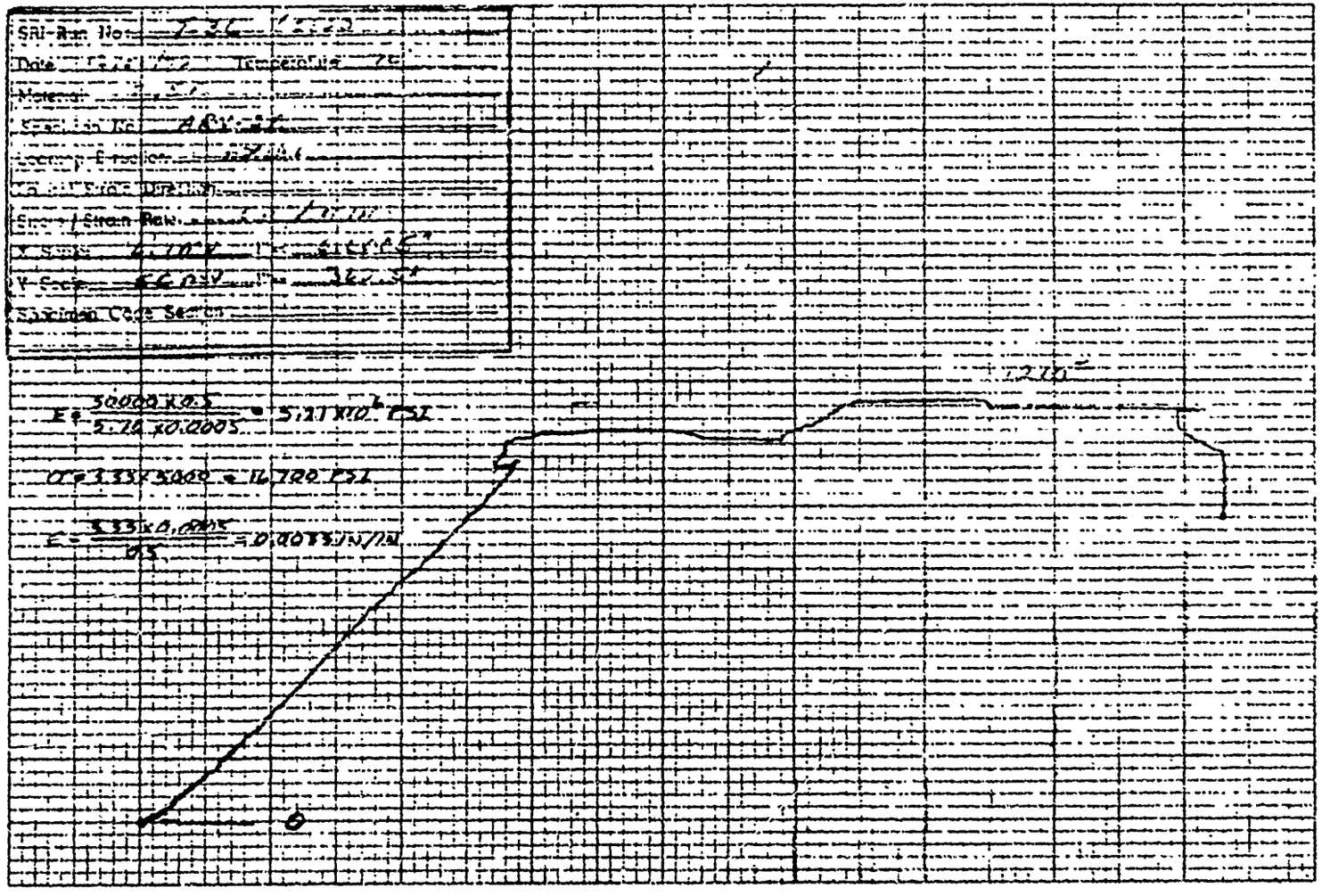

SRI Run No: T-44 (2E2C)
Date 12/5/72 Temperature 70
Material 15A
Specimen No: AR-4-2-1
Loading Direction: CIR.
Lateral Strain Direction:
Stress / Strain Rate: 0.1"/min
X Scale: 0.1mV 1"= 0.0025"
Y Scale: 5mV 1"= 47.5#
Specimen Gage Section
σ = 25/0.076 = 300 PSI
25
0

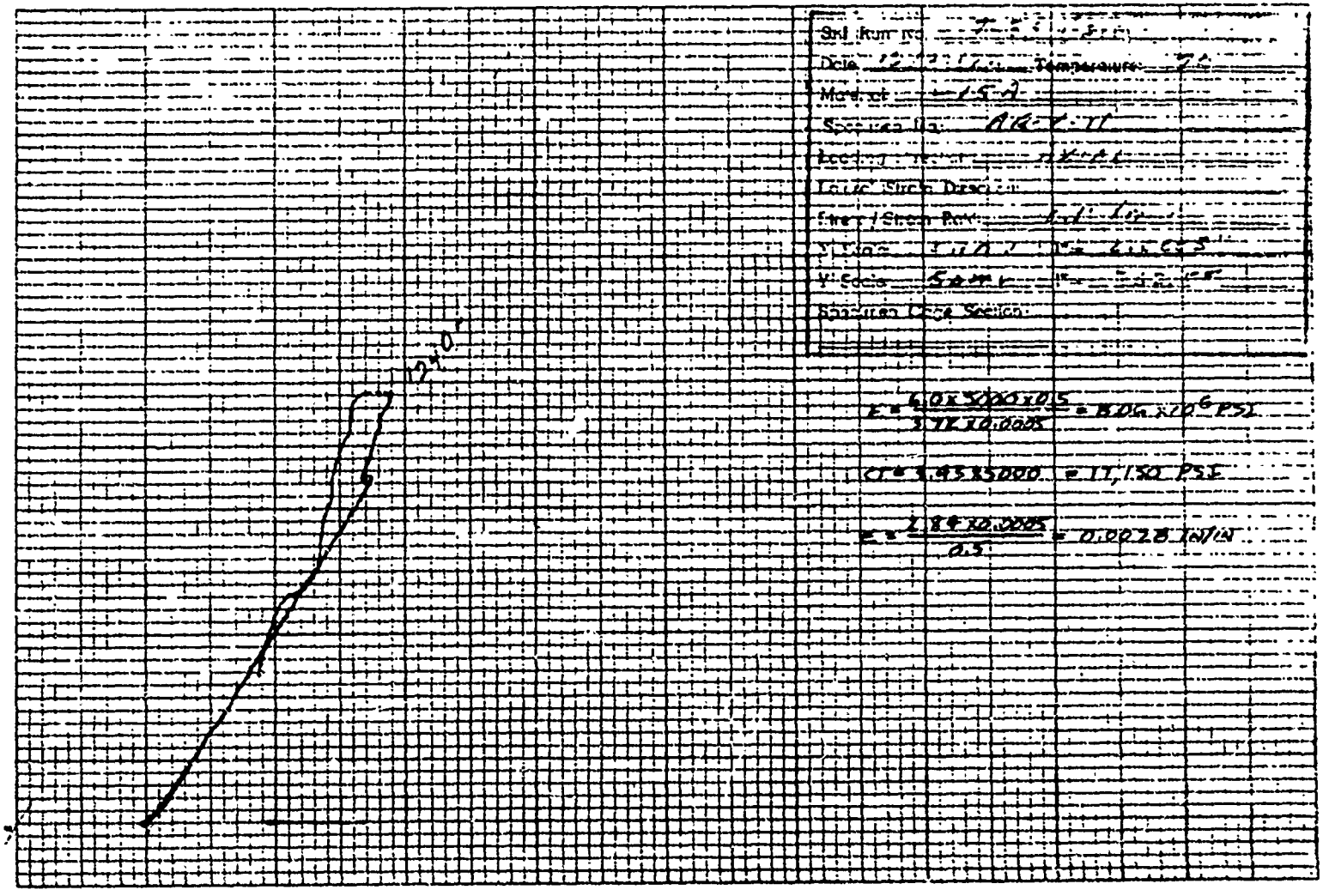

SRI Run No: T-42 (2820)
Date: 12/21/72 Temperature: 70°
Material: 18% 18A
Specimen No: AR-V-3C
Loading Direction: CIR.
Lateral Strain Direction:
Stress / Strain Rate: 0.1"/MIN
X Scale: 0.1 MV 1" = 0.0005"
Y Scale: 20 mV 1" = 100#
Specimen Gage Section:
900#
E = 6.0 x 5000 x 0.5 / 5.92 x 0.0005 = 5.06 x 10^6 PSI
σ = 4.77 x 5000 = 23,850 PSI
E = 7.10 x 0.0005 / 3.5 = 0.00071 IN/IN
0


SRI Run No: T-43 (28°C)
Date: 12/21/72 Temperature: 70
Material: 15A
Specimen No: AR-Y-4C
Loading Direction: CIR.
Lateral Strain Direction: —
Stress / Strain Rate: 0.1"/MIN
X Scale: 0.1 IN = 0.0005"
Y Scale: 20 KI = 120 #
Specimen Gage Section
E = 6.0 x 5000 x 0.5 / 4.2 x 0.0005 = 7.15 x 10^6 PSI
σ = 4.24 x 5000 = 21,200 PSI
ε = 0.24 x 0.005 / 0.5 = 0.0082 IN/IN
810
0


SRI Run No. T45° (PEEC)
Date: 12/26/72 Temperature: 70°
Material: 1564
Specimen: AR-5°-a C
C.1R
C.1MV E.0005"
Y Sig: 20 MV 95#
Specimen: Cage Section
E = 2.0 X 5000 X 0.5 / 8.0 X 0.0005 = 1.25 X 10^6 PSI
σ = 102 / 0.076 = 1340 PSI
E = 0.70 X 0.0095 / 0.5 = 0.0067 IN/IN
102#


SRI Run No: T-47 (2220)
Date: 12/22/72 Temperature: 76
Material: 156
Specimen No: AR5T-4C
Loading Direction: L/R
Lateral Strain Direction:
Stress / Strain Rate: 60"/min
X Scale: 0.10" = 0.0005"
Y Scale: 24 mil = 95°
Specimen Gage Section:
E =
σ = 174 / .027 = 2290 PSI
ε = 9.0 x 0.0005 / 0.5 = 0.0090 in/in
174#


SRI-Ran No.
Date
Temperature
Material
Specimen No.
Gage Length
Cross Head Speed
Strain Rate
X Scale
Y Scale
Specimen Cross Section
$E = \frac{30000 \times 0.5}{5.74 \times 0.0005} = 5.23 \times 10^6$ PSI
$\sigma = 3.33 \times 3600 = 11,700$ PSI
$E = \frac{3.33 \times 0.0005}{0.5} = 0.00333$ IN/IN
0
2710

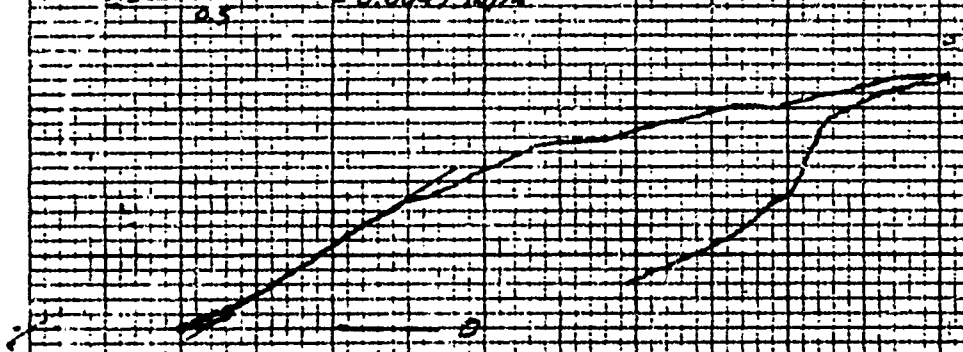

Test Number:
Date: Temperature:
Material:
Specimen ID:
Load:
Load Stress Desc:
Liner / Stress Per:
Y Load:
Y Scale:
Specimen Gage Section:
12"0"
E = 6.0 X 5000 X 0.15 / 3.14 X 0.0005 = 8.04 X 10^6 PSI
CT = 3.9385000 = 11,150 PSI
ε = 2.8 X 0.0005 / 0.5 = 0.00028 IN/IN

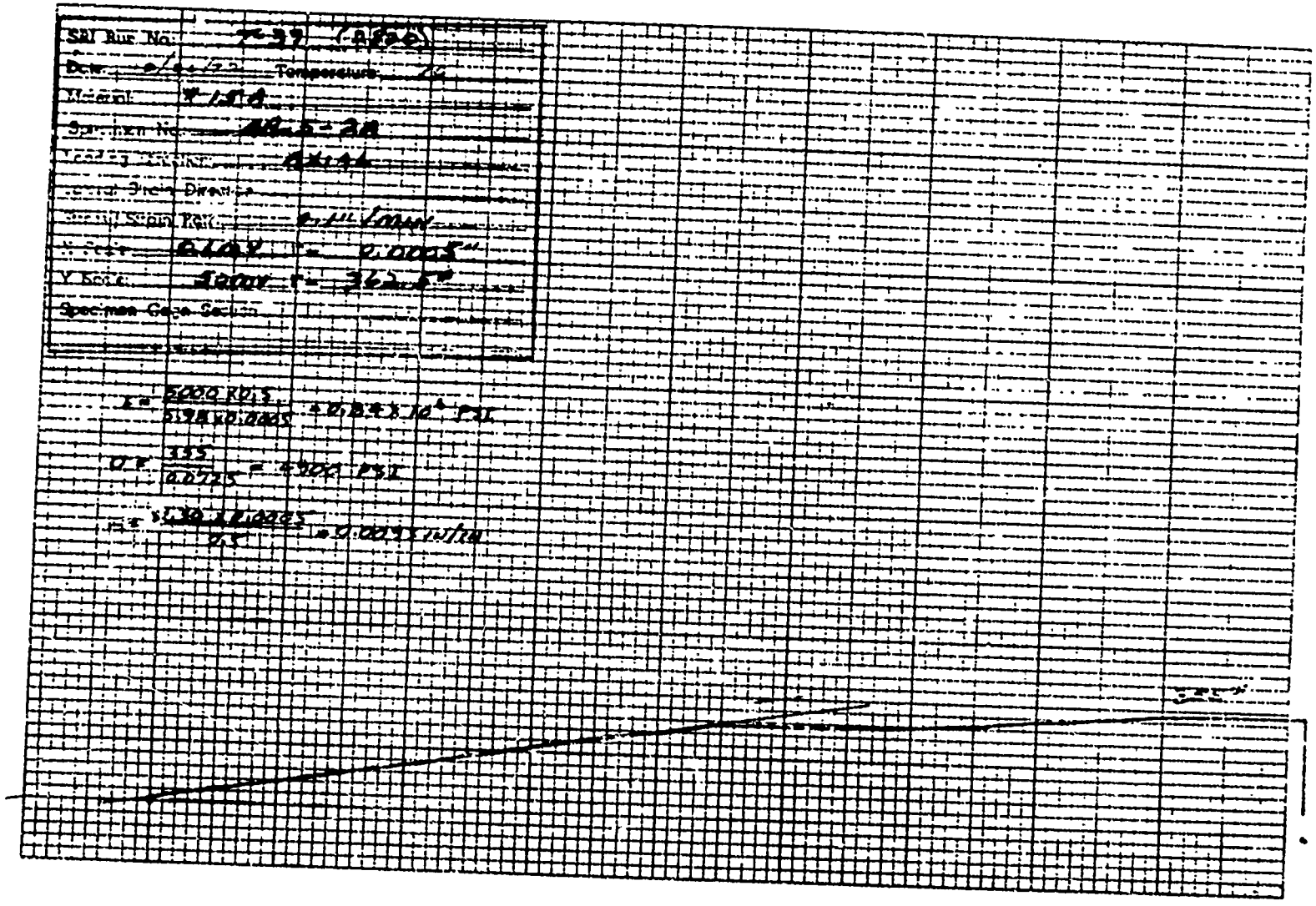
Test Run No. T-32 (2220)
Date 12/21/[illegible] Temperature 72°
Material 7154
Specimen No. AR-E-14
Loading Direction AXIAL
Type of Strain Direction
Strain Rate Selected 0.1"/min
X Scale 0.1"/IN Y Scale 0.0005"
T Scale 100/IN Area .3625"²
Specimen Gage Section

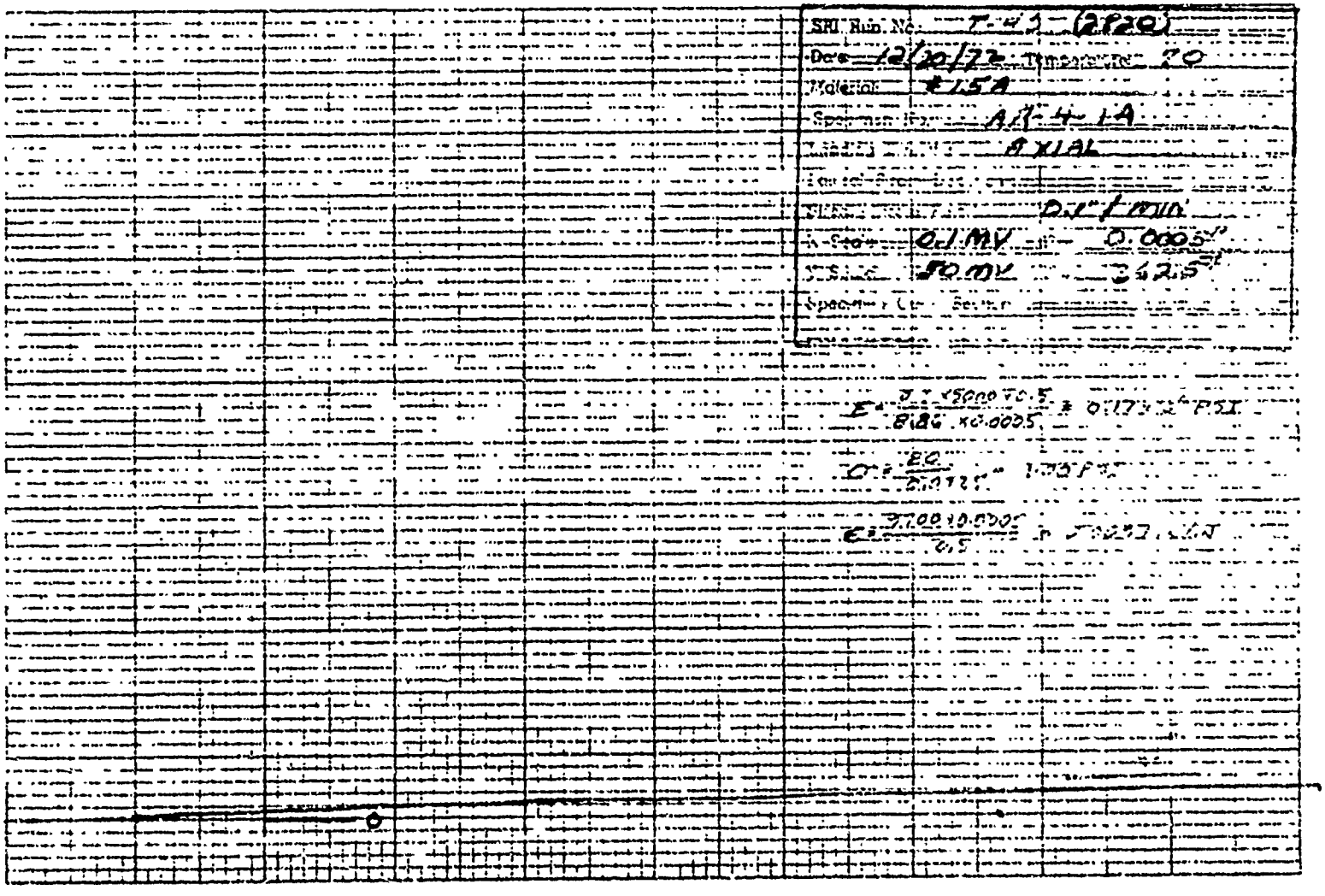
$E = \frac{30000 \times 0.1}{5.08 \times 0.0005} = 1.30 \times 10^6$ PSI

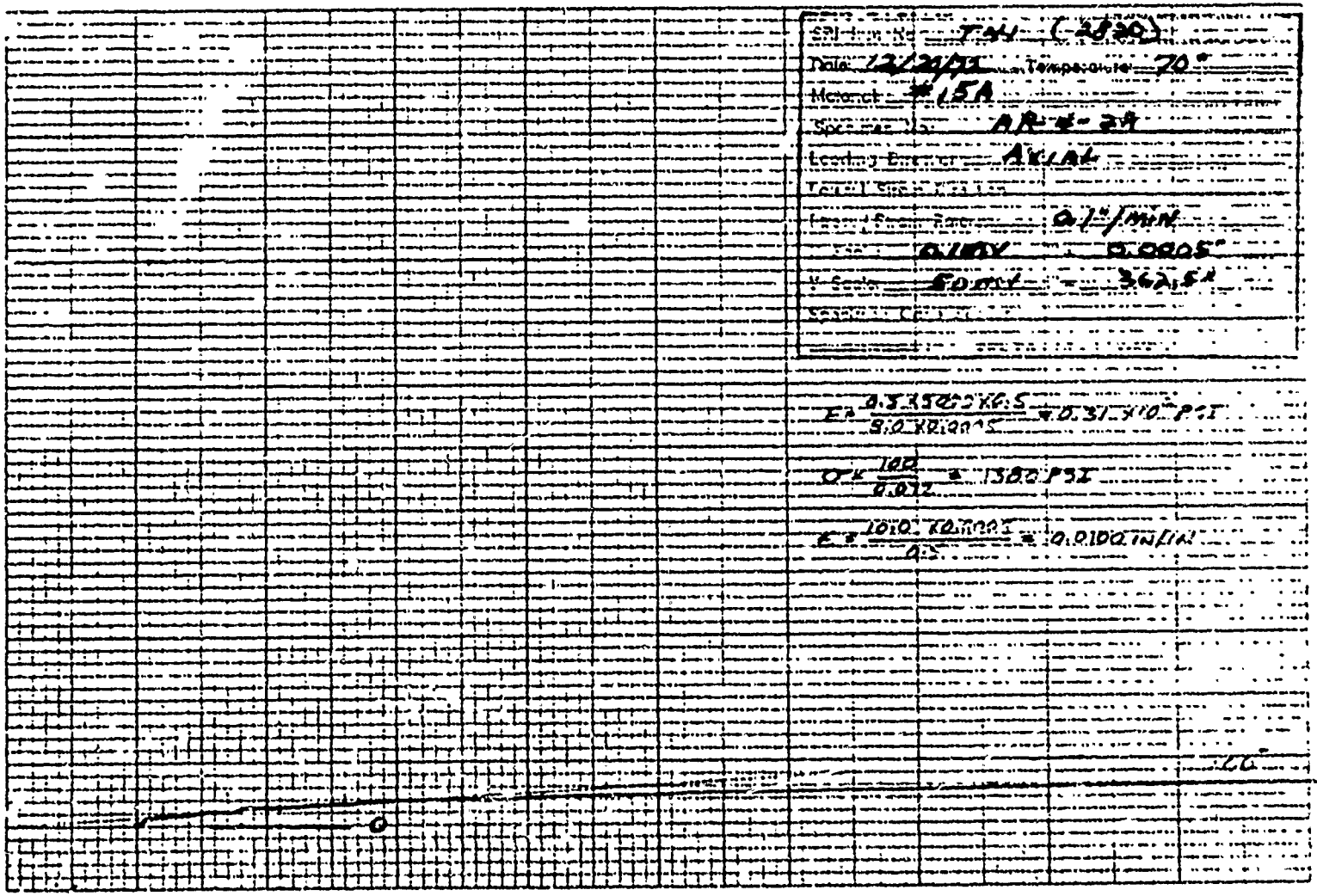
$\sigma_{7.5} = 7.5 \times 2000 = 15{,}000$ PSI

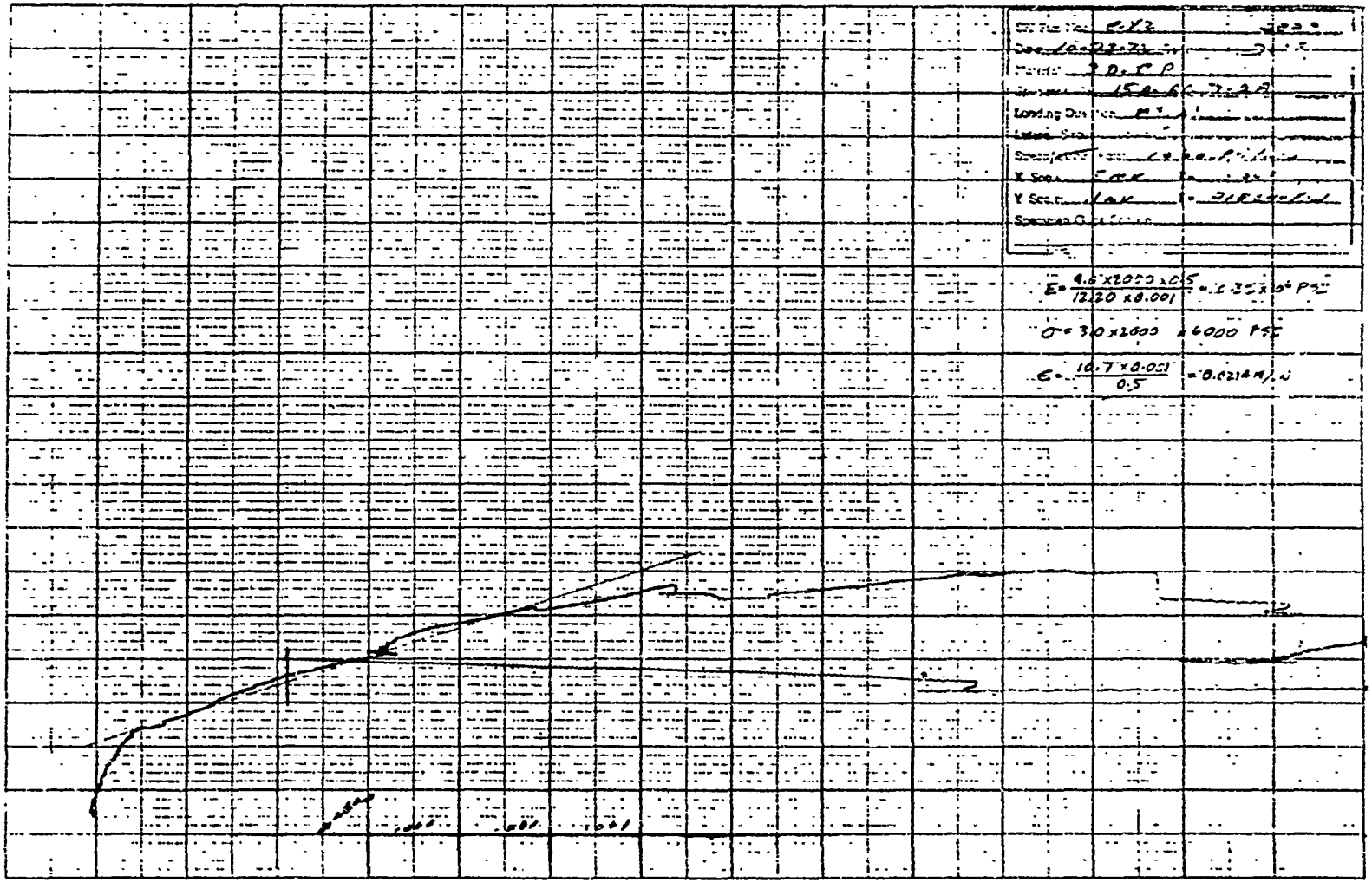
$\varepsilon = \frac{4.30 \times 0.0025}{0.5} = 0.0043$ IN/IN

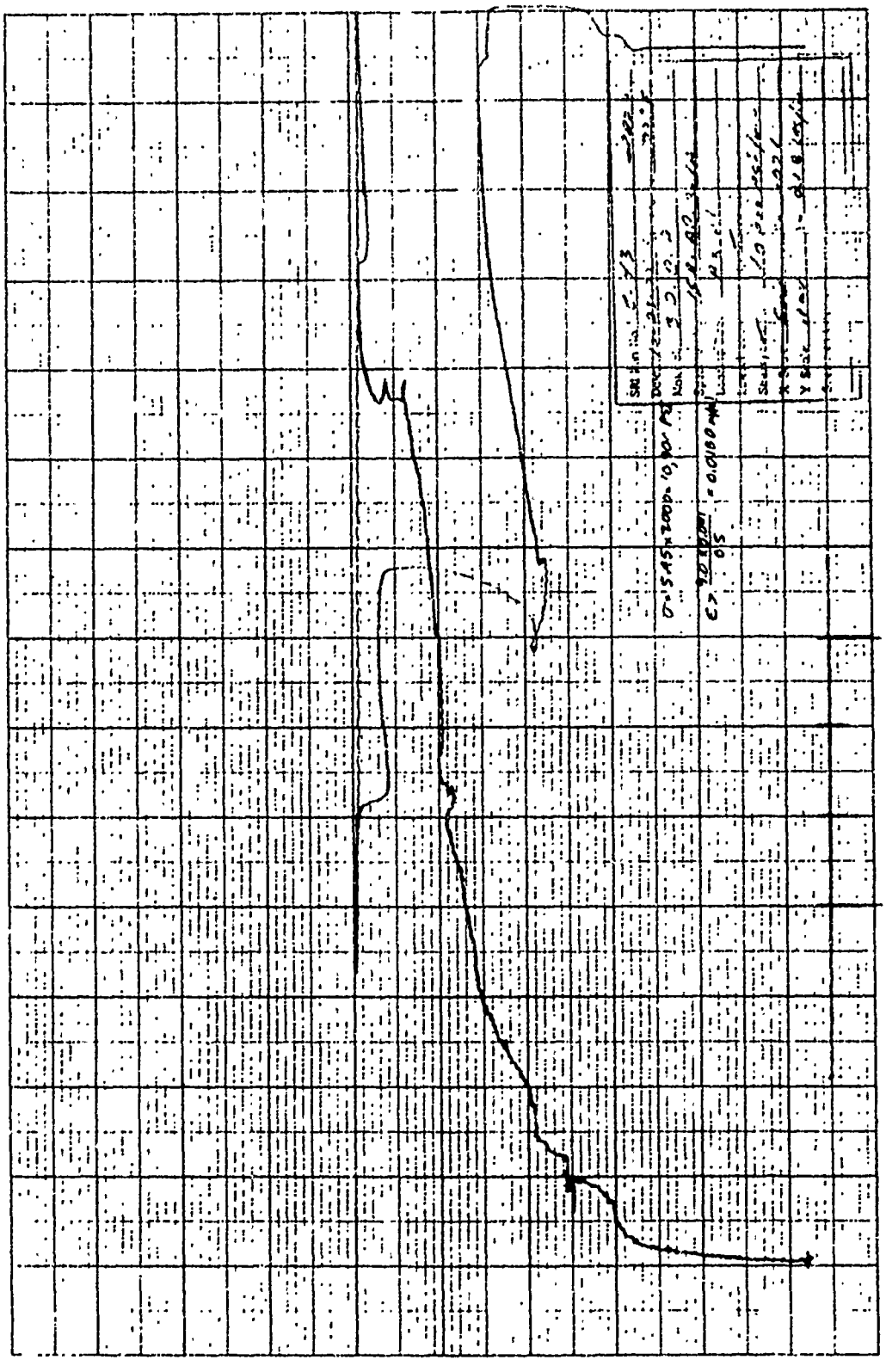


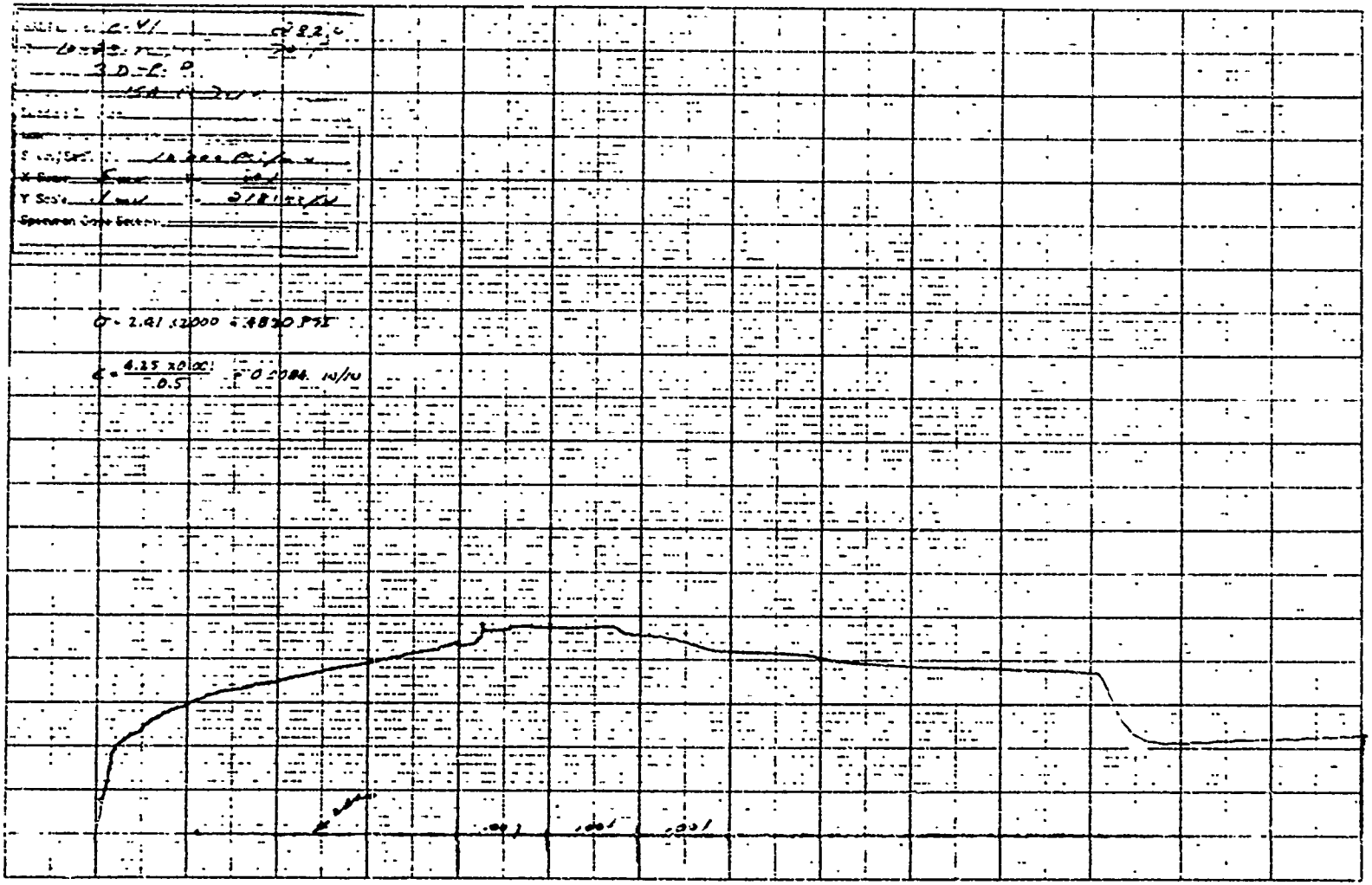

SRI Run No:
Date:
Temperature:
Material:
Specimen No:
Specimen Gage Section:

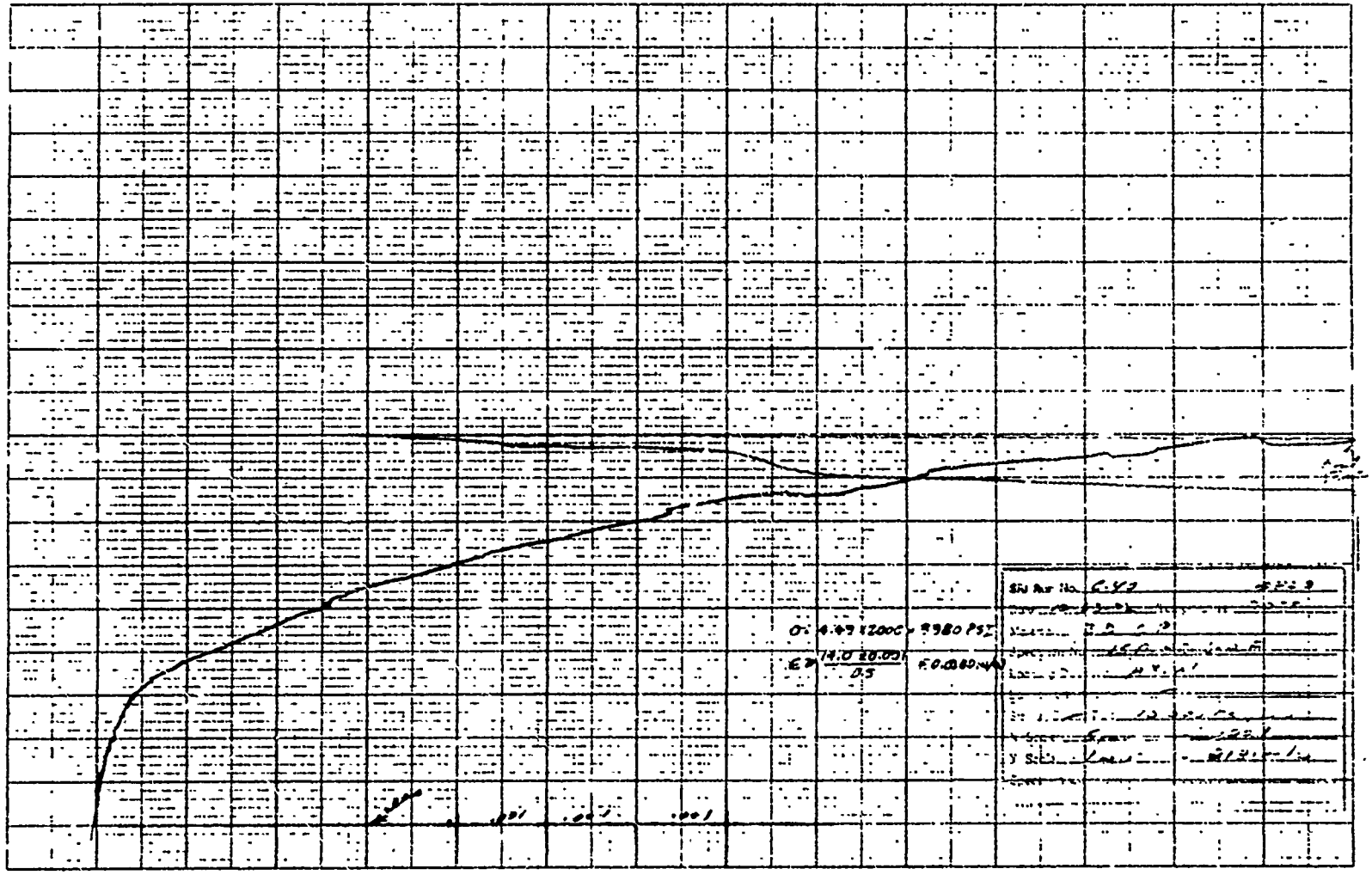

SRI Run No. T-41-(2120)
Date 12/20/72 Temperature RT
Material 6151A
Specimen No. AT-4-1A
Loading AXIAL
Strain Rate 0.1 IN/MIN
Gage Length 0.0005"
Specimen Cross Section 50 MV 3.625 in²

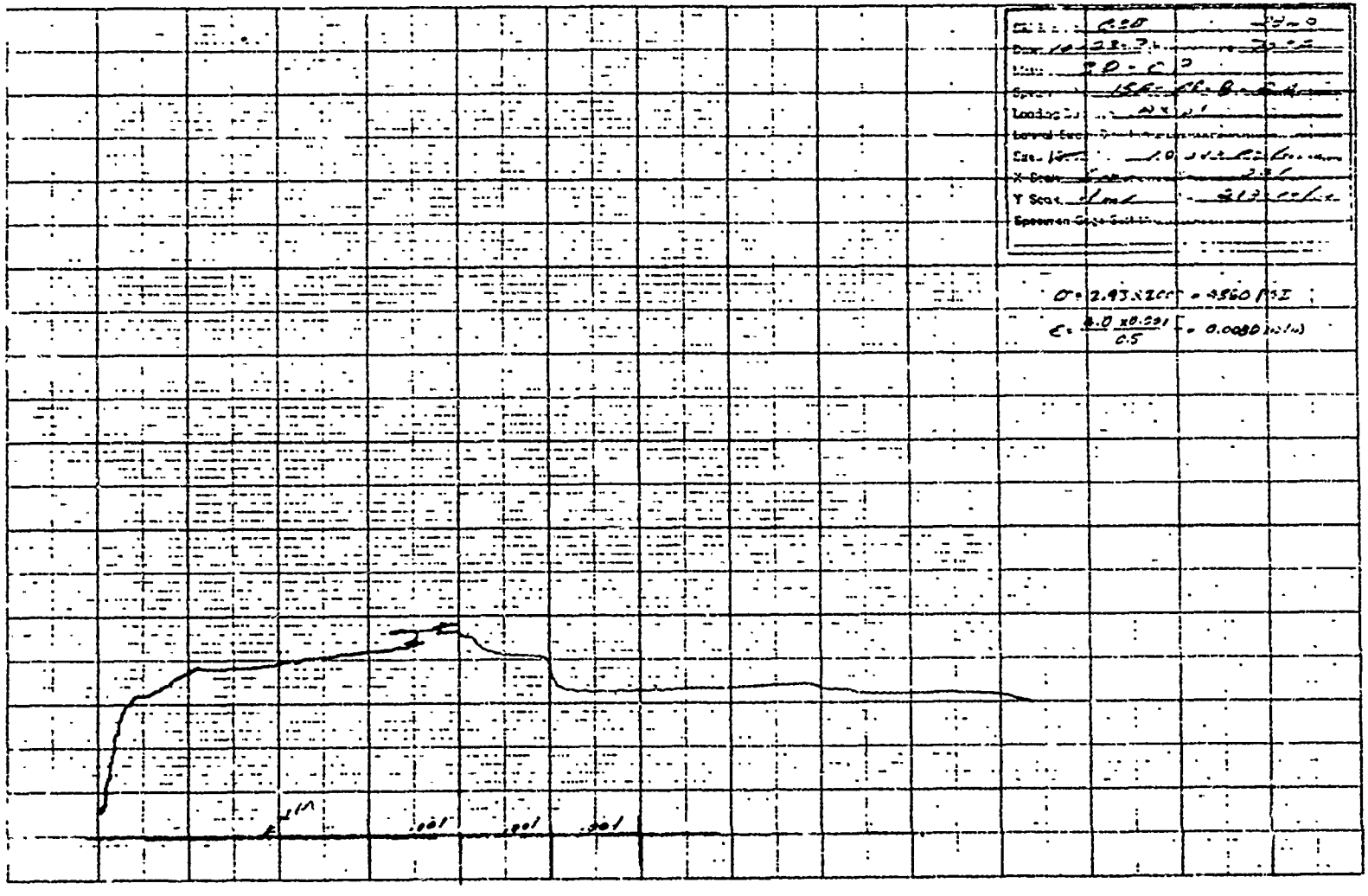

SPI
Date 12/29/92
Temperature 70°
Material #15A
Specimen No. AR-#-29
Loading Direction AXIAL
Test Speed Rate 0.1"/MIN
X-Scale 0.1"/DIV = 0.005"
Y-Scale 50mV = 362.5#
Specimen Dia.
E = 0.3350 KG/S / 9.0 KG/mm^2 = 0.37 x 10^6 PSI
σ = 100 / 0.072 = 1388 PSI
ε = 1010. KG/mm^2 / 0.5 = 0.0100 IN/IN
LC

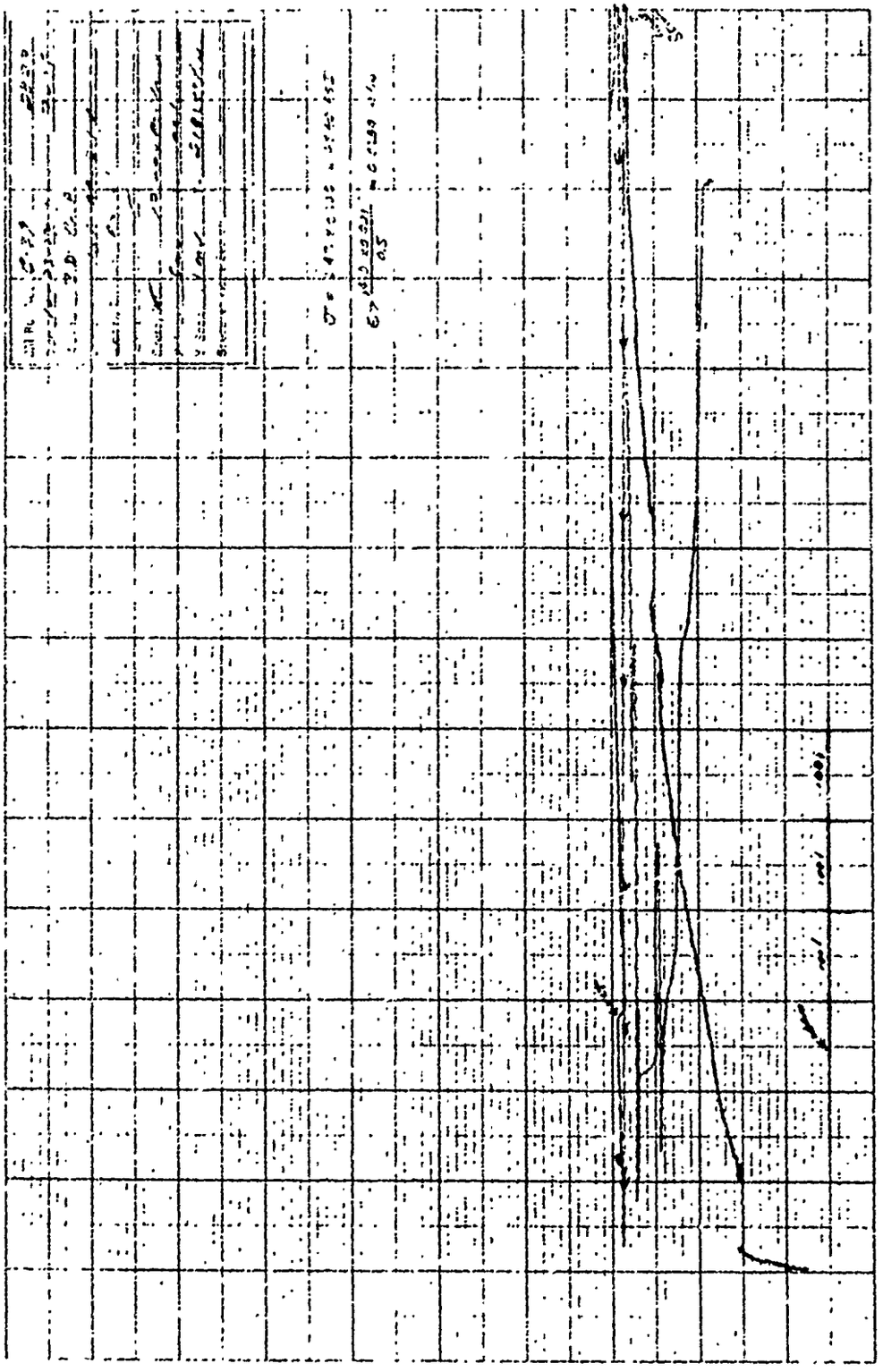

E= 4.6 x 2000 x 0.5 / 12.20 x 0.001 = 1.35 x 10^6 PSI
σ = 3.0 x 2000 = 6000 PSI
ε = 10.7 x 0.021 / 0.5 = 0.0214 in/in



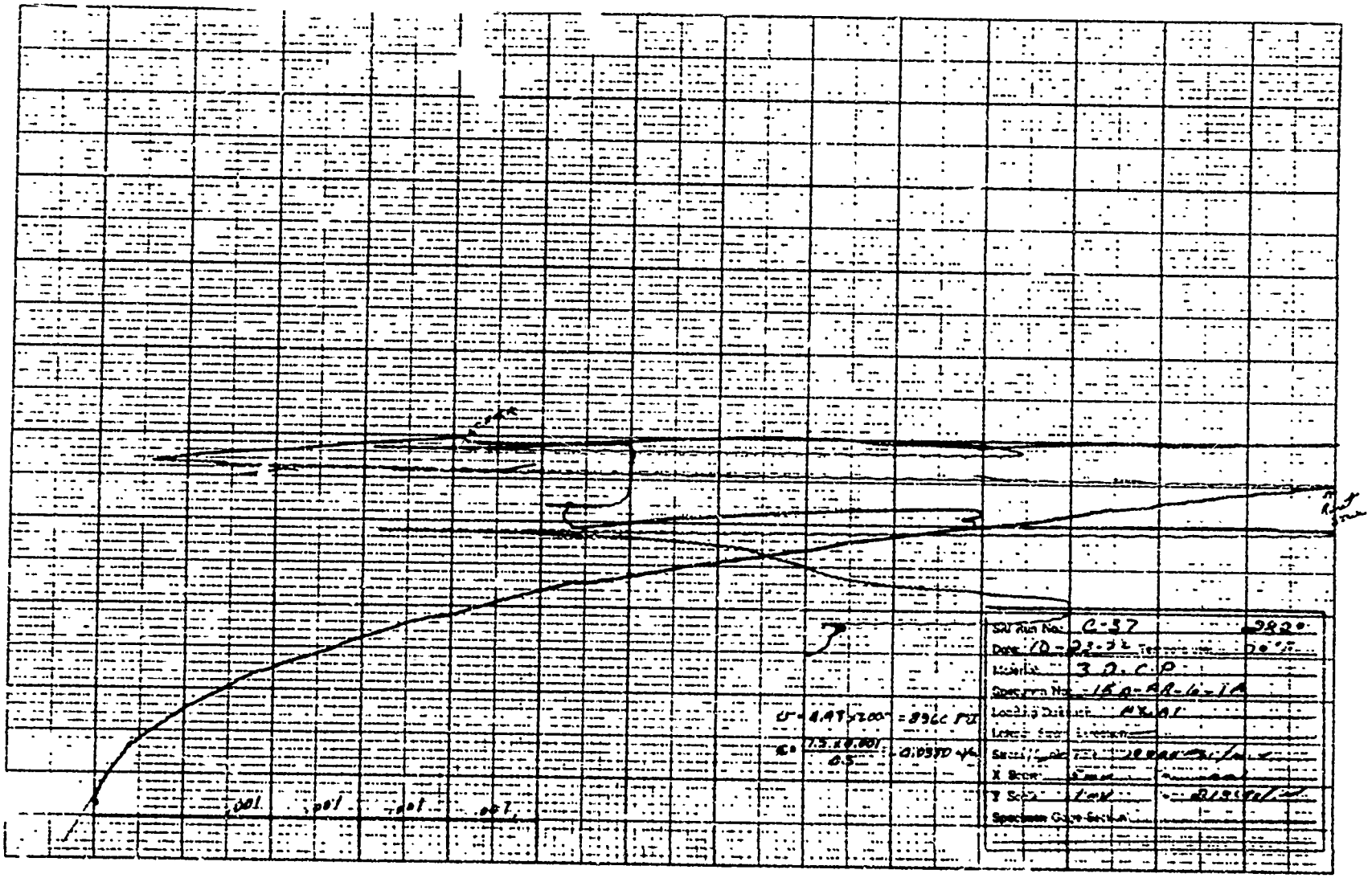

σ = 2.41 x 2000 = 4830 PSI
ε = 6.25 x 10⁻³ / 0.5 = 0.0084 in/in


σ= 4.49 X200C = 9980 PSI
E= 14.0 20.0 21 / 0.5 = 0.0360 in

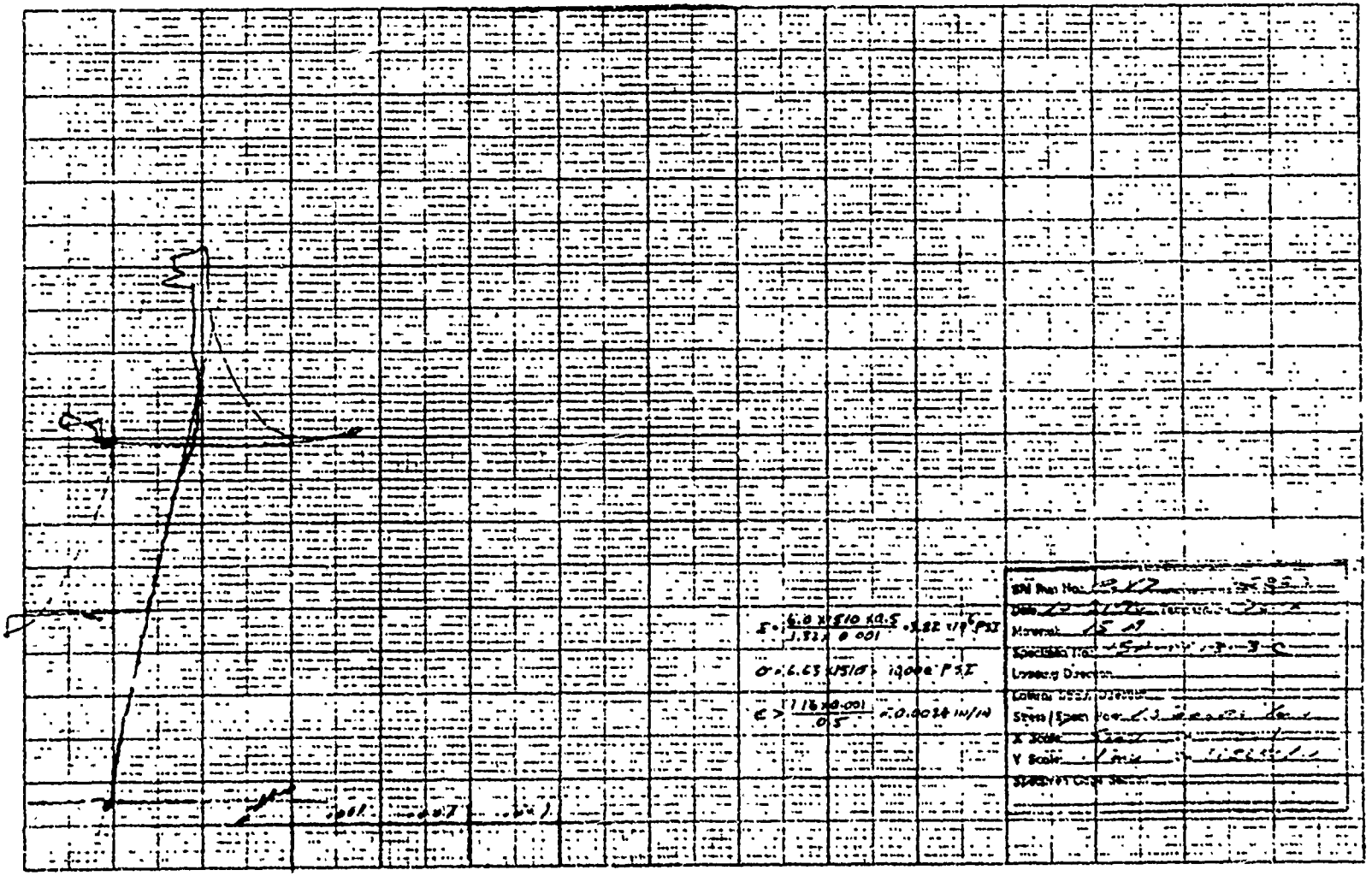

Y Scale
σ = 2.93 x 200 = 4560 PSI
ε = 0.0 x 0.291 / 0.5 = 0.0080 in/in

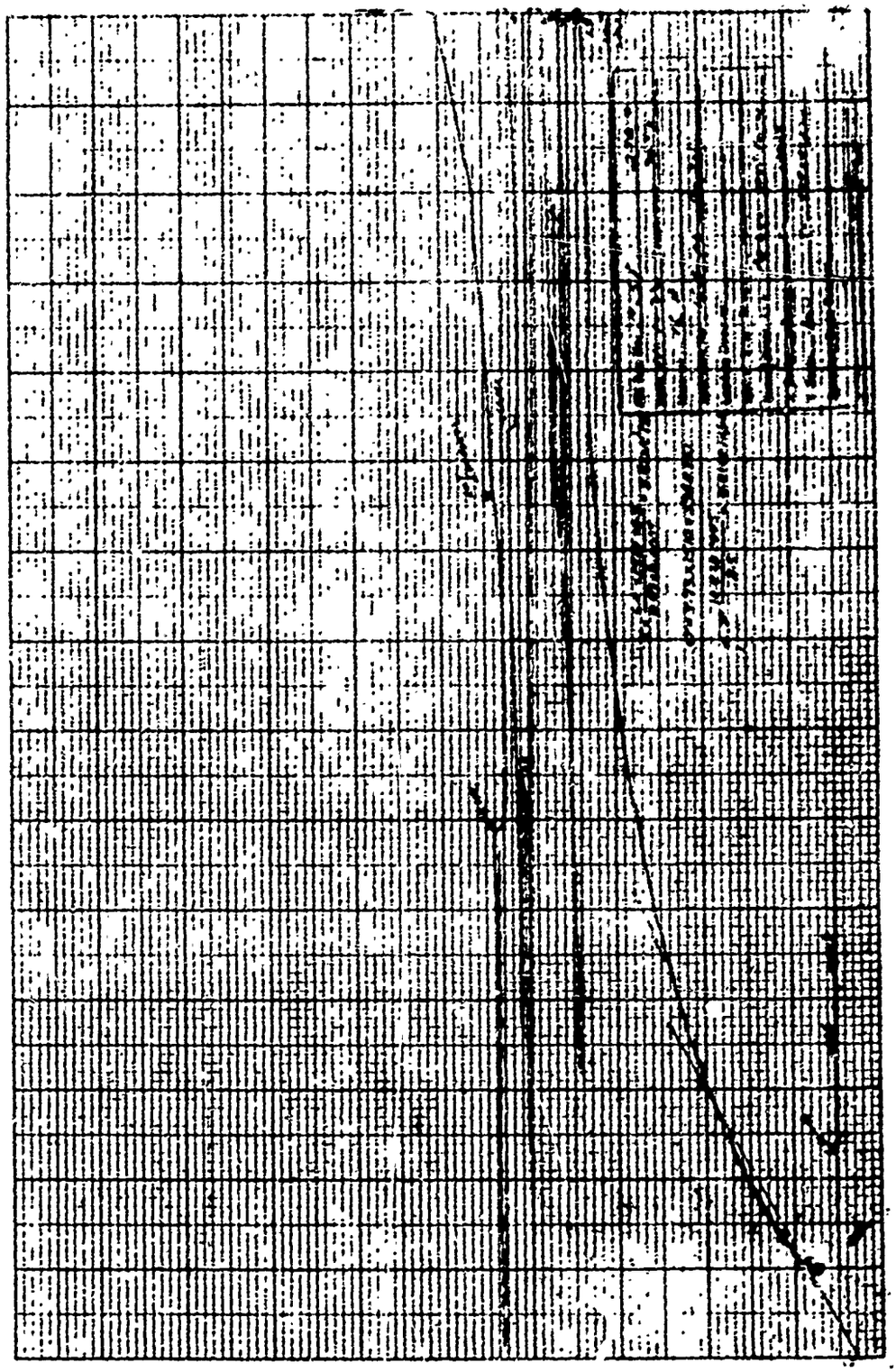


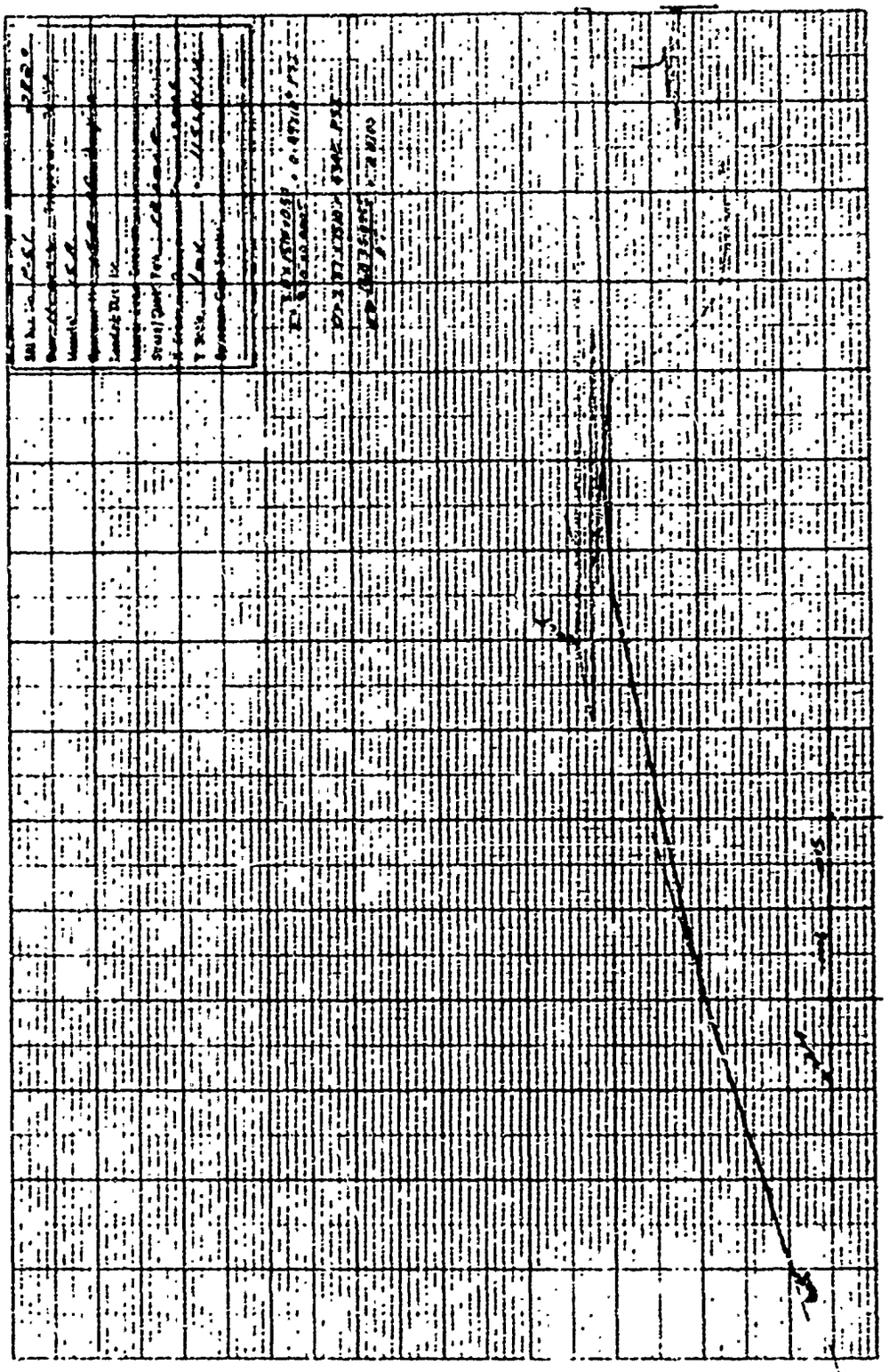
Reproduced from
best available copy.

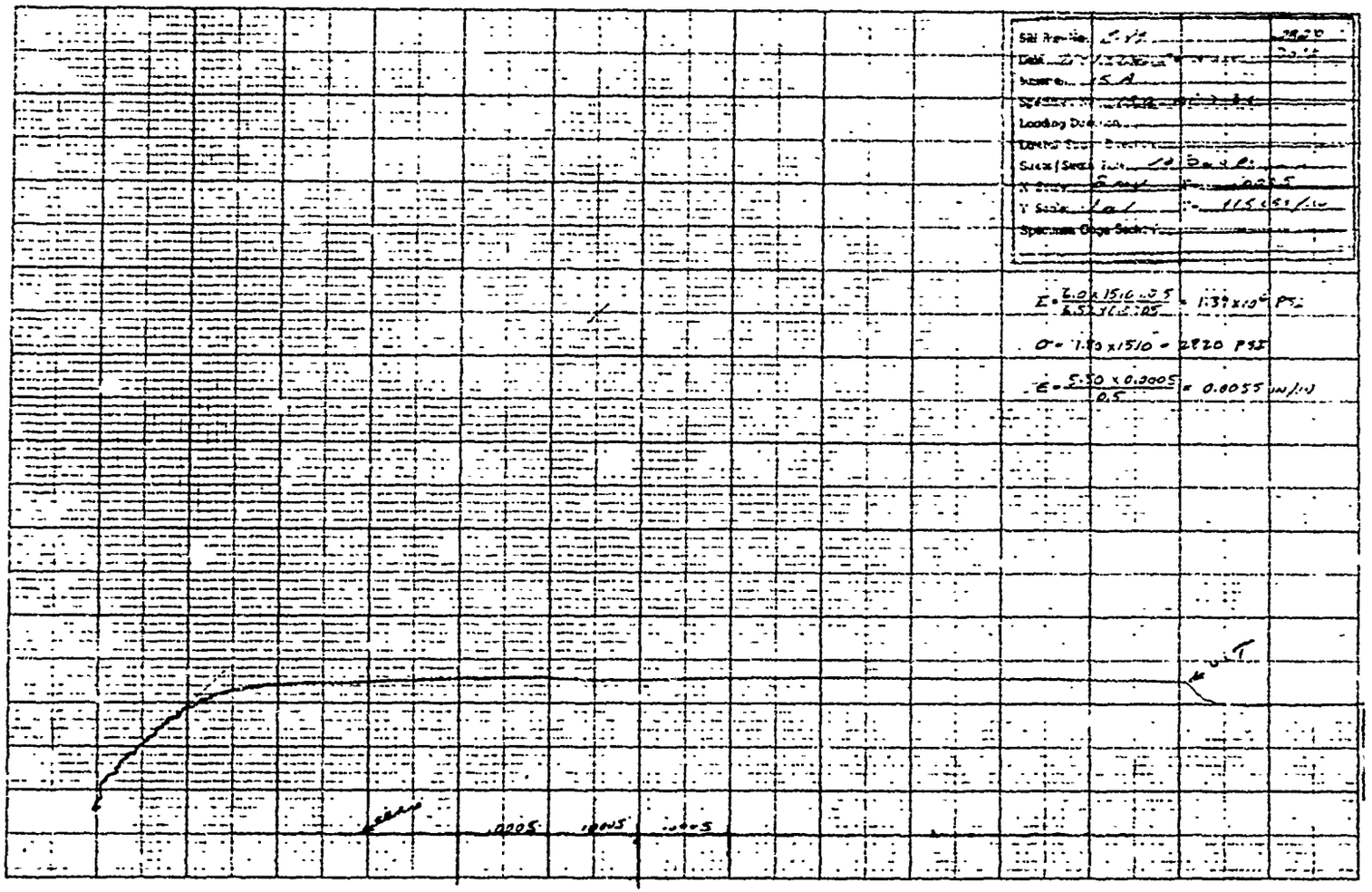

Std Run No. C-57
Date 10-23-72
Material 3 D. C. P.
Specimen No. 150-AR-16-1A
Loading Direction AXIAL
Strain Scale
X Scale
Y Scale
Specimen Gage Section
.001
.001
.001
.001

D = 3.04 x 1510 MHz
= 4590 MHz


E = 6.0 x 510 x 0.5 / 1.32 x 0.001 = 1.93 x 10^6 PSI
σ = 6.63 x 510 = 13000 PSI
ε = 1.18 x 0.001 / 0.5 = 0.0024 in/in
Stress / Strain
X Scale
Y Scale

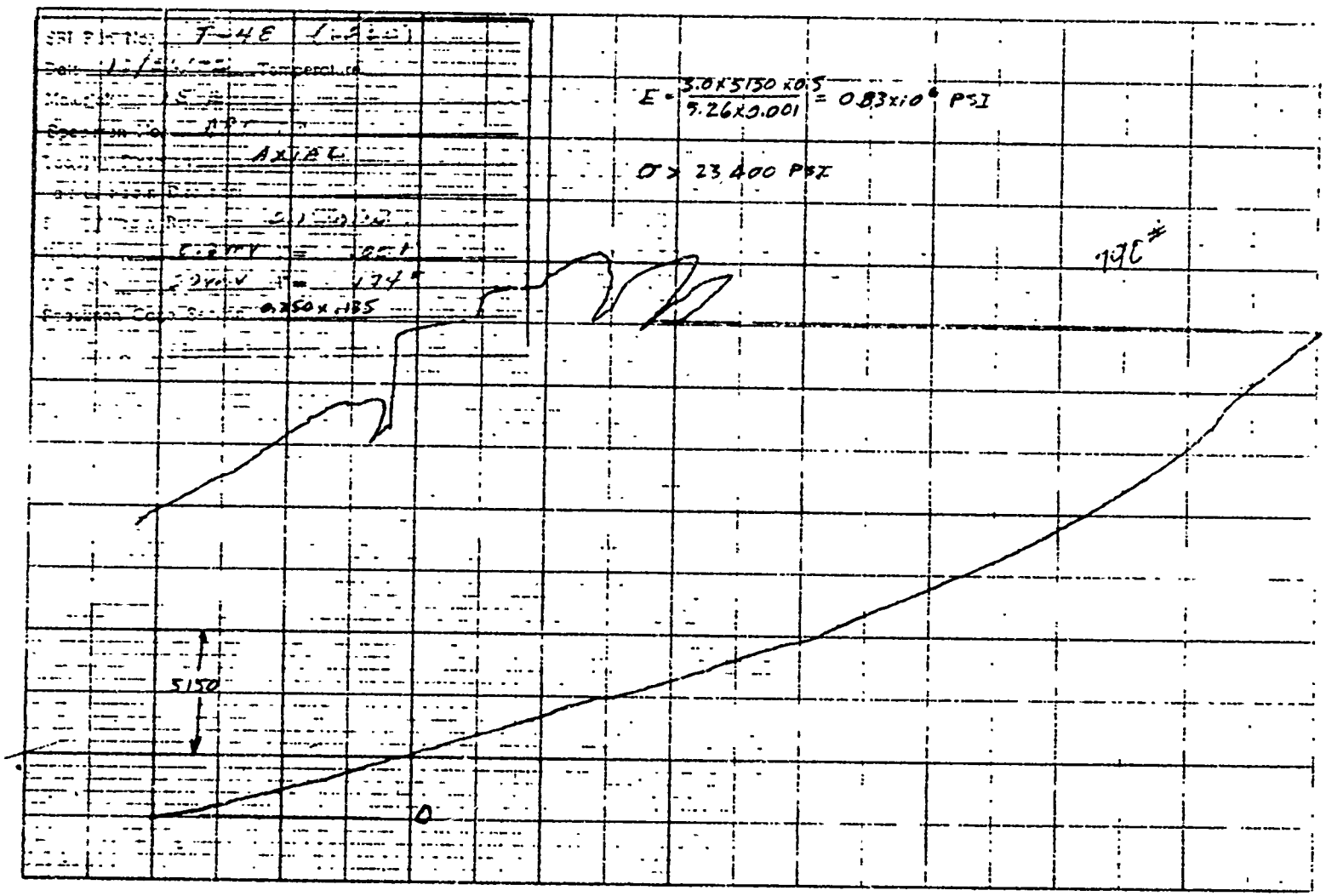


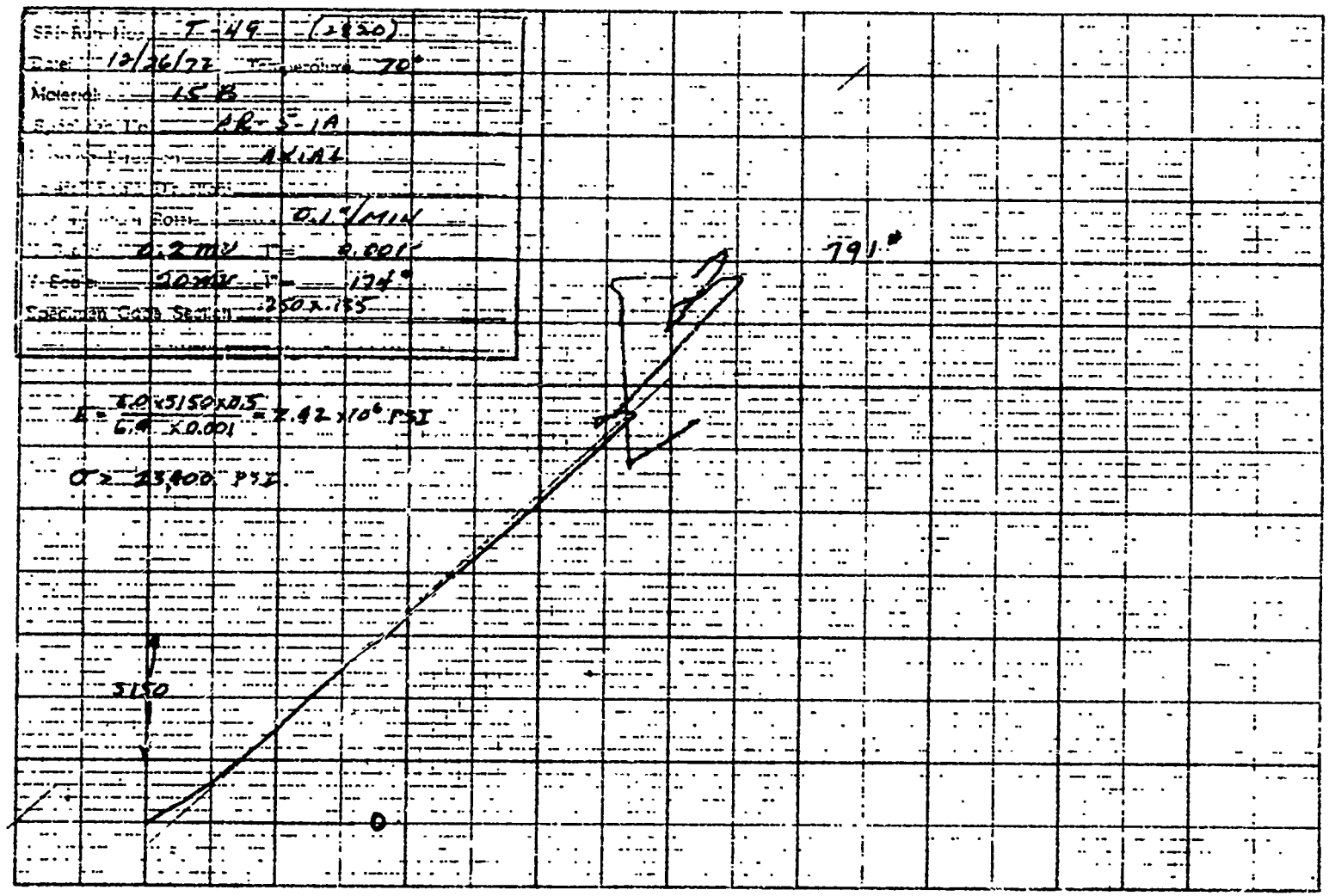


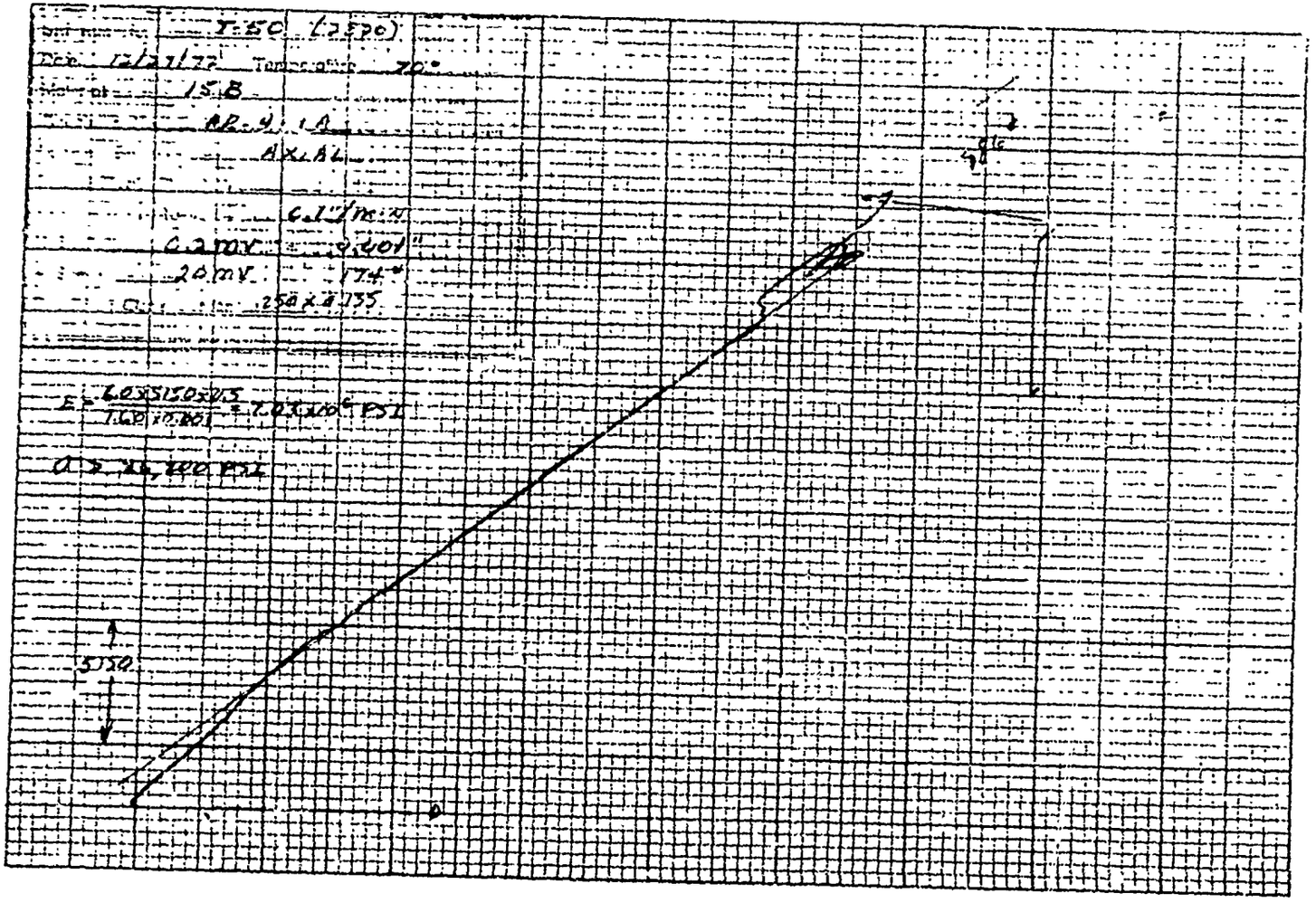

Soil Profile
Date
Name
Loading Direction
Stress / Strain Curve
X Scale
Y Scale
Specimen Shape Section
E = 6.0 x 15.16 - 0.5 / 0.5 x 1.5 x 0.05 = 1.39 x 10^6 PSI
σ = 1.89 x 15.10 = 2820 PSI
E = 5.50 x 0.0005 / 0.5 = 0.0055 in/in
.0005
.0005
.0005

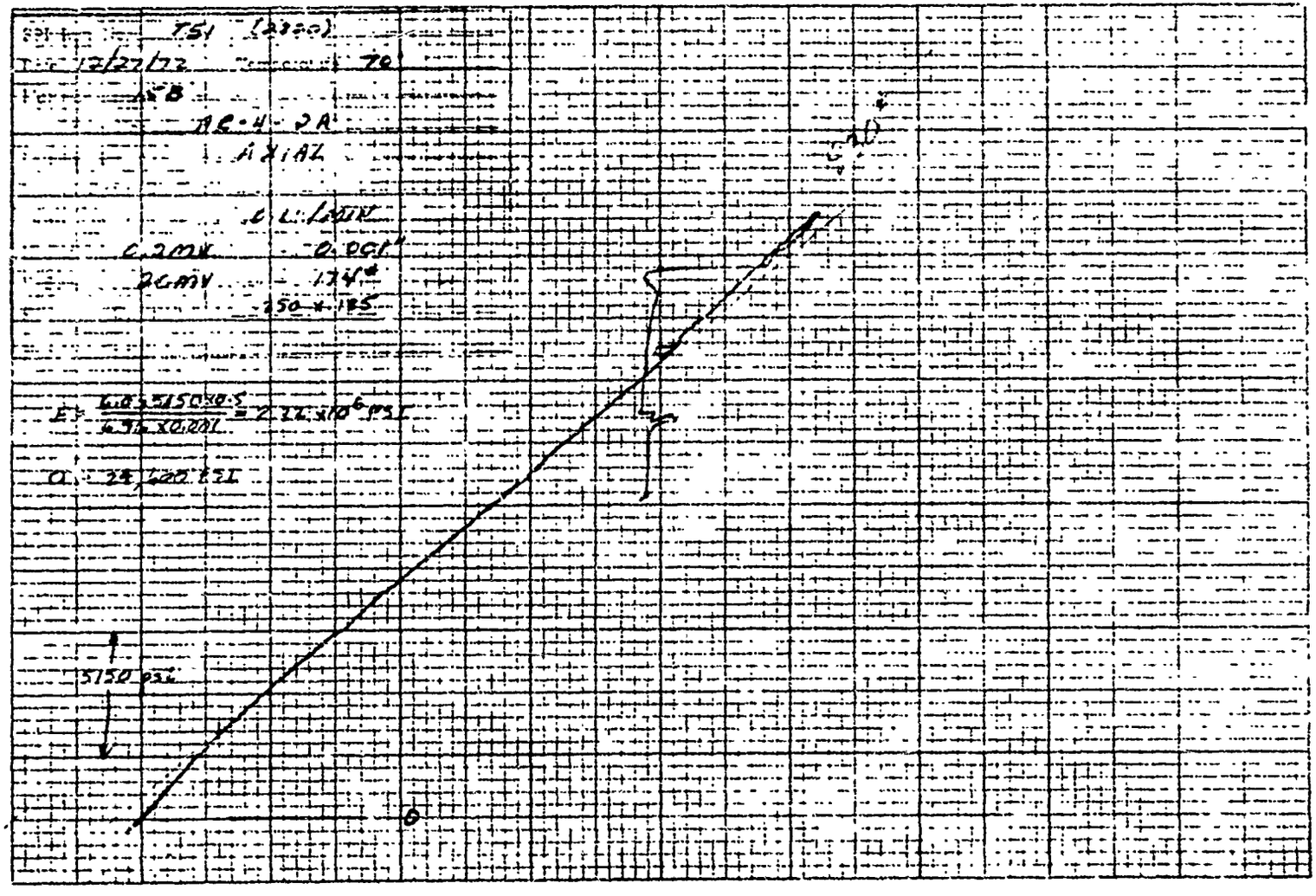
APPENDIX L

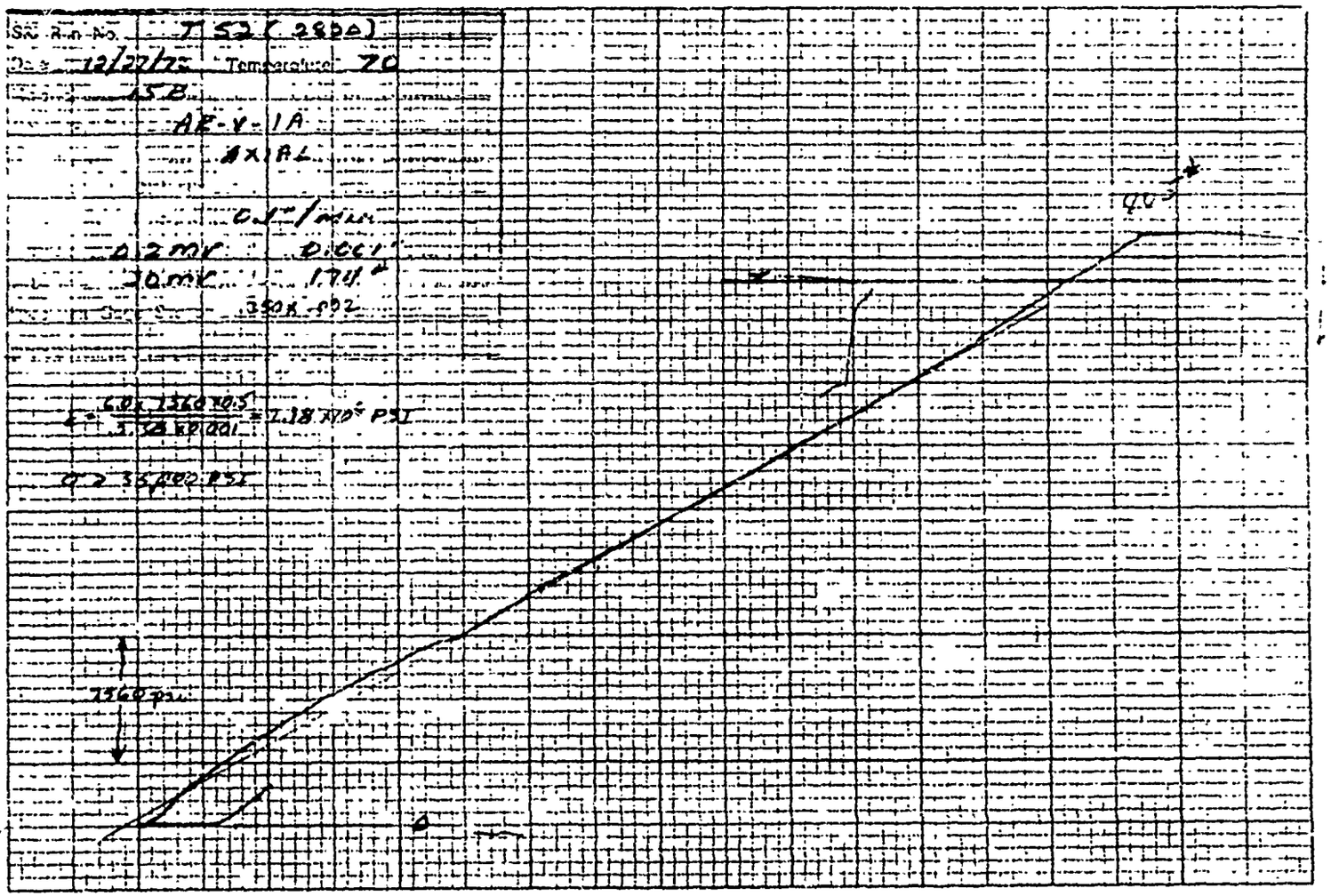
TENSILE AND COMPRESSIVE STRESS-STRAIN CURVES FOR THE QUARTZ-PHENOLIC PORTION (#15B) OF AVCO 3DC/QP - MATERIAL 15

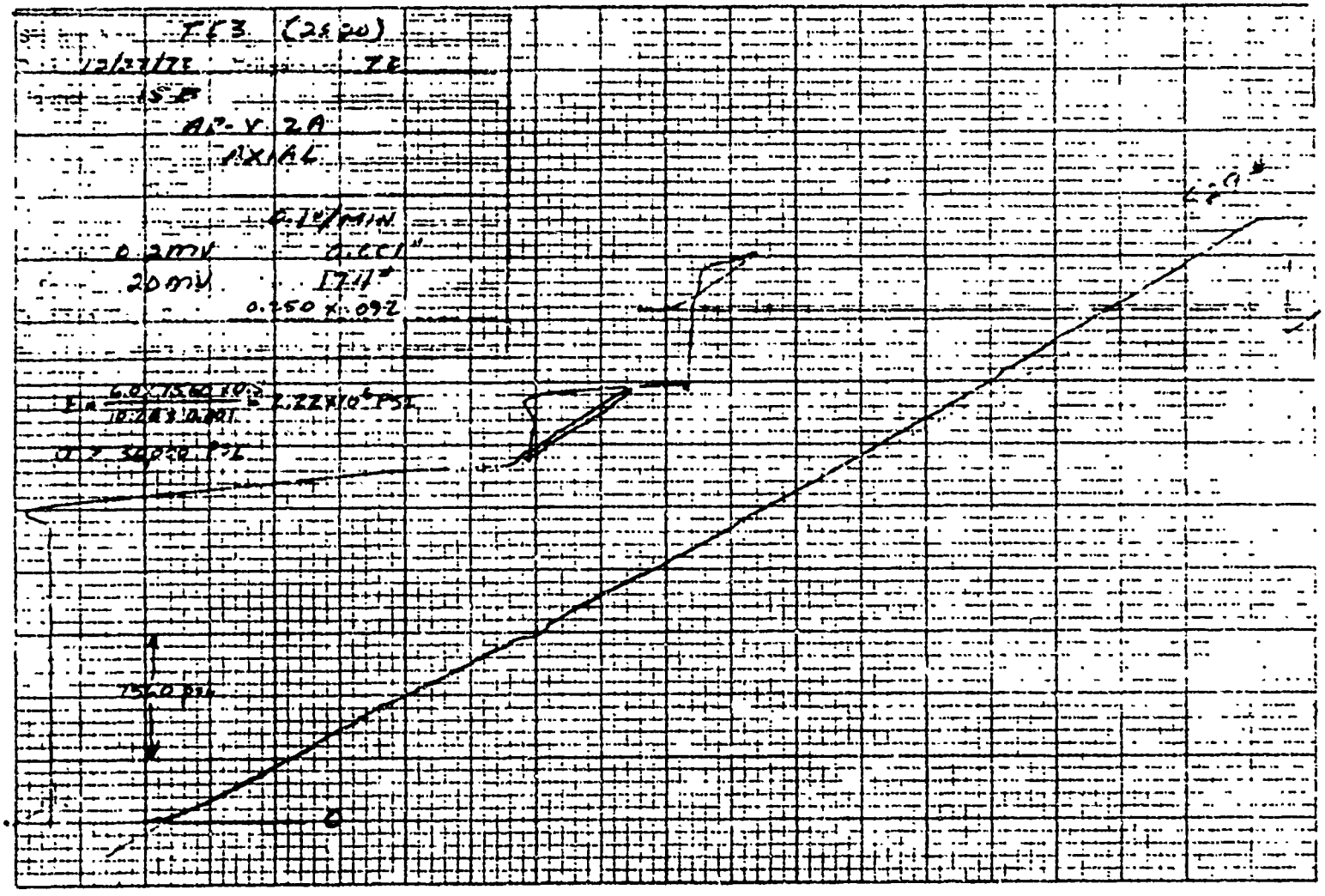

$E = \frac{3.0 \times 5130 \times 0.5}{9.26 \times 0.001} = 0.83 \times 10^6$ PSI
$\sigma >$ 23,400 PSI
5150
0

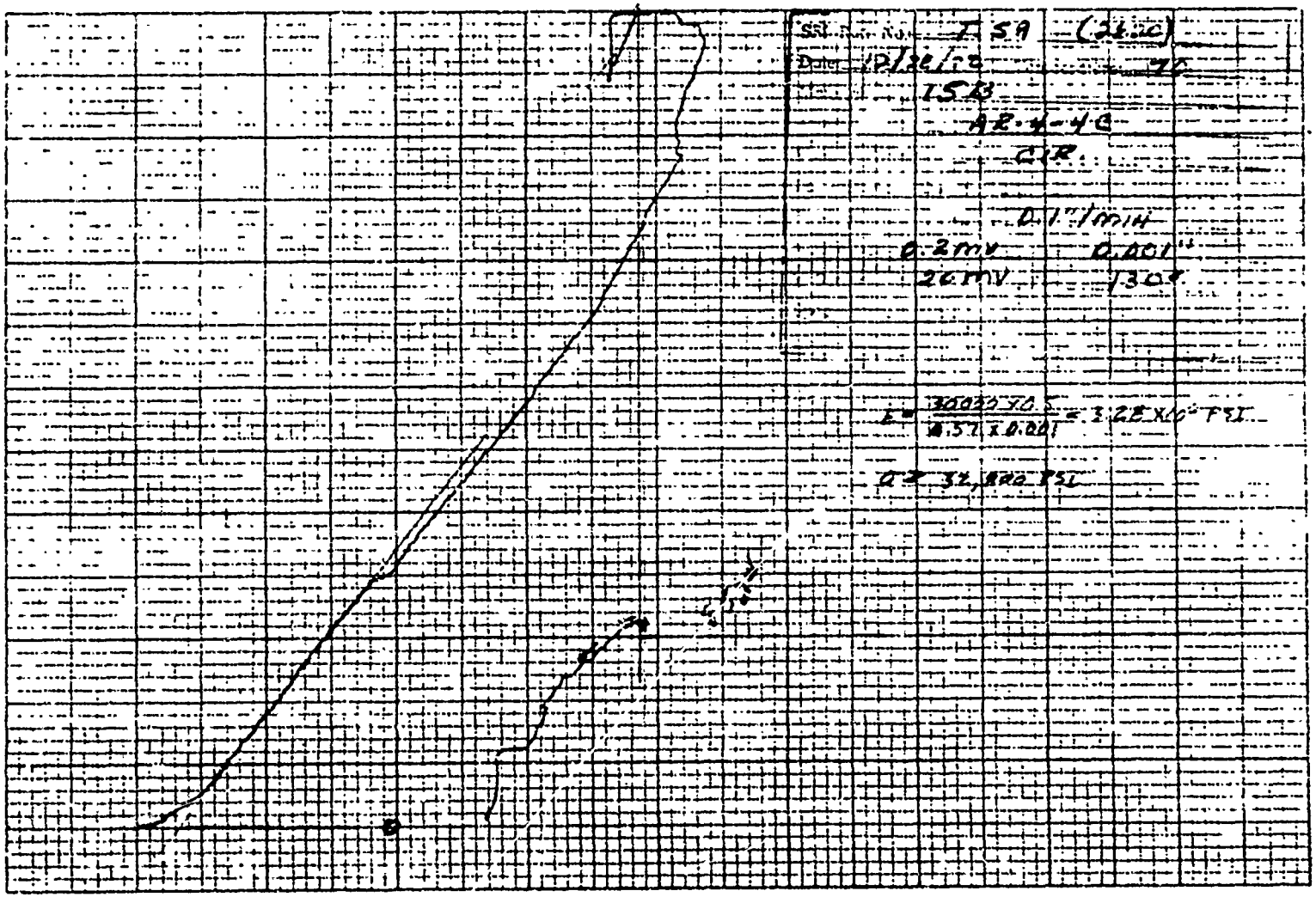

T-49 (1820)
12/26/72
70°
LS-B
AR-3-1A
AXIAL
0.1"/MIN
0.2 MV
0.001"
50 MV
134°
250 x .185
E = 2.0 x 5150 x 0.5 / 6.9 x 0.001 = 7.42 x 10^6 PSI
σ = 23,400 PSI
5150
791°

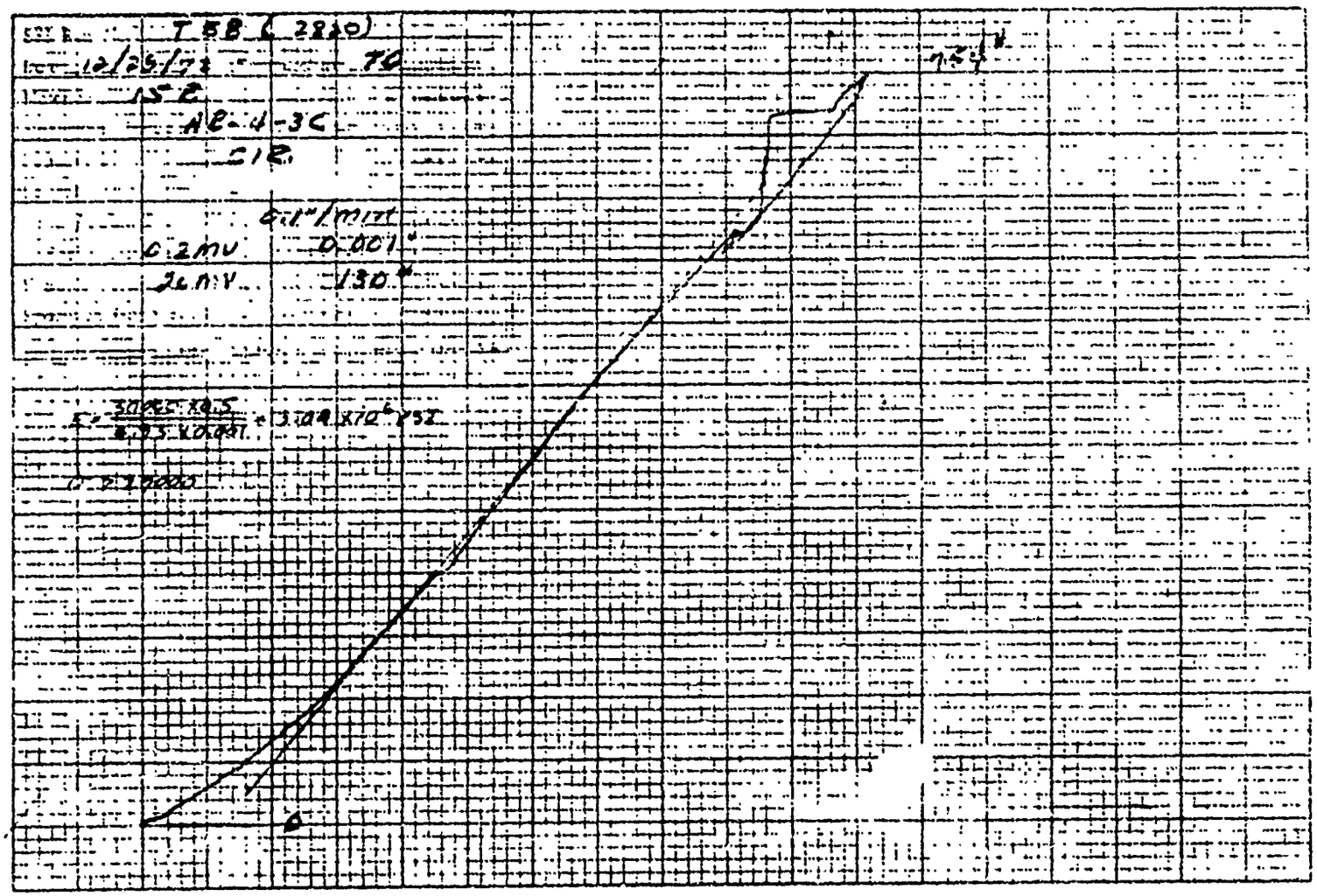

T-50 (7520)
12/21/77
70°
15.8
AR-4 : A
AXLAL
Cal/mm
Cal 70K
20 mV
250 x 4 135
E = 6.0 x 5150 x 2.5 / 7.62 x 10^-3 = 7.0 x 10^6 PSI
σ > 24,100 PSI
3550

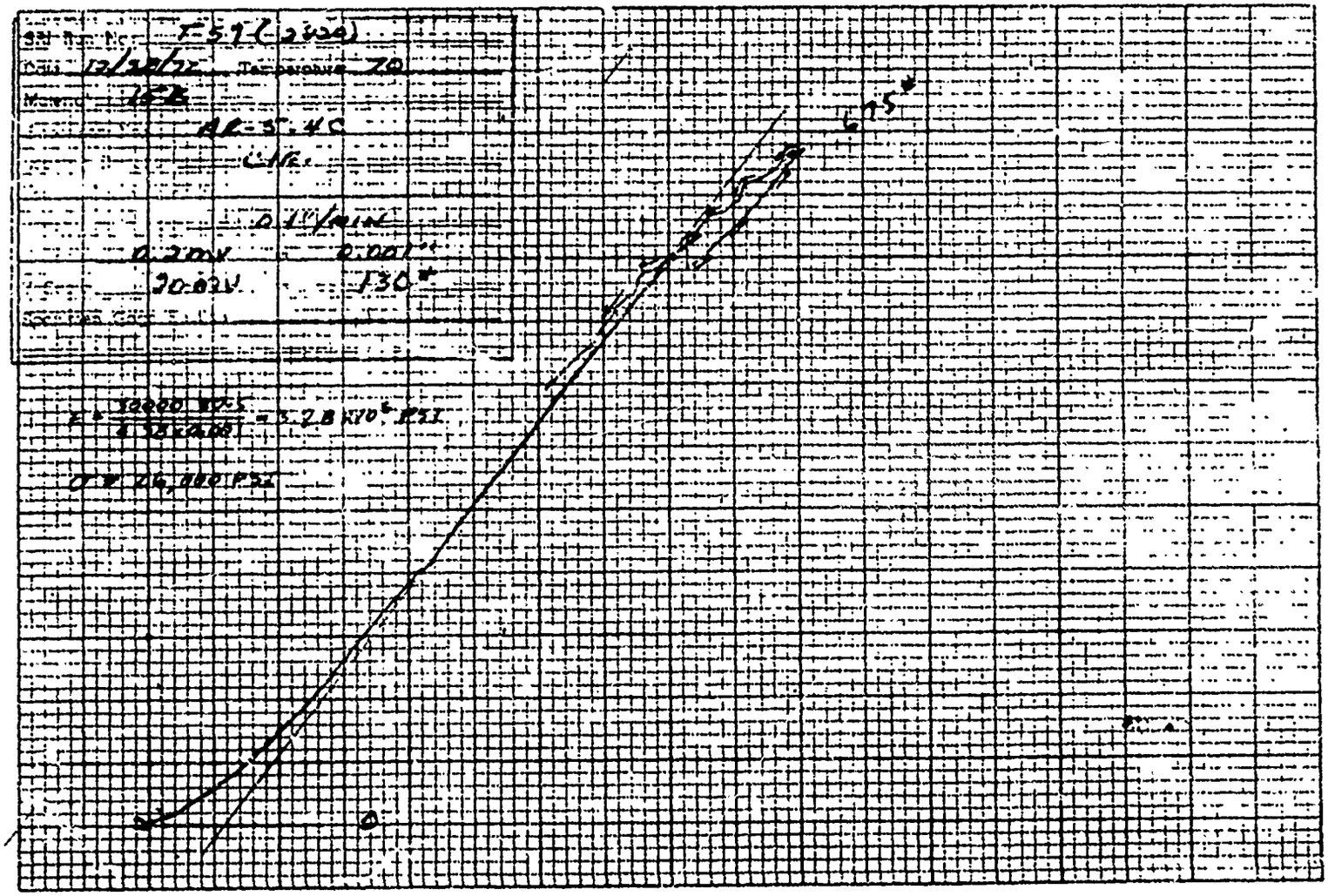

TSI (2950)
12/27/72
70
AC-4 2A
A X AZ
.6 L.L/SIN
0.2 MIN
0.091"
2 GAIN
174#
150 x 185
E = 6.0 x 5150 x 0.5 / 6.32 x 0.091 = 2.22 x 10^6 PSI
5150 PSI

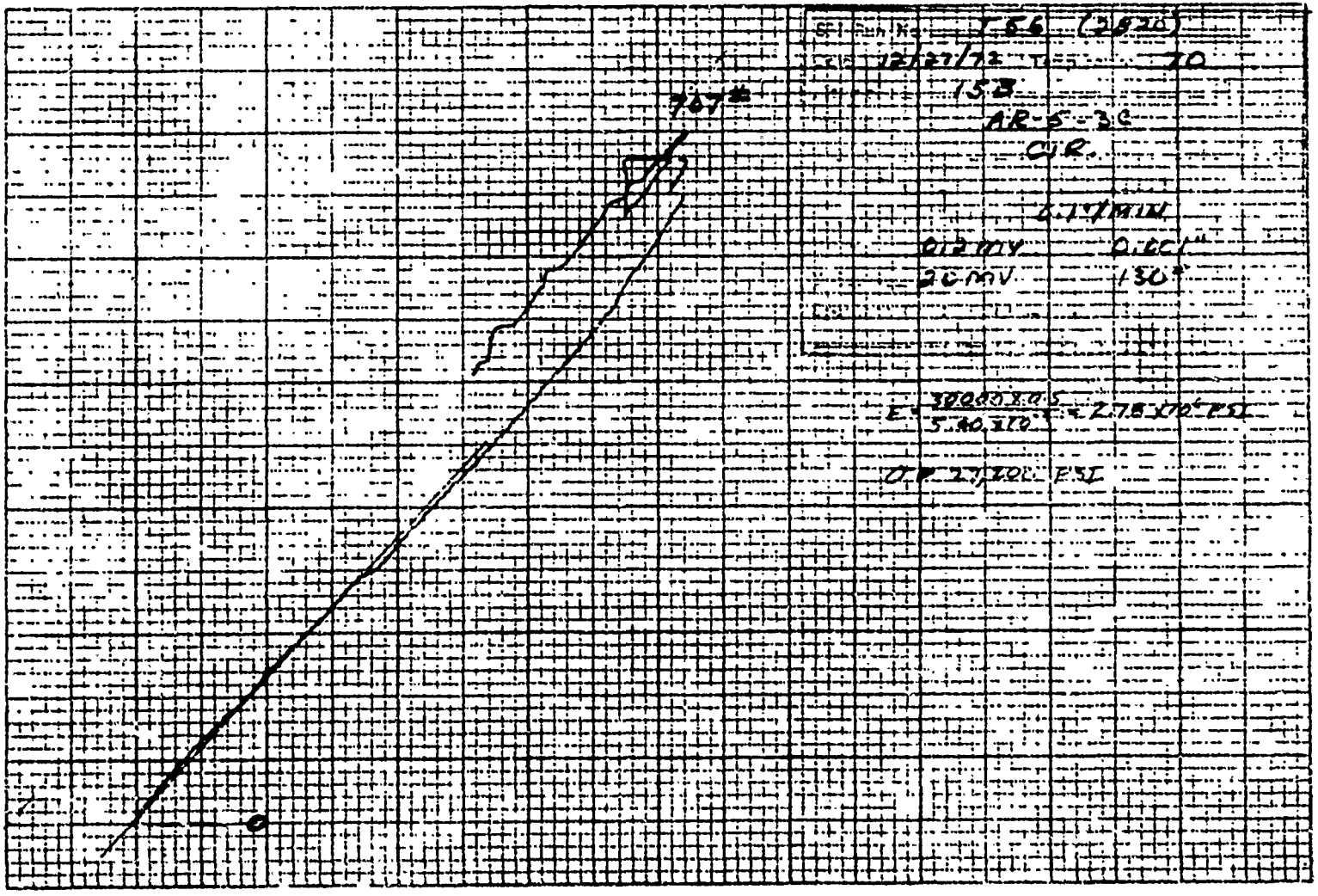

SS R-n-No. T 52 (2500)
Date 12/27/72 Temperature 20
45B
AE-V-1A
8 x 8 L
0.1"/min
0.2 mV 0.001"
20 mV 1.711"
350K 502
q = 1360 x 0.5 / 3.84 x 10^-4 x 0.01 = 1.18 x 10^6 PSI
q > 35,000 PSI
1360 psi
q = 1.18 x 10^6 PSI
q = 35,000 PSI
1360 psi
0

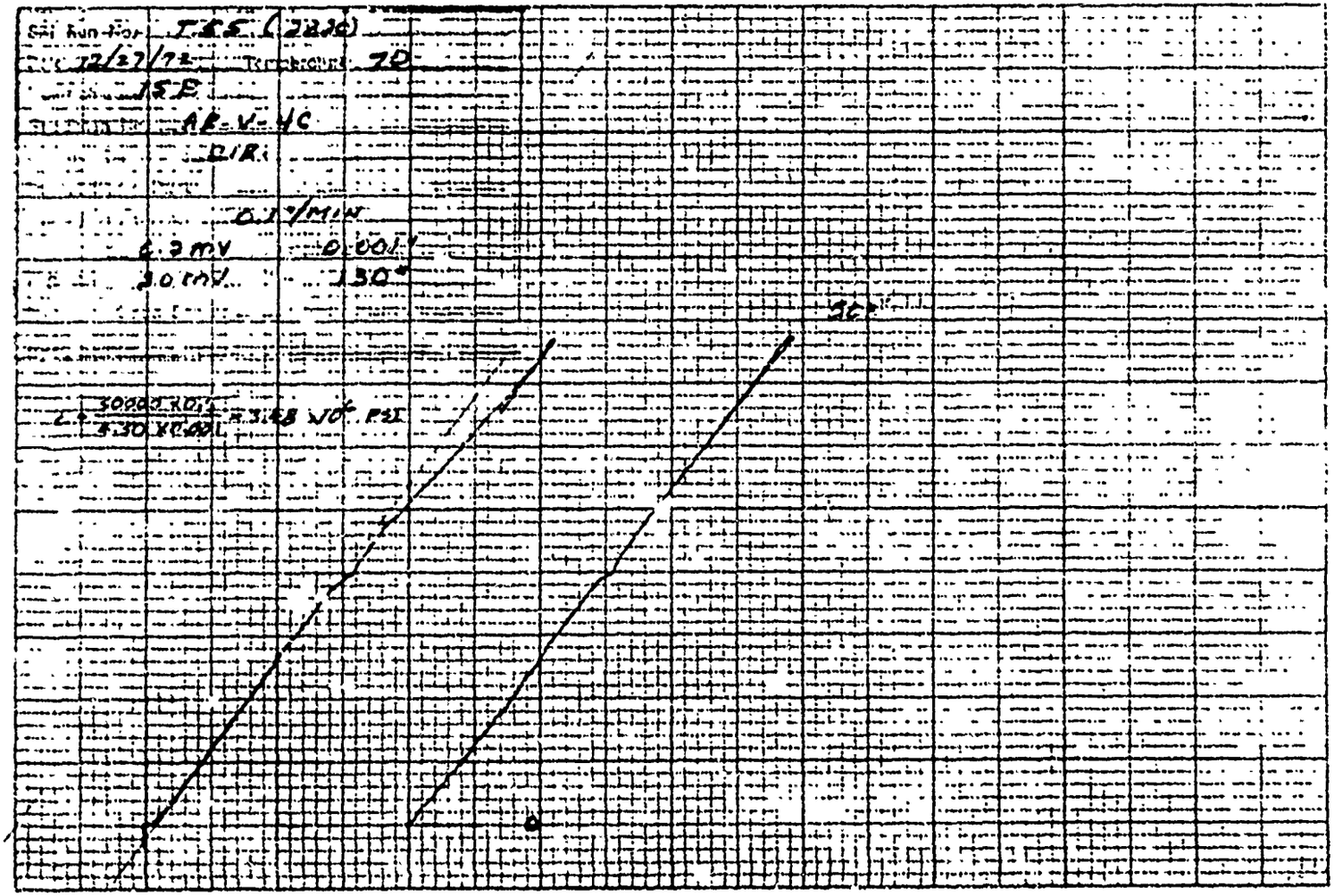

FC3 (2420)
12/27/72
ZC
SS
A1-V 2A
AXIAL
6.1"/MIN.
0.2mV
0.001"
20mV
1711#
0.750 x .092
E = 6.0 x 7560 x 10^3 / 10.283 x 0.001 = 2.22 x 10^6 PSI
σ = 30,000 PSI
7560 psi
0
ε

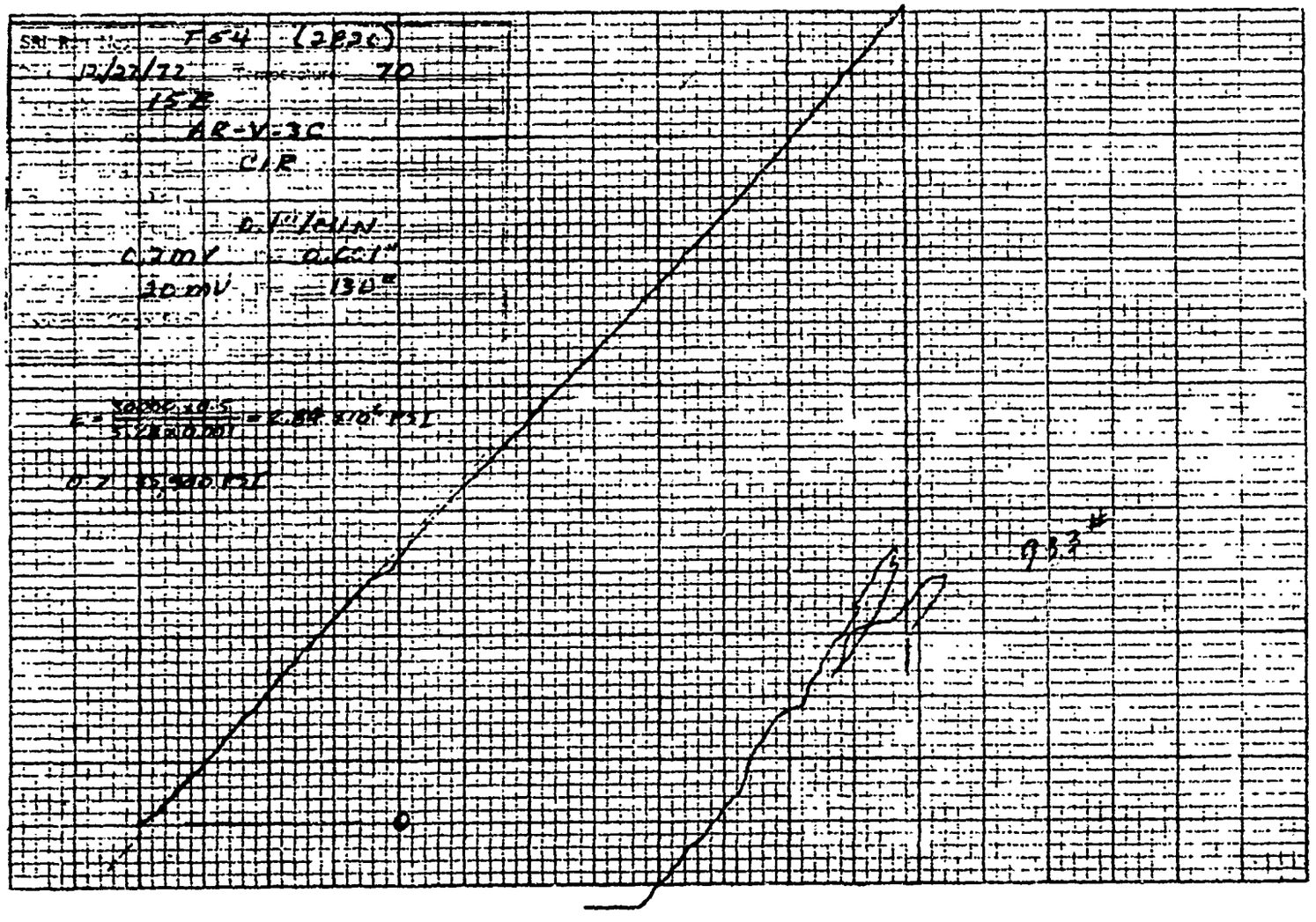

SSL No. I 59 (24.2C)
Date 12/20/79
1543
AE-4-4C
CR
0.1"/min
0.2mV 0.001"
20mV 130#
E = 30000 x 0 / 0.57 x 0.001 = 3.28 x 10^6 PSI
σ = 32,800 PSI

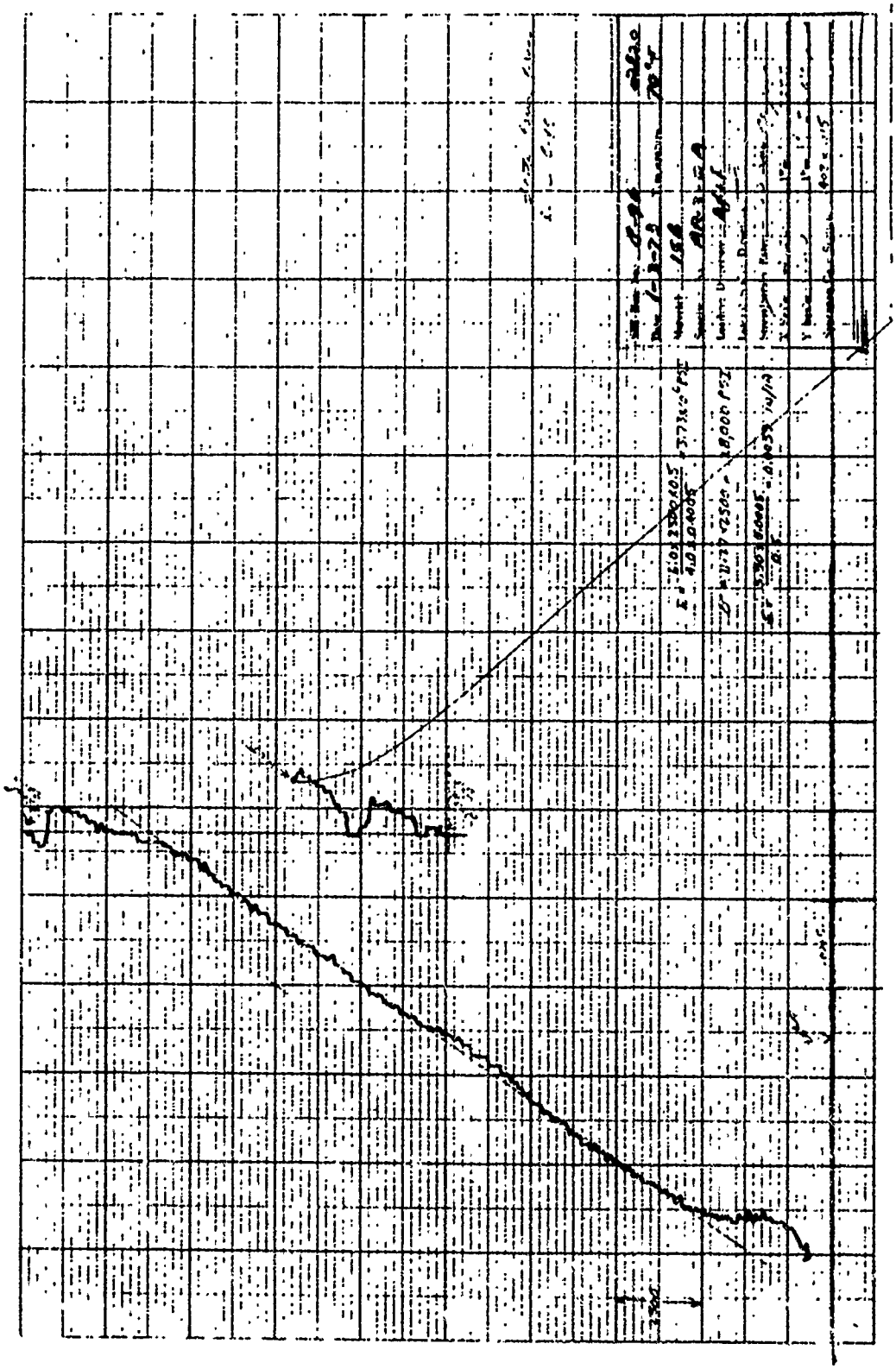

T 58 (2810)
12/25/73
TC
1.5 C
AE-4-3C
C12.
4.1"/min
0.2mV
0.001"
2.0 mV
1.30"
n = 5
σ

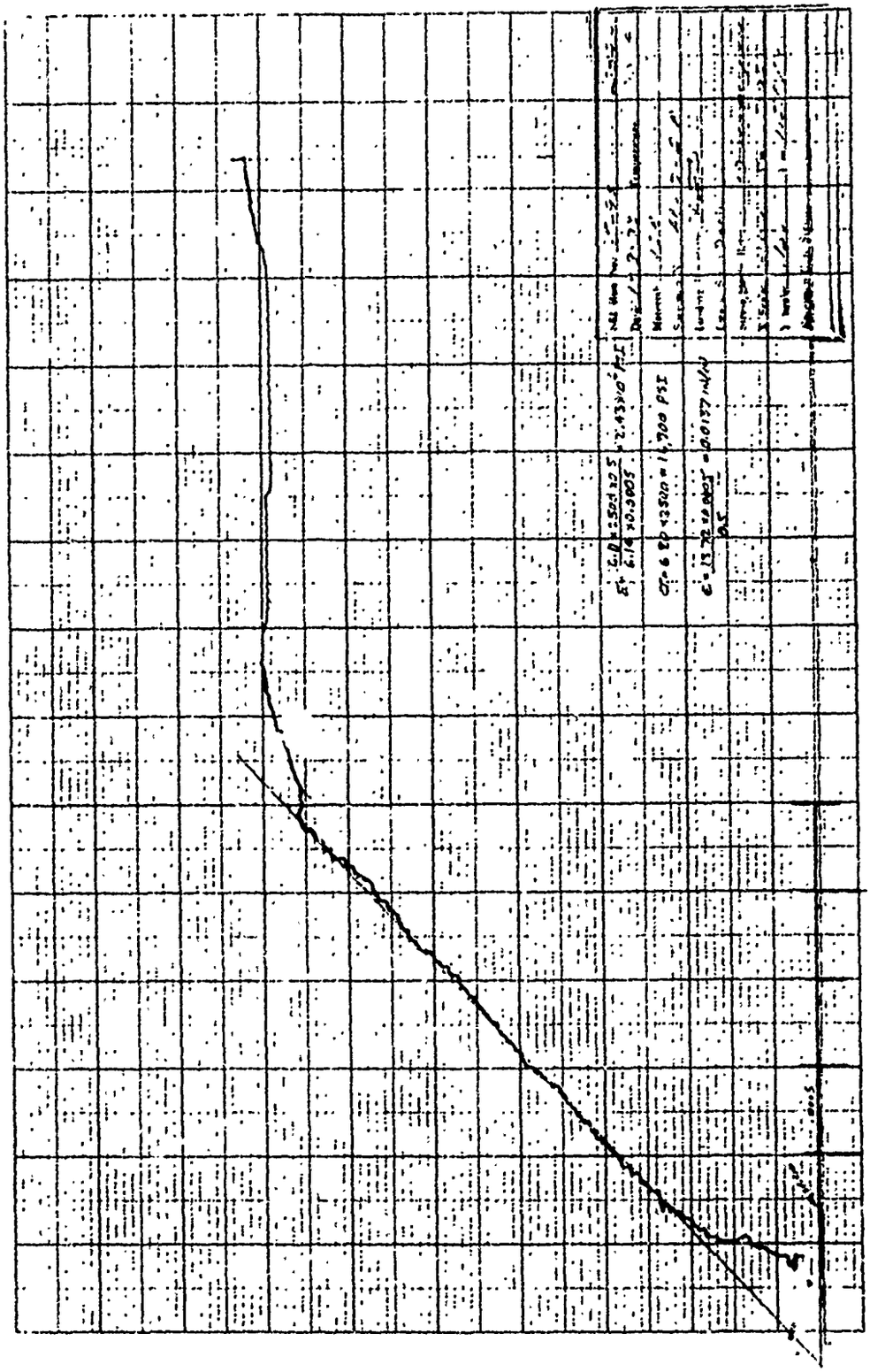

T-5.7 (2439)
Date 12/20/32
Temperature 20
AC-3.4C
0.1"/min
0.001"
130#
0.20"
20.02"
E = 32000 PSI / 0.00625 = 5.12 x 10^6 PSI
σ = 26,000 PSI
45°
0

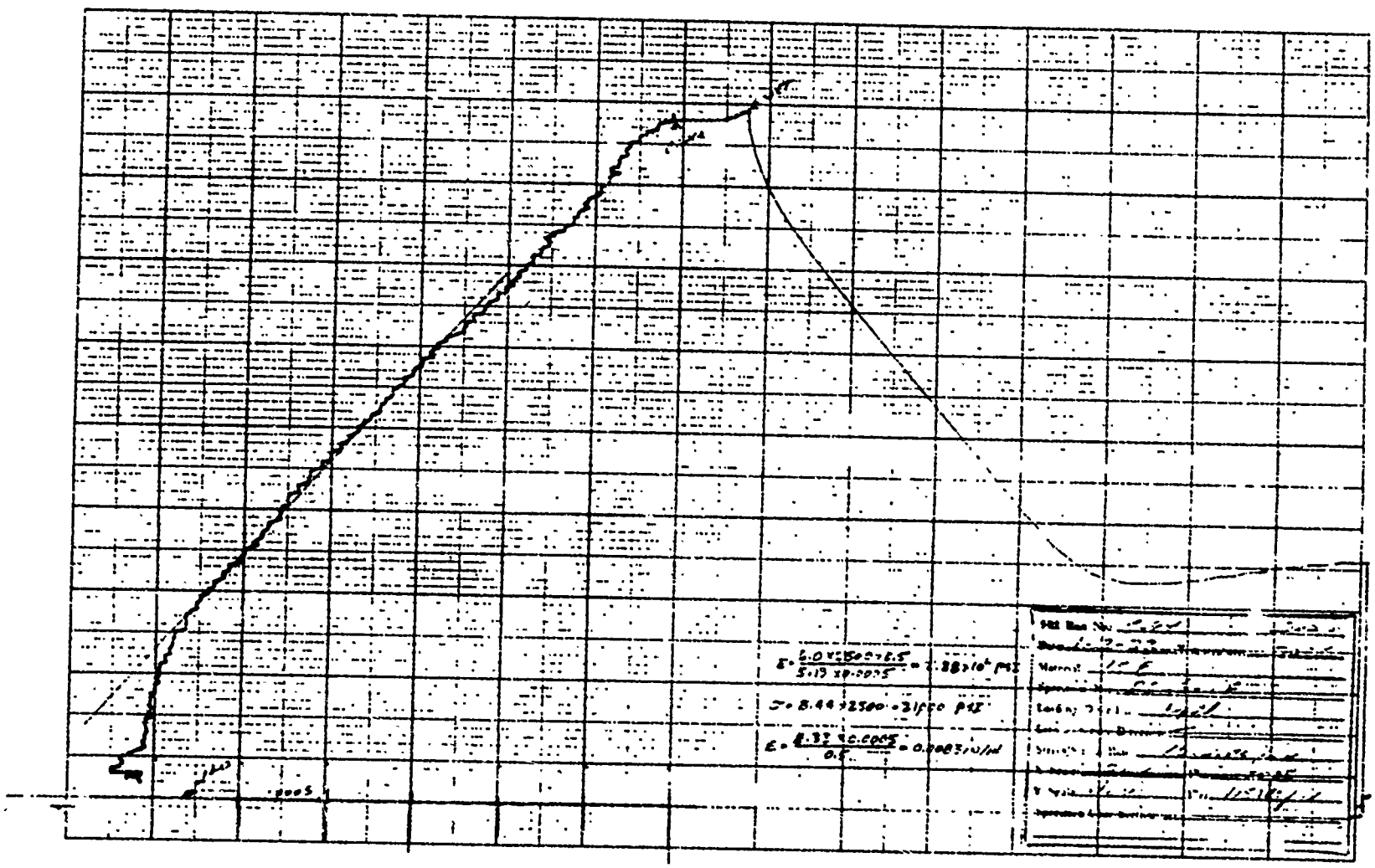

T 56 (2820)
12/27/72
70
153
AR-5-3C
C.R.
0.12 MV
20 MV
+30°
707 #
E = 390,000 x 0.5 / 5.10 x 10 = 2.78 x 10⁶ PSI
O.P. 27,200 PSI

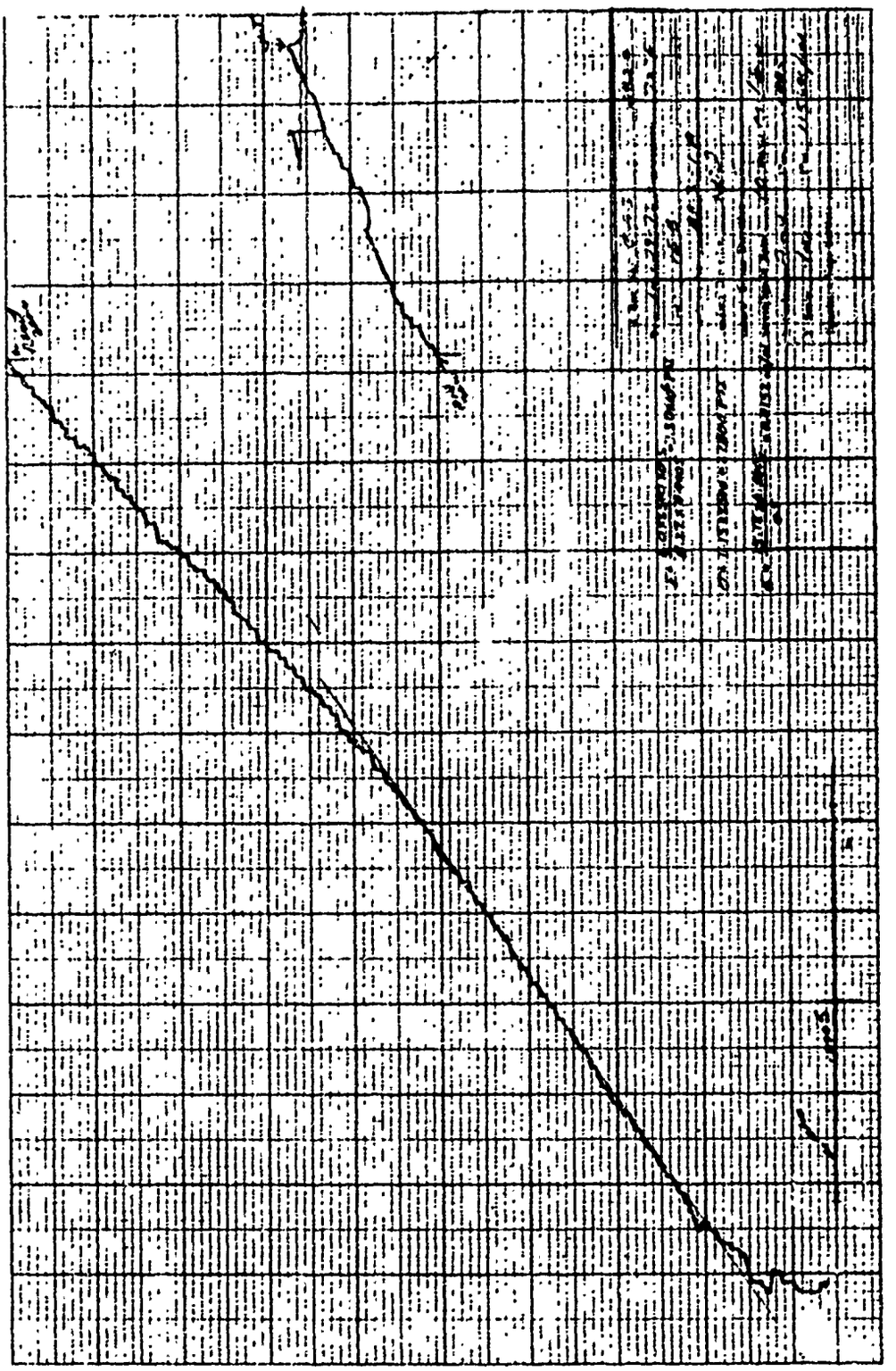

Sai Kun-Hor
12/27/72
ISE
AE-V-4C
D/R
0.1"/MIN
4.2 mV
0.001"
3.0 mV
.130"
3000 PSI
3.30 KG/CM²
= 3.48 KG/CM² PSI
90°

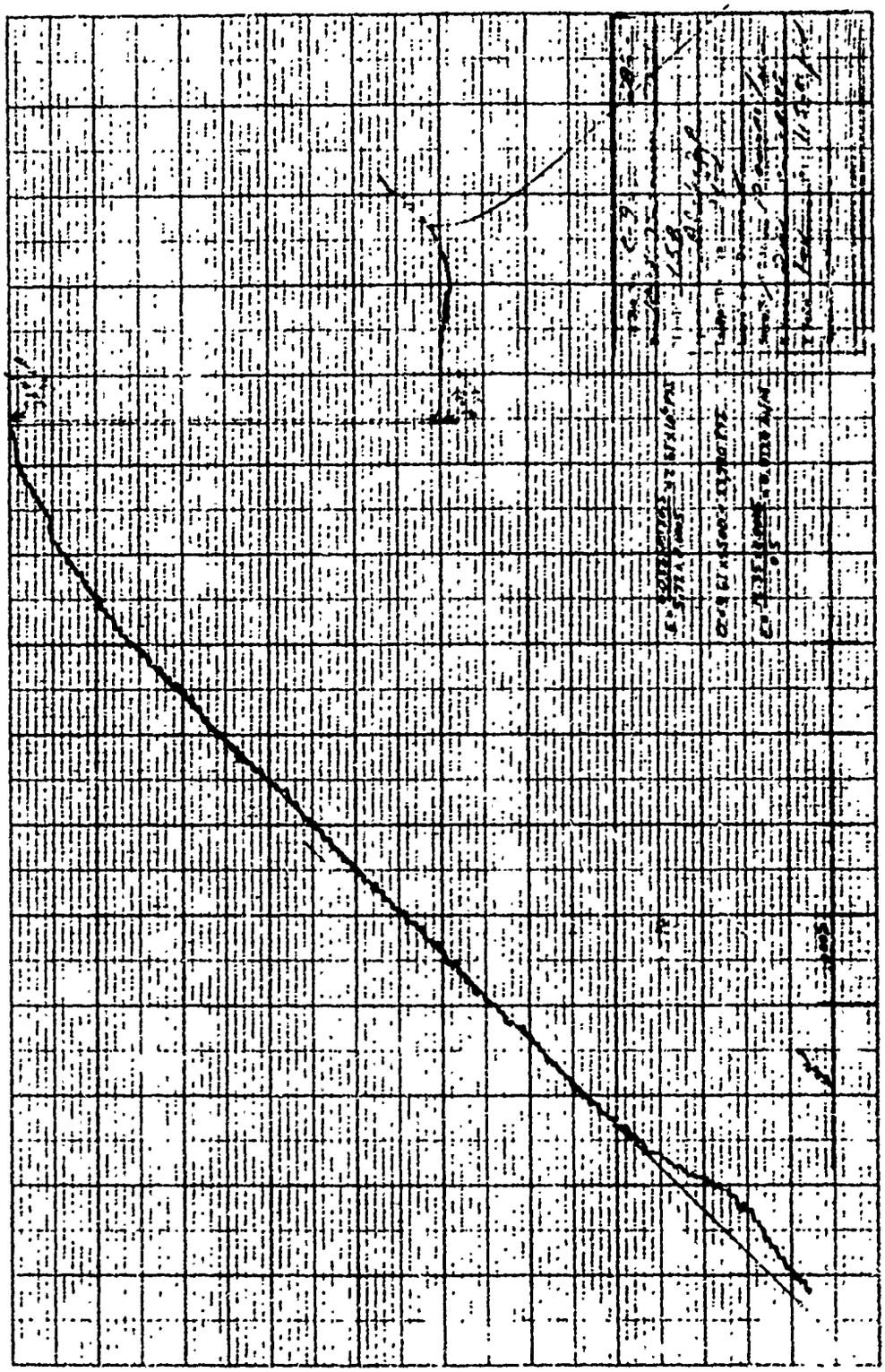

SN: F-54 (2926)
12/27/22
15°
AR-V-3C
C/R
0.1"/min
0.2mV
0.05"
20 mV
130"
933#

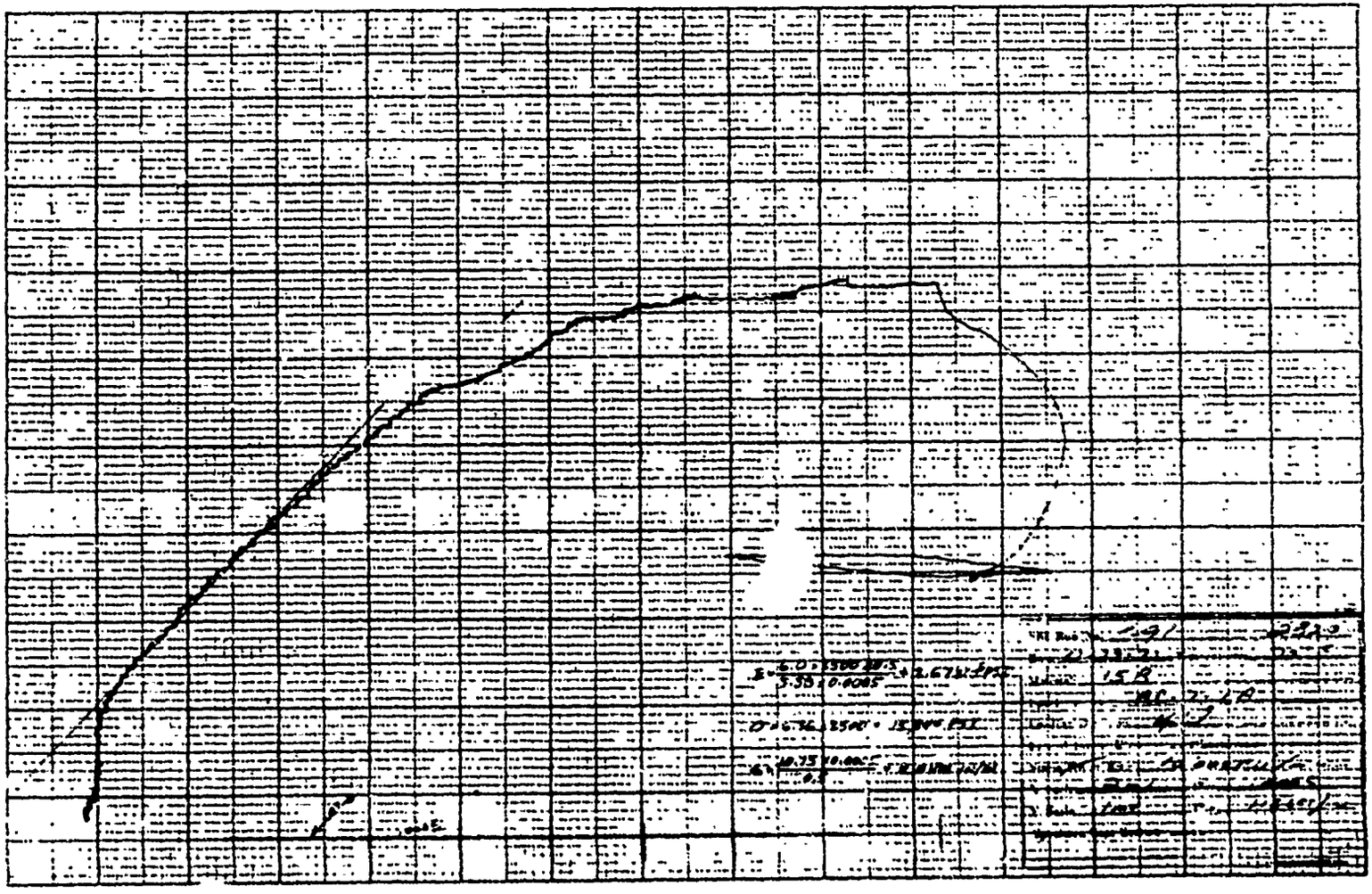


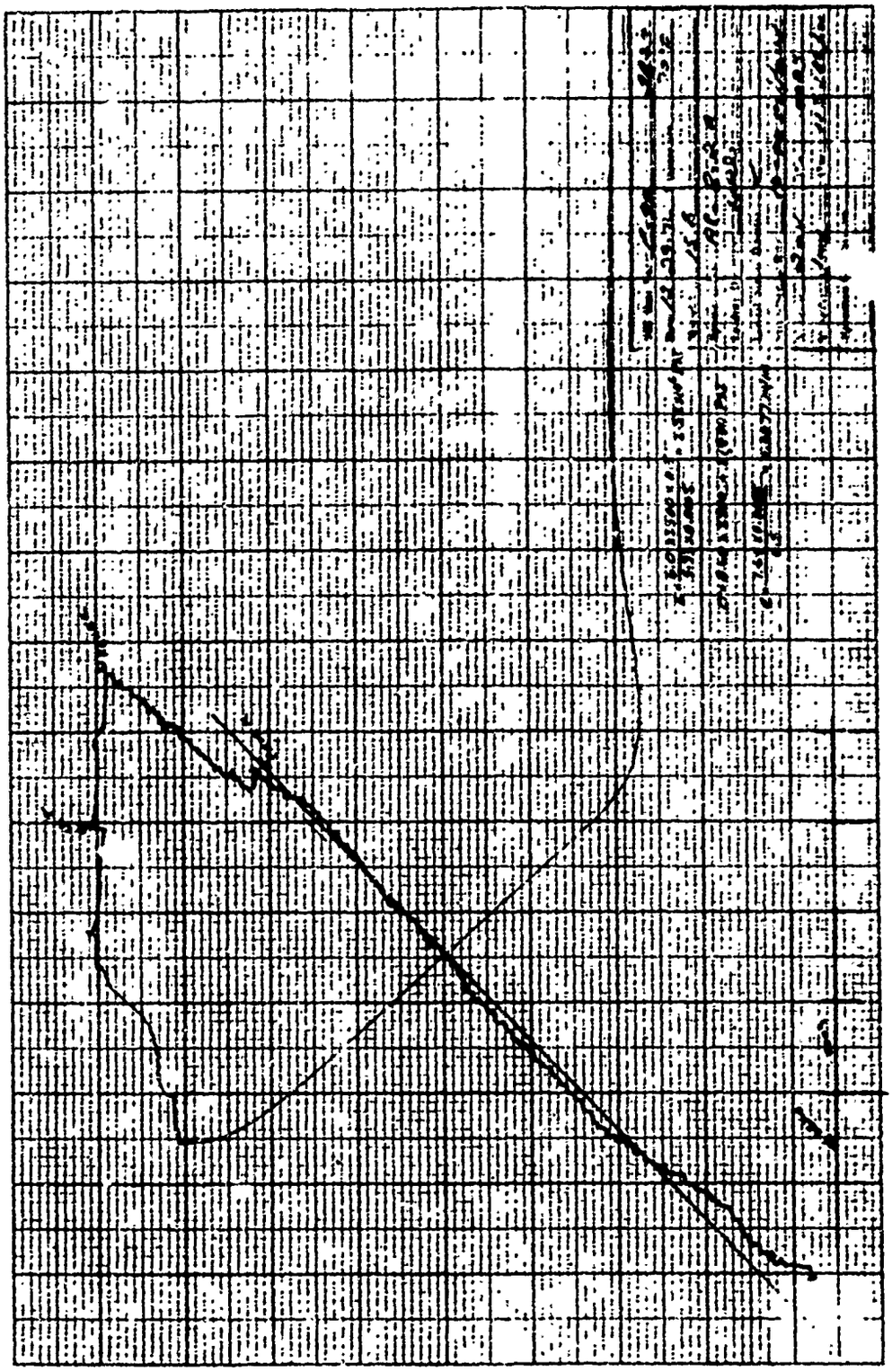


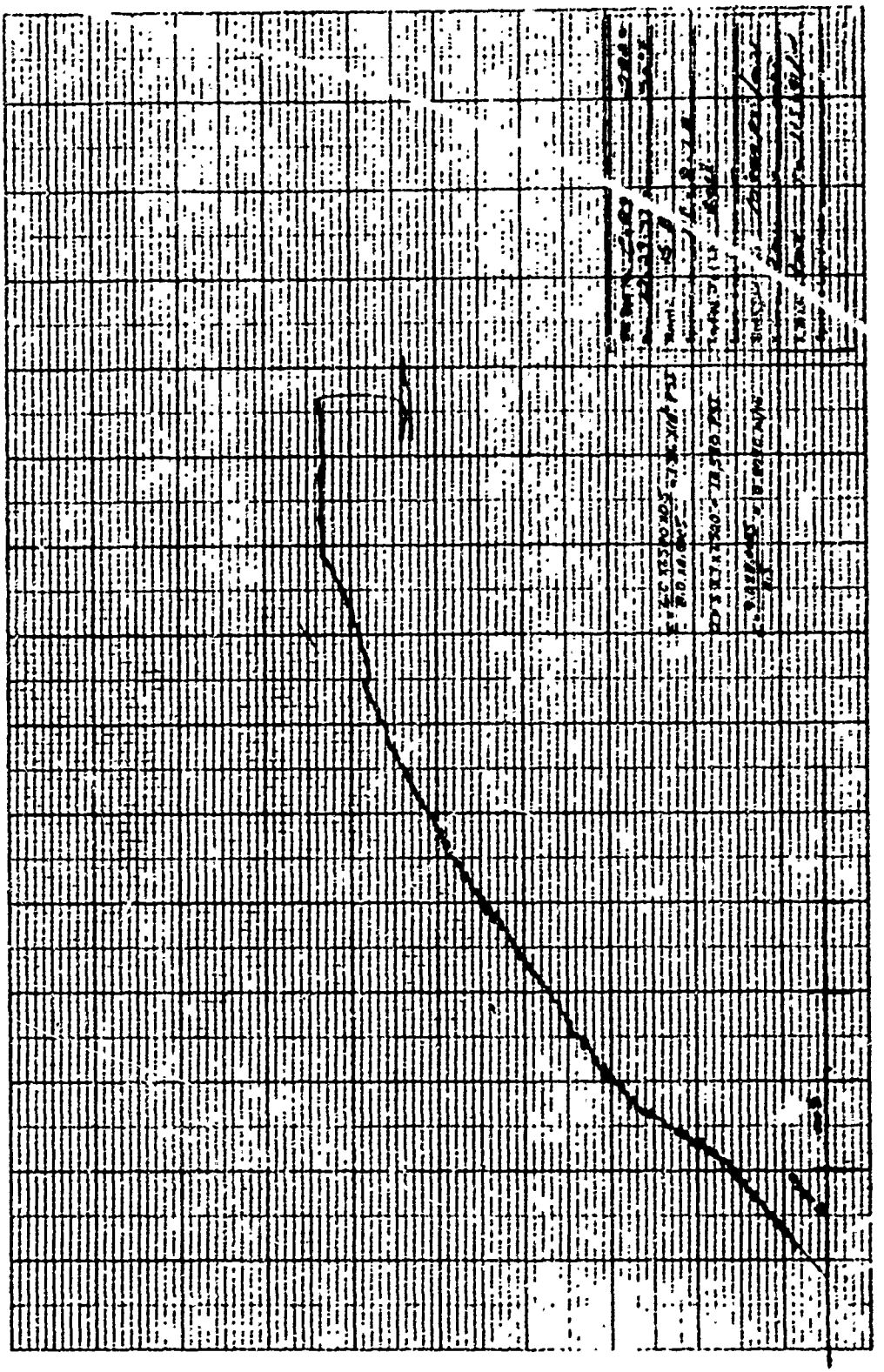

$E = \frac{6.0 \times 1500 \times 6.5}{5.19 \times 10^{-3} \times 0.75} = 1.88 \times 10^6$ psi
$T = 8.44 \times 2500 = 21100$ psi
$\varepsilon = \frac{8.32 \times 0.0015}{0.5} = 0.0083$ in/in

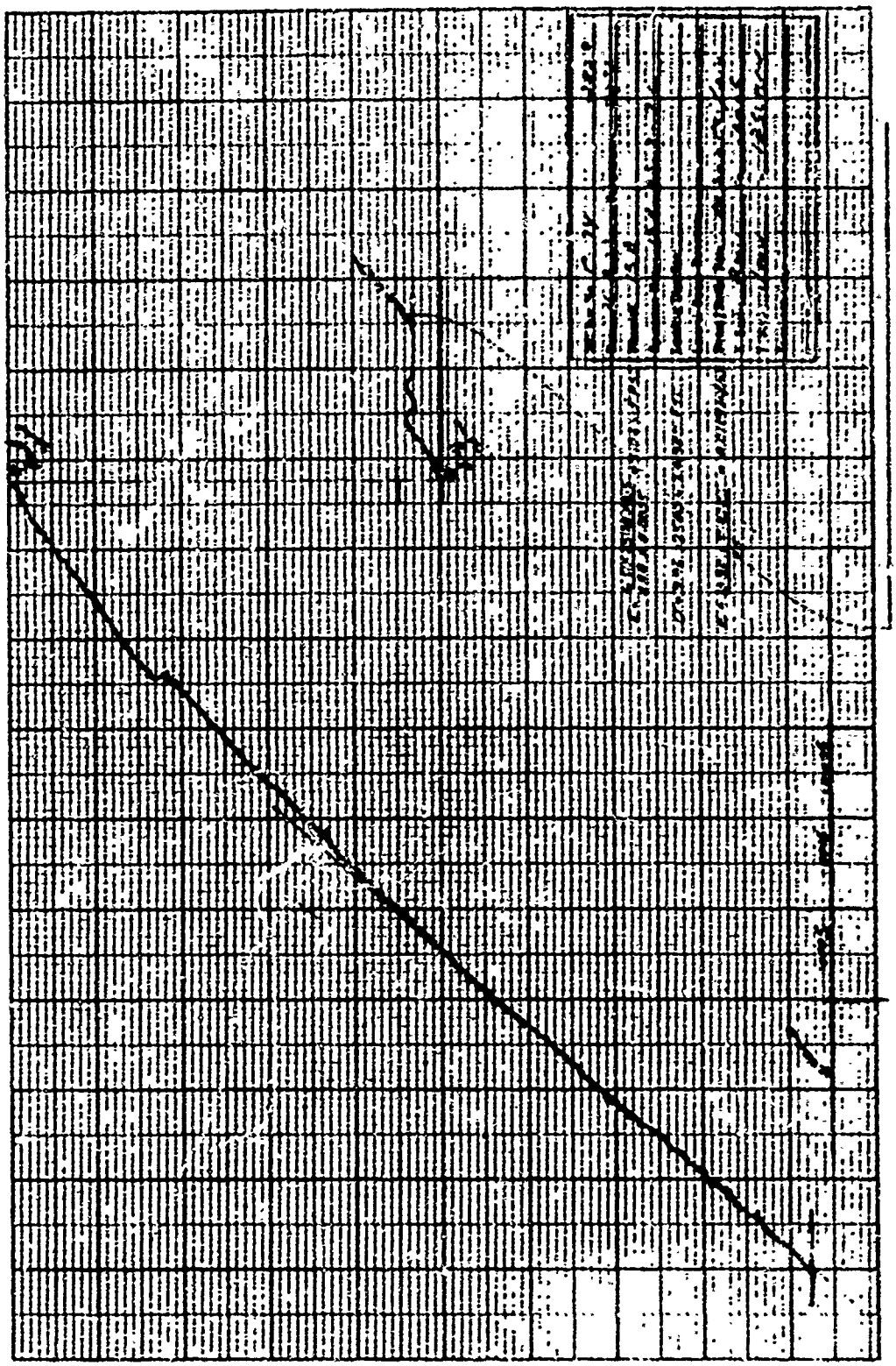


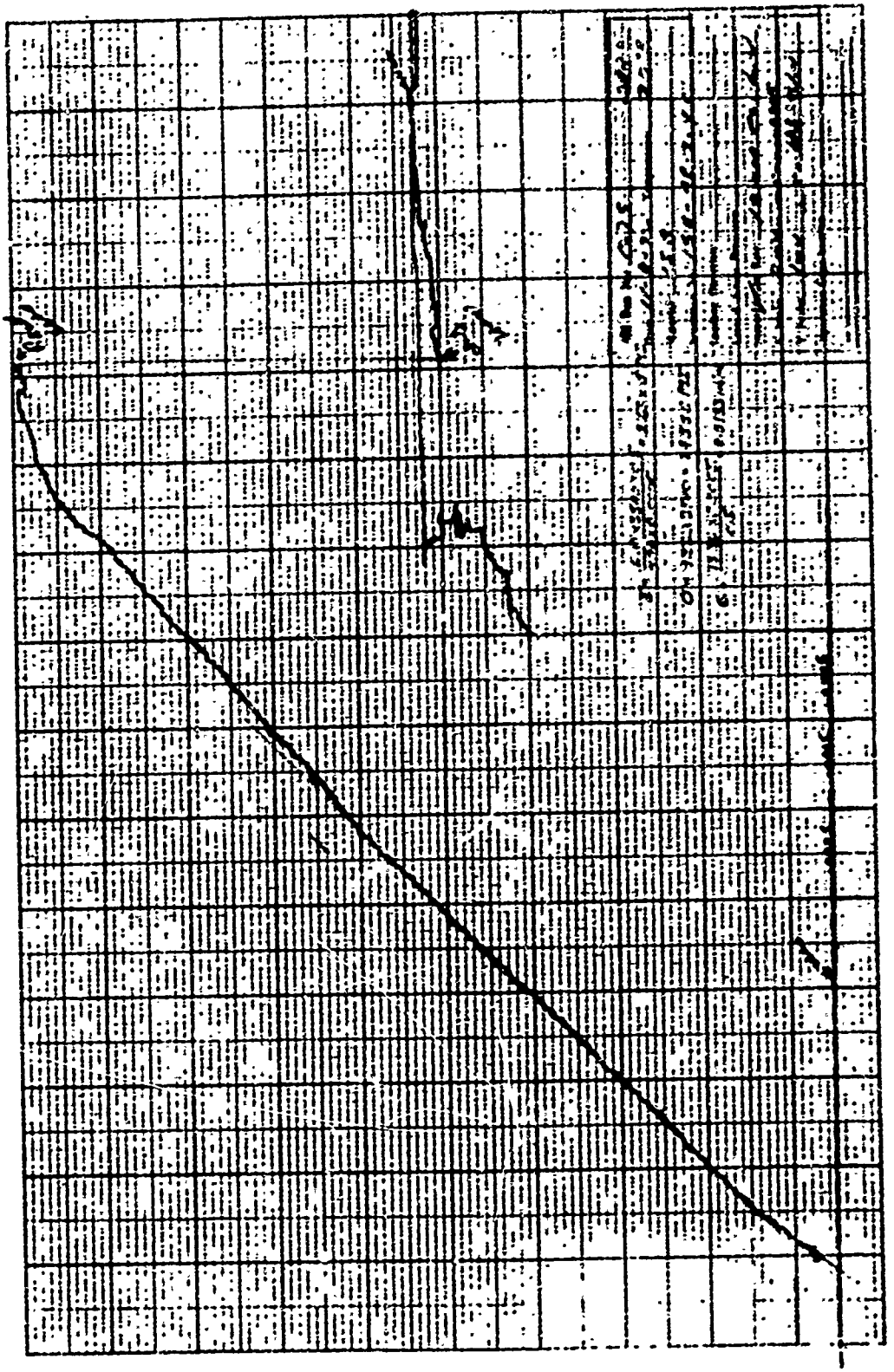


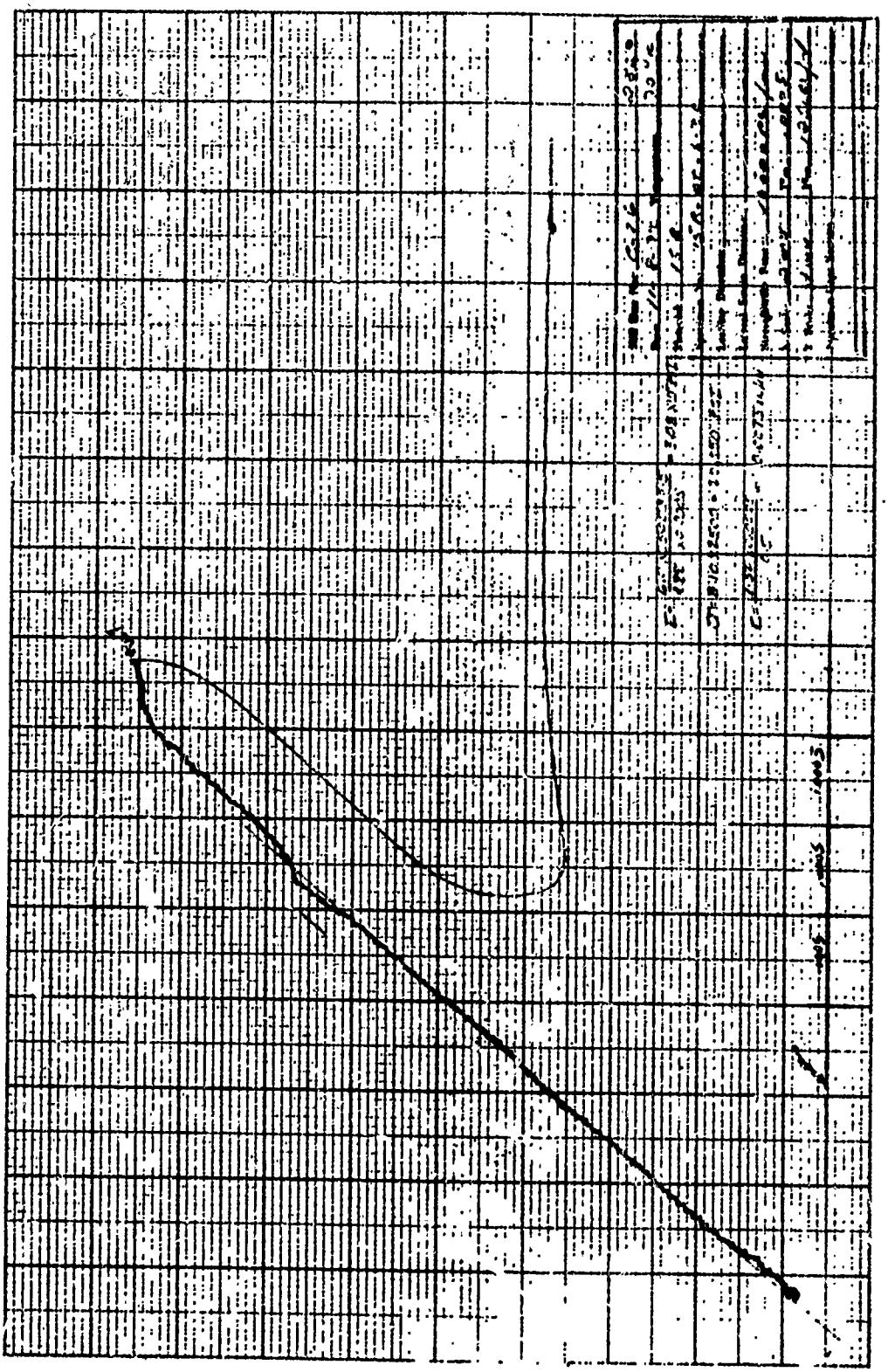


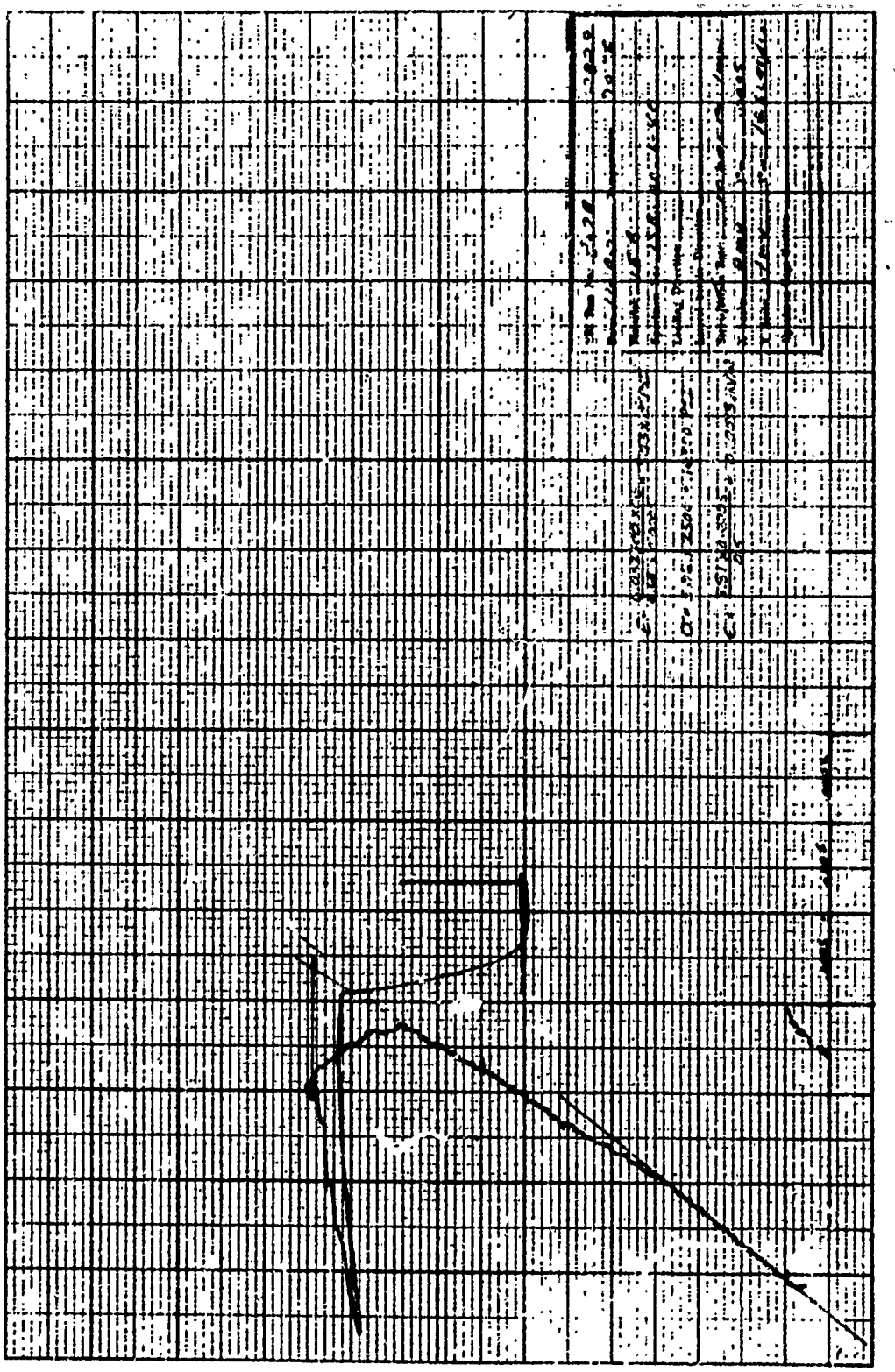




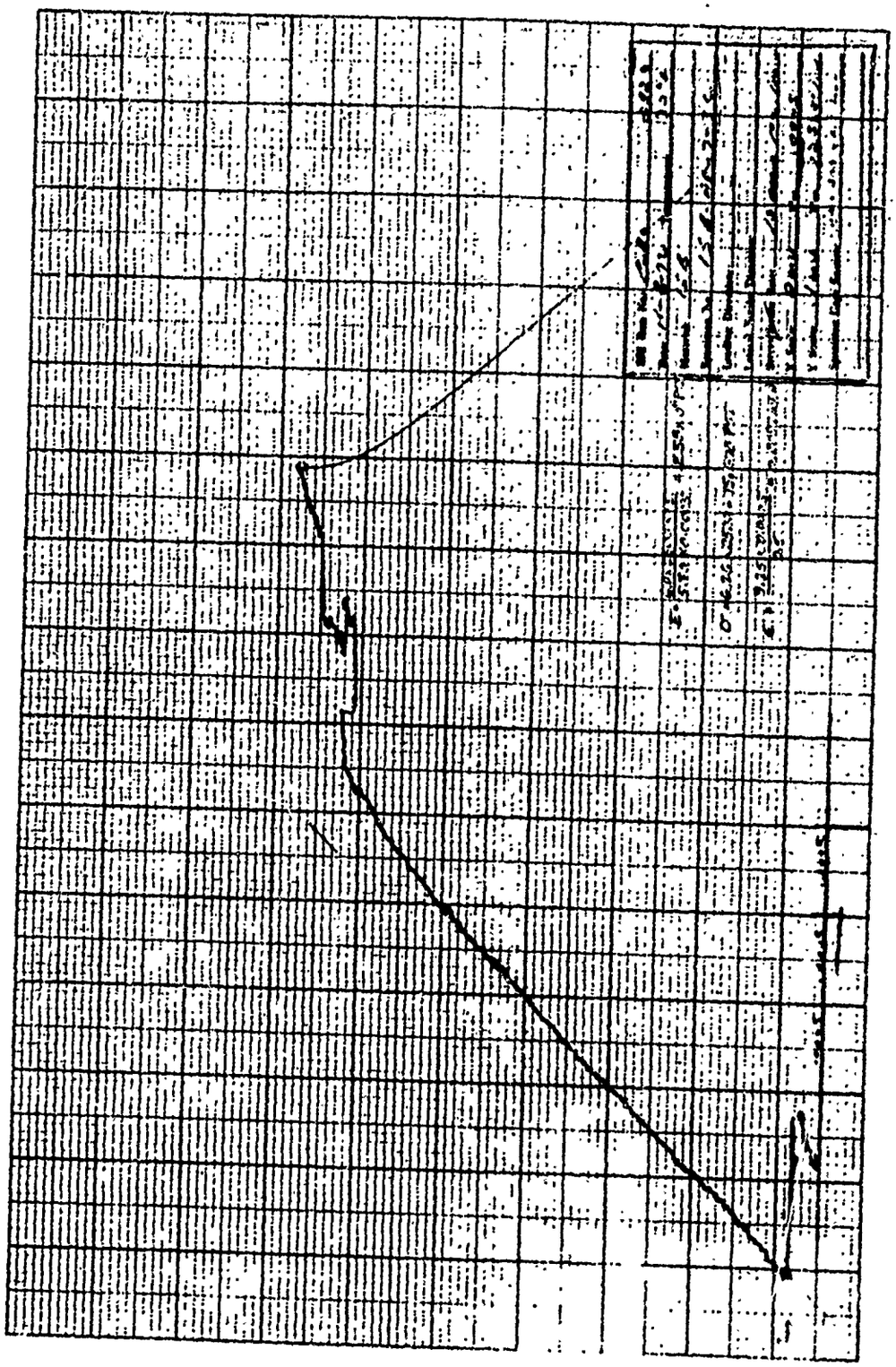


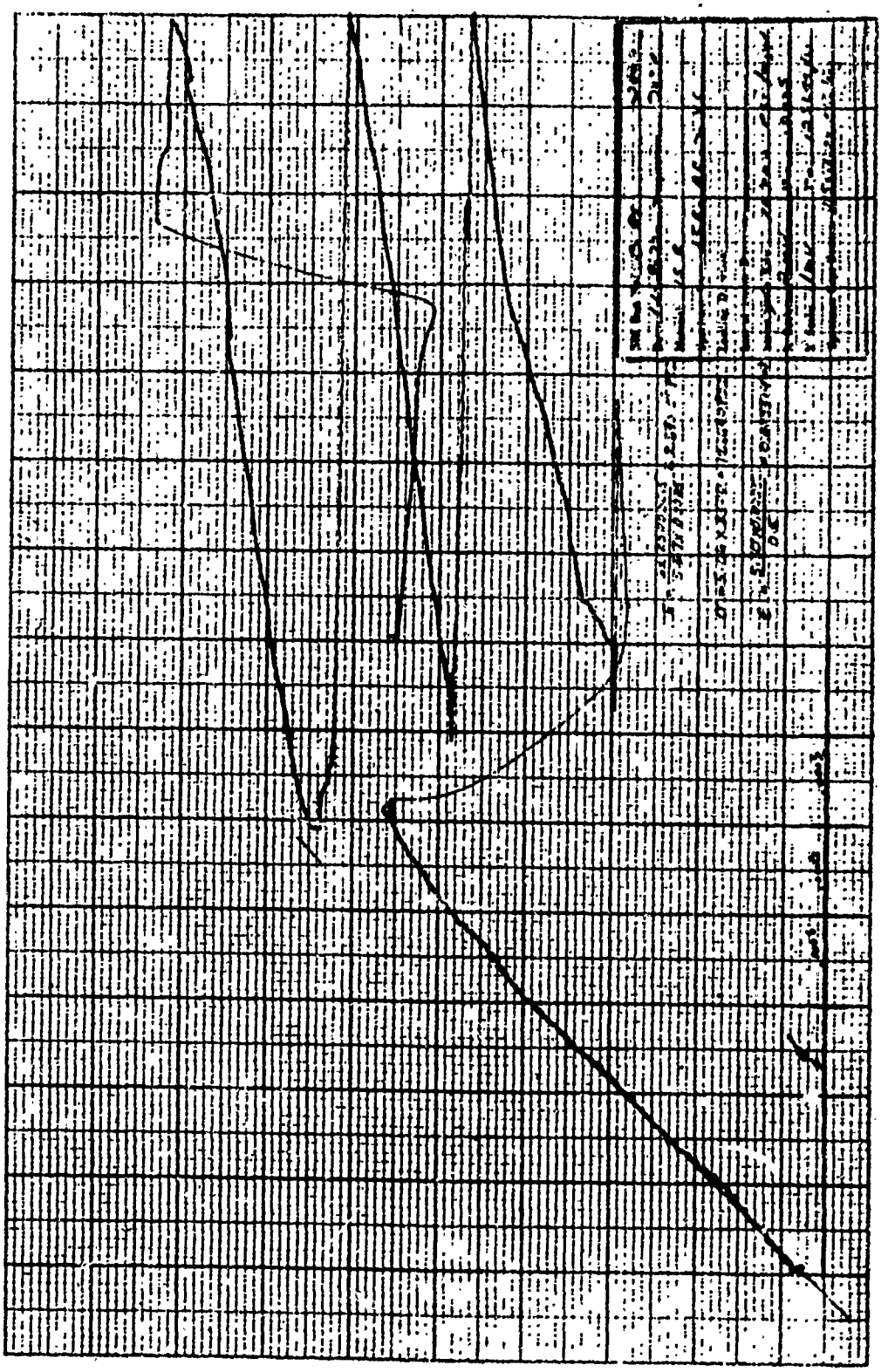


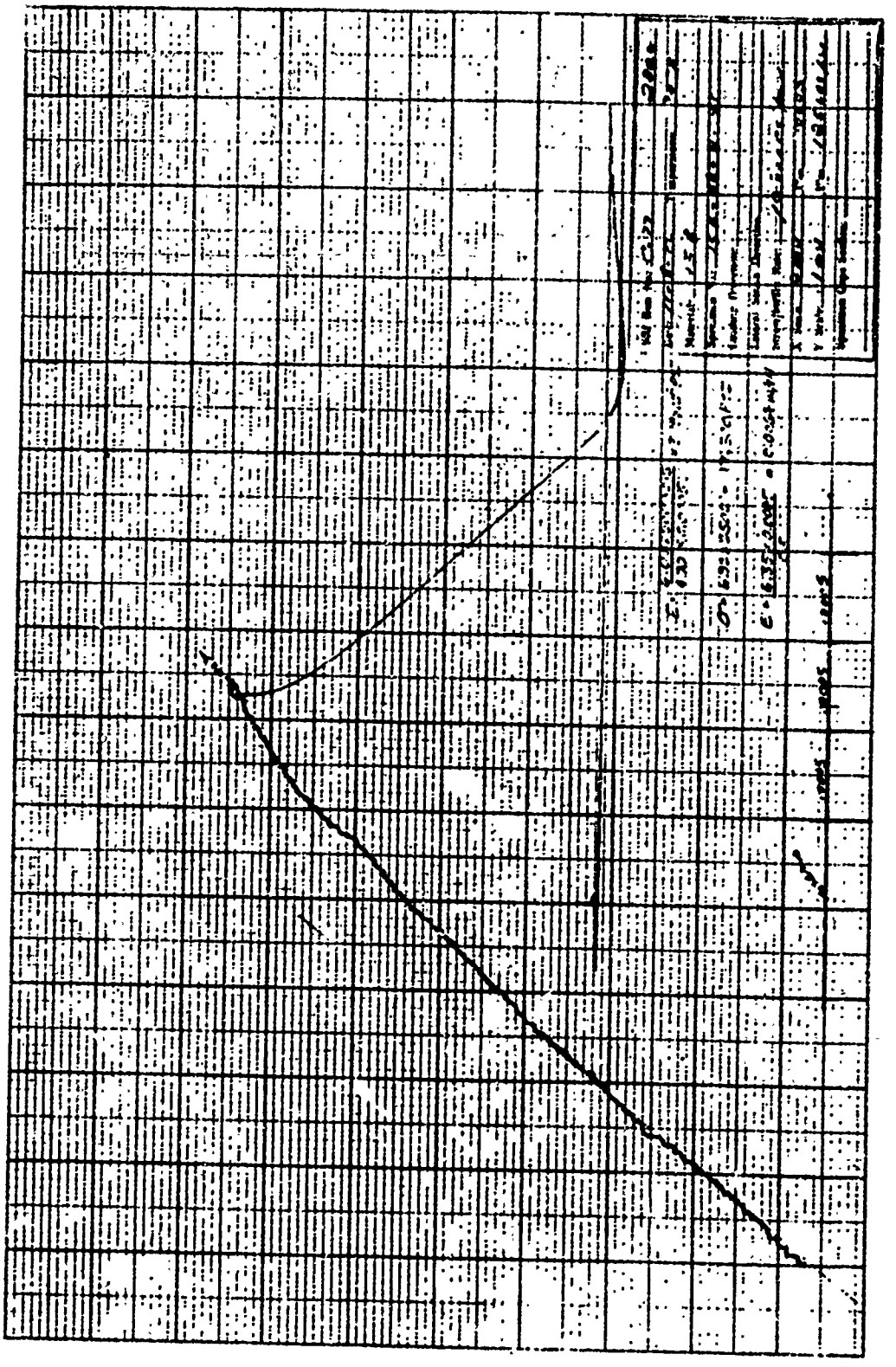


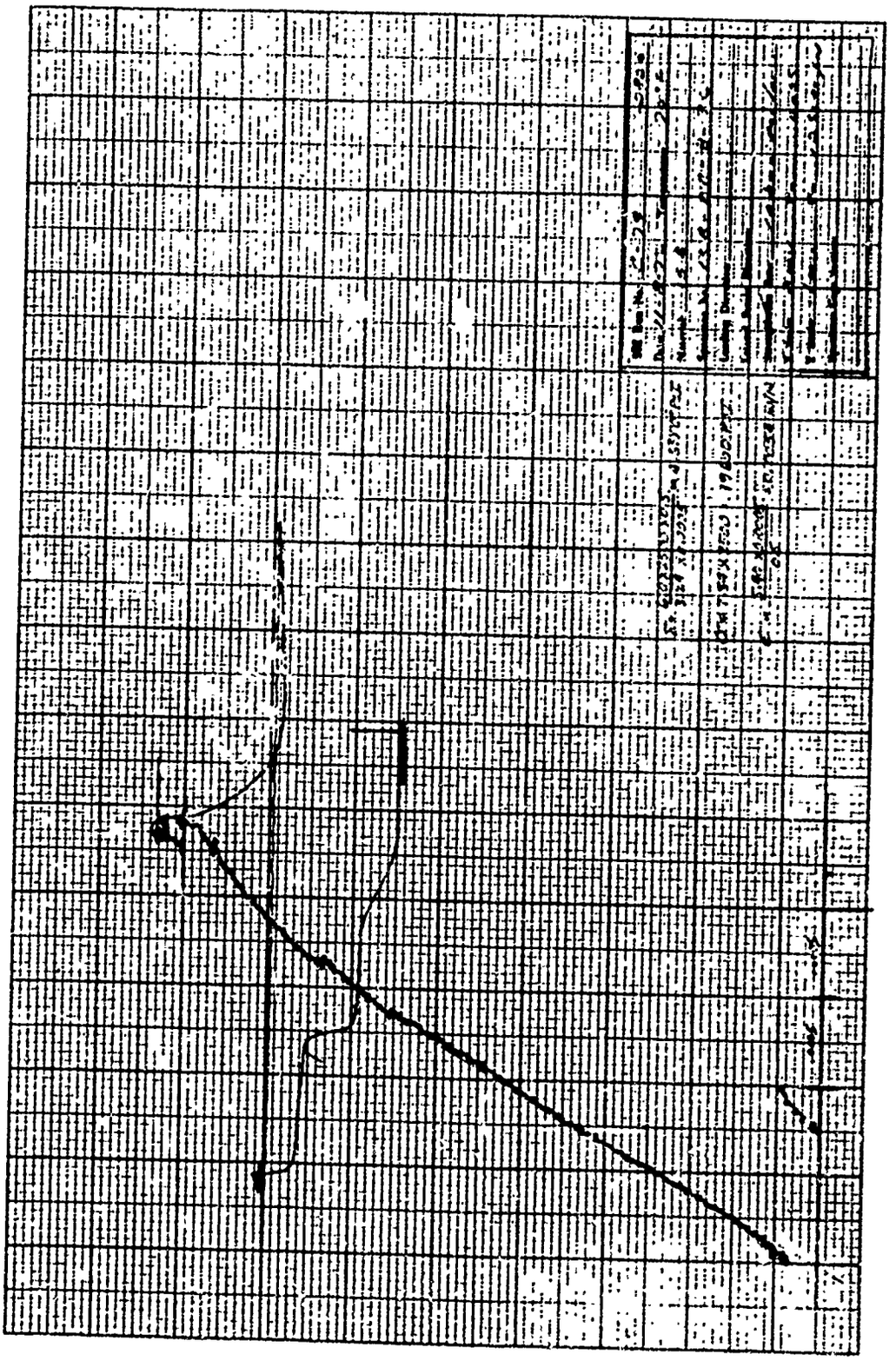


Reproduced from
best available copy.









APPENDIX M

ANOMALOUS STRUCTURE-CHANGE PROBLEM

MATERIAL #15

Material #15 (3DC/QP) was a two phase 3-D orthogonal Carbon-Quartz-Phenolic composite. The structural (inner) material was Quartz-Phenolic (3DQP), and the heat shield (outer) material was a Graphite-Phenolic (3DCP). The radials were carbon. A sketch describing the construction of the material is given in Figure M-1.

During the program, AHCA arcs of 3DC/QP and 3DCP were hit by Kaman to simulate encounter. These arcs demonstrated structure-change unlike the AHP arcs evaluated earlier. For AHCA 3DC/QP at higher levels, the inner material separated from the outer, and at lower levels, inner plies slipped off radials. At locations away from the separations little or no structure-change was detected. For AHCA 3DCP, back plies were removed with little damage occurring elsewhere. For AHP 3DC/QP arcs evaluated earlier, structure-change was volume oriented at the center of the outer material.

Photographs showing the AHCA mode of failure are given in Figures M-2 and M-3. A radiograph showing the AHP mode at different impulse levels is given in Figure M-4. Photomicrographs showing AHP Material #15 virgin and impacted (Arc 15-AR-3) and AHCA virgin and structure-change at radials are given in Figures M-5a and M-5b. A photomicrograph showing virgin AHCA Material #15 between radials is given in Figure M-6.

Because of the change in failure mode, a program was outlined to determine the source of the problem, whether geometry or material. The effort undertaken included NDT, mechanical, and thermal property characterization. NDT consisted of visual, bulk density, liquid penetrant, ultrasonic transmission, velocity, open porosity, radiographic, and light microscopy inspections. Mechanical and thermal property evaluations included flexural MOE, torsional shear, and thermal expansion. Apparatuses and test procedures used were similar to those presented in the body of this report.

The AHCA material was designed to be an improvement of AHP material by impregnation. The decrease in porosity was apparent in the AHCA material. Photomicrographs showing the two materials

are given in Figure M-7. A post cure cycle was later added to the process by AVCO in an attempt to gain back the AHP porosity. A photomicrograph showing the shrinkage effects on impregnant filled voids caused by post curing of AHCA material at Southern Research is also shown in Figure M-7.

The results of the study are given in Table M-1. Awareness of the problem first occurred when Arcs 3 and 4 from Ring 4 were hit by Kaman. Failure in Arc 3 was by rear delamination about 0.004 inch from the rear face below the impulse level where structure-change was expected, Figure M-3. The data presented in Table M-1 included results from NDT, mechanical, and thermal property evaluations on these two arcs (Columns 4 and 5), on AHP #15 virgin material (Column 1), calibration arcs from AHP #15 virgin and AHP #15 outer virgin materials (Columns 2 and 7), virgin AHCA material (Column 3), AHP Arc 15-AR-3 for comparative purposes (Column 6), and AHCA #15A (outer) material (Column 8). These data provided comparisons of the various test results on AHCA and AHP material #15 and AHCA and AHP material #15 outer for geometry and material variations.

Specimens used for geometry studies included two calibration specimens in Table M-1 (Columns 2 and 7) and 6 additional specimens injected into the program specifically for the geometry study. The two calibration specimens described in Table M-1 were from AHP material machined to the AHCA configuration (0.320/0.320 for Material #15). The six additional specimens were two #15A Arcs of AHCA material and the AHP geometry 0.660 inch thick; two Material #15A arcs of AHCA material in the AHP geometry with a ratio of outer to inner of 0.440 to 0.180; two Material #15 AHCA arcs of the AHCA geometry with an outer to inner ratio of 0.440 to 0.180. The results of the NDT evaluations on these additional specimens are given in Table M-2.

Some experimental Material #15 was also used in the program to investigate porosity effects induced by post curing and impregnation. The purpose of the experiment was to determine if porosity opened up with post cure. A ring was cut into three 120° segments, and from each segment, two Kaman arcs and a Southern Research tab were removed. The first tab end received no additional post cure or impregnation; the second tab end received low pressure impregnation plus post cure; the third tab end received high pressure impregnation of the AHCA type plus post cure. The results of NDT and radial tensile data are given in Table M-3. Some additional data included for comparative purposes

were the test results on AHP cylinder material, AHP nuclear response material, and AHCA material. As shown, porosity was influenced significantly by these process changes. The open porosity varied from 11.3 percent for virgin Tab #1 to 2.2 percent for Tab #4A, to 1.2 percent for Tab #5A. Bulk density for Tab #1 was 1.343, for Tab #4A was 1.448, and for Tab #5A was 1.460 gm/cm^3. The porosity variations were apparent visually. Photographs showing the three tab ends are given in Figures M-8 through M-10. Tab End #1 passed the nuclear response test but failed in the AHCA mode. Photomicrographs showing the material in the three tab ends are given in Figure M-11.

In addition, as mentioned earlier, specimens from AHCA Material #15 were heat treated to 500°F at Southern Research. The samples were heated using a nitrogen atmosphere to 500°F in four hours, soaked for 12 hours, and furnace-cooled back to 70°F in four hours. As shown in Figure M-7, shrinkage of impregnants occurred in voids which were filled by subsequent impregnations resulting in additional porosity at the original void interface. Results of open porosity and bulk density measurements by liquid absorption were as follows:

	Before H. T. at 500°F		After H. T. at 500°F	
Specimen	Bulk Density (gm/cm^3)	Open Porosity (%)	Bulk Density (gm/cm^3)	Open Porosity (%)
2	1.477	0.6	1.459	3.0
3	1.462	0.7	1.447	3.1

The major conclusions of this study were:

1. Porosity of AHCA #15 was lower than AHP #15;
2. Densities of AHP #15 inner and outer were higher than AHCA #15;
3. AHP #15 had higher density with higher porosity than AHCA #15 because AHP had higher fiber quantity;
4. Bleeding by AHP #15 outer (cylinder) at 140°F was probably caused from an epoxy cosmetic applied to cylinder for appearance.

5. Decoupling in AHP #15 resulted from higher porosity and lateral dissipation of energy;

6. Coupling in AHCA #15 resulted from lower porosity with increased energy transfer to backface;

7. Post curing of AHCA #15 resulted in shrinkage of impregnants in voids that had been filled by subsequent impregnations;

8. The problem with AHCA #15 was material.

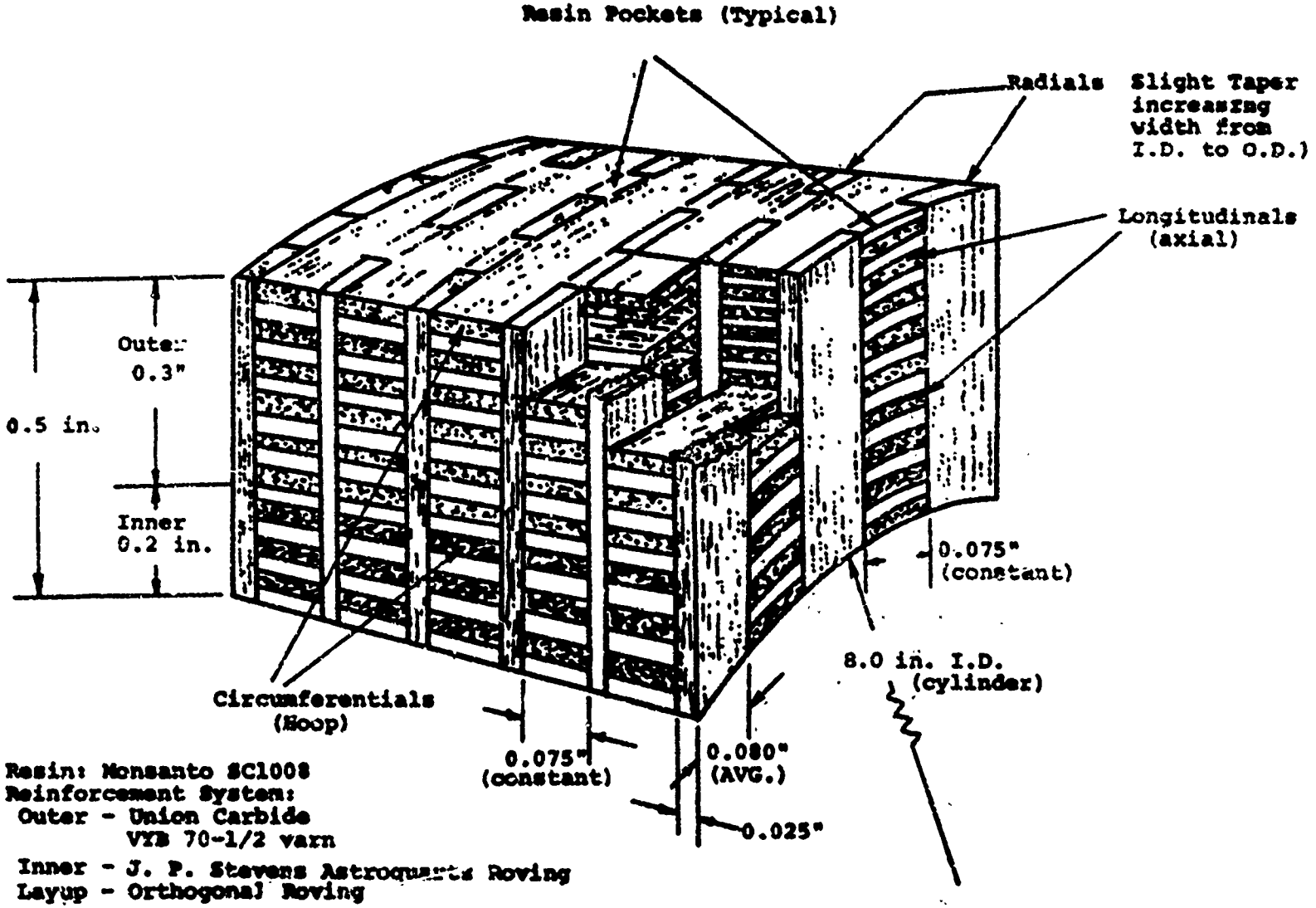
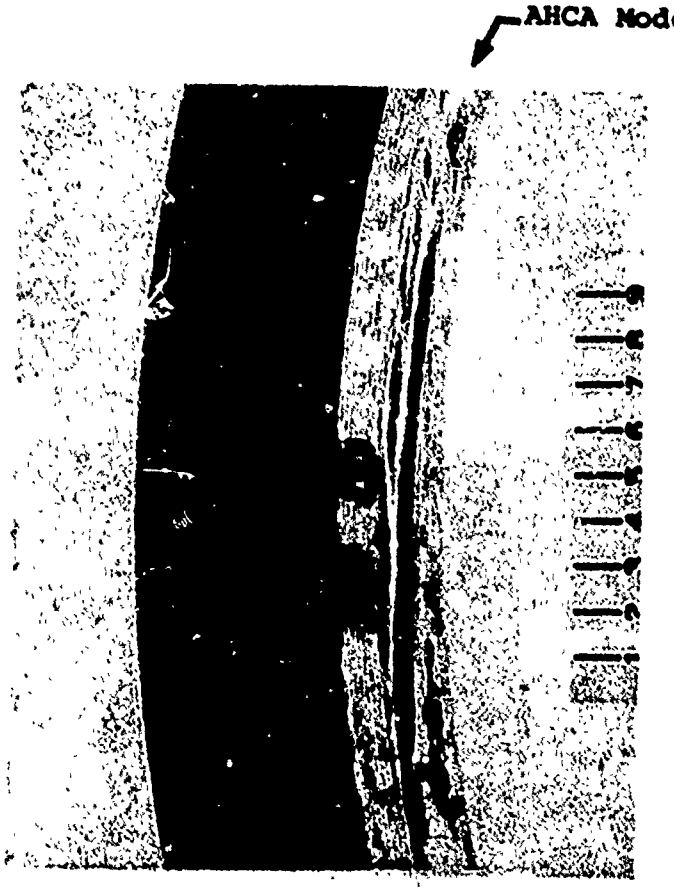


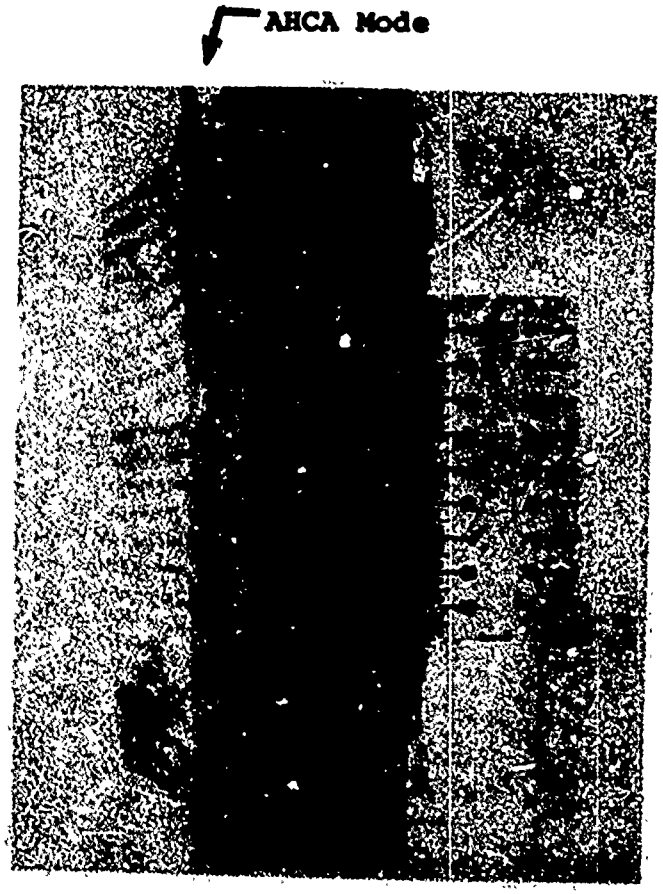
Figure M-1. AVCO Two Phase 3-D Orthogonal Quartz-Phenolic - Material #15



Figure M-2. Photograph Showing Damage to AHCA Material #15 with Increased Impulse Levels



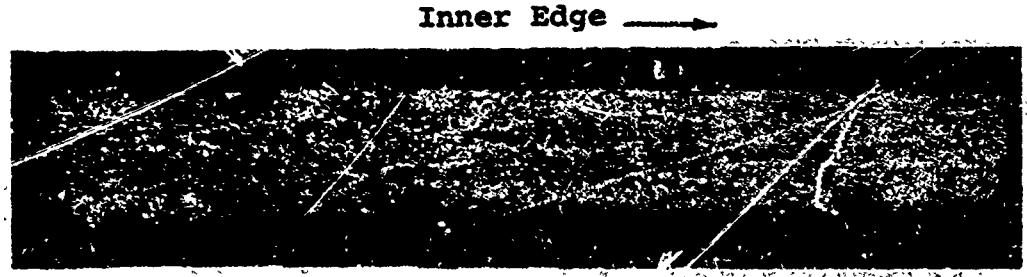
Bottom Edge
(Scale Shown)



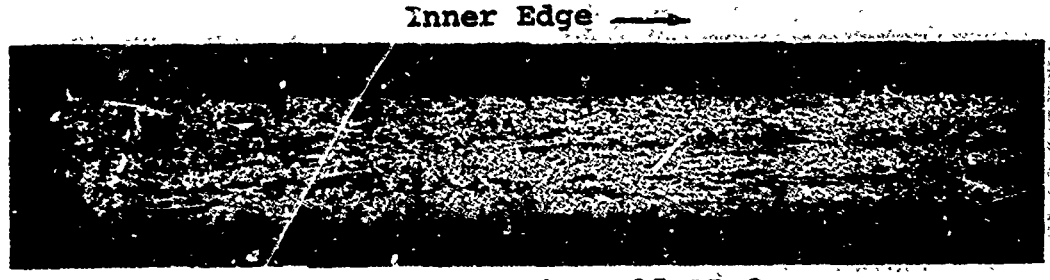
Left Edge
(Scale Shown)

Figure M-3. Photographs Showing Rear Delam in AHCA Material #15 Ring #4 Arc 3

Figure M-4. Radiograph Showing AHP Mode for Material #15

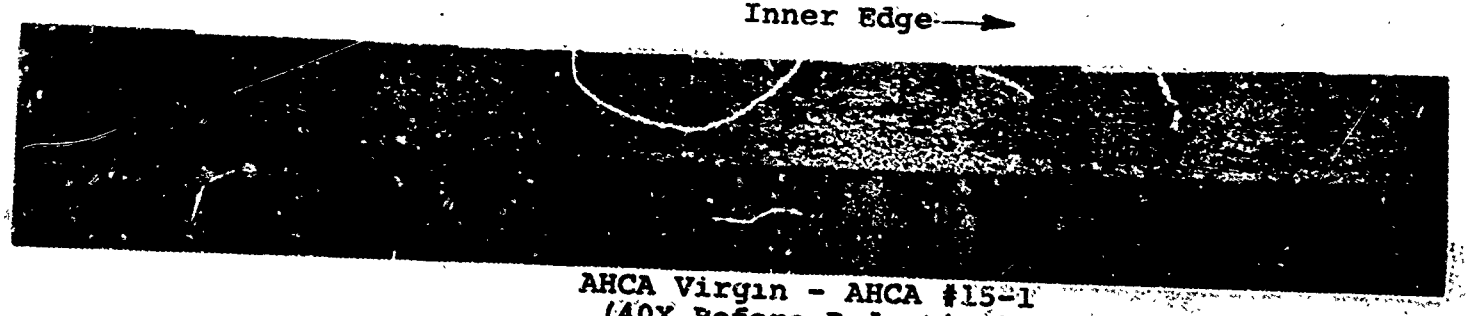


AHP Virgin - Specimen 15-AR-V
(40X Before Reduction)

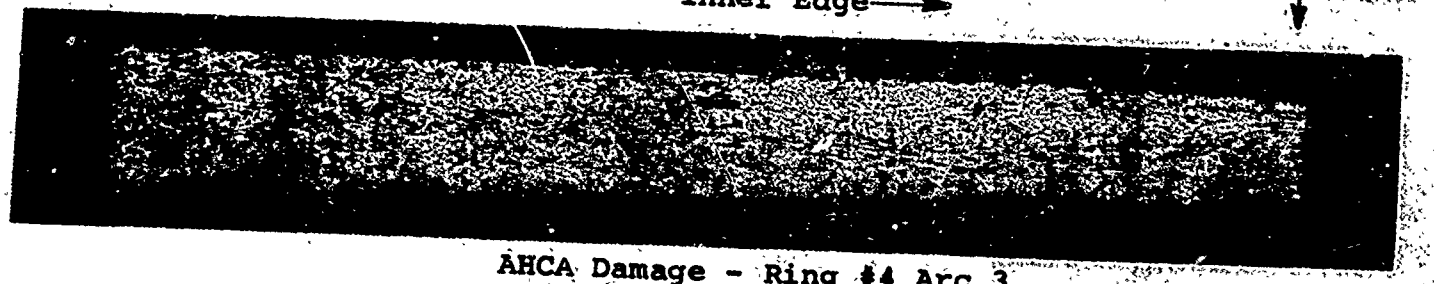


AHP Damage - Specimen 15-AR-3
(40X Before Reduction)

Figure M-5a. Photomicrographs Showing AHP and AHCA Material #15

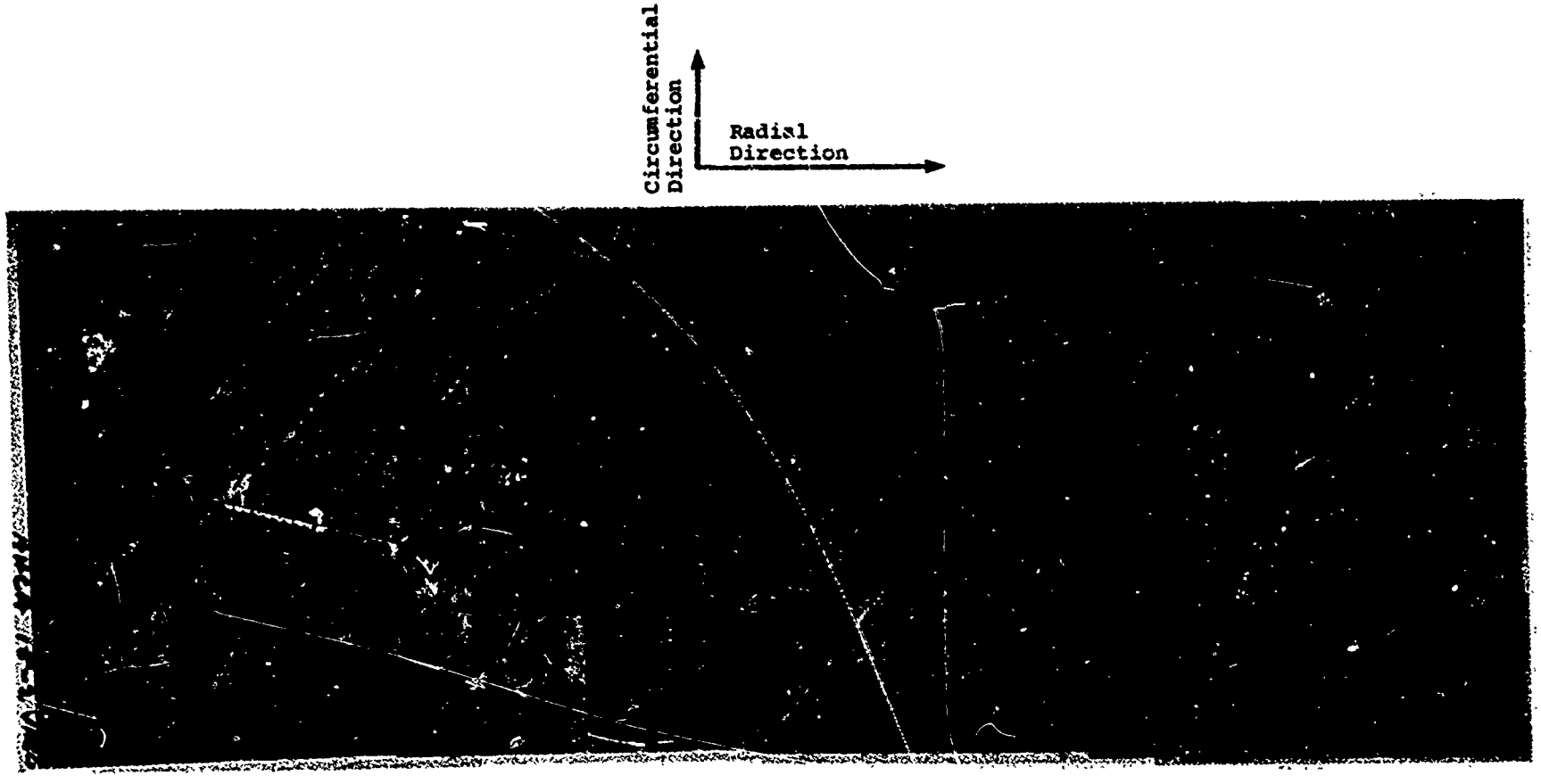


AHCA Virgin - AHCA #15-1
(40X Before Reduction)



AHCA Damage - Ring #4 Arc 3
(40X Before Reduction)

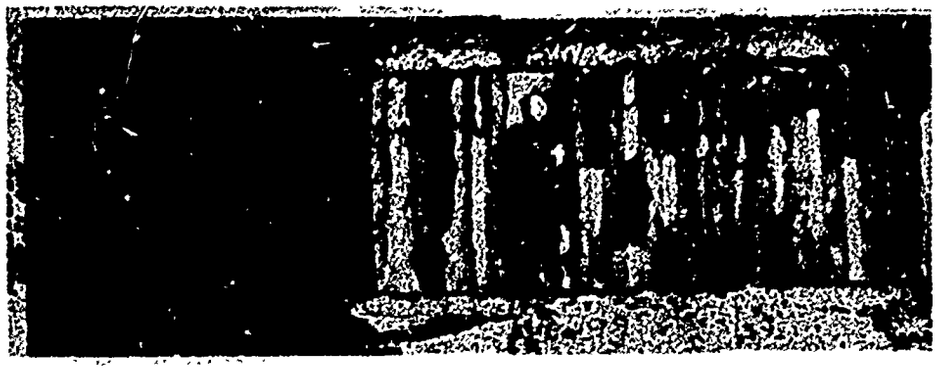
Figure M-5b.



(40X AHCA 15-2 Before Reduction)

Figure M-6. Photomicrograph Showing Virgin AHCA Material #15 Between Radials

Figure M-7. Photomicrographs Showing Virgin AHP, and AHCA Cured Material #15



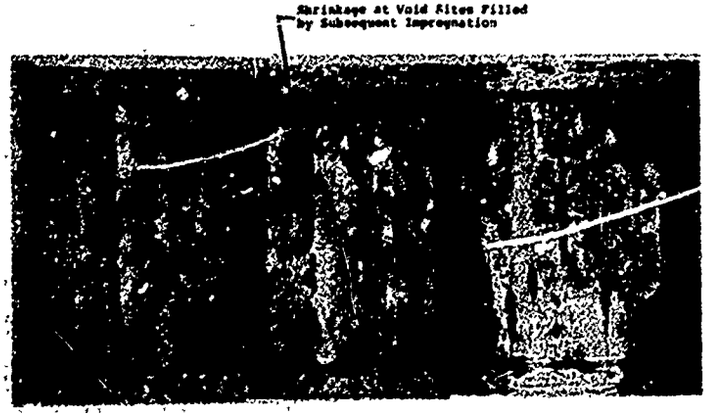
AHP Near Virgin

(15-AR-3)

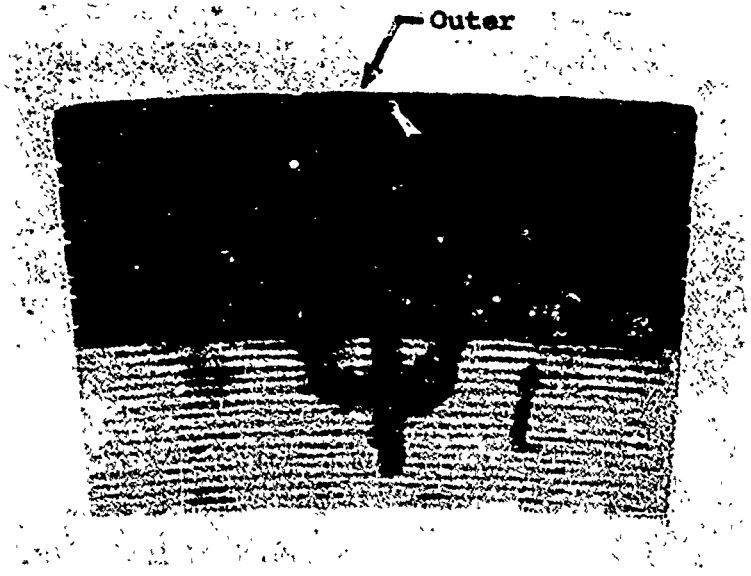
(10X before Reduction)



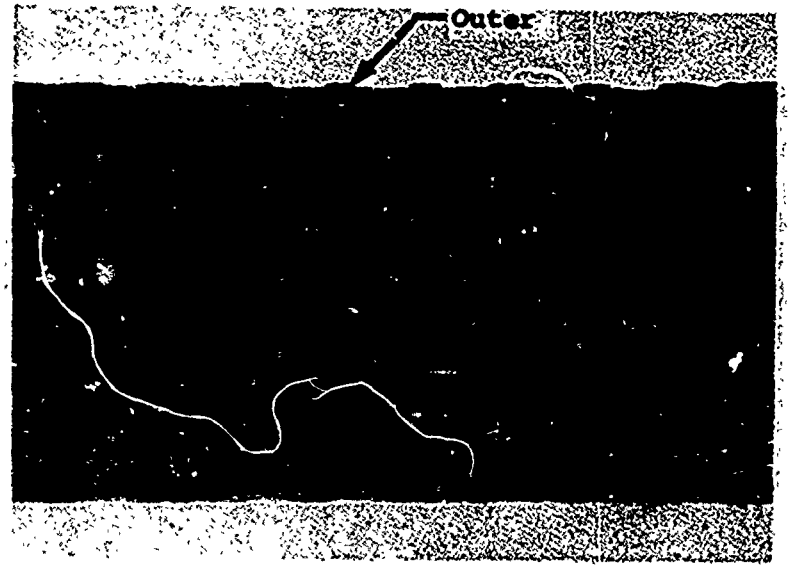
AHCA



AHCA Cured:- Heated to 500°F in 4 Hours, Soaked at 500°F for 12 Hours, and Furnace Cooled to 70°F in 4 Hours. N₂ Atmosphere

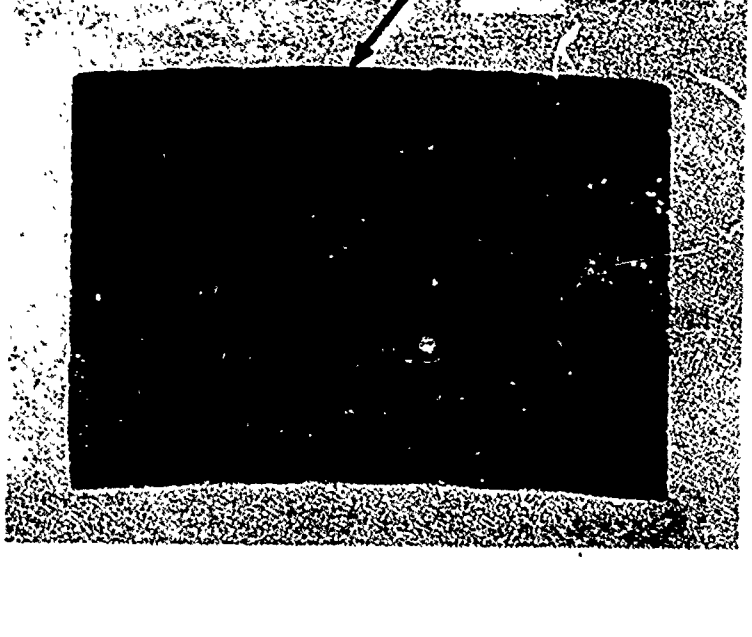


Axial View at 5X

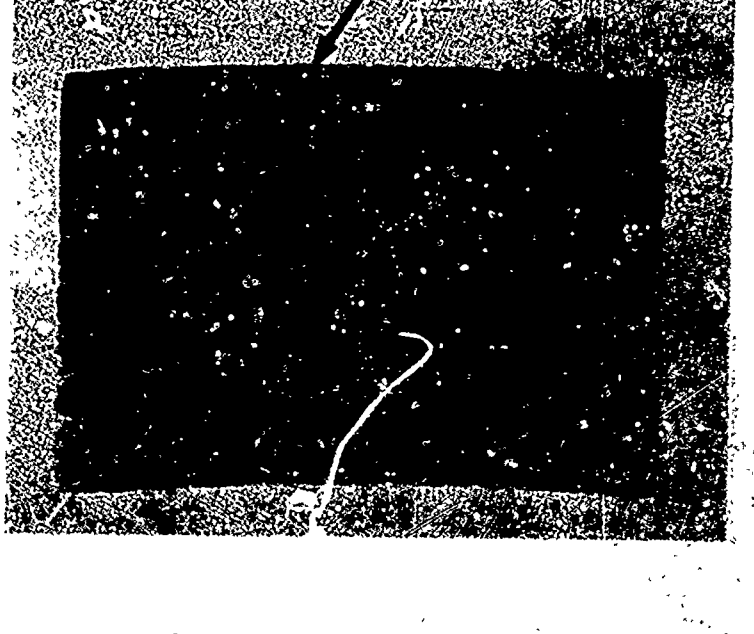


Circumferential View at 5X

Figure M-8. Photographs of Tab End #1 of Material #15

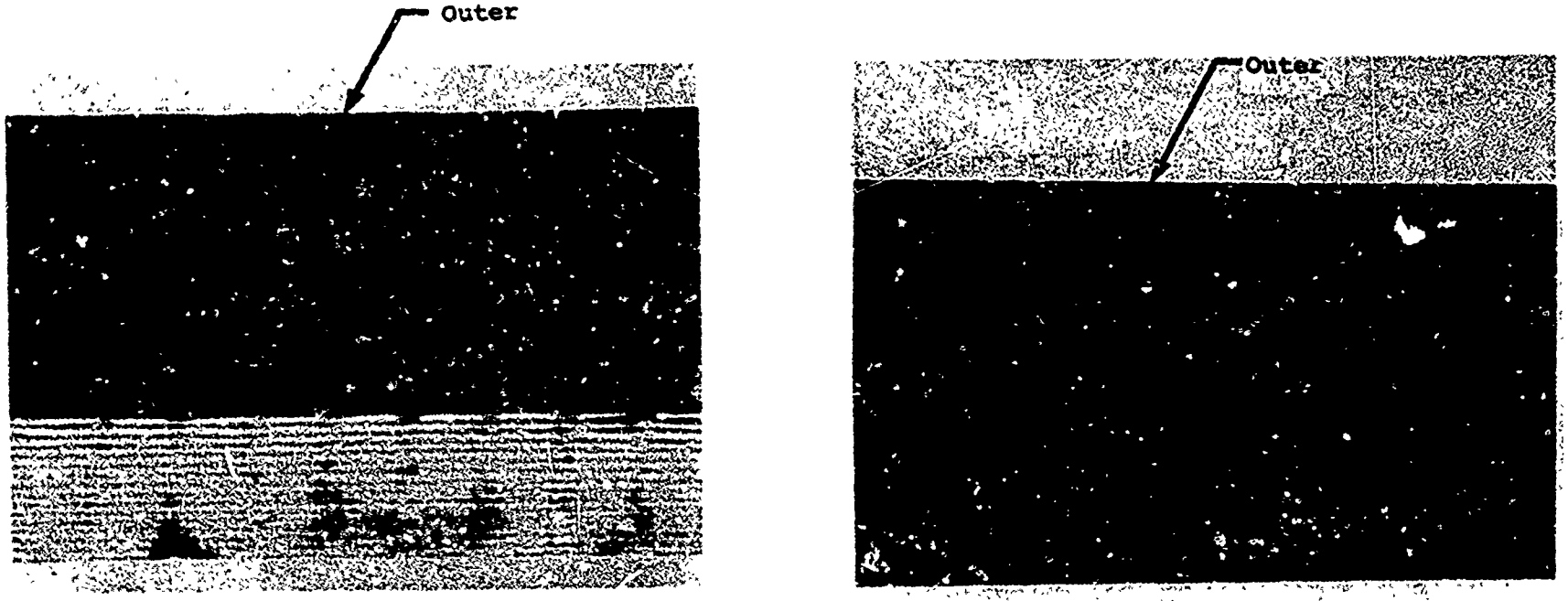


Axial View Bottom Edge at 5X



Axial View Top Edge at 5X

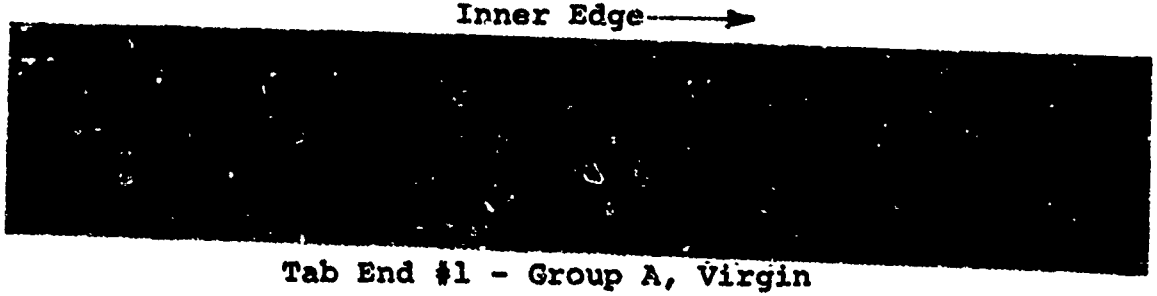
Figure M-9. Photographs of Tab End #4A of Material #15



Axial Views at 5X

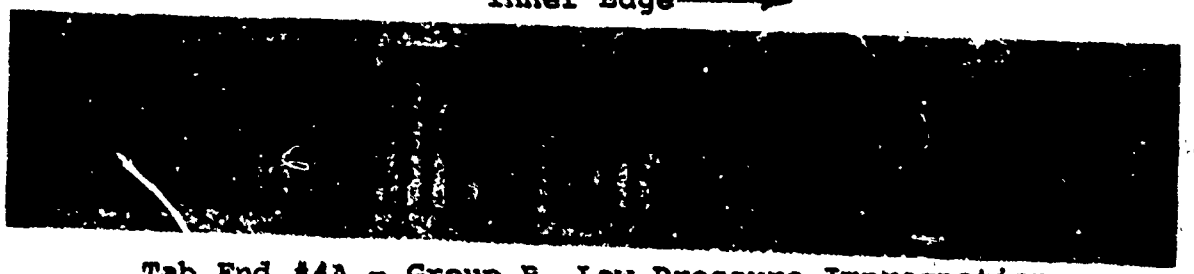
Figure M-10. Photographs of Tab End of #5A of Material #15

Inner Edge——→



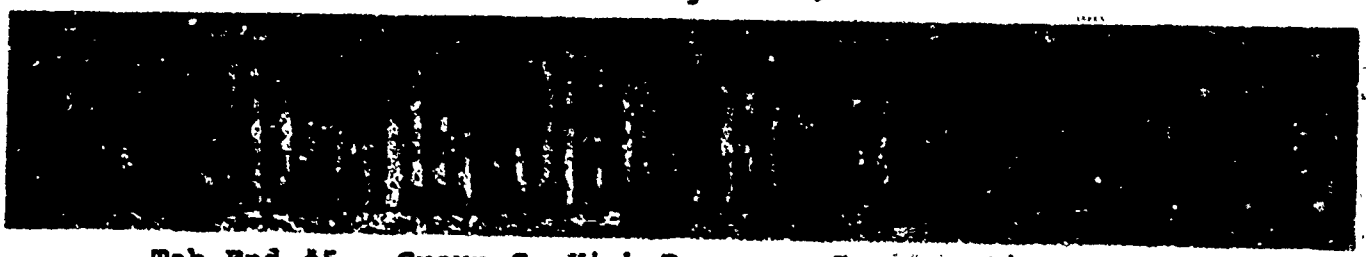
Tab End #1 - Group A, Virgin

Inner Edge——→



Tab End #4A - Group B, Low Pressure Impregnation

Inner Edge——→



Tab End #5 - Group C, High Pressure Impregnation
(40X Before Reduction)

Figure 4-11. Photomicrographs Showing Material #15 in Tab #1, #4A and #5A

Reproduced from best available copy.

TABLE D-1

COMPARISON OF ADRS 010 AND 010 OUTER ADRS

Characteristic	ADP 010[1] Substrate Fiberglass	ADP 010 Outer Substrate Fiberglass	ADRS 010[2] Substrate Fiberglass	ADRS 010[3] Phase 2 Spar 2	ADRS 010 Phase 2 Spar 3	ADP 010 Phase 2 Spar 4	ADP 010 Phase Spar Fiberglass	ADRS 010A Fiberglass
1. Top Layer	0	0	0	———	———	———	0	0
2. Thickness	0.050" 00356/0.1000	0.050"(0.356/0.1000	0.360" (0.000/0.130)	0.050"(0 [illegible])[3]	0.031" (0.000"+)[3]	0.000"	0.300"	0.300"
3. Width	1.50"	2.00"	2.00"	2.00"	2.00"	2.00"	2.00"	2.00"
4. Bulk density	1.71 g/cm³	1.000 g/cm³	1.000 g/cm³	1.579 g/cm³(1.679 g/cm³)[3]	1.00 g/cm³ (1.677 g/cm³)[3]	1.000 g/cm³	1.600 g/cm³	1.000 g/cm³
5. Radial sonic velocity	0.1570 in./usec	0.1001 in./usec	0.1000 in./usec	0.1000 in./usec	[illegible]	0.1070 in./usec	0.1000 in./usec	0.1700 in./usec
6. Axial sonic velocity	0.3000 in./ usec (1.50 in length)	0.3005 in./usec (2.99 in. length)	0.300 in./usec (1.50 in. length)	0.3720 in./usec (0.50"length)	0.3027 in./usec (0.50" length)		0.3000 in./usec (0.50" length)	0.3020 in./usec (0.50" length)
7. Radial sonic transmission	Not comparable because of thickness	-44 db	-31 db 300)	-30 db (450)	-2 db (600)	——— (450)	-44 db	-30 db
8. RMS acoustic emission	(1.10-2.77 x 10⁶ psi) not comparable because of operation geometry differences		3.00 - 4.34 x 10⁶psi	3.00-3.31 x 10⁶ psi		1.00-1.07 x 10⁶ psi	0.01-0.46 x 10⁶ psi	3.10-5.30 x 10⁶ psi (specimen warped)
9. Torsional shear strength	5630 - 6400 (bond line)		3000-5000 psi (bond line) 6000-67000 (center)				5630-6000 psi	3000-6700 psi
10. Thermal Exp. a) 0 - 300°F b) 0 - 300°F	0.30 x 10⁻⁶in./in. (axial) 0.20 x 10⁻⁶in./in. (radial)		0.30 x 10⁻⁶in./in. (axial) 0.40 x 10⁻⁶in./in. (radial)				0.35 x 10⁻⁶in./in. 0.20 x 10⁻⁶in./in.	0.33 x 10⁻⁶in./in. 0.40 x 10⁻⁶in./in.
11. Cure temp.	300°F	300°F	300°F	300°F	300°F	300°F	300°F	300°F
12. Serviceability temp.	300°F (center)		-350°F (center)				300°F	370°F
13. Visual inspection	Higher surface residual porosity & very narrow, random appearing pore regions beyond thin outer surfaces		Lower surface residual porosity & structural orientation/consistency fiber bundles	No apparent change in bond & outer thickness. In other, some localized areas of inconsistent spacing between outer adherends. In other, no apparent change.	Fig 6-6a, 6.04" deep inner circular-shaped "void" concentration. Visual scanning in outer zone(s) being covered about ADP 010 by 10-20 % depth, some 3-5% of higher density	Small chips, varying in number & surface roughness, mostly removed on lower surface exposing growth surface.	Higher surface residual porosity and very narrow, random fiber bundles	Lower surface residual porosity & structural orientation/consistency fiber bundles
14. Radiography inspection	Higher residual porosity and very orientation		Lower residual porosity, structural circumferential			Axial radiograph - normal	Higher residual porosity very circumferentially & lower optical density in center/axial layup)	Lower residual porosity circumferential & higher optical density in circum/axial layup
15. Remarks	Optimize outer 3000 at 250°F, save outer 050 and bleed				Accumulate a 1000 measurements obtained by displacement and attenuation measurements and of these weak prior correlations			
16. Shear Strength.	3.0 to 3.5% for Epoxies	3.0%	-3.0%			-0.0%		

[1] Example Values

TABLE M-2

NDT RESULTS ON AMCA MATERIAL #15 AND #15A
ARCS IN AMP AND AMCA GEOMETRY

Material	Geometry	Specimen	Density (gm/cm³)	Velocity (in./μsec)		Radial Transmission (Added db)	Remarks
				Radial	Axial		
15A	AMP-0.62 Thick	1	1.408	0.1855	0.3703	33	1. Specimens 15-1 through 15-4 were 0.64 inch thick rather than 0.62 inch thick.
		2	1.407	0.1940	0.3733	34.5	
15	AMCA-0.440/0.180	15-1	1.494	0.1824	0.3722	46	2. No anomalies by visual and Partek penetrant inspections.
		15-2	1.494	0.1846	0.3781	45.5	
15	AMP-0.440/0.180	15-3	1.494	0.1839	0.3701	46	3. Circumferential low-density (material) striations at 0.12, 0.25, and 0.35 inch from inner edge in Specimen 15A-2 by radiography.
		15-4	1.495	0.1842	0.3771	44.5	

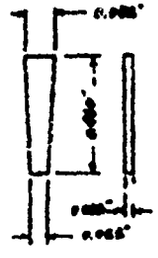
TABLE N-3.

NDE AND MECHANICAL RESULTS ON AVCO HEMISPHERICAL 15 TAB ENDS

Specimen Number	Description	Bulk Density gm/cm³	Thickness inch	Axial Velocity in./μsec	Radial Velocity in./μ sec	Radial Transmission Added db	Open Porosity %	Radial Tensile Data: Ultimate Radial Tensile Load, lb	Radial Tensile Data: Shear Length	Radial Tensile Data: Failure Plane Location	Remarks
Tab 91	Group A (Virgin)	1.363	0.509	0.3642 (1.5")[a]	0.1768 (0.5")[a]	16(3/8" aperture)	11.3	128 136	0.16 0.14	CF bond line (CF & OF) (CF & OF)	1. Visual porosity variations apparent on surfaces of tab ends
Tab 84A	Group B, Low Press. Imp.	1.448	0.509	0.3648 (1.5")[a]	0.1774	14(3/8" aperture)	2.2	247 238	0.12 0.10	OF	2. No anomalies by radiograph in tab ends
Tab 85A	Group C, High Pressure Impregnated	1.468	0.600	0.2995 (1.6")[a]	0.1705	22(3/8" aperture)	1.2	275 229	0.10 0.15	OF OF	
15AR-V	AMP/Mech-Thermal	1.447	0.469	0.300 (1.5")[a]	0.1805[a] (0.45")[a]	27(3/8" aperture) 40(1-1/2" aperture)	-----	---	---	---	3. Spec 15-AR-V Used for attenuation correlation with tab ends
MDT-1	AMP/Mech-Thermal	-----	-----	------	------	----------	0.5	---	---	---	
MDT-8	AMP/Mech-Thermal	-----	-----	------	------	----------	0.5	---	---	---	4. Open porosity for MDT-8 measured with tab ends for correlation
15-BB-10	AMP/Nuclear Response	1.469		0.300 (1.5")[a]	0.1578 (0.45")[a]	----------	5.2 3.4	268 286[c]	0.10 0.10	OF OF	
AMCA-15		1.480		0.300 (2.26")[a]	0.1682 (0.55")[a]	~37 db (1-1/2" aperture)	1.1 1.0	250 265 274	0.14 0.10 0.10	OF OF OF	

Notes:

a. Numbers in parenthesis are specimen lengths
b. Measurements for Ramen ends using 1-1/2" aperture with 41db added for virgin measurements
c. Centerline of specimen was between radials instead of aligned with a radial as in the other specimens



Sheet